

Welcoming Address

Dear Colleague,

It is a pleasure to welcome you in Salt Lake City for the third edition of The International Conference on Image Formation in X-ray Computed Tomography, also known as “The CT meeting”.

The idea for this meeting came about six years ago, following a wish from many to have a venue where CT scientists could meet together to discuss in depth all aspects that impact the image formation process in CT. These aspects include dose evaluation and dose reduction strategies, non-linearity effects and compensation schemes for these effects, image reconstruction algorithms, spectral decomposition, dynamic effects, geometrical calibration, phase-contrast physics, and image quality assessment.

Pleasantly, the meeting this year attracted a few more submissions than in 2012. However, in an effort to further increase the quality of the presentations, which is already very high, and to also increase the merit of receiving a classical poster presentation, the bottom 5% of submissions was rejected. Whereas 57 presentations were given at the first meeting, in 2010, and 104 at the second meeting, in 2012, 105 presentations will be given this year, including a special session on homeland security applications. The breadth of the topics being covered is amazing. I am grateful to all authors for submitting their work. As in 2010 and 2012, oral presentations have been allocated significant time to allow for in-depth discussion between the attendees. Also, comfortable poster sessions have been planned, and attractive locations have been selected to promote discussion during the meals.

The meeting could not be a success without a great scientific committee. I would like to take the opportunity here to once again thank the following scientists, for their support, as well as for their help with the evaluation of submitted abstracts, which was critical in shaping the scientific program:

Yoram Bresler	University of Illinois at Urbana-Champaign; InstaRecon, Inc.; IL, USA
Guang-Hong Chen	University of Wisconsin-Madison, WI, USA
Carl Crawford	Csuptwo, LLC, WI, USA
Michel Defrise	Vrije Universiteit of Brussels, Belgium
Bruno De Man	GE Global Research Center, NY, USA
Rebecca Fahrig	Stanford University, Stanford, CA, USA
Jeff Fessler	University of Michigan, MI, USA
Thomas Flohr	Siemens Healthcare Sector, Germany
Arundhuti Ganguli	Varian Medical Systems, CA, USA
Stephen Glick	UMass Medical School, MA, USA
Michael Grass	Philips Research Laboratories, Hamburg, Germany
Joachim Hornegger	University of Erlangen-Nuremberg, Germany
Jiang Hsieh	GE Healthcare, WI, USA
Steve Jiang	University of California, San Diego, CA, USA
Marc Kachelriess	German Cancer Research Center (DKFZ), Heidelberg, Germany
Alexander Katsevich	University of Central Florida, FL, USA
Thomas Koehler	Philips Research Laboratories, Hamburg, Germany
Hiroyuki Kudo	University of Tsukuba, Japan
Patrick La Riviere	University of Chicago, IL, USA

Guenther Lauritsch	Siemens Healthcare Sector, Germany
Harry Martz	Lawrence Livermore National Laboratory, CA, USA
Michael McNitt-Gray	David Geffen School of Medicine at UCLA, CA, USA
Kyle Myers	Office of Science and Engineering Labs, CDRH, FDA, MD, USA
Johan Nuyts	Katholieke Universiteit, Belgium
Jed Pack	GE Global Research Center, NY, USA
Xiaochuan Pan	University of Chicago, IL, USA
Norbert Pelc	Stanford University, Stanford, CA, USA
Roland Proksa	Philips Research Laboratories, Germany
Jeff Siewerdsen	Johns Hopkins University, MD, USA
Mike Silver	Toshiba Medical Research Institute, IL, USA
Josh Star-Lack	Varian Medical Systems, CA, USA
Web Stayman	Johns Hopkins University, MD, USA
Karl Stierstorfer	Siemens Healthcare Sector, Germany
Katsuyuki Taguchi	Johns Hopkins University, MD, USA
Xiangyang Tang	Emory University, GA, USA
Srinivasan Vedantham	UMass Medical School, MA, USA
Ge Wang	Rensselaer Polytechnic Institute (RPI), NY, USA
Bruce Whiting	University of Pittsburgh, PA, USA
Adam Wunderlich	Office of Science and Engineering Labs, CDRH, FDA, MD, USA
Hengyong Yu	Wake Forest University Health Sciences, NC, USA
Lifeng Yu	Mayo Clinic, MN, USA
Zhou Yu	Toshiba Medical Research Institute, IL, USA

Once again, we were also fortunate to receive generous support from

- ✓ Siemens AG, Healthcare Sector
- ✓ Toshiba Medical Systems Corporation
- ✓ GE Healthcare
- ✓ Varian Medical Systems

This financial support is essential to accommodate a lower registration fee for graduate students. This year, we have 142 attendees out of which a third are students.

Finally, I am thankful to Andrew Karellas for his continuous support and advice, particularly regarding the associated special issue of Medical Physics; I am grateful to Katharina Schmitt and Zhicong Yu for providing me with a very strong hand; and I am grateful for the help from my colleague, Larry Zeng, without whom I could not run such a conference.

I wish you all a pleasant meeting.

Frederic Noo, Ph.D.
 General Chair
 Utah Center for Advanced Imaging Research (UCAIR)
 Department of Radiology
 University of Utah
 E-mail: noo@ucair.med.utah.edu

Table of contents

Session M1: Spectral CT imaging
 Moderated by Bresler Y (University of Illinois & Instarecon) and Glick S (UMass Medical School)

Optimization-based direct inversion of spectral CT data into a materials decomposition Sidky E Y, Gilat-Schmidt T, Pan X <i>The University of Chicago, Chicago IL, USA; Marquette University, Milwaukee WI, USA</i>	1
Maximum a posteriori reconstruction of CT images using pixel-based latent variable of tissue types Nakada K, Taguchi K, Fung G S K, Amaya K <i>Tokyo Institute of Technology, Tokyo, Japan; Johns Hopkins University, MD, USA</i>	5
A generalized vectorial total-variation for spectral CT reconstruction Rigie D S, La Riviere P J <i>The University of Chicago, Chicago IL, USA</i>	9
Statistical image reconstruction for metal artifact correction using kV and selective MV imaging Wu M, Constantin D, Star-Lack J, Fahrig R <i>Stanford University, Stanford, CA, USA; Varian Medical Systems, Inc. Palo Alto, CA, USA</i>	13

Session M2: Dose and image quality
 Moderated by Das M (University of Houston) and Stierstorfer K (Siemens Healthcare Sector)

Dose reconstruction for real-time patient-specific dose estimation in CT De Man B, FitzGerald P, Jin Y, Yin Z, Edic P M, Yao Y, Tian X, Samei E <i>GE Global Research, Niskayuna, NY, USA; GE Global Research, Shanghai, China; Duke University, Durham, NC, USA</i>	17
CT protocol optimization at the dawn of iterative reconstruction: challenges and solutions Li K, Tang J, Chen G H <i>University of Wisconsin-Madison, WI, USA; GE Healthcare, Waukesha, WI, USA</i>	21
Application of task-based measures of image quality to evaluation of image reconstruction methods in X-ray CT Xu J, Elshahaby F, Fuld M K, Fung G S K, Tsui B M W <i>Johns Hopkins University, MD, USA; Siemens Medical Solutions, Inc., Malvern, PA, USA</i>	25
Mixed confidence estimation for iterative CT reconstruction Perlmutter D S, Kim S M, Kinahan P E, Alessio A M <i>University of Washington, Seattle, WA, USA</i>	29

Session M3A: Premium posters – Image quality evaluation and optimization
 Moderated by Gilat-Schmidt T (Marquette University) and Pack J D (GE Global Research)

Vessel overlap sparsity index – A predictive metric for 3D+T accuracy Royalty K, Szczykutowicz T, Rohkohl C, Kowarschik M <i>Siemens Medical Solutions USA, Inc.; University of Wisconsin, Madison, WI, USA; Siemens AG, Healthcare Sector, Forchheim, Germany</i>	33
Noise-weighted spatial domain FBP algorithm Zeng G L <i>Weber State University, Ogden, UT, USA; University of Utah, UT, USA</i>	37
A new redundancy weighting scheme for non-stationary data Taguchi K, Cammin J <i>Johns Hopkins University, MD, USA</i>	44
Construction of an atlas of filter configurations for fluence field modulated CT Szczykutowicz T P, Mistretta C A <i>University of Wisconsin-Madison, WI, USA</i>	48

Feasibility study on ultra-low dose 3D scout of organ based CT scan planning Yin Z, Yao Y, Montillo A, Edic P M, De Man B <i>GE Global Research, Niskayuna, NY, USA; GE Global Research, Shanghai, China</i>	52
Task-based comparison of linear forward projection models in iterative CT reconstruction Schmitt K, Schoendube H, Stierstorfer K, Hornegger J, Noo F <i>Siemens AG, Healthcare Sector, Germany; University of Erlangen-Nuremberg, Erlangen, Germany; University of Utah, UT, USA</i>	56
Clinical data evaluation of C-arm-based motion compensated coronary artery reconstruction Schwemmer C, Lauritsch G, Kleinfeld A, Rohkohl C, Müller K, Hornegger J <i>Friedrich-Alexander-Universität Erlangen-Nürnberg, Erlangen, Germany; Siemens AG, Healthcare Sector, Forchheim, Germany</i>	60
Parameter determination for optimization-based image reconstruction in cone-beam CT for image-guided radiation therapy Han X, Pearson E, Sidky E Y, Pelizzari C A, Pan X <i>The University of Chicago, IL, USA</i>	64
Validation of motion artifact metric optimization reconstruction (MAM) Bruder H, Fung G S K, Rohkohl C, Allmendinger T, Stierstorfer K <i>Siemens Healthcare Sector, Forchheim, Germany; John Hopkins University, MD, USA</i>	68

Session M3B: Premium posters – Spectral CT imaging Moderated by Gilat-Schmidt T (Marquette University) and Pack J D (GE Global Research)

Experimental investigation of hybrid region-of-interest spectral CT imaging with a photon-counting detector Gilat-Schmidt T, Zimmerman K C <i>Marquette University, Milwaukee, WI, USA</i>	71
Dual-energy-based beam hardening correction in digital volume tomography (DVT) Schueller S, Stannigel K, Huelsbusch M, Sawall S, Ulrici J, Hell E, Kachelrieß M <i>German Cancer Research Center (DKFZ), Heidelberg, Germany; Institute of Medical Physics, Friedrich–Alexander–University (FAU) Erlangen–Nuremberg, Erlangen, Germany; Sirona Dental Systems GmbH, Bensheim, Germany</i>	75
Dictionary learning and low rank based multi-energy CT reconstruction Zhang Y, Yu H, Mou X, Wang G <i>Xi’an Jiaotong University, Xi’an, Shaanxi, China; Beijing Center for Mathematics and Information Interdisciplinary Sciences, Beijing, China; Wake Forest University Health Sciences, Winston-Salem, NC, USA ; Rensselaer Polytechnic Institute, Troy, NY, USA</i>	79
CNR analysis of dual energy technologies Jin Y, Gao H, Pack J D, Wiedmann U, De Man B <i>GE Global Research Center, Niskayuna, NY, USA; GE Healthcare, Waukesha, WI, USA</i>	83
Spectrum binning approach for multi-material beam hardening correction (MMBHC) in CT Yang Q, Wu M, Maass N, Maier A K, Hornegger J, Fahrig R <i>Friedrich-Alexander-Universität Erlangen-Nuremberg, Germany; Stanford University, CA, USA; Siemens AG, Healthcare Sector, Erlangen, Germany</i>	87
Guided noise reduction for spectral CT with energy-selective photon counting detectors Manhart M, Fahrig R, Hornegger J, Doerfler A, Maier A <i>Friedrich-Alexander-Universität Erlangen-Nürnberg, Germany; Universitätsklinikum Erlangen, Erlangen, Germany; Stanford University, CA, USA</i>	91

Session M4: Model-based Iterative CT Reconstruction
 Moderated by Fessler J A (University of Michigan) and Taguchi K (Johns Hopkins University)

Modified noise modeling for robust statistical reconstructions	95
Bergner F, Brendel B, Bippus R, Muenzel D, Noel P B, Koehler T <i>Philips Technologie GmbH, Innovative Technologies, Research Laboratories, Hamburg, Germany; Technische Universitaet Muenchen, Munich, Germany</i>	
Improved statistical models in iterative CT reconstruction for PET attenuation correction	99
Kim S M, Alessio A M, Perlmutter D S, Thibault J-B, De Man B, Kinahan P E <i>University of Washington, Seattle, WA, USA; GE Healthcare, Waukesha, WI, USA; GE Global Research Center, Niskayuna, NY, USA</i>	
Optimized momentum steps for accelerating X-ray CT ordered subsets image reconstruction	103
Kim D, Fessler J A <i>University of Michigan, Ann Arbor, MI, USA</i>	
Adaptive sparsifying transforms for iterative tomographic reconstruction	107
Pfister L, Bresler Y <i>University of Illinois, Urbana Champaign, IL, USA</i>	
Integration of component knowledge in penalized-likelihood reconstruction with morphological and spectral uncertainties	111
Stayman J W, Tilley S II, Siewerdsen J H <i>Johns Hopkins University, Baltimore, MD, USA</i>	

Session T1: Homeland Security applications
 Moderated by Crawford C (Csuptwo, LLC) and Martz H (Lawrence Livermore National Laboratory)

Explosive detection in aviation applications using CT	116
Parker L <i>Department of Homeland Security, USA</i>	
Threat liquid identification in hand-held baggage	117
Faby S, Brehm M, Knaup M, Powell K, Ayoub M, Cantwell B, Radley I, Iovea M, Kachelrieß M <i>German Cancer Research Center (DKFZ), Heidelberg, Germany; Kromek Ltd, Sedgefield, Co Durham, United Kingdom; ACCENT PRO 2000 s.r.l. (AP2K), Bucharest, Romania</i>	
Algorithmic improvements to SIRT with application to X-Ray CT of luggage	121
Gregor J <i>University of Tennessee, Knoxville, TN, USA</i>	
Sinogram sparsified metal artifact reduction technology (SSMART)	125
Do S, Karl W C <i>Massachusetts General Hospital and Harvard Medical School, Boston, MA, USA; Boston University, MA, USA</i>	
Sinogram restoration for security screening CT applications	129
Vargas P, La Riviere P <i>University of Chicago, IL, USA</i>	
Artifact reduction in dual-energy CT reconstruction for security applications	133
Martin L, Karl W C, Ishwar P <i>Boston University, Boston, MA, USA</i>	
Simultaneous segmentation and reconstruction for dual-energy CT: experimental results	137
Tracey B H, Miller E L <i>Tufts University, Medford MA, USA</i>	

Compressed sensing as a tool for scanning very large objects with high energy X-ray computed tomography Schoen T, Firsching M, Reims N, Sukowski F, Dittmann J <i>Fraunhofer Institute for Integrated Circuits IIS, Fuerth, Germany; Julius-Maximilians-University, Wuerzburg, Germany</i>	141
Investigation of simulation software for explosive-detection CT imaging Gilat-Schmidt T <i>Marquette University, Milwaukee, WI, USA</i>	145
Efficient and accurate correction of beam hardening artifacts Champley K, Bremer T <i>Lawrence Livermore National Laboratory, Livermore, CA, USA</i>	149

Session T2: Invited talks Moderated by McCollough C (Mayo Clinic) and Tsui B (Johns Hopkins University)
--

Radiation dose in x-ray computed tomography McNitt-Gray M <i>University of California Los Angeles, CA, USA</i>	
Model observers: perspective from nuclear medicine Gifford H <i>University of Houston, TX, USA</i>	
Breast CT imaging: state-of-the-art Vedantham S <i>UMass Medical School, MA, USA</i>	

Session T3: Classical posters -- New directions

Human and model observers performance in low contrast detection tasks with CT phantom images acquired at different dose levels Hernandez-Giron I, Geleijns J, Calzado A, Joemai R M S, Veldkamp W J H <i>Universitat Rovira i Virgili, Reus, Spain; Universidad Complutense de Madrid, Spain; Leiden University Medical Center, The Netherlands</i>	153
X-ray tube potential modulation in spectral CT Li X, Wang X, Zou Y <i>Johns Hopkins University, Baltimore, MD, USA; Toshiba Medical Research Institute USA, Vernon Hills, IL, USA</i>	157
Motion-compensated cardiac CT with extended projection data range Cammin J, Tang Q, Taguchi K <i>Johns Hopkins University, MD, USA; Toshiba Medical Research Institute USA, Vernon Hills, IL, USA</i>	161
Texturization: a generalized image quality comparison method Do S, Pourjabbar S, Khawaja R, Padole A, Singh S, Kalra M <i>Massachusetts General Hospital and Harvard Medical School, Boston, MA, USA</i>	165
Motion compensated backprojection versus backproject-then-warp for motion compensated reconstruction Brendel B, Bippus R, Kabus S, Grass M <i>Philips Technologie GmbH, Innovative Technologies, Research Laboratories, Hamburg, Germany</i>	169
Optimal kVp selection for contrast CT imaging based on a projection-domain method Rui X, Jin Y, FitzGerald P F, Alessio A, Kinahan P, De Man B <i>GE Global Research Center, Niskayuna, NY, USA; University of Washington, Seattle, WA, USA</i>	173
A cone-beam reconstruction algorithm for dose-minimized short scan and super short scan Xia Y, Dennerlein F, Bauer S, Berger M, Hornegger J, Maier A <i>Friedrich-Alexander-University Erlangen-Nuremberg, Erlangen, Germany; Siemens AG, Healthcare Sector, Germany</i>	178

Fast and accurate stratification of tomographic scans for motion artifacts	182
Ho H, Nett B E, Pack J D <i>GE Healthcare, WI, USA; GE Global Research Center, Niskayuna, NY, USA</i>	
Constrained TV-minimization image reconstruction for dynamic micro-CT data with reduced angular sampling	186
Chen B, Liu X, Zhang Z, Davis A, Han X, Sidky E Y, Pan X <i>The University of Chicago, Chicago, IL, USA; Bruker microCT, Kontich, Belgium</i>	
A modified 4D ROOSTER method using the Chambolle-Pock algorithm	191
Mory C, Jacques L <i>Universite catholique de Louvain, Louvain-la-Neuve, Belgium; Universite de Lyon, France</i>	
Regularised GMRES-type methods for X-ray computed tomography	194
Coban S B, Lionheart W R B <i>The University of Manchester, Manchester, UK</i>	
Performance evaluation of OS-SPS and CG for differential phase-contrast X-ray tomography	198
Fehringer A, Brendel B, Hahn D, Noël P B, Pfeiffer F, Koehler T <i>Technische Universität München, Munich, Germany; Philips Technologie GmbH, Innovative Technologies, Hamburg, Germany</i>	
Estimation of missing fan-beam projections using frequency consistency conditions	203
Pohlmann M, Berger M, Maier A, Hornegger J, Fahrig R <i>Stanford University, CA, USA; Friedrich Alexander Universitaet Erlangen-Nuremberg, Erlangen, Germany</i>	
Experimental investigation of multi-energy CT material decomposition using artificial neural networks	208
Zimmerman K C, Gilat-Schmidt T <i>Marquette University, Milwaukee, WI, USA</i>	
A simple and efficient super-short-scan algorithm of fan-beam reconstruction for multiple circular trajectories: solution towards the truncated data	212
Chen L, Rodet T, Gac N <i>Universite Paris-Sud-CNRS-Supelec, France; Ecole Normale Superieur de Cachan, France</i>	
Sampling analysis of a dual source and dual detector CT system	216
Cao G, Hsieh J <i>GE Healthcare, Waukesha, WI, USA</i>	
Quantitative uniformity of iodinated contrast across the Z-coverage of large cone-angle CT	220
Gao H, Cohen A, Imai Y <i>GE Healthcare, Waukesha, WI, USA</i>	
Quantifying Hotelling observer performance for detection of small signals in CT images produced by linear reconstruction algorithms	224
Sanchez A A, Sidky A Y, Pan X <i>The University of Chicago, IL, USA</i>	
Optimization-based reconstruction exploiting spectral information in CT	228
Pan X, Chen B, Zhang Z, Pearson E, Sidky E Y, Han X <i>The University of Chicago, IL, USA</i>	
Tomosynthesis image quality assessment based on micro-CT	233
Cordes A, Levakhina Y M, Buzug T M <i>Universitaet zu Luebeck, Luebeck, Germany</i>	
Effect of reconstruction method on optimal acquisition parameters for lesion detection-localization in digital breast tomosynthesis	237
Liang Z, Gifford H C, Das M <i>University of Houston, TX, USA</i>	
Optimization of prior parameter for noise control in iterative computed tomography reconstruction	241
Yamakawa K, Kojima S <i>Hitachi Central Research Laboratory, Tokyo, Japan</i>	

Synchrotron-based microtomography: exploiting tunable, monochromatic, parallel X-rays for non-destructive materials characterization	245
Willey T M, van Buuren T, Lauderbach L, Gagliardi F, Overturf G <i>Lawrence Livermore National Laboratory, USA</i>	
2D filtered backprojection for fan-beam CT with independent rotations of the source and the detector	249
Rit S, Clackdoyle R <i>Universite de Lyon, France; Laboratoire Hubert Curien, CNRS, France; Universite Jean Monnet, Saint Etienne, France</i>	
A GPU-accelerated Katsevich algorithm with CUDA for fast, scalable, helical cone-beam CT	253
Ward W C, Lattimore B M, Hunter J F <i>Los Alamos National Laboratory, Los Alamos, NM, USA</i>	
General thresholding representation for the Lp regularization and its application in computed tomography	257
Miao C, Yu H <i>Wake Forest University Health Sciences, Winston-Salem, NC, USA</i>	
GPU-based implementation for interior tomography	261
Liu R, Yu H <i>Wake Forest University Health Sciences, Winston-Salem, NC, USA</i>	
Solid lung nodule volumetry: effects of dose reduction and reconstruction algorithms	265
Young S, McNitt-Gray M F <i>University of California Los Angeles, CA, USA</i>	
Considerations on an advanced adaptive filter	270
Schoendube H, Raupach R, Stierstorfer K <i>Siemens AG, Healthcare Sector, Forchheim, Germany</i>	
Improved trajectories in C-Arm computed tomography for non-circular fields of view	274
Herbst M, Schebesch F, Berger M, Fahrig R, Hornegger J, Maier A <i>Friedrich-Alexander-Universitaet Erlangen-Nuremberg, Erlangen, Germany; Stanford University, Stanford, CA, USA</i>	
Reduction of dose by focusing the X-ray beam to a specific region of interest: Monte Carlo assessment	279
Oktay M B, Noo F <i>University of Utah, UT, USA</i>	

Session T4: Phase contrast CT & Few-view CT
Moderated by De Man B (GE Global Research) and Tang X (Emory University)

Grating based differential phase contrast CT imaging without mechanical phase stepping	283
Ge Y, Li K, Garrett J, Chen G-H <i>University of Wisconsin-Madison, Madison, WI, USA</i>	
X-ray phase-contrast computed tomography in helical mode without phase stepping	287
Marschner M, Willner M, Herzen J, Noel P B, Pfeiffer F <i>Technische Universitaet Muenchen, Garching, Germany; Institute of Materials Research, Helmholtz-Zentrum Geesthacht, Geesthacht, Germany</i>	
Fast splitting-based ordered-subsets X-ray CT image reconstruction	291
Nien H, Fessler J A <i>University of Michigan, Ann Arbor, MI, USA</i>	
Tomographic image reconstruction from continuous projections	295
Cant J, Palenstijn W J, Behiels G, Sijbers J <i>University of Antwerp, Belgium; Agfa Healthcare NV, Belgium</i>	
Preliminary evaluation of dental cone-beam CT image from reduced projection data by constrained-TV-minimization	299
Zhang Z, Han X, Kusnoto B, Sidky E Y, Pan X <i>The University of Chicago, IL, USA; The University of Illinois at Chicago, IL, USA</i>	

Session W1: Advanced cone-beam imaging techniques and algorithms
 Moderated by Chen G-H (University of Wisconsin-Madison) and Sidky E Y (University of Chicago)

Old ideas new again: a system concept for fast CT using semi-conventional approaches Besson G M <i>ForeVision Technologies Corporation, USA</i>	303
Mitigating cone-beam artifacts via shift-variant data usage for large cone-angle scans Pack J D, Zeng K, Budde A, Yin Z, De Man B <i>GE Global Research Center, Niskayuna, NY, USA; GE Healthcare, Waukesha, WI, USA</i>	307
Efficient and exact C-arm cone-beam imaging for axially extended field-of-view using the ellipse-line-ellipse trajectory Yu Z, Lauritsch G, Hornegger J, Noo F <i>University of Utah, Salt Lake City, USA; Siemens AG, Healthcare Sector, Forchheim, Germany; University of Erlangen-Nuremberg, Erlangen, Germany</i>	311
New inversion formula for the X-ray transform and its application to CT reconstruction Oeckl S <i>Fraunhofer-Entwicklungszentrum Roentgentechnik EZRT, Fuerth, Germany</i>	315

Session W2: Data consistency conditions and applications
 Moderated by Xu J (Johns Hopkins University) and Yu Z (Mayo Clinic)

Data consistency conditions for 2D truncated parallel projections Clackdoyle R, Desbat L <i>Laboratoire Hubert Curien, CNRS, Saint Etienne, France; TIMC-IMAG laboratory, CNRS UMR, Grenoble, France; Joseph Fourier University, Grenoble, France</i>	319
Fanbeam data consistency conditions for applications to motion detection Clackdoyle R, Rit S, Hoskovec J, Desbat L <i>Laboratoire Hubert Curien, CNRS, Saint Etienne, France; TIMC-IMAG laboratory, CNRS UMR, Grenoble, France; Joseph Fourier University, Grenoble, France; CREATIS laboratory, CNRS and INSERM, Lyon, France; Université Jean Monnet, Saint Etienne, France</i>	324
Motion compensated fan-beam CT by enforcing Fourier properties of the sinogram Berger M, Maier A, Xia Y, Hornegger J, Fahrig R <i>Stanford University, CA, USA; Friedrich-Alexander-Universitaet Erlangen-Nuremberg, Erlangen, Germany</i>	329
Redundancies in X-ray images due to the epipolar geometry for transmission imaging Aichert A, Maass N, Deuerling-Zheng Y, Berger M, Manhart M, Hornegger J, Maier A K, Doerfler A <i>Friedrich-Alexander-Universität Erlangen-Nürnberg, Erlangen, Germany; Siemens AG, Healthcare Sector, Erlangen and Forchheim, Germany; Universitätsklinikum Erlangen, Germany</i>	333
Geometrical jitter correction in computed tomography Maass N, Dennerlein F, Aichert A, Maier A <i>Siemens AG, Healthcare Sector, Erlangen, Germany; Friedrich-Alexander-University Erlangen-Nuremberg, Germany</i>	338

Session W3A: Premium poster – Model-based iterative CT reconstruction
 Moderated by Szczykutowicz T (University of Wisconsin-Madison) and Yu Z (Toshiba Medical Research Institute, USA)

An efficient technique for multi-phase model based iterative reconstruction Xu S, Pal D, Thibault J-B <i>Southern Illinois University, Carbondale, IL, USA; GE Healthcare, Waukesha, WI, USA</i>	343
---	-----

Multiscale interior tomography using 1D generalized total variation	347
Lee M, Ward J P, Unser M, Ye J C <i>KAIST, Korea; EPFL, Switzerland</i>	
Application of incremental algorithms to CT image reconstruction for sparse-view, noisy data	351
Rose S, Andersen M S, Sidky E Y, Pan X <i>The University of Chicago, IL, USA; Technical University of Denmark, Denmark</i>	
GPU accelerated structure-exploiting matched forward and back projection for algebraic iterative cone beam CT reconstruction	355
Thompson W M, Lionheart W R B <i>University of Manchester, UK</i>	
Duality-based projection-domain tomography solver for splitting-based X-ray CT reconstruction	359
McGaffin M G, Fessler J A <i>University of Michigan, Ann Arbor, MI, USA</i>	
Iterative CT reconstruction using models of source and detector blur and correlated noise	363
Tilley S II, Siewerdsen J H, Stayman J W <i>Johns Hopkins University, Baltimore, MD, USA</i>	
CT reconstruction of surfaces from binary objects	368
Sawall S, Kuntz J, Maier J, Flach B, Schueller S, Kachelrieß M <i>German Cancer Research Center (DKFZ), Heidelberg, Germany</i>	

Session W3B: Premium poster – Data simulation & corrections for physical effects
Moderated by Szczykutowicz T (University of Wisconsin-Madison) and Yu Z (Toshiba Medical Research Institute, USA)

Statistical framework for synthetic object addition to CT projections	372
Zabic S, Brown K M, Eck B <i>Philips Healthcare, Cleveland, OH, USA; Case Western Reserve University, Cleveland, OH, USA</i>	
Development of a cardiac CT simulation platform: an integration of 4D anthropomorphic phantom with stent models and an accurate CT projector	376
Fung G S K, Stierstorfer K, Taguchi K, Segars W P, Bruder H, Fuld M, Flohr T G, Tsui B M W <i>Johns Hopkins University, Baltimore, MD, USA; Siemens Healthcare, Forchheim, Germany; Duke University, Durham, NC, USA.</i>	
Axial cone beam BPF/DBPF reconstruction with 3D weighting and butterfly filtering	380
Tang S, Wang W, Tang X <i>Xi'an University of Posts and Telecommunications, Xi'an, Shaanxi, China; Emory University, Atlanta, GA, USA</i>	
Reduction of cone artifacts in CT with incomplete source trajectories	384
Sunnegardh J, Schoendube H, Flohr T <i>Siemens Healthcare, Forchheim, Germany</i>	
Bilateral filtering for X-ray phase-contrast imaging	388
Allner S, Koehler T, Fehring A, Willner M, Pfeiffer F, Noël P B <i>Technische Universität München, Munich, Germany; Philips Technologie GmbH, Innovative Technologies, Hamburg, Germany</i>	
Metal artifact reduction using l1 and non-local penalties with iterative sinogram correction	393
Kim K, Ye J C, El Fakhri G, Li Q <i>Massachusetts General Hospital and Harvard Medical School, MA, USA; Korea Advanced Institute of Science and Technology, Daejeon, Korea</i>	

Scatter deconvolution in X-ray cone-beam CT using data consistency	397
Kim C, Park M, Sung Y, Lee J H, Choi J, Cho S <i>Korea Advanced Institute of Science and Technology, Daejeon, Korea; Samsung Advanced Institute of Technology, Suwon, Korea</i>	
A sparse Monte Carlo method for high speed, high accuracy scatter correction for soft-tissue imaging in cone-beam CT	401
Zbijewski W, Sisniega A, Stayman J W, Yorkston J, Aygun N, Koliatsos V, Siewerdsen J H <i>Johns Hopkins University, Baltimore, MD, USA; Carestream Health, Rochester, NY, USA</i>	

<p>Session W4: X-ray cone-beam imaging in interventional radiology Moderated by Kachelriess M (DKFZ) and Stayman J W (Johns Hopkins University)</p>
--

Deformable 3D–2D registration for CT and its application to low dose tomographic fluoroscopy	405
Flach B, Kuntz J, Brehm M, Kueres R, Bartling S, Kachelrieß M <i>German Cancer Research Center (DKFZ), Heidelberg, Germany; University of Erlangen–Nuremberg, Erlangen, Germany; University Medical Center Mannheim, Mannheim, Germany</i>	
Nesterov’s method for accelerated penalized-likelihood statistical reconstruction for C-arm cone-beam CT	409
Wang A S, Stayman J W, Otake Y, Kleinszig G, Vogt S, Siewerdsen J H <i>Johns Hopkins University, Baltimore, MD, USA; Siemens Healthcare, Erlangen, Germany</i>	
Patient-bounded extrapolation for 3D region of interest reconstruction in C-arm CT	414
Xia Y, Bauer S, Maier A, Berger M, Hornegger J <i>Friedrich-Alexander-University Erlangen-Nuremberg, Erlangen, Germany; Siemens AG, Healthcare Sector, Germany</i>	
Catheter artifact reduction (CAR) in dynamic cardiac chamber imaging with interventional C-arm CT	418
Müller K, Lauritsch G, Schwemmer C, Maier A K, Taubmann O, Abt B, Köhler H, Nöttling A, Hornegger J, Fahrig R <i>Friedrich-Alexander-Universität Erlangen-Nürnberg, Erlangen, Germany; Siemens AG, Healthcare Sector, Forchheim, Germany; Herz- und Kreislaufzentrum, Rotenburg an der Fulda, Germany; Stanford University, CA, USA</i>	

Optimization-based direct inversion of spectral CT data into a materials decomposition

Emil Y. Sidky¹, Taly Gilat-Schmidt², and Xiaochuan Pan¹

Abstract—A one-step inversion algorithm for spectral computed tomography (CT) is developed that yields material decomposition maps from multi-energy X-ray transmission data as what could conceivably be measured with photon-counting X-ray detectors. This approach is potentially desirable because incorporation of many physical constraints can be implemented directly on the material maps. Use of such constraints may stabilize reconstruction from spectral CT data thereby improving noise properties. Performing the proposed one-step image reconstruction can also aid in design of spectral CT acquisition parameters such as setting energy window thresholds.

I. INTRODUCTION

Spectral CT has recently gained much attention as research on photon-counting detectors with energy resolving capability progresses [1,2]. Spectral CT may yield images free of beam-hardening artifacts and may possibly provide quantitative information particularly for imaging involving K-edge contrast agents [3]. Image reconstruction for spectral CT is the topic of this conference contribution.

Image reconstruction for spectral CT falls into two broad categories: pre-reconstruction and post-reconstruction methods. Pre-reconstruction methods process the multi-energy transmission data to estimate sinograms of various physical quantities such as monochromatic attenuation or material maps, while post-reconstruction involves combining images reconstructed from data acquired at different energy windows. The latter method potentially suffers from beam-hardening and is not quantitative because the X-ray transmission data in the extended energy windows are processed with the negative logarithm, as is done in standard CT, yielding only an approximately self-consistent sinogram. Pre-reconstruction methods on the other hand aim at estimating a consistent sinogram of a physical map of the subject, but the downside is that the preprocessing is fairly unstable and can amplify noise.

¹The University of Chicago, Department of Radiology MC-2026, 5841 S. Maryland Avenue, Chicago IL, 60637.

²Marquette University, Department of Biomedical Engineering, PO Box 1881, Milwaukee WI, 53201.

The approach taken here is more aligned with pre-reconstruction methods in that we aim for quantitative CT, but we seek to perform the reconstruction in a single-step inversion. With standard pre-reconstruction techniques there are two steps: preprocessing to obtain sinograms of physical subject maps, followed by reconstruction of these maps. Here, we directly relate the physical maps to the spectral CT data, and invert this model implicitly through optimization. Use of optimization also allows us to enforce physically motivated constraints that can help to stabilize reconstruction. This approach is facilitated by recent developments on algorithms for large-scale constrained optimization. In particular we make use of the Chambolle-Pock (CP) algorithm [4,5] to solve the formulated optimization problem for spectral CT image reconstruction.

In this work, we make use of the materials decomposition approach for spectral CT. The data model, optimization formulation, and its inversion are presented in Sec. II. Results are shown in Sec. III for simulated spectral CT data using the FORBILD head phantom aiming at revealing the stability of image reconstruction for data taken in two versus five energy windows.

II. METHODS

For developing the image reconstruction algorithm for spectral CT, we employ a data model which contains only the essential spectral physics

$$I_{w,\ell} = \int dE S_w(E) \exp \left[- \int_{\ell} dt \mu(E, \vec{r}(t)) \right], \quad (1)$$

where $I_{w,\ell}$ is the transmitted X-ray intensity along ray ℓ in energy window w ; $S_w(E)$ is the product of beam spectrum and detector response for energy window w ; and $\mu(E, \vec{r}(t))$ is the energy dependent linear X-ray attenuation coefficient. Direct reconstruction of $\mu(E, \vec{r}(t))$ is impractical because transmission intensity is measured in only a few energy windows. Employing physical modeling can help reduce the dimensionality of the unknown attenuation map. Here, we employ the material map decomposition method where μ is expressed in terms of materials

that are expected to be in the subject

$$\mu(E, \vec{r}(t)) = \sum_m \left(\frac{\mu_m(E)}{\rho_m} \right) \rho_m f_m(\vec{r}[t]), \quad (2)$$

where ρ_m is the density of material m ; $\mu_m(E)/\rho_m$ is the mass attenuation coefficient of material m ; and $f_m(\vec{r})$ is the occupation fraction of material m at location \vec{r} . In the rest of the text we refer to $f_m(\vec{r})$ as a material map, and it is these quantities that we aim to reconstruct from the measurements $I_{w,\ell}$. Physically, $f_m(\vec{r})$ cannot be less than zero nor greater than one. If there are multiple materials at \vec{r} , for example contrast agent and blood, f_m can take on a fractional value.

Combining Eq. (1) with Eq. (2) presents us with our data model which relates the quantities measured, $I_{w,\ell}$, with the quantities we seek, $f_m(\vec{r})$. One-step inversion of this model affords us the opportunity to directly code constraints on $f_m(\vec{r})$. Working toward setting up our desired optimization problem, we discretize the integrations in Eq. (1) and write the data fidelity term in terms of the negative logarithm of the transmission intensity:

$$\mathbf{g}(\mathbf{f}_m) = -\ln(I_{w,\ell}^{\text{DD}}(\mathbf{f}_m)) \text{ for all } w, \ell \text{ and,} \quad (3)$$

where \mathbf{g} is a vector containing the negative logarithm of the transmission intensity at all rays and energy windows; \mathbf{f}_m is a discrete pixel representation of material map m ; and the DD superscript on I indicates discretization of the integrations in the definition of $I_{w,\ell}$. The reason for introducing the negative logarithm in Eq. (3) is that it yields a nearly linear relationship between \mathbf{g} and \mathbf{f}_m .

The optimization problem investigated in this work takes the following form

$$\{\mathbf{f}_m^* | m = 1, \dots, M\} = \arg \min_{\{\mathbf{f}_m | m=1, \dots, M\}} \frac{1}{2} \|\mathbf{g}(\mathbf{f}_m) - \mathbf{g}_{\text{data}}\|_2^2 \quad (4)$$

$$\text{such that } 0 \leq \mathbf{f}_m \leq 1; \sum_m \mathbf{f}_m \leq 1;$$

$$\text{and } \|\nabla \mathbf{f}_m\|_1 \leq \gamma_m,$$

where the bound constraints on \mathbf{f}_m reflect physical bounds on the material maps; the sum constraint ensures that the partial volumes of each material does not exceed unity within each voxel; and the final constraint bounds the total variation (TV) norm to a value γ_m for each material map. The sum constraint could also be formulated as an equality, because each voxel must be filled with some combination of substances. But in such a case, air needs to be included among the material maps. We prefer to drop representation of an air map and allow for voxels which are only partially filled. The constraints on the TV of each map is known to improve robustness of the

image reconstruction against view-angle undersampling and it may also help stabilize the inverse problem against the near linear dependence in energy of the material attenuation coefficients.

The proposed optimization problem in Eq. (4) may not be convex, because the quadratic function in the objective involves the function $\mathbf{g}(\mathbf{f}_m)$, which may have locations where it is concave. Aside from the objective, all the constraints are convex. The deviation from convexity is, however, slight because $\mathbf{g}(\mathbf{f}_m)$ is approximately linear. Although the CP algorithm is derived for convex optimization, it turns out that we can apply it to this constrained optimization problem by using reweighting; we have recently employed this strategy to an optimization with more severe nonconvexity [6]. In this work, we consider only inversion of the spectral CT data into tissue maps, but we point out that these maps can be then used to form other types of images such as the attenuation map at a single energy. Furthermore, other decomposition techniques can be formulated in a similar way.

III. RESULTS

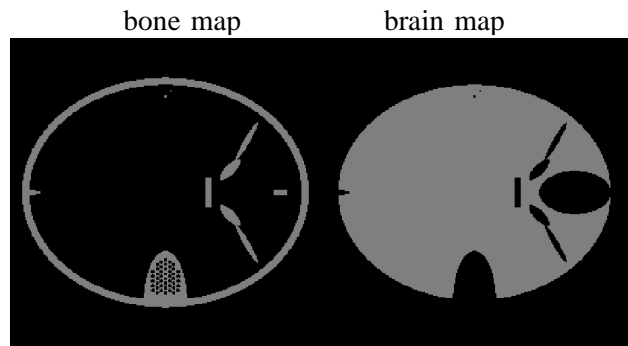


Fig. 1. Material maps \mathbf{f}_m for the Head phantom used for the spectral CT simulation. The maps are 256×256 pixelized arrays and the values are one at pixels containing the corresponding material and zero otherwise. The images are shown in a gray scale window [0.8,1.2].

To demonstrate application of Eq. (4) to image reconstruction for spectral CT, we simulate transmission data at multiple energy windows for the head phantom. We modify the phantom so that all soft tissues in the phantom are assigned brain tissue and bone remains bone as shown in Fig. 1. In this way the phantom has only two materials. The mass attenuation curves used in the simulation are the measured values for bone and brain as listed in the tables compiled by Hubbell and Seltzer [7]. The specific question we investigate is if the number of energy windows has an impact on stability of the image reconstruction.

The X-ray spectrum is modeled for a 120 kV X-ray source, and it is plotted in Fig. 2. On the detector side,

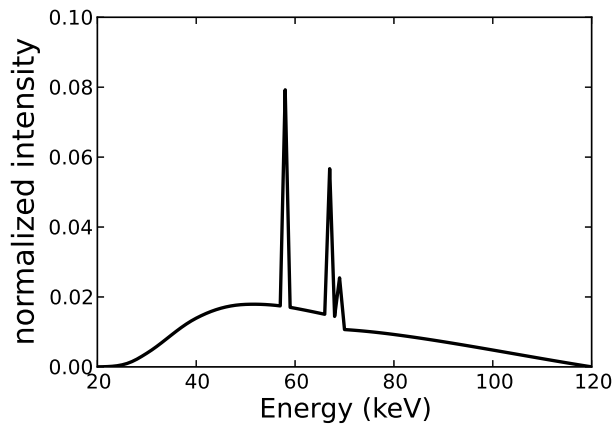


Fig. 2. Normalized spectrum of typical 120kV X-ray source.

we take two ideal window configurations: one where five energy windows span the range from 20 to 120 keV in intervals of 20 keV, and one where this same range is covered by two windows of width 50 keV. The scanning configuration is circular fan-beam with a source-to-isocenter distance of 50 cm and a source-to-detector distance of 100 cm. The number of views for the simulation is 128 and the detector is a linear array consisting of 512 equally spaced bins.

The first two sets of results are computed from ideal noiseless data for two energy windows in Fig. 3 and five energy windows in Fig. 4. By ideal data, we mean that the model for the image reconstruction is the same as the one that generates the data. In this case it is possible to drive the data discrepancy to zero. Also, because we are testing ideal recovery, we set the TV constraint parameters γ_m to the actual values from the corresponding phantom material maps. To obtain a sense of stability we view the material map estimates for different root-mean-square-error (RMSE) values of the data discrepancy along the trajectory of the map iterates. Because the data are ideal it is possible to drive the data RMSE to zero. The figures show images of the intermediate map estimates and corresponding RMSE metrics. The interesting point is that the reconstruction provided by solving Eq. (4) for both cases is fairly robust because the given data RMSE values are reasonably large. The results with noisy data, below, corroborate this point. It is also clear that the five window data provides more stable reconstruction, as might be expected. The images contain fewer artifacts and the image RMSEs are lower for the five window data as compared with the two window data.

In order to obtain some sense of the impact of data noisy, we employ the five-window spectral CT configuration and add noise to the transmission measurements with a Gaussian model that resembles a Poisson distribution. The variance at each ray and within each energy window

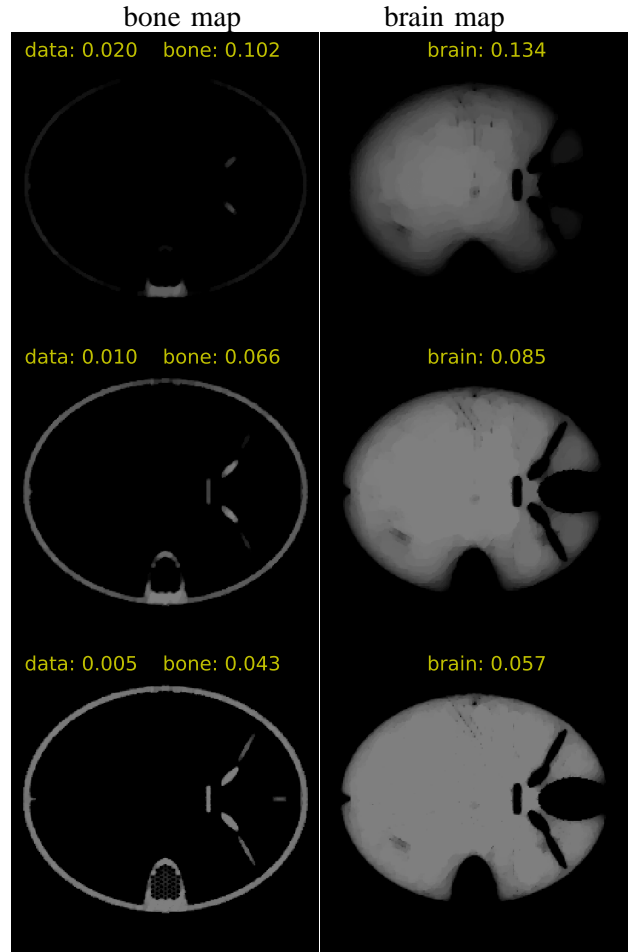


Fig. 3. Reconstructed material maps for ideal noiseless two energy window transmission data. The images shown, in the gray scale [0.8,1.2], come from a single run of the CP algorithm. The rows are distinguished by different levels of progress as measured by root-mean-square-error (RMSE) data discrepancy, labeled in the left column of images, between estimated and given spectral CT data. Note that iteration number correlates inversely with data discrepancy. Also given is the RMSE of the images with respect to the corresponding phantom material map. These numbers together with the images give a sense of the stability of the image reconstruction.

is taken to be one over the transmitted flux assuming 2×10^5 photons are incident. The results are shown in Fig. 5. Note that results for a data RMSE of 0.005 are not available because of inherent inconsistency induced by the noise model. It is clear from the images that some artifacts are introduced into the map reconstruction by the noise. But an interesting point is that the image RMSE values are actually lower for the same data RMSE in the noisy case. This results from the fact that there is actually a fair amount of uniform image bias in the noiseless results.

IV. SUMMARY

We have formulated an optimization-based method for direct inversion of spectral CT data into material maps. Many physical constraints are incorporated, which aid in stabilizing the inversion. Preliminary results indicate that

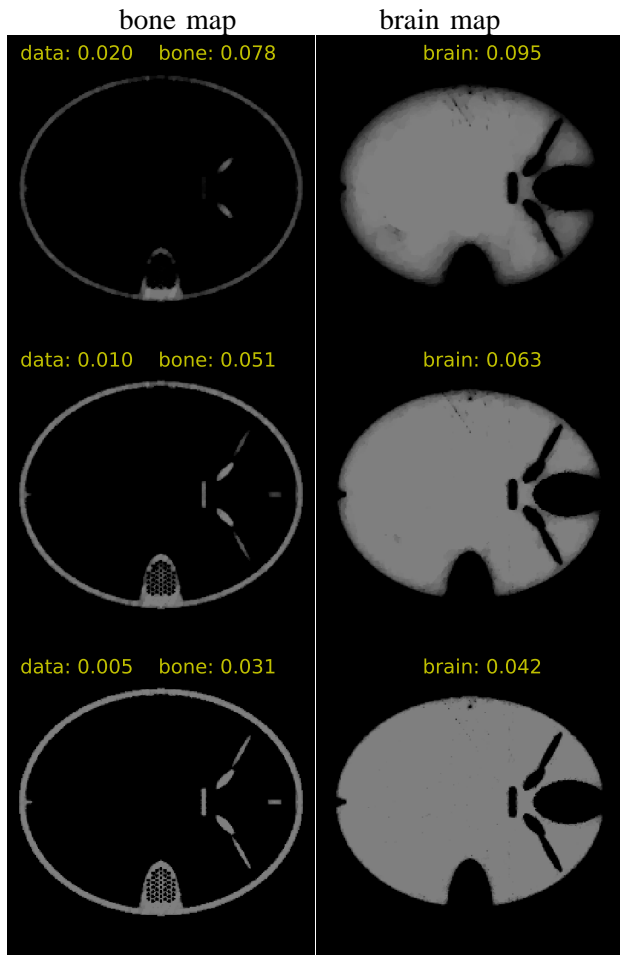


Fig. 4. Same as Fig. 3 except the reconstruction was performed for ideal noiseless five energy window transmission data.

the method is robust against noise. Many extensions of these preliminary results will be investigated. In particular, we will introduce other soft tissues into the phantom while a two-material basis expansion, and correspondingly we will seek other convex formulations of the physical constraints to account for the presence of multiple soft tissues. We will also investigate phantoms with K-edge contrast agents using a three-material basis expansion. The use of the CP algorithm will allow us the flexibility to prototype alternate optimization problems for these more complex situations. Finally, we will add other physical factors to the data model such as scatter, and include non-ideal response of the photon-counting detectors.

V. ACKNOWLEDGMENT

This work was supported in part by NIH Grant Nos. R21-EB015094, R01-CA158446, R01-CA120540, and R01-EB000225. The contents of this article are solely the responsibility of the authors and do not necessarily represent the official views of the National Institutes of Health.

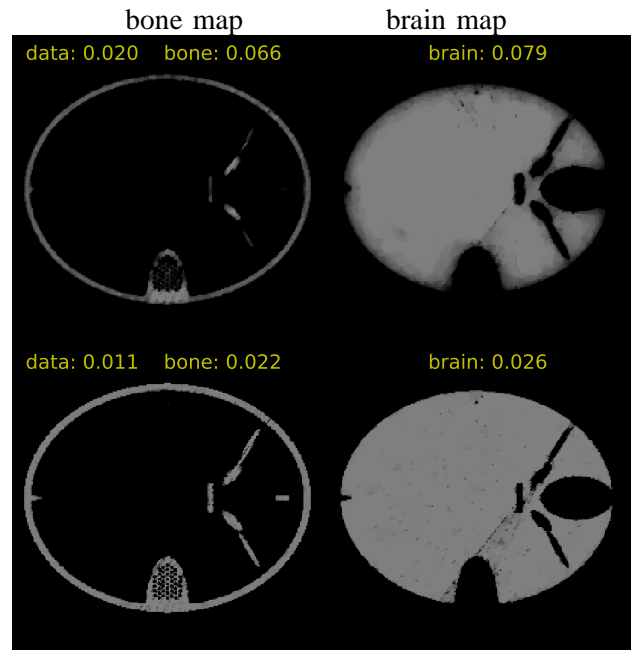


Fig. 5. Same as Fig. 4 except the reconstruction was performed for noisy five energy window transmission data. The simulated incident integrated flux per bin and energy window is 2×10^5 photons. The minimum data RMSE was 0.011 due to the data inconsistency from the simulated noise.

REFERENCES

- [1] J. P. Schlomka, E. Roessl, R. Dorscheid, S. Dill, G. Martens, T. Istel, C. Bäumer, C. Herrmann, R. Steadman, G. G. Zeitler, A. Livne, and R. Proksa, "Experimental feasibility of multi-energy photon-counting K-edge imaging in pre-clinical computed tomography," *Phys. Med. Biol.*, vol. 53, no. 15, pp. 4031–4048, 2008.
- [2] X. Wang, D. Meier, K. Taguchi, D. J. Wagenaar, B. E. Patt, and E. C. Frey, "Material separation in x-ray CT with energy resolved photon-counting detectors," *Med. Phys.*, vol. 38, no. 3, pp. 1534–1546, 2011.
- [3] S. Feuerlein, E. Roessl, R. Proksa, G. Martens, O. Klass, M. Jeltsch, V. Rasche, H.-J. Brambs, M. H. K. Hoffmann, and J.-P. Schlomka, "Multienergy photon-counting K-edge imaging: Potential for improved luminal depiction in vascular imaging 1," *Radiology*, vol. 249, no. 3, pp. 1010–1016, 2008.
- [4] A. Chambolle and T. Pock, "A first-order primal-dual algorithm for convex problems with applications to imaging," *J. Math. Imag. Vis.*, vol. 40, pp. 120–145, 2011.
- [5] E. Y. Sidky, J. H. Jørgensen, and X. Pan, "Convex optimization problem prototyping for image reconstruction in computed tomography with the Chambolle-Pock algorithm," *Phys. Med. Biol.*, vol. 57, pp. 3065–3091, 2012.
- [6] E. Y. Sidky, R. Chartrand, J. M. Boone, and X. Pan, "Constrained TpV minimization for enhanced exploitation of gradient sparsity: Application to CT image reconstruction," *J. Trans. Engineer. Health Med.*, vol. 2, pp. 1800418, 2014, DOI: 10.1109/JTEHM.2014.2300862.
- [7] J. H. Hubbell and S. M. Seltzer, "Tables of X-ray mass attenuation coefficients and mass energy-absorption coefficients from 1 keV to 20 MeV for elements $Z = 1$ to 92 and 48 additional substances of dosimetric interest," Tech. Rep. 5632, NIST, Ionizing Radiation Division, Physics Laboratory National Institute of Standards and Technology Gaithersburg, MD 20899, 1996.

Maximum a Posteriori Reconstruction of CT Images Using Pixel-based Latent Variable of Tissue Types

Kento Nakada, Katsuyuki Taguchi, George S. K. Fung, and Kenji Amaya

Abstract—We propose a new framework to jointly perform image reconstruction, material decomposition, and tissue type identification for Photon counting detector CT (PCD-CT) by applying maximum a priori (MAP) estimation with pixel-based latent variables for tissue types. With the latent variables, the proposed method utilizes region-based coupled Markov random field to describe continuity and discontinuity of human organs, and Gaussian mixture model to incorporate statistical relation between tissue types and their attenuation characteristics. The proposed method estimate CT images and their tissue types jointly, which enables us to not only identify tissue types more accurately, but also reconstruct CT images with decreased noise and enhanced sharpness thanks to the information about human tissue types. The performance of the proposed method is quantitatively compared with a quadratic penalized likelihood method and filtered backprojection.

I. INTRODUCTION

Iterative reconstruction methods for x-ray computed tomography (CT) have improved tradeoffs of the spatial resolution and noise of images compared with analytical methods. Most of iterative methods estimate images by penalized maximum likelihood (PML) method. While the likelihood term is based on rigorous statistics of measured data, the regularization (or prior) term is empirical and can be inaccurate. For example, in the Huber prior [1] the transition point between the quadratic and the linear penalties is defined without exact knowledge of the tissue type the pixel-of-interest belongs to, and the same parameter set is applied to any tissue types, which refers to biological compounds such as adipose, heart muscle, liver parenchyma, lungs, ribs, spines, and iodine-enhanced blood. We hypothesize that more accurate regularization can be performed with knowledge of tissue types pixels-of-interest belong to, and therefore, the image quality can be improved. The values of neighboring image pixels of linear attenuation coefficients are expected to vary smoothly and continuously when they are in the same tissue, while the values may be discontinuous at organ boundaries. Moreover, a suitable level of discontinuity can be obtained for each boundary from the tissue types on both sides of the boundary. The challenge is how to obtain the knowledge of the tissue types for all image pixels.

Photon counting detector-based (PCD-)CT counts the number of transmitted x-ray photons within three or more energy

K.N and K.A are with the department of Mechanical and Environmental Informatics at Tokyo Institute of Technology School of Information Science and Engineering, Meguro, Japan (email: nakada.k.ac@m.titech.ac.jp, kamaya@a.mei.titech.ac.jp).

K.T and G.S.K.F are with the Russell H. Morgan Department of Radiology and Radiological Science at the Johns Hopkins University School of Medicine, Baltimore, MD (email: ktaguchi@jhmi.edu).

windows, which allows for the use of three basis functions in material decomposition [2]. A linear combination of three basis functions—e.g., photoelectric effect, Compton scattering, and discontinuity at the K-edge of contrast agent—can accurately model the energy-dependent linear attenuation coefficient of any materials involved in clinics except for metallic implants [3]. The coefficients of basis functions, which we call characteristic coefficients in this paper, are functions of the chemical composition of the attenuator, thus, are unique to tissue types [4].

We propose a novel image reconstruction method, JE-MAP, which jointly estimates images of the energy-dependent linear attenuation coefficients and tissue types from PCD data through material decomposition process. JE-MAP algorithm employs maximum a posteriori (MAP) joint estimation based on pixel-based latent variables for tissue types. The prior information with region-based coupled Markov random field model [5] and Gaussian mixture model are used. Compared with the primitive version [6], we have designed a new prior for better describe the level of discontinuity, implemented a more computationally efficient optimization algorithm, and performed a systematic and thorough quantitative evaluations.

II. METHODS

A. Problem Modeling

The energy-dependent linear attenuation coefficients at photon energy E , $x(E)$, can be described as a linear combination of three basis functions, $\Phi_n(E)$, $n = 1, 2, 3$,

$$x(E) = \sum_{n=1}^3 w_n \Phi_n(E), \quad (1)$$

$$\Phi(E) = \left(\frac{E^{-3}}{E_0^{-3}}, \frac{f_{\text{KN}}(E)}{f_{\text{KN}}(E_0)}, \frac{f_{\text{I}_0}(E)}{f_{\text{I}_0}(E_0)} \right), \quad (2)$$

where E^{-3} denotes the photoelectric effect, $f_{\text{KN}}(E)$ is the Klein-Nishina function for Compton scattering, $f_{\text{I}_0}(E)$ is a mass attenuation coefficient of iodine element, and E_0 is the reference energy. We call the coefficients vector w characteristic coefficients. Our goal is to estimate characteristic coefficients and the tissue type for each image pixel from measured PCD sinogram data.

We introduce latent variables z_i to express the tissue type at each image pixel i , $i = 1, \dots, I$, using so called Potts model represented by the 1-of- K scheme [7].

$$z_i \in \{(1, 0, \dots, 0)^T, \dots, (0, 0, \dots, 1)^T\}, z_i \in \{0, 1\}^K. \quad (3)$$

Thus, each image pixel is labeled by one of K tissue types.

Now let $\mathbf{W} = \{\mathbf{w}_i | i = 1, \dots, I\}$ represent a set of the characteristic coefficients on the tomographic image, and $\mathbf{Z} = \{z_i | i = 1, \dots, I\}$ be a set of the latent variables. Furthermore, let $j = 1, \dots, J$ represent a set of index of detector pixel, and then $\hat{\mathbf{Y}} = \{\hat{\mathbf{y}}_j | j = 1, \dots, J\}$ be a set of PCD-CT measurements on sinograms, where each pixel is given by $\hat{\mathbf{y}}_j = (\hat{y}_{(j,1)}, \dots, \hat{y}_{(j,b)})$ which indicates photon counts detected by each of b energy bins.

B. Cost functions

The problem of image reconstruction, material decomposition, and tissue type identification can be formulated as joint MAP estimation regarding \mathbf{W} and \mathbf{Z} as random variables, whose solution can be obtained by

$$(\mathbf{W}^*, \mathbf{Z}^*) = \arg \min_{\mathbf{W}, \mathbf{Z}} \left\{ -\ln p(\hat{\mathbf{Y}} | \mathbf{W}) - \ln p(\mathbf{W}, \mathbf{Z}) \right\},$$

s.t. $\mathbf{w}_i \geq \mathbf{0}$ ($i = 1, \dots, I$), (4)

where $p(\hat{\mathbf{Y}} | \mathbf{W})$ is likelihood distribution, and $p(\mathbf{W}, \mathbf{Z})$ is prior distribution.

1) *Likelihood Modeling*: We assume an ideal photon counting detectors, that is, there is no pulse pileup effect [8] or spectral response effect [9]. Thus the probability of photon counts $\hat{\mathbf{Y}}$ given the object is expressed as Poisson distribution with sufficiently large expected value, which can then be approximated to by a Gaussian distribution.

$$-\ln p(\hat{\mathbf{Y}} | \mathbf{W}) = \frac{1}{2} \sum_{j=1}^J (\hat{\mathbf{y}}_j - \mathbf{y}_j)^T \Sigma_{\text{dtc},j}^{-1} (\hat{\mathbf{y}}_j - \mathbf{y}_j), \quad (5)$$

$$\mathbf{y}_j = h(\mathbf{w}_{\text{proj}j}), \quad (6)$$

$$\Sigma_{\text{dtc},j} = \text{diag}(y_{j1}, y_{j2}, \dots, y_{jb}), \quad (7)$$

where $\mathbf{y}_j \in \mathbb{R}^b$ and $\Sigma_{\text{dtc},j} \in \mathbb{R}^{b \times b}$ means the expected values and the covariance matrix of detected photon counts in b energy bins at j th pixel on the sinogram, function $h : \mathbb{R}^3 \rightarrow \mathbb{R}^b$ relates line integral of the characteristic coefficients, \mathbf{w}_{proj} , to the expected photon counts through Eq.(1) and Beer's law.

2) *Prior Distribution Modeling*: We define the prior distribution as a combination of a region-based coupled Markov random field (MRF) model [5] and statistical distribution between \mathbf{W} and \mathbf{Z} ,

$$\ln p(\mathbf{W}, \mathbf{Z}) := \ln p_{\text{MRF}}(\mathbf{W}, \mathbf{Z}) + \ln p_{\text{sta}}(\mathbf{W}, \mathbf{Z}). \quad (8)$$

Region-based Coupled MRF Model: We adopt a region-based coupled MRF model to express geometrical continuity and discontinuity of human organs, regarding characteristic coefficients as observable variables and tissue types as latent variables. Let $ne(i)$ be a set of index of neighboring voxels around image pixel i . Considering Potts model of tissue types,

we design the region-based coupled MRF model as follows,

$$-\ln p_{\text{MRF}}(\mathbf{W}, \mathbf{Z}) = \mathcal{E}(\mathbf{W}, \mathbf{Z}) + \ln B_{\text{MRF}}, \quad (9)$$

$$\mathcal{E}(\mathbf{W}, \mathbf{Z}) = \frac{1}{2} \sum_{i=1}^I \sum_{i' \in ne(i)} \left\{ \beta_1 (z_i \cdot z_{i'}) (\mathbf{w}_i - \mathbf{w}_{i'})^2 + \beta_2 (1 - z_i \cdot z_{i'}) \{ (\mathbf{w}_i - \mathbf{w}_{i'}) - (\boldsymbol{\mu}(z_i) - \boldsymbol{\mu}(z_{i'})) \}^2 \right\}, \quad (10)$$

where $\mathcal{E}(\mathbf{W}, \mathbf{Z})$ represents the energy function of Gibbs distribution and B_{MRF} means the normalization constant. $\boldsymbol{\mu}(z_i)$ represents the statistical expected value of characteristic coefficients which correspond to z_i . When two tissue types z_i and $z_{i'}$ are the same, the first term of Eq.(10) encourages the smoothness. In contrast, when the tissue types are different, the second term encourages the difference in pixel values at the boundary of organs to be close to the expected difference. Two parameters, β_1 and β_2 balances the effect of the two terms.

Gaussian Mixture Model: We model statistical relation between characteristic coefficients and tissue types. The expected values of \mathbf{w} for z_i were obtained from NIST database [10], and we assumed that \mathbf{w} is multivariate Gaussian distributed. We then modeled the relationship between \mathbf{w} 's and all tissue types for a image pixel using a multivariate Gaussian mixture model.

$$-\ln p_{\text{sta}}(\mathbf{W}, \mathbf{Z}) = -\beta_3 \sum_{i=1}^I \left\{ \ln p(z_i) + \ln p(\mathbf{w}_i | z_i) \right\}$$

$$= \beta_3 \sum_{i=1}^I \left\{ \ln K + \sum_{k=1}^K z_i^{(k)} \left\{ \frac{1}{2} (\mathbf{w}_i - \boldsymbol{\mu}_k)^T \Sigma_k^{-1} (\mathbf{w}_i - \boldsymbol{\mu}_k) + \ln C_k \right\} \right\}, \quad (11)$$

where β_3 is a weighting parameter, $z_i^{(k)}$ means the k th element of z_i , and $\boldsymbol{\mu}_k$, Σ_k , and C_k are the expected value, covariance matrix, and normalization constant of the multivariate Gaussian distribution for k th tissue type, respectively. Here we assumed $p(z_i)$ is uniformly distributed.

C. Constraint Optimization

1) *Approximation of Likelihood*: For the purpose of solving this optimization problem easily with a quadratic programming, we approximate the non-linear likelihood function to a quadratic surrogate function, i.e., in Eq.(5),

$$\hat{\mathbf{y}}_j - \mathbf{y}_j \approx J_h(\hat{\mathbf{w}}_{\text{proj}j} - \mathbf{w}_{\text{proj}j}), \quad (12)$$

where J_h means a Jacobian matrix of function h . By rewriting Eq.(5) as a function of \mathbf{w}_{proj} , a quadratic programming can be used in the iteration assuming that the distribution of \mathbf{w}_{proj} can be approximated by multivariate Gaussian model [11].

2) *Iterative Method*: In addition, to avoid combinatorial explosion of discrete variables z , we adopt Iterative Conditional Modes algorithm [12], which updates parameters of each pixel successively. For pixel i , the sub-minimizer w_i is found while z_i being fixed at one of K tissue types. Since the cost function becomes convex over w_i in each update, its constrained minimization can be computed analytically with the Karush-Kuhn-Tucker conditions. After performing the sub-minimization procedure for all K tissue types, the characteristic coefficients w_i^{new} and tissue type z_i^{new} which give the minimum cost are selected and used in the succeeding process.

III. EVALUATION METHODS

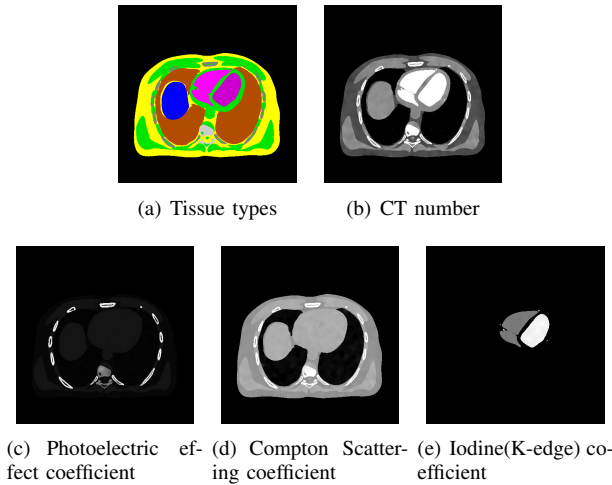


Fig. 1. Thorax of a modified XCAT phantom. Geometrical textures were added to each tissue, such that pixel values inside an organ are not homogeneous. (a) Nine tissue types including air indicated by different colors. (b) The monochromatic CT image at 70 keV. WW 600 HU and WL 0 HU. (c-e) The distributions of three characteristic coefficients.

A. Phantom and scan

We used a modified thorax image of XCAT phantom with nine tissue types shown in Fig.1. The phantom image covered $40 \times 40 \text{ cm}^2$ by 512×512 pixels, and geometrical texture was added to make image pixel values inside an organ heterogeneous. We simulated noisy projections of parallel beams with Poisson noise with tube voltage, 140 kV; incident x-ray, 10^5 counts per projection ray; 360 projections over 180° ; 4 energy thresholds at 0, 40, 70, 100 keV. 100 noise realizations were performed.

B. Reconstruction and tissue type classification

First, material decomposition was performed to obtain three sinograms of the characteristic coefficients from PCD data. Then, images of the characteristic coefficients were reconstructed using the following three methods: FBP, PML, and JE-MAP. The FBP images were used as an initial estimate of PML and JE-MAP. For each image pixel, a tissue type is chosen which gives the minimum L2-norm distance from statistical expected values to the image pixel value.

FBP: FBP with ramp filter was performed on each of the three sinograms of the characteristic coefficients independently to obtain the corresponding image.

PML: PML minimizes the likelihood of data (Eq. (5)) with a quadratic regularizer weighted by 2×10^5 .

JE-MAP: JE-MAP was performed with $\beta_1 = 2 \times 10^5$, $\beta_2 = 30$, and $\beta_3 = 1.0$. The covariance matrix Σ_k was sampled from the phantom and scaled by $\beta_4 = 2.5 \times 10^{-2}$.

IV. EVALUATION RESULTS

Figure 2 presents the estimated tissue types and monochromatic CT images at 70 keV from one noise realization and Fig. 3 shows profiles along the line shown in Fig. 2(f). These results showed that JE-MAP decreased the image noise while maintaining the sharpness and the accuracy of tissue types at the boundaries of organs.

Figure 4 shows bias and standard deviation of CT images at 70 keV and the accuracy of tissue type identification, both calculated over 100 noise realizations. The results are also summarized in Table I. It can be seen that JE-MAP provided the least noise and had small biases in general; however, negative biases were found with iodine-enhanced blood in the heart.

The tradeoffs between the spatial resolution and image noise were studied. The image noise was quantified by standard deviation values averaged over adipose regions. The spatial resolution was quantified by fitting the error function to horizontal edge profiles at the contour of the phantom. The measurements were performed on images blurred by different Gaussian filters. The obtained tradeoff curves were shown in Fig. 5, where the left top end-point of the curves was obtained from the images reconstructed by the corresponding method. JE-MAP provided the best tradeoff performance.

These results showed that JE-MAP improved the accuracy of tissue type identification for the entire image, while also improving the edge sharpness and image noise. A problem was found in biases with soft tissues, which we think was attributed to suboptimal parameters $\beta_1, \beta_2, \beta_3, \beta_4$. JE-MAP tends to mislabel liver tissue as muscle, because their true characteristic coefficients had a significant overlap. The expected values were very close and their sample variances were large.

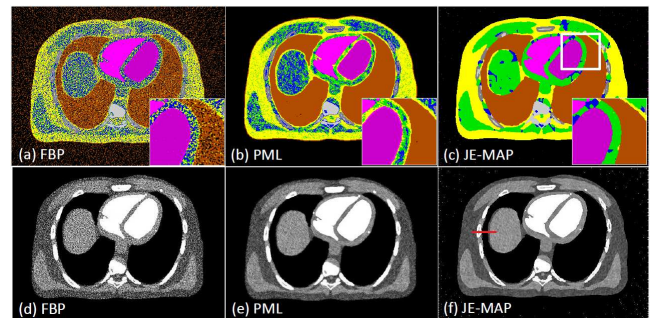


Fig. 2. Images of (a-c) the estimated tissue types and (d-f) monochromatic CT images at 70 keV. WW 600 HU, WL 0 HU.

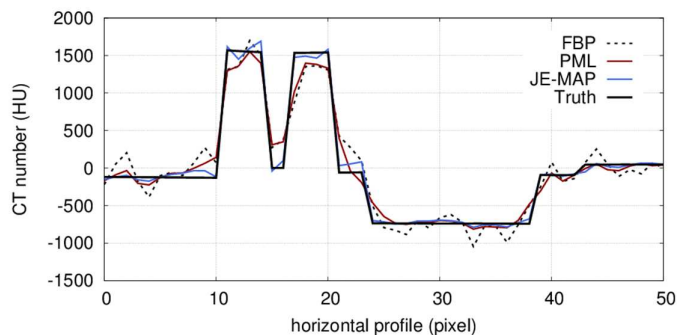


Fig. 3. Profiles of CT images at 70keV along the line in Fig.2(f) through adipose, rib, lung, thin layer of adipose, and liver.

TABLE I

IMAGE NOISE AND THE ACCURACY OF TISSUE TYPE IDENTIFICATION.

	FBP	PML	J.E.
Stdev. (HU)	112.4	48.1	35.8
Accuracy(%)	58.5	78.9	89.2

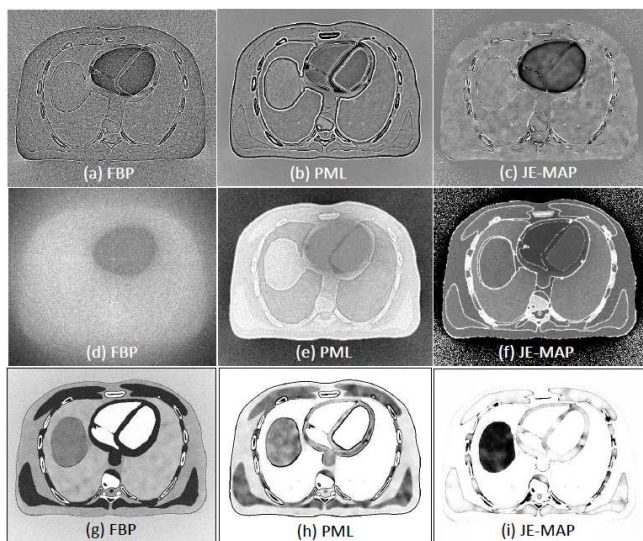


Fig. 4. Results of 100 noise realizations: (a-c) bias and (d-f) noise of CT images and (g-i) the accuracy of tissue type identification. Display window width and level are: (a-c) 100 HU, 0 HU, (d) 100 HU, 100 HU, (e,f) 30 HU, 60 HU, (d) 100 HU, 100 HU, and (g-i) 50%, 100%.

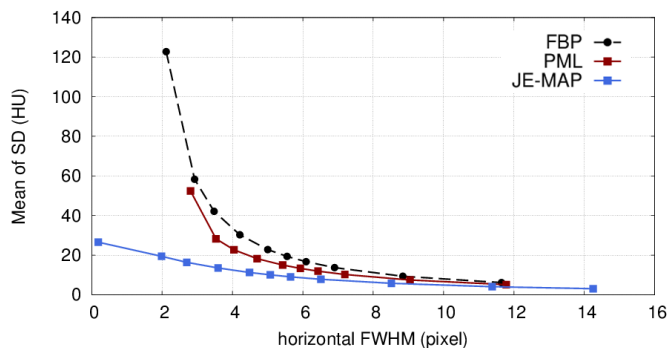


Fig. 5. Noise-resolution tradeoff curves.

V. CONCLUSION

In this paper, we have proposed a new joint estimation framework employing MAP estimation using pixel-based latent variables for tissue types. The method combines the geometrical information described by region-based coupled MRF, statistical relation between tissue types and material-based characteristic coefficients, and noise models of PCD data, and makes possible the continuous MAP estimation of CT image and tissue types directly from detected photon counts. The quantitative evaluation showed that proposed method estimates images with better accuracy of tissue type identification, noise reduction, and edge preservation than the sequential method using simple quadratic penalty. Meanwhile the quantitative noise realization results also show that it has a problem with bias and wrong identification of tissues with very close attenuation characteristics. However, The joint estimation framework has potential to further improve its performance by introducing more information about tissues in human body, e.g., the location, size, and number of tissues, or limited variation of neighboring tissues, which can be formulated by pixel-based latent variables.

REFERENCES

- [1] P. J. Huber, *Robust statistics*. Springer, 2011.
- [2] R. E. Alvarez and A. Macovski, "Energy-selective reconstructions in x-ray computerised tomography," *Physics in medicine and biology*, vol. 21, no. 5, p. 733, 1976.
- [3] E. Roessl and R. Proksa, "K-edge imaging in x-ray computed tomography using multi-bin photon counting detectors," *Physics in medicine and biology*, vol. 52, no. 15, p. 4679, 2007.
- [4] X. Wang, D. Meier, K. Taguchi, D. J. Wagenaar, B. E. Patt, and E. C. Frey, "Material separation in x-ray ct with energy resolved photon-counting detectors," in *Proceedings of SPIE*, vol. 7961, 2011, p. 79611V.
- [5] S. Z. Li, *Markov random field modeling in image analysis*. Springer, 2009.
- [6] K. Nakada, K. Amaya, K. Taguchi, and G. S. Fung, "Joint estimation of tissue types and linear attenuation coefficients for photon counting ct," in *Abstract of IEEE Medical Imaging Conference*, 2013.
- [7] R. Hasegawa, M. Okada, and S. Miyoshi, "Image segmentation using region-based latent variables and belief propagation," *Journal of the Physical Society of Japan*, vol. 80, no. 9, p. 3802, 2011.
- [8] K. Taguchi, M. Zhang, E. C. Frey, X. Wang, J. S. Iwanczyk, E. Nygard, N. E. Hartsough, B. M. Tsui, and W. C. Barber, "Modeling the performance of a photon counting x-ray detector for ct: Energy response and pulse pileup effects," *Medical physics*, vol. 38, no. 2, p. 1089, 2011.
- [9] S. Srivastava, J. Cammin, G. S. Fung, B. M. Tsui, and K. Taguchi, "Spectral response compensation for photon-counting clinical x-ray ct using sinogram restoration," in *Physics of Medical Imaging*, 2012.
- [10] J. H. Hubbell and S. M. Seltzer, "Tables of x-ray mass attenuation coefficients and mass energy-absorption coefficients," *National Institute of Standards and Technology*, 1996.
- [11] C. Schirra, S. Xu, T. Koehler, B. Brendel, A. Thran, D. Pan, M. Anastasio, and R. Proksa, "Statistical reconstruction of material decomposed data in spectral ct," *IEEE Transactions on Medical Imaging*, vol. 32, no. 7, pp. 1249–1257, 2013.
- [12] J. Besag, "On the statistical analysis of dirty pictures," *Journal of the Royal Statistical Society. Series B (Methodological)*, pp. 259–302, 1986.

A generalized vectorial total-variation for spectral CT reconstruction

David S. Rigie and Patrick J. La Rivière

Abstract—In this work we introduce a novel generalization of the total-variation semi-norm for vector-valued images and demonstrate its potential usefulness for reconstructing sparse-view, spectral CT data. The proposed vectorial TV (VTV) encourages a common edge structure among spectral channels. We show that it leads to a simple optimization problem that can be efficiently minimized using the primal-dual algorithm proposed by Chambolle et al [1] and present the results of a simulation study. We find that the coupling between channels results in better apparent image quality and improved overall reconstruction accuracy when compared with independent, channel-by-channel reconstruction.

I. INTRODUCTION

Over the past few years, there has been a growing interest in iterative reconstruction algorithms for CT using total-variation (TV) regularization, which others have shown can lead to high quality reconstructions from highly undersampled projection data [2]. Simultaneously, rapid advances in energy-discriminating detectors have generated a surge of interest in spectral CT, where the broad x-ray tube spectrum is sampled into multiple “color” channels of data, which could lead to the elimination of common artifacts [3], patient dose reduction [4], and entirely new clinical applications of CT [5], [6].

In this work we will propose a generalization of the total-variation semi-norm for reconstructing such multi-energy datasets. The simplest way to apply the existing TV-based reconstruction methods to spectral CT is to separately reconstruct the projection data from each spectral channel, but we will show that superior reconstructions can be obtained by using a generalized, vectorial TV norm that leverages the strong spatial correlations in the image domain between the various channels.

Our proposed vectorial TV (VTV) is motivated by the notion that images reconstructed from different channels should have a common edge structure. The conventional TV pertains to scalar image functions and its application to CT reconstruction is motivated by the idea that the gradient-magnitude image should be approximately sparse. Our VTV generalizes this approach for vector image functions and is based on the nuclear norm of the Jacobian derivative. In addition to introducing a desirable coupling between the spectral channels, this VTV has a simple dual formulation and can be handled readily by many of the recent primal-dual algorithms with virtually no increase in computational burden.

In this work we will give some basic theoretical motivation

David Rigie and Patrick J. La Rivière are with the Department of Radiology at the University of Chicago

for our generalized VTV, provide update equations for VTV constrained spectral CT reconstruction based on the primal-dual algorithm by Chambolle et al. [1], and briefly discuss some preliminary simulation results.

II. THEORY

A. Definitions and notation

First, we will establish some of our notational choices to avoid confusion. In this work we will refer to two different kinds of matrix norms. The first type is the “entry-wise” p -norm, which for matrix X is defined as

$$\|X\|_p = \left(\sum_{i,j} |X_{ij}|^p \right)^{1/p}. \quad (1)$$

For $p = 2$ we get the common “Frobenius norm”.

The second type is the “Schatten p -norm”, which arises when applying the ℓ_p -norm to the vector of singular values associated with X . We will use the uncommon notation $\|\cdot\|_{S_p}$, where specifically for a matrix X , the Schatten p -norm is given by

$$\|X\|_{S_p} = \left(\sum_i |\sigma_i|^p \right)^{1/p}, \quad (2)$$

where σ_i denotes the i^{th} singular value of X . Some common special cases are the “nuclear norm” ($p = 1$), the Frobenius norm ($p = 2$), and the “spectral norm” ($p = \infty$).

B. Constrained TV image reconstruction

For conventional, non-spectral CT the basic framework for TV-based image reconstruction is summarized by the following optimization problem,

$$\underset{u}{\operatorname{argmin}} \{ \|u\|_{\text{TV}} \quad \text{s.t.} \quad \|Au - f\|_2 \leq \epsilon \} \quad (3)$$

where A is the projection matrix, u is the desired image, and ϵ is a parameter that balances the trade-off between data fidelity and regularity. Next we will define the conventional TV semi-norm $\|\cdot\|_{\text{TV}}$ and develop the motivation for our generalized VTV.

C. The scalar TV

The total-variation semi-norm typically employed for CT reconstruction is given by equation 4.

$$\|u\|_{\text{TV}} = \sum_{j=1}^{\mathcal{L}} \|\nabla_j u\|_2, \quad (4)$$

The operator ∇_j is the discrete approximation to the gradient at pixel j , and \mathcal{L} is the total number of image pixels. In addition to its usefulness for handling sparse data, this penalty is both edge-preserving and convex, which are important properties that should, ideally, be preserved in any potential generalization to multi-spectral data.

D. The proposed vectorial TV

Now we consider extending this notion to spectral CT, where the image and data vectors consist of \mathcal{M} different spectral channels.

$$\mathbf{u} = \begin{pmatrix} u_1 \\ \vdots \\ u_M \end{pmatrix}, \quad \mathbf{f} = \begin{pmatrix} f_1 \\ \vdots \\ f_M \end{pmatrix} \quad (5)$$

The VTV that we propose is given by equation 6.

$$\|\mathbf{u}\|_{\text{VTV}} = \sum_{j=1}^{\mathcal{L}} \|D_j \mathbf{u}\|_{S_1}, \quad (6)$$

Since \mathbf{u} is now a vector function, where each pixel corresponds to a vector of ‘‘color’’ values, the quantity $D_j \mathbf{u}$ is the discrete approximation of the $\mathcal{M} \times \mathcal{N}$ Jacobian matrix at pixel j , where \mathcal{M} and \mathcal{N} refer to the number of spectral channels and spatial dimensions, respectively. We have replaced the ℓ_2 -norm of the gradient with the nuclear norm (a.k.a. Schatten 1-norm) of the Jacobian. At pixel j the Jacobian has the following structure

$$D_j \mathbf{u} = \begin{bmatrix} \leftarrow (\nabla_j u_1)^T \rightarrow \\ \vdots \\ \leftarrow (\nabla_j u_M)^T \rightarrow \end{bmatrix}_{\mathcal{M} \times \mathcal{N}}, \quad (7)$$

where each row is given by the discrete gradient of the corresponding spectral channel.

We hypothesize that a sensible penalty for sparse spectral CT reconstruction should try to minimize the rank of this Jacobian over all pixels. The rank of the Jacobian will be zero in constant-valued regions of the image, and it will be one when the gradient vectors of each spectral channel point in the same direction. Such a rank minimizing penalty would encourage gradient-sparse solutions in the same way as the conventional TV and it would also favor solutions that have common edge directions in all channels. Figure 1 gives a graphical illustration of the Jacobian for an ROI of a multi-spectral image.

A true rank minimizing penalty would seek to minimize $\|\cdot\|_{S_0}$, but this would lead to an optimization problem that is non-convex and NP-hard, so instead we use $\|\cdot\|_{S_1}$ as a convex surrogate. We do not provide specific justification for this relaxation, but such a substitution is implicit in all TV penalties.

Some other possible vectorial TVs have been proposed in the field of color image processing [7], [8], but to our knowledge the one described here is original, and the application of any VTV to CT reconstruction has yet to be studied. For

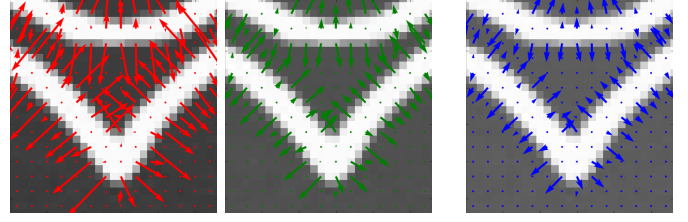


Fig. 1. Closeup ROI images of the NCAT phantom at 60 (left), 80 (middle), and 100 keV (right) with their gradient vector-fields superimposed. Each row of the Jacobian matrix corresponds to a point in one of these vector-fields. It will have a low rank if the directions are consistent between energy channels.

brevity, we do not present those other variants in this work because our proposed VTV exhibited better performance in all of our experiments.

E. Efficient minimization

Using this newly proposed VTV, our primal optimization problem is given by equation 8.

$$\operatorname{argmin}_{\mathbf{u}} \{ \|\mathbf{u}\|_{\text{VTV}} \quad \text{s.t.} \quad \|A\mathbf{u} - \mathbf{f}\|_2 \leq \epsilon \} \quad (8)$$

where the operator A is simply the CT projection matrix applied to each channel of \mathbf{u} . In order to efficiently solve this problem, we employ the primal-dual algorithm proposed by Chambolle and Pock [1].

The basic premise is to recast (8) into a saddle-point problem and to alternate between gradient descent steps in the primal variable and ascent steps in the dual variables using a proximal splitting scheme [9]. The saddle-point problem equivalent to (8) is

$$\min_{\mathbf{u}} \max_{\zeta, \mathbf{q}} \left\{ -\langle \mathbf{u}, \operatorname{Div}(\zeta) \rangle + \langle \mathbf{q}, A\mathbf{u} - \mathbf{f} \rangle - \delta_S(\zeta) - \epsilon \|\mathbf{q}\|_2^2 \right\}, \quad (9)$$

where $\delta_S(\zeta)$ is an indicator function defined as

$$\delta_S(\zeta) = \begin{cases} \infty & \sigma_{\max}(\zeta) \leq 1 \\ 0 & \text{otherwise} \end{cases}, \quad (10)$$

and the Div operator is the discrete divergence operator applied to each spectral channel of ζ . The update equations follow from this saddle-point problem in a straight-forward manner. The details on how to apply the CP algorithm to related optimization problems can be found in Sidky et al [10].

III. SIMULATION STUDY

A. Basic setup

To investigate the merits of the proposed vectorial TV regularizer, we carried out a simple 2D simulation experiment on a pixelized anthropomorphic phantom composed of bone and water, shown in figure 2. Our phantom is derived from a pixelization of the NCAT phantom [11]. We simulated 100 views of noisy, projection data at 60, 80, and 100 keV with a detector sampling of 896 bins and performed constrained TV reconstructions using both a naive, channel-by-channel approach and the proposed vectorial TV. All images were



Fig. 2. An anthropomorphic thorax phantom, composed of bone and soft-tissue (water)

reconstructed onto a 512×512 grid with 1 mm pixels. To isolate the effects of the VTV regularizer in this pilot study, we make several unrealistic assumptions. First, each energy-channel of spectral CT data is perfectly mono-energetic, removing any nonlinear, beam-hardening effects. Secondly, the same CT system matrix is used for both data generation and reconstruction, and finally, the noise-level in each energy channel is approximately equalized by fixing the number of transmitted photons. We don't believe that any of these assumptions will critically change our findings and plan on relaxing them in future investigations.

B. Selecting the parameter ϵ

Our optimization problem (8) has one free parameter, ϵ that controls the trade-off between data-fidelity and regularity. In practice, the best choice of ϵ will depend on how noisy the data is and the particular clinical task. However, we do not attempt to seek out an "optimal" value of ϵ because we are only interested in comparing our VTV to a channel-by-channel application of the conventional TV. In that case, it is only important that we use the same ϵ when making the comparison. For our purposes, it is particularly important that we use this data-constrained TV minimization framework, as opposed to the equivalent unconstrained optimization problem, because our proposed vectorial TV has inherently different scale than the conventional TV. This would make it very difficult to achieve a fair comparison when using the unconstrained form.

Since, in this simulation study, we have the ground truth images available to us, we can use them to establish a baseline for reasonable ϵ values. Particularly we calculate a reference value, ϵ^* as

$$\epsilon^* = \|A\mathbf{u}_{\text{true}} - \mathbf{f}\|_2, \quad (11)$$

where \mathbf{u}_{true} is the ground truth image data and \mathbf{f} is our noisy projection data. Then we perform reconstruction selecting $\epsilon = \gamma\epsilon^*$, where $0 < \gamma < 1$. For this study, we used γ values of 0.2, 0.5, and 1.0 in order to evaluate the impact of our VTV for different levels of regularization.

C. Results

The 60, 80, and 100 keV energy channel images were reconstructed, and a post-reconstruction, image-domain material decomposition was performed. Since we simulated perfectly monochromatic data, the decomposition amounts to solving a

TABLE I
IMAGE RMSE VALUES FOR THE CONVENTIONAL TV APPLIED CHANNEL-BY-CHANNEL (TV_S) AND THE PROPOSED VTV

	ϵ/ϵ^*	TV_S			VTV		
		0.2	0.5	1.0	0.2	0.5	1.0
60 keV image	0.057	0.025	0.015	0.048	0.023	0.011	
80 keV image	0.040	0.017	0.010	0.036	0.016	0.007	
100 keV image	0.035	0.014	0.008	0.032	0.013	0.005	
bone image	0.560	0.228	0.074	0.477	0.216	0.045	
water image	0.752	0.303	0.086	0.649	0.288	0.039	

trivial linear system. Figure 3 shows the results for the soft-tissue and bone channels for three different choices of ϵ . Note that the material decomposition process tends to amplify noise and artifacts, which makes it easier to visualize errors in the reconstructions.

Qualitatively, we observe that using our vectorial TV regularizer has a universally positive impact on the images, reducing artifacts and producing much cleaner edges. We observed this trend for all energy channels and epsilon values. Additionally, we observe that the overall image accuracy is improved, which can be seen from the RMSE values in table I.

IV. SUMMARY

In summary, we have introduced a novel generalization of the total-variation semi-norm for reconstructing spectral CT data. It possesses many of the desirable properties of the conventional TV penalty and introduces a coupling between spectral-channels that encourages a consistent edge structure. In our simulation experiment, we showed that our VTV penalty results in cleaner edges and reduced artifacts compared to separately reconstructing each channel. An additional benefit is that the resulting optimization problem is no more difficult than the conventional constrained TV minimization problem, and we have provided simple updates based on the primal-dual CP algorithm.

In the future we plan on testing our VTV penalty under more realistic data conditions and exploring alternative applications. Conceptually, our extension of the conventional TV is quite general and could conceivably be useful for a wide variety of problems involving multi-channel data with a consistent edge structure.

V. ACKNOWLEDGEMENTS

We would like to acknowledge support from Toshiba Medical Systems and NIH grants R01CA134680.

REFERENCES

- [1] A. Chambolle and T. Pock, "A first-order primal-dual algorithm for convex problems with applications to imaging," *Journal of Mathematical Imaging and Vision*, vol. 40, no. 1, pp. 120–145, May 2011. [Online]. Available: <http://link.springer.com.proxy.uchicago.edu/article/10.1007/s10851-010-0251-1>

CHANNEL-BY-CHANNEL TV

PROPOSED VTV

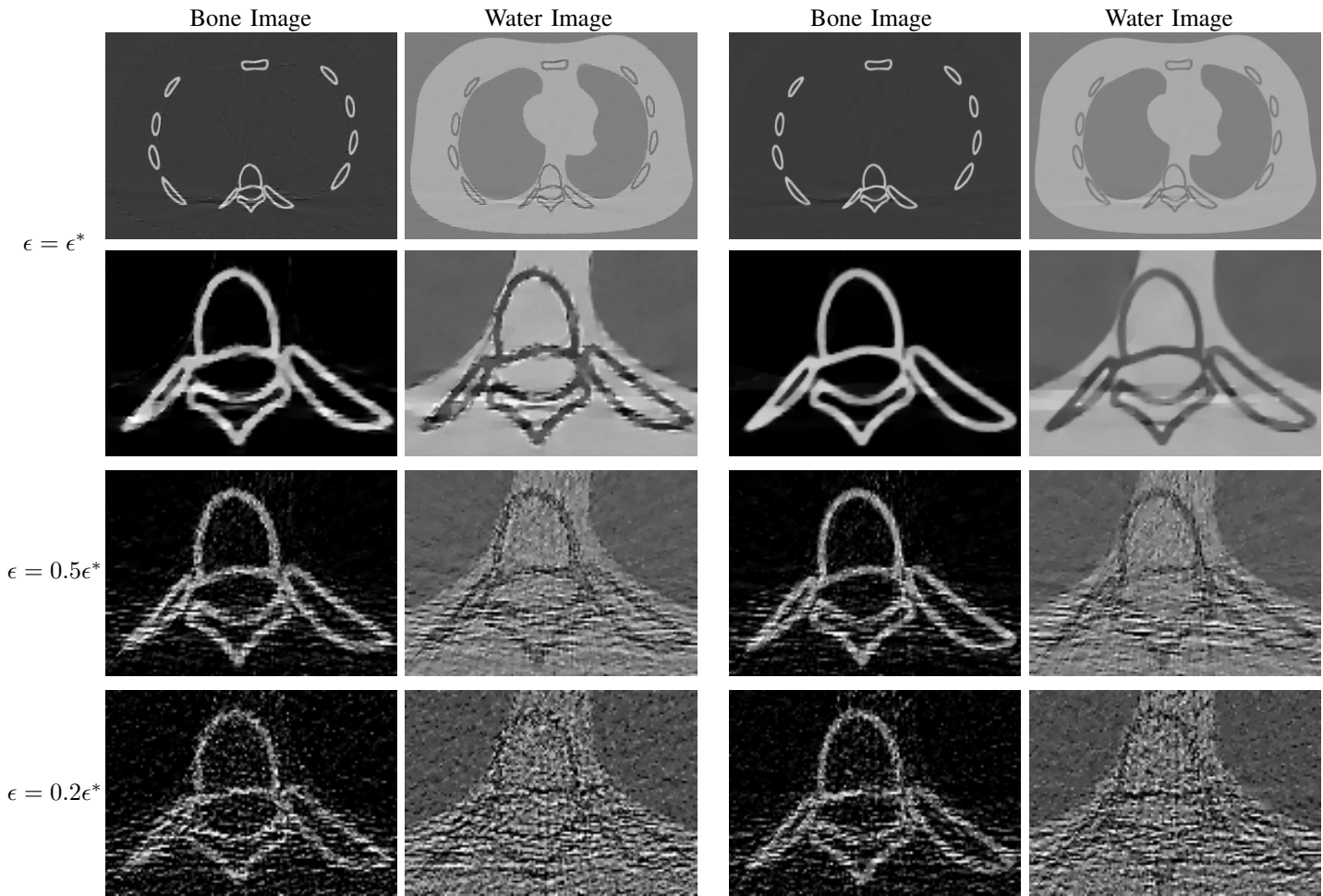


Fig. 3. Bone and water images computed post-reconstruction from the channel-by-channel TV reconstructed images (left) and the proposed vectorial TV constrained images (right) from 100 views of noisy data at 60, 80, and 100 keV. The first two rows correspond to $\epsilon = \epsilon^*$, while the next two rows correspond to $\epsilon = 0.5\epsilon^*$ and $\epsilon = 0.2\epsilon^*$ respectively.

[2] E. Y. Sidky, C.-M. Kao, and X. Pan, "Accurate image reconstruction from few-views and limited-angle data in divergent-beam CT," *Journal of X-Ray Science and Technology*, vol. 14, no. 2, pp. 119–139, Jan. 2006. [Online]. Available: <http://iopscience.metapress.com/content/1JDUV1CLL3F9E2BR>

[3] R. E. Alvarez and A. Macovski, "Energy-selective reconstructions in x-ray computerised tomography," *Physics in Medicine and Biology*, vol. 21, no. 5, p. 733, Sep. 1976. [Online]. Available: <http://iopscience.iop.org/0031-9155/21/5/002>

[4] W. H. Sommer, A. Graser, C. R. Becker, D. A. Clevert, M. F. Reiser, K. Nikolaou, and T. R. C. Johnson, "Image quality of virtual noncontrast images derived from dual-energy CT angiography after endovascular aneurysm repair," *Journal of Vascular and Interventional Radiology*, vol. 21, no. 3, pp. 315–321, Mar. 2010. [Online]. Available: <http://www.sciencedirect.com/science/article/pii/S1051044309011178>

[5] A. N. Primak, J. G. Fletcher, T. J. Vrtiska, O. P. Dzyubak, J. C. Lieske, M. E. Jackson, J. C. Williams Jr, and C. H. McCollough, "Noninvasive differentiation of uric acid versus NonUric acid kidney stones using dual-energy CT," *Academic Radiology*, vol. 14, no. 12, pp. 1441–1447, Dec. 2007. [Online]. Available: <http://www.sciencedirect.com/science/article/pii/S1076633207005235>

[6] C. Sun, F. Miao, X.-m. Wang, T. Wang, R. Ma, D.-p. Wang, and C. Liu, "An initial qualitative study of dual-energy CT in the knee ligaments," *Surgical and Radiologic Anatomy*, vol. 30, no. 5, pp. 443–447, Jul. 2008. [Online]. Available: <http://link.springer.com/article/10.1007/s00276-008-0349-y>

[7] B. Goldluecke, E. Strelakovsky, and D. Cremers, "The natural vectorial total variation which arises from geometric measure theory," *SIAM Journal on Imaging Sciences*, vol. 5, no. 2, pp. 537–563, Jan. 2012. [Online]. Available: <http://epubs.siam.org/doi/abs/10.1137/110823766>

[8] P. Blomgren and T. Chan, "Color TV: total variation methods for restoration of vector-valued images," *IEEE Transactions on Image Processing*, vol. 7, no. 3, pp. 304–309, Mar. 1998.

[9] P. L. Combettes and J.-C. Pesquet, "Proximal splitting methods in signal processing," in *Fixed-Point Algorithms for Inverse Problems in Science and Engineering*. Springer, 2011, pp. 185–212.

[10] E. Y. Sidky, J. H. Jrgensen, and X. Pan, "Convex optimization problem prototyping for image reconstruction in computed tomography with the ChambollePock algorithm," *Physics in Medicine and Biology*, vol. 57, no. 10, p. 3065, May 2012. [Online]. Available: <http://iopscience.iop.org/0031-9155/57/10/3065>

[11] W. Segars, B. M. Tsui, D. S. Lalush, E. C. Frey, M. A. King, and D. Manocha, "Development and application of the new dynamic nurbs-based cardiac-torso (NCAT) phantom." *School of Nursing Faculty Publication Series*, vol. 42, no. 5, Jan. 2001. [Online]. Available: http://scholarworks.umass.edu/nursing_faculty_pubs/86

Statistical Image Reconstruction for Metal Artifact Correction Using kV and Selective MV Imaging

Meng Wu, Dragos Constantin, Josh Star-Lack, and Rebecca Fahrig

Abstract—The goal of this study is to improve the image quality of radiotherapy planning CTs for patients with metal implants or fillings by completing the missing kilovoltage (kV) projection data with selectively acquired megavoltage (MV) data that do not suffer from photon starvation. Using the two imaging systems that are available on current radiotherapy devices, the metal streaking artifacts are avoided and the soft tissue contrast is restored, even in the areas where the kV data cannot contribute any information. We implemented two statistical image reconstruction methods, dual-energy penalized least squares (PWLS) and polychromatic maximum likelihood (PML), for combining kV and selective MV data. The PML method can reduce the beam hardening artifact caused by the metal in the low energy MV X-ray data. Cramer-Rao Lower Bound for Compound Poisson model is used to select the MV beam energy. The PML method using a 2.5 MVp beam can possibly provide soft tissue contrast and lower radiation dose than using a 6 MVp beam

Keywords—CT, Reconstruction, Metal artifact reduction, Compound Poisson

I. INTRODUCTION

Streak artifacts caused by metal objects such as dental fillings, surgical instruments, and orthopedic hardware may obscure important diagnostic information in X-ray computed tomography (CT) images. Radiotherapy planning is often times flawed or even rendered impossible if the structures of interest, that are to be segmented in the planning CT, lie on the same imaging plane as high-density objects inside the patient's body [1]. Plans are inaccurate due to the streak artifacts that result from the photon starvation along the X-ray paths traversing the metal objects. Filling the metal-affected regions with data that produce an overall smooth image is not sufficient to restore all the image details. In order to improve the image quality of radiotherapy planning CTs for patients with metal implants or fillings, we proposed to complete the kilovoltage (kV) projection data with selectively acquired Megavoltage (MV) projection data.

Recent radiotherapy devices often include detectors for both kV and MV cone beam CT imaging [2]. Since the high-energy MV X-ray beam does not suffer from photon starvation, a combination of the on-board imaging devices may provide a streak-free and high-resolution CT reconstruction even for the

soft tissue that is in the same image plane as the metal objects. In addition, the multi-leaf collimators on the radiotherapy device allow restriction of the additional MV acquisition onto the metal implants, and thus the improvement of image quality can be achieved at a moderate dose increase for the patient [3].

The new challenge in image reconstruction is how to modify the MV projection data so that it can be used to complete the missing information in the kV projections. A lower energy MV X-ray spectrum may provide higher soft tissue contrast, higher quantum detection efficiency, and lower radiation doses to the patient. However, the low energy MV X-ray spectrum may have beam hardening artifacts caused by the high density metal object [4]. The wide spectrum of the MV X-ray beam also causes higher noise, especially when using the current energy integrating detector rather than novel photon counting detectors [5]. In this study, we investigated the use of statistical reconstruction methods for kV/MV combined imaging to achieve better image quality using relatively lower MV energy.

II. METHODS

A. Measurement model

The expected X-ray energy integrating signal measured in the projections is

$$E(Y_i^{\text{CP}}) = \int \varepsilon \eta(\varepsilon) b_i(\varepsilon) e^{-[\mathbf{A}\mu(\varepsilon)]_i} d\varepsilon, \quad (1)$$

where $b_i(\varepsilon)$ denotes the number of X-ray photons of the i th ray (pixel) at the energy ε , $\eta(\varepsilon)$ denotes the energy-dependent detector quantum efficiency, $[\mathbf{A}\mu]_i$ denotes the discrete line integral in matrix form, and $\mu(\varepsilon)$ denotes the energy-dependent X-ray attenuation coefficients of the object.

The energy integrating detector signal follows the Compound Poisson (CP) statistical model [6], [7]:

$$Y_i^{\text{CP}} \sim \int \varepsilon \text{Poisson}\{\eta(\varepsilon) b_i(\varepsilon) e^{-[\mathbf{A}\mu(\varepsilon)]_i} d\varepsilon\} + n_i, \quad (2)$$

where n_i denotes additive signals (e.g. electronic noise) that are often modeled as a Gaussian random variable $\mathcal{N}(r_i, \sigma_i^2)$. When the X-ray energy is low (around 100kVp), the energy integrating effect is small. Then it is appropriate to use the simple Poisson (SP) model for the detector signal as

$$Y_i^{\text{SP}} \sim \text{Poisson}\left\{\int \eta(\varepsilon) b_i(\varepsilon) e^{-[\mathbf{A}\mu(\varepsilon)]_i} d\varepsilon\right\} + n_i, \quad (3)$$

Unlike SP, the mean and variance of the CP model are different. The variance of the CP signal is

$$\text{Var}(Y_i^{\text{CP}}) = \int \varepsilon^2 \eta(\varepsilon) b_i(\varepsilon) e^{-[\mathbf{A}\mu(\varepsilon)]_i} d\varepsilon. \quad (4)$$

This work is supported by the NIH Grant 5R01CA138426-05.

Meng Wu is with the Department of Electrical Engineering, Stanford University, Stanford, CA, 94305, USA, e-mail: mengwu@stanford.edu.

Dragos Constantin and Josh Star-Lack are with Varian Medical Systems, Inc. Palo Alto, CA, 94304, USA, e-mail: dragos.constantin@varian.com and Josh.StarLack@varian.com.

Rebecca Fahrig is with the Department of Radiology, Stanford University, Stanford, CA, 94305, USA, e-mail: fahrig@stanford.edu.

There is no explicit probability mass function of the CP distribution, and the likelihood function is very complicated. One way to simplify the noise model is to scale the signal, such that the mean and the variance of the signal are equal [7]. Then we can approximate the scaled CP signal

$$\tilde{Y}_i = \frac{Y_i^{\text{CP}}}{\epsilon} \sim \text{Poisson}\left\{\frac{1}{\epsilon} \int \epsilon \eta(\epsilon) b_i(\epsilon) e^{-[\mathbf{A}\mu(\epsilon)]_i} d\epsilon\right\} \quad (5)$$

with the SP model, under which the maximum likelihood reconstruction method is developed. The scale factor ϵ is given by

$$\epsilon = \sqrt{\frac{\text{Var}(Y^{\text{CP}})}{\mathbb{E}(Y^{\text{CP}})}}. \quad (6)$$

Using the mean energy of the X-ray spectrum is usually good enough. If the output spectra do not vary very much, one ϵ value can be applied to the entire set of data. For the SP model, the scaling is equivalent to $\epsilon = 1$.

B. kV/MV penalized weighted least squares (PWLS)

The PWLS algorithm has been used for dual-energy (DE) X-ray CT iterative reconstruction under the assumption that both beams are monochromatic. The algorithm forms a quadratic approximation of the Poisson log-likelihood function and minimizes piecewise differences of the image at the same time [8], [9]. The DE PWLS algorithm with proper modification may also be applicable for kV/MV image reconstruction. Ideally, the DE PWLS algorithm minimizes the object function

$$\Phi(\mu(\epsilon)) = \|\mathbf{A}^{\text{kV}}\mu(\epsilon^{\text{kV}}) - l^{\text{kV}}\|_{w^{\text{kV}}}^2 + \|\mathbf{A}^{\text{MV}}\mu(\epsilon^{\text{MV}}) - l^{\text{MV}}\|_{w^{\text{MV}}}^2 + \beta R(\mu(\epsilon)). \quad (7)$$

where \mathbf{A}^{kV} and \mathbf{A}^{MV} denote projection matrices for the two geometries. The least-squares weights w_i and logged sinogram l_i are computed as

$$w_i = \frac{\{Y_i - r_i\}_+^2}{\epsilon Y_i + \sigma_i^2}, \quad l_i = \log\left(\frac{\int \epsilon b_i(\epsilon) \eta(\epsilon) d\epsilon}{\max\{Y_i - r_i, s\}}\right), \quad (8)$$

where r_i and σ_i^2 denote the mean and variance of the additive signals, s is a small positive number. The argument R is the regularization function of the image. The Huber function of the 6 neighboring pixel differences is used as the penalty function of image roughness in this study.

Both $\mu(\epsilon^{\text{kV}})$ and $\mu(\epsilon^{\text{MV}})$ denote the linear attenuation coefficients of same scan object at different x-ray energies ϵ^{kV} and ϵ^{MV} , and have to be reconstructed together. However, unlike the conventional dual-energy CT system, the kV and selective MV system has only one complete set of projection data. One complete sinogram is not sufficient to reconstruct two density maps of the two basis materials directly as in [8]. To overcome this limitation, we fixed the ratios of the soft tissue and bone. Thus, only one combined density must be solved. We first computed the fraction maps of two materials from a prior image using a metal artifact reduction (MAR) reconstruction [10]. Then the ratios of the densities between the soft tissue

and the bone are fixed throughout the iterative reconstruction. The fraction maps of two base materials are given by

$$f_{\text{soft},j} = \begin{cases} 1 & \text{if } \mu_j^{(0)} \leq \mu_{\text{soft}}^{\text{kV}} \\ \frac{\mu_{\text{bone}}^{\text{kV}} - \mu_j^{(0)}}{\mu_{\text{bone}}^{\text{kV}} - \mu_{\text{soft}}^{\text{kV}}} & \text{if } \mu_{\text{soft}}^{\text{kV}} < \mu_j^{(0)} < \mu_{\text{bone}}^{\text{kV}} \\ 0 & \text{if } \mu_j^{(0)} \geq \mu_{\text{bone}}^{\text{kV}} \end{cases} \quad (9)$$

$$f_{\text{bone},j} = 1 - f_{\text{soft},j},$$

where $f_{\text{soft},j}$ and $f_{\text{bone},j}$ denote the fractions of soft tissue and bone of the j th voxel, and $\mu_j^{(0)}$ denotes the attenuation coefficient value in the prior reconstruction. $\mu_{\text{soft}}^{\text{kV}}$ and $\mu_{\text{bone}}^{\text{kV}}$ are linear attenuation coefficients of the soft tissue and the bone at the effective energy ϵ^{kV} of the kV X-ray. Thus the linear attenuation coefficients of the object can be expressed as

$$\begin{aligned} \mu_j(\epsilon^{\text{kV}}) &= (m_{\text{soft}}^{\text{kV}} f_{\text{soft},j} + m_{\text{bone}}^{\text{kV}} f_{\text{bone},j}) \rho_j = m_j^{\text{kV}} \rho_j \\ \mu_j(\epsilon^{\text{MV}}) &= (m_{\text{soft}}^{\text{MV}} f_{\text{soft},j} + m_{\text{bone}}^{\text{MV}} f_{\text{bone},j}) \rho_j = m_j^{\text{MV}} \rho_j, \end{aligned} \quad (10)$$

where m_j^{kV} and m_j^{MV} denote the pre-computed combined mass attenuation coefficient of the j th voxel for the kV and MV spectrum, and ρ_j denotes the combined density of the scanned object that is unknown. Because the PWLS method is based on the monochromatic X-ray assumption, it is not necessary to segment out the metal object that is only covered by the MV data.

By fixing the fractions of the two base materials, we obtain the following object function for the kV/MV imaging:

$$\Phi(\rho) = \|\mathbf{A}^{\text{kV}} \mathbf{M}^{\text{kV}} \rho - l^{\text{kV}}\|_{w^{\text{kV}}}^2 + \gamma \|\mathbf{A}^{\text{MV}} \mathbf{M}^{\text{MV}} \rho - l^{\text{MV}}\|_{w^{\text{MV}}}^2 + \beta R(\mathbf{M}^{\text{kV}} \rho) \quad (11)$$

Matrices \mathbf{M}^{kV} and \mathbf{M}^{MV} are diagonal matrices of the combined kV and MV dependent mass attenuation coefficients (10). The parameter γ magnifies the MV soft tissue contrast to ensure that the kV/MV PWLS method has more uniform impulse response. The scaling factor γ also it increases the impact of the noise in the MV data on the final reconstruction, but the soft tissue contrast is more desirable in this study.

C. kV/MV polychromatic maximum likelihood (PML)

Using a lower energy MV X-ray spectrum (e.g. 2.5 MVp instead of 6 MVp) may increase beam hardening due to the energy-dependent attenuation coefficients of the metal object. The kV/MV PWLS method, based on the monochromatic assumption, may not be able to correct the beam hardening artifacts. Hence, we studied a statistical polychromatic reconstruction method [7], [9] to correct the beam hardening artifacts when using relatively low energy MV X-rays. Similar to the kV/MV PWLS method, the object function of the PML method is

$$\begin{aligned} \Phi(\rho) &= \sum_i \left(Y_i^{\text{kV}} \log \hat{Y}_i^{\text{kV}}(\rho) + \hat{Y}_i^{\text{kV}}(\rho) \right) \\ &+ \gamma \sum_i \left(\frac{Y_i^{\text{MV}}}{\epsilon} \log \frac{\hat{Y}_i^{\text{MV}}(\rho)}{\epsilon} + \frac{\hat{Y}_i^{\text{MV}}(\rho)}{\epsilon} \right) + \beta R(\mathbf{M}^{\text{kV}} \rho) \end{aligned} \quad (12)$$

where $\hat{Y}_i^{\text{kV}}(\rho)$ and $\hat{Y}_i^{\text{MV}}(\rho)$ are computed using Eqn. (1). The SP likelihood function is used for the kV projections for simplicity. The material fraction maps are extended to more than two materials, because the metal objects have to be segmented out and used for beam hardening prediction in Eqn. (1). The calculation of the material fraction maps is similar to Eqn. (10) with more than two thresholds.

D. MV energy comparison

To compare the efficiency of MV X-ray beams with different energies, the Cramer-Rao Lower Bound (CRLB) for estimating soft tissue changes in the projection signal is used. The Fisher information of the x-ray projection signal with SP distribution in Eqn. (3) is

$$I(t) = -\mathbf{E}_t \left[\frac{\partial^2}{\partial t^2} \log p(Y \parallel \hat{Y}(t)) \right] = \frac{1}{\hat{Y}(t)} \left(\frac{\partial \hat{Y}(t)}{\partial t} \right)^2 \quad (13)$$

where $p(Y \parallel \hat{Y}(t))$ denotes the probability density function of the detector signal Y with mean parameter $\hat{Y}(t)$, and t denotes a small soft tissue thickness change along the X-ray paths. The mean parameter is given by

$$\hat{Y}(t) = B \int \eta(\varepsilon) \hat{b}(\varepsilon) e^{-t\mu_{\text{soft}}(\varepsilon) - q(\varepsilon)} d\varepsilon, \quad (14)$$

where B denotes the total photon counts of the attenuated X-ray beam, $\hat{b}(\varepsilon)$ denotes the normalized x-ray spectrum, and $q(\varepsilon)$ denotes the total amount of attenuation of X-rays passing through the patient body, which are assumed to be constants when computing the CRLB

$$\frac{\partial \hat{Y}(t)}{\partial t} = -B \int \eta(\varepsilon) \hat{b}(\varepsilon) \mu_{\text{soft}}(\varepsilon) e^{-t\mu_{\text{soft}}(\varepsilon) - q(\varepsilon)} d\varepsilon. \quad (15)$$

Insert Eqn. (14) and Eqn. (15) into Eqn. (13), and we can obtain the CRLB of the soft tissue signal for a given spectrum using the SP model

$$\text{CRLB}^{\text{SP}}(t \parallel B, \hat{b}(\varepsilon)) \approx \frac{1}{B} \frac{\int \eta(\varepsilon) \hat{b}(\varepsilon) e^{-q(\varepsilon)} d\varepsilon}{\left(\int \eta(\varepsilon) \hat{b}(\varepsilon) \mu_{\text{soft}}(\varepsilon) e^{-q(\varepsilon)} d\varepsilon \right)^2}, \quad (16)$$

and the CRLB using the CP model is further corrupted by the additional noise caused by the energy integrating effect. We approximate the CRLB of CP by replacing the mean and variance terms

$$\text{CRLB}^{\text{CP}}(t \parallel B, \hat{b}(\varepsilon)) \approx \frac{1}{B} \frac{\int \varepsilon^2 \eta(\varepsilon) \hat{b}(\varepsilon) e^{-q(\varepsilon)} d\varepsilon}{\left(\int \varepsilon \eta(\varepsilon) \hat{b}(\varepsilon) \mu_{\text{soft}}(\varepsilon) e^{-q(\varepsilon)} d\varepsilon \right)^2}. \quad (17)$$

E. Simulations

A numerical dental phantom including two metal fillings is used in the simulation in order to assess the ability to recover missing information. The phantom contains one gold and one amalgam filling with diameters about 5 mm. The phantom

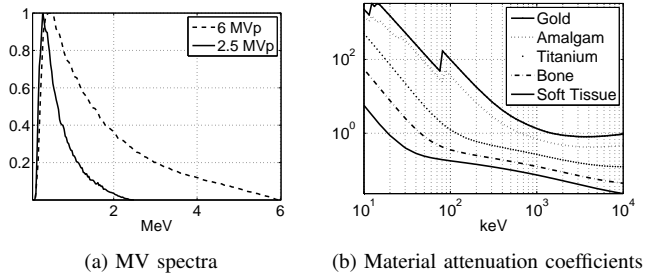


Fig. 1: X-ray spectra and material attenuation coefficients used in the simulations. (a) 2.5 MVp and 6 MVp spectra. (d) Energy dependent attenuation coefficient of soft tissue, bone, titanium, amalgam, and gold.

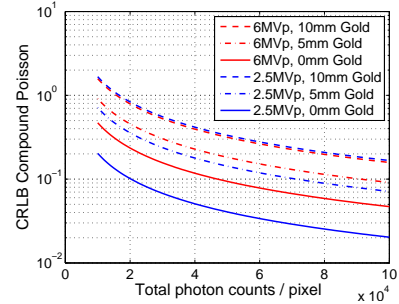


Fig. 2: The CRLB values as a function of total photon counts / pixel for 2.5 MVp and 6MVp x-ray beam penetrating different thicknesses of gold.

also features two bar-shaped soft tissue patterns. The soft tissue pattern uses adipose tissue that is 150 HU smaller than the surrounding soft tissue material. All anatomical features are specified as materials whose energy-dependent attenuation profile is derived from the NIST database. The cone-beam CT projections were simulated based on the TrueBeam radiotherapy system (Varian Medical System, Palo Alto, CA). The collimated kV and MV detectors data contain 512×16 pixels with 0.768 mm and 0.784 mm widths, respectively. Both the beams have 480 projections for a 360° rotation. The source-to-detector distance is 1000 mm, and the source-to-axial distance is 500 mm. The reconstructed volume has $400 \times 400 \times 6$ voxels with spacing of 0.4 mm \times 0.4 mm \times 2 mm.

The simulation used a 120 kVp spectrum (mean: 54.7 keV, standard deviation: 19.9 keV) to generate kV projections. A 2.5MVp beam (mean: 677 keV, standard deviation: 428 keV) and a 6 MVp beam (mean: 1.66 MeV, standard deviation 1.24 MeV) were used to generate the MV projections. The normalized MV spectra are shown in Figure 1. The MV detector was assumed to be made by 1.5 cm thick CdWO_4 pixelated scintillators with total 20% loss. The MV projections were restricted to the shadow that the fillings cast onto the detector, plus a margin of 3 pixels to each side. The X-ray beam intensities are 4×10^5 counts / pixel for the kV projection, 6×10^4 counts / pixel for the 2.5 MVp beam, and 6×10^4 counts / pixel for the 6 MVp beam. The parameters $\gamma = 30(\text{PWLS})/100(\text{PML})$ and $\beta = 1 \times 10^4$ for both the MV X-ray spectra and the reconstruction methods. Separable quadratic surrogate with 16 ordered subsets is used to optimize the object

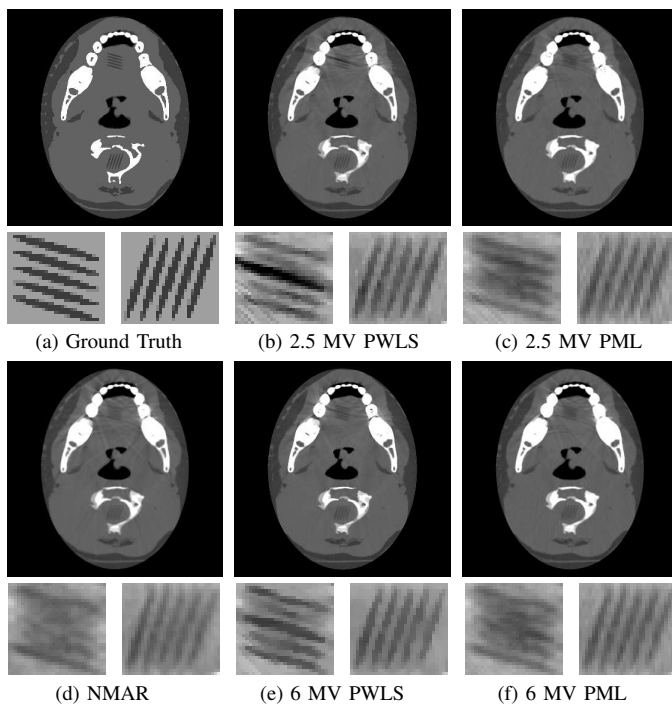


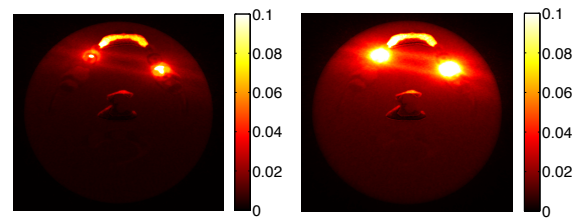
Fig. 3: Image reconstruction results. The images are displayed at the window level $[-400, 800]$ HU, and ROI images are displayed at the window level $[-200, 200]$ HU. The NAMR image is reconstructed using the normalized metal artifact reduction method [10].

functions of the kV/MV PWLS and the PML methods [9].

III. RESULTS

Figure 2 shows the CRLB values as a function of total photon counts / pixel for the 2.5 MVp and 6 MVp X-ray beam penetrating different thicknesses of gold. The patient has thickness of 20 cm soft tissue and 2 cm bone. When the metal thicknesses are 0 mm and 5 mm, the 2.5 MVp beam has a smaller CRLB than 6 MVp beam using the CP model. The two MV beams have similar CRLB values when the thickness of the gold object is 10 mm. Because most of the photons in the 2.5 MVp spectrum are blocked by the gold, and more photons in the 6 MVp beam reach the detector. The larger number of detected photons cancels the drawback of energy integrating effect of the 6 MVp beam.

Figure 3 shows the reconstructed images using our proposed image reconstruction methods. Two regions of interest (ROI) of the soft tissue patterns are displayed below each image. The left ROI image is the upper soft tissue pattern that is between the two metal fillings. Both the iterative reconstruction methods could effectively reduce streak artifacts and recover the missing soft tissue information in the kV data. The images using 2.5 MVp X-ray beam have similar soft tissue contrast as using 6 MVp beam. However, the PWLS method using 2.5 MVp beam has beam hardening artifact, the dark line between the two fillings. The PML method can effectively reduce the



(a) 2.5 MVp dose map (Gy) (b) 6 MVp dose map (Gy)

Fig. 4: MV dose distribution maps using Geant4 Monte Carlo simulations.

beam hardening artifact. The root mean squared error (RMSE) of the soft tissue patterns using the PML method and the 2.5 MVp beam are 53 HU and 45 HU. The PML images using the 6 MVp beam have similar RMSE values as those of the soft tissue patterns.

Geant4 Monte Carlo dose simulation shows that the MV dose to the patient is low due to the collimation onto the fillings. Figure 4 shows the MV dose distribution maps of the two phantoms. Using the 2.5 MVp beam delivers less radiation dose to the soft tissue and the tooth than 6 MVp beam, while providing similar the metal artifact correction results.

In conclusion, our proposed statistical image reconstruction algorithms using kV selective MV data can partially restore the lost information caused by the metal objects. The PML method allows use of a lower energy X-ray beam without having beam hardening artifacts.

REFERENCES

- [1] M. Bal and L. Spies, "Metal artifact reduction in CT using tissue-class modeling and adaptive prefiltering," *Med. Phys.*, vol. 33, no. 8, p. 2852, 2006.
- [2] H. Li, W. Giles, J. Bowsher, and F.-F. Yin, "A dual cone-beam CT system for image guided radiotherapy: initial performance characterization," *Med. Phys.*, vol. 40, p. 021912, Feb. 2013.
- [3] O. Morin, A. Gillis, M. Descovich, J. Chen, M. Aubin, J.-F. Aubry, H. Chen, A. R. Gottschalk, P. Xia, and J. Pouliot, "Patient dose considerations for routine megavoltage cone-beam CT imaging," *Med. Phys.*, vol. 34, no. 5, p. 1819, 2007.
- [4] M. R. Paudel, M. Mackenzie, B. G. Fallone, and S. Rathee, "Evaluation of metal artifacts in MVCT systems using a model based correction method," *Med. Phys.*, vol. 39, pp. 6297–308, Oct. 2012.
- [5] M. J. Tapiovaara and R. Wagner, "SNR and DQE analysis of broad spectrum X-ray imaging," *Phys. Med. Biol.*, vol. 30, pp. 519–529, June 1985.
- [6] I. A. Elbakri and J. A. Fessler, "Efficient and accurate likelihood for iterative image reconstruction in X-ray computed tomography," *Proc. SPIE Medical Imaging*, vol. 5032, pp. 1839–1850, 2003.
- [7] G. M. Lasio, B. R. Whiting, and J. F. Williamson, "Statistical reconstruction for x-ray computed tomography using energy-integrating detectors," *Phys. Med. Biol.*, vol. 52, pp. 2247–66, Apr. 2007.
- [8] P. Sukovic and N. H. Clinthorne, "Penalized weighted least-squares image reconstruction for dual energy X-ray transmission tomography," *IEEE Trans. Med. Imag.*, vol. 19, pp. 1075–81, Nov. 2000.
- [9] I. A. Elbakri and J. A. Fessler, "Statistical image reconstruction for polyenergetic X-ray computed tomography," *IEEE Trans. Med. Imag.*, vol. 21, pp. 89–99, Feb. 2002.
- [10] E. Meyer, R. Raupach, M. Lell, B. Schmidt, and M. Kachelrieß, "Normalized metal artifact reduction (NAMR) in computed tomography," *Med. Phys.*, vol. 37, no. 10, p. 5482, 2010.

Dose reconstruction for real-time patient-specific dose estimation in CT

Bruno De Man, Mingye Wu, Paul FitzGerald, Yannan Jin, Zhye Yin, Peter M Edic, Yangyang Yao, Xiaoyu Tian, Ehsan Samei

Abstract— We present a new method for *reconstructing* absorbed dose on a per voxel basis, directly from the actual projection data. While the method is approximate, preliminary results indicate that the method may offer a favorable tradeoff between computational efficiency and accuracy. From the volumetric dose estimates, traditional dose metrics such as organ dose, skin dose, average absorbed dose and effective dose can readily be computed without requiring a quantum-based approach such as Monte Carlo. This method will not replace measurements or Monte Carlo approaches but we expect that it will prove useful in applications where real-time patient-specific dose estimation is required.

Keywords—*Computed Tomography, Radiation dose.*

I. INTRODUCTION

X-ray computed tomography (CT) has become one of the most widespread diagnostic tools in medicine. While clinically invaluable, CT's associated radiation dose now makes up a significant portion of the overall population dose [1]. Increased awareness has driven CT vendors and users alike to improve the design and use of CT by optimizing the scan region, tube current, tube voltage, x-ray detection and reconstruction (Figure 1).

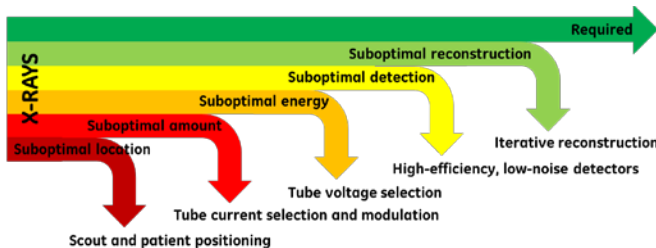


Figure 1: Opportunities for dose reduction in CT design and clinical use.

An important factor in minimizing dose is the ability to *estimate* it. Assessing dose levels can be useful in multiple contexts:

- Research and development of CT hardware and algorithms
- Prospectively, before the clinical user decides

Bruno De Man (deman@ge.com), Paul FitzGerald, Yannan Jin and Zhye Yin are with the CT Systems and Application Laboratory, GE Global Research, Niskayuna, NY. Peter M Edic is with the CT, X-ray and Functional Imaging organization, GE Global Research, Niskayuna, NY. Yangyang Yao and Mingye Wu are with the X-ray and CT Laboratory, GE Global Research, Shanghai, China. Xiaoye Tian and Ehsan Samei are with Medical Physics, Biomedical Engineering, Duke University, Durham, NC

to go ahead with the scan

- Prospectively, as part of an automated or manual scan planning process
- Retrospectively, to report the dose that was used during a scan

Depending on the purpose, time may be an important factor and time-consuming dose estimation methods may need to be substituted with more approximate but faster techniques. In other situations, accuracy may be more important, and organ-by-organ estimates may be desired.

Several methods exist for estimating dose in CT [2]. The CT dose index (CTDI) metric uses a pencil ionization chamber positioned at discrete locations inside a fixed-size circular PMMA phantom. The size-specific dose estimate (SSDE) metric applies patient size-dependent correction factors to CTDI values, for a more relevant estimate of dose in the specific patient. Obviously, cylindrical phantoms are crude approximations of patient anatomy and don't offer doses specific to individual organs. In an era of increased focus towards precision medicine (and precision imaging), including patient-specific and organ-specific scan optimization [3], the CTDI and SSDE metrics are severely limited.

Monte Carlo (MC) simulation is generally considered as the gold standard for CT dose estimation [4]. MC-based approaches produce voxel-based estimates of the absorbed dose, from which average absorbed dose, risk indices, effective dose, and organ doses can be computed. However, their quantum nature makes them noisy and computationally expensive. Massive parallelization such as using graphics cards (GPU) may make them more practical [5].

In this work, we propose a new approach for CT dose estimation, inspired by numerical ray tracing operations. The goal was to make a patient-specific voxel-based estimate without the overhead of a quantum-based approach. While the approach is based on significant approximations, we hypothesize that it is still substantially more accurate than lookup-based approaches such as CTDI and SSDE. Section II gives a detailed description of the new approach. Section III contains initial evaluation results.

II. METHODS

A. Projection-domain dose estimation

The proposed method is best understood from the patient's perspective. Reasonable questions to ask about an x-ray beam are: (1) how much energy is *applied* to the patient, (2) how much energy *interacts* with the patient and (3) how much energy is *absorbed* in the patient. The applied energy is defined as the x-ray energy arriving at the patient in a given x-ray beam (E_{incident} in Figure 1). Some of that energy will go straight through the patient ($E_{\text{transmitted}}$), some of it will be absorbed (E_{absorbed}), and some of it will be scattered ($E_{\text{scattered}}$). A large portion of the scattered x-rays will be absorbed elsewhere in the patient, but some will escape from the patient.

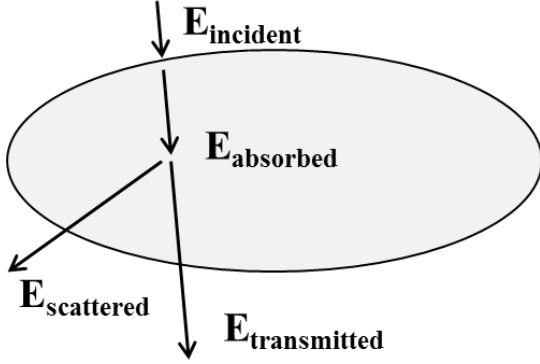


Figure 2: Schematic view of interaction processes of an x-ray beam with a patient.

We define the *interaction energy* as the energy that interacts with the patient, either through scattering or through absorption. It is the amount of energy that was removed from the primary beam prior to reaching the detector, by a combination of the physical attenuation processes in the patient (photo-electric absorption, Compton scatter and, in the case of high energies, pair formation). This can be readily computed by subtracting the transmitted energy from the applied energy, both of which can be derived from the detected signals, with and without the patient in the scanner. In the case of an energy-integrating detector, the detected signal is simply the total energy absorbed by the detector. In the case of a photon-counting detector, an energy-weighted sum over all energy bins would yield a similar estimate. Figure 3 shows the air signal (I_{air}) and the transmitted signal ($I_{\text{transmitted}}$) for a single CT view. Integrating the interaction energy across all detector channels results in the total interaction energy for a particular x-ray projection measurement or view. The striped area in Figure 3 is a measure for the total interaction energy for that view.

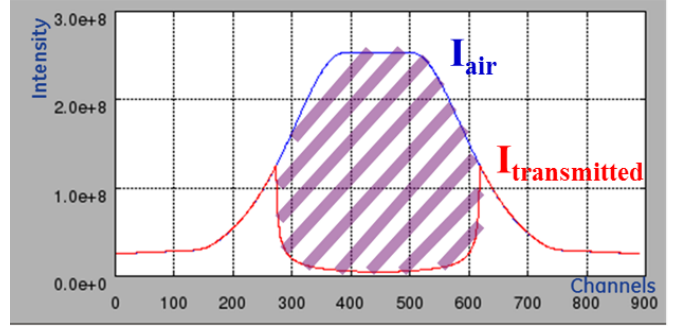


Figure 3: Air signal and transmitted signal for a single CT view.

Absorbed dose is defined as ‘absorbed’ energy per unit mass. We hypothesize that the interaction energy is ‘correlated’ (not equal) to the absorbed energy: the first includes scattered energy and the latter does not. However, we hypothesize that for certain scan parameters there exists a monotonic relationship between absorbed energy and interaction energy, hence making it possible to use the latter to estimate the former. The fact that most scattered x-rays are absorbed elsewhere (and most likely nearby) may be a good justification for this. A detailed description of this projection-domain dose estimation is presented in [6].

B. Dose reconstruction

We now take this idea a step further and apply it to each piece of tissue the x-ray beam encounters. We first consider a single x-ray beam with energy $E_{\text{inc}(0)}$ as it enters the first row or slab in the image with attenuation μ , voxel size d and incidence angle θ . The energy interacting with the first row in the image is computed as

$$E_{\text{abs}(1)} = E_{\text{inc}(0)} * (1 - \exp(-\mu * d / \cos\theta)), \quad (1)$$

and the remaining energy as the beam enters the next row is computed as (see Figure 4):

$$E_{\text{inc}(1)} = E_{\text{inc}(0)} * \exp(-\mu * d / \cos\theta). \quad (2)$$

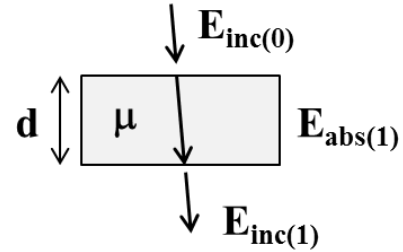


Figure 4: Schematic view of interaction processes of an x-ray beam with a slab of thickness d and linear attenuation coefficient μ .

Typically, a given voxel will only account for a portion of the absorbed energy $E_{\text{abs}(1)}$, proportional to its footprint in the beam compared to the footprint of the entire beam. The challenge is to define an algorithm that correctly tracks energy losses as a beam propagates through the voxel grid. At the same time, the lost energy needs to be distributed correctly across the corresponding voxels. We impose the following two criteria: (1) after propagating through the entire voxel grid, the energy loss should be consistent with

the loss computed from the line integral through that voxel grid (sum of the losses equals the loss over the sum) and (2) for a uniform/smooth phantom and a uniform/smooth flux profile, the dose distribution should also be uniform/smooth.

One approach is to start from a ray-driven projector, such as Siddon's intersection-length method [7] or Joseph's interpolation-based method [8], and deposit the corresponding energy losses in the respective voxels. For instance, for Joseph's method, the incremental energy deposited in voxel j may be computed as

$$E_{abs(j)} = E_{abs(j)} + a_{i,j} * E_{inc(n)} * (1 - \exp(-\mu_{eff} * d / \cos\theta)) \quad (3)$$

$$\mu_{eff} = a_{i,j} * \mu_j + a_{i,j+1} * \mu_{j+1} \quad \text{with} \quad a_{i,j} + a_{i,j+1} = 1 \quad (4)$$

where $a_{i,j}$ is the interpolation coefficient for voxel j and ray i , and $E_{inc(n)}$ is the beam energy after penetration through the previous slab. However, in order to satisfy the second criterion of uniformity and smoothness, the result needs to be normalized. Thus for each view, we compute

$$E_{abs(j)} = E_{abs(j)} / \sum_i a_{i,j}. \quad (5)$$

For Siddon's method a similar type of normalization can be applied.

We've chosen a distance-driven implementation [9], since it naturally takes care of the normalization.

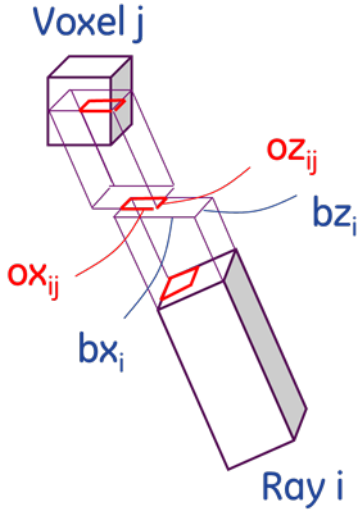


Figure 5: Geometric illustration of overlap coefficients for voxel j and ray i .

The distance-driven overlap kernel (Figure 5) was used to compute the relative footprint of a voxel inside the beam, so the interaction energy for voxel j from beam i is computed as

$$E_{abs(j)} = (ox_{ji} * oz_{ji}) / (bx_i * bz_i) * E_{inc(n)} * (1 - \exp(-\mu_j * d / \cos\theta)), \quad (6)$$

where ox_{ji} and oz_{ji} are the overlap coefficients between voxel j and beam i in the x and z direction, respectively, and bx_i and bz_i are the beam widths of beam i in the x and z direction, respectively. The linear attenuation coefficient μ is obtained from a CT reconstruction (either filtered backprojection or iterative reconstruction). Note that the sum of all interaction energies across the slabs equals the

total interaction energy from the sinogram based method, since

$$1 - \exp(-p_1) + \exp(-p_1)(1 - \exp(-p_2)) + \exp(-p_1 - p_2)(1 - \exp(-p_3)) + \dots = 1 - \exp(-p_1 - p_2 - p_3 - \dots), \quad (6)$$

where p_i is attenuation at the i^{th} row of image. We assumed above that the projection is more vertical, hence we track the beam from row to row (in y) (from xz -slab to xz -slab). For projections that are more horizontal, the same procedure is followed from column to column (or from yz -slab to yz -slab), and the index x is replaced by y , similar to the standard distance-driven approach [9].

III. RESULTS AND DISCUSSION

The projection-domain dose estimation was previously [6] demonstrated to have good correspondence with Monte Carlo based results, as illustrated in Figure 6.

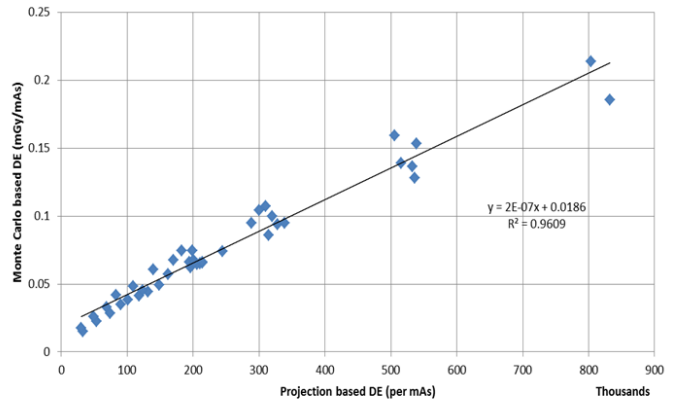


Figure 6: Transfer function from projection-domain dose estimates to Monte Carlo dose estimates. The results were obtained for a helical body phantom including a variety of tube voltages (80,100,120,140kVp) and tube currents.

Figure 7 shows a 2D dose reconstruction for a single view for a simple phantom consisting of two embedded squares with different attenuation. The x-ray source location for this view was at the top center; green reflects the highest absorbed dose and red reflects zero absorbed dose. As expected, the dose decreases rapidly as x-rays propagate through the phantom, and it increases with local density.

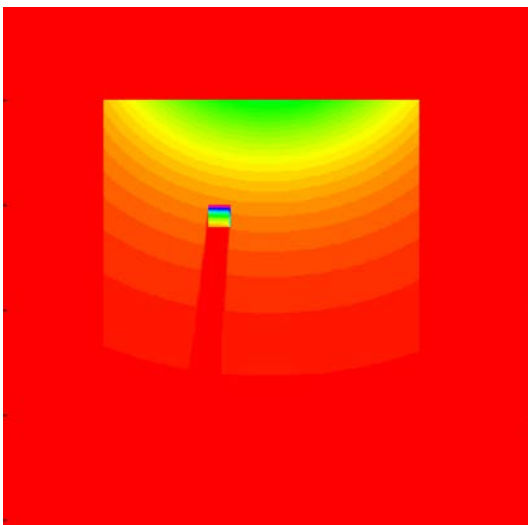


Figure 7: 2D dose reconstruction for a single view for a simple phantom consisting of two embedded squares.

Figure 8 shows a 3D dose reconstruction for a clinical CT scan. Yellow represents the highest absorbed dose (near the skin) and black represents zero absorbed dose (in air).

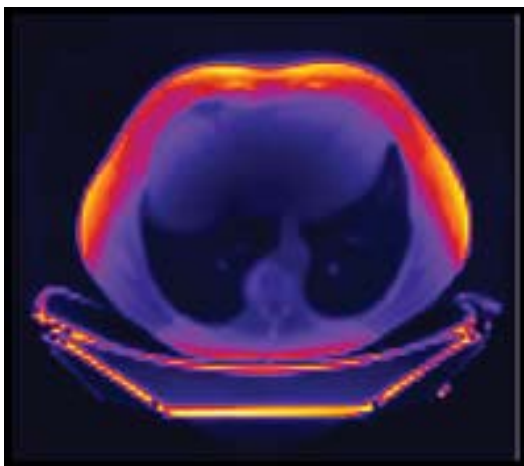


Figure 3: 3D dose reconstruction for a clinical CT scan of the thorax. Yellow is highest dose and black is lowest dose.

While the methodology is already implemented, we still need to apply a conversion from interaction energy to dose. This conversion is currently implemented as a single scale factor. However, accuracy could be further improved by empirically compensating for the scatter effect. For example, more photons are likely to scatter out of the patient for interactions near the edge of the patient's skin than deep within the patient. Potential uncertainty associated with the scatter in and out of the projection plane also needs to be quantified.

To compute absorbed dose, we normalize the interaction energy by mass. The mass in each voxel is estimated from μ , obtained from the reconstructed image:

$$m = \mu / (\mu/\rho) * v \quad (7)$$

with (μ/ρ) the estimated mass attenuation coefficient and v the voxel volume.

If a good estimate of the spectrum is available, the polychromatic nature of the x-rays can be taken into account as well. The spectrum is divided in a number of energy bins, and the above procedure is repeated for each energy bin. The total dose is the sum of the doses at each energy.

More rigorous validation based on comparison to a Monte Carlo baseline is in progress and is planned to be presented at the time of the conference. The current 3D dose reconstruction implementation is based on a monochromatic single-material model and will be extended to a polychromatic multi-material model. Finally, our goal is to optimize the accuracy by including location dependent scatter correction factors.

We have presented a new approach for fast, patient-specific estimation of CT dose in each voxel. We hope that this approach will prove useful in real-time or quasi-real-time applications, such as organ dose, skin dose and effective dose prediction and reporting.

REFERENCES

- [1] R. Fazel, H. M. Krumholz, Y. Wang, J. S. Ross, J. Chen, H. H. Ting, N. D. Shah, K. Nasir, A. J. Einstein, and B. K. Nallamothu, "Exposure to low-dose ionizing radiation from medical imaging procedures.," *N. Engl. J. Med.*, vol. 361, pp. 849–857, 2009.
- [2] H. H. Knox and R. M. Gagne, "Alternative Methods of Obtaining the Computed Tomography Dose Index," *Health Phys.*, vol. 71, no. 2, 1996.
- [3] J. Sperl, D. Beque, B. Claus, B. De Man, B. Senzig, and M. Brokate, "Computer-assisted scan protocol and reconstruction (CASPAR)-reduction of image noise and patient dose.," *IEEE Trans. Med. Imaging*, vol. 29, no. 3, pp. 724–32, Mar. 2010.
- [4] A. Ding, J. Gu, A. V Trofimov, and X. G. Xu, "Monte Carlo calculation of imaging doses from diagnostic multidetector CT and kilovoltage cone-beam CT as part of prostate cancer treatment plans.," *Med. Phys.*, vol. 37, pp. 6199–6204, 2010.
- [5] W. Chen, D. Kolditz, M. Beister, R. Bohle, and W. A. Kalender, "Fast on-site Monte Carlo tool for dose calculations in CT applications," *Medical Physics*, vol. 39, p. 2985, 2012.
- [6] X. Tian, Z. Yin, B. De Man, and E. Samei, "Projection-based dose metric: accuracy testing and applications for CT design," pp. 866829–866829–9, Mar. 2013.
- [7] R. L. Siddon, "Fast calculation of the exact radiological path for a three-dimensional CT array.," *Med. Phys.*, vol. 12, no. 2, pp. 252–255, 1985.
- [8] P. M. Joseph, "An Improved Algorithm for Reprojecting Rays through Pixel Images.," *IEEE Trans. Med. Imaging*, vol. 1, pp. 192–196, 1982.
- [9] B. De Man and S. Basu, "Distance-driven projection and backprojection in three dimensions," *Phys. Med. Biol.*, vol. 49, no. 11, pp. 2463–2475, 2004.

CT Protocol Optimization at the Dawn of Iterative Reconstruction: Challenges and Solutions

Ke Li, Jie Tang and Guang-Hong Chen

Abstract—The past decade has witnessed tremendous advances in CT technology, among which iterative reconstruction (IR) algorithms have drawn much recent attention due to the promise of generating clinically acceptable CT images at very low dose levels. However, the nonlinear nature of IR has brought new challenges to the optimization of CT scanning protocols, as the dependence of CT image quality and diagnostic performance on CT scanning parameters have been fundamentally modified. This work features a new experimental framework that aims at addressing these challenges. It enables various aspects of the physical characteristics of IR images to be accurately measured and their dependences on CT scanning parameters to be understood. The method offers a potential solution to the task-based CT protocol optimization for IR with the goal of maximizing diagnostic performance with the lowest possible radiation dose.

I. INTRODUCTION

CT iterative reconstruction (IR) algorithms have drawn much attention during the last decade because of the promise of generating clinically acceptable CT images at very low dose levels. While IR may offer additional flexibilities to the CT reconstruction process, its nonlinear nature has brought new challenges to the scanning process: The dependence of CT image quality and diagnostic performance on scanning parameters (e.g., exposure level, slice thickness, etc) have been fundamentally modified by IR, therefore the direct use of CT protocols developed in the era of filtered backprojection (FBP) is not appreciate for both dose and diagnostic performance considerations. As a result, CT protocols must be carefully re-optimized at the advent of IR algorithms to help fully utilize their potential in dose reduction and/or diagnostic performance improvement.

This paper reports an experimental framework that aims at addressing the challenges in optimizing CT protocols for IR. The framework is based on a task-based approach to quantify the physical characteristics of IR images. It uses image ensembles generated by consecutive CT scanning of anthropomorphic physical phantoms of different sizes and containing lesions of different sizes/contrast levels. To investigate the dependence of spatial resolution on CT scanning parameters in IR, ensemble averaging was performed across the repeated CT scans to reduce noise, which allows spatial resolution performance at the edges of low contrast lesions to be accurately measured

K. Li and G.-H. Chen are with Department of Medical Physics and Department of Radiology, University of Wisconsin-Madison, WI; J. Tang is with GE Healthcare, Waukesha, WI

even at low dose level. The ensemble averaging approach also relaxes the requirement of radial- and slice-averaging traditionally used to measure low-contrast spatial resolution, which enables local spatial resolution assessment at irregularly-shaped features of interest (e.g., lung/tissue interface). To investigate the dependence of noise on CT scanning parameters in IR, noise ensembles generated by the repeated CT scans are used to calculate noise standard deviation (σ) maps, which strongly depends on the local contrast level in IR. These meticulously-designed spatial resolution/noise measurements also enables further understanding of possible tradeoff relationship and their joint contributions to the overall CT image quality, which was quantified by an image domain-based and human observer-validated channelized Hotelling observer (CHO) measurement method.

II. EXPERIMENTAL METHODS

A. Data acquisition, image reconstruction and phantoms

The study used a 64-slice clinical CT scanner (Discovery CT750 HD, GE Healthcare, Waukesha, WI) equipped with both a standard reconstruction engine and a statistical model-based iterative reconstruction engine (Veo[®], GE Healthcare, Waukesha, WI) to acquire CT images of a pediatric phantom (ATOM 10-year-old pediatric phantom, Model 706, CIRS Inc., Norfolk, VA). The scanner was collimated to a 20-mm-thick section in the thoracic region of the phantom. The physical dimensions of cross-section of the phantom at this position is approximately 20 cm (AP) \times 17 cm (LR). The phantom was scanned at a fixed scanning time of 0.5 seconds and at four different mA levels (40, 80, 120, 160), which correspond to CTDI_{vol} of 3.99, 7.99, 11.98, 15.97 mGy, respectively. These exposure levels will be referred in the remainder of the paper as 25%, 50%, 75%, and 100% dose, respectively. The x-ray tube potential was fixed at 120 kV. The slice thickness and slice interval were both 0.625 mm. Each reconstruction generated a stack of 32 axial CT images. At each dose level, the CT scan was repeated for either $M = 100$ times (when low contrast inserts were used) or $M = 50$ times (otherwise).

The image quality of Veo was evaluated locally at several representative landmarks in the phantom, including a Nylon pin that connects Sections 15-16 of the pediatric phantom together and the anatomical interfaces of lung tissue/bone and lung tissue/soft tissue. In addition, a $\varnothing=37$ mm factory QA insert that fits into the phantom and contains cylindrical targets with two different contrasts values (13 HU and 33 HU) was used (Soft tissue

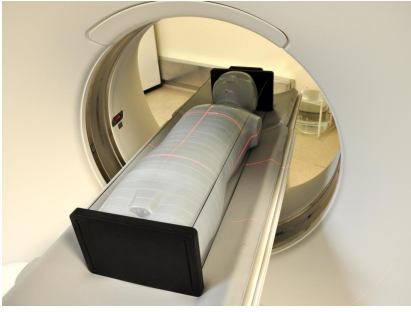


Fig. 1. The anthropomorphic pediatric phantom used in our study.

TABLE I
CT CONTRAST VALUES OF EIGHT OBJECTS IN THE PHANTOM.

	Material	Background	Contrast (HU)
Object 1	+1% Soft tissue	Soft tissue	13
Object 2	+2% Soft tissue	Soft tissue	33
Object 3	Nylon	Soft tissue	62
Object 4	Water	PMMA	120
Object 5	11.2 mg/mL I	PMMA	224
Object 6	16 mg/mL I	PMMA	346
Object 7	Soft tissue	Lung	814
Object 8	Bone	Lung	1710

insert, Model 700-QA, CIRS Inc., Norfolk, VA). Finally, a $\varnothing=38$ mm in-house acrylic phantom plug that contains $\varnothing=5.0$ mm cylindrical cavity was used to replace the QA insert. The cavity was filled with iodine solutions of three different concentrations (8, 11.2 16 mg/mL) to provide three additional contrast values. Therefore, the study covered a total of 8 contrast levels, which provides a relatively rich database for understanding the contrast dependence of various physical characteristics of Veo. The experimentally measured mean contrast values of these objects are listed in Table I.

B. Spatial resolution measurement method

This work characterized the spatial resolution of IR in the spatial domain using point spread function (PSF), which is given by taking the spatial derivative of the system edge spread function before being normalized by the area under the curve:

$$\text{PSF}(x_{\perp}) = \frac{dI(x_{\perp})/dx_{\perp}}{\int dx_{\perp} \{dI(x_{\perp})/dx_{\perp}\}} \quad (1)$$

where x_{\perp} denotes the direction running normal to an edge of interest, I denotes image pixel value with the unit of [HU]. For circular objects, any lines going through their centers are normal to their edges; for objects with irregular boundaries, the tangent lines of each point on the edge was firstly located by taking the spatial gradient of the edge central line, then the normal direction of each point on the edge was calculated from the tangent line.

While the entire PSF curve serves as a complete descriptor of spatial resolution, there is often a need to quantify the spatial resolution with a numerical figure of merit (FOM). For example, the spatial frequencies corresponding to the 50% and 10% MTF values (i.e. f_{50} and f_{10} respectively) are often used as the FOMs of spatial resolution [1]. To quantify the spatial resolution of IR using

a number, the full width at half maximum (FWHM) of the PSF was used as the FOM of spatial resolution in this work.

C. Noise measurement method

In this work, the noise standard deviation was measured locally for each imaging task from the ensembles of repeated scans by

$$\sigma(x, y) = \sqrt{\frac{1}{M-1} \sum_{i=1}^M [I_i(x, y) - \bar{I}(x, y)]^2}, \quad (2)$$

in which the mean image pixel value \bar{I} is given by

$$\bar{I}(x, y) = \frac{1}{M} \sum_{i=1}^M I_i(x, y). \quad (3)$$

D. Channelized Hotelling observer measurement method

To quantify the joint contributions of spatial resolution and noise to the final CT image, a FOM for the overall image quality is needed. This work employed the image-domain-based channelized Hotelling observer (CHO) analysis and used the CHO detectability index [2], [3] as the FOM. The CHO method has been validated by human observers to work with CT images generated by nonlinear iterative reconstruction methods [4]. In this work, the CHO method was implemented using the Gabor channel basis, which has been previous validated to have close resemblance with human observer responses [4]. Parameters of the channel basis functions (e.g., central frequency, bandwidth, cutoff frequency, etc.) were chosen to be consistent with this earlier work.

III. RESULTS

A. Dependence of spatial resolution on CT scanning parameters

Figure 2 shows that the spatial resolution of Veo strongly depends on the imaging task: the span of the PSF measured with low contrast object 1 is significantly wider than that measured with the high contrast object 7. The crossover contrast is about 200 HU at 25% exposure level. Similarly, the spatial resolution of Veo demonstrated a strong dependence on the exposure level: The FWHM of PSF always increases with decreasing exposure level, and the crossover contrast dropped to about 70 HU at 100% exposure level.

B. Dependence of noise on CT scanning parameters

Noise standard deviation (σ) maps measured locally on the objects of interest are shown in Fig. 3. Note that the display level used for the σ maps of Veo is only 31% of that of FBP, which indicates that Veo generated images with much smaller noise magnitude than FBP. However, noise in Veo images demonstrated a strong contrast dependence; edges of high contrast objects (e.g., Object 6) lead to significantly larger σ in their immediate neighborhoods

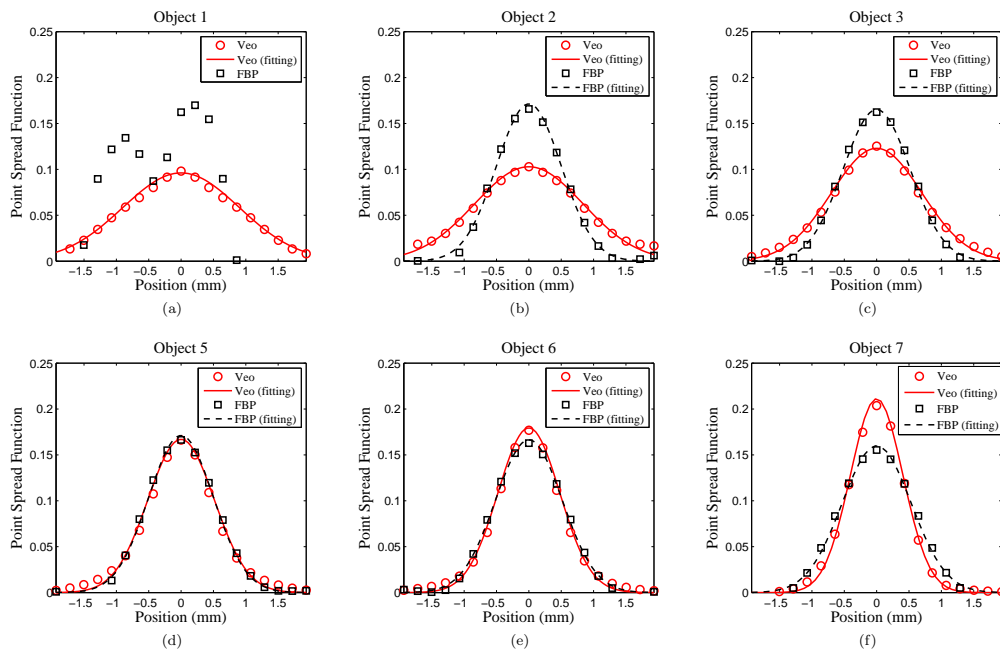


Fig. 2. Representative experimental PSF measured at 25% dose level. The FBP result of the low contrast Object 1 in (a) was too noisy to enable the (Gaussian) fitting.

(than in other areas with uniform signal level), while edges of low contrast objects (e.g., Object 4) lead to a uniform noise reduction. This suggests that noise magnitude in Veo has a strong contrast dependence even at a given exposure level. Fig. 4 summarizes this phenomenon by displaying σ as a function of both contrast and dose level. It clearly demonstrates that, in addition to the well-known dose dependence, noise of Veo images measured locally at the edge of an object increased with increasing contrast level at any x-ray exposure level.

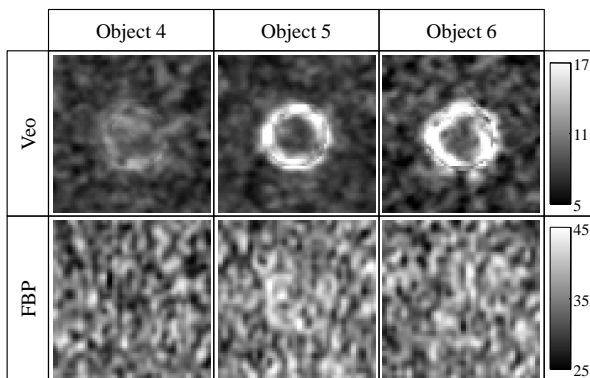


Fig. 3. Noise standard deviation (σ) maps measured at 25% dose in the neighborhood of three representative objects. Noise magnitude on the edges of these objects demonstrated a strong dependence on imaging task in IR.

Previous studies have demonstrated that Veo lead to significant noise reduction in the uniform regions of test objects [5], [6]. An immediate question based on the results in Fig. 4(a) is, how does the noise of Veo images compared with that of FBP images if the noise was strictly measured on the edges of test objects? To address this question,

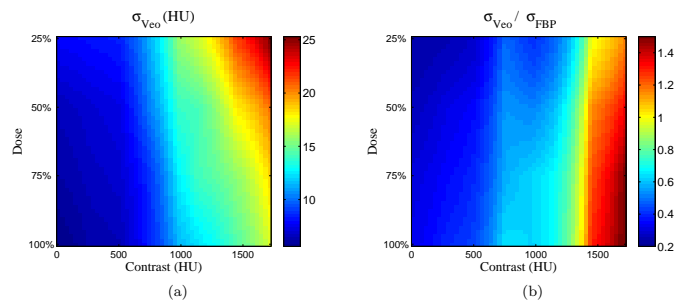


Fig. 4. Summary of dependence of noise on x-ray exposure level and imaging task. (a) Absolute σ of Veo; (b) Ratio in σ between Veo and FBP.

the noise standard deviation of Veo images (σ_{Veo}) was divided by that of FBP images (σ_{FBP}) measured at each dose/contrast level and the results are shown in Fig. 4(b). It demonstrates that, even when assessed right on the edges of test objects, in most cases Veo still lead to significant noise reduction. Only when the contrast level exceeded 1300 HU did Veo generate higher noise than FBP at the edges. The crossover contrast increased slightly with decreasing dose level.

C. Dependence of overall image quality on CT scanning parameters

Fig. 5 shows the CHO detectability indices for the detection of six different objects. The actual ROI images are provided in the figure to facilitate the readers to evaluate their image quality. For both FBP and Veo, d' increased with object contrast and radiation dose; at any contrast/dose level being tested, Veo always led to better overall CT image quality. The relative increment in d'

		Object 1 (contrast = 13 HU); W/L=40/60		Object 2 (contrast = 33 HU); W/L=60/80	
		25% dose	100% dose	25% dose	100% dose
Veo		$d' = 4.3$	$d' = 7.3$	$d' = 12.5$	$d' = 22.0$
		$d' = 2.9$	$d' = 4.2$	$d' = 7.7$	$d' = 14.5$
FBP		$d' = 31.7$	$d' = 54.4$	$d' = 72.7$	$d' = 116.2$
		$d' = 16.4$	$d' = 32.5$	$d' = 33.8$	$d' = 67.5$

		Object 4 (contrast = 99 HU); W/L=100/200		Object 5 (contrast = 224 HU); W/L=190/310	
		25% dose	100% dose	25% dose	100% dose
Veo		$d' = 31.7$	$d' = 54.4$	$d' = 72.7$	$d' = 116.2$
		$d' = 16.4$	$d' = 32.5$	$d' = 33.8$	$d' = 67.5$
FBP		$d' = 31.7$	$d' = 54.4$	$d' = 72.7$	$d' = 116.2$
		$d' = 16.4$	$d' = 32.5$	$d' = 33.8$	$d' = 67.5$

Fig. 5. CHO detectability indices (d') as a function of exposure level and imaging task. The ROI images were cropped from the original DICOM CT images.

varied between 48% to 114% depending on contrast and dose level. These results have two indications: (1) for low contrast detection tasks, the influence of the aggressive noise reduction outweighs spatial resolution degradation in Veo; (2) for high detection tasks, despite the relative increment in edge noise, the edge enhancement feature and the denoising feature in the surrounding uniform regions introduced by Veo can effectively improve the overall CT image quality.

IV. DISCUSSIONS

A. Novelities

- The noise and spatial resolution characterization were done locally using noise ensembles generated by repeated scans, which addressed the concern of noise/resolution nonstationarity introduced by IR algorithms.
- As an earlier study has shown that uniform phantoms may not be sufficient to characterize the performance of IR algorithms [7], our study used an anthropomorphic phantom that contains realistic and anisotropic anatomy.
- The local noise measurement allowed noise at edges of objects to be quantified. Our results clearly demonstrate the need to quantify noises at DC regions and edges separately in IR. This is fundamentally different from FBP.
- Noise at edges of objects were characterized at eight contrast levels and the results show that edge noise

may be strongly correlated with edge contrast in IR.

- Spatial resolution were characterized at edges with eight contrast levels, including an ultra challenging case of 13 HU. Our results show that the edge noise and edge sharpness may have a tradeoff in IR.
- The joint contributions of noise and spatial resolution to image quality were assessed **in the image domain** using the CHO detectability analysis to help understand the benefit of IR.

B. Limitations and future works

- Compared with actual patients, the anatomical structure in the anthropomorphic phantom is still relatively simple. Due to the nonlinearity of MBIR, to what extent results drawn from this work can be generalized to clinical cases warrants further study.
- Although the CHO method has been validated to have good correlation with physicist readers for a specific IR algorithm, whether it can accurately represent the diagnostic performance of physicians for other IR algorithm is still unknown and need to be addressed through carefully designed human observer experiments.

V. CONCLUSION

In summary, an experimental framework was developed to help relate CT scanning parameters with CT imaging performance in IR. The framework enabled experimental findings of several unique characteristics of IR, indicating that some of the rules-of-thumb used by imaging physicists to optimize CT protocols have been challenged. Extra efforts must be made when prescribing CT scanning protocols when IR is used so that its potential clinical benefit can be maximized.

REFERENCES

- [1] S. Richard, D. B. Husarik, G. Yadava, S. N. Murphy, and E. Samei, "Towards task-based assessment of CT performance: System and object MTF across different reconstruction algorithms," *Med. Phys.* **39**(7), pp. 4115–4122, 2012.
- [2] K. J. Myers and H. H. Barrett, "Addition of a channel mechanism to the ideal-observer model," *J. Opt. Soc. Am. A* **4**, pp. 2447–2457, Dec 1987.
- [3] C. K. Abbey, H. H. Barrett, and D. W. Wilson, "Observer signal-to-noise ratios for the ML-EM algorithm," *Proc. SPIE* **2712**, pp. 47–58, 1996.
- [4] L. Yu, S. Leng, L. Chen, J. M. Kofler, R. E. Carter, and C. H. McCollough, "Prediction of human observer performance in a 2-alternative forced choice low-contrast detection task using channelized Hotelling observer: Impact of radiation dose and reconstruction algorithms," *Med. Phys.* **40**(4), p. 041908, 2013.
- [5] D. Pal, S. Kulkarni, G. Yadava, J.-B. Thibault, K. Sauer, and J. Hsieh, "Analysis of noise power spectrum for linear and non-linear reconstruction algorithms for CT," in *Nuclear Science Symposium and Medical Imaging Conference (NSS/MIC), 2011 IEEE, Nuclear Science Symposium and Medical Imaging Conference (NSS/MIC), 2011 IEEE*, pp. 4382–4385, 2011.
- [6] B. Chen, S. Richard, and E. Samei, "Relevance of MTF and NPS in quantitative CT: Towards developing a predictable model of quantitative performance," *Proc. SPIE* **8313**, p. 83132O, 2012.
- [7] J. Solomon and E. Samei, "Are uniform phantoms sufficient to characterize the performance of iterative reconstruction in ct?," *Proc. SPIE* **8668**, pp. 86684M–1, 2013.

APPLICATION OF TASK-BASED MEASURES OF IMAGE QUALITY TO EVALUATION OF IMAGE RECONSTRUCTION METHODS IN X-RAY CT

J. Xu, F. Elshahaby, M. K. Fuld, G. S. K. Fung, and B. M. W. Tsui

Abstract—Iterative reconstruction (IR) methods for x-ray CT is a promising approach to improve image quality or reduce radiation dose to patients. The goal of this work was to use task based image quality measures and the channelized Hotelling observer (CHO) to evaluate both analytic and IR methods for clinical x-ray CT applications. We performed realistic computer simulations at different radiation dose levels, from a clinical reference low dose D_0 to $75\%D_0$ and $37.5\%D_0$. A fixed size and contrast lesion was inserted at different locations in the liver of the phantom to simulate a weak signal. The simulated data were reconstructed on a commercial CT scanner using the vendor-provided analytic and IR methods. The reconstructed images were analyzed by CHOs with both rotationally symmetric (RS) and rotationally oriented (RO) channels, and with different numbers of lesion locations (5, 10, and 20) in a signal known exactly (SKE), background known exactly but variable (BKEV) detection task. The area under the receiver operating characteristic curve (AUC) was used as a summary measure to compare IR and analytic methods; the AUC was also used as the equal performance criterion to derive the potential dose reduction factor of IR. In general, there was a good agreement in the relative AUC values of different reconstruction methods using CHOs with RS and RO channels, although the CHO with RO channels achieved higher AUCs than RS channels. The improvement of IR over analytic methods depends on the dose level. At $75\%D_0$, the performance improvement was statistically significant. The potential dose reduction factor also depended on the detection task. For the SKE/BKEV task involving 10 lesion locations, a 25% dose reduction at D_0 was achieved; the same claim cannot be made for the SKE/BKEV task involving 20 lesion locations.

I. METHOD

A. Data generation

The XCAT phantom was developed for multi-modality imaging research [1]. Using parametric non-uniform rational B-spline surfaces to describe organ shapes, it is capable of modeling the accurate human anatomy with cardiac and respiratory motions; the parametric approach makes it easy to simulate variations of anatomy and physiology in a patient population. DRASIM is a vendor-developed computer simulation package for in-house system design and optimization [2]. The native DRASIM was able to simulate projections using geometric phantoms, but it has accurate models for x-ray generation and detector physics for Siemens scanners. Combining the strengths of both tools, the XCAT/DRASIM package [3] inherits the physics models in DRASIM and enhances it with realistic human anatomy from the XCAT, so that patient-like CT projection can be obtained. The XCAT/DRASIM package

has been used to investigate performance issues of both photon counting and energy-integrating CT systems [4]–[6].

Our clinical interest was low contrast lesion detection in the liver. The projection data of the body background and the liver lesions were separately generated using the XCAT/DRASIM package with parameter settings in Table I. With the exception of the x-ray source energy, these parameters followed standard clinical protocols of chest, abdomen, and pelvis exams. We simulated monochromatic x-ray projection at 70 keV, which was chosen to approximate the effective energy of 140 kVp polychromatic tube spectrum. Both the z- and in-plane flying focal spots were switched off. The decision to simulate monochromatic x-ray beam was based on the available reconstruction methods. As we will discuss in Section I-B, the simulated projection will be uploaded to a Siemens CT scanner for image reconstruction. At the point where the projection data access the data processing pipeline, the reconstruction engine assumes that the projections are ideal line integrals, and any beam-hardening effects have been pre-corrected. A monochromatic simulation is a simplification of the complex x-ray data generation process, and removes extraneous factors that are non-central to our study.

TABLE I: Parameter settings in computer simulations.

pitch	rotation speed	slice width	views per 2π
30.7 mm	0.5 sec	1.2 mm	1152
detector channels	detector rows	source energy*	dose levels
736	32	70 keV	$(1, \frac{3}{4}, \frac{3}{8}) \times D_0$

* The monochromatic energy 70 keV was chosen to approximate the effective energy of a 140 kVp polychromatic tube spectrum.

We simulated noisy projection data of the body background from the XCAT phantom. A total of 6 gantry rotations (6 x 1152 views) was used to cover the liver. The noise levels were adjusted by changing the tube current mA settings in DRASIM. We used three mA settings corresponding to three dose levels, $(1, \frac{3}{4}, \frac{3}{8}) \times D_0$. At each dose level, 200 noise realizations were generated. To relate D_0 to clinical dose measures, we used the reconstructed image of the XCAT phantom at D_0 and compared the noise standard deviations within several liver region-of-interests (ROIs) with a patient data set of similar body size (33 cm lateral), scanned and reconstructed using the same parameters. The noise standard deviations were comparable (~ 25 HU). Expressed as CTDIvol, the scanner radiation output for the patient acquisition was 11.74 mGy.

The low contrast lesions were modeled by 5 mm diameter spheres with density of 1% of water. A total of 20 lesions distributed through the liver were generated. Noise-free projections of the lesions were simulated using parameters in Table. I. For each of the three dose levels, 100 noise realizations of the body background projection were added to

J. Xu, G. S. K. Fung, and B. M. W. Tsui are with the Division of Medical Imaging Physics, Department of Radiology, Johns Hopkins University. E-mail: jxu@jhmi.edu.

F. Elshahaby is with the Department of Electrical and Computer Engineering, Johns Hopkins University

M. K. Fuld is with Siemens Medical Solutions, Inc., Malvern, PA.

the lesion image to form lesion-present projection; the other 100 body background projections were used as lesion-absent projection.

As the x-ray projection formation process is nonlinear, the lesions should ideally be inserted in the XCAT phantom and noisy projection simulated from the combined phantom. Our data generation essentially approximated the nonlinear forward process by a linear one, and assumed that the noise in the lesion-only projection was negligible. Such an approximation can be justified by using weak signals. That is the presence or absence of low contrast lesions mainly affects the mean of the projection, but not much the noise of it. An advantage of this approach was that adjusting the lesion contrast could be achieved by tuning a weight coefficient of the lesion projection without regenerating the body background projection, which would be time-consuming. This can result in tremendous computation savings when trying to determine a proper range of the lesion contrast so that the detection task is neither too easy ($AUC \approx 1$) nor too difficult ($AUC \approx 0.5$).

B. Image reconstruction

The simulated projection data were reformatted using a vendor-provided proprietary program so that they could be uploaded to and reconstructed on a 128-slice commercial scanner (Siemens Definition Flash, Siemens Healthcare). Each data set was reconstructed using both an analytical weighted filtered backprojection (WFBP) method [7] and a sinogram affirmed iterative reconstruction (SAFIRE) method (version VA40). The reconstructed image characteristics can be controlled by a variety of kernels for both methods, *e.g.*, B41F for WFBP and a corresponding I41F for SAFIRE, and an additional strength parameter of 1 - 5 for SAFIRE. We selected 4 kernels, B31F, B41F, B50F, and B70F for WFBP reconstruction, and the corresponding kernels I31F, I41F, I50F, and I70F were used for SAFIRE reconstruction, each with strengths of 1, 3, and 5. These kernels were selected based on the noise-resolution tradeoff [Fig. 1] calculated using a 20 cm water QA phantom scan. The QA phantom was scanned at CTDIvol of 27.2 mGy, using a 120 kVp spectrum and the same geometric parameters listed in Table I. It can be seen in Fig. 1 that the selected kernels cover a wide range on the noise-resolution tradeoff curve. Unlike the iteration numbers in IR methods which often provide tradeoff between resolution and noise, increasing SAFIRE strength can reduce noise without sacrificing resolution. In other words, the strength parameter cannot be identified with the iteration numbers.

In total, there were 16 reconstructed images (WFBP with 4 kernels, and SAFIRE with 4 kernels x 3 strengths) for each projection data set. This was repeated for the 100 lesion-present and 100 lesion-absent at the three dose levels. The reconstruction voxel size was $(0.35 \text{ mm})^3$, with a FOV of $(180 \text{ mm})^3$ enclosing the liver. The reconstructed image slice thickness and slice interval were both 1.5 mm.

C. Application of the channelized Hotelling observer

The reconstructed images were sent to our computer cluster. Unless noted otherwise, all postprocessing were performed

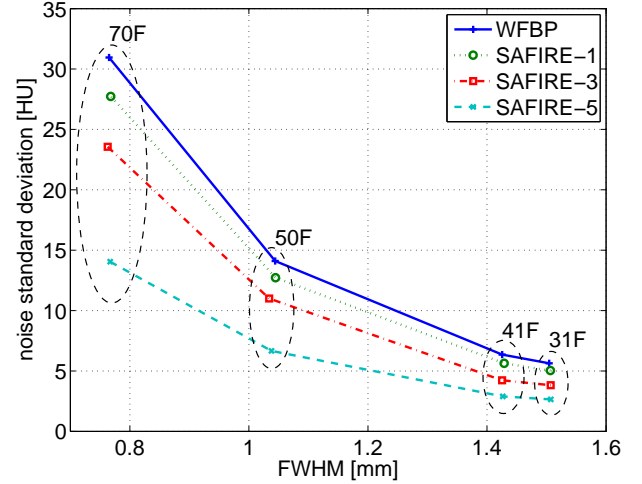


Fig. 1: The noise-resolution tradeoff of WFBP and SAFIRE with difference kernels and SAFIRE strengths. The notations 31F, 41F, etc, denote B31F, B41F for WFBP, and I31F, I41F for SAFIRE. Compared with WFBP, increasing SAFIRE strength reduces image noise while preserving resolution at the corresponding kernels.

using our in-house analysis tools. From the 3D stack of reconstructed images, the transaxial image slice across the lesion center was located. A 64×64 ROI centered on the lesion location for all 20 lesions was cropped and then processed using CHO analysis. This is the single slice CHO approach used in [8]. Below we describe the two channel mechanisms and define the lesion detection task.

1) *Rotationally symmetric square channels*: These channels have been widely applied in nuclear medicine; they were found to correlate well with human observer performance in various defect detection tasks [9], [10]. We used 5 octave-wide rotationally symmetric channels. In the (2D) frequency domain, these channels consisted of annular passbands of the form $[\frac{1}{64}, \frac{1}{32}]$ $[\frac{1}{32}, \frac{1}{16}]$ $[\frac{1}{16}, \frac{1}{8}]$ $[\frac{1}{8}, \frac{1}{4}]$ $[\frac{1}{4}, \frac{1}{2}]$ cycles per pixel. The frequency domain channels were transformed to the spatial domain; the DC components in the spatial channels were explicitly eliminated by subtracting the average value of the channel profiles.

2) *Gabor channels*: These channels have been applied in recent works in evaluating CT images [11]–[13]. The spatial domain channel profiles are of the form

$$g(x, y) = \exp\left\{-\frac{4 \log 2 [(x - x_0)^2 + (y - y_0)^2]}{w_s^2}\right\} \times \cos[2\pi f_c((x - x_0) \cos \theta + (y - y_0) \sin \theta) + \xi] \quad (1)$$

The parameters x_0, y_0 were the lesion centers, $(32, 32)$ in this work. The other parameters follow previous works. Specifically, two phase parameters $\xi = 0, \pi/2$, four frequency channels with central frequency $f_c = \frac{3}{128}, \frac{3}{64}, \frac{3}{32}, \frac{3}{16}$ cycles per pixel, five orientations $\theta = 0, 2\pi/5, 4\pi/5, 6\pi/5, 8\pi/5$, and w_s is the spatial channel width, given by $w_s = 4 \log 2 / (\pi w_f)$, w_f the bandwidth of the frequency channels, $1/64, 1/32, 1/16$, and $1/8$ cycles per pixel for the central frequencies f_c that we used. In total there was 40 channels. Similar to the calculation in the square channels, the DC component of the

spatial domain channel profiles was eliminated.

3) *CHO training and testing, and ROC analysis*: The spatial channel profiles were applied to the 64 x 64 transaxial image slice containing the lesion center, obtaining 5-component (square channels) and 40-component (Gabor channels) feature vectors for each reconstructed image. For each channel mechanism, all feature vectors from the 20 lesion locations were assembled, those feature vectors corresponding to lesions at 1-5, 1-10, and 1-20 [Table II] were selected and used in CHO training and testing. For example, when 5 locations were selected, lesions at locations 1 to 5 were used in CHO training and testing. There were 500 lesion-present feature vectors (5 locations and 100 noise realizations) and 500 lesion-absent feature vectors.

We used the leave-one-out training and testing paradigm [14]. Let there be m lesion-absent and n lesion-present feature vectors. To obtain the rating values for ROC analysis, one of the m lesion-absent feature vectors was held out, while the remaining $m - 1$ lesion-absent and n lesion-present feature vectors were used to estimate the mean and the covariance matrix of the feature vectors. The CHO template w_{CHO} was applied to the previously held-out sample, and a rating value was obtained. By holding out a different sample each time from the lesion-absent (present) class, we would obtain m (n) rating values for the lesion-absent (present) class.

These rating values were analyzed by the nonparametric ROC approach in [15], available in the ROC-kit of the University of Chicago, to estimating AUCs, the standard deviations of the AUCs, and the correlation between two AUCs. The estimated AUC statistics were then used to calculate the one-sided p-value for the null hypothesis that the two AUCs under consideration were the same. In this work, the statistical significance was defined to be $p < 0.05$. This procedure was performed for 5, 10, and 20 lesion locations at all three dose levels and using CHOs with square and Gabor channels.

TABLE II: Locations of the 20 liver lesions.

index	location	index	location
	(x, y, z) mm		(x, y, z) mm
1	(-99, 5, 532.5)	11	(-65, 35, 472.5)
2	(-99, -35, 532.5)	12	(-85, -15, 472.5)
3	(-99, 5, 519)	13	(-91, -55, 472.5)
4	(-99, -35, 519)	14	(-59, 33, 459)
5	(-69, 33, 502.5)	15	(-91, -3, 459)
6	(-103, -3, 502.5)	16	(-91, -43, 459)
7	(-99, -39, 502.5)	17	(-89, 9, 442.5)
8	(-65, 33, 489)	18	(-89, -35, 442.5)
9	(-99, 5, 489)	19	(-83, 5, 421.5)
10	(-99, -43, 489)	20	(-67, -59, 421.5)

If we only use a single lesion location in the CHO analysis, the detection task is a simple signal known exactly (SKE), background known exactly (BKE) task. On the one hand, the simplicity of the task may not reflect well the complexity of clinical diagnosis; on the other hand, results from our single lesion analysis did not have the statistical significance to differentiate the performance of different reconstruction methods. Combining multiple lesion locations helps to reduce the error bars of the AUC estimates. At the same time, using multiple lesion locations transformed the detection task to a special case of an SKE/BKEV, background known exactly but

variable, task. The backgrounds at different lesion locations have the same mean since the liver background has uniform intensity. But the noise statistics at different lesion locations are different due to the helical scan geometry. The overall covariance matrix from multiple lesion locations is a (uniform) mixture of the covariance matrices at the individual lesion locations. The number of lesions included in the CHO analysis determines the statistical variations in the SKE/BKEV task.

II. RESULTS

A. Detection task performance comparison

Our results showed that the kernel choices did not affect much the AUCs for either WFBP or SAFIRE, and higher SAFIRE strengths improved AUC values. As representatives from the two methods, we analyzed the statistical significance in the performance difference between WFBP with kernel B31F and SAFIRE at strength 5 (SAFIRE-5) with the corresponding kernel I31F. This analysis was performed for all three dose levels, using CHOs with both square and Gabor channels, and in the SKE/BKEV detection task with background variations from 5, 10, and 20 lesion locations. Table. III listed the AUC values and their standard deviations for WFBP (B31F) and SAFIRE-5 (I31F), and the calculated one-sided p values. For CHOs with square or Gabor channels, despite their difference in the absolute AUC values, there was agreement regarding statistical significance results in the performance difference.

TABLE III: The AUC values and test for statistical significance between WFBP (B31F) and SAFIRE-5 (I31F) at different dose levels.

D_0				
	WFBP (B31F)	SAFIRE-5 (I31F)		
	AUC1 \pm stdv1	AUC2 \pm stdv2	$p(p_1)$	
s	5 loc	0.839 \pm 0.012	0.860 \pm 0.011	0.092
	10 loc	0.840 \pm 0.0086	0.865 \pm 0.0079	0.016
	20 loc	0.829 \pm 0.0063	0.854 \pm 0.0058	0.0024
g	5 loc	0.89 \pm 0.010	0.903 \pm 0.0093	0.15
	10 loc	0.887 \pm 0.0072	0.906 \pm 0.0064	0.028
	20 loc	0.870 \pm 0.0055	0.890 \pm 0.0050	0.0056
$75\%D_0$				
	WFBP (B31F)	SAFIRE-5 (I31F)		
	AUC1 \pm stdv1	AUC2 \pm stdv2	$p(p_1)$	
s	5 loc	0.812 \pm 0.013	0.852 \pm 0.012	0.0099
	10 loc	0.810 \pm 0.0094	0.839 \pm 0.0087	0.011
	20 loc	0.783 \pm 0.0071	0.808 \pm 0.0067	0.0036
g	5 loc	0.85 \pm 0.012	0.88 \pm 0.010	0.030
	10 loc	0.853 \pm 0.0083	0.878 \pm 0.0075	0.0083
	20 loc	0.826 \pm 0.0064	0.851 \pm 0.0059	0.0018

s: square channels; g: Gabor channels.
The shaded cells mark those p-values that are < 0.05 .

B. Dose reduction potential of IR

The improvement in detection task performance can be traded for reduced radiation dose at the same performance. To quantitatively estimate the dose reduction potential of SAFIRE over WFBP, we compared the performance of WFBP (B31F) at dose D_0 with that of WFBP (B31F) and SAFIRE-5 (I31F) at dose $75\%D_0$. A 25% dose reduction at D_0 by using SAFIRE can be claimed when two conditions are *both* satisfied: (1) the

TABLE IV: Evaluation of dose reduction potential of SAFIRE versus WFBP.

		D_0	$75\%D_0$				25% dose reduction @ D_0 ?	
		WFBP (B31F)	WFBP (B31F)			SAFIRE-5 (I31F)		
		AUC1 \pm stdv1	AUC2 \pm stdv2	$p(p_2)$	AUC2 \pm stdv2	$p(p_3)$		
s	5 loc	0.839 \pm 0.012	0.812 \pm 0.013	0.064	0.852 \pm 0.012	0.21	No*	
	10 loc	0.840 \pm 0.0086	0.810 \pm 0.0094	0.0088	0.839 \pm 0.0087	0.49	Yes	
	20 loc	0.829 \pm 0.0063	0.783 \pm 0.0071	2.6 e-07	0.808 \pm 0.0067	0.012	No	
g	5 loc	0.89 \pm 0.010	0.85 \pm 0.012	0.0071	0.88 \pm 0.010	0.28	Yes*	
	10 loc	0.887 \pm 0.0072	0.853 \pm 0.0083	0.00057	0.878 \pm 0.0075	0.18	Yes	
	20 loc	0.870 \pm 0.0055	0.826 \pm 0.0064	6.2 e-08	0.851 \pm 0.0059	0.011	No	

The notation * marks a disagreement in results using the square and Gabor channels.

performance degradation of WFBP (B31F) from D_0 to $75\%D_0$ is significant; and (2) the performance difference between WFBP (B31F) at D_0 and SAFIRE-5 (I31F) at $75\%D_0$ is not significant. Condition (1) is to ensure that the starting dose level D_0 is appropriate for the specific task considered, and decreasing from D_0 will incur a performance loss in the detection task without using advanced algorithms such as IR. Table IV summarizes our analysis.

From Table IV, it is seen that 25% dose reduction at D_0 can be claimed for the SKE/BKEV detection task with 10 lesion locations. The same conclusion can be drawn using CHOs with either square or Gabor channels. Dose reduction cannot be claimed for the task involving 5 or 20 lesion locations. For 20 lesion locations, the 25% dose reduction was rejected by violating condition (2). The results for 5 lesion locations are interesting in that there is a disagreement in conclusions between CHO using square channels and Gabor channels. This disagreement was in the performance loss of WFBP at D_0 and $75\%D_0$. For the CHO with Gabor channels, 25% dose reduction at D_0 can be claimed. For the CHO with square channels, the 25% dose reduction was rejected by violating condition (1).

III. CONCLUSIONS

We applied channelized Hotelling observers (CHO) in an SKE/BKEV lesion detection task to evaluate the image quality of analytic and iterative image reconstruction methods for CT applications. For the CHO implementation, we considered two channel mechanisms with rotationally symmetric (RS) and rotationally oriented (RO) channels. It was shown that the CHO with RO channels achieved higher AUC values than the CHO with RS channels. There was in general a good agreement in the relative AUC values of different reconstruction methods (with kernel choices and IR strength variations) between the two channel mechanisms. The image quality improvement of IR over the analytic method depended on the dose levels in the projection data. In our examples, the performance improvement at $75\%D_0$ was significant, Dose reduction from D_0 to $75\%D_0$ was demonstrated for the SKE/BKEV task involving 10 lesion locations.

REFERENCES

- [1] W. P. Segars, M. Mahesh, T. J. Beck, E. C. Frey, and B. M. Tsui, "Realistic CT simulation using the 4D XCAT phantom," *Medical Physics*, vol. 35, pp. 3800–3808, August 2008.
- [2] K. Stierstorfer, "User documentation: DRASIM – deterministic radiological simulation." Siemens AG, apr 2005.

- [3] G. S. K. Fung, K. Stiefstorfer, K. Taguchi, W. P. Segars, T. Flohr, and B. M. W. Tsui, "A realistic CT/Human-Model simulation package," in *The 2nd International Conference on image formation in X-ray computed tomography*, (Salt Lake City, Utah), pp. 66–69, June 2012.
- [4] T. Weidinger, T. Buzuga, T. Flohr, G. Fung, S. Kappler, K. Stierstorfer, and B. Tsui, "Investigation of ultra low-dose scans in the context of quantum counting clinical CT," in *Proc. of SPIE Vol.*, vol. 8313, pp. 83134B–1, 2012.
- [5] K. Taguchi and J. S. Iwanczyk, "Vision 20/20: Single photon counting x-ray detectors in medical imaging," *Medical physics*, vol. 40, no. 10, p. 100901, 2013.
- [6] J. Xu and B. Tsui, "Quantifying the importance of the statistical assumption in statistical x-ray CT image reconstruction," *Medical Imaging, IEEE Transactions on*, vol. 33, no. 1, pp. 61–73, 2014.
- [7] K. Stierstorfer, A. Rauscher, J. Boese, H. Bruder, S. Schaller, and T. Flohr, "Weighted FBP – a simple approximate 3D FBP algorithm for multislice spiral CT with good dose usage for arbitrary pitch," *Physics in medicine and biology*, vol. 49, no. 11, p. 2209, 2004.
- [8] H. Liang, S. Park, B. D. Gallas, K. J. Myers, and A. Badano, "Image browsing in slow medical liquid crystal displays," *Academic radiology*, vol. 15, no. 3, pp. 370–382, 2008.
- [9] S. Wollenweber, B. Tsui, D. Lalush, E. Frey, K. LaCroix, and G. Gullberg, "Comparison of Hotelling observer models and human observers in defect detection from myocardial SPECT imaging," *Nuclear Science, IEEE Transactions on*, vol. 46, no. 6, pp. 2098–2103, 1999.
- [10] E. Frey, K. Gilland, and B. Tsui, "Application of task-based measures of image quality to optimization and evaluation of three-dimensional reconstruction-based compensation methods in myocardial perfusion SPECT," *IEEE Transactions on Medical Imaging*, vol. 21, pp. 1040–1050, Sept. 2002.
- [11] A. Wunderlich and F. Noo, "Image covariance and lesion detectability in direct fan-beam x-ray computed tomography," *Physics in medicine and biology*, vol. 53, no. 10, p. 2471, 2008.
- [12] L. Yu, S. Leng, L. Chen, J. M. Kofler, R. E. Carter, and C. H. McCollough, "Prediction of human observer performance in a 2-alternative forced choice low-contrast detection task using channelized Hotelling observer: Impact of radiation dose and reconstruction algorithms," *Medical Physics*, vol. 40, no. 4, pp. –, 2013.
- [13] S. Leng, L. Yu, Y. Zhang, R. Carter, A. Y. Toledano, and C. H. McCollough, "Correlation between model observer and human observer performance in CT imaging when lesion location is uncertain," *Medical Physics*, vol. 40, no. 8, pp. –, 2013.
- [14] G. Sgouros, E. C. Frey, W. E. Bolch, M. B. Wayson, A. F. Abadia, and S. T. Treves, "An approach for balancing diagnostic image quality with cancer risk: Application to pediatric diagnostic imaging of ^{99m}Tc -Dimercaptosuccinic acid," *Journal of Nuclear Medicine*, vol. 52, no. 12, pp. 1923–1929, 2011.
- [15] E. R. DeLong, D. M. DeLong, and D. L. Clarke-Pearson, "Comparing the areas under two or more correlated receiver operating characteristic curves: a nonparametric approach," *Biometrics*, pp. 837–845, 1988.

ACKNOWLEDGMENT

The project was supported in part by a JHU-Siemens research contract. The authors would like to thank Dr. Elliot Fishman, Beatrice Mudge, and all staff at Body CT, Johns Hopkins Outpatient Center for their technical assistance and generous support for scanner time. The authors would like to thank Katsuyuki Taguchi for his suggestions to this work.

Mixed Confidence Estimation for Iterative CT Reconstruction

David S. Perlmutter, Soo Mee Kim, Paul E. Kinahan, Adam M. Alessio

Abstract—We present a statistical analysis of our previously proposed Constrain-Static Target-Kinetic algorithm for 4D CT reconstruction. This method, where framed iterative reconstruction is only performed on the dynamic regions of each frame, while static regions are fixed across frames to a composite image, was proposed to reduce computation time. In this work, we generalize the previous method to describe any application where a portion of the image is known with higher confidence (static, composite, lower-frequency content, etc.) and a portion of the image is known with lower confidence (dynamic, targeted, etc.). We show that by splitting the image space into higher and lower confidence components, CSTK can lower the estimator variance in both regions compared to conventional reconstruction. We present a theoretical argument for this reduction in estimator variance and verify this argument with proof-of-principle simulations. This method allows for reduced computation time and improved image quality for imaging scenarios where portions of the image are known with more certainty than others.

I. INTRODUCTION

Specific CT imaging applications can have the property that certain regions in the image are known with more confidence than other regions. For example, in dynamic contrast enhanced acquisitions, large regions of the field of view may stay static for each time frame (essentially no change), while targeted regions have varying contrast kinetics. Conventionally, independent reconstructions would be performed for each frame. Several methods have been proposed that use a low-resolution composite image, reconstructed from a time-averaged sinogram, to aid reconstruction. Composite images have been used as a weight applied to filtered back projection [1] images and as a prior term in a total variation minimization algorithm [2]. We propose a method that uses all frames to reconstruct the static regions and uses individual frames to reconstruct only the kinetic portion (Constrain-Static Target-Kinetic). This application could be characterized as having side-information to increase the confidence of the static region, while desiring an optimal image of the lower-confidence, kinetic region. This class of methods is advantageous for both substantially reducing reconstruction time and reducing noise in the lower-confidence region.

This general approach could be applied in all applications where side-information could increase the confidence in specific regions, leading to improved image quality in the lower-confidence area. An obvious application is with multi-frame or gated images where portions of the image do not change between frames (higher confidence regions). Other applications could include images where regions are assumed or known

to have lower frequency content than others. For example, when imaging the lungs, it could be assumed that extra-lung content has much lower spatial frequency and therefore could be known with more confidence than intra-lung content.

In our previous work [3] [5], we proposed the Constrain-Static Target-Kinetic (CSTK) reconstruction algorithm as a method to reduce computation time in 4D CT image reconstruction by devoting full computational resources to only the dynamic region of interest. This paper extends that work by presenting an analytic argument, based on an estimator variance analysis [6], that CSTK also improves noise levels throughout the image, including the dynamic region of interest. We feel this analysis can be extended to the situations above, where locally varying performance can be leveraged. We verify our analytic argument with simulation studies.

A. CSTK Algorithm

Constrain-Static Target-Kinetic reconstruction (CSTK) is a method to reduce computation time of most iterative 4D CT reconstruction algorithms. It comprises the following steps; 1) classify each image pixel as either *static* or *kinetic* across frames, perhaps using a high-noise estimate of each frame, 2) form a low-noise, low-resolution "composite image" to initialize all frames, and 3) update only the kinetic pixels in each frame. The resulting computation reduction scales linearly with the percentage of dynamic pixels, minus the time to form the composite image. Previous work [3] showed two applications, Retrospective Gated CT Angiography and Dynamic Perfusion CT, in which CSTK provided similar image quality to conventional OSEM reconstruction with 50% dynamic pixels, and therefore 50% compute time.

II. STATISTICAL FORMULATION

A. Static Model

We start by adopting the standard quadratic approximation to the static transmission tomography problem. We wish to estimate the x-ray attenuation coefficients of each pixel in an image, $\theta = [\theta_1, \dots, \theta_m]^T \in \mathbb{R}^m$, from observations $Y = [y_1, \dots, y_n]^T \in \mathbb{R}^n$, where $y_i = -\log(p_i/I_0)$ are the post-log-corrected, measured sinogram bins. By taking the second order Taylor series expansion of the Poisson likelihood [4], the system model can be approximated as,

$$P(Y|\theta) \approx N(A\theta, Q) \quad (1)$$

where A is the tomographic model, a forward projection operator, and $Q = \text{diag}(1/p_i)$. Recognizing this as a weighted

Imaging Research Lab, University of Washington, Seattle, WA USA (email: dperl@uw.edu)

least squares problem, the maximum likelihood estimator $\hat{\theta}_{ML}$ can be written explicitly as the least squares solution,

$$\hat{\theta}_{ML} = \arg \max_{\theta} P(Y|\theta) = (A^T W A)^{-1} A^T W Y \quad (2)$$

Where $W = Q^{-1}$. It is easy to show that $\hat{\theta}_{ML}$ is unbiased ($E[\hat{\theta}_{ML}] = \mu_{\hat{\theta}} = \theta$) and that $Cov[\hat{\theta}_{ML}] = \Sigma_{\hat{\theta}} = (A^T W A)^{-1}$. If we choose to add a quadratic prior term to control noise amplification, the solution becomes,

$$\hat{\theta}_{MAP} = \arg \max_{\theta} P(\theta|Y) = (A^T W A + R)^{-1} A^T W Y \quad (3)$$

where R describes the prior term. In the following we will assume no prior for simplicity, although this analysis could be extended to the quadratic prior case.

B. Dynamic Model

We now consider the 4D extension to the static problem in which we want to estimate multiple images over K time frames, or $\theta = [\theta^1, \dots, \theta^K]^T$ from $Y = [Y^1, \dots, Y^K]^T$, where each $\theta^j \in \mathbb{R}^m$, $Y^j \in \mathbb{R}^n$. A straightforward approach is to treat each frame as a separate static estimation problem, i.e.,

$$\hat{\theta}_{ML}^j = (A^T W^j A)^{-1} A^T W^j Y^j \quad (4a)$$

$$\mu_{\hat{\theta}_{ML}}^j = \theta^j \quad \Sigma_{\hat{\theta}_{ML}}^j = (A^T W^j A)^{-1} \quad (4b)$$

but this solution ignores potentially useful information about θ^j in Y^{-j} , where the $-j$ superscript indicates all frames besides j . To improve on this, we separate the parameter space into a *static* and *dynamic* component, namely, $\theta^j = [\theta_s, \theta_d^j]^T$. Previous work on CSTK [3] suggests practical ways to do this partitioning. It is assumed that θ_s is constant across all frames, and θ_d^j constant only across frame j . This assumption allows us to factor the posterior distribution as,

$$P(\theta^j | Y) = P(\theta_s, \theta_d^j | Y^j, Y^{-j}) \quad (5)$$

$$= P(\theta_d^j | Y^j, \theta_s) P(\theta_s | Y). \quad (6)$$

The first term in eq. (6) is the conditional of eq. (1), and so is itself multivariate Gaussian variate. The second term is a marginal of the composite image, which is Gaussian distributed if the composite is Gaussian distributed. Although this may not be true for arbitrary composite images, we restrict the composite image to unbiased linear estimators of eq. (1), which we call $\hat{\theta}^c$ with covariance $\Sigma_{\hat{\theta}^c}$. Thus, if:

$$\Sigma_{\theta} = \begin{bmatrix} \Sigma_{ss} & \Sigma_{sd} \\ \Sigma_{ds} & \Sigma_{dd} \end{bmatrix}$$

then,

$$P(\theta_s | Y) = N(\theta_s, \Sigma_{ss}^c) \quad (7a)$$

$$P(\theta_d^j | Y^j, \theta_s) = N(\mu_{d|s}^j, \Sigma_{d|s}^j) \quad (7b)$$

$$\mu_{d|s}^j = \mu_{\theta_d}^j + \Sigma_{ds}^j (\Sigma_{ss}^j)^{-1} (\hat{\theta}^c - \theta_s) \quad (7c)$$

$$\Sigma_{d|s}^j = \Sigma_{dd}^j - \Sigma_{ds}^j (\Sigma_{ss}^j)^{-1} \Sigma_{sd}^j \quad (7d)$$

where eq. (7a) come directly from the marginal distribution and eqs. (7b) to (7d) from the conditional distribution of a multivariate Gaussian. Notice that eq. (7b) depends on θ_s only

linearly through its mean. This ensures that the product of eq. (7a) and eq. (7b) is also Gaussian, parameterized by

$$\mu_{\theta}^j = [\theta_s, \theta_d^j]^T \quad (8a)$$

$$\Sigma_{\theta}^j = \quad (8b)$$

$$\begin{bmatrix} \Sigma_{ss}^c & \Sigma_{ds}^j (\Sigma_{ss}^j)^{-1} \Sigma_{ss}^c \\ \Sigma_{ss}^c (\Sigma_{ss}^j)^{-1} \Sigma_{sd}^j & \Sigma_{d|s}^j + \Sigma_{ds}^j (\Sigma_{ss}^j)^{-1} \Sigma_{ss}^c (\Sigma_{ss}^j)^{-1} \Sigma_{sd}^j \end{bmatrix}.$$

Equation (8) is the main result of this paper. Notice that $\hat{\theta}_{CSTK} = \mu_{\theta}^j$ is unbiased, as might be expected (this would not be true if we included a prior term). Also, the covariance can be directly compared with eq. (4), the straightforward reconstruction approach. First, the static pixel variance under CSTK is simply Σ_{ss}^c . A reasonable choice for the composite image would be the average of each frame estimate, θ^j , in which case $\Sigma_{\theta}^c \approx \frac{1}{K} \Sigma_{\hat{\theta}_{ML}}^j$. More interestingly, the dynamic pixel variance (lower right term of 8b), is the sum of two terms; $\Sigma_{d|s}^j$, and a correction factor, Σ^* , where,

$$\Sigma^* = \Sigma_{ds}^j (\Sigma_{ss}^j)^{-1} \Sigma_{ss}^c (\Sigma_{ss}^j)^{-1} \Sigma_{sd}^j - \Sigma_{ds}^j (\Sigma_{ss}^j)^{-1} \Sigma_{sd}^j.$$

To better understand 8b, consider two cases; when $\Sigma_{ss}^c = \mathbf{0}$ and $\Sigma_{ss}^c = \Sigma_{ss}^j$. In the first case, the full dataset Y provides perfect information about θ_s , and the covariance of the dynamic portion of the image, θ_d^j , reduces to the conditional covariance $\Sigma_{d|s}^j$, which is guaranteed to be smaller than Σ_{dd}^j . In the second case, the covariance of the static portion of the composite image equals the covariance of the static portion of a single frame; i.e. the composite image did not improve the estimate of θ_s . Then $\Sigma^* = \mathbf{0}$, and the covariance is simply Σ_{dd}^j . In practice, we expect to lie somewhere in between these two bounds; the composite provides some extra, but not perfect, information about θ_s , which helps lower the covariance of *both* dynamic and static pixel estimates.

C. Numerical Validation

To validate our analysis we compared our predicted covariance with those measured from simulations of a small, 10x10 pixel image. We used a sinogram of 15 detectors x 16 views to make explicit computation of the pseudoinverse tractable. We added Gaussian noise according to the approximate signal model in eq. (1). Figure 1 shows the predicted variance of each pixel using simple framed recon and CSTK, from eq. (4) and eq. (8), respectively. While the true image is static, we nonetheless treat the inner pixels (red pixels in fig. 1, upper left) as dynamic, and collected 10 frames of data. The CSTK image shows dramatic variance reduction in the static region, but also significant reduction in the inner, dynamic region. We then computed $\hat{\theta}_c$, $\hat{\theta}_{ML}^j$, and $\hat{\theta}_{CSTK}$ using Y , Y^1 , and the CSTK method. Figure 1 shows that the predicted, theoretical variance of a single row of pixels agrees well with the sample variance over 1000 noise realizations. Figure 1 also shows the average variance of over all dynamic pixels as the number of frames increases. The framed recon is constant, since it doesn't share information across frames, while the composite image shows the typical $\frac{1}{N}$ variance reduction. The CSTK variance initially decreases rapidly, then plateaus to the average variance of Σ_{dd}^j .

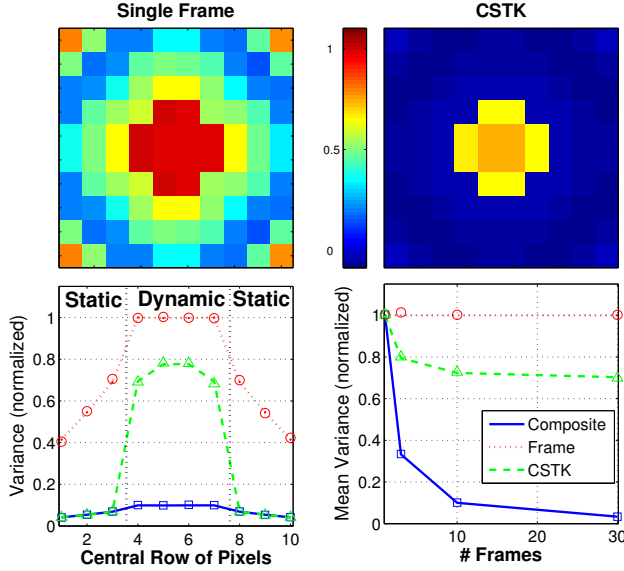


Fig. 1: First row presents theoretical variance image for single frame reconstruction and CSTK. The CSTK estimate achieves lower variance everywhere, including the central, dynamic region (yellow region, in upper right). Lower left: Profile through central row of variance image for 3 reconstruction methods, with simulated values as datum and theoretical values as lines. Lower right: Average pixel variance of the dynamic region as a function of frames acquired. Simulated data are datum and theoretical values are lines.

III. EXPERIMENTAL RESULTS

To demonstrate the utility of these results in a more realistic dynamic CT scenario, we simulated data from a 128×128 dynamic target, pictured in the top row of fig. 4 (the central object is moving continuously at a rate of 8 pixels per frame, where a frame is a full 360 degree revolution of the detector). The dynamic pixels were chosen a priori as an ellipse, pictured in fig. 2. Note, the dynamic pixels are not truly constant within a frame, as assumed in the statistical analysis. The measurement sinogram was 200 detectors \times 150 views per frame for 5 frames, with Poisson distributed noise; $p_i \sim \text{Poisson}(\lambda_i)$, where $\lambda_i = I_0 e^{-\sum_j c_{i,j} \theta_j}$ across line of response i . For reconstruction, we use iterative coordinate descent (ICD), but only update dynamic pixels. The choice of composite image is important, and must balance low-noise and computation time. We chose our composite image to be the ICD reconstruction of the average sinogram across all frames.

Figure 4 compares the CSTK reconstruction of each frame with that of simple framed recon. The CSTK noise appears lowest, particularly in the static region. However we are primarily concerned with performance in the dynamic region. We present the image roughness (pixel-to-pixel variance) in the uniform portion of the dynamic region and total RMSE in the dynamic region. Both metrics are normalized and shown above each image. Figure 3 compares the convergence of both methods. To fairly account for the composite compute time, T_c , in CSTK, the CSTK data is offset by T_c/K , the time to compute reconstruction from averaged sinogram. From fig. 3 and fig. 4, the CSTK method achieves about 15% less noise

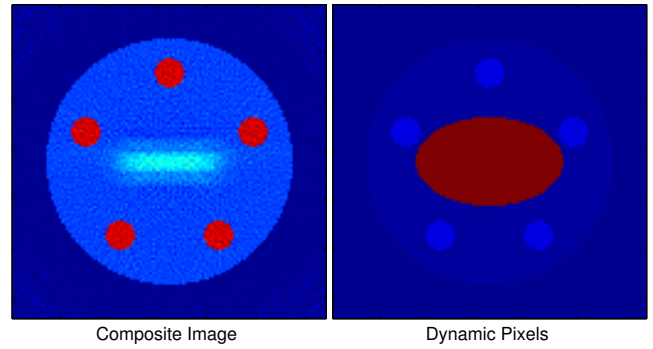


Fig. 2: Left: Composite image using ICD on the full dataset, \mathbf{Y} . Right: Mask for elliptical region of dynamic pixels.

in the dynamic region in 90% less compute time than simple frame recon. Both factors should increase with number of frames and the percentage of static pixels, as long as the static/dynamic pixel segmentation remains accurate.

IV. CONCLUSION AND FUTURE WORK

We have shown that CSTK reconstruction, applied to ML estimation of cardiac gated CT imaging, can both save computation time *and* lower noise throughout the image. The results confirm the intuition that side information, in the form of increased confidence of particular parameters, can decrease noise. As the strength of the side information increases, i.e. more frames or a higher percentage of static pixels in CSTK and the correlation between side information and pixels of interest increases, the noise reduction is greater. Future work is needed to better understand the effect of CSTK in MAP reconstruction, when a prior term is added to the cost function. We believe mixed confidence estimation can be extended to other applications where local image quality can either benefit

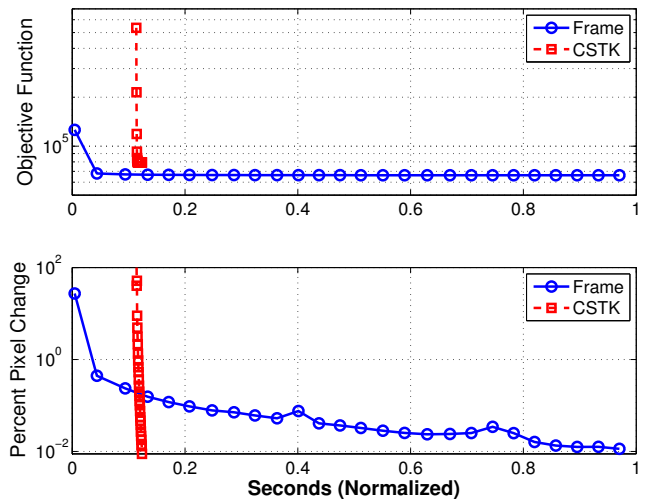


Fig. 3: Convergence metrics for reconstruction of first frame. Each data point is a full iteration of ICD. Top: Negative log-likelihood value vs. computation time for simple framed (blue) and CSTK (red) recon. Bottom: Mean percent pixel change vs. computation time. Algorithm was terminated when mean pixel change was $< 1\%$.

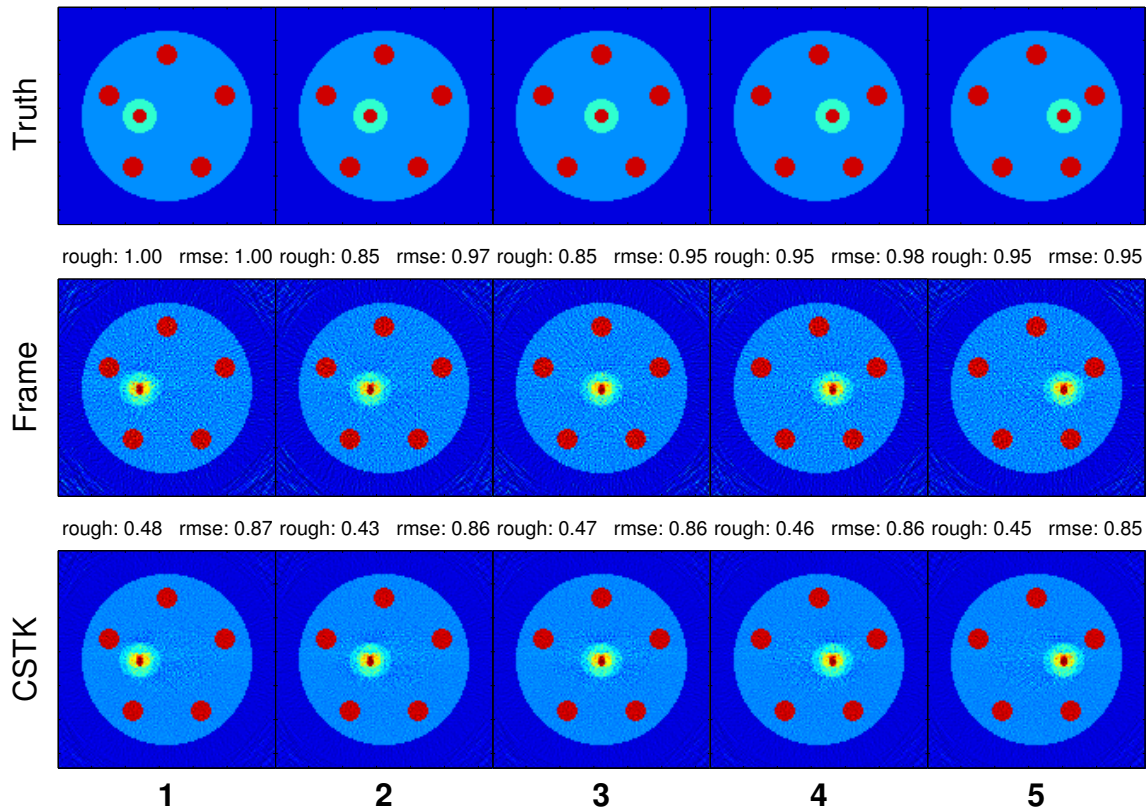


Fig. 4: Top row: Truth image in the center of each time frame. Row 2-3: Framed ML, and CSTK estimate for each frame. Above each image are image quality metrics of dynamic pixels only. RMSE is the total root mean squared error of the reconstruction. 'rough' is the standard deviation of pixels in a flat patch in the dynamic region. Both metrics are normalized.

from side information or be traded for improved performance elsewhere.

V. ACKNOWLEDGMENTS

We thank Drs. Patrick La Riviere and Bruno De Man for helpful conversations. This work is supported by the National Institutes of Health under grants R01-HL109327 and R01-CA115870.

REFERENCES

- [1] M. Supanuch and et al. Radiation dose reduction in time-resolved ct angiography using highly constrained back projection reconstruction. *Phys Med Biol*, 54(14):4575–93, Jul 2009.
- [2] G.H Chen, J. Tang, and S. Leng. Prior image constrained compressed sensing (piccs): a method to accurately reconstruct dynamic ct images from highly undersampled projection data sets. *Med Phys*, 35(2):660–3, Feb 2008.
- [3] A. Alessio and P. La Riviere. Constrain static target kinetic iterative image reconstruction for 4D cardiac CT imaging. *Proc. SPIE*, 7873:78730S–78730S–7, 2011.
- [4] K. Sauer and C. Bouman. A local update strategy for iterative reconstruction from projections. *Signal Processing, IEEE Transactions on*, 41(2):534–548, Feb 1993.
- [5] A. Alessio and P. Kinahan. Statistical reconstruction of targeted regions with application to CT and PET cardiac imaging. *American Journal of Roentgenology (supplement)*, 186(4):A46, 2006.
- [6] J. Fessler. Mean and variance of implicitly defined biased estimators (such as penalized maximum likelihood): applications to tomography. *Image Processing, IEEE Transactions on*, 5(3):493–506, Mar 1996.

Vessel Overlap Sparsity Index – A Predictive Metric for 3D+T Accuracy

Kevin Royalty, Timothy Szczykutowicz, Christopher Rohkohl, and Markus Kowarschik

Abstract—3D+T methods such as 4D DSA encode time-varying contrast information measured in only a few projections into an *a priori* 3D angiographic dataset. The methods have been shown to be accurate for cases where there are limited occurrences of overlapping vessels in the projection views. However, as the complexity of the 3D data increases, the algorithms are required to incorporate additional methods to correct for these occurrences that result in underdetermined problems. To date, the complexity of the 3D datasets has been described only in the context of “sparsity”, where only the number of non-zero voxels (relative to the total number of voxels) is considered. In this work, we propose a novel metric called the vessel overlap sparsity index (VOSI) to characterize the complexity of a given 3D dataset and evaluate its performance in predicting the results of a simple 3D+T algorithm that does not correct for overlap. We demonstrate in phantom experiments, that VOSI outperforms the standard sparsity metric in terms of predictability of the mean squared error metric (MSE) for scenarios of varying complexity. The strong correlation of VOSI and MSE makes it possible to characterize the complexity of given datasets and can serve as a baseline metric for comparing the overlap correction algorithms of various 3D+T algorithms for a 3D dataset of a given VOSI metric value.

I. INTRODUCTION

Recently, new methods for generating time-resolved 3D angiography have been developed by several groups[1]–[6]. These methods use an *a priori* segmented 3D vascular model, typically derived from rotational angiography (3D DSA). The segmented voxels are then used to define a sparse subset voxels that are encoded with time-varying measured data from x-ray projections at one or more fixed or rotating gantry positions. The projections are acquired such that the flow of a contrast agent through the vascular anatomy is captured.

The resulting 3D+T dataset has the potential to add clinical

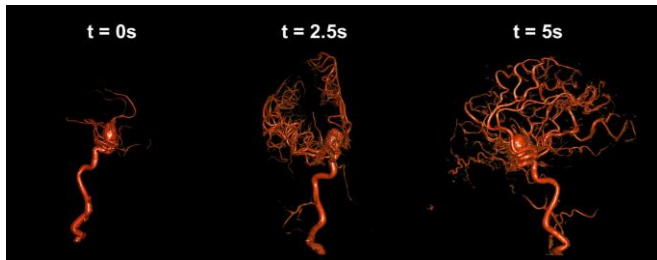


Fig. 1. Volume-rendered 4D DSA reconstruction result for three different time points (0s, 2.5s, and 5s), viewed at three unique orientations.

value by presenting the time-resolved angiographic data in 3D, allowing the user to rotate and view the 3D+T image from any

K. Royalty – Siemens Medical Solutions USA, Inc.; Department of Biomedical Engineering – University of Wisconsin, Madison, WI: kroyalty@wisc.edu

T. Szczykutowicz – Department of Radiology – University of Wisconsin, Madison, WI

C. Rohkohl, M. Kowarschik – Siemens AG, Healthcare Sector, Forchheim, Germany

arbitrary projection at any reconstructed time point. Volume rendering techniques can also be applied to this data to further enhance the physician’s ability to understand depth and morphological details of the vascular anatomy. Figure 1 shows an example of the 4D DSA algorithm[1], [2] results visualized with a volume rendering display

3D+T algorithms such as 4D DSA have been shown to be very accurate for simple anatomical situations where there is little to no overlap between vascular structures along a projection ray, often referred to as “sparse” vascular anatomy. However, as the vascular anatomy becomes increasingly complex and less “sparse”, the number of overlapping vascular structures in the measured projection increases. This situation leads to an increasingly underdetermined system of unknown voxel time attenuation (TAC) values $V(X, t)$ (where X represents the 3D voxel location) relative to our measured projection values $P(U, t)$, where U represents 2D coordinates in the coordinate system for the measured projection at time t . Each 3D+T algorithm uses varying assumptions and techniques (which range significantly in complexity and computational requirements) to calculate corrected $V(X, t)$ values for vessel overlap situations. Regardless of the 3D+T approach, as the incidence of vessel overlap increases, the more difficult the problem becomes to recover the correct TAC values.

Currently, there is no accepted method or metric used to evaluate and characterize the complexity of a given 3D DSA dataset for use in generating 3D+T results. Literature related to the topic of undersampled signal recovery commonly refers to these datasets as having a necessary level (or amount) of sparsity[7], [8]. In this case, they are defining sparsity as a vector with very few non-zero elements relative to the total size of the vector. Increasing the number of blood vessels will decrease the sparsity of the 3D DSA volume, lead to an increased number of overlap occurrences, and potentially reduce the accuracy of the 3D+T result. However, the classic definition of sparsity for the 3D DSA volume is not sufficient to predict the results of the 3D+T algorithm alone. Due to the projection geometry, the spatial locations and distributions of the vessels also plays a significant factor in the accuracy of the 3D+T results. Figures 2 and 3 provide a simple example to illustrate this point.

Figure 2 shows a cross-sectional slice of a simple digital phantom with three vessels. In four different scenarios, the average distance between the vessels was increased by approximately a factor of two (Fig.2 a-d). It is important to note that each scenario exhibits the same sparsity as defined by the number of non-zero voxels. Only the positions of the vessels have changed. Each vessel was assigned a unique TAC as shown in the right pane. Using a forward projection, this

data can then be used to generate measured projection data, which can then in turn be used to generate 3D+T results. For the purposes of this paper,

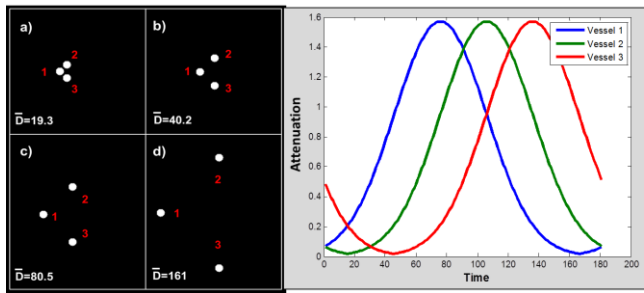


Fig. 2. Left: Simple 3 vessel phantom model with increasing distance between the 3 vessels (a,b,c,d). Right: TAC curve functions assigned to each of the 3 vessels.

we will use a basic 3D+T algorithm derived from the 4D DSA method[1], [2]. However, in order to best analyze the results and develop an appropriate metric, we will not implement a method for vessel overlap correction in this work in order to best establish an initial correlation between the metric and 3D+T results. Figure 3 shows the results of the basic 3D+T algorithm with no overlap correction (green) for increasing distance between vessels compared to the ground truth (blue).

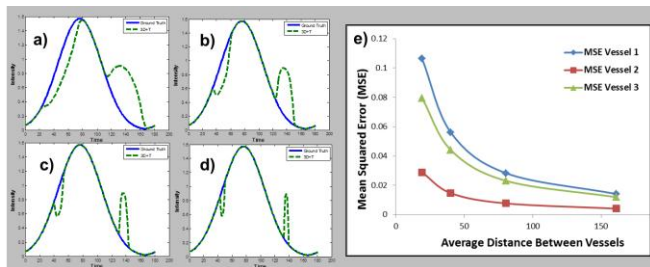


Fig. 3. Left: Vessel location #1 3D+T TAC results (green-dashed line) for increasing average distance between vessels compared to ground truth (blue line) (a-d). Right: Mean Squared Error plots for each vessel as a function of average distance between vessels.

These examples clearly show that the accuracy of the 3D+T results are influenced not only by the number vessels present, but also by the spatial distribution of these vessels. The goal of this research was to develop a vessel overlap sparsity index (VOSI) metric that is capable of more accurately predicting the quality of 3D+T results given specific anatomy. The VOSI metric has the potential to characterize the complexity of a given dataset and offer guidance as to when 3D+T algorithms can accurately be applied for clinical cases where the ground truth is not known. The VOSI metric will also provide a data-dependent metric by which 3D+T implementations can be compared for their ability to accurately recover TAC information for cases of a known VOSI metric value.

II. METHODS AND MATERIALS

A. Digital Phantom Design

In order to support the initial development of the vessel overlap incidence metric, two series of digital phantom slices were developed. In the future, this concept can be extended to incorporate the full z-axis series of slices (3D volume).

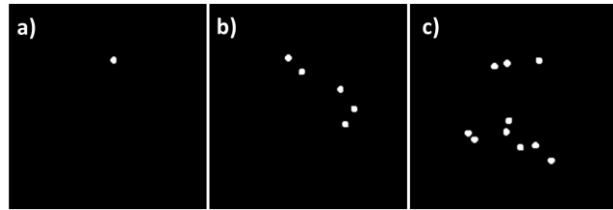


Fig. 4. Example digital phantom slices with increasing number of randomly placed vessels (1, 5, and 10 vessels).

The first series of phantom slices consist of 3 different slices, each with an increasing number of simulated vessel cross sections with a uniform diameter. The simplest of these consist of a single vessel, with the most complex slice having 10 vessels as shown in Figure 4. The locations of the vessels are randomly selected for each slice, with the constraint that no vessel may overlap with another vessel. The second series of phantom slices also consisted of 3 slices, each with a decreasing radius within which a constant number of vessels ($n=10$) are randomly distributed relative to the total field of view (FOV) of the slice. The radius decreased from 75% of the total FOV to 35% of the FOV in steps of 20%.

For the purposes of this initial work, all calculations were performed using simulated rotational acquisitions with parallel ray geometry using Matlab R2013a (The Mathworks, Inc., Matick, MA). This technique can be extended to support fan beam and cone beam geometry as applicable.

B. Methods for Generation of Ground Truth Datasets

For each digital phantom slice dataset, voxels that define a unique vessel within the slice were assigned a randomly generated TAC to represent the time-varying contrast kinetics for that particular vessel. For all cases, a total number of 180 time steps were used. The TAC curve was generated as a Gaussian distribution in time with a randomly assigned time shift within the interval of $[-45, 45]$ time steps and a randomly assigned standard deviation (σ) within the interval $[-11, 11]$. After the TACs were assigned to each vascular voxel in the 2D slice, the resulting dataset represents the ground truth data that will be used to evaluate the accuracy of the 3D+T result.

After the time-resolved ground truth voxel data was generated, each time step was then reprojected for each angular step to create a series of time-varying projections that range from $[0^\circ, 179^\circ]$ with an angular step size of 1° . This

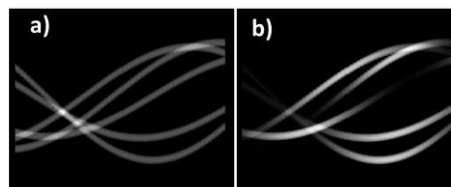


Fig. 5. a) Sinogram of constraint 3D data (single slice). b) Sinogram of time-varying projections based on the ground truth phantom

data represents the measured projection values that are then used as input to the 3D+T algorithm. Figure 5 demonstrates an example of this data. Figure 5a shows the sinogram of the

static 3D slice after reprojection. Figure 5b shows the sinogram of the ground truth 3D+T digital phantom after the reprojection of each time step.

C. Vessel Number Area Histogram

The VOSI metric is based on the dose volume histogram concept commonly used in radiation therapy[9]. Realizing that 3D+T reconstruction accuracy is strongly related to the degree of overlap of vessels within a projection data set, the VOSI metric measures the percent of the sinogram in which vessels can be uniquely counted or distinguished. For example, Figure 6a shows slice with a total of 10 vessels. Figure 6b displays the corresponding sinogram for Figure 6a. For each view angle in the sinogram, a determination was made of how many unique vessels could be distinguished. A unique vessel was defined as one or more nonzero values bordered by zero values. In the case of vessel overlap, two or more vessels will be counted in the sinogram as a single nonzero series of values for a given view angle and therefore considered as a single vessel. Figure 6c is a plot of the number of distinguished vessels as a function of view angle. Figure 6d is a plot of what we refer to as the vessel number area histogram. This histogram plots the percent of the sinogram at or above a given vessel number. The VOSI metric is then calculated as

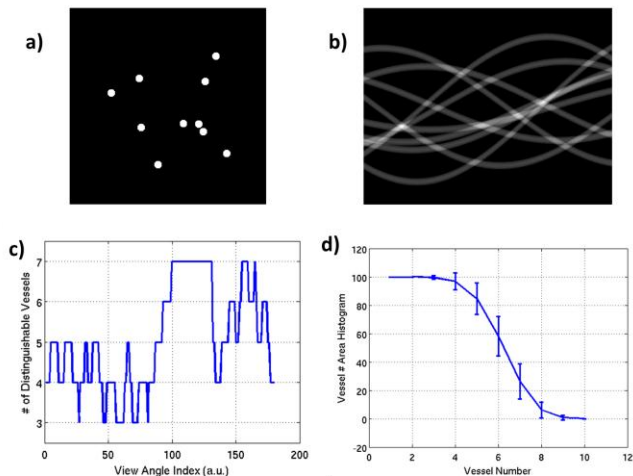


Fig. 6. a) Vessel phantom (n=10). b) Sinogram of (a). c) Vessel detection as a function of view angle. d) Vessel number area histogram

the ratio of the area under the curve of the vessel number area histogram to the ideal vessel number area histogram. The area under an ideal vessel number area histogram (where all vessels are detected correctly) is calculated as 100% multiplied by the number of vessels in each slice. Due to vessel overlap, the known vessel number cannot be determined from the sinogram, and was calculated from the actual image slice using connected components analysis. In practice the known vessel number can easily be determined from the segmentation of an *a priori* 3D DSA image volume.

D. Methods for Evaluation of 3D+T Results

The original static slice data (*a priori* 3D DSA volume) and the measured time-varying projections are then used as input to the 3D+T algorithm defined in the introduction. For evaluation, the results of the 3D+T algorithm are then compared to the original ground truth data using a mean squared error (MSE) analysis.

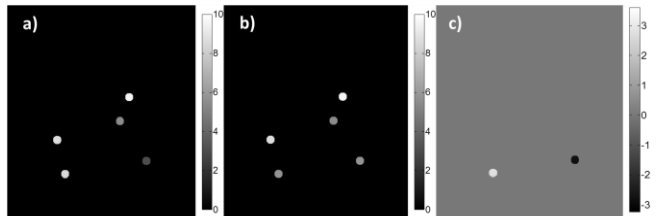


Fig. 7. a) Ground truth slice for t=179. b) 3D+T result for t=179. c) Residual comparison image used to calculate MSE

Figure 7 shows an example of a time frame from the ground truth data (Figure 7a), the 3D+T result from the same time frame (Figure 7b), and the residual comparison image (Figure 7c). The MSE was calculated across all time points for each vessel. The average MSE was then calculated across all vessels for each slice providing a composite MSE value for each vessel phantom configuration. This composite MSE value was then used to evaluate the performance of our metric. In order to establish a large sample size of simulation results, each series of phantoms (increasing vessel number and decreasing FOV) were generated and evaluated for 30 unique vessel position instances. Results were averaged across the 30 instances and the performance of the VOSI metric was compared to the MSE of the 3D+T results.

III. RESULTS

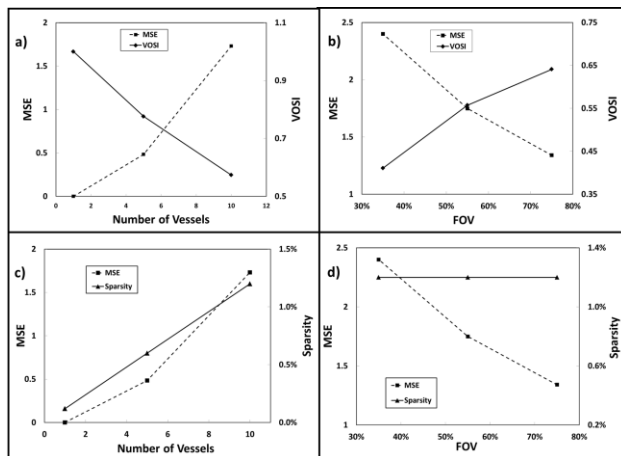


Fig. 8. a) Plot of MSE as a function of vessel number compared with VOSI metric as a function of vessel number. b) Plot of MSE as a function of FOV compared with VOSI metric as a function of FOV. c-d) Results of sparsity metric substituted for VOSI.

In the simulations that were performed across the two series of phantoms (increasing vessel number and decreasing FOV), the VOSI metric showed a very close inverse correlation to the MSE results of the 3D+T simulations. Figure 8 provides a graphical representation of the MSE and VOSI results as a

function of vessel number (Figure 8a) and FOV constraint (Figure 8b). Both Figure 8a and Figure 8b demonstrate a close inverse relationship between the VOSI metric and the MSE results of the 3D+T calculations. Figure 8c and 8d plot the same relationship substituting sparsity for the VOSI metric. Figure 8c shows a strong correlation between sparsity and the MSE results for increasing vessel number. However, Figure 8d demonstrates the failure of the sparsity metric to correlate with MSE results. Figure 9a and Figure 9b show

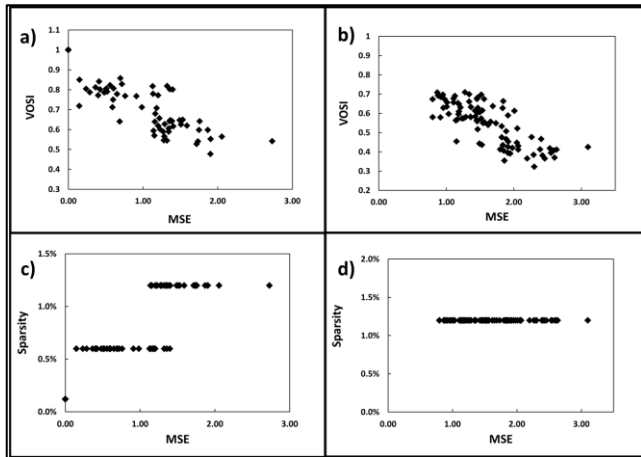


Fig. 9. a) Scatter plot of VOSI vs MSE for vessel number series (n=90). b) Scatter plot of VOSI vs MSE for FOV series (n=90). c) Scatter plot of sparsity vs MSE for vessel number series. d) Scatter plot of sparsity vs MSE for FOV series.

scatter plots of the VOSI versus MSE metric for all simulation data points (n=90) for the vessel number and FOV series respectively.

The Pearson correlation coefficient for VOSI and MSE was calculated for each series (increasing vessel number and FOV) and also shows a strong inverse correlation ($r=-0.91$, $p<0.01$ and $r=-0.78$, $p<0.01$ respectively), further confirming the results shown in Figures 8 and 9 for the VOSI metric. The Pearson correlation coefficient was also calculated for sparsity and MSE, confirming a strong correlation between sparsity and MSE for vessel number, but no correlation for FOV ($r=0.90$, $p<0.01$ and $r=0$, $p=1$ respectively).

The VOSI metric can be examined as a function of slice number (or z-axis position) as shown in Figure 10a-c. In this

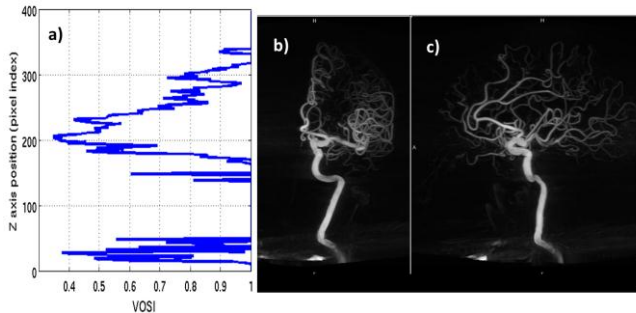


Fig. 10. a) Plot of VOSI metric as a function of z-axis position. b) Anterior view of 3D DSA aligned with 10a to demonstrate the anatomical regions with highest overlap issues. c) Lateral view of 3D DSA also aligned to 10a

case, the VOSI metric can be used to identify the areas within

a 3D volume that are most likely to have vessel overlap that will impact the 3D+T results.

Alternatively, a composite VOSI score can be assigned to a given 3D DSA volume. In these cases, it is suggested to weight the composite VOSI metric to a percentage of the lowest total VOSI scores of the slices. Future work will be aimed at developing guidelines for establishing the composite VOSI metric.

IV. SUMMARY

In summary, the VOSI metric demonstrates a very strong inverse correlation with 3D+T results for vessel phantoms of various complexities. In practice the VOSI metric can be used to classify the complexity of given datasets for use with 3D+T algorithms. As shown in this work the VOSI metric can be used to predict the performance of a 3D+T algorithm that does not include corrections for vessel overlap. In practice, 3D+T algorithms that include overlap correction techniques can be evaluated against phantoms of varying VOSI scores in order to establish a baseline in which to judge the performance of the overlap correction. In other words, for a dataset with a given VOSI value, the MSE error associated with a given 3D+T algorithm can be estimated and compared with other approaches.

REFERENCES

- [1] B. Davis, K. Royalty, M. Kowarschik, C. Rohkohl, E. Oberstar, B. Aagaard-Kienitz, D. Niemann, O. Ozkan, C. Strother, and C. Mistretta, "4D Digital Subtraction Angiography: Implementation and Demonstration of Feasibility," *Am. J. Neuroradiol.*, Apr. 2013.
- [2] C. A. Mistretta, E. Oberstar, B. Davis, E. Brodsky, and C. M. Strother, "4D-DSA and 4D fluoroscopy: preliminary implementation," pp. 762227-762227, Mar. 2010.
- [3] I. Waechter, J. Bredno, R. Hermans, J. Weese, D. C. Barratt, and D. J. Hawkes, "Model-based blood flow quantification from rotational angiography," *Med. Image Anal.*, vol. 12, no. 5, pp. 586-602, Oct. 2008.
- [4] I. Waechter, J. Bredno, J. Weese, D. C. Barratt, and D. J. Hawkes, "Using flow information to support 3D vessel reconstruction from rotational angiography," *Med. Phys.*, vol. 35, no. 7, pp. 3302-3316, Jun. 2008.
- [5] A. D. Copeland, R. S. Mangoubi, M. N. Desai, S. K. Mitter, and A. M. Malek, "Spatio-Temporal Data Fusion for 3D+T Image Reconstruction in Cerebral Angiography," *IEEE Trans. Med. Imaging*, vol. 29, no. 6, pp. 1238-1251, 2010.
- [6] H. Schmitt, M. Grass, R. Suurmond, T. Köhler, V. Rasche, S. Hähnel, and S. Heiland, "Reconstruction of blood propagation in three-dimensional rotational X-ray angiography (3D-RA)," *Comput. Med. Imaging Graph.*, vol. 29, no. 7, pp. 507-520, Oct. 2005.
- [7] E. J. Candes, J. Romberg, and T. Tao, "Robust uncertainty principles: exact signal reconstruction from highly incomplete frequency information," *IEEE Trans. Inf. Theory*, vol. 52, no. 2, pp. 489-509, 2006.
- [8] C. A. Mistretta, "Undersampled radial MR acquisition and highly constrained back projection (HYPR) reconstruction: Potential medical imaging applications in the post-Nyquist era," *J. Magn. Reson. Imaging*, vol. 29, no. 3, pp. 501-516, 2009.
- [9] F. M. Khan, "The Physics of Radiation Therapy," *CERN Document Server*, 2003. [Online]. Available: <http://cds.cern.ch/record/1101043>. [Accessed: 23-Jan-2014].

Noise-Weighted Spatial Domain FBP Algorithm

Gengsheng L. Zeng

Abstract—The purpose of this paper is to implement a noise-weighted FBP algorithm in the form of “convolution” backprojection, but this “convolution” has a spatially variant integration kernel. Noise-weighted filtered backprojection (FBP) algorithms have been developed in recent years, with filtering being performed in the Fourier domain. The noise weighting makes the ramp filter in the FBP algorithm shift-varying. It is not efficient to implement shift-varying filtration in the Fourier domain. It is known that Fourier-domain multiplication is equivalent to spatial-domain convolution. An expansion method is suggested in this paper to obtain a closed-form integration kernel. The noise weighted FBP algorithm can now be implemented in the spatial domain efficiently. The total computation cost is less than that of the Fourier domain implementation. Computer simulations are used to show the three-term expansion method to approximate the filter kernel. A clinical study is used to verify the feasibility of the proposed algorithm.

Keywords—Image reconstruction; analytical reconstruction algorithm; tomography; noise modeling; CT; Convolution

I. INTRODUCTION

The filtered backprojection (FBP) algorithm has been in use for several decades [1-5]. It is the workhorse of x-ray CT image reconstruction. A drawback of the FBP algorithm is that it may produce very noisy images. Algorithms based on optimization of an objective function are able to incorporate the projection noise model and produce less noisy images than the FBP algorithm. Usually these algorithms are iterative algorithms [6-10]. In order to shorten the computation time of an iterative algorithm, effort has been made to transform a regular iterative algorithm into an iterative FBP algorithm [11]. Another approach to noise control is to apply an adaptive filter or nonlinear filter to the projection measurements [12, 13]. We recently developed a non-iterative FBP algorithm that can model the projection noise on a view-by-view or ray-by-ray basis [14, 15].

One drawback of the noise-weighted FBP algorithm presented in [15] is that the modified ramp filtering must be implemented in the Fourier domain, because we did not know the expression of the spatial-domain “convolution” kernel. It is not efficient to implement shift-varying filtration in the Fourier domain. Projection data at each view must be filtered multiple times (say, 11 times) if the Fourier domain filtering method is used as suggested in [15]. It is known that Fourier-domain multiplication is equivalent to spatial-domain convolution. In principle, any FBP algorithm with Fourier-domain filtering can find its equivalent FBP algorithm that performs filtering in the spatial domain as convolution, if the convolution kernel can be readily obtained.

G. L. Zeng is with the Department of Engineering, Weber State University, Ogden, UT 84408, USA, and the Utah Center for Imaging Research, Department of Radiology, University of Utah, Salt Lake City, UT 84108, USA. E-mail: larryzeng@weber.edu. (801) 581-3918

This paper will implement the noise-weighted FBP algorithm presented in [15] in the form of “convolution” backprojection. However, this “convolution” is not a true convolution operation, because the integration kernel varies according to the noise variance. An expansion method will be suggested in this paper to obtain a closed-form integration kernel so that the “convolution” can be computed efficiently.

II. METHODS

Part A of this section will review and summarize what we already know about the noise-weighted FBP algorithm, according to our recent publications [14, 20]. Part B is the main contribution of this paper, and the Fourier-domain filtering in the noise-weighted FBP algorithm will be converted into spatial-domain filtering in the form of a dot product, which is similar to convolution.

A. Noise-weighted FBP algorithm

The noise-weighted FBP algorithm was derived based on minimizing the following weighted least-squares objective function $v(f)$ with a data fidelity term and a Bayesian penalty term:

$$v(f) = \|[Rf](s, \theta) - p(s, \theta)\|_w^2 + \beta \|f(x, y) ** c(x, y) - g(x, y)\|^2 \quad (1)$$

where the image to be reconstructed is $f(x, y)$ and its Radon transform is $[Rf](s, \theta)$, which is defined as [5]

$$[Rf](s, \theta) = \int_{-\infty}^{\infty} \int_{-\infty}^{\infty} f(x, y) \delta(x \cos \theta + y \sin \theta - s) dx dy. \quad (2)$$

In (2), δ is the Dirac delta function, θ is the detector rotation angle, and s is the line-integral location on the detector. The Radon transform $[Rf](s, \theta)$ is the line-integral of the object $f(x, y)$. Image reconstruction is to solve for the object $f(x, y)$ from its Radon transform $[Rf](s, \theta)$. The first term in (1) is the data fidelity term that encourages the Radon transform of $f(x, y)$ to be close to the measured projections $p(s, \theta)$. In the first term, the norm is the conventional L_2 norm with a weighting function w . The second term in (2) is the Bayesian term that encourages a filtered version of $f(x, y)$ to look like a prior image $g(x, y)$.

The function $c(x, y)$ is a symmetric image domain convolution kernel and “**” represents the image domain 2D convolution. If $c(x, y)$ is the 2D Dirac delta function $\delta(x, y) = \delta(x) \cdot \delta(y)$, then the Bayesian term encourages $f(x, y)$ to be similar to $g(x, y)$. For example, $f(x, y)$ can be a high-noise dynamic image and $g(x, y)$ can be a low-noise slow-motion image by averaging images from adjacent time frames.

If $g(x, y) = 0$ and $c(x, y) = \delta(x, y)$, the Bayesian regularization term encourages a minimum norm solution.

Note: There was a mistake in the Appendix A of [19] where we said that when $c(x, y) = 1$ the regularization term encourages a minimum norm solution. If $g(x, y) = 0$ and $c(x, y)$ is a Laplacian kernel (i.e., the sum of second-order partial-derivative kernels), the regularization term encourages a smooth image.

After minimizing the objective function (1) by using the calculus of variations,²¹ the optimal solution $f(x, y)$ must satisfy an Euler-Lagrange equation,¹⁹ which is an integral equation and may not have an explicit solution if the weighting function w depends on both variables s and θ . If we restrict that the weighting function w only depends on θ with $\tan \theta = \omega_y / \omega_x$, not on s , an explicit solution of the optimal solution $f(x, y)$ can be obtained in the Fourier domain:

$$F(\omega_x, \omega_y) = \frac{w(\theta) \cdot B(\omega_x, \omega_y) + \beta \cdot G(\omega_x, \omega_y) \cdot C(-\omega_x, -\omega_y)}{\frac{w(\theta)}{\sqrt{\omega_x^2 + \omega_y^2}} + \beta \cdot |C(\omega_x, \omega_y)|^2} \\ = \frac{\sqrt{\omega_x^2 + \omega_y^2} \cdot B(\omega_x, \omega_y) + \beta \cdot \frac{C(-\omega_x, -\omega_y) \sqrt{\omega_x^2 + \omega_y^2}}{w(\theta)} \cdot G(\omega_x, \omega_y)}{1 + \beta \cdot \frac{\sqrt{\omega_x^2 + \omega_y^2} \cdot |C(\omega_x, \omega_y)|^2}{w(\theta)}} \quad (3)$$

where B , C , F , and G are the 2D Fourier transform of b , c , f , and g , respectively. The derivation of (3) was given in [18, 19]. It is interesting to see two extreme cases of (3). In the case of $\beta = 0$, (3) becomes

$$w(\theta)F(\omega_x, \omega_y) = w(\theta) \cdot B(\omega_x, \omega_y) \sqrt{\omega_x^2 + \omega_y^2}$$

or (assuming $w(\theta) \neq 0$)

$$F(\omega_x, \omega_y) = B(\omega_x, \omega_y) \sqrt{\omega_x^2 + \omega_y^2}. \quad (3a)$$

In the case of $\beta = \infty$, (3) becomes

$$F(\omega_x, \omega_y) |C(\omega_x, \omega_y)|^2 = G(\omega_x, \omega_y) \cdot C(-\omega_x, -\omega_y)$$

or

$$F(\omega_x, \omega_y) \cdot C(\omega_x, \omega_y) = G(\omega_x, \omega_y). \quad (3b)$$

Eq. (3a) enforces the data fidelity term in the objective function (1), and (3b) enforces the Bayesian penalty term in (1). Here $b(x, y)$ is the pure backprojection of the raw projections without any filtering. Using the Central Slice Theorem,⁵ an FBP algorithm can be readily obtained from (3) as

$$f(x, y) = \int_0^\pi q(s, \theta) \big|_{s=x \cos \theta + y \sin \theta} d\theta, \quad (4)$$

where q is the filtered version of the combined data $p_{combined}$:

$$p_{combined}(s, \theta) = p(s, \theta) + \frac{\beta}{w(\theta)} \cdot p_g(s, \theta) \quad (5)$$

and the convolution kernel $h_{w(\theta)}(s)$ for the filter is a modified ramp filter kernel and is defined as

$$h_{w(\theta)}(s) = \text{1D Inverse FT} \left\{ \frac{|\omega|}{1 + \beta \cdot \frac{|\omega| \cdot |C_1(\omega)|^2}{w(\theta)}} \right\}. \quad (6)$$

Thus, the function q used in (4) is the convolution of $p_{combined}$ and $h_{w(\theta)}(s)$ with respect to variable s :

$$q(s, \theta) = p_{combined}(s, \theta) * h_{w(\theta)}(s). \quad (7)$$

It is interesting to notice that when $\beta = 0$, the filter defined in (6) is reduced to the conventional ramp filter and the noise weighting is not effective. Therefore, it is importance to include a Bayesian term in the objective function if you intend to enforce noise weighting in an FBP reconstruction.

In (6), $C_1(\omega)$ is a central section of $C(\omega_x, \omega_y)$. If $c(x, y) = \delta(x, y)$, then $C_1(\omega) = 1$. In (5), the secondary data $p_g(s, \theta)$ are generated from the prior image $g(x, y)$ by first convolving with the filter kernel $c(x, y)$, second performing forward projection, and third ramp filtering. In order to understand the reason that a ramp filtering procedure is needed in generation of $p_g(s, \theta)$, we notice that $b(x, y)$ is the backprojection of $p(s, \theta)$ and $g(x, y)$ is the backprojection of $p_g(s, \theta)$ [at this moment, let us temporally assume $c(x, y) = \delta(x, y)$], and that $b(x, y)$ is a blurred image and $g(x, y)$ is sharp image as $f(x, y)$.

In the rest of the paper except for Part E in this section, we will only consider the case of $c(x, y) = \delta(x, y)$ and $g(x, y) = 0$ for the sake of simplicity. In this special case, we have

$$h_{w(\theta)}(s) = \text{1D Inverse FT} \left\{ \frac{|\omega|}{1 + \frac{\beta}{w(\theta)} \cdot |\omega|} \right\}, \quad (8)$$

and

$$f(x, y) = \int_0^\pi [p(s, \theta) * h_{w(\theta)}(s)] \big|_{s=x \cos \theta + y \sin \theta} d\theta. \quad (9)$$

We denote the filter's Fourier-domain transfer function as

$$H_{w(\theta)}(\omega) = \frac{|\omega|}{1 + \frac{\beta}{w(\theta)} \cdot |\omega|}. \quad (10)$$

The above discussion is under the assumption that the noise weighting $w(\theta)$ is a function of view angle θ . This view-by-view noise-weighting scheme can be extended to a ray-by-ray noise weighting scheme in an *ad hoc* manner [15]. For ray-based noise weighting, w is a function of the ray: $w = w(\text{ray}) = w(s, \theta)$. At each view angle θ , we quantize the ray-based weighting function into $n+1$ values: w_0, w_1, \dots, w_n , which in turn give $n+1$ different filters as defined in (10). That is,

$$H_k(\omega) = |\omega| / (1 + \beta \cdot |\omega| / w_k), \text{ for } k = 0, 1, \dots, n. \quad (11)$$

Using these $n+1$ filters, $n+1$ sets of filtered projections are obtained. Before backprojection, one of these $n+1$ projections is selected for each ray according to its proper weighting function. Only one backprojection is performed using the selected filtered projections.

B. Spatial domain implementation

It is well known that using FFT and IFFT to implement convolution is more computationally efficient than calculating convolution directly in the spatial domain. Let the detector size be N . If the filter is shift invariant, the spatial domain convolution takes $O(N^2)$ arithmetical operations, while the FFT/IFFT method computes can it with $O(N \log N)$ operations. However, if the filter is shift variant, the spatial domain implementation still takes $O(N^2)$ arithmetical operations, while the FFT/IFFT method computes it using $O(N^2 \log N)$ operations.

At the end of Part A, the spatially varying filter was implemented by Fourier-domain multiplication and using $n+1$ filters with the help of quantization. In our previous implementations, the value n was selected as 10. Without using the quantization method, one would use 1024 filters to filter the projections 1024 times, if there were 1024 detection channels (or detection cells) on the detector. Therefore, it is not efficient to perform filtering in the Fourier domain if the filter is shift variant.

On the other hand, it is much more efficient if filtering is implemented in the spatial domain as integration when the kernel is spatially varying. If the integration kernel has a closed-form expression, the computation cost for spatial-domain filtering is the same as that of convolution, both using a dot product for implementation.

A routine method to find a discrete filter kernel $h_w(n)$ is to evaluate the following integral [5], which is the 1D inverse Fourier transform of the transfer function defined in (10) with $w(\theta)$ replaced by $w(s, \theta)$ and s replaced by integer n :

$$h_w(n) = \int_{-1/2}^{1/2} H_{w(s,\theta)}(\omega) e^{-i2\pi n\omega} d\omega = 2 \int_0^{1/2} \frac{\omega}{1 + \frac{\beta}{w} \cdot \omega} \cos(2\pi n\omega) d\omega, \quad (12)$$

where we used the property that the transfer function $H_w(\omega)$ is an even function. After quantization, w in (12) is w_k . It is unlikely that the integral in (12) has an explicit closed-form expression.

Our method is to find a finite expansion of the function $H_w(\omega)$ and the expansion should have closed-form inverse Fourier transform. Since $1/(1 + \beta_0 \omega)$ with $\beta_0 > 0$ is a monotonically decreasing function on $[0, 1/2]$, we have decided to use the following approximation:

$$\frac{\omega}{1 + \beta_0 \cdot \omega} \approx \frac{\omega}{3} (e^{-\beta_0 \omega} + e^{-\beta_1 \omega} + e^{-\beta_2 \omega}) \quad \text{with } \beta_0 = \frac{\beta}{w}, \quad (13)$$

where the parameters β_1 and β_2 are to be determined. The range of ω is $[0, 1/2]$. The approximation (13) is already exact at $\omega = 0$. We further request that (13) to be exact at $\omega = 1/4$ and $\omega = 1/2$. Thus, we have two unknowns (β_1 and β_2) and two equations:

$$\frac{1}{1 + \beta_0/2} = \frac{1}{3} (e^{-\beta_0/2} + e^{-\beta_1/2} + e^{-\beta_2/2}), \quad (14)$$

$$\frac{1}{1 + \beta_0/4} = \frac{1}{3} (e^{-\beta_0/4} + e^{-\beta_1/4} + e^{-\beta_2/4}). \quad (15)$$

Solving these two equations yields

$$\beta_1 = -4 \cdot \ln\left(\frac{A + \sqrt{2B - A^2}}{2}\right), \quad \beta_2 = -4 \cdot \ln\left(\frac{A - \sqrt{2B - A^2}}{2}\right), \quad (16)$$

where

$$A = \frac{3}{1 + \beta_0/4} - e^{-\beta_0/4}, \quad B = \frac{3}{1 + \beta_0/2} - e^{-\beta_0/2}. \quad (17)$$

Using the above results and an integral table, the closed-form filter kernel (12) can be obtained as ($n \neq 0$):

$$\begin{aligned} h_w(n) &= \frac{2}{3} \int_0^{1/2} \omega (e^{-\beta_0 \omega} + e^{-\beta_1 \omega} + e^{-\beta_2 \omega}) \cos(2\pi n\omega) d\omega \\ &= \frac{-2}{3} \sum_{k=0}^2 \frac{(-1)^k e^{-\frac{\beta_k}{2}} (\beta_k^3 + 4\beta_k \pi^2 n^2 + 2\beta_k^2 - 8\pi^2 n^2) - 2\beta_k^2 + 8\pi^2 n^2}{(\beta_k^2 + 4\pi^2 n^2)^2}, \end{aligned} \quad (18)$$

and

$$h_w(0) = -\sum_{n \neq 0} h_w(n) = -\sum_{n=1}^2 h_w(n). \quad (19)$$

The purpose of (19) is to guarantee that $H_w(0) = 0$. The filter kernel $h_w(n)$ is an even function with respect to index n .

If we take the limit of $\beta \rightarrow 0$, (18) reduces to

$$h(n) = \begin{cases} 1/4 & n = 0 \\ 0 & n = \pm 2, \pm 4, \pm 6, \dots \\ -1/(\pi n)^2 & n = \pm 1, \pm 3, \pm 5, \dots \end{cases} \quad (20)$$

which is the well-known convolution kernel for the conventional ramp filter.

C. Selection of β and weights w

The newly derived FBP algorithm's filter kernel depends on $\beta_0 = \beta/w(s, \theta)$, which in turn depends on the Bayesian term control parameter β and the current ray weighting factor $w(s, \theta)$.

The principle of selecting both β and $w(s, \theta)$ is exactly the same as that for the Fourier-domain implementation. Both methods can use the same β and $w(s, \theta)$ values. There is a trade-off consideration for the objective function (1). A larger β value emphasizes the regularization Bayesian term more, and

usually encourages a smoother image with a lower resolution. Setting β to zero or an extremely small positive value results in a high resolution but noisy image. As discussed in Reference 16, the FBP algorithm is somewhat equivalent to an iterative algorithm with an iteration number of infinity. Also, when $\beta = 0$, the relative noise weighting is not effective. By “relative” we mean that the projection rays compete with each other, and some rays are emphasized while others are de-emphasized by assigning a set of weights $w(s, \theta)$, one for each ray. The weights are also relative, meaning that you can scale the weights $w(s, \theta)$ by a constant value. However, this scaling value affects the selection of the value of β . Usually, the weights $w(s, \theta)$ are selected as the reciprocal of the noise variance (or a function of the variance) of projection value of the associated ray.

One may argue that in an iterative algorithm the noise weighting is always effective, regardless whether there is a Bayesian term or not. When a system of linear equations is not consistent due to noise, noise weighting is commonly used to define an acceptable "solution." When a linear system has a unique solution, the noise weighting should not affect the final (unique) solution. However, an iterative algorithm can only present a result with a finite number of iterations. Even though the final solution is unique, the noise weighting can alter the path towards to unique solution. Because the final solution is usually very noisy, early algorithm termination is the most common method for regularization. The effects of multiple convergent paths and early termination make the noise weighting effective in an iterative algorithm, regardless whether there is an explicit Bayesian regularization term or not. An effective regularization is always applied in one way or another.

One may ask under what conditions an imaging system can provide a unique (but maybe noisy) solution. An imaging system is usually modeled as an over-determined linear system, in which the number of unknowns (i.e., the image pixels) is less than the number of equations (i.e., the number of detection rays or cells or channels). Due to noise, this linear system is inconsistent and it does not have a solution. Let such a system be denoted in the matrix form as

$$AX = P, \quad (21)$$

where X is a vector contains all unknown image pixels, A is the projection matrix, and P is the array of noisy projections. However, its associated normal equation or weighted normal equation shown below, respectively, can give a unique least-squares solution:

$$A^T AX = A^T P \text{ or } A^T WAX = A^T WP, \quad (22)$$

where W is a certain weighting matrix. As discussed in [16], an FBP algorithm can be viewed as a solution to the least-squares problem, which is the unique solution to the “normal equation,” which is formulated in the continuous image domain.

D. The case of $c = \delta$ and $g \neq 0$

In the case of $c = \delta$ and $g \neq 0$, the Bayesian term encourages a solution $f(x, y)$ that looks like $g(x, y)$ as much as

possible while satisfies the projections as much as possible. For this special situation, (3) becomes

$$F(\omega_x, \omega_y) = \frac{\sqrt{\omega_x^2 + \omega_y^2}}{1 + \beta \cdot \frac{\sqrt{\omega_x^2 + \omega_y^2}}{w(\theta)}} [B(\omega_x, \omega_y) + \frac{\beta}{w(\theta)} \cdot G(\omega_x, \omega_y)]. \quad (23)$$

From the derivation in Part B, we conclude that the filter kernel $h_w(n)$ for this case is the same as that defined in (18) and (19). The only change is to replace the projections $p(s, \theta)$ by the combined projections

$$p_{combined}(s, \theta) = p(s, \theta) + \frac{\beta}{w(\theta)} \cdot p_g(s, \theta), \quad (24)$$

where the secondary data $p_g(s, \theta)$ are generated from the prior image $g(x, y)$ by first performing forward projection and then ramp filtering.

E. The case of c being a Laplacian filter and $g = 0$

If the filter c in Bayesian term of (1) is not a delta function δ , but is a Laplacian filter, which is a second-order derivative filter and is usually used as an edge detector, this Bayesian term penalizes sharp edges and high frequency noise. The 1D Fourier transform of the Laplacian kernel is ω^2 . Thus, the modified ramp filter for this case will have a Fourier-domain transfer function as

$$H_{w(\theta)}(\omega) = \frac{|\omega|}{1 + \frac{\beta}{w(\theta)} \cdot |\omega|^3}. \quad (25)$$

This function (25) has a faster high frequency gain drop-off rate than (10). Unfortunately, for this situation, the following approximation

$$\frac{\omega}{1 + \beta_0 \cdot \omega^3} \approx \frac{\omega}{3} (e^{-\beta_0 \omega} + e^{-\beta_1 \omega} + e^{-\beta_2 \omega}) \text{ with } \beta_0 = \frac{\beta}{w} \quad (26)$$

is rather poor. The Taylor expansion approximation

$$\frac{\omega}{1 + \beta_0 \cdot \omega^3} \approx \omega(1 + a\omega + b\omega^2) \text{ with } \beta_0 = \frac{\beta}{w} \quad (27)$$

is also poor if $\beta_0 \omega > 1$. A third option is the following expansion approximation

$$\frac{\omega}{1 + \beta_0 \cdot \omega^3} \approx \frac{\omega}{3} (e^{-\beta_0 \omega^2} + e^{-\beta_1 \omega^2} + e^{-\beta_2 \omega^2}) \text{ with } \beta_0 = \frac{\beta}{w}. \quad (28)$$

The range of ω is $[0, 1/2]$. The approximation (28) is already exact at $\omega = 0$. We further request that (28) to be exact at $\omega = 1/2^{4/3}$ and $\omega = 1/2$. Thus, we have two unknowns (β_1 and β_2) and two equations:

$$\frac{1}{1 + \beta_0 / 8} = \frac{1}{3} (e^{-\beta_1 / 8} + e^{-\beta_2 / 8} + e^{-\beta_2 / 8}), \quad (29)$$

$$\frac{1}{1+\beta_0/16} = \frac{1}{3}(e^{-\beta_0/16} + e^{-\beta_1/16} + e^{-\beta_2/16}). \quad (30)$$

Solving these two equations yields

$$\beta_1 = -16 \cdot \ln\left(\frac{A + \sqrt{2B - A^2}}{2}\right), \beta_2 = -16 \cdot \ln\left(\frac{A - \sqrt{2B - A^2}}{2}\right) \quad (31)$$

where

$$A = \frac{3}{1+\beta_0/16} - e^{-\beta_0/16} \text{ and } B = \frac{3}{1+\beta_0/8} - e^{-\beta_0/8}. \quad (32)$$

It can be verified that the fit (28) is satisfactory. The problem is that the definite integral

$$h_w(n) = \frac{2}{3} \int_0^{1/2} \omega (e^{-\beta_0 \omega^2} + e^{-\beta_1 \omega^2} + e^{-\beta_2 \omega^2}) \cos(2\pi n \omega) d\omega \quad (33)$$

can only be expressed in terms of the special function *erf* called the "error function." One could use a lookup table for the function *erf* or use further approximation of the function *erf*.

To date we do not yet have any good results for this special case: either the fits (26) and (27) are poor, or the inverse Fourier transform (33) does not have a closed-form expression. The example in Part E shows that the spatial-domain filtering method developed in Part B is not universal, and it can be inefficient if no closed-form kernels are available. In this case, it is better to use the Fourier-domain filtering.

F. Kernel for curved-detector fan-beam FBP algorithm

The discussion so far is about the development of a modified ramp filter that is suitable for the parallel-beam or flat-detector fan-beam imaging geometries. For the curved-detector fan-beam imaging geometry, its convolution kernel $h_{curve}(n)$ is a scaled version of the parallel-beam or the flat-detector fan-beam geometry's convolution kernel $h(n)$ [5]:

$$h_{curve}(n) = \left[\frac{n/D}{\sin(n/D)} \right]^2 h(n), \quad (34)$$

where D is the fan-beam focal length. Applying the curved-detector fan-beam relationship (34) to the newly developed noise-weighted kernel (18) yields

$$h_{curve,w}(n) = \frac{-2}{3} \left[\frac{n/D}{\sin(n/D)} \right]^2 \times \sum_{k=0}^2 \frac{(-1)^k e^{-\frac{\beta_k}{2}} (\beta_k^3 + 4\beta_k \pi^2 n^2 + 2\beta_k^2 - 8\pi^2 n^2) - 2\beta_k^3 + 8\pi^2 n^2}{(\beta_k^2 + 4\pi^2 n^2)^2} \quad (35)$$

III. IMPLEMENTATION AND DATA SETS

A. Implementation of the proposed FBP algorithm

Like the conventional convolution backprojection FBP algorithm, the proposed FBP algorithm first filters the projection data with a spatially variant, noise weighted, ramp

filter, and the filtering is performed in the spatial domain by evaluating a dot product. The filtered data are then backprojected into the image domain. Since the backprojection procedure of our algorithm is identical to the conventional backprojection, we only discuss the discrete implementation of the filtering procedure below.

We denote the discretely sampled projections as $p_d(n, m)$, where n is the index on the detector and m is the index of the view angle. We use a subscript d to indicate discretely sampled functions. For any fixed view angle m , do the following:

Loop through the detector cell index n :

Step 1: Consider the noise model of $p_d(n, m)$ and estimate the variance of the measurement $p_d(n, m)$. Let the weighting factor $w_d(n, m)$ be the reciprocal of the variance (or a function of the variance).

Step 2: Evaluate the spatial-domain filter kernel $h_w(n)$ according to (18) and (19).

Step 3: Calculate filtered projection value $q_d(n, m)$ using a dot product:

$$q_d(n, m) = \sum_k h_w(k-n) \cdot p_d(k, m). \quad (36)$$

Next n

In forming the spatial-domain filter kernel $h_w(n)$, one needs to select a Bayesian term control parameter β . A larger β gives a smoother and less noisy image. This value is chosen by trial-and-error and by incorporating with the selection of the weighting function w .

B. Low-dose cadaver CT data

To illustrate the feasibility of the proposed spatial-domain filtering FBP algorithm, a cadaver torso was scanned using an x-ray CT scanner with a low-dose setting. Data were collected with a diagnostic scanner (Aquilion ONE™, Toshiba America Medical Systems, Tustin, CA, USA; raw data courtesy of Leiden University Medical Center).

The imaging geometry was curved-detector cone-beam, the x-ray source trajectory was a circle of radius 600 mm. The detector had 320 rows, the row-height was 0.5 mm, each row had 896 channels, and the fan angle was 49.2°. A low-dose noisy scan was carried out. The tube voltage was 120 kV and current was 60 mA. There were 1200 views uniformly sampled over 360°. The reconstructed image array was 840 x 840 and the image resolution was 0.5 mm. The noise weighting factor for this data set was chosen as $w = \exp(-0.3 p)$, where p is the line-integral measurement. The Bayesian term control parameter β was chosen as 1.0×10^{-7} .

Only the central slice of image volume was reconstructed. The images were reconstructed by the conventional fan-beam FBP algorithm without noise weighting and by the proposed FBP algorithm with noise weighting using spatial-domain modified ramp filtering.

IV. RESULTS

Fig. 1 shows the Fourier-domain transfer functions of 4 filters according to approximation (13), for $\beta_0 = 0.1, 1, 5,$ and $20,$ respectively. The original functions represented by the left-hand-side of (13) are shown in solid curves, and the three-term expansions represented by the right-hand-side of (13) are shown in dotted curves. Approximations are shown to be fairly accurate, and more accurate approximations are obtained for smaller β_0 values.

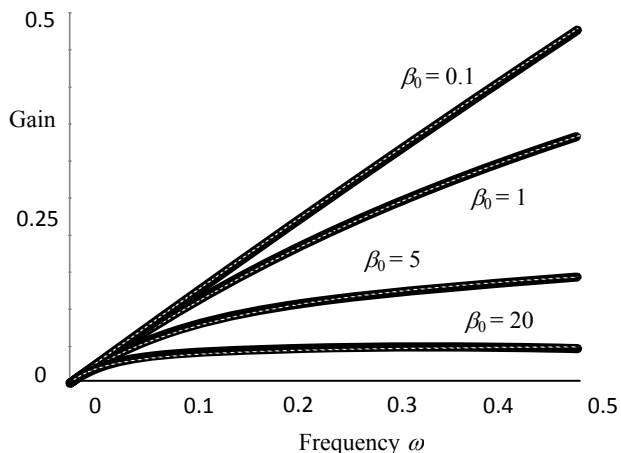


Fig. 1. Four pairs of Fourier-domain transfer functions according to approximation (13). The original functions represented by the left-hand-side of (13) are shown in solid curves, and the three-term expansions represented by the right-hand-side of (13) are shown in dotted curves.

Since an accurate approximation is usually achieved in a small region close to a point of interest, for example, about $\beta_0\omega = 0$. In order to obtain a good approximation in a large region with only few terms, it is important to select the basis functions that look similar to the original functions to be expanded. This was the reason that we chose $\{e^{-\beta_0\omega}\}$ to expand $1/(1+\beta_0\omega)$, and $\{e^{-\beta_0\omega^2}\}$ to expand $1/(1+\beta_0\omega^3)$. This was also the reason that we did not use Taylor expansion for $1/(1+\beta_0\omega)$ or $1/(1+\beta_0\omega^3)$, because when $\beta_0\omega > 1$ the approximation errors are large. Unfortunately, the functions $\{e^{-\beta_0\omega^2}\}$ or $\{\omega e^{-\beta_0\omega^2}\}$ do not have closed-form inverse Fourier transform expressions.

Fig. 2(a) shows the conventional (without noise weighting) fan-beam convolution backprojection reconstruction of a transverse slice in the abdominal region of the cadaver. The x-rays through the arms are attenuated more than x-rays in other orientations, and create the left-to-right streak artifacts in the middle of the image. Fig. 2(b) shows the reconstruction result using the proposed noise-weighted FBP with spatial-domain filtering implementation. The streak artifacts are effectively removed. Fig. 2(c) is the gold standard image, which is the conventional fan-beam convolution backprojection reconstruction using the standard dose CT data. The tube voltage was 120 kV and current was 500 mA.

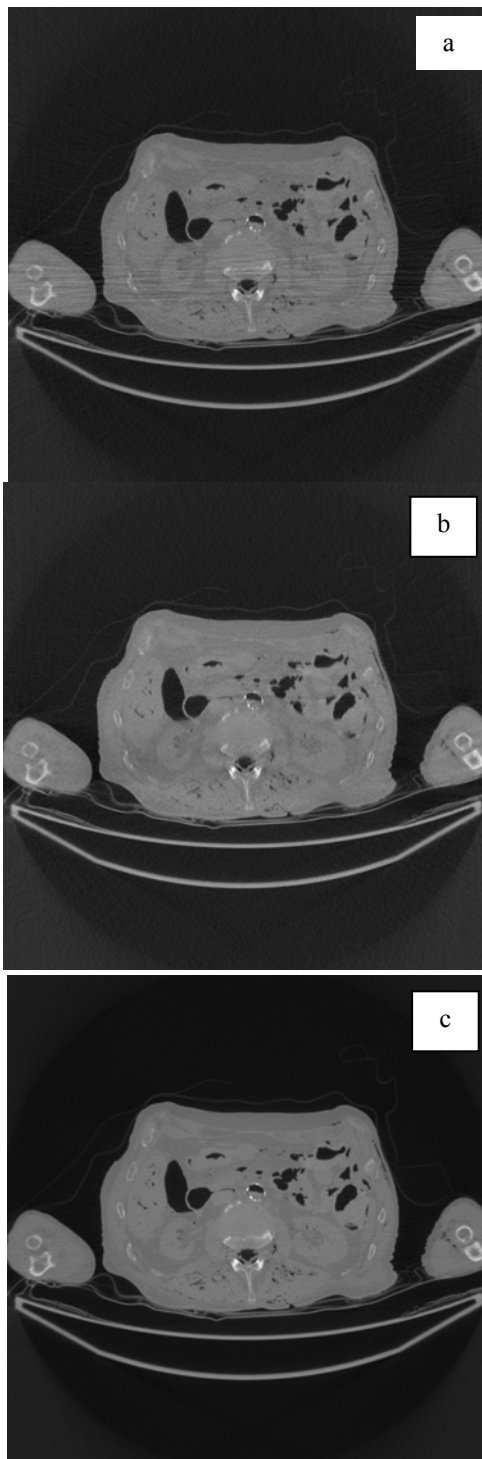


Fig. 2. Images reconstructed using low-dose CT clinical cadaver data. (a) Conventional convolution backprojection reconstruction. (b) Proposed noise-weighted FBP reconstruction with spatial-domain filtering. (c) Gold-standard: conventional convolution backprojection reconstruction using regular dose CT data.

V. CONCLUSIONS

This paper developed a spatial-domain implementation method for our previously proposed noise-weighted FBP

algorithm. Owing to the spatially variant nature of noise weighting, the filter in the FBP algorithm varies from ray to ray and it is not very efficient to implement it in the Fourier domain.

In spatial-domain implementation, filtering is achieved by performing a dot product of the projections with an integration kernel. This kernel function is discrete for a discrete implementation. To be efficient (meaning, fast computation), we require the kernel have an explicit closed-form expression. It is unlikely that the noise-weighted ramp filter $|\omega|/(1+\beta_0|\omega|)$ has a closed-form inverse Fourier transform, but it can be accurately approximated by $(|\omega|/3) \cdot (e^{-\beta_0|\omega|} + e^{-\beta_1|\omega|} + e^{-\beta_2|\omega|})$, which has a closed-form inverse Fourier transform expression. Thus, an explicit expression of the integral kernel can be obtained.

This approach of obtaining a closed-form integration kernel is not universal. We gave a counter-example of a noise-weighted ramp filter $|\omega|/(1+\beta_0|\omega|^3)$, for which we were unable to find a closed-form integration kernel.

ACKNOWLEDGMENTS

The author thanks Raoul M. S. Joemai of Leiden University Medical Center for collecting and providing the cadaver CT scan raw data.

REFERENCES

[1] J. Radon, "Über die Bestimmung von Funktionen durch ihre Integralwerte längs gewisser Mannigfaltigkeiten," *Ber. Verh. Sächs. Akad. Wiss. Leipzig, Math.-Nat. K1* **69** 262–267 (1917)

[2] R. N. Bracewell, "Strip integration in radio astronomy," *Aus. J. Phys.* **9** 198-217 (1956)

[3] B. K. Vainstein, "Finding structure of objects from projections," *Kristallografiya*, **15** 984-902 (1970)

[4] L. A. Shepp and B. F. Logan, "The Fourier reconstruction of a head section," *IEEE Trans. Nucl. Sci.* **NS-21** 21-43 (1974)

[5] G. L. Zeng, *Medical Image Reconstruction, A Conceptual Tutorial*, Springer, Beijing (2010)

[6] A. Dempster, N. Laird and D. Rubin, "Maximum likelihood from incomplete data via the EM algorithm," *J. R. Stat. Soc. Series B* **39B**, 1–38 (1977)

[7] L. A. Shepp and Y. Vardi, "Maximum likelihood reconstruction for emission tomography," *IEEE Trans. Med. Imag.* **1** 113–122 (1982)

[8] K. Langer and R. Carson, "EM reconstruction algorithms for Emission and Transmission tomography," *J. Comp. Ass. Tomogr.* **8** 302-316 (1984)

[9] S. German and D. E. McClure, "Statistical methods for tomographic image reconstruction," *Bull. Int. Statist. Inst.*, **LII-4** 5-21 (1987)

[10] H. M. Hudson and R. S. Larkin, "Accelerated image reconstruction using ordered subsets of projection data," *IEEE Trans. Med. Imag.* **13** 601–609 (1994)

[11] A. H. Delaney and Y. Bresler, "A fast and accurate Fourier algorithm for iterative parallel-beam tomography," *IEEE Trans. Image Proc.*, **5** 740-753 (1996)

[12] J. Hsieh, "Adaptive streak artifact reduction in computed tomography resulting from excessive x-ray photon noise," *Med. Phys.* **25** 2139-2147 (1998)

[13] M. Kachelrieß, O. Watzke, and W. A. Kalender, "Generalized multi-dimensional adaptive filtering for conventional and spiral single-slice, multi-slice, and cone-beam CT," *Med. Phys.* **28** 475-490 (2001)

[14] G. L. Zeng, "A filtered backprojection MAP algorithm with non-uniform sampling and noise modeling," *Med. Phys.* **39** 2170-2178 (2012)

[15] G. L. Zeng and A. Zamyatin, "A filtered backprojection algorithm with ray-by-ray noise weighting," *Med. Phys.* **40**, 031113 (2013); <http://dx.doi.org/10.1118/1.4790696> (7 pages), Online Publication Date: 28 February 2013

[16] G. L. Zeng, "A filtered backprojection algorithm with characteristics of the iterative Landweber algorithm," *Med. Phys.* **39** 603-607 (2012)

[17] G. L. Zeng, "Filtered backprojection algorithm can outperform maximum likelihood EM algorithm," *Int. J. Imag. Sys. Tech.* **22** 114-120 (2012)

[18] G. L. Zeng, Y. Li, and E. R. V. DiBella, "Non-iterative reconstruction with a prior for undersampled radial MRI data," *Int. J. Imag. Sys. Tech.* **23** 53-58 (2013)

[19] G. L. Zeng, Y. Li and A. Zamyatin, "Iterative total-variation reconstruction vs. weighted filtered-backprojection reconstruction with edge-preserving filtering," *Phys. Med. Biol.* **58** 3413-3432 (2013)

[20] G.L. Zeng G L, "Noise weighted FBP algorithm versus ML-EM algorithm," *J. Nucl. Med Tech.* **41** 283-288 (2013)

[21] B. van Brunt, *The Calculus of Variations*, Springer, New York (2004)

A new redundancy weighting scheme for non-stationary data

Katsuyuki Taguchi and Jochen Cammin

Abstract—The same projection data (or line integrals) is often measured multiple times, e.g., twice from opposite directions during one gantry rotation. Such redundant data must be normalized by applying redundancy weighting, which assumes that the noise of the data is uniform. This assumption, however, does not hold with tube current modulation techniques. The variance of data, which is inversely related to the tube current, varies significantly by a factor of 2-20. To improve how the projection data is used during reconstruction, we developed a new redundancy weighting scheme. It not only honors the data statistics, but also controls how much to honor from 100% ($\alpha_s=1.0$) to 0% ($\alpha_s=0.0$) by a parameter α_s . The proposed weighting scheme reduces to the conventional redundancy weighting scheme when $\alpha_s=0.0$. In this work, we evaluated the performance of the proposed scheme using computer simulations targeting at myocardial perfusion CT imaging.

Index Terms—CT, redundancy, statistics

I. PURPOSES

THE same CT projection data (or line integrals) is often measured multiple times, e.g., twice from opposite directions during one gantry rotation. Such redundant data must be normalized by applying redundancy weighting, which assumes that the noise of the data is uniform. This assumption, however, does not hold with tube current

modulation techniques. For monochromatic x-rays, the variance of data is proportional to the expected data, which is affected by the following factors: the x-ray intensity exiting the x-ray tube, and the attenuation of x-rays with the bowtie filter and the object. Assuming that the bowtie filter is symmetric with respect to fan- and cone-angles, the variance of the redundant data for the same ray is proportional to the tube current values used to acquire the projections. To improve how the projection data is used during reconstruction, we developed a new redundancy weighting scheme. It not only honors the data statistics, but also controls how much to honor from 100% ($\alpha_s=1.0$) to 0% ($\alpha_s=0.0$) by a parameter α_s . The proposed weighting scheme reduces to the conventional redundancy weighting scheme when $\alpha_s=0.0$.

We will evaluate the new weighting scheme using myocardial CT perfusion (CTP) imaging. CTP imaging has shown promise in improving the positive predictive value of cardiac CT examinations. One major challenge with CTP is the presence of halfscan artifacts, due to which measured pixel values of the same tissue vary as much as 30-50 Hounsfield unit (HU) from one heart beat to another and sometimes from lesion to lesion [1, 2]. This fluctuation of pixel values is larger than the targeted ischemic contrast one wishes to detect (i.e., 10-30 HU) and degrade both the perfusion defect detection performance and the reproducibility of the CTP test.

The halfscan artifacts are associated with the halfscan algorithm [3, 4] which is the generic cardiac CT image reconstruction method implemented in all CT scanners. Let d_R define the effective angular range of projection data used for image reconstruction (Fig. 1). The halfscan method uses a d_R of 0.5 rotations, and causes streaks in images that rotate with the “central angle,” which is the projection angle that corresponds to the center of d_R . A patient’s heart beat is a voluntary motion and it is impossible to mechanically control the central angle for each heartbeat and each scan. Thus, pixel values may vary from one image slice to another if several axial scans are performed to cover the entire heart, and also from one scan to another. Various factors make projections taken from the opposite direction slightly different, and they include cone-angle and scattered radiation. The former becomes a problem because the halfscan weight is designed to handle the redundancy of 2D Radon data in fan-beam geometry but is applied to 3D Radon data in cone-beam geometry prior to filtered backprojection. The inconsistency is noticeable when the cone-angle is large [5].

We propose to improve CTP using a larger d_R , a motion compensated image reconstruction technique, and a tube current modulation technique (Fig. 2). The motion

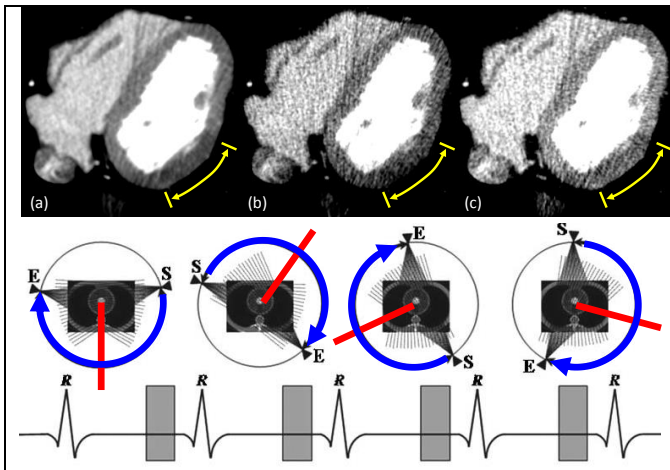


Figure 1. (Top) Synthesized patient images at mid-diastole show typical halfscan artifacts. WW/WL = 200/100 HU. (a) The true image with perfusion defect of 24.4 ± 5.8 HU (range, 7.8-34.3 HU) (yellow arrow). (b,c) Images reconstructed by halfscan method when the scan started from (b) 0° and (c) 180° . Averaged pixel values inside myocardium varied significantly from (a) the true value of 80.2 HU to (b) 69.3 HU or (c) 100.8 HU. (Bottom) Diagram modified from Ref. [1] shows that images are reconstructed from halfscan data (blue arcs, $d_R=0.5$ rotation, see Fig. 2) at different central angles (red lines).

K. T. and J. C. are with the Russell H. Morgan Department of Radiology and Radiological Science at the Johns Hopkins University School of Medicine, Baltimore, MD (email: ktaguchi@ihmi.edu).

compensated reconstruction will minimize the motion artifacts; the tube current modulation will allow for a larger d_R while limiting the radiation dose to patient. The tube current is set higher at I_H for the cardiac phase-of-interest for a duration of d_H and lower at I_L for the other phases. This makes the statistical variation of projection data for the same

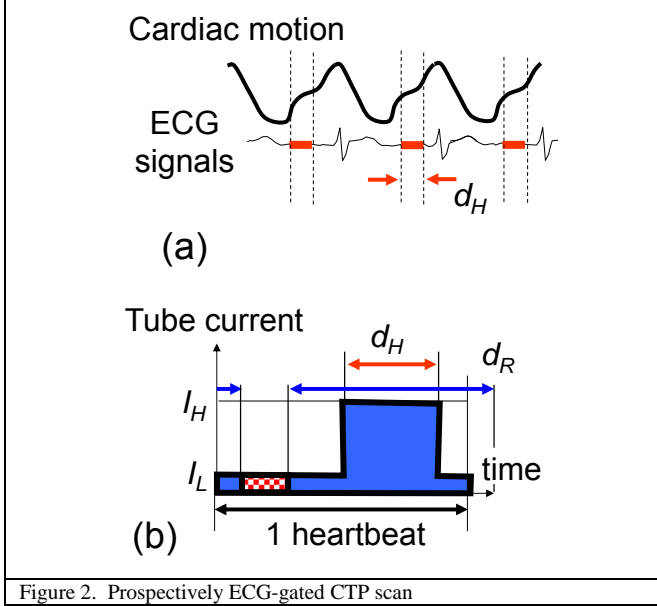


Figure 2. Prospectively ECG-gated CTP scan

ray-of-interest varying strongly: the fluctuations are smaller during I_H and larger during I_L . In this work, we evaluate the performance of the proposed scheme using computer simulations targeting at myocardial perfusion CT imaging.

II. THEORY

A. The current redundancy weight

Let $g(\beta, \gamma, \alpha)$ be cone-beam projections of an object f measured along a continuous circular orbit with a radius of R , where (β, γ, α) denote projection-, ray-, and cone-angle, respectively. The image can be reconstructed using a weighted filtered backprojection over the range where the redundancy weight w is non-zero:

$$\hat{f} = \frac{R}{2\pi} \int \frac{1}{L^2(x, \beta)} [(w \times g) * h_{ramp}] d\beta, \quad (1)$$

where h_{ramp} is a ramp filter kernel, L is the distance from the focus to the reconstruction point projected onto an xy -plane, w is a weighting function that normalizes the redundancy of data g . That is, when the 2D redundancy is considered (Fig. 3):

$$\sum_n w(\beta_{c(n)}, \gamma_{c(n)}) = 1, n=0, \pm 1, \pm 2, \pm 3, \dots, \quad (2)$$

$$\beta_{c(n)}(\beta, \gamma) = \begin{cases} \beta + n\pi + 2\gamma & n = \text{odd} \\ \beta + 2n\pi & n = \text{even} \end{cases}, \quad (3)$$

$$\gamma_{c(n)}(\gamma) = \begin{cases} -\gamma & n = \text{odd} \\ \gamma & n = \text{even} \end{cases}. \quad (4)$$

A 1D function is used to define the effective range of non-zero values and enforce the smoothness along β and γ :

$$s(\beta, \beta_R) = \text{rect}[(\beta - \beta_0)/\beta_R] \otimes h_s(2\beta/\beta_{f1}), \quad (5)$$

$$\text{rect}(t) = \begin{cases} 0 & \text{if } |t| > 1/2 \\ 1/2 & \text{if } |t| = 1/2, \\ 1 & \text{if } |t| < 1/2 \end{cases}, \quad (6)$$

$$h_s(t) = \begin{cases} 1 - 3|t|^2 + 2|t|^3 & \text{if } |t| \leq 1 \\ 0 & \text{if } |t| > 1 \end{cases}, \quad (7)$$

$$\beta_R = \pi d_R, \quad (8)$$

where β_R and d_R correspond to the full-width-at-half-maximum of the projection angular range used for image reconstruction in radians and in rotations, respectively, β_0 is the central projection angle of the range (see Figs. 1-2), \otimes is a convolution operation, h_s is a 1D smoothing kernel, and β_{f1} is the feathering range, which must be larger than the full fan-angle. A smooth redundancy weighting function can be obtained by

$$w_1(\beta, \gamma, \beta_R) = s(\beta, \beta_R) / \sum_n s(\beta_{c(n)}(\beta, \gamma), \beta_R) \quad (9)$$

and is used in the place of w in Eq. (1) for the current method.

B. The proposed redundancy weight

We will first propose a new redundancy weighting scheme which honors the data statistics, then combine it with the current scheme to control how much to honor the statistics.

When multiple line integrals are acquired at different tube current values at $I(\beta_1), I(\beta_2), \dots$ the relative variance of

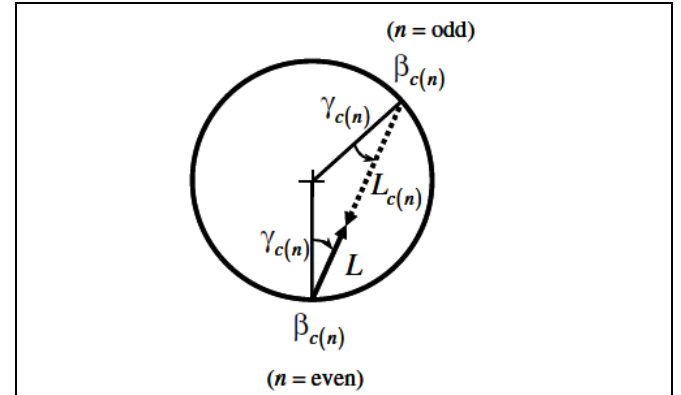


Figure 3. Two-dimensional redundant data

the acquired line integrals can be approximated by an inverse of the tube current values, $\text{var}(g(\beta_1)) : \text{var}(g(\beta_2)) : \dots = I^{-1}(\beta_1) : I^{-1}(\beta_2) : \dots$, due to the logarithm process to convert counts into line integrals. An image can be decomposed into multiple images each of which are reconstructed only from a ray-of-interest. Let us consider the noise of the partial image. When the image reconstruction is performed using Eq. (1), the image variance at the mid-point of a given ray-of-interest (when $L = L_{c(n)}$ in Fig. 3) can be modeled by

$$\sigma^2 = C \times \sum_n w^2(\beta_{c(n)}) \sigma_0^2 / I(\beta_{c(n)}), \quad (10)$$

where C and σ_0^2 are constant. The image noise is minimized when each datum is weighted by $I(\beta)$, honoring data statistics. However, such weights may produce image artifacts because if any discontinuities exist in $I(\beta)$, they would result in discontinuities in w along γ , which would then be amplified by the ramp filtering process. Thus, a 1D smooth function is used to enforce the smoothness and

$$q(\beta, \beta_H) = [(I_H - I_L) \times \text{rect}[(\beta - \beta_0)/\beta_H] + I_L] \otimes h_s(2\beta/\beta_{f2}), \quad (11)$$

$$\beta_H = 2\pi d_H, \quad (12)$$

where d_H is the duration in gantry rotations that corresponds to higher tube current value I_H (see Fig. 2) and $2\beta_{f2}$ are the feathering range.

Using two functions q and s , we get a redundancy weight w_2 that honors statistics, guarantees the smoothness, and limits the effective range of non-zero values to β_R :

$$w_2(\beta, \gamma, \beta_R, \beta_H) = q(\beta, \beta_H) s(\beta, \beta_R) / \sum_n [q(\beta_{c(n)}, \beta_H) s(\beta_{c(n)}, \beta_R)]. \quad (13)$$

Finally the proposed weights are obtained by a weighted summation of two weights w_1 and w_2

$$w_{new}(\beta, \gamma, \beta_R, \beta_H, \alpha_s) = (1 - \alpha_s) \times w_1 + \alpha_s \times w_2, \quad (14)$$

and used in the place of w in Eq. (1). The parameter α_s controls how much to honor the data statistics from 100% ($\alpha_s=1.0$) to 0% ($\alpha_s=0.0$).

III. EVALUATION METHODS

A. Noise analysis

Assuming that an on-centered cylinder or sphere is scanned without changing the x-ray energy, the noise at the origin was estimated. We calculated normalized image noise standard deviation, σ/σ_0 , using Eqs. (10) and (14) with various scan and reconstruction parameters such as I_L/I_H , d_H , d_R , and α_s , and further normalized it by that of the current halfscan method ($d_R=0.5$ rot. and $\alpha_s=0.0$).

B. Synthesized patient data

A synthesized patient image with a static heart with a perfusion defect was scanned with a tube current modulation using the following parameters: $I_H=875$ mA, $I_L/I_H=0.1$, $d_H=0.75$ rot., 0.3 sec/rot., and 1000 projections/rot. The scan started from 12 different angles, each 30° apart, and 5 noise realizations were performed for each angle, resulting in 60 scans in total.

Images were reconstructed using the following four parameter sets: (1) $d_R=0.5$ rot., $\alpha_s=0.0$ (halfscan); (2) $d_R=1.0$ rot., $\alpha_s=0.0$; (3) $d_R=1.0$ rot., $\alpha_s=0.5$; and (4) $d_R=1.0$ rot., $\alpha_s=1.0$.

Twenty-eight ROIs were placed on the myocardium. The standard deviation of the mean values of the same ROI over

the starting angles is measured, and the average of the standard deviation values over 28 ROIs was used to quantify the strength of halfscan artifacts. Image noise was quantified by the standard deviation of pixel values within ROIs averaged over all five noise realizations and 28 locations. Perfusion ratios were quantified using the myocardial signal density ratio [6, 7], and perfusion defect detection tests were performed by sweeping the threshold values.

IV. EVALUATION RESULTS

A. Noise analysis

Figure 3(a) shows plots of s , q , and w for $\gamma=0$ over β with $\alpha_s=0.0$ and 1.0 when $I_L/I_H=0.2$, $d_H=0.75$ rot., $d_R=1.50$ rot., $\beta_{f1}=28.6^\circ$, and $\beta_{f2}=50.0^\circ$. It can be seen that w with $\alpha_s=0.0$ was almost constant at 0.33 as most rays were measured three times over 1.5 rotations. In contrast, w with $\alpha_s=1.0$ was larger when q was larger where tube current I_H provided a better data statistics. Figures 3(b)-(c) show that the middle part of w with $\alpha_s=1.0$ vary with γ as the halfscan weight, while w with $\alpha_s=0.0$ was similar to the overscan weight [4].

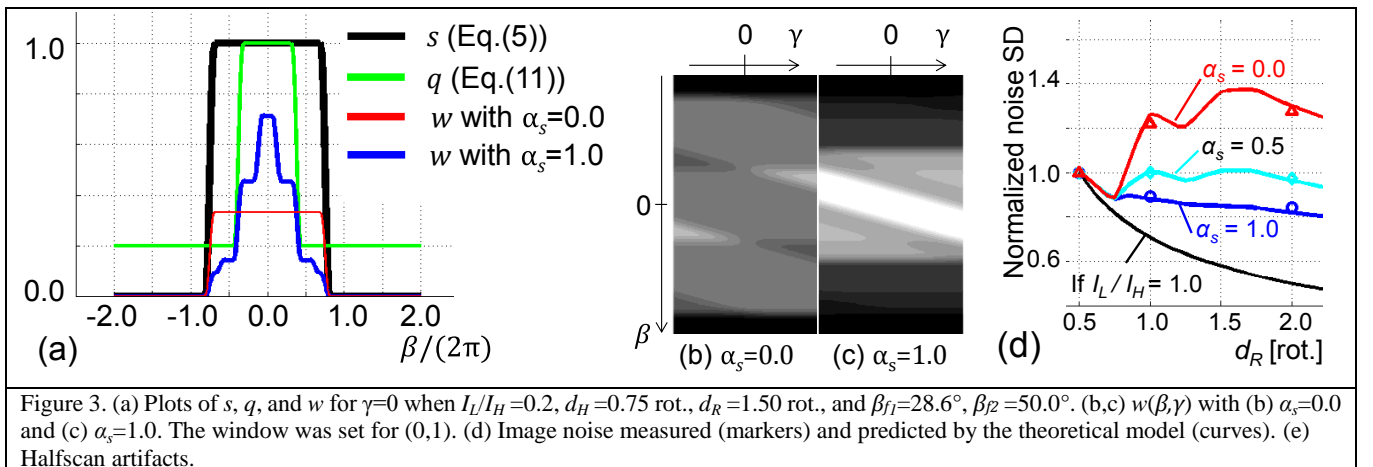
Figure 3(d) presents that (i) the estimated image noise with $\alpha_s=0.0$ increases with using a larger projection angular range d_R ; and (ii) the least image noise was achieved when statistics were completely honored with $\alpha_s=1.0$, while $\alpha_s=0.5$ was a close second.

B. Synthesized patient data

Images of one noise realization reconstructed by the four parameter sets were shown in Fig. 4 (a-d). Results are summarized as follows. (i) The measured image noise agreed with the expected value predicted by the theoretical model. (ii) The image noise observed at the myocardium confirmed the findings discussed in Sec. IV.A.

Regarding the measured halfscan artifacts (Fig. 4(e)), the following observations can be made. (i) Halfscan artifacts were as large as 14.5 HU with the halfscan algorithm ($d_R=0.5$ rot.). (ii) Regardless of the value of α_s , the use of larger d_R decreased the artifacts substantially. (iii) The halfscan artifacts were the least with the conventional weighting scheme ($\alpha_s=0.0$) and was 3.4 HU or 23% of the halfscan method, while $\alpha_s=0.5$ resulted in 4.8 HU or 33%.

The result of the perfusion defect detect detection test was



presented in Fig. 4(f) and summarized as follows. First, perfusion detection performance was better with $d_R=1.0$ rot. than with halfscan (left, $d_R=0.5$ rot.) in terms of the area-under-the-ROC-curve (AUC) values (0.935-0.938 versus 0.908, $P < 0.001$), the positive predictive value (PPV) at a negative predictive value of 95% (69.0-70.6% vs 58.0%, $P < 0.003$), and sensitivity at a false positive rate of 0.10 (0.80-0.89 vs 0.65, $P < 0.001$). Thus, it is critical to increase d_R , the projection angular range. Second, among the three methods, $\alpha_s=0.5$ provided the best performance index values, although the difference was not statistically significant.

V. DISCUSSION AND CONCLUSIONS

We have developed a new redundancy weighting scheme which not only honors the data statistics but also controls how much to honor by the parameter α_s . The results of the study showed that the proposed method allowed for a tradeoff between the image noise and halfscan artifacts when applied to CT perfusion imaging with tube current modulations. In the future, one can change the parameter α_s adaptively, e.g., keeping α_s smaller (thus, favoring equal weights) for projections up to 1 gantry rotation and making it larger (thus, favoring statistics) for the others.

One might think that the performance of CTP may not be sufficient even after the improvement. This is a challenging case with a heterogeneous and weaker perfusion defect. Our previous study with about twice as severer and homogeneous perfusion defect showed that the performances were improved by the proposed method ($P < 0.001$) and the improved indices were satisfactory: AUC, 0.994 vs 0.973; PPV, 100% vs 78.2%; sensitivity, 1.00 vs 0.89.

To our knowledge, incorporating statistical weights into redundancy weights has not been discussed. The use of redundancy weights in addition to statistical weights in iterative reconstruction methods has been discussed recently, and the merit was found in accelerated convergence [8]. The results of this study imply that there may be other merit such as decreased halfscan artifacts when both the redundancy and statistics of data are taken into account.

VI. ACKNOWLEDGEMENT

This work was supported in part by NIH/NHLBI Grant No. R01 HL087918.

REFERENCES

- [1] A. N. Primak, Y. Dong, O. P. Dzyubak, S. M. Jorgensen, C. H. McCollough, and E. L. Ritman, "A technical solution to avoid partial scan artifacts in cardiac MDCT," *Medical Physics*, vol. 34, pp. 4726-4737, 2007.
- [2] A. M. Huber, V. Leber, B. M. Gramer, D. Muenzel, A. Leber, J. Rieber, M. Schmidt, M. Vembar, E. Hoffmann, and E. Rummeny, "Myocardium: Dynamic versus Single-Shot CT Perfusion Imaging," *Radiology*, vol. 269, pp. 378-386, 2013.
- [3] D. L. Parker, "Optimal short scan convolution reconstruction for fanbeam CT," *Med Phys*, vol. 9, pp. 254-7, Mar-Apr 1982.
- [4] C. R. Crawford and K. F. King, "Computed tomography scanning with simultaneous patient translation," *Medical Physics*, vol. 17, pp. 967-982, 1990.
- [5] K. Taguchi, "Temporal resolution and the evaluation of candidate algorithms for four-dimensional CT," *Medical Physics*, vol. 30, pp. 640-50, Apr 2003.
- [6] R. T. George, C. Silva, M. A. S. Cordeiro, A. DiPaula, D. R. Thompson, W. F. McCarthy, T. Ichihara, J. A. C. Lima, and A. C. Lardo, "Multidetector Computed Tomography Myocardial Perfusion Imaging During Adenosine Stress," *Journal of the American College of Cardiology*, vol. 48, pp. 153-160, 2006.
- [7] R. T. George, T. Ichihara, J. A. C. Lima, and A. C. Lardo, "A Method for Reconstructing the Arterial Input Function during Helical CT: Implications for Myocardial Perfusion Distribution Imaging," *Radiology*, vol. 255, pp. 396-404, 2010.
- [8] K. Schmitt, H. Schöndube, K. Stierstorfer, J. Hornegger, and F. Noo, "Challenges posed by statistical weights and data redundancies in iterative X-ray CT reconstruction," presented at the The 12th international meeting on fully three-dimensional reconstruction in radiology and nuclear medicine, Lake Tahoe, California, 2013.

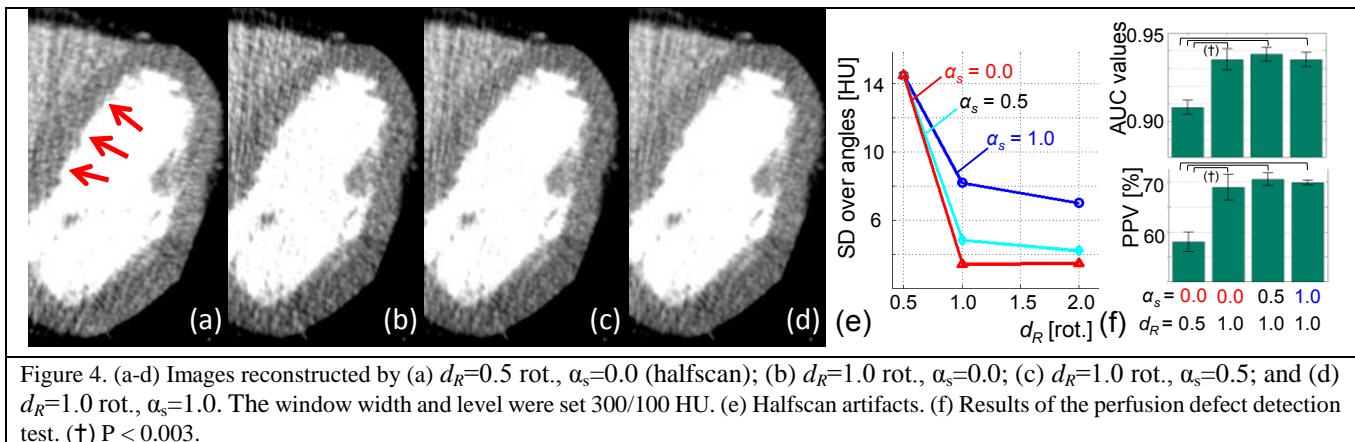


Figure 4. (a-d) Images reconstructed by (a) $d_R=0.5$ rot., $\alpha_s=0.0$ (halfscan); (b) $d_R=1.0$ rot., $\alpha_s=0.0$; (c) $d_R=1.0$ rot., $\alpha_s=0.5$; and (d) $d_R=1.0$ rot., $\alpha_s=1.0$. The window width and level were set 300/100 HU. (e) Halfscan artifacts. (f) Results of the perfusion defect detection test. (†) $P < 0.003$.

Construction of an atlas of filter configurations for fluence field modulated CT

Timothy P. Szczykutowicz, Ph.D., Charles A. Mistretta, Ph.D.

Abstract—Purpose: Fluence field modulated CT (FFMCT) and volume of interest (VOI) CT imaging applications require adjustment of the profile of the X-ray fluence incident to a patient as a function of view angle. The unique fluence profile at each angle, however, must be known in order to perform the log normalization step used to obtain the projection line integrals required for CT image reconstruction. Since current FFMCT prototypes can theoretically take on an infinite number of configurations, measuring a calibration data set for all possible positions would be difficult. Therefore, the present work aims to calculate an atlas of configurations that will span all of the possible body regions, patient sizes, patient positioning, and imaging modes (FFMCT and VOI imaging). The hypothesis here is that there exists some finite number of unique modulator configurations that effectively “span” the infinite number of possible fluence profiles with minimal loss in performance. **Methods:** CT images of a head, shoulder, thorax, abdominal, and pelvis anatomical slices were dilated and contracted to model small, medium, and large sized patients. The modulator configurations required to compensate for each image were computed assuming a FFMCT prototype (digital beam attenuator, DBA) was set to equalize the detector exposure using the algorithm described in Szczykutowicz and Mistretta 2013a. The Pearson correlation coefficient was computed between each of the DBA configurations and used to determine the atlas set of configurations that effectively “span” all clinically required configurations. **Results:** The results demonstrate that the technique works and allows reduction in the total number of required wedge configuration from tens of thousands to only a few hundred. Numerical results demonstrate that the mean change in image noise between a constrained (limited to 38 wedge configurations) and an unconstrained (limited to 900 wedge configurations) DBA configuration was 6%. The number of incident photons delivered using an atlas was found to be within 2% of the unconstrained case. **Conclusions:** The methodology proposed in this work will enable DBA-FFMCT and DBA-VOI imaging in the clinic without the need for patient specific air-scans to be performed. In addition, the methodology proposed here is directly applicable to other modulator designs such as piecewise linear, TomoTherapy MVCT, or inverse geometry CT.

T.P. Szczykutowicz and C.A. Mistretta are with the Departments of Radiology and Medical Physics University of Wisconsin-Madison 1111 Highland Avenue Madison, WI 53705 C.A. is also with the Department of Biomedical Engineering at the University of Wisconsin-Madison Email: szczykutowicz@wisc.edu

I. INTRODUCTION

The use of different kV, tube current, and bowtie filter sizes on today’s state-of-the-art CBCT and CT modalities allow for a modulation of the fluence incident onto patients. However, on many commercially available CBCT and CT systems, one is not free to choose any combination of kV, mA, and bowtie filter. Often only several kV stations are available (typically around 4), the mA is often restricted due to tube heating constraints, and at most 3 different sized bowtie filters are available (often, CBCT does not employ bowtie filters). While some of these limits are due to engineering constraints, some are mandatory to keep the amount of system calibration logistically feasible. The need for system calibration in CBCT and CT stems from the requirement to obtain projection data for image reconstruction. In order to create line integral projection data from transmitted signal intensity measurements, the fluence incident to the patient must be known. This is commonly referred to as collecting “air-scan” data as it is collected with no phantom object in place, hence the scan is taken entirely of air. This can be observed easily by considering Beer’s law ($I = I_o \cdot \exp(-P)$). One desires the projection line integral P , one measures the signal recorded at the detector transmitted through the patient I , therefore the quantity incident to the patient, I_o must be known. In CBCT and CT imaging, I_o varies as a function of fan angle due to the bowtie filter and the heel effect for a given mA and kV. As the mA and kV can change as a function of view angle due to dose modulation, calibration tables must be made or models of the response of I_o as a function of fan angle, kV, bowtie filter, and mA must be obtained.

The experimental implementation of FFMCT developed in our previous work (Szczykutowicz and Mistretta 2013a, 2013b, and 2014[1], [2], [3]) used a scan specific method to calculate the “air scan” data I_o . While this approach allowed for artifact free DBA-FFMCT and DBA-VOI images to be created, it required an air scan be performed using the same wedge configurations as were used to acquire the scan data in which the phantom object was in the beam. In a clinical environment, this type of work flow would not be feasible, especially in an interventional CT or CBCT setting where the patient cannot easily be moved out of the scan field of view in the middle of a procedure.

The X-ray optics are complicated for the DBA as

it is currently designed as two separate wedges (right triangular prisms). In addition, the beam hardening due to the wedges must be modeled accurately. These two issues have made creating a model for the attenuation from the DBA wedge difficult. Therefore, in this paper, we take the same approach as that of today’s CBCT and CT vendors; we assume physical measurements can be obtained for a range of operating points and that these operating points will “span” the range of clinically required configurations.

The methodology presented here could also be applicable to the FFMCT technology implemented by other research groups such as Hsieh and Pelc[4], [5] or the simulation work being carried out by Bartolac and Jaffray [6], [7], [8]. In addition, the technique described in this work should have applications in volume of interest imaging (VOI) [9], [10], [11], [12]. All of these techniques rely on imaging with a fluence field that changes from view to view or changes on a patient to patient basis.

II. MATERIALS AND METHODS

In this paper, the guiding assumption is that it is possible to use only a sub-set of all possible wedge configurations with a negligible effect in terms of dose and image quality. In other words, if the wedge configuration for a given phantom at a given view angle is restricted to be selected from a set of pre-calibrated atlas positions, the difference in the incident fluence profile from the ideal configuration and the atlas configuration should be minimal.

A. Atlas calculation for DBA-FFMCT

The ideal atlas will be capable of “spanning” all patient body regions, sizes, and offcenterings (see Figure 1a). Different body regions must be simulated to create an “ideal” atlas due to the different tissue inhomogeneities present in different body regions (i.e. the shoulders represent a large change in attenuation in the lateral direction but not so much in the anterior-posterior direction while the thorax has a large change in attenuation over the anterior-posterior projections due to the lung fields and mediastinum). Different body sizes will require different thicknesses of DBA wedge configurations as well as engage more wedges further from the iso-ray than would be used for smaller patients. Different patient offcenterings must be simulated because even for the same body region and patient size, the DBA configuration must change as the patient is moved away from iso-center.

The total number of view angles (denoted by $NumViews$) used in the atlas computation is equal to the number of body regions times the number of body sizes times the number of offcentering positions times the number of view angles for each body region/body size/offcentering configuration; 360 view angles were

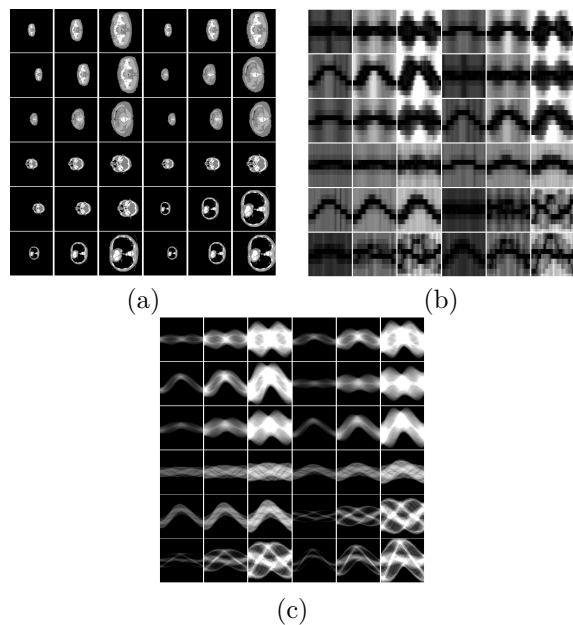


Fig. 1. (a) View of all of the digital phantoms used to construct the atlas set of wedge configurations. (b) Wedge configurations (thicknesses) for each of the sinograms shown in Figure (c); horizontal axis is view angle, vertical axis is wedge index for each of the sub figures. (c) Sinograms for each of the images shown in (b); horizontal axis is view angle, vertical axis is detector index for each of the sub figures.

used for each specific body size/region/offcentering simulation. 888 detector elements and a source to isocenter distance of 541 mm was used. The number of DBA wedges ($nDBA$) was 10.

The atlas construction method computes the Pearson correlation ($C_{j,k}$ where each pair of j, k denotes the Pearson Correlation coefficient of the j th view angle with the k th view angle) coefficient between wedge configurations ($H(i,v)$ where i is the detector index and v is the view angle index) spanning multiple body regions, sizes, and offcenterings. j, k and v range from 1 to $NumViews$. $H(i,v)$ is calculated using the method described in Szczykutowicz and Mistretta 2013a[1]. The wedge configurations are depicted in Figure 1b. The sinograms corresponding (i.e. used to determine the wedge configurations) to Figure 1b are shown in Figure 1c.

For each j in $C_{j,k}$, all view angles k having a Pearson Coefficient larger than a threshold (denoted by tr) are averaged. The result is a vector of wedge configurations denoted by $\overline{H(i,v)}$ (i.e. for each wedge combination, all other combinations that are similar to that combination are averaged). The number of “unique” configurations within are determined in an iterative manner. “Unique” is defined as the case when, for a given configuration, the Pearson correlation coefficient computed between that configuration and all other configurations is less than tr . In order to extract only the “unique” configuration from within $\overline{H(i,v)}$, each configuration is compared to all other combination as follows. The first ($v = 1$)

configuration in $\overline{H(i,v)}$ is added to the atlas library. Then, starting with the second ($v = 2$) configuration in $\overline{H(i,v)}$, each configuration is compared with the other entries in the library. If the Pearson correlation coefficient is less than tr for all atlas library members, then that configuration is added to the atlas library. This process is repeated for all view angles ($v = 1$ to $numViews$) and produces a small subset of average DBA wedge configurations that “span” the space of all the configurations in $H(i,v)$ (all body regions, sizes, and off-centerings). During an actual DBA scan, the DBA would simply be restricted to such a set for which the air-scan can be pre-calculated.

B. Creation of the different body regions

Head, shoulder, thorax, abdominal, and pelvis anatomical CT axial slices were obtained (IMAIOS SAS image gallery, Montpellier, France). The images were converted to Hounsfield units using tissue attenuation values taken from NIST[13] for cortical bone, soft tissue, and fat and a simple image based threshold for each of the materials. These slices were then dilated using 2 dimensional linear interpolation and shifted to simulate patient off centering. The dilation amounts, as can be seen from Figure 1a were tuned such that the slices occupied almost the entire 50 cm imaging field of view. At the smallest dilation amounts, the anatomy occupied roughly 1/3 of the field of view. Since 360 degree rotation scans were simulated, the rotation of the anatomy within the slices was not varied. The off centering amounts were 0, 3, and 8 cm.

C. Atlas construction for volume of interest DBA imaging

It turns out the number of wedge positions required for VOI imaging as implemented by our group previously [14], [3] is actually given by the Gauss integer summation expression,

$$\# \text{ of unique positions} = \frac{nDBA(nDBA + 1)}{2}. \quad (1)$$

Equation 1 can be derived considering that only two positions are possible for each wedge (when the DBA is implementing VOI imaging), each wedge can either be set to its thickest or thinnest configuration. Considering also that a maximum of 1 VOI is imaged during an acquisition, for $nDBA$ wedges, we can have 1,2, ... $nDBA$ wedges open (thinnest position) and the rest of the wedge closed (thickest position) at a total of $nDBA$, $nDBA - 1$, ...1 positions. Summing the total number of positions is simply the sum of integers 1 to $nDBA$. Assuming all of the possible DBA-VOI configuration are put into the atlas, there should be no difference in performance between using an atlas and not using an atlas for DBA-VOI imaging. More complicated VOI approaches would likely require a non binary wedge positioning scheme [7].

D. Quantifying performance loss with atlas

In order to quantify the changes in image quality and dose when using the atlas method, a numerical simulation was performed. The DBA was simulated, and CT images reconstructed using the framework described by Szczykutowicz and Mistretta 2013 [1]. The change in image quality was studied by considering the change in the voxel standard deviation between constrained and unconstrained DBA-FFMCT acquisitions. 10 noise instances were simulated for a DBA-FFMCT acquisition free to take on any wedge configuration and 10 noise instances were simulated for a DBA-FFMCT acquisition constrained to a subset of the configurations used in the unconstrained case. A tr value of 0.99 was used to calculate the atlas for the constrained DBA-FFMCT acquisition. Voxel standard deviation maps were created from the 10 runs for each acquisition type and the percent change in these maps was computed.

To compare the dose between non restricted and atlas constrained DBA-FFMCT, the total number of photons incident onto the phantoms was compared.

III. RESULTS AND DISCUSSION

A. Atlas creation

Figure 2a depicts the Pearson correlation coefficient ($C_{j,k}$) for each of the wedge configurations shown in Figure 1b. The thresholded version of Figure 2a is shown in Figure 2b. Figure 2c depicts $\overline{H(i,v)}$, the result of averaging over each of the similar configurations within the thresholded $C_{j,k}$. Using the algorithm described in Section II-A, $\overline{H(i,v)}$ is reduced to the final set of wedge configuration as shown in Figure 2d. This atlas construction method reduced the number of “air scan” projection from 12,960 unique wedge configurations to only 410.

B. Numerical results quantifying performance loss due to atlas

Figure 3 depicts the result of constraining a DBA-FFMCT acquisition to only 38 out of 900 configurations. In this case the atlas for the constrained DBA-FFMCT acquisition was created from the configurations used for the unconstrained DBA-FFMCT acquisition using $tr = 0.99$. Figure 4 depicts the percent change in the voxel standard deviation between the two acquisitions. The mean percent change in standard deviation over the phantom (i.e. excluding the air outside the phantom) was 6%.

Comparing the total number of photons incident onto the phantoms: a relative “dose” of 0.9835 for the constrained case relative to the unconstrained acquisition was observed.

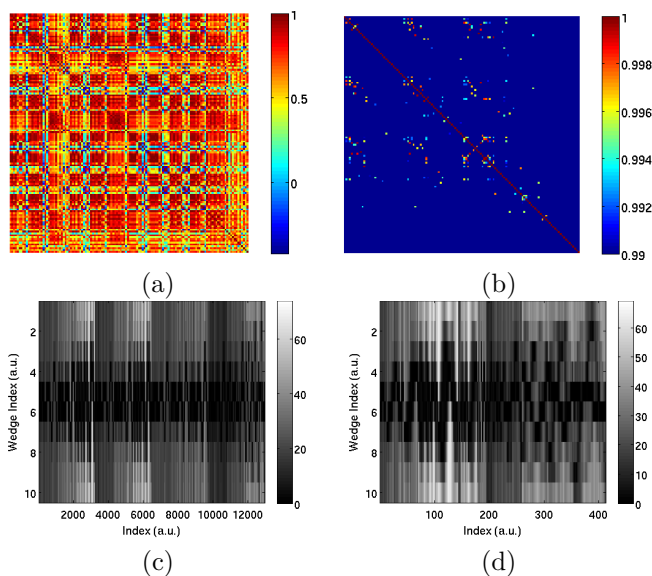


Fig. 2. (a) Cross correlation coefficient calculated for each wedge position with every other wedge position combination. The diagonal in this image has a value of 1 as it represents each of the wedge configurations shown in Figure 1b correlated with themselves. (b) Thresholded version of Figure 2a. All values below a correlation coefficient value of 0.99 ($tr = 0.99$ in this case) have been set to zero. (c) For each of the cases over the threshold as shown in (b), the mean wedge configurations are displayed in this figure. (d) The correlation between each of the configurations shown in (c) was calculated and only one wedge configuration was kept for each group of wedge positions having correlation coefficients of 0.99 or higher. This reduced the total number of required wedge positions from 12,960 to 410.

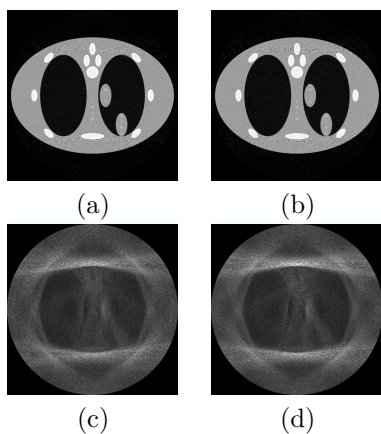


Fig. 3. (a) and (b) depict constrained and non constrained DBA FFMCT CT images respectively. (c) and (d) depict the voxel standard deviation of 10 independent noisy instances of (a) and (b) respectively. Images (a) and (b) are displayed at $[0\ 0.054]$ mm^{-1} . Images (c) and (d) are displayed at $[0\ 9.4E-3]$ mm^{-1} .

IV. CONCLUSIONS

This work outlines a clinically feasible solution for the determination of air scan free DBA-FFMCT CT imaging. In addition, the methodology presented here could also be applicable to the FFMCT technology implemented by other research groups such as Hsieh and Pelc[4], [5] or the simulation work being carried out by Bartolac and Jaffray.[6], [7], [8] In addition, the tech-

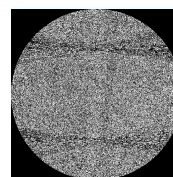


Fig. 4. Percent difference between images 3c and 3d. The image is displayed using a range -20 to 20 %.

nique described in this work should have applications in volume of interest imaging (VOI).[9], [10], [11], [12] All of these techniques rely on imaging with a fluence field that changes from view to view or changes on a patient to patient basis.

REFERENCES

- [1] T. Szczykutowicz and C. Mistretta, "Design of a digital beam attenuation system for computed tomography: Part i. system design and simulation framework," *Medical Physics* **40**, (2013).
- [2] —, "Design of a digital beam attenuation system for computed tomography: Part ii. performance study and initial results," *Medical Physics* **40**, (2013).
- [3] T. Szczykutowicz and M. C.A., "Experimental realization of fluence field modulated ct using digital beam attenuation," *Physics in Medicine and Biology* **55**, (2014).
- [4] S. S. Hsieh and N. J. Pelc, "The feasibility of a piecewise-linear dynamic bowtie filter," *Medical physics* **40**, 031910, (2013).
- [5] —, "Optimized control of a dynamic, prepatient attenuator," in *SPIE Medical Imaging*, International Society for Optics and Photonics, 2013, 86 681Q–86 681Q.
- [6] S. Bartolac, S. Graham, J. Siewerdsen, and D. Jaffray, "Compensator Approaches for Intensity Modulated Computed Tomography," *International Conference on Image Formation in X-ray Computed Tomography* **1**, no. 1, 101, (2010).
- [7] —, "Fluence field optimization for noise and dose objectives in ct," *Medical Physics* **38**, S2, (2011).
- [8] S. Bartolac and D. Jaffray, "Fluence Field Modulated Computed Tomography," *International Conference on Image Formation in X-ray Computed Tomography* **2**, no. 2, 119–122, (2012).
- [9] D. Kolditz, Y. Kyriakou, and W. Kalender, "Volume-of-interest (voi) imaging in c-arm flat-detector ct for high image quality at reduced dose," *Medical physics* **37**, 2719, (2010).
- [10] D. Heuscher and F. Noo, "Ct dose reduction using dynamic collimation," in *Nuclear Science Symposium and Medical Imaging Conference (NSS/MIC), 2011 IEEE*, IEEE, 2011, 3470–3473.
- [11] —, "Ct dose reduction using dynamic collimation," in *The Second international conference on image formation in X-ray computed tomography*, 2012, 115–118.
- [12] L. Chen, L. Yu, S. Leng, and C. McCollough, "Ct volume-of-interest (voi) scanning: Determination of radiation reduction outside the voi," *RSNA SSK15-07*, (2011).
- [13] J. Hubbell and S. Seltzer, "Tables of x-ray mass attenuation coefficients and mass energy-absorption coefficients 1 kev to 20 mev for elements z= 1 to 92 and 48 additional substances of dosimetric interest," National Inst. of Standards and Technology-PL, Gaithersburg, MD (United States). Ionizing Radiation Div., Tech. Rep., 1995.
- [14] T. Szczykutowicz and C. Mistretta, "Volume of interest ct implemented with a dynamic bowtie filter," in *Proceedings of SPIE*, 8313, 2013, 97.

Feasibility study on ultra-low dose 3D scout of organ based CT scan planning

Zhye Yin, Yangyang Yao, Albert Montillo, Peter M Edic, Bruno De Man

Abstract—3D volumetric CT images hold the potential to become a rich source of information for 3D organ segmentation and far exceed that made available through 2D radiograph images. Acquiring and generating 3D volumetric images for scan preparation purposes, i.e. 3D scout, while delivering radiation dose equivalent to conventional 2D radiograph is challenging. We explore various acquisition parameters and post-processing methods to reduce dose of a 3D scout while reducing the noise and maintaining the edge strength around the target organ. We demonstrated that similar edge strength and noise to the conventional dose CT scan can be achieved with 3D scout acquisition and post-processing while being dose neutral to a 2D scout acquisition.

Keywords— CT acquisition protocol; low dose; 3D scout; organ segmentation; IQ metric

I. INTRODUCTION

Segmentation or extraction of organ boundaries from the 2D radiograph preparatory scans, i.e. 2D scouts, has been explored before [1-3]. Due to overlapping nature of tissues projected onto a 2D scout, segmentation of adjacent soft tissue organs has proven to be very challenging. In a clinical setting, 3D helical acquisitions are often used to precisely localize target organs before the main scan but the radiation dose for such preparatory scans is quite high. In this paper, we propose a 3D volumetric preparatory scan, i.e. 3D scout, to segment target organs for scan planning while delivering radiation dose similar to conventional 2D scout.

The dose from a conventional 2D scout acquisition is a small fraction of the dose from the main scan, typically 0.4%-2%. Therefore, acquiring an ultra-low dose 3D scout delivering similar dose to conventional 2D scout while maintain image quality sufficient for organ segmentation is immensely challenging. Reconstructed images from such a low dose acquisition contain high noise and image artifacts such as streaks. Consequently conventional edge and region based image segmentation methods [4-5] tend to yield low segmentation accuracy [6-8]. More advanced model based organ segmentation (MBS) methods hold greater potential to overcome some of these challenges, however even these can fail when the noise or streaks are prominent [9-11].

In this work, we explored various ultra-low dose acquisition and post-processing strategies to reduce the radiation dose of a 3D scout. To evaluate each strategy, we defined the image quality metrics that reflect organ ‘segmentability’, i.e. ability to segment, rather than using a specific segmentation approach so that our experiments are largely independent of the specific organ segmentation algorithm. Though multiple body regions such as head, chest and abdomen are routinely scanned, we focus on the abdomen and specifically the liver organ since it is one of the most challenging organs due to its shape complexity, intersubject shape variability, and low boundary contrast. However it is straightforward to extend our work and methodology to other organs and applications.

Table I. Key DOE parameters

DOE	mA	rotation speed	mAs	# of views	dose%	
Without noise reduction techniques						
1	2000	0.4	800	1000	N/A	Ground Truth
2	600	0.4	240	1000	100%	Baseline
3	240	0.4	24	250	10%	Pulsed Acq.
4	240	0.4	12	125	5%	Pulsed Acq.
5	120	0.4	12	250	5%	Pulsed Acq.
6	120	0.4	6	125	2.5%	Pulsed Acq.
7	60	0.4	6	250	2.5%	Pulsed Acq.
8	60	0.4	3	125	1.25%	Pulsed Acq.
Noise Reduction techniques						
9	60	0.4	3	125	1.25%	Detector rebin(4)
10	60	0.4	3	125	1.25%	Detector rebin(9)
11	60	0.4	3	125	1.25%	Smooth Kernel
12	60	0.4	3	125	1.25%	Fast Iter. Recon
Combination of noise reduction techniques						
13	60	0.4	3	125	1.25%	Kernel+D.Rebin
14	60	0.4	3	125	1.25%	Kernel+Rebin+Iter
Electronic Noise Reduction						
15	60	0.4	12	250	5%	2x exposure
16	60	0.4	6	125	2.5%	2x exposure
17	60	0.4	3	62	1.25%	2x exposure

Zhye Yin, yin@research.ge.com, Albert Montillo, Peter Edic and Bruno De Man are with GE Global Research in Niskayuna, NY. Yangyang Yao is with GE Global Research in Shanghai, China.

II. METHODOLOGY

To achieve ultra-low dose for 3D scout, we proposed two low dose acquisition methods and three post-processing and reconstruction approaches.

For low dose acquisition, we reduced the dose of 3D scout by reducing mA and by reducing the number of views while maintain same exposure time per view, i.e. by emulating pulsed acquisition. Detailed acquisition parameters in our design of experiments (DOE) are shown in Table 1, DOE1-DOE8. To simulate ultra-low dose 3D scout, we use CATSIM with the anthropomorphic xCAT phantom [12-13]. A 3rd generation axial scan mode is adopted for simplicity and 8 rows of detectors are positioned over the liver region.

We simulated three denoising and reconstruction techniques: detector rebinning, smooth reconstruction kernel and fast iterative reconstruction algorithm such as ASIR, shown in Table 1, DOE9-14. Since organ segmentation algorithms mostly utilize the gradient information along the boundary, spatial resolution becomes less critical for the success. First, we proposed 2 by 2 and 3 by 3 detector rebinning approaches where the detector cells in neighboring rows and columns, 4 pixels and 9 pixels respectively, are combined into one effective cell. Second, since filter kernels for the FBP type reconstruction algorithms can be tuned to yield smooth and less noisy images, we select the smoothest reconstruction kernel available which can be aggressively modified further to achieve more smoothing in future. Finally, we emulated fast iterative reconstruction which typically has 50% noise reduction capability by simulating multiple acquisitions at same location with random noise seeds and averaging those runs.

Since electronic noise in CT acquisition sometimes dominates overall noise characteristic and makes it difficult to de-noise, we additionally simulated acquisitions with prolong exposure and compared the difference, shown in Table 1, DOE15-17.

All images are reconstructed with conventional FBP reconstruction algorithm with 1mm by 1mm by 0.625mm voxel size. The DFOV is 360mm and scan time per revolution is 0.4s. We simulated a noiseless scan, shown in Table 1, DOE1 and a conventional main scan with 240mA·s, shown in Table 1, DOE2. The dose percentage shown in the last column in Table 1 was computed relative to DOE2, the conventional main scan.

We devised two image quality metrics for organ segmentability. The first metric measures the noise at the interior portion of liver using 2cm by 2cm rectangular region of interest (ROI), shown as dotted box in Figure 1(a). The organ interior noise σ is expressed as the standard deviation of voxel intensities from a ROI in the liver interior:

$$= \text{stdev}(\text{rectangular ROI}), \quad (1)$$

The success of organ segmentation in ultra-low dose 3D scout is highly dependent of the contrast changes along the boundary of organ. High frequency artifacts such as streaks, increased noise, and blurred boundary due to heavy post-processing all can impair the success of organ segmentation. To measure the strength of the contrast change at the boundary, we propose a new metric, normalized edge strength (NES) which adds normalization to prior metrics [14]. We manually extract the ground truth boundary from the liver in the reconstruction image of xCAT phantom using VV 4D slicer [15]. This boundary is represented by a piecewise linear polygonal curve and shown in blue in Figure 1(b). We extract the intensity profile along this curve from the image and denote the intensity profile along the boundary curve as $c(t)$ where t parameterizes arc length along c , i.e. boundary curve. A clearly defined edge will have a high intensity gradient perpendicular to the boundary and a low gradient parallel to the boundary. To measure the perpendicular gradient, we evenly distribute 7mm line segments straddling the boundary, illustrated with green line segments in Figure 1(b). We extract the intensity profiles along those line segments and denote them as $s(r)$ where r parameterizes arc length along s , i.e. line segment. Finally, we define the normalized edge strength (NES) of a boundary as:

$$NES = \frac{\text{trimmean} \left(\left\{ \max \left| \frac{ds_t(r)}{dr} \right| \right\}_{i=1}^N, 5 \right)}{\text{trimmean} \left(\left\{ \left| \frac{dc(t)}{dt} \right| \right\}, 5 \right)} \quad (2)$$

For robustness to outliers, instead of taking average of gradients, we trimmed the highest and the lowest 2.5% values. For a vector input v , the $\text{trimmean}(v, 5)$ function computes the mean of elements in v , excluding the highest and lowest 2.5% values.

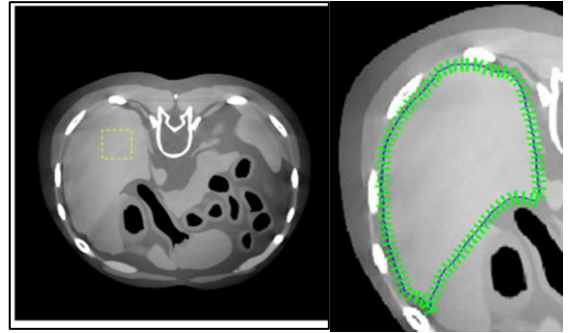


Figure 1: (a) liver region with 2cm by 2cm rectangular ROI in yellow for noise measurement (b) interpolated ground truth contour to measure NES (magnified view)

III. RESULTS AND ANALYSIS

The reconstructed images at iso-plane for each DOE are shown in Figure 2. Qualitatively we observe that as mA and number of views drop, images rapidly lose soft tissue contrast and the boundary of liver becomes invisible, shown in Figure 2(6), (7) and (8). Images with combination of various denoising techniques result in noisy but more visible organ

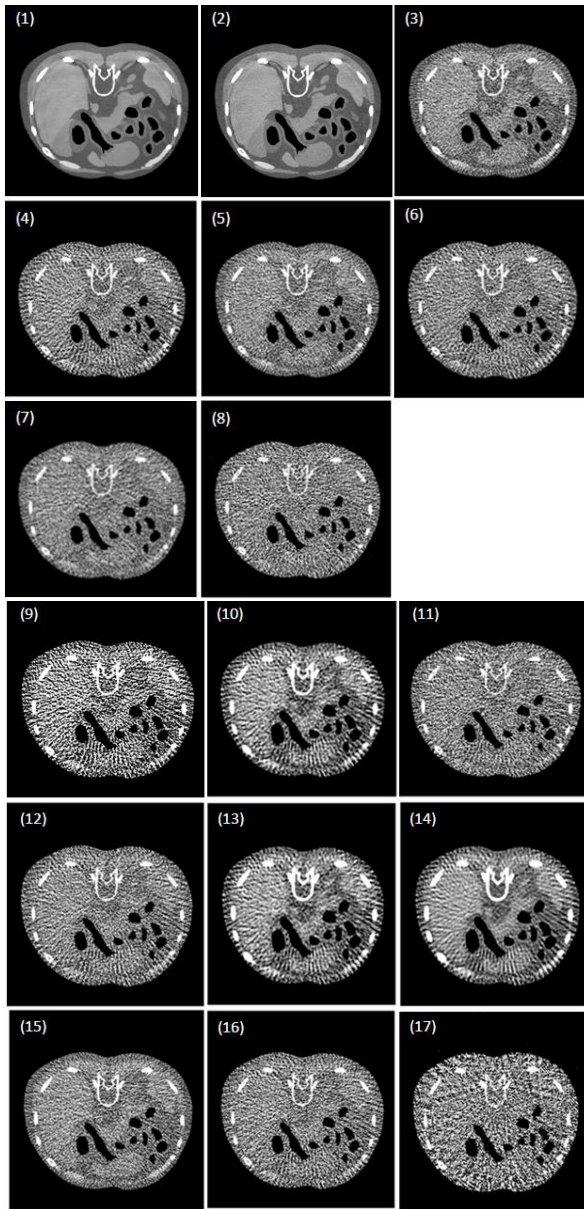


Figure 2: 3D scout with various acquisitions and post-processing techniques are shown. See Table 1 for details.

boundaries, shown in Figure 2(10), (13) and (14). Especially, the image processed with the combination of 9-pixel detector rebinning, smooth reconstruction kernel and fast iterative reconstruction, shown in Figure 2(14), presents with well-defined liver boundary while delivering only fraction of dose, 1.25%, from the baseline (DOE2, Figure 2(2)). By allowing twice the x-ray exposure time per view, electronic noise was suppressed, as shown in Figure 2(15), (16) and (17). To deliver similar dose while allowing longer exposure, the number of views was aggressively reduced to 62, only 6.2% of 1000 views in the baseline case. However, we observe that

images reconstructed without dedicated sparse view reconstruction algorithm have very high noise and invisible organ boundaries, shown in Figure 2(17).

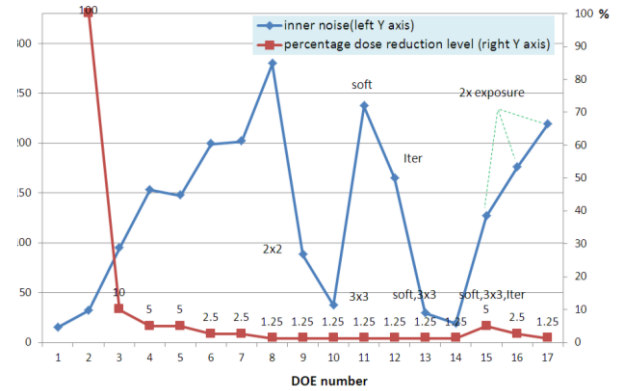


Figure 3: interior noise metric and % dose from 240mAs baseline scan are shown in red and blue lines respectively. Each detector rebinning is labeled as 2x2 and 3x3. Smooth reconstruction kernel is labeled “soft”. Fast iterative reconstruction is labeled “Iter”.

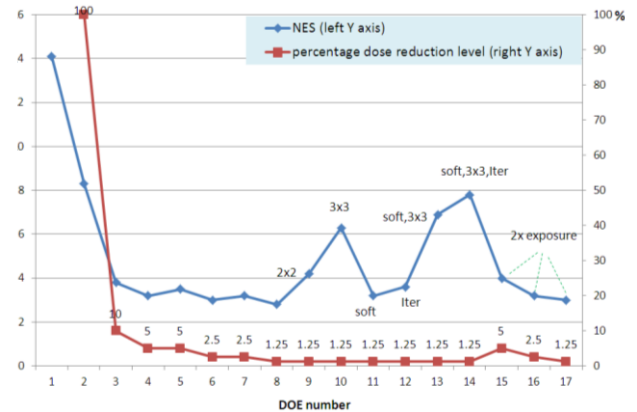


Figure 4: Normalized edge strength (NES) and % dose from 240mAs baseline scan are shown in red and blue respectively. Each detector rebinning is labeled as 2x2 and 3x3. Smooth reconstruction kernel is labeled as soft. Fast iterative reconstruction is labeled as Iter.

To objectively and quantitatively compare the performance of various simulated 3D scout acquisitions, we plot both image quality metrics and % dose for every DOE shown in Table 1. Noise performances of various 3D scout acquisitions and post processing techniques are shown by the blue line in Figure 3 while the red line shows corresponding % dose level. DOE1 was simulated with 2000mA to produce noise-free ground truth. DOE2 was simulated with 240mAs with full number of views and served as baseline. With combination of three denoising approaches, the interior noise metric successfully reached the level of the baseline, DOE2, with only 1.25% of dose level in DOE2. Similarly, the performance of normalized edge strength (NES) of various 3D scout

acquisitions and post processing techniques are shown by the blue line in Figure 4 while the red line indicates corresponding % dose level. We observe that normalized edge strength (NES) increases greatly for 2 by 2 and 3 by 3 detector rebinning technique, DOE9 and DOE10, while the dose percentage is as low as 1.25%. On the other hand, smooth reconstruction kernel and fast iterative reconstruction emulation don't improve normalized edge strength (NES) as much as detector rebinning. The combination of detector rebinning, smooth reconstruction kernel and fast iterative reconstruction techniques (DOE14) improves the normalized edge strength (NES) ever further, reaching nearly the level of full dose acquisition (DOE2).

IV. CONCLUSION

We investigated the feasibility of 3D volumetric preparatory scan, i.e. 3D scout, with ultra-low dose that is comparable to the dose of a conventional 2D scout while providing sufficient image quality, especially edge strength and uniformity, to make soft tissue organ boundaries prominent to facilitate segmentation and subsequent scan planning purposes. We proposed to reduce dose by reducing mA and the number of views while maintaining x-ray exposure time per view. We also proposed additional reconstruction and post-processing approaches to further improve image quality. We defined two image quality metrics to measure the edge strength at the boundary and noise uniformity inside of organs. We demonstrated that 3D scout can achieve equivalent image quality as a regular 240mAs diagnostic scan while delivering only 1.25% of dose. This work presents an approach that allows investigating the feasibility of 3D scout independent of the organ segmentation algorithm. In future, we plan to investigate the feasibility of 3D scout with further reduced streaking artifacts, to improve image quality visually and to further evaluate with learning-based organ localization algorithm that we are developing [2-3].

REFERENCES

- [1] Tao, Y., Peng, Z., Krishnan, A., Zhou, X.: Robust learning-based parsing and annotation of medical radiographs. *IEEE Transactions on Medical Imaging* 30(2), 338-350 (2011)
- [2] Montillo, A.*, Song, Q.*, Liu, X., Miller, J.: Parsing radiographs by integrating landmark set detection and multi-object active appearance models. In: *SPIE Medical Imaging* (2013)
- [3] Qi Song*, Albert Montillo*, Roshni Bhagalia, and Srikrishnan V, Organ localization using joint AP/LAT view landmark consensus detection and hierarchical active appearance models, In *Proc. of Medical Computer Vision Workshop, Medical Image Computing and Computer-Assisted Intervention (MICCAI)*, 2013
- [4] Linda G. Shapiro and George C. Stockman (2001): "Computer Vision", pp 279-325, New Jersey, Prentice-Hall, ISBN 0-13-030796-
- [5] R. C. Gonzalez and R.E. Woods, *Digital Image Processing 2nd Edition*, Prentice Hall, New Jersey, 2002

- [6] Seifert, S., Barbu, A., Zhou, S., Liu, D., Feulner, J., Huber, M., Suehling, M., Cavallaro, A., Comaniciu, D.: Hierarchical parsing and semantic navigation of full body CT data. *SPIE Medical Imaging* 7259, 02:1-8 (2009)
- [7] Potesil, V., Kadir, T., Platsch, G., Brady, M.: Personalization of pictorial structures for anatomical landmark localization. In: *IPMI*. pp. 333-345. Springer (2011)
- [8] Zhang, S., Zhan, Y., Dewan, M., Huang, J., Metaxas, D., Zhou, X.: Deformable segmentation via sparse shape representation. *Medical Image Computing and Computer-Assisted Intervention—MICCAI 2011* (2011) 451–458
- [9] T.F. Cootes and C.J. Taylor and D.H. Cooper and J. Graham (1995). "Active shape models - their training and application". *Computer Vision and Image Understanding* (61): 38–59. [1]
- [10] S. C. Mitchell, J. G. Bosch, B. P. F. Lelieveldt, R. J. van der Geest, J. H. C. Reiber, and M. Sonka. 3-d active appearance models: Segmentation of cardiac MR and ultrasound images. *IEEE Trans. Med. Imaging*, 21(9):1167–1178, 2002
- [11] T.F. Cootes, G. J. Edwards, and C. J. Taylor. Active appearance models. *ECCV*, 2:484–498, 1998
- [12] Bruno De Man, Samit Basu, Naveen Chandra, Bruce Dunham, Peter Edic, et al. "CatSim: a new computer assisted tomography simulation environment", *Proc. SPIE* 6510, *Medical Imaging 2007: Physics of Medical Imaging*, 65102G (March 14, 2007)
- [13] W.P. Segars, M. Mahesh, T.J. Beck, E.C. Frey, B.M. Tsui, "Realistic CT simulation using the 4D XCAT phantom," *Medical physics* 35, 3800-3808 (2008).
- [14] Montillo, J. Udupa, L. Axel, D. Metaxas, Interaction between noise suppression and inhomogeneity correction in MRI , In *Proc. of SPIE: Medical Imaging*, volume 5032, pages 1025-1036, 2003
- [15] VV-4D slicer, an opensource image tool available from <http://www.creatis.insa-lyon.fr/rio/vv/>

Task-based comparison of linear forward projection models in iterative CT reconstruction

K. Schmitt, H. Schöndube, K. Stierstorfer, J. Hornegger, F. Noo

Abstract—Iterative reconstruction methods are currently under extensive investigation for x-ray computed tomography. A major step in the design of iterative reconstruction algorithms is the choice of the forward projection model, particularly because the decision being made at this level affects both bias and noise properties of the reconstruction, in addition to choices made later in the algorithm design. In this work, we compare three important forward projection models that rely on linear interpolation: Joseph’s method, the distance-driven method, and the bilinear interpolation method. The comparison focuses on task-based assessment, using a signal-known-exactly/background-known-exactly binary classification task under various geometrical settings. The study is applied to two-dimensional fan-beam x-ray CT reconstructions with several noise realizations.

I. INTRODUCTION

Currently, significant effort is spent on the development of statistical iterative reconstruction algorithms for CT imaging, particularly for the aim of enabling CT exams with a lower dose. This effort needs to be accompanied with a careful assessment of image quality, because both bias and noise properties of the CT reconstruction can change dramatically according to the choices being made in the selection of the algorithm and the associated parameters. To achieve an objective comparison of image reconstruction algorithms in CT, a task-based metric should be considered [1].

A comparative evaluation of Joseph’s method, the distance-driven method and the bilinear interpolation method was presented in 2013 in [2]. In that work, basic metrics measuring bias and noise properties were used to quantify image quality, and no significant differences were found between these three linear interpolation models. Here, this study is refined in two aspects: i) new geometries that challenge further each forward projection model are introduced, ii) task-based assessment is used to evaluate the image quality.

II. BACKGROUND

Joseph’s method [3] and the distance-driven method [4] follow the same idea. This idea is to evaluate each line integral with a simple sum in x or y together with a linear interpolation between grid points in y or x , respectively. In Joseph’s method the direction of summation is chosen according to the direction of the line: if the line is mostly parallel to the x axis,

K. Schmitt, H. Schöndube and K. Stierstorfer are with Siemens AG, Healthcare Sector. J. Hornegger is with the Pattern Recognition Lab, University of Erlangen-Nürnberg, Erlangen, Germany. F. Noo is with the Department of Radiology, University of Utah, Salt Lake City, Utah, USA.

The concepts presented in this paper are based on research and are not commercially available. This work was partially supported by NIH grant R01 EB007236; its content is solely the responsibility of the authors and do not necessarily represent the official views of the NIH.

the summation is in x , otherwise it is in y . In the fan-beam geometry, this definition implies that the direction of summation may change from one line to another, across views as well as within views. In the distance-driven approach, the direction of summation is fixed for all lines within a fan-beam view, i.e., the position of the x-ray source defines the summation direction for all rays within the view. Moreover, the distance-driven approach takes the detector width into account, whereas Joseph’s method does not. This last aspect implies that, in the distance-driven method, more image pixels may be used for some rays.

The concept behind the bilinear method is to use bilinear interpolation to estimate the value of the linear attenuation coefficient at all points along the line defining the x-ray measurement, and then integrate (sum) these values together [5]. This concept can be efficiently implemented using a basis function description involving B-splines of order 1. Since the basis function approach yields a continuous model for the image, the definition of line integrals modeling the CT measurements is straightforward, as explained in Horbelt [6]. In particular, a different treatment according to the direction of the line is not needed.

III. EVALUATION METHODOLOGY

A. Iterative reconstruction technique

Let c be the vector of unknown image values, let g be the vector grouping the CT measurements, and let A be the matrix that links c to the CT measurements. Reconstruction was performed using Landweber iterations, which are given by the following equation:

$$c^{(n+1)} = c^{(n)} + \beta \cdot A^T (g - Ac^{(n)}) . \quad (1)$$

In this equation, β is a convergence controlling factor that was chosen as 0.90 times $2/\sigma_{max}$ where σ_{max} is the maximum singular value of the matrix A . The initial image vector, $c^{(0)}$, was always chosen as the *zero* vector. Conceptually, the above iterative step can be interpreted as a steepest gradient descent method to find the minimum-norm minimizer of

$$J(c) = \|Ac - g\|^2 , \quad (2)$$

which amounts to modelling the CT measurements as Gaussian deviates with equal variance.

Note that the minimum-norm minimizer of $J(c)$ was never reached in our evaluations as reconstruction was always stopped after a fixed number of iterations. When this number increases, resolution typically improves at the cost of noise and discretization errors, which progressively increase. This trade-off was used as a regularization means. All results are reported as an indirect function of the number of iterations,

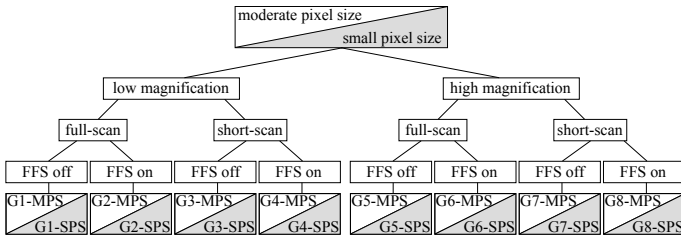


Fig. 1: Labeling of the 16 geometrical settings.

using a figure-of-merit related to resolution. The results were obtained by storing every fifth iteration, starting with the result from the first iteration, and stopping after 1000 iterations.

B. Geometrical settings

Our comparison study includes 16 different realistic geometries. We differentiate between moderate pixel size (MPS) and small pixel size (SPS), low and high magnification, full-scan and short-scan, flying focal spot (FFS) off and FFS on. These aspects allow us to probe various features of the forward projection models. For example, pixel size is an important factor for both Joseph’s and the bilinear method, since, in some views, some pixels may not contribute to any ray when the pixel size is too small. On another hand, high magnification may impact the distance-driven method more since the summation direction does not change within a view for this method. Also, the data redundancies that are present within a full-scan may allow artifact/noise cancellations that are not feasible with a short-scan. Note that the results in [2] only used two geometries: the moderate pixel size with low and high magnification.

The same label concept is used for the moderate and the small pixel size, as shown in figure 1. Thus, each geometrical setting is associated with a number and an abbreviation denoting the pixel size. For instance, G1-MPS denotes geometrical setting 1 with moderate pixel size, where geometrical setting G1 is defined using low magnification, full-scan mode and no flying focal spot.

All image and data acquisition parameters are summarized in table I. Square pixels were used in each geometrical setting. The pixel grid was always centered on the origin, and the computations were only carried out over the pixels that were within 13 cm from the origin. For both magnifications, the parameters were chosen so as to achieve the same resolution at field-of-view (FOV) center. For the short scan, the rotation of the source was over 240 degrees, starting from the x -axis.

C. Data simulation

Simulations were performed in fan-beam geometry (3rd generation CT curved detector) using the FORBILD head phantom. The simulation model included a sub-sampling of the x-ray tube focal spot, of each detector element, and of each source position. These settings allowed us to model the shift-variant effect of the x-ray tube anode angle, β , on resolution; to model the blurring that results from continuous x-ray emission; and to model the blurring that results from the finite size of the focal spot and detector elements. In total,

		pixel size		magnification	
		moderate (MPS)	small (SPS)	low	high
		$\Delta = 0.75$ mm	$\Delta = 0.375$ mm	$R_0 = 57$ cm	$R_0 = 36$ cm
		$N_x = 351$	$N_x = 701$	$N_u = 380$	$N_u = 380$
		$N_y = 351$	$N_y = 701$	$\Delta u = 0.75$ mm	$\Delta u = 0.75$ mm
		FFS			
		off		on	
		$u_{\text{off}} = \Delta u/4$		$u_{\text{off}} = \Delta u/8$	
scan mode	full	$N_\lambda = 1200$	$N_\lambda = 2400$	$N_{in} = 60,000$	$N_{in} = 30,000$
	short	$N_\lambda = 800$	$N_\lambda = 1600$	$N_{in} = 90,000$	$N_{in} = 45,000$

TABLE I: Fanbeam scanning parameters: Δ is the size of the pixels, N_x and N_y are the number of pixels in x and y , R_0 is the radius of the source trajectory, N_u is the number of detector pixels, Δu is the detector pixel size at FOV center, N_λ is the number of projections, u_{off} is the detector pixel offset, N_{in} is the number of photons emitted along each ray.

each CT measurement was simulated as an average of 405 line integrals. The computation of each line integral was based on analytical expressions, and the average was performed before applying the logarithm. The x-ray tube focal spot size was $0.12 \text{ cm} \times 0.09 \text{ cm}$, and the anode angle was $\beta = 7^\circ$.

All evaluations with noise involved 50 noise realizations for each geometrical setting. Poisson noise was used with a fixed number of incoming photons, N_{in} , for each ray. This number changed from one geometry to the next to ensure that the total exposure was always the same. The different values that were used for N_{in} are listed in Tab. I. Note that no compensating bowtie and no tube current modulation were included in the noise simulation.

D. Resolution measurement

The modulation transfer function (MTF) was used to evaluate resolution. This function was obtained using a phantom that consists only of the central low contrast ellipse within the FORBILD head phantom. For any reconstruction of this phantom, an edge profile that gives the reconstructed value as a function of the distance from the ellipse was computed. Then, the MTF was obtained as the Fourier transform of the differentiated edge profile. Since the selected reconstruction method is linear, this approach is suitable to evaluate the resolution achieved within the neighborhood of the large low-contrast ellipse in reconstructions of the FORBILD head phantom. Given that the resolution varies from one forward projection model to the other and also changes at a different pace with the number of iterations for each model, we present all figures-of-merit as a function of $\nu_{0.5}$, the frequency at which the MTF value is down by 50%.

IV. IDEAL OBSERVER STUDY

Image quality was evaluated using the ideal observer applied to a signal-known-exactly/background-known-exactly (SKE/BKE) binary classification task. Class 1 contains all images where the signal is normal, and class 2 contains all images where the signal corresponds to a disease. The area under the receiver-operating-characteristic (ROC) curve, called AUC, was used as the measure of performance.

A. Theory

The noise in the fan-beam data was assumed to be Gaussian distributed, and the signal was chosen so that it has negligible effect on the data statistics. Under these assumptions, both image classes are characterized by the same covariance matrix, Σ , and $AUC = \Phi(\text{SNR}/\sqrt{2})$ where SNR is the signal-to-noise ratio of the observer and Φ is the cumulative distribution function for the standard normal distribution. By definition,

$$\text{SNR} = \sqrt{\Delta\mu^T \Sigma^{-1} \Delta\mu}, \quad (3)$$

where $\Delta\mu = \mu_2 - \mu_1$ is the difference between the mean image under class 2 (μ_2) and the mean image under class 1 (μ_1).

When only a finite number of images are available, statistical variability can be an issue. To maximize the statistical power of the study, the known-means approach described in [7], [8] was employed. Briefly, AUC was estimated as $\widehat{\Phi}(\text{SNR}/\sqrt{2})$ with

$$\widehat{\text{SNR}} = \gamma \sqrt{\Delta\mu^T S^{-1} \Delta\mu} \quad \text{and} \quad \gamma = \frac{\sqrt{\frac{2\pi}{m+n}}}{B\left(\frac{m+n-p}{2}, \frac{1}{2}\right)} \quad (4)$$

where p is the number of pixels centered on the signal location, m and n are the number of measurements for class 1 and class 2, respectively, B is the Euler Beta function, and S is the pooled sample covariance matrix. The values chosen for m , n and p are discussed later, in section IV.C.

Using the results in [7], the standard deviation for our AUC point estimator can be approximated by

$$\sigma = \Phi'(\widehat{\text{SNR}}/\sqrt{2}) \cdot \tau \cdot \widehat{\text{SNR}} \quad \text{with} \quad \tau = \sqrt{\frac{\eta}{l-1} - \frac{1}{2}} \quad (5)$$

where Φ' is the derivative of Φ , $l = m + n - p$, and $\eta = (l + p)\gamma^2/2$.

B. task-selection

A discrimination task that is representative of a medical task was sought. The class 1 signal was defined as a circle with radius r_c and center point C . The class 2 signal was created from the class 1 signal as follows. First, the class 1 signal was truncated using four clipping lines at a distance of $\pm d_c$ of C in the vertical and horizontal directions, as shown in figure 2. The remaining part of the signal looks like a square with blunt edges. Four circles of radius r_l at distance $\pm d_l$ from C were superimposed on this square to yield the class 2 signal. In each class, the difference between the signal and the background was 10HU and the lesion was centered in the central low contrast ellipse of the FORBILD head phantom. The medical analogy to our two classes is the classification between lesions with a fuzzy or sharp boundary, as fuzziness is often a marker for malignancy.

Various expressions of the class 2 signal were obtained by varying d_l and r_c while using a fixed value for r_c and d_c . The involved values were $d_l = 0.30, 0.34, \dots, 0.50\text{cm}$, $r_l = 0.25, 0.27, \dots, 0.37\text{cm}$, $r_c = 0.65\text{cm}$ and $d_c = 0.55\text{cm}$.

To find a preferred setting for the class 2 signal, 10,000 noisy filtered backprojection (FBP) reconstructions were performed at three resolution levels in geometry G1-MPS. Then,

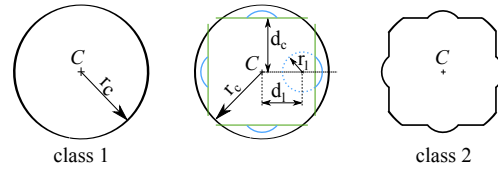


Fig. 2: (left) Class 1 is a circle with radius r_c . (middle) This draft shows how the (right) lesion object of class 2 was obtained.

		r_l [cm]						
		0.25	0.27	0.29	0.31	0.33	0.35	0.37
d_l [cm]	0.30	0.792	0.777	0.748	0.706	0.653	0.594	0.560
	0.34	0.751	0.712	0.663	0.609	0.572	0.601	0.667
	0.38	0.675	0.625	0.586	0.599	0.655	0.720	0.782
	0.42	0.604	0.602	0.645	0.704	0.764	0.818	0.863
	0.46	0.639	0.690	0.746	0.799	0.845	0.882	–
	0.50	0.728	0.779	0.825	0.863	–	–	–
	0.50	0.728	0.779	0.825	0.863	–	–	–

TABLE II: AUC values obtained using 10,000 FBP noise reconstruction with no apodization.

the AUC value corresponding to the various expressions of the class 2 signal were computed. For this computation, a choice had to be made on the number of pixels involved in the definition of μ_1 and μ_2 . We decided to use all pixels that were at a distance 8.25 mm or less from C . The results of this preliminary experiment are shown in table II for a reconstruction with no apodization. Only small differences were observed when changing the resolution of the reconstruction.

Based on the results in table II, the signal corresponding to $d_l = 0.34$ cm, $r_l = 0.27$ cm and $AUC = 0.712$ was selected for class 2. Also, we decided to carry out all further evaluations of AUC based on this signal with the pixels that are at distance 8.25 mm or less from C . This last decision yield $p = 373$ in the MPS setting and $p = 1513$ in the SPS setting.

C. Controlling statistical variability

A well-known statistical difficulty associated with the utilization of the ideal observer is the large number of measurements required for classes 1 and 2 altogether. Basically, $m + n$ needs to be larger than p , which is particularly challenging given the above values of p . To overcome this problem while using only 50 noise realizations for each geometry (which already entail significant computer resources), the following approach was adopted. Instead of considering that each noise realization provides only one sample for the computation of S , we considered that each noise realization provides 49 samples. Thus, the total number of samples involved in our computation of AUC was 2450. To obtain the 49 samples, the noise properties were assumed to be slowly varying around the signal location. More specifically, one sample was obtained using the p pixels centered on C , as expected, and the other 48 samples were obtained using p pixels centered on shifted locations. These locations were on a 7×7 grid centered on C with a pitch of 18 mm.

To validate the above concept, the AUC value obtained by using 10,000 FBP reconstructions was computed by using either 1 or 49 samples per noise realization. The result was an AUC value of 0.7251 for the approach with 49 samples, and a value of 0.7122 for the other case. This result provided enough confidence for utilization of the approximation.

At the same time, to determine how reliable formula 5 would remain to evaluate statistical variability, the 10,000 FBP reconstruction were split into 200 sets of 50 noise realizations, yielding each one AUC value. The standard deviation over these 200 values was computed and compared to the mean value obtained from 5. The result was a sigma value of 0.00295 in the first case versus 0.00310 in the second case, demonstrating excellent agreement.

Note that the tests described above were performed in setting G1-MPS with no apodization on the ramp filter. No significant differences were expected for different settings and resolution level.

D. Results

The results are shown in two formats that allow assessing dependence on resolution as well as on geometry for each pixel size. The first format displays the mean AUC value over the geometries as a function of $\nu_{0.5}$ for any given pixel size. This format was straightforwardly applied for the MPS setting. On the other hand, some adjustment were needed in the SPS setting, because a saturation in resolution was observed for geometries 3 and 4 in this setting. The adjustment amounted to apply the mean over the eight geometries only for $\nu_{0.5} \in [1.58, 5.43]$ lp/cm, and to use the mean over the remaining geometries for $\nu_{0.5} \in (5.43, 6.79]$ lp/cm.

The second format displays the AUC value after averaging over the frequency range. This average value is reported in a bar plot for each pixel size, as a function of the geometrical settings. In the MPS case, the average was taken over $\nu_{0.5} \in [1.58, 6.29]$ lp/cm. In the SPS case, the average was over $\nu_{0.5} \in [1.58, 5.43]$ lp/cm.

Figure 3 shows the results obtained in the MPS case. As can be seen, there is practically no difference in performance between the three forward projection models. The standard error associated with these plots was as follows. In the first format, the standard deviation value for each point on the curves was about 0.0011 for each forward projection model. In the second format, the standard deviation on each bar was about 0.0031. These numbers convey high statistical accuracy, and also convey that the small differences observed in each format are not statistically significant.

Figure 4 shows the results obtained in the SPS case. As can be seen, there is again practically no difference in performance between the three forward projection models. The standard error associated with these plots was as follows. In the first format, the standard deviation value for each point on the curves was about 0.0016 for each forward projection model. In the second format, the standard deviation on each bar was about 0.0046. As in the MPS case, These numbers convey high statistical accuracy, and also convey that the small differences observed in each format are not statistically significant.

V. DISCUSSION AND CONCLUSION

We have presented the results of a task-based comparison of three classical linear forward projection models. The comparison was extensive in terms of geometrical settings, including cases that challenge each model. The results show

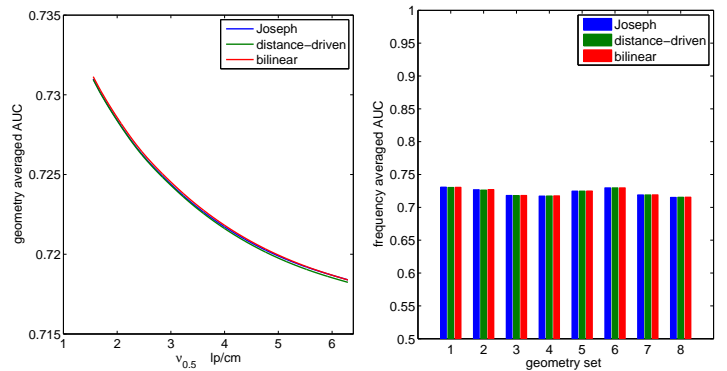


Fig. 3: Results for the MPS case. (left) AUC value averaged over geometries as a function of $\nu_{0.5}$, the frequency at which the MTF reaches 50% of its peak value. (right) AUC value averaged over $\nu_{0.5}$ for each geometrical setting.

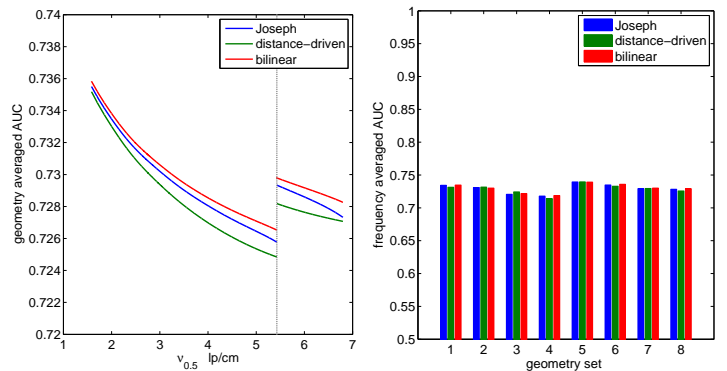


Fig. 4: Results for the SPS case. (left) AUC value averaged over geometries as a function of $\nu_{0.5}$; the average only includes all geometries for $\nu_{0.5} < 5.43$; geometries 3 and 4 could not be included. (right) AUC value averaged over $\nu_{0.5}$ for each geometrical setting.

that the choice of the model had very little influence on performance for the task, even though important differences could be noted visually, in terms of pixel noise variance and correlation among pixels (not shown in this abstract). Overall, these difference seem to balance out, so that there is no net effect on task performance. In the future, we will investigate if such observation can also be made when using human observers and also when using more challenging tasks.

REFERENCES

- [1] H. H. Barrett and K. J. Myers, *Foundations of Image Science*, Wiley, 2004.
- [2] K. Schmitt, H. Schöndube, K. Stierstorfer, J. Hornegger, and F. Noo, "Comparative evaluation of linear interpolation models for iterative reconstruction in X-ray CT," *Proc. SPIE 8668, Medical Imaging*, 2013.
- [3] P. M. Joseph, "An improved algorithm for reprojecting rays through pixel images," *IEEE Trans. Med. Imag.*, **1**, pp. 192–196, Nov 1982.
- [4] B. De Man and S. Basu, "Distance-driven projection and backprojection in three dimensions," *Physics in Medicine and Biology* **49**, pp. 2463 – 2474, 2004.
- [5] A. C. Kak and M. Slaney, *Principles of computerized tomographic imaging*, Society for Industrial and Applied Mathematics, 2001.
- [6] S. Horbelt, M. Liebling, and M. Unser, "Discretization of the radon transform and of its inverse by spline convolutions," *IEEE Transactions on Medical Imaging* **21**, pp. 363–376, Apr 2002.
- [7] A. Wunderlich and F. Noo, "Estimation of Channeled Hotelling Observer Performance With Known Class Means or Known Difference of Class Means," *IEEE Trans. Med. Imag.* **28**(8), pp. 1198–1207, 2009.
- [8] A. Wunderlich and F. Noo, "New Theoretical Results on Channeled Hotelling Observer Performance Estimation With Known Difference of Class Means," *IEEE Trans. Nuc. Sci.* **60**(1), pp. 182–193, 2013.

Clinical Data Evaluation of C-arm-based Motion Compensated Coronary Artery Reconstruction

Chris Schwemmer, Günter Lauritsch, Albrecht Kleinfeld, Christopher Rohkohl, Kerstin Müller, and Joachim Hornegger

Abstract—Angiographic C-arm systems are capable of performing computed tomography (CT) imaging for assisting in therapy planning, performance and assessment. Due to the long acquisition time, C-arm CT of dynamic structures is challenging. Cardiac motion has to be estimated and compensated in the reconstruction step. The quality of the motion estimation algorithm mainly dictates the resulting image quality. A common strategy to reduce the requirement of motion estimation is to exclude problematic heart phases by ECG-gating. A small ECG window improves the temporal resolution, but the usage of fewer data leads to undersampling artifacts. In contrast, larger ECG windows yield better image quality at the account of stronger cardiac motion artifacts. The bootstrapping approach presented here allows increasing the size of the ECG window in an iterative manner. The technique was evaluated on a clinical data set of 58 cases. Image quality was assessed by a human observer. Vessel sharpness and diameter were determined by a semi-automatic evaluation tool. The vessel diameter in 3-D was compared to a gold standard measurement in the 2-D projection images. Good image quality was achieved. The diameter of the arteries was determined reliably. The evaluation study clearly shows the benefit of using more projection data for dynamic image reconstruction. Besides avoiding undersampling artifacts a sharper reconstruction filter kernel can be applied. There is no clear choice in using either an 80% or 100% width of the ECG gating window. While using (almost) all acquired projection data, the technique appears efficient in dose and contrast agent.

Keywords—C-arm computed tomography, cardiac imaging, motion compensation, image reconstruction, clinical evaluation

I. INTRODUCTION

Angiographic C-arm systems are capable of performing computed tomography (CT) imaging. 3-D imaging in the catheter laboratory assists in therapy planning, performance and assessment. However, due to the long acquisition time of several seconds, CT imaging of dynamic structures like coronary arteries is a challenging task. In recent years various approaches were developed that account for cardiac motion in the reconstruction step [1], [2], [3], [4] by first estimating the coronary motion from the acquired data and then compensating it in the image reconstruction algorithm.

C. Schwemmer, K. Müller and J. Hornegger are with Pattern Recognition Lab, Department of Computer Science, and Erlangen Graduate School in Advanced Optical Technologies (SAOT), Friedrich-Alexander-Universität Erlangen-Nürnberg, Erlangen, Germany, email: chris.schwemmer@cs.fau.de. C. Schwemmer, G. Lauritsch, A. Kleinfeld and C. Rohkohl are with Siemens AG, Healthcare Sector, Forchheim, Germany.

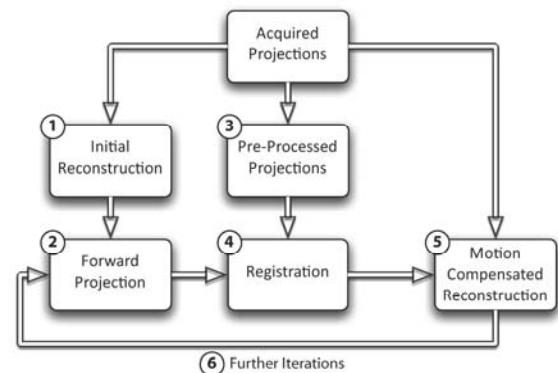


Fig. 1. Overview of the motion estimation and compensation reconstruction framework.

The quality of the motion estimation algorithm is a key factor for the resulting image quality. Any type of error is strongly propagated into the quality of the motion compensated reconstructed image. Especially data from heart phases with strong motion, e.g. systole might degrade reconstruction results significantly. Therefore a common technique is to use that prior knowledge and to exclude the strong motion phases by ECG-gating of the input data. However, there is a trade-off in ECG-gating. A small ECG window improves temporal resolution but the utilization of few data leads to undersampling artifacts. A large ECG window yields better image quality but strong cardiac motion yields errors in estimation and compensation.

The approach [4] presented here allows for flexibility in ECG gating. In particular, it allows increasing the size of the ECG window by an iterative bootstrapping [5]. Finally, all acquired data might be used for the final image reconstruction step. So far, no investigations about the optimal size of the ECG window have been performed. This paper reports on an empirical study on 58 human, clinical data sets. Different algorithmic parameters are investigated on that ensemble.

II. MOTION COMPENSATED IMAGE RECONSTRUCTION

A. Brief description of the algorithm

A detailed description can be found in [3][4]. A short summary is given here. Fig. 1 shows an overview of the components. (Step 1): An initial ECG-gated reconstruction is performed. (Step 2): Non-vascular tissue is removed by a thresholding operation. The vascular structure is forward projected using a maximum intensity forward projection. (Step 3): The original projection images are pre-processed using a morphological top-hat operation and a thresholding,

so that non-vascular tissue is removed. (Step 4): The pre-processed original projections and the forward projections are registered using affine and deformable 2-D-2-D registration in a multi-resolution scheme. (Step 5): A motion-compensated, ECG-gated reconstruction is performed using the deformation field from the registration step. (Step 6): The procedure is repeated either for further refinement or for increasing the number of acquisition data used for image reconstruction.

B. Iterative bootstrapping approach for ECG windowing

The iterative loop of step 6 is used for enlarging the width of the ECG window and therefore improving image quality. ECG gating is defined by the center at heart phase h_r and the width ω of the gating window. h_r and ω are expressed as a fraction of the heart cycle in the range of 0 and 1.

Three iteration cycles are performed. Cycle 1 is started with an initial image using an ECG gating window of width $\omega=0.4$. This cycle determines a first approximation of the motion field since the motion artifacts of the initial image degrade motion estimation. Cycle 2 refines motion estimation using the motion-compensated image of cycle 1. Cycle 3 allows increasing the ECG gating window width. Two variants are investigated using $\omega=0.8$ and $\omega=1.0$.

III. CLINICAL EVALUATION

A. Patient population

This study investigates 58 human cases. The coronaries were contrasted selectively. Rotational angiograms were acquired of 39 left coronary arteries (LCA) and 19 right coronary arteries (RCA). Heart rate and variability are critical parameters: The length of the heart's rest-phase with minimal motion is reduced by increasing heart rate. ECG-gating relies on a periodic motion during different cardiac cycles. A variability of the heart rate is likely to degrade the temporal resolution. The median heart rate during acquisition was 71bpm. 18, 18, and 22 cases showed low (<60bpm), medium (between 60bpm and 75bpm), and high (>75bpm) heart rate. The median heart rate variability was 1.3bpm with 50 cases smaller 5bpm and 8 cases above.

B. Image acquisition and reconstruction parameters

Images were acquired on an Artis zeego system (Siemens AG, Healthcare Sector, Forchheim, Germany) using a large flat panel detector of size 40cm×30cm. An acquisition rotation lasts 5s at a frame rate of 30fps achieving 133 projection images in total. Detector resolution is 308 μ m pixel length in each direction. Acquisitions were performed under strict breath-hold. Normal sinus heart rhythm occurred without any regulation drugs. Contrast agent was injected directly into the coronaries at a flow rate of 1-2ml/s, achieving a total contrast burden below 10ml.

All reconstructed volume images show an isotropic voxel length of 500 μ m. The ECG gating window center was set to end systolic and end diastolic heart phases in 7 and 51 cases. The median of h_r was 75%. Four reconstructed volume images will be compared. (Initial): Initial image with ECG window width $\omega=0.4$ reconstructed from 45-56 projection images using a smooth filter kernel. (RMC

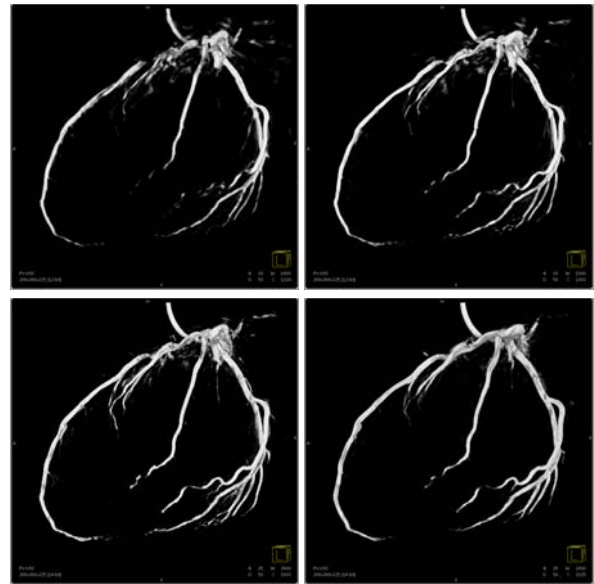


Fig. 2. Volume rendered image of a left coronary artery. Top left: Initial image. Top right: RMC 40%. Bottom left: RMC 80%. Bottom right: RMC 100%.

40%): Motion-compensated reconstruction after iteration 2 with $\omega=0.4$ and using a smooth filter kernel. (RMC 80%): Motion-compensated reconstruction after iteration 3 with $\omega=0.8$ and using a normal filter kernel. (RMC 100%): Motion-compensated reconstruction after iteration 3 with $\omega=1.0$ and using a normal filter kernel.

C. Visual image inspection

Image quality was assessed visually by a human observer. The coronary tree was divided into segments according to Ref. [6]. Each segment was scored using grades from 0 (not visible), 1 (substantial artifact), 2 (moderate), to 3 (perfect).

D. Quantitative evaluation tool CoroEval

The semi-automatic evaluation tool CoroEval computes vessel sharpness and diameter from volume images of magnetic resonance or C-arm CT [7]. CoroEval requires a centerline segmentation which can be performed either manually using CoroEval or by an external tool. The centerline is smoothed and sampled regularly at an interval of 1.0mm. At each sample point ten radial profile lines are extracted, smoothed and examined. Nine points of interest are detected at each profile line: The maxima at the vessel center, the left and the right minima beyond the border of the vessel, and for each side the point of 20%, 50%, 80% of the difference between maximum and minimum.

1) *Vessel sharpness.* Let d_l and d_r be the distances of the 20% and 80% points on the left and right side of the maximum, respectively. The vessel sharpness s on a profile line is defined as $s = 2/(d_l + d_r)$. The vessel sharpness at a centerline sample point is just the average of the sharpness measures of all profile lines.

2) *Vessel diameter.* The elliptical shape of a vessel cross-section is taken into consideration. An ellipse is fit to the 50% points of each profile line after outlier detection.

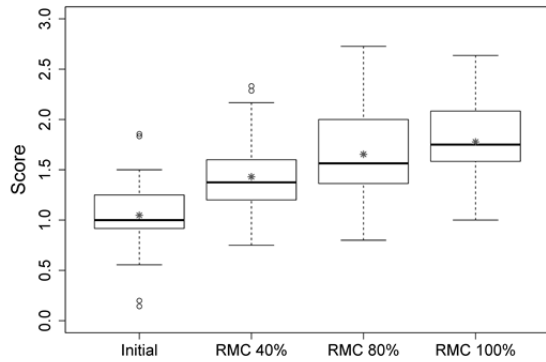


Fig. 3. Image quality score for all vessel sections examined by a human observer. The average over all vessel segments is computed.

The diameter of the cross-section is just the radius of a circle which has the same area as the constructed ellipse.

E. Ground truth of vessel size

As a ground truth the vessel diameter was measured in the 2-D projection data by the validated Quantitative Coronary Analysis (QCA) tool of the *syngo* Workplace – Angio/Quant package (Siemens AG, Healthcare Sector, Forchheim, Germany). The QCA tool segments the coronary artery automatically after manual detection of the start and end point of the section. Length measurements are calibrated by the known diameter of the contrasting catheter.

F. Statistical analysis

The statistical distribution of the evaluation results is shown in boxplots. The box contains the middle 50% of all values (interquartile range IQR). Within the box, the median is shown by a thick line, the mean by a star. The whiskers extend to the last data value within 1.5·IQR of the box. More extreme values are shown as circles.

Statistical significance of the difference of the means of two distributions was tested with t-tests. Since all four reconstructions for a specific dataset were generated from the same projection data, paired t-tests with Bonferroni correction [8] for multiple testing were used. The significance of all results shown in the following is $p < 0.001$.

IV. RESULTS

A. Visual image inspection

As an example Fig. 2 shows volume rendered images of a left coronary artery using all four methods to be compared. Increasing the ECG gating window width from $\omega=0.4$ (RMC 40%) to $\omega=0.8$ (RMC 80%) clearly improves image quality. The comparison of $\omega=0.8$ (RMC 80%) and $\omega=1.0$ (RMC 100%) is ambivalent. Using all projection data at RMC 100% removes background noise, but some final parts of distal vessels vanish at the same time.

Fig. 3 displays the image quality score of a human observer. The shown score is computed as the average of the scores given for each vessel segment. Reconstructing from all projection data ($\omega=1.0$) achieved the best image impression. Fig. 4 shows the same score evaluated for vessel sections of large diameter only. The quality scores

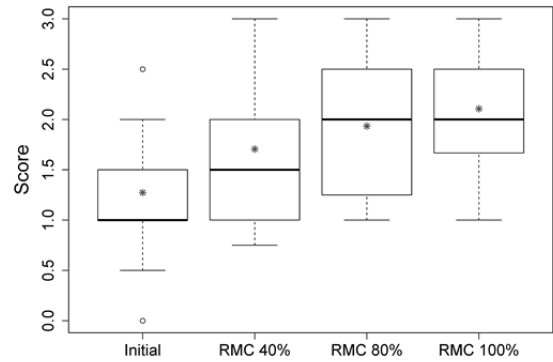


Fig. 4. Image quality score of large vessel sections examined by a human observer. The average over all vessel segments is computed.

improve for all images reconstructed using motion compensation.

B. Quantitative evaluation

1) *Success rate*. Quantitative analysis is performed only for cases with a successful vessel segmentation for all reconstructed volumes. 31 of 39 LCA and 15 of 19 RCA cases are assessed, 12 are rejected. In six of them the segmentation failed for the initial image only. In the other six cases no reconstructed image could be segmented. In five cases this is due to acquisition errors such that not sufficient contrast agent is admitted into the coronary arteries. In one case the failing reason is not known.

2) *Vessel sharpness*. According to Fig. 5 motion-compensated reconstruction using an ECG-gating window width of $\omega=0.8$ yields the sharpest vessel edges. Regarding this property $\omega=0.8$ seems to be optimal in the trade-off between temporal resolution and sufficient input data.

3) *Vessel diameter*. For ground truth values, a QCA measurement has to be performed in 2-D projection images. In 24 and 15 of LCA and RCA cases appropriate data sets were found displaying the desired vessel in good quality and contrast. The main branch of the vessel is selected and the average of the diameter deviation on that selection is plotted in Fig. 6. Intra-observer variations in using QCA on projection images at different angulations are indicated as dashed green lines. The standard deviation of repeated QCA measurements was 0.14mm. All volume images reconstructed using motion-compensation slightly underestimate the diameter value, while the initial image overestimates it. Most values of the RMC diameters are located inside the variance region of the ground truth. However, the median of RMC 80% is slightly below the variance region.

V. DISCUSSION

The gain of using more projection data for motion-compensated image reconstruction is clearly seen. On the other side there is no clear answer which width of the ECG gating window might be optimal. The investigated quality properties either prefer $\omega=0.8$ or $\omega=1.0$.

The image quality score of the human observer in Fig. 3 seems to be disappointing since the largest median value is still below 2 (moderate image quality). However, we have

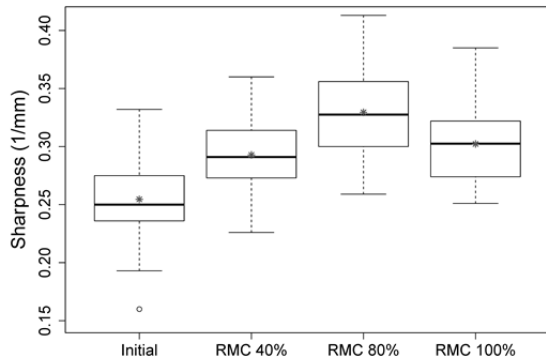


Fig. 5. Vessel sharpness as an average over all sampling points of the centerline.

to keep in mind that all cases are considered in that study even those deficient acquisitions having not sufficient contrast agent into the vessels. Further, distal vessels are included in the quality score as well. Motion estimation of distal vessels is quite complex since larger structures dominate the cost function. Distal vessels are not relevant for most clinical applications since e.g. percutaneous coronary interventions (PCI) solely focus on dilating stenosis of proximal to mid vessel sections, which feed a large portion of the myocardial mass. The image quality scores from vessels having larger diameter values significantly improve.

The diameter of the vessels is measured reliably. The observed deviations might be explained by measurement errors. There is also a variance in the ground truth values. The diameter of elliptical vessels alters with the viewing angle in 2-D.

VI. CONCLUSION

The proposed reconstruction technique using motion estimation and compensation was evaluated on a clinical data set of 58 cases. Good image quality was achieved. The diameter of the coronary arteries was determined reliably in consideration of the variance in the ground truth.

The evaluation study clearly shows the benefit of using more projection data for image reconstruction. Undersampling artifacts can be reduced and a sharper reconstruction filter kernel can be applied improving spatial resolution. On the other hand temporal resolution is reduced when increasing the width of the ECG-gating window. Most of the object motion can be estimated and compensated. However, some remains. There is no clear choice in using either an 80% or 100% width of the ECG-gating window, yet.

The presented method allows dynamic imaging of coronary arteries in the catheter laboratory using an angiographic C-arm system. While using (almost) all acquired projection data the technique appears efficient in dose and contrast agent.

ACKNOWLEDGMENT

The authors gratefully acknowledge funding of the Erlangen Graduate School in Advanced Optical Technologies (SAOT) by the German Research Foundation

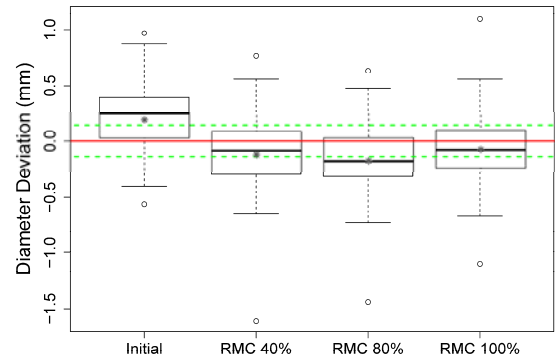


Fig. 6. Deviation of the vessel diameter measured in 3-D by CoroEval and in 2-D by QCA as an average over the selected vessel section. The full red line indicates zero value, the dashed green line the intra-observer variations in using QCA on projection images at different angulations.

(DFG) in the framework of the German excellence initiative. The authors also would like to thank Prof. Dr. D. Böcker and Dr. P. Skurzewski, St. Marienhospital Hamm, Germany for acquiring clinical data.

Disclaimer: The concepts and information presented in this paper are based on research and are not commercially available.

REFERENCES

- [1] C. Blondel, G. Malandain, R. Vaillant, N. Ayache, Reconstruction of Coronary Arteries From a Single Rotational X-Ray Projection Sequence, *IEEE Trans. Medical Imaging*, Vol. 25, pp. 653-663, 2006.
- [2] E. Hansis, D. Schäfer, O. Dössel, M. Grass, Projection-based motion compensation for gated coronary artery reconstruction from rotational x-ray angiograms, *Phys. Med. Biol.*, Vol. 53 pp. 3807-3820, 2008.
- [3] C. Rohkohl, G. Lauritsch, L. Biller, M. Prümmer, J. Boese, J. Hornegger, Interventional 4D motion estimation and reconstruction of cardiac vasculature without motion periodicity assumption, *Medical Image Analysis*, Vol. 14, pp. 687-694, 2010.
- [4] C. Schwemmer, C. Rohkohl, G. Lauritsch, K. Müller, J. Hornegger, Residual motion compensation in ECG-gated interventional cardiac vasculature reconstruction, *Phys. Med. Biol.*, Vol. 58, pp. 3717-3737, 2013.
- [5] C. Schwemmer, C. Rohkohl, G. Lauritsch, K. Müller, J. Hornegger, Opening Windows – Increasing Window Size in Motion-Compensated ECG-gated Cardiac Vasculature Reconstruction, *Proc. of Fully Three-Dimensional Image Reconstruction in Radiology and Nuclear Medicine Conference*, June 16-21, 2013, Lake Tahoe, California, USA, pp. 51-54.
- [6] W.G. Austen, J.E. Edwards, R.L. Frye, G.G. Gensini, V.L. Gott, L.S.C. Griffith, D.C. McGoon, M.L. Murphy, B.B. Roe, A reporting system on patients evaluated for coronary artery disease, Report of the Ad Hoc Committee for Grading of Coronary Artery Disease, Council on Cardiovascular Surgery, American Heart Association, in: *Circulation Journal of the American Heart Association*, Vol. 51, pp. 5-40, 1975.
- [7] C. Schwemmer, C. Forman, A. Maier, J. Hornegger, CoroEval – A Multi-platform, Multi-modality Tool for the Evaluation of 3-D Coronary Vessel Reconstructions, *Phys. Med. Biol.*, submitted, 2013.
- [8] J. Shaffer, Multiple hypothesis testing, *Annu. Rev. Psychol.*, Vol. 46, pp. 561-584, 1994.

Parameter Determination for Optimization-Based Image Reconstruction in Cone-Beam CT for Image-Guided Radiation Therapy

Xiao Han, *Member, IEEE*, Erik Pearson, Emil Y. Sidky, Charles A. Pelizzari, *Member, IEEE*, and Xiaochuan Pan, *Fellow, IEEE*

Abstract—Advanced optimization-based algorithms have been demonstrated to be capable of yielding cone-beam CT (CBCT) images of improved quality than conventional, analytic-based algorithms under a number of clinically relevant imaging conditions. It has been recognized that appropriate selection of parameters for optimization-based algorithms is crucial when the algorithm is tailored to reconstructing images of optimal utility in the specified imaging tasks. In this work, we investigate the strategy for determination of a key parameter for an optimization-based algorithm in the contexts of three imaging tasks relevant to clinical image-guided radiation therapy (IGRT). We acquired CBCT data of a calibration phantom with a clinical imaging configuration, and performed image reconstruction by using the adaptive-steepest-descent-POCS (ASD-POCS) algorithm with a range of the parameters. Technical-efficacy metrics were designed and computed for quantitatively characterizing the impact of the algorithm parameter on the image utility for the specified tasks, from which the optimal selection of the parameter was determined. The parameter-determination strategy developed in this study can be applied for achieving a fully exploration of image-quality potential for current CBCT systems under clinical imaging conditions.

I. INTRODUCTION

Cone-beam CT (CBCT) has seen remarkable growth over the past decade in a wide range of clinical applications, such as image-guided radiation therapy (IGRT). Current CBCT systems employ the FDK algorithm for image reconstruction, which poses limitations to fully exploration of image quality. Meanwhile, the FDK algorithm also requires densely-sampled data along the angular direction, which in general contribute to a relatively high radiation exposure to the imaged patient.

In recent years, advanced optimization-based algorithms have been actively developed for application to image reconstruction in CBCT. They have been demonstrated in a number of imaging conditions to be capable of yielding high-quality reconstructions and less susceptible to sparse

X. Han and E. Y. Sidky are with the Department of Radiology, The University of Chicago, IL 60637 (e-mail: xiaohan@uchicago.edu; sidky@uchicago.edu).

E. Pearson and C. A. Pelizzari are with the Department of Radiation & Cellular Oncology, The University of Chicago, IL 60637 (email: epearson@uchicago.edu; c-pelizzari@uchicago.edu).

X. Pan is with the Departments of Radiology and Radiation & Cellular Oncology, The University of Chicago, IL 60637 (e-mail: xpan@uchicago.edu).

angular sampling. Whereas a variety of optimization-based algorithms have been proposed and investigated, it has been recognized that the selection of parameters for these algorithms play a pivotal role in achieving the full potential of reconstruction quality. Adequate selection of parameters is dependent upon the specific imaging task. In this work, based upon one of the optimization-based algorithms, we conduct a study on determination of one of the key algorithm parameters that perform optimally for three imaging tasks that are relevant to clinical IGRT.

II. MATERIALS AND METHODS

A. CBCT data

We scanned a standardized calibration phantom, the Catphan phantom, at three sections for characterizing different image-quality properties. Schematic illustrations [1] of the three sections, CTP515, CTP528, and CTP404, are displayed in Fig. 1. The CBCT system for data acquisition was an on-board imaging (OBI) system on a Trilogy linear accelerator (Varian Medical Systems, Palo Alto, CA). The scan was performed with a clinical imaging configuration, referred to as “high-quality head”, in which projection data were collected over a 200-degree range at about 360 views. At each angular view an X-ray exposure was taken at 100 kVp, 80 mA and 25 ms.

B. Reconstruction-algorithm framework

We denote the measured data by an M -element vector \mathbf{g} , the reconstruction image by an N -element vector \mathbf{f} , and the system matrix by an $M \times N$ matrix \mathcal{H} . The reconstruction is formulated as a constrained total-variation (TV)-minimization program

$$\mathbf{f}^* = \operatorname{argmin} \|\mathbf{f}\|_{TV} \text{ s.t. } D(\mathbf{f}) \leq \epsilon \text{ and } f_j \geq 0, \quad (1)$$

where \mathbf{f} is expanded as $512 \times 512 \times 70$ voxels, each corresponding to a cuboid volume of $0.488 \times 0.488 \times 2.5\text{mm}^3$; $\|\mathbf{f}\|_{TV}$ denotes the image total-variation (TV); f_j the value of the j -th voxel of \mathbf{f} , $j = 1, 2, \dots, M$; ϵ the tolerance parameter for D , which is the Euclidean data divergence between model data and actual data, averaged per pixel [2, 3]:

$$D(\mathbf{f}) = (1/M) \sqrt{(\mathcal{H}\mathbf{f} - \mathbf{g})^T (\mathcal{H}\mathbf{f} - \mathbf{g})}. \quad (2)$$

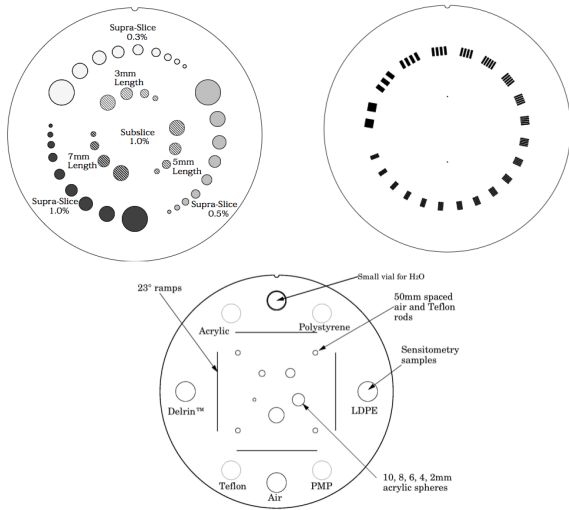


Figure 1. Schematic illustrations [1] of the three sections of the Catphan phantom CTP515 (top left), CTP528 (top right), and CTP404 (bottom), which are used in the study.

We employ the adaptive-steepest-descent-POCS (ASD-POCS) [2, 3] algorithm to numerically achieve the solution to the reconstruction program in Eq. (1). As the basic framework of the algorithm, two operations, a steepest-descent step for lowering image TV, and a POCS step for reducing data divergence, are performed in an alternating manner. Details of the algorithm framework and workflow can be found elsewhere [2–5].

C. Parameter determination

A number of parameters need to be selected for the ASD-POCS algorithm when adapted to reconstructing images from the acquired CBCT data. Among them, the parameter ϵ in Eq. (1) is of particular importance to designing the feasible set of solutions to the reconstruction program. Because inconsistencies inevitably exist between measured data and the assumed linear model, ϵ prescribes an upper bound of allowable $D(\mathbf{f})$, which establishes a balance between the enforcement of data constraint and the imposition of image regularity. In principle, a lower ϵ pushes for a more stringent agreement between data and model, which can help revealing finer image details but can potentially also lead to amplified noise. On the other hand, a higher ϵ seeks to promote image smoothness, which can be effective in suppressing image noise, at a potential cost of blurring high-spatial-frequency details. Therefore, a universally “optimal” choice of ϵ may not exist. Instead, ϵ needs to be tailored to suit the specific imaging task. In this work, we first obtained the lower bound for ϵ , $D_{min}(\mathbf{f})$, by using the POCS algorithm, i.e., without imposing any image regularization. Above this lower bound, a range of ϵ was selected for formulating the reconstruction program. Characterization studies were then conducted for images reconstructed with each selected ϵ on their utilities for the specified imaging task. The range of ϵ that performs optimally for each imaging

task was then identified from the characterization result, which can be used as guidance for determining algorithm parameters in similar imaging tasks.

Additional algorithm parameters, such as the expansion of image vector \mathbf{f} , can also have significant impact on the reconstruction performance, whereas their determination is beyond the scope of the work. In the following, we focus on the determination of ϵ , and we simply selected those additional parameters in accordance to common CBCT imaging protocols in clinical IGRT practice.

III. RESULTS

We summarize in this section results of parameter determination for each of the three imaging tasks.

A. Task 1: Contrast-resolution study

We first conducted a contrast-resolution study on the images of the CTP515 section. By applying the ASD-POCS algorithm, we obtained the solutions to the reconstruction program in Eq. (1) corresponding to a range of ϵ . On each of these solution images, we calculated the contrast-to-noise ratio (CNR) from the 7mm 1%-contrast insert, and plot it as a function of ϵ in Fig. 2. A peak can be observed from the curve around ϵ_2 , indicating that an image of “optimal” CNR on this insert is achieved. The shape of this CNR curve can be understood by examining the reconstructed images. A reconstruction with a lower ϵ such as ϵ_1 contains a high level of noise, yielding a lower CNR. When ϵ increases to a range near ϵ_2 , the contrast is preserved and noise significantly suppressed. After that, the smoothness of background continues to improve with larger ϵ , such as ϵ_3 , albeit at a cost of reduced contrast as the “signal” now visibly merges to the “background”. Furthermore, by computing CNRs for other inserts, we have obtained curves of similar shape. We show two of these curves in Fig. 2, which were computed for the 9mm 0.5%- and 15mm 0.3%-contrast inserts, after normalization to the maximum of the CNR curve corresponding to the 7mm 1%-contrast insert. It is worth of noting that all three CNR curves reach their respective peaks at approximately the same value of ϵ , suggesting that a range of ϵ may exist that can yield “optimal” contrast resolution for all low-contrast inserts under consideration. Therefore, for the imaging task at hand, one can make selection of ϵ around ϵ_2 . Additional images and analysis will be presented at the conference.

B. Task 2: Spatial-resolution study

Next, we investigated the impact of ϵ on the spatial-resolution property by characterizing ASD-POCS reconstructions of the CTP528 section with varying ϵ . We computed the modulation transfer function (MTF) by using an empirical technique [6] from images reconstructed with a range of ϵ , and plot in Fig. 3 modulations at the spatial frequency of 7 and 9 lp/cm as functions of ϵ . A monotonically decreasing trend can be observed in both

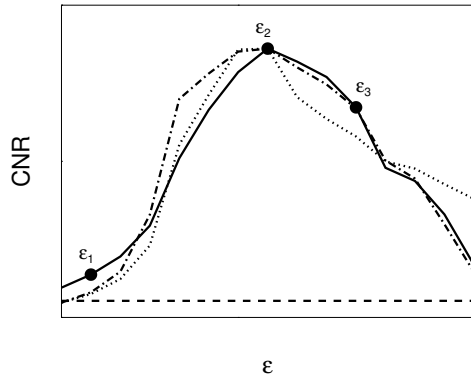


Figure 2. CNRs, calculated from ASD-POCS reconstruction of the CTP515 section on the 7mm 1.0%- (solid line), 9mm 0.5%- (dotted line), and 15mm 0.3%-contrast (dash-dotted line) inserts, plotted as functions of the parameter ϵ used. The CNR computed from the FDK reconstruction on the 7mm 1.0%-contrast insert is plotted as the horizontal dashed line as reference.

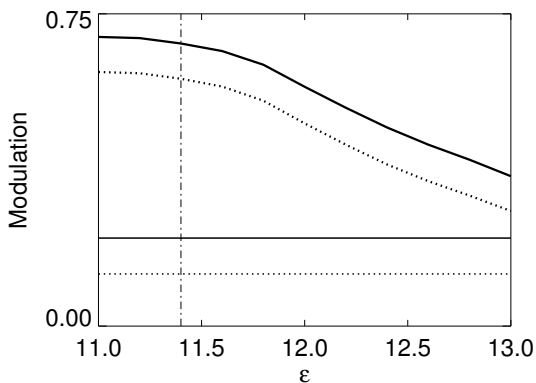


Figure 3. Modulations at spatial frequencies of 7 (solid curve) and 9 lp/cm (dotted curve) computed from CTP528 images reconstructed by use of the ASD-POCS algorithm as functions of ϵ . Solid and dotted horizontal lines represent the counterparts computed from the FDK reference.

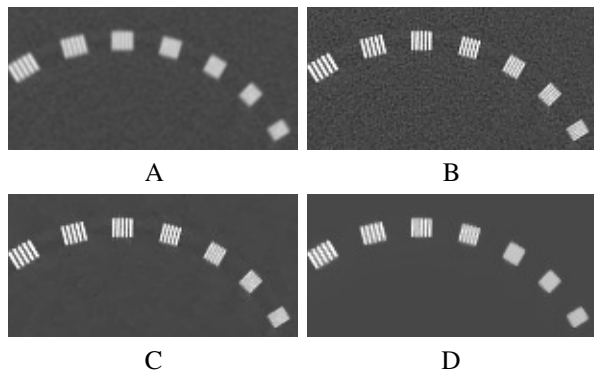


Figure 4. ROI Images of the CTP528 section of the FDK reference (A) and ASD-POCS reconstructions with $\epsilon=11.0$, 11.4, and 12.2. Bar patterns with spatial frequency of 7 – 13 lp/cm are enclosed within the ROI. Display grayscale: $[0.15, 0.6] \text{ cm}^{-1}$. The background smoothness of the ASD-POCS reconstruction displayed in panel C is matched to that of the FDK reference in panel A.

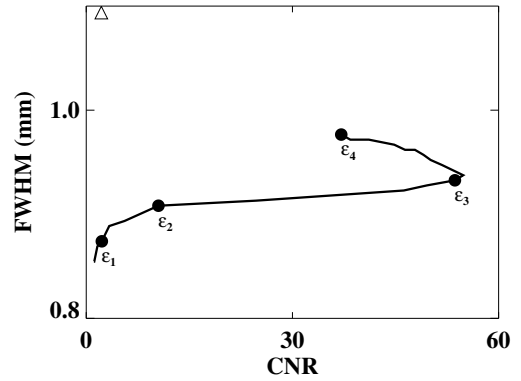


Figure 5. FWHMs of the wire ramp as a function of the CNR of the acrylic insert, computed from the ASD-POCS reconstructions of the CTP404 section with ϵ increasing from ϵ_1 to ϵ_4 . Four images obtained with ϵ_1 , ϵ_2 , ϵ_3 , and ϵ_4 are represented by solid dots. The FDK reference is represented by Δ .

curves, indicating degraded spatial resolution when a higher ϵ is used. Nevertheless, the ASD-POCS reconstruction has modulations higher than those of the FDK reference, which is plotted as baselines in the same figure, for the entire range of ϵ under study. In particular, we identified the ASD-POCS reconstruction with background noise magnitude, quantified by calculating the standard deviation over a uniform background region-of-interest (ROI), matched with that of the FDK reference. We indicate the ϵ that yields this reconstruction in Fig. 3 by a vertical, dash-dotted line. At this particular operating point of ϵ , the ASD-POCS reconstruction has background noise magnitude similar to that of the FDK reference, while MTFs exhibit an approximately three-fold improvement. This quantitative-metric-based observation is also corroborated by visualization assessment shown in Fig. 4. Bar patterns at spatial frequency of up to 8 lp/cm can be visually resolved in the FDK reference image, which is consistent with clinical quality-assurance guidelines [7–9] under comparable imaging conditions. As comparison, bar patterns at spatial frequency of 11 lp/cm appear to be resolved in the ASD-POCS reconstruction. Therefore, for the imaging task under consideration, ϵ can be determined by use of the above-mentioned method for yielding images of optimal spatial resolution without incurring over-amplified background noise.

C. Task 3: Combined contrast-resolution and spatial-resolution study

Finally, we investigated image reconstruction of the CTP404 section, where both high-spatial-frequency structures and low-contrast structures are present. Therefore, contrast resolution and spatial resolution are simultaneously considered in this imaging task. From ASD-POCS reconstructions obtained with a range of ϵ , we characterized contrast resolution and spatial resolution by technical-efficacy metrics. The contrast resolution was quantified by

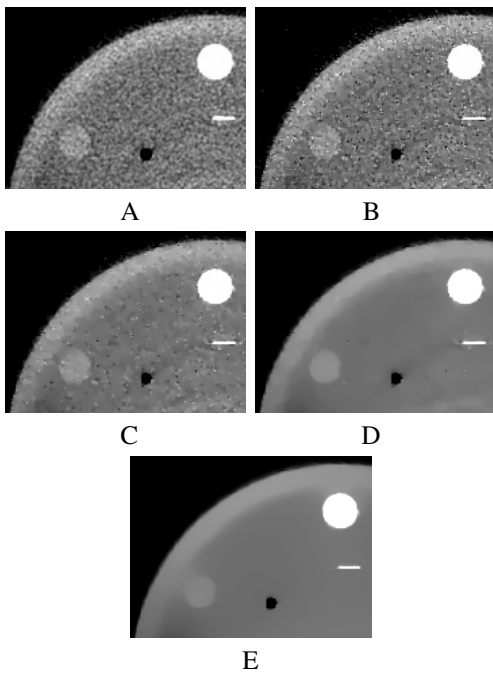


Figure 6. ROI images within the middle transverse slice of the CTP404 section reconstructed by use of the ASD-POCS algorithm with ϵ_1 (B), ϵ_2 (C), ϵ_3 (D), and ϵ_4 (E), indicated in Fig. 5. The FDK reference is displayed within the same ROI in panel (A). Display window: $[0.26, 0.3] \text{ cm}^{-1}$.

calculating CNRs of the acrylic insert over ROIs selected within and immediately outside of the insert. On the other hand, the spatial resolution was measured by computing the lateral broadening of the tungsten wire ramp. Specifically, we plot the profile across the wire, and fit the profile with a Gaussian function. The full width at half maximum (FWHM) of the fitted Gaussian function was then used as the metric for quantifying spatial resolution. We show the result in Fig. 5 by plotting FWHM as a function of CNR. The curve exhibits an initial sharp trade-off between spatial resolution and contrast resolution when ϵ is small, followed by a rather flat region as ϵ increases, where contrast resolution is quickly gained at a slow degradation of spatial resolution, and finally, a turning point after which contrast resolution and spatial resolution both degrade. As a benchmark, the FDK reference is represented in the same plot by a triangle, which has the FWHM larger than the entire ASD-POCS curve, and CNR smaller than almost all the points on the curve. To corroborate the quantitative-metric-based observation, we display ASD-POCS reconstructions with four ϵ values marked in Fig. 5. One can observe that a larger ϵ helps significantly in suppressing background noise, while the sharpness of the wire suffers little appreciable loss, thereby enhancing the contrast resolution while preserving the spatial resolution. This trend continues until ϵ increases beyond the turning point in Fig. 5, when the low-contrast structure starts to visibly merge into the background and thus loses the contrast. Therefore, for the imaging task under consideration, one may select ϵ close to ϵ_3 , for a simultaneous gain of contrast resolution and preservation of spatial resolution.

IV. DISCUSSION

We have investigated the determination of a parameter in the ASD-POCS algorithm that is crucial to tailoring the algorithm to three common imaging tasks, which are frequently encountered in applications such as IGRT. For a given imaging task, once the optimal range of the parameter is identified by use of the techniques described above, it can be applied to reconstruction problems involving a class of subjects of similar sizes and structural components. Therefore, a fully exploration of image-quality potential from current CBCT systems may be performed by utilization of this parameter-determination strategy.

ACKNOWLEDGMENT

This work was supported in part by NIH R01 Grant Nos. CA120540, CA158446, and EB000225. The contents of this article are solely the responsibility of the authors and do not necessarily represent the official views of the National Institutes of Health.

REFERENCES

- [1] D. Goodenough, "Catphan 500 and 600 manual," 2004.
- [2] E. Y. Sidky, C.-M. Kao, and X. Pan, "Accurate image reconstruction from few-views and limited-angle data in divergent-beam CT," *J. X-Ray Sci. and Technol.*, vol. 14, pp. 119–139, 2006.
- [3] E. Y. Sidky and X. Pan, "Image reconstruction in circular cone-beam computed tomography by constrained, total-variation minimization," *Phys. Med. Biol.*, vol. 53, pp. 4777–4807, 2008.
- [4] J. Bian, J. H. Siewerdsen, X. Han, E. Y. Sidky, J. L. Prince, C. A. Pelizzari, and X. Pan, "Evaluation of sparse-view reconstruction from flat-panel-detector cone-beam CT," *Phys. Med. Biol.*, vol. 55, pp. 6575–6599, 2010.
- [5] X. Han, J. Bian, D. R. Eaker, T. L. Kline, E. Y. Sidky, E. L. Ritman, and X. Pan, "Algorithm-enabled low-dose micro-CT imaging," *IEEE Trans. Med. Imaging*, vol. 30, pp. 606–620, 2011.
- [6] R. T. Droege and R. L. Morin, "A practical method to measure the mtf of ct scanners," *Medical physics*, vol. 9, p. 758, 1982.
- [7] S. Yoo, G.-Y. Kim, R. Hammoud, E. Elder, T. Pawlicki, H. Guan, T. Fox, G. Luxton, F.-F. Yin, and P. Munro, "A quality assurance program for the on-board imager," *Med. Phys.*, vol. 33, pp. 4431–4447, 2006.
- [8] J.-P. Bissonnette, D. J. Moseley, and D. A. Jaffray, "A quality assurance program for image quality of cone-beam CT guidance in radiation therapy," *Med. Phys.*, vol. 35, pp. 1807–1815, 2008.
- [9] S. Kim, S. Yoo, F. Yin, E. Samei, and T. Yoshizumi, "Kilovoltage cone-beam CT: Comparative dose and image quality evaluations in partial and full-angle scan protocols," *Med. Phys.*, vol. 37, p. 3648, 2010.

Validation of Motion Artifact Metric Optimization Reconstruction (MAM)

Herbert Bruder¹, George S K Fung², Christopher Rohkohl¹, Thomas Allmendinger¹, Karl Stierstorfer¹

Abstract—

We evaluated the Motion Artefact Metric Optimization (MAM) method [1] as a candidate for motion compensated reconstruction in cardiac CT and demonstrate its potential for clinical use. The potential of MAM was investigated based on two simulation studies: one using a realistic model of the RCA of cylindrical shape with a realistic motion curve (A) and a second one using the 4D-XCAT [2] model at different heart-rates ranging from 60bpm to 80bpm (B). Different CT acquisition modes have been simulated (64 slice single source cardiac spiral, 64 slice dual source cardiac spiral at low and high pitch, respectively). It was shown, that in the experiment (A) MAM reconstructions are close to the ground truth at most cardiac phases. Also, in experiment (B) MAM improved the distal and proximal RCA segment even at high heart-rates. Motivated by these results, MAM reconstruction was evaluated on clinical data and proved to effectively reduce motion artifacts. However, both in simulation studies and clinical data the dual source acquisition with improved temporal resolution delivered superior cardiac image data compared to single source cardiac data, which have been processed with MAM. Moreover, the benefit of MAM in Dual Source cardiac CT can be to increase the range of valid heart-rates for the high-pitch FLASH acquisition. This is demonstrated using 4D-XCAT phantom and clinical dual source FLASH data, respectively.

Index-Terms: Cardiac CT, ECG correlated reconstruction, temporal resolution, 4D-XCAT phantom, motion compensation, motion vector field, motion artifact metric.

Bruder H, Rohkohl C, Allmendinger T, Stierstorfer K are with SIEMENS, Healthcare Division, Siemenstr. 1, 91301 Forchheim, Germany. E-mail: herbert.bruder@siemens.com
Fung G S K is with Johns Hopkins University, Maryland, USA

I. INTRODUCTION

The imaging of cardiac structures, in particular the coronary arteries in (CT) is clinically important and at the same time technically challenging. Coronary arteries are small, rapidly moving vessels which require high temporal resolution of the reconstructed images. In a CT system, the temporal resolution is limited by hardware constraints, primarily by the fastest possible gantry rotation speed. Alternative system designs can improve temporal resolution. Currently, a temporal resolution of 65 ms can be achieved with the latest generation of dual source scanners. CT scanning of the heart is controlled by the patient's ECG and usually performed in cardiac phases with low motion, e.g., the diastolic phase. The duration of the quiescent heart phases shortens with increasing heart rate, at the same time vessel velocities increase. Even though reconstruction is retrospectively correlated to the quiet heart phase, this may cause image quality degradation by motion artifacts in particular in less advanced CT systems and may even affect image quality in high-end CT systems.

An alternative approach to improve temporal resolution is the development of reconstruction algorithms that account for the object motion during data acquisition. There are a variety of different approaches to this problem. However, common to almost all of them, is that a motion vector field is computed in four dimensions, initially. This motion vector field is input to a motion-compensated reconstruction. Motion compensation is achieved by warping the voxel space either prior to backprojection or after backprojection.

Three ways of estimating the motion vector field can be discerned. One way is to compute the motion vector field from 3D-3D registration of reconstructions at adjacent cardiac phases. Yet another approach is based on modeling the vessel. Partial images of reconstructions with subsequent portions of the measurement data are then matched to partial images of the vessel model. This match provides time-dependent motion fields [3].

Our approach is based on the definition of motion artifact metrics (MAM) which aim at the quantification of motion artifacts of the coronary arteries in a 3-D reconstructed image. Minimizing the metrics allows for iteratively estimating local motion vector fields. In section II we give a

short outline of the method. In addition, two simulation experiments are discussed, which are viable for evaluation of the MAM technique.

II. METHOD

A. Basic idea of MAM reconstruction

The proposed algorithm for motion estimation and compensation consists of several steps. A local parametric motion model $\mathcal{M}(t, \mathbf{x}, \mathbf{s})$ is used to describe local deformable motion as a function of time. The parameters \mathbf{s} are local motion vectors. An analytic reconstruction algorithm based on the FDK algorithm but incorporating the motion model is used to compute motion-compensated image data [4]. We restrict our algorithm to the coronary arteries and artifacts caused by their motion. Therefore, the first step of the algorithm is the definition of a region of interest for motion estimation (M-ROI). It is determined by segmentation of the coronary arteries from the initial image data. The estimation of the motion parameters \mathbf{s} is formulated as the minimization of a motion artifact metric $L(\mathbf{s})$ inside the M-ROI. The minimization is iteratively performed by a gradient descent algorithm. Each iteration consists of the reconstruction of a motion compensated image using the momentary $\mathcal{M}(t, \mathbf{x}, \mathbf{s}_k)$, the computation of the respective MAM value $L(\mathbf{s}_k)$ and the computation of its derivative $\partial L(\mathbf{s}_k) / \partial \mathbf{s}_k$ to obtain an updated motion vector \mathbf{s}_{k+1} for the next iteration.

B. Simulation experiments

Experiment A: A computer simulation was designed to evaluate the MAM approach. It is based on a simple but realistic model of the right coronary artery (RCA) with regard to morphology and motion curve. The simulated CT system used a 64×0.6 mm detector in a sequential (axial) acquisition mode with 285 ms rotation time.

Experiment B: Yet another simulation study was employed using the 4DXCAT [2] phantom and 64×0.6 mm detector in a helical acquisition mode with 285 ms rotation time.

Two different scanner types were simulated: a single-source system and a dual source system with two source-detector pairs 90° ahead of each other [5]. Dual source data were also simulated in a high-pitch mode to cover the entire heart in a single heart-beat during the end-diastolic heart phase. In a clinically environment this so-called FLASH mode is limited to moderate heart-rates, because the time period to cover the entire heart extends to one rotation time. The question is: can this heart rate limitation be eased using MAM reconstruction?

III. EVALUATION

In this section we evaluate the two simulation studies and check the potential of MAM in case of clinical data.

A. Evaluation of simulation data

In experiment A a heart-beat of 70bpm was simulated. Reconstructions were performed from 20% to 80 % cardiac

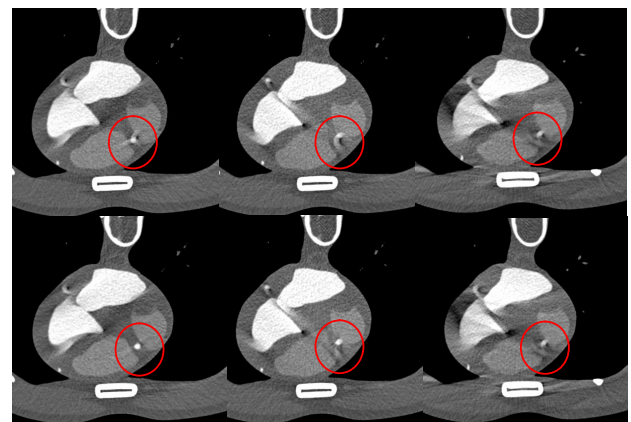
phase with step width of 2 %. The MAM reconstructions were compared to standard FBP reconstruction without motion compensation and respectively, to motion compensated reconstruction with ground truth motion vector field. MAM reconstruction was performed with two different motion artifact metrics: the image entropy, respectively a non-negativity constraint for image artifacts. Using a normalized cross correlation measure, it was shown that MAM reconstruction results come close to the ground truth at most of the phases. However, if the motion direction points orthogonal the recon range, motion artefacts are quite severe, and it takes a lot more iterations to reduce artefacts to an acceptable level.

In experiment B using the 4D-XCAT phantom, heart-rates from 60 bpm to 80 bpm have been simulated. The data were acquired both in single source and dual source helical acquisition mode. The MAM reconstruction was limited to the RCA. It proved to be efficient up to 80 bpm (Fig. 1). The reconstruction of dual source data with temporal resolution of 75 ms was superior at any heart rate. MAM also proved to be helpful to remove artefacts of dual source FLASH scans at high heart rates.

B. Evaluation of clinical data

Similar results as in simulation experiment B were obtained with clinical data. Fig. 2 shows the evaluation of dual source helical acquisition data. The ECG-correlated reconstruction of this type of data can be done either in a Single-Source mode using only data from one detector or in a Dual-Source mode using data of both detectors. We evaluated two cardiac phases in the end-diastole of the cardiac cycle. Again MAM reconstruction proved to reliably reduce motion artefacts. However, dual source reconstruction proved to be superior. We also demonstrate the efficiency of MAM reconstruction in case of FLASH dual source data. A cardiac perfusion dataset acquired in the high pitch FLASH mode at a heart rate of 75 bpm was processed with MAM. It was shown that motion artifacts were largely reduced.

Fig.1: Reconstructions of 4D-XCAT phantom (upper row) Reconstruction of Single Source data without motion compensation (middle row) MAM reconstruction of RCA of Single Source data. The heart-rate is increased from 60 bpm to 80 bpm from left to right. Please note, that the MAM volume was restricted to the RCA branch.



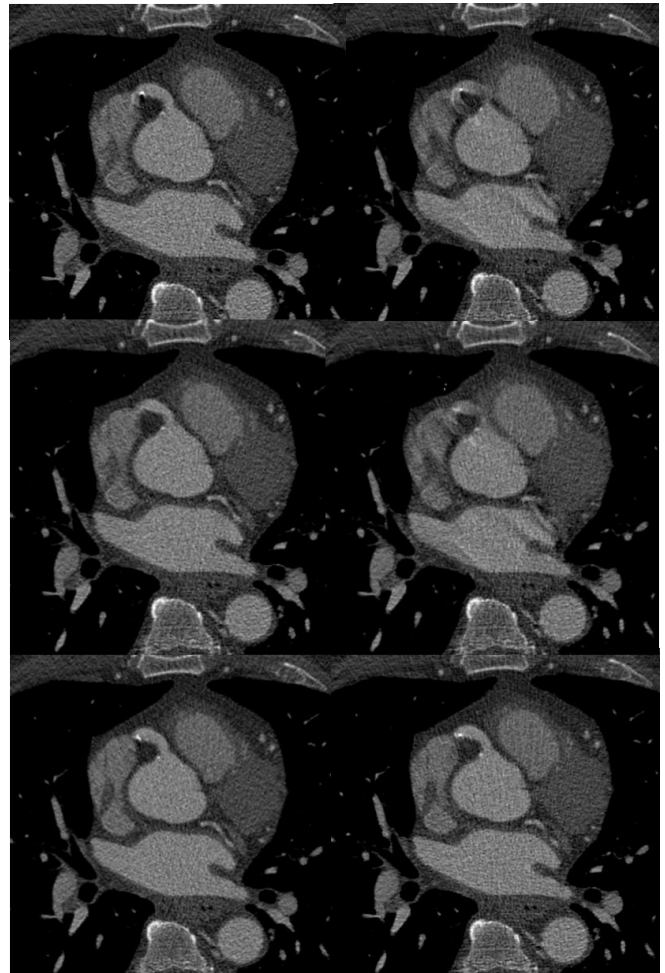
IV. CONCLUSION

In this work we tried to answer the question to what extent the Motion Artifact Metric Optimization (MAM) reconstruction is able to reduce motion artifacts in cardiac CT. If so, this would encourage to scan patients at higher heart rates. Consequently the administration of beta blockers could be reduced. Also, low-end CT systems with slower rotation of the gantry would benefit. Both, the evaluations of simulation data (e.g. with 4D-XCAT phantom) and clinical data, respectively, have shown, that motion compensation with MAM reconstruction can significantly enhance best phase reconstructions of single-source data. This opens the way to scan patients with higher heart rates. Also, it could be conceived to extend cardiac CT imaging to low-end CT systems with slow gantry rotation. It was also shown, that for Dual Source acquisition data motion compensation is not needed, because the intrinsic high temporal resolution of this acquisition technique is sufficient to robustly obtain motion artifact free image data in the diagnostic phases. The only exception is the cardiac FLASH acquisition that covers the entire heart in one cardiac cycle with maximum table feed. Today this acquisition mode is limited to moderate heart rates. Using MAM, it was shown, that this heart rate limitation could be eased. Thus the FLASH technique, which is extremely dose efficient, can be extended to a larger number of patients.

V. REFERENCES

1. Rohkohl, C., Bruder, H., Stierstorfer, K., Flohr, T., 'Improving Best-Phase Image Quality in Cardiac CT by Motion Correction with MAM Optimization', Med. Phys. (2013)
2. W.P.Segers et al., '4D-XCAT phantom for multimodality imaging research', Med.Phys. 37(9), 2010
3. Pack, J, et al. US 2011/0142313 A1
4. D. Schäfer, J. Borgert, V. Rasche, and M. Grass, 'Motion-compensated and gated cone beam filtered back-projection for 3-D rotational x-ray angiography', IEEE Trans. Med. Imaging **25**(7), 898–906 (2006).
5. Flohr T., Bruder, H., et al., 'Image reconstruction and image quality evaluation for a dual source CT scanner', Med. Phys. **35** 5882 (2008)

Fig.2 Reconstruction of patient data (heart rate 74bpm) at different heart phases (upper row) Reconstruction of Single Source data without motion compensation (middle row) MAM reconstruction of Single Source data (bottom row) Reconstruction of Dual Source data without motion compensation. (left) heart phase 70% (right) heart phase 75% of RR cycle.



Experimental Investigation of Hybrid Region-of-Interest Spectral CT Imaging with a Photon-Counting Detector

Taly Gilat Schmidt¹ and Kevin C. Zimmerman¹

Abstract—This study experimentally investigated the performance of a hybrid spectral CT acquisition method that acquires truncated spectral CT data for a central region of interest (ROI) while acquiring conventional energy-integrating data for the full field of view (FOV). ROI imaging may be beneficial for reducing pulse-pileup artifacts by reducing the dynamic range of the x-ray projections. In the proposed method, the conventional CT image is used as prior information to estimate spectral data outside of the ROI. A cylindrical rod phantom was scanned on a bench-top spectral CT system using a photon-counting detector with four energy bins. The photon-counting data recorded above the lowest energy threshold was used to approximate the prior conventional CT image. Reconstructed PMMA and aluminum basis images were compared for full FOV, truncated, and hybrid imaging methods. Images reconstructed from the truncated sinograms demonstrated cupping artifacts with increased error towards the edge of the ROI. The truncation artifacts were reduced by merging and blending the basis sinogram data inside the ROI with data outside the ROI that was estimated from the prior conventional image. For the blended data, the error in the PMMA basis image was less than 10% for the central 2.5 cm of the 4.25-cm-ROI, and less than 15% for the central 3 cm of the ROI. Overall, the results suggest preliminary experimental feasibility of a hybrid imaging method that acquires spectral data inside an ROI and conventional CT data for the full FOV, which may be beneficial for reducing pulse-pileup effects.

I. INTRODUCTION

Spectral CT using photon-counting detectors has the potential for improved material decomposition compared to dual-kV approaches. Photon-counting detectors with pulse-height analysis can sort detected photons into discrete energy bins. However, the recorded spectral information may be degraded by non ideal effects, such as pulse pileup. Pulse pileup occurs when multiple photons reach the detector within the counting period, resulting in errors in the number and energy of detected photons. Pulse-pileup artifacts are expected to be greater at the periphery of the field of view (FOV) where the object attenuation is low compared to the center of the FOV. Pulse pileup may be avoided by imaging a region of interest (ROI) where the dynamic range is expected to be limited [1].

This study experimentally investigated a hybrid spectral CT acquisition method that acquires truncated spectral CT data for a central ROI while acquiring conventional CT data for the full FOV. The conventional CT image is used as prior information for reconstructing basis images within the ROI. This method was previously investigated through simulations

¹ Department of Biomedical Engineering, Marquette University, Milwaukee WI

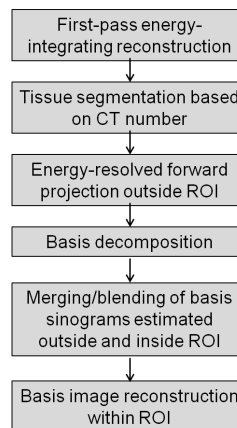


Fig. 1. Proposed algorithm for reconstructing ROI basis images from truncated spectral CT data with prior conventional CT image data.

modeling an ideal photon counting detector [2]. The current study is the first to investigate this hybrid imaging method on an experimental system with spectral degradations such as pulse-pileup and charge sharing. Alternative approaches for hybrid spectral CT imaging have also been investigated [3].

II. METHODS AND MATERIALS

A. Hybrid Spectral CT Imaging

We previously proposed an algorithm for performing material decomposition and reconstructing basis images for an ROI using prior energy-integrating data from the entire FOV [2]. The steps of the proposed algorithm are illustrated in Figure. 1. Conventional detectors image the full FOV, while energy-resolving detectors with B energy bins image a smaller ROI. Images of the full FOV are first reconstructed from the energy-integrating data using a conventional reconstruction technique. The resulting prior image is segmented based on Hounsfield Unit (HU) values into K materials. The previous simulation study determined that a coarse segmentation into a small number of materials (3 -6) provided sufficient accuracy [2]. A polyenergetic forward projection is performed on the segmented volume to estimate data in the B energy bins of detectors outside the ROI.

Material decomposition is performed on a ray-by-ray basis for both the measured projection data within the ROI and the estimated spectral data outside the ROI. M basis sinograms encompassing the entire FOV are then formed by merging

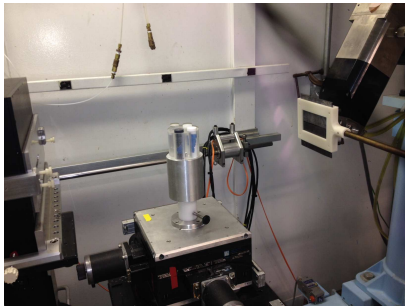


Fig. 2. Bench-top spectral CT system with a photon-counting detector used in experimental study.

the basis projections decomposed from the measured and estimated spectral data. Blending the basis sinograms at the boundaries of the truncated data may be performed to reduce discontinuities. Finally, M basis images are reconstructed from the decomposed sinograms using conventional techniques (i.e., filtered backprojection).

Because material decomposition is performed independently for each ray, the error in the estimated spectral data outside the ROI does not affect the decomposition into basis sinograms within the ROI. However, the error in the estimated data outside the ROI is expected to introduce errors into the ROI during reconstruction of the ROI basis images.

B. Experimental Study

Experimental data were acquired on a bench-top spectral CT system shown in Figure 2. The bench-top system consists of a CdZnTe detector (NEXIS, Nova R & D, Riverside, CA) with two pixel rows, each consisting of 128, 1 mm pixels, and a maximum of five energy thresholds per pixel. The system also contains a microfocus x-ray source (Fein-Focus-100.50, YXLON Intl, Hamburg, Germany) with a 3 micron effective focal spot.

A 6.35-cm-diameter cylindrical PMMA phantom was scanned, as shown in Figure 2. The phantom contained 2-cm-diameter cylindrical inserts of PMMA, Teflon, low-density polyethylene (LDPE), and air. The system was operated at 100 kV and 40 μ A, and energy measurements were performed with energy thresholds of 30, 40, 50, and 60 keV. The detector recorded the number of detected photons with energy above each threshold. Two hundred projections were acquired over 360 degrees, with a 1.9-second acquisition per view. The source-to-detector distance was 72 cm. The source-to-isocenter distance was 41 cm.

The recorded counts from successive energy measurements were subtracted to calculate the number of photons detected in energy bins of [30 - 40], [40 - 50], [50 - 60], and [60 - 100] keV. The energy-bin data for each detector pixel at each view angle were decomposed into basis materials of PMMA and aluminum using an empirical decomposition method previously proposed by Alvarez [4]. The resulting PMMA and aluminum basis sinograms encompass the complete phantom FOV and are referred to as the full FOV data. The full FOV basis sinograms were reconstructed into PMMA and aluminum basis images using filtered backprojection. These full FOV basis

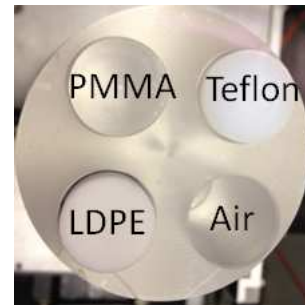


Fig. 3. PMMA phantom used in experimental study with Teflon, air, and low-density polyethylene inserts.

images served as the gold-standard images for the investigated hybrid method.

The proposed hybrid acquisition method was investigated by extracting the central 7.5-cm of sinogram data for each energy bin. These truncated energy-bin sinograms correspond to a 4.26-cm-diameter ROI within the phantom. A conventional CT acquisition of the full FOV was approximated by using the data detected above the lowest energy threshold, which corresponds to a photon-counting acquisition without energy selective information.

A full FOV photon-counting image was reconstructed from the photon-counting sinogram. The resulting 'conventional' image was segmented into air, PMMA, and Teflon regions using Hounsfield Unit ranges of [-2000 to -200], [-200 to 280] and [200 to 2000], respectively. A spectral forward projection was performed through the segmented image to generate estimated energy-bin data outside of the ROI. The forward projection algorithm modeled the mean energy of each energy bin. The estimated energy-bin sinograms were decomposed into PMMA and aluminum basis sinograms using a maximum likelihood method [5].

The basis sinogram data decomposed from the measured energy-bin data within the ROI was combined with the basis sinogram data estimated from the conventional CT image outside of the ROI, resulting in merged hybrid basis sinograms. The estimated basis sinograms outside of the ROI were blended with the measured basis sinograms inside the ROI using the previously proposed method [2].

PMMA and aluminum basis images were reconstructed within the 4.26-cm-diameter ROI from the full FOV, truncated, merged, and blended sinograms using filtered backprojection.

III. RESULTS

Figure 4 displays the 'conventional' photon-counting image reconstructed from the data measured above the lowest energy bin. Figure 4 also displays the resulting segmented image that was forward projected to estimate the energy-bin data outside of the ROI.

Figure 5 displays the PMMA and aluminum basis sinograms decomposed from the full FOV energy-bin data, the truncated ROI energy-bin data, and from the hybrid acquisition method that estimated the energy-bin data outside the ROI from a prior conventional image. The hybrid sinogram is displayed with

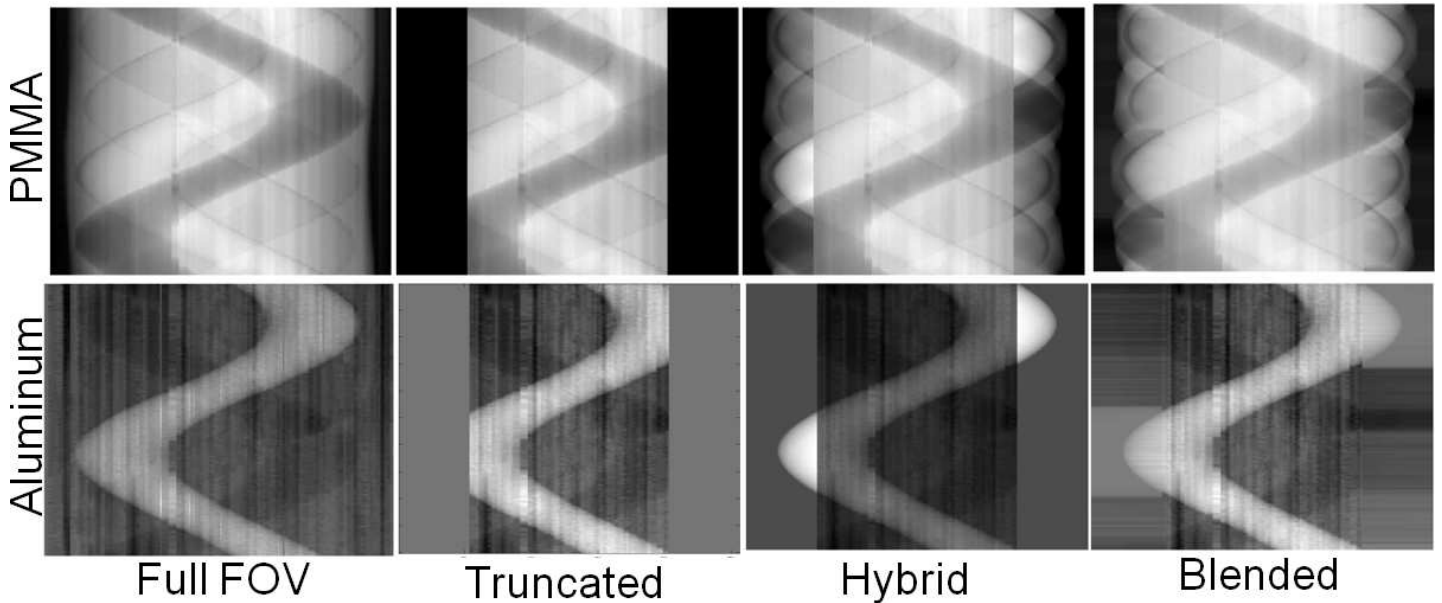


Fig. 5. PMMA and aluminum basis sinograms decomposed from the full FOV energy-bin data, the truncated ROI energy-bin data, and from the hybrid acquisition method with and without blending.

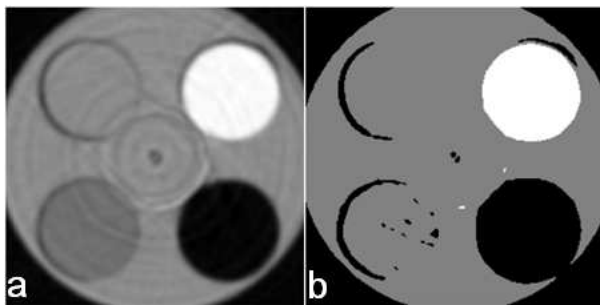


Fig. 4. (a) 'Conventional' CT image reconstructed from the photon-counting data measured above the lowest energy threshold. (b) Conventional CT image segmented into air, PMMA, and Teflon regions.

and without blending. As seen in Figure 5, blending reduced the discontinuities at the edge of the ROI.

Figure 6 displays the PMMA and aluminum basis images reconstructed from the full FOV data, the truncated ROI data, and the hybrid ROI data with and without blending. All images suffer from ring artifacts due to pixel-to-pixel variations and instabilities within the detector. In order to demonstrate preliminary feasibility of the hybrid imaging method, the goal of this work is to demonstrate similar basis image values in the hybrid ROI images compared to the full FOV images, even though the full FOV images may contain decomposition errors. Figures 7 and 8 plot horizontal profiles through PMMA and Teflon regions of the reconstructed basis images.

As seen in Figures 6 - 8, images reconstructed from the truncated sinograms contained cupping artifacts with increasing error towards the edge of the ROI. The truncation artifacts were reduced by merging the data within the ROI with data outside the ROI that was estimated from the prior conventional image. Blending the measured sinograms within the ROI with the estimated sinograms outside the ROI further reduced the

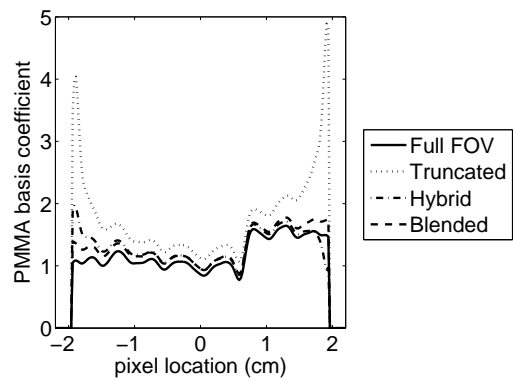


Fig. 7. Horizontal profile through the PMMA basis images reconstructed from full FOV, truncated, and hybrid acquisitions, with and without blending. The selected profile was through the PMMA background and Teflon rod insert.

truncation errors.

IV. DISCUSSION AND CONCLUSIONS

Reconstructing the ROI from truncated data resulted in errors that ranged from 300% at the edge of the ROI and 30% at the center of the ROI for the PMMA basis image. This error was reduced to 80% at the edge of the ROI to 10% at the center of the ROI by merging the basis sinograms estimated from the prior conventional image with the measured basis sinograms inside the ROI. Blending the estimated and measured sinograms further reduced the error to 30% at the edge of the ROI and 10% at the center of the ROI. For the blended data, the error in the PMMA basis image was 10% or less for central 2.5 cm of the 4.25-cm-ROI, and less than 15% for the central 3 cm of the ROI.

As seen in Figure 8, the truncated and blended aluminum basis images had good agreement with the full FOV data. This is because the aluminum basis image is generally sparse,

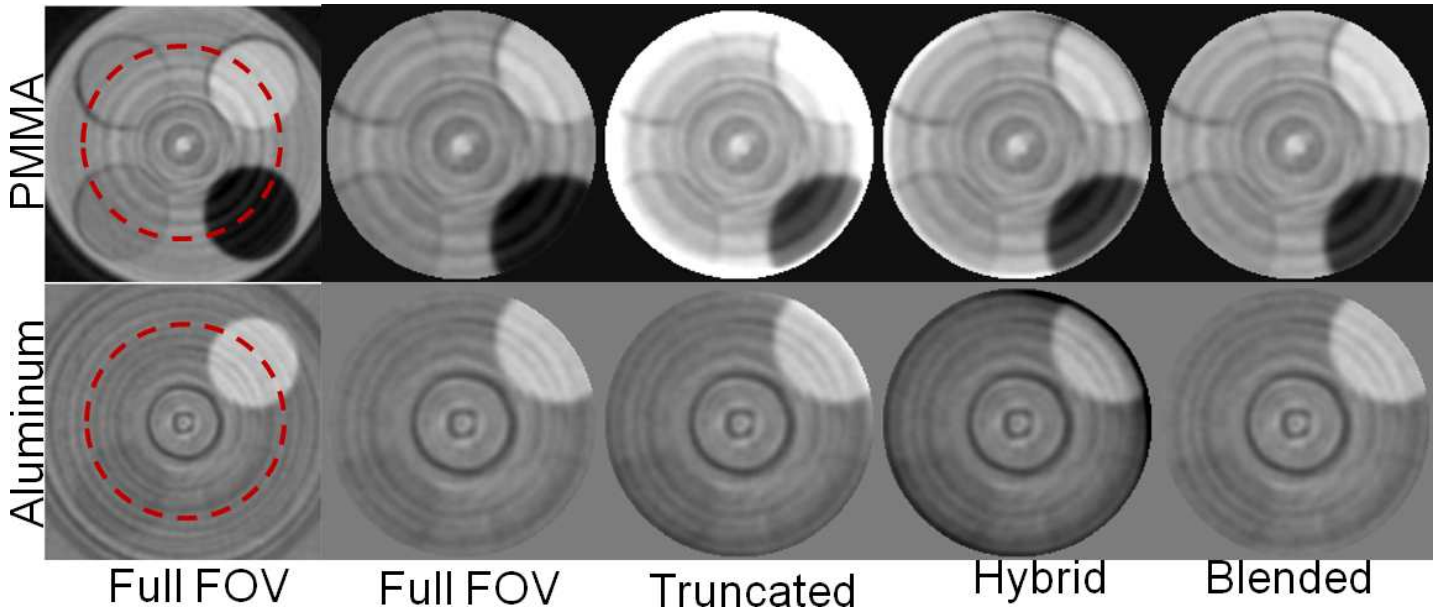


Fig. 6. PMMA and aluminum basis images reconstructed from the full FOV energy-bin data, the truncated ROI energy-bin data, and from the hybrid acquisition method with and without blending. The images on the left illustrate the ROI on the full FOV reconstructed image.

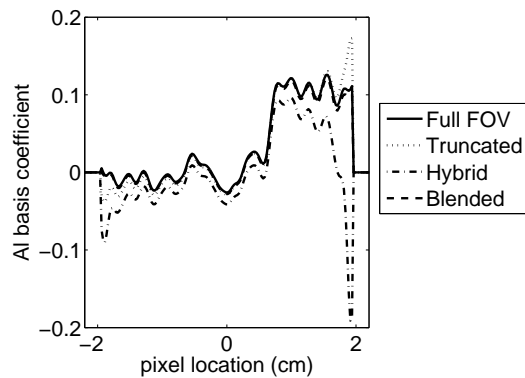


Fig. 8. Horizontal profile through the aluminum basis images reconstructed from full FOV, truncated, and hybrid acquisitions, with and without blending. The selected profile was through the PMMA background and Teflon rod insert.

thus the error from the missing data outside the ROI is small. Merging the hybrid sinogram data without blending increased the error in the aluminum basis image. This is likely due to differences in decomposition in the measured and estimated data, due to nonidealities in the experimental data. The forward projector used to estimated data outside of the ROI assumed an ideal detector.

Future work is planned to investigate improved blending and decomposition methods to reduce the errors in the reconstructed basis images. Overall, the results suggest preliminary experimental feasibility of a hybrid imaging method that acquires spectral data inside an ROI and conventional CT data for the full FOV, which may be beneficial for reducing pulse-pileup effects.

V. ACKNOWLEDGMENTS

This work was supported by NIH Grant number R21EB015094. The contents of this article are solely the

responsibility of the authors and do not necessarily represent the official views of the National Institutes of Health.

REFERENCES

- [1] K. Taguchi, S. Srivastava, H. Kudo, and W. Barber, "Enabling photon counting clinical x-ray CT," in *Nuclear Science Symposium Conference Record (NSS/MIC), 2009 IEEE*. IEEE, 2009, pp. 3581–3585.
- [2] T. G. Schmidt and F. Pektas, "Region-of-interest material decomposition from truncated energy-resolved ct," *Medical Physics*, vol. 38, no. 10, pp. 5657–5666, 2011. [Online]. Available: <http://link.aip.org/link/?MPH/38/5657/1>
- [3] J. Bennett, A. Opie, Q. Xu, H. Yu, M. Walsh, A. Butler, P. Butler, G. Cao, A. Mohs, and G. Wang, "Hybrid spectral micro-ct: System design, implementation, and preliminary results," *Biomedical Engineering, IEEE Transactions on*, vol. 61, no. 2, pp. 246–253, Feb 2014.
- [4] R. Alvarez, "Estimator for photon counting energy selective x-ray imaging with multibin pulse height analysis," *Medical Physics*, vol. 38, p. 2324, 2011.
- [5] E. Roessl and R. Proksa, "K-edge imaging in x-ray computed tomography using multi-bin photon counting detectors," *Physics in Medicine and Biology*, vol. 52, no. 15, pp. 4679–4696, 2007. [Online]. Available: <http://stacks.iop.org/0031-9155/52/4679>

Dual-Energy-based Beam Hardening Correction in Digital Volume Tomography (DVT)

Sören Schüller, Kai Stannigel, Markus Hülsbusch, Stefan Sawall, Johannes Ulrici, Erich Hell,
and Marc Kachelrieß

Abstract—Streak artifact reduction required by beam hardening is a well known task in computed tomography (CT) image reconstruction. Dual- or multi-energy CT provides additional spectral information compared to a standard single-energy CT scan, which can be used to solve this task. As a special kind of a CT system, a digital volume tomograph (DVT) is used in the dental field to deliver high contrast and highest spatial resolution. In this work, we develop an algorithm which takes all these important image quality features into account. The demonstrated results show a reduction of beam hardening, while contrast, noise and spatial resolution are preserved. To reach these goals we perform linear weighting of dual-energy images and use different mixed images as a basis of correction employing frequency-split and non-linear blending.

Index Terms - DVT, beam hardening correction, dual-energy, frequency split

I. INTRODUCTION

In digital volume tomography (DVT) the image quality often suffers from beam hardening (BH) artifacts. The artifacts appear in the vicinity of strong attenuating objects like bones, teeth or implants which are densely positioned in the dentition. The polychromatic nature of x-ray radiation causes the BH artifacts. Several publications [1]–[3] have shown that suitable combinations of the low- and high-energy images of a dual-energy scan can provide images with different image characteristics like reduced BH and metal artifacts as well as an improved contrast-to-noise ratio (CNR). However, the solutions are mutually exclusive and only one parameter can be optimized at the same time. For example metal artifact reduced images always suffer from high noise [4] and need post-processing by noise reduction techniques like adaptive filtering, which might degrade spatial resolution.

In the dental field, a special need for high spatial resolution and high contrasts exists [5], [6]. The evaluation of the periodontium is a good example. This structure is the connection between each tooth and the jaw bone and is, for this reason, essential for a solid anchorage. State-of-the-art DVTs perform at high spatial resolution ($\gtrsim 100 \mu\text{m}$) [7] to visualize the bounding layers correctly [6]. Each BH reduction technique

leading to a blurring or a contrast reduction is not acceptable especially for dental diagnostics. We therefore propose a new method for the reduction of BH which maintains the high contrast and spatial resolution provided by the DVT imaging system.

The idea behind our algorithm is to decompose our initial dual-energy reconstructions into a set of basis images, each of them optimizing a certain image characteristic, i.e. best contrast, lowest noise, and minimal BH. These images are combined using frequency split (FS) (like used in [8]) and non-linear blending (NB) (like used in [3]) to yield in a BH-reduced reconstruction which meets dental demands.

The blending allows for a preservation of contrast and the frequency split maintains spatial resolution. All benefits will only be acceptable if the overall dose of the proposed dual-energy scan and correction technique does not exceed the dose of a state of the art DVT scan.

II. METHODS AND MATERIALS

To minimize BH artifacts we utilize the fact that BH occurs with different strengths in the low- and high-energy images. By using a linear weighting between these images, the artifacts can be significantly reduced. This kind of weighting, however, leads to increased image noise and a decrease of the CNR in the resulting BH-reduced image. To overcome this issue we propose a voxel-wise non-linear blending between the soft-tissue regions of the previously generated BH-reduced image and the strong attenuating regions, e.g. teeth, of the low-energy image which shows a high contrast. After all, the combination of the low frequencies of the non-linear blended image and the high frequencies of a minimal noise image re-establishes fine structures and low image noise. A schematic overview of the algorithm is presented in figure 1. The proposed algorithm performs in image domain because the angular sampling between the two dual-energy scans might differ. If not noted otherwise all reconstructions are performed using a filtered back-projection, in our case the Feldkamp-Davis-Kress (FDK) [9] reconstruction without any further post-processing.

A. Data Acquisition

Cadaver heads were scanned on a Galileos DVT (Sirona, The Dental Company, Bensheim, Germany). Each scan was performed over an angular range of 210° and the number of projections was 200 per scan. The following scans were performed:

- reference scan f_{Ref} : 98 kV, 12 mA
- low energy f_{L} : 65 kV, 36 mA

Sören Schüller: German Cancer Research Center (DKFZ), Im Neuenheimer Feld 280, Heidelberg, Germany and Institute of Medical Physics, Friedrich–Alexander–University (FAU) Erlangen–Nürnberg, Henkestr. 91, 91052 Erlangen, Germany and Sirona Dental Systems GmbH, Fabrikstr. 31, Bensheim, Germany.

Dr. Kai Stannigel, Dr. Markus Hülsbusch, Dr. Johannes Ulrici, and Dr. Erich Hell: Sirona Dental Systems GmbH, Fabrikstr. 31, Bensheim, Germany.

Dr. Stefan Sawall, and Prof. Dr. Marc Kachelrieß: German Cancer Research Center (DKFZ), Im Neuenheimer Feld 280, Heidelberg, Germany and Institute of Medical Physics, Friedrich–Alexander–University (FAU) Erlangen–Nürnberg, Henkestr. 91, 91052 Erlangen, Germany.

Corresponding author: soeren.schueller@dkfz.de

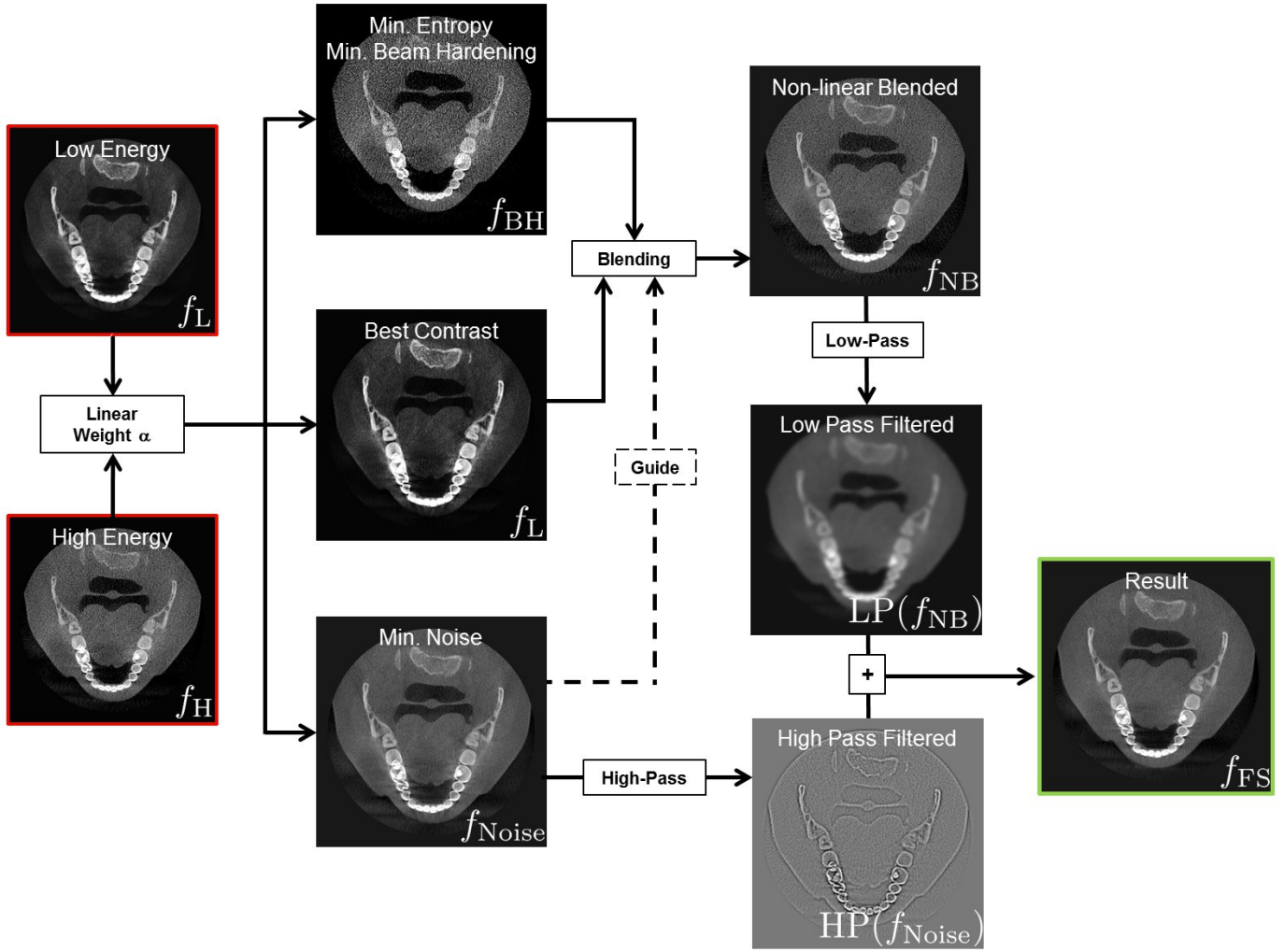


Fig. 1. Block diagram of the whole algorithm. Linear weighting of f_L and f_H generating f_{BH} , f_L , and f_{Noise} . f_{Noise} is used as a guide for the non-linear blending of f_L and f_{BH} . The final image f_{FS} is generated by a voxel-wise summation of the high pass of f_{Noise} and the low pass of f_{NB} .

- high energy f_H : 120 kV, 18 mAs, 2 mm copper pre-filter

The performed reference scan is the gold standard of the Galileos DVT and includes proprietary post-processing steps. For a better comparison all images are without post-processing. The dual-energy scan has the same dose as the reference scan.

B. Linear Weighting to Minimize Noise

A simple way to obtain images with desired properties from a low f_L and high f_H image, which were acquired at different tube voltages, is by a linear combination with weight α :

$$f_\alpha = (1 - \alpha)f_L + \alpha f_H. \quad (1)$$

Linear weighting was used, because linear weighted images are equivalent to pseudo monochromatic images.

If there are no correlations between the image noise in f_L and f_H equation 2 describes the noise $\sigma(f_\alpha) = \sqrt{\text{Var}(f_\alpha)}$ for each linear combination α :

$$\text{Var}(f_\alpha) = (1 - \alpha)^2 \text{Var}(f_L) + \alpha^2 \text{Var}(f_H). \quad (2)$$

The optimal α_{Noise} to achieve minimal noise can be obtained by derivation of equation 2:

$$\alpha_{Noise} = \frac{\text{Var}(f_L)}{\text{Var}(f_L) + \text{Var}(f_H)}. \quad (3)$$

C. Linear Weighting to Maximize Contrast

To choose the image with the maximal contrast between soft-tissue and bone, the energy dependent attenuation can be taken into account. The relative distance (contrast) between bone and soft-tissue is greater for low energies. The initial low energy image is used as the maximal contrast image. It would also be possible to use a linear combination with $\alpha < 0$ which has an even better contrast but results in an increased noise level (see equation 2).

In general the contrast $C(A, B, \alpha)$ between regions of interest A and B of a linear mixed image f_α is given as

$$C(A, B, \alpha) = (1 - \alpha)(f_L(A) - f_L(B)) + \alpha(f_H(A) - f_H(B)). \quad (4)$$

This equation is later used in section II-E and III.

D. Linear Weighting to Minimize Beam Hardening

The linear weighting coefficient α_{BH} for an image with minimal BH is determined by evaluating the entropy S concerning the gray-value distribution $k_\alpha(b)$, i.e. the histogram with B Bins, inside the soft-tissue regions (figure 2) for different linear combinations in the range of $1 \leq \alpha \leq 4$.

$$S_\alpha = - \sum_{b=1}^B k_\alpha(b) \log k_\alpha(b) \quad (5)$$

The dependency between entropy and w is shown in figure 3. The impact of BH on the image quality decreases with

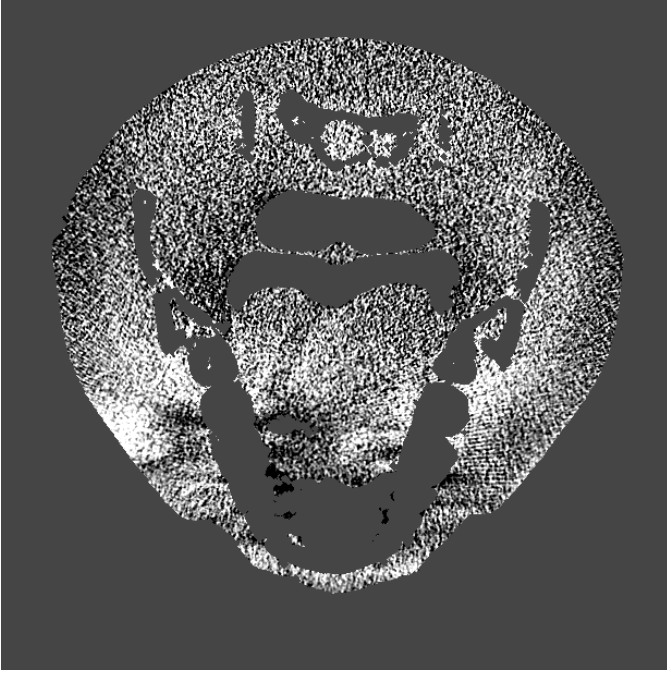


Fig. 2. Soft-tissue region which is used to estimate the BH. All homogeneous gray voxels are not taken into account.

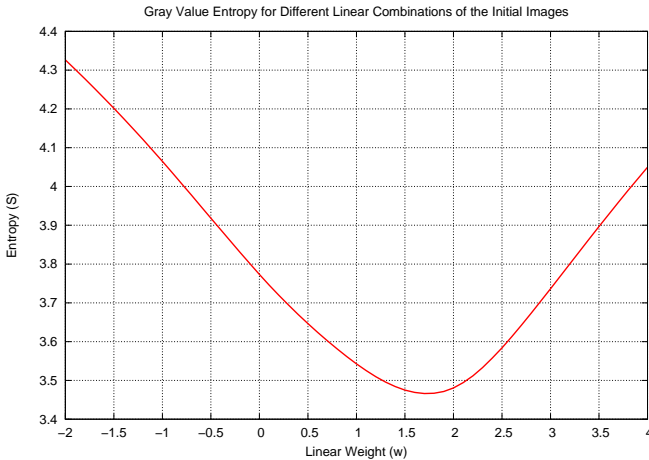


Fig. 3. Entropy of different linear combination calculated over the soft-tissue region, in which the streaks appear. The plot shows a well-defined minimum at $w_{\text{BH}} = 1.7$.

higher mean energies of the spectrum. So in fact an image with less BH can only be achieved for combinations above f_{H} , i.e. $\alpha > 1$. It would also be possible to use other cost functions, like total variation, to detect BH streaks in the soft-tissue. But our choice turned out to be less prone to noise and sampling artifacts.

E. Non-linear Blending

Our main task is to obtain an image with reduced BH artifacts. Equation 2 and 4 illustrate that by directly taking the BH-reduced image f_{BH} as the final image automatically a reduced contrast and a higher noise level compared to the initial dual-energy images appears. To recover the contrast we combine the soft-tissue regions of the BH-reduced image f_{BH} with the high density regions (bone, teeth,...) of the maximum contrast image $f_{\alpha=0}$ by a voxel-wise non-linear blending which is guided by the minimal noise image f_{Noise} . Because of the low noise in f_{Noise} all regions can be assigned correctly.

F. Frequency Split

Performing a FS on the low noise image f_{Noise} and the non-linear blended images f_{NB} followed by a combination of the results is the final step of the algorithm. The final image consist of the high frequency information of f_{Noise} , which reestablish all edges, and the low frequency information of the non-linear blended image f_{NB} , which contains high contrast and minimal BH in the soft-tissue regions. The FS performs in the image domain by simply using a long range 3D binomial filter. The low-pass (LP) image is simply the filtered image itself. To obtain the high-pass (HP) image, the low-pass image is subtracted from the unfiltered image. Finally, the voxel-wise addition of the HP and LP yields the desired image f_{FS} with high spatial resolution, high contrast and low noise.

III. RESULTS

All results are compared to a standard DVT scan f_{Ref} which has the same dose as the whole dual-energy scan. Figure 4 illustrates the preserved spatial resolution. Fine structures in f_{FS} can be as good as in f_{Ref} and f_{L} identified with the advantages of lower noise and more homogeneity inside uniform regions. Figure 5 illustrates the potential of the proposed BH artifact reduction in DVT images. The reduction of the streaks can also be seen in tiny spaces between the teeth, where a diagnosis can be strongly affected by this kind of artifacts.

TABLE I

COMPARISON OF THE CNRS OF ALL INITIAL AND PRODUCED IMAGES ALONG THE IMAGING CHAIN. THE ROIS ARE INDICATED IN FIGURE 5.

	Soft Tissue A	$\sigma(A)$	Bone B	$\sigma(B)$	CNR
f_{Ref}	137 HU	170 HU	1085 HU	197 HU	2.83
f_{L}	68 HU	97 HU	1459 HU	132 HU	5.98
f_{H}	137 HU	170 HU	1085 HU	197 HU	2.58
f_{Noise}	83 HU	86 HU	1376 HU	114 HU	6.41
f_{BH}	185 HU	294 HU	823 HU	344 HU	1.00
f_{NB}	175 HU	256 HU	1455 HU	134 HU	3.14
f_{FS}	181 HU	84 HU	1446 HU	111 HU	6.45

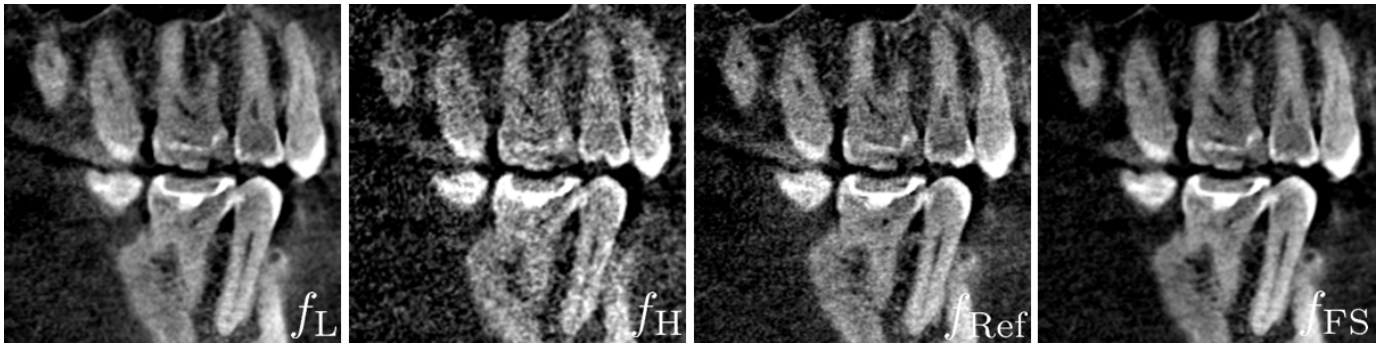


Fig. 4. Sagittal slices. Center and window are adapt for each image according the contrasts inside the ROIs. The windowing corresponds to $C = 1500$ HU, $W = 3000$ HU of f_{Ref} . Voxel size $250 \mu\text{m}^3$.

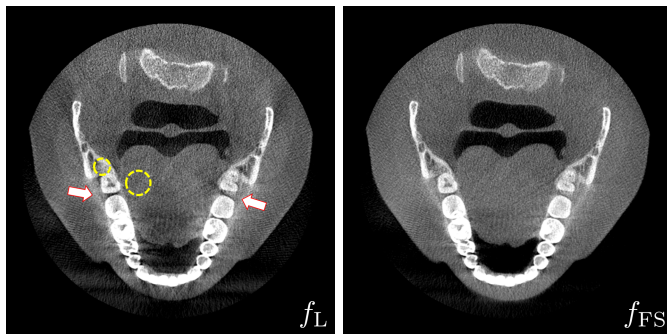


Fig. 5. The number and magnitude of the BH streaks has decreased in the f_{FS} in comparison to f_L . $C = 500$ HU, $W = 3000$ HU. Voxel size $250 \mu\text{m}^3$. The ROIs for the CNR evaluations are presented in f_L . Arrows pointing to regions which benefit from the proposed BH reduction algorithm.

A short overview of noise, contrast and CNR for the basis and final images are presented in table I. The proposed method achieves the highest CNR compared to the reference scan at 98 kV and the two single scans f_L and f_H of the dual-energy scan. This is a consequence of the properties of the non-linear blending, which retains the high contrast of f_L and the frequency split, which in an ideal case only contains the low noise level of f_{Noise} . This leads to a CNR outperforming all 3 initial reconstructions.

IV. CONCLUSION

The herein proposed method can easily and automatically reduce beam hardening artifacts in DVT routine and the results indicate that it is superior to previously published BH-correction [10] algorithms in terms of noise and dose usage. The spatial resolution which plays an important role for the dentist is not degraded by the new algorithm. It can also be noticed that reduced noise and BH in the proximity of bone and teeth structures clearly improve the capabilities for the diagnostics. As a result of the higher CNR, a dose reduction for some applications could also be possible and leads to a increased patient safety.

ACKNOWLEDGMENT

The authors would like to thank Dr. Christian Scheifele of Sektion Bildgebung und implantologische Diagnostik Department für Zahn-, Mund- und Kieferheilkunde Universitätsklinikum, Freiburg, Germany for providing the data sets. The high-speed image reconstruction software RayConStruct-IR was provided by RayConStruct® GmbH, Nürnberg, Germany.

REFERENCES

- [1] A. Coleman and M. Sinclair, "A beam-hardening correction using dual-energy computed tomography," *Physics in Medicine and Biology*, vol. 30, no. 11, p. 1251, May 1985.
- [2] F. Bamberg, A. Dierks, K. Nikolaou, M. F. Reiser, C. R. Becker, and T. R. Johnson, "Metal artifact reduction by dual energy computed tomography using monoenergetic extrapolation," *European Radiology*, vol. 21, no. 7, pp. 1424–1429, Jan. 2011.
- [3] D. R. Holmes III, J. G. Fletcher, A. Apel, J. E. Huprich, H. Siddiki, D. M. Hough, B. Schmidt, T. G. Flohr, R. Robb, C. McCollough *et al.*, "Evaluation of non-linear blending in dual-energy computed tomography," *European Journal of Radiology*, vol. 68, no. 3, pp. 409–413, Dec. 2008.
- [4] L. Yu, S. Leng, and C. H. McCollough, "Dual-Energy CT-Based Monochromatic Imaging," *American Journal of Roentgenology*, vol. 199, no. 5, pp. S9–S15, Sep. 2012.
- [5] C. Holberg, S. Steinhäuser, P. Geis, and I. Rudzki-Janson, "Cone-beam computed tomography in orthodontics: benefits and limitations," *Journal of Orofacial Orthopedics/Fortschritte der Kieferorthopädie*, vol. 66, no. 6, pp. 434–444, Sep. 2005.
- [6] Y. Doshi, A. Mani, P. Marawar, P. Mishra *et al.*, "A clinical study on mobility of teeth as assessed through their damping characteristics and progress of periodontal disease using advanced diagnostic aids: Mobilometer and florida probe," *Journal of the International Clinical Dental Research Organization*, vol. 2, no. 1, p. 12, Nov. 2011.
- [7] Y. Kyriakou, D. Kolditz, O. Langner, J. Krause, and W. Kalender, "Digital volume tomography (DVT) and multislice spiral CT (MSCT): an objective examination of dose and image quality," in *RöFo. Fortschritte auf dem Gebiet der Röntgenstrahlen und der bildgebenden Verfahren*, vol. 183, no. 02. Thieme, Oct. 2010, pp. 144–153.
- [8] E. Meyer, R. Raupach, M. Lell, B. Schmidt, and M. Kachelrieß, "Frequency split metal artifact reduction (FSMAR) in computed tomography," *Medical Physics*, vol. 39, p. 1904, Mar. 2012.
- [9] L. Feldkamp, L. Davis, and J. Kress, "Practical cone-beam algorithm," *Journal of the Optical Society of America*, vol. 1, no. 6, pp. 612–619, Jun. 1984.
- [10] Y. Kyriakou, D. Prell, W. A. Kalender, and M. Kachelrieß, "Empirical beam hardening correction for CT," *IEEE Medical Imaging Conference Record*, pp. M08–4, 7 pages, Oct. 2009.

Dictionary Learning and Low Rank based Multi-energy CT Reconstruction

Yanbo Zhang, Hengyong Yu, Xuanqin Mou and Ge Wang

Abstract—Multi-energy CT promises much richer information. How to fully use spectral datasets is a hot topic. Because images in different energy channels are highly correlated, the low rank regularization is well motivated. On the other hand, our previous work has shown that the dictionary learning based reconstruction method can suppress image noise remarkably. In this paper, a novel multi-energy CT reconstruction method is developed by combining dictionary learning and low rank regularization. The proposed method is compared to two other algorithms using a simulated mouse thorax phantom containing iodine. The proposed method outperforms the competing methods in the simulation.

I. INTRODUCTION

Multi-energy CT produces an attenuation map of an object with a spectral dimension, commonly presented in multiple energy channels simultaneously. This new information can be used to discriminate materials in a chemically specific fashion. Currently, multi-energy CT reconstruction attracts an increasing attention. Xu et al. developed a statistical interior tomography method with total variation (TV) regularization for hybrid true-color micro-CT [1]. In that study, images in each energy channel were reconstructed independently similar to conventional CT. However, since the multi-energy datasets are collected from the same object, attenuation coefficients in different channels are highly correlated. Hence, the multi-energy reconstruction can be improved if the relationships among spectral component images are fully utilized. In 2011, Gao et al. proposed a PRISM method to model a multi-energy image as the superposition of a low-rank matrix and a sparse matrix and formulate the reconstruction problem in a coupled optimization via compressive sensing [2]. Recently, Chu et al. [3] [4] and Semerci et al. [5] proposed multi-energy CT reconstruction methods using low rank tensor and TV regularization. These methods yielded promising numerical results.

In our previous work, a dictionary learning based reconstruction method has been applied to utilize image sparsity

This work was supported in part by the National Natural Science Foundation of China (No. 61172163), as well as the NSF CAREER Award (CBET-1149679).

Yanbo Zhang and Xuanqin Mou are with the Institute of Image Processing and Pattern Recognition, Xi'an Jiaotong University, Xi'an, Shaanxi 710049, China, and also with Beijing Center for Mathematics and Information Interdisciplinary Sciences, Beijing, 10048 China. (e-mail: yanbozhang007@163.com, xqmou@mail.xjtu.edu.cn).

Hengyong Yu is with the Biomedical Imaging Division, VT-WFU School of Biomedical Engineering and Sciences, Wake Forest University Health Sciences, Winston-Salem, NC 27157 USA (e-mail: hyu@wfbmc.edu).

Ge Wang is with the Biomedical Imaging Center/Cluster, CBIS, Dept. of BME, Rensselaer Polytechnic Institute, Troy, NY 12180 USA (e-mail: wangg6@rpi.edu).

for low dose CT, whose performance is superior to that with the TV constraint. In this paper, we propose a multi-energy CT reconstruction method by combining dictionary learning and low rank regularization.

II. RELATED WORK

A. Tensor Unfolding [3] [6]

A tensor is a multidimensional array. An n -way (or n th-order) tensor is defined as $\mathcal{X} \in \mathbb{R}^{I_1 \times I_2 \times \dots \times I_n}$, whose (i_1, i_2, \dots, i_n) element is denoted as $x_{i_1 i_2 \dots i_n}$, and $1 \leq i_k \leq I_k, k = 1, 2, \dots, n$.

A tensor can be transformed into a matrix using an *unfolding* operator, which is an element reordering process. The mode- k *unfolding* of $\mathcal{X} \in \mathbb{R}^{I_1 \times I_2 \times \dots \times I_n}$ is denoted by $X_{(k)}$,

$$\text{unfold}_k(\mathcal{X}) \triangleq X_{(k)} \in \mathbb{R}^{I_k \times (I_1 \dots I_{k-1} I_{k+1} \dots I_n)}. \quad (1)$$

B. Multi-energy CT with TV Regularization

A simple way to reconstruct multi-energy CT is to reconstruct each component image independently, just like conventional CT reconstruction [1]. An iterative reconstruction method with TV regularization can be expressed as

$$\min_{\mathbf{x}_i} \|A\mathbf{x}_i - \mathbf{y}_i\|^2 + \lambda_{TV} TV(\mathbf{x}_i), \quad (2)$$

where A is a system matrix, \mathbf{x}_i and \mathbf{y}_i are vectors corresponding to the 2D image X_i and the projection dataset Y_i in the i th energy channel respectively.

C. Multi-energy CT with TV and Low Rank Regularization

In multi-energy CT, let $\mathcal{X} \in \mathbb{R}^{I_1 \times I_2 \times I_3}$ be a 3-way tensor, where I_1 and I_2 are the width and height of a CT image respectively, and I_3 is the number of spectral channels. $\mathcal{X} = \{X_i\}_{i=1,2,\dots,I_3}$ and $\mathcal{Y} = \{Y_i\}_{i=1,2,\dots,I_3}$, where X_i and Y_i are a CT image and an acquired sinogram corresponding to the i th energy channel respectively. Similar to the method proposed by Chu et al. [4], the reconstruction of spectrally dependent attenuation coefficients is reduced to the following optimization problem:

$$\min_{\mathcal{X}} \left\| A\mathcal{X}_{(3)}^T - \mathcal{Y}_{(3)}^T \right\|_F^2 + \lambda_* \|\mathcal{X}\|_* + \lambda_{TV} TV(\mathcal{X}), \quad (3)$$

where the first term is the sum of errors in spectral channels, and the superscript T denotes the transpose operator. The tensor \mathcal{X} can be turned into matrixes using the *unfolding* operation as $\mathcal{X}_{(1)} \in \mathbb{R}^{I_1 \times (I_2 \times I_3)}$, $\mathcal{X}_{(2)} \in \mathbb{R}^{I_2 \times (I_1 \times I_3)}$ and $\mathcal{X}_{(3)} \in \mathbb{R}^{I_3 \times (I_1 \times I_2)}$. $\|\cdot\|_F$ represents the Frobenius norm, and

$\|\mathcal{X}\|_*$ is the generalized tensor nuclear norm which is defined as

$$\|\mathcal{X}\|_* = \sum_{k=1}^3 \gamma_k \|\mathcal{X}_{(k)}\|_*, \quad (4)$$

where γ_k is a weighting factor. Tomioka et al. [6] proposed a more general form in which γ_k can be different. In this work, we only consider the correlation of images between different energy channels. Therefore, we set γ_1 and γ_2 to be zero and γ_3 to be one. $TV(\mathcal{X})$ indicates the TV regularization for channels separately.

III. METHOD

In our previous work [7], it has been shown that the dictionary learning based algorithm outperforms the TV minimization method for low-dose CT. A well trained dictionary can sparsely represent a single image, while low rank tensors are intended to encourage the correlation between images in different channels. Hence, we are motivated to combine the merits of dictionary learning and low rank tensor regularization, and formulate the CT reconstruction as the following optimization.

$$\min_{(\mathcal{X}, \alpha)} \left\| A\mathcal{X}_{(3)}^T - \mathcal{Y}_{(3)}^T \right\|_F^2 + \lambda_* \|\mathcal{X}\|_* + \lambda_D \left(\sum_s \|\mathbf{E}_s(\mathcal{X}) - \mathbf{D}\alpha_s\|_2^2 + \sum_s v_s \|\alpha_s\|_0 \right), \quad (5)$$

where $D \in \mathbb{R}^{N \times K}$ is a dictionary matrix with K atoms, each of which has $\sqrt{N} \times \sqrt{N}$ pixels. The dictionary can be obtained via training from a given image, which is described in detail in section V. $\alpha_s \in \mathbb{R}^{K \times 1}$ is the representation vector. The operator $\mathbf{E}_s = \{e_{ki}^s\} \in \mathbb{R}^{N \times (I_1 I_2 I_3)}$ extracts the s th patch from a component image of the tensor, and $e_{ki}^s \in \{0, 1\}$. $\|\cdot\|_0$ represents the l_0 -norm, namely, the number of nonzero entries. The two variables \mathcal{X} and α can be optimized using an alternating minimization scheme. Thus, the objective function becomes

$$\begin{cases} \mathcal{X}^{n+1} = \arg \min_{\mathcal{X}} \left\| A\mathcal{X}_{(3)}^T - \mathcal{Y}_{(3)}^T \right\|_F^2 + \lambda_* \|\mathcal{X}\|_* \\ \quad + \lambda_D \sum_s \|\mathbf{E}_s(\mathcal{X}) - \mathbf{D}\alpha_s^n\|_2^2 \\ \alpha^{n+1} = \arg \min_{\alpha} \sum_s \|\mathbf{E}_s(\mathcal{X}^{n+1}) - \mathbf{D}\alpha_s\|_2^2 + \sum_s v_s \|\alpha_s\|_0 \end{cases} \quad (6)$$

The first objective function in Eq. (6) is difficult to solve directly. Inspired by the optimization method proposed in [8], we implement the algorithm in Eq. (7). Specifically, the first step in Eq. (7) uses OS-SART.

$$\begin{cases} \mathcal{X}^{n+1/2} = \arg \min_{\mathcal{X}} \left\| A\mathcal{X}_{(3)}^T - \mathcal{Y}_{(3)}^T \right\|_F^2 \\ \mathcal{X}^{n+1} = \arg \min_{\mathcal{X}} \left\| \mathcal{X} - \mathcal{X}^{n+1/2} \right\|_F^2 + \lambda_* \|\mathcal{X}\|_* \\ \quad + \lambda_D \sum_s \|\mathbf{E}_s(\mathcal{X}) - \mathbf{D}\alpha_s^n\|_2^2 \end{cases} \quad (7)$$

To solve the second step of Eq. (7), an intermediate variable $\mathcal{D} = \mathcal{X}$ and a difference variable \mathcal{V} are introduced. Then,

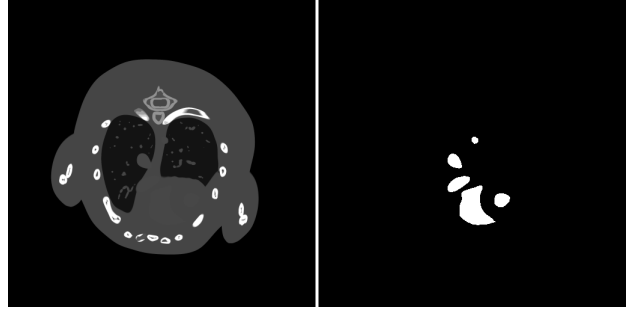


Fig. 1. The mouse thorax phantom (left) and the iodine contrast agent (right).

the objective function is split into the three steps in Eq. (8). The first step of Eq. (8) has an explicit solution given by Eq. (9), where d_j^n and v_j^n are entries of \mathcal{D}^n and \mathcal{V}^n , respectively. The second step is solved using the generalized singular value thresholding (G-SVT) formula [2].

$$\begin{cases} \mathcal{X}^{n+1} = \arg \min_{\mathcal{X}} \left\| \mathcal{X} - \mathcal{X}^{n+1/2} \right\|_F^2 + \mu_* \|\mathcal{D}^n - \mathcal{X} - \mathcal{V}^n\|_F^2 \\ \quad + \lambda_D \sum_s \|\mathbf{E}_s(\mathcal{X}) - \mathbf{D}\alpha_s^n\|_2^2 \\ \mathcal{D}^{n+1} = \arg \min_{\mathcal{D}} \mu_* \|\mathcal{D} - \mathcal{X}^{n+1} - \mathcal{V}^n\|_F^2 + \lambda_* \|\mathcal{D}\|_* \\ \mathcal{V}^{n+1} = \mathcal{V}^n + \mathcal{X}^{n+1} - \mathcal{D}^{n+1} \end{cases} \quad (8)$$

$$x_j^{n+1} = \frac{x_j^{n+1/2} + \mu_*(d_j^n - v_j^n) + \lambda_D \sum_{i=1}^N e_{ij}^s [\mathbf{D}\alpha_s^n]_i}{1 + \mu_* + \lambda_D \sum_{i=1}^N \sum_{l=1}^{I_1 I_2 I_3} e_{ij}^s e_{il}^s} \quad (9)$$

The update of α in Eq. (6) is basically equivalent to solving a constrained problem, which can be solved using an orthogonal matching pursuit (OMP) algorithm [9]. The sparsity level L_0^S and the precision level ε control the sparse representation. The OMP process will stop when either $\|\alpha_s\|_0 \geq L_0^S$ or $\|\mathbf{E}_s(\mathcal{X}^{n+1}) - \mathbf{D}\alpha_s\|_2^2 \leq \varepsilon$.

The workflow of the proposed algorithm can be summarized as follows. In this work, we applied a simple stopping criteria for the iterative algorithm, i.e., the algorithm should be stopped after a fixed number of iterations.

Algorithm 1 Dictionary Learning and Low Rank based Multi-energy CT Reconstruction.

Initialization:

Set parameters $\lambda_D, \lambda_*, \mu_*, L_0^S$ and ε ;
Initialize $\mathcal{X}^0 = \mathcal{D}^0 = \mathcal{V}^0 = 0$.

Repeat until the stopping criteria is met:

- Step 1: OS-SART;
 - Step 2: Eq. (9);
 - Step 3: Solving $\mathcal{D}^{n+1} = \arg \min_{\mathcal{D}} \mu_* \|\mathcal{D} - \mathcal{X}^{n+1} - \mathcal{V}^n\|_F^2 + \lambda_* \|\mathcal{D}\|_*$ using G-SVT;
 - Step 4: $\mathcal{V}^{n+1} = \mathcal{V}^n + \mathcal{X}^{n+1} - \mathcal{D}^{n+1}$;
 - Step 5: Updating α using OMP.
-

IV. EXPERIMENT

A. Experimental Setup

In this study, an equi-spatial fan-beam geometry was assumed. There were 512 detector elements of width 0.1 mm per element. Totally, 640 projections were uniformly collected over a full scan range. The distance from the source to the system origin was 132 mm, and the distance from the source to the detector was 180 mm. A 50 kVp X-ray spectrum was used, which was generated from the SpectrumGUI software [10]. The spectrum was divided into four spectral channels: 15-22 keV, 23-27 keV, 28-33 keV and 34-50 keV. In the experiment, a realistic mouse thorax phantom [11] was used, in which 1.2% by weight iodine contrast agent was introduced into the blood circulation. Figure 1 shows the original mouse thorax phantom and the added iodine contrast agent.

The reconstructed CT images were $512 \times 512 \times 4$ tensors with area $0.075 \text{ mm} \times 0.075 \text{ mm}$ per pixel. Both noise-free and noisy (2×10^4 photons in total emitted along each x-ray path) projections were simulated. In the case of a blank scan, the four energy channels received about 18.2%, 22.4%, 26.1% and 32.6% of total photons respectively.

B. Parameter selection

The parameters were empirically selected to achieve satisfactory performance. In this study, $\lambda_D = \lambda_* = 0.05$, $\mu_* = 0.5$, $L_0^S = 6$, the maximum iteration number was 20, and each projection dataset were divided into 40 subsets. The parameter ε , which is crucial for denoising, depends on the noise level. However, projection noise in different energy channels may be different. Thus, we selected ε values separately for the energy channels.

We employed a semi-empirical way to determine the parameter ε_i for each energy channel. Let γ_i be the median ratio of the detected photon numbers in detector bins between the i th energy channel and the sum over all the channels. Because the variation is equal to the number of photons for Poisson noise, γ_i reflects relative noise levels across the channels. After the logarithm transform, ε_i can be defined as $\varepsilon_i = \varepsilon_0 \log(1/\gamma_i)$, where $\varepsilon_0 = 0.0013$ in this paper.

V. RESULTS AND DISCUSSIONS

In order to have a dictionary, we first reconstructed an image with TV regularization from a single channel projection dataset. Then, image patches of 8×8 pixels were extracted from the image for dictionary learning. The learned dictionary has 256 atoms as shown in Fig. 2.

In this study, we compared the images reconstructed using the conventional FBP, TV regularization method (corresponding to Eq. 2), TV and low rank regularization (corresponding to Eq. 3), and dictionary learning and low rank regularization method. For fair comparison, we carefully adjusted the parameters so that all the methods would achieve optimal results. The reconstructed images are shown in Fig. 3. It can be seen from the 1st channel images in rows 3 and 4 that the results in row 4 has fewer noise, which is attributed to low rank regularization. By comparing the bottom two rows, it can be

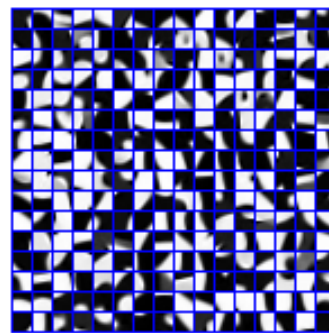


Fig. 2. Learned dictionary.

observed that channels 3 and 4 lost substantial details in the lung region in row 4, while the proposed method can keep details well for all the channels and reduce noise effectively. The superior performance of the proposed method must come from two factors: dictionary is better than TV for denoising, and the semi-empirically selected parameters can adapt to various noise levels in different energy channels.

In conclusion, based on the dictionary learning and low rank regularization, we have developed a novel reconstruction method for multi-energy CT. The proposed algorithm can reduce noise significantly and provide more details at the same time. In the near future, we will systematically evaluate our methodology using real datasets and optimize its preclinical and clinical potential.

REFERENCES

- [1] Q. Xu, H. Yu, J. Bennett, P. He, R. Zainon, R. Doesburg, A. Opie, M. Walsh, H. Shen, A. Butler, P. Butler, X. Mou, and G. Wang, "Image reconstruction for hybrid true-color micro-CT," *IEEE Transactions on Biomedical Engineering*, vol. 59, no. 6, pp. 1711–1719, 2012.
- [2] H. Gao, H. Yu, S. Osher, and G. Wang, "Multi-energy CT based on a prior rank, intensity and sparsity model (PRISM)," *Inverse Problems*, vol. 27, no. 11, p. 115012, 2011.
- [3] J. Chu, L. Li, Z. Chen, G. Wang, and H. Gao, "Multi-energy CT reconstruction based on low rank and sparsity with the split-Bregman method (MLRSS)," in *Nuclear Science Symposium and Medical Imaging Conference (NSS/MIC), 2012 IEEE*. IEEE, 2012, pp. 2411–2414.
- [4] J. Chu, W. Cong, L. Li, and G. Wang, "Combination of current-integrating/photon-counting detector modules for spectral CT," *Physics in Medicine and Biology*, vol. 58, no. 19, p. 7009, 2013.
- [5] O. Semerci, N. Hao, M. E. Kilmer, and E. L. Miller, "Tensor-based formulation and nuclear norm regularization for multi-energy computed tomography," *arXiv preprint arXiv:1307.5348*, 2013.
- [6] T. G. Kolda and B. W. Bader, "Tensor decompositions and applications," *SIAM review*, vol. 51, no. 3, pp. 455–500, 2009.
- [7] Q. Xu, H. Y. Yu, X. Q. Mou, L. Zhang, J. Hsieh, and G. Wang, "Low-dose X-ray CT reconstruction via dictionary learning," *Medical Imaging, IEEE Transactions on*, vol. 31, no. 9, pp. 1682–1697, 2012.
- [8] B. Zhao, H. Gao, H. Ding, and S. Molloi, "Tight-frame based iterative image reconstruction for spectral breast CT," *Medical Physics*, vol. 40, no. 3, p. 031905, 2013.
- [9] Y. C. Pati, R. Rezaifar, and P. Krishnaprasad, "Orthogonal matching pursuit: Recursive function approximation with applications to wavelet decomposition," in *Signals, Systems and Computers, 1993. 1993 Conference Record of The Twenty-Seventh Asilomar Conference on*. IEEE, pp. 40–44.
- [10] <http://spectrumgui.sourceforge.net/>.
- [11] W. P. Segars, B. M. Tsui, E. C. Frey, G. A. Johnson, and S. S. Berr, "Development of a 4-D digital mouse phantom for molecular imaging research," *Molecular Imaging & Biology*, vol. 6, no. 3, pp. 149–159, 2004.

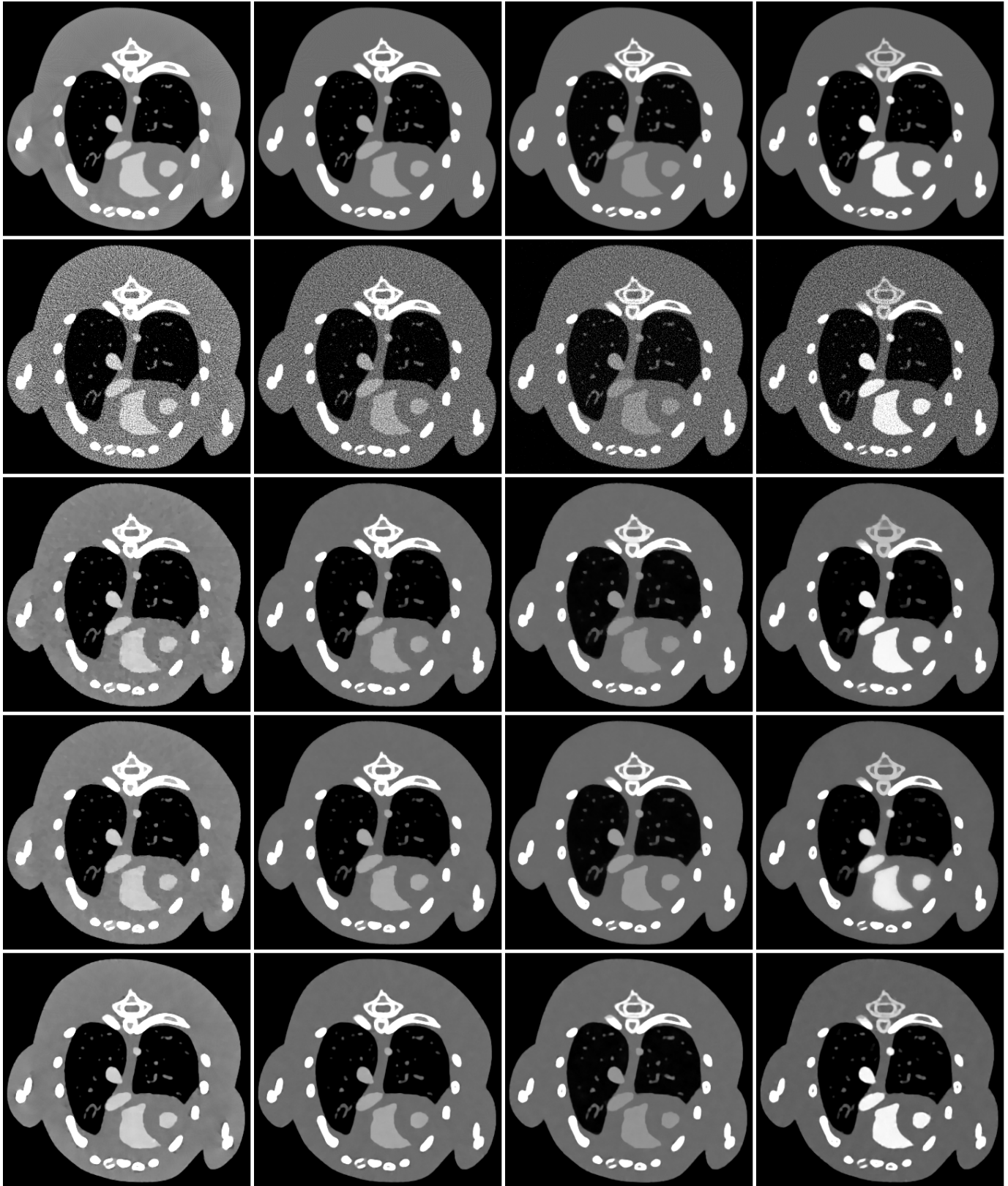


Fig. 3. Reconstructed images in the four energy channels. The columns from the left to the right correspond to the 1-4 energy channels, respectively. The images in the top two rows were reconstructed using FBP from the noise-free and noisy projection datasets, respectively. The images in rows 3-5 are iteratively reconstructed from the noisy projection dataset using TV regularization, TV and low rank regularization, and dictionary learning and low rank regularization, respectively. The display windows are $[0.4, 1.4] \text{ cm}^{-1}$, $[0.2, 1.0] \text{ cm}^{-1}$, $[0.1, 0.8] \text{ cm}^{-1}$ and $[0.1, 0.6] \text{ cm}^{-1}$ for channels 1-4, respectively.

CNR Analysis of Dual Energy Technologies

Yannan Jin, Hewei Gao, Jed Pack, Uwe Wiedmann and Bruno De Man

Abstract—We present a comparative study of different dual energy techniques in X-ray computed tomography (CT), based on dual kVp, dual layer detectors and photon-counting detectors. A projection-based contrast-to-noise ratio (CNR) analysis tool was developed to evaluate the dual energy performance. The spectral power (CNR at maximum tube output) and spectral dose efficiency (dose-normalized CNR) were defined as the metrics in this study. The results indicated that the spectral dose efficiency of dual kVp was about 25%-45% higher than that of the dual layer, while the difference in spectral power between dual kVp and dual layer approaches were below 10%. Energy-discriminating photon-counting technique had superior performance on both metrics if it could provide sufficient count rate capability of 100 Mcps/mm². With currently available count rate of 20 Mcps/mm², however, the practical application of this technique is limited by the spectral power. The validation results also demonstrated that the projection-based CNR analysis could achieve similar results compared to the full-blown simulation with image reconstruction.

Index Terms—dual-energy, CNR Analysis, spectral power, spectral dose efficiency

I. INTRODUCTION

DUAL-energy computed tomography (DECT) differentiates and classifies materials by utilizing attenuation values acquired using two different energy spectra. The idea of DECT dates back to the early 1970s when Hounsfield first proposed to use an image-based method to distinguish iodine and calcium [1]. Since then several CT configurations have been developed to realize the dual-energy technique. One of the first configurations used multi-layer detector [2] which was recently implemented into commercial product [3]. Other approaches such as the rotate-rotate acquisition, dual-source technology [4] and fast kV switching technique [5] also found their way to the products. Moreover, the direct-conversion energy-discriminating photon counting detector [6] is also deemed as a promising technique in the future.

The main aim of this study is to perform a quantitative comparison of the major dual energy approaches. A projection-based screening tool was developed to evaluate two main figures of merit: the spectral power and spectral dose efficiency. A first class of approaches studied here is based on dual tube voltage (dual kVp) imaging, which is representative for fast kVp switching [5], for dual-source CT and for rotate-rotate acquisitions. It is compared to dual energy based on dual layer [3] and photon-counting [6] detectors.

Finally, we also provide a broader comparison of all dual energy approaches, highlighting specific system advantages and challenges associated with each technology.

Yannan Jin, Jed Pack, Uwe Wiedmann and Bruno De Man are with GE Global Research Center, Niskayuna, NY 12309 USA (email: jin@ge.com)
Hewei Gao is with GE Healthcare, Waukesha, WI 53188 USA

II. MATERIALS AND METHODS

A. Systems and operating modes

In this paper we simulated two CT systems: Discovery CT750 HD (GE Healthcare, Waukesha, WI) for the implementation of dual kVp and photon counting technique and Brilliance iCT system (Philips Healthcare, Best, The Netherlands) for the dual layer technique. The operating parameters of the corresponding CT systems were acquired from the CEP report [7] and vendor brochures [8].

Table 1 shows the parameters used in the simulation, including the tube voltages at low and high energy, the maximum tube current and tube power, material and thickness of the added filtration, specifications of detector layers as well as the scanning time and gantry rotation speed.

Table 1: Operating parameters used for dual energy comparison study.

	dkVp const mA	dkVp const power	DL 120kVp	DL 140kVp	PC 20Mcps	PC 100Mcps
kV_LOW	80	80	120	120	140	140
kV_HIGH	140	140	120	140	140	140
Duty_LOW	60%	60%	100%	100%	100%	100%
Duty_HIGH	40%	40%	100%	100%	100%	100%
Power (kW)	100	100	120	120	100	100
mA_LOW	714	1250	1000	857	150	714
mA_HIGH	714	714	1000	857	150	714
Detector Absorption	100%	100%	top layer: 1mm ZnSe inter-layer: 25mm Sn bottom layer: 100%		100%	100%

The two settings for the dual kVp approach correspond to equal mA and equal tube power at low and high energy. The duty ratio between the low and high energy represents the time percentage allocated to the low and high kVp during fast switching.

For the dual layer system we used 1 mm ZnSe as the top scintillator and added 25 μ m Sn inter-layer filter according to [3]. As shown in Table 1, tube voltages at 120 kV and 140 kV were included for comparison. Note that the duty ratio between low and high energy cannot be adjusted for the dual layer approach.

For photon counting (PC) system, we studied CdTe detector with periodic count rate (N_0) of 20 Mcps/mm² and 100 Mcps/mm². The constraint on the maximum tube current was added to avoid complications of pile-up effect. The spectral response model of PC was implemented according to literature which was validated using synchrotron [9]. Note that we used 0.5 \times 0.5 mm² detector pixel size which was different from what was used in [9]. The corresponding energy tail in the response function due to charge sharing, fluorescence and K-escape was assumed to be 20% in this study. We did not consider losses due to rejection of photons that fall outside a

certain energy range: certain photon-counting solutions have detector sub-pixels with varying energy thresholds, but rejecting a subset of the photons is not a desirable approach.

B. Projection-based analysis tool

The motivation of developing a projection-based analysis tool is to enable quick screening of various dual energy technologies, in terms of CNR or dose efficiency, without going through the time-consuming full dual-energy simulation and reconstruction.

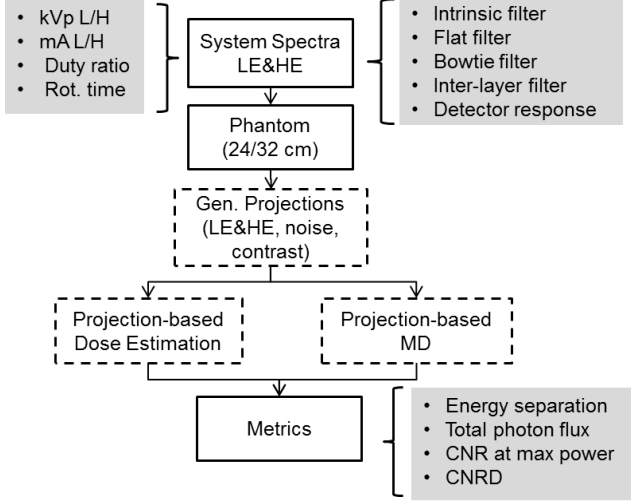


Figure 1: Framework of the developed dual energy analysis tool

The framework of this analysis tool is illustrated in Figure 1. The system spectra for LE & HE are first computed using the tube spectra under the selected kVp, mA, duty ratio, and rotation time, plus filtration by intrinsic/flat/bowtie/inter-layer filters (if any), as well as detector response. Two sizes of water phantoms were selected for two different purposes of analyses: “medium” (24 cm) for dose-normalized CNR and “large” (32 cm) for CNR at maximum power, respectively. To simulate the contrast agent we inserted 3 cm of 10 mg/cc iodine. The spectrum files used in this study are produced by the XSPECT package (v3.5), and then filtered with the nominal intrinsic filtration of a typical X-ray tube. With the system spectra and phantom defined, dose estimation, and projection generation followed by material decomposition were then conducted independently in the projection domain for the central ray. They were used together to compute the metrics (defined in the next section). Please refer to literature for the implementation details about projection generation [10], dose estimation [11] and material decomposition [12].

C. Evaluation criteria

Spectrum-based energy separation/photon flux can be used as an indicator to estimate the noise level and its amplification after material decomposition. For more quantitative comparison, we need to take a closer look at the noise distribution after material decomposition.

As shown in Figure 2, the area of the noise cloud in the basis material space represents the material separability which reflects the overall dual energy performance. Note that the

direction of the red arrow is called ‘Optimal keV’, along which the monochromatic image (mono) has the least noise; the direction of the light blue arrow is orthogonal to the red arrow, along which the mono has the worst noise and indeed represents the material separability.

The mono projection is synthesized by linearly combining the decomposed water and iodine at a specific energy:

$$mono(E) = \mu_{wa}(E)L_{wa} + \mu_{io}(E)L_{io},$$

where μ_{wa} and μ_{io} are linear attenuation coefficients of water and iodine; L_{wa} and L_{io} are the path length of water and iodine equivalent materials. If we normalize the μ , the mono projection can be rewritten as the dot product of two vectors:

$$mono = \left(\frac{\mu_w}{\sqrt{\mu_{wa}^2 + \mu_{io}^2}}, \frac{\mu_{io}}{\sqrt{\mu_{wa}^2 + \mu_{io}^2}} \right) \cdot (L_{wa}, L_{io}),$$

Similarly, the orthogonal mono projection can be synthesized by:

$$mono^\perp = \left(-\frac{\mu_{io}}{\sqrt{\mu_{wa}^2 + \mu_{io}^2}}, \frac{\mu_{wa}}{\sqrt{\mu_{wa}^2 + \mu_{io}^2}} \right) \cdot (L_{wa}, L_{io}),$$

As discussed above, the area of the noise cloud reflects the material separability. Therefore the metric for evaluation is defined as:

$$CNR = \sqrt{\frac{1}{\pi \cdot std(mono) \cdot std(mono^\perp)}} \\ = \sqrt{\frac{1}{\pi \cdot std\left(\frac{\mu_{wa}}{\sqrt{\mu_{wa}^2 + \mu_{io}^2}}L_{wa} + \frac{\mu_{io}}{\sqrt{\mu_{wa}^2 + \mu_{io}^2}}L_{io}\right) \cdot std\left(\frac{-\mu_{io}}{\sqrt{\mu_{wa}^2 + \mu_{io}^2}}L_{wa} + \frac{\mu_{wa}}{\sqrt{\mu_{wa}^2 + \mu_{io}^2}}L_{io}\right)}}$$

The final metrics used in the evaluation are spectral power and spectral dose efficiency. The *spectral power* corresponds to CNR^2 at the maximum tube power, which reflects the best performance a dual energy CT system could possibly achieve regardless of dose constraints. The *spectral dose efficiency* corresponds to CNR^2 at normalized dose which indicates the material separability at a given dose level. We believe that these metrics best represent what really matters in the dual energy images. For comparison, others have published a *spectral separability* metric, which does not clearly account for misclassified voxels and may favor high power rather than dose-efficiency.

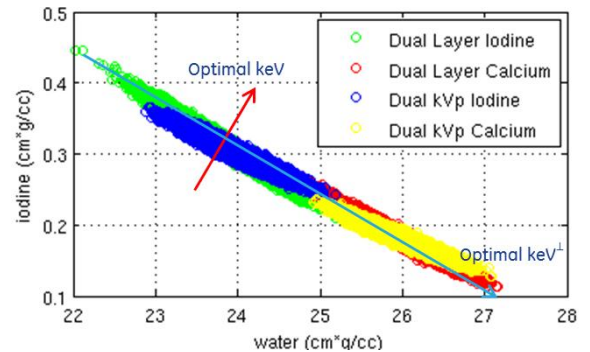


Figure 2: Noise cloud of basis materials after projection-based material decomposition for dual kVp and dual layer technologies.

III. RESULTS

A. Energy separation and photon flux

As mentioned in section II.C, previous studies have used the energy separation and photon flux as good indicators for spectral dose efficiency and spectral power, respectively. The separation of effective energy for different DE technologies is listed in Table 2. All techniques have reasonable to good energy separation in air, except for dual layer operated at 120 kVp. In a more realistic scenario, after passing through 24cm or 32cm water phantoms, the energy separation for dual kVp techniques improves dramatically, the energy separation of dual layer degrades significantly and the energy separation of photon counting detectors remains good.

The photon flux corresponding to the maximum tube power output detected at each detector cell per view is shown in Figure 3. Dual kVp at constant mA has rather low flux at the low kVp, while the constant power version has a more balanced photon flux. Both dual layer techniques have a higher number of photons, especially at the low energy, however due to the limited energy separation the photons will be less *useful* in contributing to spectral information, as illustrated by the analysis in the next section.

Table 2: Comparison of energy separations of dual energy technologies.

Energy Separation (keV)	In Air	Water (24 cm)	Water (32 cm)
dkVp - const mA	23	29	32
dkVp - const P	23	29	32
dlayer - 120 kV	19	15	14
dlayer - 140 kV	24	20	19
PC - 20 Mcps	32	30	29
PC - 100 Mcps	32	30	29

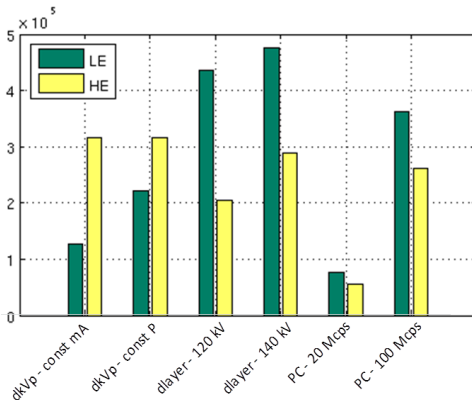


Figure 3: Comparison of photon flux at maximum tube power for different dual energy technologies after attenuated by 24 cm water.

B. Spectral power and spectral dose efficiency

In this section, we provide the more quantitative evaluation of spectral power and spectral dose efficiency for 0.8 sec body scan from different dual energy modalities. The simulation of spectral dose efficiency and spectral power correspond to 24 cm and 32 cm diameter phantoms, respectively. As shown in

Table 3, the CNR results from all the dual energy technologies were normalized to dual kVp with constant mA which was the baseline in this study. The spectral dose efficiency of dual kVp approach was about 25%-45% higher than that of the dual layer approach. The spectral power of dual kVp and dual layer approaches were comparable. The photon-counting approach has the highest spectral dose efficiency and spectral power capability if the system could be operated at 100 Mcps/mm² count rate. At the currently stage with 20 Mcps/mm² the spectral power of photon counting system was about 45%-60% lower than dual kVp or dual layer approaches.

The energy levels of the monochromatic projection were optimized to maximize the CNR.

Table 3: Comparison of DE performances of dual energy technologies.

Body scan	Spectral dose-efficiency	Spectral power
dkVp - const mA	1.00	1.00
dkVp - const P	1.21	1.38
dlayer - 120 kV	0.71	1.00
dlayer - 140 kV	0.76	1.48
PC - 20 Mcps	1.31	0.56
PC - 100 Mcps	1.31	2.76

C. Validation of analysis tool

To validate the projection-based tool (CatFiQ) developed in this study, we used image-based full-blown simulation in CatSim [10] to validate the results. Three sizes of phantoms (16/24/32 cm water cylinder) were used to compare the CNR² in monochromatic images normalized by the total dose (CNR²/D). The parameters of ‘dkVp const power’ and ‘PC 100 Mcps’ specified in Table 1 were used for simulation.

Both CatFiQ and CatSim simulation were conducted 20 times and the mean value of the CNR²/D in the dose was compared. The error bar was the standard deviation of CNR²/D from these tests. The dose was calculated using the Monte Carlo-based function CatDose within the CatSim package. The results were normalized to dkVp.

As shown in Figure 4, the results from CatFiQ and CatSim matched with each other. The result indicated that for all the object sizes the projection-based method was a good estimation of the dual energy performance.

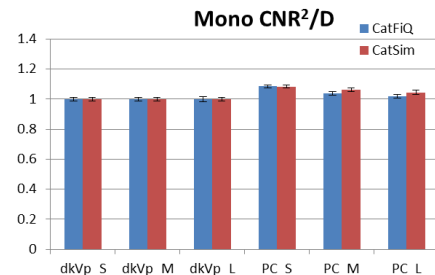


Figure 4: Validation of the dual energy evaluation tool (CatFiQ) with image-based full-blown simulation (CatSim [10]) for small/medium/large phantoms using dual kVp and photon counting CT.

Table 4: Overview of different implementations of dual energy technologies

	Spectral CT			Image-based Dual Energy CT	
	Fast kVp switching	Dual layer	Photon-counting	2T2D	Rotate-Rotate
Projection MD Capable	+	+	+	-	-
Temporal Skew	<1ms	0ms	0ms	80ms	500ms
Adjustable Duty Ratio	+	-	+	+	+
Full FOV	+	+	+	-	+
Cross Scatter	None	Between 2 layers	None	Between 2 beams	None

IV. DISCUSSION

It should be noted that Figure 3 shows the dual layer had more photon flux arriving at the detector than the dual kVp, but the results in Table 3 shows that the spectral power of dual layer was about the same as dual kVp. This discrepancy was due to the spectral overlap in the dual layer approach which amplified the noise in the material decomposition process and impaired the CNR even at the maximum power output.

The dose efficiency and spectral power used in this paper is not necessarily the only metrics that should also be taken into account for dual energy techniques. Other considerations, such as temporal skew, adjustable duty ratio, full field-of-view capability as well as the impact of cross scatter are also important factors for a CT system. In Table 4 we tried to compare these features on different implementations of dual energy technologies. Note that the projection-based approaches grouped as ‘spectral CT’ can provide beam hardening-free monochromatic images with the potential for quantitative analysis; in contrast, the image-based approaches grouped as ‘dual energy CT’ are straightforward to implement but the beam hardening artifacts in the reconstructed datasets undermine the MD accuracy.

The purpose of this study is to get a good understanding of the fundamental differences between dual energy systems, not including the entire correction/calibration, reconstruction and post-processing chain. Consequently this study does not include techniques such as iterative reconstruction or correlated noise reduction. We think the results are still highly relevant since better projection data should result in better images for a fixed reconstruction chain, although the relative importance of certain criteria may vary.

V. SUMMARY

In summary, a dual energy benefits study was conducted for a variety of dual energy technologies: dual kVp, dual-layer, and photon counting with realistic energy response. A projection-based evaluation tool was developed to fast screen different technologies without full CT simulation and reconstruction. The metrics for comparing different dual energy approaches were the scan-time-normalized CNR at maximum power and the optimal dose-normalized CNR. The results indicated that the spectral dose efficiency of dual kVp was about 25%-45% higher than that of the dual layer, while the spectral power of dual kVp and dual layer approaches were comparable. Specifically, the spectral power of dual kVp

with constant power was about 38% higher than that of dual layer at 120kV. The Photon-counting technique had superior performance if it could provide sufficient count rate capability. With current count rate, however, this technique is still limited by the spectral power. The validation results also demonstrated that the projection-based CNR analysis used in this paper could achieve similar results compared to the full-blown simulation with image reconstruction.

Future works include modeling and investigation of the material decomposition for photon-counting CT with multiple energy bins; modeling and correction of the pileup effect in photon counting CT and analysis of the clinical implications using the realistic patient data.

ACKNOWLEDGEMENTS

The authors would like to thank Naveen Chandra, Vance Robinson, Pete Edic, Bob Senzig, Jiang Hsieh, Paavana Sainath, Yasuhiro Imai, Vladimir Lobastov, Brian Yanoff, Geng Fu, Feng Chen, Girijesh Yadava, Eric Tkaczyk, Mark Frontera, Ron Hockersmith, and Aziz Ikhlef for valuable contributions and feedback.

REFERENCES

- [1] G. N. Hounsfield, "Computerized transverse axial scanning (tomography): Part 1. Description of system," *British Journal of Radiology*, vol. 46, pp. 1016-1022, 1973.
- [2] F. Kelcz, P. M. Joseph, and S. K. Hilal, "Noise considerations in dual energy CT scanning," *Medical Physics*, vol. 6, pp. 418-425, 1979.
- [3] Ami Altman and Raz Carmi, "A Dual-Energy CT Based on A Double Layer Detector." *AAPM Annual Meeting*, 2013
- [4] Petersilka, Martin, et al. "Technical principles of dual source CT." *European journal of radiology* 68.3 (2008): 362-368.
- [5] Wu, Xiaoye, et al. "Monochromatic CT image representation via fast switching dual kVp." *SPIE Medical Imaging*. International Society for Optics and Photonics, 2009.
- [6] Taguchi, Katsuyuki, et al. "Image-domain material decomposition using photon-counting CT." *Medical Imaging*. International Society for Optics and Photonics, 2007.
- [7] CEP Buyer's Guide to multislice CT scanners, Report CEP08028
- [8] PHILIPS Brilliance iCT Brochure
- [9] Schlomka, JPea, et al. "Experimental feasibility of multi-energy photon-counting K-edge imaging in pre-clinical computed tomography." *Physics in medicine and biology* 53.15 (2008): 4031.
- [10] De Man, Bruno, et al. "CATSIM: a new computer assisted tomography simulation environment." *Medical Imaging*. International Society for Optics and Photonics, 2007.
- [11] Tian, Xiaoyu, et al. "Projection-based dose metric: accuracy testing and applications for CT design." *SPIE Medical Imaging*. International Society for Optics and Photonics, 2013.
- [12] R. E. Alvarez and A. Macovski, "Energy-selective reconstructions in X-ray computerised tomography," *Physics in Medicine and Biology*, vol. 21, pp. 733-744, 1976.

Spectrum Binning Approach for Multi-Material Beam Hardening Correction (MMBHC) in CT

Qiao Yang, Meng Wu, Nicole Maass, Andreas K. Maier, Joachim Hornegger, and Rebecca Fahrig

Abstract—In CT, the nonlinear attenuation characteristics of polychromatic X-rays cause beam hardening artifacts in the reconstructed images. When datasets contain multiple materials in the field of scan, the performance of state-of-the-art beam hardening correction approaches is limited by high computational load and reduced correction efficiency. An image based multi-material beam hardening correction (MMBHC) method is introduced by conserving original reconstruction attenuation in a material density map, and obtaining beam hardening artifacts by polychromatic forward projecting of the original CT images. By decomposing the attenuation coefficient into photoelectric and Compton scattering components, the spectrum can be parameterized and presented with several energy bins. In this paper, the MMBHC algorithm is accelerated by using a proposed spectrum binning (SB) method to reduce the required prior knowledge from full spectrum to three energy bins. The approach has a significant computational time reduction by use of material number independent forward projection and parameterized energy spectrum with fewer bins. Moreover, representing the spectrum with a few parameters instead of optimizing full spectrum increase the stability of the MMBHC process. The algorithm has been evaluated with a simulated phantom on 3D cone beam geometry. In comparison to correction results with full spectrum information, the results with optimized three bins spectrum shows comparable artifact reduction efficiency while providing significant reduction on computational time.

Index Terms—Polychromatic X-ray, beam hardening correction, spectrum binning, CT reconstruction

I. INTRODUCTION

A. Purpose of this work

In computed tomography (CT), analytical reconstruction techniques such as filtered backprojection (FBP) are based on the assumption that X-ray radiation is monoenergetic, and the total attenuation of incident X-rays is linearly related to the thickness of the object along the ray. In reality, X-ray beams consist of a continuous energy spectrum, and material attenuation coefficients are energy dependent. When a polychromatic X-ray passes through the substances, due to the non-linearity, reconstruction images will contain cupping and streaking artifacts, which are so-called beam hardening artifacts.

Various beam hardening correction (BHC) algorithms have been developed for X-ray CT, both analytically [1]–[3] and iteratively [4]–[7]. However, when multiple materials appear in a scanned dataset, such as contrast agent or metal implants in clinical CT or most industrial CT cases, state-of-the-art

approaches have large computational complexity and limited correction performance.

B. State of the art

In previous work [8], a practical multi-material BHC approach which employs a CT-value conserving material decomposition technique was presented. The method separates reconstructed images into density images and images containing material information, which has the advantage that segmentation errors, which result in invalid material properties for a voxel, have only minor effects on the beam hardening correction.

It has been presented that energy dependent attenuation coefficients can be decomposed into a linear combination of photoelectric and Compton scattering components [5]. Wu et al. have proposed a modified optimization problem for polychromatic statistical reconstruction algorithms, and simplified the algorithms with a spectrum binning method to reduce the full spectrum [9]. An evaluation study to examine the robustness of the method with mismatched spectra are published in [10].

C. Outline

In this paper, a method that applies spectrum binning to accelerate the MMBHC approach is presented. The original CT value conserving density map is combined with photoelectric and Compton scattering components which are calculated from attenuation decomposition. By polychromatic forward projecting the two components separately, polychromaticity enhanced images are obtained to calculate the beam hardening artifacts. In the next section, a review of the MMBHC approach and the spectrum binning method is given and the derivation of the combined algorithm is discussed in detail. In Section III, the results from the simulated phantom are illustrated and quantitative evaluation is performed.

II. METHOD

A. Multi-material beam hardening correction (MMBHC)

When a monochromatic X-ray beam traverses a homogeneous object, according to Lambert-Beer's law, the total attenuation is linearly related to the intersection length of the object and the ray. However, in practical setups, the emitted X-ray photons have varying energies and the detector response is also energy-dependent. The measured intensity of a polychromatic beam Y_{poly} on detector pixel i can be written as the sum of monochromatic contributions for each energy

Q. Yang, A. K. Maier, and J. Hornegger are with the Pattern Recognition Lab, Department of Computer Science, Friedrich-Alexander-University Erlangen-Nuremberg, Germany. E-mail: qiao.yang@cs.fau.de. M. Wu and R. Fahrig are with the Department of Radiology, Stanford University, USA. N. Maass is with the Siemens AG, Healthcare Sector, Erlangen, Germany

bin E in the X-ray spectrum ($E \in [0, E_{max}]$):

$$Y_{poly,i} = \int_0^{E_{max}} b_{0,i}(E) \cdot \exp\left(-\int_{L_i} \mu(E, \mathbf{r}) dl\right) dE, \quad (1)$$

where $b_{0,i}(E)$ is the normalized source-detector energy spectrum, L is the path length of the corresponding ray direction. Denote \mathbf{r} as the spatial location on the reconstruction grid, and $\mu(E, \mathbf{r})$ is the spatial distribution of the attenuation coefficient which depends on spectrum energy E .

When a dataset consists of M materials, the mass attenuation coefficient for material m at specific energy E_0 can be written as $\kappa_m(E_0) = \mu_m(E_0)/\rho_m$, with ρ_m being the reference material density. In [8], a multi-material beam hardening correction scheme is proposed, which separates reconstructed images $g(\mathbf{r})$ into images containing material information $\kappa_m(E)$ and spatial density images $\rho_m(\mathbf{r})$. Thus, (1) can be rewritten as

$$Y_{poly,i} = \int_0^{E_{max}} b_{0,i}(E) \cdot \exp\left(-\sum_{m=1}^M \kappa_m(E) \int_{L_i} \rho_m(\mathbf{r}) dl\right) dE. \quad (2)$$

Instead of using the reference material density ρ_m , material density at spatial location \mathbf{r} is applied:

$$\rho_m(\mathbf{r}) = \frac{f_m(\mathbf{r}) \cdot g_{initial}(\mathbf{r})}{\kappa_m(E_0)}, \quad (3)$$

where $f_m(\mathbf{r})$ is the binary mask of material m that is obtained from automatic k-means segmentation [11] at location \mathbf{r} . By polychromatically forward projecting the original beam hardening affected volume $g_{initial}$, additional beam hardening is introduced and added up onto the existing artifacts. The difference between $g_{initial}$ and the reconstruction image $g_{calc}(\mathbf{r})$ from recalculated polychromatic attenuation can be used to estimate the beam hardening error:

$$\hat{g}_{BH}(\mathbf{r}) = g_{calc}(\mathbf{r}) - \text{Gauss}(0, \sigma) * g_{initial}(\mathbf{r}), \quad (4)$$

with $\arg \min_{\sigma} \|\hat{g}_{BH}(\mathbf{r})\|_2$. Note that a spatial resolution matching Gaussian filtering is applied. Then the beam hardening image $\hat{g}_{BH}(\mathbf{r})$ is subtracted from the initial reconstruction to obtain a beam hardening corrected image

$$g_{corrected}(\mathbf{r}) = g_{initial}(\mathbf{r}) - \hat{g}_{BH}(\mathbf{r}). \quad (5)$$

Since errors may occur during segmentation due to severe artifacts, an iterative scheme can be used for more accurate image updates.

B. Spectrum binning (SB)

De-Man et al. had decomposed the energy dependent attenuation coefficients into linear combinations of photoelectric and Compton scattering components [5]. Therefore, the attenuation coefficients of a certain substance can be represented as:

$$\mu_m(E) = \phi_m \Phi(E) + \theta_m \Theta(E), \quad (6)$$

where $\Phi(E)$ and $\Theta(E)$ are base functions of energy dependent photoelectric and Compton scattering components, and ϕ_m and θ_m represent the m th material dependence of the two

components. For a multi-material case, from (6) the attenuation coefficient can be decomposed to:

$$\begin{aligned} \mu(E, \mathbf{r}) &= \left(\Phi(E) \sum_{m=1}^M \phi_m f_m(\mathbf{r}) + \Theta(E) \sum_{m=1}^M \theta_m f_m(\mathbf{r}) \right) \\ &= \Phi(E) \phi(\mathbf{r}) + \Theta(E) \theta(\mathbf{r}). \end{aligned} \quad (7)$$

$\phi(\mathbf{r})$ and $\theta(\mathbf{r})$ are the amount of photoelectric and scattering components from all materials at spatial location \mathbf{r} .

Using this expression, the detector signal from full spectrum information is

$$\begin{aligned} \hat{Y}^{\text{full}} &= \int_0^{E_{max}} b_0(E) \\ &\cdot \exp\left(-\Phi(E) \int_{L_i} \phi(\mathbf{r}) dl - \Theta(E) \int_{L_i} \theta(\mathbf{r}) dl\right) dE. \end{aligned} \quad (8)$$

Wu et al. [9] developed an optimal spectrum binning strategy, which uses a reduced number of energy bins instead of full spectrum information. Define (ϕ_t, θ_t) as the pairs of line integrals of photoelectric and Compton scatter components over total distance \mathbf{t} that are spaced over the equivalent range of materials, $\mathbf{t} = [L_1 \ L_2 \ \dots \ L_M]$. The approximated expected signals using spectrum binning can be expressed as

$$\hat{Y}^{\text{SB}}(\underline{\phi}_t, \underline{\theta}_t; \mathbf{B}_s, \Phi_s, \Theta_s) = \sum_{s=1}^S B_s \cdot \exp(-\Phi_s \phi_t - \Theta_s \theta_t) \quad (9)$$

Φ_s and Θ_s are the corresponding values of each bin s . The energy bin sizes B_s need to satisfy the constraints that the sum of all bins is identical to the integral over the spectrum:

$$\sum_{s=1}^S B_s = \int_0^{E_{max}} b(E) dE, \quad B_s > 0 \quad \text{for } s = 1, 2, 3, \dots, S. \quad (10)$$

The optimal bin sizes \mathbf{B}_s , and the values of Φ_s and Θ_s are determined by optimizing

$$\arg \min_{\mathbf{B}_s, \Phi_s, \Theta_s} \|\log(\hat{Y}^{\text{full}}(\underline{\phi}_t, \underline{\theta}_t)) - \log(\hat{Y}^{\text{SB}}(\underline{\phi}_t, \underline{\theta}_t, \mathbf{B}_s, \Phi_s, \Theta_s))\|_1. \quad (11)$$

Empirical results show that the L_1 distance provides relatively good BHC results.

C. MMBHC-SB

Define $\hat{p}_i(E) = \int_{L_i} \mu(E, \mathbf{r}) dl$ as the line integral through the volume along ray i . From Eq. (2) and (3), $\hat{p}_i(E)$ can be written as

$$\hat{p}_i(E) = \sum_{m=1}^M \int_{L_i} \kappa_m(E) \cdot \frac{f_m(\mathbf{r}) \cdot g_{initial}(\mathbf{r})}{\kappa_m(E_0)} dl. \quad (12)$$

From the MMBHC approach, the spatial density image calculated from the original reconstruction is used instead of the true material density. A ratio density map is calculated as

$$\alpha_m(\mathbf{r}) = \frac{f_m(\mathbf{r}) \cdot g_{initial}(\mathbf{r})}{\rho_m \cdot \kappa_m(E_0)}. \quad (13)$$

The effective energy E_0 should be material dependent. At the segmentation step, the updated centroids from k-means

clustering correspond to the effective attenuation coefficients for each material [11]. The effective energy of each material are then be determined.

Applying Eq. (7) and Eq. (13) to Eq. (12), the line integral $\hat{\rho}^S$ for each discrete energy bin can be formulated as

$$\hat{\rho}_i^S = \Phi_s \sum_{m=1}^M \int_{L_i} \phi_m \alpha_m(\mathbf{r}) dl + \Theta_s \sum_{m=1}^M \int_{L_i} \theta_m \alpha_m(\mathbf{r}) dl. \quad (14)$$

The polychromatically reprojected sinogram can be calculated as

$$\hat{Y}_{\text{calc}}^{\text{MMBHC-SB}} = \sum_{s=1}^S B_s \cdot \exp(-\hat{\rho}_i^S). \quad (15)$$

D. Experiments

In order to evaluate the performance of the algorithm, polychromatic cone-beam CT simulations with added Poisson noise were carried out. The digital phantom has a soft tissue basis of 20 cm in diameter, two cortical bone columns of 4 cm in diameter and two titanium columns of 3 cm in diameter. Source-isocenter-distance is 80 cm and source-detector-distance is 120 cm. Each dataset consists of 640 projection images over an angular range of 360° , with a size of 512×512 pixels at an isotropic resolution of $0.8 \times 0.8 \text{ mm}^2$. The image reconstruction was performed on a $320 \times 320 \times 320$ voxel grid with spacing of $0.8 \times 0.8 \times 0.8 \text{ mm}^3$. Fig. 1 shows the attenuation coefficients of the three simulated materials and attenuation decomposition results for the case of cortical bone.

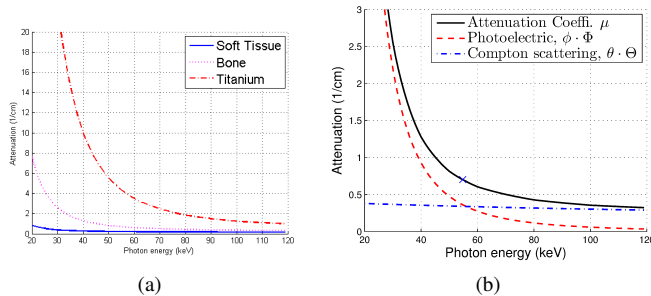


Fig. 1. (a) Attenuation coefficients of soft tissue, cortical bone and titanium. (b) Decomposition of attenuation coefficient into photoelectric and Compton scatter components for cortical bone (Eq. (6)).

III. RESULTS AND DISCUSSION

The original reconstruction and correction results including line profiles are shown in Fig. 2. It can be seen that the FDK reconstruction suffers from cupping and streaking artifacts. The center image is obtained using the previous approach [8] with full spectrum information (120 energy bins), while the right image is calculated with a parameterized spectrum of three energy bins. Both are the correction results after the first iteration. The second row of Fig. 2 shows line profiles corresponding to each reconstructed image. It can be observed that the correction using three energy bins has comparable overall performance, with little over-correction on cortical bone. The material total lengths which are chosen for spectrum parameter optimization will result in different correction performance for each material.

As discussed before, since the polychromatic energy spectrum has different impact on different materials, the effective energy for each material has to be chosen independently. Table I shows effective energies of the three materials at each iteration. The values are obtained from k-means clustering of the reconstructed image, therefore segmentation errors which are caused by artifacts will influence the results. The segmentation improvement is illustrated in Fig. 3(a). The percentage of missegmented voxels converges quickly at the first iteration, further iterations only marginally improve the results. Fig. 3(b) shows the error volume of attenuations $\log(\hat{Y}^{\text{full}}) - \log(\hat{Y}^S)$ corresponding to different materials' thicknesses. Maximum thickness values of different materials have been chosen according to relations between material attenuation coefficients at efficient energies.

Iterations	Soft tissue (keV)	Bone (keV)	Titanium (keV)
Original Recon.	58	72	91
1st iteration	65	71	85
2nd iteration	70	77	84
3rd iteration	71	76	84

TABLE I
EFFECTIVE ENERGY FROM K-MEANS CLUSTERING FOR EACH MATERIAL AT EACH ITERATION.

Regarding computation time, the proposed algorithm has a large reduction of execution time for two reasons. Firstly, the number of polychromatic forward projection increases with the number of substances in the previous MMBHC approach. In the current method, increasing the material number only results in a marginal increase in computational time, because it forward projects the two components from attenuation decomposition. Moreover, the proposed approach only uses three energy bins in the polychromatic model instead of a full spectrum, which results in a significant reduction of computation load.

IV. CONCLUSION

In this paper, we have derived an accelerated multi-material beam hardening correction approach using only a few energy bins instead of full spectrum information. As shown in the results, using the optimized three energy bins can provide effective beam hardening artifact reduction after the first iteration. The main advantage of the algorithm is the significant reduction of computation time. The number of forward and back-projections is not influenced by the number of materials, but depends on photoelectric and Compton scattering components obtained from attenuation decomposition.

ACKNOWLEDGMENT

The authors gratefully acknowledge funding of the Erlangen Graduate School in Advanced Optical Technologies (SAOT) by the German Research Foundation (DFG) in the framework of the excellence initiative.

Disclaimer: The concepts and information presented in this paper are based on research and are not commercially available.

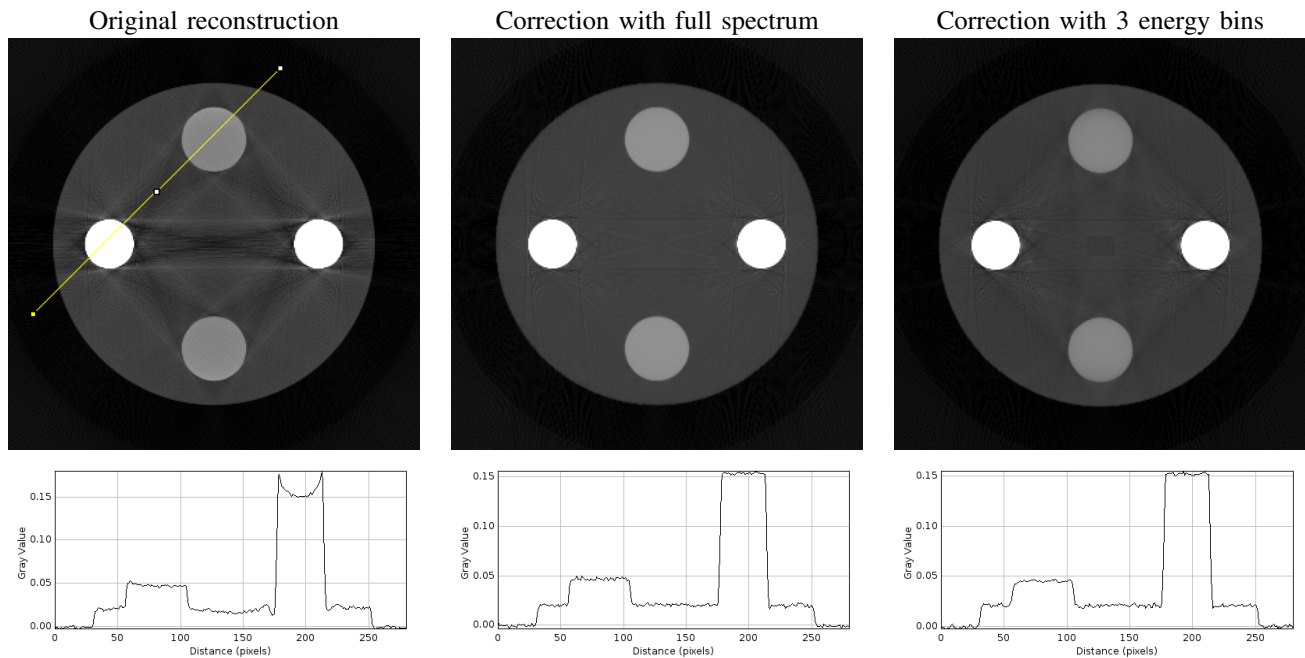


Fig. 2. Results of original analytical reconstruction, correction from previous MMBHC approach, and proposed algorithm with three energy bins. Corresponding line profiles are plotted. Correction images are results after the first iteration. Reconstructed images are displayed with window level $[0.05; 0.09] \text{ mm}^{-1}$.

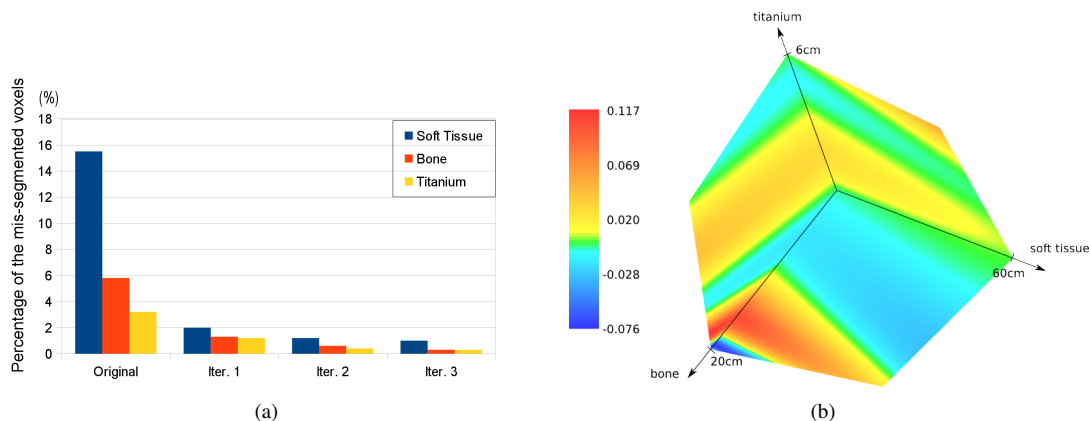


Fig. 3. (a) Percentage of incorrectly segmented voxels for three materials from original reconstruction and at each iteration step. (b) Attenuation error volume at three materials' various thicknesses using spectrum binning methods.

REFERENCES

- [1] P. Joseph and R. Spital, "A method for correction bone induced artifacts in computed tomography scanners," *Journal of computer assisted tomography*, 1978.
- [2] M. Kachelriess, K. Sourbelle, and W. A. Kalender, "Empirical cupping correction: a first-order raw data pre-correction for cone-beam computed tomography," *Med Phys*, vol. 33, no. 5, pp. 1269–1274, May 2006.
- [3] C. Maaß, E. Meyer, and M. Kachelriess, "Exact dual energy material decomposition from inconsistent rays (MDIR)," *Medical Physics*, vol. 38, no. 2, pp. 691–700, 2011.
- [4] I. A. Elbakri and J. A. Fessler, "Statistical image reconstruction for polyenergetic X-ray computed tomography," *IEEE Trans Med Imaging*, vol. 21, no. 2, pp. 89–99, Feb. 2002.
- [5] B. De Man, J. Nuyts, P. Dupont, G. Marchal, and P. Suetens, "An iterative maximum-likelihood polychromatic algorithm for CT," *IEEE transactions on medical imaging*, vol. 20, no. 10, pp. 999–1008, Oct. 2001.
- [6] N. Menvielle, Y. Goussard, D. Orban, and G. Soulez, "Reduction of Beam-Hardening Artifacts in X-Ray CT," *Conference proceedings : Annual International Conference of the IEEE Engineering in Medicine and Biology Society*, vol. 2, pp. 1865–8, Jan. 2005.
- [7] G. Van Gompel, K. Van Slambrouck, M. Defrise, K. J. Batenburg, J. de Mey, J. Sijbers, and J. Nuyts, "Iterative correction of beam hardening artifacts in CT," *Medical physics*, vol. 38, no. 7, p. S36, Jul. 2011.
- [8] Q. Yang, N. Maass, M. Tian, M. Elter, I. Schasiepen, A. Maier, and J. Hornegger, "Multi-material beam hardening correction (MMBHC) in computed tomography," in *Proc. Intl. Mtg. on Fully 3D Image Recon. in Rad. and Nuc. Med.*, 2013, pp. 533–536.
- [9] M. Wu, Q. Yang, A. Maier, and R. Fahrigr, "A practical statistical polychromatic image reconstruction for computed tomography using spectrum binning," in *SPIE 2014, to appear*, 02 2014.
- [10] Q. Yang, M. Wu, A. Maier, J. Hornegger, and R. Fahrigr, "Evaluation of spectrum mismatching using spectrum binning approach for statistical polychromatic reconstruction in CT," *Bildverarbeitung fuer die Medizin 2014, to appear*, 2014.
- [11] M. Tian, Q. Yang, A. Maier, I. Schasiepen, N. Maass, and M. Elter, "Automatic histogram-based initialization of k-means clustering in CT," in *Bildverarbeitung fuer die Medizin 2013*. Springer Berlin Heidelberg, 2013, pp. 277–282.

Guided Noise Reduction for Spectral CT with Energy-Selective Photon Counting Detectors

Michael Manhart, Rebecca Fahrig, Joachim Hornegger, Arnd Doerfler and Andreas Maier

Abstract—We investigate the use of joint bilateral filtering for noise reduction in energy-selective photon counting detectors. A guidance image from all energy channels is computed, which steers a non-linear filter to denoise each energy bin individually. Our novel approach is evaluated with cone beam data simulated using a numerical cardiac phantom. Results indicate that the method increases cross-talk between energy channels only at a very slight level. In terms of noise reduction, the method is successful. The rRMSE is reduced by about 60% and the SNR is increased from 3.3 to 72.9 for the channel with the lowest photon count.

I. INTRODUCTION

Spectral CT (S-CT) facilitates the quantitative measurement of material properties in X-ray computed tomography (CT). Popular diagnostic applications are bone removal, measurement of blood volume in the lung or quantification of contrast agent concentrations (e.g., in the myocardium) [1]. S-CT data can be acquired using energy-selective photon counting detectors [2]. The energy-selective detectors assign incoming X-ray photons to energy bins. Figure 1 visualizes an idealized binning of an X-ray photon spectrum into 3 bins. The binned data can be reconstructed separately to obtain volumes with energy-selective attenuation coefficients. This can be utilized, for instance, to reconstruct contrasted and non-contrasted images from a single acquisition. Since iodine contrast agent has a K-edge of 33.2 keV, it will not be visible in high energy bins (e.g., bins around 140 keV) [3]. Because the full spectral data is acquired in one shot, contrasted and non-contrasted images will be perfectly aligned. This is particularly beneficial for imaging of moving organs, e.g., cardiac and lung imaging.

However, by splitting the acquired photons into bins the noise statistics of the corresponding projection images suffer. Especially bins covering only the low energy portion of the spectrum energy distribution are corrupted by noise. For instance, Figure 2a shows a numerical projection image of the spectral data corresponding to Bin 1 in Figure 1. Due to the low energy of this bin with respect to the spectrum distribution, the projection image is obviously noisy. Thus an expedient noise reduction method is required to obtain appropriate image quality at clinically acceptable dose levels.

Iterative reconstruction algorithms have shown superior image quality [4], but suffer from high computational de-

A. Maier, J. Hornegger, and M. Manhart are with Pattern Recognition Lab, Department of Computer Science, Friedrich-Alexander-Universität Erlangen-Nürnberg, Germany. M. Manhart and A. Doerfler are with Department of Neuroradiology, Universitätsklinikum Erlangen, Erlangen, Germany. R. Fahrig is with Department of Radiology, Stanford University, CA, USA. J. Hornegger is with Erlangen Graduate School in Advanced Optical Technologies (SAOT). Email: andreas.maier@cs.fau.de

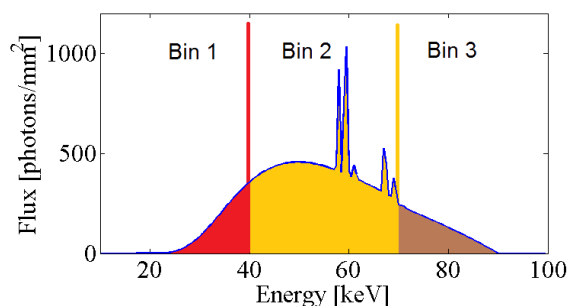


Figure 1: Binning of a X-ray spectrum into 3 bins.

mand. Alternative computationally faster methods have been proposed, which apply adaptive, anisotropic filters in a pre-processing step on the projection data [5] or in a post-processing step on reconstructed images [6], [7]. The advantage of projection space denoising is that for photon counting detectors the noise can be modeled accurately and easily using Poisson statistics. Up to now, projection space denoising methods using noise adaptive filter kernels [5], [8], [9], as well as methods using edge preserving filters [10] and combinations of both methods [11] have been presented.

In this work we extend the idea of projection based denoising by edge preserving filtering to S-CT data of energy-selective detectors. We guide the edge preserving filter using information from the fully acquired spectrum. The novel approach is evaluated using the CONRAD cone beam reconstruction and simulation framework [12] with data from a numerical cardiac phantom.

II. METHODS

A. Energy-Selective Detector

The energy-selective photon counting detector assigns incoming photons into $b = 1 \dots B$ bins. Each bin covers a spectral bandwidth of ΔE and the spectral bandwidth of the first bin starts at energy level E^0 . Let $\mathbf{x} = (u, v)$ be the spatial location of the detector pixel with column index u and row index v . The expected photon count $I_b(\mathbf{x})$ measured for bin b at location \mathbf{x} is given by

$$I_b(\mathbf{x}) = I^0 \int_{E^0+(b-1)\Delta E}^{E^0+b\Delta E} S(E) \exp\left(-\int_{L(\mathbf{x})} \mu(E, l) dl\right) dE, \quad (1)$$

where I^0 denotes the number of photons per mm^2 arriving at the detector in the unattenuated case and $S(E)$ denotes the spectral distribution with the area under the curve normalized

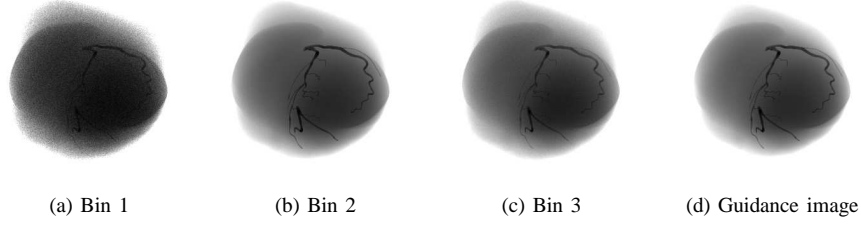


Figure 2: Energy-selective projection images and guidance image for joint bilateral filtering.

to one. The X-ray attenuation is defined by $\mu(E, l)$ and depends on the photon energy E and the spatial position l on the line $L(\mathbf{x})$, which points from the X-ray source to the detector pixel \mathbf{x} . Accordingly, the log-transformed image $P_b(\mathbf{x})$ is given by

$$P_b(\mathbf{x}) = -\log \frac{I_b(\mathbf{x})}{I_b^0} \text{ with } I_b^0 = \int_{E^0+(b-1)\Delta E}^{E^0+b\Delta E} I^0 S(E) dE. \quad (2)$$

B. Joint Bilateral Filtering

For guided edge preserving noise reduction we apply joint bilateral filtering (JBF) [13]. The JBF is a variant of the bilateral filter [14], where the edge preservation is controlled by a guidance image. Each intensity of a filtered image $P'(\mathbf{x})$ is computed as a weighted average of the intensities of the original image $P(\mathbf{x})$ in a spatial neighborhood $\mathcal{N}_{\mathbf{x}}$

$$I'(\mathbf{x}) = \frac{\sum_{\mathbf{o} \in \mathcal{N}_{\mathbf{x}}} I(\mathbf{x} + \mathbf{o}) \mathcal{W}(\mathbf{x}, \mathbf{o})}{\sum_{\mathbf{o} \in \mathcal{N}_{\mathbf{x}}} \mathcal{W}(\mathbf{x}, \mathbf{o})}, \quad (3)$$

$$\text{with } \mathcal{W}(\mathbf{x}, \mathbf{o}) = \mathcal{G}_{\sigma^S}(\mathbf{x} - \mathbf{o}) \cdot \mathcal{G}_{\sigma^R}(I^G(\mathbf{x}) - I^G(\mathbf{x} + \mathbf{o})),$$

where $\mathcal{G}_{\sigma}(\mathbf{z}) = \exp(-0.5 \cdot \|\mathbf{z}\|_2^2 / \sigma^2)$ denotes a Gaussian kernel. The weighting term \mathcal{W} consists of the spatial closeness term \mathcal{G}_{σ^S} controlled by the domain parameter σ^S and the range similarity term \mathcal{G}_{σ^R} controlled by the range parameter σ^R and by the guidance image I^G .

C. Guided Range Filtering

To exploit the complete spectral information for the edge preservation, the guidance image is formed by the sum over all spectral bins. Therefore the guidance image to filter the binned projection images $I_b(\mathbf{x})$, $b = 1 \dots B$ is defined by

$$I^G(\mathbf{x}) = \sum_{b=1}^B I_b(\mathbf{x}) \quad (4)$$

Note that the summation inherently includes an uncertainty weighting as the signal-to-noise ratio is proportional to the number of measured photons. The range parameter σ^R is set to the minimal contrast difference D in the guidance image, which should be preserved.

D. Guided Filtering in Reconstruction Domain

The idea of JBF can also be applied after reconstruction of the image. In this case, however, the guidance image cannot be simply created by a sum of the individual reconstructed volumes $f_b(\mathbf{y})$. Note that $\mathbf{y} = (x, y, z)$ is used to index the volume space. In order to create a suitable guidance image, the image contributions have to be scaled according to their reliability. In our case, we picked an inverse variance weighting and denote the variance in bin b with σ_b^2 . This leads to the following guidance image

$$f^G(\mathbf{y}) = \sum_{b=1}^B \frac{f_b(\mathbf{y})}{\sigma_b^2}. \quad (5)$$

As this method operates in the image domain (ID), we refer to it as ID-JBF.

E. Experimental Setup

We simulated a static instance of the human heart as described in [15]. The contents of the heart chambers were simulated as water with a density of 1.06. The heart muscle was simulated as water with a density of 1.05. In addition, the coronary arteries were filled with a solution of Iopromide ($C_{18}H_{24}I_3N_3O_8$) that contained 0.76 g of contrast agent per gram of water. The density of this solution was set to 1.40 g/cm³ which is typical for a clinical contrast agent (e.g., Ultravist[®] 370). The simulated spectrum is shown in Fig. 1. Its properties were adjusted such that its half-value-layer is comparable to that of a clinical C-arm system. We set the tube voltage to 90 kVp and the time-current product to 0.1 mAs. In this configuration, we have $I_1^0 = 948$, $I_2^0 = 28982$, and $I_3^0 = 10103$ photons per mm² arriving at each detector bin, if no object is hit between source and detector. In the present experiment, we did not simulate cross-talk between the energy bins and the detection efficiency was 100% at all energies. While this might not be the case in a real detector, it maximizes the independence between the energy bins and allows us to study correlations between the energy bins that are introduced by the denoising method. We did not perform an optimization of the energy thresholds in the present study to maximize the iodine contrast, as the focus of the study is denoising and not material separation. The bins were equally spaced between 10 and 100 keV according to the sampling range of the spectrum, i.e., $E^0 = 10$ keV and $\Delta E = 30$ keV. All simulations and algorithms were created using our open-source

flat panel simulation and reconstruction framework CONRAD [12].

JBF filtering was performed in intensity space before conversion to line-integral space. The intensity difference in the contrast filled vessels D was found to be 1000 in the guidance image. We picked $\sigma^S = 9$ and $\sigma^R = 100$ for the projection-based filtering. Then a standard Feldkamp short-scan reconstruction was performed using a Shepp-Logan filter [16]. We simulated 495 projections over an angular range of 200 degrees, which is the short-scan range of our 620×480 detector. Detector element size was 0.6×0.6 mm², the source detector distance 1200 mm, and the source to center of rotation distance was 750 mm. The heart fit all projections in all views, thus no truncation correction had to be performed. After reconstruction onto an 256³ image grid with 0.5×0.5×0.5 mm³ voxels, we investigated the use of ID-JBF. Here, we chose the parametrization as $\sigma^S = 5$ and $\sigma^R = D$. The guidance image weightings σ_b^2 were determined by estimating the noise variance inside homogenous regions of the corresponding reconstructed images. JBF filtering and back-projection was implemented in OpenCL.

Errors were measured using structural similarity [17], linear correlation coefficient, and the relative root means square error (rRMSE), that is the RMSE scaled by the maximum intensity.

III. RESULTS

Table I displays structural similarity and correlations between the different reconstruction approaches. All denoising methods show improved results compared to the ground truth. While correlations increase slightly, the structural similarity between the three bins is preserved by all methods. Thus, we can conclude that the JBF does not cause the three energy bins to display identical information.

Figure 3 shows the center slices of the different reconstructions of Bin 1. All reconstructions are shown at the same window and level [10, 110 HU]. The ground truth image (Figure 3a) nicely differentiates between the heart chambers and the heart muscle. The excessive noise in Bin 1 does not permit differentiation of the two heart chambers (Figure 3b, rRMSE 3.10%, SNR 3.3). JBF filtering in the projection domain allows visualization of a slight contrast between the two heart chambers. Streaking from polychromatic effects is emphasized (Figure 3c, rRMSE 1.33%, SNR 29.0). ID-JBF only is not able to recover the separation between the heart chambers and the muscle tissue (Figure 3d, rRMSE 1.20%, SNR 47.6). Additional filtering in the image domain reduces noise and streak artifacts further (Figure 3e, rRMSE 1.26 %, SNR 72.3).

IV. DISCUSSION

We applied the idea of joint bilateral filtering to energy-resolving detectors. First results demonstrate that the method is feasible. We were able to restore low-contrast image data in a very noisy channel. The comparisons between the channels showed that the method introduces very little cross-talk between the different energy bins, and their similarity is only slightly increased.

An advantage of bilateral filters is that they are very easy to configure. We require only two parameters which can be easily obtained from the guidance image. The first one is σ^S which controls the locality of desired smoothing. It can be chosen in the same way as a normal Gaussian filter. The second parameter σ^R describes the amount of edge preservation. A good rule-of-thumb way of setting it is to measure the lowest contrast from the image that needs to be preserved (D). In case of projection-based filtering, however, we recommend setting σ^R to 10% to 20% of this value, as the preservation of very small signal changes at the edge of high contrast contours is crucial. Otherwise, streaking artifacts can arise in the reconstructed images. In our present study, we already introduced such slight streaking.

At present, we only investigated JBF and did not include further modifications such as ray-by-ray weighting [5], [9] or projection stack filtering [8]. Integration of both techniques into this method is straight-forward, as the filter kernel is designed for each ray individually anyway. Thus, we would expect only minor increases in terms of run time. However, this will require a different object, as we did not observe strong streak noise in our reconstructions. Another topic for future work is the straight-forward extension of JBF in the image domain to 3D.

V. CONCLUSIONS

We created a joint bilateral filter for energy-selective detectors. First results are encouraging. We found that only little cross-talk is introduced between the channels. The SNR was improved from 3.3 to 72.3 while preserving a low rRMSE error.

ACKNOWLEDGMENTS

The authors gratefully acknowledge funding of the Medical Valley national leading edge cluster, Erlangen, Germany, diagnostic imaging network, sub-project BD 16, research grant nr. 13EX1212G.

REFERENCES

- [1] M. Balda, "Quantitative Computed Tomography," Ph.D. dissertation, Friedrich-Alexander-Universität Erlangen-Nürnberg, 2011.
- [2] D. Niederlohner, F. Nachtrab, T. Michel, and G. Anton, "Using the Medipix2 detector for photon counting computed tomography," in *Nuclear Science Symposium Conference Record*, vol. 4. IEEE, 2005, pp. 2327–2331.
- [3] N. Maaß, S. Sawall, M. Knaup, and M. Kachelrieß, "Dose minimization for material-selective CT with energy-selective detectors," in *Nuclear Science Symposium and Medical Imaging Conference (NSS/MIC)*. IEEE, 2011, pp. 4447–4452.
- [4] J.-B. Thibault, K. D. Sauer, C. A. Bouman, and J. Hsieh, "A three-dimensional statistical approach to improved image quality for multislice helical CT," *Medical Physics*, vol. 34, no. 11, pp. 4526–4544, 2007.
- [5] M. Kachelrieß, O. Watzke, and W. A. Kalender, "Generalized multi-dimensional adaptive filtering for conventional and spiral single-slice, multi-slice, and cone-beam CT," *Medical Physics*, vol. 28, no. 4, pp. 475–490, 2001.
- [6] H. Bruder, R. Raupach, J. Sunnegardh, M. Sedlmair, K. Stierstorfer, and T. Flohr, "Adaptive iterative reconstruction," in *SPIE Medical Imaging*, vol. 7961, 2011, pp. 79 610J–1 79 610J–12. [Online]. Available: <http://dx.doi.org/10.1117/12.877953>
- [7] Z. Li, L. Yu, J. D. Trzasko, J. G. Fletcher, C. H. McCollough, and A. Manduca, "Adaptive non-local means filtering based on local noise level for CT denoising," in *SPIE Medical Imaging*. International Society for Optics and Photonics, 2012, pp. 83 131H–83 131H.

Image	GT Bin 1	GT Bin 2	GT Bin 3	Bin 2	Bin 3
Ground truth (GT) Bin 1	1.0 (1.0)	0.78 (0.97)	0.62 (0.99)	0.78 (0.97)	0.62 (0.99)
No Filtering Bin 1	0.95 (0.91)	0.67 (0.87)	0.52 (0.91)	0.69 (0.90)	0.56 (0.92)
JBF Bin 1	0.98 (0.98)	0.76 (0.95)	0.60 (0.98)	0.79 (0.99)	0.64 (0.99)
ID-JBF Bin 1	0.98 (0.98)	0.75 (0.95)	0.60 (0.98)	0.78 (0.98)	0.64 (0.99)
JBF + ID-JBF Bin 1	0.98 (0.98)	0.76 (0.65)	0.60 (0.98)	0.79 (0.99)	0.64 (0.99)

Table I: Structural similarity and linear correlation (in brackets) for the different reconstruction methods. All JBF combinations deliver significant improvements compared to the baseline reconstruction (No Filtering Bin 1) in terms of noise reduction. Visual inspection of ID-JBF, however, demonstrates that it is not able to preserve the low-contrast difference between heart chambers and muscle (cf. Figure 3d).

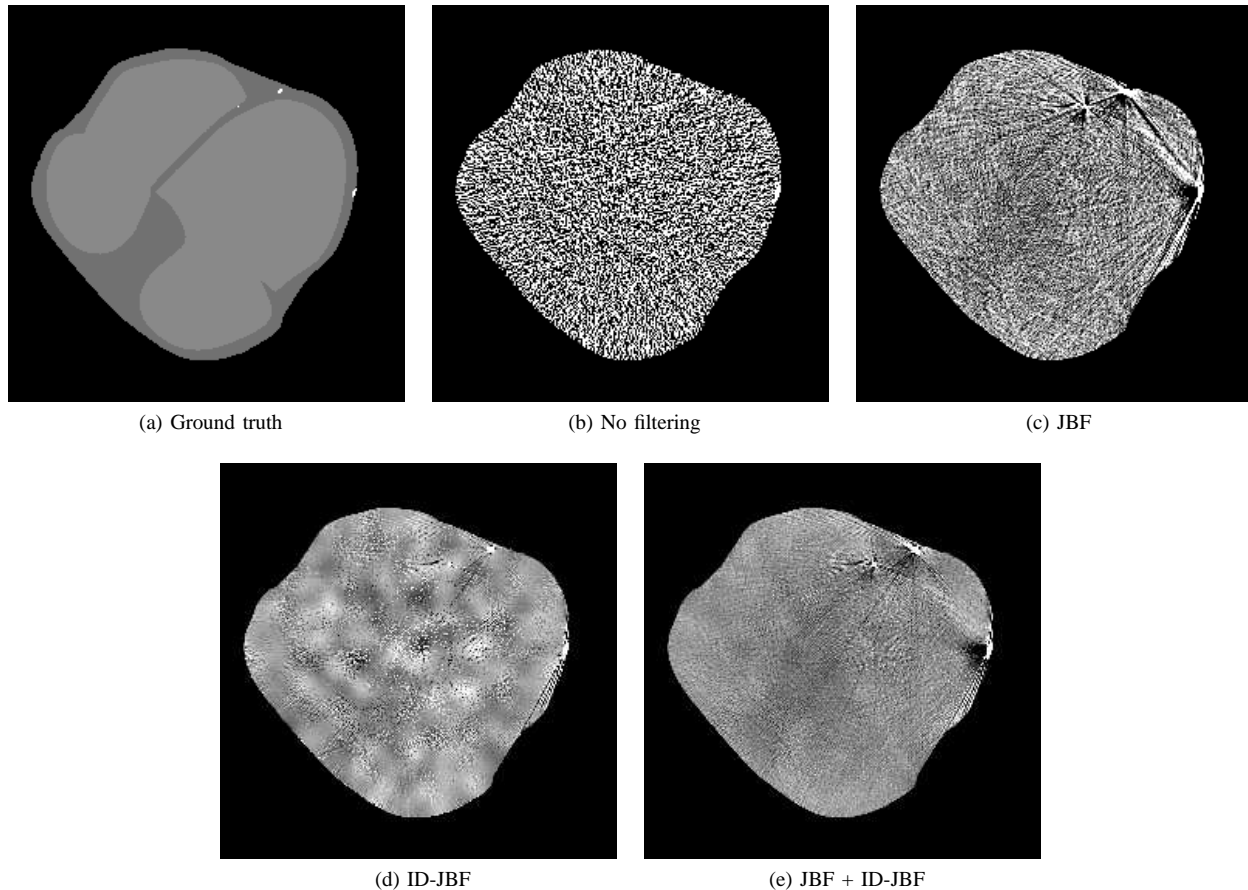


Figure 3: Comparison between the different reconstruction methods in the central slice of Bin 1 [10, 110 HU].

- [8] A. Maier, L. Wigström, H. Hofmann, J. Hornegger, L. Zhu, N. Strobel, and R. Fahrig, “Three-dimensional anisotropic adaptive filtering of projection data for noise reduction in cone beam CT,” *Medical Physics*, vol. 38, no. 11, pp. 5896–5909, 2011. [Online]. Available: <http://www5.informatik.uni-erlangen.de/Forschung/Publikationen/2011/Maier11-TAA.pdf>
- [9] G. L. Zeng and A. Zamyatin, “A filtered backprojection algorithm with ray-by-ray noise weighting,” *Medical Physics*, vol. 40, no. 3, pp. 031 113–1–7, 2013.
- [10] A. Manduca, L. Yu, J. D. Trzasko, N. Khaylova, J. M. Kofler, C. M. McCollough, and J. G. Fletcher, “Projection space denoising with bilateral filtering and CT noise modeling for dose reduction in CT,” *Medical Physics*, vol. 36, no. 11, p. 4911, 2009.
- [11] L. Yu, A. Manduca, M. Jacobsen, J. D. Trzasko, J. G. Fletcher, D. R. DeLone, and C. H. McCollough, “Adaptive modulation of bilateral filtering based on a practical noise model for streaking and noise reduction in multi-slice CT,” in *Proc SPIE Medical Imaging*, vol. 7622, 2010, p. 76222O.
- [12] A. Maier, H. Hofmann, M. Berger, P. Fischer, C. Schwemmer, H. Wu, K. Müller, J. Hornegger, J.-H. Choi, C. Riess, A. Keil, and R. Fahrig, “CONRAD - A software framework for cone-beam imaging in radiology,” *Medical Physics*, vol. 40, no. 11, pp. 111 914–1–8, 2013.
- [13] G. Petschnigg, R. Szeliski, M. Agrawala, M. Cohen, H. Hoppe, and K. Toyama, “Digital photography with flash and no-flash image pairs,” *ACM Transactions on Graphics (TOG)*, vol. 23, no. 3, pp. 664–672, 2004.
- [14] V. Aurich and J. Weule, “Non-linear Gaussian filters performing edge preserving diffusion,” in *Mustererkennung 1995*, ser. Informatik aktuell, G. Sagerer, S. Posch, and F. Kummert, Eds. Springer Berlin Heidelberg, 1995, pp. 538–545.
- [15] A. Maier, H. G. Hofmann, C. Schwemmer, J. Hornegger, A. Keil, and R. Fahrig, “Fast simulation of X-ray projections of spline-based surfaces using an append buffer,” *Physics in Medicine and Biology*, vol. 57, no. 19, pp. 6193–6210, 10 2012.
- [16] G. L. Zeng, *Medical image reconstruction: A conceptual Tutorial*, 1st ed. Berlin, Germany: Springer, 2010.
- [17] Z. Wang, A. Bovik, H. Sheikh, and E. Simoncelli, “Image quality assessment: from error visibility to structural similarity,” *Image Processing, IEEE Transactions on*, vol. 13, no. 4, pp. 600–612, April 2004.

Modified Noise Modeling for Robust Statistical Reconstructions

Frank Bergner¹, Bernhard Brendel¹, Rolf Bippus¹, Daniela Muenzel², Peter B. Noel², Thomas Koehler¹

Abstract—Statistical, iterative reconstruction has become a major topic for computed tomography (CT) in the last years as computational efforts have become feasible. In comparison to conventional filtered-backprojection methods the iterative methods highly rely on a consistent model and consistent data. Motion and inconsistencies can cause strong artifacts in the resulting images. In statistical reconstructions side information about the distribution of noise in the measured data is available. A simple modification of this noise modeling is proposed, which enables the down-weighting of systematic deviations in the measured data, making the statistical reconstruction more robust against inconsistencies.

I. INTRODUCTION

In recent years the increase in computation power has enabled new iterative reconstruction methods in computed tomography. Although the computation times for reconstructing images are still beyond the ones for conventional, analytic methods like filtered backprojection, the iterative methods have been adopted to the clinical workflow. They offer significant dose reductions while maintaining the diagnostic confidence in the images.

One major drawback of iterative, statistical methods is that they rely on a consistent system model. The reconstruction will try to “explain” the projection data by generating an image that fits the measured data best. However, modeling all possible effects that might have occurred during the acquisition is almost impossible. Motion, beam-hardening, or out-of-field-of-view data usually do not undergo a special treatment but appear as artifacts in the final image. One possible way to reduce some of the artifacts is an additional weighting applied to the projections [1], [2]. A drawback of these methods is that the weighting reduces the utilization of measured data for the reconstruction, which implies a suboptimal use of radiation dose.

In CT a valid model for the noise induced by the incoming X-ray photons (ignoring the electronic detector noise) is a Poisson distribution, i.e. the mean number of photons equals the expected variance in the detector pixel. By using this knowledge and error propagation one can obtain an estimate for the noise in the line integral values or relative attenuations for each detector pixel. This variance estimate is then used, for instance, in a weighted least-squares (WLS) cost function in a statistical reconstruction [3].

In this abstract a method is proposed which incorporates the projection noise model in a modified way to make the

reconstruction more robust against systematic deviation and outliers. From the projection data one can get estimates about the actual noise level and implement outlier rejection methods for the difference between the forward-projected image and the raw data. If both deviate too much for a detector pixel, e.g. by three times the assumed standard deviation, then the impact of the pixel in the cost function could be reduced. In the following sections a practical outlier rejection is described and evaluated for clinical data.

II. METHOD

For the reconstruction we usually approximate the maximum likelihood (ML) cost function as a WLS problem, in which the statistical weights are derived by error propagation from the Poisson noise model. We also add a regularization term in order to reduce noise in the image domain. For the derivation of the mathematics in our proposed method we focus in the following on the WLS term. The regularization term will remain unchanged.

A. Algorithm

We use a WLS cost function of

$$L(\mu) = \sum_i \frac{w_i}{2} \left(\sum_j a_{ij} \mu_j - y_i \right)^2$$

and modify it to

$$L_{\text{Huber}}(\mu) = \sum_i \frac{w_i}{2} \Psi \left(\sum_j a_{ij} \mu_j - y_i, \delta_i \right)$$

with Ψ being the Huber potential function and δ_i being the individual Huber parameters for each pixel. The factors a_{ij} are the entries of the system matrix and describe the linear coupling of the attenuation value of the j -th voxel μ_j to the i -th projection pixel. y_i is the line integral value in this pixel. The statistical weight w_i for the pixel can be estimated from the measured intensity values from an energy integrating detector or directly from photon numbers in case of a photon counting detector. From the statistical weights, which usually have the property $w_i \propto 1/\sigma_i^2$, one can derive the estimate of the standard deviation σ_i of the individual pixels. For energy integrating detectors, more accurate estimates including the electronic noise can be used [4]. The Huber parameter δ describes the transition point between the quadratic and the linear part of the Huber potential function

$$\Psi(x, \delta) = \begin{cases} 0.5x^2, & \text{if } x \leq \delta \\ \delta(x - 0.5\delta) & \text{otherwise.} \end{cases}$$

¹ Philips Technologie GmbH, Innovative Technologies, Research Laboratories, Hamburg, Germany

² Department of Radiology, Technische Universität München, Germany

Values greater than δ are penalized in the Huber potential less than in a quadratic potential. In order to iteratively solve the above cost function a separable paraboloid surrogate approach is used, which calculates a diagonal approximation of the Hessian for the given problem at the point of the current image $\mu^{(n)}$ [5]. The corresponding modified cost function of the n th iteration depending on the update $\Delta\mu_j$ and its tangent surrogate $\tilde{L}_\Psi(\Delta\mu)$ above it are

$$\begin{aligned} L_\Psi(\Delta\mu) &= \sum_i \frac{w_i}{2} \Psi \left(\sum_j a_{ij} (\mu_j^{(n)} + \Delta\mu_j) - y_i, \delta_i \right) \\ &= 0.5 \sum_i \frac{w_i}{2} \Psi \left(\sum_j \alpha_{ij} \frac{a_{ij}}{\alpha_{ij}} \Delta\mu_j + e_i^{(n)}, \delta_i \right) \\ &\leq 0.5 \sum_i \frac{w_i}{2} \sum_j \alpha_{ij} \Psi \left(\frac{a_{ij}}{\alpha_{ij}} \Delta\mu_j + e_i^{(n)}, \delta_i \right) \\ &= \tilde{L}_\Psi(\Delta\mu) \end{aligned}$$

with

$$\alpha_{ij} = \frac{a_{ij}}{\sum_j a_{ij}} \quad \text{and} \quad e_i^{(n)} = a_{ij} \mu_j^{(n)} - y_i.$$

The values $e_i^{(n)}$ are the differences between the forward-projected image in iteration n and the measured line integral data. The inequality stems from Jensen's inequality, and the procedure is also known from literature as De Pierro's trick [5]. Taking the derivative twice for the m th voxel at the current point $\Delta\mu_j = 0$ yields the Hessian diagonal elements

$$\left. \frac{d^2 \tilde{L}(\Delta\mu)_\Psi}{d\Delta\mu_j^2} \right|_{\Delta\mu_j=0} = \sum_i a_{ij} \frac{w_i}{2} \ddot{\Psi} \left(e_i^{(n)}, \delta_i \right) \sum_j a_{ij}.$$

The result is almost the same as for the conventional method with quadratic term, in which one performs a forward projection of the volume with all voxels set to 1, does a weighting of the projection and performs a backprojection into a volume. For the quadratic part of the Huber penalty, i.e. for $|e_i^{(n)}| \leq \delta_i$, the diagonal approximation will be exactly the same. For all other values in the linear part of the function a paraboloid approximation of the Huber function is used, which is also described in [5] and which handles the vanishing second derivative in the linear part of the potential. The larger the difference between the measured values and the forward projected image are, the lower the curvatures of the paraboloid will be, which are defined by the diagonal Hessian. The cost function becomes less strict for large differences compared to a purely quadratic cost function.

B. Evaluation

For the evaluation of the method several patient datasets with different inconsistencies are used. These include breathing motion, heart motion, and metal artifacts. Each dataset is reconstructed and compared to the conventional WLS method. Furthermore, in order to evaluate the impact of the given method on image resolution, a reconstruction

of a CatPhan phantom (The Phantom Laboratory, Salem, NY, USA) dataset is performed with a fixed regularization strength.

For the reconstructions, a GPU reconstruction framework with spherical symmetric basis functions, so-called blobs, is used [6], [7]. A start image is generated prior to each iterative reconstruction to increase the speed of convergence [8]. In order to further speed-up the reconstruction the ordered subset heuristics is used, i.e. the dataset is divided into sets of geometrically distant projections. The subset sizes are chosen such that approximately 20 rays contribute to the update of each blob in every sub-iteration. We also add a Huber regularization term in the image domain to the reconstruction in order to stabilize the reconstruction and reduce the noise in the images. The scaling of the regularization term in comparison to the data term is performed automatically using a controlling mechanism described in [9]. As the scaling factor might be slightly different between the individual reconstructions, one will possibly observe differences in the resolution.

III. RESULTS

The convergence speed of iterative reconstruction did not change with the described modification of the cost function. The reconstructed images shown here are the results from the 10th iteration, if not stated otherwise. An estimated Huber delta of $\delta_i \approx 3\sigma_i$ was used.

Fig. 1 shows the reconstruction of a dataset, in which the patient was breathing during the helical acquisition. The conventional reconstruction shows motion artifacts like duplicated structures at various positions e.g. near the ribcage and also the heart. The blurring and the duplicated structures are slightly reduced by the proposed method. Still some artifacts remain because of the severity of the data inconsistencies introduced by the patient motion. In the difference image the motionless regions near the table and the spine of the patient contain hardly any further anatomical structure. Thus, one can assume that the majority of the cost function terms belonging to those regions are not affected by the modification.

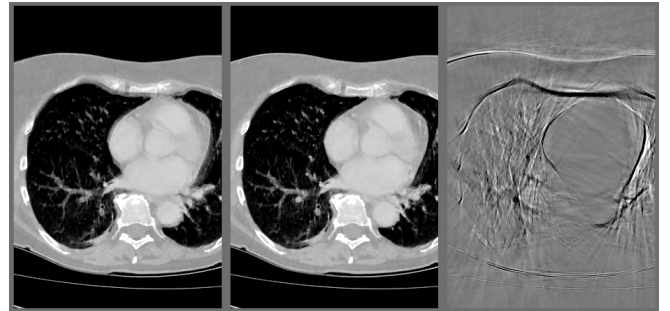


Fig. 1. Reconstruction of a dataset affected by breathing motion. The left image shows the conventional WLS result, the center image the one using the proposed method, and the right one shows the difference between both (Level/window = -200/1200 HU, 0/400 HU for the difference image)

A similar behavior can be found for concatenated cardiac step-and-shoot scans. For these the scanner acquires data

for several bed positions using a circular trajectory. In order to reduce dose the scan is gated at a predicted state in the cardiac cycle. The conventional reconstruction in Fig. 2 (left images) shows the impact of an inaccurate prediction in the gating. Both scans have a slight mismatch in the acquired motion phases leading to bright and dark streaks and blurred anatomy (yellow arrow) in the statistical reconstruction. In this case, the artifacts can also be reduced by the proposed method (center images). In an axial view through one of the motion affected slices (top row) one can see that the artifacts are reduced to a more convenient level. The motion artifacts of the heart coronary indicated by the yellow rectangle are not reduced by the method. The coronal view in the lower row shows the reduction of artifacts in the region between both scans. The difference image reveals that these even spread into the lung and affect vessels there.

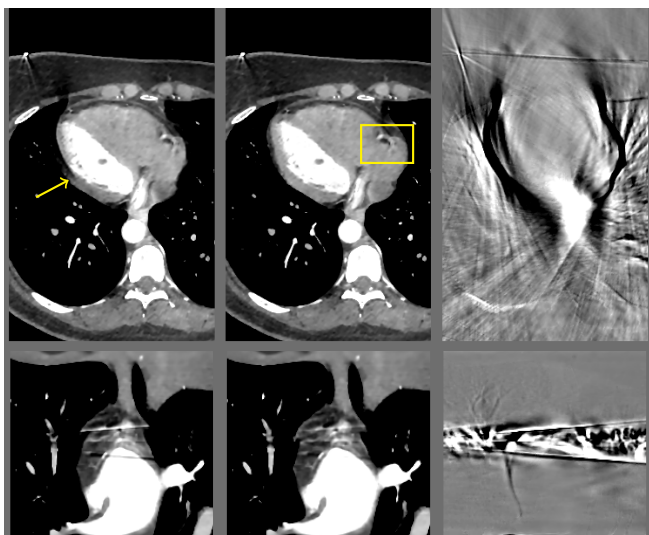


Fig. 2. Reconstruction of a cardiac image based on a prospectively gated step-and-shoot protocol in a axial (top) and coronal view (bottom). The columns show the conventional method (left), the proposed methods (center), and the difference between both (right). (Level/window = 50/500 HU and 0/100 HU for the difference image)

In Fig. 3 the reconstructions of a head dataset with metal artifacts are shown for both a conventional statistical approach (left image) and the proposed method (center image). This time 1000 iterations were performed since the metal region has a very slow convergence rate. The difference image on the right shows that the Huber function for the raw data mainly affects the region of the teeth, as intended. Although the differences appear significant they are barely visible in the reconstructions themselves. It cannot be concluded whether the proposed method gives a better result in this case.

In order to evaluate the impact of the modified raw data penalty on the image resolution, reconstructions of the resolution section of the CatPhan were performed. For the CatPhan data the regularization strength was chosen constant without regularization control in order to have a numerically exact comparison. In this case a quadratic regularization in the image space was chosen, which is does

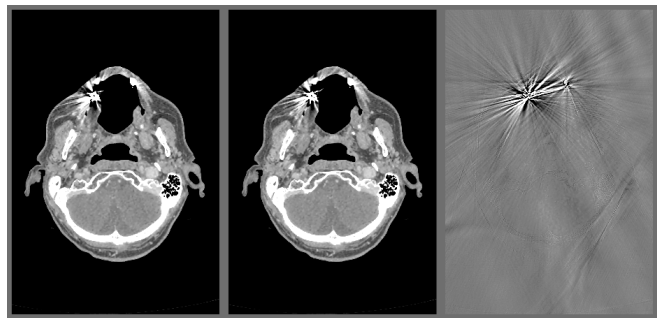


Fig. 3. Reconstruction of a head with dental implants. The columns show the conventional method (left), the proposed methods (center), and the difference between both (right). (Level/window = 100/500 HU, 0/200 HU for the difference image)

not have edge-preserving properties and is therefore better suited to evaluate the impact on the image resolution and noise. The results are shown in Fig. 4. The leftmost image shows the conventional reconstruction, the center image shows the proposed methods with $\delta_i \approx 3\sigma_i$ and the right image with $\delta_i \approx \sigma_i$. Around the high contrast inserts one can see dark streaks, which become more apparent in the difference images for smaller δ_i . This can be explained by high-frequent content being blurred by the regularization and leading to high differences in the projection domain. Therefore, the streaks are getting stronger for $\delta_i \approx \sigma_i$ as the view-dependent loss of resolution is being penalized less in the projections. Image noise is measured from the standard deviation within the regions of interest (ROIs) indicated by yellow circles. The noise is almost unchanged for $\delta_i \approx 3\sigma_i$ but drops for $\delta_i \approx \sigma_i$ as noise in the projection domain is penalized less strong due to the linear range of the Huber potential. The same reconstruction but with edge-preserving

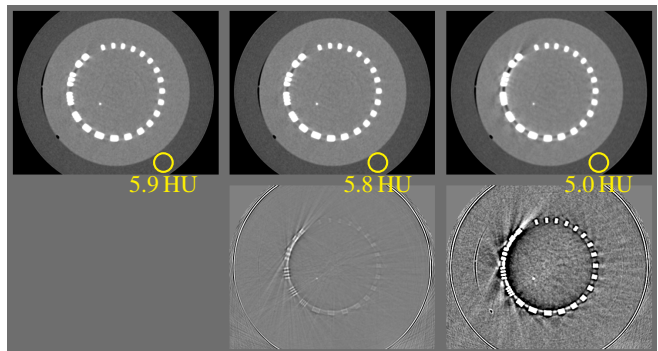


Fig. 4. Reconstruction of the resolution pattern section of the CatPhan with quadratic regularization. The columns show the conventional method (left), the proposed method with $\delta_i \approx 3\sigma_i$ (center), and the proposed method with $\delta_i \approx \sigma_i$ (right). The bottom row shows the corresponding difference images with respect to the reference at the top left. (Level/window = 100/500 HU, 0/50 HU for the difference image)

Huber regularization on the image are shown in Fig. 5. Here only a slight decrease in resolution can be observed at the edges of the high-contrast objects for $\delta_i \approx \sigma_i$. Streaks are not visible as the regularization does not blur the resolution inserts. For $\delta_i \approx 3\sigma_i$ only minor differences can be seen at the border of the phantom but almost none at the high contrast inserts, so the image resolution remains unchanged

in comparison to the conventional WLS case. The overall noise level is in the same order of magnitude as in the case of quadratic regularization. The same drop in noise for low δ_i values can be observed.

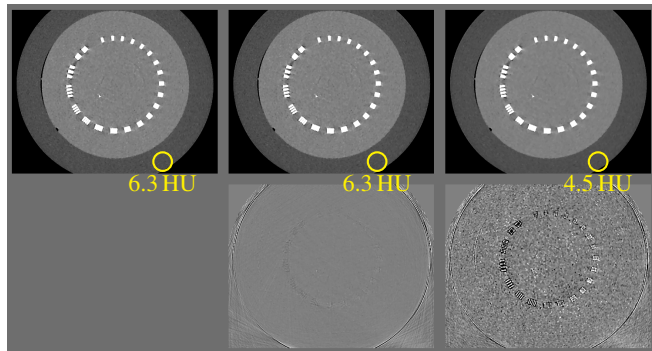


Fig. 5. Reconstruction of the resolution pattern section of the CatPhan with Huber regularization. The columns show the conventional method (left), the proposed method with $\delta_i \approx 3\sigma_i$ (center), and the proposed method with $\delta_i \approx \sigma_i$ (right). The bottom row shows the corresponding difference images with respect to the reference at the top left. (Level/window = 100/500 HU, 0/50 HU for the difference image)

IV. DISCUSSION

The results demonstrate that the proposed modification of the statistical reconstruction with an implicit outlier rejection based on a Huber potential gives an advantage in most cases over the conventional approach without reducing the spatial resolution or introducing artifacts when the Huber parameters δ_i are chosen moderately and an edge-preserving image regularization is used. If the Huber parameters are chosen too tightly the reduced influence of the raw data term of the cost function paired with a non-edge-preserving regularization impedes an accurate reconstruction of high-frequency image content. In the case of the CatPhan the differences in the projections led to a wrong view-dependent weighting of the projection pixels which resulted in black streaks between the high contrast resolution inserts of the phantom similar to beam-hardening artifacts. The introduced artifacts were less severe for the image space Huber regularization, which is known to preserve edges and high-contrast objects better. In this case the differences to the conventional reconstruction were negligible if $\delta_i \approx 3\sigma_i$ was used. The image noise dropped slightly for $\delta_i \approx \sigma_i$ in the case of the edge-preserving image regularization, but it remained almost the same for $\delta_i \approx 3\sigma_i$. So one can assume that most raw-data differences remained below the $3\sigma_i$ boundary.

In the case with dental implants the method did not show improvements in this case. One possible explanation is the already reduced impact of the projected metal in the cost function as the statistical weights are very low for these detector pixel. In these regions the noise estimation also becomes problematic since only few photons are measured in combination with the electronic noise of the detector. Although the method does not appear to be well-suited for inconsistencies from metal it at least does not introduce new

artifacts. In the cases with heart and breathing motion the statistical pixel weight was on a normal scale compared to the metal penumbra. Thus, the proposed method showed more significant improvements on in these cases. It was not able to improve the temporal resolution e.g. for one of the moving coronary arteries. For these the inconsistencies are not large enough to be affected by the Huber penalty in projection domain.

One issue of the proposed method is that the estimation of the pixel standard deviation stems from the noisy raw data and is, therefore, a random variable itself. Although the used estimates are rather coarse, the method seems to be sufficiently robust. Nevertheless, more datasets have to be evaluated in order to exclude systematic deviations related to the noise estimation. A different, more accurate solution could be the inclusion of an outlier rejection into the noise model, i.e. into the probability density function, in combination with an expectation maximization algorithm. This would imply an adjustment of the estimated noise in the projection values according to the current image but on the other hand could reduce the convergence speed. Alternatively, one could also try to estimate the variances of the pixels from the forward projected volume, which incorporates noise corrected values in the ideal case. This procedure would be similar fast as the conventional WLS approach. In this case one would have to check whether the cost function remains convex and guarantees convergence.

V. CONCLUSION

The proposed extension of a statistical reconstruction has been shown to reduce certain artifacts caused by inconsistencies in the measured data. The algorithm parameters must be chosen carefully when being combined with image space regularization.

REFERENCES

- [1] K. Zeng, B. De Man, and J.-B. Thibault, in *Proceedings of the Fully 3D*, 2009, pp. 242–245.
- [2] H. Takahashi, T. Goto, K. Hirokawa, and O. Miyazaki, in *Proceedings of the Fully 3D*, 2011, pp. 355–258.
- [3] J. A. Fessler, “Statistical image reconstruction methods for transmission tomography,” in *Handbook of Medical Imaging, Vol. 2*, M. Sonka and J. M. Fitzpatrick, Eds., chapter 1, pp. 1–70. SPIE Press, Bellingham, WA, 2000.
- [4] J. Ma, Z. Liang, Y. Fan, Y. Liu, J. Huang, W. Chen, and H. Lu, *Medical Physics*, vol. 39, no. 7, pp. 4051–4065, 2012.
- [5] H. Erdogan and J. A. Fessler, *IEEE Trans. Med. Imag.*, vol. 18, no. 9, pp. 801–814, 1999.
- [6] R. Bippus, T. Koehler, F. Bergner, B. Brendel, E. Hansis, and R. Proksa, in *Proceedings of the 3D’2011 Conference*, Potsdam, Germany, 2011, pp. 68–71.
- [7] R. M. Lewitt, *Phys. Med. Biol.*, vol. 37, no. 3, pp. 705–716, 1992.
- [8] K. M. Brown, S. Zabic, and T. Koehler, *Proc. SPIE Med. Imag. Conf.*, p. 831339, 2012.
- [9] F. Bergner, B. Brendel, P. B. Noël, M. Dobritz, and T. Koehler, in *Proceedings of the 2nd CT Meeting*, Salt Lake City, Utah, USA, 2012, pp. 267 – 270.

Improved Statistical Models in Iterative CT Reconstruction for PET Attenuation Correction

Soo Mee Kim, Adam M. Alessio, David S. Perlmutter, Jean-Baptiste Thibault, Bruno De Man, and Paul E. Kinahan

Abstract— CT-based attenuation correction (CTAC) in PET/CT and SPECT/CT can be performed with extremely low-dose (high noise) acquisitions. These acquisitions, however, can suffer from photon starvation noise-induced artifacts. There have been numerous efforts to develop low-dose compensation methods to improve CT image quality. In this study, we investigated the application of improved first and second order statistical models in iterative CT reconstruction for extremely low-dose CT acquisitions. Three approaches of non-positivity correction prior to the log-conversion step were evaluated for estimating first order statistics. The three non-positivity correction methods used were fixed- and varying-thresholds and a mean-preserving filter (MPF). As expected, the MPF method yielded improved discrimination of lung regions, a higher signal-to-noise ratio, and a lower RMSE compared with the two threshold approaches. We also evaluated the impact of different models of second order statistics used in weighted least-squares (WLS) reconstruction. These included previously proposed models based on simple approximations of (1) Poisson or (2) combined Poisson and Gaussian processes, as well as more accurate weighting based on sample estimates from 1000 realizations. Using the directly estimated sample variance, the performance of the WLS reconstruction was enhanced over using the approximate weighting terms. We conclude that using improved first and second order statistical models can lead to improved reconstructions for extremely low-dose acquisitions.

I. INTRODUCTION

CT has played a crucial role in attenuation correction for quantitative PET imaging, giving patient-specific attenuation information in hybrid PET/CT systems. While respiratory-gated PET images are widely applied to disease diagnosis and treatment monitoring, it has increased the importance of phase-matched attenuation correction for quantitative accuracy of PET images. However, the repeated CT acquisitions at multiple respiratory-gated phases lead to increased patient radiation doses [1].

Recently, there have been several efforts (e.g., down-sampling of raw data sinogram, sinogram smoothing, or other denoising techniques [1]) to reduce excessive CT radiation dose. Iterative reconstruction is one approach that enables lower dose scans by incorporating data noise models that generally lead to improved SNR in reconstructed images.

In this study, we investigated the application of improved models of the first and second order statistics in iterative CT

reconstruction for very high-noise CT data. We evaluated the impact of these models with realistic simulations of low-dose CT acquisitions.

II. METHODS

For CT iterative reconstruction, we considered the weighted least square (WLS) problem, which maximizes an approximation to the negative Poisson log-likelihood of the CT projection data. We apply iterative reconstruction to post-log data, which enables use of the existing data processing steps used for the numerous pre-corrections. The log-likelihood, $L(\boldsymbol{\mu})$ has a quadratic form given by a second-order Taylor series expansion [2]:

$$\hat{\boldsymbol{\mu}} = \underset{\boldsymbol{\mu}}{\operatorname{argmax}} \{-L(\boldsymbol{\mu})\} \approx \underset{\boldsymbol{\mu}}{\operatorname{argmax}} \left\{ \frac{1}{2} \sum_i W_i (p_i - \langle \mathbf{D}\boldsymbol{\mu} \rangle_i)^2 \right\}. \quad (1)$$

In Eq. (1), p_i is one measured projection value corresponding to sinogram element i , in the attenuation domain (i.e., post-log data) and the projection operator, $\langle \mathbf{D}\boldsymbol{\mu} \rangle$, computes the mean projection through line integrals of given attenuation map, $\boldsymbol{\mu}$, with a system matrix \mathbf{D} for fan-beam CT geometry. In WLS, the measured projection (p_i) and the weight (W_i) in diagonal matrix correspond to first and second order statistical properties, respectively. We investigated first order statistic of non-positivity correction methods that enable the log-conversion step from raw CT measurement to the attenuation domain, to reduce bias in reconstruction, as well as second order statistic models representing the projection variance in the diagonal matrix. By incorporating more accurate statistical properties into iterative reconstruction, we hope to improve image quality even for extremely low dose CT scans.

A. First order statistic models

A CT projection data (p_i) in the attenuation domain is calculated by computed the logarithm of the measured detector count (λ_i):

$$p_i = \log(\lambda_T / \lambda_i), \quad (2)$$

where λ_T is the x-ray intensity prior to body attenuation. The detector count is from quantum detection and electronics processes having probability density functions, $f_Q(m_q, \sigma_q^2)$ and $f_D(m_e, \sigma_e^2)$. The mean and variance of λ_i are

$$m_{\lambda_i} = E[\lambda_i] = m_{q,i} + m_{e,i} \quad \text{and} \quad \sigma_{\lambda_i}^2 = \operatorname{Var}[\lambda_i] = \sigma_{q,i}^2 + \sigma_{e,i}^2, \quad (3)$$

if the sources of noise are uncorrelated.

Figure 1 demonstrates the processing steps of dark current offset correction and non-positivity correction (Eq. 4).

$$\tilde{\lambda}_i = f_{NP}(\lambda_i - m_{e,i}). \quad (4)$$

Soo Mee Kim, David S. Perlmutter, Adam M. Alessio, Paul E. Kinahan are with the Department of Radiology, University of Washington, Seattle, WA 98185, USA (e-mail: smeekim@uw.edu, dperl@uw.com, alessio@uw.edu, kinahan@uw.edu).

J.-B. Thibault is with GE Healthcare, Waukesha, WI 53188 USA

Bruno De Man is with the CT Systems and Applications Laboratory, GE Global Research Center, Niskayuna, NY 12309, USA

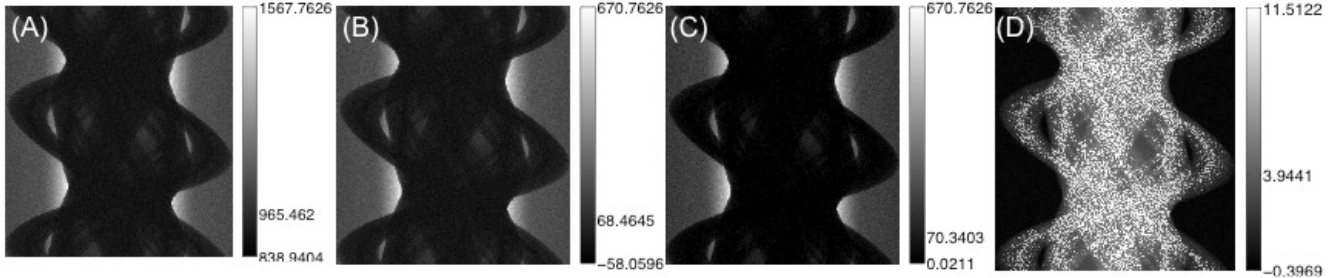


Fig. 1. Representative simulated sinograms from a 80 kVp, 0.5 mAs acquisition. Procedure of log-conversion from intensity to attenuation domain sinogram (left to right): (A) Raw sinogram in intensity domain, (B) offset subtracted sinogram, (C) non-positivity corrected sinogram by fixed threshold (FTH), and (D) projection sinogram in attenuation domain after computing the logarithm (Eq. 2).

The post-corrected measurement ($\tilde{\lambda}_i$) will have a mean ($m_{\tilde{\lambda}_i}$) and variance ($\sigma_{\tilde{\lambda}_i}^2$) after offset subtraction and non-positivity correction. Offset subtraction of the electronic noise mean (m_e) of shifts the actual measurement mean in Eq. (3) to better represent the quantum mean (m_q) while preserving the measurement variance. However, the offset subtraction can increase the number of non-positive values. The non-positive portion substantially increases at lower dose CT scans.

Non-positivity correction replaces the negative and zero entries with a positive value prior to log conversion. Non-positivity correction can affect the estimate of both mean and variance of the corrected measurement and can lead to a discrepancy with the statistical models.

Here, we investigated three different non-positivity correction approaches based on thresholds (TH) and a mean-preserving filter. Fixed threshold approach (FTH) uses a function,

$$f_{\text{TH}}(\lambda; \varepsilon_\theta) = \begin{cases} \lambda, & x \geq \varepsilon_\theta \\ \varepsilon_\theta, & \lambda < \varepsilon_\theta \end{cases}. \quad (5)$$

It is important to set the threshold value to minimize bias from the true mean.

We also use a varying threshold (VTH) method that varies the thresholds (ε_θ) over rotation angles (θ) as shown in Fig. 2(A). The path length (L_θ) is estimated from the current projection data through edge detection of the most extreme attenuated beams for each angle. Then, we assume a uniform attenuating medium along this estimated path length having the linear attenuation coefficient for water (μ_w) at 70 keV within the object boundary. The variable threshold value, ε_θ , was computed as follows

$$\varepsilon_\theta = \lambda_T \exp(-\mu_w \cdot L_\theta). \quad (6)$$

The mean-preserving filter (MPF) method [3] uses a local smoothing filter that preserves the local means using a non-linear function,

$$f_{\text{MPF}}(\lambda; \alpha) = \alpha \log \left(\exp\left(\frac{\lambda}{\alpha}\right) + 1 \right). \quad (7)$$

The difference between the input and result of this function is forward dispersed to neighboring sinogram bins.

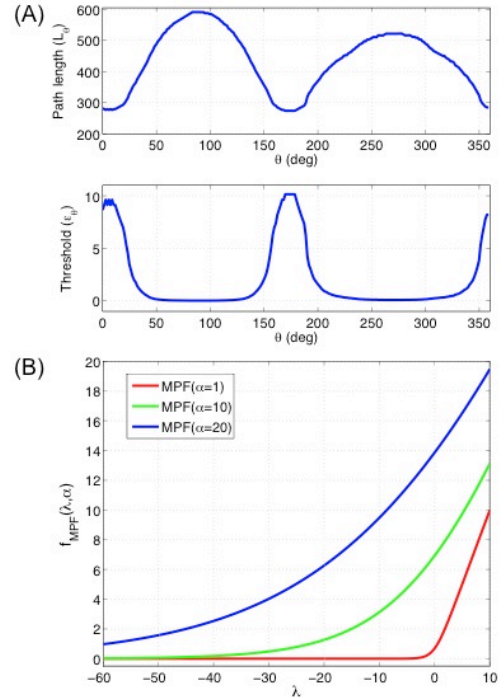


Fig. 2. (A) Varying path lengths (L_θ) and threshold values (ε_θ) over rotation angle, (B) MPF function with different parameters, $\alpha=1, 10$, and 20 .

Larger values of α will have a greater likelihood of ensuring positive values throughout the data but will lead to more bias as shown in Fig. 2(B).

B. Second order statistic models

WLS reconstruction requires a diagonal weight matrix, \mathbf{W} (Eq. 1). When implemented as a minimum variance unbiased estimator for attenuation images, each element, W_i , is the reciprocal of the variance (σ_p^2) of the CT projection in the attenuation domain. The attenuation domain (post-log) variance is related to statistical properties of the corrected, intensity domain measurements. An approximate form of the post-log variance has been proposed using a first order Taylor series expansion of the logarithm function [3]:

$$\begin{aligned} \sigma_{p_i}^2 &= E \left[(m_{\tilde{p}_i} - \tilde{p}_i)^2 \right] = E \left[\log^2 \left(\frac{\tilde{\lambda}_i}{m_{\tilde{\lambda}_i}} \right) \right] \\ &\approx E \left[\left(1 - \frac{\tilde{\lambda}_i}{m_{\tilde{\lambda}_i}} \right)^2 \right] = \frac{E \left[(m_{\tilde{\lambda}_i} - \tilde{\lambda}_i)^2 \right]}{m_{\tilde{\lambda}_i}^2} = \frac{\sigma_{\tilde{\lambda}_i}^2}{m_{\tilde{\lambda}_i}^2}. \end{aligned} \quad (8)$$

Assuming only a Poisson noise for the CT imaging process, the conventional diagonal matrix for practical WLS reconstruction has been expressed by the real measurement of a random variable $\tilde{\lambda}_i$ in intensity domain as follows

$$\frac{1}{\sigma_{pi}^2} \cong \frac{m_{\tilde{\lambda}_i}^2}{\sigma_{\tilde{\lambda}_i}^2} \cong \frac{m_{qi}^2}{\sigma_{qi}^2} = m_{qi} \propto \tilde{\lambda}_i = W_{q,i}. \quad (9)$$

Here, the projection variance is inversely proportional to the measured detector count [4].

One improvement beyond this model is to include the contribution of electronic noise, as proposed in [3]. In this model, the projection variance in Eq. (8) become

$$\frac{m_{\tilde{\lambda}_i}^2}{\sigma_{\tilde{\lambda}_i}^2} \cong \frac{m_{qi}^2}{(m_{qi} + \sigma_{ei}^2)} \propto \frac{\tilde{\lambda}_i^2}{(\tilde{\lambda}_i + \sigma_{ei}^2)} = W_{qe,i}. \quad (10)$$

In Eq. (9) and (10), $\tilde{\lambda}_i$ is a corrected realization of the quantum mean of a Poisson in intensity domain.

These second order statistical models do not account for several effects. Actual CT measurements are compound Poisson distributed. Furthermore, the processing steps of offset subtraction and non-positivity correction can have a

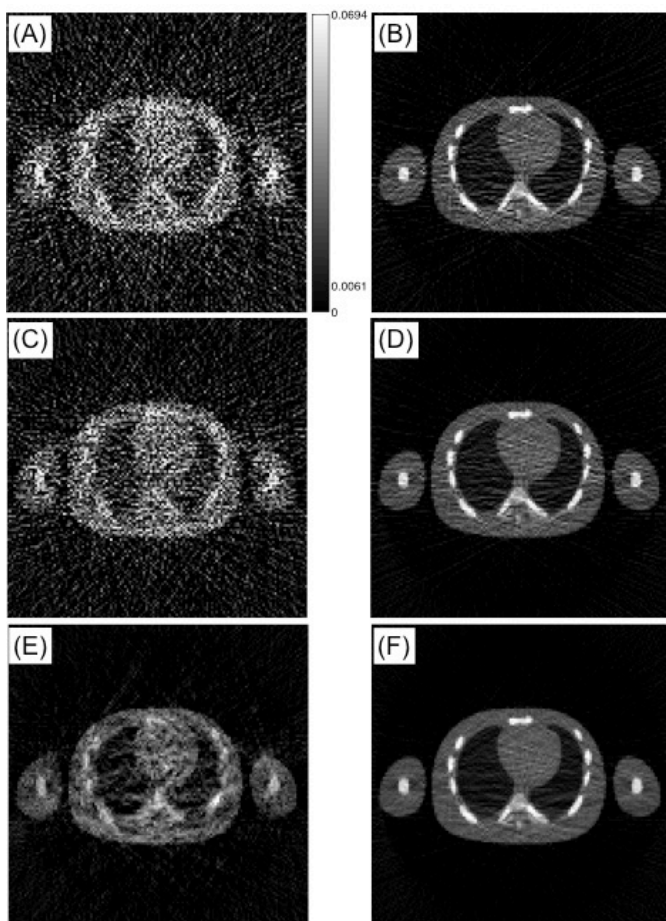


Fig. 3. FBP results with ramp filter of noisy data from tube currents of 0.5 and 10 mA; all noisy data were pre-corrected by offset subtraction and non-positivity correction; (A) 0.5mA-fixed threshold (FTH, RMSE:1.48), (B) 10mA-FTH (RMSE:0.38), (C) 0.5mA-varying thresholds (VTH, RMSE:1.11), (D) 10mA-VTH (RMSE:0.3), (E) 0.5mA-MPF ($\alpha=20$, RMSE:0.48), and (F) 10mA-MPF (RMSE:0.18).

variable influence on the data statistics depending on the number of non-positive entries. Finally, with the log-conversion, the entire processing chain is non-linear, which makes it difficult to predict the final actual variance.

C. Simulation and Evaluation

CT simulations were performed of the NCAT phantom using the CatSim simulator [5], which generates poly-energetic compound Poisson data with Gaussian electronic noise contributions. In the simulation, we set different noise levels corresponding to a tube current of 0.5 and 10 mA. From 1000 realizations, the sample mean and variance of the corrected measurement were calculated as follows

$$\tilde{m}_{\lambda,i} \approx \frac{1}{N} \sum_{n=1}^N \tilde{\lambda}_{i,n} \quad \text{and} \quad \sigma_{\tilde{\lambda}_i}^2 \approx \frac{1}{N-1} \sum_{n=1}^N (m_{\tilde{\lambda}_i} - \tilde{\lambda}_i)^2. \quad (11)$$

The image quality was evaluated in terms of root mean squared error (RMSE).

III. RESULTS

Figure 3 compares the FBP reconstructions with ramp filter of data corrected with different non-positivity correction approaches: fixed threshold (FTH), varying thresholds (VTH) over rotation angles, and MPF with $\alpha=20$. The VTH method resulted in less RMSE than the FTH method (1.48 vs 1.11 1/mm). MPF (E and F) gave better discrimination of lung regions, visually higher signal to noise ratio, and lower RMSE compared with threshold approaches (A to D).

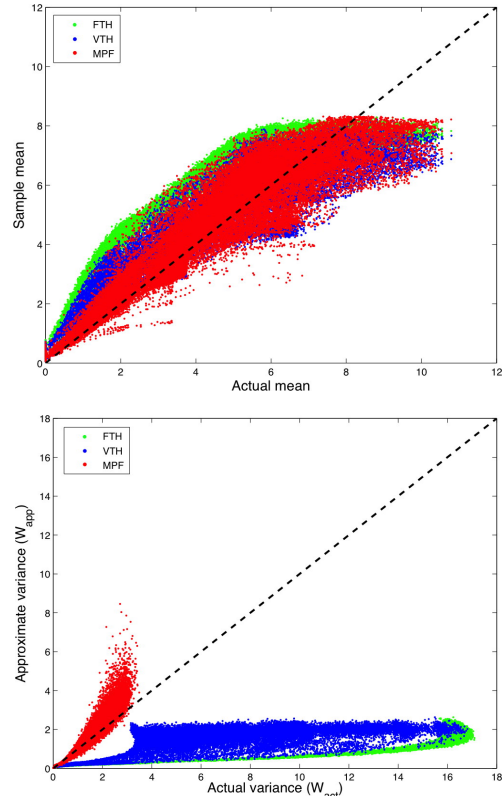


Fig. 4. Scatter plots of post-log mean (top) and projection variance (bottom). Approximate projection variances from Eq. (8) are plotted versus actual sample projection variance computed from 1000 realizations, which were processed by FTH (green), VTH (blue), and MPF (red) corrections.

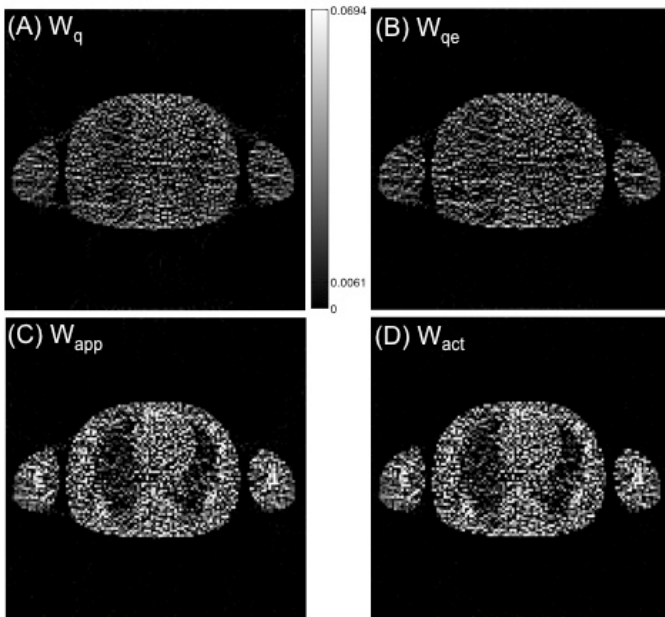


Fig. 5. Iterative reconstructions of 0.5 mA data after non-positivity correction using the VTH method and using different estimates of variance. Variance estimates were: (A) W_q (RMSE:0.9), (B) W_{qe} (RMSE:0.9), (C) W_{app} (RMSE:1.07), and (D) W_{act} (RMSE:1.08).

Figure 4 shows scatter plots of the mean estimated from corrected noisy data compared to the noise-free mean. The MPF resulted in values more in keeping with the actual mean, although it is clear that all of the non-positivity correction techniques result in biased measurements. Figure 4 also presents approximate and actual projection variances. The approximate variance (W_{app}) of the post-log data was computed from the sample mean and variance of 1000 corrected, pre-log sinograms as presented in Eq. (8). MPF compared to variable thresholding resulted in approximate variances more in keeping with the actual variance (W_{act} , sample variance of 1000 corrected, post-log sinograms).

Figure 5 and 6 show WLS reconstructions with different weighting matrices for a low-dose scan of 0.5 mA. The measurements were corrected through offset subtraction and non-positivity corrections, VTH and MPF ($\alpha=20$), as shown in Fig. 5 and 6 respectively. The weighting terms were W_q , W_{qe} , W_{app} , or W_{act} , in which the variance was estimated from Eq. (9) or (10) or calculated from multiple realizations for Eq. (8) or directly calculated from post-log measurements from multiple realizations.

In comparing the practical weighting matrices W_q vs W_{qe} , there were no visual differences or significant differences in RMSE with the addition of the electronic noise component. If we had access to multiple realizations (not practical) or if better models can be developed for the post-log low-dose projection measurements, the results using W_{app} and W_{act} show that there are potential improvements with these better second order statistics. In the case of VTH in Fig. 5, W_{app} and W_{act} show improved visual image quality, but give higher RMSE than W_q and W_{qe} , due to the increased background noise in the reconstructed image.

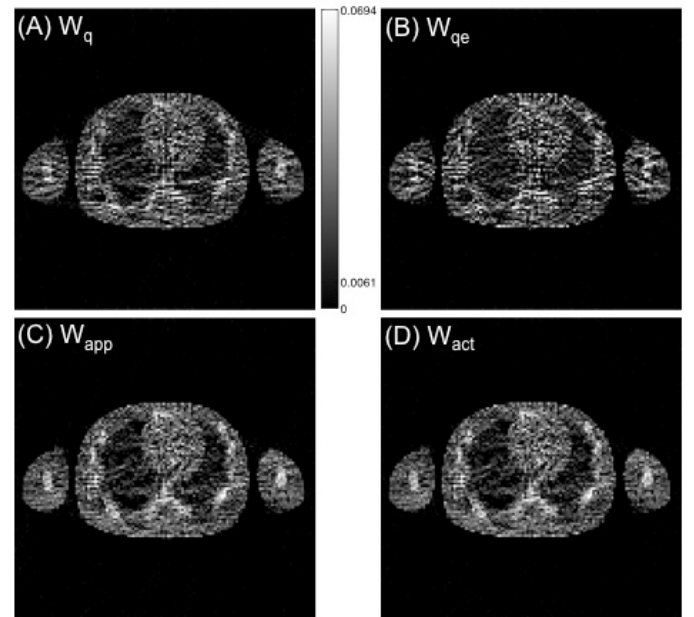


Fig. 6. Iterative reconstructions of 0.5 mA data after non-positivity correction using the MPF method and using different estimates of variance. Variance estimates were: (A) W_q (RMSE:0.68), (B) W_{qe} (RMSE:0.78), (C) W_{app} (RMSE:0.58), and (D) W_{act} (RMSE:0.57).

IV. CONCLUSION AND FUTURE WORK

We propose and evaluate correction techniques and variance estimation techniques for low-dose CT data. In effect, these steps improve our estimates of the first and second order statistics of the measurements. For models of the first order statistics, the MPF gave improved image quality in terms of visual signal-to-noise ratio and RMSE, compared with threshold approaches. Use of accurate variance measures yielded images with improved image quality compared to simple, practical models based on only Poisson or combined Poisson and Gaussian processes, demonstrating that there is potential value to developing methods to better estimate second order statistics. The improved first and second order models can lead to improved image quality in iterative reconstruction of extremely low-dose scans.

ACKNOWLEDGMENT

This work is supported by NIH grant R01-CA115870 and R01-HL109327.

REFERENCES

- [1] T. Xia, A. M. Alessio, B. De Man, R. Manjeshwar, E. Asma, and P. E. Kinahan, "Ultra-low dose CT attenuation correction for PET/CT," *Phys. Med. Biol.*, vol. 57, pp. 309–328, Jan. 2012.
- [2] K. Sauer and C. Bouman, "A local update strategy for iterative reconstruction from projections," *IEEE Trans. Sig. Proc.*, vol. 41, pp. 534–548, Feb. 1993.
- [3] J.-B. Thibault, C. A. Bouman, and K. D. Sauer, "A recursive filter for noise reduction in statistical iterative tomographic imaging," *Computational Imaging IV: Proc. of SPIE-IS&T Electronic Imaging*, vol. 6065, 2006.
- [4] C. A. Bouman and K. Sauer, "A unified approach to statistical tomography using coordinate descent optimization," *IEEE Trans. Image Proc.*, vol. 5, pp. 480–492, Mar. 1996.
- [5] B. D. Man, S. Basu, N. Chandra, B. Dunham, P. Edic, and M. Iatrou, "CatSim: a new computer assisted tomography simulation environment," *Proceedings of SPIE*, vol. 6510, pp. 1–8, Mar. 2007.

Optimized Momentum Steps for Accelerating X-ray CT Ordered Subsets Image Reconstruction

Donghwan Kim and Jeffrey A. Fessler

Abstract—Recently, we accelerated ordered subsets (OS) methods for low-dose X-ray CT image reconstruction using momentum techniques, particularly focusing on Nesterov’s momentum method. This paper develops an “optimized” momentum method that is faster than Nesterov’s method. Drori and Teboulle’s original version requires substantial memory space and computation time per iteration. Therefore, we design an efficient implementation approach of the optimized momentum method that uses storage and computation comparable to Nesterov’s method. We also propose to combine it with OS methods. We examine the acceleration of the proposed algorithm using 2D X-ray CT simulation data.

I. INTRODUCTION

We consider low-dose X-ray CT image reconstruction solving the following optimization problem:

$$\hat{x} = \arg \min_x \Psi(x), \quad (1)$$

where a function $\Psi(x)$ belongs to a set $\mathcal{F}_L(\mathbb{R}^{N_p})$ of convex and continuously differentiable functions with L -Lipschitz continuous gradient. Specifically in X-ray CT reconstruction, we use a penalized weighted least squares (PWLS) cost function [1]:

$$\Psi(x) = \frac{1}{2} \|y - Ax\|_W^2 + R(x), \quad (2)$$

where $x \in \mathbb{R}^{N_p}$ is an unknown image, $y \in \mathbb{R}^{N_d}$ is a noisy measured sinogram data, $A \in \mathbb{R}^{N_d \times N_p}$ is a projection operator [2], a diagonal matrix $W \in \mathbb{R}^{N_d \times N_d}$ provides statistical weighting [3], and $R(x)$ is an edge-preserving regularization function.

In X-ray CT, iteratively minimizing the cost function $\Psi(x)$ requires long computation times due to the computationally expensive operators A and A' . Ordered subsets (OS) methods [4], [5], which use only submatrices of A and A' per iteration, have been used widely for computational efficiency. However, traditional OS methods require many iterations to be used practically, so we recently proposed to combine them with Nesterov’s momentum method [6], yielding OS-momentum methods [7] that have faster initial convergence.

Nesterov’s momentum method achieves the optimal convergence rate $O(1/n^2)$ where n counts the number of iterations [8]. But, the constant of the convergence rate can be large in Nesterov’s method, motivating Drori and Teboulle (hereafter “DT”)’s optimized momentum¹ approach [9]. That

D. Kim and J. A. Fessler are with the Dept. of Electrical Engineering and Computer Science, University of Michigan, Ann Arbor, MI 48109 USA (e-mail: kimdongh@umich.edu, fessler@umich.edu).

Supported in part by NIH grant R01-HL-098686 and equipment donations from Intel Corporation.

¹Momentum methods here refer to iterative algorithms that have access to only the first-order information of the cost function such as the value and the gradient of the objective as well as the Lipschitz constant L .

work constructs a momentum method that achieves the fastest possible convergence. However, each iteration of the optimized momentum method in [9] requires substantial memory space and computational cost for storing and (weighted-)summing all previous gradients. Here we propose a practical approach to circumvent this burden.

Section II and III review Nesterov’s momentum method [6] and DT’s optimized momentum method [9]. Section IV discusses the computational burden of the optimized momentum method and provides a much more practical approach. We combine this proposed computationally-efficient optimized momentum method with OS methods, and examine the acceleration using 2D CT simulation data, compared to OS methods with Nesterov’s method.

II. NESTEROV’S MOMENTUM METHOD

Table I summarizes Nesterov’s momentum method [6], which reduces to a gradient descent (GD) method when $t^{(n)} = 1$ for all $n \geq 0$. The difference between $z^{(n+1)}$ and $z^{(n)}$ plays the role of momentum with carefully chosen coefficient $t^{(n)}$, where $(t^{(n)} - 1)/t^{(n+1)}$ increases from 0 to 1 as the algorithm iterates. This algorithm requires only one extra image storage and minimal additional computation in line 5 of Table I compared to GD, while significantly accelerating convergence.

1:	Initialize $x^{(0)} = z^{(0)}$ and $t^{(0)} = 1$.
2:	for $n = 0, 1, \dots, N - 1$
3:	$t^{(n+1)} = \frac{1}{2} \left(1 + \sqrt{1 + 4 [t^{(n)}]^2} \right)$
4:	$z^{(n+1)} = x^{(n)} - \frac{1}{L} \nabla \Psi(x^{(n)})$
5:	$x^{(n+1)} = z^{(n+1)} + \frac{t^{(n)} - 1}{t^{(n+1)}} (z^{(n+1)} - z^{(n)})$

TABLE I
NESTEROV’S MOMENTUM METHOD [6]

Nesterov’s method in Table I satisfies the following convergence rate inequality² at any n th iteration [6]:

$$\Psi(z^{(n)}) - \Psi(\hat{x}) \leq \frac{2L \|x^{(0)} - \hat{x}\|^2}{(n + 1)^2} \quad (3)$$

for all functions $\Psi(x)$ in $\mathcal{F}_L(\mathbb{R}^{N_p})$. The right term of (3) is the worst-case bound of Nesterov’s momentum method [6]; Section III reviews the optimized momentum method that achieves the lowest worst-case bound.

In [7], we combined Nesterov’s method in Table I with OS methods [4], [5] for X-ray CT reconstruction (2) by replacing

²DT [9] numerically showed that the sequence $\{x^{(n)}\}$ in Table I satisfies the inequality (3) of $\{z^{(n)}\}$ for many choices of n .

$\nabla\Psi(x)$ by the following approximation:

$$\nabla\Psi(x) \approx MA'_m W_m (A_m x - y_m) + \nabla R(x) \quad (4)$$

for $m = 1, \dots, M$, where A_m , W_m and y_m are submatrices of A , W and y corresponding to m th subset of projection views out of total M subsets, yielding M -times reduced computational cost per update. So, we count one iteration after we visit M subsets considering the use of A and A' per update. Combining OS and Nesterov's momentum provided fast M^2 -times initial acceleration [7], unlike M -times acceleration from conventional OS methods.

III. OPTIMIZED MOMENTUM METHODS

A. Achievable convergence rate of momentum methods

Nesterov's method [6] in Table I achieves the optimal rate $O(1/n^2)$, since Nesterov [8] found one function in $\mathcal{F}_L(\mathbb{R}^{N_p})$ that cannot be minimized faster than $O(1/n^2)$ by all momentum methods using only the gradient information and the Lipschitz constant L [8]. In particular, any momentum method generating $\{x^{(n)}\}$ satisfies the following lower bound:

$$\frac{3L\|x^{(0)} - \hat{x}\|^2}{32(n+1)^2} \leq \Psi(x^{(n)}) - \Psi(\hat{x}) \quad (5)$$

for at least one function $\Psi(x)$ in $\mathcal{F}_L(\mathbb{R}^{N_p})$. The constant in (3) is $\frac{64}{3}$ -times larger than that in (5), showing potential room for improving Nesterov's method in Table I.

B. Optimized momentum in N -iterations (OptMom- N)

DT [9] proposed an optimized momentum method that minimizes the upper-bound of $\Psi(x^{(N)}) - \Psi(\hat{x})$ for a given total number of iterations N among all possible momentum methods, achieving a lower bound with a constant smaller than 2 in (3) (but larger than $3/32$ in (5)). Our work was inspired by [9].

All momentum algorithms using a Lipschitz constant L can be written in the following general form [9]:

$$x^{(n+1)} = x^{(n)} - \frac{1}{L} \sum_{k=0}^n h_k^{(n)} \nabla\Psi(x^{(k)}) \quad (6)$$

for $n = 0, \dots, N-1$, where each update is a weighted sum of all previous gradients with (precomputed) coefficients $\{h_k^{(n)}\}$. A constant-step GD has the form (6) with $h_k^{(n)} = 1$ for $k = n$, and 0 otherwise. Nesterov's method in Table I has this form (6) with the following coefficients [9]:

$$\bar{h}_k^{(n)} = \begin{cases} \frac{t^{(n)}-1}{t^{(n+1)}} \bar{h}_k^{(n-1)}, & 0 \leq k \leq n-2 \\ \frac{t^{(n)}-1}{t^{(n+1)}} (\bar{h}_{n-1}^{(n-1)} - 1), & k = n-1 \\ 1 + \frac{t^{(n)}-1}{t^{(n+1)}}, & k = n \end{cases} \quad (7)$$

for $n = 0, \dots, N-1$ and $t^{(n)}$ in Table I. These coefficients $\{\bar{h}_k^{(n)}\}$ are independent of N , and Table II shows a few of them. The analysis using (6) and (7) means that both Table I and the algorithm (6) with $\{\bar{h}_k^{(n)}\}$ in (7) will generate the same sequence of images. However, using (7) in (6) would require storing all previous gradients and (weighted)-summing all of them at each update, whereas Table I uses a computationally efficient recursion.

Coefficients $\{\bar{h}_k^{(n)}\}$ for Nesterov's momentum method [6]					
n \ k	0	1	2	3	4
0	1.0000				
1	0.0000	1.2818			
2	0.0000	0.1223	1.4340		
3	0.0000	0.0649	0.2305	1.5311	
4	0.0000	0.0389	0.1380	0.3180	1.5988

Coefficients $\{\hat{h}_k^{(n)}\}$ of DT's momentum method [9] for $N = 5$					
n \ k	0	1	2	3	4
0	1.6180				
1	0.1741	2.0194			
2	0.0756	0.4425	2.2317		
3	0.0401	0.2350	0.6541	2.3656	
4	0.0178	0.1040	0.2894	0.6043	2.0778

TABLE II
COEFFICIENTS OF NESTEROV'S $\{\bar{h}_k^{(n)}\}$ (7) AND DT'S $\{\hat{h}_k^{(n)}\}$ (9)
MOMENTUM METHODS.

DT [9] consider measuring the worst-case bound for a given number of iterations N , a given upper bound B of the distance between $x^{(0)}$ and \hat{x} , and a given candidate set of coefficients $\{h_k^{(n)}\}$:

$$P_{N,B}(\{h_k^{(n)}\}) \triangleq \max_{\Psi(x) \in \mathcal{F}_L(\mathbb{R}^{N_p})} \left\{ \Psi(x^{(N)}) - \Psi(\hat{x}) \right\} \quad (8)$$

$$\text{s.t. } x^{(n+1)} = x^{(n)} - \frac{1}{L} \sum_{k=0}^n h_k^{(n)} \nabla\Psi(x^{(k)}), \quad n = 0, \dots, N-1,$$

$$\|x^{(0)} - \hat{x}\| \leq B.$$

Since this problem (8) is intractable due to the functional constraint $\Psi(x) \in \mathcal{F}_L(\mathbb{R}^{N_p})$, DT relax (8) by replacing the functional constraint on $\Psi(x)$ by a basic property of the $\mathcal{F}_L(\mathbb{R}^{N_p})$ functions [8, Theorem 2.1.5]:

$$\frac{1}{2L} \|\nabla\Psi(x) - \nabla\Psi(z)\|^2 \leq \Psi(x) - \Psi(z) - \nabla\Psi(z)'(x - z)$$

for all $x, z \in \mathbb{R}^{N_p}$. Even then, the problem needs several mathematical tricks to finally be transformed to a solvable semidefinite programming (SDP) problem.³

DT [9] use (8) to find the "optimized" coefficients $\{\hat{h}_k^{(n)}\}$ that minimize the worst-case bound for a given N as:

$$\{\hat{h}_k^{(n)}\} = \arg \min_{\{h_k^{(n)}\}} P_{N,B}(\{h_k^{(n)}\}), \quad (9)$$

and similarly, the problem (9) eventually becomes an SDP problem in [9]. Here, a solution $\{\hat{h}_k^{(n)}\}$ of (9) is independent of B [9]. An update (6) using the optimized coefficients $\{\hat{h}_k^{(n)}\}$ computed from (9) for a given N becomes an optimized momentum method in N -iterations (OptMom- N) [9].

For example, Table II shows the optimized coefficients $\{\hat{h}_k^{(n)}\}$ for $N = 5$ computed from (9), achieving the following inequality at the final $N = 5$ th iteration:

$$\Psi(x^{(5)}) - \Psi(\hat{x}) \leq 0.67 \frac{L\|x^{(0)} - \hat{x}\|^2}{(5+1)^2}. \quad (10)$$

The constant here is less than half of that of Nesterov's method in (3) for $n = 5$. This (more than twice) acceleration has been confirmed for multiple choices of N in [9].

³We used CVX [10] to solve SDP programs in our experiments.

Similar to combining Nesterov's momentum with OS methods [7], here we consider combining DT's OptMom- N framework with OS methods to achieve faster convergence than OS methods with Nesterov's momentum. However, the substantial computational cost and storage requirements remain large in (6) in general. The next section describes a practical approach to reducing this burden while maintaining fast convergence rate.

IV. PROPOSED EFFICIENT IMPLEMENTATION OF OPTIMIZED MOMENTUM METHODS IN N -ITERATIONS

The general momentum methods in (6) require storing all previous gradients and (weighted-)summing them at each update. In contrast, Table I provides a clever method that uses minimal extra memory and is computationally efficient, implicitly using the coefficients in (7). In this paper, we propose an efficient version of DT's OptMom- N framework [9] in terms of memory and computation, instead of using the general recursion (6), by constraining the coefficients $\{h_k^{(n)}\}$ so that the implementation is efficient while preserving the fast convergence rate.

To transform the general momentum method (6) into a computationally efficient algorithm, we consider two modifications of (6). Firstly, we constrain the method to store at most $n_w + 1$ linear combinations of gradient vectors in $\{G_0, \dots, G_{n_w}\}$, so that the extra memory relative to GD is a fixed amount instead of growing with each iteration. This restriction is essential for a method to be practical in 3D CT. Secondly, we constrain the coefficients $\{h_k^{(n)}\}$ to satisfy the following condition:

$$h_{k-1}^{(n)} = \beta_k h_k^{(n)}, \quad (11)$$

for all $1 \leq k \leq n - n_w$ and $0 \leq n < N$, where $\{\beta_k\}$ is a set of multiplicative factors that we will optimize. The condition (11) enables the method to update recursively a weighted-sum of a part of previous gradients $\{\nabla\Psi(x^{(0)}), \dots, \nabla\Psi(x^{(n-n_w)})\}$ in one image memory space G_0 at the $n(\geq n_w)$ th iteration as:

$$G_0^{(n)} \triangleq \sum_{k=0}^{n-n_w} \frac{h_k^{(n)}}{h_{n-n_w}^{(n)}} \nabla\Psi(x^{(k)}) = \sum_{k=0}^{n-n_w} \left(\prod_{l=k+1}^{n-n_w} \beta_l \right) \nabla\Psi(x^{(k)})$$

$$= \beta_{n-n_w} G_0^{(n-1)} + \nabla\Psi(x^{(n-n_w)}). \quad (12)$$

We use the remaining memory space $\{G_1, \dots, G_{n_w}\}$ for storing the n_w most recent gradients $\{\nabla\Psi(x^{(n-n_w+1)}), \dots, \nabla\Psi(x^{(n)})\}$ separately. Table III describes the corresponding efficient implementation of (6) for coefficients $\{h_k^{(n)}\}$ that satisfy the constraint (11).

1:	Initialize $x^{(0)}$, N , n_w , and $G_l = 0$ for $l = 0, \dots, n_w$.
2:	Choose $\{\beta_k\}_{k=1}^{N-n_w}$ and $\{\{h_l^{(n)}\}_{l=n-n_w}^n\}_{n=0}^{N-1}$.
3:	for $n = 0, 1, \dots, N - 1$
4:	if $n \leq n_w - 1$
5:	$G_{n+1} \leftarrow \nabla\Psi(x^{(n)})$
6:	else
7:	$G_0 \leftarrow \beta_{n-n_w} G_0 + G_1$
8:	$G_l \leftarrow G_{l+1}$ for $l = 1, \dots, n_w - 1$
9:	$G_{n_w} \leftarrow \nabla\Psi(x^{(n)})$
10:	endif
11:	$x^{(n+1)} = x^{(n)} - \frac{1}{L} \left(\sum_{l=1}^{n_w} h_{n-n_w+l}^{(n)} G_l + h_{n-n_w}^{(n)} G_0 \right)$

TABLE III
PROPOSED EFFICIENT IMPLEMENTATION OF OPTIMIZED MOMENTUM METHODS IN N -ITERATIONS.

To optimize the factors $\{\beta_k\}$ in (11) and Table III, we insert the condition (11) in (9) and solve a modified SDP problem. Alternatively, as a simpler approach, we can project the optimized coefficients computed from (9) onto the subspace of coefficients satisfying (11). Interestingly, we found empirically that the optimized coefficients $\{\hat{h}_k^{(n)}\}$ computed from (9) satisfy the condition (11) for any⁴ $n_w \geq 1$. Thus, we chose the smallest $n_w = 1$, which requires same memory space and computational cost as Nesterov's method in Table I. Finally, the momentum method in Table III with $n_w = 1$, $\{\beta_k \triangleq \hat{h}_{k-1}^{(N-1)} / \hat{h}_k^{(N-1)}\}_{k=1}^{N-n_w}$ and $\{\{\hat{h}_l^{(n)}\}_{l=n-n_w}^n\}_{n=0}^{N-1}$ using $\{\hat{h}_k^{(n)}\}$ in (9) becomes our proposed efficient implementation of an optimized momentum in N -iterations (EffOptMom- N).

⁴We recently found an analytical solution for $\{\hat{h}_k^{(n)}\}$ of (9) that we will submit to arXiv in near future.

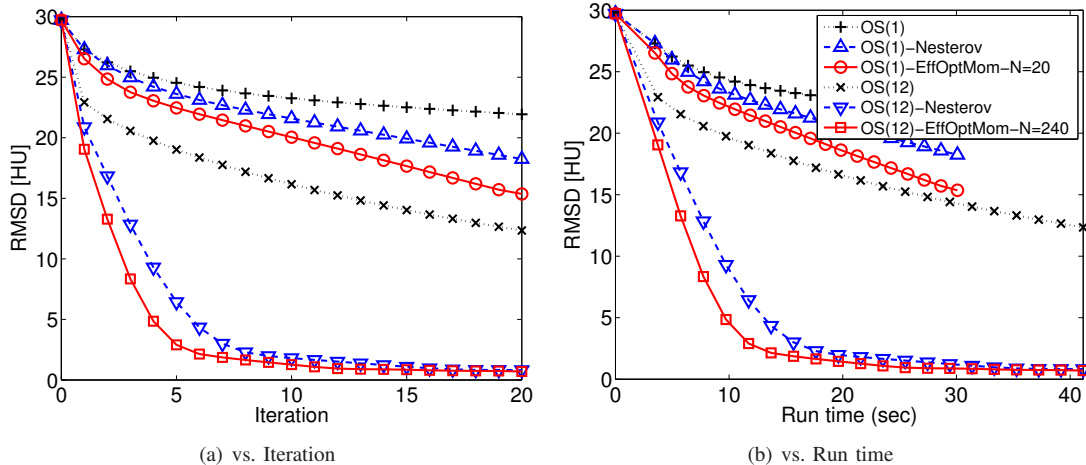


Fig. 1. Plots of RMSD [HU] versus (a) iteration and (b) run time (sec) for OS methods using 1 and 12 subsets with and without momentum techniques. Each iteration of OS methods with 12 subsets performs 12 sub-iterations.

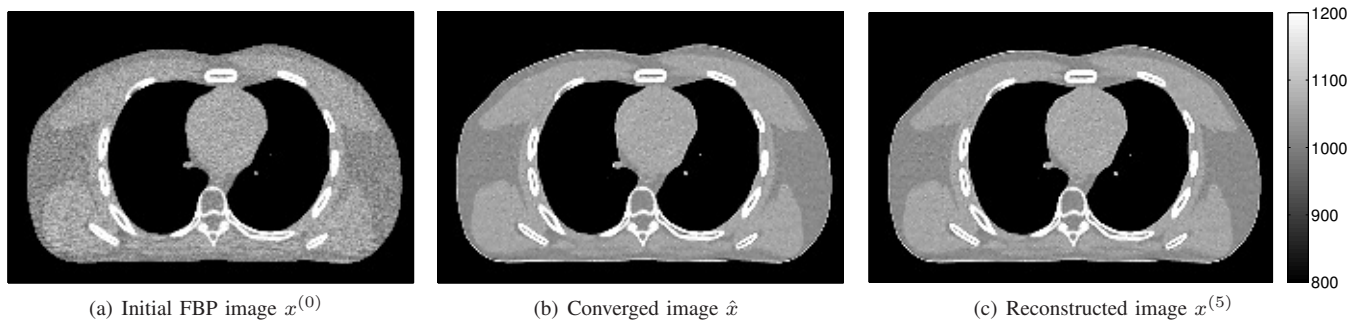


Fig. 2. 2D XCAT simulation: (a) an initial FBP image $x^{(0)}$, (b) a converged image \hat{x} , and (c) a reconstructed image $x^{(5)}$ from 5 iterations of the proposed OS(12)-EffOptMom- $N = 240$ algorithm using 12 subsets.

For further acceleration, we combine the efficient version of the optimized momentum method in Table III with OS methods, by replacing $\nabla\Psi(x)$ with (4). We expect this OS-EffOptMom- N method to converge faster than OS methods with Nesterov’s momentum method. We also replaced the $1/L$ factor in Table III with a diagonal matrix D^{-1} based on separable quadratic surrogates [5], [11]; this D is easier to compute than the (smallest) Lipschitz constant L .

V. RESULTS

We simulated 2D fan-beam CT 492×444 noisy sinogram data from a 512×512 XCAT phantom image [12]. We reconstructed a 256×256 image from the sinogram using OS methods (1 and 12 subsets) with and without momentum techniques for 20 iterations.

Fig. 1 illustrates the root mean square difference (RMSD) between $x^{(n)}$ and the converged image \hat{x} in Hounsfield Units (HU):

$$\text{RMSD}^{(n)} = \frac{\|x^{(n)} - \hat{x}\|}{\sqrt{N_p}} \text{ [HU]} \quad (13)$$

versus both iteration and run time, to evaluate the convergence rate. The results show that two momentum techniques provide acceleration. Particularly, the proposed EffOptMom- $N = 20$ algorithm reaches the converged image faster than Nesterov’s method in both iteration and run time, as expected. Even though the (Eff)OptMom- N algorithm is known to achieve the fast convergence only at the final N th iteration, the algorithm shows acceleration within all N iterations in this experiment.

In Fig. 1, using 12 subsets in OS methods accelerated all algorithms, even though it slightly increased the computation time per iteration for executing 12 sub-iterations per each iteration. The EffOptMom- N algorithm with OS(12) method for 20 iterations requires $N = 240$ sub-iterations, leading to solving a large SDP problem (9) with $N = 240$ to compute the optimized coefficients $\{\hat{h}_k^{(n)}\}$. However, these coefficients can be precomputed for a given N regardless of the data set, so we can neglect the computation of SDP problem in practice (and in Fig. 1). Considering a large $N = 240$, we note that an (inefficient) OptMom- $N = 240$ framework would require 240 image space, while our proposed efficient implementation uses only one extra image space for storing a linear combination of previous gradients.

Fig. 2 shows an initial filtered back-projection (FBP) image $x^{(0)}$, a converged image \hat{x} , and a reconstructed image from 5 iterations of the proposed EffOptMom- N algorithm with OS(12) method. The result indicates that we can reach nearby the converged image within very few iterations using the proposed algorithm.

VI. CONCLUSION

We proposed an efficient implementation of optimized momentum [9] in N -iterations for X-ray CT image reconstruction and showed that it converges faster in both N -iterations and run time than Nesterov’s method. We combined it with OS methods for further acceleration, leading to faster convergence than our previous combination of OS methods and Nesterov’s momentum method [7]. We will next investigate this acceleration in real 3D CT data.

REFERENCES

- [1] J-B. Thibault, K. Sauer, C. Bouman, and J. Hsieh, “A three-dimensional statistical approach to improved image quality for multi-slice helical CT,” *Med. Phys.*, vol. 34, no. 11, pp. 4526–44, Nov. 2007.
- [2] Y. Long, J. A. Fessler, and J. M. Balter, “3D forward and back-projection for X-ray CT using separable footprints,” *IEEE Trans. Med. Imag.*, vol. 29, no. 11, pp. 1839–50, Nov. 2010.
- [3] K. Sauer and C. Bouman, “A local update strategy for iterative reconstruction from projections,” *IEEE Trans. Sig. Proc.*, vol. 41, no. 2, pp. 534–48, Feb. 1993.
- [4] H. M. Hudson and R. S. Larkin, “Accelerated image reconstruction using ordered subsets of projection data,” *IEEE Trans. Med. Imag.*, vol. 13, no. 4, pp. 601–9, Dec. 1994.
- [5] H. Erdoğan and J. A. Fessler, “Ordered subsets algorithms for transmission tomography,” *Phys. Med. Biol.*, vol. 44, no. 11, pp. 2835–51, Nov. 1999.
- [6] Y. Nesterov, “A method for unconstrained convex minimization problem with the rate of convergence $O(1/k^2)$,” *Dokl. Akad. Nauk. USSR*, vol. 269, no. 3, pp. 543–7, 1983.
- [7] D. Kim, S. Ramani, and J. A. Fessler, “Ordered subsets with momentum for accelerated X-ray CT image reconstruction,” in *Proc. IEEE Conf. Acoust. Speech Sig. Proc.*, 2013, pp. 920–3.
- [8] Y. Nesterov, *Introductory lectures on convex optimization: A basic course*, Kluwer, 2004.
- [9] Y. Drori and M. Teboulle, “Performance of first-order methods for smooth convex minimization: A novel approach,” *Mathematical Programming*, 2013.
- [10] M. Grant, S. Boyd, and Y. Ye, “Disciplined convex programming,” 2006.
- [11] D. Kim, D. Pal, J-B. Thibault, and J. A. Fessler, “Accelerating ordered subsets image reconstruction for X-ray CT using spatially non-uniform optimization transfer,” *IEEE Trans. Med. Imag.*, vol. 32, no. 11, pp. 1965–78, Nov. 2013.
- [12] W. P. Segars, M. Mahesh, T. J. Beck, E. C. Frey, and B. M. W. Tsui, “Realistic CT simulation using the 4D XCAT phantom,” *Med. Phys.*, vol. 35, no. 8, pp. 3800–8, Aug. 2008.

Adaptive Sparsifying Transforms for Iterative Tomographic Reconstruction

Luke Pfister* and Yoram Bresler*

Abstract—A major challenge in computed tomography imaging is to obtain high-quality images from low-dose measurements. Key to this goal are computationally efficient reconstruction algorithms combined with detailed signal models. We show that the recently introduced adaptive sparsifying transform (AST) signal model provides superior reconstructions from low-dose data at significantly lower cost than competing dictionary learning methods. We further accelerate this technique for tomography by utilizing the Linearized Alternating Direction Method of Multipliers (L-ADMM) to remove the need to solve an expensive least-squares problem that requires computing multiple forward and backward projections. Numerical experiments on data from clinical CT images show that adaptive sparsifying transform regularization outperforms total-variation and dictionary learning methods, and combining our regularizer with L-ADMM provides for faster reconstructions than standard ADMM.

I. INTRODUCTION

The increased use of x-ray computed tomography (CT) in medical imaging has been accompanied by increased concerns about the x-ray exposure to the patient population. The ability to reconstruct high quality images from low-dose data has therefore become a central problem in CT. Advances in image reconstruction algorithms are key to achieving this goal. Unlike the standard filtered backprojection (FBP) algorithm, iterative reconstruction algorithms incorporate detailed models of data acquisition, noise statistics, and the signal to reconstruct. These algorithms are commonly developed as the solution to the penalized weighted-least squares (PWLS) problem [1]

$$\min_x \frac{1}{2} \|y - Ax\|_W^2 + \lambda J(x). \quad (1)$$

The first term represents a statistically weighted fidelity measure between the data vector $y \in \mathbb{R}^M$, containing the log of received photon counts, and the reprojected image Ax . The diagonal weighting matrix W consists of statistical weights w_i and can be motivated as a quadratic approximation to the negative log-likelihood of the image given the photon counts.

The regularization functional $J : \mathbb{R}^N \rightarrow \mathbb{R}$ improves the conditioning of (1) and encourages solutions that obey a prescribed signal model. Signal models based on sparse representations have shown to be effective for both low-dose and limited data tomography. These models have classically been instances of *analysis* sparsity, in which the image becomes sparse when acted on by a fixed linear transformation called an analysis operator. Many regularizers, such as total-variation, promote images that are sparse under finite differencing operators and are thus piecewise constant. This type

of regularization can replace complex texture by flat, patchy regions. Regularization with more sophisticated analysis operators, such as shearlets, has been shown to better preserve complex texture at the expense of performance on uniform regions [2].

Recent years have shown the promise of signal models that are directly adapted to the signal of interest. A popular approach is to represent small, overlapping patches of the image as the linear combination of a few columns of a dictionary. Many algorithms have been proposed to fit a dictionary to a given set of data. Algorithms that jointly learn a dictionary while reconstructing the image have been shown to outperform traditional regularization techniques in both low-dose [3] and limited-data tomography [4]. More recently, algorithms have been developed to adaptively learn analysis operators based on manifold methods [5], variable-splitting methods [6], and modifications of dictionary learning algorithms [7].

Unfortunately, both synthesis and analysis learning algorithms scale poorly with data size and are prohibitively expensive for practical tomographic reconstruction. An alternative signal model is to assume that our signal satisfies $\Phi x = z + e$, where z is sparse and e is small. This is called the *transform model* and stipulates that x should be approximately sparse when acted on by the matrix $\Phi \in \mathbb{R}^{k \times k}$, which we call a sparsifying transform. Algorithms have been proposed to learn sparsifying transforms directly from data [8], [9]. Allowing a small deviation from exact sparsity facilitates transform learning algorithms that are much faster than competing synthesis dictionary and analysis operator learning algorithms. Adaptive sparsifying transforms have been shown to be effective in MRI reconstruction from sparsely sampled data [10].

In this paper, we show that adaptive sparsifying transform (AST) regularization outperforms both TV and synthesis dictionary methods for low-dose CT imaging, while operating at a speed rivaling that of TV [11]. Our algorithms use the Alternating Direction Method of Multipliers (ADMM) to provide a computationally efficient solution to the resulting optimization problem. The computational cost of the algorithms is dominated by solving an unweighted least squares problem that requires many applications of A and A^T . We propose the use of the Linearized ADMM algorithm to circumvent this least-squares problem and further accelerate AST-regularized tomographic reconstruction. Numerical experiments are performed using reprojected clinical images. The results show that AST regularization outperforms dictionary learning and total variation methods and that Linearized ADMM provides an appreciable decrease in computation time.

*Dept. of Electrical and Computer Engineering, University of Illinois at Urbana-Champaign

This work was supported in part by the National Science Foundation (NSF) under grants CCF-1018660 and CCF-1320953.

II. ALGORITHM

Our goal is to reconstruct our image $x \in \mathbb{R}^N$ from noisy projection data $y \in \mathbb{R}^M$ while simultaneously learning a sparsifying transform Φ that acts on $\sqrt{k} \times \sqrt{k}$ patches of x . We accomplish this by solving

$$\min_{x, z, \Phi} \frac{1}{2} \|y - Ax\|_W^2 + \frac{\lambda}{2} \sum_j \|\Phi E_j x - z_j\|_2^2 + \lambda (\gamma \|z_j\|_0 + \alpha (\|\Phi\|_F^2 - \log \det \Phi)), \quad (\text{P1})$$

where λ , γ and α are positive scalar parameters, and $\|z_j\|_0$ is the ℓ_0 quasinorm that counts the number of nonzero elements in z_j . The matrix $E_j \in \mathbb{R}^{k \times N}$ extracts the j th $\sqrt{k} \times \sqrt{k}$ vectorized patch and removes its mean. The second term in (P1) penalizes the sparsification error of patches from x , while the third term encourages sparsity in the z_j . The final two terms ensure that the learned transform is both non-singular and well conditioned. The minimization problem (P1) can be viewed as a PWLS problem where the regularizer is itself the solution of a minimization problem.

We solve (P1) using an alternating minimization algorithm. With x and the z_j fixed, we update Φ by solving

$$\Phi^{k+1} = \arg \min_{\Phi} \sum_j \|\Phi E_j x - z_j\|_2^2 + \alpha (\|\Phi\|_F^2 + \log \det \Phi), \quad (2)$$

which can be solved in closed-form [12], requiring only three products of $k \times N$ and $N \times k$ matrices and one Cholesky decomposition and one SVD of $k \times k$ matrices. Typically $k \ll N$ and so the solution of (2) is cheap.

With x and Φ fixed, we update each z_j by solving

$$z_j^{k+1} = \arg \min_{z_j} \gamma \|z_j\|_0 + \frac{1}{2} \|\Phi E_j x - z_j\|_2^2. \quad (3)$$

The solution of (3) is given in closed form by setting to zero all entries with magnitude less than $\sqrt{\gamma}$, an operation known as *hard thresholding*. We will write this update as $z_j = \mathcal{T}_{\gamma}(\Phi E_j x)$.

In practice, we ensure that Φ is a good transform for the current image by alternating between updating Φ and the z_j a few times before proceeding to the image update phase.

The image update phase begins by fixing Φ and the z_j . Then, (P1) reduces to the weighted least squares problem

$$x^{k+1} = \arg \min_x \frac{1}{2} \|y - Ax\|_W^2 + \lambda \sum_j \|\Phi E_j x - z_j\|_2^2. \quad (4)$$

Owing to the size of A , direct inversion is impossible and we must resort to iterative methods. The large dynamic range in W causes the Hessian $A^T W A + \lambda \sum_j E_j^T \Phi^T \Phi E_j W$ to be poorly conditioned and many iterations are required, while the placement of W makes this problem highly shift-variant and prohibits the use of efficient Fourier preconditioners [13].

Ramani & Fessler [14] proposed the use ADMM to mitigate these problems by introducing an auxiliary variable $u \in \mathbb{R}^M$. The constraint $u = Ax$ is used to split the data fidelity term and separate the projection operator A from the statistical weighting matrix W . Applying ADMM to the new constrained

optimization problem results in an algorithm consisting of the following update steps:

$$x^{k+1} = \arg \min_x \frac{\lambda}{2} \sum_j \|\Phi E_j x - z_j\|_2^2 + \frac{\mu}{2} \|u^k - \eta^k - Ax\|_2^2 \quad (5)$$

$$u^{k+1} = \arg \min_u \frac{1}{2} \|y - u\|_W^2 + \frac{\mu}{2} \|u^k - \eta^k - Ax\|_2^2 \quad (6)$$

$$\eta^{k+1} = \eta^k - (u^{k+1} - Ax^{k+1}). \quad (7)$$

These subproblems are solved in an alternating fashion. Subproblem (6) is solved as

$$u^{k+1} = (W + \mu I)^{-1} (Wy + \mu (Ax^{k+1} + \eta^k)), \quad (8)$$

which is computationally inexpensive as $W + \mu I$ is diagonal. Similarly, (7) requires only vector additions and is cheap.

The bulk of computation occurs during the solution of subproblem (5). This is an unweighted least-squares problem and is amenable to Fourier-based preconditioners. However, even when an efficient preconditioner is used, the solution of (5) requires many products with A and A^T and thus remains computationally expensive.

We propose to accelerate this step by using the Linearized ADMM (L-ADMM) approach. This technique has been developed under many names and in multiple contexts; see [15] and the references within. We begin by introducing a new inertia term into the x -update subproblem (5):

$$x^{k+1} = \arg \min_x \frac{\lambda}{2} \sum_j \|\Phi E_j x - z_j\|_2^2 + \frac{\mu}{2} \|u^k - \eta^k - Ax\|_2^2 + \|x - x^k\|_Q^2 \quad (9)$$

where Q is a positive-definite matrix that can be chosen to improve the conditioning of this least squares problem. In particular, we take $Q = \delta I - \mu A^T A$ and the updated image is now given by the solution of

$$Gx^{k+1} = \lambda \sum_j E_j^T \Phi^T z_j + \delta x^k + \mu A^T (u^k - \eta^k - Ax^k) \quad (10)$$

where $G \triangleq \lambda \sum_j E_j^T \Phi^T \Phi E_j + \delta I$. We have used the matrix Q to eliminate the influence of $A^T A$ from the Hessian G .

The solution of (10) depends on the boundary conditions present in the patch extraction operators E_j . As the region of interest in CT images is surrounded by air, which provides zero attenuation, we are free to extract patches that wrap around the image boundary without incurring distortion. In this case, the quantity $\sum_j E_j^T \Phi^T \Phi E_j + \delta I$ is circularly shift-invariant and can be diagonalized using a 2D DFT. During the image update phase, Φ is held constant, so this diagonalization can be computed and stored. The solution of (10) can be computed in closed form and only requires a product with A and A^T as well as a 2D FFT/IFFT pair. This represents a significant improvement over the multiple products with $A^T A$ that are required to solve (5) using the conjugate gradient method. Note that as we do not solve a least squares problem, we do not need to precondition $A^T A$. This may prove especially beneficial for high angle cone beam CT and other geometries where circulant preconditioners are less effective.

Algorithm 1 L-AST-CT

INPUT: Initial transform Φ , observed data y **OUTPUT:** Reconstructed image x

```
1: Set  $\gamma$  by using power iteration on  $A^T A$ 
2:  $x^0 \leftarrow \text{FBP}(y)$ 
3:  $z_j^0 \leftarrow \mathcal{T}_\gamma(\Phi E_j x^0) \quad \forall j$ 
4: repeat
5:   repeat
6:     Update  $\Phi$  by solving (2)
7:      $z_j^k \leftarrow \mathcal{T}_\gamma(\Phi E_j x) \quad \forall j$ 
8:   until Halting condition
9:    $\tilde{G} \leftarrow$  diagonalization of  $\lambda \sum_j E_j^T \Phi^T \Phi E_j + \delta I$ 
10:   $i \leftarrow 0, u^0 \leftarrow Ax^k, v^0 \leftarrow \vec{0}$ 
11:  repeat
12:     $\zeta \leftarrow \text{FFT2} \left[ \lambda \sum_j E_j^T \Phi^T z_j + \right.$   

                               $\left. \delta x^k + \mu A^T (u^k - \eta^k - Ax^k) \right]$ 
13:     $\tilde{x}^{i+1} \leftarrow \text{IFFT2} \left[ \tilde{G}^{-1} \zeta \right]$ 
14:     $u^{i+1} \leftarrow (W + \mu I)^{-1} (Wy + \mu (A\tilde{x}^{i+1} + v^i))$ 
15:     $v^{i+1} \leftarrow v^i - (u^{i+1} - A\tilde{x}^{i+1})$ 
16:     $i \leftarrow i + 1$ 
17:  until Halting condition
18:   $x^{k+1} \leftarrow \tilde{x}^{i+1}$ 
19: until Halting condition
```

The parameter δ must be chosen to make $\delta I - \mu A^T A$ positive definite, so we require that $\delta > \mu \|A^T A\|_2$. We estimate this lower bound by performing power iteration on $A^T A$, and we take δ to be slightly larger than this estimate.

Note that the update (10) can alternatively be derived by linearizing the Augmented Lagrangian term in (5) about the point x^k and adding additional quadratic regularization. We choose to use the Q -norm notation as it clearly shows the required lower bound for δ . The overall algorithm, which we call L-AST-CT, is presented as Algorithm 1. We initialize the algorithm by taking x^0 to be a Hamming-weighted FBP of the data y . Our initial sparsifying transform is a separable approximation of the 2D finite differencing matrix.

III. EXPERIMENTS

The algorithm was implemented using NumPy 1.8 and SciPy 0.13 on a computer containing an Intel i5-2520m processor with two cores and 6GB of RAM. The projection operator A simulates the central slice of the GE Light-speed geometry, with 888 detector bins and 984 projections spaced between 0 and 360° . Forward and back projections were performed using a multithreaded C implementation of the distance-driven projector and backprojector to ensure a matched projector and backprojector pair.

Our error metric is the root mean square error (RMSE), defined for $x \in \mathbb{R}^N$ as $\text{RMSE} = \sqrt{\sum_{k=1}^N (x_k - \bar{x}_k)^2 / N}$, where x_k is the k -th index of x and \bar{x} is the ground truth image. We compare the performance of AST-CT to Hamming-weighted FBP reconstruction and two iterative reconstruction algorithms. The first uses total-variation regularization. We use ADMM to split the non-differentiable regularization term and refer to this algorithm as TV-CT. The second, which we call DL-CT, uses a regularizer of the form $J(x) = \min_{D, a_j} \sum_j \|E_j x - Da_j\|_2^2 + \gamma \|a_j\|_0$. The update for a is

solved using orthogonal matching pursuit from the efficient SPAMS¹ toolbox, and the dictionary update is performed using K-SVD. We use ADMM to separate W and A . In both TV-CT and DL-CT, we do not linearize the x -update step, but instead use a circulant preconditioner to improve the rate of convergence.

The parameters λ and γ were determined empirically by sweeping over a large range of values and choosing the parameter that corresponded to the lowest RMSE. For L-AST-CT and DL-CT, the ADMM parameter μ was chosen to ensure that the Hessian is well-conditioned, and for TV-CT it was chosen according to the strategy in [14]. The dictionary for DL-CT is of size 64×121 and is initialized with a DCT matrix, while in L-AST-CT the sparsifying transform is 64×64 and initialized with a separable approximation to the finite differencing matrix. Both algorithms use 8×8 patches with maximal overlap.

We evaluate the performance of the algorithm on data formed by reprojecting a 512×512 pixel clinical-dose CT image of a human abdomen. The clinical data consists of overlapping 0.9mm slices with 0.45mm overlap. The slices have noise standard deviation of 21 HU, as measured over a flat region in the liver. We form a ground truth image \bar{x} by averaging together 5 consecutive slices of the clinical data. This reduces streaking present in our \bar{x} . We form clinical dose data by taking the k -th detector measurement to be $y_k = -\log(P(I_0 \exp[-A\bar{x}]_k) / I_0)$, where $P(t)$ represents a Poisson random variable with mean t . Setting I_0 to 2.0×10^6 results in a noise level that matches that of the original slices. We synthesize low-dose data by taking $I_0 = 5 \times 10^5$ which corresponds to dose reduction by a factor of 4.

The TV-CT algorithm was run for 300 iterations. For DL-CT, each outer-loop iteration consists of five dictionary and sparse code updates followed by updating the image by performing 10 ADMM iterations. For L-AST-CT, the outer-loop consists of 10 sparsifying transform and sparse code updates followed by updating the image with a minimum of 30 L-ADMM iterations. In both cases, we repeat the ADMM/L-ADMM steps until the cost function has decreased. We use a total of 30 outer-loop iterations for L-AST-CT and DL-CT.

Figure 1 show the images reconstructed with each algorithm and the magnitude of the difference between the reconstructed images and \bar{x} . FBP suffers from the expected streaking behavior due to the reduction in dose. The TV-CT reconstruction shows no streaking artifacts, but has patchy artifacts in textured areas such as the bone. Reconstructions with adaptive regularization show low error in both the bone and soft tissue. We see that L-AST-CT outperforms DL-CT in the bone regions.

Table II illustrates the amount of time spent on updating the signal models in single outer-loop iteration of DL-CT and L-AST-CT. Even with the highly efficient multithreaded C implementations provided by SPAMS, the dictionary learning steps are significantly more expensive than the sparsifying transform updates. As an alternative benchmark, the time to perform 10 ADMM image update iterations in DL-CT is

¹Available: <http://spams-devel.gforge.inria.fr/>

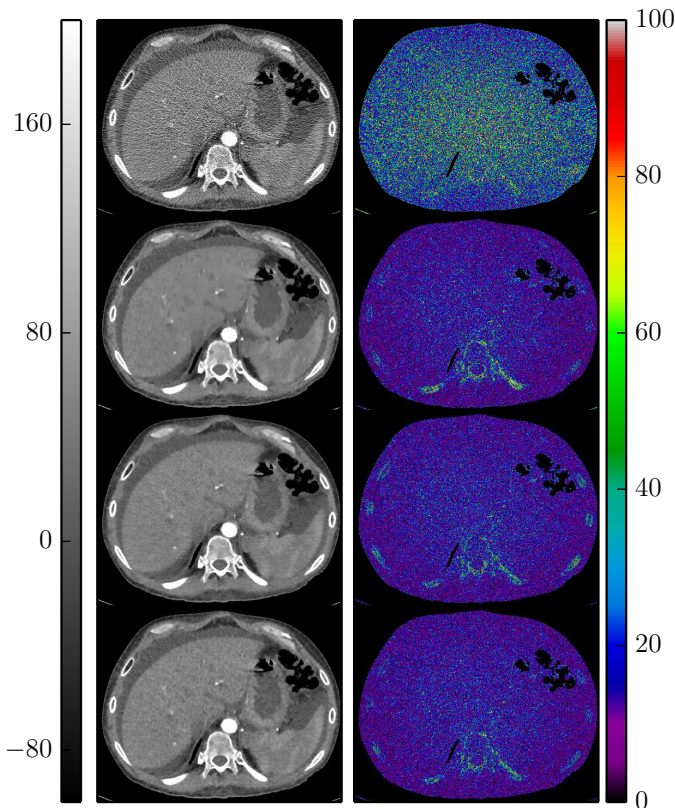


Fig. 1: Left column: Reconstruction from low-dose projections. Right column: Magnitude of error between reconstruction and \bar{x} . From top to bottom: FBP, TV-CT, DL-CT, L-AST-CT. All units in HU

TABLE I: RMSE in HU of reconstructions from low-dose data.

	Clinical dose FBP	Low dose FBP	L-AST-CT	DL-CT	TV-CT
RMSE	19	33	16	18	18

85 seconds. This shows that the use of dictionary learning regularization has nearly tripled the reconstruction time, while the overhead incurred by AST regularization is negligible.

We next evaluate the influence of the linearized x update step. We initialized Φ to be a separable finite differencing matrix and calculated the resulting z_j . We then fixed these variables and ran 4000 iterations of the usual ADMM algorithm to solve (4). The resulting image is denoted x^* . We then solved (4) using ADMM and L-ADMM and evaluate the distance from convergence as the RMSE between x^k and x^* . For ADMM, the least squares problem is solved by CG with a circulant preconditioner to the Hessian to accelerate convergence. Figure 2 shows the rate of convergence of both ADMM and L-ADMM. The quantity ϵ illustrates the RMSE of the ADMM reconstruction after performing the minimum 10 iterations. These results show that while L-ADMM requires more iterations to reach the value ϵ , it does so in roughly half the time as ADMM.

REFERENCES

[1] K. Sauer and C. Bouman, "A local update strategy for iterative reconstruction from projections," *IEEE Trans. Signal Process.*, vol. 41, no. 2, pp. 534–548, 1993.

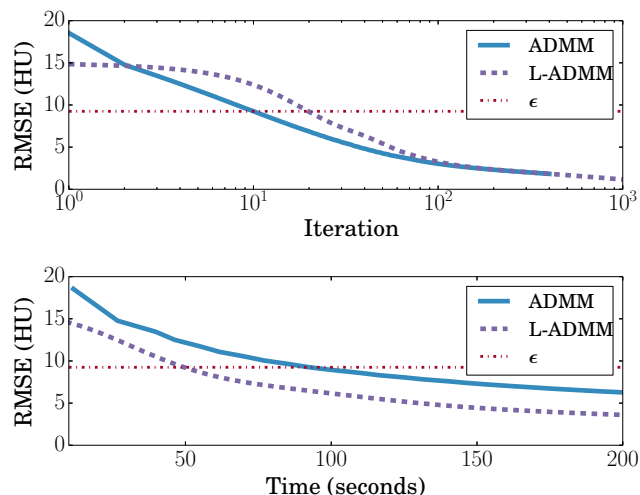


Fig. 2: Rate of convergence for ADMM and L-ADMM.

TABLE II: Amount of time to perform dictionary and transform learning steps. Units: seconds

	D/Φ Update	a/z Update	Total
DL-CT	87.5	60.3	147.8
L-AST-CT	4.4	0.2	4.6

[2] B. Vandeghinste, B. Goossens, R. Van Hoken, C. Vanhove, A. Pizurica, S. Vandenberghe, and S. Staelens, "Iterative CT reconstruction using shearlet-based regularization," *Proc. SPIE 8313 Medical Imaging*, vol. 8313, pp. 83 133I–83 133I–7, 2012.

[3] Q. Xu, H. Yu, and X. Mou, "Low-dose x-ray CT reconstruction via dictionary learning," *IEEE Trans. Med. Imag.*, vol. 31, no. 9, pp. 1682–1697, Sep. 2012.

[4] H. Y. Liao and G. Sapiro, "Sparse representations for limited data tomography," in *2008 5th IEEE International Symposium on Biomedical Imaging: From Nano to Macro*. IEEE, May 2008, pp. 1375–1378.

[5] S. Hawe, M. Kleinstueber, and K. Diepold, "Analysis operator learning and its application to image reconstruction," *IEEE Trans. Image Process.*, vol. 22, no. 6, pp. 2138–2150, June 2013.

[6] M. Yaghoobi, S. Nam, R. Gribonval, and M. E. Davies, "Constrained overcomplete analysis operator learning for cosparsely signal modelling," *IEEE Trans. Signal Process.*, vol. 61, no. 9, pp. 2341–2355, May 2013.

[7] R. Rubinstein, T. Peleg, and M. Elad, "Analysis K-SVD: A dictionary-learning algorithm for the analysis sparse model," *IEEE Trans. Signal Process.*, vol. 61, no. 3, pp. 661–677, Feb. 2013.

[8] S. Ravishanker and Y. Bresler, "Learning sparsifying transforms," *IEEE Trans. Signal Process.*, vol. 61, no. 5, pp. 1072–1086, 2013.

[9] S. Ravishanker and Y. Bresler, "Learning doubly sparse transforms for image representation," in *2012 19th IEEE International Conference on Image Processing*, no. 2. IEEE, Sep. 2012, pp. 685–688.

[10] S. Ravishanker and Y. Bresler, "Sparsifying transform learning for compressed sensing MRI," in *International Symposium on Biomedical Imaging*, 2013.

[11] L. Pfister, "Tomographic reconstruction with adaptive sparsifying transforms," M.S. thesis, University of Illinois at Urbana-Champaign, 2013.

[12] S. Ravishanker and Y. Bresler, "Closed-form solutions within sparsifying transform learning," in *Acoustics Speech and Signal Processing (ICASSP), 2013 IEEE International Conference on*, 2013.

[13] J. Fessler and S. Booth, "Conjugate-gradient preconditioning methods for shift-variant PET image reconstruction," *IEEE Trans. Image Process.*, vol. 8, no. 5, pp. 688–99, Jan. 1999.

[14] S. Ramani and J. Fessler, "A splitting-based iterative algorithm for accelerated statistical x-ray CT reconstruction," *IEEE Trans. Med. Imag.*, vol. 31, no. 3, pp. 677–688, Mar. 2012.

[15] X. Zhang, M. Burger, and S. Osher, "A unified primal-dual algorithm framework based on bregman iteration," *Journal of Scientific Computing*, vol. 46, no. 1, pp. 20–46, Jan. 2011.

Integration of Component Knowledge in Penalized-Likelihood Reconstruction with Morphological and Spectral Uncertainties

J. Webster Stayman, Steven Tilley II, Jeffrey H. Siewerdsen

Abstract—Previous investigations [1-3] have demonstrated that integrating specific knowledge of the structure and composition of components like surgical implants, devices, and tools into a model-based reconstruction framework can improve image quality and allow for potential exposure reductions in CT. Using device knowledge in practice is complicated by uncertainties in the exact shape of components and their particular material composition. Such unknowns in the morphology and attenuation properties lead to errors in the forward model that limit the utility of component integration. In this work, a methodology is presented to accommodate both uncertainties in shape as well as unknown energy-dependent attenuation properties of the surgical devices. This work leverages the so-called known-component reconstruction (KCR) framework [1] with a generalized deformable registration operator and modifications to accommodate a spectral transfer function in the component model. Moreover, since this framework decomposes the object into separate background anatomy and "known" component factors, a mixed fidelity forward model can be adopted so that measurements associated with projections through the surgical devices can be modeled with much greater accuracy. A deformable KCR (dKCR) approach using the mixed fidelity model is introduced and applied to a flexible wire component with unknown structure and composition. Image quality advantages of dKCR over traditional reconstruction methods are illustrated in cone-beam CT (CBCT) data acquired on a testbench emulating a 3D-guided needle biopsy procedure – i.e., a deformable component (needle) with strong energy-dependent attenuation characteristics (steel) within a complex soft-tissue background.

Index Terms—CT Reconstruction, Polyenergetic Beam Model, Metal Artifacts, Interventional cone-beam CT.

I. INTRODUCTION

Surgical devices including implants and tools are often present during imaging studies. This is particularly true for interventional imaging scenarios when such devices are delivered and placement of implants is assessed post-procedure. The devices themselves are often responsible for decreased image quality due to beam hardening, photon starvation, and other artifacts associated with metal components. A plethora of metal artifact correction schemes exist to mitigate such artifacts - often through strategies that replace low-fidelity data or treat those data as missing. Alternate approaches that avoid eliminating data through incorporation of component prior knowledge have

also been proposed. [1-3] These methods rely on a parameterization of the reconstruction problem where not only are traditional attenuation values estimated, but so are registration parameters associated with objects known to be in the imaging field - changing the traditional reconstruction problem into a joint registration and reconstruction.

While such methods have demonstrated the potential to greatly improve image quality, especially in the vicinity of the device, approaches like known-component reconstruction (KCR) typically rely on precise knowledge of the device. For example, the shape of the surgical device is presumed to be known precisely (e.g., from a CAD model) and the material composition is known so that attenuation of x-rays passing through the device can be modeled. Unfortunately, such information is not always available and the structure of components may not be precisely known.

Interventional imaging scenarios have the advantage that the surgical device is available pre-procedure allowing for a degree of calibration. This opportunity is leveraged in the following work that generalizes the KCR framework to allow for deformable registrations of a component whose composition is homogenous but unknown using an "in-air" calibration scan to characterize the energy-dependence of both the "known" component and the imaging system. The proposed deformable KCR (dKCR) approach incorporates a sophisticated forward model that integrates spectral effects, a nonlinear partial volume model, and detector blur.

The proposed dKCR method is applied to cone-beam CT testbench data of a phantom containing a metal wire of unknown composition and structure (diameter, length, and curvature), and compared to traditional reconstructions.

II. METHODS

A. Deformable Object Model and Forward Model

The KCR framework previously introduced a modified object model for integration of component knowledge. This model for a single known component in the field of view is

$$\mu(\mu_*, \lambda) = \mathbf{D}\{\mathbf{W}(\lambda)s_c\} \mu_* + \mathbf{W}(\lambda)\mu_c. \quad (1)$$

where μ_* denotes a vector of attenuation values representing the (unknown) background anatomy, μ_c is a vector of attenuation values for the (partially known) component, s_c is a mask that is zero for voxels inside the component and one outside, and $\mathbf{D}\{\cdot\}$ is an operator that converts a vector to a diagonal matrix. The operator \mathbf{W} represents a transformation operator parameterized by the vector λ

J. Webster Stayman, Steven Tilley II, and Jeffrey H. Siewerdsen are with the Department of Biomedical Engineering, Johns Hopkins University, Baltimore, MD 21212 USA (contact info: phone: 410-955-1314; fax: 410-955-1115; e-mail: web.stayman@jhu.edu).

This work supported in part by NIH grant R21EB014964.

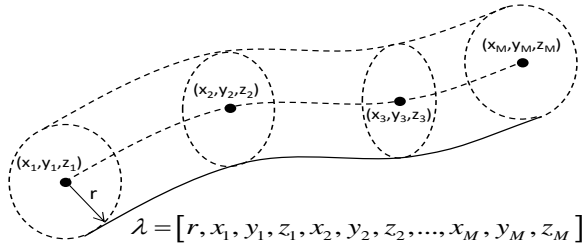


Fig. 1. A deformable cylinder that could represent a variety of components including needles, guide wires, and fixation rods. The curvature along the long axis of the cylinder is parameterized using a cubic b-spline with control points spaced along the length while an additional parameter defines the radius.

which allows for registration of the component and the associated mask.

In [1], a rigid transformation operator was used in (1); however, this form is general and provides the opportunity to accommodate additional uncertainty about components beyond position and pose. Consider a component with unknown morphology as in Figure 1. This class of deformed cylinder morphologies can be accommodated using the formulation in (1) with an appropriate selection of μ_C (i.e., a cylinder) and a parameterization λ comprised of control points along the deformed trajectory of the cylinder as well as the radius of the cylinder. In this work, a cubic b-spline parameterization of the curvature of the central axis of the cylinder is adopted. Note that more general parameterizations such as deformable meshes that define the shape of the component also fit into this framework but entail higher dimensional parameter vectors.

With the object model defined, a forward model may be adopted for use in model-based reconstruction. A traditional monoenergetic physical model is a convenient choice that leads to a relatively computationally efficient algorithm:

$$\bar{y}(\mu_*, \lambda) = \mathbf{D}\{g\} \exp(-\mathbf{A}\mu(\mu_*, \lambda)) \quad (2)$$

where \mathbf{A} denotes the system matrix that applies the projection operation and the vector g contains ray-dependent gain factors including detector sensitivities and x-ray beam intensity.

B. A Refined Forward Model for Known Components

The simple forward model in (2) is sufficient for many imaging applications; however, unmodeled beam

hardening, nonlinear partial volume (NLPV), and source/detector blur effects for measurements that include metal components can contribute to significant degradations in image quality. A more sophisticated forward model has the potential to mitigate artifacts associated with metal components; however, such modifications of the forward model are typically coupled with increased computational complexity.

Consider the two forward model choices in Figure 2: first, the standard forward model of (2); and second, a high-fidelity model that seeks to mitigate partial volume effects through fine sampling of both the image volume and detector pixels using a "high-resolution" system matrix, \mathbf{A}_{HR} , and a summation over detector subsamples. This formulation also permits detector blur modeling through weighted sums. The computational complexity increases cubically as voxel size decreases and increases with the square as detector subsample size decreases.

The object model in (1) provides an excellent opportunity to refine the object model for measurements associated with the component without adding a great deal of computation complexity. Consider the following decomposition of the forward model in (2) that leverages the object model in (1)

$$\begin{aligned} \bar{y}(\mu_*, \lambda) &= \mathbf{D}\{g\} \exp\left(-\mathbf{A}\left[\mathbf{D}\{\mathbf{W}(\lambda)s_C\}\mu_* + \mathbf{W}(\lambda)\mu_C\right]\right) \\ &= \mathbf{D}\{g\} F_A(\mu_*, \lambda) F_C(\mu_*, \lambda) \end{aligned} \quad (3)$$

$$F_A(\mu_*, \lambda) = \exp(-\mathbf{A}\mathbf{D}\{\mathbf{W}(\lambda)s_C\}\mu_*) \quad (4)$$

$$F_C(\lambda) = \exp(-\mathbf{A}\mathbf{W}(\lambda)\mu_C) \quad (5)$$

where F_A and F_C represent functional forms for the survival probabilities of x-ray photons as they pass through the background anatomy and the component voxels, respectively.

Thus, one can potentially refine the physical model for the component only (which is arguably where a sophisticated model is most important) which involves a smaller volume and smaller projection area than would be required for the entire image volume. The more compact support in both image and projection domains means that such high-fidelity component models can be applied efficiently in terms of storage and computation as compared with approaches that attempt a high-fidelity model for the entire image volume.

Consider the following model that incorporates a high-

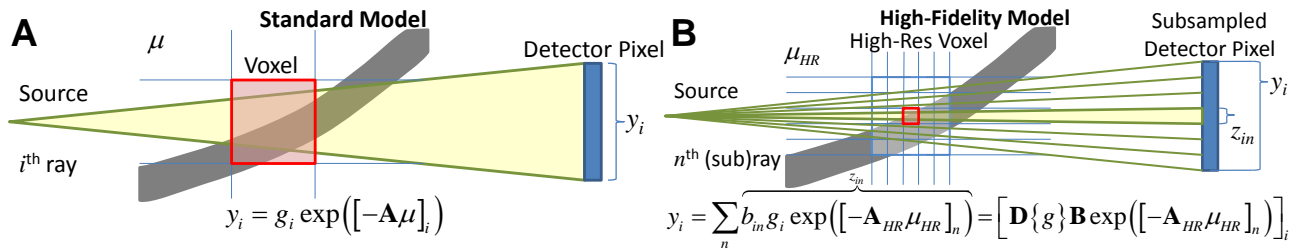


Fig. 2. An illustration of two different forward models with varying data fidelity. A) A standard forward model versus B) a high-fidelity model that can better approximate real-world physics by modeling detector aperture and partial volume effects using a high-resolution projector (\mathbf{A}_{HR}) and an integration over the detector aperture (with subelements z_m). Furthermore, with an additional weighting term, b_m , one can also accommodate predetection blur (e.g., due to light spread in the scintillator of a flat-panel detector). In general there is significant computational cost associated with such high-fidelity models.

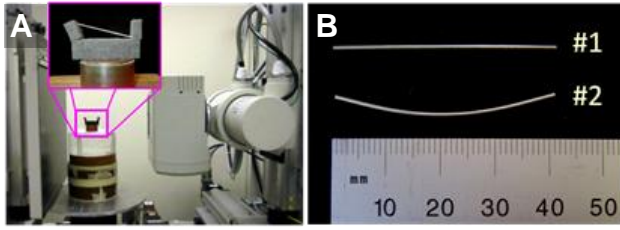


Fig. 3. (A) Experimental setup for imaging and calibration scans. In-air calibration measurements are conducted using a thin foam holder that is essentially radiolucent. (B) Two stainless steel wire components are used in the experiments: Wire #1 is straight and used for calibration scans, while wire #2 has an (unknown) curve applied before it is placed in the test phantom.

resolution projector, detector subsampling, and detector blur:

$$F_C^{HR}(\lambda) = \mathbf{B} \exp[-\mathbf{A}_{HR} \mathbf{W}(\lambda) \mu_{C_{HR}}]. \quad (6)$$

A similar model (without detector blur effects) was leveraged in [4] and demonstrated superior control of nonlinear partial volume effects in simulated monoenergetic data. However, application of the KCR methodology to real data without spectral modeling yields significant beam hardening artifacts. Recognizing again that spectral effects are most pronounced for the measurements including a metal component suggests an additional refinement of the component model where the polyenergetic beam and attenuation are modeled as:

$$F_C^{HR,\varepsilon}(\lambda) = \mathbf{B} \sum_{\varepsilon} I(\varepsilon) \exp[-\mathbf{A}_{HR} \mathbf{W}(\lambda) \mu_{C_{HR}}(\varepsilon)] \quad (7)$$

where we have assumed that the energy dependent attenuation of the component, $\mu_{C_{HR}}(\varepsilon)$, and the combined effects of the spectral distribution of the x-ray beam and detector sensitivity $I(\varepsilon)$ are known. Somewhat analogous polyenergetic forward models have been used in [5]; however, material segmentation issues are automatically handled here by the explicit decoupling of the component and background anatomy models. One drawback of (7) is that the energy-dependence of the component and imaging system must be characterized and known (as presumed in [2]), which can be difficult for components of unknown composition.

Note that for a component composed of a homogeneous material, we may replace the summation in (7) with the following relation

$$F_C^{HR,\tilde{s}}(\lambda) = \mathbf{B} f(-\mathbf{A}_{HR} \mathbf{W}(\lambda) \tilde{s}_{C_{HR}}) \quad (8)$$

where $f(\cdot)$ is a "spectral transfer function" relating path lengths through the component (represented by transformation and projection of the component mask $\tilde{s}_{C_{HR}}$) to survival probabilities. Even for a homogeneous component, this function needs to incorporate deviations from a standard monoenergetic Beer's law model. For example, one possible model uses a polynomial expansion inside an exponential:

$$f(l; \{\kappa_k\}_{k=1}^K) = \exp[\kappa_1 l + \kappa_2 l^2 + \kappa_3 l^3 + \dots + \kappa_K l^K] \quad (9)$$

where the values of κ_k are determined by the particular component and system characteristics. (A monoenergetic

system would be represented with $\kappa_1 = -\mu_C$ and $\kappa_k = 0$ for $k > 1$.) Estimation of κ_k is addressed in the following section.

C. Spectral Calibration

When the composition of a component is unknown, but a sample component is available prior to imaging (as in interventional scenarios), the unknown κ values in (9) may be estimated by performing a scan of the component alone (in air) using the same x-ray technique that will be used in the interventional scan. In this case, there is no background anatomy and the forward model (3) reduces to

$$\bar{y}_C(\lambda, \sigma_b, \{\kappa_k\}_{k=1}^K) = \mathbf{D}\{g\} F_C^{HR,\tilde{s}}(\lambda, \sigma_b, \{\kappa_k\}_{k=1}^K) \quad (10)$$

where the mean measurement model is a function of the unknowns, including the morphology (given by λ), system blur (here, presumed Gaussian with parameter σ_b), and spectral parameters (κ). Using (10) as a forward model, we may construct a maximum likelihood estimator for the unknown parameters that characterize the system and component:

$$\{\hat{\lambda}, \hat{\sigma}_b, \{\hat{\kappa}_k\}_{k=1}^K\} = \arg \max L(\lambda, \sigma_b, \{\kappa_k\}_{k=1}^K; y) \quad (11)$$

where y denotes the noisy measurement vector. In this work, a Poisson noise distribution is presumed and a Nelder-Mead optimization algorithm is used to solve (11). Note that the $\hat{\lambda}$ estimated in this calibration are only important for proper estimation of $\hat{\sigma}_b$ and $\hat{\kappa}$. These $\hat{\lambda}$ are not used in subsequent reconstructions when background anatomy is present and component is in a different position and/or shape.

D. Deformable Known-Component Recon. (dKCR)

For subsequent reconstructions, the following dKCR forward model is adopted where the measurements are a function of μ_* and λ with additional fixed characterization parameters as estimated from in-air scans:

$$\bar{y}(\mu_*, \lambda) = \mathbf{D}\{g\} F_A(\mu_*, \lambda) F_C^{HR,\tilde{s}}(\lambda; \hat{\sigma}_b, \{\hat{\kappa}_k\}_{k=1}^K) \quad (12)$$

Again, there is no requirement that the shape or pose of the known component be maintained between the calibration and patient scans. We note that (12) models spectral effects associated with the component but not the anatomy. While beam hardening is expected with the anatomy it is typically less severe than the component, though one could similarly modify FA to accommodate spectral effects as well (e.g., using a water-based beam hardening model). As with previous implementations of KCR, (12) is used to form a penalized-likelihood objective function:

$$\{\hat{\mu}, \hat{\lambda}\} = \arg \max L(\mu, \lambda; y) - \beta R(\mu) \quad (13)$$

which is solved using an alternating maximization scheme, as in [1], using separable paraboloidal surrogates image updates [6] and Nelder-Mead updates for the registration estimates.

III. RESULTS/DISCUSSION

The dKCR methodology with a simple prescan calibration for components of unknown material

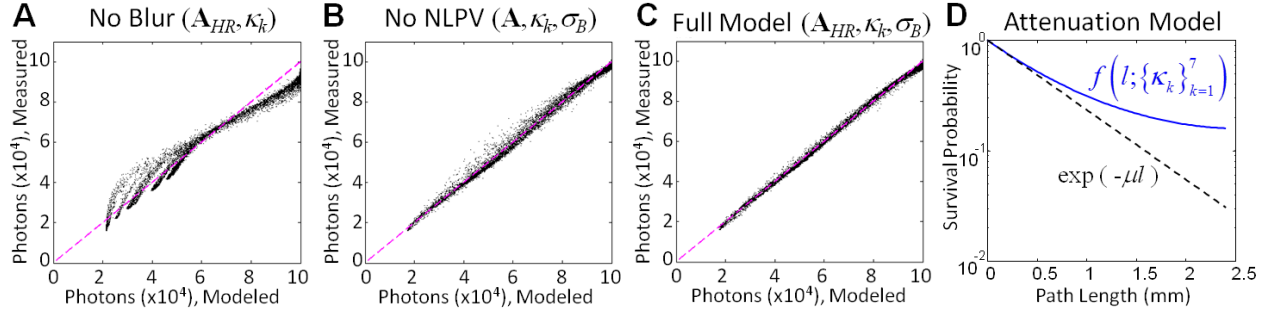


Fig. 4. In-air spectral calibration results using wire #1. Goodness-of-fit plots (e.g. measured vs. modeled projection values) show the relative importance of different aspects of high-fidelity forward models in spectral calibration including the following cases: (A) a no-blur model with 2x upsampling for both projections and the volume; (B) a no upsampling model with blur estimation; and (C) both blur estimation and 2x upsampling. (D) The component material attenuation model for the estimated from case (C) as compared with a standard monoenergetic model. These plots show the classic increase in the number of counts seen for longer material path lengths due to beam hardening as compared with a monoenergetic model.

composition was applied to the scenario of tomographic imaging of a wire component within patient anatomy. These investigations were conducted on a cone-beam CT (CBCT) testbench (see Figure 3). The testbench used a 55 cm source-to-detector distance, 43 cm source-to-axis distance, projection data of 600x116 pixels with 0.278 mm pitch and 360 angles over 360°. Nominal image volumes for reconstruction were 512x512x150 with 0.18 mm voxels. For NLPV modeling, a factor of two decrease in voxel and pixel size were used (corresponding to 0.139 mm pixels and 0.09 mm voxels). All acquisitions used 80 kVp and 115 mAs. Gain scans were used to estimate an effective number of photons for the Poisson models equal to 10^5 photons per detector element in the unattenuated beam.

A. System and Component Calibration

To investigate a scenario of CBCT-guided needle intervention, in-air calibration of a straight wire (wire #1) was performed on the testbench. A radiolucent foam holder was used to position the wire at an incline and thereby achieve a wide range of material path lengths over which the calibration would be accurate. The system blur and spectral calibrations used the estimator in (11) with $K=7$ and eight control points for λ (although the wire was straight in the calibration scan).

Results of this calibration using different fidelity component models (i.e., by setting $\sigma_b=0$ or using **A** instead of **A_{HR}**) are illustrated in Figure 4. To compare the goodness-of-fit for various models, the measurements (y) versus the estimated model (\bar{y}_C) from (10) are plotted for a subset of projection data with material path lengths greater than zero. The best agreement is found using the full model, with decreased goodness-of-fit when system blur and/or NLPV effects are not included in the system model. In relative terms, the system blur estimation appears significantly more important than NLPV modeling, suggesting that detector (and perhaps source) blur play an important role for this flat-panel-based CBCT system. The blur was estimated to be $\hat{\sigma}_B = 0.72$ pixels, equal to 0.47 mm full-width half-maximum.

Using the spectral calibration results from the full system model, the calibrated attenuation transfer function in (9) could then be evaluated. This function is shown in Figure 4D. As compared with a monoenergetic Beer's law model, one observes the typical increase in survival probability at longer material path lengths due to beam hardening.

B. Calibrated dKCR on CBCT Testbench Data

The dKCR approach outlined in (12) and (13) was applied to a test phantom (Figure 5A) approximately 80 mm in diameter and composed of water and a mixture of acrylic spheres ranging from 3.2 to 9.5 mm in diameter. A medium-contrast line pair phantom (9 lp/cm constructed from polycarbonate and acetal) was placed among the spheres along with the curved stainless steel wire #2 (Figure 3B) which served as the (partially) known component.

These studies used the same acquisition protocol and x-ray technique as for the pre-scan spectral calibration. System and component calibration estimates from the previous subsection were incorporated in (12). Raw data were scatter-corrected by simple subtraction of a single scalar from all measurements equal to 2.4% of the unattenuated beam.

Three reconstruction approaches were investigated: 1) Traditional filtered-backprojection (FBP), 2) penalized-likelihood estimation (PLE), and 3) the proposed calibrated dKCR approach. The latter two methods used quadratic regularization, and all three methods were qualitatively matched in terms of spatial resolution in the background anatomy. Both FBP and PLE performed somewhat comparably in this scenario with significant artifacts associated with the metal wire. Because of the inherent decoupling of the background anatomy and the component wire, the dKCR reconstruction allows for creation of an overlay image (from $\mathbf{W}(\hat{\lambda})\hat{s}_{cm}$) from which the estimated component shape can be shown in red. The dKCR approach was able to accurately estimate the curvature of the wire within the phantom. Moreover, the higher fidelity model

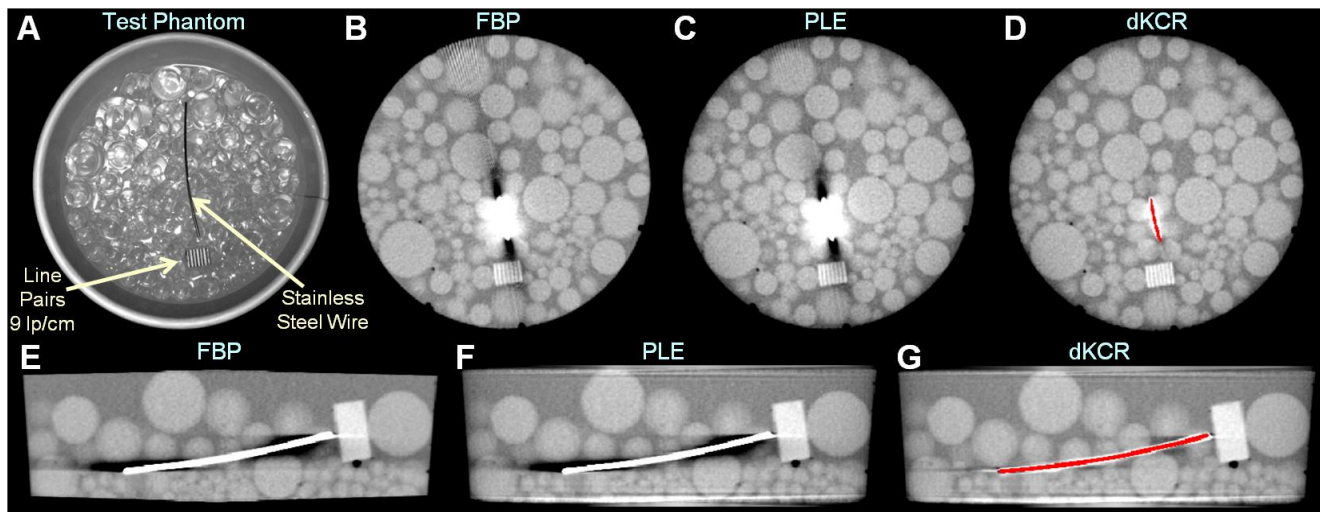


Fig. 5. Illustration of various reconstruction methods using (A) Test phantom comprised of acrylic spheres and water, medium-contrast line pairs, and wire #2. Axial and sagittal reconstructions of CBCT testbench data of the test phantom using (B)(E) FBP, (C)(F) penalized-likelihood, and (D)(G) dKCR. All images above use a window/level of 450 HU/225HU and 0.18 mm voxels in-plane with slice thicknesses of 1.8 mm for axial slices and 3.6 mm for sagittal slices.

associated with projections through the wire component provided a reconstruction with reduced artifacts in the vicinity of the wire. Some residual artifacts remain at the transition between the component and background, as well as at the ends of the wire. These residual errors may be due to slight mismatches between the class of shapes allowed by the deformation model and the actual physical morphology.

C. Conclusion

Application of the dKCR approach using components with both morphological and spectral uncertainties has been applied in real CBCT data on a testbench emulating an image-guided needle insertion. The results suggest a promising way to mitigate artifacts associated with homogeneous metal components without a sophisticated physical model of the component, using instead a simple pre-scan spectral calibration and a deformable model in joint registration and reconstruction. Potential applications include a range of interventional imaging scenarios, including procedures with guide wires, catheters, implants, and fixation hardware.

REFERENCES

- [1] J. W. Stayman, *et al.*, "Model-based tomographic reconstruction of objects containing known components," *IEEE Trans Med Imaging*, vol. 31, pp. 1837-48, Oct 2012.
- [2] W. Zbijewski, *et al.*, "CT Reconstruction Using Spectral and Morphological Prior Knowledge: Application to Imaging the Prosthetic Knee," in *The Second International Conference on Image Formation in X-Ray Computed Tomography*, Salt Lake City, UT, 2012.
- [3] D. L. Snyder, *et al.*, "Deblurring subject to nonnegativity constraints when known functions are present with application to object-constrained computerized tomography," *IEEE Trans Med Imaging*, vol. 20, pp. 1009-17, Oct 2001.
- [4] J. W. Stayman, *et al.*, "Overcoming nonlinear partial volume effects in Known-Component Reconstruction of cochlear implants," in *SPIE Medical Imaging*, Orlando, FL, 2013, pp. 86681L-1 -- 6.

- [5] I. A. Elbakri and J. A. Fessler, "Statistical image reconstruction for polyenergetic X-ray computed tomography," *IEEE Trans Med Imaging*, vol. 21, pp. 89-99, Feb 2002.
- [6] H. Erdogan and J. A. Fessler, "Ordered subsets algorithms for transmission tomography," *Phys Med Biol*, vol. 44, pp. 2835-51, Nov 1999.

Explosive Detection in Aviation Applications Using CT

Laura Parker

Abstract— CT scanners are deployed world-wide to detect explosives in checked and carry-on baggage. While similar to single- and dual-energy multi-slice CT scanners used today in medical imaging, some recently developed explosives detection scanners employ multiple sources and detector arrays to eliminate the mechanical rotation of a gantry, provide photon counting detectors for spectral imaging, and produce limited number of views to reduce cost. For each bag scan, the resulting reconstructed images are processed by threat detection algorithms to screen for explosives and other threats. Human operators review the images only when these automated algorithms report the presence of possible threats. The US Department of Homeland Security (DHS) has requirements for future scanners that include dealing with a larger number of threats, higher probability of detection, lower false alarm rates and lower operating costs. One tactic that DHS is pursuing to achieve these requirements is to augment the capabilities of the established security vendors with third-party algorithm developers. A third-party in this context refers to academics, national laboratories, and companies other than the established vendors. DHS is particularly interested in exploring the model that has been used very successfully by the medical imaging industry, in which university researchers develop algorithms that are eventually deployed in commercial medical imaging equipment. The purpose of this presentation is to review the presently deployed scanners and their concept of operations, and to discuss opportunities for third-parties to develop advanced reconstruction and threat detection algorithms.

Laura Parker is with the Department of Homeland Security, USA

Threat Liquid Identification in Hand-Held Baggage

Sebastian Faby, Marcus Brehm, Michael Knaup, Keith Powell, Mohammed Ayoub,
Benjamin Cantwell, Ian Radley, Mihai Iovea, and Marc Kachelrieß

Abstract—We present an approach for threat liquid identification in bottles transported on a belt extracted from hand-held baggage using a scan configuration that allows to acquire at least two projections from different view angles along with spectral information for each projection. The main difficulty with this scenario is obtaining a reconstruction of the bottle from few projections only. To achieve this, a parameterized bottle shape model is fitted to the projection data to fully describe the bottle and its filling. This step, together with a material decomposition carried out in projection space, makes it possible to determine material-characteristic parameters of the liquid. These parameters finally allow for a threat/benign classification of the respective liquid. Simulations were carried out to assess the performance of the proposed method using energy-selective photon counting detectors. The results show the high potential of this method.

Index Terms—Threat detection, liquid identification, bottle scanner, multi energy, material classification, few view CT.

I. INTRODUCTION

With the plans to permit passengers to take liquids aboard an airplane in their hand baggage comes the need for reliable threat liquid detection at the security check at the airport. The main requirements on those threat liquid detection devices are a high probability of detection and a low probability of false alarm along with a high throughput and all this at reasonable costs. Especially the latter puts constraints on the design of such devices, leading to the elimination of rotating gantry-based approaches or other methods with a high number of acquired projections, which is as a consequence impairing a simple tomographic reconstruction of scanned objects. This demands for a method for accurate object reconstruction from a very low number of projections, e.g. from two projections from different view angles in a dual view system. To allow for liquid identification, at least two material-specific quantities have to be derived from the projection data. This is requiring the system to be multi energy capable, e.g. by employing an energy-selective photon counting detector. In this work we present a method for threat liquid identification that is capable of operating under the above-mentioned minimal requirements, i.e. a dual view multi energy system using a belt for bottle transportation. This allows to acquire projection data from many slices of the bottle during its transportation through the scanner. The two pillars of our method are a tomographic

reconstruction procedure that is fitting a parameterized bottle shape model to the acquired projection data, i.e. the reconstruction, and a material decomposition for the determination of material characteristic parameters, which will allow liquid identification.

II. MATERIALS AND METHODS

In a system configuration that restricts the number of available projections to only a very few, all conventional reconstruction approaches like the filtered backprojection fail to give usable results. A possible scan configuration is shown in figure 2, which illustrates a classical dual view system consisting two source-detector pairs, where the bottles are lying on a belt. Some sort of reconstruction, however, is necessary to be able to separate the contribution of the bottle wall from the liquid in the measured projections and to determine the density. This is crucial to be able to determine the liquid's attenuation coefficient. Therefore, a central part of our work presented here will be a special reconstruction approach that allows to reconstruct the scanned bottle using a parameterized bottle shape model. The next important step is to derive material-specific information. The concept of using the effective atomic number Z_{eff} and the electron density ρ_e to describe a material's or material mixture's attenuation behavior is well known and used in many applications. A comprehensive discussion on this topic is given for example in reference [1]. We chose to determine these quantities based on a decomposition into two materials. This will be motivated in the following.

All materials that will have to be dealt with in the context of threat liquid identification are either organic compounds or other materials containing mostly the elements C, H, O and N. Certain threat materials may also contain K, Cl, or S. All these elements have a relatively low atomic number Z . The element with the highest atomic number to be found in significant amounts is probably Fe with $Z = 26$, e.g. in steel bottle walls. Its K-edge at 7.1 keV is situated at such a low energy that it does not play a role in the x-ray imaging process. We therefore assume the absence of K-edge discontinuities. This means that all relevant materials can be approximately described by two parameters since the x-ray absorption is governed by two basic physical effects in the energy range considered here, i.e. the photoelectric effect and Compton scattering. This motivates the application of a projection-based material decomposition into two basis materials. Every material is then approximated by the respective contributions of the two basis materials. To obtain the coefficients of the basis materials for the scanned liquid from the material-decomposed projection data the reconstruction is necessary. These coefficients allow

S. Faby, M. Brehm, Dr. M. Knaup and Prof. Dr. M. Kachelrieß are with the Division of Medical Physics in Radiology, German Cancer Research Center (DKFZ), Im Neuenheimer Feld 280, 69120 Heidelberg, Germany (e-mail: sebastian.faby@dkfz.de).

Dr. Keith Powell, Dr. Mohammed Ayoub, Dr. Benjamin Cantwell and Ian Radley are with Kromek Ltd, NetPark, Thomas Wright Way, Sedgfield, Co Durham, TS21 3FD, United Kingdom.

Dr. Mihai Iovea is with ACCENT PRO 2000 s.r.l. (AP2K), Nerva Traian 1, K6, Ap. 26 Bucharest, S3, Romania 031041.

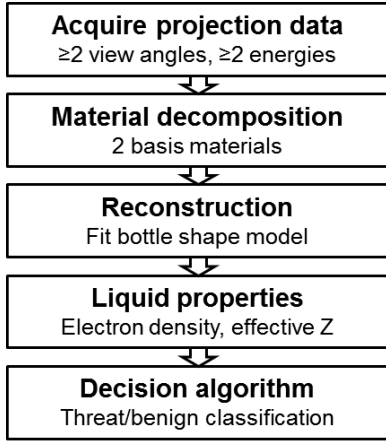


Fig. 1. Workflow of the proposed threat liquid identification method.

in the end to calculate Z_{eff} and ρ_e . The procedure of our proposed workflow is therefore as follows: First a minimum of two projections of the bottle from different view angles with each providing spectral information are acquired. These projections are then independently decomposed into two basis materials. The decomposed projection data are then used to fit the parameterized bottle shape model. This reconstruction step gives two coefficients from the two sets of basis material projection data. With these two coefficients Z_{eff} and ρ_e are calculated. The last step will then be a decision algorithm that compares these material-characteristic quantities to a database of reference materials to come up with a threat/benign decision for the scanned bottle. The single parts of the workflow summarized in figure 1 will be described now in more detail.

A. Scan geometry

For optimal results the single projections should be acquired at favorable angles that allow to identify important features of the scanned bottle, like its fill level. The case of two projections, which will be studied here, is defined in figure 2. It makes sense to acquire a horizontal projection, showing the fill level, the vertical bottle position and dimension, and a vertical projection, which defines the horizontal bottle position and dimension (see also figure 4). The two projections should be acquired at an angle of 90° for maximum information. Precise knowledge of the scan geometry is important to obtain correct material-characteristic parameters since the density scales with object size.

B. Material decomposition

The material decomposition of the projection data is based on a maximum likelihood approach [2], [3], which is able to deal with $B \geq 2$ energy information and decompose into $M \leq B$ basis materials. The spectral information is provided by an energy-selective photon counting detector with $B \geq 2$ energy bins.

With the definition of an analytical spectral forward model the expected number of photons, i.e. the expected intensity λ_b

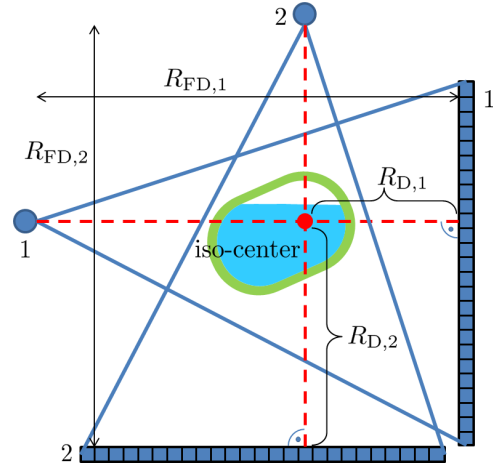


Fig. 2. Scan geometry for an orthogonal dual view system. The two source-detector distances are denoted R_{FD} and the iso-center-detector distances R_{D} .

in energy bin b can be computed:

$$\lambda_b(p_1, \dots, p_M) = \int dE I_{0,b}(E) e^{-\sum_m p_m \mu_m(E)}. \quad (1)$$

The expectation value depends on the basis material intersection lengths p_m , which are the quantities of interest here: p_1, \dots, p_M . The detected air spectra $I_{0,b}(E)$ need to be known and the energy dependency of the attenuation coefficients $\mu_m(E)$ of the basis materials is required as well. These spectra have to be calibrated for the specific scan system. Under the assumption of measuring independent Poisson-distributed random variables n_b , the likelihood function $P(n_1, \dots, n_B | p_1, \dots, p_M)$ is given by:

$$P = \prod_{b=1}^B \frac{(\lambda_b(p_1, \dots, p_M))^{n_b}}{n_b!} e^{-\lambda_b(p_1, \dots, p_M)}. \quad (2)$$

The log-likelihood function $L(n_1, \dots, n_B | p_1, \dots, p_M)$ is:

$$L \approx \sum_{b=1}^B n_b \ln \lambda_b(p_1, \dots, p_M) - \lambda_b(p_1, \dots, p_M). \quad (3)$$

The simplex method of Nelder and Mead [4] is used to solve this. An estimation of the basis material intersection lengths \hat{p}_m is obtained in the end.

C. Bottle shape model

The parameterized bottle shape model that is used to reconstruct the material-decomposed projection data is shown in figure 3. The model is essentially a box with rounded corners and a constant wall thickness w . This model is able to reproduce any shape from a rectangle, a box with rounded corners, an ellipse to a circle. With this flexibility every regular bottle shape can be represented. Highly irregular bottles can probably nevertheless be correctly handled since the optimization procedure will find a good average solution. The parameters of interest are the attenuation coefficient of the wall $\mu_{w,b}$ and the liquid $\mu_{l,b}$ for every energy bin b . Since we do not carry out the parameter optimization on the spectral projection data but on the material-decomposed

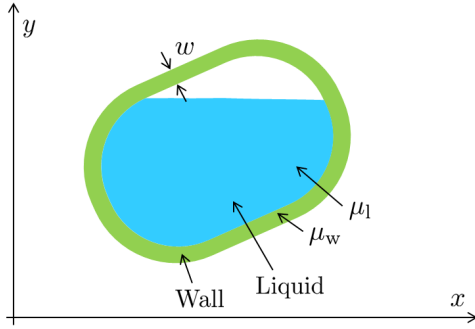


Fig. 3. Parameterized bottle shape model. The model is a box with rounded corners and wall thickness w , consisting of a wall and a liquid part. To the wall is assigned the attenuation coefficient μ_w and to the liquid μ_l .

projection data containing intersection lengths, we actually estimate material concentrations $c_{\text{wall},m}$ and $c_{\text{liquid},m}$ for the wall and the liquid for the two basis materials $m = 1, 2$. The material concentrations signify the relative density of the liquid compared to the one of the two basis materials. Please note that these coefficients are globally assigned to the liquid and the wall. Spatial variations can therefore not be resolved.

All the parameters of the bottle shape model have to be determined in a fitting procedure. This bottle shape model can be described completely analytically, making the intersection length calculation through the object fast.

D. Bottle shape reconstruction

The bottle shape reconstruction is the central part of our method. Its basic concept is to find all bottle shape parameters such that the intersection lengths through the estimated bottle shape model p_{est} are as similar as possible to the intersection lengths obtained by the material decomposition from the measured projection data p_{meas} (figure 4). This is done slice by slice since the detectors are line arrays. The cost function to be optimized is mainly defined as the difference of p_{meas} and p_{est} . To minimize this cost function the simplex method of Nelder and Mead [4] is used. Since the Nelder-Mead algorithm can only supply local a solution here, good starting points for the parameter optimization are required. We found this initial estimation to be crucial for a correct and fast convergence. We use an initial estimation based on information extracted from the unprocessed projection data. Line profiles of the projection data provide good estimates for many of the open parameters (see the projections in figure 4). The Nelder-Mead algorithm is re-initialized several times after its convergence during the optimization procedure to avoid local minima. The optimization is stopped if no further improvement of the cost function value is achieved compared to the previous initialization of the Nelder-Mead algorithm. The result of interest of the bottle shape reconstruction are the material concentrations of the liquid for the basis materials BM1 $c_{\text{liquid},1}$ and BM2 $c_{\text{liquid},2}$. They will be used to calculate the corresponding Z_{eff} and ρ_e .

E. Liquid identification and decision

After the material concentrations of the liquid for the basis materials BM1 and BM2 have been determined, now named

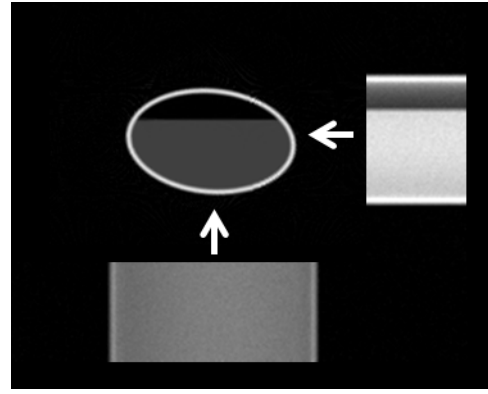


Fig. 4. Reconstruction of a bottle cross-section using the model shown in figure 3 from a horizontal and a vertical projection acquired in the geometry of figure 2. The projections are shown here for only one energy bin. Noise was added to the projections during the simulation process.

c_{BM1} and c_{BM2} , Z_{eff} and ρ_e can be calculated using reference values for the two basis materials [1]. The electron density relative to the one of water can then be determined as a function of the material concentrations:

$$\rho_e(c_{\text{BM1}}, c_{\text{BM2}}). \quad (4)$$

The same applies for the effective atomic number:

$$Z_{\text{eff}}(c_{\text{BM1}}, c_{\text{BM2}}, k). \quad (5)$$

The free parameter k was adapted to represent liquids well. Z_{eff} and ρ_e are calculated for each slice of the bottle separately and have then to be post-processed to obtain a final result for the whole bottle.

Having finally obtained these sought material-characteristic parameters, their values can now be compared to a database containing Z_{eff} and ρ_e of various threat and benign materials to come to a decision whether the respective liquid is dangerous or not. This could be realized e.g. by simply looking at the distances to all the other materials in $Z_{\text{eff}}-\rho_e$ -space.

F. Simulations

The threat liquid identification method described above was validated with simulations of an energy-selective photon counting detector with five energy bins based on directly converting semiconductor material. Extensive simulations were carried out testing the method in various scenarios. Amongst others the following parameters were varied: Bottle size and shape, fill level, wall material and thickness, and noise level. All this was done each for a total of twelve threat and benign liquids in the bottle. These simulations serve as an error propagation using the Monte Carlo technique: A single slice is evaluated 50 times in a row, with each single repetition having a different noise realization. For the resulting Z_{eff} and ρ_e the mean of all repetitions is taken. The expected error of Z_{eff} and ρ_e is then given by one standard deviation Δ determined from the 50 independent repetitions. The standard scenario “normal size” is based on an elliptical bottle with the two half axes being 50 mm and 30 mm, a glass wall of 3 mm thickness and a relative fill level of 75%. The noise level is

TABLE I
SIMULATION RESULTS OF WATER FOR DIFFERENT SCENARIOS BASED ON
PHOTON COUNTING DETECTOR TECHNOLOGY.

Scenario	ρ_e	Z_{eff}	$\Delta\rho_e$	ΔZ_{eff}
Normal size	0.99962	7.48910	0.00285	0.02591
Half size	0.99754	7.54164	0.00470	0.03855
Double size	0.99829	7.48219	0.00573	0.04558
Decreased # photons	0.99823	7.53671	0.00620	0.06711
Al wall	0.99937	7.49172	0.00250	0.02116
Rectangular bottle	1.00004	7.47307	0.00299	0.03124
Almost empty bottle	1.00162	7.43038	0.02237	0.11739

defined by 10^5 photons per ray, using an 80 kVp spectrum. The detector consists of 512 pixels with 0.5 mm pixel size in the iso-center. For the “half size” and the “double size” scenarios the half axes and the wall thickness were halved and doubled. The photon number per ray was reduced by one order of magnitude to 10^4 in the “decreased # photons” case. The “Al wall” case features a 0.1 mm aluminium wall instead of a 3 mm glass wall. The elliptical bottle shape is changed to a rectangular one with 100 mm and 60 mm side length for the “rectangular bottle” scenario. For the “almost empty bottle” case the relative fill level was reduced from 75% to 10%.

III. RESULTS AND DISCUSSION

The results of the simulations for the different scenarios are shown in table I. Generally, the error of the electron density is smaller than the one of the effective atomic number. The error is always well below 0.01 for the electron density and 0.075 for the effective atomic number, i.e. a relative error of 1%, even for the “decreased # photons” case, disregarding however the “almost empty bottle” scenario. In this scenario the bottle shape reconstruction suffers from a reduced amount of available data on the liquid. The results for Z_{eff} sometimes show a bias, which is often due to local minima close to the true solution. The “double size” case is a scenario with increased noise as well since the large bottle is highly absorbing. The photon counting detector was simulated assuming an energy resolution of $\text{FWHM} = 7 \text{ keV}$, but no additional degrading detector effects were taken into account.

The results for the other eleven liquids are quite similar to the results shown here for water. In all cases the different liquids could be separated from all the others using the average of all slices. Only for very few liquids with very similar properties and in a case with high standard deviation could a confusion for a single slice alone become possible. This confusion, however, would never lead to a wrong threat/benign decision, it would only lead to mistaking one threat for another threat or one benign for another benign liquid.

After having proved the method’s fitness in simulations, the construction of a dual view prototype system is now ongoing. Adaptation of the bottle shape reconstruction and especially of the initial estimation to this specific system together with a calibration of the scan geometry and the material decomposition are expected to yield a comparable standard deviation of the material-specific parameters over the

different slices as in the simulations. Improvements will also come from making use of the available slice data, e.g. using the result of the previous slice as initialization for the following slice. So far each slice was always processed independently.

IV. CONCLUSION

A threat liquid identification method was presented that is able to work with different numbers of projections, as long as a minimum of two views from different angles are available and the detectors are providing spectral information. The simulation results obtained with this method are very promising. The method might not just be able to classify a liquid as threat or benign, it might even be capable of identifying the liquid.

ACKNOWLEDGMENT

This work was supported by Eurostars project E! 7308 DCXScan. Parts of the reconstruction software were provided by RayConStruct® GmbH, Nürnberg, Germany.

REFERENCES

- [1] D. F. Jackson and D. J. Hawkes, “X-ray attenuation coefficients of elements and mixtures,” *Physics Reports*, vol. 70, no. 3, pp. 169–233, 1981.
- [2] E. Roessl and R. Proksa, “K-edge imaging in x-ray computed tomography using multi-bin photon counting detectors,” *Physics in Medicine and Biology*, vol. 52, pp. 4679–4696, 2007.
- [3] J. P. Schlomka, E. Roessl, R. Dorscheid, S. Dill, G. Martens, T. Istel, C. Bäumer, C. Herrmann, R. Steadman, G. Zeitler, A. Livne, and R. Proksa, “Experimental feasibility of multi-energy photon-counting K-edge imaging in pre-clinical computed tomography,” *Physics in Medicine and Biology*, vol. 53, no. 15, pp. 4031–4047, 2008.
- [4] J. A. Nelder and R. Mead, “A simplex method for function minimization,” *The Computer Journal*, vol. 7, pp. 308–313, 1965.

Algorithmic Improvements to SIRT with Application to X-Ray CT of Luggage

Jens Gregor

Abstract—In this paper we discuss algorithmic improvements to SIRT including near-optimal relaxation, scalar preconditioning, minimum norm based Tikhonov regularization, data driven weighting of the residual errors associated with the least squares problem being solved, and a conjugate gradient implementation. The showcase application is X-ray CT imaging of luggage for aviation security.

I. INTRODUCTION

As part of the standard security measures for safe air travel, passenger luggage is typically screened by an X-ray CT based system prior to being loaded onto the air plane to determine if explosives are present. Imaging challenges to be dealt with include beam hardening and metal artifacts such as streaking and shading. The Department of Homeland Security recently sponsored a project which had as its goal to investigate the use of iterative reconstruction in connection with X-ray CT based screening of luggage. This paper reports on the algorithmic developments carried out for the SIRT (Simultaneous Iterative Reconstruction Technique) algorithm [1].

Having been applied to a wide range of inverse problems in medicine, biology and engineering, SIRT is an example of a Richardson Iteration which is a classical numerical method for solving a linear system of equations. We have previously shown that near-optimal relaxation can be achieved by means of eigenvalue analysis and introduced a scalar-preconditioned version called PSIRT [2]. That work established a closed-form expression for the largest eigenvalue and argued for the smallest eigenvalue being negligible but left it undefined. More recently, we reported a simple way to compute an upper bound on the smallest eigenvalue based on trace analysis of the system matrix and added Tikhonov regularization in the form of a minimum norm constraint within the relaxed PSIRT framework [3]. Following a summary of these results, we here show that data driven weighting of the residual errors associated with the least squares problem being solved can be incorporated in a manner consistent with our previous work. We also remind the reader that SIRT can be embedded within a conjugate gradient algorithm and show that such an implementation eliminates the need for the heuristic method of ordered subsets which which often is used to make SIRT be fast enough for practical use.

II. ALGORITHMIC DEVELOPMENTS

Let x and b denote image and log-normalized projection data, A the system matrix that connects the two, and R and

C two diagonal matrices of inverse row and column sums of A . Then SIRT solves the weighted least squares problem

$$x^* = \operatorname{argmin} \|Ax - b\|_R^2. \quad (1)$$

The solution is computed using the relaxed iteration

$$x^{(k+1)} = x^{(k)} + \alpha CA^T R(b - Ax^{(k)}). \quad (2)$$

In practice, updating takes place using an ordered subsets approach. Also, we use $x^{(0)} = 0$. See [2], [4] for details.

A. Near-Optimal Relaxation

SIRT is a Richardson Iteration [5]. Convergence is guaranteed if $0 < \alpha < 2/\lambda_{\max}$ with the fastest rate of convergence obtained for $\alpha^* = 2/(\lambda_{\max} + \lambda_{\min})$. Here λ_{\max} and λ_{\min} refer to the largest and smallest eigenvalues of matrix $CA^T RA$. Assuming A has full column rank, both eigenvalues are strictly positive.

Stemming from the fact that non-negative matrices CA^T and RA are both stochastic, it follows that $\lambda_{\max} = 1$. This implies $1 \leq \alpha^* = 2/(1 + \lambda_{\min}) < 2$. Empirical comparisons of residual norms have consistently found $\alpha = 1.99$ to converge twice as fast as $\alpha = 1.00$ in terms of requiring half as many iterations to achieve the same residual error. This indicates $\lambda_{\min} \ll 1$. We here detail a straightforward pathway for quantifying this finding.

The trace of an $N \times N$ matrix is equal to the sum of the eigenvalues of that matrix [6]. Clearly, the smallest eigenvalue must be less than or equal to the average of all eigenvalues. For SIRT, we can establish an even tighter bound, namely,

$$\lambda_{\min} \leq \frac{\operatorname{tr}(CA^T RA) - 1}{N - 1} \quad (3)$$

where we have subtracted off the value of the largest eigenvalue and computed the average of the remaining eigenvalues. We will use λ_{\min}^* to refer to this bound below.

B. Scalar Preconditioning

Matrix C serves to precondition the normal equations associated with (1). We have introduced an alternative scalar preconditioning scheme [2]. The resulting PSIRT algorithm is given by

$$x^{(k+1)} = x^{(k)} + \alpha p A^T R(b - Ax^{(k)}) \quad (4a)$$

$$p = 1/\|A\|_1 \quad (4b)$$

where $\|A\|_1 = \max_j \sum_i a_{ij}$ denotes the maximum column sum of the system matrix. The advantage of PSIRT over

J. Gregor is with the Department of Electrical Engr. & Computer Science, University of Tennessee, Knoxville, TN 37996. Email: jgregor@eecs.utk.edu.

SIRT is best seen when solving a large problem using ordered subsets and the code is executed in a distributed environment. Each ordered subset requires its own image-sized matrix C . When memory limitations preclude storage of these, SIRT is forced to recompute them on a per-iteration basis. This is costly in itself, but in a distributed computing environment a global reduction is needed to create a complete local copy on each node. In contrast, PSIRT can compute and store the scalars that replace the C matrices during the first iteration. This eliminates the need for computation and communication thereof during the subsequent iterations.

C. Tikhonov Regularization

The condition number of matrix A is given by the ratio of its largest and smallest singular values [6]. A small condition number indicates that the linear system $Ax=b$ can be solved with great precision. A large condition number conversely indicates that no algorithm can guarantee to find a solution with any provable accuracy.

Tikhonov regularization is a widely used technique for improving the numerical stability of an algorithm for solving a poorly conditioned linear system [7]. In our case, it leads to the weighted least squares problem

$$x^* = \operatorname{argmin} \|Ax - b\|_R^2 + \beta \|Qx\|_2^2 \quad (5)$$

where matrix Q is chosen to emphasize structural characteristics of x that are undesirable. Hyperparameter β establishes a trade-off between the data term (left norm) and the model term (right norm). A small value of β places more emphasis on the data term. We show that this is needed to maintain the rate of convergence achievable when regularization is not used. A large value of β places more emphasis on the model term. We show that this is needed to achieve the regularization.

We obtain a SIRT-like update scheme by preconditioning the normal equations associated with (5) by matrix C followed by matrix splitting

$$x^{(k+1)} = (I - \alpha\beta CQ)x^{(k)} + \alpha CA^T R(b - Ax^{(k)}). \quad (6)$$

We consider the special case where $Q = I$ for which preference is given to a minimum norm solution. Combined with the scalar preconditioning used by PSIRT, a simplified update scheme can be derived. That is,

$$x^{(k+1)} = (1 - \alpha\beta p)x^{(k)} + \alpha p A^T R(b - Ax^{(k)}). \quad (7)$$

Near-optimal relaxation results when $\alpha^* = 2/(1 + \lambda_{\min}^* + 2\beta p)$. This in turn implies that $\alpha^* > 1.99$ results if $\beta p < 0.0025$ under the assumption that λ_{\min}^* is negligible.

The condition number for the underlying linear system is given by

$$\kappa = \sqrt{\frac{\sigma_{\max}^2 + \beta p}{\sigma_{\min}^2 + \beta p}} \quad (8)$$

where σ_{\max} and σ_{\min} denote the largest and smallest singular values of matrix $pA^T R A$. Regularization is thus needed when σ_{\min} is close to zero. This occurs when λ_{\min}^* is close to zero since $\sigma_{\min} \leq \lambda_{\min}^*$. In this case, the approximation $\kappa = \sigma_{\max}/\sqrt{\beta p}$ implies that even a relatively small value

of βp has the potential to greatly improve the conditioning and thus the numerical stability of a PSIRT reconstruction. Case in point, $\beta p = 0.0025$ yields $\kappa = 20\sigma_{\max}$ which is a substantial improvement over the unregularized case. In practice, a smaller value of βp may be needed to prevent the data term from being dominated by the model term which could lead to excessive smoothing. This increases the condition number but the end result is still better than not regularizing at all.

D. Data Driven Weighting

Regularization addresses the fact that the imaging geometry may lead to a poorly conditioned system matrix. Another problem that needs to be addressed is that of heavily attenuated data being less trustworthy than lightly attenuated data. This is an important problem because the log-normalization applied to the projection data causes a least squares solver like SIRT to place more emphasis on the former than on the latter. The solution is to weight the residual errors in a data driven manner.

Define $b = -\log\{\lambda/\lambda_T\}$ where λ and λ_T denote the beam intensity at the detector and the source, respectively. In a seminal paper, Sauer and Bouman [8] showed that a Poisson likelihood model of X-ray attenuation can be approximated by a weighted least squares problem, namely,

$$L(\lambda|x) = 0.5\|Ax - b\|_D^2 + f(\lambda) \quad (9)$$

where $D = \operatorname{diag}\{\lambda\}$. Function f represents terms that are constant with respect to x . These can be discarded when seeking to determine the x that maximizes the data likelihood. We here show that this and other weighting schemes can be incorporated into the developed SIRT framework.

Let $A = [a_{ij}]$ and $b = [b_i]$ and define $w = [w_i]$ to be the diagonal of weight matrix W . The residual error for the i^{th} equation of the associated weighted least squares problem can then be expressed as

$$\epsilon_i^2 = w_i \left(\sum_j a_{ij} x_j - b_i \right)^2. \quad (10)$$

The transformations $\tilde{A} = [\sqrt{w_i} a_{ij}]$ and $\tilde{b} = [\sqrt{w_i} b_i]$ allow us to write $\|Ax - b\|_W^2 = \|\tilde{A}x - \tilde{b}\|_2^2$. By furthermore introducing $\tilde{R} = [1/\sum_j \tilde{a}_{ij}]$ and $\tilde{C} = [1/\sum_i \tilde{a}_{ij}]$, we can express a SIRT-like W -weighted least squares problem indirectly, namely,

$$x^* = \operatorname{argmin} \|\tilde{A}x - \tilde{b}\|_{\tilde{R}}^2. \quad (11)$$

We note that the normal equations for the standard version of SIRT can be expressed as

$$P^T R(b - Ax) = 0 \quad (12)$$

where $P = [a_{ij}/\sum_h a_{hj}]$. Using the equality $\tilde{R}(\tilde{b} - \tilde{A}x) = R(b - Ax)$, the normal equations for the W -weighted version of SIRT can similarly be expressed as

$$Q^T R(b - Ax) = 0 \quad (13)$$

where $Q = [\sqrt{w_i} a_{ij}/\sum_h \sqrt{w_h} a_{hj}]$.

We have thus shown that, when incorporated as proposed here, data driven weighting is equivalent to modifying the back

projector. We note that matrix Q is stochastic like matrix P regardless of the choice of weight vector w. This guarantees SIRT and PSIRT remain convergent and that near-optimal relaxation and minimum norm regularization can be achieved as described above.

In the experimental results section we compare unweighted reconstruction with two exponential weighting schemes. Let $w = [\exp\{-kb_i\}]$. Then $k = 0$ yields the unweighted case, $k = 1$ corresponds to the Poisson likelihood weighting apart from a scaling factor, and $k = 2$ is a quadratically boosted version of the latter. We refer to these three cases as W0, W1, and W2. Different values of k are possible as are functionally different weighting schemes. Neither is pursued here.

E. Conjugate Gradient Implementation

SIRT quickly establishes the low-frequency content of an image but then enters into a long and slow process during which the high-frequency content is recovered. As an alternative to ordered subsets, a SIRT-like problem can be formulated which is then solved using a conjugate gradient algorithm [9] Specifically, let $M = [a_{ij}/\sqrt{r_i c_j}]$, $u = [x_j/\sqrt{c_j}]$ and $v = [b_i/\sqrt{r_i}]$, where $r_i = \sum_j a_{ij}$ and $c_j = \sum_i a_{ij}$. Then apply a conjugate gradient algorithm to the following least squares problem

$$u^* = \operatorname{argmin} \|Mu - v\|_2^2 + \beta \|u\|_2^2. \quad (14)$$

The regularization term can be dropped if we fold it into the linear system of equations being solved. That is,

$$\hat{M} = \begin{bmatrix} M \\ \beta I \end{bmatrix} \quad \text{and} \quad \hat{v} = \begin{bmatrix} v \\ 0 \end{bmatrix}.$$

The reconstructed image is obtained from u^* through a simple transformation, namely, $x^* = [\sqrt{c_j} u_j]$. Even without use of preconditioning, we have found this CGSIRT approach to converge as fast as ordered subsets versions of PSIRT.

III. EXPERIMENTAL RESULTS

We have applied the above variants of SIRT to fan-beam data of luggage obtained using an Imatron C300 which is a fifth generation CT scanner from the 1990s. Data was acquired for 864 view angles covering 216 degrees. The fan-beam angle was 41.3 degrees and 864 equiangular rays were sampled. Polynomial beam hardening correction was applied. A 512x512 image was reconstructed for each data set. PSIRT was executed for 64 iterations using $\alpha = 1.99$ and 32 ordered subsets. This corresponds approximately to 4,096 iterations of a standard SIRT implementation. CGSIRT was executed for 64 iterations.

The geometry of the Imatron C300 was modeled using a system matrix based on area intersection. The system matrix contained 950 million non-zero elements. We determined that $\lambda_{\min}^* = 0.00089$ which supported using a relaxation factor of 1.99 for PSIRT and emphasized the need to regularize both PSIRT and CGSIRT. This was in turn carried out using $\beta = 0.04$ which was found to provide a good trade-off between improving the condition number of the iteration matrix and not causing excessive smoothing of the reconstructed image.

Figure 1 illustrates the log-normalized projection data for the unweighted and weighted cases described above. Notice that bright pixels in W0 (max 9.40) are mapped to become dark in W1 and even darker in W2. Conversely, dark pixels in W0 are mapped to become bright in W1 (max 0.75) and W2 (max 0.37). This mapping corresponds to a change in influence of the projection data on the reconstruction: larger values correspond to more influence, smaller values to less.

Figure 2 shows the CGSIRT reconstructions without regularization as well as with regularization. Notice how metal artifacts seen in the W0 reconstructions are suppressed in the regularized W1 and W2 reconstructions. One example is the broad valley that runs horizontally through the large water container in the middle of the image and continues through the box shaped object to the right of it. Another example is the Gibbs ringing seen for the two circular metal enclosed objects toward the top and the right of the image. The overall level of background noise is also reduced.

We cannot show the comparable PSIRT images due to space limitations. Generally speaking, we found them to be visually similar to the CGSIRT images although many edges were not quite as well defined indicating slower convergence. This was reflected also when comparing the least square residual errors.

We make no claims that these are the best reconstructions possible. The goal has been to illustrate that near-optimal relaxation, minimum norm regularization and data driven weighting can be achieved simultaneously.

We close by commenting in the computational cost of the proposed algorithms. Using a single Dell Precision PC with dual, quad-core 2.26 GHz Xeon CPUs and 10 GB of memory, it took 20 seconds to initialize the system matrix, and approximately 2 seconds for a multi-threaded implementation to compute each PSIRT and CGSIRT iteration. These times include computation and printing of miscellaneous types of log information to file. The cost to weight the projection data and the system matrix and subsequently map the problem to the form solved by CGSIRT was approximately equal to the cost of two iterations.

ACKNOWLEDGMENT AND DISCLAIMER

This paper is based upon work supported by the U.S. Department of Homeland Security, Science and Technology Directorate, under Task Order Number HSHQDC-12-J-00056. The views and conclusions are those of the author and should not be interpreted as necessarily representing the official policies, either expressed or implied, of the U.S. Department of Homeland Security.

REFERENCES

- [1] A. Kak and M. Slaney, *Principles of CT Imaging*, SIAM, 2001.
- [2] J. Gregor and T. Benson, "Computational analysis and improvement of SIRT," *IEEE Trans. Medical Imaging*, 27: 918-924, 2008.
- [3] J. Gregor, "Tomographic neutron imaging using SIRT," *Fully 3D*, Lake Tahoe, 2013.
- [4] J. Gregor, "Distributed CPU multi-core implementation of SIRT with vectorized matrix kernel for micro-CT," *Fully 3D*, Germany, 2011.
- [5] Y. Saad and H.A. van der Horst, "Iterative solution of linear systems in the 20th century," *J. Comp. Applied Math.*, 123: 1-33, 2000.
- [6] R. Horn and C. Johnson, *Matrix Analysis*, Cambridge Univ. Press, 1985.

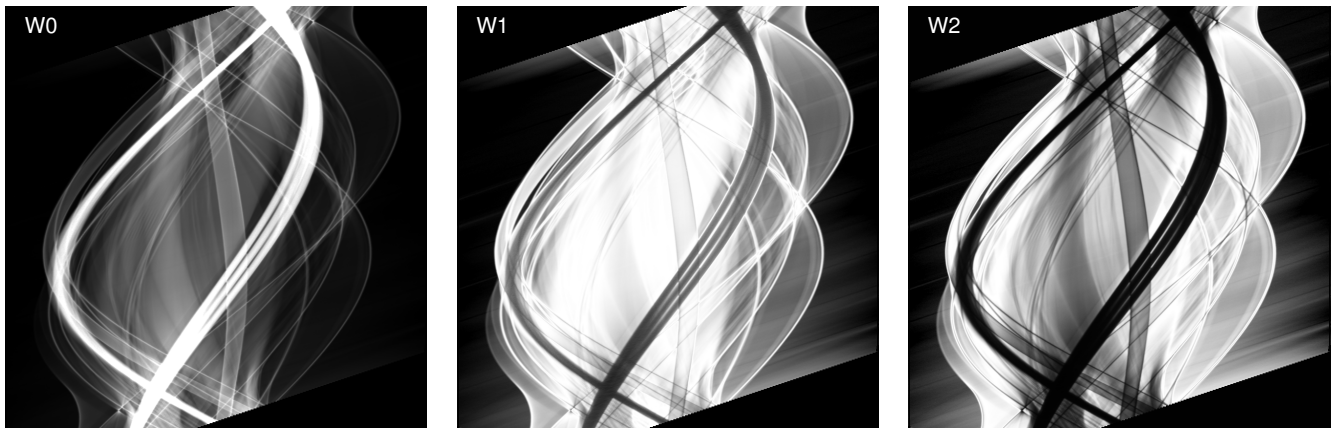


Fig. 1. Projection data illustrating the effect of weighting. W0 is raw data. W1 and W2 represent two different exponential weighting schemes.

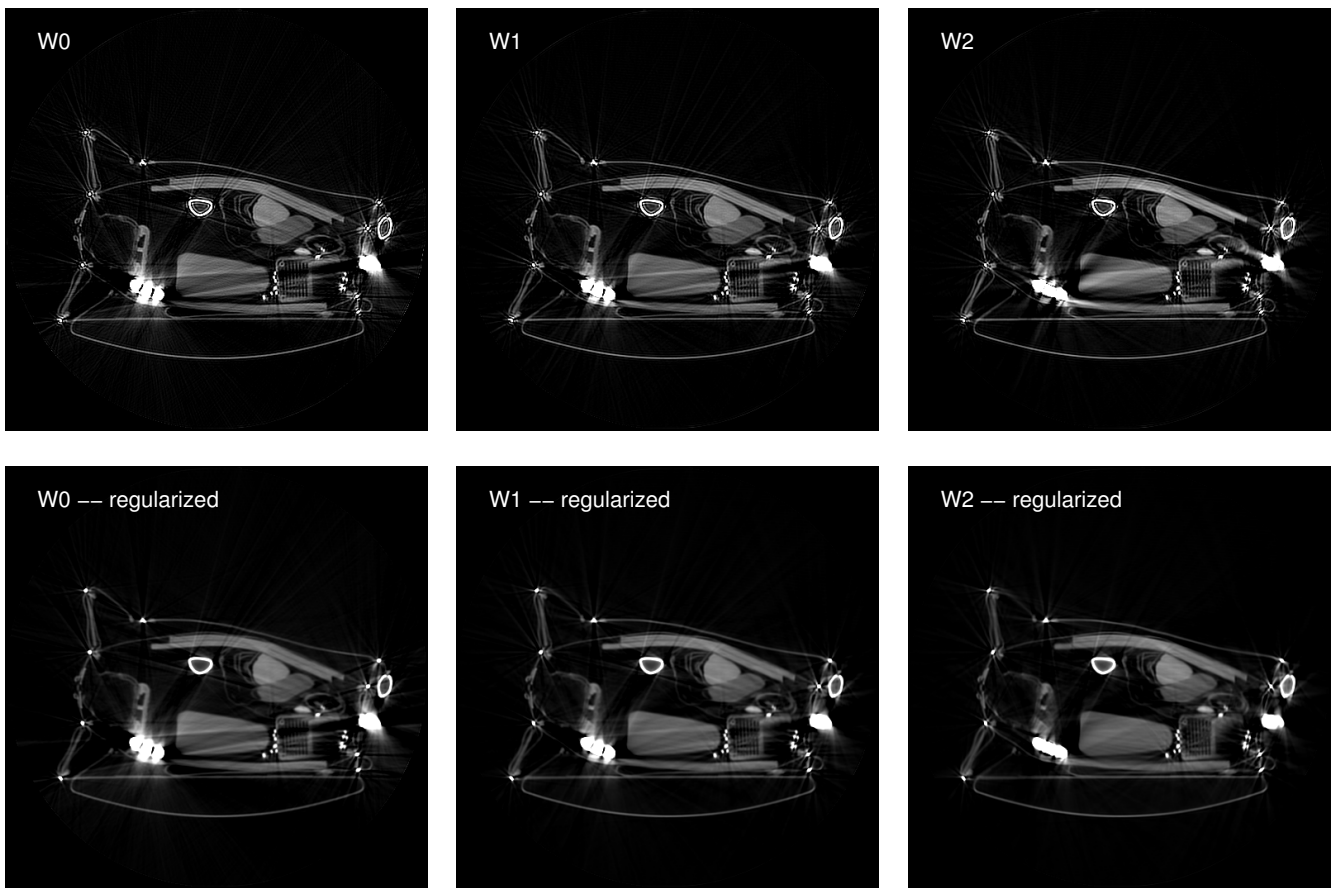


Fig. 2. CGSIRT reconstructions for the three versions of the projection data without regularization (top row) as well as with regularization (bottom row).

- [7] W. Press, S. Teukolsky, W. Vetterling and B. Flannery, *Numerical Recipes*, Cambridge Univ. Press, 2007.
- [8] K. Sauer and C. Bouman, "A local update strategy for iterative reconstruction from projections," *IEEE Trans. Signal Proc.*, 41: 534–548, 1993.
- [9] A. van der Sluis and H.A. van der Horst, "SIRT and CG-type methods for the iterative solution of sparse linear least-squares problems," *Linear Algebra and its Applications*, vol. 130, pp. 257–302, 1990.

Sinogram Sparsified Metal Artifact Reduction Technology (SSMART)

Synho Do¹ PhD and W. Clem Karl² PhD

Abstract—The use of Computed Tomography (CT) scans is an essential component of a wide variety of fields in our world today, most notably in security and medicine. However, the presence of metal in an object that needs to be scanned causes significant artifacts which considerably detracts from the quality of the image produced. This presents a major concern, especially when used in security to scan baggage for their contents, as they frequently contain metal objects in them. The most popular technique used to combat this problem has been taking the specific data sets that are affected by the metal and replacing them with data sets estimated using the unaffected data. However, this technique renders it impossible to get the true value leading to not only inaccurate estimations, but also inaccurate images. In this paper, we present the Sinogram Sparsified Metal Artifact Reduction Technique (SSMART) for Electron Beam Computed Tomography (EBCT) data. We hypothesize that rather than replacing the affected data sets with estimations, simply removing and reconstructing the images without them can lead to images of increased quality and accuracy.

Index Terms—Metal artifact reduction, Iterative reconstruction technique, Electron Beam CT, compressed sensing

I. INTRODUCTION

In recent years, there have been significant improvements made in two different techniques to combat the problem of metal artifacts in CT imaging improving the algorithm in itself, and adding spectral information to improve the quality of the image. While in the medical field, Metal Artifact Reduction (MAR) is used only when dealing with patients who have metallic implants in their bodies, it is a constant necessity for scanning baggage in the security field, where the presence and amount of metal is much more frequent and severe.

The fundamental problem of MAR is the nonlinear effects of measurements by the corruption or shifting of the energy spectra [1] [2] [3]. It has been speculated that MAR is a problem without a simple, generalized solution, and the solutions [4] [5] [6] [7] [8] [9] [10] currently used are limited to the correction of mild artifacts and local artifacts.

We present a novel metal artifact reduction algorithm using Electron Beam Computed Tomography (EBCT) scanner data (i.e., IMATRON C300). Our algorithm takes advantage of accurate forward system modeling and Iterative Reconstruction Technique (IRT) using the compressed sensing theory to

This research was funded by the center of Awareness and Localization of Explosives Related Threats (ALERT) at Northeastern University and the Department of Homeland Security (DHS). ¹Massachusetts General Hospital and Harvard Medical School, Dept. of Radiology, Boston, MA, email: sdo@mgh.harvard.edu ²Boston University, Dept. of Electrical and Computer Engineering, Boston, MA, email:wckarl@bu.edu

reconstruct images from incomplete data sets (i.e., Sparse ray-sums).

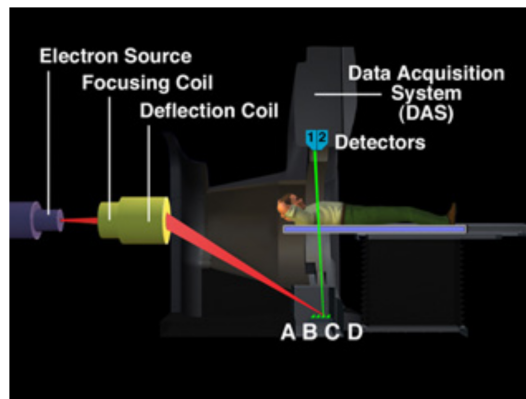


Fig. 1. A configuration of Electron Beam Computed Tomography (EBCT)

In this paper, we propose that rather than to replace the identified corrupted measurements with inaccurate ones, we simply exclude them in the fidelity term of the energy functional so that the corrupted measurements are not included in the image formation process. In doing so, we would effectively change the MAR problem from being about inaccurate data correction to sparse data image reconstruction.

The proposed algorithm, called the Sinogram Sparsified Metal Artifact Reduction Technique (SSMART), has shown robust and effective metal artifacts (i.e., streaking artifacts, low frequency shadowing artifacts etc.) reduction results with sparse sinogram data in even high clutter cases. The SSMART results were compared to Xrec (i.e., FBP) results by visual inspections and segmentation algorithms (i.e., CCL and Tumbler[11]).

II. METHODS

A. System Models

EBCT have multiple formats of sinogram in the pre-processing stages. To achieve an image of the highest quality, we used the native geometry model of EBCT. It requires the accurate system modeling of EBCT as shown in Figure 2. Of the two concentric half circles, and the bigger circle depicts an electron beam target (source ring), while the smaller is for detector modules. The radius of the source ring is 900.0 mm. The 864 channel detector modules that measure over 216 degree has a 676.0 mm radius. The reconstruction field of view is a 475.0 mm circle. The system can collect full sinogram data within 116.16 ms (total sweep time) without any gantry motion.

B. Image Reconstruction Algorithm

The FBP type image reconstruction algorithm (Xrec) is implemented on the system and is used as the conventional method for the comparison. The main idea of SSMART is to remove and simply not use less reliable ray-sums that passed metal components in the fidelity term. The metal passed ray-sums go through beam hardening, spectral shifting, intensity clipping etc. effects and it is very hard to correct all of these with the measurements from an energy integration detector.

As shown in Figures 3, 4, 5, and 6, when there are artifacts, we focused on the measurements which didn't pass through the metal objects. In order to use only reliable data, we had to develop a decision rule to determine metal passed ray-sums on the image domain and an image reconstruction method to reconstruct an image without metal component and additional artifacts. In this reconstruction, the number of measurements became smaller than the number of unknowns, making it an under-determined problem. Therefore, we developed a Sinogram Sparsified Reconstruction to solve this problem.

As shown in **Algorithm 1**, SSMART consists of pre-correction steps (2-5) and post compensation steps (9-11) with Sinogram Sparsified Iterative Reconstruction (SSIR). The two pre and post-image reconstruction steps can be replaced by a conventional FBP algorithm.

Algorithm 1 SSMART

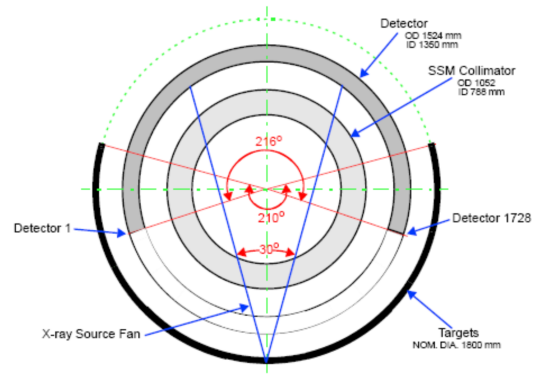
- 1: **procedure** $X_{ss} = \operatorname{argmin} E(Y_{ss}, X) + \alpha E(X)$
 - 2: $\hat{X} = H^{-1}Y$ (FBP or IRT)
 - 3: $X_M \leftarrow \hat{X}[0, Th]$ (Metal Image Mask)
 - 4: $X_S \leftarrow \hat{X} - (X_M[i] - Th)$ (Soft Image Mask)
 - 5: $Y_M \leftarrow HX_M$ (Metal Sinogram Mask)
 - 6: **for** each integer k in L **do** (SSIR)
 - 7: $\hat{X}_S \leftarrow H^{-1}[\Psi, \Phi]Y_S$
 - 8: **end for**
 - 9: $X_E \leftarrow (X - \hat{X}_S) \times X_M'$
 - 10: $Y_E \leftarrow HX_E$
 - 11: $Y_{ss} \leftarrow Y - Y_E$
 - 12: $X_{ss} \leftarrow H^{-1}Y_{ss}$ (FBP or IRT)
 - 13: **end procedure**
-

III. RESULTS

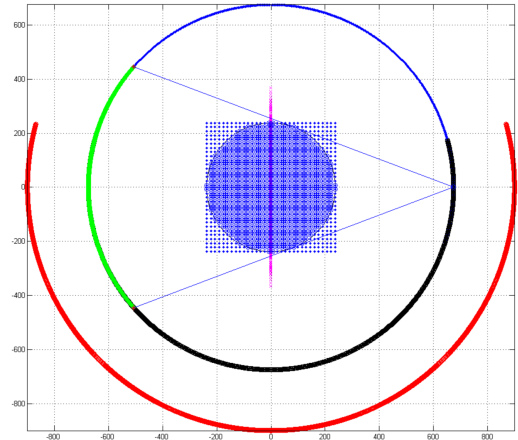
A. Clouds

In the clouds plot, SSMART reduced clouds sizes a sign of better image reconstruction. The clouds plot was on metrics we used to evaluate the image quality of SSMART compared to Xrec. The automatic segmentation algorithm was applied to both SSMART and Xrec images. As shown in Figure 7, three class clouds (i.e., water, doped water, and rubber sheet) were displayed in the plots by mean (X-axis) and standard deviation (Y-axis). Each class is composed of multiple small dots, and each dot represents the segmentation results of a single object. To form a cloud, the distribution of multiple measurements (=dots) was calculated for each class from multiple slides for Xrec and SSMART independently.

Firstly, the clouds areas were calculated and plotted to show significant area reductions in SSMART from all three classes.



(a)



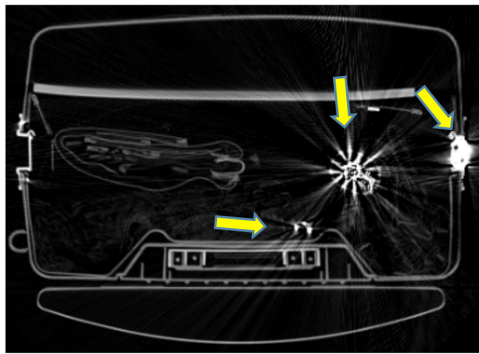
(b)

Fig. 2. A diagram of EBCT: (a) A descriptive diagram of EBCT, (b) An accurate modeling of EBCT for every image pixels and source/detector elements locations

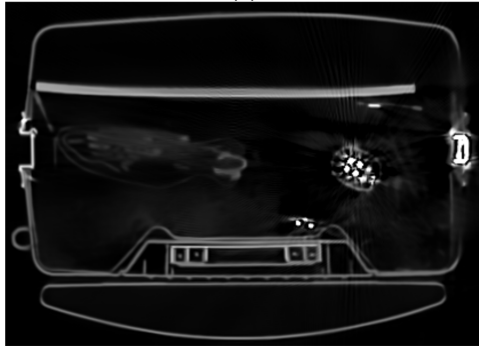
The cloud area of water class in the Xrec image was 18473, as compared to the 11552 in SSMART, a significant reduction. The cloud area of Doped water in the Xrec image was 3916, while in SSMART it was 1741. The cloud area of the Rubber sheet area in Xrec image was 23539, reduced to 8365 by SSMART. Secondly, the first Principal Component (PC) values were also calculated to measure the longer diameters of ellipsoids in the clouds. As shown in the plot in Figure 7, the PC-1 was increased a little in SSMART for Water class from 12469 to 12553, but all other PC-1s were decreased significantly for both the Doped water class (from 8959 to 1527) and the Rubber sheet class (from 20957 to 5156). Thirdly, the outliers in the Xrec clouds plot were absent in the those of SSMART. A few dots were plotted near 600 (Y-axis) in Xrec plot but those went down to 300 in the SSMART plot to make the clouds compact.

B. Image Comparison

It is important to observe images visually as radiologists do. In this study, metal artifacts in Xrec are noticeably suppressed in SSMART. In Figures 3 and 4, we compared SSMART with Xrec displaying in the same contrast window. As we marked with arrows in Figure 3, the streaking artifacts in Xrec images were significantly reduced in SSMART images. The low



(a)



(b)

Fig. 3. Image comparison for streaking artifacts reduction: (a) Xrec images with severe streaking metal artifacts, (b) SSMART image with streaking artifacts suppression.

frequency shading artifact in the Figure 4 was also suppressed in the SSMART image. The boundaries of metal components were clearly defined in SSMART images as compared to fuzzy boundaries in Xrec images. However, SSMART images looked more blurry than those of Xrec because of strong regularization.

Even though the strong regularization in SSMART caused images smooth, the segmentation results from SSMART are superior to those from Xrec as shown in Figure 5 and 6.

IV. CONCLUSION

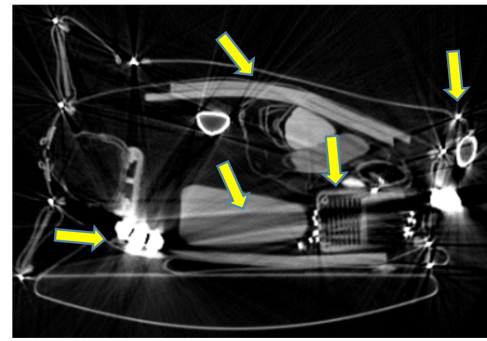
The proposed SSMART suppressed metal artifacts effectively, improving the accuracy in the following segmentation.

ACKNOWLEDGMENT

The authors gratefully acknowledge Dr. Carl R. Crawford, John Beaty, and Dr. Michael Silevitch for their support. We also acknowledge Stratovan Inc. for the automatic segmentation tasks.

REFERENCES

- [1] Fabian Bamberg, Alexander Dierks, Konstantin Nikolaou, Maximilian F Reiser, Christoph R Becker, and Thorsten RC Johnson, "Metal artifact reduction by dual energy computed tomography using monoenergetic extrapolation," *European radiology*, vol. 21, no. 7, pp. 1424–1429, 2011.
- [2] Young Han Lee, Kwan Kyu Park, Ho-Taek Song, Sungjun Kim, and Jin-Suck Suh, "Metal artefact reduction in gemstone spectral imaging dual-energy ct with and without metal artefact reduction software," *European radiology*, vol. 22, no. 6, pp. 1331–1340, 2012.



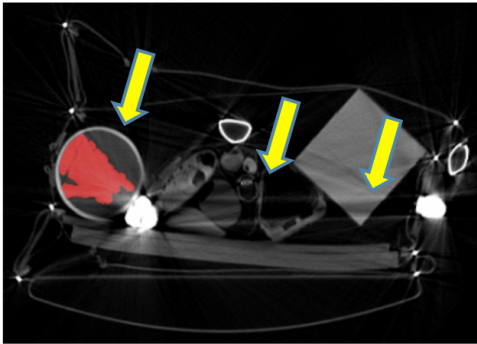
(a)



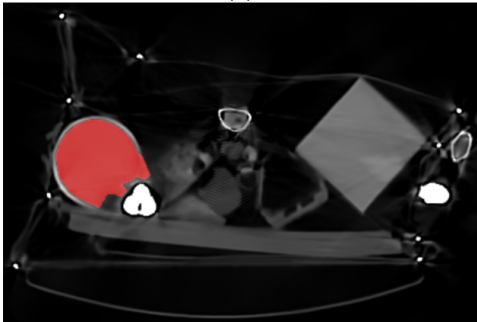
(b)

Fig. 4. Image comparison for low frequency shadowing artifact suppression: (a) Xrec images with severe shadowing metal artifacts, (b) SSMART image with low frequency shadowing artifact suppression.

- [3] R Guggenberger, S Winklhofer, G Osterhoff, GA Wanner, M Fortunati, G Andreisek, H Alkadhi, and P Stolzmann, "Metallic artefact reduction with monoenergetic dual-energy ct: systematic ex vivo evaluation of posterior spinal fusion implants from various vendors and different spine levels," *European radiology*, vol. 22, no. 11, pp. 2357–2364, 2012.
- [4] Xiaomeng Zhang, Jing Wang, and Lei Xing, "Metal artifact reduction in x-ray computed tomography (ct) by constrained optimization," *Medical physics*, vol. 38, no. 2, pp. 701–711, 2011.
- [5] Raoul MS Joemai, Paul W de Bruin, Wouter JH Veldkamp, and Jacob Geleijns, "Metal artifact reduction for ct: Development, implementation, and clinical comparison of a generic and a scanner-specific technique," *Medical physics*, vol. 39, no. 2, pp. 1125–1132, 2012.
- [6] Guido Hilgers, Tonnis Nuver, and André Minken, "The ct number accuracy of a novel commercial metal artifact reduction algorithm for large orthopedic implants," *Journal of Applied Clinical Medical Physics*, vol. 15, no. 1, 2014.
- [7] Katrien Van Slambrouck and Johan Nuyts, "Metal artifact reduction in computed tomography using local models in an image block-iterative scheme," *Medical physics*, vol. 39, no. 11, pp. 7080–7093, 2012.
- [8] Seemeen Karimi, Pamela Cosman, Christoph Wald, and Harry Martz, "Segmentation of artifacts and anatomy in ct metal artifact reduction," *Medical physics*, vol. 39, no. 10, pp. 5857–5868, 2012.
- [9] Bärbel Kratz, Imke Weyers, and Thorsten M Buzug, "A fully 3d approach for metal artifact reduction in computed tomography," *Medical physics*, vol. 39, no. 11, pp. 7042–7054, 2012.
- [10] Esther Meyer, Rainer Raupach, Michael Lell, Bernhard Schmidt, and Marc Kachelrieß, "Frequency split metal artifact reduction (fsmar) in computed tomography," *Medical physics*, vol. 39, no. 4, pp. 1904–1916, 2012.
- [11] David Wiley, "Method and apparatus of identifying objects of interest using imaging scans," Feb. 4 2014, US Patent 8,644,578.

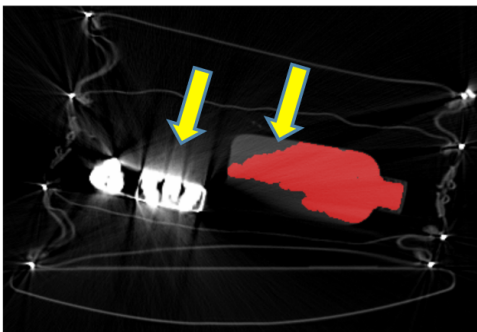


(a)

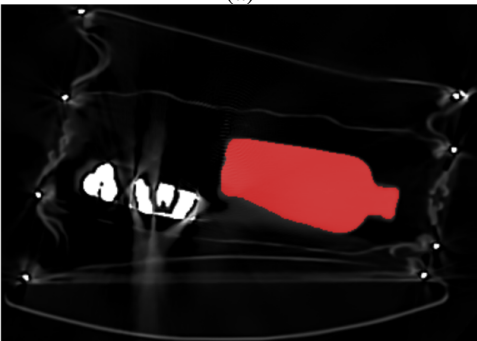


(b)

Fig. 5. Automatic segmentation results (water bottle) comparison: (a) Xrec image, (b) SSMART shows a significant improvement in accuracy.



(a)



(b)

Fig. 6. Automatic segmentation results (water bottle) comparison: (a) Xrec image with automatic target detection algorithm, (b) SSMART shows better result in boundary segmentation.

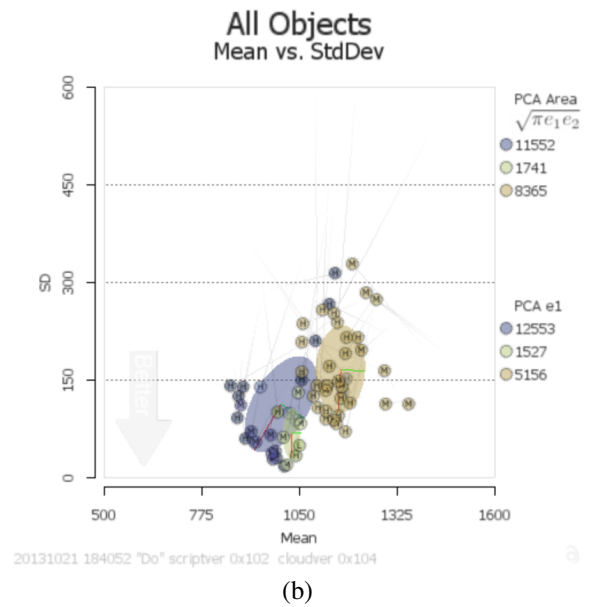
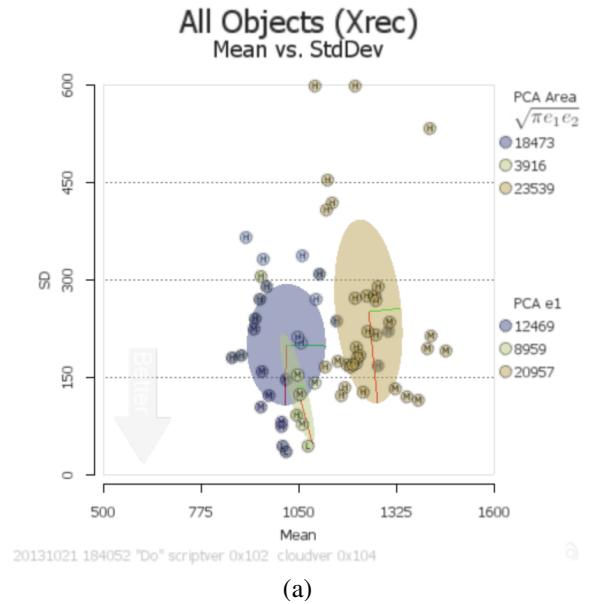


Fig. 7. Performance comparison by cloud metrics: The cloud plots show scatter dots for targets by the means (X-axis) and the standard deviation or targets (Y-axis) for (a) Xrec and (b) SSMART. SSMART shows significant improvements by the smaller size clouds positioned in the bottom of plot.

Sinogram restoration for security screening CT applications

Phillip Vargas and Patrick La Riviere

Abstract—In this work, we apply metal artifact reduction and sinogram restoration algorithms to security screening luggage datasets that were acquired using an Imatron medical CT scanner. The goal is to reduce noise and especially artifacts that can impede the automatic threat recognition algorithms that are routinely applied to CT images of checked luggage. We couple the sinogram restoration with metal artifact reduction algorithms and demonstrate a clear reduction in certain kinds of streak artifacts, leading to improved segmentation and classification accuracy in a wide range of cases. However, secondary artifacts were occasionally observed that produced significant bias in CT values. This leads to a spreading of the mean-value clouds and a reduced level of segmentation precision.

Keywords—security screening, explosive detection, computed tomography, sinogram restoration

I. INTRODUCTION

The goal of this work was to implement sinogram domain preprocessing coupled with standard analytic reconstructions such as filtered backprojection (FBP) in order to reduce noise and artifacts in reconstructed baggage screening images.

Computed tomography (CT) measurement data, whether in the medical or security fields, are degraded by a number of physical factors that cause the data to deviate from the ideal model assumed by all analytic image reconstruction algorithms. These factors include off-focal radiation, detector afterglow, detector crosstalk, scatter, beam hardening, and metal-induced photon starvation, and they will generally produce artifacts and degradations in reconstructed images unless corrected or otherwise massaged (some compensation schemes for detector crosstalk simply add crosstalk across detector module boundaries, where the sudden lack of crosstalk would yield a ring artifact in the image). In current practice, many such effects are addressed by a sequence of independent sinogram-preprocessing steps, including recursive corrections for detector afterglow and deconvolution for off-focal radiation, that have the potential to amplify data noise.

The noise level in measured CT transmission data is also a major determinant of the ultimate visual quality and diagnostic utility of the reconstructed images. Noise arises from two principal sources in CT: quantum noise, which is a consequence of photon-counting statistics, and electronic noise, which arises in the photodiode and other components of the detector electronics.

We have previously developed methods in the medical context in which we formulate CT sinogram preprocessing as a statistical restoration problem in which the goal is to obtain the best possible estimate of the line integrals needed for reconstruction from the set of noisy, degraded detector measurements [1]. We developed a general imaging model relating the degraded measurements to the ideal sinogram of line integrals and propose to estimate the ideal line integrals by iteratively maximizing an appropriate penalized statistical likelihood function. The maximization algorithm is based on the separable paraboloidal surrogates strategy developed by Fessler [2].

The essential idea is to approximate a difficult optimization problems by a series of simpler ones (“surrogates”), especially quadratic ones (hence “paraboloidal”) and ones in which each pixel can be acted on independently at each iteration (hence “separable”). Image reconstruction can then proceed by use of existing, non-iterative approaches or even iterative approaches since many iterative algorithms being considered for CT do not try to model the effects that are corrected by sinogram restoration. We have demonstrated that the approach can successfully correct for sinogram degradations, effectively eliminating the image artifacts caused by beam hardening and off-focal radiation. We also demonstrate that the proposed approach can achieve lower noise levels at a given resolution than can many existing approaches.

Here we couple this approach with a metal artifact reduction (MAR) algorithm. The goal is to see whether this combination of very computationally efficient algorithms can achieve some of the benefits of fully iterative image reconstruction algorithms at a fraction of their computational cost.

II. METHODS

A. Metal artifact reduction

For metal artifact reduction, we implemented the most promising algorithm from the literature on medical CT medical artifact reduction. Called frequency-splitting metal artifact reduction (FSMAR) [3], the approach seeks to address two principal problems with many previous metal artifact reduction algorithms: their potential to introduce additional, secondary artifacts when estimating metal-corrupted projection data, and their tendency to obscure important

The authors are with the Department of Radiology, The University of Chicago.

details near the metal inclusion. A flow chart of the algorithm is shown in Fig 1.

The algorithm starts with a raw-data inpainting method called normalized metal artifact reduction (NMAR) previously developed by the same group [4] and depicted in Fig 2. This approach improves on previous inpainting approaches through a normalization and denormalization of the data before and after the interpolation of the data in the metal shadow. This mitigates inconsistencies between the inpainted and existing data, reducing the chance of introducing secondary artifacts, streaks that can arise when the inpainted data is not a consistent projection of any plausible object. The normalization is based on forward projection of a metal-free prior image that is obtained by multithreshold segmentation of the initial uncorrected image. The metal shadow itself is identified through the forward projection of the metal component of the segmentation. The measured sinogram is divided by the normalization sinogram, interpolation is performed across the metal gaps, and then the interpolated sinogram is multiplied by the normalization sinogram to return to the correct scaling.

The FSMAR step of the algorithm attempts to restore some high frequency information near the metal structures that may have been lost during the NMAR process. Both the original and MAR corrected images are then low- and high-

$$Y_i^{meas} = G_i \sum_{m=1}^M E_m \text{Poisson} \left\{ \sum_{j=1}^{N_y} b_{ij} I_j \lambda_m^{(j)} \exp \left[- \int_{L_j} \mu(\mathbf{x}, E_m) dl \right] + s_m^{(i)} \right\} + \text{Normal} \{ d_i, \sigma_i^2 \}.$$

In the first term, which represents the effects of photon-counting statistics, I_j is the incident X-ray intensity along the j^{th} measurement line. These I_j are, of course, polychromatic, and so we further assume they are grouped into discrete energy bins E_m , $m = 1, \dots, M$, with probabilities $\lambda_m^{(j)}$ satisfying

$$\sum_{m=1}^M \lambda_m^{(j)} = 1.$$

The superscript j on $\lambda_m^{(j)}$ reflects the fact that the energy distributions of photons emerging from an X-ray tube can be spatially varying due to the use of bow-tie filters as well as to the heel effect. The function $\mu(\mathbf{x}, E)$ is the energy-dependent attenuation map, which we would ideally like to reconstruct, although from single-energy data we typically seek to reconstruct $\mu(\mathbf{x}, E_r)$, the attenuation map at some reference energy. The term $s_m^{(i)}$ is the number of scattered photons of energy E_m contributing to measurement Y_i . In this model, the i th measurement is seen to receive contributions not just from the i th attenuation line but from other attenuation lines j not equal to i with weight b_{ij} . This could model, for example, the effects of off-focal radiation, which results in contributions from other points in the sinogram lying on a locus that can be determined by the geometry of the X-ray tube's off-focal halo,

pass filtered. The high-pass filtered original image is then added back to the corrected image with a spatially varying weight that is maximum at the center of metal objects and falls off rapidly as you move away from the metal. This seeks to balance resolution recovery with noise and streak control.

B. Sinogram restoration

We employ a model for raw CT data that incorporates the statistical and deterministic effects discussed above. The model applies equally well to single-slice, multi-slice, and cone-beam scanners and to both conventional and helical modes of operation. We assume that the CT scan produces a set of measurements that are organized into a one-dimensional (1D) vector \mathbf{y}^{meas} , with elements y_i^{meas} , $i = 1, \dots, NY$, where NY is the total number of measurements in the scan, given by the product of the number of detector elements and the number of projection views acquired.

We assume that each y_i^{meas} is a realization of a random variable Y^{meas} whose statistics are compound Poisson, as described by the following model:

the X-ray collimation, and the detector geometry. The weights b_{ij} could also model the source and detector response functions as well as crosstalk and detector lag, although if these effects are significant they introduce noise correlations that should be accounted for by a different model.

Each detected photon contributes to the measured detector signal in proportion to its energy E_m , which accounts for the factor of E_m in this expression; the constant of proportionality (the gain) is denoted G_i . The detected signal is read out through detector electronics having dark current d_i and electronic readout noise assumed to be normally distributed with variance σ_i^2 .

We assume that I , G , d , σ^2 , the average energy of the incident beam, and an energy-averaged and normalized estimated scatter term are all known or measurable. While it would naturally be useful to be able to reconstruct $\mu(\mathbf{x}, E)$ for all energies E , this is generally not possible without the use of fully iterative reconstruction methods and fairly strong assumptions about the material composition of the object being imaged, such as assuming that the density of a given material fully determines its spectral properties (very dense objects are assumed to be bone-like, unit density assumed to be water like). Such assumptions are somewhat unrealistic for medical imaging and highly inappropriate in the security context. In single-energy CT, the goal is generally the more modest one of reconstructing the attenuation map $\mu(\mathbf{x}, E_r)$ at

some reference energy E_R . To achieve this, one needs first to estimate a set of “monochromatic” attenuation line at the reference energy, from the set of measurements $y^{\text{meas}}, i = 1, \dots, N_Y$. These estimated line integrals can then be input to a standard analytic reconstruction algorithm.

In the present work, we focused solely on the effects of Poisson noise, often the source of distracting streaks in images and did not attempt to model the other non-idealities of the Imatron scanner, but many of these effects could readily be accommodated with this framework.

III. RESULTS

A. Visual results showing improved uniformity and reduced streaks

Fig. 1 shows improvement in uniformity and circularity of the beads in the left hand panel and of the water in the center of the right hand panel. There is perhaps some evidence of overcompensation in the water cylinder.

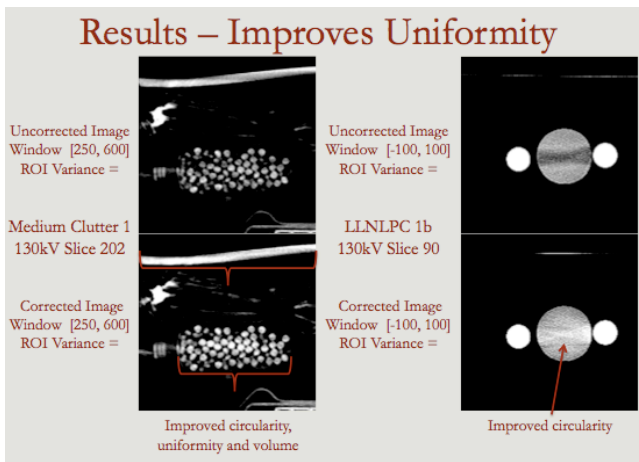


Figure 1: Demonstration of improved uniformity.

Fig. 2 shows a reduction in streak artifacts without loss of resolution for fine lines and small objects.

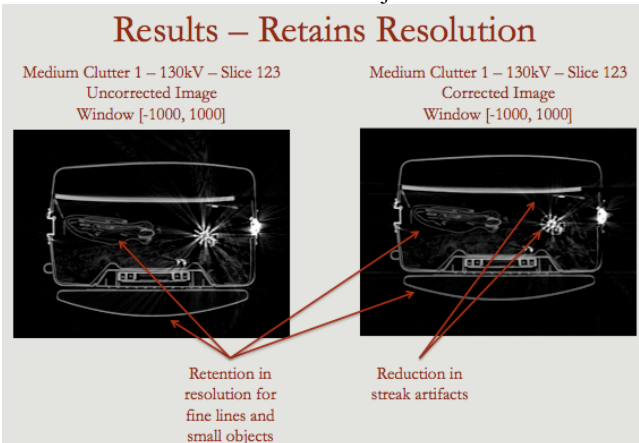


Figure 2: Demonstration of resolution retention.

Fig. 3 shows mitigation of object splitting, with a strong dark streak splitting the water bottle being greatly reduced in magnitude. Some mild new hyperintense streaks are observed, however.

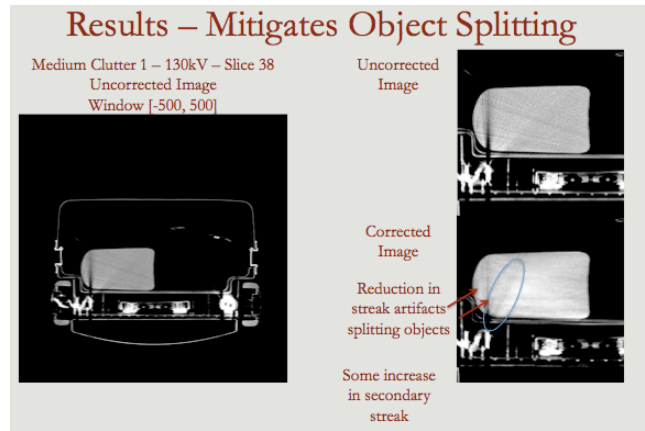


Figure 3: Demonstration of reduced streaks..

B. Result showing improved segmentation performance

Figure 4 shows a situation where the sinogram processing algorithm has mitigated a streak artifact yielding improved segmentation relative to that achieved from the xrec image. The segmentation was performed using connected-component labeling. The segmentation is still not perfect, with a portion of the arc still missing, but it demonstrates that improved image quality can lead to improved segmentation performance.

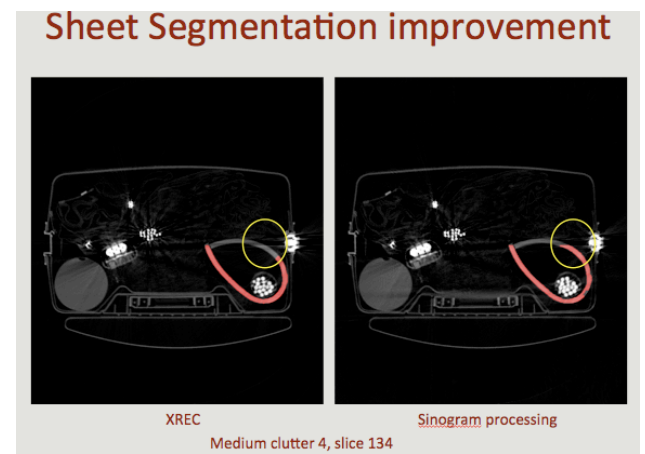


Figure 4: Illustration of CCL segmentation improvement.

C. Quantitative results

Quantitative results were generated by study participant Stratovan Inc. in which known objects were segmented manually and the various reconstruction approaches could be judged on their ability to support manual segmentation and also quantitative accuracy of CT number within the object boundaries. An example of such a plot is shown in Fig. 5.

IV. CONCLUSIONS

The sinogram processing demonstrated mixed success. There was a clear reduction in certain kinds of streak artifacts, leading to improved segmentation accuracy in a wide range of cases. However, secondary artifacts were occasionally observed that produced significant bias in HU values. This led to a spreading of the mean clouds and a reduced level of segmentation precision.

One of the great strengths of the sinogram processing approach is the very low computational cost. The MAR algorithm involves a single segmentation and reprojection step and the sinogram restoration algorithm a small number of sinogram-domain iterations with the overall computational burden being on the order of the analytic reconstruction or a single iteration of an iterative reconstruction algorithm. It is possible that further parameter optimization in the sinogram processing could limit the outlier cases observed and yield performance comparable to the fully iterative approaches at a very low computational cost.

Alternatively, the sinogram processed data could be input to one of the fully iterative approaches, which might speed convergence while benefiting from the ability of fully iterative approaches to enforce edge preserving more naturally than can be done in the sinogram domain.

ACKNOWLEDGMENTS

This material is based upon work supported by the U.S. Department of Homeland Security, Science and Technology Directorate, under Task Order Number HSHQDC-12-J-00056. The views and conclusions contained in this document are those of the authors and should not be interpreted as necessarily representing the official policies, either expressed or implied, of the U.S. Department of Homeland Security.

REFERENCES

- [1] La Rivière, P. J., and Bian, J., and Vargas, P. A., "Penalized-likelihood sinogram restoration for computed tomography," *IEEE Trans. Med. Imag.*, 25, pp. 1022-1036, 2006.
- [2] H. Erdoğan and J. A. Fessler, "Monotonic algorithms for transmission tomography," *IEEE Trans. Med. Imaging* 18, pp. 801-814 (1999).
- [3] Meyer et al., "Frequency split metal artifact reduction (FSMAR) in computed tomography," *Med. Phys.* 39, pp. 1904 - 1916 (2012).
- [4] Meyer et al., "Normalized metal artifact reduction (NMAR) in computed tomography," *Med Phys* 37, pp. 5482-93 (2010)

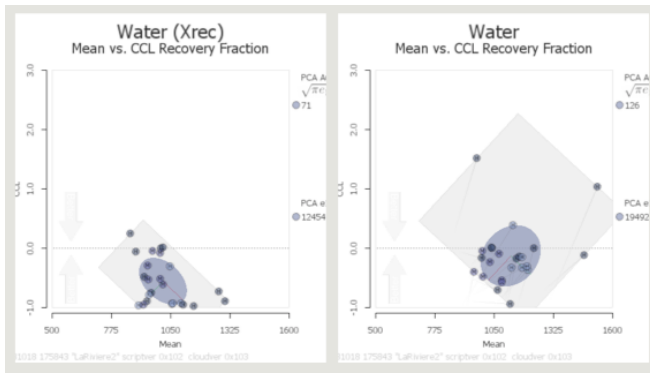


Figure 5: Mean vs CCL cloud plots.

D. Results showing limitations of the approach

In Fig 6, we show an image that produced one of the two outlier dots in the water cloud. It can be seen to suffer from substantial "blooming" artifacts and hyperintense streaks. This could be caused by failure of the MAR algorithm, leading to introduction of secondary artifacts. This issue needs to be investigated further.

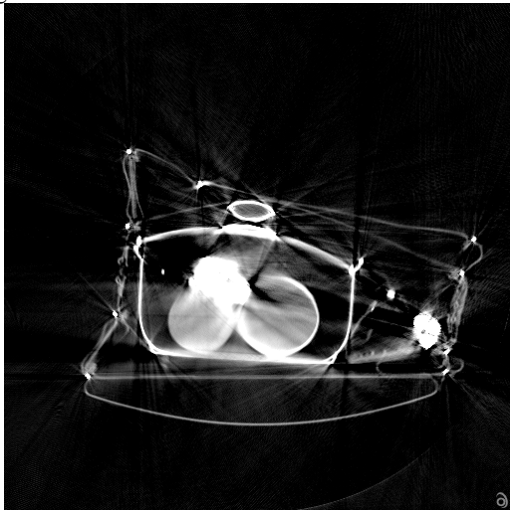


Figure 7: Reconstructed image producing one of the outlier dots in water cloud. The application of MAR has apparently introduced secondary artifacts leading to bright shading in the water cylinders. This gives rise to an artificially high HU value for the water.

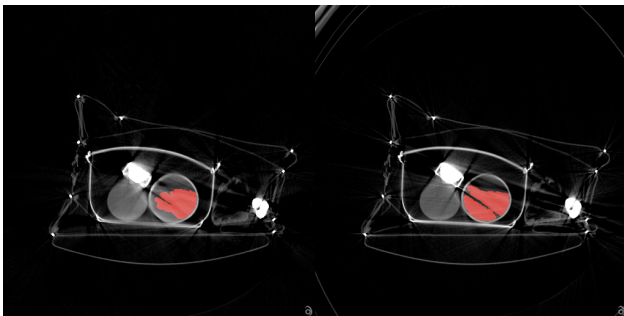


Figure 8: (Left) Our result. (right) Xrec result. Our result mitigates the main dark streak artifact diving the xrec segmentation, but the hyperintense swath in the lower left of the cylinder causes its omission from the segmentation.

Artifact reduction in dual-energy CT reconstruction for security applications

Limor Martin, W. Clem Karl and Prakash Ishwar

Abstract—In this paper we present a structure-preserving dual-energy (SPDE) CT reconstruction method for security, which provides enhanced estimates of material-dependent basis coefficient images. In security applications many different materials may be scanned in various degrees of clutter and metal objects are common. Image noise and metal artifacts are often severe and can lower the accuracy of material identification. The proposed approach aims at mitigating metal artifacts and improving material parameter accuracy. The basis coefficient images are generated jointly as the solution of a single model-based optimization problem. An auxiliary variable corresponding to a mutual boundary-field is estimated as well and applied to the basis coefficient images to reduce object splitting and material variability. In addition, metal aware data weighting is included to reduce streaks. We evaluate the performance of the method both visually and quantitatively using simulated dual-energy data. We demonstrate a significant reduction in noise and metal artifacts compared to a baseline filtered back projection (FBP) method.

I. INTRODUCTION

Dual-energy X-ray computed tomography (DECT) is a powerful tool for non-destructive evaluation, used for security and medical purposes. With DECT two energy-selective sets of tomographic measurements are acquired, allowing enhanced material discrimination relative to conventional single-energy computed tomography (CT). Several DECT techniques have been suggested since the 1970s [1], [2], [3]. In general, the goal is to reconstruct a small number of material-specific basis coefficient images, such as the photoelectric and Compton coefficients, from the energy-selective measurements. Usually filtered back-projection (FBP) is used for image formation and there is no unified treatment of metal artifacts. In the security application, where DECT is used for scanning checked luggage, many different materials may be scanned in various degrees of clutter and metal objects are common. In this application, image noise and metal artifacts can be severe and lead to less reliable image estimates. Therefore, different reconstruction techniques may be appropriate.

In this paper we describe a structure-preserving dual-energy (SPDE) reconstruction method for the formation of enhanced

This material is based upon work supported by the U.S. Department of Homeland Security, Science and Technology Directorate, under Award Number 505035-78050. The views and conclusions contained in this document are those of the authors and should not be interpreted as necessarily representing the official policies, either expressed or implied, of the U.S. Department of Homeland Security.

The authors would like to thank Prof. T. G. Schmidt of Marquette University for providing the simulated data and spectra estimates, Prof. C. A. Bouman and Dr. P. Jin of Purdue University for providing the Imatron forward projection matrix, and Prof. P. J. La Rivière of University of Chicago for providing the Imatron FBP code.

Authors are with the Department of Electrical and Computer Engineering at Boston University, Boston, MA 02215 USA (E-mail: limor@bu.edu).

basis coefficient images. We form the images as the solution of an optimization problem which explicitly models the physical tomographic projection process. Metal induced streaking is reduced by appropriately down-weighting unreliable data. A boundary-preserving prior based on [4] is incorporated to improve object localization. In particular, we estimate a mutual boundary-field along with the material-parameter images. The boundary-field provides accurate object localization and helps to suppress the splitting and streaking effects of metal artifacts. This method extends our work in [5]. Here we incorporate an additional parameter in the problem formulation, which allows a more reliable boundary-field estimate.

We test our method on simulated dual-energy measurements of a suitcase phantom containing water bottles and metal. We show that with SPDE both noise and metal artifacts in the reconstructed basis coefficient images are greatly reduced, which can lead to more accurate material identification.

II. DUAL-ENERGY CT RECONSTRUCTION

In DECT two sets of measurements are acquired with different energy spectra by either changing the source spectrum or using energy-sensitive detectors. Typically these measurements are acquired at a “high” energy and a “low” energy, corresponding to emphasis on high or low energies respectively, which we denote here with an “H” or “L” subscript. The measured photon counts are modeled as follows [6]:

$$\begin{aligned} I_L(\theta, t) &= \int w_L(E) e^{-\int_{\mathcal{L}_{\theta,t}} \mu(\vec{r}, E) dl} dE \\ I_H(\theta, t) &= \int w_H(E) e^{-\int_{\mathcal{L}_{\theta,t}} \mu(\vec{r}, E) dl} dE \end{aligned} \quad (1)$$

where θ is the projection angle, t is the projection displacement, E is the energy level, \vec{r} is the spatial location, $w_L(E)$ and $w_H(E)$ are the low and high spectral weighting functions at energy E , $\mu(\vec{r}, E)$ is the linear attenuation coefficient (LAC) at location \vec{r} and energy E , and $\int_{\mathcal{L}_{\theta,t}} \mu(\vec{r}, E) dl$ is the line integral of $\mu(\vec{r}, E)$ over the ray path defined by θ and t .

Typically, the LAC $\mu(\vec{r}, E)$ is decomposed with respect to some known basis and the following model is assumed [2]:

$$\mu(\vec{r}, E) = a_1(\vec{r}) f_1(E) + a_2(\vec{r}) f_2(E) \quad (2)$$

where $a_1(\vec{r})$ and $a_2(\vec{r})$ are the basis coefficients of the material at location \vec{r} and $f_1(E)$ and $f_2(E)$ are the basis functions.

Using decomposition (2), the measurements (1) become:

$$\begin{aligned} I_L(\theta, t) &= \int w_L(E) e^{-(A_1(\theta,t) f_1(E) + A_2(\theta,t) f_2(E))} dE \\ I_H(\theta, t) &= \int w_H(E) e^{-(A_1(\theta,t) f_1(E) + A_2(\theta,t) f_2(E))} dE \end{aligned} \quad (3)$$

where $A_1(\theta, t) = \int_{\mathcal{L}_{\theta, t}} a_1(\vec{r}) dl$ and $A_2(\theta, t) = \int_{\mathcal{L}_{\theta, t}} a_2(\vec{r}) dl$. The quantities $A_1(\theta, t)$ and $A_2(\theta, t)$ for a set of θ and t points are called the coefficient sinograms.

In many DECT methods the goal is to reconstruct the coefficient images, $a_1(\vec{r})$ and $a_2(\vec{r})$ given the dual energy measurements $I_L(\theta, t)$ and $I_H(\theta, t)$. Since the problem is nonlinear and high-dimensional, a well-known solution approach is to separate it into two sub-problems [1]. In the first sub-problem, the nonlinear set of equations (3) is solved for $A_1(\theta, t)$ and $A_2(\theta, t)$ given $I_L(\theta, t)$ and $I_H(\theta, t)$. This is implemented, for example, by polynomial fitting [1] or least squares [3]. The second sub-problem is reconstruction of the basis coefficient images $a_1(\vec{r})$ and $a_2(\vec{r})$. This is usually modeled as a linear problem and solved by applying FBP individually to $A_1(\theta, t)$ and $A_2(\theta, t)$.

III. PROPOSED APPROACH

Our focus in this work is on improving the solution of the second sub-problem in DECT, i.e., reconstruction of the basis coefficient images from the basis coefficient sinograms. This problem is related to the field of multi-sensor image fusion. Each basis coefficient sinogram may be regarded as observations obtained from a different measurement channel/modality. In [7], Weisenseel et al. proposed a shared boundary fusion formulation as part of a framework for fusion of medical imaging modalities. We incorporate the main principles from this work in our approach. We utilize the mutual structure information and reconstruct the coefficient images jointly. In this way, object localization may be improved in both images. An illustration contrasting the similarities and differences between the typical DECT and the proposed approaches is shown in Figure 1.

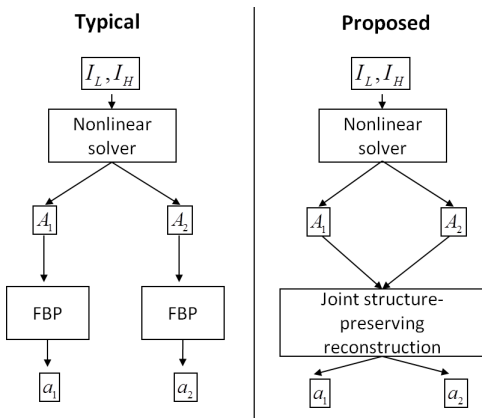


Fig. 1. Typical approach (left) and proposed approach (right).

A. General formulation

We consider the discretized problem, where \underline{I}_L and \underline{I}_H denote vectors containing dual-energy measurements for a set of θ and t points, and \underline{A}_1 and \underline{A}_2 are vectors containing the photoelectric and Compton sinograms at the same points. Similarly, \underline{a}_1 and \underline{a}_2 are stacked basis coefficient images at a set of spatial locations \vec{r} .

We introduce an auxiliary variable \underline{s} corresponding to the mutual edge field of \underline{a}_1 and \underline{a}_2 . Given \underline{A}_1 and \underline{A}_2 , we jointly estimate \underline{a}_1 , \underline{a}_2 , and \underline{s} by solving the following problem:

$$\begin{aligned} \underset{(\underline{a}_1 \geq 0, \underline{a}_2 \geq 0, \underline{s})}{\text{minimize}} \quad & \{ \|\underline{A}_1 - T\underline{a}_1\|_{W_I}^2 + \|\underline{A}_2 - T\underline{a}_2\|_{W_I}^2 \\ & + \lambda_1^2 \|D\underline{a}_1\|_{W_1(\underline{s})}^2 + \lambda_2^2 \|D\underline{a}_2\|_{W_2(\underline{s})}^2 \\ & + \lambda_3^2 \|\underline{a}_1\|_2^2 + \lambda_4^2 \|\underline{a}_2\|_2^2 \\ & + \lambda_5^2 \|D\underline{s}\|_2^2 + \lambda_6^2 \|\underline{s}\|_2^2 \} \end{aligned} \quad (4)$$

where λ_i , $i = 1, \dots, 6$, are non-negative regularization parameters, W_I is a nonnegative diagonal data weighting matrix, $W_1(\underline{s})$ and $W_2(\underline{s})$ are nonnegative diagonal weighting matrices which depend on \underline{s} and control the smoothing of the photoelectric image and Compton image respectively, T is the tomographic system forward projection operator, and D is a derivative operator. The weighted norm is defined as $\|v\|_M^2 = v^T M v$. The weights W_I , $W_1(\underline{s})$, and $W_2(\underline{s})$ are described in Sections III-B and III-C below.

Three effects are explicitly captured in the formulation (4). First, the tomographic model T is explicitly used. Second, explicit use is made of an object boundary-field \underline{s} to mitigate and limit the propagation of artifacts. Third, the sinogram data are weighted through W_I to reduce the effect of unreliable rays due to the presence of low count rays caused by metal.

B. Streak mitigation by a mutual boundary-field

The matrices $W_1(\underline{s})$ and $W_2(\underline{s})$ control the smoothing of basis coefficient images \underline{a}_1 and \underline{a}_2 respectively, and are used to ameliorate metal induced streaks and splits. They are formulated as follows:

$$W_i(\underline{s}) = \text{diag} \left((1 - \epsilon_i)(1 - \underline{s})^2 + \epsilon_i \right), \quad i \in \{1, 2\} \quad (5)$$

where \underline{s} is the boundary-field and $\epsilon_i \in [0, 1]$.

The contribution of \underline{a}_1 and \underline{a}_2 to the boundary-field estimate \underline{s} and the effect of \underline{s} on the smoothing of \underline{a}_1 and \underline{a}_2 are controlled by $W_1(\underline{s})$ and $W_2(\underline{s})$. The parameters ϵ_1 and ϵ_2 allow the inclusion of different boundary-field contributions from the coefficient images. This flexibility is useful when one of the coefficients has more reliable structure information than the other. Further, these parameters are useful as annealing parameters to aid in convergence of the solution iterations.

C. Data weighting to mitigate metal artifacts

In the presence of metal and high clutter some rays are significantly attenuated and the measured values for these rays are very small. Since few photons are measured, these data points are less reliable. We apply explicit data weighting to account for this phenomenon. The weighting matrix W_I is given by

$$W_I = \text{diag} \left((\underline{I}_H^2 + c)^{-1} \right) \quad (6)$$

where c is a constant and the square is element-wise. This weighting reduces the contribution of the unreliable, low count, rays which go through dense metal objects. The weighting is based on the high-energy sinogram because it is more reliable.

D. Optimization approach

The cost function in (4) depends on three coupled variables - \underline{a}_1 , \underline{a}_2 , and \underline{s} - and the resulting optimization problem is non-quadratic. In the absence of the non-negativity constraint, the following equations must hold at the optimum:

$$(T^T W_I T + \lambda_1^2 D^T W_1(\underline{s}) D + \lambda_3^2) \underline{a}_1 = T^T W_I \underline{A}_1 \quad (7)$$

$$(T^T W_I T + \lambda_2^2 D^T W_2(\underline{s}) D + \lambda_4^2) \underline{a}_2 = T^T W_I \underline{A}_2 \quad (8)$$

$$(B + \lambda_5^2 D^T D) \underline{s} = B \underline{u} \quad (9)$$

where

$$B = \text{diag}(\lambda_1^2(1 - \epsilon_1)[D\underline{a}_1]_j^2 + \lambda_2^2(1 - \epsilon_2)[D\underline{a}_2]_j^2 + \lambda_6^2)$$

$$[\underline{u}]_j = \frac{\lambda_1^2(1 - \epsilon_1)[D\underline{a}_1]_j^2 + \lambda_2^2(1 - \epsilon_2)[D\underline{a}_2]_j^2}{\lambda_1^2(1 - \epsilon_1)[D\underline{a}_1]_j^2 + \lambda_2^2(1 - \epsilon_2)[D\underline{a}_2]_j^2 + \lambda_6^2}$$

We iteratively solve (7) and (8) for \underline{a}_1 and \underline{a}_2 while keeping \underline{s} fixed, and solve (9) for \underline{s} while keeping \underline{a}_1 and \underline{a}_2 fixed. We enforce the non-negativity constraint in (4) by projecting the solution onto the constraint set at every iteration.

In practice we use ϵ_1 and ϵ_2 as annealing parameters in the optimization process. We adaptively vary their values at each iteration of the numerical solution. This approach allows us to gradually progress from a more blurred solution to a sharper solution. In addition, we can control the individual contributions of the coefficient images \underline{a}_1 and \underline{a}_2 to the estimation of the mutual boundary-field. More details are provided in the experiments section.

IV. EXPERIMENTAL RESULTS

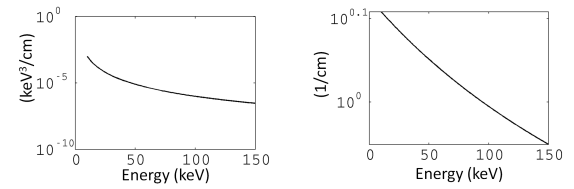
A. Experimental setup

We tested our method on simulated dual-energy data. The simulations were performed using analytical ray tracing software and were based on the properties of the Imatron C300 electron-beam medical scanner. Dual-energy measurements were simulated with estimates of the 95kVp and 130kVp Imatron spectra (kVp denotes the maximum voltage applied to the X-ray tube). The spectra are shown in Figure 2c. The simulations included scatter and electronic noise.

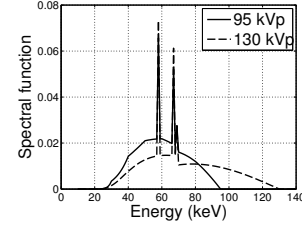
In security applications a common choice of basis functions for the LAC decomposition (2) is the photoelectric and Compton basis functions shown in Figures 2a and 2b [3]. We used these basis functions in our formulation and reconstructed the photoelectric and Compton coefficient images.

We processed two-dimensional scan slices. We used rebinned parallel measurements with 720 angles and 1024 bins. The reconstructed images are 512×512 with pixel spacing of 0.928 mm. The photoelectric and Compton sinograms were estimated from the dual-energy measurements using Matlab's 'lsqnonlin' least-square function and equation (3). We assumed that the spectral functions were known. As a baseline method we applied the Imatron FBP inversion algorithm to the photoelectric and Compton sinograms individually. We label this method FBP in results to come.

In the implementation of SPDE we initialized the photoelectric image \underline{a}_1 and the Compton image \underline{a}_2 as the results of one iteration of the image-based decomposition method proposed in [8]. We initialized the boundary-field \underline{s} with



(a) Photoelectric function $f_1(E)$ (b) Compton function $f_2(E)$



(c) Estimated scanner spectra

Fig. 2. Top: Photoelectric and Compton basis functions. Bottom: estimates of the Imatron system spectra used in the simulations normalized to unit sum.

all zeros. The data weighting parameter c in (6) was set to 5, based on sinogram values of rays going through metal (around 6-8). The regularization parameters λ_i in (4) were chosen empirically as the following: $\lambda_1 = 5$, $\lambda_2 = 3$, $\lambda_3 = 0.2$, $\lambda_4 = 0.01$, $\lambda_5 = 0.5$, $\lambda_6 = 0.5$. A relative iteration error stopping criterion was used, and a total of five iterations were performed. We calculated the intermediate linear inversions using Matlab's 'lsqr' function and an estimate of the Imatron forward projection matrix. With the current implementation SPDE is more computationally intensive than FBP, but it is comparable to other model-based iterative approaches.

We made use of the parameters ϵ_1 and ϵ_2 to guide the SPDE solution to a globally acceptable answer. We exploited the fact that the Compton sinogram is more informative on object structure than the photoelectric sinogram. In the first iteration we set ϵ_1 to 1 and ϵ_2 to 0.5. In the second iteration we set ϵ_1 to 1 and ϵ_2 to 0. After that we set both parameters to 0. With this choice of parameters only the Compton component contributed to the boundary-field estimate in the first two iterations. In this manner we obtained a more reliable boundary-field \underline{s} early on.

B. Reconstruction results

We show the results for a slice with different benign objects in a plastic suitcase. The suitcase contains an oval object of water, a round object of water in a Teflon container, a square object of water in a steel container and a round object of water in an aluminum container. There is also a rubber sheet and two small steel balls. The remainder of the suitcase is filled with styrofoam to simulate clothing. Figure 3 shows the reconstructed photoelectric and Compton images with FBP and SPDE, as well as the ground truth images. Ground truth values were obtained by finding the least-squares fit of the LAC curve of each material and the photoelectric and Compton basis functions. The mutual boundary-field estimated with SPDE is shown in Figure 3g. It can be seen that noise and streaking are significantly less visible in the SPDE results relative to FBP in both the photoelectric and Compton images. In addition, the artifacts caused by the metal in the suitcase

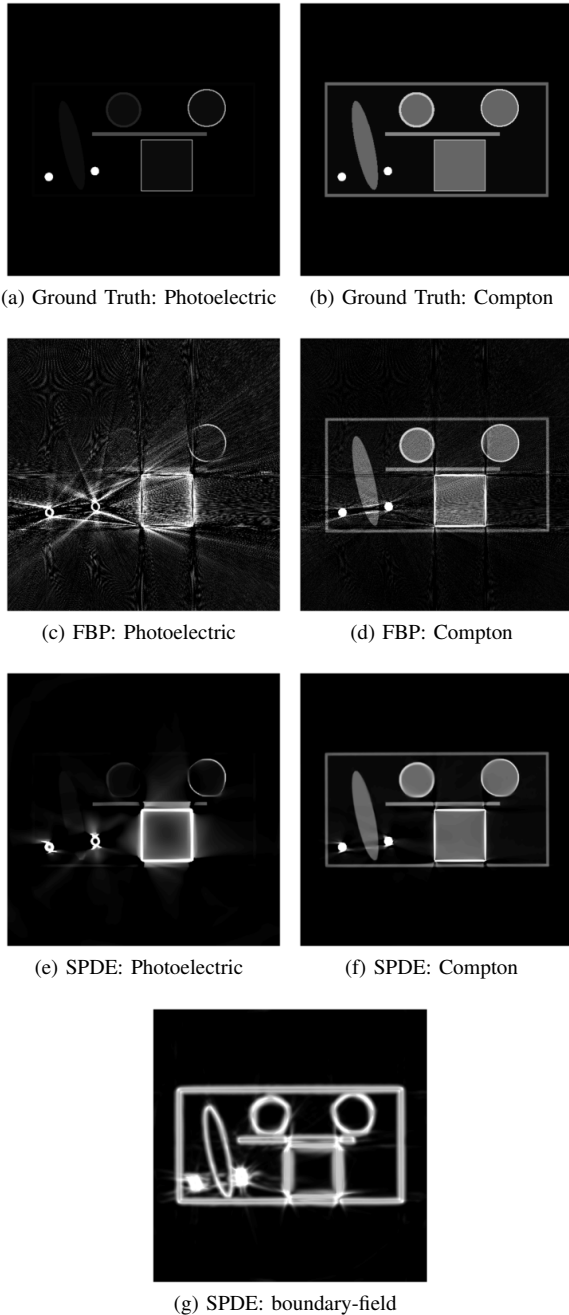


Fig. 3. Top row: ground truth photoelectric and Compton coefficient images. Second row: FBP reconstructions. Third row: SPDE reconstructions. Fourth row: estimated mutual boundary-field by SPDE. Photoelectric units are keV^3/cm and the gray scale range is $[0, 7E4]$. Compton units are $1/\text{cm}$ and the gray scale range is $[0, 0.4]$.

(steel balls) are greatly reduced by SPDE. For example, in Figure 3d there is a thick black streak at the bottom of the oval water object and it is much less visible in Figure 3d.

C. Quantitative evaluation

For each of the four water objects in the suitcase phantom we calculated the mean percent error (MPE) of the estimated photoelectric and Compton values relative to the ground truth. We also calculated the signal to noise ratio (SNR) of the photoelectric and Compton values, where SNR was defined

as the mean divided by the standard deviation. The results are shown in Figure 4. It can be seen that the mean errors are significantly lower for SPDE than for FBP. For the oval water object with no container, for example, with SPDE the mean error of the photoelectric coefficient is reduced by 90% and the mean error of the Compton coefficient is reduced by 80% relative to FBP. In addition, the SNR values for SPDE are much higher than for FBP, indicating that the noise is greatly reduced. For example, for the water object with no container, with SPDE the SNR of the photoelectric coefficient is increased by over 20,000% and the SNR of the Compton coefficient is increased by almost 400% relative to FBP.

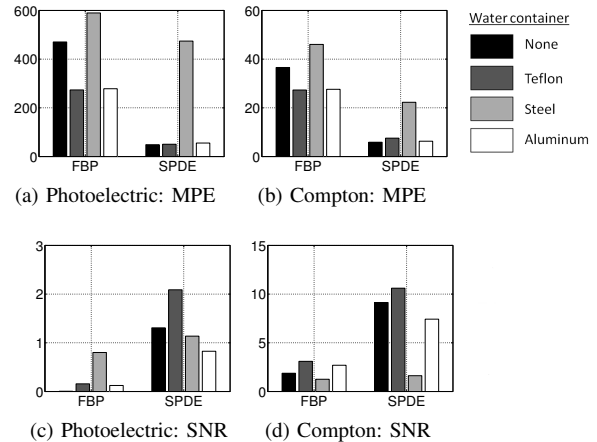


Fig. 4. Metrics calculated for Photoelectric values (left) and Compton values (right) in water objects for FBP and SPDE. Top: Mean percent error (lower is better). Bottom: SNR (higher is better).

V. CONCLUDING REMARKS

In this paper we presented and tested a structure-preserving dual-energy reconstruction method, SPDE. We demonstrated that it reduces noise and metal artifacts in basis coefficient images while keeping boundary localization. This may increase the accuracy of material identification in security applications.

REFERENCES

- [1] R. E. Alvarez and A. Macovski, "Energy-selective reconstruction in x-ray computerized tomography," *Phys. Med. Biol.*, vol. 21, no. 5, pp. 733–744, 1976.
- [2] J. A. Fessler, I. A. Elbakri, P. Sukovic, and N. H. Clinthorne, "Maximum-likelihood dual-energy tomographic image reconstruction," in *Proc. SPIE*, 2002, vol. 4684, pp. 38–49.
- [3] Z. Ying, R. Naidu, and C. R. Crawford, "Dual energy computed tomography for explosive detection," *Journal of X-ray Science and Technology*, vol. 14, no. 4, pp. 235–256, 2006.
- [4] D. Mumford and J. Shah, "Optimal approximations by piecewise smooth functions and associated variational problems," *Communications on Pure and Applied Mathematics*, vol. 42, no. 5, pp. 577–685, 1989.
- [5] L. Martin, W. C. Karl, and P. Ishwar, "Structure-preserving dual-energy reconstruction for luggage screening," Submitted to the IEEE International Conference on Acoustics, Speech and Signal Processing, ICASSP 14, 2014.
- [6] A. C. Kak and M. Slaney, *Principles of Computerized Tomographic Imaging*. Society of Industrial and Applied Mathematics, 2001.
- [7] R. A. Weisenseel, W. C. Karl, and R. C. Chan, *Multi-sensor image fusion and its applications*, chapter Multisensor Data Inversion and Fusion Based on Shared Image Structure, CRC Press, 2005.
- [8] B. Heismann and M. Balda, "Quantitative image-based spectral reconstruction for computed tomography," *Medical physics*, vol. 36, no. 10, pp. 4471–4485, 2009.

Simultaneous segmentation and reconstruction for dual-energy CT: Experimental results

Brian H. Tracey and Eric L. Miller

Abstract—Dual- or multi-energy computed tomography systems that can provide improved material identification are of great interest in airport luggage screening. While dual-energy luggage scanning systems are commercially available, dual-energy reconstruction remains challenging because data sensitivity varies greatly depending on the material parameter being estimated, and because prior information about materials of interest is imprecise. Here we extend earlier work [1] that uses a variational framework to perform simultaneous segmentation and reconstruction focusing on materials of interest, by introducing novel regularization terms and by developing a more computationally tractable variation of the previous approach. Experimental results with realistic luggage show that material property estimates can be stabilized by estimating foreground values, which can be expected to make material identification more robust.

1. INTRODUCTION

There is growing interest in exploiting dual- or multi-energy Computed Tomography (CT) systems that provide information on material properties as well as geometry by exploiting the energy dependence of X-ray absorption [2], [3]. Previously [1], our group developed an approach to geometric image formation for dual-energy CT reconstruction that exploited prior knowledge of the Compton and photoelectric coefficients of materials of interest. This approach is designed specifically for airport luggage screening application. Because the materials being scanned may vary greatly (as opposed to medical CT, where the tissue properties in the human body are relatively constrained) it is appropriate to represent the scene using Compton and photoelectric coefficient images, which capture the relevant X-ray physics. We further separate these images into background and foreground regions, with objects of interest captured in the foreground. Because we employ a variational framework, regularization terms can be designed to help stabilize reconstruction of the photoelectric image, which is typically much more difficult to reliably estimate than the Compton image [4], [1].

In this paper we describe extensions of this earlier work and apply the method to experimental data. A high-level description of the overall processing flow, with both ‘background’ and ‘foreground’ image formation, is shown in Fig. 1. In the first stage of processing, iterative reconstruction is applied to the dual energy data to form Compton and photoelectric coefficient images for the entire scene (denoted ‘background’). Here, we use patch-based regularization terms to stabilize the background photoelectric image, described in detail elsewhere [5]. In this paper we focus on the second stage of

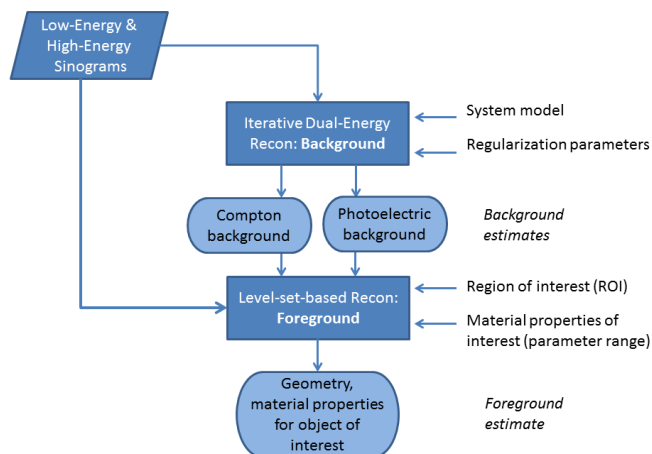


Fig. 1. Flowchart showing concept of background and foreground image formation. Low- and high-energy scans are processed using iterative reconstruction to form background images of the full scene. Further processing is used to reprocess data corresponding to a user-specified region of interest, with the goal of localizing foreground materials of interest whose nominal material properties are known.

processing (‘Foreground’ box in Fig. 1). In this stage, further processing is carried out within a user-specified region of interest (ROI), with the goal of producing improved shape and material property estimates of any objects in the ROI that correspond to materials of interest (such as contraband). During this step, the background image is assumed to be correct outside the ROI, and the location and exact material properties of the foreground object (i.e. material of interest) is iteratively estimated using the sinogram data. This two-stage approach differs from [1], in which foreground and background are jointly estimated. While computational speed was not a primary focus of our work, separating the two stages was important as otherwise the time needed to process experimental data would have been prohibitive.

2. ITERATIVE RECONSTRUCTION APPROACH

Typical X-ray sources used in CT applications generate an energy spectra roughly between 20 KeV and 140 KeV [6]. In this energy range the X-ray attenuation is dominated by Compton scatter and photoelectric absorption. The energy- and spatial-dependent attenuation can be modeled as [4].

$$\mu(x, y, E) = c(x, y)f_{KN}(E) + p(x, y)f_p(E) \quad (2.1)$$

where $\mu(x, y, E)$ is the total attenuation and $c(x, x)$ and $p(x, y)$ are the material dependent Compton scatter and photo-

B. Tracey and E. Miller are with Tufts University, Electrical and Computer Engineering Dept., Medford MA, USA 02155.

electric absorption coefficients respectively. The quantity f_{KN} is the Klein-Nishina cross section for Compton scattering [4]. We seek to solve for Compton and photoelectric coefficients and use these as ‘fingerprints’ allowing material identification.

As noted above, we further separate the region being imaged into *foreground* and *background*. The foreground is modeled as piece-wise constant objects of interest with Compton coefficient c_f and photoelectric coefficient p_f , although the approach could be extended to textured objects. For a domain $\Omega \subset \mathcal{D}$ which represents the support of the foreground objects, a characteristic function $\chi(x, y)$ is defined as

$$\chi(x, y) = \begin{cases} 1, & \text{if } (x, y) \in \Omega \\ 0, & \text{if } (x, y) \in \mathcal{D} \setminus \Omega. \end{cases} \quad (2.2)$$

Then, the Compton image can be written as

$$c(x, y) = \chi(x, y)c_f + [1 - \chi(x, y)]c_b(x, y). \quad (2.3)$$

In discretized form, the Compton and photoelectric images are

$$\begin{aligned} \mathbf{c} &= \boldsymbol{\chi} c_f + (\mathbf{I} - \text{diag}(\boldsymbol{\chi})) \mathbf{c}_b \\ \mathbf{p} &= \boldsymbol{\chi} p_f + (\mathbf{I} - \text{diag}(\boldsymbol{\chi})) \mathbf{p}_b \end{aligned} \quad (2.4)$$

where $c_b(x, y)$, $p_b(x, y)$ and $\chi(x, y)$ have been unwrapped lexicographically into vectors \mathbf{c}_b , \mathbf{p}_b , and $\boldsymbol{\chi}$, where $\text{diag}(\boldsymbol{\chi})$ is a diagonal matrix whose entries are the values of the unwrapped characteristic function χ . We next assume the dual-energy CT system acquires low-energy and high-energy sinograms. These are modeled as vectors of additive Poisson-Gaussian random variables, with i^{th} raypath of the the low-energy sinogram \mathbf{Y}_L given by

$$[\mathbf{Y}_L(\boldsymbol{\theta})]_i = \text{Poisson} \{ [\bar{\mathbf{Y}}_L(\boldsymbol{\theta})]_i \} + \text{Normal}(0, \sigma_{e,L}) \quad (2.5)$$

and the high-energy sinogram $[\mathbf{Y}_H(\boldsymbol{\theta})]_i$ being similar. The Poisson variables account for the X-ray counting statistics, while the Gaussian terms captures detector electronics noise. The corresponding mean values are given as

$$[\bar{\mathbf{Y}}_L]_i = \int S_L(E) \exp(-f_{KN}(E) \mathbf{A}_{i*} \mathbf{c}(\boldsymbol{\theta}) - f_p(E) \mathbf{A}_{i*} \mathbf{p}(\boldsymbol{\theta})) dE. \quad (2.6)$$

Here, \mathbf{A}_{i*} is the i^{th} row of \mathbf{A} , where \mathbf{A} is the *system matrix* capturing the mapping from image pixels to raypaths, calculated for example using ray-trace methods [7], [8], and $S_L(E)$ is the low X-ray spectra. The high-energy sinogram $[\bar{\mathbf{Y}}_H]_i$ is similar but with an integration over the high-energy spectrum $S_H(E)$. Note that scatter contributions are neglected here, as we assume that scatter corrections are applied to measured data in pre-processing [9]. To complete our model of the acquired data, we assume that the data have been normalized and transformed logarithmically, giving a low-energy measurement of $[\mathbf{m}_L(\boldsymbol{\theta})]_i = -\ln \frac{[\mathbf{Y}_L(\boldsymbol{\theta})]_i}{Y_{0,L}}$ with analogous expression for the modeled high-energy sinogram.

We denote the *measured* (normalized, logarithmic-transformed) as \mathbf{y}_L and \mathbf{y}_H and stack them into a vector $\mathbf{y}^T = [\mathbf{y}_L^T, \mathbf{y}_H^T]$. We then seek a solution that minimizes a sum of data fidelity and regularization terms:

$$\arg \min_{\boldsymbol{\theta}} F(\boldsymbol{\theta}) = \frac{1}{2} (\mathbf{y} - \mathbf{m}(\boldsymbol{\theta})) \boldsymbol{\Sigma} (\mathbf{y} - \mathbf{m}(\boldsymbol{\theta}))^T + R_{BG}(\boldsymbol{\theta}) + R_{FG}(\boldsymbol{\theta}) \quad (2.7)$$

where $\boldsymbol{\Sigma}$ is the noise covariance matrix [1], and R_{BG} and R_{FG} are background and foreground regularization terms, which are discussed in the next section.

In solving this problem, we are *simultaneously segmenting* (by estimating the foreground region χ) and *reconstructing* the image (by estimating the background Compton and photoelectric coefficients $c_b(x, y)$ and $p_b(x, y)$ and foreground material properties c_f and p_f). Here we briefly review our approach, but refer the reader to [1] for details. In estimating χ , we make use of level set concepts, which are widely used in image processing [10] as well as image formation [11]. We define the characteristic function $\chi(x, y)$ as the zero level set of a Lipschitz continuous object function $\mathcal{O} : \mathcal{D} \rightarrow \mathbb{R}$ such that $\mathcal{O}(x, y) > 0$ in Ω , $\mathcal{O}(x, y) < 0$ in $\Omega \setminus \mathcal{D}$ and $\mathcal{O}(x, y) = 0$ in $\partial\Omega$. The characteristic function is then defined as

$$\chi(x, y) = H(\mathcal{O}(x, y)) \quad (2.8)$$

where H is the step function. In practice, smoothed approximations of H_ϵ and its derivative δ_ϵ are used [12]. In our particular level set approach, we simplify the problem using a parametric level set (PaLS) approach [13] which represents the object function $\mathcal{O}(x, y)$ parametrically using a predefined basis set. Here we chose that basis set to be a family of exponential radial basis functions (RBF’s), which as described in [1] allow a flexible description of object shape.

A. Regularization terms for iterative solver

In solving the iterative problem above, we introduce regularization terms (different from those in [1]) which encourage stable recovery of the photoelectric coefficient, which as noted above is challenging to estimate. For *background* regularization, we regularize the PE image based on patch-wise similarities found from the Compton image. Here we are adapting a regularization approach originally proposed by Buades *et al* [14] and recently applied to iterative PET inversion [15]. The concept behind this regularization is that in some applications, a stable ‘reference’ image is available to guide the inversion of a less stably estimated image with similar geometry. For multi-energy CT we can exploit the relative stability of the inverted Compton image and use it as a reference image to guide photoelectric coefficient inversion. The geometry from the reference image is captured by calculating patch-wise similarity weights from the reference, as found in the non-local means (NLM) denoising algorithm [14], and using these weights to smooth the noisier image. We therefore define a regularization term:

$$R_{BG} = \lambda_{NLM} \int \left(p_b(x, y) - NL^{(C)} p_b(x, y) \right)^2 dx dy \quad (2.9)$$

where $NL^{(C)}$ represents non-local smoothing using weights calculated using the Compton image as a reference. For details on this regularization approach see [5], [16].

To regularize the *foreground*, we define several terms:

$$R_{FG}(\boldsymbol{\theta}_{FG}) = R_s(\mathbf{a}) + R_{prop}(c_f, p_f) + R_{balloon}(\mathbf{a}) \quad (2.10)$$

The first term is the commonly used penalty term [10], [17] that encourages objects of interest to have a small area:

$$R_s(\mathbf{a}) = \lambda_1 \|H(\mathcal{O})\|_1. \quad (2.11)$$

where $\|\cdot\|_1$ indicates cardinality, i.e. the number of pixels where $\chi(x, y) = 1$. The second term captures our prior knowledge about the expected physical properties of the objects of interest, and specifies a subset Γ of allowable values for the object values in the (p_f, c_f) parameter space. In general, many chemical compounds of interest may exist, so the set of allowable parameter values could be comprised of a number of disconnected regions. However, for simplicity here we consider the case where the constraint set is elliptical in shape. We define $\Gamma \in \mathcal{R}^2$ as an ellipse with the center (c_0, p_0) major axis σ_p and minor axis σ_c . Then, we can write a non-linear inequality constraint as

$$\frac{(c_f - c_0)^2}{\sigma_c^2} + \frac{(p_f - p_0)^2}{\sigma_p^2} < 1 \quad (2.12)$$

We transform this inequality constraint into a penalty term:

$$R_{prop}(c_f, p_f) = \lambda_2 \max\left(g_1(p_f, c_f), 0\right) \quad (2.13)$$

where

$$g_1(p_f, c_f) = \frac{(c_f - c_0)^2}{\sigma_c^2} + \frac{(p_f - p_0)^2}{\sigma_p^2} - 1 \quad (2.14)$$

thus penalizing solutions that violate Eq. 2.12.

The foreground penalties above were used in previous work by our group [1], and showed good performance on simulated data examples, where the objects being imaged were perfectly homogeneous and there was minimal mismatch between the data and model. In processing experimental data, we found it necessary to include an additional regularization term. This term was motivated by success of the widely used Total Variation (TV) penalty [18] in stabilizing image reconstruction. In principle, we could seek to minimize TV for the overall (background + foreground) Compton and photoelectric images. However, it is clear (if the background image is held constant) that minimizing the overall Total Variation is equivalent to maximizing the area of the foreground object. We can then define a ‘balloon force’ term as a rough surrogate for a TV penalty:

$$R_{balloon}(\mathbf{a}) = \lambda_3 (\|\mathcal{D}\| - \|\mathcal{H}(\mathcal{O})\|_1). \quad (2.15)$$

where $\|\mathcal{D}\|_1$ is the cardinality of the image domain. This penalty is clearly very closely connected to the size penalty R_s . For experimental data, we found best results by including the balloon force but disabling the size penalty (setting $\lambda_1 = 0$). The balloon force provides a means for rewarding solutions that find homogeneous foreground objects.

B. Implementation considerations

In [1], the PALS approach was used to find foreground objects located anywhere in the image. In addition, foreground and background estimates were improved iteratively using a cyclic descent approach until both converged. The problems examined in [1] were however much smaller than those considered in this report, both spatially (images were 100×100 pixels, instead of 512×512 as examined here) and in terms of the number of rays (3000, vs. 737,280 for the data shown below). We therefore make the following simplifications:

- *Restrict foreground search region:* While the background estimate is found over the full image, the foreground region is restricted to a region of interest (ROI) is specified by the user (see Fig. 1). A set of basis functions is then defined to cover only this grid region, and the search for foreground objects is restricted to this region. In future work, the ROI could be automatically identified.
- *Keep background constant:* Rather than iteratively estimating background and foreground, for the results below we hold the background image constant. Thus the estimate outside the ROI is fixed, and the estimate inside the ROI is equal to the background estimate except where the object characteristic function $\chi(x, y)$ is nonzero.

Much of the computational load in minimizing Eq. 2.7 comes from the need to recompute forward projections during each iteration. These projections are expressed in Eq. 2.6 as the terms $\mathbf{A}_{i*}\mathbf{c}$ (with similar terms $\mathbf{A}_{i*}\mathbf{p}$ for photoelectric). As most of the scene is fixed, we can split the projection into non-ROI and ROI parts, so that for the Compton image

$$\mathbf{A}_{i*}\mathbf{c} = \mathbf{A}_{i*}\mathbf{c}_{bkg} + \mathbf{A}_{i*}^{ROI}\mathbf{c}_{ROI} \quad (2.16)$$

where \mathbf{c}_{ROI} is the Compton estimate in the ROI, \mathbf{A}_{i*}^{ROI} is the portion of the system matrix containing rays which intersect the ROI, and \mathbf{c}_{bkg} is the background image with the ROI zeroed out. $\mathbf{A}_{i*}\mathbf{c}_{bkg}$ (and analogous photoelectric terms) are pre-computed and used on each iteration.

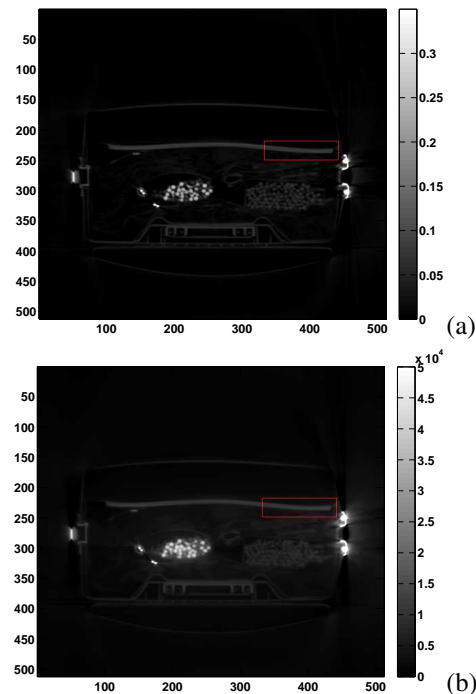


Fig. 2. Estimated background Compton (a) and photoelectric(b) images, with overlaid Region of Interest (ROI) covering part of the sheet.

3. EXPERIMENTAL RESULTS

We generated processing results from a set of dual-energy scans performed on the Imatron C300 scanner. This commercial single-energy scanner was re-purposed for dual-energy

studies by performing sequential scans of the object, with X-ray source voltage adjusted between scans and registration controlled by a precise belt drive system. Figure 2 shows a representative suitcase scan which contains beads inside a bottle, folded clothes, and a rubber sheet object. Because the sheet object should be relatively homogeneous, it is an interesting test case for foreground recovery. Figure 2 shows the estimated background Compton and photoelectric scenes. To restrict computation, we consider an ROI that covers one end of the sheet, as shown.

The results of background and foreground estimation for the Compton image in the ROI are shown in Fig. 3. While the sheet appears generally homogeneous in the background estimate, some variation is clearly seen. A very similar image is seen for photoelectric coefficients.

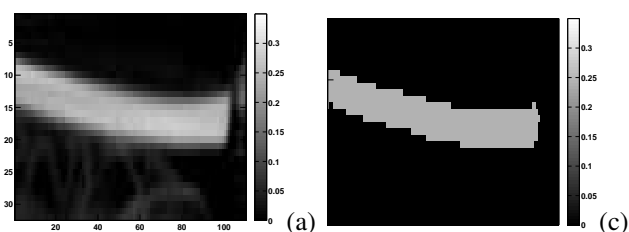


Fig. 3. Top: background Compton image for selected ROI. Bottom: estimated foreground object in ROI.

Fig. 4 shows the histogram of Compton and photoelectric background estimates in the segmented region, as compared to the single-valued foreground estimate. For this example, significant scatter was seen in the Compton background image as well as the photoelectric background. This scatter is eliminated in the single-valued foreground estimates.

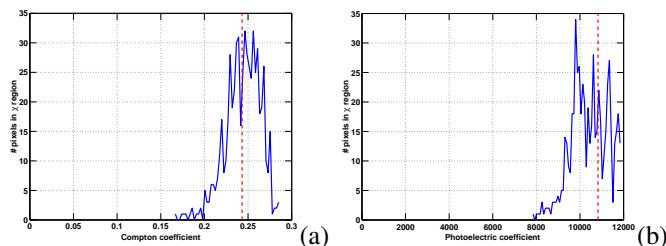


Fig. 4. Histograms of background estimate in segmented level set region, along with single-valued estimate resulting from level set estimation.

4. CONCLUSIONS AND FUTURE WORK

In this paper we developed a computationally lower-cost implementation of the simultaneous segmentation and reconstruction method introduced in [1], and demonstrated on experimental data that the method can lead to potentially useful segmentations of homogenous objects such as sheets and liquids. The variation in estimated material properties, in particular estimated photoelectric coefficients, is greatly reduced compared to previous approaches. An important future extension of this work is to consider extensions that will allow us to segment and reconstruct textured objects, building on related work in the image processing domain [19], [20].

5. ACKNOWLEDGMENTS

This material is based upon work supported by the U.S. Department of Homeland Security, Science and Technology Directorate, under Task Order Number HSHQDC-12-J-00056. The views and conclusions contained in this document are those of the authors and should not be interpreted as necessarily representing the official policies, either expressed or implied, of the U.S. Department of Homeland Security.

REFERENCES

- [1] O. Semerci and E.L. Miller. A parametric level-set approach to simultaneous object identification and background reconstruction for dual-energy computed tomography. *Image Processing, IEEE Transactions on*, 21(5):2719–2734, may 2012.
- [2] Z. Ying, R. Naidu, and C.R. Crawford. Dual energy computed tomography for explosive detection. *J. of X-ray Sci. and Tech.*, 14(4):235–256, 2006.
- [3] P.M. Shikhaliyev. Energy-resolved computed tomography: first experimental results. *Physics in medicine and biology*, 53:5595, 2008.
- [4] R.E. Alvarez and A. Macovski. Energy-selective reconstructions in x-ray computerized tomography. *Phys. Med. Biol.*, 21(5):733–744, 1976.
- [5] B. H. Tracey and E.L. Miller. Stabilizing dual-energy computed tomography reconstructions using patch-based regularization. *submitted, Inverse Problems*, 2014.
- [6] J. Beutel. *Handbook of medical imaging: Physics and psychophysics*, volume 1. Spie Press, 2000.
- [7] Robert L. Siddon. Fast calculation of the exact radiological path for a three-dimensional CT array. *Medical Physics*, 12(2):252–255, 1985.
- [8] Bruno De Man and Samit Basu. Distance-driven projection and backprojection in three dimensions. *Physics in Medicine and Biology*, 49(11):2463+, May 2004.
- [9] J. H. Siewerdsen, M. J. Daly, B. Bakhtiar, D. J. Moseley, S. Richard, H. Keller, and D. A. Jaffray. A simple, direct method for x-ray scatter estimation and correction in digital radiography and cone-beam CT. *Medical Physics*, 33(1):187–197, 2006.
- [10] T. F. Chan and L. A. Vese. Active contours without edges. 10(2):266–277, February 2001.
- [11] O. Dorn, E.L. Miller, and C.M. Rappaport. A shape reconstruction method for EM tomography. *Inverse problems*, 16:1119–1156, 2000.
- [12] S. Osher and R. P. Fedkiw. *Level Set Methods and Dynamic Implicit Surfaces, Applied Mathematical Sciences*, volume 153. New York: Springer, 2002.
- [13] A. Aghasi, M. Kilmer, and E. Miller. Parametric level set methods for inverse problems. *SIAM J. Imaging Sciences*, 4(2):618–650, 2011.
- [14] Anoni Buades, Bartomeu Coll, and Jean-Michel Morel. Image enhancement by non-local reverse heat equation. Technical report, CMLA, 2006.
- [15] Guobao Wang and Jinyi Qi. Penalized likelihood PET image reconstruction using patch-based edge-preserving regularization. *IEEE transactions on medical imaging*, 31(12):2194–2204, December 2012.
- [16] B.H. Tracey and E. L. Miller. Geometric image formation for target identification in multi-energy computed tomography. SPIE, 2013.
- [17] Oliver Dorn and Dominique Lesselier. Level set methods for inverse scattering. *Inverse Problems*, 22(4):R67–R131, 2006.
- [18] Leonid I. Rudin, Stanley Osher, and Emad Fatemi. Nonlinear total variation based noise removal algorithms. *Physica D: Nonlinear Phenomena*, 60(1-4):259–268, November 1992.
- [19] D. Freedman and T. Zhang. Active contours for tracking distributions. *Image Processing, IEEE Transactions on*, 13(4):518–526, 2004.
- [20] K. Ni, X. Vresson, T. Chan, and S. Eshedoglu. Local histogram based segmentation using the Wasserstein distance. *Int J. Comput Vis*, 84:97–111, 2009.

Compressed Sensing as a tool for Scanning Very Large Objects with High Energy X-ray Computed Tomography

Tobias Schön¹, Markus Firsching², Nils Reims², Frank Sukowski², Jonas Dittmann³

Abstract—We propose a novel high-energy X-ray Computed Tomography system for inspecting very large objects like automobiles and sea freight containers. In this context we discuss appropriate strategies for efficient scanning and reconstruction methods. Due to scattering radiation the system uses a line detector which leads to longer acquisition times compared to planar detectors. In order to reach adequate scanning times the number of projections is reduced and Compressed Sensing techniques are used for the reconstruction. The image quality is discussed with respect to its suitability for applications in the field of industrial non-destructive testing as well as security. We present an experimental evaluation with real data of a sea freight container scanned at the high-energy testing facility of the Fraunhofer Development Center for X-ray Technology. The image quality is quantitatively assessed by a separate test specimen. We can show that Computed Tomography of very large, complex objects is technologically feasible.

I. INTRODUCTION

TODAY, X-ray Computed Tomography (CT) is widely used as a tool for industrial non-destructive testing (NDT) and security. However, conventional CT devices pose limitations regarding specimen dimensions and material thicknesses. Nowadays, there are several fields of technology requiring inspection of objects or components which are too large in diameter or size to be covered by conventional X-ray imaging technology: wings of airplanes, wind power plants, automobiles and sea freight containers [1]. Therefore, there is need of a high energy CT system capable of inspecting very large objects (VLO) in 3D.

During the last 5 years, the Fraunhofer Development Center for X-ray Technology (Fraunhofer EZRT) in Fürth, Germany, has evaluated appropriate technologies and several construction designs for building a high-energy test facility for scanning VLOs. In particular, the efforts focused on the following: high-energy X-ray physics, 3D image processing for inspection of large objects, material-selective CT as well as the development of radiation-resistant X-ray sensors and high-intensity X-ray sources. [2] describes the complete overview of planning, design, construction and installation of the high-energy test facility in detail. Fig. 1 shows the CT system which is installed at the Fraunhofer EZRT.

¹Process Integrated Inspection Systems, A Dept. of the Development Center for X-ray Technology (Fraunhofer-EZRT), division of Fraunhofer Institute for Integrated Circuits IIS in cooperation with Fraunhofer IZFP, Fürth, Germany
²Application Specific Methodology and Systems, A Dept. of the Fraunhofer-EZRT
³Chair for X-ray Microscopy, Julius-Maximilians-University, Würzburg
Contact: tobias.schoen@iis.fraunhofer.de

In this paper we mainly focus on the reconstruction and image quality with respect to an efficient scanning time which is an important point in the field of NDT and security.



Fig. 1. The high-energy test facility is installed at the Fraunhofer EZRT, Fürth, Germany, and allows for reconstruction volumes of 3.2 meters in diameter and 5 meters in height.

First we outline the components of the CT system and compare it with state of the art X-ray systems. Due to scattering radiation the system uses a line detector which leads to longer scanning times compared to planar detectors. In order to realize shorter acquisition time which is an important factor in the field of NDT and security the number of projections are gradually reduced. For the reconstruction, compressed sensing (CS) techniques [3] were used to reach an adequate image quality compared to the standard reconstruction method, i.e. filtered backprojection (FBP) [4]. We outline the test specimen which we used for the quantitative evaluation of the image quality. The next section shows real data results using a sea freight container. The image quality is discussed depending on the different number of projections as well as on the reconstruction algorithm. Finally, we give an outlook to future work.

II. MATERIAL AND METHODS

This novel CT system utilizes a 9 MeV linear accelerator (LINAC) from Siemens to achieve high penetration lengths in both dense and high-Z materials. In contrast to standard industrial CT systems, flat panel detectors are not a practical option to scan VLO effectively due to technological limitations and X-ray attenuation physics at high energies. The X-ray attenuation is mainly determined by Compton scattering and a line detector provides a significantly better image quality which is mainly due to masking of the vertical plane scattering. The implemented line detector array (LDA) has an overall length of about 4 meters with a pixel size of $400 \mu\text{m}$. The system allows for reconstruction volumes of 3.2 meters in diameter and 5 meters in height. The maximum capacity of the turn table is 10000 kg. Table I shows the acquisition parameters used for the reconstruction in the result section.

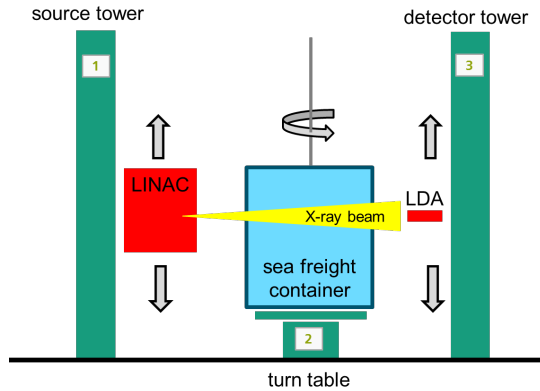


Fig. 2. The LINAC which is mounted on the source tower (1) and the LDA which horizontally aligned mounted on the tower at the opposite side (3) are translated synchronously in vertical direction in order to scan the VLO resulting in large images with a maximum size of 4 by 5 meters.

TABLE I
THE GEOMETRY AND RECONSTRUCTION PARAMETERS FOR THE
SCANNING OF THE 10" ISO SEA FREIGHT CONTAINER:

parameter	value
projection pixel count	2048×841
projection pixel size	$1.95 \text{ mm} \times 3 \text{ mm}$
distance source to rotation center	9913 mm
distance source to detector	11858 mm
angular scan range	180°
reconstructed matrix	$2048 \times 2048 \times 841$
voxel size	$1.5 \text{ mm} \times 1.5 \text{ mm} \times 3 \text{ mm}$

Currently, two different scanning modes are implemented. If only few layers of the objects have to be reconstructed a classical sinogram mode is possible where a variable angular range (typically 180° up to 360°) is acquired and a single slice is reconstructed. Subsequently, the LDA and LINAC are moved in vertical direction for the next vertical scanning position of the object. In the case of high vertical sampling rates which typically occurs by the inspection of large objects, the sinogram mode is inefficient particularly with regard to the scanning times. Therefore, in the second mode the linear axes of the detector and of the high energy source can move

synchronously while the detector is exposed. After the object has been completely scanned vertically the turn table is rotated with the angular increment and the next vertical scan starts, as indicated in Fig 2. Due to the imaging geometry, the reconstruction algorithm has to cope with uncommon 2D-projections, this means fan beam geometry in lateral direction, but parallel beam in vertical dimension. This is the standard scanning mode for inspection of VLO and the relevant acquisition geometry concerning this paper. A conventional single row helical scanning as known in medical CT is not implemented yet due to technical limits of the currently used frame grabber. Thus, the usage of this powerful sampling mode and a direct comparison with this set up is not possible for the moment.

Compared to standard industrial CT systems which generally use flat panel detectors this setup generates higher scanning times due to the usage of a LDA. So, in order to reach an adequate acquisition time which is an important factor in the field of NDT and security the number of projections are reduced. But, reducing the number of projections considerably causes image artifacts with standard reconstruction methods like FBP. To avoid this, CS-based reconstruction algorithms are employed to reach a sufficient image quality for typical testing situations in NDT and security. The result section shows reconstruction by CS-algorithm using gradually reduced numbers of projections. This means, reconstructions with 250, 125, 50 and 25 projections all with the angular scan range of 180° . The algorithm was adapted to this acquisition geometry, so that this uncommon 2D-projections can be directly processed. The time-consuming steps, i.e. mainly forward and backprojection step, were implemented via GPU parallelization in order to reach an adequate reconstruction time.

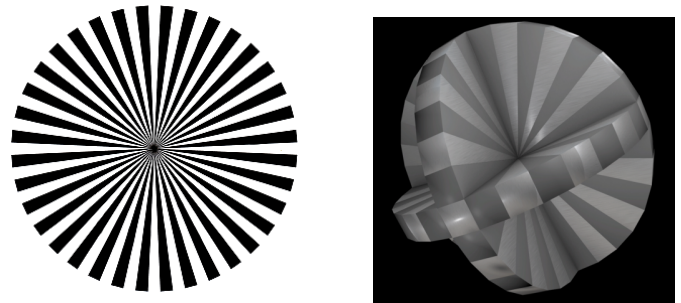


Fig. 3. The developed test specimen (right) can be interpreted as a 3D extension of the Siemens star (left).

For the quantitative evaluation of the image quality we developed a test specimen. The specimen is called "EZRT star" and can be interpreted as a 3D extension of the Siemens star which is often used to test the resolution of optical instruments and printers or displays, see Fig 3. The EZRT star consists of three patterns of "spokes" in direction of the three principal axes. The spokes radiate from a common center and become wider with increasing distance to the center. The actual specimen was placed inside the container and used to evaluate the spatial resolution in the real scans.

Real data was acquired by the high energy test facility using



Fig. 4. Test container which was prepared with typical house moving cargo with a variety of different objects (left: photography, right: radiography).

a 10" iso sea freight container which was prepared to represent typical house moving cargo with a variety of different objects, see Fig. 4. The geometry and reconstruction parameters are listed in Table I. In order to scan the complete height of the container 841 detector lines with a size of 3 mm per line were acquired for each 2D-projection. The exposure time per 2D-projection was 26,880 s and 250 projections were acquired with a scan range of 180°. The complete measurement took about 3h. A detector binning in horizontal direction was used to achieve 2048 pixels and 1.95 mm pixel size. Therefore, this data-set possesses a non-isotropic resolution.

The CS-based algorithm is an iterative alternating gradient descent method inspired by the work of Sidky et al. [5], [6]. Instead of the classical algebraic reconstruction techniques (ART) [7] the simultaneous ART (SART) [8] is chosen and a new stepsize heuristic is used in the Total-Variation (TV) minimization step. A variant of this method was presented in [9].

In all reconstructions 25 global iterations were used, each consisting of 3 SART iterations and 30 TV gradient descent steps. As a final step 3 more SART iterations were applied. All reconstruction images are displayed with the identical gray value contrast [0.0; 0.1].

III. RESULTS

Fig. 5 shows reconstructions of a central horizontal slice through the container using varying number of projections: 250, 125, 50, 25 (from top to bottom). The container could not be placed on the center of the turn table to avoid a collision with the detector. Therefore, artifacts at the bottom of the reconstructed slices can clearly be identified due to limited angle problems in that regions. Especially, the image quality of the outer shape of the container differs because of this.

The EZRT star was placed inside of the container as depicted on the left side in Fig. 6. The grey values of the EZRT star were evaluated by line profiles with two different radii: 36mm and 24mm (Fig. 6, right). Figure 7 depicts the line profiles for both radii using the reconstructions with 250, 125, 50 and 25 number of projections.

Fig. 5 as well as the line profiles in Fig. 7 demonstrate that an image quality with comparatively high quality can be obtained with 250 projections (green line in Fig. 7) and also with 125 projections (yellow line in Fig. 7). However, the image quality decreases significantly by reducing the number of projections to 50 (blue line in Fig. 7) and, especially, to 25

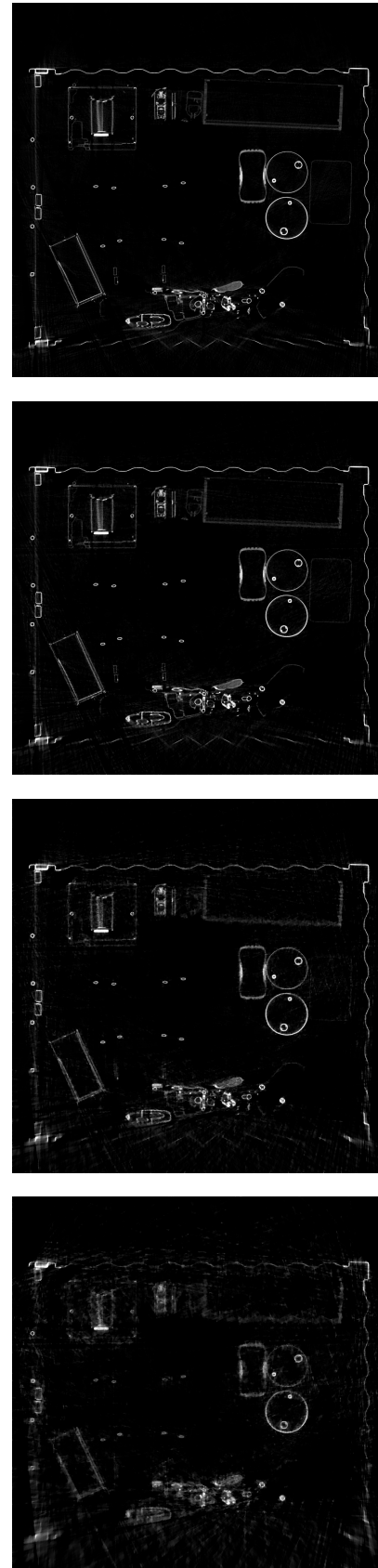


Fig. 5. A central horizontal slice of the container using varying number of projections for the reconstruction: 250, 125, 50, 25 (from top to bottom).

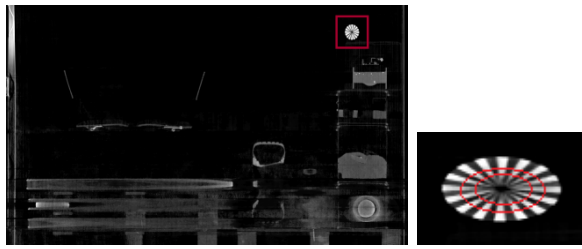


Fig. 6. The EZRT star was placed inside of the container and a vertical slice was used for the evaluation (left). The grey values of the EZRT star are evaluated by line profiles with two different radii: 36mm and 24mm (right).

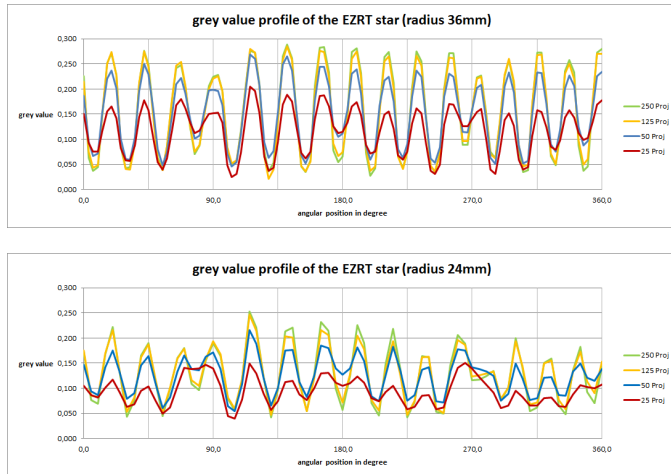


Fig. 7. The line profiles of the EZRT star with two different radii 36mm (top) and 24mm (bottom) using the reconstructions with 250, 125, 50 and 25 number of projections.

projections (red line in Fig. 7). In this case the outer shape of the container as well as the structures of the different objects inside the container appear to be more and more blurred (see bottom of Fig. 5).

IV. CONCLUSION AND FUTURE WORK

We proposed a new high-energy X-ray CT system for very large objects. In order to reach an adequate scanning time the number of projections were gradually reduced and CS-based reconstruction techniques were deployed. The image quality was analyzed by a test specimen. We could demonstrate that CT of very large, complex objects is technologically feasible by scanning a sea freight container. The complete measurement period of the container took about 3h. Using CS-techniques allows a significant reduction in scanning time for scanning VLO by high-energy X-ray CT which increases the desirability in the field of NDT and security. However, the best possible choice for the reduction of the number of the projections strongly depends on the particular application.

Future efforts will be made in investigating our approach by further real data and in improving the quality by exploring several ways:

- The image quality is going to be analyzed more thoroughly in terms of verifying the isotrop spatial resolution by using the EZRT star and compared with results of FBP.

- A verification by scanning additional VLOs, e.g. complete cars, well be done particularly with regard to higher horizontal and vertical resolutions.
- Evaluation of CS-methods to reduce the reconstruction time as well as the number of projections subject to the testing situation.
- Comparison with a helical scanning mode especially in respect to the scanning time at high-energy X-ray CT system.

ACKNOWLEDGMENT

The authors would like to thank the Fraunhofer EMI, especially Stefan Moser and Victoria Heusinger, for their support during the container scanning.

REFERENCES

- [1] M. Firsching and et al., "3-D scanning of sea freight containers using MeV x-rays," IEEE Nuclear Science Symposium and Medical Imaging Conference Record (Seoul, Korea), 2013.
- [2] T. Fuchs and et al., "High-energy 3-d x-ray computed tomography on very large objects," *NDT&E International*, vol. to be published, 2014.
- [3] E. Candes, "Robust uncertainty principles: exact signal reconstruction from highly incomplete frequency information," *IEEE Transactions on Information theory*, vol. 52, pp. 489–509, 2006.
- [4] L. Feldkamp, L. Davis, and J. Kress, "Practical cone-beam algorithm," *J. Opt. Soc. Amer.*, vol. 1, pp. 612–619, 1984.
- [5] E. Y. Sidky, C. M. Kao, and X. Pan, "Accurate image reconstruction from few-views and limited-angle data in divergent-beam ct," *Journal of X-ray Science and Technology*, vol. 14, pp. 119–139, 2006.
- [6] E. Y. Sidky and X. Pan, "Image reconstruction in circular cone-beam computed tomography by constrained, total-variation minimization," *Physics in medicine and biology*, vol. 53, no. 17, 2008.
- [7] G. Gordon, R. Bender, and G. T. Herman, "Algebraic reconstruction techniques (art) for three-dimensional electron microscopy and x-ray photography," *J. Theoret. Biol.*, vol. 29, pp. 471–481, 1970.
- [8] A. H. Andersen and A. C. Kak, "Simultaneous algebraic reconstruction technique (sart): a superior implementation of the art algorithm," *Ultrasonic Imag.*, vol. 6, pp. 81–94, 1984.
- [9] J. Dittmann, T. Schön, S. Zabler, and R. Hanke, "Tomographic reconstruction from few x-ray projections using a simultaneous combined reconstruction techniques (sart) and total variation (tv) minimization method," Proceedings of 1st International Conference on Tomography of Materials and Structures (Gent, Belgium), 2013.

Investigation of Simulation Software for Explosive-Detection CT Imaging

Taly Gilat Schmidt¹

Abstract—This study investigated the feasibility of simulating CT data for explosive-detection applications by quantifying the agreement between simulated and experimental data. Simulated data has the potential to impact the development of explosive-detection imaging systems and algorithms, by providing a test data with known ground truth and by enabling testing of a wide variety of design parameters. In this work, simulations were performed that modeled x-ray transmission, scatter, polyenergetic spectra, Poisson noise, electronic noise, finite focal spot and detector aperture effects. The following metrics were compared between simulated and experimental data: the reconstructed Hounsfield Unit (HU) values, reconstructed noise standard deviation, scatter-to-primary ratio (SPR), cupping due to beam hardening and scatter, and the visual similarity of streaks due to beam hardening and metal. The results demonstrated that the simulated data matched the experimental mean values to within 1% to 9.6% percent, depending on the object and spectrum. The noise standard deviation of the simulated data was within 10% of the experimental data for five of the reconstructed objects and within 20%-30% for three of the objects. The SPR of the simulated and experimental data matched to within 13%, while the scatter cupping artifact matched to within 1 HU. The artifacts due to metal and beam hardening were visually similar in the experimental and simulated images.

I. INTRODUCTION

Simulated data has the potential to impact the development of explosive-detection imaging systems and algorithms, by providing a large library of test data with known ground truth. Simulations may reduce the time to market and development cost for new CT scanners, as a wide variety of design parameters can be tested without the expense of physical implementation. Furthermore, simulations may be used to predict scanner performance.

Numerous simulation tools are available for X-ray and CT simulation and have been applied to medical imaging applications. X-ray-based imaging for explosive detection is challenging, due to the wide range of materials and objects that may be present in the field of view. In security imaging, shading and streak artifacts due to beam hardening, scatter, and photon starvation are particularly problematic, as they increase the feature clouds associated with threats and confuser objects. When the feature clouds of a threat and a confuser overlap, the probability of detection decreases while the probability of false alarm increases. In order for simulations to be beneficial for development of explosive-detection systems, simulated data must present the same artifacts and challenges as experimental data.

¹ Department of Biomedical Engineering, Marquette University, Milwaukee WI

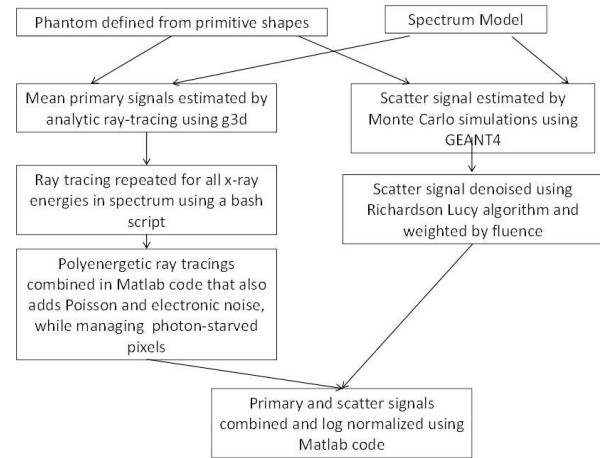


Fig. 1. Flow chart of simulation methods

In this work, simulated datasets were generated and validated by quantitatively comparing images reconstructed from simulated and experimental data. A secondary goal of this work was to define mathematical suitcase phantoms that can be used for reconstruction, segmentation, and threat recognition algorithm development.

II. METHODS AND MATERIALS

A. Simulation Methods

Figure 1 displays a flow chart of the simulation methods. The simulations modeled the geometry and scanning parameters of the Imatron C300 CT scanner, for which raw data of objects relevant to security imaging were available. Data was simulated assuming both 95 kV and 130 kV spectra, which were modeled using the SPEC78 software [1]. The raw spectrum output by SPEC78 was attenuated by modeling the 0.381-mm 304 stainless steel window of the Imatron source and the energy-absorption effects of the 2.3-mm cadmium tungstate detector. The x-ray fluence (180,000 photons per ray in the sinogram for the 95 kV spectrum, and 170,000 photons per ray for the 130 kV spectrum) was estimated by calculating the signal-to-noise ratio in raw air-scan data.

Bag phantoms (i.e., bag models) were defined as a combination of primitive 3D shapes: ellipsoids, cylinders, cones and boxes. The dimensions, orientation and positions of the primitive objects were specified in a text file. The primitive shapes can be further defined as the portion of a primitive shape on one side a defined plane. The material composition of primitive shapes was defined by specifying the linear attenuation coefficient as modeled with the NIST XCOM database

[2]. Intersections of objects were handled by assigning each object a precedence level.

The g3d simulation software was used to analytically calculate the path-length (i.e., ray tracing) of defined rays through the software phantoms. The g3d software models the scanner geometry, including the source focal spot dimensions and location, the detector dimensions and location, and gantry rotation [3].

The Geant4 Monte Carlo tool kit was used to model scatter in this work [4]. Geant4 models and tracks the stochastic trajectory of individual x-ray photons through the defined phantom. In this work, 10 billion photons were tracked for each of the 2588 view angles in the native Imatron geometry assuming the 95 kV and 130 kV spectra. The Monte Carlo simulation software used in this work output two sinograms: the detected scatter signal and the detected primary signal.

The simulated scatter signal was noisy, as the number of simulated photons was kept low to reduce computation time. The scatter signal generally contains low frequencies [5]. Therefore, the mean scatter signal was estimated by denoising the Monte Carlo output with the Richardson-Lucy algorithm [6], [7]. The mean scatter signal was normalized by the photon fluence modeled in Geant4, and then multiplied by the photon fluence of the Imatron scanner.

The ray-tracing and Monte Carlo simulation outputs were combined, followed by the modeling of Poisson and electronic noise as described in Figure 1.

B. Validation Study

The purpose of this work was to quantify the agreement between simulated and experimental data with respect to reconstructed values, noise, scatter-to-primary ratio (SPR) and artifacts.

The 95 kV and 130 kV spectra models were validated by comparing the experimental transmission through an aluminum step phantom as measured on the Imatron scanner with the transmission estimated using the spectral models.

CT data of graphite (2.54-cm-radius, 3.81-cm-radius), magnesium (1.27-cm-radius), and aluminum (2.63-cm-radius) cylinders were experimentally acquired and simulated. The raw experimental data and the simulated data were processed and reconstructed using the same algorithms. The mean and standard deviation of the reconstructed Hounsfield Unit (HU) values were calculated in regions of interest (ROIs) and compared for the experimental and simulated data.

The simulated scatter signal was validated by comparing the simulated SPR in projections of a 2000-ml water phantom to the SPR estimated in the experimental images. For the experimental data, SPR was estimated as the difference between sinograms with and without scatter correction, divided by the scatter-corrected sinogram. For simulated data, SPR was calculated as the ratio of the detected scatter signal to the detected primary signal.

The scatter simulation methods were further validated by comparing images of the water phantom reconstructed from simulated data and experimental data without scatter correction. The difference between images reconstructed with

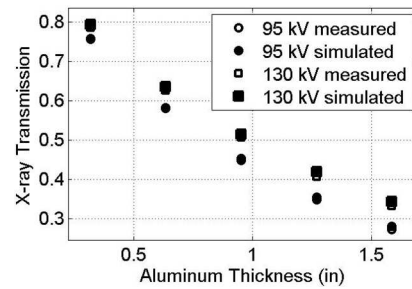


Fig. 2. Transmission through aluminum step phantom as measured through experiments and simulations.

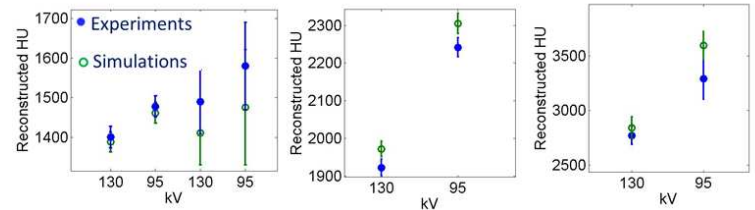


Fig. 5. A comparison of reconstructed Hounsfield Unit (HU) values in regions of interest within the cylinder objects reconstructed from experimental and simulated data. The error bars represent one standard deviation.

scatter and images reconstructed after scatter correction was calculated for both experimental and simulated data in order to evaluate the level of cupping artifact.

III. RESULTS

The plot in Figure 2 compares the transmission through an aluminum wedge phantom as estimated by experiments and simulations. The transmission estimated through simulations was within 2% of the transmission measured through experiments.

Figure 3 compares the reconstructed images and the central horizontal profile through the phantom for the graphite and magnesium cylinders reconstructed from experimental and simulated data. Figure 4 displays the comparison for graphite and aluminum cylinders. Figure 5 compares the mean and standard deviation of the Hounsfield Unit values in the images reconstructed from experimental and simulated data.

The results demonstrated that the simulated data matched the mean values to within 1% to 9.6% percent, depending on the object and spectrum. In the case of the 9.6% error (aluminum at 95 kV), the mean of the simulated data was within one standard deviation of the HU values reconstructed from experimental data. Comparing the size of the error bars in Figure 5 demonstrates that the simulated and experimental data resulted in similar noise standard deviation. The noise standard deviation of the simulated data was within 10% of the experimental data for five of the reconstructed objects and within 20%-30% for three of the objects. The horizontal profiles plotted in Figures 3 and 4 demonstrate similar cupping artifacts within the cylinders for simulated and experimental data.

Figure 6 plots the simulated and experimental SPR at 130 kV. The mean simulated SPR was within 13% of the SPR in

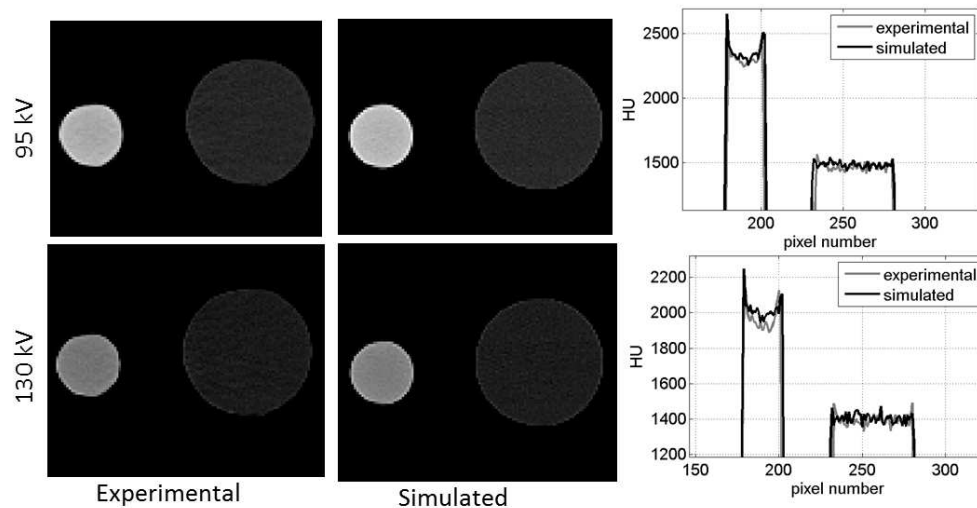


Fig. 3. Comparison of graphite and magnesium cylinders reconstructed from Imatron and simulated data at 95 kV and and 130 kV. All images are displayed at the same window/level. The central horizontal profile through the objects is also plotted.

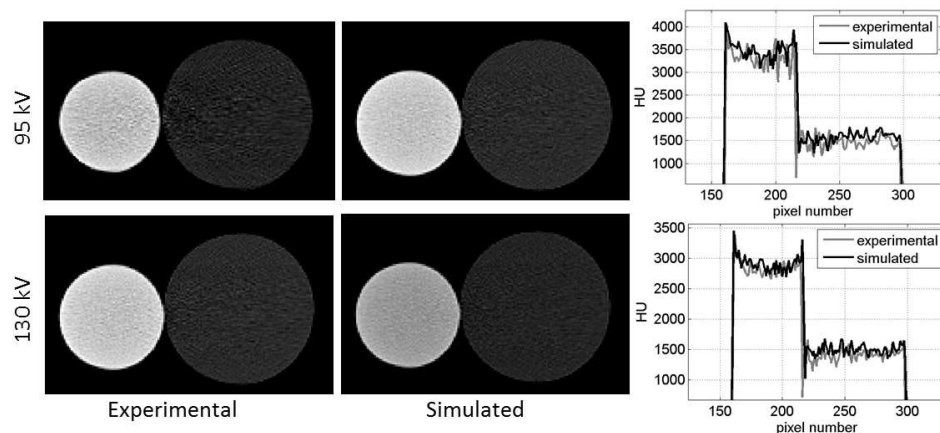


Fig. 4. Comparison of graphite and aluminum cylinders reconstructed from Imatron and simulated data at 95 kV and and 130 kV. All images are displayed at the same window/level. The central horizontal profile through the objects is also plotted.

the experimental data for both the 95 kV and 130 kV data. The simulated SPR was noisier, as the number of simulated photons was reduced because Monte Carlo simulation time is proportional to the number of simulated photons. The noisy signal did not affect the final simulated data, as the simulated scatter data were denoised prior to combination with the ray-tracing data.

Figure 7 compares the scatter cupping artifact for simulated and experimental data, which was calculated as the difference between images reconstructed with scatter and images reconstructed after scatter correction. The cupping artifact due to scatter in the simulated images was within 1 HU of the artifact seen in the experimental images.

A library of simulated data was generated using the developed software tools. Figure 8 displays a slice of one simulated suitcase phantom that may be a useful tool for comparing reconstruction, segmentation, and automatic threat recognition algorithms. The suitcase contains four water objects in four different containers: steel, aluminum, Teflon, and no container.

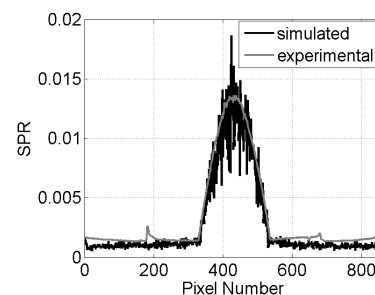


Fig. 6. The scatter-to-primary ratio for one projection of a water cylinder phantom as estimated by simulations and by experiments at 130 kV.

These water objects could be used to generate feature clouds for comparing algorithms. The suitcase also contains a Teflon sheet, as well as two stainless steel spheres. Figure 8 demonstrates that the simulated data contains realistic streak artifacts due to scatter and metal. The metal objects were positioned such that the resulting metal artifacts make it challenging to

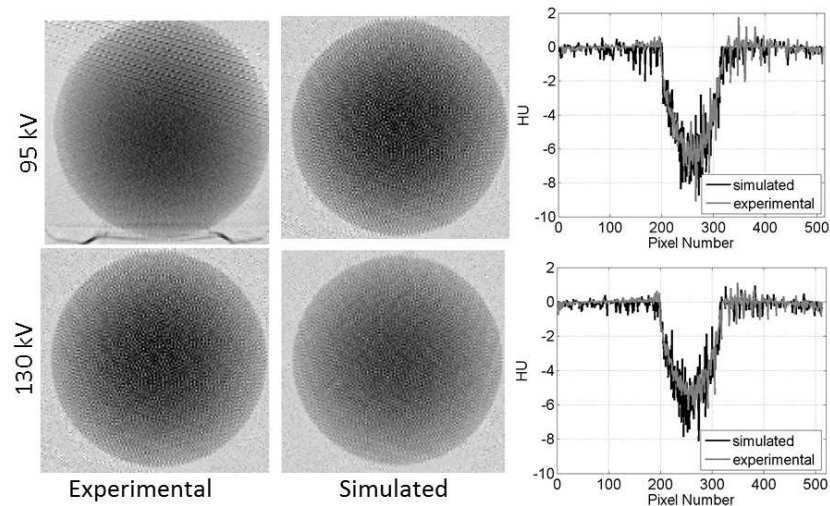


Fig. 7. Comparison of the scatter artifact in the simulated and scanned water cylinder at 95 kV and 130 kV. All images are displayed at the same window/level. The central horizontal profile through the water cylinder is also plotted. The scatter artifact images were generated by subtracting the images with scatter from the scatter corrected images.

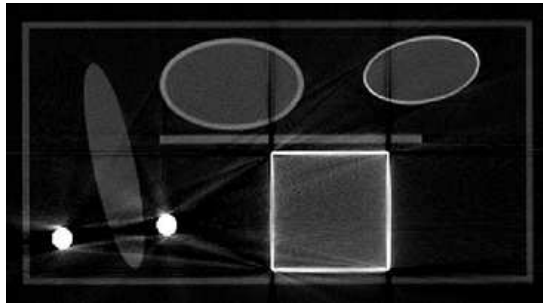


Fig. 8. Image reconstructed from simulated data of a suitcase phantom.

segment the water and sheet objects.

IV. DISCUSSION AND CONCLUSIONS

The results demonstrated that the simulated data matched the experimental reconstructed HU values to within 9%, noise within 10% for five of eight objects (and within 20-30% for three objects), SPR within 13%, and scatter artifact within 1 HU. One limitation of this work was the small number of objects used to validate the simulation software. Another limitation was that spatial resolution was not used as a metric to evaluate the match between the simulated and experimental data. A comparison of spatial resolution metrics such as Modulation Transfer Function (MTF) is recommended for future work. Another limitation is that the work flow for performing simulations (Figure 1) was not streamlined, as it requires two different simulators, bash scripts, and Matlab code. Modifying the code for new geometries may be challenging. Additional work is required to improve the flexibility and usability of the simulation tool and to quantify the level of agreement between experimental and simulated data for artifacts such as streaks. Overall, the results present the preliminary feasibility of simulation tools to model CT-based explosive detection systems.

V. ACKNOWLEDGMENTS

This material is based upon work supported by the U.S. Department of Homeland Security, Science and Technology Directorate, under Task Order Number HSHQDC-12-J-00056. The views and conclusions contained in this document are those of the authors and should not be interpreted as necessarily representing the official policies, either expressed or implied, of the U.S. Department of Homeland Security.

REFERENCES

- [1] K. Cranley, B. Gilmore, G. Fogarty, and L. Desponds, "IPEM Report 78: catalogue of diagnostic x-ray spectra and other data," The Institute of Physics and Engineering in Medicine (IPEM), Tech. Rep. 78, 1997.
- [2] M. Berger, J. Hubbell, S. Seltzer, J. Chang, J. Coursey, R. Sukumar, and D. Zucker, "XCOM: Photon cross sections database," *NIST Standard Reference Database*, vol. 8, pp. 87–3597, 1998.
- [3] C. Crawford and K. King, "Computed tomography scanning with simultaneous patient translation," *Medical Physics*, vol. 17, no. 6, pp. 967–982, 1990.
- [4] S. Agostinelli, J. Allison, K. Amako, J. Apostolakis, H. Araujo, P. Arce, M. Asai, D. Axen, and EtAl, "G4—a simulation toolkit," *Nuclear Instruments and Methods in Physics Research Section A: Accelerators, Spectrometers, Detectors and Associated Equipment*, vol. 506, no. 3, pp. 250–303, 2003.
- [5] L. Zhu, N. R. Bennett, and R. Fahrig, "Scatter correction method for x-ray CT using primary modulation: Theory and preliminary results," *Medical Imaging, IEEE Transactions on*, vol. 25, no. 12, pp. 1573–1587, Dec. 2006.
- [6] W. Richardson, "Bayesian-based iterative method of image reconstruction," *J. Opt. Soc. Amer.*, vol. 62, pp. 55–59, 1972.
- [7] L. Lucy, "An iterative technique for the rectification of observed distributions," *Astronom. J.*, vol. 74, pp. 745–754, 1974.

Efficient and Accurate Correction of Beam Hardening Artifacts

Kyle Champley and Timo Bremer

Abstract—The polychromatic energy-spectra of X-ray tubes used in Computed Tomography (CT) produce so-called *beam hardening* artifacts in the reconstructed images. These artifacts diminish the quantitative accuracy and qualitative appearance of the CT images. Modern model-based beam hardening correction (BHC) algorithms are effective at removing these artifacts, but are extremely computationally expensive. In this paper we develop a new model-based BHC algorithm that is both effective and computationally efficient. The method consists of two nested loops. The outer loop estimates the energy dependence on the measured ray-sums of the attenuation map and the inner loop determines the sinogram data that fits the energy-weighted forward model of CT data.

I. INTRODUCTION

X-ray Computed Tomography (CT) allows one to non-destructively obtain images of the structural makeup of an object of interest. A number of physical effects in the measured data may diminish the qualitative and quantitative accuracy of the image. This paper deals with the correction of so-called *beam-hardening* artifacts.

The attenuation of a monochromatic X-ray beam through a uniform object is given by $-\log(I/I_0) = \mu l$, where I_0 and I are the intensity of the beam before and after the beam travels through the object, μ is the attenuation coefficient (at the given energy of the beam), and l is the path-length through the object.

The relationship between the attenuation of a polychromatic X-ray beam through an object and the attenuation map is highly nonlinear. The rate of absorption and scattering of X-rays depends on the X-ray energy and the material composition. Lower energy X-rays are absorbed at a higher rate which causes the beam to *harden*. The violation of the assumed linear relationship between the measurements and the object attenuation map by the polychromatic X-ray CT spectra introduces *beam hardening* artifacts into the reconstructed CT images.

Methods for beam hardening correction (BHC) have been developed over the past several decades [1], [2], [3], [4], [5], [6], [7], [8] to mitigate beam hardening artifacts. Earlier approaches [1], [2], [3], [4] may be categorized as post-reconstruction techniques. These methods are computationally efficient, but not as accurate as state-of-the-art model based iterative methods [5], [6], [8] which are computationally intensive.

In this paper we introduce a new computationally-efficient and quantitatively accurate model-based BHC algorithm. We

test our algorithm with simulated and measured data and compare its performance with a BHC algorithm developed by Fuchs [3].

II. X-RAY CT MODEL

Let γ be the X-ray energy (keV), $d(\gamma)$ be the energy-dependent detector response, and $s(\gamma, L)$ be the source spectra that depends on a particular ray-path, L . Assuming that no scattered radiation is measured by the detectors, the expectation of a radiograph can be modeled by

$$I(L) := \int d(\gamma) s(\gamma, L) e^{-\int_L \mu(\gamma, \mathbf{x}) d\mathbf{x}} d\gamma,$$

where $\mu(\gamma, \mathbf{x}) \text{ cm}^{-1}$ is the energy-dependent attenuation map of the object being scanned and $\mathbf{x} \in \mathbb{R}^3$ is a location in space. Define the *air scan* as the radiograph with the object removed from the field of view. Then its expectation is given by

$$I_0(L) := \int d(\gamma) s(\gamma, L) d\gamma.$$

The normalized radiograph is given by

$$\begin{aligned} \frac{I(L)}{I_0(L)} &= \int \hat{m}(\gamma, L) e^{-\int_L \mu(\gamma, \mathbf{x}) d\mathbf{x}} d\gamma, \\ \hat{m}(\gamma, L) &:= \frac{d(\gamma) s(\gamma, L)}{\int d(\gamma) s(\gamma, L) d\gamma}. \end{aligned}$$

The attenuation map can be reconstructed (with beam-hardening artifacts) from a *sinogram* which is given by

$$p(L) := -\log\left(\frac{I(L)}{I_0(L)}\right) \approx P\mu(\bar{\gamma}, L) \quad (1)$$

$$P\mu(\bar{\gamma}, L) := \int_L \mu(\bar{\gamma}, \mathbf{x}) d\mathbf{x}, \quad (2)$$

where P is the forward projection operator and $\bar{\gamma} = \int \gamma \hat{m}(\gamma) d\gamma$ is the mean effective energy of the system. Equation (2) is only exact for $\hat{m}(\gamma, L) = \delta(\gamma - \bar{\gamma})$, where $\delta(\cdot)$ is the dirac delta functional.

A. Energy-Dependent Attenuation of Compounds

The attenuation coefficient of a material can be broken up in components of electron density (electrons mol / cm³) and cross section (cm² mol⁻¹/electrons). The absorption and scattering cross section of a material depends on its effective atomic number (also called effective-Z), i.e.,

$$\mu(\gamma, \mathbf{x}) = \sigma(\gamma, Z(\mathbf{x}))\rho(\mathbf{x}),$$

The authors are with Lawrence Livermore National Laboratory, Livermore, CA. Corresponding author: Kyle Champley (champley1@llnl.gov)

where σ is the cross section, ρ is the density, and $Z(\mathbf{x})$ is the spatially-variant effective-Z map. The photon energy-dependent absorption and scattering cross section for the elements can be found in tables [9]. We shall denote these quantities by $\sigma(\gamma, Z)$ where $Z \in \mathbb{Z}$ is the atomic number of the element. The cross sections of the elements can be extended to non-integer Z by linear interpolation.

These energy-dependent attenuation coefficients can be approximated by the Compton-Photoelectric basis given by

$$\begin{aligned}\mu(\gamma, \mathbf{x}) &\approx b_c(\gamma)f_c(\mathbf{x}) + b_p(\gamma)f_p(\mathbf{x}) \\ b_c(\gamma) &:= 2\pi r_0^2 N_A \\ &\times \left\{ \frac{1+\alpha}{\alpha^2} \left[\frac{2(1+\alpha)}{1+2\alpha} - \frac{1}{\alpha} \log(1+2\alpha) \right] \right. \\ &\left. + \frac{1}{2\alpha} \log(1+2\alpha) - \frac{1+3\alpha}{(1+2\alpha)^2} \right\} \frac{\text{mol}^{-1}\text{cm}^2}{\text{electron}} \\ b_p(\gamma) &:= \gamma^{-3},\end{aligned}$$

where r_0 is the classical electron radius and N_A is Avogadro's number.

Now consider the attenuation maps f_1 and f_2 at the two energies γ_1 and γ_2 . Then there exists f_p and f_c such that

$$\begin{aligned}f_1 &= b_c(\gamma_1)f_c + b_p(\gamma_1)f_p \\ f_2 &= b_c(\gamma_2)f_c + b_p(\gamma_2)f_p\end{aligned}$$

and conversely

$$\begin{aligned}f_c &= b_1(\gamma_1)f_1 + b_2(\gamma_1)f_2 \\ f_p &= b_1(\gamma_2)f_1 + b_2(\gamma_2)f_2,\end{aligned}$$

where

$$b_1(\gamma) := \frac{b_p(\gamma_2)b_c(\gamma) - b_c(\gamma_2)b_p(\gamma)}{b_p(\gamma_2)b_c(\gamma_1) - b_c(\gamma_2)b_p(\gamma_1)} \quad (3)$$

$$b_2(\gamma) := \frac{b_c(\gamma_1)b_p(\gamma) - b_p(\gamma_1)b_c(\gamma)}{b_c(\gamma_1)b_p(\gamma_2) - b_p(\gamma_1)b_c(\gamma_2)} \quad (4)$$

and thus

$$\mu(\gamma, \mathbf{x}) \approx b_1(\gamma)f_1(\mathbf{x}) + b_2(\gamma)f_2(\mathbf{x}).$$

III. DEVELOPMENT OF BEAM HARDENING CORRECTION ALGORITHM

We wish to determine $p := Pf$, where f is the attenuation map at energy $\bar{\gamma}$. Assume that the energy-dependent attenuation map, μ , can be broken up into a finite number of material components by

$$\mu(\gamma, \mathbf{x}) = \sum_{i=1}^M \hat{\sigma}_i(\gamma) a_i(\mathbf{x}),$$

where $\hat{\sigma}_i(\gamma) = \frac{\sigma(\gamma, Z_i)}{\sigma(\bar{\gamma}, Z_i)}$ is the normalized cross section (unit less) of the materials with effective-Z of Z_i and $a_i(\mathbf{x})$ are spatially-dependent attenuation maps (at $\bar{\gamma}$) for each material. Note that this model allows the attenuation map to fluctuate (by variable density) for a given material. The choice of $\{Z_i\}_{i=1}^M$ should be such that different materials can be reasonably determined by either a priori knowledge of the object

being scanned or by applying a set of parametric transfer functions to f such as $a_i(\mathbf{x}) := T_i(f)(\mathbf{x})$, where

$$T_i(f)(\mathbf{x}) := \begin{cases} f(\mathbf{x}), & f(\mathbf{x}) < \mu_1, \\ \frac{\mu_i - f(\mathbf{x})}{\mu_i - \mu_{i-1}} \mu_{i-1}, & \mu_{i-1} \leq f(\mathbf{x}) < \mu_i, \\ \frac{f(\mathbf{x}) - \mu_i}{\mu_{i+1} - \mu_i} \mu_i, & \mu_i \leq f(\mathbf{x}) < \mu_{i+1}, \\ f(\mathbf{x}), & \mu_M < f(\mathbf{x}), \\ 0, & \text{otherwise.} \end{cases} \quad (5)$$

Note that $f = \sum_i a_i$ and μ_i are the attenuation coefficients of our basis elements at the mean effective energy. Other transfer functions may be used, but are not discussed in this paper.

Using the above we can separate the spectra effects of $P\mu(\gamma, L)$ from its value at the mean energy by

$$\begin{aligned}P\mu(\gamma, L) &= \frac{P\mu(\gamma, L)}{P\mu(\bar{\gamma}, L)} P\mu(\bar{\gamma}, L) \\ &= \frac{\sum_{i=1}^M \hat{\sigma}_i(\gamma) P a_i(L)}{\sum_{i=1}^M \hat{\sigma}_i(\bar{\gamma}) P a_i(L)} P f(L) \\ &= \sum_{i=1}^M \hat{\sigma}_i(\gamma) \frac{P a_i(L)}{\sum_{j=1}^M P a_j(L)} P f(L) \\ &=: c(\gamma, L) p(L).\end{aligned} \quad (6)$$

This method requires M forward projections to estimate $c(\gamma, L)$. We now show how one can estimate $c(\gamma, L)$ with only one forward projection using equations (3, 4). Now consider the two energies $\bar{\gamma}$ and γ_{peak} , where γ_{peak} is the peak energy of the spectra. Then using equations (3, 4), we may define basis functions $b_{mean}(\gamma)$ and $b_{peak}(\gamma)$ such that

$$\mu(\gamma, \mathbf{x}) \approx b_{mean}(\gamma)f(\mathbf{x}) + b_{peak}(\gamma)f_{peak}(\mathbf{x}).$$

Then using a similar argument as above we find

$$\begin{aligned}P\mu(\gamma, L) &\approx \left[b_{mean}(\gamma) + b_{peak}(\gamma) \frac{P f_{peak}(L)}{P f(L)} \right] P f(L) \\ &=: c(\gamma, L) P f(L),\end{aligned} \quad (7)$$

where $f_{peak}(\mathbf{x}) := \sum_{i=1}^M \hat{\sigma}_i(\gamma_{peak}) a_i(\mathbf{x})$.

IV. ITERATIVE ESTIMATION OF MODEL PARAMETERS

In this section we describe how to iteratively determine the beam hardening model parameters, $c(\gamma, L)$ and in turn the beam hardening corrected sonogram data, $p(L)$.

Suppose that the effective atomic number of the material with the lowest effective atomic number in the model is given by Z_1 . For example, in medical CT $Z_1 = 7.42$, the effective atomic number of water. Also let A be the filtered backprojection (FBP) operator. Then our algorithm is given by

- 1) Initialize $n = 0$ and $p_{0,0} := -\log\left(\frac{I}{I_0}\right)$
- 2) Set $c_n(\gamma)$:

$$\begin{aligned}c_n(\gamma) &:= \begin{cases} \hat{\sigma}_1(\gamma), & n = 0, \\ b_{mean}(\gamma) + b_{peak}(\gamma) \frac{P f_{n,peak}}{P n,0}, & n \geq 1 \end{cases} \\ f_n &:= A p_{n,0}, \quad n \geq 1 \\ f_{n,peak} &:= \sum_{i=1}^M \hat{\sigma}_i(\gamma_{peak}) T_i(f_n), \quad n \geq 1\end{aligned}$$

- 3) Use Newton's Method to find sinogram data that matches polychromatic model (for $k = 0, 1, \dots, K-1$):

$$p_{n,k+1} := p_{n,k} + \frac{\int \hat{m}(\gamma) e^{-p_{n,k} c_n(\gamma)} d\gamma}{\int c_n(\gamma) \hat{m}(\gamma) e^{-p_{n,k} c_n(\gamma)} d\gamma} \times \left[\log \left(\int \hat{m}(\gamma) e^{-p_{n,k} c_n(\gamma)} d\gamma \right) + p_{0,0} \right]$$

- 4) Update beam corrected sinogram: $p_{n+1,0} := p_{n,K-1}$
 5) Increment n and repeat steps 2 through 4

For notational simplicity we have dropped the arguments of L from the above equations.

Thus the inner loop (in k) uses Newton's method to determine the best match between the measured data and the polychromatic forward model of the data. This model requires knowledge of $c(\gamma, L)$ which is iteratively estimated in the outer loop (in n) of the algorithm.

Note that the first iteration (in n) of the algorithm does not require a reconstruction and the first image reconstructed has already been partially corrected for beam hardening artifacts.

V. METHODS

We tested our algorithm on both simulated and measured data from an Imatron electron-beam CT (EBCT) scanner. The spectra and detector response of the measured data are unknown; we only know that the spectra has a peak energy of 130 keV. We modeled this spectra using the techniques proposed in [10]. Using this spectra model and uniform detector response, i.e., $d(\gamma) = 1$, the mean effective energy of the system is estimated to be $\bar{\gamma} = 61.27$. We partitioned our BHC model into three components: water, aluminum, and titanium.

To provide a basis for comparison, we also implemented a BHC method developed by Fuchs [3]. The method is given by

$$\begin{aligned} p_0 &:= -\log(I/I_0) \\ p_1 &:= 2p_0 + \log \left(\int \hat{m}(\gamma) e^{-\hat{\sigma}_i(\gamma) p_0} d\gamma \right) \\ g_{n,i} &:= PT_i(f_n) \\ p_{n+1} &:= p_0 + \sum_{i=1}^M g_{n,i} \\ &+ \log \left(\int \hat{m}(\gamma) e^{-\sum_{i=1}^M \hat{\sigma}_i(\gamma) g_{n,i}} d\gamma \right). \end{aligned}$$

The Fuchs algorithm shares some similarities with our algorithm. In our algorithm, the forward model of the corrected data essentially matches the measured data. This is not true for the Fuchs algorithm.

A list of attenuation coefficients and effective-Z of the materials used in our simulations is shown in Table I. The FBP reconstruction of the phantoms used in our simulations are shown in Figure 1. We simulated 500 views (over 180°) of parallel-beam data with 512 rays per view using analytic ray-tracing techniques and a polychromatic spectra with peak energy of 130 keV. Noise was not included in the simulation so we could isolate the beam hardening artifact and correction.

The Imatron CT data is comprised of a single-row of fan beam projections with 888 views (over 222°) and 864 rays per view. Multiple axial slices were taken in step-and-shoot mode.

TABLE I
MATERIAL PROPERTIES

material	electron density	Z	attenuation	HU
graphite	0.9012 $\frac{\text{electrons mol}}{\text{cm}^3}$	6	0.3140 cm^{-1}	1542
water	0.554 $\frac{\text{electrons mol}}{\text{cm}^3}$	7.42	0.2040 cm^{-1}	1000
magnesium	0.8610 $\frac{\text{electrons mol}}{\text{cm}^3}$	12	0.4370 cm^{-1}	2147
aluminum	1.3009 $\frac{\text{electrons mol}}{\text{cm}^3}$	13	0.7290 cm^{-1}	3581
silicon	1.1580 $\frac{\text{electrons mol}}{\text{cm}^3}$	14	0.7210 cm^{-1}	3543
titanium	2.0710 $\frac{\text{electrons mol}}{\text{cm}^3}$	22	3.2820 cm^{-1}	16121

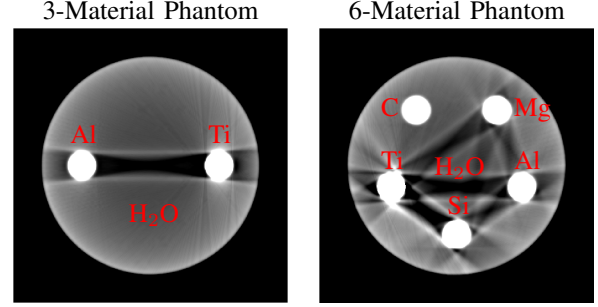


Fig. 1. FBP Reconstructions. Window: [900 1100] HU.

VI. RESULTS

Results are shown in Figures 2, 3, 4, and 5.

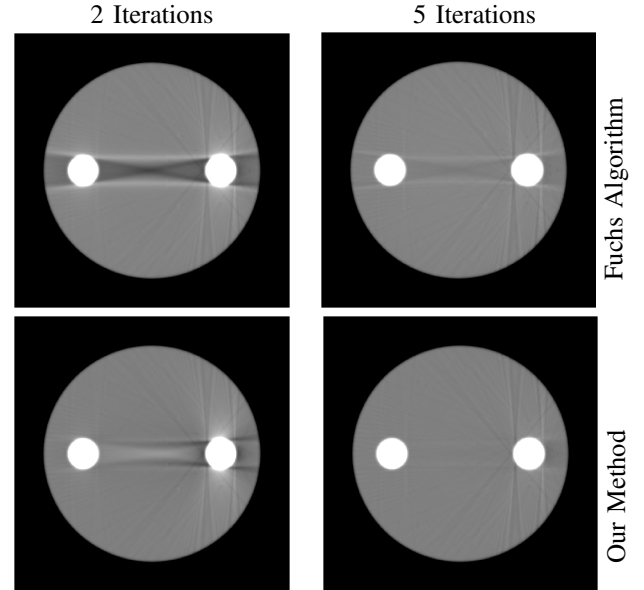


Fig. 2. Reconstructed images are the 3-material phantom. Window: [900, 1100] HU.

VII. DISCUSSION AND CONCLUSION

In this paper we have developed and tested an efficient and accurate model-based beam hardening correction algorithm for X-ray CT. Experiments show that the algorithm effectively converged in five iterations, removing streaks and improving quantification. Our algorithm seemed to converge significantly faster than the algorithm developed by Fuchs et al. and the image quality of our algorithm is shown to be superior for the same number of iterations.

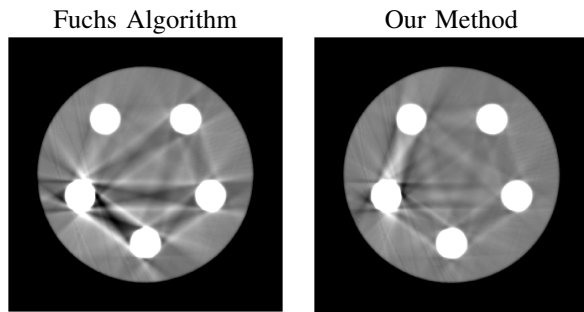


Fig. 3. Reconstructed images of the 6-material phantom after 2 iterations of each BHC algorithm. Window: [900, 1100] HU.

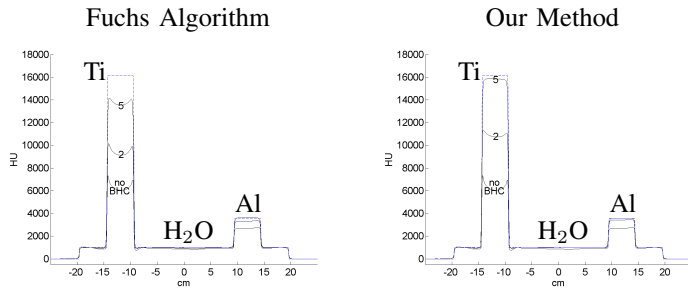


Fig. 4. Cross sectional plots through the reconstructed image of the 6-material phantom after two iterations of each BHC method. The numbers on the cross section plots represent the number of iterations of the BHC algorithm. The dashed line is the true cross section.

The *inner loop* of the BHC algorithm (the iteration in k) converges rapidly and can be computed in parallel because each measurement is processed independently. In our experiments nearly all data samples converged to within ten decimal places in three iterations or less. The computational complexity of our algorithm and the Fuchs algorithm is primarily driven by the number of forward and backprojection operations that are required per iteration. Our algorithm requires one forward projection and one backprojection per iteration while the Fuchs algorithm requires M (the number of materials in the model) forward projections and one backprojection per iteration. No forward or back projections are required for the first iteration of either algorithm, but one must perform an extra backprojection at the conclusion of both algorithms to produce an output image. Thus the number of forward and back projections required for N iterations is given by $2(N - 1) + 1$ and $(M + 1)(N - 1) + 1$ for our algorithm and the Fuchs algorithm, respectively.

The main novel aspect of our algorithm is in the separation of the beam hardening model parameters, $c(\gamma, L)$, and the desired monochromatic sinogram, $p(L)$, described by equations (6, 7). This allows one to exactly determine the data that fits the given material model by computation of the inner loop in our algorithm. The outer loop updates the material model.

VIII. ACKNOWLEDGEMENT

This work performed under the auspices of the U.S. Department of Energy by Lawrence Livermore National Laboratory under Contract DE-AC52-07NA27344. The Imatron data was

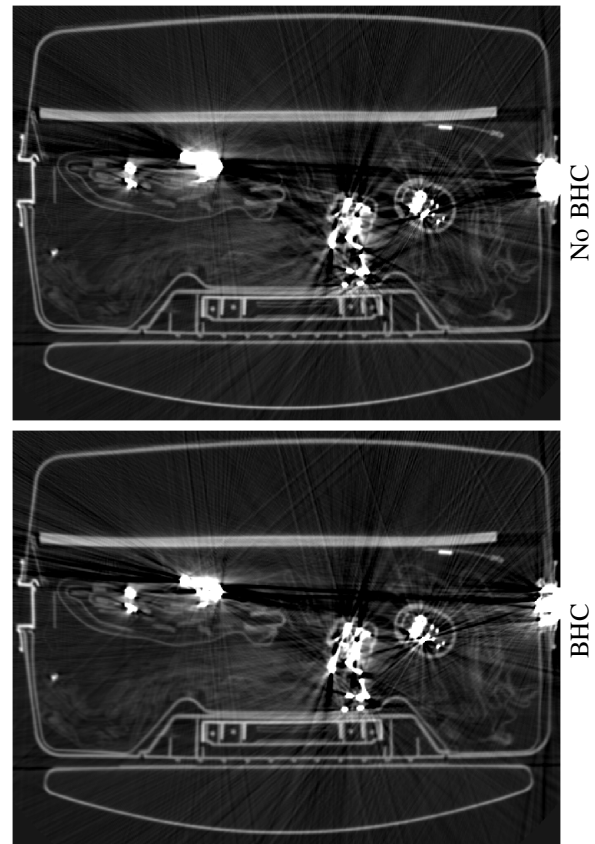


Fig. 5. Reconstructed images of luggage scanned on the Imatron EBCT scanner with display window [-200, 2000] HU.

provided courtesy of the COE for Explosives ALERT at Northeastern University.

REFERENCES

- [1] G. Herman and S. Trivedi. A comparative study of two postreconstruction beam hardening correction methods. *IEEE Trans. Med. Imaging*, 2:128–135, 1985.
- [2] P. Joseph and C. Ruth. A method for simultaneous correction of spectrum hardening artifacts in ct images containing both bone and iodine. *Med. Phys.*, 24:1629–1634, 1997.
- [3] T. Fuchs. Strahlauhfärtungskorrekturen in der computer-tomographie. *Ph.D. dissertation, Institut für Medizinische Physik, Friedrich-Alexander Universität*, 1998.
- [4] J. Hsieh, R. Molthen, C. Dawson, and R. Johnson. An iterative approach to the beam hardening correction in cone beam ct. *Med. Phys.*, 27:23–29, 2000.
- [5] Bruno De Man, Johan Nuyts, Patrick Dupont, Guy Marchal, and Paul Suetens. An iterative maximum-likelihood polychromatic algorithm for CT. *IEEE Trans. Med. Imag.*, 20:999–1008, 2001.
- [6] I. Elbakri and J. Fessler. Segmentation-free statistical image reconstruction for polyenergetic x-ray computed tomography with experimental validation. *Phys. Med. Biol.*, 48:2453–2477, 2003.
- [7] Marc Kachelrieß and Willi A. Kalender. Improving pet/ct attenuation correction with iterative ct beam hardening correction. *IEEE Nuclear Science Symposium Conference Record*, M04-5:1905–1909, 2005.
- [8] G. Van Gompel, K. Van Slambrouck, M. Defrise, K. Batenburg, J. de Mey, J. Sijbers, and J. Nuyts. Iterative correction of beam hardening artifacts in ct. *Med. Phys.*, 38:36–49, 2011.
- [9] M.J. Berger, J.H. Hubbell, S.M. Seltzer, J. Chang, J.S. Coursey, R. Sukumar, D.S. Zucker, and K. Olsen. *XCOM: Photon Cross Section Database (version 1.5)*. National Institute of Standards and Technology, Gaithersburg, MD, 2010.
- [10] G.G. Poludniowski. Calculation of x-ray spectra emerging from an x-ray tube. part ii. x-ray production and filtration in x-ray targets. *Med. Phys.*, 34:2175–2186, 2007.

Human and model observers performance in low contrast detection tasks with CT phantom images acquired at different dose levels

I. Hernandez-Giron^{1,2}, J. Geleijns³, A. Calzado², R. M. S. Joemai³, W. J. H. Veldkamp³

Abstract— Purpose: To study low contrast detectability (LCD) performance in CT phantom images using two model observers and compare it with human observers results in a 2-alternative forced choice (2-AFC) experiment.

Introduction: Low contrast sensitivity of CT scanners is regularly assessed by subjective scoring of low contrast detectability within CT phantom images. These studies might be biased since low contrast objects are in general arranged in fixed patterns known by the observers beforehand.

Methods and Materials: Images of the low contrast module of the Catphan 500 phantom were used for the evaluations. The phantom contains three series of low contrast disk patterns (diameter 2 -15 mm; contrast 0.3, 0.5, and 1.0%). The images were acquired at different dose levels, varying the CT mAs. Two model observers (non-prewhitening matched filter with an eye filter and Hotelling) were implemented in a software program to automatically measure LCD using the images as inputs. To validate the results, human observers scored images in a 2-AFC experiment.

Results: The expected improvement in LCD with increasing mAs was reproduced by both, the models and the human observers. Both models were more efficient than the humans in these tasks. The efficiency of NPWE compared to humans was between 0.5 and 0.65 for 1% and 0.5% contrast objects. The internal noise added to Hotelling to match human results was $\approx 2\text{HU}$.

Conclusion: We have developed an automated method to investigate LCD in CT based on different model observers. The observers reproduced the trends showed by the human observer and showed similar LCD values than the human after corrections by efficiency and internal noise addition. This method can be a useful tool to predict human in CT detection tasks and also be used to evaluate image reconstruction algorithms or dose reduction strategies, among others, in an objective way.

I. INTRODUCTION

The number of CT scans performed worldwide per year has continually grown in the past decades. Nowadays it is one of the most used radiologic imaging techniques. In parallel, the concern about the radiation dose related to these examinations has increased. Protocol optimization is essential to obtain images containing the relevant diagnostic information acquired at the lowest achievable dose following the ALARA criteria. Several improvements have been incorporated in CT to achieve this goal and to extend the medical indications of this technique. Different studies have shown that a significant variation in image quality and

dose can exist between the different CT manufacturers for equivalent diagnostic indications.

Different parameters are used to assess image quality, among them, low contrast detectability (LCD), which consists in determining the smallest object visible for certain contrast value at a given dose level. It can be subjectively assessed by several observers scoring the detectability of objects on CT phantom images. These studies are time consuming and expensive due to the high number of observers and observations required. Besides, the results might be biased if the observers know beforehand the spatial distribution of the objects in the phantom, and a great inter and intra-observer variability may appear.

As an objective alternative, computer model observers intend to predict the performance of human observers in the image analysis. They can be a useful tool when investigating the influence of acquisition and reconstruction parameters in image quality or the effect of object size, shape and contrast in detection tasks.

In a previous work, we presented and validated an objective statistical method, implemented in Matlab, with a model observer (non-prewhitening matched filter with an eye filter, NPWE) to investigate the influence of different CT acquisition parameters on LCD and dose applied to a different CT scanner [1]. An improved version of the method has been developed and additionally, a channelized Hotelling (CHO) model observer with internal noise has been implemented. Both models were applied to CT phantom images acquired at different dose levels. Their results were compared with those obtained by human observers scoring the same images in a 2-alternative forced choice (2-AFC) experiment. The goal of this work is to study the LCD performance of both model observers and study their capability to predict human observer results.

II. MATERIALS AND METHODS

For this study, images of the Catphan 500 phantom were acquired with a 320-detector row CT scanner (Aquilion ONE, Toshiba, Japan) selecting 64x0.5 mm as beam collimation, FOV of 240 mm, helical acquisition (pitch 0.828) and 120 kV, for 50-100-200-400 mAs, respectively. Image reconstruction was performed with 5 mm slice thickness selecting a *soft body* FC12 kernel.

¹Unitat de Física Mèdica. Universitat Rovira i Virgili. Facultat de Medicina i Ciències de la Salut, Reus (Spain)

²Departamento de Radiología, Universidad Complutense de Madrid, Madrid (Spain)

³Radiology Department, Leiden University Medical Center, Leiden (The Netherlands)

*irene.debroglie@gmail.com

The phantom contains three groups of 9 low contrast cylindrical objects each (with diameters 2-15 mm and 0.3, 0.5 and 1.0% contrast, respectively, Fig. 1) and it was scanned 20 times. After discarding the images with artifacts and nearby the borders, sets of 80 images were obtained.

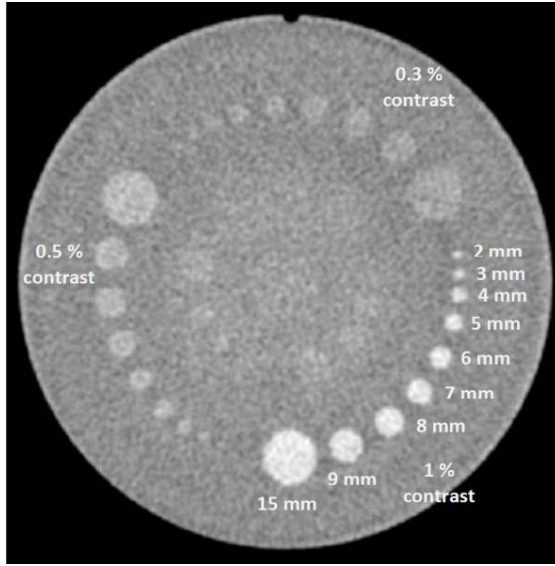


Fig.1. Catphan phantom low contrast module

The software uses a predefined pattern of templates of the distribution and sizes of the objects in the phantom, which is rescaled and rotated to fit the CT images. Low contrast detectability values for all the objects in the images are automatically calculated using two model observers:

NPWE observer: The eye filter used in the model was $E(f) = fe^{-bf}$, with b chosen such that $E(f)$ peaked at 4 cycles per degree [2] and assuming a fixed viewing distance of 50 cm from the monitor. Templates of the low contrast objects (previously blurred with the measured PSF) were correlated with the acquired images of the phantom and from the distribution of test statistics, a discrimination index d' was calculated (Eq. (1)); where $\langle \cdot \rangle$ is the mean and $\sigma(\cdot)$ is the standard deviation of the respective distributions [1, 3]. This index can be used as a measure of detection performance and related to object diameter and contrast. Proportion correct (PC) values can be determined according to Eq. (2). As, just by chance, in a 2-AFC experiment a PC=50% may be obtained, we propose a threshold of PC=75% to decide whether objects were visible or not. Psychometric fits were performed for each mAs and contrast applying Eq. (3), where λ tallies with the detectability threshold (PC=75%).

$$d' = \frac{\langle T \rangle_1 - \langle T \rangle_2}{\sqrt{\frac{1}{2}\sigma_1^2 + \frac{1}{2}\sigma_2^2}} \quad (1) \quad PC = 0.5 + 0.5 \operatorname{erf}\left(\frac{d'}{2}\right) \quad (2)$$

$$PC = 0.5 + \frac{0.5}{1 + e^{-f \log\left(\frac{d}{\lambda}\right)}} \quad (3)$$

Hotelling observer (CHO): This model uses channels to emulate neuronal response in the visual cortex. Gabor channels were used for this task, following Eq. (4) [4, 5]:

$$Ga(x, y) = \exp[-4(\ln 2)((x - x_o)^2 + (y - y_o)^2)/\omega_s^2] \cdot \cos[2\pi f_c((x - x_o)\cos\theta + (y - y_o)\sin\theta) + \beta] \quad (4)$$

where ω_s is the channel width, f_c is the central frequency and β is a phase factor [4]. As first approach we implemented the proposed conditions by Yu et al [5] and Leng et al [6] as their studies were also based on CT phantom images. The parameters were selected as follows: 6 channel passbands: [1/128–1/64], [1/64–1/32], [1/32–1/16], [1/16–1/8], [1/8–1/4] and [1/4–1/2] cycles/pixel; central frequencies f_c : 3/256, 3/128, 3/64, 3/32, 3/16 and 3/8 cycles/pixel; 5 orientations θ (0, $2\pi/5$, $4\pi/5$, $6\pi/5$ and $8\pi/5$); 2 phase factors β (0 and $\pi/2$). This configuration led to 60 channels in total. After applying the model to the CT images, SNR (equivalent to d') and PC were obtained for all the series.

Human observer 2-AFC study: To validate the trends shown by the models, a 2-AFC pilot human observer study was carried out with two observers, each of them scoring pairs of crops (object/background samples) extracted from the different sets of images for the 1% and 0.5% contrast groups. These crops (55x55 pixels) were obtained after applying a correction to wipe-out the nearby objects in the phantom, as shown in Fig. 2. For each mAs, reconstruction technique, and object size each observer scored 80 pairs of images (the same used for the models). This was done twice, to assess intra-observer variability. In total, for each mAs and contrast value 2880 pairs of images were analyzed. The scoring was performed in an i-MAC 27" DICOM calibrated monitor according to recommended visualization conditions, with fixed values window level/width (the latter taken as 3σ , being σ the average STD of the background samples of each series).

A routine was developed in Matlab to perform the 2-AFC study: two images were displayed together with the template; the one which is supposed to contain the object must be clicked on and scoring results are automatically stored in an output file. The images with/without signal were displayed randomly at left or right and also shuffled from the original image folders.

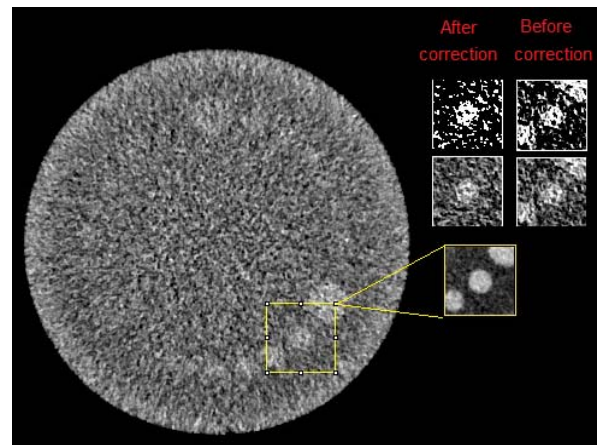


Fig.2. Background correction to wipe-out nearby objects in Catphan images. Inside the yellow square in this figure, a Z-projection of all the images in the series is shown before applying the correction.

The analysis of the intra and inter-observer consistency in both sessions was performed using the Wilcoxon signed rank test for matched-pair samples (consistent results for p-value ≥ 0.05) by separately comparing the scores for each object size and mAs. Using the deperated scoring results, detectability profiles (PC curves as a function of object diameter) were obtained for each observer and image series. Psychometric fits were calculated as in Eq. (3) to obtain the detectability threshold for the human observer. PC fitted values were transformed back into d' values.

Correlation between human and models: For NPWE, an efficiency η was estimated (Eq. (5)) for 1% and 0.5% contrast:

$$\eta = \left(\frac{d'_{human}}{d'_{NPWE}} \right)^2 \quad (5)$$

For channelized Hotelling model, internal noise, α , was added to the decision variables in the model to try to mimic the human results, in the range (0-20 HU).

III. RESULTS

Detectability increased with object diameter and contrast and with increasing mAs, as expected, for the human observer and both models.

In Fig. 3, d' NPWE values are shown as a function of object diameter and mAs for 0.5% contrast objects. The detectability thresholds as a function of mAs were in the range (2.9–1.6mm) for 0.5% and (1.8–1.4mm) for 1% contrast.

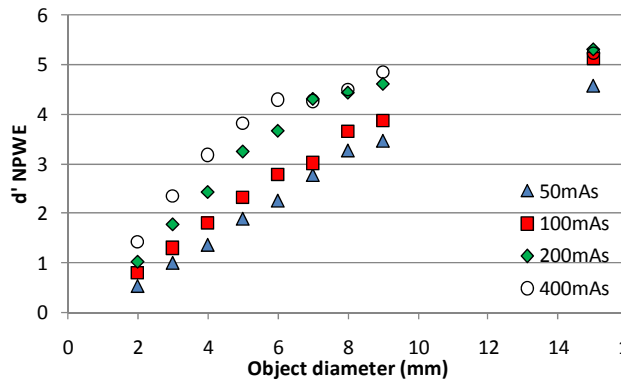


Fig. 3. Detectability index d' as a function of object diameter for the NPWE model observer and all mAs for 0.5% contrast objects.

In Fig. 4, the psychometric fits obtained for the average human observer and 0.5% contrast are shown. The detectability thresholds were (4 –2.2mm) for 0.5% and (1.9 –1.6mm) for 1% contrast.

In Fig. 5, d' for the average human is plotted as a function of PC. Due to the shape of the curve (Fig. 5) it is difficult to measure d' when its value is above 3, approximately, (i. e. $PC \approx 0.98$) in a 2-AFC experiment. Only the values below this threshold were used to determine the efficiency of the NPWE model observer.

The efficiency values between the average human and NPWE were 0.5 and 0.67 for 1% and 0.5% contrast, respectively.

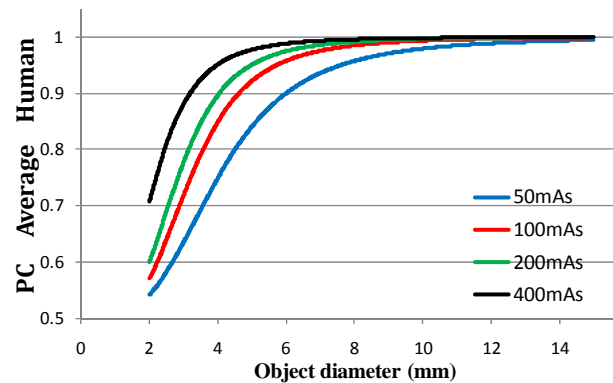


Fig. 4. Psychometric fits of the average human observer PC values as a function of object diameter and mAs for 0.5% contrast.

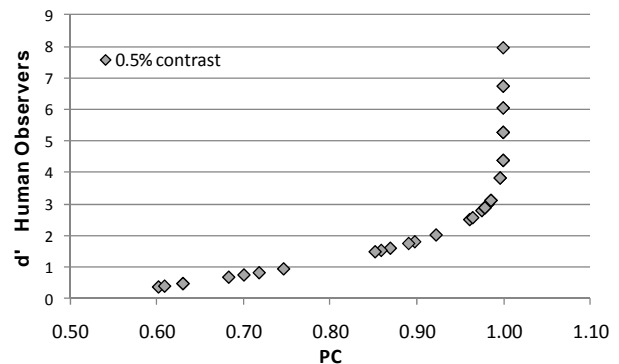


Fig. 5. Detectability index d' as a function of PC for the human observers and 0.5% contrast objects and all mAs

The CHO model gave much higher d' values than NPWE when no internal noise was applied. In Fig.6, d' values for the channelized Hotelling observer are shown for different values of internal noise (α) and the 1% contrast group. It depicts how the LCD of the CHO model is degraded as the internal noise increases.

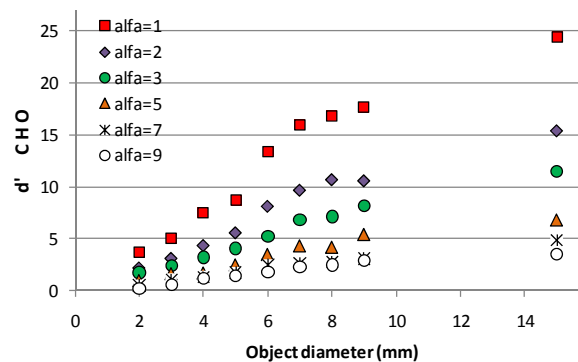


Fig. 6. Detectability index d' as a function of object diameter for the CHO model observer for different levels of internal noise (α) and 1% contrast objects.

In Fig. 7, the PC values as a function of the added internal noise for the CHO model is plotted together with the PC value for the average human for one of the analyzed conditions (2mm, 200 mAs). The point where both curves cross gives the internal noise that has to be added to the model to match the human ($\alpha=4$).

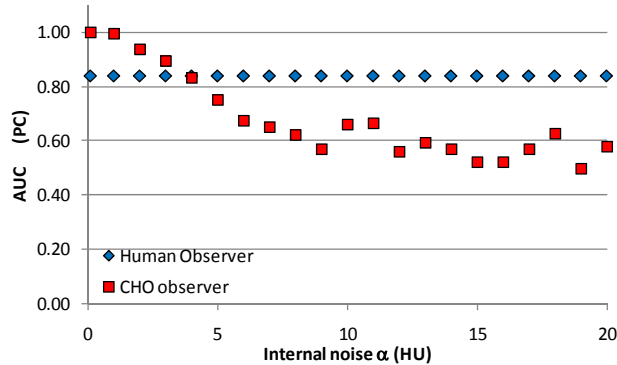


Fig. 7. Channelized Hotelling model observer PC values as a function of added internal noise for 200mAs and the 1% contrast 2mm object

This analysis was carried out for all the object sizes and mAs which showed significant differences between the human and the CHO model performance. The calculated internal noise was higher for the 0.5% contrast group and, in general, it also varied for the different mAs.

As a proof of concept, an intermediate value (4mm, 100mAs) was selected for both contrasts as reference to normalize the rest of the values using the related internal noise α . Thus, this parameter was fixed at 2.2 and 2.5 HU, for 1% and 0.5% contrast series respectively.

In Fig. 8 the psychometric fits of the PC corrected values for the NPWE model (normalized by the efficiency) and CHO model (corrected by the related internal noise factor) are shown together with the average human observer results. The figure shows the results related to 100 mAs and 0.5% contrast.

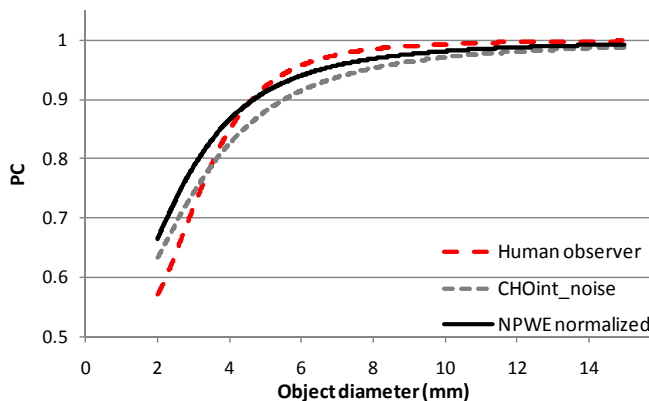


Fig. 8. Psychometric fits of PC as a function of object diameter for the human observer, CHO with internal noise ($\alpha = 2.5$ HU) and NPWE normalized by the efficiency ($\eta = 0.67$) for 100mAs and 0.5% contrast.

IV. CONCLUSIONS

Two model observers (NPWE and CHO) were implemented in a software program to automatically calculate low contrast detectability in Catphan phantom images. Images of the phantom were acquired at different dose levels and analyzed in this study.

Both models (CHO and NPWE), reproduced the trends obtained by human observers, showing an improvement of LCD with increasing object size, contrast and mAs and had better LCD performance than humans.

NPWE results were corrected by an efficiency factor, dependant on contrast, and the CHO was modified to add internal noise. Then, both models gave results much closer to the human observer.

There is still some leeway for tuning the models to reproduce more accurately human performance. For this task, an extended human observer study, including more observers is to be made in the near future. Further investigation in CHO channels and options will be made.

The method could be adapted to analyze images obtained with other phantoms and applied to specialties like mammography or tomosynthesis, amongst others. It can be a useful tool to objectively analyze the influence in LCD of different acquisition or reconstruction parameters and help in protocol optimization.

ACKNOWLEDGEMENTS

We would like to thank Christophe Opdam for his help in the implementation of the channelized model observer.

REFERENCES

- [1] Hernandez-Giron I, Geleijns J, Calzado A, Veldkamp WJH. Automated assessment of low contrast sensitivity for CT systems using a model observer. *Med Phys* 2011;38:S25–S35.
- [2] Burgess E, Jacobson FL, Judy PF. Human observer detection experiments with mammograms and power-law noise. *Med Phys* 2001;28:419–437.
- [3] Reiser I, Nishikawa RM. Identification of simulated microcalcifications in white noise and mammographic backgrounds. *Med Phys* 2006;33:2905–11.
- [4] Wunderlich A and Noo F. Image covariance and lesion detectability indirect fan-beam x-ray computed tomography. *Phys Med Biol* 2008;53: 2471–93.
- [5] Yu L, Leng S, Chen L, Kofler M, Carter RE et al. Prediction of human observer performance in a 2-alternative forced choice low-contrast detection task using channelized Hotelling observer: Impact of radiation dose and reconstruction algorithms. *Med Phys* 2013;40:041908-1-9.
- [6] Leng S, Yu L, Zhang Y, Carter RE, Toledano AY, McCollough CH. Correlation between model observer and human observer performance in CT imaging when lesion location is uncertain. *Med Phys* 2013;40:081908-1-9.

X-ray Tube Potential Modulation in Spectral CT

Xin Li, Xiaolan Wang, Yu Zou

Abstract—A constant x-ray tube potential over all imaging views has long been used in CT; however, it may not be dose efficient for a non-isotropic object, e.g., human patients. Studies have shown different optimal tube potential should be used for different size patient to reduce the CT dose if the target contrast is highly energy dependent. This work is to study the image quality improvement and dose reduction benefit of x-ray tube potential modulation for photon counting based spectral CT. Algorithms are developed to determine the optimal tube potential and tube current for phantoms with clinical relevant dimensions. Several tube potential and/or current modulation protocols, taking into consideration tube power limitation, tube potential switching frequency, and available tube potential options, are studied and compared. Simulation results showed that tube potential modulation protocols achieve better contrast-to-noise ratio compared with non-modulation protocols at the same dose level.

I. INTRODUCTION

CT dose is of great concern due to the significant increase in the use of CT nowadays. Different strategies have been developed to reduce the radiation dose without compromising image quality: Reducing tube current, using low tube voltage when the patient size is small and the target contrast is highly energy dependent, individualized scanning parameters such as automatic exposure control, advanced imaging reconstruction or processing methods or parameters, etc. [1]

Selecting optimal tube potential for a particular size patient has been of interest to reduce CT dose [2, 3]. These studies have found when the target contrast is highly energy dependent, smaller tube potential is preferred for a smaller size patient, while larger tube potential is preferred for a bigger size patient. However, the tube potential is fixed for the patient during the scan in those studies.

Since patient shape is often elliptical, i.e. the pathway through the patient is thicker for some views and thinner for other views, we are interested in modulating tube potential for different views. In this study we studied the image quality improvement and dose benefit of tube potential modulation for photon counting based spectral CT imaging. Photon counting spectral CT is suitable of performing tube potential modulation due to two reasons: On one hand, existing commercial x-ray tube is capable of tube potential modulation, at least slow modulation with a switching frequency limit; More importantly, the projection-domain decomposition enables straightforward image interpretation of projections at different tube potentials, whereas it is

challenging for non-spectral CT reconstruction due to the change of spectrum during a scan.

II. METHODS

In this study, monochromatic images at selected energy are generated as the final image to be evaluated, which is comparable to conventional CT reconstructed image at effective energy. There are three main parameters of interest to be optimized for a specific object:

- During the acquisition of spectral CT data, two parameters: *X-ray tube potential* and *current* for each view. Once determined, the spectral CT measurements can be decomposed into basis material projections by an iterative projection-domain decomposition method [4].
- Basis material images can then be reconstructed and monochromatic images at any energy can be derived by the method proposed by Lehmann [5]. *The energy of the monochromatic image* is the third parameter to be determined.

We propose the following 3-step method to determine these parameters: X-ray tube potential kVp, x-ray tube current mA, and the monochromatic energy E. For simplicity, we will denote the three parameters using kVp, mA and E in the following content.

A. Optimize x-ray tube potential kVp

We determined kVp by maximizing dose efficiency of each view with x-ray tube power constraint. The dose efficiency is defined as below ([2]):

$$\text{Dose Efficiency} = \frac{\text{CNR}}{\sqrt{\text{dose}}} \quad (1)$$

where CNR is the contrast to noise ratio and dose is the total energy deposited in the object. The contrast is calculated as the attenuation coefficient difference of target and background at the effective energy for each view. Since the definition of dose efficiency is mA independent, we can use it to optimize kVp before determine mA.

B. Optimize x-ray tube current mA

The x-ray tube current mA is determined by equalizing count level for each view and then the whole mA pattern will be scaled to a predetermined dose level. This requires knowledge of the outer dimension of the patient/phantom.

Xin Li is with Department of Electrical and Computer Engineering, Johns Hopkins University, Baltimore, MD 21218 USA.

Xiaolan Wang and Yu Zou are with Toshiba Medical Research Institute USA, Vernon Hills, IL 60061 USA.

C. Optimize monochromatic image energy E

We determined E after material decomposition which achieves the best image quality of the final image in terms of CNR.

D. Phantoms and simulations

We studied two elliptical water phantoms: 350mm*250mm (phantom 1), and 450mm*250mm (phantom 2), as shown in Fig. 1. Both water phantoms have a 7mm radius of calcium insert at the center. Noisy spectral CT projections are generated with the following energy bins: 20-40keV, 40-60keV, 60-80keV, 80-120keV, 120-140keV with 1200 views over 360 degree.

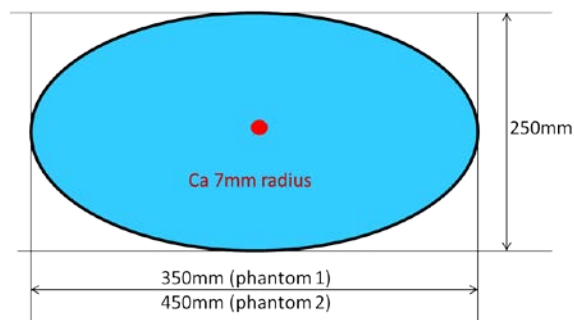


Fig. 1. Elliptical water phantoms with main axis size 350mm*250mm (phantom 1) and 450mm*250mm (phantom 2) with a 7mm radius calcium insert at the center.

E. Imaging protocols

We studied six imaging protocols summarized in Table I. For protocol 1 and 2, there will be no kVp modulation (120kVp), with fixed and modulated mA, two protocols currently used in CT. For protocol 3, we obtain the kVp and mA modulation pattern with our proposed method. Available kVps are 40 -120 in 10 kVp increment, and 135 kVp. We consider protocol 3 to be the best kVp and mA modulation protocol. Protocols 4-6 are kVp modulation protocols with more constraints. For protocol 4, we add a 20 ms kVp switching speed constraint. For protocol 5,6, we are only using 80 kVp and 120 kVp as the optional tube potential, which are available in commercial CT x-ray tubes and with modulated and fixed mA. All protocols are under current x-ray tube power limit of 75 kW.

F. Image evaluations

To evaluate the image quality of the final monochromatic image, we use the contrast-to-noise-ratio (CNR) as a figure of merit. The contrast is measured as the difference of the mean in the calcium ROI and the mean of the two nearby water ROIs. Noise is the averaged noise of the two water ROIs.

TABLE I. IMAGING PROTOCOLS

Protocol	kVp	mA	kVp switching frequency 20 Hz
1	120	255(phantom 1) 135(phantom 2)	Yes
2	120	Modulated	Yes
3	Modulated	Modulated	No
4	Modulated	Modulated	Yes
5	80, 120	Modulated	Yes
6	80, 120	No modulation within each kVp	Yes

III. RESULTS

A. Modulation pattern

The kVp and mA modulation pattern for the two phantoms are shown in Figs. 2-5. The discrete choices of kVp are to simplify the simulation. And more realistic and better kVp modulation pattern can be considered in the future studies. The abrupt jump of mA is due to the abrupt change of kVp when count level at each view is matched.

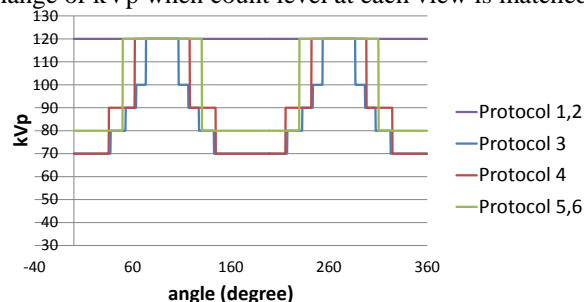


Fig. 2. kVp modulation pattern for phantom 1 for the six imaging protocols.

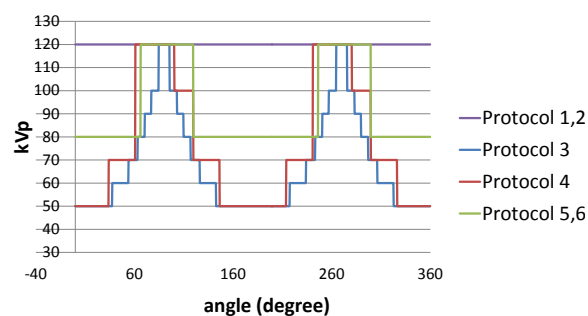


Fig. 3. kVp modulation pattern for phantom 2 for the six imaging protocols.

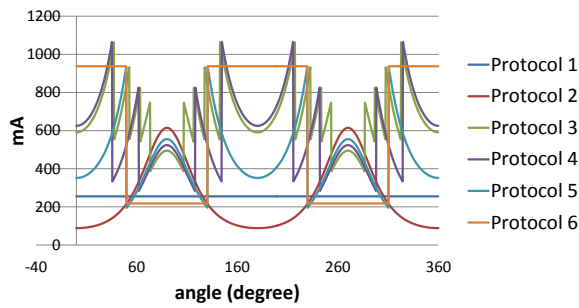


Fig. 4. mA modulation pattern for phantom 1 for the six imaging protocols.

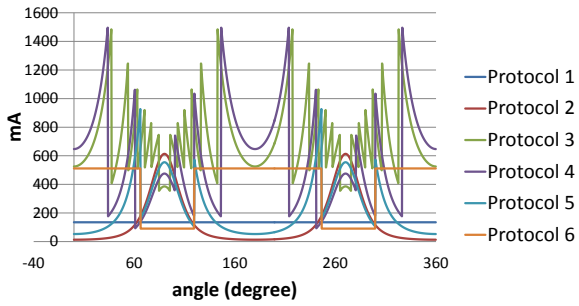


Fig. 5. mA modulation pattern for phantom 2 for the six imaging protocols.

B. Image contrast

The plot of image contrast for the two phantoms at different monochromatic energy E for the six protocols is shown in Figs. 6-7. The contrast of the monochromatic image largely depends on its energy E , as predicted by [5]: The attenuation coefficient of an object is determined by an energy independent, and an energy dependent part. For certain target and background, the contrast between the two only depend on energy.

C. Image noise

The plot of image noise for the six protocols at different monochromatic energy E for the two phantoms is shown in Figs. 8-9. The noise is affected by all three parameters: kVp, mA and E . The kVp modulation protocol decreases the noise of the monochromatic images with lower E . This is intuitively true: For lower energy images, noise is lowered by using measurement from lower energy.

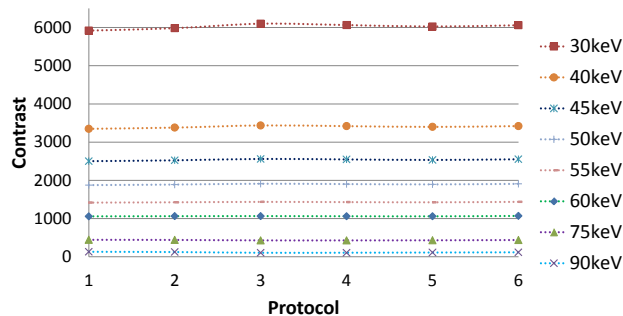


Fig. 6. Contrast plot for phantom 1 for the six imaging protocols at different E : 30, 40, 45, 50, 55, 60, 75, 90 keV.

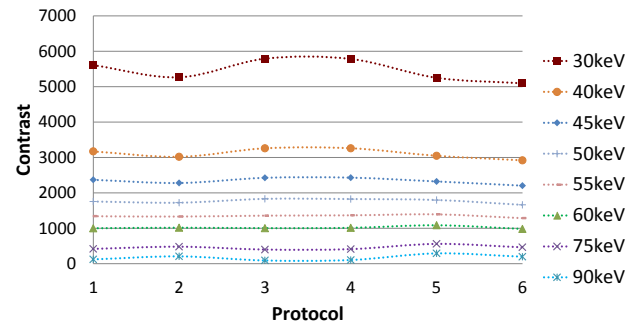


Fig. 7. Contrast plot for phantom 2 for the six imaging protocols at different E : 30, 40, 45, 50, 55, 60, 75, 90 keV.

D.

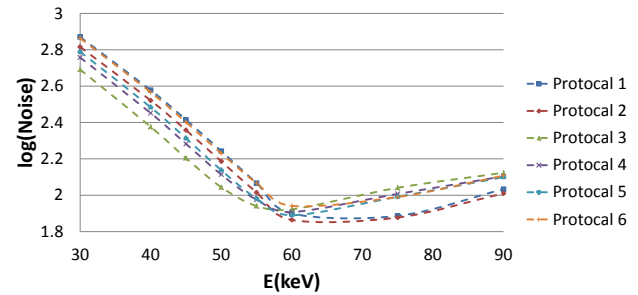


Fig. 8. Noise plot for phantom 1 at different E for the six imaging protocols.

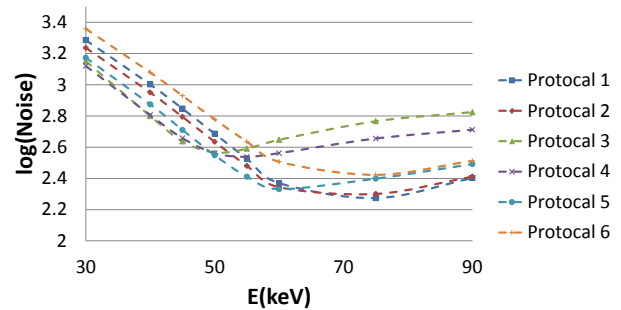


Fig. 9. Noise plot for phantom 2 at different E for the six imaging protocols.

E. Image CNR

The plot of CNR at the optimal monochromatic energy E is shown in Figs. 10-11. And the optimal images for the six imaging protocols are shown in Figs. 12-13. Visibly protocol 3 achieves the best image quality in terms of CNR at the same dose level. This is especially apparent for phantom 2, which have a larger aspect ratio so the benefit of kVp modulation is more significant.

The optimal monochromatic energy and corresponding optimal CNR for phantoms 1 and 2 are summarized in Tables II and III. Protocol 3 achieves the best CNR, which can be traded for lowest dose at the same CNR. Protocols 4 and 5 also have satisfactory CNR or dose benefit.

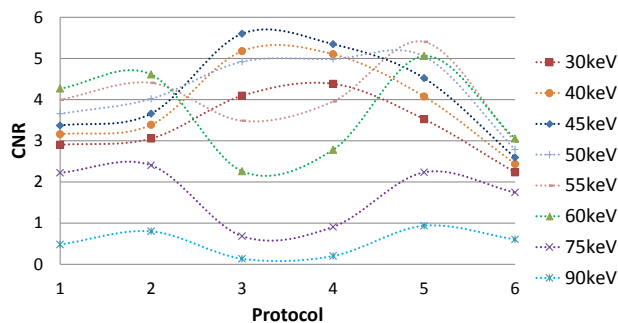


Fig. 10. CNR plot for phantom 1 at the optimal monochromatic energy for the six imaging protocols.

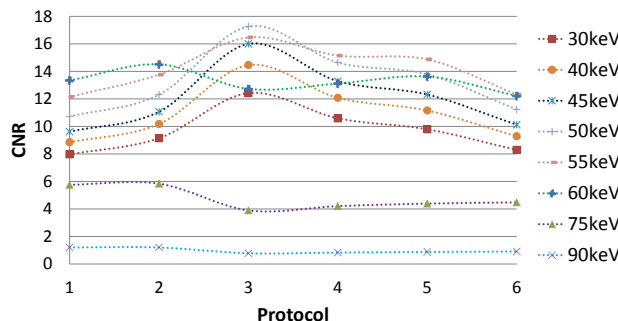


Fig. 11. CNR plot for phantom 2 at the optimal monochromatic energy for the six imaging protocols.

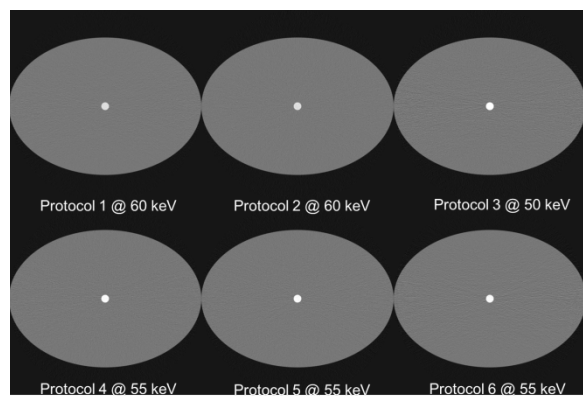


Fig. 12. Optimal images for the six imaging protocols for phantom 1.

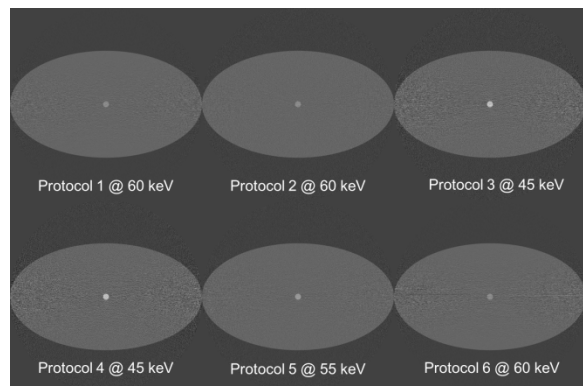


Fig. 13. Optimal images for the six imaging protocols for phantom 2.

TABLE II. OPTIMAL MONOCHROMATIC ENERGY AND CNR AND DOSE BENEFIT FOR PHANTOM 1

Protocol #	Optimal keV	Optimal CNR	CNR* (wrt #3)	Dose** (wrt #3)
1	60	13.34	0.77	1.67
2	60	14.52	0.84	1.42
3	50	17.27	1.00	1.00
4	55	15.15	0.88	1.30
5	55	14.87	0.86	1.35
6	55	12.32	0.71	1.97

TABLE III. OPTIMAL MONOCHROMATIC ENERGY AND CNR AND DOSE BENEFIT FOR PHANTOM 2.

Protocol #	Optimal keV	Optimal CNR	CNR* (wrt #3)	Dose** (wrt #3)
1	60	4.27	0.76	1.72
2	60	4.61	0.82	1.48
3	45	5.60	1.00	1.00
4	45	5.32	0.95	1.10
5	55	5.10	0.96	1.07
6	60 (55)	3.06	0.55	3.36

(For Table II and III, CNR* is the CNR with respect to CNR of protocol 3 at the same dose level; Dose** is the estimated dose level with respect to dose level of protocol 3 at the same CNR. The numbers in the Dose column is a simple calculation from numbers in CNR column assuming the same contrast and CNR.)

IV. CONCLUSIONS

We developed a 3-step parameter optimization method to optimize the tube potential, tube current and monochromatic energy for kV-modulated spectral CT. Results demonstrated the dose benefit of kV modulation in photon counting based spectral CT, in terms of improved CNR in human-size objects. More realistic kVp and mA modulation patterns can be considered in the future study and the benefit of kV modulation are expected to retain.

ACKNOWLEDGMENT

We thank Toshiba Medical Research Institute USA for their valuable support of this work.

REFERENCES

- [1] T. Kubo, P.-J. P. Lin, W. Stiller *et al.*, "Radiation Dose Reduction in Chest CT: A Review," *American Journal of Roentgenology*, vol. 190, no. 2, pp. 335-343, 2008/02/01, 2008.
- [2] W. A. Kalender, P. Deak, M. Kellermeier *et al.*, "Application- and patient size-dependent optimization of x-ray spectra for CT," *Medical Physics*, vol. 36, no. 3, pp. 993-1007, 2009.
- [3] L. Yu, H. Li, J. G. Fletcher *et al.*, "Automatic selection of tube potential for radiation dose reduction in CT: A general strategy," *Medical Physics*, vol. 37, no. 1, pp. 234-243, 2010.
- [4] Y. Zou, and M. D. Silver, "Analysis of fast kV-switching in dual energy CT using a pre-reconstruction decomposition technique." *Proc. SPIE 6913, Medical Imaging 2008: Physics of Medical Imaging*.
- [5] L. A. Lehmann, R. E. Alvarez, A. Macovski *et al.*, "Generalized image combinations in dual KVP digital radiography," *Medical Physics*, vol. 8, no. 5, pp. 659-667, 1981.

Motion-compensated cardiac CT with extended projection data range

J. Cammin*, Q. Tang, and K. Taguchi

Abstract—We investigate using a larger projection data range for cardiac CT compared to the conventional halfscan and combine it with motion estimation and motion-compensated reconstruction. Radiation dose concerns can be addressed by proper tube current modulation. The larger data range helps to reduce halfscan artifacts and motion compensation helps to reduce motion artifacts. We studied the potential benefits of this approach for coronary CT angiography (CTA) by measuring the accuracy of the stenosis grade from soft plaque in the right coronary artery. Synthesized patient data were used to provide realistic images while at the same time having access to the true motion vectors and stenosis grade. The motion-estimation combined with motion-compensated reconstruction significantly improved the image quality at rapid cardiac phases. The relative accuracy of the measured stenosis grade at mid-diastole decreased by only 4% when the dose was reduced by 75%, however, the difference was statistically not significant (t -statistics=0). The results indicated that a larger projection data range may be used to improve the accuracy of diagnostic tasks or to reduce the dose while maintaining measurement accuracies.

Index Terms—cardiac CT, motion estimation, motion compensation, atherosclerosis, soft plaque, CTA

I. INTRODUCTION

Cardiac CT imaging provides high contrast, high quality, non-invasive imaging of the heart and coronary tree to help with the detection of heart diseases. However, despite continuing technological improvements, there are limitations in spatial and temporal resolution resulting in image artifacts. Further artifacts stem from the halfscan reconstruction algorithm used in all commercial scanners and lead to fluctuating pixel values for the same tissue type depending on the projection angle. These limitations reduce the accuracy and precision of diagnostic tasks. The relatively high dose of cardiac CT exams is also a concern.

We propose to address some of these problems by using a wider projection data range for reconstruction with appropriate tube current modulation. Since a larger data range is more

sensitive to motion we estimate the motion and use the motion information during reconstruction.

The proposed method was evaluated for coronary CT angiography (CTA). CTA is an established, non-invasive method to detect coronary stenosis from soft or calcified plaques [1], [2]. It has a large negative predictive value but currently suffers from a relatively large fraction of false positives [3]. Therefore, improving the accuracy of the stenosis measurement by reducing motion and halfscan artifacts has direct clinical relevance.

Furthermore, we used synthesized patient data with a manually implanted stenosis and known motion for evaluation. This approach combines the advantages of using clinically realistic data but also knowing the true values of the stenosis grade and motion.

A. Halfscan reconstruction

The current halfscan reconstruction algorithm uses a data range w_R corresponding to 0.5 gantry rotations [4], [5] (Fig. 1b). The range has to be small because motion during the reconstruction window is not compensated for. Data acquired outside this range is neglected but contributes to the radiation dose. Despite the minimum data range used for reconstruction, motion artifacts can be severe for rapid cardiac phases. Therefore, images are typically reconstructed only for a quiescent phase (usually at mid-diastole).

The halfscan reconstruction also leads to streak artifacts that rotate with the location of the center of the reconstruction w_R [6]. For CTA, however, it is expected that motion artifacts are the dominating limitation.

B. Increased projection data range with tube current modulation

Halfscan artifacts can be reduced by using a larger projection data range w_R . In order to limit the total radiation dose, the tube current will be set to a fraction c_1 (compared to the tube current for conventional protocols) for the range w_A around the phase of interest and to a smaller fraction c_2 outside of w_A (see Fig. 1b).

Using a larger data range, however, requires compensating for the cardiac motion to avoid or reduce motion artifacts. We have already developed an image-based motion estimation algorithm for CT and demonstrated that motion artifacts in cardiac CT can be reduced when the algorithm is combined with motion-compensated reconstruction [7].

This work was supported in part by NIH grants R44 EB008612, R01 HL087918 and AHA grant BGIA 0865315E.

J.C. and K.T. are with the Russell H. Morgan Department of Radiology and Radiological Science, The Johns Hopkins School of Medicine, Baltimore, MD 21287, USA (phone: 410-502-3773; fax: 410-614-1060; e-mail: jcammin1@jhmi.edu).

Q.T. was with the Russell H. Morgan Department of Radiology and Radiological Science, The Johns Hopkins School of Medicine, Baltimore MD 21287 and is now with Toshiba America Research Inc., Vernon Hills, IL 60061, USA.

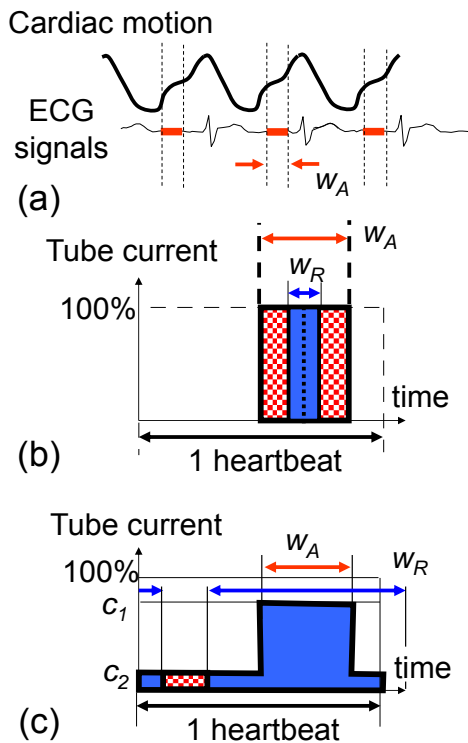


Fig. 1: The current and the proposed tube current modulation for ECG-gated cardiac CT.

II. MATERIALS AND METHODS

A. Synthesized patient data with coronary soft plaque

In order to have access to the true location and magnitude of the coronary stenosis but to also use realistic data, we implemented a soft plaque into clinically acquired patient data.

A patient was selected from a data base of 68 patients who underwent ECG-gated, contrast-enhanced cardiac CT at the Johns Hopkins Hospital. The selected patient had an average heart rate of (52 ± 3) bpm and no visible plaque. Images were reconstructed using filtered back-projection at 20 cardiac phases.

The soft plaque was implemented manually in the image volume reconstructed at mid-diastole (image f^0 (75%RR)). The soft plaque was located in the right coronary artery (RCA) as shown in Fig. 2.

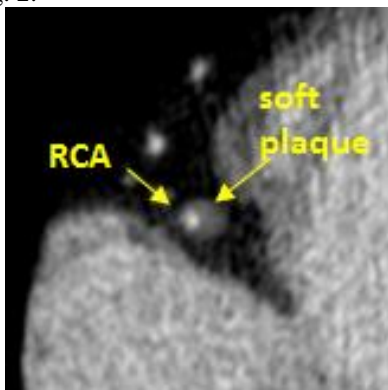


Fig. 2: Soft plaque implemented in the RCA of the original patient image at mid-diastole.

B. Cardiac motion estimation and motion ground truth

The 4-dimensional (4D) cardiac motion was estimated on the original 20 phase images (without synthesized plaque) using our previously developed image-based motion estimation algorithm iME [7]. Briefly, the cardiac motion is estimated by non-rigid, 4D registration of a quiescent reference phase to all other phases. The motion model is based on b-splines and the cost function is the weighted squared difference of pixel values between reference and target volume with regularization in both space and time. The optimization algorithm is a nested conjugate gradient method.

The obtained 4D motion vector field (MVF) was then altered with known disturbances to avoid presenting the same motion to iME again when estimating the motion on the synthesized patient images. The altered MVF, \vec{v}_t , provides the ground truth of the cardiac motion.

C. Projection data and tube current modulation

Projection data was obtained by forward projecting the synthesized patient image f^0 (75%RR). Heart rates of 60 bpm and 90 bpm were simulated and the image was warped to the corresponding cardiac phase for each projection angle using the ground truth MVF \vec{v}_t . Noise was added to the projection data corresponding to the tube current at each projection angle. Seven scenarios of tube current modulations were simulated as shown in Table 1. Each scan was repeated 10 times. Note that scenarios #5 and #6 were designed to yield the same total dose as the conventional half scan with $c_1=100\%$, $c_2=0\%$ (scenario #1).

Table 1: Tube current modulations and scan conditions. $w_A=0.37-0.40$. The tube current was 875 mA for $c_1=100\%$.

#	c_1	c_2	condition	Noise (HU)
1	100%	0%	60 bpm, $w_R=0.50$	16.7
2	100%	20%	60 bpm, $w_R=0.75$	14.0
3	50%	10%	60 bpm, $w_R=0.75$	20.8
4	25%	5%	60 bpm, $w_R=0.75$	30.7
5	70%	16%	60 bpm, $w_R=0.75$	17.6
6	70%	16%	60 bpm, $w_R=1.00$	15.3
7	70%	16%	90 bpm, $w_R=0.75$	16.3

D. Image reconstruction

Images were reconstructed using our iterative approach of motion-estimation and motion-compensated reconstruction (MCR) as reported previously [7] with five iterations of iME-MCR. The MCR algorithm is based on Schäfers motion-tracking cone-beam backprojection [8]. The projection data windows w_R used for reconstruction are listed in Table 1. The size of the reconstructed image volume was $512 \times 512 \times 332$ voxels with size $0.43 \times 0.43 \times 0.50$ mm³.

E. Evaluations

The areal stenosis grade d was calculated in one slice within a region-of-interest (ROI) containing the RCA as $d = 1 - N_{90 \text{ HU}} / N_{0 \text{ HU}}$, where $N_{90 \text{ HU}}$ is the number of pixels

with pixel value > 90 HU and $N_{0 \text{ HU}}$ is the number of pixels with pixel value > 0 HU. The measured stenosis grade was compared to the true stenosis grade which was obtained from the reconstructed image at 75% RR simulated without cardiac motion and without noise.

The accuracy of the MVF was calculated as the 3D Euclidian distance between the estimated MVF and the “ideal” MVF obtained from noise-free images with $c_1=c_2=100\%$ and $w_R=0.75$.

III. RESULTS

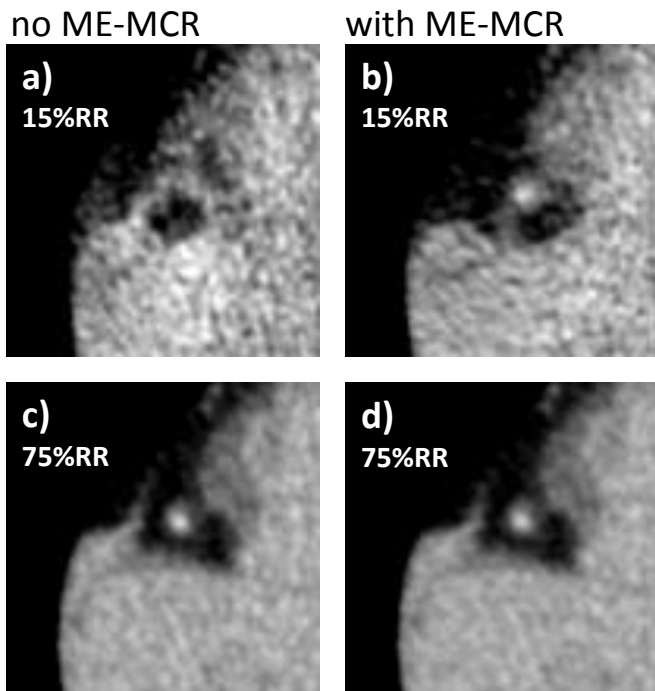


Fig. 3: Reconstructed image around the RCA at a rapid phase (15%RR) and a quiescent phase (75%RR) a)+c) halfscan without motion compensation and b)+d) proposed method with motion compensation.

The results for CTA can be summarized as follows:

1. The motion artifacts at rapid cardiac phases were visibly reduced with iME-MCR (Fig. 3a and b).
2. At mid-diastole (a quiescent phase), the sharpness of the RCA was similar for the halfscan with $w_R = 0.5$ and iME-MCR with $w_R = 1.0$ but the noise was slightly lower (Fig. 3c and d) and last column in Table 1).
3. The accuracies of the estimated motion vector fields near the RCA, averaged over all 20 cardiac phases, are listed in Table 2 for a subset of all generated scenarios. The accuracies were 1 mm for the halfscan method and 0.6 mm or better for the cases with increased data range $w_R=0.75$.
4. Reducing the dose to 50% or 25% did not affect the accuracy of the stenosis grade in a statistically significant way (t -statistics was zero), see Fig. 4. However, in all cases the measured stenosis grade showed large variations over different noise realizations (error bars in the figure).

5. The average accuracy of the stenosis grade at a heart rate of 90 bpm was comparable to the accuracy at a heart rate of 60 bpm, but the standard deviation was slightly increased.

Table 2: Accuracies of the estimated motion vector fields.

#	c_1	c_2	condition	Accuracy (mm)
1	100%	0%	60 bpm, $w_R=0.50$	1.00
2	100%	20%	60 bpm, $w_R=0.75$	0.10
3	50%	10%	60 bpm, $w_R=0.75$	0.59
4	25%	5%	60 bpm, $w_R=0.75$	0.65
5	70%	16%	60 bpm, $w_R=0.75$	0.58

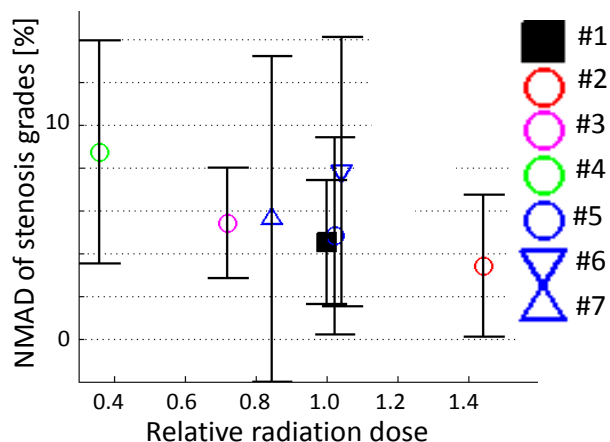


Fig. 4: Accuracy of the stenosis grade. The numbers #1 to #7 correspond to the settings for tube current modulations and reconstruction data range listed in Table 1.

IV. CONCLUSION

We investigated extending the data range used for image reconstruction in cardiac CT. Motion artifacts were limited with iterated motion estimation and motion-compensated reconstruction. The methods were evaluated on synthesized patient data with a stenosis from soft plaque in the RCA.

The accuracy of the estimated motion vector fields in the RCA region was 1 mm or better and showed only weak dependence on the total dose.

The accuracy of the measured stenosis grade was unaffected by different tube current modulation schemes even when the radiation dose was reduced to one fourth (although the noise increased). The accuracy at an increased heart rate of 90 bpm was statistically not different than the accuracy at a heart rate of 60 bpm.

V. REFERENCES

- [1] G. L. Raff, M. J. Gallagher, W. W. O’Neill, and J. A. Goldstein, “Diagnostic accuracy of noninvasive coronary angiography using 64-slice spiral computed tomography,” *J Am Coll Cardiol*, vol. 46, no. 3, pp. 552–7, 2005.

- [2] M. Gilard, J.-C. Cornily, P.-Y. Pennec, C. Joret, G. Le Gal, J. Mansourati, J.-J. Blanc, and J. Bosch, "Accuracy of Multislice Computed Tomography in the Preoperative Assessment of Coronary Disease in Patients With Aortic Valve Stenosis," *J. Am. Coll. Cardiol.*, vol. 47, no. 10, pp. 2020–2024, May 2006.
- [3] J. B. Shreibati, L. C. Baker, and M. A. Hlatky, "Association of coronary CT angiography or stress testing with subsequent utilization and spending among Medicare beneficiaries," *JAMA J. Am. Med. Assoc.*, vol. 306, no. 19, pp. 2128–2136, Nov. 2011.
- [4] D. L. Parker, "Optimal short scan convolution reconstruction for fanbeam CT," *Med Phys*, vol. 9, no. 2, pp. 254–7, 1982.
- [5] M. D. Silver, "A method for including redundant data in computed tomography," *Med Phys*, vol. 27, no. 4, pp. 773–4, 2000.
- [6] A. N. Primak, Y. Dong, O. P. Dzyubak, S. M. Jorgensen, C. H. McCollough, and E. L. Ritman, "A technical solution to avoid partial scan artifacts in cardiac MDCT," *Med. Phys.*, vol. 34, no. 12, pp. 4726–4737, 2007.
- [7] Q. Tang, J. Cammin, S. Srivastava, and K. Taguchi, "A fully four-dimensional, iterative motion estimation and compensation method for cardiac CT," *Med. Phys.*, vol. 39, no. 7, pp. 4291–4305, 2012.
- [8] D. Schafer, J. Borgert, V. Rasche, and M. Grass, "Motion-compensated and gated cone beam filtered back-projection for 3-D rotational X-ray angiography," *Med. Imaging IEEE Trans.*, vol. 25, no. 7, pp. 898–906, 2006.

Texturization: A Generalized Image Quality Comparison Method

Synho Do PhD*, Sarvenaz Pourjabbar MD, Ranish Khawaja MD, Atul Padole MD, Sarabjeet Singh MD, and Mannudeep Kalra MD

Abstract—In this paper, we present the texturization method, which compares the quality of multiple scanners and algorithms without the need of phantom scans. It removes the high-principal components of an image, leaving just the texture information. This information is then converted into a quantitative Texture Spectral Density (TSD) plot.

The TSD plots provide a simple quantitative means for cross-vendor and cross-algorithm comparison by comparing the texture spectral power per unit of frequency bandwidth over multiple image reconstruction algorithms. The results of TSD were found to be very easy and useful to compare multiple image reconstruction algorithms for low dose imaging experiments for multiple vendors and multiple image reconstruction algorithms. As further research is done with this method, there are multiple potential applications for it in the clinical field.

Index Terms—Computed Tomography, Low Dose Imaging, Iterative Reconstruction Technique, Image Quality, Texturization

I. INTRODUCTION

X-ray Computed Tomography (CT) imaging is the fastest, most efficient, and most practical imaging modality in the clinical setup today. Its uniqueness comes from its ability to provide a quantitative value (the attenuation coefficient) of each pixel value, a higher resolution image, and micro-second level temporal resolution. However, in order to minimize potential health risks that can be caused by the radiation exposure CT scans entail, the current trend in the field is to reduce radiation dose As Low As Reasonably Achievable (ALARA) [1] [2].

As a result, various CT scanner vendors have proposed several algorithms to sustain image quality even in low dose radiation (i.e., < 1 mSv), including image-based Iterative Reconstruction (IR) algorithms [3] [4] [5] [6] [7] [8] and raw-data (i.e., Sinogram) based algorithms [9] [10] [11]. This presents various problems for different situations.

They are limited to the use of standard phantoms to measure conventional image quality metrics [12] [13].

- The current method for comparison requires co-registration, which is only possible when using either phantoms or cadavers with repeated scans (no motion is involved).
- Since phantoms are homogenous and comprised of inserts for specific purposes, they result in a different imaging physics (i.e., scattering, diffraction, nonlinear

polychromatic effect etc.) than if actual patients were used, rendering them an unideal comparison platform.

Cross-vendor and cross-algorithm comparison is not easy.

- Each algorithm has multiple parameter settings to control the strength of regularization, and the details of the internal functions are usually either published without specifics or not disclosed to the public at all.
- In larger hospitals where there may be scanners from different vendors, there is no simple way for medical doctors to know the differences between them, making them unable to optimize scanning protocol for individual cases.
- A larger hospital would need to scan their phantoms in each different scanner to compare them, which is both time-consuming and inefficient.

In this paper, we propose a novel approach for the comparison of multiple algorithms from different companies. Using the concept of singular value decomposition (SVD), we remove the common components of all the images, leaving just the texture information, a better platform for comparison.

In Section II, we describe our texturization algorithm in detail. In Section III, we describe data collection and image comparison. Finally, we discuss potential applications in Section IV.

II. METHODS

We hypothesize that an image (I) is composed of contrast (C), edge (E), texture (T), and noise (ϵ):

$$I = C + E + T + \epsilon \quad (1)$$

Each component is unique and important in medical imaging for the diagnosis of disease except for noise. While most IR algorithms produce high quality images, small but noticeable variations in texture exist between them. When we visually compared IR images, clinicians were quick to notice the difference in texture of the images.

A. Co-registered images

To formulate this difference in texture, we first define two co-registered images I_a and I'_a :

$$\begin{aligned} I_a &= C_a + E_a + T_a + \epsilon_a \\ I'_a &= C'_a + E'_a + T'_a + \epsilon'_a \end{aligned} \quad (2)$$

Massachusetts General Hospital and Harvard Medical School, Department of Radiology, Boston, MA, email: sdo@mgh.harvard.edu

Therefore, when we subtract one co-registered image from the other:

$$\begin{aligned} I_a - I'_a &= (C_a + E_a + T_a + \epsilon_a) \\ &\quad - (C'_a + E'_a + T'_a + \epsilon'_a) \\ &= (T_a - T'_a) + (N_a - \epsilon'_a) \end{aligned} \quad (3)$$

where, $C_a \approx C'_a$ and $E_a \approx E'_a$. In this case, we can easily distinguish the differences in texture between the two co-registered images.

B. Two different images

In the same way, when we compare *two different* images I_a and I_b :

$$\begin{aligned} I_a &= C_a + E_a + T_a + \epsilon_a \\ I_b &= C_b + E_b + T_b + \epsilon_b \end{aligned} \quad (4)$$

So by subtracting both contrast (C) and edge (E) from each image by using $f(I) = C + E$, we get:

$$\begin{aligned} I_a - f(I_a) &= (C_a + E_a + T_a + \epsilon_a) - (C_a + E_a) \\ &= T_a + \epsilon_a \\ I_b - f(I_b) &= (C_b + E_b + T_b + \epsilon_b) - (C_b + E_b) \\ &= T_b + \epsilon_b \end{aligned} \quad (5)$$

This allows us to easily compare two different images even though they are not co-registered. We subtracted two high-principal components from each image for detailed comparison, an idea similar to Principal Component Analysis (*PCA*), which is frequently used to distinguish differences for face recognition algorithms in the image processing field. We rank the *PCs* and remove the primary ones from each image, allowing us to observe the differences in texture (and noise) maps. Another novelty of texturization is that we use Total Variation (*TV*) as a simple and direct method to compute the contrast (C) and edge (E) of an image. The *TV* of an image is:

$$TV(I) = \int_0^1 \int_0^1 |\nabla I| dx dy \quad (6)$$

where $\nabla I = (\frac{\partial I}{\partial x}, \frac{\partial I}{\partial y})$ denotes the gradient and $|(x, y)| = \sqrt{(x^2 + y^2)}$ denotes the Euclidean norm, to ensure $TV(I) = C + E$ with a stopping criteria.

Next, we compute the conventional Noise Spectral Density (NSD) [14], which calculates the noise power per unit of bandwidth in 2D polar coordinate Fourier domain. In this paper, we call this Texture Spectral Density (TSD).

III. RESULTS

We followed the IRB protocol of MGH to collect two consecutive patient scans: one normal routine clinical dose scan and one low dose scan (< 1 mSv). We reconstructed images from three different scanners (GE, Siemens, and Philips) and also used a post-processing software (SafeCT). We then implemented texturization on the three groups of images for the three vendors. The image reconstruction algorithms tested were:

- GE: High (normal) dose FBP, Low dose FBP, and Low dose ASIR (30%, 50%, 70%, and 90% blending)
- Siemens: High (normal) dose FBP, Low dose FBP, and Low dose SAFIRE (S1, S2, and S3)
- Philips: High (normal) dose FBP, Low dose FBP, iDose (L2 and L4), and IMR (L1 Body-SP, L1 Body-R, L1 Body-S, L2 Body-R, and L2 Body-S)
- Medic Vision: SafeCT (Chest-4, Lung-1 and Lung-2)

We generated texturization results, shown in Figure 1, 2, and 3.

As can be seen in Figures 1, 2, and 3, by removing the common components of all the images, we were able to see just the texture information, which provides a more quantitative and re-producible metric for image quality comparison. Because the texturization of images doesn't necessarily require co-registration, we were able to use patient data to extract a spectral signature of each image for comparison. Also, as can be seen in Figures 4, 5, 6, 7, 8, and 9, TSD provides a simple way to compare different scanners and algorithms, allowing medical doctors to easily see the differences between them and optimize scanning protocol for different situations. The results of TSD were not only easy to generate, but also easy to compare and make cross-comparisons.

IV. DISCUSSIONS AND CONCLUSION

In this paper, we propose a novel approach for the comparison of multiple algorithms from different companies. Most notably, it doesn't exclusively require the use of phantoms, as texturization of images doesn't require a homogenous region, sharp steps, or specific inserts to provide a standard. Also, rather than depending on scheduled calibrations of scanners to ensure optimal image quality, texturization would allow us to use the patient data to continuously monitor deviations in the parameters.

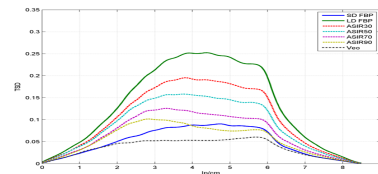


Fig. 4: Texture spectral density comparison plot for GE images (FBP, ASIR and Veo) in Figure 1

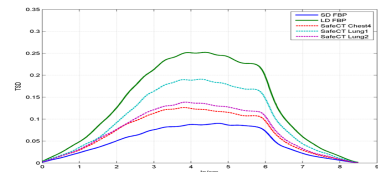


Fig. 5: Texture spectral density comparison plot for GE FBP and SafeCT in Figure 1

REFERENCES

- [1] Thomas L Slovis, "Children, computed tomography radiation dose, and the as low as reasonably achievable (alara) concept," *Pediatrics*, vol. 112, no. 4, pp. 971-972, 2003.

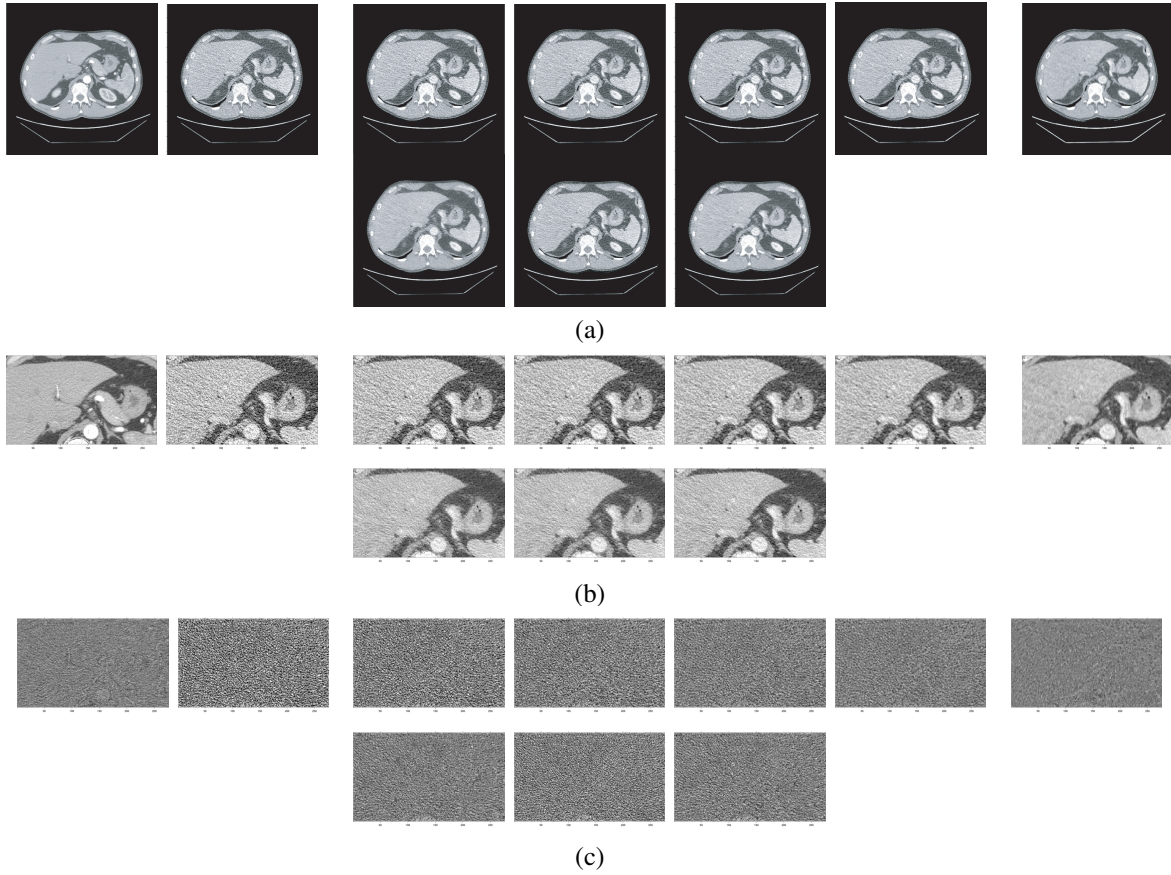


Fig. 1: Texturization method applied on GE Scanner images and SafeCT images: (a) From left to right, FBP (normal dose and low dose), ASIR Images (Parameters: 30%, 50%, 70%, and 90% blending), Veo, and SafeCT images (Parameters: Chest4, Lung1, and Lung2), (b) Zoomed images, (c) Texture maps

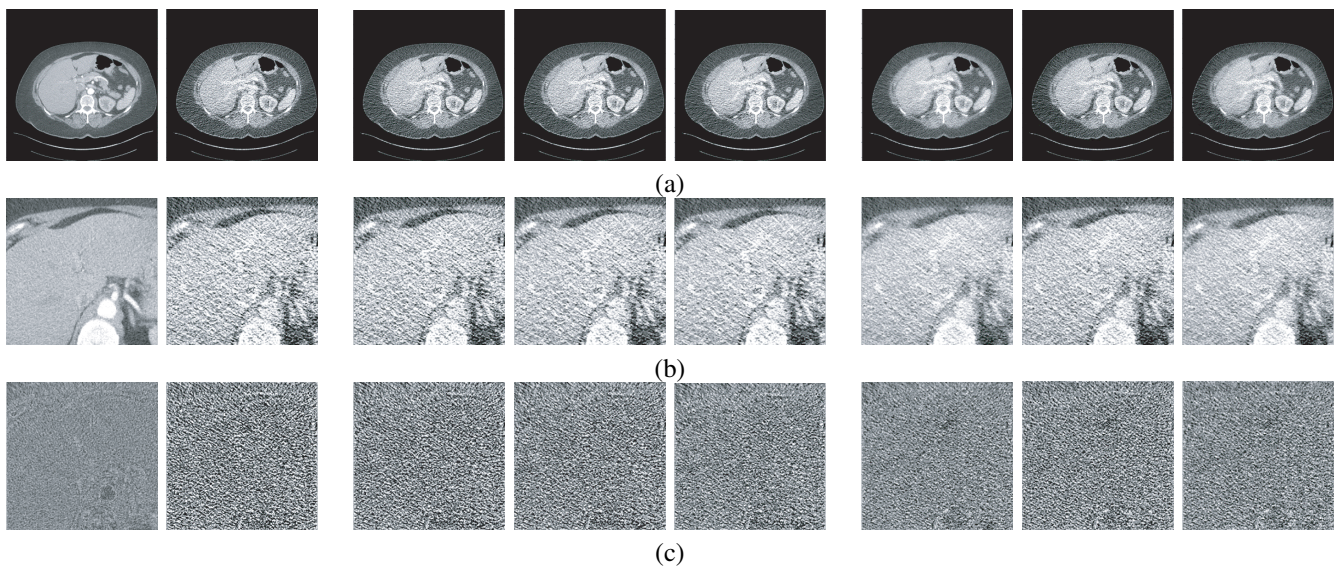


Fig. 2: Texturization method applied on Siemens scanner images: (a) From left to right, FBP(normal dose and low dose), SAFIRE images (Parameters: S1, S2, and S3), and SafeCT images (Parameters: Chest 4, Lung1, and Lung2), (b) Zoomed images, (c) Texture maps

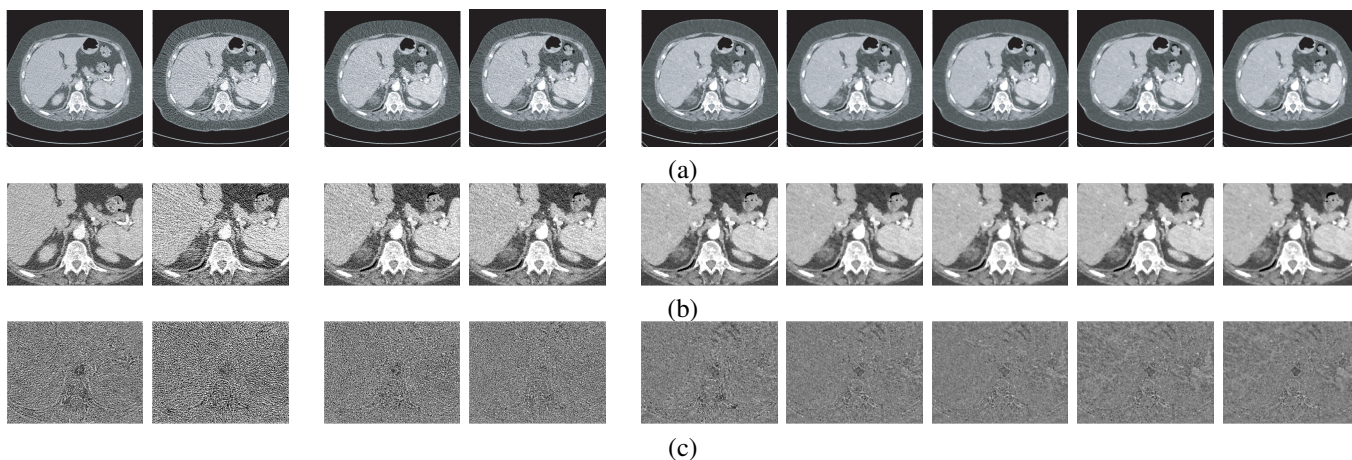


Fig. 3: Texturization method applied on Philips scanner images: (a) From left to right, FBP (normal dose and low dose), iDose (Parameters: L2 and L4), and IMR images (Parameters: L1 Body-SP, L1 Body-R, L1 Body-S, L2 Body-R, and L2 Body-S), (b) Zoomed images, (c) Texture maps

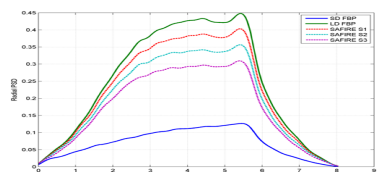


Fig. 6: Texture spectral density comparison plot for Siemens (FBP and SAFIRE) in Figure 2

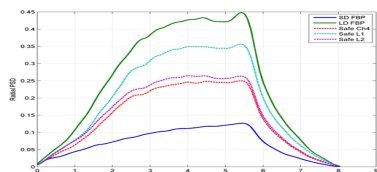


Fig. 7: Texture spectral density comparison plot for Siemens FBP and SafeCT in Figure 2

- [2] Keith J Strauss and Sue C Kaste, "The alara (as low as reasonably achievable) concept in pediatric interventional and fluoroscopic imaging: striving to keep radiation doses as low as possible during fluoroscopy of pediatric patients white paper executive summary," *Pediatric radiology*, vol. 36, pp. 110–112, 2006.
- [3] Daniele Marin, Rendon C Nelson, Sebastian T Schindera, Samuel Richard, Richard S Youngblood, Terry T Yoshizumi, and Ehsan Samei, "Low-tube-voltage, high-tube-current multidetector abdominal ct: Im-

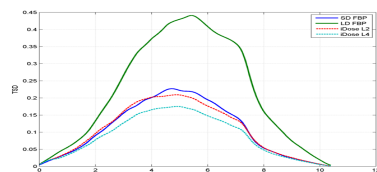


Fig. 8: Texture spectral density comparison plot for Philips FBP and iDose in Figure 3

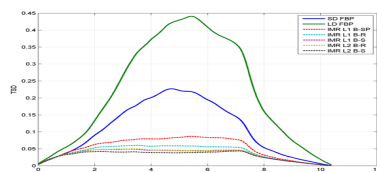


Fig. 9: Texture spectral density comparison plot for Philips FBP and IMR in Figure 3

proved image quality and decreased radiation dose with adaptive statistical iterative reconstruction algorithm initial clinical experience 1," *Radiology*, vol. 254, no. 1, pp. 145–153, 2009.

- [4] Alvin C Silva, Holly J Lawder, Amy Hara, Jennifer Kujak, and William Pavlicek, "Innovations in ct dose reduction strategy: application of the adaptive statistical iterative reconstruction algorithm," *American Journal of Roentgenology*, vol. 194, no. 1, pp. 191–199, 2010.
- [5] Anna Winklehner, Christoph Karlo, Gilbert Puippe, Bernhard Schmidt, Thomas Flohr, Robert Goetti, Thomas Pfammatter, Thomas Frauenfelder, and Hatem Alkadhi, "Raw data-based iterative reconstruction in body cta: evaluation of radiation dose saving potential," *European radiology*, vol. 21, no. 12, pp. 2521–2526, 2011.
- [6] Rui Wang, U Joseph Schoepf, Runze Wu, Ryan P Reddy, Chuanchen Zhang, Wei Yu, Yi Liu, and Zhaoqi Zhang, "Image quality and radiation dose of low dose coronary ct angiography in obese patients: sinogram affirmed iterative reconstruction versus filtered back projection," *European journal of radiology*, vol. 81, no. 11, pp. 3141–3145, 2012.
- [7] Mannudeep K Kalra, Mischa Woisetschlager, Nils Dahlstrom, Sarabjeet Singh, Maria Lindblom, Garry Choy, Petter Quick, Bernhard Schmidt, Martin Sedlmair, Michael A Blake, et al., "Radiation dose reduction with sinogram affirmed iterative reconstruction technique for abdominal computed tomography," *Journal of computer assisted tomography*, vol. 36, no. 3, pp. 339–346, 2012.
- [8] Yoshinori Funama, Katsuyuki Taguchi, Daisuke Utsunomiya, Seitaro Oda, Yumi Yanaga, Yasuyuki Yamashita, and Kazuo Awai, "Combination of a low tube voltage technique with the hybrid iterative reconstruction (idose) algorithm at coronary ct angiography," *Journal of computer assisted tomography*, vol. 35, no. 4, pp. 480, 2011.
- [9] Ken Sauer and Charles Bouman, "A local update strategy for iterative reconstruction from projections," *Signal Processing, IEEE Transactions on*, vol. 41, no. 2, pp. 534–548, 1993.
- [10] Jean-Baptiste Thibault, Ken D Sauer, Charles A Bouman, and Jiang Hsieh, "A three-dimensional statistical approach to improved image quality for multislice helical ct," *Medical physics*, vol. 34, no. 11, pp. 4526–4544, 2007.
- [11] Synho Do, W Clem Karl, Zhuangli Liang, Mannudeep Kalra, Thomas J Brady, and Homer H Pien, "A decomposition-based ct reconstruction formulation for reducing blooming artifacts," *Physics in medicine and biology*, vol. 56, no. 22, pp. 7109, 2011.
- [12] Rebecca Fahrig, Robert Dixon, Thomas Payne, Richard L Morin, Arundhuti Ganguly, and Norbert Strobel, "Dose and image quality for a cone-beam c-arm ct system," *Medical physics*, vol. 33, no. 12, pp. 4541–4550, 2006.
- [13] Frédéric A Miéville, François Gudinchet, Francis Brunelle, François O Bochud, and Francis R Verdun, "Iterative reconstruction methods in two different mdct scanners: Physical metrics and 4-alternative forced-choice detectability experiments—a phantom approach," *Physica medica*, vol. 29, no. 1, pp. 99–110, 2013.
- [14] Marie Foley Kijewski and Philip F Judy, "The noise power spectrum of ct images," *Physics in medicine and biology*, vol. 32, no. 5, pp. 565, 1987.

Motion Compensated Backprojection versus Backproject-then-Warp for Motion Compensated Reconstruction

Bernhard Brendel^a, Rolf Bippus^a, Sven Kabus^a and Michael Grass^a

Abstract—Motion Compensated Backprojection (MCBP) and Backproject-then-Warp (BPW) are two methods described in literature to incorporate motion vector fields (MVF) into motion compensated reconstruction. However, a comparison of the two methods is not available so far. Here, both methods are compared based on simulated data. It is analyzed how many warping-operations of the BPW method are needed to achieve comparable image quality as the MCBP method. This is of interest, since the computational demand for the BPW method increases with the number of warping operations, while the dependency of the computational demand on the number of given MVFs for the MCBP method is negligible.

I. INTRODUCTION

Conventional CT reconstruction is based on the assumption that the scanned object is static during data acquisition. This assumption is a good approximation for most regions of the human body, since scanners provide today a high data acquisition speed such that many scans take only a few seconds or less. For the heart, which is a fast moving organ, this assumption is not valid, even with modern CT hardware. The consequence is a blurring of anatomical structures in the reconstructed images, prohibiting in some cases a reliable diagnosis of small structures. This is especially true for coronary artery vessels, which are small (a few mm in diameter) and move quite fast [1].

To improve image quality in these cases, approaches for motion compensated reconstruction have been developed [2]–[9]. One important group of these approaches comprises two steps: In the first step, the motion of the anatomical structure of interest is estimated. In the second step, the reconstruction is performed using the estimated motion to obtain an improved representation of the anatomical structure of interest in the image [2]–[7].

In most cases the estimation of motion is based on the reconstruction of images without motion compensation for different time points (i.e., for different motion states) [2]–[7]. Image registration is performed between these images to extract the motion, represented by a motion vector field (MVF). This MVF has to be incorporated into the reconstruction in the second step.

Two possible methods to incorporate the MVF into the reconstruction are discussed here. One method is introduced

in [3]. It is a FBP based method, which incorporates the MVF into the backprojection step of the FBP. Consequently, this method is called motion compensated backprojection (MCBP) in the following. The second method is introduced in [6], [7]. It utilizes the linearity of the FBP to incorporate the MVF. Different portions of the projection data are reconstructed separately, resulting in a set of partial images. A FBP reconstruction from all projections and the summation of the partial images deliver the same image result. The portions are chosen such that they belong to different motion states of the anatomical structure of interest. Each partial image is warped by the corresponding MVF to achieve the same motion state for all images in the set. Finally, the warped partial images are summed up to obtain the motion compensated image. In the following this method will be called backproject-then-warp (BPW).

The aim of the work presented here is to compare MCBP and BPW with respect to their reconstruction performance and resulting image quality for moving objects. The motion estimation step (i.e., the generation of the MVFs) is not discussed. Consequently, simulated data is used and ideal MVFs are generated to exclude influences of the motion estimation step from this comparison.

II. METHOD

In motion compensated reconstruction, a reference motion state has to be chosen. When imaging the heart, the motion state corresponds to a heart phase, which reoccurs in each heart beat. Thus, the reference motion state is determined by choosing a reference heart phase.

Since an ECG is recorded during the data acquisition, each projection is related to a heart phase. For the reconstruction, intervals of projections placed symmetrically around the reference heart phase are used. These intervals are chosen as narrow as possible, but such that the completeness condition for reconstruction is fulfilled. Each interval of projections is acquired within a finite time interval, which directly translates to a corresponding interval of heart phases (see Fig. 1). For motion compensated reconstruction, MVFs have to be available which describe the displacements of the anatomical structure of interest between the heart phases within this interval and the reference heart phase.

Due to practical reasons, MVFs are only determined for a discrete set of heart phases. Thus, for most projections

^a Philips Technologie GmbH, Innovative Technologies, Research Laboratories, Hamburg, Germany

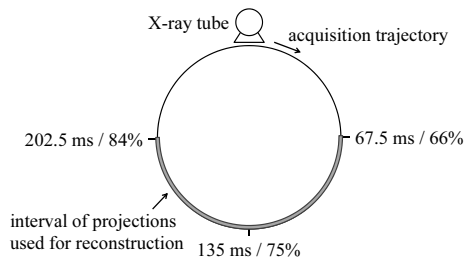


Fig. 1. Visualization of the projection interval selected for an axial reconstruction. The reference heart phase is chosen to be 75%. To fulfill the completeness condition, the projection interval has to comprise 180° of the rotation. In this example (270 ms rotation time, 80 bpm heart rate) this corresponds to a time interval of 135 ms (67.5 ms to 202.5 ms) / a heart rate interval of 18% (66% to 84%). Thus, MVFs have to be available to describe the motion between the reference phase of 75% and the heart phases within the interval of 66% to 84%.

MVFs have to be interpolated from this given set of MVFs. The way of handling the given MVFs is different for MCBP and BPW as described in the following.

A. MCBP

The first step of the MCBP method is the projection filtering as it is done in FBP. Then, the backprojection of each filtered projection is performed as follows: The MVF for the currently considered projection is interpolated along the temporal axis (e.g., linearly) from the set of given MVFs. Then, the interpolated MVF is applied to the location of each voxel within the image to determine where it would have been in the heart phase of the current projection. After that, the ray of the current projection is determined which runs through this (moved) location. The contribution of this ray is added to the voxel. Since in most cases no ray exactly hits a given location, linear interpolation is involved in the last step. In the general case of multicycle helical acquisition, the moved location has to be considered to correctly determine aperture and pi-partner weighting. A detailed description is given in [2], [3], [10].

B. BPW

For the sake of brevity, BPW is explained here for an axial acquisition trajectory, but an extension to multicycle helical acquisitions is straight forward. As for the MCBP, the first step of the BPW method is the conventional projection filtering. Then, the set of projections is divided into subintervals. Each subinterval corresponds to a narrower interval of heart phases as compared to the complete set of projections (see Fig. 2). For each subinterval a separate “sub-image” is reconstructed, but the weighting in the backprojection is chosen such that the sum of all sub-images is identical to the reconstruction of the complete interval of projections. In the next step, for each subinterval a MVF corresponding to the mean heart phase of this subinterval is interpolated from the given MVFs. The interpolated MVF is then applied to warp the corresponding sub-image. After the warping of all sub-images they are summed up to get the final image. The method is illustrated in Fig. 3. A detailed description is given in [6].

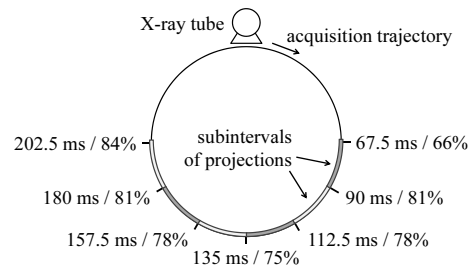


Fig. 2. Visualization of the partitioning of the complete set of projections into subintervals based on the example given in Fig. 1. Each subinterval corresponds here to a time interval of 22.5 ms / heart phase interval of 3%.

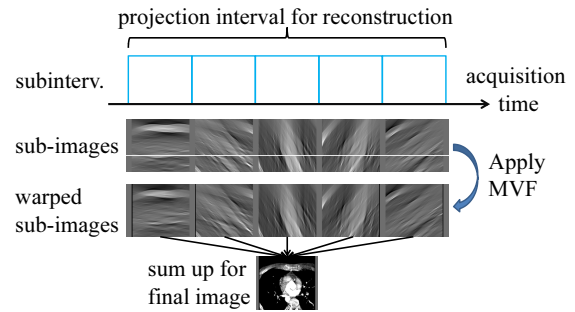


Fig. 3. Illustration of the BPW method.

It turns out that a partitioning of the projections into non-overlapping subintervals (as illustrated in Fig. 2 and Fig. 3) leads to streak artifacts in the final image. To avoid these artifacts, overlapping subintervals can be used [6], [7].

C. MCBP versus BPW

There are some notable differences between MCBP and BPW. One quite important aspect is that MCBP interpolates for each projection an individual MVF, while for BPW the same (interpolated) MVF is used for all projections within one subinterval.

Regarding the computation time, two differences are remarkable. The computational demand of MCBP does not depend on the number of given MVFs. For BPW this is theoretically also true, but to fully use the information of the given MVFs, the number of subintervals should be at least equal to the number of given MVFs. Since the warping of the sub-images generates additional computational demand for BPW, there is an indirect relation between the number of given MVFs and computational demand of BPW.

On the other hand, the backprojection method has to be modified significantly for MCBP and has a substantially higher computational demand as compared to the conventional backprojection method. For BPW, the backprojection method has to be changed only slightly. The computational demand for the backprojection of all subintervals is roughly equal to the computational demand for the backprojection of the complete interval of projections as long as the subintervals do not overlap. If the subintervals overlap, there is an additional computational demand, which linearly increases with the amount of overlap.

D. Simulations

Simulated data is used to compare both methods. The phantom consists of 27 spheres with a diameter of 4 mm and attenuation value of 1000 HU. The spheres are placed on a 3x3x3 grid in space with a distance of 20 mm in each direction. A 200 mm long cylinder with a diameter of 200 mm and an attenuation value of 0 HU is used as background. An axial and a “sagittal” view through the phantom are shown in Fig 4. The central sphere is moving along a line with a sinusoidal velocity profile with a peak-to-peak deflection of 14 mm and a frequency of 80 cycles/minute. The motion line is tilted by 45° with respect to the rotation axis of the simulated CT system (see Fig 4). All other spheres are not moving.

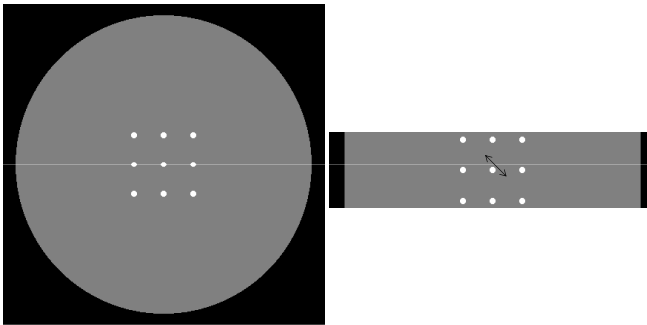


Fig. 4. Axial (left) and sagittal (right) slice through the phantom used for simulations. The black arrow illustrates the motion direction of the central sphere. All other spheres do not move.

The simulated CT system has a source-detector distance of 1040 mm and a isocenter-detector distance of 470 mm. Data is simulated in wedge rebinned geometry. The simulated projections have 648x256 values and a size of 256x80 mm² (projected to the center of rotation). 1200 views are acquired within one rotation. The rotation time is 270 ms. A helical trajectory is simulated with a pitch of 14.4 mm.

Reconstructions are performed for the time point of maximal motion (i.e., the reference motion state is the central position). Ideal MVFs representing exactly the motion of the central sphere are generated based on the knowledge of the phantom. For BPW reconstructions with different numbers of equally wide subintervals are performed. For all of these reconstructions ideal MVFs are generated for the center of each subinterval, thus an interpolation of MVFs is not necessary. For MCBP, reconstructions with different numbers of given (ideal) MVFs are performed. These given MVFs are equally distributed over the relevant interval of heart phases. In the MCBP processing, a linear interpolation of the given MVFs is applied, to get individual MVFs for each projection.

III. RESULTS

In Fig. 5 sagittal slices through reconstructions for a simulation without motion and for a simulation with motion as described in the preceding section are shown. Both reconstructions are done conventionally without motion com-

ensation. As can be seen, severe motion artifacts occur for the motion case. Here and in the following only the central sphere and its surrounding are shown to illustrate artifacts more clearly.

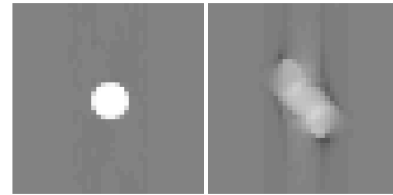


Fig. 5. Sagittal slice through the central sphere of the phantom shown in Fig. 4. Left: Reconstruction of a simulation without motion. Right: Reconstruction of a simulation with motion. Both reconstructions are done without motion compensation. (Window/Level: 2000/0HU)

In Fig. 6 reconstruction results are shown for motion compensated reconstructions using the MCBP approach. As mentioned above MCBP based reconstructions were performed for different numbers of given MVFs. The illustration shows that the quality of the reconstruction does not depend on the number of given MVFs in this case, which is due to the fact that the motion in the interval around the time point of maximal motion is nearly linear for a sinusoidal motion, corresponding well to the linear interpolation of the given MVFs in the MCBP processing.

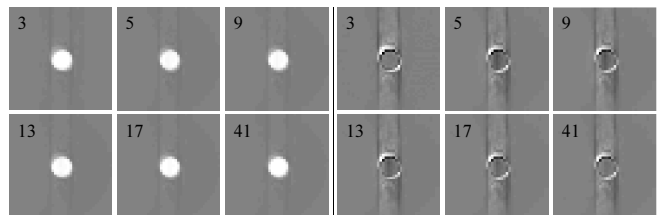


Fig. 6. Sagittal slice through the central sphere of the phantom shown in Fig. 4. Left: 6 images reconstructed with the MCBP approach for different number of given MVFs, as indicated by the numbers in the images (Window/Level: 2000/0HU) Right: Differences of the reconstructions on the left to the reconstruction shown in Fig. 5 on the left (Window: 500HU).

In Fig. 7 reconstruction results are shown for motion compensated reconstructions using the BPW approach with non-overlapping subintervals. As mentioned above BPW based reconstructions were performed for different numbers of subintervals. As can be seen, the quality of the reconstruction depends significantly on the number of subintervals here. Up to a number to 13 subintervals significant improvements in the sharpness of the moving sphere can be achieved. Beyond 13 subintervals only marginal additional improvements can be achieved. This dependence is due to the fact that BPW uses the same MVF for all projections within one subinterval. Thus, if the subintervals are too large there is a significant deviation between the assumed motion of the sphere for a certain projection and the real motion, leading to the remaining blurring in the reconstruction.

Fig. 8 illustrates the same results for the BPW approach with overlapping subintervals. The results with respect to sharpness of the sphere are especially for low numbers

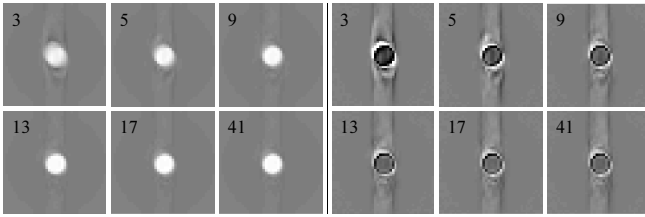


Fig. 7. Same illustrations as in Fig. 6, this time for the BPW method with non-overlapping subintervals. The numbers in the images indicate here how many subintervals were used.

of subintervals inferior as compared to BPW with non-overlapping subintervals. For 13 and more subintervals the results of BPW with and without overlapping are very similar.

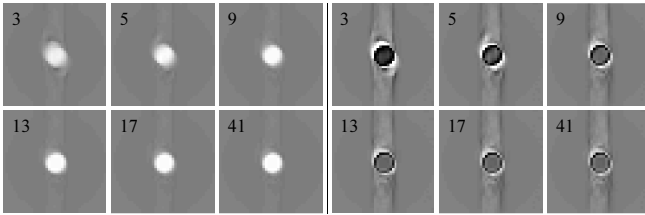


Fig. 8. Same illustrations as in Fig. 7, this time for the BPW method with overlapping subintervals.

Another difference of BPW with and without overlapping is illustrated in Fig. 9. Here, axial difference images for 5 and 13 subintervals / given MVFs are shown for all three approaches. For 5 subintervals, there are significant differences between all three methods. BPW without overlapping shows significant additional streak artifacts as compared to BPW with overlapping. Both BPW approaches show much higher differences as compared to the MCBP approach. For 13 subintervals, these differences are not significant anymore, and the results for both BPW approaches are very similar to the result achieved with the MCBP approach.

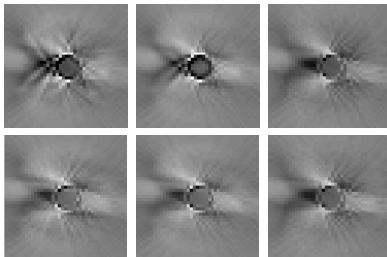


Fig. 9. Axial difference images showing the central sphere of the phantom. Again differences of the motion compensated reconstruction with respect to the reconstruction shown in Fig. 5 on the left are taken. Top: 5 subintervals / given MVFs. Bottom: 13 subintervals / given MVFs. Left: BPW with non-overlapping subinterval. Middle: BPW with overlapping subintervals. Right: MCBP (Window: 500HU).

IV. DISCUSSION

Three methods to integrate MVFs in motion compensated reconstruction were compared in this work based on images.

First of all it should be noted that a prerequisite for all methods for motion compensated reconstruction is that the given MVFs represent the motion of the structure of interest with an adequate precision. Nevertheless, for BPW in many cases it makes sense to choose the number of subintervals higher than the number of given MVFs and to interpolate MVFs for certain subintervals to get results comparable to the MCBP approach. This is illustrated here by the fact that MCBP achieves good results already for 3 given MVFs, while for the BPW approaches about 13 subintervals are necessary to achieve comparable results. This is due to the fact that MCBP uses in the implementation applied here linear interpolation to get MVFs for each projection, while the application of the MVFs in the BPW approaches corresponds to a nearest-neighbor interpolation of the MVFs between the centers of the subintervals, which is an inferior approach for inartificial, continuous motion.

Since roughly comparable results are achievable for MCBP and BPW, a decision which approach is the method of choice depends mainly on implementation effort and computational demand. Here two questions have to be answered, which mainly depend on available software framework and thus cannot be answered generally:

- Is the implementation of a modified backprojection for MCBP more or less effort than the implementation of subinterval-reconstruction and warping for BPW?
- Is the additional computational demand of the modified backprojection in MCBP higher or lower than the additional computational effort of backprojecting overlapping subintervals and warping and in BPW?

It should be noted that for the results shown here, the difference between overlapping and non-overlapping subintervals for BPW becomes marginal once the number of subintervals increases to the point where BPW can compete with MCBP in terms of image quality.

REFERENCES

- [1] M. Vembar, M. J. Garcia, D. J. Heuscher, R. Haberl, D. Matthews, G. E. Boehme, and N. L. Greenberg, *Med Phys*, vol. 30, no. 7, pp. 1683–1693, 2003.
- [2] D. Schaefer, J. Borgert, V. Rasche, and M. Grass, *IEEE J. Med. Imag.*, vol. 25, no. 7, pp. 898–906, 2006.
- [3] U. van Stevendaal, J. von Berg, C. Lorenz, and M. Grass, *Med Phys*, vol. 35, no. 7, pp. 3239–3251, 2008.
- [4] K. Taguchi and H. Kudo, *IEEE J. Med. Imag.*, vol. 27, no. 7, pp. 907–917, 2008.
- [5] A. A. Isola, A. Ziegler, T. Koehler, W. J. Niessen, and M. Grass, *Phys Med Biol*, vol. 53, no. 23, pp. 6777–6797, 2008.
- [6] Roshni Bhagalia, Jed D. Pack, James V. Miller, and Maria Iatrou, *Med Phys*, vol. 39, no. 7, pp. 4245–4254, 2012.
- [7] Jed Pack and Bernhard Claus, *The second international conference on image formation in X-ray computed tomography*, pp. 322–325, 2012.
- [8] Hermann Schomberg, *Nuclear Science Symposium and Medical Imaging Conference (NSS/MIC), 2011 IEEE*, pp. 4077–4079, 2011.
- [9] Christopher Rohkohl, Herbert Bruder, Karl Stierstorfer, and Thomas Flohr, *Med Phys*, vol. 40, no. 3, pp. 031901, 2013.
- [10] Thomas Koehler, Tobias Klinder, Udo van Stevendaal, Cristian Lorenz, and Peter Forthmann, *Tsinghua Science and Technology*, vol. 15, no. 1, pp. 87–95, 2010.

Optimal kVp Selection for Contrast CT Imaging Based on a Projection-domain Method

Xue Rui^{1*}, Yannan Jin¹, Paul F FitzGerald¹, Adam Alessio², Paul Kinahan² and Bruno De Man¹

Abstract— Computed Tomography (CT) has been in clinical use for several decades. The number of CT scans has increased significantly worldwide, which results in increased radiation dose delivered to the general population. Many technologies have been developed to minimize the dose from CT scans, including scanner hardware improvements, task-specific protocol design and advanced reconstruction algorithms. In this study, we focused on selection of X-ray tube voltage and filtration to achieve optimal dose efficiency given required image quality, more specifically the contrast to noise ratio. Our approach differs from previous studies in two aspects. Typically, Monte-Carlo simulation is used to estimate dose in simulations, but this is computationally costly. We instead use a projection-domain dose estimation method. No image reconstruction is required for the projection-domain method, which further simplifies the analysis. This study also includes tantalum, a new contrast agent, in addition to soft tissue (water), bone and iodine contrast. Optimal tube voltages and filtration are identified as a function of phantom size. The simulation analysis is confirmed with a limited phantom study.

Keywords—Computed Tomography, Contrast Imaging, Optimal Spectrum.

I. INTRODUCTION

CT is widely used in various clinical applications, such as cardiac imaging, colonography, angiography and urology [1]–[3]. The number of CT scans performed every year has dramatically increased, resulting in an increase in radiation dose delivered to the population. This dose increase has led to great concern within the medical community. In 2010, the Food and Drug Administration announced the regulation towards the CT manufacturers to avoid unnecessary radiation exposures during scans [4] to lower the radiation risk to patients especially for those exposed to multiple CT scans.

Many technologies have been developed to optimize components of image quality and minimize patient dose, through improved hardware, scanning protocol design and reconstruction algorithms. Dose reduction techniques such as tube-current modulation and low-voltage protocols have been developed [5]. Iterative reconstruction algorithms show a great advantage in providing high quality images with much lower dose [6]–[8]. A computer assisted scan protocol and reconstruction method has been proposed to achieve the best tradeoff between radiation dose and image quality for task- and patient-specific cases [9]. With the combination of the all these advanced techniques, it is expected to see the averaged

effective dose decrease by 2 to 3 fold compared to the current value of about 10 mSv [10].

In this study, we focus on the selection of optimal X-ray tube voltage considering the dose efficiency of different contrast materials. Typically, contrast to noise ratio (CNR) is chosen to represent the required image quality. The dose-normalized CNR (CNRD) therefore can be used to evaluate the dose efficiency given the desired CNR [11]. To accurately calculate the CNR and dose in the analysis usually requires image reconstruction and Monte Carlo dose simulation, which are both time-consuming. A projection-domain dose estimation method has been proposed and compared with Monte Carlo dose simulation [12]. In this paper, we use the projection-domain screening method which uses relatively simple analytical estimates of contrast, noise and dose. Contrasting material such as iodine is often injected into the patient to enhance the vasculature. Recently, tantalum has been evaluated as a contrast agent. Tantalum has several potential performance advantages over iodine as a contrast agent, and is hoped to offer an alternative to avoid known issues associated with iodine [13]–[15]. We used our projection-domain screening method to estimate the optimal X-ray tube voltage for the highest CNRD within soft tissue, and between soft tissue and bone, iodine and tantalum. The simulations included electronic noise and quantum noise. The simulation results were confirmed with measurements on a clinical CT scanner.

II. METHOD: PROJECTION DOMAIN ANALYSIS

A. Analytical Representation for the Noise in the Projection Measurement

We first consider a projection ray passing through the object with a path length of L and attenuation coefficient of μ . Assuming the incoming photon counts is a Poisson random variable I_0 with the mean of N_0 , then the transmitted photon count is a Poisson random variable I_t with mean and variance of $N_t = N_0 e^{-\mu L}$.

For an energy-integrating detector, the variance of the noise in the transmitted projection ray I_t prior to the log operation is

$$\sigma_{me}^2 \approx g^2 E^2 N_t + \sigma_e^2,$$

where g is the system gain and represents the conversion factor from energy to the number of electrons, E is the energy of X-ray photons detected by the detector, and σ_e^2 is the variance of the electronic noise associated with the detector cell.

¹CT Systems and Application Laboratory, GE Global Research Center, Niskayuna, NY

²Department of Radiology, University of Washington, Seattle, WA

*ruix@ge.com

For a polychromatic beam, the noise in the projection can be obtained by viewing the polychromatic spectrum as a summation over finite energy bins,

$$I_t = \sum_k I_k = \sum_k I_{k0} e^{-\mu_k L}.$$

where for energy bin E_k , I_{k0} is the incoming photon count with mean and variance of N_{k0} , I_k is the transmitted photon count with mean and variance of N_k , and μ_k is the attenuation coefficient of the object.

The noise in the pre-log data can therefore be written as

$$\sigma_{photon}^2 = \sum_k g^2 E_k^2 N_k + \sigma_e^2.$$

For a polychromatic beam, the signal detected for the transmitted X-ray photons is a summation across all the energy bins. Therefore, the projection value p after the logarithm operation is

$$p = -\ln \frac{\sum E_k I_k}{\sum E_k I_{k0}}.$$

Using the Taylor expansion, the variance of p can be derived from the variance of the pre-log data based on approximately linearizing the logarithm operation.

$$\sigma_{proj}^2 \approx \left(\frac{\sum_k g^2 E_k^2 N_k + \sigma_e^2}{(\sum_k g E_k N_k)^2} \right).$$

B. Analytical Representation of the Contrast for Different Materials

The contrast used in this analysis is also obtained from the projection domain. It is defined as the difference in attenuation coefficients between the object of interest and background. In the simulation, along the path of the projection ray, a small amount of the contrast material is inserted in place of the background material (typically, water is used as a background material in this simulation). Water and iodine contrast is analyzed as an example.

We used water contrast as a representative contrast for soft-tissue to soft-tissue contrast. By applying a small perturbation of the normal background water density, the water contrast is computed as:

$$C_{water}(E) = (1 + \epsilon)\mu_{water}(E) - \mu_{water}(E),$$

where ϵ is a small constant (we used 0.05).

The iodine contrast is defined as:

$$C_{iodine}(E) = \mu_{iodine}(E) - \mu_{water}(E).$$

Bone and tantalum contrast mechanisms are defined the same way as iodine. For a polychromatic beam, the contrast is defined as the flux-weighted average of the monochromatic contrast,

$$C = \frac{\sum_k C_k N_k}{\sum_k N_k}.$$

C. Dose Estimation

An accurate estimation of dose such as can be achieved with Monte Carlo simulation is always computationally costly. In our method, to simplify the calculation but still provide a reasonable estimate of the dose, we calculate the energy of the X-ray photons absorbed by the subject. In our previous publication, this method was demonstrated to be a reasonable approximation of the dose absorbed in the subject [12].

For a monochromatic beam with energy E , the deposited energy of the projection ray is

$$D_e = E N_0 (1 - e^{-\mu_e L}) = E N_0 - E N_t,$$

where μ_e is the attenuation coefficient of the object.

The dose for polychromatic beam is simply calculated as a summation of the energy for absorbed X-ray photons in all energy bins.

$$D_e = \sum_k D_{ek}.$$

D. Overall evaluation

The figure-of-merit used in the study is dose weighted contrast-to-noise ratio (CNRD):

$$CNRD = \frac{C}{\sigma \sqrt{D}},$$

where C is the contrast, σ represents the noise in the measurement, and D is the dose delivered to the patient.

III. SIMULATION CONDITIONS AND PHANTOM MEASUREMENT

A. Simulation Conditions

We chose a circular water cylinder as our simulation object. For the contrast analysis, the center pixel is replaced by the contrasting material to introduce a small change in the projection value. Three sizes of the water cylinder were used, with diameters of 20 cm, 24 cm and 35 cm chosen to respectively represent pediatric, small adult and large adult abdomen scans.

Four different types of contrast were evaluated in the simulation, including water, bone, iodine and tantalum. We also evaluated the effect of extra filtration of the spectrum on the dose efficiency curve. Since the mA level does not affect the shape of the dose efficiency curve, we only simulated at one mA level.

The spectrum files used in this study are produced by the XSPECT package (v3.5), and then filtered with the nominal intrinsic filtration of a typical X-ray tube. We evaluated spectra with X-ray tube voltages ranging from 60 kVp to 160 kVp, which is a slightly broader range than the typically-used clinical X-ray tube voltages, which range from 80 kVp to 140

kVp. Each spectrum is represented in 0.5 keV increments. In this study, we applied a 0.5mm Cu filter to the X-ray spectrum and compared its performance with the original spectrum.

B. Phantom Measurements

To verify the simulation results, we measured a 24 cm CTDI phantom (fabricated in-house from a commercial 32 cm CTDI phantom, made of PMMA (Plexiglas)) with contrast material inserted at the center using a GE Healthcare Lightspeed VCT scanner. The concentrations of iodine and tantalum contrast were both 20 mg/cc. The contrast agent was installed in a custom-made vial, which was inserted in the modified CTDI phantom. The vial provided a 13 mm diameter cross-section of contrast agent, of which a 10 mm diameter region of interest (ROI) was used. For the background, an annular ROI was used, with a 20 mm inside diameter and a 24 mm diameter outside diameter. For the water contrast we inserted a vial with water and measured the contrast relative to the PMMA. This is not quite the same as the simulated water contrast with only a density perturbation. The contrast was determined as the difference in the average CT number in the contrast agent ROI and the background ROI; the noise was determined as the standard deviation in the background ROI. We measured the water, iodine, and tantalum contrast material at four tube voltages: 80, 100, 120, and 140 kVp; the tube current (mA) was selected to achieve approximately the same dose level, represented by CTDI as measured in that phantom. The scanning parameters are included in Table 1. We did not explore the effect of electronic noise at very low tube current [16].

TABLE I. PHANTOM MEASUREMENT PARAMETERS

Voltage (kVp)	Current (mA)	CTDI (mGy)
80	300	1.536
100	165	1.553
120	105	1.558
140	75	1.561

IV. RESULTS AND DISCUSSION

A. Simulation Results

The simulated dose efficiency curves for water (soft tissue), bone, iodine and tantalum are plotted in Figure 1 for the three different phantom sizes. The CNRD curves are normalized to 1.0 at their maximum values for all cases (i.e. with and without filtration).

For the simulation based on the 20 cm phantom, low kVp produces the highest dose efficiency for bone and iodine imaging. For tantalum, the optimal voltage is around 100 kVp. The CNRD curve for water is rather flat, with a decrease below 80kVp.

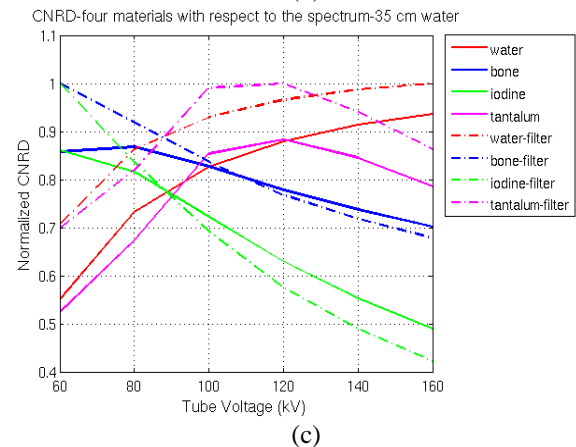
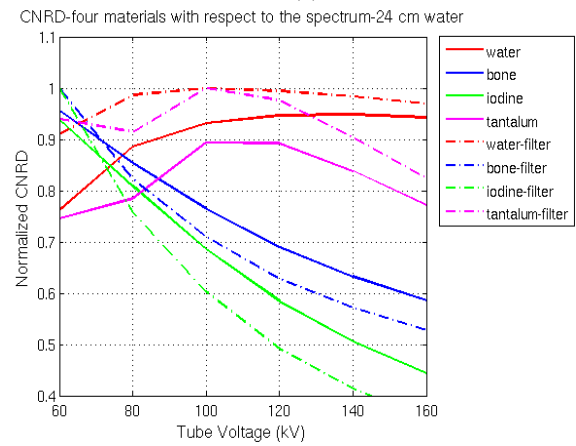
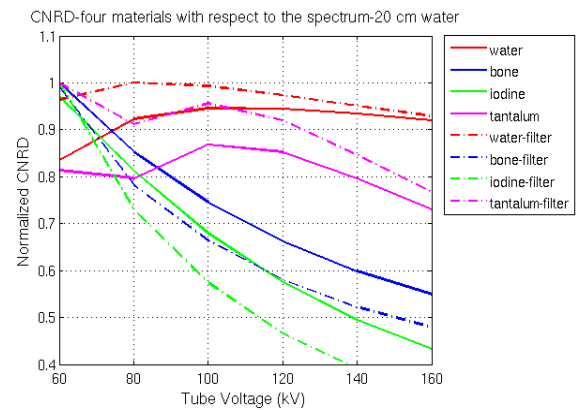


Figure 1. The simulation results for the Dose efficiency (CNRD) curves at different phantom sizes: (a) 20 cm, (b) 24 cm, and (c) 35 cm phantoms respectively. Four contrast mechanisms (water, bone, iodine, and tantalum) show distinctive dose efficiency curves. An optional 0.5 mm Cu filter is used to harden the spectra.

When the phantom size becomes larger, soft tissue imaging is more dose efficient at higher kVp compared with the smaller phantom size. For the 24 cm phantom, the optimal voltage for soft tissue is around 140 kVp. For bone and iodine contrast, lower kVp is still more dose efficient. The optimal value for

tantalum is between 100 to 120 kVp. For the 35 cm phantom, the soft tissue requires higher tube voltage for better dose efficiency. Iodine contrast still requires low kVp. The optimal tube voltage for bone contrast is around 80 kVp. For tantalum, the most dose-efficient voltage increased to 120 kVp. With the 0.5 mm Cu filter added, the dose efficiency at a given tube voltage is improved for soft tissue and tantalum imaging. For the 20 cm phantom, the dose efficiency for bone and iodine decreases with the Cu filter, since the lower energy photons are filtered out from the spectrum.

B. Phantom Measurements

The 24 cm CTDI phantom measurement results from the clinical scanner are shown in Figure 2. At the same dose, iodine has the highest CNR at 80 kVp, water has the highest CNR at 140 kVp, and tantalum has the highest CNR at 100 kVp. These equal dose CNR curves match our simulation screening method (Figure 1) reasonably well: the iodine CNR curve drops by about 50% in the 80-140kVp range, the tantalum CNR curve peaks at 100-120kVp and the water CNR curve monotonically increases. As expected, the latter shows a significantly higher increase in the measurements since they actually reflect PMMA to water contrast.

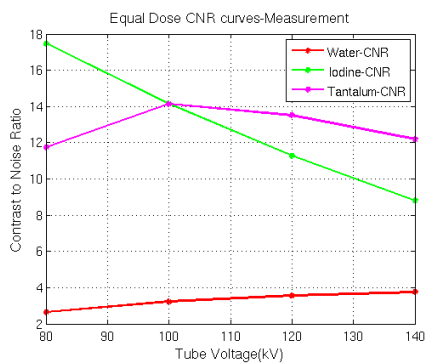


Figure 2. The CNR curves for iodine, tantalum and water contrast for equal dose measurement, using a 24 cm CTDI phantom.

V. CONCLUSION

In this study, we used a projection-domain screening method to evaluate the dose efficiency over a range of X-ray tube voltages for different contrast materials, including soft tissue, bone, iodine and tantalum at different phantom sizes. For bone and iodine contrast, low kVp is always more dose efficient (as has been previously shown), and some filtration will improve dose-efficiency at that low kVp, for larger phantoms only. For soft tissue imaging, with small phantom sizes, the optimal value of the tube voltage is around 100~120 kVp, but the curve is very flat, so there is no clear preference. With increasing phantom size, this optimal tube voltage increases. Filtration can improve dose-efficiency by 5-10%. The most dose efficient tube voltage for tantalum contrast imaging is between 100~120 kVp, depending on the phantom size. This value is closer to that of soft tissue contrast, thus making it easier to develop scanning protocols considering both materials.

To verify our simulation results, CTDI phantom measurements were performed on a GE Lightspeed VCT scanner to determine CNRD for water, iodine and tantalum. The measurements (Figure 2) confirmed that the project-domain analysis (Figure 1) gave a very good prediction of the relative performance of various spectra for all contrast mechanisms and phantom sizes. The projection domain method provides a quick screening method for selection of the spectrum, with much less computational cost compared to full image reconstruction and Monte-Carlo dose simulation. The study did not include very low tube currents where electronic noise would start to dominate, hence the conclusions should not be extrapolated to very low signal scenarios. Similarly, the study did not take into account practical upper limits on tube current: the most dose-efficient spectrum may not always achieve the desired image quality. Finally, this study did not take into account algorithmic noise reduction techniques. To first order, we expect that those will not change our conclusions, although it is conceivable that they might favor low kVp protocols, combining high iodine and bone contrast with good noise suppression.

ACKNOWLEDGMENTS

This work was supported in part by the National Institutes of Health under grant R01 CA160253. The content is solely the responsibility of the authors and does not necessarily represent the official views of the National Institutes of Health. We thank Michael J. Flynn and the Henry Ford Health System for the XSPECT software used to generate the spectra in this study.

REFERENCES

- [1] J. Hsieh, *Computed tomography: principles, design, artifacts, and recent advances*, vol. PM188. SPIE Press, 2003, p. 388.
- [2] D. Fleischmann and F. E. Boas, "Computed tomography--old ideas and new technology," *Eur. Radiol.*, vol. 21, no. 3, Mar. 2011.
- [3] M. Prokop, M. Galanski, A. J. van der Molen, and C. M. Schaefer-Prokop, *Spiral and Multislice Computed Tomography of the Body*. 2003.
- [4] FDA, "Initiative to Reduce Unnecessary Radiation Exposure from Medical Imaging." Center for Devices and Radiological Health.
- [5] E. Dougeni, K. Faulkner, and G. Panayiotakis, "A review of patient dose and optimisation methods in adult and paediatric CT scanning," *Eur. J. Radiol.*, vol. 81, no. 4, pp. e665-e683, 2012.
- [6] J.-B. Thibault, K. D. Sauer, C. A. Bouman, and J. Hsieh, "A three-dimensional statistical approach to improved image quality for multislice helical CT," *Med. Phys.*, vol. 34, no. 11, pp. 4526-4544, 2007.
- [7] J. Nuyts, B. De Man, J. A. Fessler, W. Zbijewski, and F. J. Beekman, "Modelling the physics in the iterative reconstruction for transmission computed tomography," *Phys. Med. Biol.*, vol. 58, no. 12, pp. R63-96, Jun. 2013.
- [8] B. De Man and J. A. Fessler, "Statistical iterative reconstruction for X-ray computed tomography," in *Biomedical Mathematics*, G. Wang, Y. Censor, and J. Ming, Eds. Springer, 2009.
- [9] J. Sperl, D. Beque, B. Claus, B. De Man, B. Sengiz, and M. Brokate, "Computer-assisted scan protocol and reconstruction (CASPAR)-reduction of image noise and patient dose," *IEEE Trans. Med. Imaging*, vol. 29, no. 3, pp. 724-32, Mar. 2010.
- [10] T. Lee and R. K. Chhem, "Impact of new technologies on dose reduction in CT," *Eur. J. Radiol.*, vol. 76, no. 1, pp. 28-35, 2010.

- [11] W. A. Kalender, P. Deak, M. Kellermeier, M. van Straten, and S. V. Vollmar, "Application- and patient size-dependent optimization of x-ray spectra for CT," *Med. Phys.*, vol. 36, no. 3, p. 993, 2009.
- [12] X. Tian, Z. Yin, B. De Man, and E. Samei, "Projection-based dose metric: accuracy testing and applications for CT design," pp. 866829–866829–9, Mar. 2013.
- [13] G. Gamsu, "Tantalum , A New Contrast Agent for Tracheobronchography New Concepts in the Management of Mycosis Fungoides," *West. J. Med.*, vol. 120, no. 2, p. 150, 1974.
- [14] P. J. Bonitatibus, A. S. Torres, B. Kandapallil, B. D. Lee, G. D. Goddard, R. E. Colborn, and M. E. Marino, "Preclinical assessment of a zwitterionic tantalum oxide nanoparticle X-ray contrast agent," *ACS Nano*, vol. 6, no. 8, pp. 6650–8, Aug. 2012.
- [15] T. As, B. P. J. Jr, C. Re, G. Gd, F. Pf, L. Bd, and M. Me, "Biological performance of a size-fractionated core-shell tantalum oxide nanoparticle x -ray contrast agent," *Invest Radiol.*, vol. 47, no. 10, pp. 578–87, 2012.
- [16] T. Xia, A. M. Alessio, B. De Man, R. Manjeshwar, E. Asma, and P. E. Kinahan, "Ultra-low dose CT attenuation correction for PET/CT.," *Phys. Med. Biol.*, vol. 57, no. 2, pp. 309–28, Jan. 2012.

A Cone-beam Reconstruction Algorithm for Dose-minimized Short Scan and Super Short Scan

Yan Xia, Frank Dennerlein, Sebastian Bauer, Martin Berger, Joachim Hornegger, and Andreas Maier

Abstract—Recently, we proposed an approach that deploys dynamic collimation to shield unnecessary redundant data in circular cone-beam data acquisition, enabling a dose-minimized short scan and super short scan. In this paper, we suggest a new reconstruction algorithm that produces images from these acquisitions that are superior to those restored by traditional short scan FDK-type algorithms. The method involves two stages: First, an initial volume was reconstructed by using a truncation correction method. However, this reconstruction suffers from the streaking artifacts in slices away from the mid-plane due to implicit sharp binary weighting to the cone-beam data. Then, we forward project this initial volume to fill the original projection areas that were shielded by collimation, so that a second reconstruction with a smooth Parker-weighting scheme can be applied to reduce the streaking effects. The evaluation is performed on clinical data with the simulated dose-minimized acquisition scans. The results demonstrate that the proposed algorithm achieves image quality that is comparable to non-collimated FDK short scan reconstruction, with minimized dose to the patient.

I. INTRODUCTION

Today, clinicians typically rely on 3D C-arm CT imaging for interventional procedures in neuroradiology since 3D images offer more detailed anatomical information and higher low-contrast resolution than 2D angiography. 3D scans, however, cause a considerable amount of effective dose for a low-contrast scan of the patient's head [1]. Under such circumstances, it is the practical significance to reduce the radiation dose to the patient without compromising image quality.

There are many practical C-arm CT reconstruction algorithms that employ a weighting scheme (e.g., Parker weights [2]) to approximately compensate for the fact that during a partial circle scan some data are measured once, while other measurements are observed twice. In [3], we investigated the possibility to block redundant rays during the short scan acquisition by successively moving the collimator into the ray path at the beginning or end of the scan. We calculated that using this method the dose reduction for a C-arm CT with a fan angle of 20° is 10%, while for a diagnostic CT with a fan angle of 50° the reduction reaches 23%. Using dynamic collimation to shield redundant data is equivalent to applying a sharp binary weight. Direct use of this weight

Y. Xia, M. Berger, J. Hornegger and A. Maier are with the Pattern Recognition Lab, Friedrich-Alexander-University Erlangen-Nuremberg, 91058 Erlangen, Germany. Y. Xia and J. Hornegger are also with the Erlangen Graduate School in Advanced Optical Technologies (SAOT), Friedrich-Alexander-University Erlangen-Nuremberg, 91052 Erlangen, Germany. F. Dennerlein and S. Bauer are with Siemens AG, Healthcare Sector, Germany.

Disclaimer: The concepts and information presented in this paper are based on research and are not commercially available.

leads to large numerical errors due to its discontinuities, which was already demonstrated in [4]. To compensate these artifacts, we apply a robust truncation correction algorithm - Approximated Truncation Robust Algorithm for Computed Tomography (ATRACT) [5]. As shown in [3], ATRACT reconstructions from binary-weighted minimal complete data yields satisfying reconstruction results in mid-plane. But for slices away from the mid-plane, unacceptable streaking artifacts appear in the constructions due to the missing information in the cone-beam geometry.

In this paper, we present an approach that provides improved image quality even if only the binary-weighted minimal complete data is acquired. The basic idea of the algorithm is to forward project an initial reconstruction (with streaking artifacts for slices away from mid-plane) to fill the shielded areas in the original projection data, so that a second reconstruction with a smooth Parker-weighting scheme can be applied to reduce the streaking effects. Related work which deals with reducing streaking-like cone-beam artifacts proposed to blend the artifact-free parts of two initial volumes [6]. However, this blending is performed in frequency domain and the two initial volumes should fulfill some requirements. There also have been attempts involving an additional line, arc or helical scan [7], [8] to reduce streaking artifacts in cone-beam CT. But such an additional scan may complicate data acquisition and increase both the scan time and radiation dose.

II. MATERIALS AND METHODS

A. Dose-Minimized Data Acquisition

The proposed algorithm deals with the reconstruction problem in recently suggested dose-minimized acquisition scans. Below, we briefly describe these scans.

1) *Dose Saving in Short Scan* : Let us first consider data redundancy in a short scan. As shown in Fig. 1b, the data in the triangle area ABC are redundant to the data in $A'B'C'$, which means only one triangle area must be acquired to reconstruct the object. In [3] we investigated the possibility to block redundant rays during short scan acquisition by successively moving the collimator into the ray path at the beginning or end of the scan. The angular interval of short scan is $\Lambda_s = [0, \pi + 2\delta]$, where $\delta = \arcsin(R/D)$. The resulting dose reduction γ_s can be theoretically estimated as the ratio between the short scan area and the collimated redundant area:

$$\gamma_s = \frac{\frac{1}{2}2\delta \cdot 4\delta}{2\delta(\pi + 2\delta)} = \frac{2 \arcsin(R/D)}{\pi + 2 \arcsin(R/D)}. \quad (1)$$

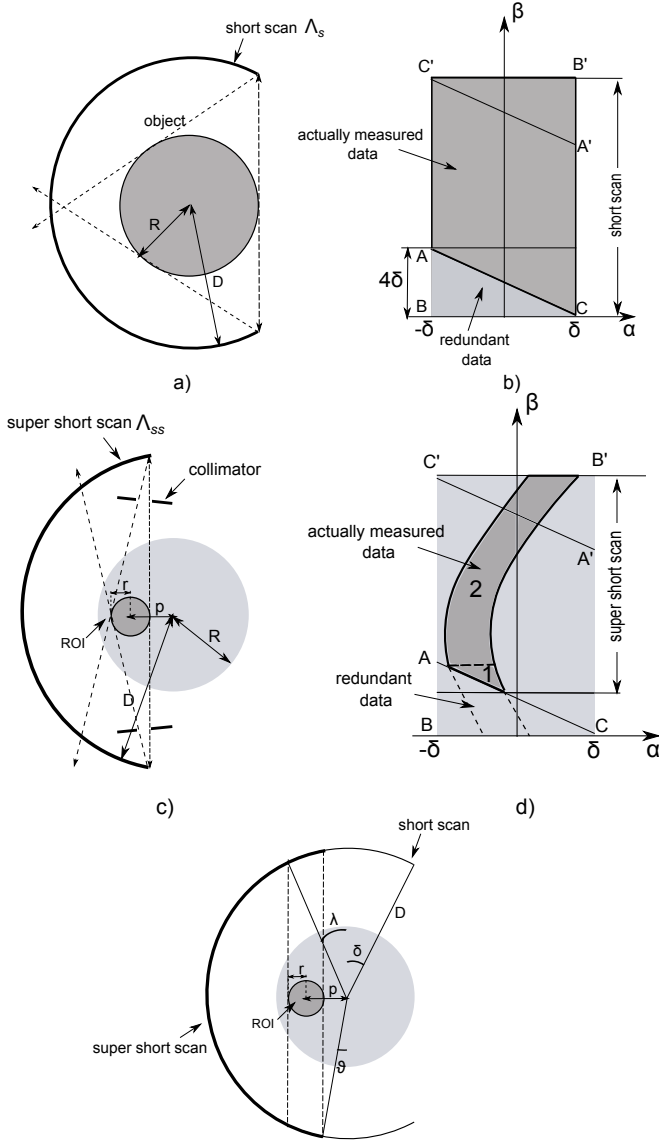


Figure 1. Illustration of the short scan and super short scan acquisition and the corresponding sinograms. a) and b): short scan with an angular interval $\Lambda_s = [0, \pi + 2\delta]$. c) and d): super short scan with an angular interval $\Lambda_{ss} = [0, \pi - 2\vartheta]$. e): potentially reduced angular range in a super short scan ($2\delta + 2\vartheta$) as well as the angular range to acquire the area 1 ($2\lambda - 2\vartheta$).

2) *Dose Saving in Super Short Scan* : A short scan acquisition is used when the entire object is to be reconstructed. However, the angular interval can be further reduced when only an ROI is required to be irradiated and reconstructed. Here we consider the off-center ROI shown in Fig. 1c. The centered ROI is just a special case when $p = 0$. When using collimation to get the truncated projections to reconstruct the specific ROI, we will only obtain the curved band in the sinogram (see Fig. 1d). However, the dashed curve band lies in the redundant region. Thus, the short scan angular range can be even further reduced and the acquisition can start at the point where the line AC intersects the ROI sinogram boundary since the scan segment below the intersect will be measured again at the area $A'B'C'$. We can apply an asymmetric collimation with changeable distance to acquire the area 1, followed by

using an asymmetric collimation with fixed distance (shown in Fig. 1d) to acquire the area 2.

Figure 1e shows that the angular interval for super short scan is $\Lambda_{ss} = [0, \pi - 2\vartheta]$, where ϑ can be determined by the radius r and location p of the ROI:

$$\vartheta = \arcsin\left(\frac{p-r}{D}\right). \quad (2)$$

With increasing distance from the iso-center and decreasing ROI radius, the angular interval decreases. Note that when the ROI is located at the iso-center ($p = 0$) and the radius of the ROI is equal to the object support ($r = R$), the interval above extends to the short scan range Λ_s . The dose reduction can be approximated by computing the ratio between the short scan range $\pi + 2\delta$ and the difference of short scan and super short scan range $2(\delta + \vartheta)$ plus half of the angular range to acquire the area 1 ($\lambda - \vartheta$) (see Fig. 1e):

$$\gamma_{ss} = \frac{2 \arcsin\left(\frac{R}{D}\right) + \arcsin\left(\frac{p-r}{D}\right) + \arcsin\left(\frac{p+r}{D}\right)}{\pi + 2 \arcsin\left(\frac{R}{D}\right)}. \quad (3)$$

This gives the relationship between the radius r , location p of the ROI and potential dose reduction in a super short scan. For instance, for an off-centered ROI with radius $r = 20$ mm and location $p = 40$ mm acquired from a C-arm CT system with standard configuration $D = 750$ mm, $\arcsin(R/D) = 10^\circ$, the potential dose reduction is $\gamma_{ss} = 13\%$.

B. New Streaking Reduction Algorithm

We present an approach that provides superior results with the minimal complete data acquired from a short scan or super short scan. The approach involves three steps. First, an initial volume is reconstructed using the ATRACT algorithm. However, this reconstruction suffers from streaking-like cone-beam artifacts in the slices away from mid-plane. Thus, we forward project the initially reconstructed volume and use the forward projections to fill the shielded areas in the original measured data. By doing so, we obtain artificial short scan data but at a lower radiation dose compared to an ordinary short scan. The last step in this pipeline is the FDK or ATRACT reconstruction with the standard Parker weights that will lead to the final reconstructed image with improved image quality, exhibiting substantially less streaking artifacts compared to the initially reconstructed volume. The flowchart of the algorithm is depicted in Fig. 2. Further details are elaborated in the following sections.

1) *Initial Reconstruction* : Blocking the redundant rays or acquiring ROI projections will result in truncated projection data, which is not compatible with conventional reconstruction algorithms. Here we apply a truncation robust algorithm (ATRACT) to deal with the truncation problem. The idea behind ATRACT is to adopt the FDK algorithm by decomposing the 1D ramp filter into two successive filter steps so that the filtering procedure is less sensitive to data truncation [5]. In this work we use a 1D version of ATRACT, in which the filtering step was adapted to a 1D Laplace filtering of the pre-weighted data and a 1D convolution-based filtering with a kernel $\ln|u|$ to get the filtered projection data [9]. It should

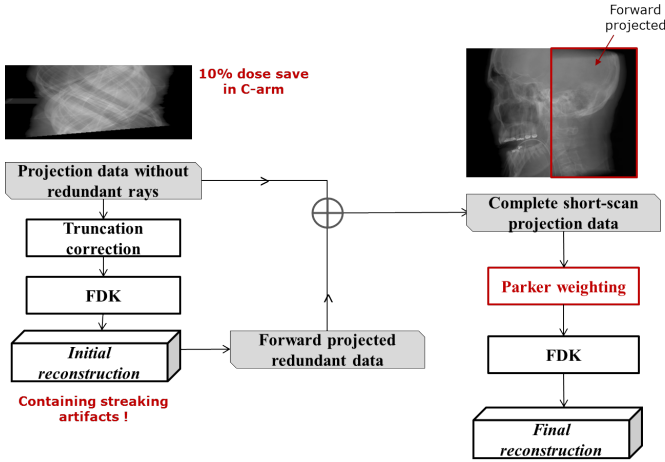


Figure 2. Flowchart of the proposed cone-beam reconstruction algorithm. First, an initial volume is reconstructed using the ATRACT algorithm. Then, we forward project the initially reconstructed volume and use the forward projections to fill the shielded areas in the original measured data. The last step involves the standard FDK algorithm or the ATRACT method, depending on complete projections or truncated ROI projections are processed.

be pointed out that the ATRACT algorithm yields accurate reconstructions in terms of truncation correction. However, as discussed before, streaking artifacts appear in off-center planes degrading image quality. That is why we propose a second reconstruction here, to compensate the streaking artifacts.

2) *Forward projection*: To perform the second reconstruction with improved image quality, it is necessary to complete the measured projections (truncated) with the information from the initial volume, so that a smooth weighting function (e.g. Parker weights) rather than the binary weighting, can be applied in the reconstruction to reduce the streaking effects. This requires the initial volume be forward projected in the original projection domain with the same detector size. In practice, the forward projection is only necessary to be performed on the redundant areas where original projections are shielded by collimation. These projections correspond to the triangle area ABC in Fig. 1b for a short scan and the dashed band in Fig. 1d for a super short scan.

3) *Adaptive combination*: The original dynamically-collimated data and the forward projected data are combined in the projection domain. Here an adjustment is needed to handle the incorrect forward projection values. To do so, an additional small overlapping region on the side of the original projection is also forward projected. Values are compared to the corresponding column of measured data in row-wise and a constant bias is added to the corresponding row in the forward projected data. Finally, the measured projections are filled by the transformed forward-projected data and the final image is reconstructed by the standard FDK algorithm or the ATRACT method, depending on the complete projections or truncated projections are processed.

C. Experimental Setup

To validate and evaluate the new method, two configurations were considered on a clinical human head dataset (data courtesy of St. Luke’s Episcopal Hospital, Houston, TX, USA).

The dataset was acquired on a C-arm CT system with 496 projections (1240×960 px) at the resolution of 0.308 mm/px.

In the first configuration, the short scan dataset was virtually cropped to mimic the removal of redundant area. The removed data correspond to the triangle area ABC in Fig. 1b. In configuration 2, we assume an off-centered ROI is reconstructed and the original short scan dataset was virtually collimated to the super short scan area that corresponds to area 1 and 2 in Fig. 1d. Note that the angular range in configuration 2 is 179° , which is much less than the standard short scan range of 200° .

The virtually collimated projections of both configurations were reconstructed onto a volume of $512 \times 512 \times 350$ voxels with an isotropic size of 0.45 mm³. The standard FDK reconstruction of the original short scan was used as the reference in each case. The data from configuration 1 and 2 were reconstructed by the proposed algorithm.

To quantify the improved accuracy obtained by the proposed algorithm, two quantitative metrics were used: the Root Mean Square Error (RMSE) and the Structural Similarity Index Measurement (SSIM) [10]. The SSIM measures the similarity of two volumes f_x and f_{Ref} and is calculated as follows:

$$\text{SSIM}(f_x, f_{\text{Ref}}) = \frac{(2\mu_x\mu_{\text{Ref}} + c_1)(2\sigma_{x,\text{Ref}} + c_2)}{(\mu_x^2 + \mu_{\text{Ref}}^2 + c_1)(\sigma_x^2 + \sigma_{\text{Ref}}^2 + c_2)}, \quad (4)$$

where μ_x and μ_{Ref} indicate the mean values of f_x and f_{Ref} , σ_x^2 and σ_{Ref}^2 indicate the variances of f_x and f_{Ref} and $\sigma_{x,\text{Ref}}$ indicates their covariance. c_1 and c_2 are two constants to stabilize the results in case the denominator is too small (in our case, $c_1 = c_2 = 0$).

III. RESULTS

The reconstruction results of the clinical dataset with configuration 1 are presented in Fig. 3. As expected, slight streaking artifacts are observed in the initial volume where ATRACT algorithm is applied. These streaking artifacts are oriented along a fixed direction associating with the truncated edge of the sinogram. In contrast, we found that the new algorithm yields almost identical image quality to the short scan FDK. The quantitative analysis in Table I also confirms the improvement of the proposed method: an RMSE of 28.3 HU is achieved compared to a larger error in the initial reconstruction (RMSE of 95.2 HU). It seems that the streaking artifacts do less impact on the structural similarity: both reconstructions yield similar SSIM results. Figure 4 shows two off-mid planes as well as a mid-plane of the ROI reconstructions with a super short scan. We can see that ATRACT (second column) is able to obtain high image quality in terms of truncation correction. No truncated-related bright ring or cupping artifacts are found within the FOV. Quantitative analysis with a SSIM of 0.93 also demonstrates this visual inspection. Note that reconstructing severely truncated data is an under-determined problem and the reconstructions will be biased by a constant. This explains the larger values in RMSE. Again, the streaking effect appears in slices that are away from the mid-plane. In contrast, no significant difference within the FOV is found between the proposed method and the reference, even in the off mid-planes.

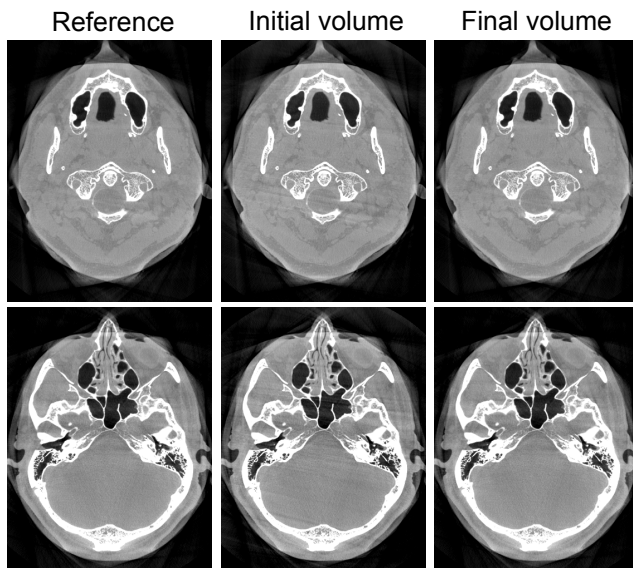


Figure 3. Reconstruction results of the binary-weighted short scan data by the proposed algorithm, in the gray scale window [-1000 HU, 1000HU]. Top row: $z = 21.6$ mm; bottom row: $z = -21.6$ mm.

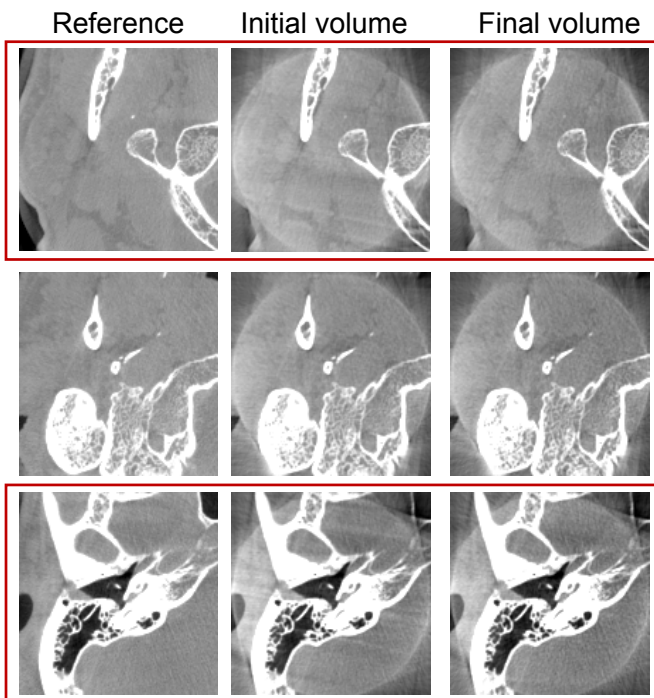


Figure 4. ROI reconstruction results of the binary-weighted super short scan data by the proposed algorithm, in the gray scale window [-1000 HU, 1000HU]. Top row: $z = 26$ mm; middle row: $z = 0$ mm; bottom row: $z = -26$ mm.

IV. DISCUSSION

The experimental results show that our newly proposed algorithm yields improved image quality for the dose-minimized short scan and super short scan data. The amount of dose reduction in short scan depends on the fan-beam angle, with up to 10% for C-arm CT and up to 23% for diagnostic CT. In super short scan, dose saving additionally depends on the position and radius of the ROIs. When the ROI in Fig. 1c is

Stage		RMSE (HU)	SSIM
Config 1	Initial volume	95.2	0.98
	Final volume	28.3	0.99
Config 2	Initial volume	160	0.93
	Final volume	155	0.94

Table I
SUMMARY OF QUANTITATIVE EVALUATION IN TWO EXPERIMENTAL CONFIGURATIONS.

located at the right side of the patient, the dose saving potential could also be kept by either shifting the scan trajectory to the right side of the patient or laterally moving the table to left direction so that the right ROI is repositioned in the left side. For a standard C-arm CT system, the latter seems to be more feasible than the former.

Future work involves to further reduce computational complexity. It would be interesting to adapt the method proposed in [11]: since both measured minimal complete data and forward projected data are 2D entities, suggesting an approach that calculates the missing data directly from the original measured projections using 2D image processing steps, rather than explicitly performing reconstruction and forward projection. The computational complexity to estimate the missing data is considerably decreased, which will further deliver the algorithm to practical use.

ACKNOWLEDGMENT

The authors gratefully acknowledge funding by Siemens AG, Healthcare Sector and of the Erlangen Graduate School in Advanced Optical Technologies (SAOT) by the German Research Foundation (DFG) in the framework of the German excellence initiative.

REFERENCES

- [1] R. Fahrig, R. Dixon, T. Payne, R. L. Morin, A. Ganguly, and N. Strobel, "Dose and image quality for cone-beam C-arm CT system," *Medical Physics*, vol. 33, no. 12, pp. 4541–4550, 2006.
- [2] D. L. Parker, "Optimal short scan convolution reconstruction for fan-beam CT," *Medical Physics*, vol. 9, pp. 254–257, 1982.
- [3] Y. Xia, M. Berger, C. Riess, J. Hornegger, and A. Maier, "Dose Reduction Achieved by Dynamically Collimating the Redundant Rays in Fan-beam and Cone-beam CT," in *Proc IEEE NSS/MIC*, 2013, to appear.
- [4] A. Naparstek, "Short-scan fan-beam algorithms for CT," *IEEE Trans. Nucl. Sci.*, vol. 27, pp. 1112–1120, 1980.
- [5] F. Dennerlein and A. Maier, "Approximate truncation robust computed tomography - ATRACT," *Physics in Medicine and Biology*, vol. 58, pp. 6133–6148, 2013.
- [6] J. D. Pack, Z. Yin, K. Zeng, and E. N. Brian, "Mitigating cone-beam artifacts in short-scan CT imaging for large cone-angle scans," in *Proc Fully 3D 2013*, 2013, pp. 300–303.
- [7] A. Katsevich, "Image reconstruction for the circle and line trajectory," *Physics in Medicine and Biology*, vol. 49, pp. 5059–5072, 2004.
- [8] C. Bontus, P. Koken, T. Kohler, and R. Proksa, "Circular CT in combination with a helical segment," *Physics in Medicine and Biology*, vol. 52, pp. 107–120, 2007.
- [9] Y. Xia, A. Maier, H. G. Hofmann, F. Dennerlein, K. Mueller, and J. Hornegger, "Reconstruction from truncated projections in cone-beam CT using an efficient 1D filtering," in *Proc SPIE*, 2013, 86681C.
- [10] Z. Wang, A. C. Bovik, H. R. Sheikh, and E. P. Simoncelli, "Image quality assessment: from error visibility to structural similarity," *IEEE Transactions on Image Processing*, vol. 13, no. 4, pp. 600–612, 2004.
- [11] F. Dennerlein, A. Jerebko, A. Fieselmann, and T. Mertelmeier, "Efficient Synthesis of Virtual Projections from a Tomosynthesis Data Set using a 2D Image Processing Method," in *Proc SPIE*, 2013, p. 86680W.

Fast and Accurate Stratification of Tomographic Scans for Motion Artifacts

Holly Ho¹, Brian E. Nett¹, and Jed D. Pack²

Abstract—In computed tomography there are several scenarios in which motion that occurs during an axial scan will manifest as artifacts in the full-scan (360° of projection data) reconstructed image. These artifacts are due to inconsistent projection data used in the reconstruction. The aim of this work is to introduce a fast, robust algorithm which calculates a metric that accurately approximates how prominent motion artifacts will be in a full-scan reconstructed image from an axial scan in CT. The method was validated using projection and image data from scans of a dynamic phantom. There was a strong correlation demonstrated between the intensity of motion artifacts in the image space and the projection space motion metric (Pearson correlation coefficient of 0.90 and a P-value of 8.8×10^{-7}).

I. INTRODUCTION

In diagnostic computed tomography (CT) there are clinical scenarios where patient motion is not anticipated, but involuntary patient motion can lead to artifacts in the reconstructed images. Examples of this include imaging of the abdomen under breath-hold conditions; where involuntary respiratory motion or peristaltic motion can lead to motion artifacts in the reconstructed images. There are a variety of methods to modify the image reconstruction algorithm in order to reduce these motion artifacts. In this work we develop a metric to identify cases where significant artifacts would be noticeable if the standard non-gated full-scan filtered back-projection reconstruction is used. The aim of this work was to enable rapid stratification of scan data based on the likelihood of image artifacts in a standard reconstruction. Therefore, we have selected a projection based metric which does not require image reconstruction in order to assess the likelihood of motion artifacts.

The context of this work is diagnostic CT scanning under breath-hold conditions. Thus, motion may occur during the scan but it is not the expected norm. In comparison there are other slowly rotating projection acquisitions, such as on C-arm systems or on-board imaging devices on radiation therapy systems, which acquire data during periods of known motion such as during the respiratory cycle. In that context projection based methods have been developed to estimate the respiratory motion[1] or to determine the portion of the projection data which is influenced by patient motion[2] so as to provide gated reconstruction of the moving regions.

II. METHODS

The core of this algorithm is built on the theory that motion artifacts in axial full-scans manifest due to inconsistent

projection data. In an axial full-scan, projections are acquired at the same spatial location but at different times in the scan. To approximate how prominent the motion artifact will be in the reconstructed image, we assume that there will be more structure in the difference between the first and last projection than in the difference between neighboring projections (e.g. the first and second projection). This algorithm isolates the structures which have moved during the scan in order to quantify the amount of motion that occurred during the scan. The hypothesis is that by constructing a metric based on the amount of object motion in the projection domain, one may predict the likelihood of the scan data to generate image artifacts upon reconstruction. In this section we provide a thorough description of the algorithm.

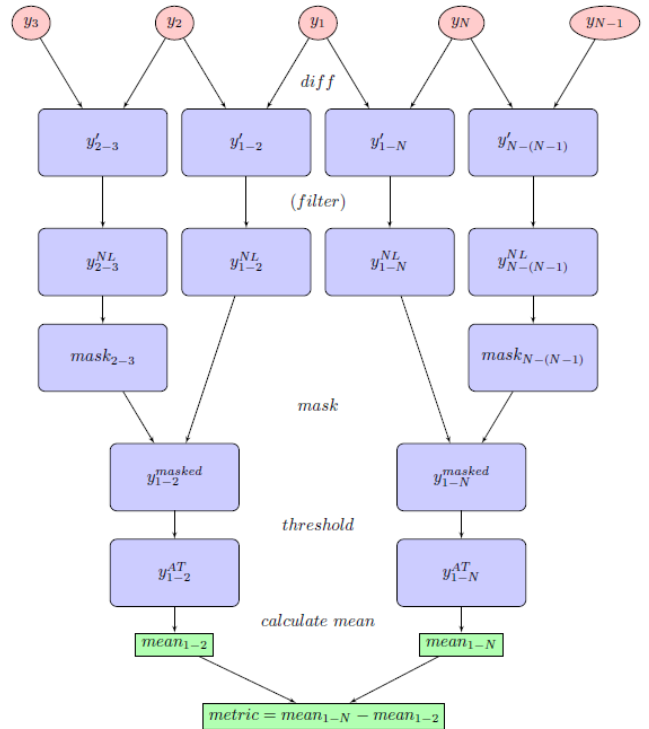


Fig. 1. Schematic diagram of the algorithm for data domain motion estimation, where the description of each step is given in the main text. Parentheses denote an optional operation.

¹GE Healthcare, 3000 N. Grandview Blvd., Waukesha, WI USA

²GE Global Research Center, One Research Circle, Niskayuna, NY USA

A. Algorithm Description

The general flow for the algorithm is depicted in Figure 1. In this implementation of the algorithm, we use five different projections for processing: $y_1, y_2, y_3, y_N,$ and $y_{(N-1)}$, where y_i refers to the index of the projection data corresponding to the i^{th} view, and N is the total number of views in one axial rotation. This algorithm can be broken down into the steps below:

- Step 1 - Take the difference of adjacent views.
- Step 2 - Apply a noise reduction filter.
- Step 3 - Mask out reoccurring features.
- Step 4 - Apply threshold.
- Step 5 - Calculate mean.
- Step 6 - Stratify.

The threshold level may be determined empirically by studying a variety of clinical cases with different levels of motion. In an ideal case where there is no projection noise Step 2 may be removed.

We begin by explaining Step 1, where we take the difference of adjacent views. In this implementation, we use the absolute value of the element-by-element difference. For every five projections of interest, we take the difference of each adjacent pair of views. This results in four difference projections: $y'_{1-2}, y'_{2-3}, y'_{1-N},$ and $y'_{N-(N-1)}$, where

$$y'_{i-j} = |y_i - y_j|$$

In the rest of the algorithm, we aim to isolate unique structures that are present in y'_{1-N} which indicate that motion occurred during the scan. We use y'_{1-2} as a basis of comparison. The remaining difference projections are used for masking out similar structures that are present in y'_{1-2} and y'_{1-N} . These structures will not be included in the calculation of the metric. The masking process is described in Step 3.

Next, we apply a noise reduction filter. In order to reduce noise in projections while still preserving structure. In this implementation we choose to apply a Non-Local Means filter[3] with a 5x5 search window. In order to calculate an appropriate noise level to use for the Non-Local Means filter, we calculate the standard deviation of the projection excluding air. To do this, we first calculate the Gonzalez-Woods threshold[4] for projections 1, 2, and N, resulting in $GW_1, GW_2,$ and GW_N . The standard deviation, σ_i , is then calculated only on the pixels whose values are greater than GW_i . The resulting filtered difference projections are $y_{1-2}^{NR}, y_{2-3}^{NR}, y_{1-N}^{NR},$ and $y_{N-(N-1)}^{NR}$, where NR denotes an image that has been filtered by a noise reduction filter.

In Step 3, we aim to remove the reoccurring features that are present in both y'_{1-2} and y'_{1-N} . These structures show up in each projection difference because the object is present in each projection, but are essentially shifted slightly due to the change in view angle. The table is an example of a reoccurring structure (i.e. the edge of the table will be present in multiple difference images even though it is not moving). These structures will not be included in the calculation of the motion estimation metric. In the case displayed in Figure 2, the

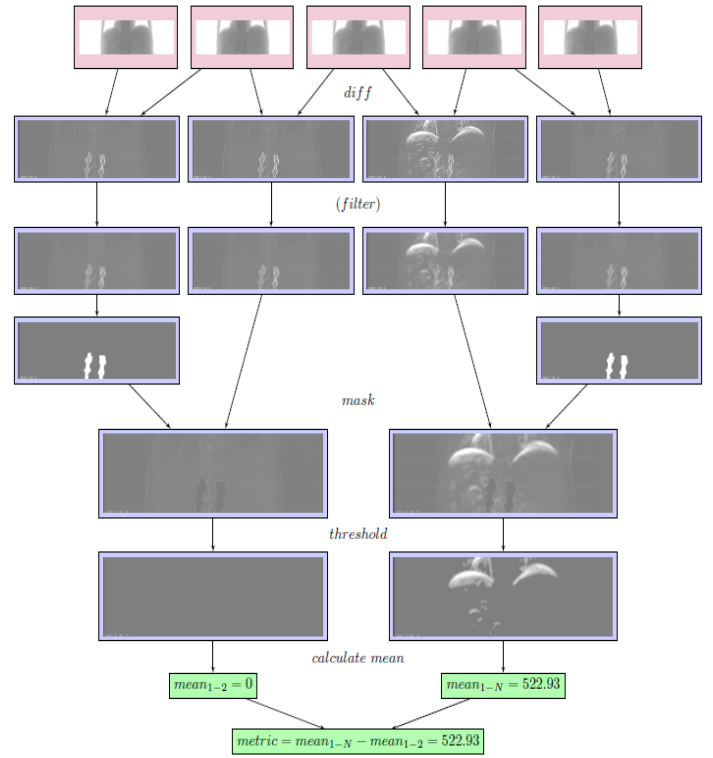


Fig. 2. Step-by-step results from a clinical case processed with the motion estimation algorithm. Motion occurred during scanning in this particular case and results in a high metric (522.93). Note that implanted hardware in the spine was removed during Step 3 of the process. The corresponding full-scan reconstruction is shown in Figure 3.

reoccurring structures are projections of implanted hardware located in the patient's spine. To remove these structures, we create two masks using (y'_{2-3} and $y'_{N-(N-1)}$), which will be applied separately to (y'_{1-2} and y'_{1-N}).

First, we calculate an auto threshold based on the maximum value of y_1 . Then we apply the threshold to y'_{2-3} and $y'_{N-(N-1)}$, resulting in a binary image. Each binary image is then dilated to account for the change in view angle. The resulting binary masks are $mask_{2-3}$ and $mask_{N-(N-1)}$. To apply the mask, we calculate an element-by-element product of the filtered difference projection and the complement of the mask:

$$y_{1-2}^{masked} = y_{1-2}^{NR} * \overline{mask_{2-3}}$$

$$y_{1-N}^{masked} = y_{1-N}^{NR} * \overline{mask_{N-(N-1)}}$$

Step 4 is the final step in isolating any structure of interest in y'_{1-N} that shows evidence of motion during the scan. In this step, an auto threshold is calculated based on y_{1-2}^{masked} . In this implementation, we use the Gonzalez-Woods threshold[4]. This threshold is applied to both y_{1-2}^{masked} and y_{1-N}^{masked} . Each pixel that is below the threshold is set to 0, and every pixel above the threshold maintains its value. The resulting projections are y_{1-2}^{AT} and y_{1-N}^{AT} , where AT denotes an image that has been filtered by the auto threshold.

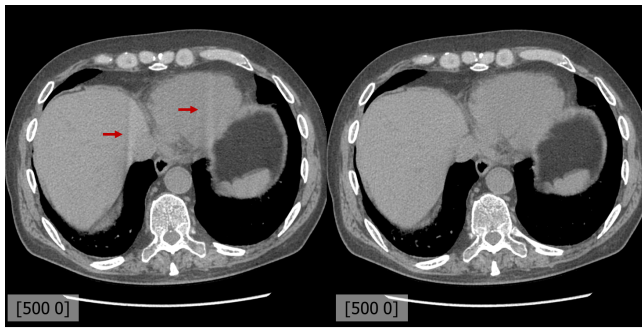


Fig. 3. (Left) Full-scan reconstruction of a clinical chest scan. Prominent motion artifacts in the liver and heart resulting from heart motion during the acquisition. The motion metric for this case is 522.93 (Figure 2). (Right) Improved reconstruction with motion artifacts noticeably reduced. Note that this patient has implanted hardware in his/her spine which is present in other slices of the volume.



Fig. 4. (Left) Full-scan reconstructed image of a clinical chest scan. No motion artifacts in the liver and heart. The projection motion metric for this case is very low (i.e. 2.81). (Right) Full-scan reconstructed image of a clinical pelvis scan. Note that this patient has hardware implanted in his/her spine. There are no motion artifacts present in this reconstructed image, and the projection motion metric is also very low (i.e. 6.79).

In Step 5 we calculate the motion metric first by measuring the mean of y_{1-2}^{AT} and y_{1-N}^{AT} , denoted as $mean_{1-2}$ and $mean_{1-N}$, respectively. Our final metric of motion is the difference between the resulting mean of each processed projection:

$$metric = mean_{1-2} - mean_{1-N}$$

Other motion metrics can also be applied such as the ratio of $mean_{1-N}$ and $mean_{1-2}$, or some other function of these two values.

A final optional step is to stratify the acquired scan data into a given category based on the level of motion which occurred during the scan. For instance the most basic stratification would be no/minimal motion cases and motion artifact corrupted cases. The stratification may be performed by comparing the motion metric for each case to the thresholds for the given categories, which are based on applying the method to many cases.

Figure 2 shows the flow of the algorithm with step-by-step images from a clinical case of a chest scan. Figure 3 shows the full-scan reconstructed image of the same clinical case. In this specific scan, motion artifacts are prominent in the heart and liver due to heart motion. Note that this patient had implanted hardware in his/her spine, and one can appreciate the need for the additional steps in the algorithm to remove the contribution of these regions from the motion metric. Additionally, Figure 4 shows the full-scan reconstructed images of two cases: (1) a chest scan with no motion artifacts and (2) a pelvis scan of a patient with implanted hardware in his/her spine with no motion. Both of these cases result in low (i.e. 2.81 and 6.79, respectively) projection motion metrics. Note that the input data has been pre-processed, which includes a projection scaling.

III. RESULTS

Projection scan data was acquired using a prototype CT system at 120 kVp, 400 mA, and a rotation time of 0.35 s. To simulate motion, we used the Quantitative Standard Pulsating

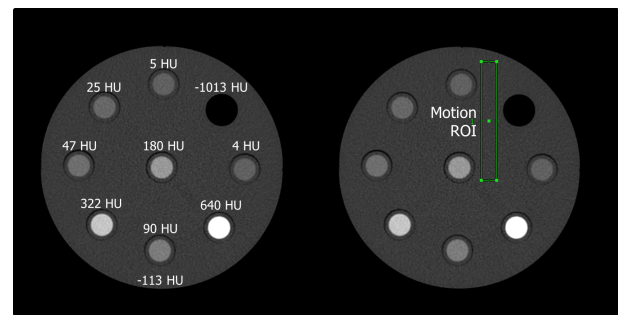


Fig. 5. (Left) Axial slice of Quantitative Standard Pulsating Phantom (FYC Fuyo Corporation), each cylinder labeled with its CT number. (Right) Axial slice showing where the ROI was placed to measure σ_{motion} .

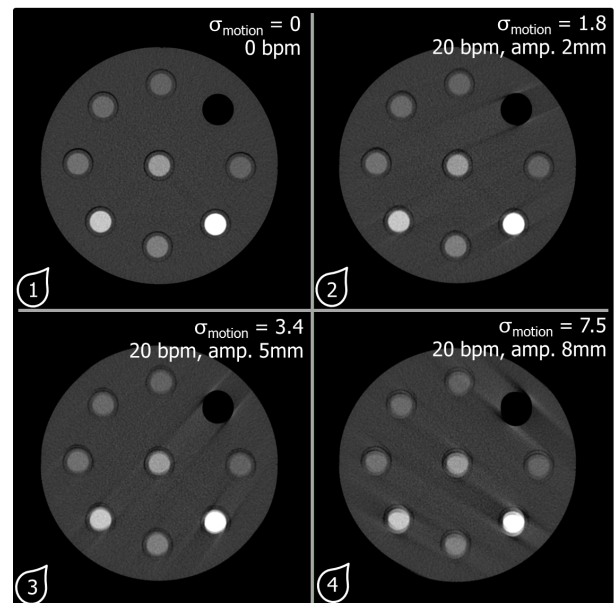


Fig. 6. Full-scan reconstruction of Kyoto Dynamic Phantom. (1) Static phantom. (2) Phantom moving at 20 bpm with 2 mm amplitude. (3) Moving at 20 bpm with 5 mm amplitude. (4) Moving at 20 bpm with 8 mm amplitude. The greater the amplitude of movement, the more prominent the motion artifact. Labels in the bottom left corner of each image correspond to annotations in Figure 7.

Phantom (FYC Fuyo Corporation). The phantom is a cylinder made of polymer that contains nine cylinders that are filled with different materials, of various attenuations. The layout of the phantom is shown in Figure 5. The phantom was moved up and down (AP direction) with a repeatable sinusoidal profile. The motion profile was specified by the frequency (measured in beats per minute, bpm) and the amplitude (mm). We acquired data of the phantom for four motion profiles:

- (1) static (0 bpm) [5 realizations]
- (2) 20 bpm, amplitude 2 mm [5 realizations]
- (3) 20 bpm, amplitude 5 mm [5 realizations]
- (4) 20 bpm, amplitude 8 mm [4 realizations]

Multiple realizations of each profile were acquired as the central view angle in each acquisition varied. The images were reconstructed using the a standard full-scan reconstruction (Figure 6) and analysis was performed in the central slice. The reconstruction was performed off-line and is not representative of any given production CT. The images were reconstructed at the same relative phase in the motion cycle, 75% of the cycle. As the amplitude of the motion increased, more motion artifacts were observed in the reconstructed images, as exhibited in Figure 6.

To evaluate the motion estimation algorithm, we are interested in comparing the motion metric to the amount of motion artifact present in the full-scan reconstructed image. To measure motion artifact in image space we first measure the standard deviation of an ROI in the full-scan reconstruction of the static phantom, σ_{static} . We then use σ_{static} as a baseline for the standard deviation due to quantum noise in the reconstructed image. To calculate σ_{motion} , we subtract σ_{static} from the measured standard deviation, σ_{meas} , of an image:

$$\sigma_{motion} = \sigma_{meas} - \sigma_{static}$$

In Figure 7, we compare σ_{motion} and the calculated motion metric for each case. The data shown in Figure 7 demonstrates a high degree of correlation, where the Pearson correlation coefficient is 0.90 with a P-value of 8.8×10^{-7} . Thus, there is a strong correlation between the motion measured in image space and the calculated motion metric in projection space. For cases where no motion artifacts are present in image space, the corresponding motion metric is very low (i.e. less than 20). For cases where strong motion artifacts were present in image space, the corresponding motion metric is very high (i.e. greater than 100). The annotations on the graph in Figure 7 correspond to the labels in the bottom left corner of each image in Figure 6. The results show that it is possible to completely separate data sets corrupted by motion artifacts from the non-motion cases in this study using a threshold of 50. Further study on clinical data is planned to validate the utility of the metric for stratification of motion in clinical exams.

IV. CONCLUSION

In this work we developed a fast and robust method for estimating motion that occurs during a full-scan axial CT acquisition. Multiple image volumes, with and without motion, were acquired and tested with the motion estimation algorithm.

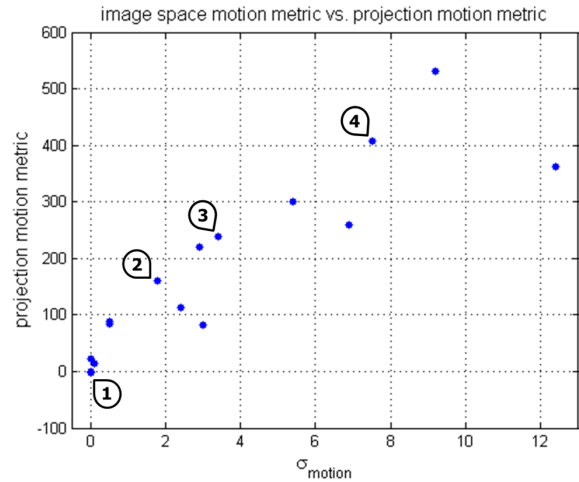


Fig. 7. Results comparing standard deviation due to motion (σ_{motion}) and calculated motion metric using the motion estimation algorithm. There is a strong correlation demonstrated between the intensity of motion artifacts in the image space and the projection space motion metric (Pearson correlation coefficient of 0.90 and a P-value of 8.8×10^{-7}). When stronger artifacts are exhibited in image space the corresponding motion metric will be high. Points on the plot with annotations correspond to reconstructed images in Figure 6.

The resulting motion metric is strongly correlated with the intensity of motion artifacts present in full-scan reconstructions.

REFERENCES

- [1] R. Zeng, J. A. Fessler, J. M. Balter. *Respiratory motion estimation from slowly rotating x-ray projections: Theory and simulation*. Med. Phys. **32**, 984. (2005).
- [2] F. Bergner, T. Berkus, M. Oelhafen, P. Kunz, T. Pan, M. Kachelrieß. *Autoadaptive phase-correlated (AAPC) reconstruction for 4D CBCT*. Med. Phys. **36**, 5695. (2009).
- [3] A. Buades, B. Coll, J. -M. Morel. *A non-local algorithm for image denoising*. IEEE Computer Society Conference on Computer Vision and Pattern Recognition. **2**, 60-65. (June 2005).
- [4] R. C. Gonzalez, R. E. Woods. *Thresholding*. Digital Image Processing, 595-611. (2002).

Constrained TV-minimization Image Reconstruction for Dynamic Micro-CT Data with Reduced Angular Sampling

Buxin Chen, Xuan Liu, Zheng Zhang, Andrew Davis, Xiao Han, *Member, IEEE*, Emil Sidky, and Xiaochuan Pan, *Fellow, IEEE*

Abstract—Micro-CT is a useful tool for preclinical research. Dynamic micro-CT with gating has been used for *in-vivo* imaging of small animals. Meanwhile, imaging time and radiation dose can be lowered by reducing the angular sampling in the dynamic scan. In this work, we investigated the applicability of constrained TV-minimization reconstruction for dynamic sparse-view data from micro-CT. Data from a single synchronized phase of an *in-vivo* pulmonary-gated scan were formed into a short-scan from which sparse-view data subsets were extracted. Results suggest that the constrained TV-minimization reconstruction, together with the ASD-POCS algorithm, is robust to the reduction of angular sampling. Images show improved contrast for features of interests under full-view data and sustaining the high contrast under sparse-view data.

I. INTRODUCTION

MICRO-computed tomography (micro-CT) is useful for *in-vivo* imaging of small animals [1], [2]. Its advantages include high resolution and high efficiency of radiation detection. However, imaging time, motion blurring, and photon statistics are three particularly challenging factors for micro-CT *in-vivo* scans. Cardiac and pulmonary gating have been proposed to reduce motion blurring by rebinning data from a single synchronized phase together [3], [4]. Meanwhile, reducing the number of angular views reduces imaging time and radiation dose, while maintaining the photon statistics for each projection view.

Total-variation (TV)-minimization based reconstruction has been proposed [5], [6] for sparse-view reconstruction and investigated for micro-CT specimen imaging [7]. In this work, we focus on applying constrained TV-minimization reconstruction program to dynamic *in-vivo* data with reduced number of angular views. The adaptive-steepest-descent-projection-onto-convex-sets (ASD-POCS) algorithm is used to solve the program. The evaluation tasks are mainly visually based, involving the delineation of the pulmonary region and visualization of the blood vessels.

B. Chen, Z. Zhang, A. Davis, X. Han, and E. Sidky are with the Department of Radiology, The University of Chicago, Chicago, IL 60637 USA.

X. Liu is with Bruker microCT, Kartuizersweg 3B, B-2550 Kontich, Belgium.

X. Pan is with the Departments of Radiology & Radiation and Cellular Oncology, The University of Chicago, Chicago, IL 60637 USA.

II. MATERIALS AND METHODS

A. Imaging System and Data Collection

A mouse was scanned *in-vivo* using the SkyScan1076 micro-CT system from Bruker microCT. The detector was placed 165 mm away from the X-ray source, and the object 125 mm away. The detector has 4000×2096 pixels, binned by a factor of 4 into 1000×524 during acquisition to keep exposure time short for dynamic scans, yielding pixel size of $45 \times 45 \mu\text{m}^2$. The tube voltage and current were set to 59 kVp and $167 \mu\text{A}$. The step-and-shoot rotation mode was used.

Dynamic data were acquired via respiratory gating. Projections from a single synchronized phase were extracted and rebinned to form a short-scan. As a result, there were in total 245 views with a 0.8-degree step size, covering 195 degree angular range. The exposure time for each of the views was 158 ms.

We focus on the central row of the detector, which forms a sinogram of 1000 bins \times 245 views, referred to as the "full-view" data. Further, subsets with reduced number of views were extracted and referred to as the "sparse-view" data. We use one half (123), one quarter (62), and one eighth (31) views, all uniformly distributed over the angular range, from the full-view data, in an effort to reduce imaging time and radiation dose, and reconstruct images from these sparse-view data.

B. Reconstruction Methods

A linear, discrete-to-discrete (D-D) model for the CT imaging process is considered here as

$$\mathbf{g}_0 = \mathcal{H}\mathbf{f}, \quad (1)$$

where \mathbf{g}_0 denotes the model-data vector, \mathbf{f} the image vector, and \mathcal{H} the projection matrix.

We design a constrained TV-minimization reconstruction program, explicitly specifying a set of solutions (i.e., reconstructed images), as below

$$\mathbf{f}^* = \operatorname{argmin} \|\mathbf{f}\|_{\text{TV}} \quad \text{s.t.} \quad |\mathcal{H}\mathbf{f} - \mathbf{g}| \leq \epsilon \quad \text{and} \quad f_j \geq 0, \quad (2)$$

where ϵ is a positive parameter accounting for the inconsistencies between the model-data \mathbf{g}_0 and measured data \mathbf{g} . Note that any physical factors that are not modeled into the system matrix \mathcal{H} , including noise, contribute to the inconsistencies.

The ASD-POCS algorithm [6] is used to solve the reconstruction program in Eqn. (2). It is the vehicle that takes

the image into the designed solution set specified by the reconstruction program. The FBP algorithm, with Parker's weighting, is also used to reconstruct images from the data. It serves here as a reference for benchmarking purpose. Central slice images are reconstructed on 740×590 arrays, with $34 \times 34 \mu\text{m}^2$ pixel size.

For sparse-view data, linear interpolation can be used to increase the data quantity in the angular direction. For any detector bin, a "view" is created by linearly interpolating the data from two adjacent views, doubling the number of views in the data set. Such method is tried on the one-half data in the sparse-view study and the reconstruction results using both ASD-POCS and FBP algorithms are shown with data before and after the angular interpolation.

III. RESULTS

We present images reconstructed from full-view data, sparse-view data, and sparse-view data after angular interpolation, using ASD-POCS and FBP algorithms, referred to as ASD-POCS images and FBP images, respectively. The reference image refers to the full-view (245) FBP image. The evaluation is done via visual inspection of the image quality, especially in areas of the lung and blood vessels. Figures show full-size images of the pulmonary region along with zoomed-in region-of-interest (ROI) images indicated by the white box in Fig. 1a for the blood vessels. For studies *A* and *B* below, FBP and ASD-POCS images are shown side-by-side for image quality comparison under the same data condition.

A. Full-view Study

Figs. 1a and 1b show that images reconstructed from full-view data are comparable between FBP and ASD-POCS. The pulmonary region is easily outlined in both images. However, the full-view FBP image displays a slightly higher noise level, especially in the pulmonary region, and some low-level streak artifacts in the peripheral skin tissues. In Figs. 1c and 1d, both ROI images show blood vessels clearly, though the ASD-POCS image, on the right, exhibits higher contrast due to the suppressed background noise.

B. Sparse-view Study

Sparse-view data reconstruction results are divided into three groups in Figs. 2, 4 and 5. The number of views decreases from one-half, to one-quarter, and to one-eighth the original number of views. For each group, full-size and ROI images are presented and placed in the same way as in the full-view study. For the first group using the one-half data, an additional figure showing full-size and ROI images from data after angular interpolation is also shown to illustrate the effect of the angular interpolation method.

1) *One Half, 123 Views*: In Fig. 2, the top row shows half-view FBP and ASD-POCS images. Compared to the corresponding full-view images, the streak artifacts and noise level are elevated in the half-view FBP image (Fig. 2a). The delineation of the pulmonary region can be compromised at the lung-heart boundary, where the noise makes it less

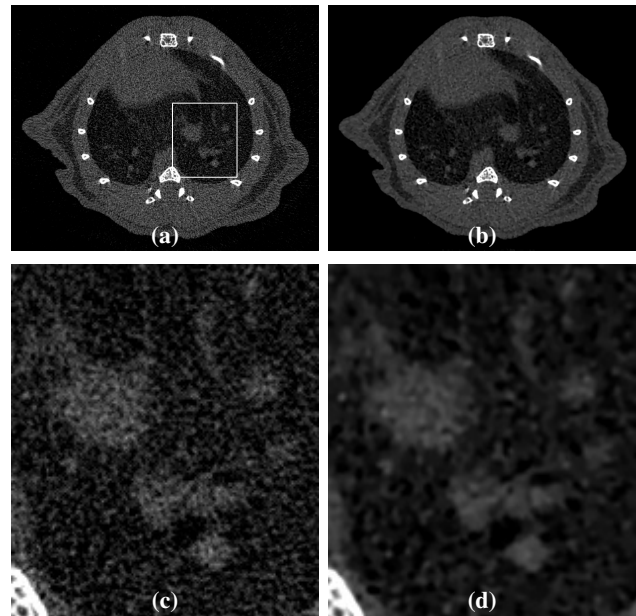


Fig. 1: Full-view data reconstruction images using FBP ((a) & (c)) and ASD-POCS ((b) & (d)). Both full size (top row) and ROI (bottom row) images are shown in a narrow displaying window of $[0.02, 0.20] \text{ mm}^{-1}$.

sharp. The ASD-POCS image (Fig. 2b) in general does not degrade much. The sharp edge of the pulmonary region and the contrast remain, as the number of views is reduced to half. On the bottom row of ROI images, streak artifacts and elevated noise level obscure the blood vessels in the FBP image ROI (Fig. 2c), especially the feature at the top right corner. The ASD-POCS image (Fig. 2d) displays clearly the blood vessels, and is very close to the full-view one (Fig. 1d).

In Fig. 3, angular interpolation seems to help reduce the streak artifacts in the FBP image (Fig. 3a) to some degree, such as, in the soft tissue region below the vertebrae, when compared to Fig. 2a. However, the noise level is not alleviated at all. Zooming in to the ROI image in Fig. 3c, we can make the same observation that the streak artifacts are less pronounced, but the noise level are as high. Moreover, tangential resolution degrades greatly along the radial direction, blurring the vasculature features of interest, especially their boundaries. The ASD-POCS image (Fig. 3b) suffers the same tangential resolution loss, while demonstrating no clear improvement over the original half-view ASD-POCS image (Fig. 2b). For the ASD-POCS ROI (Fig. 3d), a noticeably elevated noise level, compared to Fig. 2d, is observed due to the extra inconsistencies introduced in the interpolated views.

2) *One Quarter, 62 Views*: When the number of views is reduced to one-quarter, the FBP image (Fig. 4a) displays conspicuous streak artifacts and high noise level. The delineation of the pulmonary region is subject to likely errors from the noise, especially at the lung-heart boundary. On the contrary, the ASD-POCS image (Fig. 4b) shows sharp outline of the pulmonary region. While there are streaks present, the overall contrast remains high and comparable to that in Fig. 1b. Zooming in to the FBP ROI image in Figs. 4c, we find that

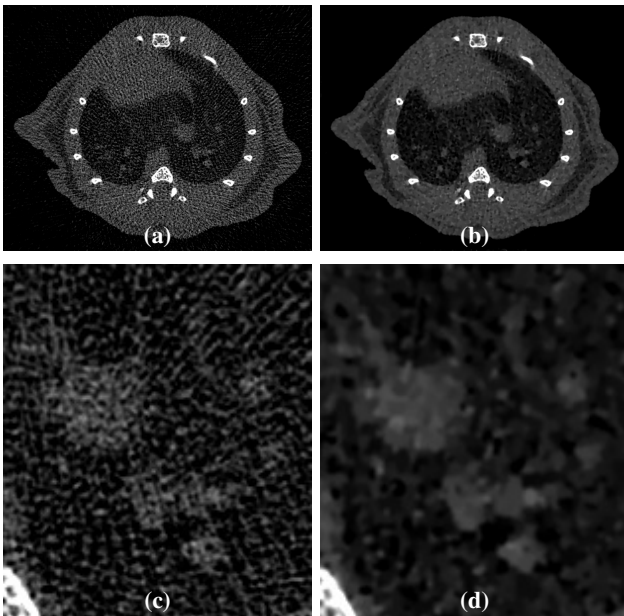


Fig. 2: Half-view data reconstruction images using FBP ((a) & (c)) and ASD-POCS ((b) & (d)). Both full-size (top row) and ROI (bottom row) images are shown in a narrow displaying window of $[0.02, 0.20] \text{ mm}^{-1}$.

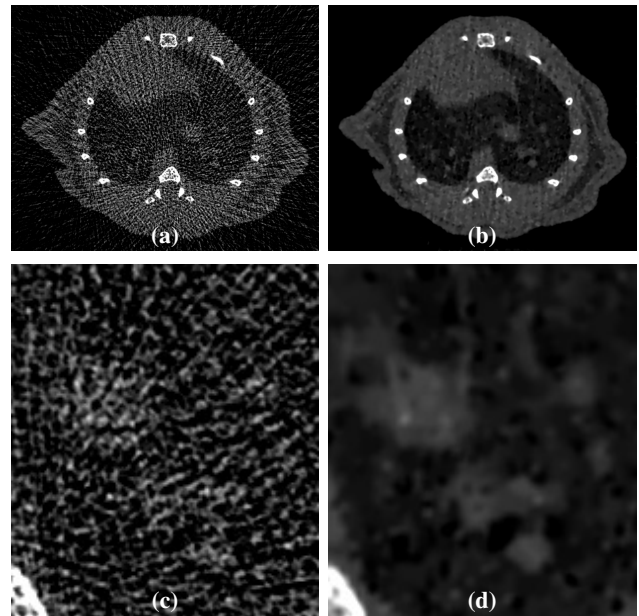


Fig. 4: Quarter-view data reconstruction images using FBP ((a) & (c)) and ASD-POCS ((b) & (d)). Both full-size (top row) and ROI (bottom row) images are shown in a narrow displaying window of $[0.02, 0.20] \text{ mm}^{-1}$.

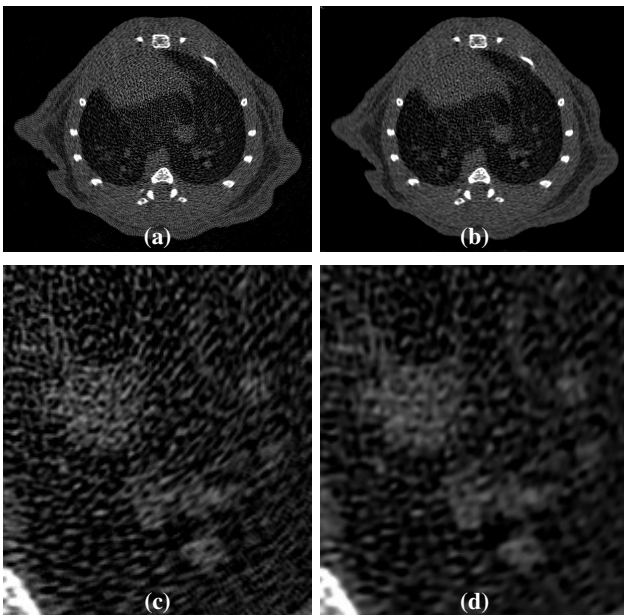


Fig. 3: Reconstruction images from half-view data after angular interpolation. FBP ((a) & (c)) and ASD-POCS ((b) & (d)) algorithms are used. Both full-size (top row) and ROI (bottom row) images are shown in a narrow displaying window of $[0.02, 0.20] \text{ mm}^{-1}$.

high-level noise severely obscures the blood vessels. As a result, the ROI image exhibits degraded image quality, with only the biggest feature barely discernible. Nevertheless, the ASD-POCS ROI (Fig. 4d) is less impacted by the reduction in angular sampling and maintains high contrast of the blood vessel features.

3) *One Eighth, 31 Views*: When the number of views is further reduced to one-eighth, the FBP image (Fig. 5a) is filled with streak artifacts and high noise level. The lung-heart boundary is blurred and smeared out by the noise, making the delineation of the pulmonary region very difficult. On the other side, the ASD-POCS image (Fig. 5b) still clearly shows the pulmonary region with relatively sharp boundary and stable contrast. For the ROI images on the bottom row, it is clear that the blood vessels can not be distinguished in the noise-filled FBP ROI image (Fig. 5c), while the ASD-POCS one (Fig. 5d), although suffering patchy artifacts, preserves almost all the features that are present in the full-view ROI (Fig. 1d).

C. Intermediate Iteration Results of ASD-POCS

A necessary optimality condition for the reconstruction program in Eqn. (2) has been derived as $c_\alpha = -1$ [6]. For practical applications, it has been suggested that iterations after c_α reaches below -0.5 do not change the reconstructed images significantly. [6], [7] In this work of real data studies, for the ASD-POCS images presented above, c_α 's have all reached -0.9 or lower. Meanwhile, we also study the evolution of the ASD-POCS image over iterations. For the full-view data, we show images at iterations 10, 20, 30, 40, 120, and 300 in Fig. 6. These images at intermediate iterations suggest that, at early iterations, such as the one in Fig. 6a, most blood vessels are reconstructed and the pulmonary outline is clearly defined. Further reduction of artifacts and increase of edge sharpness may require more iterations.

IV. DISCUSSION

In this work, we have investigated the applicability of constrained TV-minimization reconstruction for sparse-view

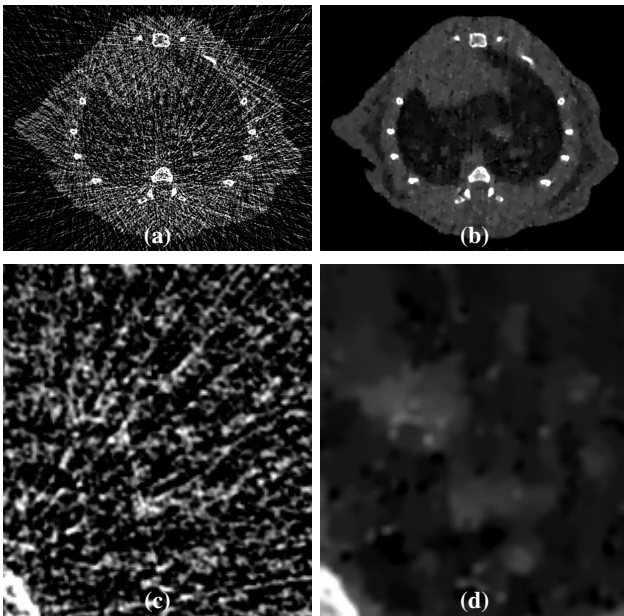


Fig. 5: One-eighth-view data reconstruction images using FBP ((a) & (c)) and ASD-POCS ((b) & (d)). Both full-size (top row) and ROI (bottom row) images are shown in a narrow displaying window of $[0.02, 0.20] \text{ mm}^{-1}$.

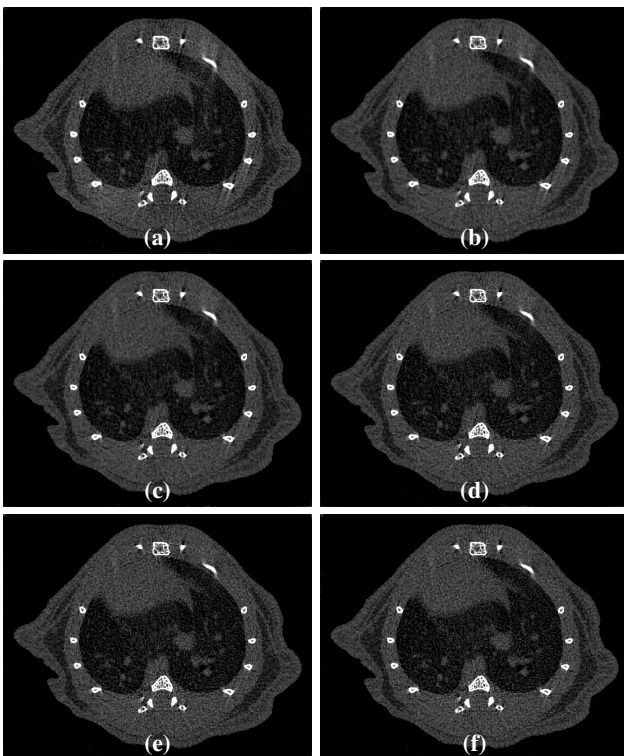


Fig. 6: Full-view data reconstruction images using ASD-POCS, at iterations (a) 10, (b) 20, (c) 30, (d) 40, (e) 120, and (f) 300.

data from micro-CT dynamic scans. As simulation studies and real data specimen studies have been reported on the ASD-POCS algorithm with micro-CT system, we focus on applying the algorithm to dynamic scans for live animals,

and reducing the radiation dose and total scanning time by using reduced number of views. The challenges here exist in the reduced angular sampling and the high noise level from the low radiation dose used. The results suggest that the ASD-POCS algorithm is overall insensitive to the reduction of angular sampling studied here. Under the low dose condition, the ASD-POCS images demonstrated improved contrast for features of interest, such as the pulmonary blood vessels, under full-view data, and sustained the high contrast under sparse-view data.

The angular interpolation showed some effectiveness in reducing the streak artifacts in both FBP and ASD-POCS images from sparse-view data. However, the reduction was trivial compared to the noise level and came at a cost of resolution degradation in the tangential direction, especially for the FBP images. As for the ASD-POCS images, angular interpolation introduced extra inconsistencies in the linear model in Eqn. (1), resulting in elevated noise level, as well as resolution loss. It is further suggested that ASD-POCS images at early iterations appear useful in terms of defining the pulmonary outline and visualizing the main blood vessels.

We stress that the utility of the reconstruction method is very much related to the task. It is worth pointing out that, if our focus is drawn to the very high contrast bone structures and the visualization of them, the sparse-view FBP images (Figs. 2a, 4a, and 5a), although plagued by streak artifacts and elevated noise level, display the bones with better resolution and higher fidelity to those in the reference image than their ASD-POCS counterparts. However, in this work under investigation, the task is focused on the pulmonary region outlines and the blood vessels, whose visualization can be compromised by the high noise level and streak artifacts. It is under this evaluation ground that the constrained TV-minimization program together with the ASD-POCS algorithm renders robust reconstruction for sparse-view dynamic data.

ACKNOWLEDGMENT

The authors would like to thank Dr. Phil Salmon and Dr. Jeroen Hostens from Bruker microCT for the data and for the discussions. The gratitude is also extended to Dr. Michel Defrise for his helpful discussions. This work was supported in part by NIH R01 Grant Nos. CA120540, CA158446, and EB000225. The contents of this article are solely the responsibility of the authors and do not necessarily represent the official views of the National Institutes of Health.

REFERENCES

- [1] S. M. Jorgensen, O. Demirkaya, and E. L. Ritman, "Three-dimensional imaging of vasculature and parenchyma in intact rodent organs with x-ray micro-ct," *American Journal of Physiology-Heart and Circulatory Physiology*, vol. 275, no. 3, pp. H1103–H1114, 1998.
- [2] E. L. Ritman, "Molecular imaging in small animals-Roles for micro-CT," *J. Cell. Biol. Suppl.*, vol. 39, pp. 216–224, 2002.
- [3] D. Cavanaugh, E. Johnson, R. E. Price, J. Kurie, E. L. Travis, and D. D. Cody, "In vivo respiratory-gated micro-ct imaging in small-animal oncology models," *Molecular imaging*, vol. 3, no. 1, pp. 55–62, 2004.
- [4] C. Badea, L. Hedlund, and G. Johnson, "Micro-ct with respiratory and cardiac gating," *Medical physics*, vol. 31, p. 3324, 2004.
- [5] E. Y. Sidky, K.-M. Kao, and X. Pan, "Accurate image reconstruction from few-views and limited-angle data in divergent-beam CT," *J. Xray Sci. Technol.*, vol. 14, pp. 119–139, 2006.

- [6] E. Y. Sidky and X. Pan, "Image reconstruction in circular cone-beam computed tomography by constrained, total-variation minimization," *Phys. Med. Biol.*, vol. 53, pp. 4777–4807, 2008.
- [7] X. Han, J. Bian, D. R. Eaker, T. L. Kline, E. Y. Sidky, E. L. Ritman, and X. Pan, "Algorithm-enabled low-dose micro-CT imaging," *IEEE Trans. Med. Imag.*, vol. 30, pp. 606–620, 2011.

A modified 4D ROOSTER method using the Chambolle-Pock algorithm

Cyril Mory¹ and Laurent Jacques²

Abstract—The 4D RecOnstructiOn using Spatial and TEmporal Regularization method is a recent 4D cone beam computed tomography algorithm. 4D ROOSTER has not been rigorously proved to converge. This paper aims to reformulate it using the Chambolle & Pock primal-dual optimization scheme. The convergence of this reformulated 4D ROOSTER is therefore guaranteed.

I. INTRODUCTION

Four dimensional cone beam computed tomography (4D CBCT) of the free breathing thorax is important for image-guided radiation therapy (IGRT). Mainly two families of methods have been proposed to handle the problem: respiratory motion compensation, in which the motion of organs during breathing is estimated and used to deform the volume during reconstruction, and respiration-correlated reconstruction, in which several volumes are computed, each one from a subset of the projections that has been acquired during the correct respiratory phase. Advances in compressed sensing have been used to improve respiration-correlated reconstruction by enforcing spatial regularity constraints [1]–[4], but only a few recent methods exploit the strong correlation between successive respiratory phases [5]–[8]. 4D ROOSTER [8], which was recently proposed for 4D cardiac CBCT, is one such method. However, it came without a rigorous proof of convergence. In this paper, we propose a reformulation of 4D ROOSTER using the Chambolle & Pock primal-dual optimization scheme [9]. The convergence of this reformulated 4D ROOSTER is therefore guaranteed.

II. THE ORIGINAL 4D ROOSTER METHOD

This algorithm assumes that a rough segmentation of the patient’s heart is available, and that movement is expected to occur only inside this segmented region. The method consists in iteratively enforcing five different constraints in an alternating manner. It starts by minimizing a quadratic data-attachment term $\sum_{\alpha} \|R_{\alpha} S_{\alpha} x - p_{\alpha}\|_2^2$, with α the projection angle, x a 4D sequence of volumes, R_{α} the forward projection operator at angle α , S_{α} a linear interpolator, and p_{α} the measured projection at angle α . This data-attachment term is minimized by conjugate gradient. Then the following regularization steps are applied sequentially: positivity enforcement, averaging along

time outside the heart region, spatial total-variation denoising, and temporal total-variation denoising. This constitutes one iteration of the main loop, the output of which is fed back to the conjugate gradient minimizer for the next iteration. This algorithm offers no convergence guarantees. In [10], [11], using the theory of non-expansive mappings, it is only proved that if the main iteration has at least one fixed point, the algorithm converges to one of them. However, we show in this paper that each step of this method can be interpreted as a proximal operator [8], thus little effort is required to make it fit into the Chambolle & Pock framework. We remind that for $f : \mathbb{R}^N \rightarrow \mathbb{R}$ a closed convex function, the proximal operator of f is defined as $\text{prox}_f(v) = \arg \min_{x \in \mathbb{R}^N} \frac{1}{2} \|x - v\|_2^2 + f(x)$.

III. CHAMBOLLE & POCK 4D ROOSTER

Setting $R = \begin{pmatrix} R_{\alpha_1} S_{\alpha_1} \\ \vdots \\ R_{\alpha_m} S_{\alpha_m} \end{pmatrix}$ and $p = \begin{pmatrix} p_{\alpha_1} \\ \vdots \\ p_{\alpha_m} \end{pmatrix}$, with m

the number of projections, the data-attachment term becomes a single L^2 norm $\sum_{\alpha} \|R_{\alpha} S_{\alpha} x - p_{\alpha}\|_2^2 = \|Rx - p\|_2^2$. The 4D ROOSTER optimization problem can then be expressed as the search for

$$\arg \min_{x \in \mathbb{R}^N} \frac{1}{2} \|Rx - p\|_2^2 + \lambda_2 \|x\|_{TV_{space}} + \lambda_3 \|x\|_{TV_{time}} + i_{\mathbb{R}^N+}(x) + i_{ROI}(x) \quad (1)$$

with x the 3D+t sequence of volumes, with in total N voxels, p the set of measured projections, with in total P pixels, $R : \mathbb{R}^N \rightarrow \mathbb{R}^P$ the forward projection operator, $\|\cdot\|_{TV_{space}}$ the spatial total-variation norm, $\|\cdot\|_{TV_{time}}$ the temporal total-variation norm, \mathbb{R}^N+ the set of sequences of volumes in which all voxels have non-negative values, ROI the set of sequences of volumes in which all voxels outside the heart have equal values, $i_{\mathbb{R}^N+}(x)$ and $i_{ROI}(x)$ their respective convex indicator functions, and $\lambda_2, \lambda_3 > 0$ two parameters weighing the relative importance of the terms. We adopt the same formalism as in [12], and therefore use the following notations:

$$\begin{aligned} F_1 : \mathbb{R}^P &\rightarrow \mathbb{R}, t \rightarrow \frac{1}{2} \|t - p\|_2^2 \\ F_2 : \mathbb{R}^N &\rightarrow \mathbb{R}, t \rightarrow \lambda_2 \|t\|_{TV_{space}} \\ F_3 : \mathbb{R}^N &\rightarrow \mathbb{R}, t \rightarrow \lambda_3 \|t\|_{TV_{time}} \\ H : \mathbb{R}^N &\rightarrow \mathbb{R} \cup \{+\infty\}, t \rightarrow i_{\mathbb{R}^N+}(t) + i_{ROI}(t) \end{aligned}$$

Because the cost function has more than two terms, we have to reformulate the problem into a search in \mathbb{R}^{3N} by

¹iMagX project, ICTEAM Institute, Université catholique de Louvain, Louvain-la-Neuve, Belgium and Université de Lyon, CREATIS ; CNRS UMR5220 ; Inserm U1044 ; INSA-Lyon ; Université Lyon 1 ; Centre Léon Bérard, France

²ISP GROUP, ICTEAM/ELEN, Université catholique de Louvain, Louvain-la-Neuve, Belgium

defining $x' = \begin{pmatrix} x_1 \\ x_2 \\ x_3 \end{pmatrix}$, with x_1, x_2 and $x_3 \in \mathbb{R}^N$, and $\prod_{1,i} = \{x' \in \mathbb{R}^{3N} \mid x_1 = x_i\}$ for $i = 2, 3$. The 4D ROOSTER optimization problem becomes

$$\begin{aligned} \arg \min_{x \in \mathbb{R}^{3N}} & F_1(Rx_1) + F_2(x_2) + F_3(x_3) \\ & + i_{\mathbb{R}^N}(x_1) + i_{ROI}(x_1) + i_{\prod_{1,2}}(x') + i_{\prod_{1,3}}(x') \end{aligned} \quad (2)$$

We define the total dimension $W = P + 2N$, the convex functions F and G and the linear operator K :

$$\begin{aligned} F : \mathbb{R}^W &\rightarrow \mathbb{R}, s = \begin{pmatrix} s_1 \\ s_2 \\ s_3 \end{pmatrix} \rightarrow \sum_{j=1..3} F_j(s_j) \\ \text{with } & s_1 \in \mathbb{R}^P, s_2 \in \mathbb{R}^N, s_3 \in \mathbb{R}^N \\ K : \mathbb{R}^{3N} &\rightarrow \mathbb{R}^W, K = \begin{pmatrix} R & 0 & 0 \\ 0 & I_N & 0 \\ 0 & 0 & I_N \end{pmatrix} \\ G : \mathbb{R}^{3N} &\rightarrow \mathbb{R}, x' \rightarrow i_{\prod_{1,2}}(x') + i_{\prod_{1,3}}(x') + H(x_1) \end{aligned}$$

With these new notations, we can write the cost function as a sum of two functions $\arg \min_{x \in \mathbb{R}^{3N}} F(Kx') + G(x')$ on which the Chambolle-Pock algorithm applies. In compact form, the Chambolle-Pock algorithm is as follows: let $v^{(0)} \in \mathbb{R}^W, x^{(0)} \in \mathbb{R}^{3N}, y^{(0)} \in \mathbb{R}^{3N}$, the update step is

$$\begin{cases} v^{(k+1)} = \text{prox}_{\gamma F^*}(v^{(k)} + \gamma K y^{(k)}) \\ x^{(k+1)} = \text{prox}_{\mu G}(x^{(k)} - \mu K^* v^{(k+1)}) \\ y^{(k+1)} = 2x^{(k+1)} - x^{(k)} \end{cases}$$

If we expand this for our problem and simplify it since $x_1 = x_2 = x_3$ and $y_1 = y_2 = y_3$, we obtain:

$$\begin{cases} v_1^{(k+1)} = \text{prox}_{\gamma F_1^*}(v_1^{(k)} + \gamma R y_1^{(k)}) \rightarrow \text{Data fidelity} \\ v_2^{(k+1)} = \text{prox}_{\gamma F_2^*}(v_2^{(k)} + \gamma y_2^{(k)}) \rightarrow \text{TV in space} \\ v_3^{(k+1)} = \text{prox}_{\gamma F_3^*}(v_3^{(k)} + \gamma y_3^{(k)}) \rightarrow \text{TV in time} \\ x^{(k+1)} = \text{prox}_{\frac{\mu}{3} H}(3x_1^{(k)} - \mu(R^* v_1^{(k+1)} \\ + v_2^{(k+1)} + v_3^{(k+1)})) \rightarrow \text{Positivity and ROI} \\ y^{(k+1)} = 2x^{(k+1)} - x^{(k)} \rightarrow \text{Update step} \end{cases}$$

Four new operators appear in this formulation. $R^* : \mathbb{R}^P \rightarrow \mathbb{R}^N$ is the back projection operator. To express the other ones, we use the relation between the proximal operator of a function and the proximal operator of its adjoint:

$$\text{prox}_{\gamma F^*}(x) = x - \gamma \text{prox}_{\frac{1}{\gamma} F}\left(\frac{1}{\gamma}x\right)$$

Therefore

$$\text{prox}_{\gamma F_1^*}(x) = x - \gamma \left(\frac{x+p}{\gamma+1}\right) = \frac{x-\gamma p}{\gamma+1}$$

The proximal operator for the spatial and temporal TV norms can be computed iteratively using the Chambolle algorithm [13], simply by using either the spatial or the temporal gradient and divergence operators

$$\begin{aligned} \text{prox}_{\frac{1}{\gamma} TV}(x) &= x - \frac{1}{\gamma} \text{div } \bar{p}, \text{ where } \bar{p} = \lim_{n \rightarrow +\infty} p^{(n)} \\ p^{(0)} &= 0 \text{ and for every voxel } i, \\ p_i^{(n+1)} &= \frac{p_i^n + h(\nabla(\text{div } p^{(n)} - \gamma x))_i}{1 + h(\nabla(\text{div } p^{(n)} - \gamma x))_i}, \text{ with } h > 0 \end{aligned}$$

And the proximal operator of γF_2^* (and similarly γF_3^*) can be obtained from the same relationship as previously

$$\begin{aligned} \text{prox}_{\gamma F_2^*}(v_2^{(k)} + \gamma y_2^{(k)}) & \\ &= v_2^{(k)} + \gamma y_2^{(k)} - \gamma \text{prox}_{\frac{1}{\gamma} F_2}\left(\frac{1}{\gamma}(v_2^{(k)} + \gamma y_2^{(k)})\right) \\ &= v_2^{(k)} + \gamma \left(y_2^{(k)} - \text{prox}_{\frac{1}{\gamma} F_2}\left(\frac{1}{\gamma}v_2^{(k)} + y_2^{(k)}\right)\right) \end{aligned}$$

With this new formulation, the modified 4D ROOSTER is guaranteed to converge. The theory of proximal algorithms also helps find the suitable parameters based on the norm of R , while they can only be determined empirically in the original method.

IV. PERSPECTIVES

4D ROOSTER can be applied to respiration-correlated 4D CBCT in order to reduce the level of streak artifacts in the reconstructions. Preliminary results are provided in Figure 1 and 2. They have been obtained using the original 4D ROOSTER method, and are compared with a standard ECG-gated FDK reconstruction. The modified 4D ROOSTER method presented in this paper will be implemented in the near future using the RTK framework [14].

REFERENCES

- [1] F. Bergner, T. Berkus, M. Oelhafen, P. Kunz, T. Pan, R. Grimmer, L. Ritschl, and M. Kachelrieß, "An investigation of 4D cone-beam CT algorithms for slowly rotating scanners," *Medical Physics*, vol. 37, no. 9, p. 5044, 2010.
- [2] Z. Qi and G.-H. Chen, "Extraction of tumor motion trajectories using PICCS-4DCBCT: a validation study," *Medical physics*, vol. 38, no. 10, pp. 5530–5538, Oct. 2011, PMID: 21992371 PMID: PMC3195374.
- [3] S. Leng, J. Tang, J. Zambelli, B. Nett, R. Tolakanahalli, and G.-H. Chen, "High temporal resolution and streak-free four-dimensional cone-beam computed tomography," *Physics in medicine and biology*, vol. 53, no. 20, pp. 5653–5673, Oct. 2008, PMID: 18812650.
- [4] E. Y. Sidky and X. Pan, "Image reconstruction in circular cone-beam computed tomography by constrained, total-variation minimization," *Physics in Medicine and Biology*, vol. 53, no. 17, pp. 4777–4807, Sep. 2008.
- [5] H. Gao, R. Li, Y. Lin, and L. Xing, "4D cone beam CT via spatiotemporal tensor framelet," *Medical Physics*, vol. 39, no. 11, pp. 6943–6946, Nov. 2012, PMID: 23127087 PMID: PMC3494730.
- [6] H. Wu, A. Maier, R. Fahrig, and J. Hornegger, "Spatial-temporal total variation regularization (STTVR) for 4D-CT reconstruction," in *Proceedings of SPIE Medical Imaging 2012*, N. J. Pelc, R. M. Nishikawa, and B. R. Whiting, Eds., San Diego, CA, USA, Feb. 2012, p. 83133J.
- [7] Z. Tian, X. Jia, B. Dong, Y. Lou, and S. B. Jiang, "Low-dose 4DCT reconstruction via temporal nonlocal means," *Medical physics*, vol. 38, no. 3, pp. 1359–1365, Mar. 2011, PMID: 21520846.

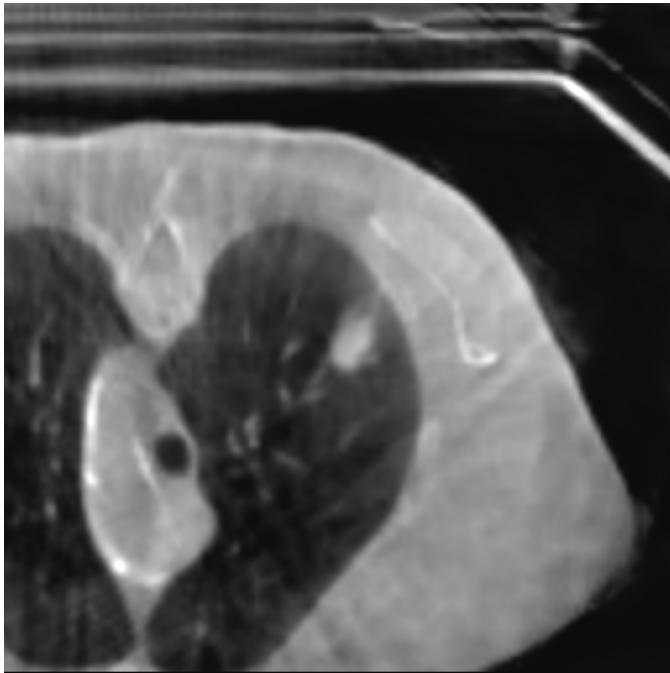


Figure 1. Respiratory-gated reconstruction of a lung tumor using 4D ROOSTER

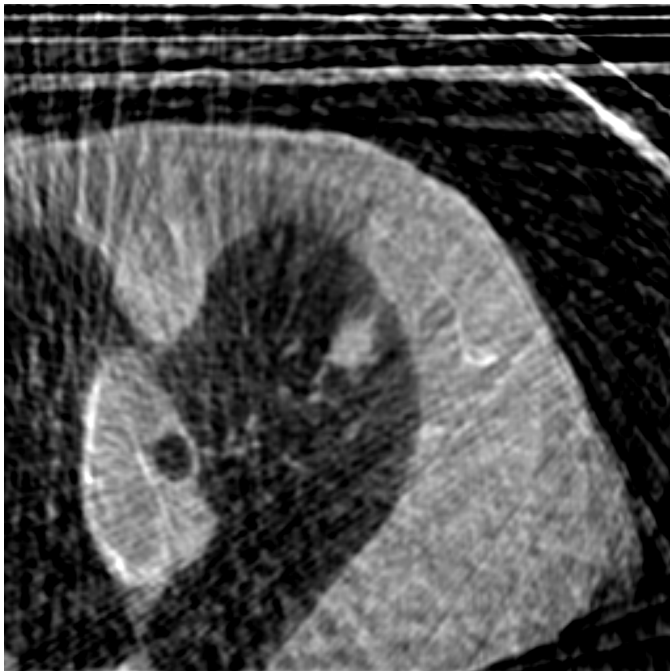


Figure 2. Respiratory-gated reconstruction of a lung tumor using the Feldkamp, Davis and Kress method

- [8] C. Mory, "Cardiac c-arm computed tomography," Ph.D. dissertation, Université Lyon 1, Feb. 2014.
- [9] A. Chambolle and T. Pock, "A first-order primal-dual algorithm for convex problems with applications to imaging," *Journal of Mathematical Imaging and Vision*, vol. 40, no. 1, pp. 120–145, May 2011.
- [10] J. J. Moreau, "Fonctions convexes duales et points proximaux dans un espace hilbertien," *Comptes Rendus de l'Académie des Sciences (Paris)*, vol. 255, pp. 2897–2899, 1962.
- [11] P. L. Combettes and J.-C. Pesquet, "Proximal splitting methods in signal processing," in *Fixed-Point Algorithms for Inverse Problems in Science and Engineering*, ser. Springer Optimization and Its Applications, H. H. Bauschke, R. S. Burachik, P. L. Combettes, V. Elser, D. R. Luke, and H. Wolkowicz, Eds. Springer New York, Jan. 2011, pp. 185–212.
- [12] A. Gonzalez, L. Jacques, C. De Vleeschouwer, and P. Antoine, "Compressive optical deflectometric tomography: A constrained total-variation minimization approach," *Journal of Inverse Problems and Imaging*, In press.
- [13] A. Chambolle, "An algorithm for total variation minimization and applications," *J. Math. Imaging Vis.*, vol. 20, no. 1-2, p. 89–97, Jan. 2004.
- [14] S. Rit, M. Vila Oliva, S. Broumische, R. Labarbe, D. Sarrut, and G. C. Sharp, "The reconstruction toolkit (RTK), an open-source cone-beam CT reconstruction toolkit based on the insight toolkit (ITK)," in *Proceedings of the International Conference on the Use of Computers in Radiation Therapy (ICCR)*, 2013.

Regularised GMRES-type Methods for X-Ray Computed Tomography

Sophia B. Coban and William R.B. Lionheart

Abstract—Slowly converging iterative methods such as Landweber or ART, have long been preferred for reconstructing a tomographic image from a set of CT data. In the recent years, a fast-converging method named CGLS has received attention for reconstructing tomographic data. However, there is a large class of methods that give more reliable solutions, when compared to CGLS. In this paper, we are going to consider the merits of the GMRES-type methods when applied to the CT problem, introduce various strategies, and compare the results with CGLS.

In computed tomography, we deal with an over-determined system of linear equations of the form

$$Ax = b, \quad (1)$$

where $A \in \mathbb{R}^{m \times n}$ is a large and sparse geometry matrix, $b \in \mathbb{R}^{m \times 1}$ is the logarithm of the ratio of initial and final intensities, and $x \in \mathbb{R}^{n \times 1}$ is the linear attenuation coefficient in voxels. For computational efficiency and mathematical flexibility, iterative methods are preferred for solving problems of this type. Additionally, since the CT problem is very large, it cannot be solved with a direct method because that would require more matrices of the same size to be stored. This emphasises the need for iterative methods. In the CT community, when *iterative reconstruction methods* are discussed, one is accustomed to think of slowly converging algebraic iterative methods such as Landweber or ART. These methods have been around for a long time and are widely used because the user has the advantage of stopping the algorithm before the data is over-fit, even though the problem is mathematically not yet minimized. However, it is understood in the recent years that by reconstructing CT data with a fast-converging method, we also avoid over-fitting the data and are able to obtain a better solution. So in theory, to obtain an exact solution with these complex, fast-converging methods, we would have memory requirements that grow with the number of iterations but in practice, we require only a fraction of this number so our memory requirements stay low. These are just a few reasons why there has been a growing interest in fast-converging methods, with the most popular one being the Conjugate Gradient method for Least Squares (CGLS). This method is mathematically equivalent to applying the original Conjugate Gradient to the normal equation, i.e.

$$A^T A x = A^T b. \quad (2)$$

School of Mathematics, The University of Manchester, Manchester, M13 9PL, UK.
www.maths.manchester.ac.uk/~scoban, www.maths.manchester.ac.uk/~bl.

The performance of the CG method depends on the fact that the geometry matrix is symmetric, which automatically works well with (2) since the product of any matrix with its transpose will always be symmetric. However, it is not always ideal to calculate the exact transpose in CT problems, and it is much more efficient to implement an inexact transpose (also known as an unmatched back projection): A certain \hat{A}^T that is close, but not equal to A^T . Of course this means that the product of $\hat{A}^T A$ is no longer a symmetric matrix, which causes some issues on the convergence and computational inefficiency with the CGLS method. This is an important point (to which we return to later on in the paper), and our main motivation for wanting to adapt alternative iterative methods in the same class as a well-established problem.

CGLS is a member of a large class of methods named the Krylov subspace (KS-)methods [8]. Those belonging to this class converge very quickly, which gives us the possibility of applying them directly to the Tikhonov system,

$$(A^T A + \lambda^2 L^T L)x = A^T b. \quad (3)$$

For the readers' convenience, we now give the definition of a Krylov subspace: An order k Krylov subspace, $\mathcal{K}_k(A, b)$, is the linear subspace spanned by the image of b under the linear transformation matrix A^p , $p = 0, 1, \dots, k - 1$ (where $A^0 = I_n$),

$$\mathcal{K}_k(A, b) = \text{span}\{b, Ab, A^2b, \dots, A^{k-1}b\}. \quad (4)$$

KS-methods are derived from (4) and are popularly used for their convergence properties, robustness and efficiency. These methods are particularly preferred for when A is large and sparse since the product of Ab is a vector, and $A^2b = A(Ab)$ is another matrix-vector operation¹. This avoids filling in the zero elements in the matrix and preserves the sparsity of A . Also, as $k \rightarrow \infty$, $A^k b \rightarrow A^{-1}b$, thus avoiding the inversion of a large and sparse matrix. Krylov subspace methods are also row (or column) action methods. This is important because in CT, the geometry matrix A is often too big to store, and the matrix-vector operations are required to be performed with one row (or column) of A at a time. So KS-methods are easily (and efficiently) adaptable for the CT problem.

Another popular method from the KS-methods class is GMRES. In the next section, we highlight the advantages and disadvantages of this method but we first give a quick introduction to GMRES and state the algorithm. We should

¹Note here that this definition is valid for square matrices. For non-square matrices, we deal with forward and back projection, rather than the powers of matrices.

note that a more detailed derivation of this method is given in [9], [5] as well as an extensive literature review. Here, we will mention only some of these references and briefly explain the GMRES variations.

GMRES-TYPE METHODS

The **Generalised Minimum Residual** (GMRES), is a KS-method that approximates a solution to (1) by evaluating

$$x_k = x_0 + V_k y. \quad (5)$$

Here, $V_k \in \mathbb{R}^{k \times k}$ is the orthonormal columns of basis for $\mathcal{K}_k(A, r_0)$, and $y \in \mathbb{R}^{k \times 1}$ is the solution to (what we refer to as) an *inner* problem, where $\|r_k\|_2$ is minimized over the Krylov subspace, $\mathcal{K}_k(A, r_0)$. The matrix V_k is obtained during what is called an *Arnoldi process*, which also returns a rectangular upper Hessenberg matrix, $H_k \in \mathbb{R}^{(k+1) \times k}$. This matrix mimics the characteristics of the coefficient matrix A and thus, it is used to obtain a solution to the inner problem, y , that minimizes the residual over $\mathcal{K}_k(A, r_0)$.

GMRES was first introduced by Saad and Schultz in 1986 [9], for solving nonsymmetric square matrices. Its convergence properties were studied by van der Horst, in 1993 [11], and its behaviour for singular and nearly singular matrices by Brown and Walker, in 1994 [1]. In the following years, there has been a great interest in the theory and applications of GMRES-type² methods: Complementing Brown and Walker's work, Calvetti proposed a GMRES-type method for singular matrices, called Range Restricted GMRES (RRGMRES) [2]. The idea, with which we experiment, was to shift $\mathcal{K}_k(A, r_0)$ by the coefficient matrix A prior to the Arnoldi process. The GMRES algorithm is given below:

ALGORITHM 1: *GMRES*

1. *Start*: Choose x_0 . Let $r_0 = b - Ax_0$, $\beta = \|r_0\|_2$ and $V_1 = r_0/\beta$.

2. *Arnoldi Process*:

for $j = 1, 2, \dots$ until convergence **do**

$$h_{(i,j)} = V_i^T A V_j, \quad i = 1, 2, \dots, j,$$

$$\omega = A V_j - \sum_{i=1}^j h_{(i,j)} V_i,$$

$$h_{(j+1,j)} = \|\omega\|_2,$$

$$V_{j+1} = \omega / h_{(j+1,j)}.$$

end for

3. *Solve*: $\|\beta e_1 - H_{k+1,k} y\|_2$ for y , where $e_1 = [1, 0, \dots, 0]^T$.

4. *Form the approximated solution*: $x_k = x_0 + V_k y$.

Step 3 can be done with the help of QR factorization coupled with Givens rotation. For the RRGMRRES algorithm, we only have to replace $V_1 = r_0/\|r_0\|_2$ by $V_1 = Ar_0/\|Ar_0\|_2$ in Step 1.

GMRES is popularly used as a deblurring technique and often compared with other iterative methods [3]. It is also used as part of new hybrid methods [4] or coupled with preconditioners [13]. In recent years, GMRES is adapted to

²Throughout the paper, we use this term to mean GMRES and its variations.

solve various other applied problems, e.g. inverse blackbody radiation problem [12], or non-rotational CT [10]. However most of these works are limited to square matrices and are concluded using simulated data.

CG is arguably the most popular KS-method because it is easy to implement, computationally inexpensive and numerically stable when applied to square, symmetric and positive-definite systems. As we mentioned earlier, CGLS is the equivalent of CG applied to $A^T A x = A^T b$, where $A^T A$ is clearly symmetric but when an unmatched back projection, \hat{A}^T , is used (where $\hat{A}^T \neq A^T$), $\hat{A}^T A$ is **not** symmetric. So CGLS has difficulties giving reliable results, whereas GMRES encounters no problems. This is because GMRES is designed to work with nonsymmetric systems as opposed to CG. Another advantage of GMRES is that, in case of a well-conditioned coefficient matrix in a square system (that is, $m = n$ in (1)), GMRES works as a direct solver and returns the exact solution in n steps. When compared to CGLS [3], examples show that the residual is much smaller and GMRES requires less computational work.

One disadvantage of GMRES is its large memory requirements. To avoid this, Saad and Schultz suggested to restart the method after a certain number of iterations (parameter m , chosen by user), clear the memory, and use the m^{th} iterate x_m as the new initial vector x_0 , before the next cycle of iterations. In our experiments, we found that for normal matrices, restarted GMRES (or GMRES(m)) does not converge at all. Our results are omitted here but can be found in [5]. However, as we have already said, the applications to CT with typical accuracies of data, we do not need that many iterations before we are over-fitting. So the disadvantage of GMRES is not an issue for us when solving the CT problem.

In our strategies, we combine GMRES and RRGMRRES with other useful tools (e.g. Tikhonov regularisation). Various test matrices from MATLAB's gallery, Hansen's Regularization Tools and AIRTools [6], [7] are used, but we include only two test cases with 1% and 10% Gaussian noise in this paper. The computations are carried out using MATLAB 2013a with a personal laptop of specifications 1.7 GHz Intel Core i7.

NUMERICAL EXPERIMENTS

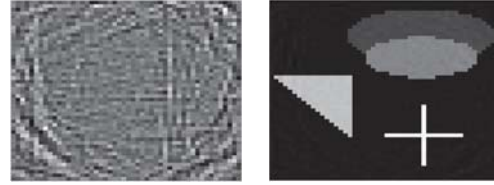
In this section, we test the accuracy and speed of GMRES, RRGMRRES and regularised GMRES methods. We have 8 strategies to compare and give results for two simulated cases: *Parallel 2D* and *FanBeam 2D*. The strategies are listed in Table I.

Test Case 1: Parallel 2D

This test case is generated using the `tomom(N, f)` function from Hansen's Regularization Tools [6]. N is chosen to be 50, i.e. matrix A has dimensions $N^2 \times N^2$. The images below are obtained for when b contains 1% noise, and the dataset is complete. For this and the next case, we assume we have no prior information about the object, so for the strategies involving Tikhonov, we take $L = I$ (and $\lambda = 10^{-4}$).

Strategy	Description
1) GMRES	<i>full</i> -GMRES algorithm, as stated in ALGORITHM 1.
2) GMRES+Tikhonov (outer)	GMRES algorithm applied to solve the Tikhonov system (3).
3) GMRES+Tikhonov (double)	GMRES algorithm applied to solve the Tikhonov system (3), and the <i>inner</i> problem in Step 3 is replaced by its Tikhonov alternative.
4) GMRES+Tikhonov +TV	GMRES algorithm applied to solve the Tikhonov system (3). The system is then plugged in TV to be solved (where the GMRES solution is used as the starting point).
5) RRGMRRES	GMRES algorithm where $V_1 = r_0/\ r_0\ $ is replaced by $V_1 = Ar_0/\ Ar_0\ $ in Step 1.
6) RRGMRRES+Tikhonov (outer)	RRGMRES algorithm applied to solve the Tikhonov system (3).
7) RRGMRRES+Tikhonov (double)	RRGMRES algorithm applied to solve both the 'outer' Tikhonov system (3) and the Tikhonov alternative of the <i>inner</i> problem in Step 3.
8) CGLS	The popular CGLS algorithm, run until the same tolerance value is satisfied.

TABLE I
THE STRATEGIES USED IN THE TEST CASES, FOLLOWED BY THEIR DESCRIPTIONS.



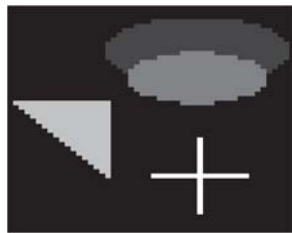
(h) RRGMRRES+Tikhonov (double) (i) CGLS (10^4 iterations)

Fig. 1. Results for *Parallel 2D* test problem with 1% noise.

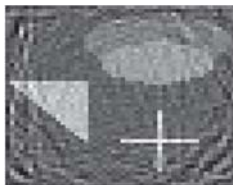
We see that the features of the exact image are distinguishable in the GMRES runs. GMRES gives much better results when we start with a problem where Tikhonov regularisation is already added. The results seem to improve further when a TV solution is computed following GMRES+Tikhonov.

RRGMRES gives similar results to GMRES, but when coupled with Tikhonov, it fails to give any reasonable solutions. This is because RRGMRRES is designed for singular or nearly singular systems, so it is not stable when the problem becomes 'less' ill-posed. We will not include RRGMRRES in the future experiments in our work.

Finally, we note that all the GMRES runs took less than N^2 iterations whereas CGLS reached the maximum iteration number, which was set by us as 10^4 .



(a) Exact image



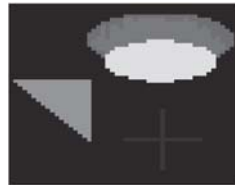
(b) GMRES



(c) GMRES+Tikhonov (outer)



(d) GMRES+Tikhonov (double)



(e) GMRES+Tikhonov+TV



(f) RRGMRRES



(g) RRGMRRES+Tikhonov (outer)

Test Case 2: *FanBeam 2D*

The second test case is generated by using the function `fanbeamtomo(N, angles, projections)` from Hansen's AIRTools Toolbox [7]. This time, N is chosen to be 200 (i.e. the image size is 200×200), the number of angles to be 180 (going from 0 to 179), and the number of projections to be 360. This means that the size of the geometry matrix, A , is $(180 \times 360) \times (200 \times 200) = 64800 \times 40000$. Additionally, we have added 10% Gaussian noise to the data vector to account for the experimental noise.

In the previous case we obtained some promising results with GMRES+Tikhonov (outer). However, for the strategies involving Tikhonov regularisation, the prior information was taken as $L = I$, and the regularisation parameter as $\lambda = 10^{-4}$. This means that starting GMRES with (3) is very close to starting GMRES with (2). So this time we run GMRES started with (2), and thus make a fairer comparison to CGLS (which is mathematically equivalent to CG started with (2)). We also compare these KS-methods to the popular iterative methods, Landweber and ART (the details of Landweber and ART algorithms can be found in [7]).



Fig. 2. Phantom image used for Test Case 2.

We run each method for 2000 iterations except for ART, which is not designed for large number of iterations. Comparing the solution norms with Landweber (at 2000th iteration), we believe that running 40 iterations of ART is a fair comparison to running 2000 iterations of GMRES. The reconstructed images are presented in Fig. 3.

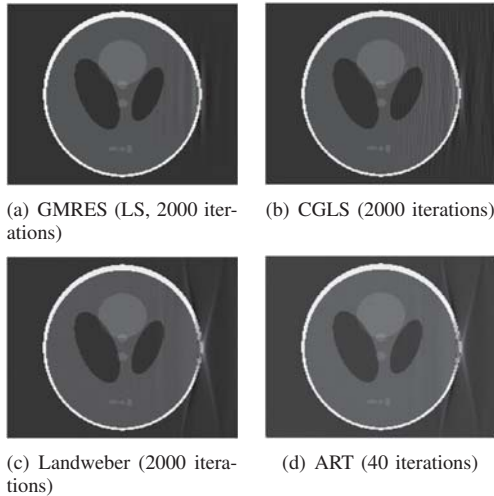


Fig. 3. Results for *FanBeam 2D* test problem with 10% noise.

Since both GMRES and CGLS are members of the KS-methods class, it is not surprising to see both reconstructions with the same features: Both Fig. 3(a) and 3(b) have converged to the phantom image well, except for the second half. This is simply because we have not iterated enough. Interestingly, after iterating for a long time, Landweber or ART are still not as close to the phantom image as GMRES or CGLS are. In fact, the image reconstructed with Landweber at 2000 iterations can be obtained with 39 iterations of GMRES, and 51 iterations of CGLS. This highlights the benefits of fast-converging methods.

When compared to CGLS, although it is difficult to see from the images, the noise is somewhat less in Fig. 3(a), and the lines on the second half of the image are less pronounced.

CONCLUSION AND FUTURE WORK

This paper briefly introduced the theory and algorithm of GMRES-type methods, as well as investigating the effects of combining GMRES and its variations with regularisation tools. A number of strategies were tested with simulated tomography data. The results achieved are promising and motivates a great number of possibilities, with which our implementation and reconstructions can be improved. They also provoke different ideas, which are all summarised and listed as future tasks below.

- 1) In our test cases, we have simulated a 2D parallel and fan beam experiments where 1% and 10% Gaussian noise was added to the tomographic data. However, to understand the benefits of regularised-GMRES, it is necessary that our strategies are tried with real datasets.
- 2) It is also necessary to apply these strategies to cases where some prior information is known and used in the

Tikhonov system. It is important to see how this would affect the reconstructed images.

- 3) Our test cases showed GMRES + Tikhonov (outer) or GMRES (LS) can be used as alternatives to CGLS. An important next step could be testing these algorithms when an unmatched back projection is used.
- 4) In addition to that, one must apply these strategies to limited data problems, were the data is obtained with fewer angles.
- 5) The algorithms we discussed can also be further optimised and parallelised for the reconstruction of larger datasets or 3D and 4D (space + time) tomography.
- 6) We must also test these ideas against the popular reconstruction methods such as CGLS and FDK to highlight the advantages and disadvantages of our strategies. CGLS and FDK are available to users at our facilities in the University of Manchester.
- 7) More detailed investigation into GMRES with normal equations (rather than applying the algorithm to $A^T Ax = A^T b$) is needed. We need a clearer picture of how that can affect the convergence when there is noise in data.
- 8) Finally, one more task we can do is to make use of appropriate preconditioners in the GMRES strategies to improve the convergence properties (especially for the real data case).

ACKNOWLEDGEMENT

This project is funded by BP through the ICAM framework.

REFERENCES

- [1] P.N. Brown and H.F. Walker. GMRES on (nearly) singular systems. *SIAM J. Matrix Anal. Appl.*, 18:37–51, 1994.
- [2] D. Calvetti, B. Lewis, and L. Reichel. GMRES-type methods for inconsistent systems. *Linear Algebra Appl.*, 316:157–169, 2000.
- [3] D. Calvetti, B. Lewis, and L. Reichel. On the choice of subspace for iterative methods for linear discrete ill-posed problems. *Int. J. Appl. Math. Comput. Sci.*, 1:1069–1092, 2001.
- [4] D. Calvetti, B. Lewis, and L. Reichel. A hybrid GMRES and TV-norm based method for image restoration, 2002.
- [5] S.B. Coban. Regularised GMRES-type methods for x-ray computed tomography. Technical report, School of Mathematics, University of Manchester, United Kingdom, September 2013. Available on request.
- [6] P.C. Hansen. Regularisation tools version 4.0 for MATLAB 7.3. *Numer. Algorithms*, 46:189–194, 2007.
- [7] P.C. Hansen and M. Saxild-Hansen. AIR Tools - a MATLAB package of algebraic iterative reconstruction methods. *Journal of Computational and Applied Mathematics*, 236:pp. 2167–2178, 2012.
- [8] A.N. Krylov. On the numerical solution of the equation by which the frequency of small oscillations is determined in technical problems. *Izv. Akad. Nauk SSSR Ser. Fiz.-Mat.*, 4, 1931.
- [9] Y. Saad and M.H. Schultz. GMRES: a generalized minimal residual algorithm for solving nonsymmetric linear systems. *SIAM J. Sci. Statist. Comput.*, 7:856–869, 1986.
- [10] Z. Sun and W.C. Karl. A non-rotational approach to computed tomography. *Poster available online: http://www.censsis.neu.edu/RICC/2010/posters/pdf/HSD_p7.pdf*, 2010.
- [11] H.A. van der Vorst and C. Vuik. The superlinear convergence of behaviour of GMRES. *J. Comput. Appl. Mathematics*, 48:327–341, 1993.
- [12] J. Wu and Z. Ma. A regularised GMRES method for inverse blackbody radiation problem. 2012.
- [13] J.F. Yin and K. Hayami. Preconditioned GMRES methods with incomplete Givens orthogonalization method for large sparse least squares problems. *J. of Comput. and Appl. Mathematics*, 226:177–186, 2009.

Performance evaluation of OS-SPS and CG for differential phase-contrast X-ray tomography

Andreas Fehringer, Bernhard Brendel, Dieter Hahn, Peter B. Noël, Franz Pfeiffer, and Thomas Koehler

Abstract—Grating-based phase-contrast computed tomography (PCCT) is a promising new imaging approach perfectly suited for revealing details of low absorption contrast at high resolution. The acquisition method provides apart from the usual absorption image a differential image of the phase shift and an ultra-small-angle scatter signal, called darkfield. Previously we presented a statistical iterative reconstruction framework to work with differential projections. We found that not only the object function has to be modified but also the solver needs to be optimized for optimal convergence. We illustrate that, in contrast to absorption imaging, the non-linear Conjugate Gradient algorithm (CG) clearly outperforms the commonly used ordered-subset Separable Paraboloidal Surrogates (OS-SPS). Even without any special adaptations, the CG converges two orders of magnitude faster for both maximum likelihood and penalized likelihood maximization. Our fast iterative approaches allow accessing new fields of application for PCCT.

I. INTRODUCTION

X-ray PCCT is a recent technique combining standard X-ray imaging with a Talbot-Lau interferometer. It allows accessing phase [1]–[4] and darkfield [5]–[8] information. The differential phase image unveils great insights into soft-tissue [9], [10] making PCCT a highly sensitive alternative to classical X-ray imaging. Clinical relevance is expected soon [11]–[15]. The high sensitivity is mainly due to the fact that the phase shift increases linearly with the thickness of the sample in contrast to the exponential increase for attenuation-based imaging. Previously we have shown that this circumstance delivers great results, e. g. for biological samples, but also introduces phase-wrapping artifacts at interfaces between materials with a big gradient of the index of refraction. In contrast to absorption CT, where saturation effects usually only occur for highly dense materials like metal [16], phase-wrapping artifacts can already be seen between soft-tissue and bone. Hahn et al. [17] demonstrated that iterative reconstruction techniques are able to successfully address this problem.

The convergence speed of an optimization algorithm depends strongly on the features of the problem that needs to be solved. It has also been observed that algorithms

A. Fehringer, D. Hahn and F. Pfeiffer are with the Chair of Biomedical Physics, Technische Universität München, Munich, Germany.

B. Brendel and T. Koehler are with Philips Technologie GmbH, Innovative Technologies, Hamburg, Germany. T. Koehler is moreover with the Institute for Advanced Study, Technische Universität München, Munich, Germany.

P.B. Noël is with the Department of Radiology, Technische Universität München, Munich, Germany.

which perform well for transmission tomography do not automatically perform well for on differential data [18]–[20]. Thus, there is a need to compare different optimization algorithms with respect to their convergence speed, which is the goal of this work.

We will first state the problem introducing the objective function for differential phase contrast tomography, the solvers investigated and a mathematical test phantom. Second, we will compare the performance and image quality of ordered-subset Separable Paraboloidal Surrogates (OS-SPS), which is widely used for iterative reconstruction in absorption computed tomography [21], [22], with those of the non-linear Conjugate Gradient (CG).

II. THE PROBLEM

On the contrary to attenuation CT, the phase-shift information in PCCT is only available in differential form. Consequently, the objective function and the whole optimization have to be adapted [23].

A. The objective function

Maximum likelihood reconstruction requires an objective function L consisting of a data term and a penalty term R . The data term ensures the consistency with the measured projections l_i by using a forward model \mathbf{A} on the current guess of the reconstructed volume δ . The regularization enforces additional constraints in order to receive a unique solution to the ill-posed problem, especially for noisy data.

The objective function for PCCT with a Gaussian noise model can be written as [23]

$$L = -\frac{1}{2} \sum_i \frac{1}{\sigma_i^2} (l_i - [\partial \mathbf{A} \delta]_i)^2 - \beta R(\delta) \quad (1)$$

where σ_i are optional weights for the measured data and β is the strength of the regularization. Note, the differential operator ∂ enables the reconstruction framework to work with differential data.

The penalties $R(\delta)$ used in the experimental evaluation below are the quadratic potential function

$$R_Q(\delta) = \sum_i \sum_{j \in \mathcal{N}_i} w_{ij} (\delta_i - \delta_j)^2$$

for homogeneous smoothing and the Huber potential function [24]

$$R_H(\delta, \gamma) = \sum_i \sum_{j \in \mathcal{N}_i} w_{ij} \begin{cases} \frac{(\delta_i - \delta_j)^2}{2\gamma^2} & \text{for } |\delta_i - \delta_j| \leq \gamma \\ \frac{|\delta_i - \delta_j|}{\gamma} - \frac{1}{2} & \text{else} \end{cases}$$

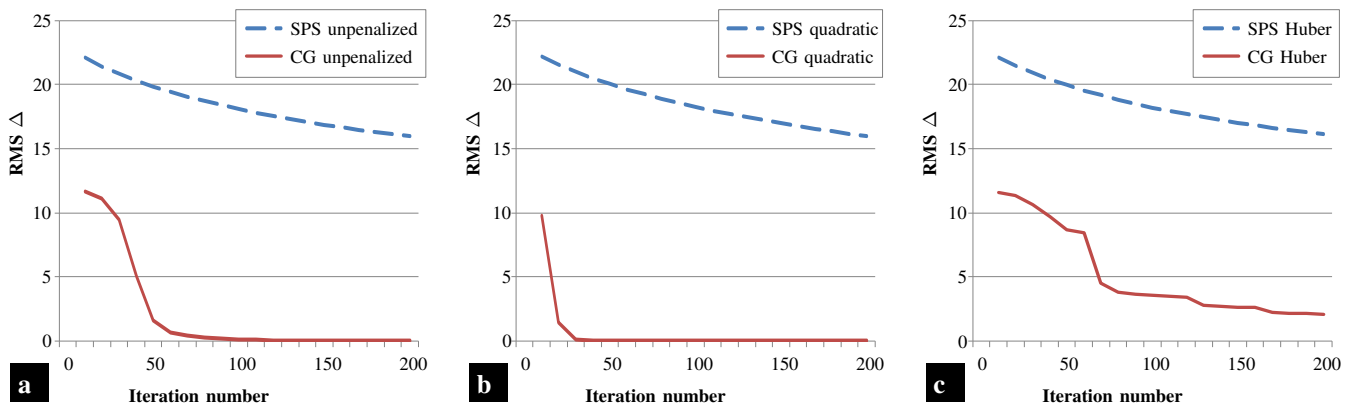


Figure 1. **The Root Mean Square error (RMS Δ) after different number of iterations OS-SPS and CG for differential phase data.** RMS Δ is a measure for how well the reconstruction fits the ideal phantom values and thus for the convergence of the algorithm. Subfigure **a** shows the progress for an unpenalized differential-phase log-likelihood, **b** for quadratic and **c** for non-quadratic Huber regularization.

With respect to RMS Δ , the CG clearly outperforms OS-SPS for all three cases in preciseness and speed of convergence. In contrast to the behavior of OS-SPS which is about equal for a, b, and c, quadratic regularization further decreases the number of iterations required for CG. The Huber regularization in the last test makes the log-likelihood function non-quadratic and thus the convergence more unsteady as well as the overall result a little less precise.

for edge-preserving smoothing. Both compute the gradient for each voxel i to all of its neighbors \mathcal{N}_i weighted with the corresponding spacial distance w_{ij} . The threshold γ in the Huber potential marks the transition from quadratic to linear behavior.

B. The investigated solvers

1) *CG*: is a general-purpose optimization method based on conjugate search directions with a variable step-size. For non-linear problems—the penalized likelihood with the Huber function in our case—CG can be extended with a line search [25]. Furthermore, it has been shown that CG can be optimized for standard iterative tomography by using appropriate preconditioning [26]. The drawback of the non-linear CG is that for each iteration the line search requires an additional forward projection of the whole dataset. We always use the non-linear CG which behaves exactly like the linear CG for purely quadratic objective functions.

2) *OS-SPS*: was developed and optimized especially for log-likelihood maximization. It operates on a paraboloidal surrogate function which tangentially touches L in each iteration. A full iteration of OS-SPS is about as computationally expensive as one iteration of linear CG involving a forward and a back projection. However, SPS can be divided into fast subiterations executing on very sparsely sampled subsets making the convergence significantly faster but also at the cost that the convergence is longer guaranteed. One iteration always denotes a complete set of subiterations in this paper. [21]

C. Experimental evaluation

The test sample is a cylindrical mathematical phantom, 10 cm in diameter, with a refractive index according to the material *breast mammary adult 1* defined in [27]. It contains 10 inhomogenities with a diameter of 5 mm each and values in the range of $\pm 6.5\%$ the background value. The differential

phase line integrals were simulated for 600 views in parallel-beam geometry and a detector of 256 elements with a total width of 11 cm. Noise was not included in the simulation.

The weights σ_i in equation (1) were chosen to be one and the regularization parameter β was optimized for suppressing aliasing artifacts in the mathematical phantom. We used 30 subsets for OS-SPS, i.e. 20 views per subset.

III. THE PERFORMANCE OF OS-SPS AND CG

In order to measure the performance of OS-SPS and CG, we reconstructed the test phantom described above in several ways. There are two purely quadratic cases for both solvers, one involving no and the other quadratic regularization. The third case is non-quadratic with Huber regularization. We always recorded the root mean square error (RMS Δ) shown in figure 1 and the reconstructed image after each iteration shown in figures 2 and 3 on page 4.

A. Results for phase data

For all three PCCT test cases, we recognized a drastically slower convergence for OS-SPS than for CG. The number of iterations required for a comparable image quality is two orders of magnitude higher. We stopped the reconstruction after 2000 iterations, although OS-SPS had not converged to a satisfying image quality.

1) *Without regularization*: figure 2 shows the reconstruction results for CG and OS-SPS after different numbers of iterations. The images after 10 and 20 iterations of CG nicely point out the character of the differential input data. The position of sharp edges, i.e. high-frequency features, can be extracted immediately. As shown in figure 1a, the low-frequency information can only be retrieved after ~ 50 iterations. Additional iterations do not significantly decrease the error. The overall high RMS Δ can be explained by the incorrect low frequencies appearing in early iterations.

2) *With quadratic regularization:* The quadratic regularization in the second fully quadratic test case helped both algorithms to recover the low frequencies faster. The CG reconstruction perfectly converged after 30 iterations as depicted by the error plot in 1b. After about 1000 iterations the OS-SPS manages to recover the border of the cylinder which was not the case in the previous two tests. However, even the 2000th iteration suffers also here from low a contrast and incorrect absolute values.

3) *With Huber regularization:* The last performance test was carried out for the penalized log-likelihood function with Huber regularization. This is also the configuration which is most suitable for reconstructions on naturally noise-affected data. As figure 3 shows, both algorithms require more time to obtain image results comparable to the two earlier cases. CG is about two times slower and has difficulties to recover the absolute values which can also be seen in the large tail of the error plot in figure 3. The visual image quality does not further improve after the first 100 iterations.

B. Results for attenuation data

We provide this section for completeness, but do not show visual results, since reconstruction with CS and OS-SPS was already investigated for attenuation data [22], [26]. In the quadratic case CG results in smaller RMS Δ after about 20 iterations, but the results suffer from overshooting effects at the border of the cylinder. OS-SPS provides visually good results already after 10 iterations. In the non-quadratic case, the OS-SPS constantly provides smaller errors. We got the first visually pleasing result after about 50 iterations.

IV. CONCLUSION

Iterative approaches for PCCT have to deal with the differential character of the phase signal. In this work we investigated the maximization of the corresponding objective function. We analyzed three test cases with a mathematical phantom: the unpenalized log-likelihood, log-likelihood with quadratic regularization and with Huber regularization, whereas the latter has a non-quadratic objective function. The convergence measured as the root mean square error over the iterations clearly illustrated that for one of the most common solver in attenuation CT, the OS-SPS, the likelihood function for differential phase contrast is an adverse problem. Non-linear CG, in contrast, converges over two orders of magnitude faster and returns a significantly improved visual result if the iterations are stopped early. We successfully showed that fast iterative reconstruction is possible for differential PCCT.

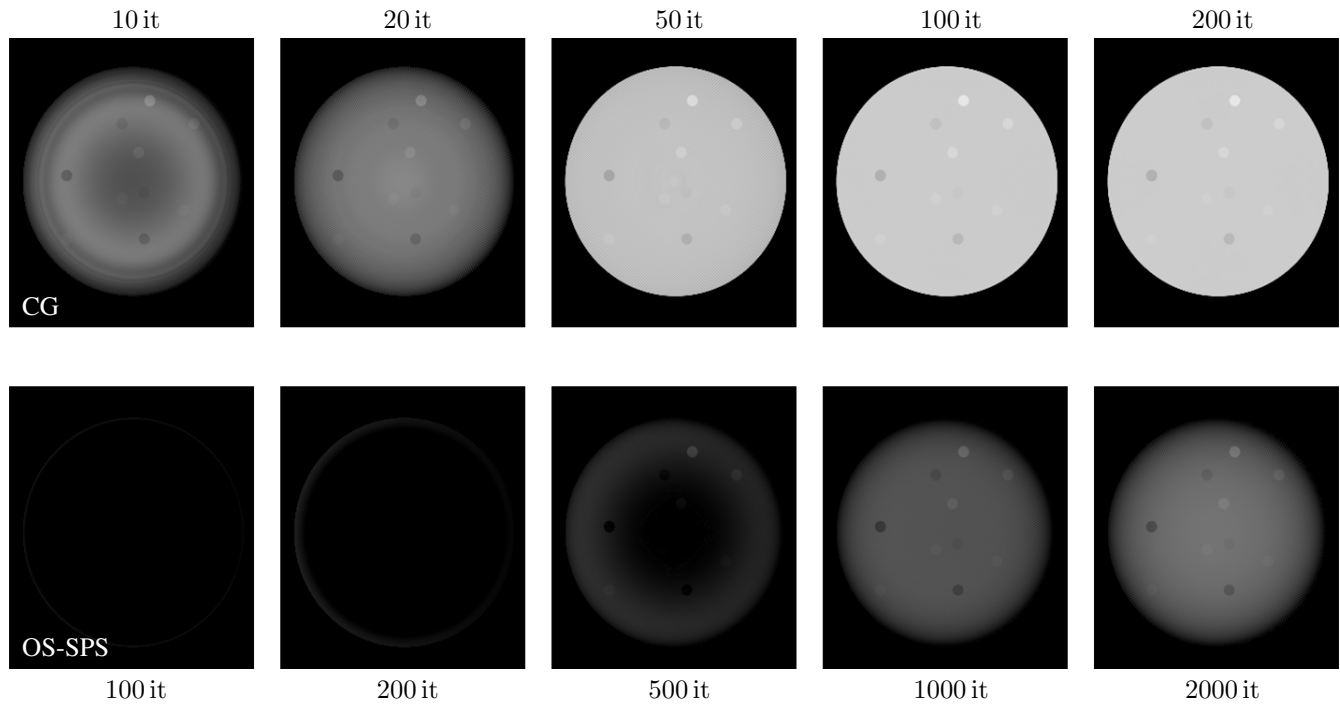


Figure 2. **The reconstruction results for differential phase data after different numbers of iterations CG and OS-SPS without penalty.** The sample shown is a mathematical test phantom consisting of different cylinders. The results in the upper row show that CG converges more than two orders of magnitude faster than OS-SPS in the lower row. CG converged after about 50 iterations whereas OS-SPS was aborted after 2000 iterations.

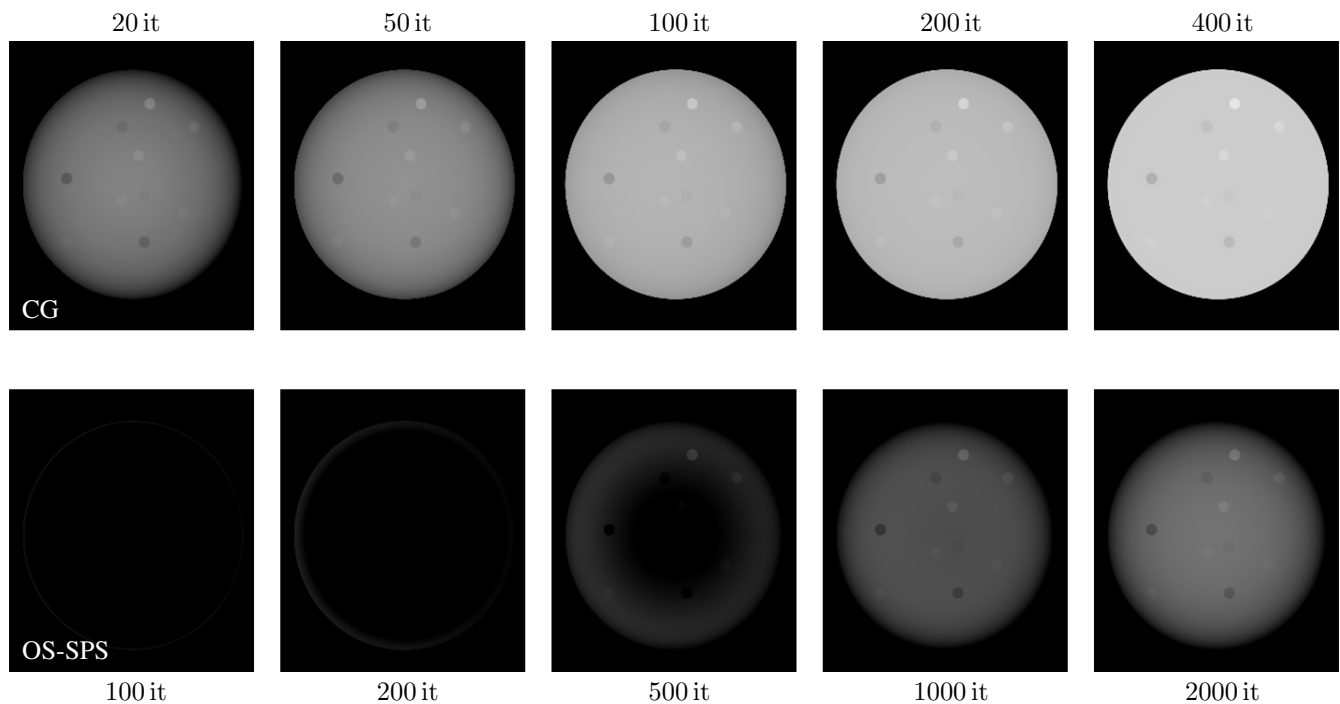


Figure 3. **The reconstruction results for differential phase data CG and OS-SPS with Huber penalty.** The additional Huber penalty does not change the general trend of CG (upper row) converging much faster as OS-SPS (lower row). The overall convergence is slower compared to figure 2 because the Huber term makes the likelihood function non-quadratic.

REFERENCES

- [1] A. Momose, S. Kawamoto, I. Koyama, Y. Hamaishi, K. Takai, and Y. Suzuki, "Demonstration of X-ray Talbot interferometry," *Japanese journal of applied physics part 2 letters*, vol. 42, no. 7B; ISSU 393, pp. L866–L868, 2003.
- [2] T. Weitkamp, A. Diaz, C. David, F. Pfeiffer, M. Stampanoni, P. Cloetens, E. Ziegler *et al.*, "X-ray phase imaging with a grating interferometer," *Optics express*, vol. 13, no. 16, pp. 6296–6304, 2005.
- [3] A. Momose, W. Yashiro, Y. Takeda, Y. Suzuki, and T. Hattori, "Phase tomography by X-ray Talbot interferometry for biological imaging," *Japanese journal of applied physics*, vol. 45, p. 5254, 2006.
- [4] F. Pfeiffer, T. Weitkamp, O. Bunk, and C. David, "Phase retrieval and differential phase-contrast imaging with low-brilliance X-ray sources," *Nature physics*, vol. 2, no. 4, pp. 258–261, 2006.
- [5] F. Pfeiffer, M. Bech, O. Bunk, P. Kraft, E. F. Eikenberry, C. Brönnimann, C. Grünzweig, and C. David, "Hard-X-ray dark-field imaging using a grating interferometer," *Nature materials*, vol. 7, no. 2, pp. 134–137, 2008.
- [6] W. Yashiro, Y. Terui, K. Kawabata, and A. Momose, "On the origin of visibility contrast in x-ray Talbot interferometry," *Optics express*, vol. 18, no. 16, pp. 16 890–16 901, 2010.
- [7] G. Potdevin, A. Malecki, T. Biernath, M. Bech, T. H. Jensen, R. Feidenhans, I. Zanette, T. Weitkamp, J. Kenntner, J. Mohr *et al.*, "X-ray vector radiography for bone micro-architecture diagnostics," *Physics in medicine and biology*, vol. 57, no. 11, p. 3451, 2012.
- [8] A. Malecki, G. Potdevin, and F. Pfeiffer, "Quantitative wave-optical numerical analysis of the dark-field signal in grating-based x-ray interferometry," *EPL (europhysics letters)*, vol. 99, no. 4, p. 48001, 2012.
- [9] F. Pfeiffer, O. Bunk, C. David, M. Bech, G. Le Duc, A. Bravin, and P. Cloetens, "High-resolution brain tumor visualization using three-dimensional x-ray phase contrast tomography," *Physics in medicine and biology*, vol. 52, no. 23, p. 6923, 2007.
- [10] D. Hahn, P. Thibault, M. Bech, M. Stockmar, S. Schleede, I. Zanette, A. Rack, T. Weitkamp, A. Sztrókay, T. Schlossbauer *et al.*, "Numerical comparison of X-ray differential phase contrast and attenuation contrast," *Biomedical optics express*, vol. 3, no. 6, p. 1141, 2012.
- [11] T. Donath, F. Pfeiffer, O. Bunk, C. Grünzweig, E. Hempel, S. Popescu, P. Vock, and C. David, "Toward clinical x-ray phase-contrast CT: demonstration of enhanced soft-tissue contrast in human specimen," *Investigative radiology*, vol. 45, no. 7, pp. 445–452, 2010.
- [12] M. Stampanoni, Z. Wang, T. Thüning, C. David, E. Roessl, M. Trippel, R. A. Kubik-Huch, G. Singer, M. K. Hohl, and N. Hauser, "The first analysis and clinical evaluation of native breast tissue using differential phase-contrast mammography," *Investigative radiology*, vol. 46, no. 12, pp. 801–806, 2011.
- [13] A. Tapfer, M. Bech, A. Velroyen, J. Meiser, J. Mohr, M. Walter, J. Schulz, B. Pauwels, P. Bruyndonckx, X. Liu *et al.*, "Experimental results from a preclinical X-ray phase-contrast CT scanner," *Proceedings of the National Academy of Sciences*, vol. 109, no. 39, pp. 15 691–15 696, 2012.
- [14] A. Sztrókay, J. Herzen, S. D. Auweter, S. Liebhardt, D. Mayr, M. Willner, D. Hahn, I. Zanette, T. Weitkamp, K. Hellerhoff *et al.*, "Assessment of grating-based X-ray phase-contrast CT for differentiation of invasive ductal carcinoma and ductal carcinoma in situ in an experimental ex vivo set-up," *European Radiology*, vol. 23, no. 2, pp. 381–387, 2013.
- [15] H. Daerr, T. Koehler, U. van Stevendaal, G. Martens, and E. Roessl, "A scanning type DPCI system: System design, processing, and experimental results," in *Proceedings of the XNPIG 2014*, vol. 2, 2014, p. 34.
- [16] B. De Man, J. Nuyts, P. Dupont, G. Marchal, and P. Suetens, "Metal streak artifacts in X-ray computed tomography: a simulation study," in *Nuclear Science Symposium, 1998. Conference Record. 1998 IEEE*, vol. 3. IEEE, 1998, pp. 1860–1865.
- [17] D. Hahn, P. Thibault, A. Fehringner, M. Bech, P. B. Noël, and F. Pfeiffer, "Bone artifact reduction in differential phase-contrast CT," in *Proceedings of the Fully3D 2013*, vol. 12, 2013, pp. 416–419.
- [18] T. Koehler, B. Brendel, and E. Roessl, "Iterative reconstruction for differential phase contrast imaging: theory and initial results," in *Proceedings of the Fully3D 2011*, vol. 11, 2011, pp. 403–406.
- [19] M. Nilchian, C. Vonesch, P. Modregger, M. Stampanoni, and M. Unser, "Fast iterative reconstruction of differential phase contrast X-ray tomograms," *Optics express*, vol. 21, no. 5, pp. 5511–5528, 2013.
- [20] M. Nilchian, C. Vonesch, S. Lefkimmiatis, P. Modregger, M. Stampanoni, and M. Unser, "Constrained regularized reconstruction of X-ray-DPCI tomograms with weighted-norm," *Optics Express*, vol. 21, no. 26, pp. 32 340–32 348, 2013.
- [21] H. Erdogan and J. A. Fessler, "Ordered subsets algorithms for transmission tomography," *Physics in medicine and biology*, vol. 44, no. 11, p. 2835, 1999.
- [22] J. A. Fessler, "Statistical image reconstruction methods for transmission tomography," *Handbook of medical imaging*, vol. 2, pp. 1–70, 2000.
- [23] T. Koehler, B. Brendel, and E. Roessl, "Iterative reconstruction for differential phase contrast imaging using spherically symmetric basis functions," *Medical physics*, vol. 38, p. 4542, 2011.
- [24] P. J. Huber, *Robust Statistics*. New York: Wiley, 1981.
- [25] J. R. Shewchuk, "An introduction to the conjugate gradient method without the agonizing pain," 1994.
- [26] J. A. Fessler and S. D. Booth, "Conjugate-gradient preconditioning methods for shift-variant PET image reconstruction," *Image Processing, IEEE Transactions on*, vol. 8, no. 5, pp. 688–699, 1999.
- [27] "Proton and neutron interaction data for body tissues," International Commission on Radiation Units and Measurements, Bethesda, MD, Tech. Rep., 1992.

Estimation of Missing Fan-Beam Projections using Frequency Consistency Conditions

Marcel Pohlmann, Martin Berger, Andreas Maier, Joachim Hornegger and Rebecca Fahrig

Abstract—Reducing radiation dose is a crucial problem in computed tomography. One approach is to undersample the projections and compensate for the missing ones using an estimation method. In this paper, we introduce a novel method to estimate missing projections in fan-beam geometry. The estimation is done by iteratively enforcing consistency conditions of the sinogram’s Fourier-Transform. The completed sinogram can be used for reconstruction using filtered backprojection algorithm to obtain images with less artifact. A comparison of our method to other state-of-the-art compensation techniques shows promising results.

Index Terms—Computed Tomography, Sparse Image Reconstruction, Projection Estimation, Spectral Analysis

I. INTRODUCTION

In X-ray computed tomography projections are sampled along a trajectory around the patient. The detector read-out of each view is written row-wise as a set of 1-D projection images, also referred to as sinogram.

In order to reduce the radiation exposure of a patient during a CT scan, the projections can be undersampled by measuring only a subset of projections. Using filtered backprojection on an undersampled sinogram might produce streak artifacts in the resulting image. To avoid those artifacts a compensation for the missing projections is needed.

Depending on the different imaging geometry every sinogram underlies data consistency conditions, e.g. the well known Ludwig-Helgason consistency condition of the two-dimensional Radon transform. These conditions have already been utilized in the field of image reconstruction from a limited number of view angles [1].

But there are also consistency conditions in the sinogram’s Fourier Space, as Edholm et al. showed by their derivation of the frequency-distance relationship for the parallel-beam sinogram [2]. This relationship attributes contributions in sinogram-frequency space to points in the object at fixed distances along the projections. Mazin et al. performed a similar derivation to arrive at corresponding properties of a fan-beam sinogram [3]. In the parallel-beam case as well as the fan-beam case, the derived property is a zero-energy region in the Fourier transform of the full scan sinogram.

In this paper, we present a method that estimates missing projection data of undersampled fan-beam sinograms by utilizing the frequency condition mentioned above.

Rebecca Fahrig is with the Department of Radiology, Stanford University, Stanford, CA, USA. Marcel Pohlmann, Martin Berger, Andreas Maier and Joachim Hornegger are with the Pattern Recognition Lab, Department of Computer Science, Friedrich Alexander Universität Erlangen-Nürnberg. This work has been supported by the Research Training Group 1774 “Heterogeneous Image Systems”, funded by the German Research Foundation (DFG).

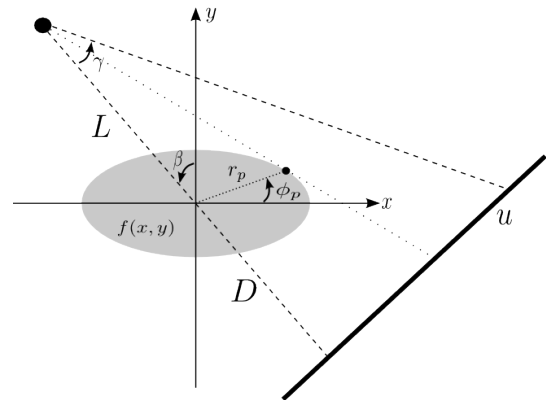


Figure 1. Fan-beam CT geometry with equally-spaced detector used for the estimation of unknown projections

II. METHOD

A. Background

Our method for the estimation of the missing data is iterative and based on the consistency-conditions of the two-dimensional Fourier transform of the fan-beam sinogram. Iterative methods similar to ours have previously been applied in a variety of other applications where a complete set of data is not available in measurement space but prior knowledge is available in a second space that is related to the first by a simple transformation, in this case the two-dimensional Fourier transformation. This type of iterative algorithm has successfully been implemented in image restoration problems such as band-limited spectral analysis [4], [5] and spectral deconvolution [6], [7]. Another estimation method for SPECT based on the consistency-condition of the two-dimensional Fourier transform of the parallel-beam sinogram is discussed in [8].

B. Theory

Using the geometry shown in Fig. 1 we denote the distance from the origin of a point of interest as r_p and its angle from the x -axis as ϕ_p , the source-to-isocenter distance as L and the isocenter-to-detector distance as D . We can model the object function $f(x, y)$ as a set of many delta function points. Forward projecting each of them we get sinograms each with a single sinusoidal curve. Adding all obtained sinograms of the single points up to one image will give us the observed sinogram. The derivations in [2] and [3] use this decomposition of the sinogram to obtain properties from its Fourier transform. Applying the two-dimensional Fourier

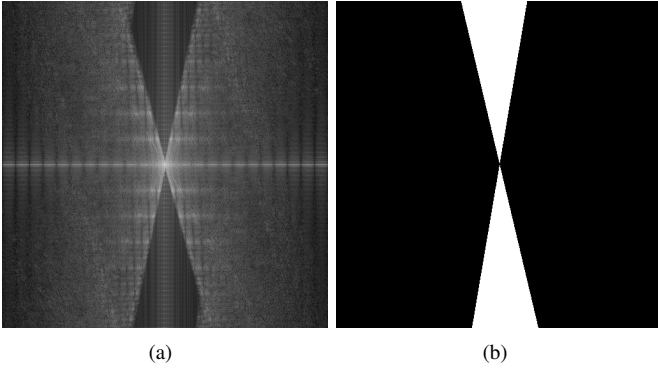


Figure 2. (a) Appearance of the Fourier transform of a fan-beam sinogram and (b) the corresponding double-wedge filter

transform on a sinogram of an arbitrary delta function will give us

$$P(\zeta, k) \approx e^{-jk(\phi_p + \frac{\pi}{2})} J_k \left((k - (L + D)\zeta) \frac{r_p}{L} \right), \quad (1)$$

where J_k denotes a Bessel function of the first kind of order k . Because Bessel functions of order k rapidly tend to zero if the argument is less than k , Eq. (1) implies that the Fourier transform is approximately zero for all frequencies (ζ, k) such that

$$\left| \frac{k}{k - \zeta(L + D)} \right| > \frac{r_p}{L}. \quad (2)$$

The Bessel function in Eq. (1) is an approximation which was determined intuitively but validated empirically in [3]. Eq. (2) parametrizes a double-wedge region in the frequency domain of the sinogram, containing negligible coefficients. The boundary of this region is described by the equation $\zeta = (k/(L + D))(1 \pm L/r_p)$. The single points of the object within a smaller radius have a larger double-wedge region than single points located at the maximum radius of our object. Since we are interested in restoring the complete sinogram and not only a region of interest, we interpret r_p as the maximum radius of the object. We can now design a fan-beam double-wedge filter for the estimation of the missing lines in our algorithm. Fig. 2 (a) shows the Fourier transform of a sinogram of an object with $r_p = 200$ mm, the double-wedge region can already be identified and (b) shows the corresponding double-wedge filter.

Modeling the observed sinogram $p(u, \beta)$ as a point-wise multiplication of the non-undersampled sinogram $p_{ideal}(u, \beta)$ with a missing projection mask $w(u, \beta)$, which contains zero-rows if the projection is not measured and ones otherwise, will initially violate the condition of the zero-energy double-wedge region. We can use the designed double-wedge filter to enforce the condition iteratively in the estimation algorithm by cutting of the high frequencies corresponding to the missing projections.

Eq. (1) describes the double wedge region in a continuous manner without respecting discretization problems. For this reason we applied a morphological erosion operation in the direction of ζ on the double-wedge filter. After this pre-processing we can be sure that we will not affect any frequencies that do not correspond to the frequency condition.

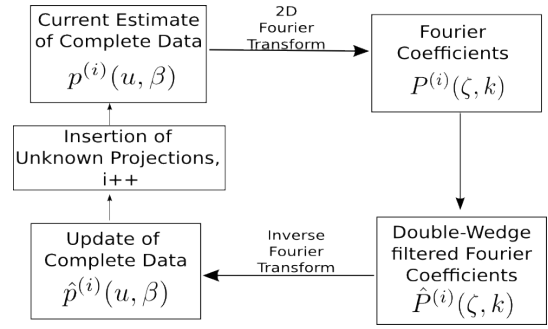


Figure 3. Flow diagram of the iterative double-wedge filtering

C. Algorithm

The main idea of the estimation algorithm is to alternate between the frequency domain to apply the double-wedge filter and the spatial domain to insert the current estimation of the missing projections.

In an initialization step, the observed sinogram has to be extended by the missing projections. Filling the missing rows with the mean value of the observed sinogram turned out to be the best choice. In that way the energy loss caused by the filtering is compensated. It is important to choose the initial values in a way that the Fourier coefficients outside the double-wedge region are not affected, because the algorithm does not perform on these coefficients.

In one iteration step $p^{(i)}(u, \beta)$, the current estimate of the complete sinogram data is zero-padded to the image size of the next power of two and Fourier transformed in order to get the Fourier coefficients $P^{(i)}(\zeta, k)$ with an increased resolution of the frequencies. At this point the eroded double-wedge filter is applied to enforce the condition of zero-energy and eliminate high frequencies referring to the missing projections. The double-wedge filtered Fourier coefficients $\hat{P}^{(i)}(\zeta, k)$ are inverse Fourier transformed to receive a updated version of the complete sinogram $\hat{p}^{(i)}(u, \beta)$ which holds new estimates of the missing projections.

Since the double-wedge filter affects the complete sinogram, we insert only the estimation of the missing projections from $\hat{p}^{(i)}(u, \beta)$ into the sinogram of the next iteration step instead of using the complete data set of the inverse Fourier transform. The iteration procedure, where i represents the current iteration step is repeated until a specific convergence criterion is reached or a fixed number of iterations are performed. The iterative procedure of the algorithm is illustrated in the flow diagram shown in Fig. 3.

Source-to-isocenter distance, L	598.5 mm
Detector-to-isocenter distance, D	598.5 mm
# of views over 2π	67, 134
# of detector channels	500
Detector channel spacing	1.0 mm
Maximum radius of object, r_p	200 mm
Kernel width for erosion	7
Resampling factor	2

Table I
SIMULATION PARAMETERS

III. RESULTS

We evaluated the algorithm on simulated data, with a phantom size of 512×512 px, which is shown in Fig. 4 (a). The maximum radius of the overall object extend is $r_p = 200$ mm. In a first experiment, 67 projections, over a full-scan trajectory of 2π , are measured and resampled by the factor of two in order to achieve 134 views for the reconstruction. The results related to this parametrization are shown in Fig. 4. In a second experiment, 134 projections, over the same trajectory, are measured and resampled up to 268 views. The results are shown in Fig. 5. The wedge filter was pre-processed by an morphological erosion operation with a kernel width of 7 px, in the direction of ζ , before applying it on the Fourier coefficients. Additional simulation parameters related to the geometry are listed in Tab. I.

In both experiments, we applied our method on the sparse data with a fixed number of 50 iterations. The result of the iterative double-wedge filter performing on an input number of 67 views is shown in Fig. 4 (c) and performing on an input number of 134 views in Fig. 5 (c). We compared the results to the reconstructions without any compensation and three other estimation techniques: Linear interpolation in the direction of β , Iterative Reconstruction-Reprojection (IRR) [9], where we achieved the best image quality with 3 iterations in the case of 67 projections and 4 iterations in the case of 134 projections, and Spectral Deconvolution [6] with a maximum number of 100 iterations. In all reconstruction results negative values resulting from the FBP have been set to zero, furthermore all pixel values outside of a region of interest corresponding to the detector length have been set to zero as well. We used a Shepp-Logan kernel within the algorithm of IRR and a Ram-Lak kernel for FBP of all final reconstructions. The intensity window for displaying the reconstruction results was chosen to be in the range of 0 to 1 for all images.

In addition to the images of the reconstructions, we calculated the error of the reconstruction with respect to the phantom using normalized root mean square error (NRMSE):

$$NRMSE = \frac{1}{x_{max} - x_{min}} \sqrt{\frac{\sum_{t=0}^{N-1} (x_{1,t} - x_{2,t})^2}{n}}, \quad (3)$$

where x_{min} and x_{max} denote the minimum and maximum intensity value of the phantom. The pixels belonging to the image of the phantom are represented by x_1 and the pixels belonging to the reconstruction are represented by x_2 . The NRMSE for the different estimation methods is listed in Tab. II. We implemented the methods using CONRAD [10], a software framework for cone-beam imaging in radiology. To get a picture of the run-time complexity for the methods used in this evaluation, we added the run-time of the estimation methods in Tab. II. Note that the computation of the results for all methods was CPU driven (Intel Xeon X5450, 16 GB RAM).

Compensation Method	NRMSE		Runtime	
	64	134	67	134
Without Compensation	8.02%	4.79%	-	-
Double-Wedge filter	5.60%	3.29%	4.68 s	8.8 s
Linear Interpolation	6.36%	3.61%	-	-
Spectral Deconvolution	6.89%	4.14%	16.55 s	34.12 s
Iterative Reprojection	7.08%	3.69%	234.49 s	467.54 s

Table II
NORMALIZED ROOT MEAN SQUARE ERROR (NRMSE) AND RUN-TIME OF
EVALUATED METHODS FOR DATA COMPLETION

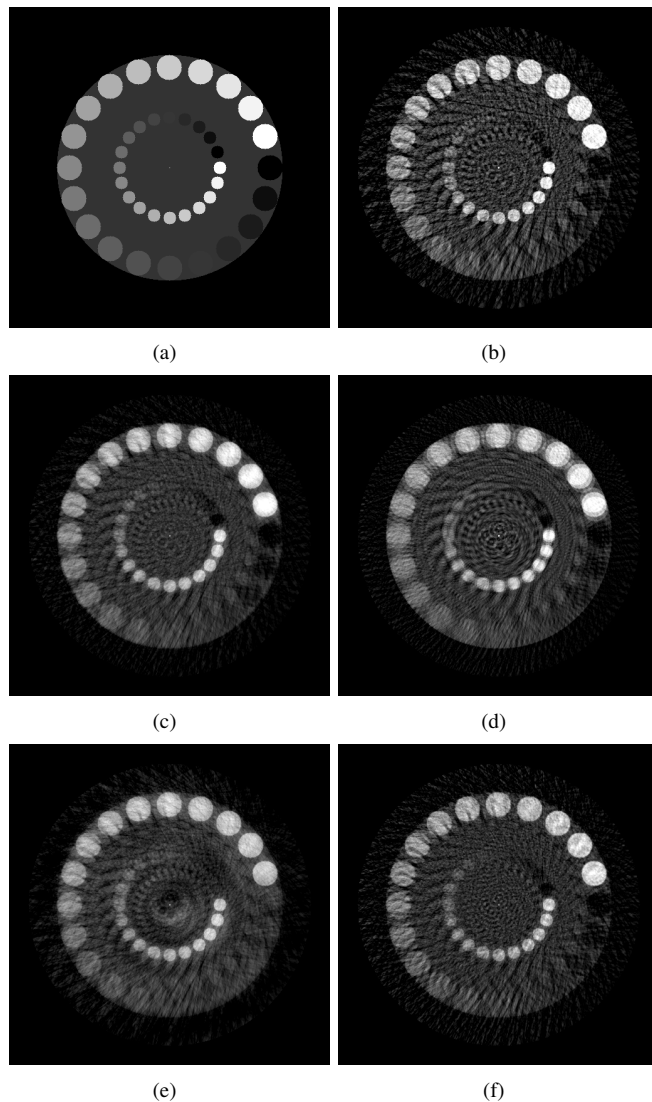


Figure 4. FBP Reconstruction results using different estimation methods for missing projections (a) phantom, (b) reconstruction of the undersampled sinogram with 67 views, (c) reconstruction of the double-wedge filtered sinogram (50 iterations), (d) reconstruction of the linear interpolated sinogram, (e) reconstruction of the sinogram filtered with spectral deconvolution (100 iterations), (f) reconstruction of the completed sinogram using IRR (3 iterations)

IV. DISCUSSION

We presented a new method to estimate missing projections in undersampled sinograms based on the principles of data consistency. In our simulation, the new method performs well

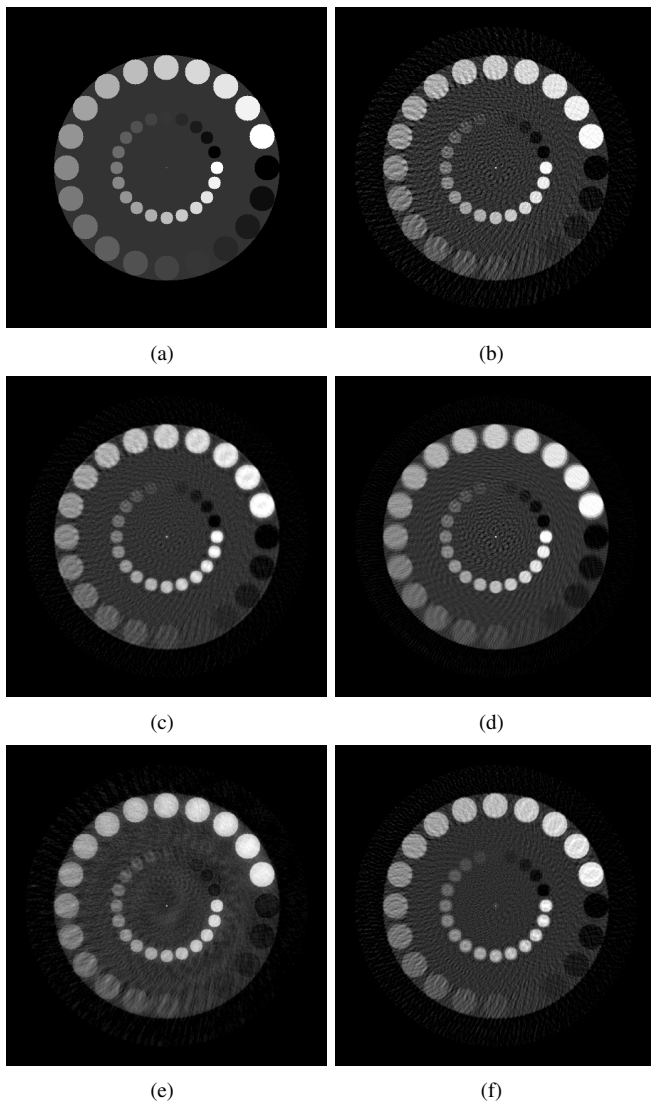


Figure 5. FBP Reconstruction results using different estimation methods for missing projections (a) phantom, (b) reconstruction of the undersampled sinogram with 134 views, (c) reconstruction of the double-wedge filtered sinogram (50 iterations), (d) reconstruction of the linear interpolated sinogram, (e) reconstruction of the sinogram filtered with spectral deconvolution (100 iterations), (f) reconstruction of the completed sinogram using IRR (4 iterations)

even on very sparse projection data. We showed that the estimated projections are consistent with the observed projections and thus result in a reconstruction with a low error. This becomes noticeable in the images of the reconstructions and the values of the NRMSE. In both results of the experiments, it can be seen that the double-wedge filter reduces streak artifacts while preserving the edges of the objects and their intensity values.

The frequency condition requires a projection set sampled along a full-scan trajectory of 2π in order to satisfy Eq. (1). Usually a projection set from, e.g. a C-arm system, is sampled with 133 projections along a trajectory of 200° . Re-binning this data set to a full-scan data set using data redundancy will provide about 240 projections as input before applying our method. The experiment with an initial number of 134 views, shown in Fig. 5, corresponds to an undersampling of such a

C-arm scan and shows promising results. The first experiments with 67 given projections shows that our method also performs good on extremely sparse data sets and its stability does not depend on the input number of projections. Our algorithm is easy to implement and might be embedded as an additional process step in other methods in order to fulfill the data consistency and therefore improve the image quality.

The parameter r_p corresponding to the object extent can directly be measured from the observed sinogram, if the geometry of the scanner is known, using trigonometry.

One limitation of the presented method is that the double-wedge filter estimates parts of the projections in a nearby neighborhood of the periphery of the object more precisely than those referring to the inner part of the object. The inner part can be seen as an object with a smaller extent and therefore requires a larger shape of the double-wedge region. This problem might be solved by iteratively decreasing the parameter r_p that corresponds to a circular region of interest and insert the resulting estimates at the corresponding positions in u -direction into the sinogram. This method will be implemented and evaluated in the future.

In upcoming experiments we are going to investigate the performance of the designed method on real data in order to evaluate the influence of complex structures, noise [11] and scattering [12]. Furthermore, the comparison with regularized iterative methods and additional non-linear filters seems beneficial [13].

The presented method to estimate missing projections in undersampled works well on simulated data. Assuming that the future evaluation using real data shows as promising results as using simulated data, iteratively enforcing consistency condition might be a good approach to reduce the radiation exposure.

REFERENCES

- [1] A. K. Louis, "Incomplete data problems in x-ray computerized tomography," vol. 48, no. 3, pp. 251–262, 1986.
- [2] P. R. Edholm, R. M. Lewitt, and B. Lindholm, "Novel properties of the fourier decomposition of the sinogram," *Proceedings of the International Workshop on Physics and Engineering of Computerized Multidimensional Imaging and Processing*, vol. Proc. SPIE 671, pp. 8–18, 1986.
- [3] S. R. Mazin and N. J. Pelc, "Fourier properties of the fan-beam sinogram," *Medical Physics*, vol. 37, no. 4, p. 1674, 2010.
- [4] A. Papoulis, "A new algorithm in spectral analysis and band-limited extrapolation," vol. 22, no. 9, pp. 735–742.
- [5] A. Papoulis and C. Chamzas, "Detection of hidden periodicities by adaptive extrapolation," *Acoustics, Speech and Signal Processing, IEEE Transactions on*, vol. 27, no. 5, pp. 492–500, 1979.
- [6] T. Aach and V. Metzler, "Defect interpolation in digital radiography-how object-oriented transform coding helps," *Medical Imaging*, pp. 17–22, 2001.
- [7] H. Kostler, M. Prummer, U. Rude, and J. Hornegger, "Adaptive variational sinogram interpolation of sparsely sampled CT data," in *Pattern Recognition, 2006. ICPR 2006. 18th International Conference on*, vol. 3, 2006, pp. 778–781.
- [8] J. S. Karp, G. Muehllehner, and R. M. Lewitt, "Constrained fourier space method for compensation of missing data in emission computed tomography," *Medical Imaging, IEEE Transactions on*, vol. 7, no. 1, pp. 21–25, 1988.
- [9] M. Nassi, W. R. Brody, B. P. Medoff, and A. Macovski, "Iterative reconstruction-reprojection: an algorithm for limited data cardiac-computed tomography," *Biomedical Engineering, IEEE Transactions on*, no. 5, pp. 333–341, 1982.

- [10] A. Maier, H. G. Hofmann, M. Berger, P. Fischer, C. Schwemmer, H. Wu, K. Müller, J. Hornegger, J.-H. Choi, C. Riess, A. Keil, and R. Fahrig, "CONRAD-A software framework for cone-beam imaging in radiology," *Medical Physics*, vol. 40, no. 11, p. 111914, Nov. 2013.
- [11] A. Maier, L. Wigström, H. Hofmann, J. Hornegger, L. Zhu, N. Strobel, and R. Fahrig, "Three-dimensional anisotropic adaptive filtering of projection data for noise reduction in cone beam CT," *Medical Physics*, vol. 38, no. 11, pp. 5896–5909, 2011. [Online]. Available: <http://www5.informatik.uni-erlangen.de/Forschung/Publikationen/2011/Maier11-TAA.pdf>
- [12] B. Bier, A. Maier, H. Hofmann, C. Schwemmer, Y. Xia, T. Struffert, and J. Hornegger, "Truncation Correction for VOI C-arm CT using Scattered Radiation," in *Proceedings of SPIE Medical Imaging 2013: Physics of Medical Imaging*, R. Nishikawa and B. Whiting, Eds., vol. 8668, 2013. [Online]. Available: <http://www5.informatik.uni-erlangen.de/Forschung/Publikationen/2013/Bier13-TCF.pdf>
- [13] C. Riess, M. Berger, H. Wu, M. Manhart, R. Fahrig, and A. Maier, "TV or not TV? That is the Question," in *Fully Three-Dimensional Image Reconstruction in Radiology and Nuclear Medicine*, R. M. Leahy and J. Qi, Eds., 2013, pp. 341–344. [Online]. Available: <http://www5.informatik.uni-erlangen.de/Forschung/Publikationen/2013/Riess13-TON.pdf>

Experimental investigation of multi-energy CT material decomposition using artificial neural networks

Kevin C. Zimmerman and Taly Gilat Schmidt

Abstract—This study investigated the use of artificial neural networks (ANN) for material decomposition of multi-energy x-ray projections. The proposed empirical neural network decomposition technique may be advantageous for spectral CT applications, as it does not require explicit prior knowledge of source or detector parameters. The neural network estimator was trained using a set of calibration scans through varying thicknesses of basis materials. In this study, the bias and standard deviation of the neural network estimator was compared to the empirical estimator previously proposed by Alvarez. Bone, soft tissue and adipose tissue were simulated and decomposed into polystyrene and polyvinyl chloride (PVC) basis material thicknesses. X-ray projections through varying thicknesses of Teflon were acquired experimentally on a bench-top spectral CT system with a photon-counting detector and decomposed into acrylic and aluminum basis material thicknesses. In addition, multi-energy CT scans of a rod phantom consisting of polymethyl methacrylate (PMMA), Teflon, low-density polyethylene (LDPE), and air were acquired experimentally and decomposed into acrylic and aluminum basis material images. The neural network decomposed Teflon into acrylic with less than 11% bias and 1.8 mm standard deviation and aluminum with less than 14% bias and 0.4 mm standard deviation. The Alvarez method decomposed Teflon into acrylic with less than 9% bias and 0.5 mm standard deviation and aluminum with less than 19% bias and 0.2 mm standard deviation. Overall, the results suggest preliminary experimental feasibility of empirical decomposition methods for multi-energy CT.

I. INTRODUCTION

Energy information from x-ray projections can be extracted by using photon-counting detectors with pulse height analysis. This multi-energy information can be used for material decomposition. Maximum likelihood estimation (MLE) can be used to accurately decompose multi-energy information, however this method requires prior knowledge of the source spectrum, energy-bin thresholds, count-rate independent spectral response effects, and pulse-pileup effects [1]. Obtaining accurate models of these effects may be challenging. Empirical methods have the advantage of requiring only system data rather than specific system parameters. This study evaluated the use of artificial neural networks to decompose multi-energy x-ray projections into basis material thicknesses. This empirical method uses a calibration data set to train the neural network. The neural network estimator bias and standard deviation was quantified through simulations and experiments and compared to an empirical decomposition method previously proposed by Alvarez[2].

K.C. Zimmerman and T.G. Schmidt are with Marquette University, Biomedical Engineering Department.

II. METHODS

A. Empirical Methods for Material Decomposition

The number of photons detected in the i^{th} energy bin, N_i can be expressed as a function of a vector of M basis materials thicknesses, \mathbf{A} .

$$N_i(\mathbf{A}) = \int_0^\infty S_i(E) \exp \left[- \sum_{j=1}^M a_j \mu_j(E) \right] dE \quad (1)$$

where a_j , the components of \mathbf{A} , are the path lengths through the M basis materials with attenuation coefficient μ_j , and S_i is the effective spectrum detected by the i^{th} bin, i.e., the number of photons at each energy detected by that bin. The effective spectrum depends on the source spectrum and detector effects such as charge charing and pulse pileup. The inversion of this equation is nonlinear and requires knowledge of the effective spectrum for each bin.

B. Training Set

Both empirical estimators investigated in this work (Neural Network and Alvarez) require a calibration training set. The training set consists of multi-energy x-ray projection measurements at varying combinations of thicknesses of the basis materials. The calibration basis material thicknesses are assumed to be known, while the multi-energy x-ray projections are measured. Each of the studied empirical methods used the known calibration thicknesses and the measured x-ray projection data to approximate the relationship between basis material thicknesses and x-ray projection measurements.

C. Neural Network Decomposition

The projection integral, \mathbf{L} is equal to $\mathbf{L} = -\log(\mathbf{N}/\mathbf{N}_o)$ where the components of \mathbf{N}_o are the number of counts detected in each bin without an object in the beam. We propose an artificial neural network to approximate the relationship between the projection integral \mathbf{L} and the basis material thicknesses \mathbf{A} . Unlike previously proposed maximum likelihood estimators [1], the proposed neural network method does not require *a priori* information about the system, such as the effective spectrum for each energy bin, $S_i(E)$.

The calibration x-ray projection measurements and known basis material thicknesses were used to train a two-layer feed-forward network with sigmoid hidden neurons and linear output neurons. The size of the input was the number of

energy bins and the size of the output was the number of basis materials. For this study, five energy bins were used for two material decomposition. The weights and the biases of the neural network were calculated from the training set using a variation of the Levenberg-Marquardt backpropagation algorithm.

After training the neural network to map multi-energy data to basis material thicknesses, calculation of basis material thicknesses given multi-energy data was performed using the neural network. The neural network performs the calculation using a series of multiplication and addition operators involving the weights and biases of the network and the multi-energy data. The Neural Network Toolbox in MATLAB was used to train the network and perform the decomposition.

D. Alvarez Decomposition

The model relating the projection integral \mathbf{L} , to the basis material thicknesses \mathbf{A} , can be approximated as,

$$\mathbf{L}(\mathbf{A}) \approx \mathbf{M}\mathbf{A} + w \quad (2)$$

where w is a zero mean multivariate normal random variable whose covariance depends on \mathbf{A} and the effective linear attenuation coefficient matrix, \mathbf{M} , is the least squares approximate solution[2]. The maximum likelihood estimator of the linearized equation in Eq. 2 is

$$\mathbf{A}_{MLE} = (\mathbf{M}^T \mathbf{R}_{L|A}^{-1} \mathbf{M})^{-1} \mathbf{M}^T \mathbf{R}_{L|A}^{-1} \mathbf{L}_{with\ noise} \quad (3)$$

where $\mathbf{R}_{L|A}$ is the covariance of the data, \mathbf{L} . In the Alvarez method, both \mathbf{M} and $\mathbf{R}_{L|A}$ are estimated from the calibration training data. The errors in the linearized model are found by calculating \mathbf{A}_{MLE} for every calibration, \mathbf{L} , and subtracting them from the known calibration basis material thicknesses, \mathbf{A} . The errors in the initial linear estimate are interpolated across the basis material thicknesses to create two look-up tables, one for each basis material. The accuracy of the look-up table is expected to increase with the number of calibration measurements.

E. Simulation Study

The simulation study used PVC and polystyrene as the basis materials. For the calibration training set, for both the neural network and Alvarez method, x-ray projections of combinations of polystyrene (0 to 18 slabs, 2.54 cm each) and polyvinyl chloride (PVC) (0 to 18 slabs, 1.27 cm each) were simulated, producing a 324-point training set. The simulations assumed an ideal multi-energy detector with 5 bins at energies [25-40], [40-50], [50-60], [60-70], and [70-100] keV. The simulations modeled a 100 kV spectrum, Poisson noise, and 2×10^6 photons per measurement, which is comparable to the number of photons detected through air in the experimental study. Thicknesses of bone (1 to 8 cm; increments of 1 cm), soft tissue (5 to 40 cm; increments of 5 cm), and adipose tissue (5 to 40 cm; increments of 5 cm) were used in order to test the performance of the estimators on materials that were not part of the calibration dataset. The material attenuation coefficients were obtained from the NIST attenuation coefficient database.

F. Experimental Setup

In the simulation study, the detector was modeled with ideal energy response. In practice, photon-counting detectors suffer from numerous non-ideal effects that degrade the energy resolution. An experimental study was performed to investigate the performance of the empirical estimators on experimental data with non-ideal spectral response. In this study, x-ray projections were acquired using a bench top energy-resolved CT system with a photon-counting detector. The system consisted of a cadmium zinc telluride (CZT) detector (NEXIS, Nova R&D, Riverside, CA), with two pixel rows, each consisting of 128 1x1 mm pixels. The detector pixel array is read out by the XENA chip (Nova R&D, Riverside, CA), which can sort detected photons into bins above user-selected thresholds. The energy thresholds for each bin were set to [25-40], [40-50], [50-60], [60-70], and [70-100] keV. Acquisitions were performed at 100 kV and 0.44 mAs. Acrylic and aluminum were used as basis materials.

For the calibration training set, x-ray projections through combinations of acrylic (0 to 4 slabs, 2.54 cm each) and aluminum (0 to 4 slabs, 0.635 cm each) were acquired, producing a 25-point training dataset. The calibration dataset was used to train a neural network for each pixel in the detector. For the Alvarez method, the calibration dataset created a separate lookup table for each pixel in the detector.

To quantify the bias and standard deviation of the neural network and Alvarez estimators, x-ray projections through varying thickness of Teflon slabs (1 to 4 slabs, 1.72 cm each; 5 trials) were acquired. For each Teflon thickness, the acquired energy-bin data was decomposed into thicknesses of the acrylic and aluminum basis materials using the trained neural networks and the Alvarez look up tables for each pixel.

To investigate the performance of the neural network estimator for multi-energy CT imaging, a CT dataset was acquired of a 6.35 cm diameter cylindrical phantom consisting of polymethyl methacrylate (PMMA), Teflon, low-density polyethylene (LDPE), and air as seen in Fig. 1. The phantom was rotated and 200 equally spaced projections were acquired over 360° with 0.076 mAs per projection angle.

For the CT dataset, aluminum and acrylic basis sinograms were estimated using both the trained neural networks and the Alvarez look up tables. The basis sinograms were reconstructed using filtered back projection to produce acrylic and aluminum basis images.

G. Performance Evaluation

For both the simulation and the experimental studies, the performance of the neural network and Alvarez estimators was evaluated by calculating the bias, as a percentage of the basis material thickness, and standard deviation in the estimated basis material thicknesses.

III. RESULTS

A. Simulation Study

Fig. 2 plots the polystyrene and PVC basis material thicknesses estimated by the neural network and Alvarez methods

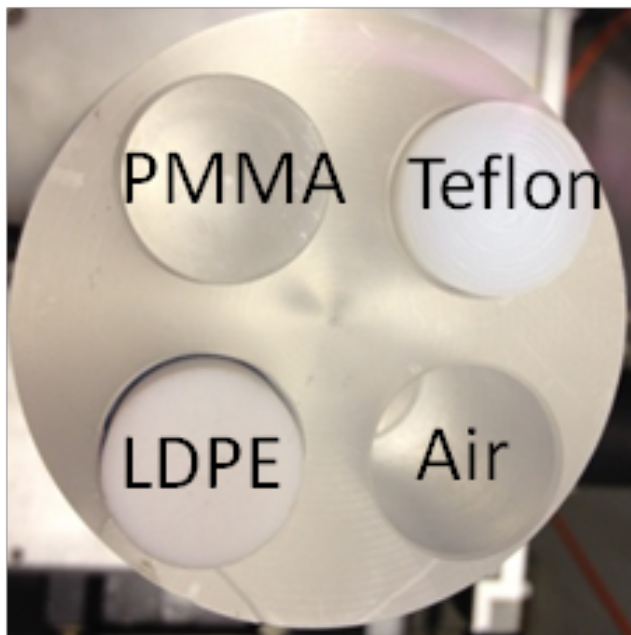


Fig. 1. Rod phantom used for CT investigation. The phantom consists of rods of PMMA, Teflon, LDPE, and air.

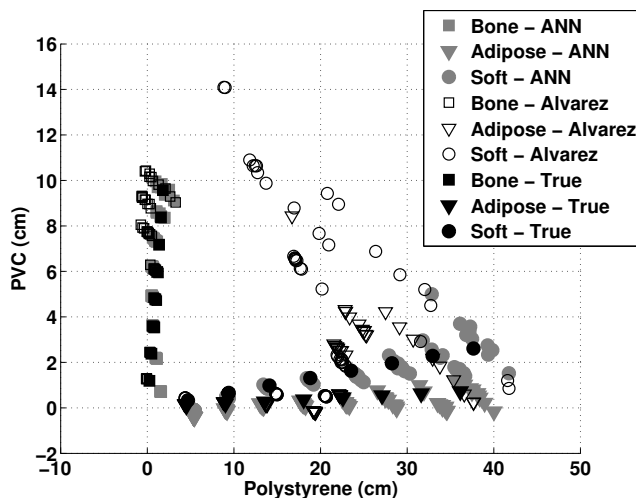


Fig. 2. Decomposition of bone, soft tissue and adipose tissue using the neural network and Alvarez method on simulated data ($n = 10$)

for the simulated bone, soft tissue and adipose tissue. All trials, materials, and thicknesses are displayed. The bias and the standard deviation of the estimates for both methods increased as the test material thicknesses increased with a greater increase for thicknesses greater than 30 cm. The bias and standard deviation of each basis material is plotted in Fig. 3.

B. Experimental Study

Fig. 4 plots the acrylic and aluminum material thicknesses estimated by the neural network and Alvarez methods from the experimental measurements through Teflon. Similar to the simulation results, the bias and the standard deviation of the estimates for both empirical methods increased with increasing

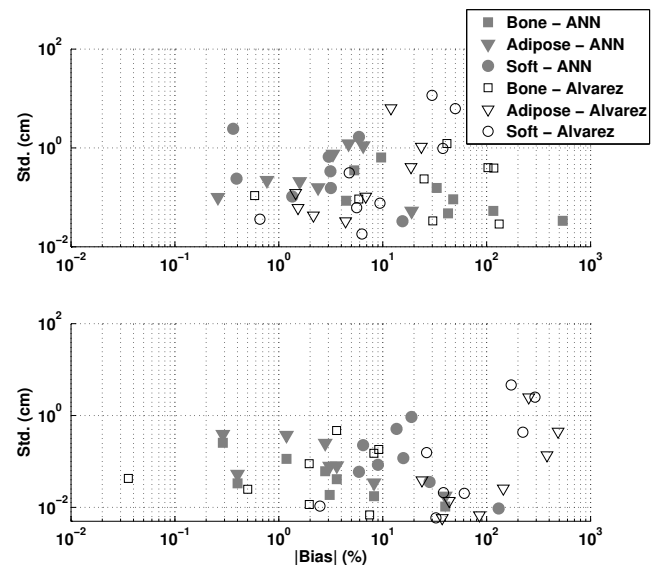


Fig. 3. The bias and standard deviation of the polystyrene (top) and PVC (bottom) basis thickness estimates for the experimental simulated data through bone, soft tissue, and adipose tissue ($n = 10$)

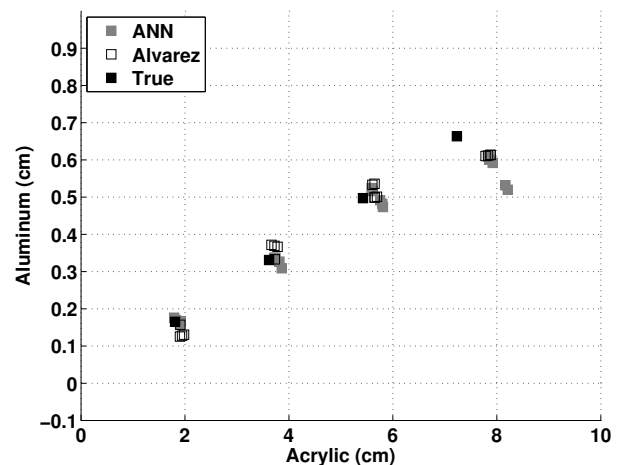


Fig. 4. Decomposition of Teflon (1 to 4 slabs; 1.27 cm each) using the neural network and the Alvarez method on experimental data. ($n = 5$)

Teflon thickness. The bias and the standard deviation of each basis material is plotted in Fig. 5.

Fig. 6 displays the acrylic and aluminum basis images reconstructed from the basis sinograms decomposed by the neural network and Alvarez estimators. As expected, the aluminum basis image contains contributions from primarily the Teflon rod, as the other phantom materials are closer in atomic number and density to acrylic. The LDPE rod decomposes into a negative value in the aluminum basis image because its effective number is not in the range of spanned by the acrylic and aluminum basis materials. The Alvarez method has slightly fewer and more stable rings in the reconstructed images than does the neural networks, suggesting that the Alvarez method may be more robust to pixel-to-pixel variations..

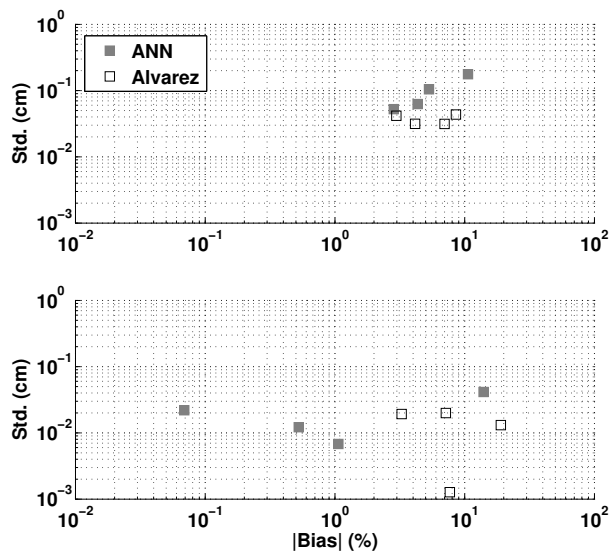


Fig. 5. The bias and standard deviation of the acrylic (top) and aluminum (bottom) basis thickness estimates for the experimental measurements through Teflon. ($n = 5$)

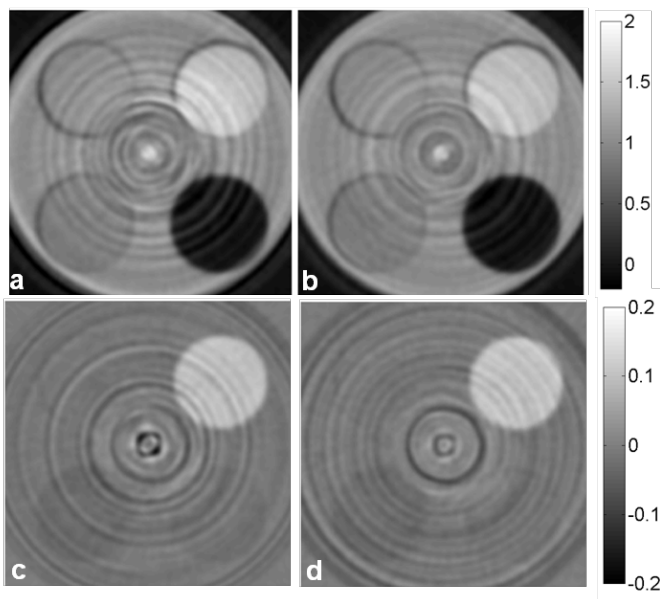


Fig. 6. Material decomposition of a rod phantom into acrylic and aluminum basis materials using both neural network and Alvarez methods. (a) Acrylic basis image using ANN. (b) Acrylic basis image using the Alvarez method. (c) Aluminum basis image using ANN. (d) Aluminum basis image using the Alvarez method.

IV. DISCUSSION

In the future, three material decomposition using K-edge materials will be desired. The training set then becomes combinations of three basis materials. The use of neural networks for three material decomposition requires the addition of weights and biases which are calculated in the training algorithm. For two material decomposition with the Alvarez method, two 2-dimensional lookup tables are required for each detector pixel. When three material decomposition is desired, three 3-dimensional lookup tables will be needed for each

detector pixel. Which is expected to have a large memory requirements as compared to the neural network.

V. CONCLUSIONS

The neural network decomposed Teflon into acrylic with less than 11% bias and 1.8 mm standard deviation and aluminum with less than 14% bias and 0.4 mm standard deviation. The Alvarez method decomposed Teflon into acrylic with less than 9% bias and 0.5 mm standard deviation and aluminum with less than 19% bias and 0.2 mm standard deviation. Overall, the neural network had a lower bias in the decomposition of Teflon into the aluminum basis material however had a higher standard deviation in the decomposition of Teflon into the acrylic basis material than the Alvarez method. Future work will investigate the performance of these estimators in the presence of higher photon flux resulting in a greater presence of pulse pileup. Also, three material decomposition of k-edge materials will be investigated using artificial neural networks. Overall, the results suggest preliminary experimental feasibility of empirical decomposition methods for multi-energy CT.

VI. ACKNOWLEDGMENTS

This work was supported by NIH Grant number R21EB015094. The contents of this article are solely the responsibility of the authors and do not necessarily represent the official views of the National Institutes of Health.

REFERENCES

- [1] Schlomka, J. P., Roessl, E., Dorscheid, R., Dill, S., Martens, G., Istel, T., Bäumer, C., Herrmann, C., Steadman, R., Zeitler, G., Livne, A., and Proksa, R., "Experimental feasibility of multi-energy photon-counting K-edge imaging in pre-clinical computed tomography," *Physics in Medicine and Biology* **53**(15), 4031–4047 (2008).
- [2] Alvarez, R., "Estimator for photon counting energy selective x-ray imaging with multibin pulse height analysis," *Medical Physics* **38**, 2324 (2011).

A simple and efficient super-short-scan algorithm of Fan-beam reconstruction for multiple circular trajectories: solution towards the truncated data

Long Chen, Thomas Rodet, and Nicolas Gac

Abstract—The sufficiency condition of the accurate reconstruction of the region of interest (ROI) in fan-beam tomography with non-truncated data was introduced by F. Noo([1]). When the detector does not cover the whole objet, R. Clackdoyle extended this condition of the accurate reconstruction of ROI in presence of the truncated data using virtual fan-beam method (VFB) [2]. In this paper, we are interested in the image reconstruction of the whole object from truncated data, since the whole object reconstruction is always preferred even with small detector, instead of the accurate reconstruction of only a region. We propose a simple and efficient super-short-scan algorithm for multiple circular trajectories to reconstruct the whole object from truncated fan-beam projections. This algorithm is validated by simulation studies.

I. INTRODUCTION

In fan-beam tomography, the short-scan (180° plus the fan angle) is a minimal complet data set to reconstruct the whole object [3]. This had been also hold even for the reconstruction of only a ROI [4]. A new sufficient condition of the accurate reconstruction of ROI was introduced in [1]. The ROI can be exactly reconstructed only and if only all the lines through the ROI are known. All the fan-beam projections should be non-truncated as the short scan.

When the detector is too small to cover all the object, the projection data is inevitably truncated. The accurate reconstruction of ROI is still able to be achieved in some cases with VFB in [2]. An optimal virtual fan-beam circular trajectory is found by rebinning the truncated projections to non-truncated projections. Additionally, the whole object reconstruction from the truncated data has been interesting, as in dental imaging, the panoramic view of the whole jaw from a medium detector. In this paper, we propose a simple and efficient super-short-scan (SS-scan) algorithm on twice and triple circular trajectories to achiev the reconstruction of the whole object. 'Simple' means the movement of the scanner is not complexe, and 'efficient' stands for as less fan-beam projections as

Long Chen is with the Laboratory of Signals and Systems, UMR8506, Université Paris-Sud-CNRS-Supélec, Gif-sur-Yvette cedex, F-91192, France

Thomas Rodet is with the Laboratory of Systems and Applications of Technologies of Information and Energy, Ecole Normale Supérieure de Cachan, Cachan cedex, F-94235, France

Nicolas Gac is with the Laboratory of Signals and Systems, UMR8506, Université Paris-Sud-CNRS-Supélec, Gif-sur-Yvette cedex, F-91192, France

possible to reconstruct the whole object. The super-short-scan projections here are not necessarily non-truncated, which are different from those in [5].

The rest of this paper is organized as follows: the proposed super-short-scans on twice and triple circular trajectories are described in section 2, we use a standard iterative least-squares method for image reconstruction in section 3. the proposed super-short-scan algorithm is evaluated by the simulation studis in section 4, and we draw the conclusion in the final section.

II. SUPER-SHORT-SCANS ON MULTIPLE CIRCLE TRAJECTORIES

In CT tomography, how to reconstruct a whole object from the truncated data is a challenge, when the detector is too small to cover all the object. Obviously, a single circular scan is able to reconstruct only a region, not the whole object. More scans are needed to achieve the whole object reconstruction. We present the proposed super-short-scans on two and three circular trajectories below.

A. Twice super-short-scans

Usually, the object support is known *a priori*. Without loss of generality, let the object support Ω be an ellipse depicted by tow semi-axis parametres (a and b , $a > b$), which is centered at origine in figure 1.(a). Two iso-centers O_1 and O_2 of scans are located symetrically to the axis Y , with distance c to the origine. The system geometry is decribed in the figure 1.(a) with distance from the X-ray source to the iso-center R , and from the source to the detector D . The length of detector is L . We have $r = L * R / D$, where r is the radius of the field of view (FOV). Obviously, r should be greater than c for the whole object reconstruction.

Intuitively, the first choice of the whole object reconstruction is to reconstruct a half ellipse from each scan. In presence of the truncated data, an optimum virtual trajectory of the X-ray is found in red solid circle using VFB ([2]), in the figure 2.(a). According to the sufficient condition in [1], two reasonable trajectories are drawn in the figure 2.(a), the scanning angle of each scan Q_1 or Q_2 is $\pi + 2 * \gamma_1$, where $\gamma_1 = \arcsin(c/R)$. As $c < r$, the angle is smaller than half of the fan angle γ_m with $\gamma_m = \arcsin(r/R)$. These tracjectories are refered to the reduced scan (R-scan). When we look at the two reduced

scans, a random pixel M in the left half of object is measured twice in one line in the figure 2.(a). The fan-beam projections of the whole object are double from the scanning range between the lines t_1 and t_2 and between t_3 and t_4 , which are the shared tangents of the object support Ω and two fields of view (FOV) of the twice scans.

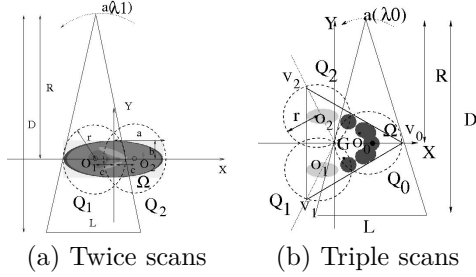


Fig. 1: System geometries of twice scans (Q_1 and Q_2) with ellipse support of the object (a). and triple scans (Q_0 , Q_1 and Q_2) for the triangular object support (b). O_i denotes the iso-center, $i = 0, 1, 2$, In (b), V_0 , V_1 , and V_2 are the three vertexes, their three iso-centers, O_0 , O_1 and O_2 , are located on the middle of the segments between the triangle gravity G and each vertex, respectively. The phantoms of Shepp-Logan (a) and simulated jaw (b) inside Ω are given here only as example.

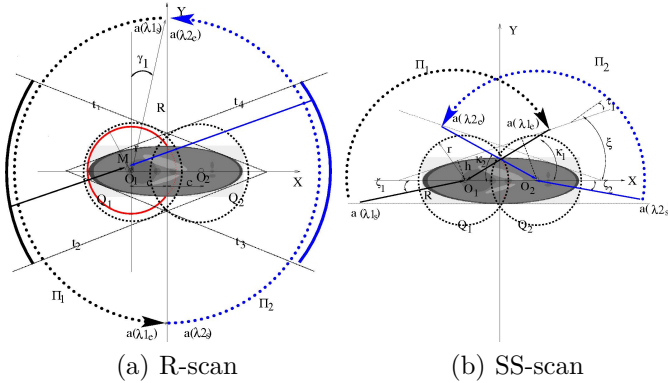


Fig. 2: Illustration of the reduced scan (a) and super-short-scan (b).

In order to reduce the data redundancy above, we propose two shorter scans referred to super-short-scans (SS-scan) in the figure 2.(b). The scanning ranges of the two super-short-scans Π_1 et Π_2 are $[\lambda_{1_s} \lambda_{1_e}]$ and $[\lambda_{2_s} \lambda_{2_e}]$ respectively. The start positions of the X-ray source $a(\lambda_{1_s})$ and $a(\lambda_{2_s})$ are on the tangent to the object support. In the figure 2.(b), the angle is defined positive in counterclockwise direction. $\zeta_1 = \zeta_2 = \arcsin(b/R)$, $\tau_1 = \arcsin(h/R) = \arcsin(\frac{r-2*c*\sin\xi}{R})$, and $\kappa_1 = \kappa_2$,

$$\lambda_{1_s} = \pi + \zeta_1, \lambda_{1_e} = \kappa_1 = \xi + \tau_1 \quad (1)$$

$$\lambda_{2_s} = -\zeta_2, \lambda_{2_e} = \pi - \kappa_2 = \pi - (\xi + \tau_1) \quad (2)$$

where the tangent angle ξ is given by

$$\tan\xi = 1/\sqrt{\left(\frac{r*c + \sqrt{(a^2 - b^2)*(r^2 - b^2) + b^2*c^2}}{r^2 - b^2}\right)^2 - 1},$$

which is derived from the solution of the tangent to the FOV of Q_1 or Q_2 and the object support function. Compared to the reduced scan, the SS scan requires less fan-beam projections. Quantitatively, the reduced projection angle is given below :

$$\Delta\Pi = \pi + 2*\gamma_1 - |\lambda_{1_e} - \lambda_{1_s}| = 2*\gamma_1 + \xi + \tau_1 - \zeta_1 \quad (3)$$

A numerical result will be given in the simulation studies, $\Delta\Pi = 30^\circ$.

B. Triple super-short-scans

When the object is much larger than the field of view of the scanner, triple scans are required for the whole object reconstruction from the truncated data. For simplification, let the object support Ω be an equilateral triangle, as in the figure 1.(b). The other parameters are defined as above.

As the object takes a great part of the FOV of each scan, no less than short-scan is able to reconstruct the part of the object inside the FOV, separately, according to Noo's sufficient condition. A good choice is short-scan. The scanning angle of short-scan is π plus the fan angle $2*\gamma_m$. The data redundancy here is larger than in case of twice scans. We propose a triple super-short-scans to decrease

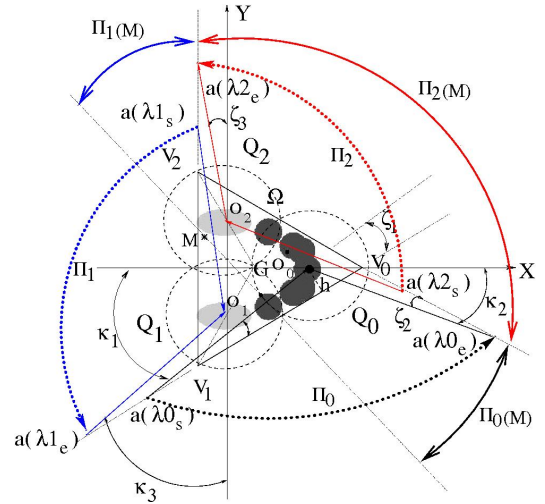


Fig. 3: Illustration of the triple super-short-scans. M is an arbitrary pixel in the object. The scanning ranges $\Pi_0(M)$, $\Pi_1(M)$ and $\Pi_2(M)$ are sufficient for the accurate reconstruction of M.

the data redundancy in the figure 3. The scanning ranges of the triple super-short-scans are Π_0 , Π_1 , and Π_2 , where $\Pi_0 = [\lambda_{0_s} \lambda_{0_e}]$, $\Pi_1 = [\lambda_{1_s} \lambda_{1_e}]$, and $\Pi_2 = [\lambda_{2_s} \lambda_{2_e}]$. In the figure 3, we have the angles $\angle O_0V_0a(\lambda_{0_s}) = \angle V_2V_0O_0 = \pi/6$ in the equilateral triangle Ω , the start and end angular

positions of Π_0 , Π_1 , and Π_2 are obtained as follows:

$$\lambda 0_s = \pi + \kappa_1, \lambda 0_e = 2 * \pi - \kappa_2 \quad (4)$$

$$\lambda 1_s = \frac{\pi}{2} + \angle O_2 O_1 a(\lambda 1_s), \lambda 1_e = \frac{3\pi}{2} - \kappa_3 \quad (5)$$

$$\lambda 2_s = -\frac{\pi}{2} + \angle O_1 O_2 a(\lambda 2_s), \lambda 2_e = \frac{\pi}{2} + \zeta_3 \quad (6)$$

where $h = r * \sin(\angle O_0 V_0 a(\lambda 0_s)) = 1/2 * r$, $\zeta_1 = \zeta_2 = \zeta_3 = \angle O_2 O_1 a(\lambda 1_s) = \arcsin(h/R) = \arcsin(\frac{r}{2*R})$, $\kappa_1 = \angle O_0 V_0 a(\lambda 0_s) + \zeta_1$, $\kappa_2 = \angle V_2 V_0 O_0 - \zeta_2$, $\kappa_3 = \pi/3 - \arcsin(\frac{r}{2*R})$, and $\angle O_1 O_2 a(\lambda 2_s) = \pi/3 + \arcsin(\frac{r}{2*R})$. All the three scanning angles $|\lambda i_e - \lambda i_s|$ of Π_i are $2/3\pi$, with $i=0,1,2$. For the whole object reconstruction, our triple super-short scans only needs 2π fan-beam projections, which are $\pi + 6 * \gamma_m$ less than those of the triple short-scans, since each short-scan needs $\pi + 2 * \gamma_m$ fan-beam projections.

We verify the sufficient condition where every lines through the object support should be known in the figure 3: Let M be an arbitrary pixel inside the object. All the lines passing M are intersected with the three colorful solid arcs (black, red, and blue). Therefore, M is able to be reconstructed exactly. This will be validated in the results of image reconstruction from the simulated data.

III. IMAGE RECONSTRUCTION

In this paper, we consider the image reconstruction as an optimisation problem. A standard iterative least-squares (ILS) method is used for image reconstruction. The analytic methods suitable for the multiple scans are beyond this topic.

In fan-beam tomography, a forward model of data acquisition is given as follows:

$$\mathbf{g} = \mathbf{H}\mathbf{f} + \epsilon \quad (7)$$

where \mathbf{g} is the measurement vector, \mathbf{H} represents the system matrix, whose element h_{ij} means the contribution of j^{th} pixel of the object on the i^{th} measurement unit, the vector \mathbf{f} describes the unknown object, and ϵ contains the detector noise and modelling errors. \mathbf{f} is estimated by minimizing the criteria function $J(\mathbf{f})$ defined below:

$$J(\mathbf{f}) = 1/2 \|\mathbf{g} - \mathbf{H}\mathbf{f}\|^2 \quad (8)$$

$$\hat{\mathbf{f}} = \arg \min_{\mathbf{f}} J(\mathbf{f}) \quad (9)$$

where $\|\cdot\|^2$ is \mathcal{L}_2 norm. In the case of the twice scans or triple scans, \mathbf{H} is rewritten as

$$\mathbf{H} = \begin{bmatrix} \mathbf{H}_1 \\ \mathbf{H}_2 \end{bmatrix}, \text{ or } \mathbf{H} = \begin{bmatrix} \mathbf{H}_0 \\ \mathbf{H}_1 \\ \mathbf{H}_2 \end{bmatrix}$$

respectively, where \mathbf{H}_0 , \mathbf{H}_1 , and \mathbf{H}_2 are the system matrices of the scans Q_0 , Q_1 , and Q_2 , separately. In case of the twice, the gradient $\nabla J(\mathbf{f})$ and the optimal step $\hat{\alpha}$ of ILS are deducted as follows:

$$\nabla J(\mathbf{f}) = \mathbf{H}_1^T (\mathbf{H}_1 \mathbf{f} - \mathbf{g}_1) + \mathbf{H}_2^T (\mathbf{H}_2 \mathbf{f} - \mathbf{g}_2) \quad (10)$$

$$\hat{\alpha} = \frac{\|\nabla J(\mathbf{f})\|^2}{\nabla J(\mathbf{f})^T (\mathbf{H}_1^T \mathbf{H}_1 + \mathbf{H}_2^T \mathbf{H}_2) \nabla J(\mathbf{f})} \quad (11)$$

where \mathbf{H}_i^T are the backprojections, $i = 1, 2$, \mathbf{g}_1 and \mathbf{g}_2 are the measurements of the scans Q_1 and Q_2 .

IV. SIMULATION STUDIES

The proposed methods of image reconstruction of the whole object from the truncated data are evaluated by the noise-free and noisy simulated data. The geometry configuration of our CT scanner fits for dental imaging, R and D are 440 and 690 mms, there are 680 units of the detector with size of $120 \mu\text{m}$, as a result, the achievable image size by a single circular scan is $52 \times 52 \text{ mm}^2$. However, in our simulation, the support size of the standard modified Shepp-Logan (MSL) phantom (Figure 5) is $72 \times 24 \text{ mm}^2$, whose attenuation coefficients are defined in matlab, and a larger simulated jaw (Figure 6) is included in an equilateral triangle support with side length 90 mm. Twice or triple circular scans are required to reconstruct the whole object. Our jaw contains 3 materials to simulate the tissue, teeth and high attenuated implants with attenuation coefficient of 0.02, 0.06 and 0.3 mm^{-1} . The fan-beam data was acquired using our ray-driven projector. To verify a stable reconstruction with the proposed method, the noisy data was generated with addition of a gaussian noise in the noise-free fan-beam projections.

The images are reconstructed in 384×384 with pixel size $200 \mu\text{m}$. The reconstructed images from the noise-free fan-beam data of MSL are presented in the left column of Figure 5. Each half of MSL is accurately reconstructed, even more the pixels inside the FOV (red dashed arc in 5.(a) and .(c)) from the reduced scan. The ILS method is able to reconstruct the MSL inside the FOV not only half of MSL from the reduced scan, as OSEM in [2]. Both twice reduced scans and twice super-short scans allow to reconstruct the whole object exactly, in the figure 5.(e) and .(g). Moreover, the scanning angle of the proposed super-short-scan decreases by 16.3%, from 184° of the reduced scan ($\pi + 2 * \gamma_1$) to 154° (equations (1) and (2)). To assure the efficacy of our proposed super-short-scan, we reduce a bit of its scanning ranges, which is referred to the SS⁻-scan, $[\lambda 1_s - \epsilon \lambda 1_e + \epsilon]$ (clockwise) and $[\lambda 1_s + \epsilon \lambda 1_e - \epsilon]$, with a small angle ϵ (one or two angular steps), in the figure 2.(b). The reconstruction result is given in the figure 5.(i). The upper and centre edge of the MSL is contaminated, clearly in the profil curves of the figure 4.(a). The reconstructed images from the noisy fan-beam data are demonstrated in the right column of Figure 5. We achieve the stable restrictions from all the noisy data. The image of SS⁻-scan (Figure 5.(j)) and the profile (Figure 4.(b)) show again that the upper and center edge of MSL is not able to be reconstructed accurately decreasing the scanning range of our SS-scans.

The reconstructed images from the noise-free data and the noisy data of the simulated jaw are given in the left column of the figure 6.(a)-(c) and in the right column 6.(d)-(f). The accurate reconstructions of the whole jaw are achieved both on the triple short-scans (Figure 6.(a) and .(c)) and the proposed SS-scans (Figure 6.(b) and

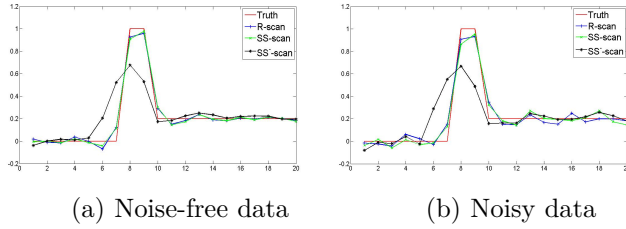


Fig. 4: Profiles of the reconstructed images of the whole MSL from SS^- -scan (a) noise-free data and (b) noisy data. The profiles are drawn along the yellow solid line in 5.(a).

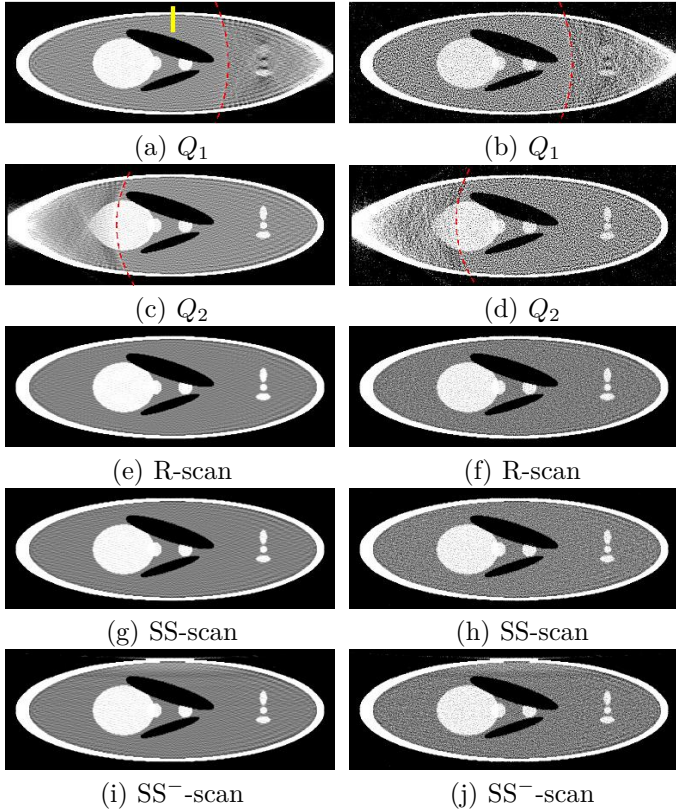


Fig. 5: Reconstructed images from the noise-free fan-beam data (left column) and the noisy fan-beam data of MSL (right column). The display window is $[0.1 \ 0.3]$.

(e). However the proposed SS-scan requires only the fan-beam projections of 120° , which is much less than 187° ($\pi + \text{the fan-beam angle} \cdot 2 \cdot \gamma_m$) of the short-scan. The scanning range using SS-scan decreases by 35.8% compared to the short-scan. Moreover, the proposed SS-scan is the minimal scan for the whole jaw reconstruction. If we reduce a few of fan-beam projections (SS^- -scan) with the scanning ranges $[\lambda i_s + \varepsilon \ \lambda i_e - \varepsilon]$, $i = 0, 1, 2$ (Figure 3), some artifacts appear in the figure 6.(c) and .(f).

V. CONCLUSION

We propose a simple and efficient super-short-scan algorithm on twice and triple circular trajectories for the whole object image reconstruction from the truncated data. The scanning angle decreases by 16.3% in the case

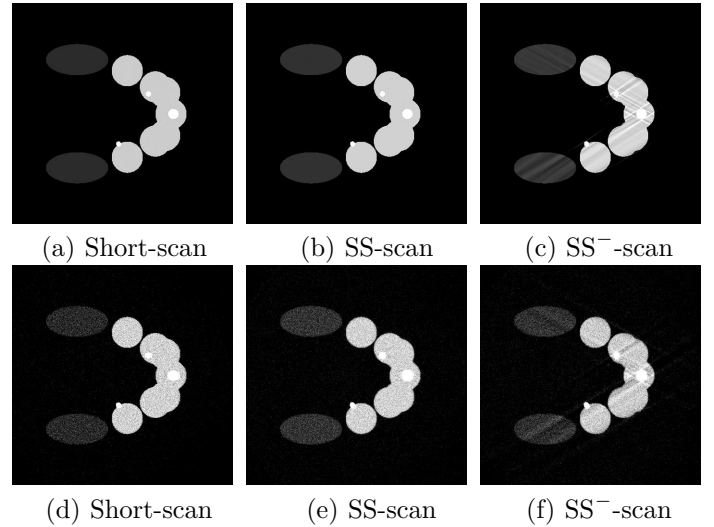


Fig. 6: Reconstructed images from the noise-free fan-beam data of the simulated jaw of the different acquisitions (a) short-scan, (b) SS-scan and (c) SS^- -scan. and from the noisy data (d) short-scan, (e) SS-scan and (f) SS^- -scan. The display window is $[0.01 \ 0.07]$.

of twice super-short scans compared to the reduced scans, and by 35.8% in the case of the proposed triple super-short scans compared to the short-scans. Our proposed super-short scans algorithms could be applied in dental imaging for a panoramic view of the whole jaw with a small detector, as well as for a fast scan and reduction of dose in other applications of CT tomography. Furthermore, these super-short scans will be easily extended in cone-beam CT tomography.

REFERENCES

- [1] F. Noo, M. Defrise, R. Clackdoyle, and H. Kudo, "Image reconstruction from fan-beam projections on less than a short scan," *Phys. Med. Biol.*, vol. 47, no. 02, pp. 2525–2546, 2002.
- [2] R. Clackdoyle, F. Noo, J. Guo, and J.A Roberts, "Quantitative reconstruction from truncated projections in classical tomography," *IEEE Trans. Nucl. Sci.*, vol. 51, no. 5, pp. 2570–2578, 2004.
- [3] D. L. Parker, "Optimal short scan convolution reconstruction for fanbeam ct," *Med. Phys.*, vol. 9, no. 2, pp. 254–257, 1982.
- [4] R. Clackdoyle and M. Defrise, "Tomographic reconstruction in the 21st century," *IEEE Signal Proc. Mag.*, vol. 27, pp. 60–80, 2010.
- [5] H. Kudo, and M. Defrise F. Noo, and R. Clackdoyle, "New super-short-scan algorithms for fan-beam and cone-beam reconstruction," in *Nuclear Science Symposium Conference Record, 2002 IEEE*, 2002, pp. 902 – 906.

Sampling Analysis of a Dual Source and Dual Detector CT System

Guangzhi Cao and Jiang Hsieh

Abstract—Dual source and dual detector CT system has advantage of improved temporal resolution and fast coverage by sampling an object simultaneously with two source/detector pairs that are 90 degree apart at high helical pitches. However, this scan mode can also result in insufficient sampling and hence image artifacts when helical pitch is very high. In this work, a detailed analysis on the sampling of a dual source and dual detector CT system is provided. The sampling efficiency of the system as a function of helical pitch is discussed. The results show that the sampling efficiency of the dual source and dual detector system decreases as the helical pitch increases. There are regions within the scan FOV that are under-sampled, which may lead to image artifacts in clinical scans.

I. INTRODUCTION

Helical scanning is a popular scan mode in computed tomography (CT) clinical applications due to its fast volumetric coverage capability. In the past decades, both the detector size and helical pitch that are used in CT scans have increased significantly. This continuing progress could enable thoracic scanning without breath holds. This is of particular importance for trauma and pediatric cases.

More recently, dual source and dual detector CT systems have been developed to further improve the temporal resolution of CT imaging [1]. The improved temporal resolution is realized by scanning an object simultaneously with two source/detector pairs that are roughly 90 degree apart at high helical pitches, and the reconstruction is performed using the combined projections data. The dual source and dual detector system reduces the temporal resolution to a quarter (plus fan angle) of gantry rotation time. The improved temporal resolution is important to mitigate the motion artifacts which is challenging to deal with in cardiac applications. However, the fast helical scan of dual source and dual detector CT systems can also lead to a significant amount of image artifacts (other than motion artifacts) as observed in clinical scans when helical pitch is high. Therefore, it is important to analyze the sampling pattern of dual source and dual detector CT systems and understand what is the cause of these image artifacts that are typical in dual source and dual detector CTs.

In this work, a detailed analysis on the sampling of dual source and dual detector CT systems is provided. The sampling efficiency of the system as a function of helical pitch is also discussed. The analysis shows as helical pitch increases, there are under-sampled regions in the scan field of view (FOV), which can lead to image artifacts that are generally observed

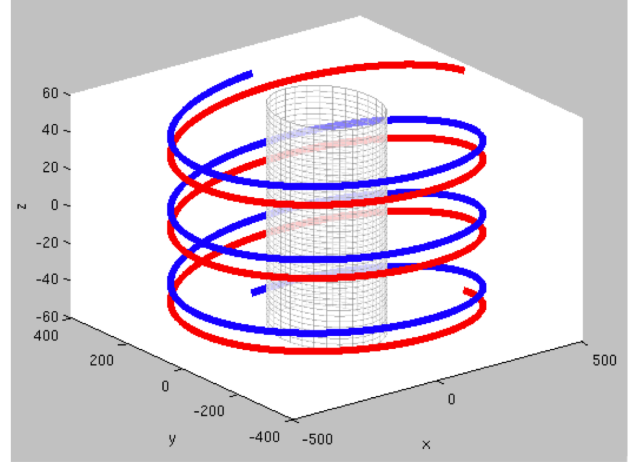


Fig. 1. Scan geometry of a dual source and dual detector CT system. The $x-y$ coordinates correspond to an object's axial plane, and the z -axis corresponds to the object moving direction.

in high pitch helical scans of dual source and dual detector CT systems.

II. METHODS

A. Notation

The two source trajectories in a helical scan of a dual source and dual detector CT system can be expressed as

$$\underline{s}_1(\beta) = (R \sin \beta, R \cos \beta, \frac{H}{2\pi}\beta), \beta \in [\beta_s, \beta_e] \quad (1)$$

$$\underline{s}_2(\beta') = (R \sin \beta', R \cos \beta', \frac{H}{2\pi}\beta'), \beta' = \beta + \frac{\pi}{2}, \quad (2)$$

where R is the radius of the helical source trajectory, β_s and β_e correspond to the starting and ending view angles of the helical trajectory of the first source/detector pair, denoted as A , and H is the distance traveled by each source per rotation along z -axis. The normalized helical pitch, denoted as h , is defined as the ratio of H over detector height at ISO, denoted as D , i.e.

$$h = \frac{H}{D}. \quad (3)$$

Figure 1 shows an illustration of the source trajectories of a dual source and dual detector system. In practice, the second source/detector pair, denoted as B , has a smaller scan field of view (FOV) due to space and other design constraints.

G. Cao and J. Hsieh are with GE Healthcare, Waukesha, WI USA. Send correspondence to guangzhi.cao@ge.com.

B. Fan-To-Parallel Rebinning

It is common for reconstruction algorithms to implement the reconstruction in the so-called cone-parallel geometry that can be obtained through row-wise fan-to-parallel rebinning in the native cone-beam geometry [2]. In the rebinned cone-parallel geometry, any projection data p can be specified by the cone angle α , view angle β and orthogonal distance t from the ISO-ray. Therefore, we can re-parameterize the projection data as $p(\alpha, \beta, t)$ in the cone-parallel geometry. Note that after row-wise cone-parallel rebinning, the curvature of the resultant virtual detector is inverted and the 1D ramp filtering in reconstruction is applied along the tangential direction of the helical source trajectory, which can significantly improve reconstruction accuracy.

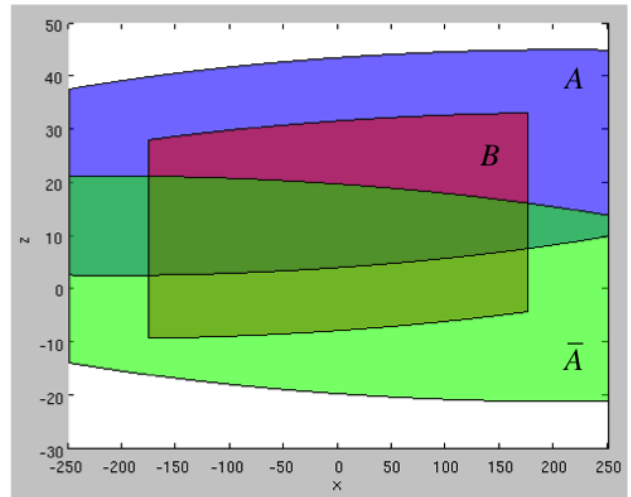
In the dual source and dual detector CT system, the rebinning process is performed separately for each source/detector pair as in a single source and single detector system. In the following section, the sampling pattern of dual source and dual detector systems is analyzed in the rebinned cone-parallel geometry.

C. Sampling Pattern and Image Artifacts

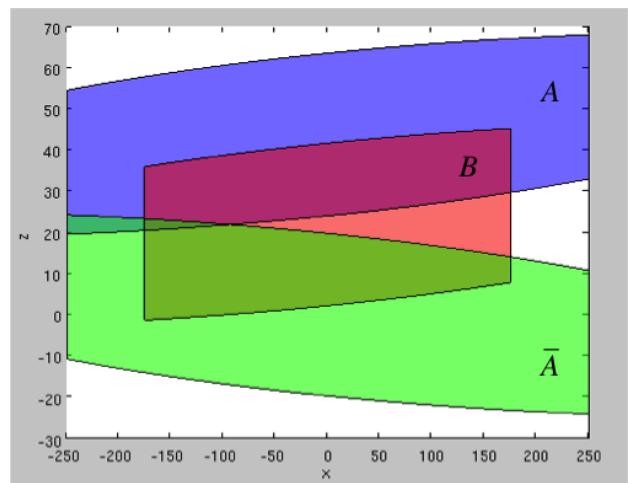
First, let us look at the sampling pattern at one view angle. In Fig. 2, the measurement from two neighboring half turns at one view angle is shown for three different pitch values. All the measurement data are projected on to a flat plane that passes the ISO center. Here we assume that detector A has a scan FOV of 500mm, and detector B has a scan FOV of 350mm. The height of the detectors is normalized to helical pitches in the figure to generalize the sampling analysis. The blue region represents the measurement of detector A in the current half turn, the brown region represents the measurement of detector B after 90 degree rotation in the current half turn; and the green region represents the measurement of detector A in the next half turn which is labeled as \bar{A} . We use the pitches $h = 1.2, 2.2$ and 3.2 as examples of low, middle and high pitches.

1) *Pitch 1.2*: From Fig. 2(a), it can be seen that at pitch 1.2 there is no region of missing measurement within the 500mm FOV. Even without the small detector B , the sampling is still complete. Actually there is a significant overlap between these three views, which means the measurement is over-complete. In this case, as long as an object is completely within the large scan FOV, any standard reconstruction algorithm, such as FDK, with an appropriate view weighting, would result in good image quality.

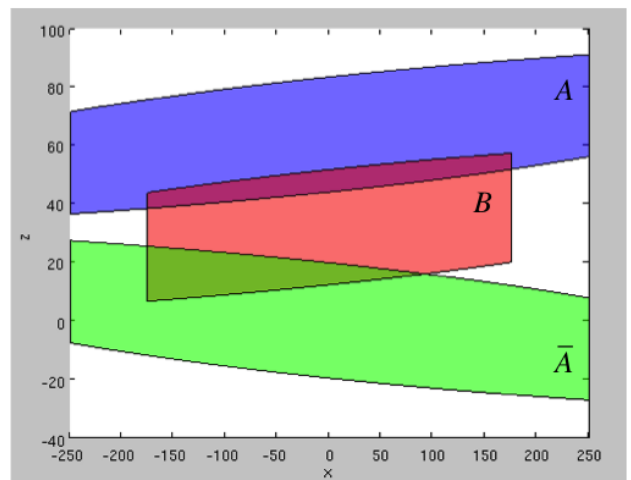
2) *Pitch 2.2*: From Fig. 2(b), it can be seen that at pitch 2.2 there is an area of missing measurement within the 500mm FOV, but the measurement is complete within the 350mm FOV of detector B after combining all these three views. In this case, if an object is completely within the small scan FOV, any standard reconstruction algorithm would result in good image quality. However, if an object contains any region that is outside the small scan FOV, these regions may not be correctly reconstructed due to missing measurement. Since this is resultant from the limited detector size in channel direction (i.e. x -axis), the corresponding artifacts is called x -truncation



(a)



(b)



(c)

Fig. 2. Projection data from two neighboring half turns at one view angle in cone-parallel geometry in a dual source and dual detector system: (a) Pitch 1.2; (b) Pitch 2.2; (c) Pitch 3.2.

artifacts. The x -truncation artifacts would even be extended further into the neighboring regions within the small FOV due

to the ramp filter that is used in reconstruction. See [3], [4] for detailed analysis and possible mitigation for this type of truncation artifacts.

3) *Pitch 3.2*: From Fig. 2(c), it can be seen that at pitch 3.2 even within the 350mm FOV there is a wedge that is not measured by any of the three views. This means that the measurement at this view angle is incomplete for the small FOV. These wedges of missing measurement have to be extrapolated along the detector row direction (i.e. z -axis) in reconstruction. This generally introduces the z -truncation artifacts. The size of the wedges increases as the helical pitch increases, and it rotates from view to view along the helical scan trajectory. See [5] for similar analysis and possible mitigation for this type of truncation artifacts.

The fact that measurement is not complete within the small FOV at pitch 3.2 in a dual source and dual detector system can also be visualized in image space. Figure 3 shows the sampling pattern of a single image slice at different z locations. The intensity of the image represents the view angle range of project measurement in radian that covers the given pixels. Therefore, if a pixel is covered by less than one π of views (i.e. 180 degree), it is under-sampled and truncation artifacts would be expected in reconstruction. The radius of the circle corresponds to the small FOV of detector B. Within the small FOV, most of the pixels get sufficient sampling. However, there are pixels within the small FOV get under-sampled, i.e. they are measured by less than 180 degree of views. These missing measurements correspond to the wedges of incomplete data in Fig. 2(c). As it can be seen, the under-sampled region rotates along the z -axis. Figure 4 shows the sampling pattern in the reformatted slice. Only the pixels that are completely sampled (i.e. ≥ 180 degree of views) within the small FOV is visualized.

III. EXPERIMENTAL RESULTS

Experiments were performed to demonstrate the effectiveness of the sampling analysis of dual source and dual detector systems as discussed above. Two phantoms were scanned at pitch 1.2 and 3.2 on a commercial dual source and dual detector system, respectively. Figure. 5(a) (b) and (c) are the image results at pitch 1.2 reconstructed in the FOV of the large detector (500mm). Figure. 5(d) (e) and (f) are the image results of the same slices at pitch 3.2 reconstructed in the FOV of the small detector (332mm). Comparing the results at the two pitches, it can be seen that there is a significant amount of image artifacts introduced at pitch 3.2. The increased artifacts confirm our analysis of under-sampled regions in the projection when the helical pitch is high.

IV. CONCLUSION

In this work, a detailed analysis on the sampling of a dual source and dual detector CT system is provided. The sampling efficiency of the system as a function of helical pitch is derived. Results show that the sampling efficiency of a dual source and dual detector system decreases as the helical pitch exceeds a threshold. In such cases, there are region within the scan FOV of the smaller detector that gets incomplete

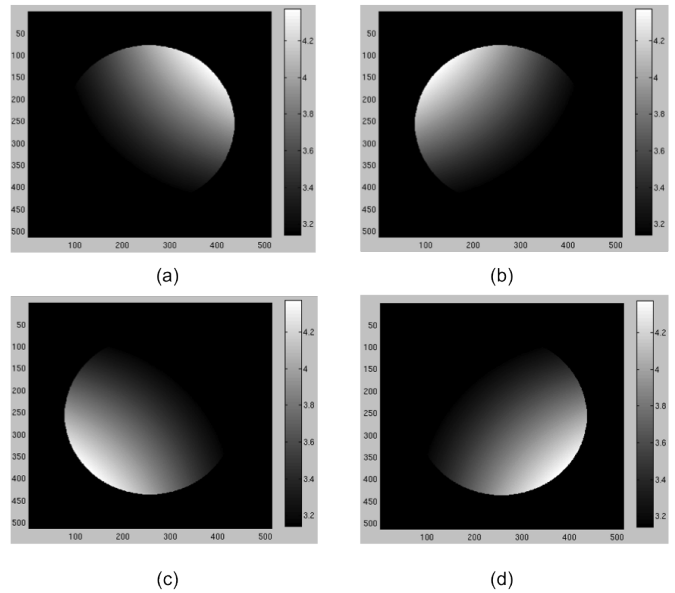


Fig. 3. Sampling pattern of a dual source and dual detector system in axial slices at different z locations at pitch 3.2. The z locations of the images correspond to: (a) $\beta = \beta_0$. (a) $\beta = \beta_0 + \pi/2$. (a) $\beta = \beta_0 + \pi$. (a) $\beta = \beta_0 + 3\pi/2$. The intensity of the image represents the view angle range of project measurement in radian that covers the given pixels. The pixels in dark are under-sampled. The radius of the circle is equal to the small FOV of detector B.

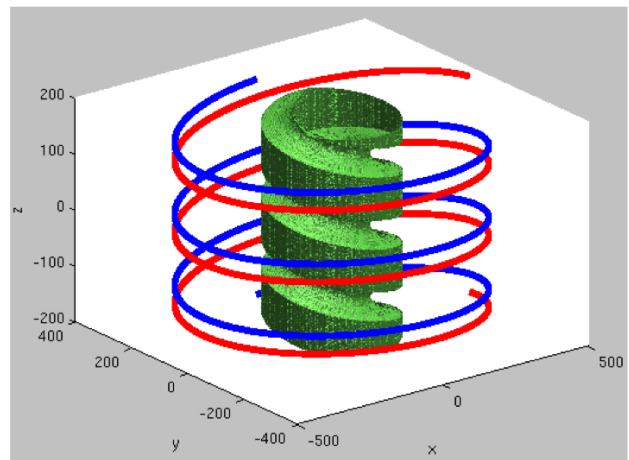


Fig. 4. Sampling pattern of a dual source and dual detector system at pitch 3.2 in 3D view. Only the pixels that are completely sampled within the small FOV is visualized.

sampling, which usually leads to increased image artifacts in clinical scans.

REFERENCES

- [1] H. Bruder, K. Stierstorfer, C. McCollough, R. Raupach, M. Petersilka, M. Grasruck, C. Suess, B. Ohnesorge, and T. Flohr, "Design considerations in cardiac ct," in *Proc. of SPIE Conf. on Medical Imaging: Image Processing*, vol. 6142, 2006.
- [2] X. Tang, J. Hsieh, R. Nilsen, S. Dutta, D. Samsonov, and A. Hagiwara, "A three-dimensional-weighted cone beam filtered backprojection (CB-FBP) algorithm for image reconstruction in volumetric CT helical scanning," *Physics in Medicine and Biology*, vol. 51, no. 4, p. 855, 2006.
- [3] J. Hsieh, E. Chao, J. Thibault, B. Grekowicz, A. Horst, S. McOlash, and T. Myers, "A novel reconstruction algorithm to extend the ct scan field-of-view," *Medical physics*, vol. 31, no. 9, pp. 2385–2391, 2004.

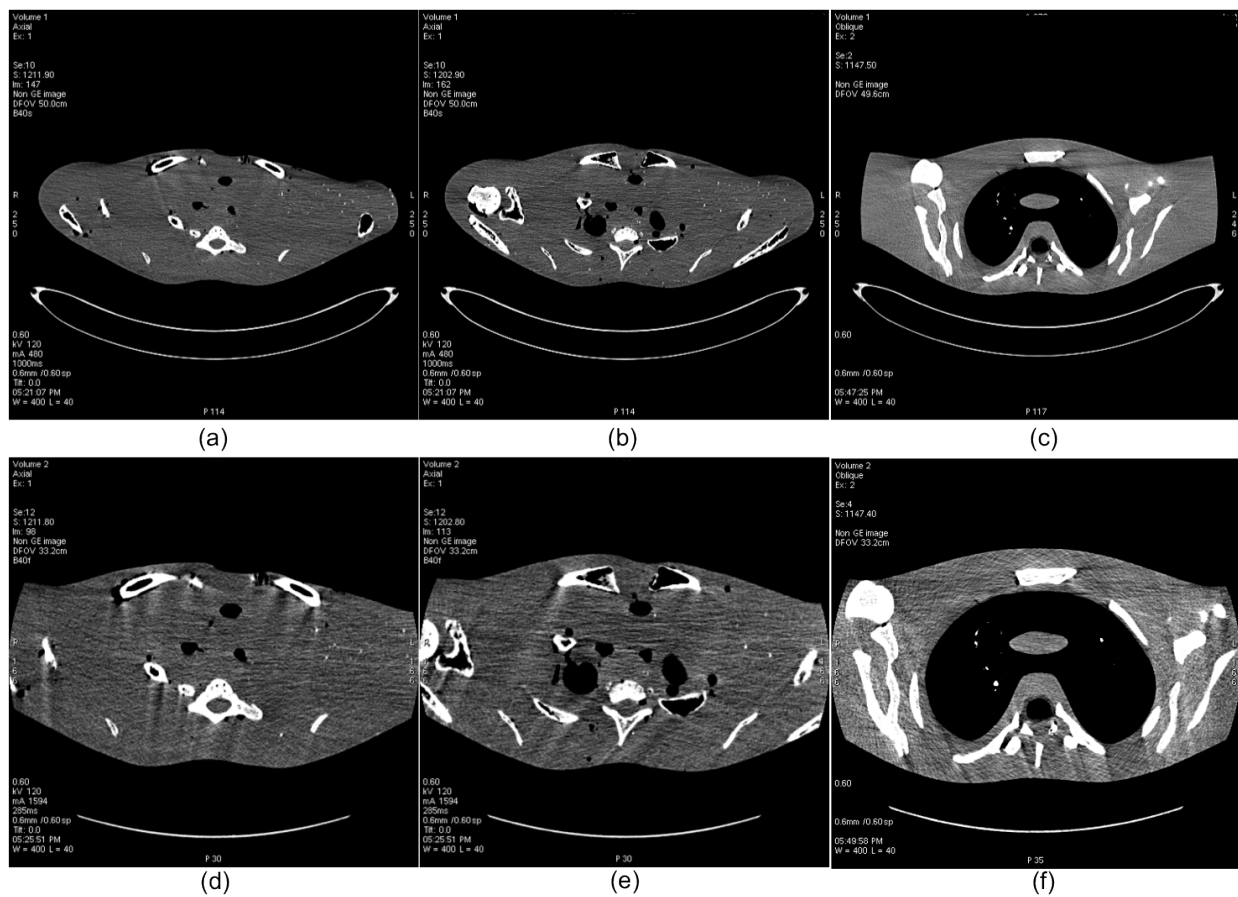


Fig. 5. Image acquired in a dual source and dual detector CT system: (a)(b)(c) Image acquired at pitch 1.2 with a FOV of 500mm; (d)(e)(f) Image acquired at pitch 3.2 with a FOV of 332mm. (W/L = 400/40)

- [4] S. Hsieh, B. Nett, G. Cao, and N. Pelc, "An algorithm to estimate the object support in truncated images," *Medical physics*.
- [5] J. Pack, B. Nett, K. Zeng, G. Cao, A. Budde, Z. Yin, B. De Man, H. Na, J. Fan, . Champley, and J. Hsieh, "Cone-beam analytic reconstruction for axial tomography," in *Fully 3D Image Reconstruction in Radiology and Nuclear Medicine*, 2013.

Quantitative Uniformity of Iodinated Contrast Across the Z-Coverage of Large Cone-Angle CT

Hewei Gao, Adam Cohen, and Yasuhiro Imai

Abstract—For multi-detector computed tomography (CT) with a Z-coverage as wide as 160 mm in axial scan, a large cone angle is required. The increased heel effect in the X-ray source present a new challenge, which may significantly affect CT number uniformity across the Z-coverage if not appropriately overcome. A native spectral solution has been developed to address the heel effect as well as other spectral issues. It is able to significantly improve the quantitative uniformity of iodinated contrast across the Z-coverage, and reduce other common physics-induced artifacts. In this paper, a comparative study is conducted to analyze the CT number uniformity on GE Revolution CT scanner operated at 80, 100, 120, and 140 kV, using a custom water phantom inserted with three tubes that are filled with three levels of iodine concentrations. Based on this phantom study, thanks to the advanced spectral solution, Revolution CT system is capable of improving quantitative uniformity of iodinated contrast down to within 7 Hounsfield Units across the whole 160 mm Z-coverage for scanning kV's and iodine contrast concentrations that are commonly used in clinical applications. Good uniformity is also achieved in a clinical cardiac CT angiography study.

Index Terms—CT number uniformity, heel effect, spectral correction

I. INTRODUCTION

THE polychromatic X-ray spectrum is a fundamental issue for conventional computed tomography (CT) as beam hardening occurs when the lower energy X-ray photons are attenuated more than those with higher energies, thus increasing the mean energy of the remaining X-ray photons. Different materials usually have different spectral response. So the conventional single-material beam hardening correction methods (e.g., water correction) that are commonly employed in clinical CT are not enough to handle dense materials such as iodine and bone [1]–[4], resulting in residual artifacts between high density objects.

For large cone angle CT system, the increased heel effect becomes a new challenge as well due to the fact that X-rays at smaller incident angles are attenuated more by the anode target itself than those at larger angles. As a result, the X-rays coming out of the target are harder at one detector side than the other. Due to the way the X-ray tube is placed in clinical CT system, the heel effect usually affects the imaging performance in the Z direction. It could easily cause more than 20 Hounsfield Units (HU) CT number shift across the Z-coverage with a moderate iodine concentration if not appropriately corrected, degrading the CT quantitative uniformity that is critical in perfusion applications.

GE Revolution CT scanner can acquire patient data in axial mode over 160 mm collimation in the Z direction. To achieve

All authors are with the GE Healthcare, Waukesha, WI 53188 (E-mail: gao@ge.com).

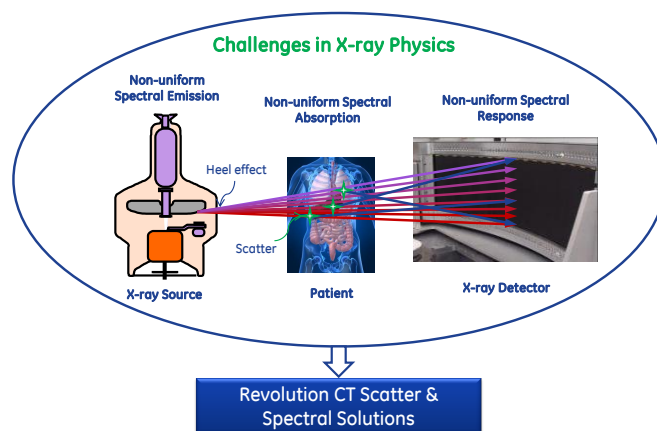


Fig. 1. Challenges in X-ray physics for a wide cone CT system.

such a wide coverage, a large cone angle is required. The Revolution CT system includes a native advanced spectral solution to address the heel effect as well as other spectral issues. It can significantly improve the quantitative uniformity of iodinated contrast across the Z-coverage, and reduces common artifacts caused by beam hardening. This paper is to present the performance of the CT number uniformity by the Revolution CT spectral solution.

II. REVOLUTION CT SPECTRAL SOLUTION

Large cone angles present the following two challenges in X-ray physics: 1) more scattered photons traveling toward the detector, 2) a larger variation in the X-ray spectra due to the increased heel effect, as illustrated in Fig. 1. Both the scatter and the spectral issues could significantly affect CT image quality [1], [5]–[7], leading to shading, cupping and ghosting artifacts in reconstructed images, as well as CT number shift and low contrast-to-noise ratio.

In Revolution CT system, a three-dimensional (3D) anti-scatter grid has been developed to provide a powerful native hardware-based solution for scattered radiation [8]. With respect to the heel effect, there is no good hardware-based solution without a severe sacrifice in X-ray photon flux [9]. A native spectral solution therefore has been developed to address not only the heel effect but also other spectral artifacts caused by patient attenuation and the non-uniformity of detector spectral response. In conjunction with 3D collimator, this significantly reduces artifacts in high atomic number materials such as iodinated contrast, bone, or other dense objects.

The spectral solution works in a straightforward way as illustrated in Fig. 2. First, a set of intermediate CT images

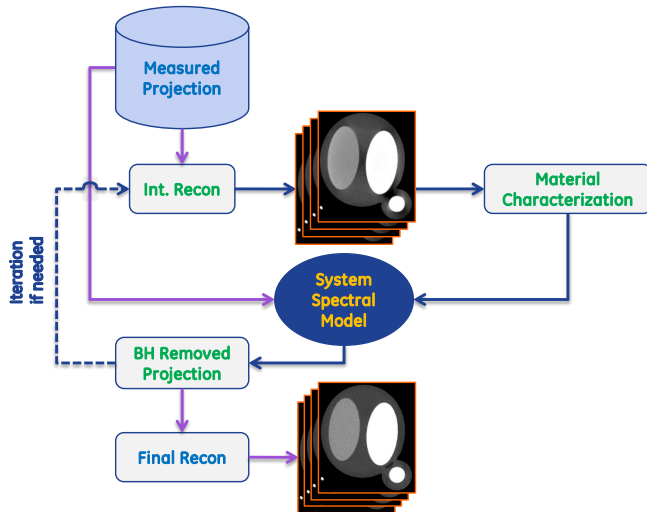


Fig. 2. The flow diagram of the Revolution CT spectral solution.

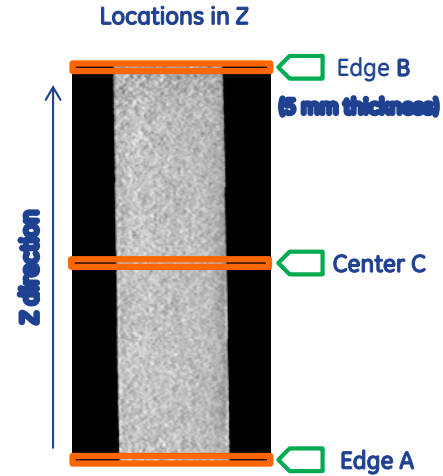


Fig. 4. The three Z-positions selected for evaluation.

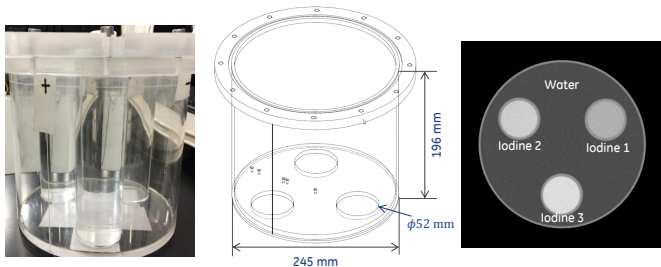


Fig. 3. Iodine-rod phantom used for quantitative uniformity study. Left: photograph; middle: dimension; right: CT image reconstructed in-plane.

are reconstructed from measured projection and then used for material characterization that follows. Once beam hardening is estimated and removed, by using the spectral model that comes from sophisticated calibration and physics modeling, final CT images will be reconstructed. Iterative corrections for multiple materials can also be applied if needed.

III. EVALUATION METHOD

To evaluate the HU uniformity across the 160 mm Z-coverage in axial scan mode, a custom phantom (as shown in Fig. 3) was scanned on Revolution CT system. It has 196 mm in height and 245 mm in diameter. There are 3 tubes symmetrically inserted in the phantom that can be filled with liquid. In our evaluation, we filled water in the tank and three different iodine concentrations (corresponding to about 230, 290 and 330 HU at 120 kV) in the tubes. Thanks to its appropriate size and structure, the phantom could generate apparent shading and cupping artifacts, as well as HU non-uniformity in the Z direction. It was scanned at four kV's that are commonly used in diagnostic mode: 80, 100, 120 and 140 kV.

All images were reconstructed using a standard kernel. As the heel effect changes monotonically from one detector side to another, the HU values of the same dense material, in general, vary monotonically along the Z direction as well. To measure the HU uniformity quantitatively, three positions in

the Z direction (“CENTER” and two “EDGES”) are selected, among which the maximum difference are computed and used as our figure of merit, i.e.,

$$\Delta = \max(HU_A, HU_B, HU_C) - \min(HU_A, HU_B, HU_C)$$

where HU_A , HU_B and HU_C represent the averaged CT numbers (over 5 mm thickness) in the three Z-positions as shown in Fig. 4. The smaller the Δ value is, the better the HU uniformity is.

It is worth noting that in order for a side-by-side comparison, a patch to the Revolution Reconstruction console is temporally added to allow disabling the spectral solution that otherwise runs natively on Revolution CT scanner in diagnostic mode.

IV. RESULTS

A. A Phantom Study

For the three iodine rods inserted into the water phantom, three regions of interest (ROIs) are evaluated, respectively, without and with the Revolution spectral solution. The reformatted images in Fig. 5 show the improvement of the iodine HU uniformity with the Revolution spectral solution turned on. Good HU uniformity also comes with removal of shading and cupping artifacts, as presented in Fig. 5 as well.

The quantitative uniformity measured by the CT number different across the whole 160 mm Z-coverage for the three iodine rods at 80, 100, 120 and 140 kV is plotted in Fig. 6, which demonstrates that, thanks to the advanced spectral solution, Revolution CT system is capable of improving quantitative HU uniformity of iodinated contrast down to within 7 HU across the whole 160 mm Z-coverage for scanning kV's and iodine contrast concentrations commonly used.

B. A CCTA Study

A clinical cardiac CT angiography (CCTA) study on Revolution CT scanner are also taken as an example to show the quantitative uniformity of the system in reality. Figure 7

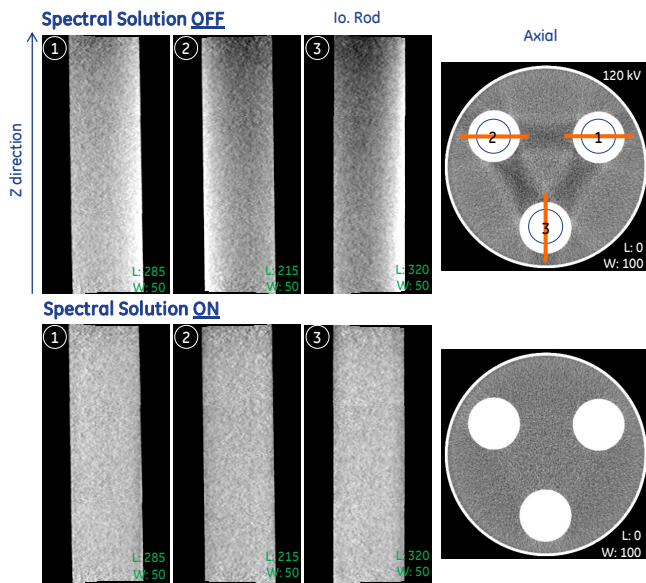


Fig. 5. Coronal/sagittal images of the iodine rods (left), axial images of the phantom (right), with the Revolution spectral solution turned OFF (top) and ON (bottom).

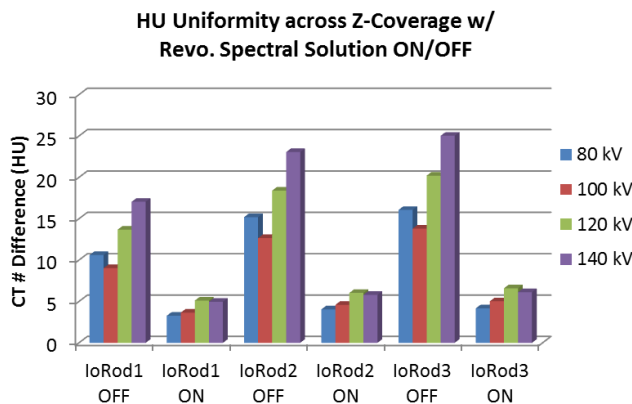


Fig. 6. CT number difference across the whole 160 mm Z-coverage.

shows clinical CCTA images on Revolution CT scanner by a single axial scan. ROIs were selected in both top and bottom regions of descending aorta (top images), and the chamber to ascending aorta (bottom images). In the top images, the averaged CT numbers of the ROIs show CT number shift across the Z-coverage are reduced from 24 HU to 1 HU with the Revolution CT spectral solution turned on. While they are reduced from 41 HU to 2 HU in the bottom images. This clearly demonstrates the capability of Revolution CT system in maintaining good quantitative uniformity across the whole Z-coverage in practical applications.

V. CONCLUSION AND DISCUSSION

The increased heel effect for wide Z-coverage CT system presents a new challenge in CT correction and reconstruction. The unique image chain on GE Revolution CT scanner features an advanced spectral solution to improve quantitative unifor-

mity of iodinated contrast. It can reduce common physics-induced artifacts from iodinated contrast, bone, and other dense objects as well. In tests performed on this evaluation the results were within 7 HU across the whole 160 mm Z-coverage for scanning kV's and contrast concentrations commonly used in diagnostics.

ACKNOWLEDGMENTS

The authors would like to thank Dr. Ricardo Cury at Baptist Hospital of Miami, FL for sharing the clinical data. Thanks also go to CT Physics/IQ team at GE Healthcare and GE Global Research.

REFERENCES

- [1] R. A. Brooks and G. D. Chiro, "Beam hardening in X-ray reconstructive tomography," *Phys. Med. Biol.*, vol. 21, no. 3, p. 390, 1976.
- [2] P. M. Joseph and R. D. Spital, "A method for correcting bone induced artifacts in computed tomography scanners," *J. Comput. Assist. Tomogr.*, vol. 2, no. 1, pp. 100–108, 1978.
- [3] G. T. Herman, "Correction for beam hardening in computed tomography," *Phys. Med. Biol.*, vol. 24, no. 1, p. 81, 1979.
- [4] G. T. Herman and S. S. Trivedi, "A Comparative Study of Two Postreconstruction Beam Hardening Correction Methods," *IEEE Trans. Med. Imag.*, vol. MI-2, no. 3, pp. 128–135, 1983.
- [5] G. H. Glover, "Compton scatter effects in CT reconstructions," *Med. Phys.*, vol. 9, no. 6, pp. 860–867, 1982.
- [6] R. Ning, X. Tang, and D. Conover, "X-ray scatter correction algorithm for cone beam CT imaging," *Med. Phys.*, vol. 31, no. 5, 2004.
- [7] J. Hsieh, *Computed Tomography: Principles, Design, Artifacts, and Recent Advances*, 2nd ed. Bellingham, WA: SPIE, 2009.
- [8] D. M. Hoffman et al, "Revolution CT system with mercury detector technology for the next generation in true volumetric imaging," 2013, white paper, GE Healthcare.
- [9] S. Mori, M. Endo, K. Nishizawa, M. Ohno, H. Miyazaki, K. Tsujita, and Y. Saito, "Prototype heel effect compensation filter for cone-beam CT," *Phys. Med. Biol.*, vol. 50, no. 22, p. N359, 2005.

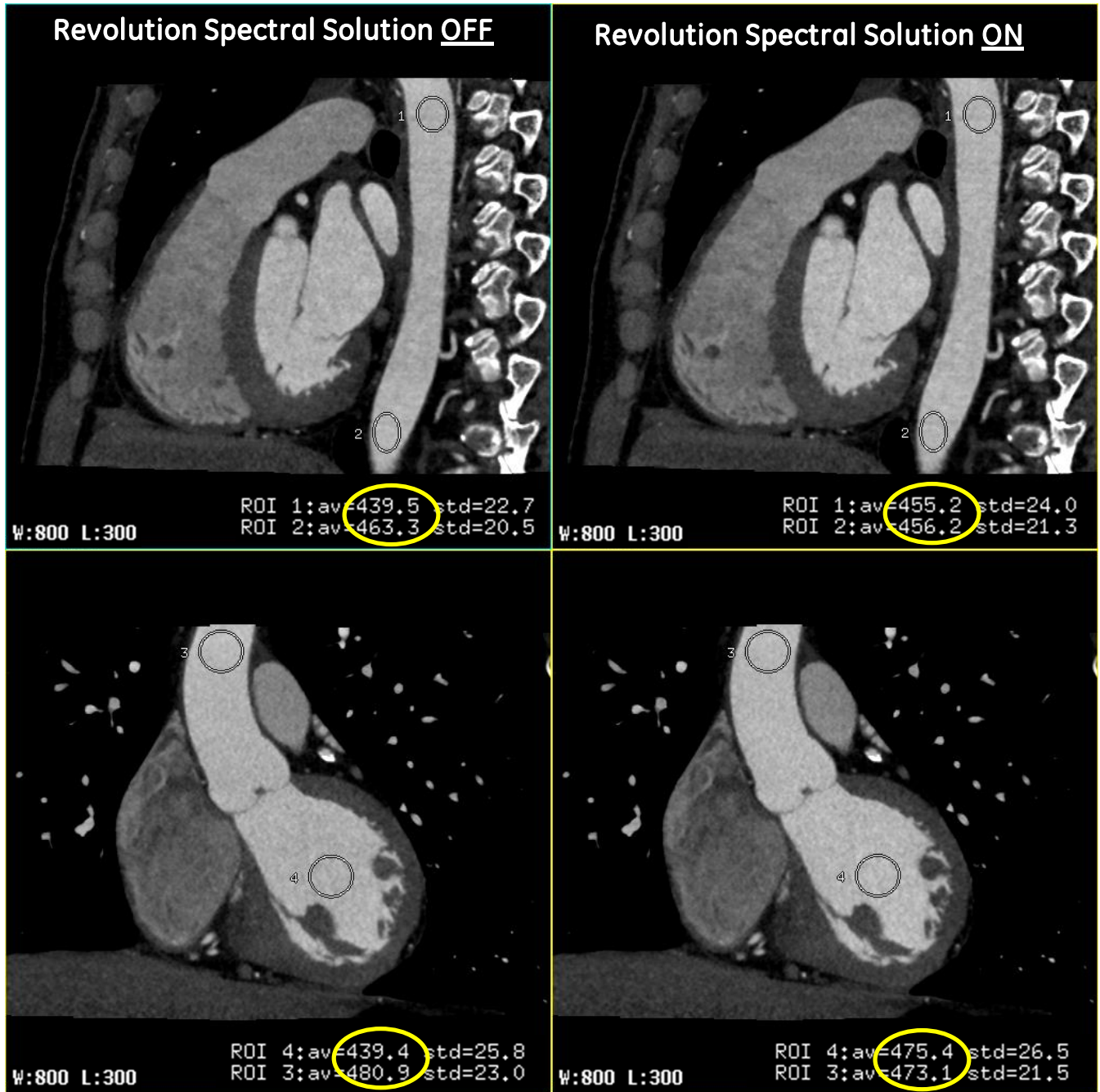


Fig. 7. CCTA images for descending aorta (top) and the chamber and ascending aorta (bottom) on Revolution CT scanner without (left) and with (right) the advanced spectral solution.

Quantifying Hotelling Observer Performance for Detection of Small Signals in CT Images Produced by Linear Reconstruction Algorithms

Adrian A Sanchez¹, Emil Y Sidky¹, and Xiaochuan Pan^{1,2}

Abstract—We present a formalism for computing Hotelling observer (HO) task performance metrics for detection of small signals in CT. The approach put forward is based on the restriction of the reconstruction to a region-of-interest containing the signal, wherein the HO metrics can be computed exactly. The method is illustrated for the detection of microcalcifications of varying size in dedicated breast CT. The results are compared to channelized Hotelling observer (CHO) results employing Laguerre-Gauss channels, as well as the results of a single human observer for reference. The proposed methodology slightly outperforms the CHO approach and has advantages in terms of computational efficiency. Both the HO and CHO methods substantially overestimate human performance, however both model observers investigated are capable of predicting the general shape of a human’s performance curve as a function of microcalcification size.

I. INTRODUCTION

The most meaningful metrics of image quality are predictive of the utility of an image with respect to a certain task. In some cases, one can make direct measurements of humans’ performance of the relevant task, thereby obtaining a measure of the quality of the images used. However, human observer experiments can be time consuming and expensive, making them unsuited to many applications, such as the optimization of multiple imaging system parameters. Further, human observer experiments have an inherent degree of variability, both between observers and even for a single observer.

In order to address some of the shortcomings of human observer experiments, many researchers have employed mathematical model observers instead. One such observer is the Hotelling Observer (HO), which is the optimal linear observer, meaning that it employs an optimal linear combination of the available measurements to perform a given task [1], [2]. The HO often constitutes a useful upper-bound on human performance[3], [4], [5], however its use in CT is limited by the nature of the CT image covariance matrix. Specifically, the image covariance matrix must be inverted to calculate HO metrics, and in the case of CT, this matrix can be large ($\sim 10^6 \times 10^6$), highly non-diagonal, and non-circulant.

In order to address the dimensionality issue of the image covariance matrix, some authors have proposed the use of efficient channels. Here, we present an alternative approach for small signals, wherein only a region of interest (ROI) around

the signal is considered, and the resulting image covariance can be stored in computer memory and directly inverted. By fully accounting for inter-pixel covariances within the ROI, we hypothesize that HO metrics for detection of small signals can be more accurately approximated and can be obtained more efficiently than with the use of efficient channels. We demonstrate the use of this approach for assessing the detectability of microcalcifications in dedicated breast CT. A quantitative comparison to the performance of a single human observer is included for reference.

II. THE CLASSIFICATION TASK

The task of microcalcification detection can be seen as a two-class classification task. Given a noisy CT image \mathbf{y} , an observer must classify the image as belonging to either a “microcalcification-present” class or a “microcalcification-absent” class. We shall refer to these two classes as H_1 and H_0 , respectively.

The performance of an observer in a two-class classification task, such as signal detection, can be quantified by means of a two-alternative forced choice (2AFC) experiment. In a 2AFC experiment, an observer is presented with two images \mathbf{y}_0 , which belongs to the class H_0 , and \mathbf{y}_1 , which corresponds to H_1 [6]. The observer then computes a scalar test statistic $t(\mathbf{y})$, commonly referred to as the decision variable, for each of the two images. The observer then assigns the signal-present decision to the image that produces the higher value of the decision variable. For each decision made, the trial is assigned a score of either 1, signifying a correct decision has been made, or 0 for an incorrect decision. The ensemble average of the scores is then the observer’s proportion of correct decisions, P_C for the detection task. For any decision variable, P_C is equal to the area under the ROC curve (AUC) for that observer and task. In practice, since we cannot access the full statistical ensemble of scores, the sample average of scores across many trials is used as an efficient, unbiased estimator of the true P_C .

III. THE HOTELLING OBSERVER

The HO’s test statistic used for classification, $t(\mathbf{y})$, is computed as a linear combination of image pixel values:

$$t = \mathbf{w}_y^T \mathbf{y}, \quad (1)$$

where \mathbf{w}_y is the optimal set of weights for the image pixels, known as the Hotelling template. The Hotelling template is in

¹The University of Chicago, Department of Radiology, Chicago, IL 60637

²The University of Chicago, Department of Radiation and Cellular Oncology, Chicago IL 60637

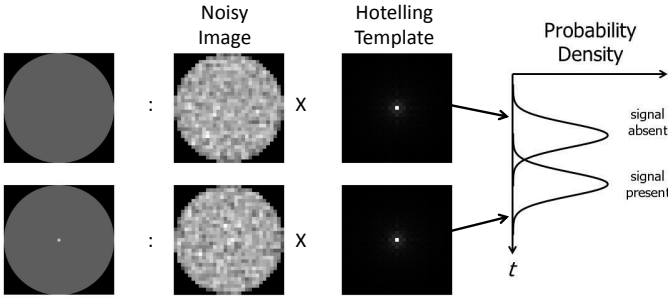


Fig. 1. In order to classify an image as corresponding to a single hypothesis, the HO computes the inner product of a noisy image with the Hotelling template. The resulting scalar test statistic t is then compared to a threshold value and assigned to a class accordingly. This is the approach of any linear observer performing a classification task, and the HO is the optimal linear observer.

turn defined as

$$\bar{K}_y w_y = \Delta \bar{y}, \quad (2)$$

where \bar{K}_y is the average of the image covariance matrix under the two hypotheses, and $\Delta \bar{y}$ is the mean difference between images from the two hypotheses. Since we assume a signal-known-exactly, background-known-exactly (SKE/BKE) paradigm, $\Delta \bar{y}$ can be obtained simply through simulation of noiseless images. The process of HO classification is outlined schematically in Fig. 1. Note that noise in the images introduces statistical variability in the outcome of the test statistic for each hypothesis. The task of the HO can then be seen as the construction of a linear test statistic which has maximally separated statistical distributions under the two hypotheses.

In this work, we considered the data vector \mathbf{g} , which represents the line-integral data obtained after applying the negative logarithm to the original projection data. Since we are restricting our discussion to CT images resulting from linear reconstruction algorithms, the action of these algorithms on \mathbf{g} is fully captured through multiplication with a reconstruction matrix A , so that the image \mathbf{y} is given by

$$\mathbf{y} = A\mathbf{g} \quad (3)$$

Ref. [6] then provides the useful result that the image covariance matrix K_y is related to the covariance of the projection data vector K_g by

$$K_y = AK_g A^\dagger, \quad (4)$$

where the superscript \dagger denotes the Hermitian conjugate, and reduces to a matrix transpose since we consider the matrix A to be real.

In order to address the issue of large dimensionality of K_y , we restrict the image to a smaller circular ROI within a 31×31 pixel² image containing the signal of interest. Given that there are 128 projection views simulated, along with 1590 detector bins, this implies that the matrix A has dimension $31^2 \times 203,520$. This matrix can be stored directly in computer memory on most systems, as can the resulting K_y

matrix with dimension $31^2 \times 31^2$. The image covariance matrix can then be inverted via a Moore-Penrose pseudo-inversion or by any direct matrix inversion method in that event that it is full rank. In practice, one can construct the transpose of the reconstruction matrix, A^T , column-wise, which requires $O(n_{\text{pix}}^2)$ operations, where n_{pix} is the number of pixels in the ROI (the matrix A^T has n_{pix} columns, the determination of each of which requires the equivalent of a single back-projection).

The noise model we assumed in this work is independent, zero-mean Gaussian noise added to the line-integral data vector \mathbf{g} . The variance of the data was based on the CT data noise model put forward by Barrett and Swindell [7]. This noise model approximates the variance in the line integral data \mathbf{g} (after applying the negative logarithm) as:

$$\text{Var}\{\mathbf{g}_i\} = \frac{1}{\bar{N}_i} + \frac{1}{\bar{N}_0} \quad (5)$$

where \bar{N}_0 is a constant representing the mean number of photons incident on and absorbed by the detector in an air scan, and \bar{N}_i is the mean number of photons incident on the i th detector pixel transmitted through the numerical phantom. The data covariance matrix K_g is then given by

$$(K_g)_{i,j} = \begin{cases} \frac{e^{\bar{g}_i+1}}{\bar{N}_0} & : i = j \\ 0 & : \text{else.} \end{cases} \quad (6)$$

where $(K_g)_{i,j} = \text{Cov}\{g_i, g_j\}$ and \bar{g}_i is the mean value of \mathbf{g}_i . \bar{N}_0 was set to approximately 140,000 per detector pixel per view, based on the mean flux of photons from an 80kVp setting necessary to produce the same dose in a 14cm diameter breast as two-view mammography [8].

Equipped with this noise model, we can then compute all of the relevant quantities for the HO. Specifically, since the data we consider are Gaussian-distributed, the HO's P_C can be computed as

$$P_C = \frac{1}{2} + \frac{1}{2} \text{erf}\left(\frac{\text{SNR}_y}{2}\right), \quad (7)$$

where

$$\text{SNR}_y^2 = w_y^T \Delta \bar{y} \quad (8)$$

is the HO's SNR.

IV. EFFICIENT CHANNELS

One potentially effective means of reducing the dimensionality of the covariance term is a judicious selection of efficient channels. With prior knowledge of the nature of the signal to be detected and the background statistics, one can select a new basis in which to express the reconstructed image which requires relatively few basis functions (channels) and still largely preserves the separability of the two distributions $t(\mathbf{y}_0)$ and $t(\mathbf{y}_1)$. Since the microcalcifications we model are circularly symmetric, we employ Laguerre-Gauss channels, which have been demonstrated to efficiently and accurately approximate the HO performance for various circularly symmetric signals [6], [9].

The resulting observer is termed the channelized Hotelling observer (CHO), and its template is defined in channel space as

$$\bar{K}_v w_v = \Delta \bar{v}, \quad (9)$$

where $\Delta \bar{v}$ is the mean difference in the channel outputs from the two classes, $\Delta \bar{v} = U^T \Delta \bar{y}$, and U is a matrix whose columns are discretized versions of the channel functions. The corresponding covariance matrix and CHO SNR are then given by

$$K_v = U^T K_y U \quad (10)$$

and

$$\text{SNR}_v^2 = w_v^T \Delta \bar{v}, \quad (11)$$

respectively. The CHO P_C is then computed as in Eqn. 7.

Direct computation of K_v requires $O(N_{\text{pix}} \times N_C)$ operations, where N_{pix} is the number of pixels in the full image, and N_C is the number of channels used. In our case, we found maximal CHO performance with at least 20 channels. However, given the computational requirements of computing HO performance within an ROI given above, this still corresponds to a roughly 75-fold increase in computational demands relative to the ROI HO outlined above.

V. HUMAN OBSERVER STUDY

In order to provide a reference for the model observer results, a human volunteer performed a 2AFC experiment for detection of microcalcifications using images simulated with the same system, noise, and phantom parameters used in the model observer studies. The human observer performed 300 2AFC trials for each of five microcalcification sizes ranging from $100\mu\text{m}$ to $200\mu\text{m}$. Three signal locations were considered, as discussed below for the HO and CHO experiments. In addition to the two image choices, \mathbf{y}_0 and \mathbf{y}_1 , presented to the observer, the reconstructed signal was also shown accompanying each pair of images. Ten trials were performed preceding the 300 recorded trials for each microcalcification size as training for the observer. The images were windowed and leveled so that the level was roughly centered on the mean pixel value and the window width roughly corresponded to two-thirds of the full range of pixel values. The specific window used was $[0.0213, 0.024]\text{mm}^{-1}$.

In order to compute a confidence interval (CI) for the true P_C , we used Papoulis's [10] expression for estimating the CI of a Gaussian-distributed estimator when the variance of the estimator is unknown. Namely, we use the fact that the probability

$$P \left\{ \hat{P}_C - \frac{s}{\sqrt{n}} z_{1-\delta/2} < P_C < \hat{P}_C + \frac{s}{\sqrt{n}} z_{1-\delta/2} \right\} > 1 - \delta = \gamma \quad (12)$$

where δ is the confidence level, γ is the confidence coefficient, s is the sample standard deviation, z_u denotes the u th percentile of the standard normal density, and n is the number of trials (300). 95% confidence intervals for P_C were then found by setting $\gamma = 0.95$ and evaluating Eqn. 12.

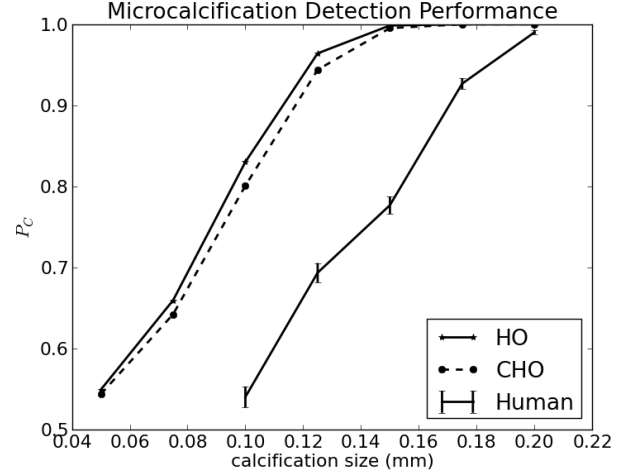


Fig. 2. The proportion of correct decisions for the HO, CHO, and human observer are shown as a function of the microcalcification size simulated. Error bars on the human performance denote 95% confidence intervals.

VI. SIMULATION PARAMETERS

The specific CT system simulated in this work is based on the system simulated in Ref. [11]. We model a flat-panel fan-beam system with a source-to-detector distance of 80cm, and a source-to-axis distance of 60cm. We consider 128 projection views equally spaced over 2π degrees and an array of 1590 detector pixels spaced over a detector width of approximately 31.8cm, for a detector pixel width of 0.2mm. For image reconstruction, the circular field-of-view is then inscribed in a $(1659 \text{ pixel})^2$ image array, with square pixels of width 0.1mm. Finally, a 0.4mm x-ray focal spot was modeled by convolving the projection data with a rect function. FBP reconstruction was used, along with a 2D Butterworth filter applied to the reconstructed images. The Butterworth filter was of order 5.0, with a cutoff of 0.25mm^{-1} .

Although only an ROI was considered for computation of $\Delta \bar{y}$, for accurate noise modeling, a full breast phantom was considered in the calculation of the data covariance matrix K_g . The breast phantom used was a uniform circle with a 7.0cm radius. The background was uniform with an attenuation value midway between adipose and fibro-glandular breast tissue [12]. The microcalcifications were circularly symmetric Gaussian functions with full widths at half-maximum defined by the microcalcification size and peak attenuation values equal to that of calcium. The attenuation was scaled with the inverse of the microcalcification diameter for diameters less than 1.0mm to account for linear partial volume averaging within the 1.0mm thick slice. Finally, the location of the microcalcification was set to the center of the field of view, 2.0cm from the center, and 4.0cm from the center, and the corresponding HO and CHO results were averaged across signal locations. This is equivalent to a signal-known-exactly-but-variable (SKEV) paradigm.

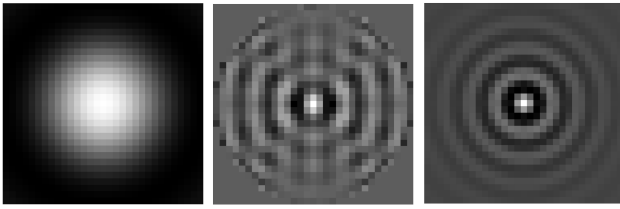


Fig. 3. Left: The reconstructed image of a $100\mu\text{m}$ microcalcification at the center of the FOV. Middle: The HO template for detection of the signal shown in the top row, when the reconstruction is restricted to a 31×31 pixel ROI. Right: The CHO template for detection of the microcalcification. The area of the images shown is the same in all three cases.

VII. RESULTS

The performance of the HO, CHO, and human observer are shown in Fig. 2 in terms of P_C for a range of microcalcification sizes. Error bars corresponding to 95% confidence intervals are shown for the human observer. Clearly, both the HO and CHO establish upper bounds on the human observer, but are not quantitatively predictive of human performance in this case. Although the significance of the disagreement is lessened somewhat by the fact that only a single human observer was used, it is worth noting that the human observer agreed closely with the detection performance predicted by Ref. [11]. More importantly, the HO was qualitatively predictive of the human's performance, suggesting that both the HO and CHO could potentially be used for rank ordering of tasks, system parameters, or reconstruction options in terms of human performance.

The fact that the ROI HO outperformed the CHO (which was based on the full reconstructed field-of-view) implies that the HO acting on the small ROI performed more closely to the true HO for the full image than did the CHO. The improved accuracy of the ROI method relative to efficient channels, taken together with the improvements in computational efficiency, imply that the ROI approach is likely preferable for detection performance evaluation for small signals. Further, the formulation put forward in this work is entirely general in that it makes no assumptions regarding the structure of the signal to be detected or of the Hotelling template. Finally, there is a further benefit to the ROI approach, which is that the efficient channels used here employ a scaling factor which must be determined through an optimization of the CHO performance for a given signal, and the CHO must also be optimized in terms of the number of channels used.

Fig. 3 shows the mean difference image between classes, $\Delta\bar{y}$ (left), along with the templates for the HO (middle) and CHO (right). Inspection of the templates for the HO and CHO reveal one limitation of the CHO, which is that it assumes that not only the signal, but also the template, is circularly symmetric and therefore expressible through the radial Laguerre-Gauss functions. In our case, the reconstructed signal was circularly symmetric, but based on the template results shown in Fig. 3, this clearly isn't a guarantee that the optimal template also possesses equivalent symmetry properties.

VIII. SUMMARY

We have demonstrated the use of the Hotelling Observer for assessment of microcalcification detection performance in a dedicated breast CT system. For small signals, the calculation of image covariance can be restricted to an ROI, and in the case investigated here, this is sufficient to outperform the use of Laguerre-Gauss channels in terms of accuracy for determining HO performance metrics. Taken with the fact that there is a substantial improvement in terms of computational efficiency when using the ROI method, this suggests that the HO performing in an ROI could be used effectively for rank ordering of imaging parameters in a task-based framework, and could potentially be used for system optimization.

ACKNOWLEDGMENTS

This work was supported in part by NIH R01 Grant Nos. CA120540, CA158446, and EB000225 and NIH T32 Grant No. EB002103-22. The contents of this article are solely the responsibility of the authors and do not necessarily represent the official views of the National Institutes of Health.

REFERENCES

- [1] K. J. Myers, "Visual perception in correlated noise (models)." 1985.
- [2] R. Fiete, H. Barrett, E. Cargill, K. Myers, and W. Smith, "Psychophysical validation of the hotelling trace criterion as a metric for system performance," in *Proceedings SPIE Medical Imaging*, vol. 767, 1987, p. 298305.
- [3] J. Yao and H. H. Barrett, "Predicting human performance by a channelized hotelling observer model," in *San Diego'92*, 1992, p. 161168.
- [4] H. H. Barrett, J. Yao, J. P. Rolland, and K. J. Myers, "Model observers for assessment of image quality," *Proceedings of the National Academy of Sciences*, vol. 90, no. 21, p. 97589765, 1993.
- [5] J. P. Rolland and H. H. Barrett, "Effect of random background inhomogeneity on observer detection performance," *JOSA A*, vol. 9, no. 5, p. 649658, 1992.
- [6] H. H. Barrett and K. J. Myers, *Foundations of Image Science*. Hoboken, New Jersey: John Wiley & Sons, Inc., 2004.
- [7] H. H. Barrett and W. Swindell, *Radiological imaging: the theory of image formation, detection, and processing*. Academic Press, 1996.
- [8] J. M. Boone, A. L. Kwan, J. A. Seibert, N. Shah, K. K. Lindfors, and T. R. Nelson, "Technique factors and their relationship to radiation dose in pendant geometry breast CT," *Medical Physics*, vol. 32, p. 3767, 2005.
- [9] B. D. Gallas and H. H. Barrett, "Validating the use of channels to estimate the ideal linear observer," *JOSA A*, vol. 20, no. 9, p. 17251738, 2003.
- [10] A. Papoulis and S. U. Pillai, "Probability, random variables and stochastic processes with errata sheet," *New York, NY, McGraw-Hill Education*, 2002.
- [11] X. Gong, A. A. Vedula, and S. J. Glick, "Microcalcification detection using cone-beam CT mammography with a flat-panel imager," *Physics in Medicine and Biology*, vol. 49, no. 11, pp. 2183-2195, Jun. 2004.
- [12] P. C. Johns and M. J. Yaffe, "X-ray characterisation of normal and neoplastic breast tissues," *Physics in medicine and biology*, vol. 32, no. 6, p. 675, 1987.

Optimization-based Reconstruction Exploiting Spectral Information in CT

Xiaochuan Pan, Buxin Chen, Zheng Zhang, Erik Pearson, Emil Sidky, and Xiao Han

Abstract—Interest exists in the development and applications of new CT systems that can collect multiple sets of data, including energy-integrating and/or photon-counting data. Practical utilities of such systems include improving image quality and, more importantly, exploiting spectral information for enabling imaging systems and configurations of clinical significance. In the work, instead of using data-based decomposition combined with standard analytic-based reconstruction, we propose an optimization-based reconstruction method for CT systems with multiple data sets. The method consists of a linearized data model, optimization program, and associated algorithm specifically designed for images resulting from data collected in such CT systems. Simulation studies using two distinct diagnostic range kV spectra show the robustness and effectiveness of the proposed method in correcting for non-linear beam hardening artifacts in CT images.

I. INTRODUCTION

Spectral CT refers to CT systems that explore and attempt to recover the underlying spectral properties of materials. As a result, materials can be differentiated by not only electron density, but also their energy dependence, leading to enhanced material contrast and benefiting radiological applications including vascular, cardiac, and abdominal imaging [1]–[4]. In addition, by incorporating the spectral properties of the materials, we can reduce the beam hardening artifacts from high contrast structures or metal objects [5], [6]. Recent interests and efforts in developing spectral CT systems that can collect multiple sets of data, including energy-integrating and/or photon-counting data, rely mostly on image- or data-based decomposition combined with standard analytic-based reconstruction [7]–[12]. While either decomposition method has certain constraints, the analytic-based reconstruction possesses additional limitations, especially on sampling condition [13]. In the work, we propose an optimization-based reconstruction method that integrates the decomposition into the reconstruction for CT systems with multiple data sets. The method consists of a linearized data model, optimization program, and associated algorithm specifically designed for images resulting from data collected with such systems. Potential utilities of the developed reconstruction method include designing, enabling, and optimizing spectral CT systems and their practical applications. Preliminary simulation studies using two distinct diagnostic range kV spectra are conducted to demonstrate the robustness and effectiveness of the proposed method in correcting for non-linear beam hardening artifacts.

X. Pan is with the Departments of Radiology & Radiation and Cellular Oncology, The University of Chicago, Chicago, IL 60637 USA.

B. Chen, Z. Zhang, E. Pearson, E. Sidky, X. Han are with the Department of Radiology, The University of Chicago, Chicago, IL 60637 USA.

II. STANDARD IMAGING MODEL

When the energy spectrum of the X-ray source and detector response is considered, one can express mathematically the natural logarithmic of the intensity measured in CT as

$$g_m = -\ln \int S(E) \exp \left[- \int_L \mu(E, \vec{r}) dl \right] dE, \quad (1)$$

where $S(E)$ denotes the normalized energy spectrum, $\mu(E, \vec{r})$ the linear attenuation coefficient at energy E and spatial location \vec{r} , and L indicates X-ray path L . It is a well-known practice to decompose $\mu(E, \vec{r})$ into contributions from relevant basis materials. While μ is in general the summation of contributions from different physical interactions (e.g., photoelectric and Compton interactions for a diagnostic X-ray energy range), each of the physical interactions can be predominant in certain basis materials. As a result, we consider in the work a decomposition of $\mu(E, \vec{r})$ into T types of basis materials as

$$\mu(E, \vec{r}) \approx \sum_{t=1}^T \mu_t(E) c_t(\vec{r}), \quad (2)$$

where t indexes basis material with $\mu_t(E)$, and $c_t(\vec{r})$ is the contribution from the t th basis material at location \vec{r} . In practical applications, the number of basis materials is typically 2 or 3, depending on if the K-edge effect is of interest in the energy spectrum studied. When additional contrast materials are considered, the number of basis materials can be larger than 3 [10].

Further, we can separate $\mu_t(E)$ into a constant plus a perturbation term [11], as $\mu_t(E)$ as

$$\mu_t(E) = \bar{\mu}_t + \Delta\mu_t(E), \quad (3)$$

where

$$\bar{\mu}_t \equiv \int S(E) \mu_t(E) dE \quad \text{and} \quad \Delta\mu_t(E) = \mu_t(E) - \bar{\mu}_t. \quad (4)$$

Using system spectrum $S(E)$ and knowledge of $\mu_t(E)$ obtained from, e.g., NIST data base, for a given material type, one can readily calculate the spectrum-averaged term $\bar{\mu}_t$ and thus the perturbative, beam-hardening term $\Delta\mu_t(E)$.

Substitution of Eqs. (2) and (3) into Eq. (1) yields

$$g_m = \sum_{t=1}^T \bar{\mu}_t \int_L c_t(\vec{r}) dl + g_{BH}, \quad (5)$$

where the non-linear, perturbation term g_{BH} is defined as

$$g_{BH} \equiv -\ln \int S(E) \exp \left[-\sum_{t=1}^T \Delta \mu_t(E) \int_L c_t(\vec{r}) dl \right] dE. \quad (6)$$

Note that, 1) for the sake of convenience and not causing confusion, we use an equal sign in Eq. (5) even though the decomposition in Eq. (2) is an approximation; and 2) g_{BH} can be estimated from knowledge of $c_t(\vec{r})$ using the above Eq. (6). This observation is particularly important, as discussed in Sec. VI, for the generalization of the optimization-based reconstruction developed below to correct for the beam hardening artifacts.

We define g as the contribution from the linear term, i.e.,

$$g = g_m - g_{BH} = \sum_{t=1}^T \bar{\mu}_t \int_L c_t(\vec{r}) dl. \quad (7)$$

The task of image reconstruction is to, from the knowledge of measurements g_m , $\mu_t(E)$ of basis material types, and energy spectra $S(E)$, determine the basis images $c_t(\vec{r})$.

III. OPTIMIZATION-BASED RECONSTRUCTION

Using Eq. (7) as a guide, we develop below an optimization-based method for image reconstruction from multiple CT data sets collected. The method consists of a discrete-to-discrete model, optimization program, and reconstruction algorithm. In the formulation, we assume that we have S sets of measurements, with typically $S \geq T$. The S sets can be obtained in different ways: (1) dual or multiple X-ray source; (2) single X-ray source, dual or multiple layer detector; (3) single X-ray source, dual or multiple kVp switching; (4) single X-ray source, dual or multiple kVp spin; (5) single X-ray source, single X-ray photon counting detector with multiple energy bins; (6) a combination of the above.

A. Discrete-to-discrete Data Model

For a total of S sets of measurements, we use (column) vector \vec{g}_m^s of size M^s to denote the s th set of measurements, each entry of which depicts the measurement of a particular X-ray. Let vector \vec{g}^s of size M^s denote the s th data set, which, according to Eq. (7), is related to the measurements through

$$\vec{g}^s = \vec{g}_m^s - \vec{g}_{BH}^s, \quad (8)$$

where vector \vec{g}_{BH}^s of size M^s denotes the beam hardening term. For the purpose of developing the data model, we assume for now that \vec{g}_{BH}^s is known, and its estimation and effect on the reconstruction will be discussed in Sec. VI below. Next, let (column) vector \vec{c}_t of size N denote the t th basis image, each entry of which represents the image value of a pixel in 2D (or a voxel in 3D) grid. For a given imaging condition that collects the s th data set, we use A^s to denote the system-geometry matrix, i.e., A^s is a discrete form of a fan- or cone-beam projection process:

$$\int_L c_t(\vec{r}) dl \rightarrow A^s \vec{c}_t. \quad (9)$$

Based on Eqs. (8) and (9), we can develop a discrete-to-discrete (DD) data model for spectral CT imaging with multiple data sets:

$$\vec{G} = \mathcal{H} \vec{C}, \quad (10)$$

where $\vec{G}^\top = (\vec{g}^{1\top}, \vec{g}^{2\top}, \dots, \vec{g}^{S\top})$, $\vec{C}^\top = (\vec{c}_1^\top, \vec{c}_2^\top, \dots, \vec{c}_T^\top)$ (\top indicates transpose),

$$\mathcal{H} = \begin{pmatrix} \bar{\mu}_1^1 d_1^1 A^1 & \bar{\mu}_2^1 d_2^1 A^1 & \cdots & \bar{\mu}_T^1 d_T^1 A^1 \\ \bar{\mu}_1^2 d_1^2 A^2 & \bar{\mu}_2^2 d_2^2 A^2 & \cdots & \bar{\mu}_T^2 d_T^2 A^2 \\ \vdots & \vdots & \ddots & \vdots \\ \bar{\mu}_1^S d_1^S A^S & \bar{\mu}_2^S d_2^S A^S & \cdots & \bar{\mu}_T^S d_T^S A^S \end{pmatrix}, \quad (11)$$

and

$$\bar{\mu}_t^s \equiv \int S^s(E) \mu_t(E) dE. \quad (12)$$

$S^s(E)$ is the energy spectrum used to collect the s th set of measurements, and d_t^s a scalar designed to control the contribution of basis image \vec{c}_t to the s th data set. For example, it is 1 for conventional energy integrating measurements, while it can be set to 0 or $\frac{1}{\bar{\mu}_t^s}$ for energy-decomposed data. Here s runs from 1 to S , and t from 1 to T .

B. Reconstruction Program

Optimization programs can be devised by use of Eqs. (10) and (11) for reconstruction of the basis images. In this work, we formulate a constrained total variation (TV)-minimization program as below

$$\begin{aligned} (\vec{c}_1^\top, \vec{c}_2^\top, \dots, \vec{c}_T^\top) &= \operatorname{argmin} \sum_{t=1}^T \|\vec{c}_t\|_{TV} \\ \text{s.t. } D_w(\vec{G}) &< \epsilon \text{ and } c_{ti} > 0, \end{aligned} \quad (13)$$

where c_{ti} denotes the image value on the i th pixel/voxel of the t th basis image,

$$\begin{aligned} D_w(\vec{G}) &= \left\| \mathcal{H} \vec{C} - \vec{G} \right\|_w^2 \\ &= \sum_{s=1}^S \left\| W^s \left(A^s \cdot \sum_{t=1}^T \bar{\mu}_t^s d_t^s \vec{c}_t - \vec{g}^s \right) \right\|_2^2, \end{aligned}$$

is a L2-norm of weighted data difference, W^s is a diagonal weighting matrix of size $M^s \times M^s$, and ϵ a positive parameter accounting for the inconsistencies between data vectors and model. The weighting matrices can be designed for balancing the contributions to the data distance not only among data within a set of measurements but also among data from different sets of measurements.

C. Reconstruction Algorithm

Based upon the ASD-POCS algorithm that was designed for solving a constrained TV-minimization optimization program [14], we develop an algorithm to solve the optimization program in Eq. (13) for \vec{c}_t . Specifically, the algorithm uses a modified projection-onto-convex-sets (POCS) for lowering the weighted data distance and the steepest descend (SD) for reducing basis-image TV. We define a composite image vector

as

$$\vec{f} = \sum_{t=1}^T \bar{\mu}_t^s d_t^s \vec{c}_t. \quad (14)$$

In the modified POCS portion, the algorithm reconstructs the composite and basis images as

$$\vec{f}^{\vec{p},q+1} = \vec{f}^{\vec{p},q} + \beta w_j^s \vec{A}_j^{s\top} \frac{g_j^s - \vec{A}_j^s \cdot \vec{f}^{\vec{p},q}}{\vec{A}_j^s \cdot \vec{A}_j^{s\top}}, \quad (15)$$

and

$$\vec{c}_t^{(p,s+1)} - \vec{c}_t^{(p,s)} = \frac{\bar{\mu}_t^s d_t^s}{\sum_{t=1}^T (\bar{\mu}_t^s d_t^s)^2} \left(\vec{f}^{\vec{p},s+1} - \vec{f}^{\vec{p},s} \right), \quad (16)$$

where g_j^s denotes datum on the j th detector bin in data set s , and w_j^s the j th diagonal element of weight matrix W^s . $\vec{f}^{\vec{p},q}$ and $\vec{c}_t^{(p,q)}$ are the q th updates at the p th iteration of the composite and basis images, while $\vec{f}^{\vec{p},s}$ and $\vec{c}_t^{(p,s)}$ are the composite and basis images after all updates from s th data set at the p th iteration. In general, q increments as (s, j) is followed by next update (s', j') . As j loops from 1 to M^s and s from 1 to S , one completes an iteration and increment p .

After the modified POCS portion described above, the basis images \vec{c}_t take TV gradient descent steps, with independent adaptive step size. Upon finishing the calculation of image TVs, we use these new images as the input in Eqs. (15) and (16) to repeat the iteration. Therefore, we alternate POCS and TV-descent update in each iteration. The pseudocode for the algorithm is present below. The balancing between the POCS update and TV-descent update and the definitions of parameters β and α_t below can be followed in Ref. [14].

Algorithm 1 reconstruction algorithm for \vec{c}_t 's

```

1: repeat {iteration}
2:   for s=1,S do {POCS update}
3:      $\vec{f} := \sum_{t=1}^T \bar{\mu}_t^s d_t^s \vec{c}_t$ 
4:      $\vec{f}_0 := \vec{f}$ 
5:     for j=1, $M^s$  do
6:        $\vec{f} := \vec{f} + \beta w_j^s \vec{A}_j^{s\top} \frac{g_j^s - \vec{A}_j^s \cdot \vec{f}}{\vec{A}_j^s \cdot \vec{A}_j^{s\top}}$ 
7:     end for
8:     for t=1,T do
9:        $\vec{c}_t := \vec{c}_t + \frac{\bar{\mu}_t^s d_t^s}{\sum_{t=1}^T (\bar{\mu}_t^s d_t^s)^2} (\vec{f} - \vec{f}_0)$ 
10:    end for
11:  end for
12:  for n=1,ngrad do {TV-descent update}
13:    for t=1,T do
14:       $\vec{c}_t := \vec{c}_t - \alpha_t * \nabla_{\vec{c}_t} \|\vec{c}_t\|_{TV}$ 
15:    end for
16:  end for
17: until stop

```

In addition, Eq. (10) can be viewed as a simple linear system and standard POCS updating formula can be used in combination with optimized updating order among the

S sets of measurements within one iteration. One of such is to alternate the update from different data sets to help accelerate convergence speed. The images shown in Sec. IV are reconstructed using such alternating POCS algorithm.

D. Necessary Optimality Condition

Even though the developed algorithm have not been shown to be a mathematical solver of the optimization program in (13), we have demonstrated, however, in extensive quantitative studies that the algorithm appears to solve numerically the program, in the absence of the non-linear term \vec{g}_{BH}^s . More importantly, under this consideration, we can derive a necessary condition on the optimality of the algorithm. This condition, referred to as the KKT condition [14], can be obtained by considering the Lagrangian,

$$L = \sum_{t=1}^T \|\vec{c}_t\|_{TV} + \lambda_0 \left(\|\mathcal{H}\vec{C} - \vec{G}\|_w^2 - \epsilon \right) - \vec{\lambda} \cdot \vec{C}, \quad (17)$$

where λ_0 and $\vec{\lambda}$ are the multipliers. The optimality condition can be obtained by letting $\nabla_{\vec{C}} L = 0$, and expressed as

$$c_\alpha = \frac{\vec{d}_{TV} \cdot \vec{d}_{data}}{|\vec{d}_{TV}| |\vec{d}_{data}|} \rightarrow -1, \quad (18)$$

where

$$\vec{d}_{TV} = \text{diag}(\vec{C}_{indicator}) (\nabla_{\vec{C}} \sum_{t=1}^T \|\vec{c}_t\|_{TV}), \quad (19)$$

$$\vec{d}_{data} = \text{diag}(\vec{C}_{indicator}) (2\mathcal{H}^\top \bar{W}^\top \bar{W} (\mathcal{H}\vec{C} - \vec{G})). \quad (20)$$

The definition of indicator image $\vec{C}_{indicator}$ is identical to that in Ref. [14], and \bar{W} is a diagonal weighting matrix of size $SM^s \times SM^s$ in which the diagonal elements are formed with those of the S diagonal weighting matrices W^s . From knowledge of reconstructed basis images at each iterations, \vec{d}_{data} and \vec{d}_{TV} can readily be calculated. This necessary condition requires that two vectors \vec{d}_{TV} and \vec{d}_{data} are pointing to opposite directions when the program is mathematically solved. In addition to information on the reduction of the weighted data distance and image TV, this condition also provides a useful check on the numerical convergence of the algorithm.

IV. RESULTS

Employing the optimization-based reconstruction method described above, we have conducted numerical phantom studies with different configurations to acquire multiple data sets. Here, we show an example of a phantom study for beam hardening correction using two distinct diagnostic spectra with 100 and 140 kVp. Two basis materials (i.e., $T = 2$) were used to represent one water-like, Compton-dominant material and the other bone-like, photoelectric-dominant material. Two sets of sinogram (i.e., $S = 2$) were simulated as the low (100kVp) and high (140kVp) X-ray spectra travel through the basis images and stop on conventional energy integrating detectors. For simplicity, the two sinogram sets have the exactly same 2D fan-beam geometry (i.e. $A^1 = A^2$) with a magnification

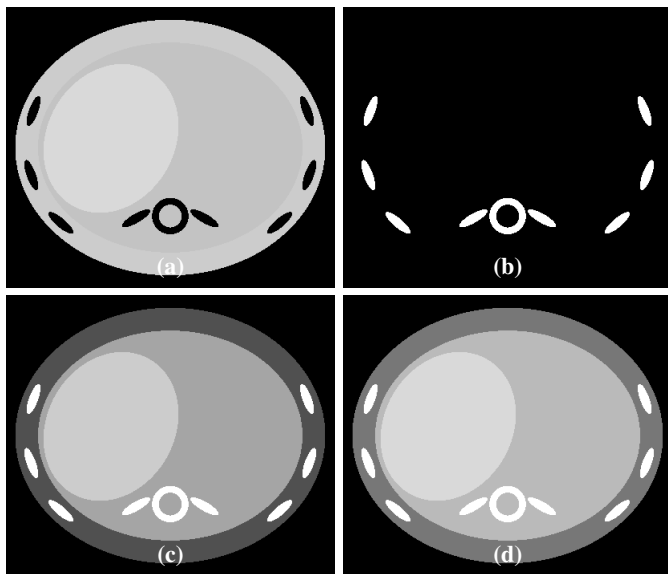


Fig. 1: Top row: basis image phantoms for the water-like, Compton-dominant material (a) and the bone-like, photoelectric-dominant material (b). The display windows are $[0.60, 1.10]$ and $[0.35, 0.55]$ for (a) and (b), respectively. Bottom row: composite images composed from basis images and $\bar{\mu}$'s averaged over the 100kVp spectrum (c) and the 140kVp spectrum (d). The display windows are $[0.18, 0.28]$ and $[0.15, 0.25]$ for (c) and (d), respectively.

factor of 1.83, a fan angle of 49° , 1200 sampling angles over 2π , and 800 detector bins. The reconstructed images, as well as the basis image phantom, are on 2D arrays of 350×410 . Following Eq. (12), we can calculate 4 spectrum-averaged $\bar{\mu}_i^s$ and compose two composite image as defined in Eq. (14) corresponding to the two spectra. The two true composite images, equivalent to monoenergetic images composed from basis images, and two true basis images are shown in Fig. 1.

We first reconstructed basis images directly from the beam hardened sinograms. In other words, \vec{g}_m^s was used to replace \vec{g}^s in the reconstruction program in Eq. (13). It is clearly an inconsistent linear system and the results are filled with beam hardening (BH) artifacts surrounding the high contrast bony structures, as shown in Fig. 2. In addition, a decreased intensity level in the reconstructed images can be observed with tight display window settings.

Next, we applied a beam hardening correction method derived based upon the reconstruction method and reconstructed basis images free of BH. In specific, Eq. (8) was plugged into Eq. (13) and the BH term \vec{g}_{BH}^s was estimated using Eq. (6) and subtracted from the measured sinogram. In effect, the BH perturbation was gradually eliminated from the measurements. Details about the BH correction method will be discussed in Sec. VI. The reconstructed basis images and corresponding composite images with BH correction are shown in Fig. 3. Displayed in tight window settings, all images are visually indistinguishable with the truth. In addition, we report the normalized image distance to truth, for the combined basis image vector \vec{C} , as 2×10^{-1} and 1×10^{-6} in the reconstructions without BH correction and with BH correction, respectively.

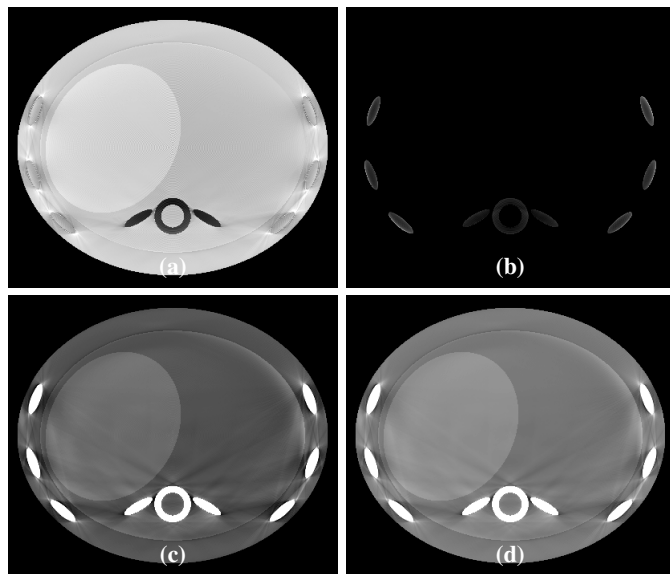


Fig. 2: Top row: reconstructed basis images without BH correction. Bottom row: composite images composed from reconstructed basis images without BH correction. Same display windows are used as in Fig. 1. Severe BH artifacts and DC shifts are noticeable in all basis images and composite images.

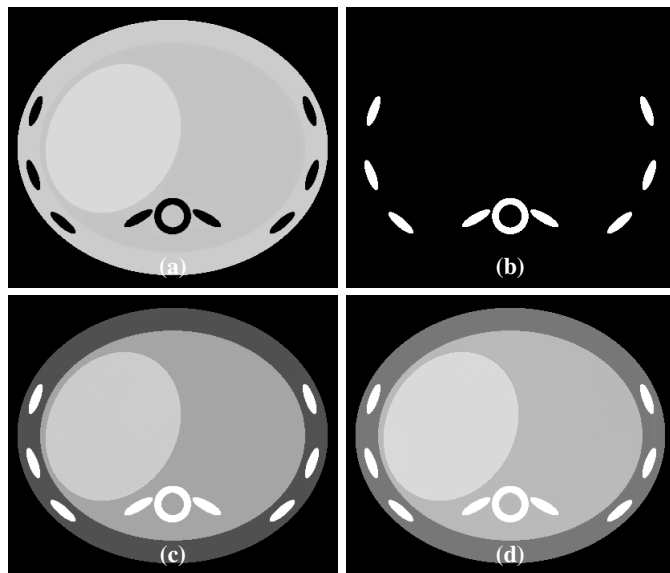


Fig. 3: Top row: reconstructed basis images with BH correction. Bottom row: composite images composed from reconstructed basis images with BH correction. Same display windows are used as in Fig. 1. All images are visually very close to the truth.

V. CONCLUSION

In the work, we have developed an optimization-based method for image reconstruction from multiple data sets with spectral CT systems. Simulation studies using two diagnostic range kV spectra suggest that the developed method is robust in adapting to existing spectral CT systems. This reconstruction method does not depend on pre- or post-reconstruction decomposition, while correcting for the non-linear beam hard-

ening artifacts, as demonstrated. Further, the method can be used for assessing the performance upper bound of a variety of spectral CT systems and their applications. It is thus of use for exploring and enabling the design and optimization of CT systems with multiple data sets that aim to explore and attempt to recover the underlying spectral properties of the objects.

VI. DISCUSSION

An interesting point arises as we draw a close inspection of the effect of the non-linear BH term \vec{g}_{BH}^s . The investigation of the proposed reconstruction program and algorithm, and the necessary optimality condition, is made available in the absence of \vec{g}_{BH}^s . However, if we take the non-linear effect into account, the weighted data distance becomes

$$D_w(\vec{G}) = \sum_{s=1}^S \left\| W^s \left(A^s \cdot \sum_{t=1}^T \bar{\mu}_t^s d_t^s \vec{c}_t - \vec{g}_m^s + \vec{g}_{BH}^s \right) \right\|_2^2. \quad (21)$$

where

$$\vec{g}_{BH}^s = -\ln \int S^s(E) \exp \left[-A^s \sum_{t=1}^T \Delta \mu_t^s(E) \vec{c}_t \right] dE, \quad (22)$$

and

$$\Delta \mu_t^s(E) = \mu_t(E) - \int S^s(E) \mu_t(E) dE. \quad (23)$$

When Eq. (22) is used in Eq. (13), the optimization program can become non-convex. We have investigated approaches to solving the non-convex optimization program. One of such approaches can be summarized to three steps: 1) at an iteration, \vec{g}_{BH}^s can be calculated by using Eq. (22) with basis images reconstructed at the previous iteration, 2) substitution of the estimated \vec{g}_{BH}^s into Eq. (21) makes the optimization program convex, and 3) the developed algorithm can then be applied to numerically solving the program by replacing g_j^s with $(g_{mj}^s - g_{BHj}^s)$. Such approach can help to handle the non-linear effect and generalize the readily developed algorithms that are mathematically solvers for a convex optimization program in the absence of the non-linear effect, such as the one in Eq. (13). Images shown in Fig. 3 are examples of results following this approach.

In addition, other optimization programs can be devised to reconstruct the basis images as well. For example, a constrained TpV-minimization program can be formulated, and algorithms for numerically solving the program can also be developed. We are investigating how developed optimization programs and algorithms respond to the non-linear effect in the context of evaluation of performance of spectral CT systems with multiple data sets and plan to report the results at the conference, along with the analysis of the impact of data noise on the study.

ACKNOWLEDGMENT

The authors are grateful to Dr. Chien-Min Kao for helpful discussion. This work was supported in part by NIH R01 Grant Nos. CA120540, CA158446, and EB000225. The contents of this article are solely the responsibility of the authors and do

not necessarily represent the official views of the National Institutes of Health.

REFERENCES

- [1] T. R. Johnson, C. Fink, S. O. Schönberg, and M. F. Reiser, *Dual energy CT in clinical practice*. Springer, 2011, vol. 201, no. 1.
- [2] Y. Watanabe, K. Uotani, T. Nakazawa, M. Higashi, N. Yamada, Y. Hori, S. Kanzaki, T. Fukuda, T. Itoh, and H. Naito, "Dual-energy direct bone removal ct angiography for evaluation of intracranial aneurysm or stenosis: comparison with conventional digital subtraction angiography," *European radiology*, vol. 19, no. 4, pp. 1019–1024, 2009.
- [3] S. Leschka, P. Stolzmann, F. T. Schmid, H. Scheffel, B. Stinn, B. Marincek, H. Alkadhi, and S. Wildermuth, "Low kilovoltage cardiac dual-source ct: attenuation, noise, and radiation dose," *European radiology*, vol. 18, no. 9, pp. 1809–1817, 2008.
- [4] A. Graser, T. R. Johnson, H. Chandarana, and M. Macari, "Dual energy ct: preliminary observations and potential clinical applications in the abdomen," *European radiology*, vol. 19, no. 1, pp. 13–23, 2009.
- [5] A. Coleman and M. Sinclair, "A beam-hardening correction using dual-energy computed tomography," *Physics in medicine and biology*, vol. 30, no. 11, p. 1251, 1985.
- [6] P. M. Joseph and C. Ruth, "A method for simultaneous correction of spectrum hardening artifacts in ct images containing both bone and iodine," *Medical Physics*, vol. 24, no. 10, pp. 1629–1634, 1997.
- [7] T. G. Flohr, C. H. McCollough, H. Bruder, M. Petersilka, K. Gruber, C. Süß, M. Grasruck, K. Stierstorfer, B. Krauss, R. Raupach *et al.*, "First performance evaluation of a dual-source ct (dsct) system," *European radiology*, vol. 16, no. 2, pp. 256–268, 2006.
- [8] T. R. Johnson, B. Krauss, M. Sedlmair, M. Grasruck, H. Bruder, D. Morhard, C. Fink, S. Weckbach, M. Lenhard, B. Schmidt *et al.*, "Material differentiation by dual energy ct: initial experience," *European radiology*, vol. 17, no. 6, pp. 1510–1517, 2007.
- [9] S. Kappler, M. Grasruck, D. Niederlöhner, M. Strassburg, and S. Wirth, "Dual-energy performance of dual kvp in comparison to dual-layer and quantum-counting ct system concepts," in *SPIE Medical Imaging*. International Society for Optics and Photonics, 2009, pp. 725 842–725 842.
- [10] J. Schlomka, E. Roessl, R. Dorscheid, S. Dill, G. Martens, T. Istel, C. Bäumer, C. Herrmann, R. Steadman, G. Zeitler *et al.*, "Experimental feasibility of multi-energy photon-counting k-edge imaging in pre-clinical computed tomography," *PMB*, vol. 53, no. 15, p. 4031, 2008.
- [11] Y. Zou and M. D. Silver, "Analysis of fast kv-switching in dual energy ct using a pre-reconstruction decomposition technique," in *Medical Imaging*. International Society for Optics and Photonics, 2008, pp. 691 313–691 313.
- [12] C. Maaß, M. Baer, and M. Kachelrieß, "Image-based dual energy ct using optimized pre-correction functions: A practical new approach of material decomposition in image domain," *Medical physics*, vol. 36, no. 8, pp. 3818–3829, 2009.
- [13] X. Pan, E. Y. Sidky, and M. Vannier, "Why do commercial CT scanners still employ traditional, filtered back-projection for image reconstruction?" *Inverse Probl.*, vol. 25, p. 123009, 2009.
- [14] E. Y. Sidky and X. Pan, "Image reconstruction in circular cone-beam computed tomography by constrained, total-variation minimization," *Phys. Med. Biol.*, vol. 53, pp. 4777–4807, 2008.

Tomosynthesis Image Quality Assessment Based on Micro-CT

Aileen Cordes, Yulia M. Levakhina and Thorsten M. Buzug

Abstract—Digital tomosynthesis (DT) is an X-ray based limited angle imaging modality. A high in-plane resolution, a low radiation dose and three-dimensionality make DT a clinically attractive technology. However, due to incomplete data sampling image artifacts are unavoidable. The quality of the reconstructed images is greatly affected by the choice of acquisition parameters such as the number of projections, the angular sampling distance and the total angular range. Each of them needs to be optimized to ensure optimal diagnostic information. This work presents a novel method to investigate the tomosynthesis performance in dependence of numerous acquisition and reconstruction parameters. The idea is to use a micro-CT projection data set to simulate tomosynthesis projections. Because the simulated projections are based on measured data, they are realistic and include physical effects such as scatter, noise and beam hardening. At the same time, the micro-CT reconstruction provides reference images that allow for a qualitative and quantitative image quality assessment. An experimental evaluation based on a human finger bone demonstrates that our method is a valid, easy and flexible tool for developing optimization rules for tomosynthesis imaging.

I. INTRODUCTION

Digital tomosynthesis is a tomographic technique for generating a stack of cross-sectional images based on a limited number of low dose two-dimensional projections taken on an arc trajectory. This modality overcomes the limitations of conventional X-ray imaging which suffers from the drawback of overlapping structures. DT is therefore considered to be of great potential in a wide range of applications to various clinical tasks [1]. It allows for better visualization of complex anatomic structures and may allow for important improvements in the accuracy of screening and diagnosis [2]. But although the benefits of such technology are clear, tomosynthesis is not without drawbacks. The limited angle condition of tomosynthesis is associated with a low depth resolution of the reconstructed volume and remaining out-of-plane artifacts [3]. A successful generation of high quality images requires a selection of multiple parameters for acquisition and reconstruction. Each of them needs to be optimized to produce images with the maximum diagnostic information and a minimum visibility of potential artifacts. Although much effort has been spent identifying optimal parameter settings in the last decade, the ideal choice is still unknown. The optimization of acquisition and reconstruction parameters continues to be an active area of research. The practical problem is the generation of suitable datasets with ground truth that reflect the actual

structures within the object to be examined. So far, an image quality assessment of DT imaging systems is usually based on physical or anthropomorphic phantoms with known ground truth. However, the phantom preparation is often difficult and time consuming. Moreover, the phantoms are typically composed of simple geometric objects and do not represent realistic anatomical structures. It is not straightforward to apply the results to imaging of clinically relevant objects. Brunner *et al.* for instance demonstrated that currently used breast phantoms are no adequate image quality evaluation phantoms for DT [4]. The use of a simulation software and digital phantoms provides more flexibility and allows for an image quality assessment based on full-reference metrics. But since the simulated tomosynthesis projections are not based on measured data, it is more difficult to include all physical side effects such as scatter, noise and beam hardening [5]. This work presents a novel approach for an evaluation of tomosynthesis image quality. The method uses micro-CT projections to simulate tomosynthesis projections. Since the simulation is based on real measurements, all physical effects are included. Moreover, the micro-CT reconstruction provides a realistic image of the structures inside the object and makes a ground truth reference image available. This way, an analysis of numerous acquisition and reconstruction parameters can be performed with both qualitative and quantitative methods. A detailed description of the transformation between the micro-CT and the tomosynthesis geometry is given in section 2. Experimental results based on a dried human finger bone are presented in section 3. Finally, the benefits and limitations of the presented method are summarized in section 4.

II. MATERIALS AND METHODS

A. Micro-CT Imaging Geometry

The micro-CT projection images have been obtained using the micro-CT system SkyScan 1172. The imaging geometry is illustrated schematically in figure 1. The micro-CT system basically consists of a cone-beam X-ray source and a two-dimensional 1.3 MP flat-panel detector. The geometry gives a focus-detector distance (FDD) of 345.16 mm. The distance between the source and the isocenter depends on the chosen magnification factor. For this study, a focus-center distance (FCD) of 257.6 mm is applied. The image acquisition involves collection of two-dimensional projection images of the object under examination which is placed on a rotating specimen disk. The X-rayed measuring field is approximately 2 cm³ in volume. During the acquisition, the object rotates over 360° with a fixed rotation step of 0.7° or 0.9°.

A. Cordes, Y. M. Levakhina and T. M. Buzug are with the Institute of Medical Engineering, Universität zu Lübeck, Lübeck, Germany (email: cordes@imt.uni-luebeck.de, levakhina@imt.uni-luebeck.de, buzug@imt.uni-luebeck.de).

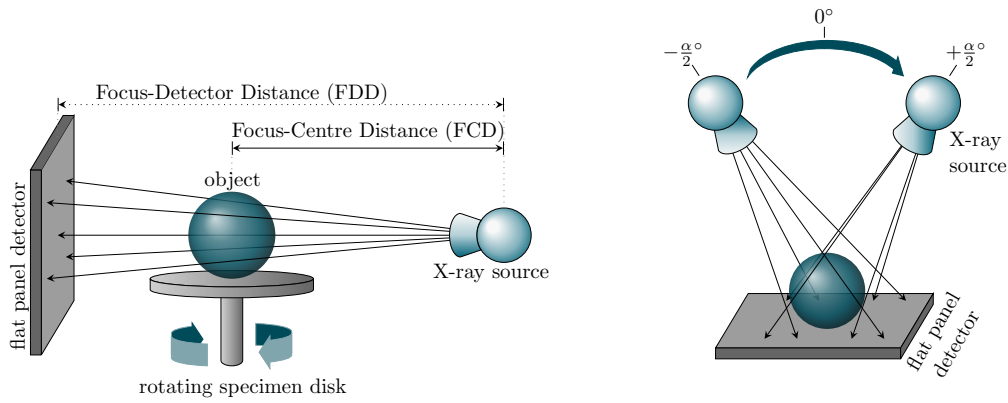


Fig. 1. Left: Micro-CT imaging geometry. The object is placed on a rotating specimen disc between a digital flat-panel detector and an X-ray source. Right: Tomosynthesis imaging geometry. The X-ray tube is moved on an arc trajectory above a stationary flat-panel detector.

B. Simulation of Tomosynthesis Projections

Similar to micro-CT, DT is performed with a flat-panel detector and uses cone-beam projections taken at varying orientations of the X-ray tube as input for the generation of cross-sectional images. But while the micro-CT image acquisition is based on a full 360° scan, the angular range is limited in tomosynthesis. During a tomosynthesis data acquisition, the X-ray tube is moved on an arc trajectory above a stationary detector [7]. A simulation of this modality can therefore be realized by selecting a subset of the micro-CT projection dataset. Subsequently, these micro-CT shadow images have to be reprojected onto a virtual tomosynthesis detector. By a suitable selection of the micro-CT projections, the angular increment between two projections, the total number of projections and the orientation of the reconstructed slices can be varied. The transformation necessary to convert the micro-CT data into tomosynthesis projections is illustrated graphically in figure 2. Here, a conversion between the micro-CT detector and the dark area of the virtual stationary detector located at distance k from the isocenter is required. A column of the micro-CT projection image at distance c from the origin of the image receptor plane is projected onto the virtual detector according to the following equation

$$s = \frac{k(c \cos(\gamma) + FDD \sin(\gamma) + cFCD)}{FDD \cos(\gamma) - c \sin(\gamma)}, \quad (1)$$

where s represents the distance from the origin in the horizontal detector plane and γ is the angle at which the projection image is acquired. Due to the symmetry of the tomosynthesis acquisition procedure, γ can take values from $-\alpha/2$ to $+\alpha/2$, where α specifies the total angular range of tube motion. The transformation (1) represents a stretching of the data in x -direction. Additionally, the individual columns must be appropriately magnified in y -direction to account for varying distances from the spot of the tube to the virtual tomosynthesis detector. The scaling factor to account for magnification differences can be calculated as follows

$$\text{scale}(c) = 1 + \frac{c \sin(\gamma) + k - \cos(\gamma)(FDD - FCD)}{\cos(\gamma + \theta) \sqrt{FDD^2 + c^2}}, \quad (2)$$

where

$$\theta = \tan^{-1} \left(\frac{c}{FDD} \right). \quad (3)$$

After performing the transformations (1) and (2) for a total number of N micro-CT projections, the resulting data represent a simulated tomosynthesis projection dataset.

C. Experimental Evaluation

Once the tomosynthesis projections are calculated, cross-sectional images can be reconstructed. Objective full-reference metrics can then be applied in order to quantify the accuracy of the tomosynthesis reconstruction. For our study, we used micro-CT projections of a dried human finger bone¹, a reconstruction algorithm based on the traditional shift-and-add method and the mutual information as figure of merit.

1) *Bone Phantom*: The bone phantom represents an anatomy of fine trabecular structures that are of great interest in the field of skeletal tomosynthesis imaging. The potential of DT to assess different pathologies of hands has been recently demonstrated in [8].

2) *Tomosynthesis Image Reconstructions*: The traditional shift-and-add reconstruction algorithm involves shifting and adding each of the projection images taken at varying X-ray source positions to produce cross-sectional images at any height above the detector [9]. By controlling the amount of shift, planes at an arbitrary depth can be reconstructed with little computational effort. The amount of shift to bring structures at distance a from the isocenter into focus is given by

$$\text{shift}(a) = FCD \sin(\gamma) \frac{k + a}{FCD \cos(\gamma) - a}. \quad (4)$$

To improve the visibility of objects within in the plane of interest, the remaining out-of-focus blurring has to be

¹The human cadavers -respectively bodies/heads/arms/legs feet etc. as parts of cadavers- were used and dissected in this examination under permission of the "Gesetz über das Leichen-, Bestattungs- und Friedhofswesen (Bestattungsgesetz) des Landes Schleswig-Holstein vom 04.02.2005, Abschnitt II, 9 (Leichenöffnung, anatomisch)". In this case it is allowed to dissect the bodies of the donors (Körperspender/in) for scientific and/or educational purposes.

reduced. This can for instance be achieved by filtering all projections with a ramp filter along each row.

3) *Figure of Merit*: A comparison of the tomosynthesis and the micro-CT reconstructions can be performed by a quantitative analysis based on full reference methods. A suitable metric for observing the agreement between the reconstructions is given by the mutual information [10]. It is defined in terms of entropy and does not require any prior knowledge about the relationship between the pixel intensities in both sets of image data.

III. RESULTS AND DISCUSSION

In order to demonstrate that the proposed method is a valuable tool to investigate the tomosynthesis performance, the image quality has been evaluated in dependence of the angular range, the angular sampling distance and the number of projections. This has been done qualitatively by means of a visual inspection and quantitatively by the use of a full reference metric.

A. Qualitative Visual-Based Evaluation

1) *The impact of the angular range α* : Figure 3 shows a micro-CT reference image and corresponding tomosynthesis reconstructions obtained with a constant rotation step of 0.7° and varying tomographic angle α . The tube movement is from left to right with respect to all images. The reconstructions demonstrate an improvement in the agreement between the tomosynthesis and the micro-CT reconstructions with an increase of α . At small angles, the visibility of structures in the plane of interest is clearly reduced since structures outside the plane of interest are less blurred and appear as unwanted out-of-plane artifacts. This result corresponds to studies performed using physical phantoms or anthropomorphic software phantoms [11], [12], [13].

2) *The Influence of the Angular Sampling Distance $\Delta\alpha$* : Figure 4 demonstrates the appearance of ripple artifacts in dependence of the angular sampling distance $\Delta\alpha$. Figures

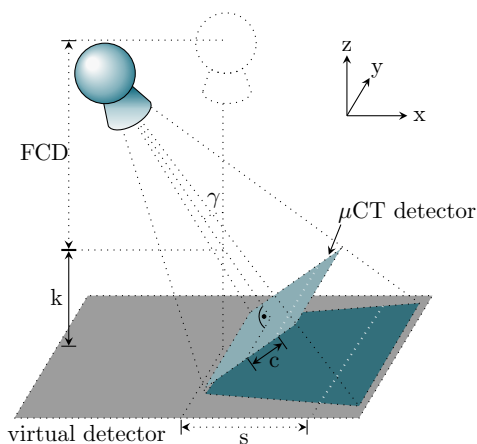


Fig. 2. Transformation between micro-CT projections and tomosynthesis projections.

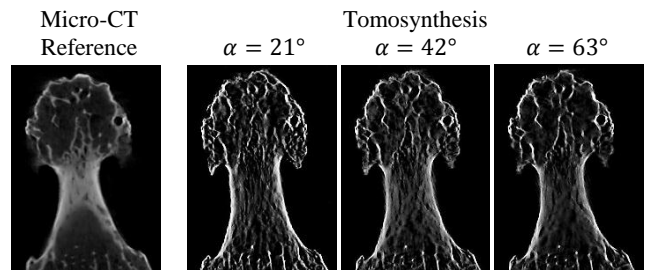


Fig. 3. Left: Micro-CT reconstruction of a human finger bone. Right: Tomosynthesis reconstructions using a constant rotation step $\Delta\alpha = 0.7^\circ$ and varying tomographic angles α .

4(b)-(c) represent a section of the slice highlighted as a white line in figure 4(a). Figures 4(e)-(f) show the cross-sectional image marked in figure 4(d). Both slices demonstrate an increasing impact of ripple artifacts with decreasing sampling density. However, the artifacts are more prominent in the second case, since the object size in the direction perpendicular to the reconstructed slice is larger. As a consequence, the object orientation should be chosen by taking into account the thickness of the measured object and the tube direction. Similar results are presented in [13], [14]. Machida *et al.* and Deller *et al.* demonstrated that ripple artifacts may be reduced by decreasing the angular step size.

B. Quantitative Evaluation

Figure 5 demonstrates the mutual information in dependence of the total angular range α and the number of projections N . The two analyzed slices differ from each other in the maximal distance of structures to the plane of interest. In figure 5(a) the object size in z -direction is limited by 5.6 mm and in figure 5(b) by 10.6 mm. Both graphs demonstrate the same tendency. At a constant number of projections, the mutual information increases first, reaches a maximum and finally decreases continuously. This result indicates that with a constant number of projections an enlargement of the tomographic angle does not necessarily lead to an improved image quality. This is directly attributed to the fact that an increase of the tomographic angle is associated with an

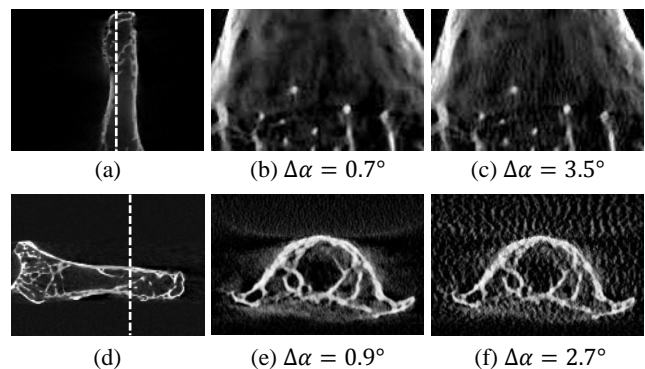


Fig. 4. Occurrence of ripple artifacts in dependence of the sampling distance $\Delta\alpha$. (b)-(c) show a section of the slice highlighted as a white line in (a), (e)-(f) show the the slice highlighted in (d).

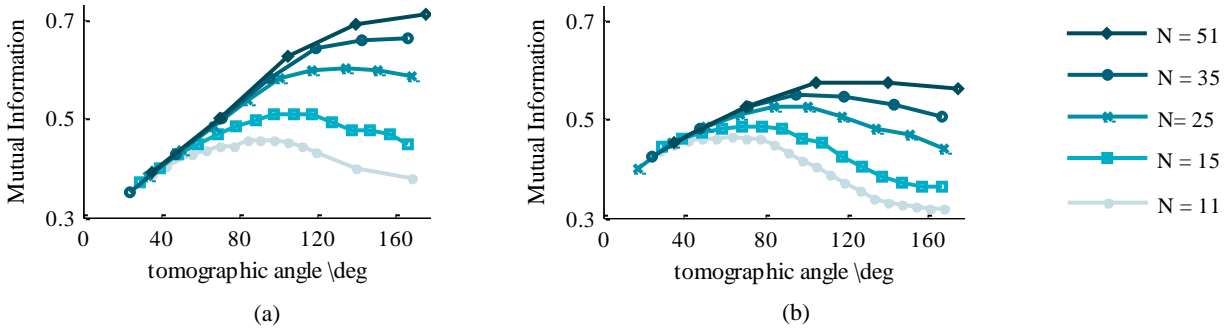


Fig. 5. Mutual Information between a micro-CT reference image and tomosynthesis reconstructions in dependence of the number of projections N and the tomographic angle α . Object sizes in z -direction: (a) 5.6 mm, (b) 10.6 mm

increasing angular step size $\Delta\alpha$. As discussed above, the lower sampling density is favorable for occurring of ripple artifacts. Consequently, the tomographic angle with the maximal value of the mutual information can be understood as a compromise between a greatest possible tomographic angle and an acceptable sampling density. Furthermore, the graphs reveal a correlation between the accessible image quality and the object size in z -direction. With a constant number of projections, the maximum value is reached at smaller angles as the object size increases. The greater influence of ripple artifacts for larger objects results in a shift of the optimal tomographic angle towards smaller angles.

IV. CONCLUSION

We have presented a novel approach for an evaluation and optimization of the tomosynthesis image quality. This method involves a simulation of tomosynthesis projections based on a micro-CT projection data set. It offers the great advantage that the simulated tomosynthesis projections are realistic and include all physical side effects. Slight inaccuracies may only occur due to the application of interpolation methods. At the same time, the micro-CT and the tomosynthesis reconstructions represent identical structures within the object to be examined. This way, ground truth reference images are directly available. A qualitative and quantitative analysis of numerous acquisition and reconstruction parameters can be performed in order to develop optimization rules for tomosynthesis imaging. The tomosynthesis image acquisition parameters including the number of projections, the angular increment between two projections and the orientation of the reconstructed cross-sectional image can simply be varied by selecting an appropriate subset of the micro-CT projection data set. No further micro-CT acquisition is required. Furthermore, provided that the size restriction according to the micro-CT manufacture specification is taken into account, the test object can be selected freely according to the requirements and goals of each specific study. Consequently, an examination of very fine structures is possible without a difficult and time consuming preparation of anthropomorphic phantoms. In our experiments, we used a micro-CT acquisition of a dried human finger bone. The results demonstrate a huge impact of the number of projections N , the angular range α , the angular sampling

distance $\Delta\alpha$. In particular, it could be shown that the optimal parameter selection largely depends on the orientation and the thickness of the investigated object. This finding corresponds to results of studies performed with physical or software phantoms indicating that the proposed method is a valuable tool for developing optimization rules for tomosynthesis imaging. At the same time, the method is easy, flexible and straightforward to implement.

REFERENCES

- [1] J. T. Dobbins and D. J. Godfrey, *Digital x-ray tomosynthesis: current state of the art and clinical potential.*, Phys. Med. Biol. 48(19): 65–106, 2003
- [2] S. P. Poplack, T. D. Tosteson, C. A. Kogel and H. M. Nagy, *Digital breast tomosynthesis: Initial experience in 98 women with abnormal digital screening mammography.*, AJR 198(3): 2907–2916, 2007
- [3] Y. H. Hu, W. Zhao, T. Mertelmeier and J. Ludwig, *Image artifact in digital breast tomosynthesis and its dependence on system and reconstruction parameters.*, IWDM 2008 Proceedings, LNCS 5116: 628–634, 2008
- [4] C. C. Brunner, R. J. Acciavatti, P. R. Bakic, A. D. A. Maidment, M. B. Williams, R. Kaczmarek and Kish Chakrabarti, *Evaluation of various mammography phantoms for image quality assessment in digital breast tomosynthesis.*, IWDM 2012 Proceedings, LNCS 7361: 284–291, 2012
- [5] N. V. Ruiter, C. Zhang, P. R. Bakic, A. Carton, J. Kuo and A. D. A. Maidment, *Simulation of tomosynthesis images based on an anthropomorphic breast tissue phantom.*, Proc. SPIE 9(2): 69182I.1–69182I.10, 2008
- [6] L. A. Feldkamp, L. C. Davis and J. W. Kress, *Practical cone-beam algorithm.*, J. Opt. Soc. Am. 1(6): 612–619, 1984
- [7] J. T. Dobbins, *Tomosynthesis imaging: At a translational crossroad.*, Med. Phys. 36(6): 1956–1967, 2009
- [8] Y. M. Levakhina, R. L. Duschka, F. M. Vogt, J. Barkhausen, and T. M. Buzug, *A dual-axis tilt acquisition geometry for digital musculoskeletal tomosynthesis.*, Phys. Med. Biol. 58(14): 4827–4848, 2013
- [9] K. R. Maravilla, R. C. Murry and S. Homer, *Digital tomosynthesis: Technique for electronic reconstructive tomography.*, AJR 141(3): 497–502, 1983
- [10] C. Stutholme, D. Hill and D. Hawkes, *An overlap invariant entropy measure of 3D medical image alignment.*, Pattern Recogn. 32(1): 71–96, 1999
- [11] B. Li, G. B. Avinash, R. Uppaluri, J. W. Eberhard and B. E. H. Claus, *The impact of acquisition angular range on the z -resolution of radiographic tomosynthesis.*, International Congress Series 1268: 13–18, 2004
- [12] C. Kontos D. and Zhang, N. Ruiter, P. Bakic and A. Maidment, *Evaluating the effect of tomosynthesis acquisition parameters on image texture: a study based on an anthropomorphic breast tissue software model.*, Digital Mammography LNCS 5116: 491–498, 2008
- [13] H. Machida, T. Yuhara, T. Mori, E. Ueno, Y. Moribe and J. M. Sabol, *Optimizing parameters for at-panel detector digital tomosynthesis.*, Radiographics 30(2): 549–562, 2010
- [14] T. Deller, K. N. Jabri, J. M. Sabol, X. Ni, G. Avinash, R. Saunders and R. Uppaluri, *Effect of acquisition parameters on image quality in digital tomosynthesis.*, In Proc. of SPIE 6510: 65101L1–11, 2007

Effect of Reconstruction Method on Optimal Acquisition Parameters for Lesion Detection-Localization in Digital Breast Tomosynthesis

Zhihua Liang^{1,2}, Howard C. Gifford², and Mini Das¹

Abstract—Previous work [1] has suggested that the optimal scan arc and number of projections for lesion detection in DBT are not greatly affected by the choice of reconstruction algorithm. We are investigating whether the same can be said for the task of lesion detection and localization. Our assessment methodology involves realistic computer simulations with digital breast phantoms and both human and model-observer LROC studies. The latter have been carried out with a visual-search (VS) model that uses gradient-template matching to guide an initial holistic search. This VS observer is intended as a human-observer model. Observer results from 2D test images reconstructed with Feldkamp FBP and iterative, maximum-likelihood methods have been obtained. Results for the FBP images are discussed in this abstract.

I. INTRODUCTION

Early detection is important to reduce breast-cancer mortality. Digital breast tomosynthesis (DBT) has recently gained FDA approval for clinical use and its potential utility as an adjunct or replacement for screening mammography is under investigation. Two-dimensional (2D) digital mammography (DM), while relatively simple in acquisition and image evaluation, suffers from problems with tissue overlap that reduce lesion conspicuity in dense breasts. DBT overcomes this issue, but presents other complications related to partial-angle tomography. Thus, it is critical to carefully assess the DBT acquisition parameters for a given diagnostic task (mass or microcalcification targets; detection or detection-localization) to help ensure optimal detection-to-dose benefits.

Several researchers have investigated the effects of scan arc β and number of projections P for DBT acquisitions. Among the evaluation methods that have been applied are artifact spread functions and modulation transfer functions. Both Zeng [1] and Chawla [2] have used Bayesian ideal observers for location-known mass-detection tasks in reconstructed images as a means of investigating optimal β and P . In [1], the authors suggest that the optimal β is fairly insensitive to the choice of reconstruction algorithm. Our objective was to examine the interplay between reconstruction algorithm and the optimal parameters when the observer task included mass localization.

Our LROC study involved simulated FBP and penalized maximum-likelihood (PML) images. Results were obtained

with human observers, a visual-search (VS) model observer [3], and a scanning channelized nonprewhitening (CNPW) observer. The FBP results are discussed herein.

II. METHODS

A. Breast and Mass Models

The breast phantoms used in this study are anthropomorphic volumes designed by Bakic *et al.* [4] at the University of Pennsylvania. We have nine unique phantoms in total, three with approximately 25% volumetric glandular fraction (VGF), three with approximately 50% VGF, and the remaining three with approximately 75% VGF. The VGFs for the latter six phantoms may be physically unrealistic, but do serve to broaden the range of detection accuracies in our studies.

Each phantom was used to create eight single-lesion (or abnormal) cases and eight lesion-absent (or normal) cases, for a total of $9 \times 16 = 144$ cases. The lesion targets were homogeneous spheres with an 8.0-mm diameter. The abnormal cases were created by adding the lesion to the Bakic phantom prior to the projection imaging. Lesions were randomly positioned within the fibroglandular compartment of the phantom. The attenuation coefficients for the masses modeled infiltrating ductal carcinoma as a function of energy and were based on empirical measurements.

B. Image Generation

A rigorous computer simulation [5] was used to generate the DBT imaging data. The projector used Siddon's ray-tracing method [6] to model x-ray transmission through the breast. The subsequent propagation of signals and noise through a CsI-based amorphous silicon flat-panel detector was based on a serial cascade model. Both focal-spot blur and scintillator blur were accounted for. Each of the 144 phantom cases was imaged 33 times, covering the parameters $P \in \{3, 7, 11, 15, 19, 21, 25, 31, 35, 41, 45, 51\}$ for $\beta = 60^\circ$ and $P \in \{3, 7, 11, 15, 19, 25, 35\}$ for $\beta \in \{15^\circ, 30^\circ, 45^\circ\}$. Poisson noise in the projections was consistent with a total dose of 1.5 mGy for each acquisition. The dose was evenly distributed over the P projections.

¹Department of Physics, University of Houston; ²Department of Biomedical Engineering, University of Houston

C. Reconstruction Method

We analyzed detection task performance for the widely used Feldkamp FBP method [7] and a penalized ML algorithm [8]. This abstract discusses FBP results only. The 3D reconstructions are postsmoothed with a 3D Butterworth filter having a 0.25-pixel^{-1} cut-off frequency. The 2D test images for the observer study were produced by extracting image slices that contained the lesion centers. The neighboring four slices (two above and two below) were also extracted. These 5 slices were combined using boxcar smoothing to form the final test image with a one-mm slice thickness, a process which is also used in clinic practice. The corresponding slices for normal images were extracted and combined in the same way.

D. Model Observers

1) *Scanning CNPW observer*: An observer's LROC data for a given 2D test image \mathbf{f} consists of a localization \mathbf{r} and a confidence rating λ . The scanning CNPW observer determines these quantities by first computing a perception measurement at each location in a given region of interest (ROI). With Ω representing the set of indices of the pixels in this ROI, the measurement for voxel $j \in \Omega$ is

$$z_j = \mathbf{w}_j^t [\mathbf{f} - \mathbf{b}]. \quad (1)$$

Here, \mathbf{b} is the noise-free background corresponding to \mathbf{f} and \mathbf{w}_j is the j th CNPW observer template. The subtraction of \mathbf{b} in Eq. 1 sets the observer's relative operating points for assessing malignancy at the various locations in Ω . Figure 1 shows an illustrative example of the image processing prescribed by Eq. 1.

For a given \mathbf{f} , the ROI included all breast tissue areas except for the breast edges. The observer template \mathbf{w}_j is shift invariant, composed from the average reconstructed mass \mathbf{s} as computed from a set of 2D training images. Image \mathbf{s}_j represents this average mass centered on pixel j . The template is formed by applying Butterworth filtering to \mathbf{s}_j and modulating the result by a set of frequency selective channels. As with our previous CNPW work [9], three difference-of-Gaussian channels were used.

The confidence rating and localization for a test image are respectively drawn from the $\arg \max$ and \max of the z_j measurements:

$$\lambda = \max_{j \in \Omega} z_j \quad (2)$$

$$\mathbf{r} = \arg \max_{j \in \Omega} z_j. \quad (3)$$

2) *VS observer*: The VS observer performs the detection-localization task as two steps, first conducting an initial search that identifies suspicious locations within Ω , followed by application of a scanning observer at only those locations. The CNPW template was used for the scanning. The initial search can be thought of as a mechanism for adding uncertainty to the scanning observer, but can actually make the scanning observer more robust computationally when the mean background \mathbf{b} is not known exactly [10].

The locations of interest in the search were determined with a gradient template-matching process. The 2D gradient field of \mathbf{s}_j is

$$\nabla \mathbf{s}_j = \left(\frac{\partial \mathbf{s}_j}{\partial x}, \frac{\partial \mathbf{s}_j}{\partial y} \right). \quad (4)$$

Both field components on the right-hand side of this equation can be viewed as images having the same dimensions as \mathbf{w}_j and \mathbf{f} . The gradient vector at the i th pixel is

$$\nabla \mathbf{s}_j(i) = \left(\frac{\partial \mathbf{s}_j}{\partial x}(i), \frac{\partial \mathbf{s}_j}{\partial y}(i) \right). \quad (5)$$

Similarly, the gradient vector for location i in \mathbf{f} is denoted as

$$\nabla \mathbf{f}(i) = \left(\frac{\partial \mathbf{f}}{\partial x}(i), \frac{\partial \mathbf{f}}{\partial y}(i) \right). \quad (6)$$

The VS observer searches for local maxima in the cross-correlation

$$v_j = \sum_{i=1}^N [\nabla \mathbf{f}(i)]^t [\nabla \mathbf{s}_j(i)] \quad (7)$$

of these two gradient fields. Integer N is the number of pixels in \mathbf{f} . Pixels j which satisfy the inequality $v_j \geq \alpha \max(v_j)$ for a fixed threshold α are taken as candidate locations for the scanning stage. Our results were obtained with the value of $\alpha = 0.95$.

Although this VS-observer framework for DBT studies has been presented previously [3], the exact form of the model has been changed for this study. The previous version used normalized-gradient matching and relied on two thresholds. The results of the current study offer the first detailed validation of the revised VS observer against human observers.

E. Observer Studies

Three nonradiologists took part in the LROC study, reading images obtained for a subset of P values and $\beta = 60^\circ$. With each (P, β) parameter pair, these observers read the 144 cases as two sets of 18 training images and 54 test images. The model observers read the same cases for the full parameter space. Observer performance was assessed on the basis of Wilcoxon (or empirical) estimates of area under the LROC curve (A_L). Human-observer performances are reported in terms of the averages over the individual observers.

III. RESULTS

Figure 2 compares the observer performances obtained for $\beta = 60^\circ$ as a function of P . The highest performance for each P was obtained with the scanning observer, which is not affected by anatomical noise. This observer only accounts for the effects of quantum noise in the images and thus achieves its highest performances at lower values of P , for which the counts per projection is greatest. By comparison, the VS observer demonstrated quantitative agreement with the human observer. This was partly by design, as the threshold value α was empirically set based on the observer data. Nonetheless, the VS and human observers exhibit similar performance trends for small values of P . Also, changes in P beyond 11 angles had little effect on the VS and human observers.

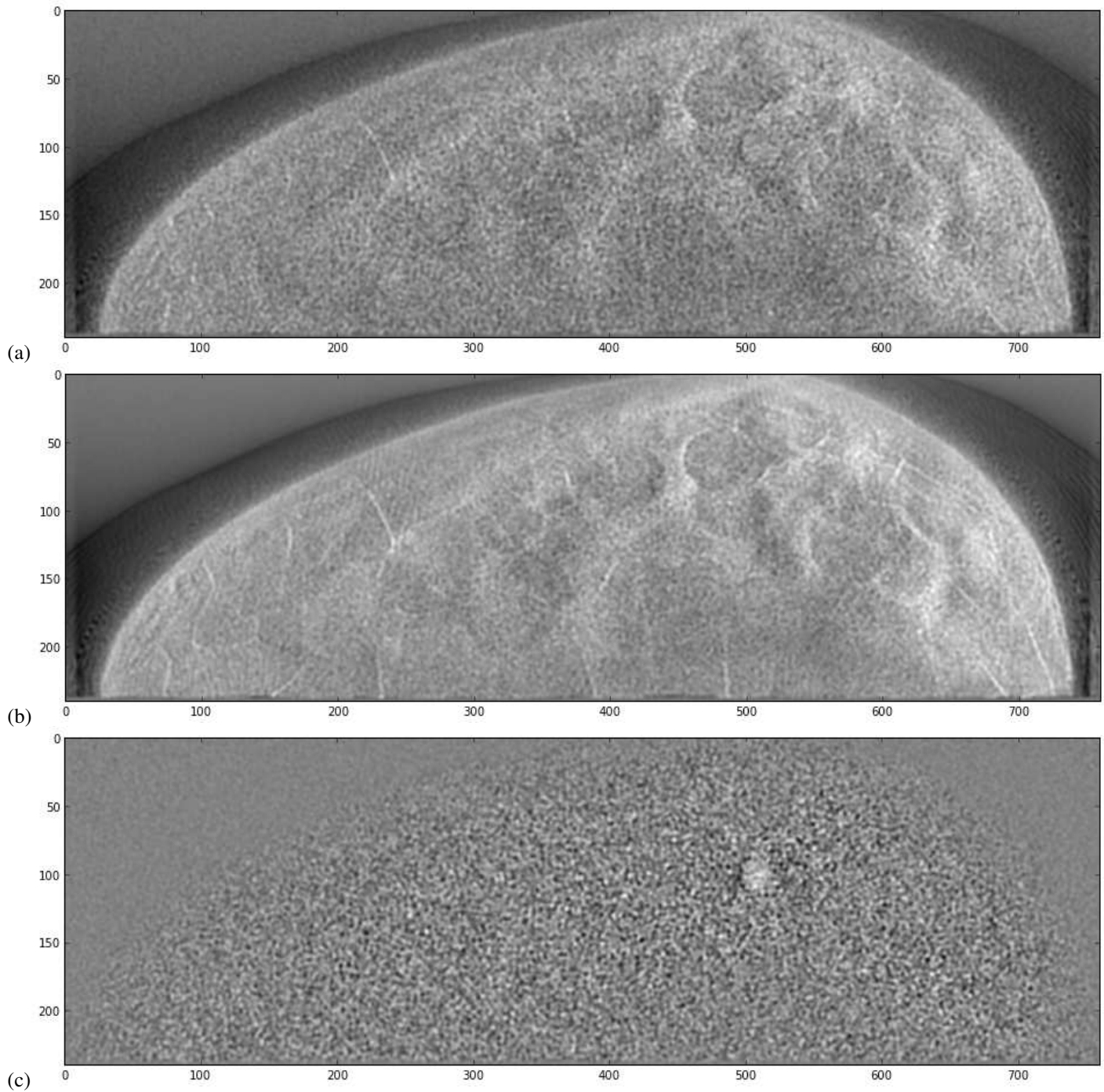


Fig. 1: Background subtraction for the model observers. (a) A noisy test image with mass; (b) the corresponding mean background; and (c) the difference image.

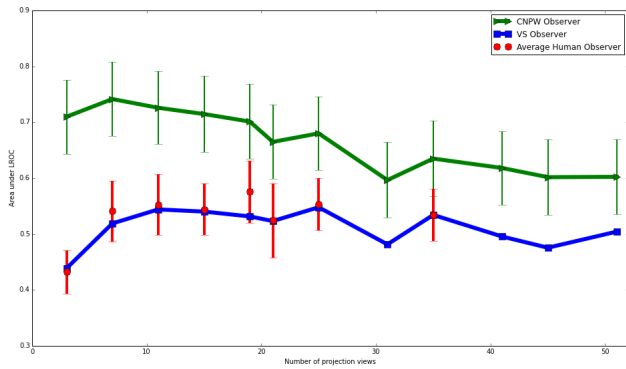


Fig. 2: Comparison of average human and model-observer performances for scan arc 60° as a function of P . The error bars represent \pm one standard deviation. The uncertainties for the VS observer (not shown) are approximately the same as those for the scanning CNPW observer.

Figure 3 presents a subanalysis of the VS and human-observer data from Fig. 2 in terms of background breast density (VGF). The lines in the plot denote VS observer performance as a function of P with the 25% (green), 50% (blue), and 75% (yellow) breast densities. Human performances are shown as discrete points. Although there are some outliers, this subanalysis indicates that these observers demonstrated very similar responses to changes in VGF.

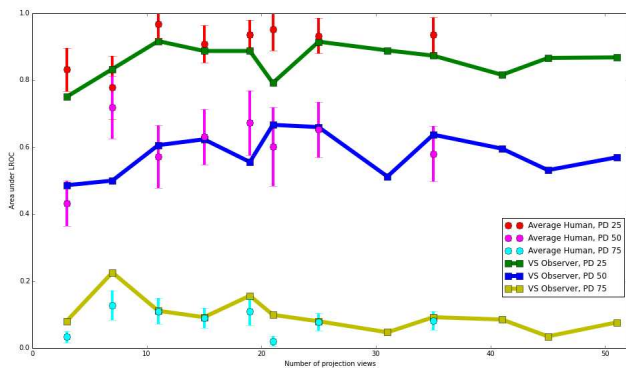


Fig. 3: Comparison of average human and VS observer performances with the 60° scan arc as a function of P and phantom VGF. The three VGF levels (or “percent densities” (PDs)) are 25%, 50%, and 75%.

An assessment of VS observer performance as a function of P and β is given in Fig. 4. Each line in this plot represents a fixed scan arc. Nominally, performance improved with increasing scan arc, although the lines for $\beta = 45^\circ$ and 60° intersect at low P . The uncertainties in A_L are fairly high (around ± 0.08 , as indicated in Fig. 2). These results also suggest a slight decrease in performance with increased P , primarily with smaller scan arcs.

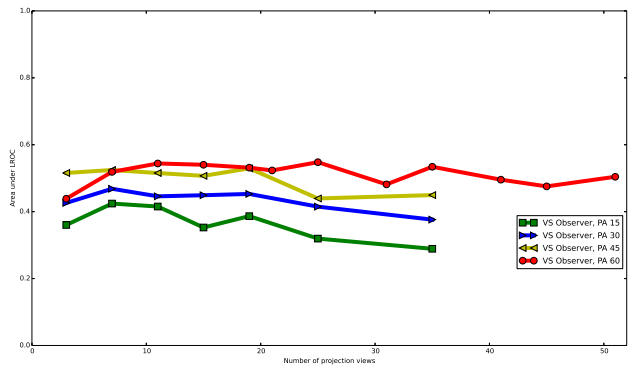


Fig. 4: VS observer performance as a function of P and β .

IV. CONCLUSION

DBT scan arcs between 45° and 60° produced the highest performances for the detection-localization task treated in this study. Performance was relatively insensitive to the number of projections. Future work will consider the effects for task variations involving different mass sizes and imaging doses.

V. ACKNOWLEDGEMENT

This work was supported by the National Institute for Biomedical Imaging and Bioengineering under grant R01-EB12070 and by the National Cancer Institute under grant K25-CA140858.

REFERENCES

- [1] R. Zeng, S. Park, P. Bakic, and K. Myers, “Is the outcome of optimizing the system acquisition parameters sensitive to the reconstruction algorithm in digital breast tomosynthesis?,” in *Breast Imaging* (A. Maidment, P. Bakic, and S. Gavenonis, eds.), vol. 7361 of *Lecture Notes in Computer Science*, pp. 346–353, Springer Berlin Heidelberg, 2012.
- [2] A. S. Chawla, J. Y. Lo, J. A. Baker, and E. Samei, “Optimized image acquisition for breast tomosynthesis in projection and reconstruction space,” *Medical Physics*, vol. 36, pp. 4859–4869, Oct. 2009.
- [3] B. A. Lau, M. Das, and H. C. Gifford, “Towards Visual-Search Model Observers for Mass Detection in Breast Tomosynthesis,” *Proceedings of SPIE*, vol. 8668, Mar. 2013.
- [4] P. R. Bakic, M. Albert, D. Brzakovic, and A. Maidment, “Mammogram synthesis using a 3D simulation. I. Breast tissue model and image acquisition simulation,” *Medical Physics*, vol. 29, pp. 2131–2139, Aug. 2002.
- [5] A. A. Vedula, S. J. Glick, and X. Gong, “Computer simulation of CT mammography using a flat-panel imager,” *Proceedings of SPIE*, vol. 5030, pp. 349–360, 2003.
- [6] R. L. Siddon, “Fast calculation of the exact radiological path for a three-dimensional CT array,” *Medical Physics*, vol. 12, no. 2, pp. 252–255, 1985.
- [7] L. Feldkamp, L. Davis, and J. Kress, “Practical cone-beam algorithm,” *Journal of the Optical Society of America*, 1984.
- [8] M. Das, H. C. Gifford, J. M. O’Connor, and S. J. Glick, “Penalized maximum likelihood reconstruction for improved microcalcification detection in breast tomosynthesis,” *IEEE Transactions on Medical Imaging*, vol. 30, pp. 904–914, Mar. 2011.
- [9] H. C. Gifford, C. Didier, M. Das, and S. J. Glick, “Optimizing breast-tomosynthesis acquisition parameters with scanning model observers,” *Proceedings of SPIE*, vol. 6917, p. 69170S, 2008.
- [10] H. C. Gifford, “A visual-search model observer for multislice-multiview SPECT images,” *Medical Physics*, vol. 40, p. 092505, Sept. 2013.

Optimization of Prior Parameter for Noise Control in Iterative Computed Tomography Reconstruction

Keisuke Yamakawa and Shinichi Kojima

Abstract—In iterative reconstruction, computed tomography (CT) image noise is reduced by using a prior term that reduces the difference between the CT value of the updated pixel and that of neighboring pixels. A serious problem with this term is that applying unoptimized parameters blurs the object or decreases the noise reduction rate. In this paper, we propose a method to control the noise reduction rate by optimizing the prior parameter δ in the prior term when applying the generalized Geman prior (GGP) for maintaining the spatial resolution. This parameter was calculated from the measured noise at each image pixel. First, the noise was measured by using image subtraction without depending on the object. Second, the parameter δ for deciding the inflection point of the prior function was calculated from the measured noise σ . The effectiveness of the optimized δ method (proposed method) compared with that of constant δ method (conventional method) was evaluated in terms of simulated CT values by using a circle phantom and an abdomen phantom. The noise reduction rate with standard deviation (SD) was used as the evaluation index. The average absolute error compared with the desired noise reduction rate was reduced from 10.8% to 2.3%. As a result, applying a suitable value for parameter δ on the basis of image noise made it possible to effectively control noise reduction in a CT image.

I. INTRODUCTION

Iterative reconstruction has been attracting attention in recent years as a method for X-ray computed tomography (CT) from the viewpoints of reducing irradiation doses while maintaining image quality [1, 2]. The reduction of irradiation doses results in increasing noise in a CT image. This method has to control noise reduction exactly to reduce the increased noise due to reduced irradiation doses to usual noise due to standard doses. In iterative reconstruction, image noise is reduced by using a prior term that reduces the difference between the CT value of the updated pixel and that of the neighboring pixels. A serious problem with this term is that applying unoptimized parameters blurs the object or decreases the noise reduction rate. Applying the constant parameter to the CT image with different noise distribution has the potential to cause non-uniform noise reduction. In conventional methods [3, 4], the prior parameters are optimized based on the measured noise in the region of interest (ROI) of every iteration. In these methods, setting the ROI to a uniform area on the object is required to measure the noise. In this paper, we propose a method to control the noise reduction rate by optimizing the prior parameter δ in a prior term when applying generalized Geman prior (GGP) [5, 6] for maintaining the spatial resolution. This parameter was calculated from the

measured noise at each image pixel. First, the noise was measured by using image subtraction [7, 8] without depending on the object. Second, the parameter δ for deciding the inflection point of the prior function was calculated from the measured noise σ . The effectiveness of the optimized δ method (proposed method) compared with that of constant δ method (conventional method) was evaluated in terms of simulated CT values by using a circle phantom and an abdomen phantom. The noise reduction rate with standard deviation (SD) was used as the evaluation index.

II. METHODS

A. Iterative reconstruction with OS-SPS

The method for iterative reconstruction is expressed as follows. In one study [9], the method used for the paper was based on ordered subsets separable paraboloidal surrogates (OS-SPS) algorithm expressed as

$$\mu_j^{(n+1)} = \mu_j^{(n)} - \frac{M \sum_{i \in S} a_{ij} w_i (\sum_{l=1}^J a_{il} \mu_l^{(n)} - y_j) + \beta \sum_{k \in N_j} d_{jk} \psi(\mu_j^{(n)} - \mu_k^{(n)})}{\sum_{i=1}^J a_{ij} w_i \sum_{l=1}^J a_{il} + \beta \sum_{k \in N_j} d_{jk} g(\mu_j^{(n)} - \mu_k^{(n)})} \quad (1)$$

where $\mu_j^{(n)}$ is the CT value at image pixel j with iteration number n , y_i represents data measured by detector i , and a_{il} is the probability that the irradiated X-rays pass image pixel l between the X-ray tube and detector i . Here, w_i is a constant value or the weight proportional to the detected X-ray photons, M is the number of subsets, $\psi(\mu_j^{(n)} - \mu_k^{(n)})$, $g(\mu_j^{(n)} - \mu_k^{(n)})$ are the prior functions that helped to reduce the random noise unrelated to the neighboring pixel k in the image, and β and d are weights in the prior functions. The iterative method consists of two terms that have different effects such as the likelihood term and the prior term. The likelihood term is used to reduce error between the measured data and the projected data from the CT image when updating the image. The prior term that reduces the difference between the CT value of the updated pixel and that of the neighboring pixels is used to reduce image noise. The derivative ψ of the GGP function ψ is used in the prior term for maintaining spatial resolution and is expressed as [5, 6].

$$P = \psi(\mu_j^{(n)} - \mu_k^{(n)}) = \frac{\delta^p (\mu_j^{(n)} - \mu_k^{(n)}) \left\{ (\mu_j^{(n)} - \mu_k^{(n)})^2 \left(1 - \frac{p}{2}\right) + \delta^2 \right\}}{\left\{ (\mu_j^{(n)} - \mu_k^{(n)})^2 + \delta^2 \right\}^{\left(\frac{p}{2} + 1\right)}} \quad (2)$$

The parameter δ is used for deciding the inflection point of the prior function, which consisted of two different functions,

K. Yamakawa, and S. Kojima are with Hitachi Central Research Laboratory, 1-280, Higashi-Koigakubo, Kokubunji-shi, Tokyo, Japan. (e-mail : keisuke.yamakawa.fd@hitachi.com).

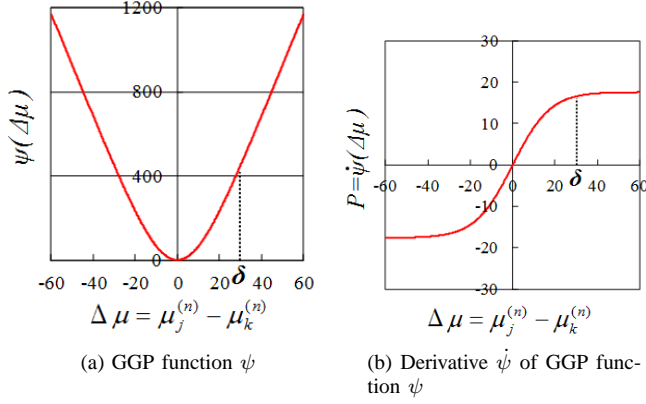


Fig. 1. Comparison between GGP function ψ and its derivative $\dot{\psi}$

and p is the prior function order. The GGP function ψ and its derivative $\dot{\psi}$ are shown in Fig. 1(a) and (b) respectively. In these figures, $\delta = 30$ and $p = 0.94$.

In the prior term, the image noise is treated as the difference $\Delta\mu$ between the CT value of the updated pixel and that of neighboring pixels and is reduced. The prior intensity P increased approximately in proportion to increasing $\Delta\mu$ when $\Delta\mu$ was less than δ [Fig. 1(b)]. The image noise is reduced in proportion to the increasing prior intensity P by the smoothing effect. As a result, the noise reduction rate results were uniform regardless of any noise. In contrast, the prior intensity P was equivalent to $\dot{\psi}(\delta)$ regardless of increasing $\Delta\mu$ when $\Delta\mu$ is larger than δ . The image noise was not reduced sufficiently for a constant prior intensity P , though the spatial resolution in the CT image was maintained by the low smoothing effect. As a result, the noise reduction rate decreased, and the spatial resolution was maintained very effectively. In the simulation [Fig. 2(a), (b)], $\delta = \sigma_{middle}$ and $p = 0.94$. The noise σ_{small} at the peripheral position was reduced excessively by the high prior intensity P_{small} when $\Delta\mu$ was much less than δ . In contrast, the prior intensity P_{large} at the center was equivalent to P_{middle} at the middle regardless of σ_{large} being much more than σ_{middle} . The noise σ_{large} was not reduced sufficiently by the constant prior intensity P_{large} when $\Delta\mu$ was much more than δ . For this reason, applying the constant parameter δ reduced non-uniform noise in accordance with the noise at each image pixel.

B. Optimization of Prior Parameter for Noise Control

We propose a method that optimizes the prior parameter δ by applying the measured noise σ_j at the pixel j of the CT image to acquire a uniform noise reduction rate.

$$\delta_j = \sigma_j \delta_w \quad (3)$$

The constant parameter δ_w was used to determine the image quality taking into account factors such as graininess of the image. For example, about 68% of the total noise was included below δ_j when δ_w was 1.0. The optimized parameter δ_j was applied in proportion to the noise σ_j in each area. [Fig. 3]. In Fig. 3, $\delta_w = 1.0$ and $p = 0.94$. The image noise was

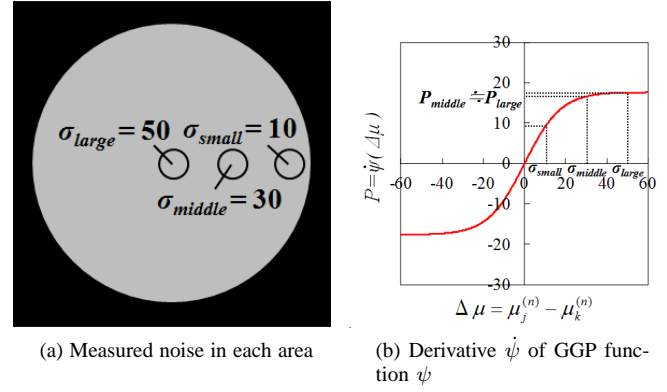


Fig. 2. Measured noise in each area and derivative $\dot{\psi}$ of GGP function ψ by applying constant parameter δ

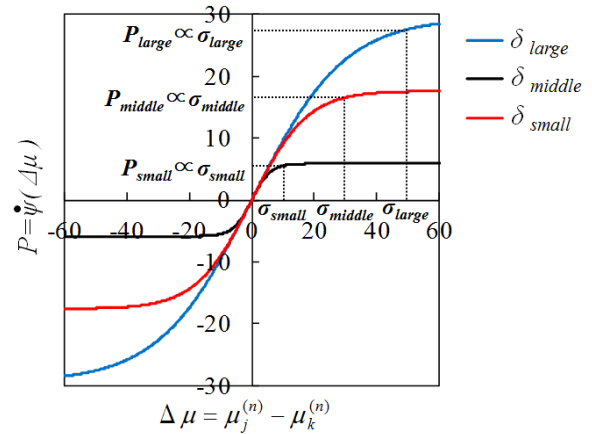


Fig. 3. Derivative $\dot{\psi}$ of GGP function by applying optimized parameter δ_j

reduced in proportion to the increased prior intensity P by the smoothing effect. As a result, the noise reduction rate results were uniform regardless of the different noise in each area.

A serious problem is that setting wide ROI made it difficult to measure the noise on the non-uniform object of CT image. In our proposed method, the image subtraction method [7, 8] was applied to measure the noise accurately without depending on the object [Fig. 4]. First, the measured data was divided evenly into non-correlated pairs such as odd and even views. Second, the SD σ of the random noise was calculated from the subtracted image, which was created from the difference between reconstructed odd and even CT image.

III. MATERIALS

The effectiveness of the proposed method was evaluated through phantom simulations. The geometry of a multi-slice scanner (Scenaria, Hitachi) was assumed. In particular, a multi-slice scanner that scanned non-helicly without generating electronic noise was used for estimating the noise reduction rate. A mid-plane slice was selected for the evaluation. The slice was 0.625 mm wide, the detector was 1.0 mm wide, and the dimensions of the image pixels were 512×512 in the x and y directions. The method was evaluated by using a circle phantom (Fig. 5(a)) and an abdomen phantom (Fig. 5(b))

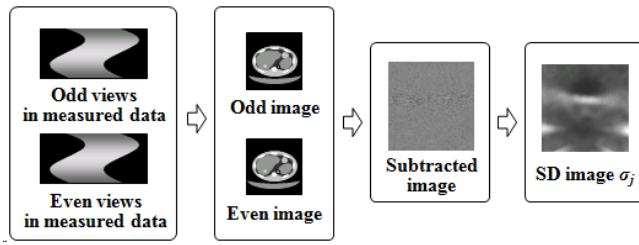


Fig. 4. Flowchart of image subtraction method

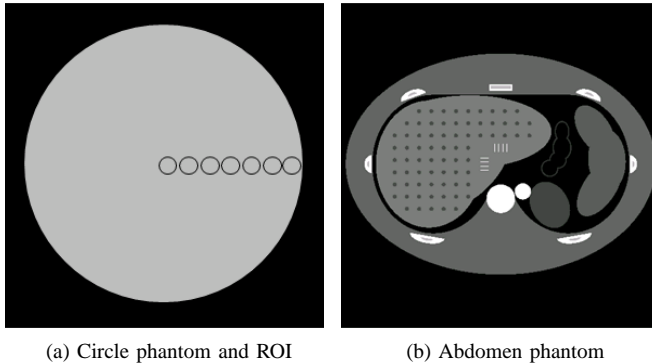


Fig. 5. Simulation phantoms and ROI for measuring noise

under mono-energy X-rays (100 [mAs]). The circle phantom mimicked the human abdomen, and the attenuation coefficient that mimicked water was uniformly set at zero [HU]. The diameter of the phantom was 400 mm and the field of view (FOV) for reconstructing the CT image was 550 mm. The abdomen phantom that mimicked the human abdomen was set as shown in Fig. 5(b). The long axis was 380 mm, the short axis was 270 mm, and the FOV was 400 mm. The number of iterations was set to 100, and the number of subsets was set to 24. The $\delta_w = 0.5$ and $\delta_w = 1.0$. Seven ROI were placed at the center and off-center to measure the SD σ of the random noise as shown in Fig. 5(a). The SD reduction rate calculated from the measured SD σ was used as the evaluated value for comparison between the conventional and proposed methods.

$$SD \text{ reduction rate } [\%] = 100 \cdot \left(1.0 - \frac{SD^{(n=100)}}{SD^{(n=0)}} \right) \quad (4)$$

The $SD^{(n)}$ was measured in the CT image when the iteration number was n . In this paper, the weight w_i in the iterative algorithm was a constant value of 1. In the conventional method, the constant parameter δ was determined by using the measured SD σ inside the ROI placed at the center and $x = 150$ mm at the off-center in the circle phantom. In the abdomen phantom, the constant parameter δ was determined by using the measured SD σ inside the ROI at the center, and $y = 120$ mm at the off-center. The $\delta_w = 0.5$ and $\delta_w = 1.0$ were multiplied by the measured SD σ . In this paper, the prior weight β was determined to acquire the desired SD reduction rate when applying each parameter δ_w . The values of $\beta_{\delta_w=0.5}$ and $\beta_{\delta_w=1.0}$ were acquired when the desired SD reduction rate was 50%.

IV. RESULTS AND DISCUSSION

The images obtained with the conventional and proposed methods are shown in Fig. 6(a) and (b) for the circle phantom when applying $\delta_w = 0.5$. The constant parameter δ that was determined from the measured noise when $x = 150$ mm (off-center) was applied in the conventional method [Fig. 6(a)]. In this method, the noise at the center of the CT image, such as salt and pepper noise, was much larger than that at the off-center compared with the proposed method. In the proposed method, the noise at the center was approximately equivalent to that at the off-center. The SD reduction rate and absolute error for the two methods in the ROI are shown in Fig. 7(a) $\delta_w = 0.5$ and (b) $\delta_w = 1.0$. The absolute error is expressed as

$$Absolute \ error = |SD \text{ reduction rate} - True \ value| \quad (5)$$

The true value was the desired SD reduction rate 50%. In particular, the average absolute error of the proposed method was reduced from 10.8% to 2.3% compared with the conventional method in Fig. 7(a) $\delta_w = 0.5$. The absolute error calculated from the conventional and proposed methods was less in Fig. 7(b) when $\delta_w = 1.0$. The reason is that the total noise was filled sufficiently below $\delta = \sigma$ in common with the conventional and proposed methods compared with when $\delta_w = 0.5$. The error of the proposed method is reduced remarkably compared with the conventional method when the δ_w is less.

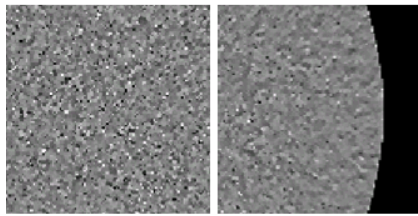
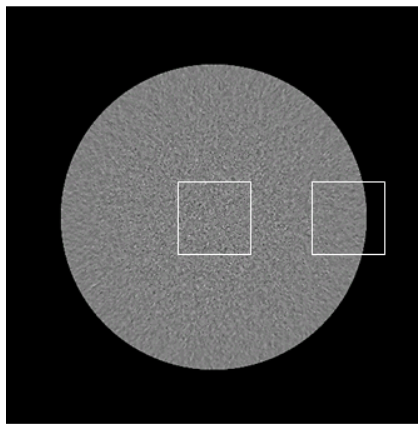
The images obtained with the conventional and proposed methods are shown in Fig. 8(a) and (b) for the abdomen phantom when applying $\delta_w = 0.5$. The constant parameter δ determined by the measured noise when $y = 120$ mm (off-center) was applied in the conventional method. In this method, the noise at the center of the CT image was much larger than that at the off-center compared with the proposed method. In the proposed method, the noise at the center was approximately equivalent to that at the off-center. Applying a suitable value for the parameter δ_j on the basis of the image noise made it possible to effectively control the uniform noise reduction in a CT image.

V. CONCLUSION

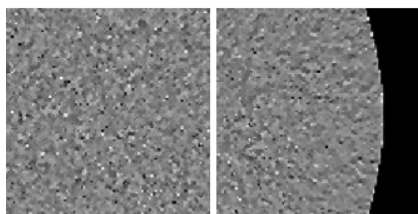
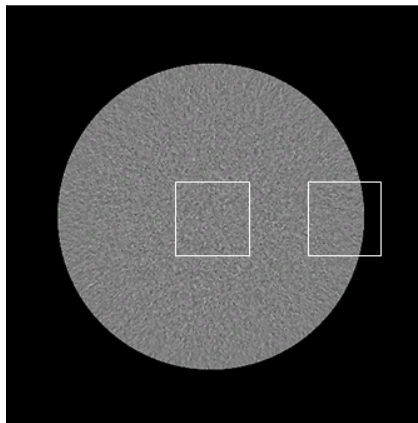
In this paper, we proposed a method to control the noise reduction rate by optimizing the prior parameter δ in the prior term when applying generalized Geman prior (GGP) for maintaining the spatial resolution. Applying a suitable value for the parameter δ on the basis of the image noise made it possible to effectively control the noise reduction in a CT image.

REFERENCES

- [1] J.-B. Thibault, K. D. Sauer, C. A. Bouman, and J. Hsieh, "A three dimensional statistical approach to improved image quality for multislice helical CT," *Med. Phys.*, vol.34, no 11, pp.4526-4544, 2007.
- [2] M. Kachelriess, "Iterative reconstruction techniques: What do they mean for cardiac CT?," *Curr. Cardiovasc. Imaging Rep.*, vol.6, pp.268-281, 2013.



(a) Conventional method



(b) Proposed method

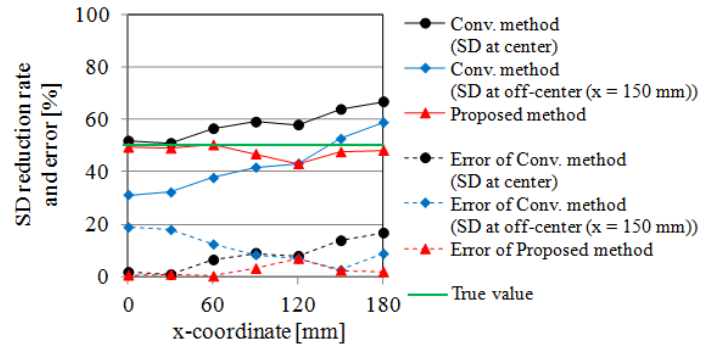
Fig. 6. Comparison of conventional and proposed methods (window width : 250, window level : 0)

[3] F. Bergner, B. Brendal, P. B. Noel, M. Dobritz, and T. Koehler, "Robust automated regularization factor selection for statistical reconstructions," The second international conference on image formation in X-ray computed tomography, pp.267-270. 2012.

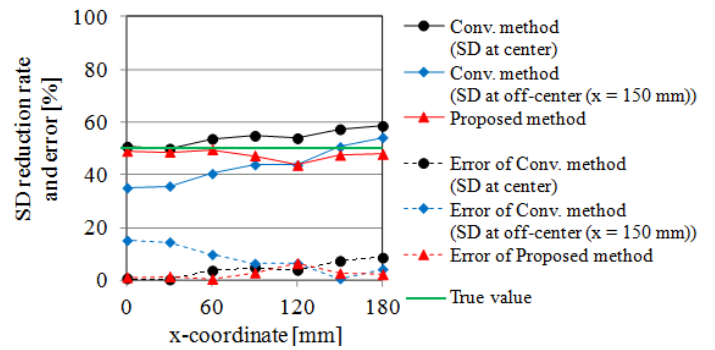
[4] K. Morikawa, "Image processing device and X-ray CT device," JP Patent 4,535,795, Sep., 2010.

[5] B. De Man, S. Basu, "Generalized Geman prior for iterative reconstruction," 14th International Conference, Medical physics; ICMP 2005, pp.358-359, 2005.

[6] B. De Man, "Statistical methods for image reconstruction," IEEE NSS and MIC Short course, 2007.

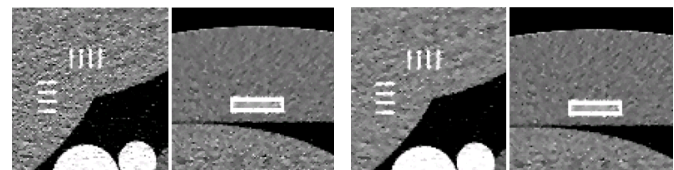
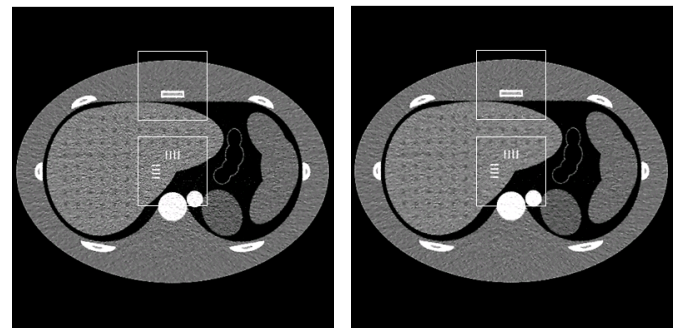


(a) $\delta_w = 0.5$



(b) $\delta_w = 1.0$

Fig. 7. Comparison of SD reduction rate and error when $\delta_w = 0.5$ and $\delta_w = 1.0$



(a) Conventional method

(b) Proposed method

Fig. 8. Comparison of conventional and proposed methods. (window width : 250, window level : 65)

[7] J. Hsieh, "METHODS AND APPARATUS NOISE ESTIMATION FOR MULTI-RESOLUTION ANISOTROPIC DIFFUSION FILTERING," US7,706,497 B2, Apr., 2010.

[8] D. Shi, "Alternative noise map estimation methods for CT images," SPIE Medical Imaging 2013: Physics of Medical Imaging 8668, 866835-1, 2013.

[9] H. Erdogan, J. A. Fessler, "Monotonic algorithms for transmission tomography," IEEE. Trans. Med. Imag., vol.18, no.9, pp.801-814, 1999.

Synchrotron-Based Microtomography: Exploiting Tunable, Monochromatic, Parallel X-rays for Non-Destructive Materials Characterization

Trevor M. Willey, Tony van Buuren, Lisa Lauderbach, Franco Gagliardi, and George Overturf

Abstract—Monochromatic, energy-tunable, and parallel x-rays generate quantitative reconstructed images in situations not amenable to conventional cone-beam microtomography. Complicated data treatment (for example, ray weighting or beam hardening correction) are largely unnecessary in situations where the unique aspects of synchrotron radiation are appropriately exploited. Two representative cases are presented here: First, an ultra-low density foam, embedded in a higher density foam and adjacent to a highly attenuating bromine-containing layer is imaged much more readily with parallel beam rays that traverse the foams but not the bromine layer in the set of images used for reconstruction. Also, the highly monochromatic beam requires little or no beam hardening correction. In the second case, multi-energy monochromatic acquisitions lead directly to quantitative compositional three dimensional microstructure in mixtures of triaminotrinitrobenzene and a chlorinated fluoropolymer binder.

I. INTRODUCTION

Synchrotron storage rings generate high-flux, monochromatic, and essentially parallel beams of x-rays. We present two examples where the capabilities of synchrotron microtomography quantitatively characterize density and composition of materials not easily investigated with laboratory-based, polychromatic cone-beam microtomography.

The first object, a few mm in diameter and less than 1 mm tall, is an ultra-low density (10 mg/cc) silica layer embedded within a higher density carbon foam (400 mg/cc), and adjacent to a highly attenuating, bromine doped layer. In order to image the silica layer, careful alignment within the x-ray beam, such that x-rays used to reconstruct this layer were only traversing carbon and silica, and careful choice of x-ray energy are required.

In the second class of objects, multiple acquisitions using monochromatic x-rays at multiple carefully chosen energies generate three dimensional composition maps of triaminotrinitrobenzene mixed with a chlorinated polymer binder. The reconstructed images show a subtle spatial concentration variation.

II. EXAMPLE USE CASES FOR SYNCHROTRON-BASED MICROTOMOGRAPHY

A. Imaging of Ultra-low Density, Embedded Materials

The first example is the use of relatively low-energy (10 keV) and parallel-beam to non-destructively determine morphology and density uniformity in embedded, ultra-low density

foams in targets used to investigate materials under extreme conditions at the National Ignition Facility (NIF) at Lawrence Livermore National Laboratory (LLNL). NIF is the worlds largest laser facility; the laser beams are used to heat and compress materials to extreme temperatures and pressures. One application of NIF is research into inertial confinement nuclear fusion.

Nuclear *fusion* promises carbon-free nuclear energy without the proliferation risks of current nuclear *fission* reactor designs. Although enormous technical challenges over the last few decades have plagued both magnetic and inertial confinement fusion, both possibilities are moving forward. NIF is the premier inertial confinement fusion research center; recent breakthroughs resulted in record yields of over $5 \cdot 10^{15}$ neutrons during one laser shot sequence, an improvement by nearly a factor of 4 within the past year [1] [2]. These shots, using the so called “high foot” laser profile, and diamond capsules, have neutron yields estimated to be well within a factor of 5 of the alpha heating regime, a threshold for “ignition” [3] along the path to generating more energy from nuclear fusion than is consumed.

One overarching challenge is to create targets to enable effective use of the enormous laser energy generated with the unique experimental capability at NIF. Successful target design places considerable demands upon the underlying materials synthesis; materials often tune the pressure profile of the initial laser shock, or emit radiation as they are heated and/or compressed. The uniformity of these materials plays a critical role, and often, ultra-low density materials are needed for these tasks.

As an example of the use of synchrotron microtomography to image embedded low-density foams, Fig. 1 presents a small sub-volume of a class of target used on NIF that uses 10 mg/cc SiO_2 aerogel, mounted within a 400 mg/cc carbon foam, atop a heavily bromine-doped layer with orders of magnitude difference in x-ray opacity. The top pane presents a CT slice acquired at 10 keV through a uniform area of the aerogel. The bottom pane presents a reconstructed volume of a similar aerogel layer along with its unintended defects. Prior to synchrotron-based tomography, our Xradia MicroCT was unable to image, let alone discern defects or density variation in this embedded, ultra-low density foam. At least using standard filtered backprojection, accurate morphology and density measurements of the SiO_2 aerogel, that has only 0.5% of the density of the bulk solid required the following: 1) A well-aligned sample in a parallel beam is the best geometry, with

The authors are with Lawrence Livermore National Laboratory.

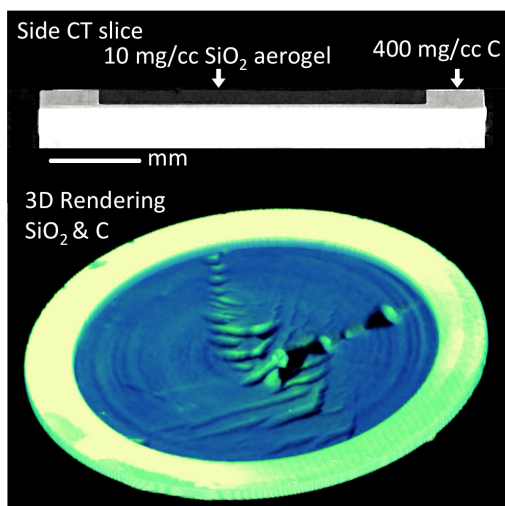


Fig. 1. CT slice (top) and 3D view of ultra-low density SiO_2 aerogel embedded in higher density carbon. Conventional, cone-beam, polychromatic microCT failed to image or even detect the SiO_2 that has 0.5% of the density of bulk material. This sample was rejected due to its defects.

the x-rays used to image the SiO_2 traversing only low density foams and not bromine layers. The higher-z bromine layer results in orders of magnitude more attenuation and thus rays that traverse any part of this layer are essentially useless for reconstructing the 10 mg/cc aerogel layer. With conventional point-source x-rays, one would either need a high source-object to object-detector distance ratio, which can reduce x-ray flux through the sample and onto the detector to unacceptably low levels, or use algorithms to address experimental errors introduced by radically different attenuation through aerogel vs. the bromine layer. 2) Monochromatic x-rays can be tuned to optimize the attenuation through these low density foams, in this case, relatively low energy, at or less than 10 keV. Higher energy x-rays do not have sufficient attenuation to image the central foam layer. Further, polychromatic conventional x-ray sources complicate analysis of density variation due to beam hardening. 3) The synchrotron source gives sufficiently high flux at relatively low energies. These three characteristics above are either impossible or non-trivial using conventional x-ray sources. These three aspects of synchrotron radiation enable measurement of the morphology and to a lesser degree, density variation in the ultra-low density SiO_2 foam layer. In this case, the foam had several rips, but otherwise had relatively uniform density. The data gave valuable feedback to enable appropriate changes in synthesis to obtain uniform embedded low-density foams. Another capsule under development requires an $100 \mu\text{m}$, 30 mg/cc carbon aerogel layer within a 2 mm diameter, $50 \mu\text{m}$ thick spherical diamond shell [4]. This interior foam layer scaffolds deuterium-tritium ice growth. Synthetic challenges fall beyond the scope of studies reported to date, particularly when one considers that formation of the nanoporous scaffold and any subsequent doping must be achieved through a hole in the wall of the capsule that is, at most, only tens of microns in diameter. Synchrotron-based tomography with high-intensity, parallel

beam, and monochromatic and tunable x-rays is a viable technique that can verify intended morphology of embedded low-density materials at micron-scale resolution.

B. Mapping Subtle Compositional Variation

The second example of the use of synchrotron tomography uses multiple acquisitions at multiple energies using monochromatic x-rays to map subtle concentration variation in low-z composites.

TATB (1,3,5-triamino-2,4,6-trinitrobenzene) is a highly insensitive energetic material often mixed with polymer binders to improve mechanical properties and enable pressing to high density. Two common formulations, named LX-17 and PBX-9502, use Kel-F 800 (poly chlorotrifluoroethylene-co-vinylidene fluoride) as a binder with nominal concentrations of 7.5% and 5%, respectively. The resultant polymer-bound explosive has higher density and better mechanical properties compared to the pure explosive alone. Samples investigated with tomography were previously observed to have a variation in binder concentration of about 1.5% on mm length scales [5] [6] with binder-rich regions surrounding binder poor regions. Figure 2 presents a three dimensional rendering of the binder concentration variation. The so-called prill structure is consistent with the formulation of these explosives where mm-sized spheres, or prills, form during the mixing of binder and explosive prior to consolidation and pressing.

This observation motivates several questions: What is the cause of this variation? Does it result purely from the formulation step where raw pure TATB is mixed with the Kel-F 800 binder? How does the production lot of TATB or Kel-F 800 contribute to the degree of heterogeneity? Can homogeneous LX-17 and/or PBX-9502 be reliably synthesized? And ultimately, what are the possible impacts of heterogeneity, if any, on mechanical and detonation properties? These questions cannot be addressed or answered without first understanding the degree of microstructural variation. To this end, synchrotron-based tomography was performed on a series of samples of LX-17 and PBX-9502 with different origins as a starting point towards answering the above questions.

Synchrotron-based x-ray computed microtomography enables quantitative determination of constituent volume frac-

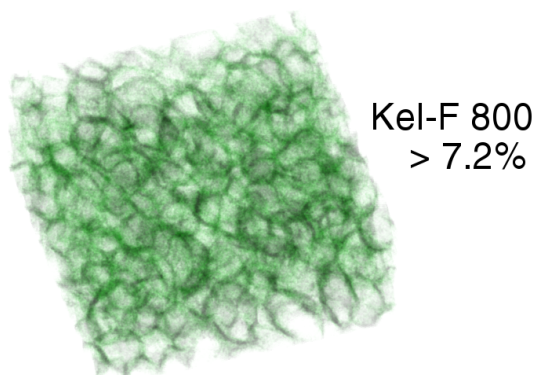


Fig. 2. A three-dimensional rendering of relatively high concentrations of the constituent Kel-F 800 binder within an LX-17 sample.

tions, voxel by voxel, in three-dimensional volumes of LX-17 and PBX-9502. Using monochromatic incident x-rays, the well-defined, well-known, and energy dependent attenuation coefficients μ [7] can be directly compared to resultant measured μ from reconstructed slices. As an example, at 20 keV, TATB and Kel-F 800 have attenuation coefficients of 1.1 and 4.1 cm^{-1} respectively; at 30 keV, these are 0.5 and 1.4 cm^{-1} . In the simple case of a mixture of two materials (e.g. TATB and Kel-F 800) these differences and nonlinearity in μ as a function of energy enable volume fraction determination through the linear relationships

$$V_{TATB} \cdot \mu_{TATB} + V_{KelF} \cdot \mu_{KelF} = \mu_{measured} \quad (1)$$

at two unique energies, and

$$V_{TATB} + V_{KelF} + V_{void} = 1 \quad (2)$$

where V is the respective volume fraction of constituents TATB, Kel-F 800 binder (*KelF*) and void, and μ are the respective linear attenuation coefficients.

This framework can be extended to N materials, requiring $N-1$ acquisitions, each at a unique energy. Generally at length scales presented, void volume generally is less than a few percent and varies little with a slight increase with decreasing binder concentration [4, 5]. The Kel-F 800 concentration can also be estimated from a single energy acquisition by assuming a void distribution as a function of μ . Figure 3 presents slices of the approximate Kel-F 800 concentration from within the interior of LX-17 and PBX-9502 samples of different manufacturing lots, labeled a through p. Figure 2 is a three dimensional rendering of the volume concentration of the constituent binder and its variation in concentration. The variation in Kel-F 800 concentration is only dependent upon lot: Several samples from within single batches possess similar binder inhomogeneity irrespective of conditioning (i.e. temperature cycling [8], age, or mechanical creep). LX-17 lots a and b are

most homogeneous, c and g are moderately homogeneous, and d, e, f, and h are heterogeneous. PBX-9502 lots are moderately homogeneous, with lots m and n being most heterogeneous. Having established the heterogeneity is purely lot dependent, the most apparent predictor of inhomogeneity to date is the type of TATB, whether the so-called dry-aminated, or wet-aminated was used to make the composite. Brown letters in Fig. 3 (e.g. LX-17 lots a and b) indicate formulations using dry-aminated TATB, while black (e.g. PBX-9502 lots m and n) are made with wet-aminated TATB. The dry-aminated lots lead to slices that are qualitatively more homogeneous than wet-aminated from inspection of the slices in Fig. 3. Conversely, lots made with wet-aminated TATB have prill boundaries. Although the use of wet- vs. dry-aminated TATB is the most apparent factor influencing degree of inhomogeneity, the TATB type is not the only parameter, and may even be coincidental with other process changes: the variation observed within the lots formulated with wet-aminated TATB indicates other factors affect the binder/TATB mixing. The microstructure from wet-aminated TATB varies from grossly heterogeneous in e to relatively homogeneous in g. Thus, these CT datasets are crucial starting point as empirical experimental input to high fidelity computational models, and in understanding how microstructure affects subtle detonation and mechanical property differences in TATB-based explosives.

In summary, two examples using advantages of synchrotron microtomography have been presented. The parallel beam and relatively low monochromatic energy are able to image ultra-low density materials, and the monochromaticity and tunability have been used to map subtle polymer concentration variation in polymer bound explosives.

LLNL-ABS-645201

REFERENCES

- [1] O. A. Hurricane, D. A. Callahan, D. T. Casey, P. M. Celliers, C. Cerjan, E. L. Dewald, T. R. Dittrich, T. Doeppner, D. E. Hinkel, L. F. Berzak Hopkins, J. L. Kline, S. Le Pape, T. Ma, A. G. MacPhee, J. L. Milovich,

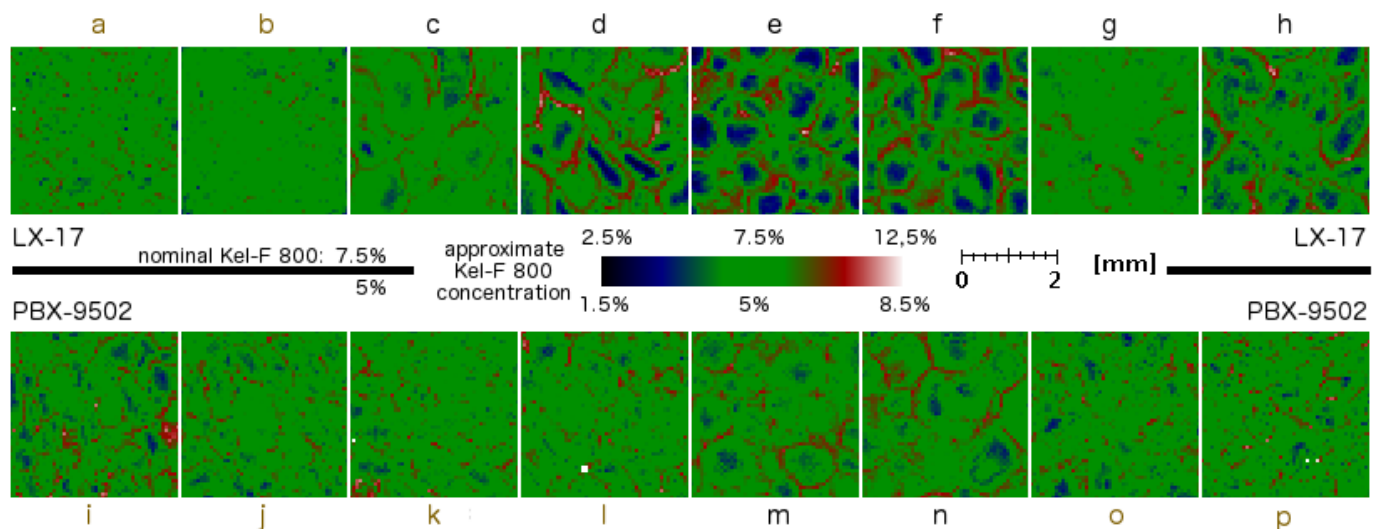


Fig. 3. Slices depicting deviation from nominal polymer binder (Kel-F 800) concentration from x-ray computed microtomography. Different batches (lots) of LX-17 (top, nominally 7.5% binder) and PBX-9502 (bottom, nominally 5% binder).

- A. Pak, H. S. Park, P. K. Patel, B. A. Remington, J. D. Salmonson, P. T. Springer, and R. Tommasini. Fuel gain exceeding unity in an inertially confined fusion implosion. *NATURE*, 506(7488):343+, FEB 20 2014.
- [2] H-S Park, O. A. Hurricane, D. A. Callahan, D. T. Casey, E. L. Dewald, T. R. Dittrich, T. Doepfner, D. E. Hinkel, L. F. Berzak Hopkins, S. Le Pape, T. Ma, P. K. Patel, B. A. Remington, H. F. Robey, J. D. Salmonson, and J. L. Kline. High-Adiabatic High-Foot Inertial Confinement Fusion Implosion Experiments on the National Ignition Facility. *PHYSICAL REVIEW LETTERS*, 112(5), FEB 5 2014.
- [3] D. E. Hinkel, M. J. Edwards, P. A. Amendt, R. Benedetti, L. Berzak Hopkins, D. Bleuel, T. R. Boehly, D. K. Bradley, J. A. Caggiano, D. A. Callahan, P. M. Celliers, C. J. Cerjan, D. Clark, G. W. Collins, E. L. Dewald, T. R. Dittrich, L. Divol, S. N. Dixit, T. Doepfner, D. Edgell, J. Eggert, D. Farley, J. A. Frenje, V. Glebov, S. M. Glenn, S. W. Haan, A. Hamza, B. A. Hammel, C. A. Haynam, J. H. Hammer, R. F. Heeter, H. W. Herrmann, D. Ho, O. Hurricane, N. Izumi, M. Gatu Johnson, O. S. Jones, D. H. Kalantar, R. L. Kauffman, J. D. Kilkenny, J. L. Kline, J. P. Knauer, J. A. Koch, A. Kritcher, G. A. Kyrala, K. LaFortune, O. L. Landen, B. F. Lasinski, T. Ma, A. J. Mackinnon, A. J. Macphée, E. Mapoles, J. L. Milovich, J. D. Moody, D. Meeker, N. B. Meezan, P. Michel, A. S. Moore, D. H. Munro, A. Nikroo, R. E. Olson, K. Opachich, A. Pak, T. Parham, P. Patel, H-S Park, R. P. Petrasso, J. Ralph, S. P. Regan, B. A. Remington, H. G. Rinderknecht, H. F. Robey, M. D. Rosen, J. S. Ross, R. Rygg, J. D. Salmonson, T. C. Sangster, M. B. Schneider, V. Smalyuk, B. K. Spears, P. T. Springer, E. Storm, D. J. Strozzi, L. J. Suter, C. A. Thomas, R. P. J. Town, E. A. Williams, S. V. Weber, P. J. Wegner, D. C. Wilson, K. Widmann, C. Yeamans, A. Zylstra, J. D. Lindl, L. J. Atherton, W. W. Hsing, B. J. MacGowan, B. M. VanWanterghem, and E. I. Moses. Progress toward ignition at the National Ignition Facility. *PLASMA PHYSICS AND CONTROLLED FUSION*, 55(12, 1-2), DEC 2013. 40th Conference of the European-Physical-Society on Plasma Physics, VTT Tech Res Ctr Finland, Espoo, FINLAND, JUL 01-05, 2013.
- [4] J. Biener, C. Dawodeit, S. H. Kim, T. Braun, M. A. Worsley, A. A. Chernov, C. C. Walton, T. M. Willey, S. O. Kucheyev, S. J. Shin, Y. M. Wang, M. M. Biener, J. R. I. Lee, B. J. Kozioziemski, T. van Buuren, K. J. J. Wu, J. H. Satcher, Jr., and A. V. Hamza. A new approach to foamed indirect-drive NIF ignition targets. *NUCLEAR FUSION*, 52(6), JUN 2012.
- [5] J.H. Kinney and T.M. Willey and G.E. Overturf. On the Nature of Variations in Density and Composition within TATB-based Plastic Bonded Explosives. *Proceedings of the 13th International Detonation Symposium*, 2006.
- [6] Willey, T. M. and Lauderbach, L. and Gagliardi, F. and Cunningham, B. and Lorenz, K. T. and Lee, Jonathan R. I. and van Buuren, T. and Call, R. and Landt, L. and Overturf, G. E. Comprehensive Characterization of Voids and Microstructure in TATB-based Explosives from 10 nm to 1 cm: Effects of Temperature Cycling and Compressive Creep. *Proceedings of the 14th International Detonation Symposium*, 2010.
- [7] The Center for X-ray Optics, Lawrence Berkeley Laboratory, X-ray Database, <http://www.cxro.lbl.gov>.
- [8] D. G. Thompson, G. W. Brown, J. T. Mang, R. DeLuca, B. Patterson, and S. Hagelberg. CHARACTERIZING THE EFFECTS OF RATCHET GROWTH ON PBX 9502. In Elert, ML and Buttlar, WT and Furnish, MD and Anderson, WW and Proud, WG, editor, *SHOCK COMPRESSION OF CONDENSED MATTER - 2009, PTS 1 AND 2*, volume 1195 of *AIP Conference Proceedings*, pages 388–391, 2 HUNTINGTON QUADRANGLE, STE 1N01, MELVILLE, NY 11747-4501 USA, 2009. Amer Phys Soc, Topical Grp, AMER INST PHYSICS. 16th Conference of the American-Physical-Society-Topical-Group on Shock Compression of Condensed Matter, Nashville, TN, JUN 28-JUL 03, 2009.

2D filtered backprojection for fan-beam CT with independent rotations of the source and the detector

Simon Rit and Rolf Clackdoyle

Abstract—A cone-beam CT scanner has recently been developed for radiotherapy imaging where the source and the flat detector can rotate independently along concentric circular trajectories. This paper investigates the reconstruction of the central slice of this system. A new filtered-backprojection algorithm has been derived that only modifies the weighting schemes of the projections and the backprojections of the standard fan-beam algorithm. The accuracy of the algorithm is demonstrated on simulated projections of a numerical phantom with source and detector trajectories that image an offset field-of-view.

I. INTRODUCTION

Cone-beam computed tomography (CT) scanners have been introduced in radiotherapy rooms to acquire three-dimensional (3D) CTs of patients prior to treatment and guide their delivery accordingly. Existing cone-beam CT scanners are generally fixed to the gantry of the linear accelerator with an x-ray source dedicated to imaging that is orthogonal to the treatment beam [1].

MedPhoton, a spin-off company of Paracelsus Medical University (Salzburg, Austria), is developing a new Patient Alignment system with an integrated x-ray Imaging Ring (PAIR, Figure 1). The system has been designed to provide greater flexibility in the positioning of the patients and to enable re-positioning of the patient based on 3D images acquired during radiotherapy. A robotic couch is mounted to the ceiling along which an imaging ring surrounding the patient table can translate in the cranio-caudal direction. The x-ray source and the flat panel detector are mounted on the ring and can rotate independently to acquire x-ray projections of any part of the patient with various incidences. The x-ray source is collimated with four motorized jaws that can dynamically adapt the dimension of the x-ray beam. The device allows, for example, the acquisition of x-ray projections for CT reconstruction with an offset field-of-view, i.e., a field-of-view that is not centered on the mechanical center-of-rotation.

By default, the source follows a conventional circular trajectory with respect to the patient and it is known that for this geometry, only the plane containing the source trajectory can be reconstructed exactly [2]. We limit our study to this plane. Two-dimensional (2D) filtered-backprojection (FBP)

S. Rit is with the Université de Lyon, CREATIS; CNRS UMR5220; Inserm U1044; INSA-Lyon; Université Lyon 1; Centre Léon Bérard, France (e-mail: simon.rit@creatis.insa-lyon.fr). R. Clackdoyle is with the laboratoire Hubert Curien, CNRS and Université Jean Monnet (UMR 5516), Saint Étienne, France. This work was partially supported by grants ANR-12-BS01-0018 (DROITE project) and ANR-13-IS03-0002-01 (DEXTER project) from the Agence Nationale de la Recherche (France).



Fig. 1. Photography of a prototype of the Patient Alignment system with an Integrated x-ray imaging Ring (PAIR).

algorithms are known for the conventional situation where the flat detector is orthogonal to the line connecting the source to the center-of-rotation [3]. FBP formulas have also been derived for displaced centers-of-rotation [4] and for noncircular trajectories [5], [6] but these situations do not cover the geometry of PAIR's central slice.

In this article, we derive a 2D FBP formula for circular trajectories with independent rotations of the source and the detector. The resulting algorithm is tested on simulated data in which the center of the field-of-view is not at the center-of-rotation.

II. RECONSTRUCTION ALGORITHM

The geometry is described in Figure 2 with the origin at the center-of-rotation. The fan-beam source follows a circular trajectory parameterized by angle β and at fixed radius R from the center-of-rotation. The source motion is therefore given by $\mathbf{v} = (-R \sin \beta, R \cos \beta)$. The flat detector lies at fixed radius R_D from the center-of-rotation and is tilted at an angle α with respect to the usual position, which would be directly opposite the x-ray source. The detector and the source can rotate independently so the tilt angle may also vary with β , and α is understood to have a β dependence. The origin of the detector is at the point closest to the center-of-rotation as shown in Figure 2.

The aim is to reconstruct the unknown two-dimensional (2D) function $f(x, y)$ from the measured line integrals

$$g(\beta, u) = \int_0^\infty f(\mathbf{v} + t\boldsymbol{\gamma}) dt \quad (1)$$

III. EXPERIMENTS

The reconstruction algorithm has been validated on simulated projections. The fixed geometric parameters were chosen to be close to those of the PAIR: the radii of the source and the detector were $R = 700$ mm and $R_D = 400$ mm and the detector measured 1024 samples in the interval $u \in [-175.3, 233.9]$ mm. As in the PAIR, the center of the detector has been intentionally shifted by 29.3 mm to enlarge the field-of-view when it is centered.

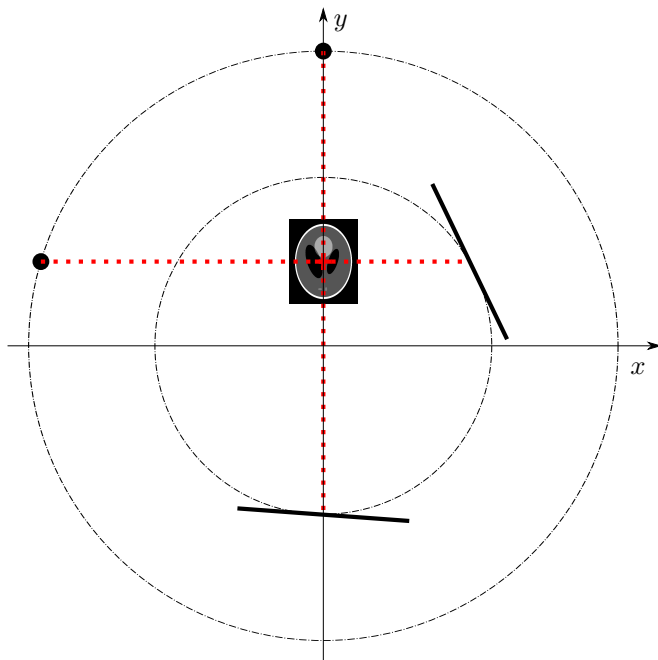


Fig. 3. Scale drawing of the experiment for the positions corresponding to projection #0 and projection #181. The phantom image is the reference slice in Figure 5. The red cross is the center of the offset field-of-view. The two red lines correspond to the source to center-of-detector lines of the two positions of the detector. The pair of angles (α, β) were about $(-4^\circ, 0^\circ)$ and $(42^\circ, 73^\circ)$ for projections #0 and #181, respectively. Corresponding vertical lines have been drawn in Figure 4. Note that the detector is not horizontal when the source to center-of-rotation line is vertical for projection #0 because the center of the detector that we align with this line is at $u = 29.3$ mm.

The angles α and β are two degrees of freedom of the scanner set by the user to acquire one projection $g(\beta, \cdot)$. We centered the offset field-of-view on point $(0, 200)$ mm of the y-axis (Figure 3). The source position β was set to enforce an equiangular spacing at the center of the offset field-of-view of the 720 projections. The variation of the speed of the source rotation (Figure 4) has been accounted for in the discretization of Equation 2 with a variable $\Delta\beta$ -weight between projections. The tilt angle α was set to align the source, the center of the offset field-of-view and the center of the detector for every projection. Figure 4 illustrates the β and $\beta+\alpha$ values according to projection number where β is the angle of the source to center-of-rotation line with the y-axis and $\alpha + \beta$ is the angle of the detector with the x-axis (Figure 2). These curves would have been parallel lines if the offset field-of-view had been centered on the center-of-rotation but we varied the speed of the rotation of the source and the detector in order to focus on the chosen offset field-of-view.

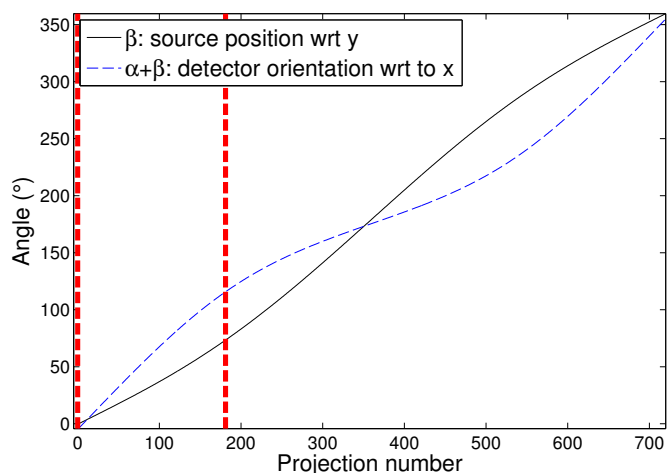


Fig. 4. Variations of β and $\alpha + \beta$ according to the projection number in the simulated projections of the phantom. Note that the source rotates more slowly (lower slope) when near the center of the offset field-of-view at the begin and the end of the scan. Similarly for the detector which is close to the offset field-of-view at the middle of the scan. The two vertical dashed lines correspond to the two positions that have been represented in Figure 3.

The phantom was slice $z = -0.25$ of the 3D version of the Shepp Logan phantom described in [3], centered on point $(0, 200)$ mm and scaled to 69 by 92 mm to fill the offset field-of-view. The reconstruction lattice was also centered on this point and made of 400×500 pixels of 0.4×0.4 mm².

IV. RESULTS

Several images of the phantom are shown in Figure 5: (1) the reference image illustrates the original phantom, (2) a naive modification of the existing equispaced FBP described in the following, and (3) the image obtained using the proposed fan-beam FBP algorithm. The naive modification of the existing equispaced FBP consisted in assuming that the source to center-of-rotation line was orthogonal to the detector during the weighting of projection images which comes down to weighting the projection by $\cos(\sigma - \alpha)$ instead of $\cos(\sigma)$ in Equation 9 while filtering and backprojecting the weighted projections in a similar manner. Images are displayed with two different gray scales, one to illustrate the large discrepancy between the naive reconstruction and the reference, and another narrow one to illustrate the accuracy of the new FBP algorithm.

Profiles along the lines drawn in Figure 5 are plotted in Figure 6. Accurate values have been reconstructed with small fluctuations ($\simeq 0.1\%$) around the expected values.

V. DISCUSSION AND CONCLUSIONS

A 2D FBP algorithm has been derived and validated for the reconstruction of the central slice of a cone-beam CT system, the PAIR, where the source and the detector can rotate independently. The new FBP algorithm is very similar to the conventional one [3]: only the weights of the projections and the backprojections need to be modified.

Other equispaced fan-beam geometries have been proposed but they did not cover this geometry. Gullberg *et al* derived

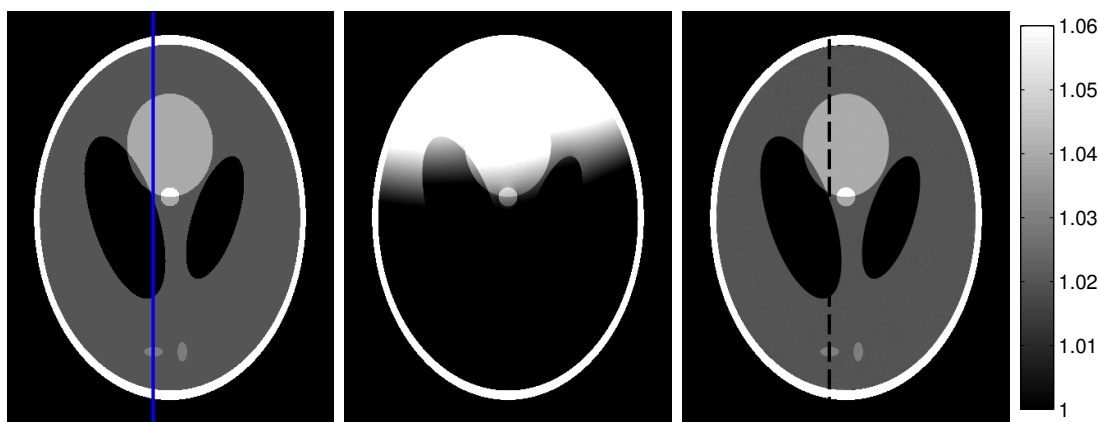


Fig. 5. Left: reference image of the phantom. Middle: naive modification of existing equispaced FBP. Right: new FBP algorithm.

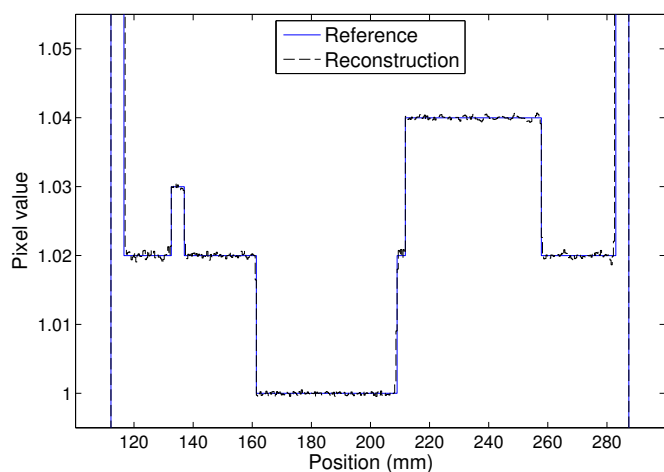


Fig. 6. Vertical profiles along the lines drawn on the reference and the reconstructed images of Figure 5.

a reconstruction formula for a fixed offset τ of the detector [4] which is covered by the new formula. Their formula may be obtained from Equation 9 by linking the parameterizations with $\tau = R \sin \alpha$. Other formulas are for non-circular source trajectories [5], [6].

Independent rotations of the source and the detector enable offset field-of-views. Offset field-of-views are essential in PAIR to image areas which could not be imaged otherwise due to the limited size of the detector. A side effect of moving the center of the offset field-of-view is the reduction of its maximum size with increasing distances between the center-of-rotation and the center of the offset field-of-view.

The formula is inaccurate if projections are truncated which is expected in many practical situations. One solution is to use a short scan with a source arc that is opposite the center of the offset field-of-view with respect to the center-of-rotation. Short scan acquisitions can be reconstructed with an appropriate weighting scheme as proposed for the conventional FBP algorithm [7], provided that the arc is greater than $\pi + 2\sigma_{\max}$ where σ_{\max} is the maximum value taken by $|\sigma|$. An alternative is to use an appropriate weighting scheme that accounts for redundant acquisition lines to truncate projections on one side

only [8]. If it is insufficient, the derivation of other algorithms for region-of-interest reconstruction [9] will be required.

Three-dimensional reconstruction is beyond the scope of this article. Exact reconstruction is only possible in the central plane but the FDK algorithm is commonly used [10]. Future work includes the derivation of a practical algorithm for the geometry of the PAIR.

REFERENCES

- [1] D.A. Jaffray, J.H. Siewerdsen, J.W. Wong, and A.A. Martinez, "Flat-panel cone-beam computed tomography for image-guided radiation therapy," *Int J Radiat Oncol Biol Phys*, vol. 53, no. 5, pp. 1337–1349, Aug 2002.
- [2] H. Tuy, "An inversion formula for cone-beam reconstruction," *SIAM Journal of Applied Mathematics*, vol. 43, pp. 91–100, 1983.
- [3] A.C. Kak and M. Slaney, *Principles of computerized tomographic imaging*. IEEE Press, 1988.
- [4] G.T. Gullberg, C.R. Crawford, and B.M. Tsui, "Reconstruction algorithm for fan beam with a displaced center-of-rotation," *IEEE Trans Med Imaging*, vol. 5, no. 1, pp. 23–29, 1986.
- [5] F.S. Weinstein, "Formation of images using fan-beam scanning and noncircular source motion," *JOSA*, vol. 70, no. 8, pp. 931–935, 1980.
- [6] C.R. Crawford, G.T. Gullberg, and B.M. Tsui, "Reconstruction for fan beam with an angular-dependent displaced center-of-rotation," *Med Phys*, vol. 15, no. 1, pp. 67–71, 1988.
- [7] D.L. Parker, "Optimal short scan convolution reconstruction for fanbeam CT," *Med Phys*, vol. 9, no. 2, pp. 254–257, 1982.
- [8] P.S. Cho, A.D. Rudd, and R.H. Johnson, "Cone-beam CT from width-truncated projections," *Computerized Medical Imaging and Graphics*, vol. 20, no. 1, pp. 49–57, 1996.
- [9] R. Clackdoyle and M. DeFRise, "Tomographic reconstruction in the 21st century," *IEEE Signal Process. Mag.*, vol. 27, no. 4, pp. 60–80, 2010.
- [10] L.A. Feldkamp, L.C. Davis, and J.W. Kress, "Practical cone-beam algorithm," *J Opt Soc Am A*, vol. 1, no. 6, pp. 612–619, 1984.

A GPU-Accelerated Katsevich Algorithm with CUDA for Fast, Scalable, Helical Cone-Beam CT

William C. Ward, Brandon M. Lattimore, James F. Hunter

Abstract—A very fast implementation of the Katsevich exact helical reconstruction algorithm has been coded and demonstrated using CUDA on a variety of GPUs. The performance demonstrates good scalability and the algorithm was designed for large volumes that cannot be held in core memory during processing. This implementation differs from previous work in that the entire computation chain is performed on the GPU(s) as soon as raw projection files are loaded. CPU processing tasks after setup are limited to the retrieval and scaling of projection data, storage of completed reconstructions, and the scheduling of GPU tasks. CPU and GPU processing are made fully concurrent so that the latency of both CPU—GPU transfers and CPU—disk I/O are masked from the sustained processing throughput while backprojecting. An interleaved slice scheme is used to effectively utilize resources in multi-GPU configurations. This algorithm is three orders-of-magnitude faster than the serial implementation it replaced and compares favorably to both our GPU-accelerated Feldkamp algorithms and to other known accelerated helical reconstructors. Overall performance approaches real-time processing, with reconstruction rates that meet or exceed the available I/O bandwidth in most cases. Performance comparisons, centering solutions, and example reconstructions are presented.

I. INTRODUCTION

A. Background and Motivation

For the routine cone-beam reconstruction of 3-D tomographic datasets, the approximation proposed by Feldkamp *et. al.* [1] (FDK) has long been the gold standard, particularly for Non-Destructive Evaluation (NDE) applications that make liberal use of large format flat panel detectors or lens-coupled digital camera systems. Recently, cone-beam FDK and parallel Filtered BackProjection (FBP) implementations based on CUDA across multiple GPUs have been implemented under MPI, OpenMP, and also a hybrid (MPI with local OpenMP) mode to help manage a large reconstruction workload that includes volume sizes up to $(4k)^3$. To overcome some limitations of FDK reconstructions, the exact helical algorithm developed by Katsevich[2] and in particular the work on the method by Noo *et. al.*[3] to implement native geometries stimulated strong interest from the NDE community. NDE applications are often driven toward large cone angle, tall detectors, high magnification, and long objects. All of these challenges can potentially be addressed by helical scans. However, scan geometry is also highly variable in the practice of NDE inspection; seldom are two scans identical. Post-scan isocenter correction is frequently needed, regardless of the nominal system alignment.

A version of the Noo/Katsevich algorithm has been incorporated in LANL reconstruction codes since 2006. Regardless,

helical reconstructions with experimental datasets had not been performed until 2013 because of two limitations: 1) computation time was prohibitive for large problem size, and 2) no isocenter corrections were implemented to compensate for small panel-to-rotary axis misalignments. This work exploits the latest GPU hardware to address both of these weaknesses in an effort to make helical CT as commonplace as FDK imaging for NDE tomographic studies.

B. Related Work

The time-line for acceleration efforts of helical CT reconstruction has a natural dependence on the evolution of computer hardware and software of the last decade. Parallelization of the Katsevich algorithm was implemented on a Linux cluster by Deng *et. al.* [4] who achieved basically linear speedup across 32 compute nodes for volumes up to 512^3 . Fontaine and Lee [5] employed OpenMp on a single server of 8 cores and exploited SIMD instructions available on the system to achieve an impressive speedup ratio. They also make the interesting observation, foreshadowing GPU computation considerations, that frontside bus bandwidth created an upper limit on usable thread count. OpenMP and maximization of the resources on a single server will generally scale better than MPI on a local computing model because threads under OpenMP need not subdivide the local memory space.

Yan *et. al.* [6] used a different approach to achieve good GPU acceleration of the FBP operation only; filtering operations were performed on the multicore CPUs of the host system. The FBP step was performed in OpenGL under the Cg framework by rendering the projections directly to an imaging space bound to a floating point texture (cyclic render-to-texture) and employing the graphics pipeline to effectively turn the FBP calculation into a true drawing process. Yan observed greater than a factor of 20 speedup on this single GPU platform over the 32-processor cluster of earlier work (only FBP times were compared).

Steckmann, Knaup, and Kachelrieß [7] developed a voxel-weighting scheme that allows highly optimized backprojection with vectorization enabled by symmetry. Their method is applied to approximate spiral cone-beam reconstruction with rebinning in all dimensions and pre-computed storage of all required detector coordinates and voxel weightings. The resulting reduction in complexity allows for FBP performance approaching that of optimized parallel backprojection and yields good image quality demonstrated with up to 256-row detectors. While limited $\pi/4$ symmetry has been exploited before in a Katsevich-type method ([5]), the Steckmann approach has not yet been extended to the exact methods and the size

Los Alamos National Laboratory, Los Alamos, NM USA 87545; Corresponding author: ww@lanl.gov LA-UR-14-20971

of problems targeted by this work would add to the difficulty. The pre-computation cost of weights and coordinates for each new (volatile) geometry and the restrictions of fixed isocenter and cylindrical FOV are further disincentives to pursue this optimization in place of the more direct approach.

C. Defining and Achieving Real-Time Performance

All of the referenced authors presenting accelerated methods base their timing on data that is already fully loaded to CPU memory. The goal of this work is to achieve an end-to-end real-time throughput of exact Katsevich-based helical reconstructions including all I/O operations. Conveniently, the concept of “real-time” is application-specific, so a precise definition is elusive. Scientific industrial CT applications are by nature much slower than medical applications: resolution is primary, dose management is not. A single scan may last for hours and offline storage (and retrospective reconstruction) is essential. “Real-world real-time” performance of the end-to-end process of loading projections, reconstruction, and storing a completed volume back to a permanent repository is the bounding metric. By this definition an optimal system design, hardware and software, will provide enough processing power to complete the reconstruction tasks as quickly as it can move the necessary data through the file system. Still, early information about the progress of a scan is useful in all applications and the best implementation will start producing output slices as soon as useable subset of projections is available from the source. In other terms, this method is designed to facilitate temporal locality of initial projections and the first reconstructed slices.

II. ALGORITHMIC APPROACH AND IMPLEMENTATION

An adaptation of the cone beam cover method (Yang[8]) is adopted and optimized for single-board systems with one or more suitable GPUs and a strong compliment of CPU cores. Coarse-grained parallelism is pursued on the CPU, (e.g. disk transfers). Most every image-related task exhibits ‘embarrassing parallelism’ and is handled effectively by the GPU.

OpenMP scheduling is used to feed all the image processing steps—differentiation, filtering and back projection—to the GPU. Asynchronous scheduling for CPU↔GPU memory copies and GPU Kernel launches frees the CPU to perform file I/O tasks asynchronously and thereby mask the latency as completely as possible.

Algorithm 1 presents pseudo-code for the algorithm design optimizing concurrent CPU/GPU use. Coordinates and dimensions relevant to the implementation sections below are summarized in Figure 1.

1) *Filtering Steps 1&2: Differentiation:* The Katsevich algorithm requires the first derivative of each projection, taken at constant line direction $\underline{\theta}_c$,

$$g'(\lambda, \underline{\theta}_c) = \lim_{\varepsilon \rightarrow 0} \frac{g(\lambda + \varepsilon, \underline{\theta}_c) - g(\lambda - \varepsilon, \underline{\theta}_c)}{2\varepsilon} \quad (1)$$

where coordinate transformation of $\underline{\theta}_c$ provides the projection value in the flat detector plane coordinates u, w :

$$g_1(\lambda, u, w) = g(\lambda, \underline{\theta}_c) \quad (2)$$

Algorithm 1: GPU Filtering & Back Projection With Concurrent I/O (per GPU)

```

// vertical extent of VOI block
Data: Chunk size  $N_C$ 
// Batch size is F(#cores, GPU memory, max
// texture length)
Data: Batch size  $N_b$ 
while slices remain do
  Find range of projections influencing slices
  Zero slices in chunk (MemSet)
  while batch( $g$ )  $\in$  range do // Inner Loops are
  Concurrent!
1   foreach  $g \in$  batch do // Preload
2     Load  $g$  (disk⇒CPU⇒GPU)
     _____ Wait(Compute Idle?) _____ ↓↓
3   Copy batch to texture
4   next batch ( $g[i + N_b - 2]$ )
5   for  $i$  in  $[1..N_b - 1]$  do // Compute
     _____ Wait(Preload Complete?) _____ ↑↑
6     Filter  $g[i]$  to  $g^F$ 
7     Copy  $g^F \Rightarrow$  FBP texture
8     BackProject  $g^F$  over chunk (all valid  $z$ )
9   MemCpy chunk GPU⇒CPU
10  foreach slice  $S$  in chunk do Store  $S$  // no-wait
11  next chunk ( $S[n + N_C]$ )

```

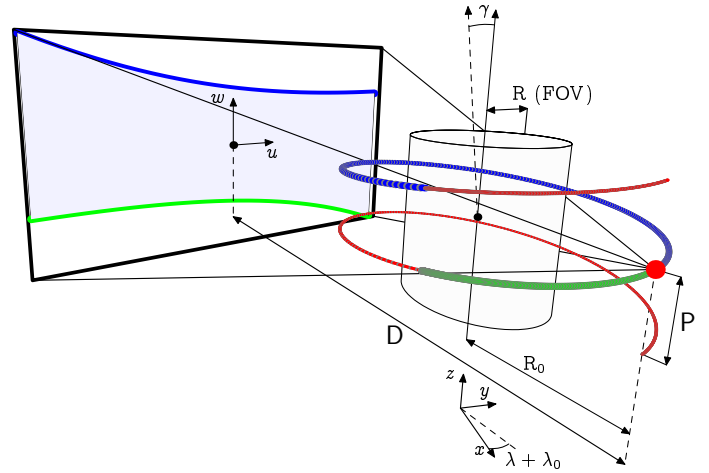


Fig. 1. Helical geometry and variables. Tam-Danielsson window is shaded.

Noo *et al.*[3] propose two practical alternatives for efficient estimation of the derivative, but this work uses a direct computation of equation (1) that is well-suited to the GPU architecture. With a stack of $N + 2$ projections loaded to a layered 2-D texture representing $\{g(\lambda_{-1}), g(\lambda_0), \dots, g(\lambda_N)\}$, the GPU is used to compute in hardware (‘fetch’) bilinear interpolations at points $g(\lambda_{i-1}, u, v), g(\lambda_i, u, v), g(\lambda_{i+1}, u, v)$ without any computational cost. The 2-D texture also alters the locality of the projections for better 2-D access to reduce cache hits. The $[\lambda + \varepsilon, \lambda - \varepsilon]$ interpolates are generated in the conventional way from the three points centered at $g(\lambda_i, u, v)$.

This process generates N filtered projections.

Kernel is the designation given to a GPU function executed by every thread of a parallel *Kernel Launch* (This usage is unrelated to the mathematical *kernel* employed during a convolution.) Within the same GPU differentiation Kernel it is convenient to implement length-correction weighting:

$$g_2(\lambda, u, w) = \frac{D}{\sqrt{D^2 + w^2}} g_1(\lambda, u, w). \quad (3)$$

2) *Centering (Misalignment Correction)*: The hardware-based interpolation in the implementation of Filtering Step 1 provides an opportunity to inexpensively correct for misalignment of the acquisition system. If the transverse plane of the rotational axis is misaligned by a horizontal shift a_0 and an angle γ to the vertical axis of the detector (see Fig. 1) then more accurate reconstruction can be obtained by rotating each raw projection about its center by the γ . If (u_m, w_m) are the uncorrected coordinates, then the corrected coordinates are given by

$$\begin{aligned} u &= u_m \cos \gamma + w_m \sin \gamma + a_0, \\ v &= -u_m \sin \gamma + w_m \cos \gamma. \end{aligned} \quad (4)$$

(The shift of u coordinate must also be replicated while indexing the boundaries of the Tam-Danielsson window.)

3) *Filtering Steps 3–5: Convolution with Hilbert kernel*: The 1-D Hilbert transform in u can be implemented as a convolution of $g_3(\lambda, u, \psi) = g_2(\lambda, u, w_\kappa(u, \psi))$ with the Hilbert kernel h_H , where w_κ defines a κ -line of angle ψ across the Tam-Danielsson window in the detector plane. The interpolation of (u, w) points to (u, ψ) space is termed Forward Rebinning. With the Hilbert kernel

$$h_H(s) = - \int_{-\infty}^{+\infty} d\sigma \operatorname{sgn}(\sigma) e^{i2\pi\sigma s} = \frac{1}{\pi s}, \quad (5)$$

the convolution theorem is used to efficiently perform the convolution by FFT/IFFT; therefore, the Fourier transform of h_H is required:

$$\widehat{h}_H(\xi) = -i \operatorname{sgn}(\xi) \quad (6)$$

and the filtered result along each κ -line is computed by

$$g_4(\lambda, u, \psi) = \operatorname{IFFT} \left(\operatorname{FFT} (g_3(\lambda, u, \psi)) \cdot \widehat{h}_H \right). \quad (7)$$

In the final filtering step, $g^F(\lambda, u, w) = g_4(\lambda, u, \hat{\psi}(u, w))$ applies a coordinate transformation, designated Backward Rebinning, to invert step 3. These three GPU Kernels (forward rebin, Hilbert transform, backward rebin) work in sequence with NVIDIA cuFFT API calls to complete the filtering.

4) *Back Projection*: Each filtered projection g^F is copied to a texture buffer and projected by a single Kernel launch over the applicable slices of the VOI chunk in memory (see Fig. 1 for geometry and upper/lower limits of the Tam-Danielsson window). Each voxel rod $[x_i, y_j, *]$ is assigned to a thread which loops over the applicable Z-strip where the projection crosses those voxels. Pre-calculated upper and lower limits (blue and green curves in Fig. 1) of the w coordinate are

read from two 1-D textures for easy interpolation. Transition regions near the boundaries are progressively weighted as recommended by Noo *et. al.*[3]. All projections pertaining to slices in the loaded VOI are completed before it is released.

A. GPU Memory Management

All projections and VOI segments are held, at some point, in global GPU memory. The scheme outlined below is flexible and minimizes required memory allocation so that reconstructions of any practical size will perform well without altering the approach. If most of the latency of I/O transactions is successfully masked, performance is nearly constant regardless of how many chunks the VOI is divided into.

1) *Volume Of Interest Blocking*: The reconstructed volume is divided into N_C chunks, as necessary. Every projection which contains lines required by the chunk is read in, differentiated, filtered, back-projected across the resident volume, and then discarded. With pre-fetch and the speed of the GPU, the cost of reprocessing reused projections is less than the bidirectional I/O needed to store and retrieve previously filtered projections. In practice the chunk size will consume the majority of the GPU memory, however, a smaller chunk size may be optimal overall in order to distribute writes so that the write cache of the file system is not overrun.

2) *Raw Projections Input Buffer*: Two buffers in global GPU memory of size $(N_b \times N_{rows} \times N_{col})$ are used to facilitate asynchronicity in the projection filtering and I/O processes. The first buffer is filled with raw projections as soon as they are available. [Algorithm 1: line 2] Once complete, this buffer is copied to a bound texture area of equal size and thereafter the CPU is free to fill the space with a new set of projections. [Algorithm 1: line 4] For asynchronous copy/compute overlap, it is a prerequisite that the host memory used in CPU \leftrightarrow GPU transfers be pinned (aligned and non-pageable) under the CUDA API. For the Fermi or Kepler generations of GPUs (Compute Capability ≥ 2.0), maximum texture length implies $N_b \times N_{rows} < 2^{16}$, hence the maximum useful size of both buffer and texture is limited to 256–512 MB each in practice.

3) *Filtering Space*: Filtering and differentiation stages in the Katsevich algorithm involve multiple bilinear interpolations so several steps are configured to exploit the hardware-based interpolation available with an image loaded to a `cudaArray` and bound to a texture. Floating point ‘fetches’ from a point $[x, y]$ near $[i, j]$ in a texture map $P[]$ then simply take the form of floating point indexing: $p = P[x, y]$. GPU workspace is also required to perform the 1-D $\times N_{\kappa}$ -lines convolution that embodies the Hilbert transform across κ -lines.

4) *Current Projection Texture*: The completed filtered projection g^F is copied to an additional texture (a bound `cudaArray`, $N_{rows} \times N_{col}$) from which it can be back projected exploiting hardware interpolation. [Algorithm 1: line 7] This also permits filtering on the next projection to start as soon as resources are available.

B. Asynchronicity and CPU/GPU Task Overlap

Two types of asynchronous operations improve throughput. Asynchronous GPU operations permit data transfers from

Host-to-Device (HtoD or DtoH) to occur concurrently with computation. These concurrencies improve performance by 3–5%. More important is asynchronicity between CPU operations and GPU computation which can nearly double overall performance.

C. Multi-GPU Task Partitioning and Synchronization

Many workstations and servers now have adequate power and slot space for 2 or more high performance GPUs. The performance of 2- and 4-GPU servers is discussed in the next section. Each additional GPU offers a potential linear increase in total memory and processing power, but it is not obvious at first glance how to best subdivide the workload. The most effective scheme, to first order, is also the easiest to configure. Instead of dividing VOI chunks sequentially, the slices can be interleaved in much the same way as a striped RAID array is formed from multiple disks. Each GPU is assigned 3 CPU threads (input, output, and computation) and dispatched asynchronously to complete its slices independently. Each GPU utilizes the same range of projections so disk I/O is minimized.

III. PERFORMANCE ANALYSIS

Giga-Updates is the standard metric for problem size, defined for parallel projection as voxel count \times total projections/ 2^{30} . Helical reconstructions are more complicated to quantify so the code sums actual updates as it progresses. Table 1 gives a summary of results for previous Katsevich-type parallelizations in the literature. The Hyperfast algorithm of Steckmann *et. al.* is also provided for comparison purposes. Figure 2 shows multiple GPU scaling along with an indication of the dependence on problem size (negligible, with a doubling of projection count). In both summaries, raw data represents the execution time of the FBP only (since I/O latency is buried, this is somewhat realistic, and is the most valid metric to compare with other memory-resident FBP times). The ‘SS’ data refers to the sustainable, steady-state rate that should be achievable for any problem size, including concurrent disk I/O. This is measured from the start of first upload to the GPU until the end of the last download of VOI slices. This net rate is within 70–80% of the raw performance in most cases. Multi-GPU scaling is also quite acceptable. Deviations from a linear speedup are not fully understood, but the primary culprits are latencies due to simultaneous demands on CPU resources.

A sample reconstruction visualization is provided for a long object: a AAA battery. Fig. 3 is produced from a helical CT with at 5:1 magnification and 1000 projections over 3 turns.

REFERENCES

[1] L. Feldkamp, L. Davis, and J. Kress, “Practical cone-beam algorithm, *J. Opt. Soc. Amer. A, Opt. Image Sci., Vis.*, 1984, vol. 1, no. 6, pp. 612–619.

[2] A. Katsevich, “Theoretically exact filtered backprojection-type inversion algorithm for spiral CT, *SIAM J. Appl. Math.*, 2002, vol. 62, no. 6, pp. 2012–2026.

[3] F. Noo, J. Pack, and D. Heuscher, “Exact helical reconstruction using native cone-beam geometries”, *Phys.Med. Biol.*, 2003, vol. 48, no. 23, pp. 3787–3818.

[4] J. J. Deng, H. Y. Yu, J. Ni, T. He, S. Y. Zhao, L. H. Wang, and G. Wang, “A parallel implementation of the Katsevich algorithm for 3-D CT image reconstruction, *J. Supercomput.*, 2006, vol. 38, no. 1, pp. 35–47.

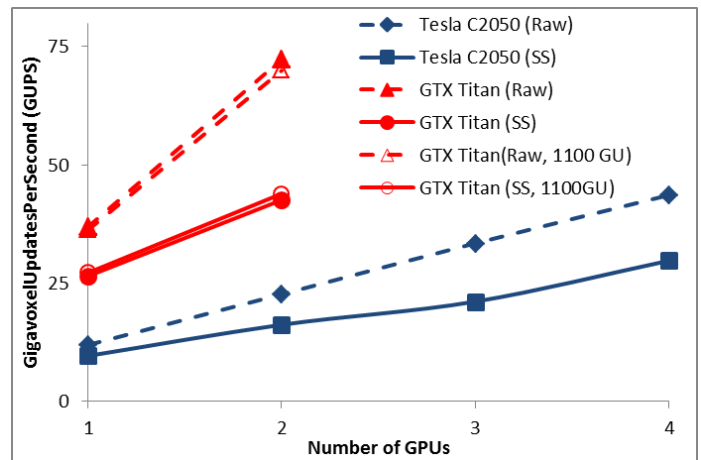


Fig. 2. GPU performance scaling for multi-GPU server configurations. For GTX Titan, both 1100 GigaUpdate and 580 GigaUpdate cases are shown. Raw results are FBP only; Steady State(SS) are full system performance.

TABLE I
GPU KERNEL AND OVERALL THROUGHPUT PERFORMANCE

	Hardware	GUPS(raw)	GUPS(SS)
Other Authors: 1–60 GigaUpdates size, typ.			
Yang <i>et. al.</i>	32-node cluster	0.21	
Yan <i>et. al.</i>	8800 GTX	4.9	
Steckmann <i>et. al.</i>	24-core CPU	17*	(approx. method)
1000 projections (581.4 GigaUpdates total)			
Present Work	Quadro K2100M	5.19	3.94
-	GTX 680	18.87	14.91
-	Tesla C2050(x1)	11.90	9.59
-	Tesla C2050(x2)	22.62	16.17
-	Tesla C2050(x3)	33.40	21.07
-	Tesla C2050(x4)	43.59	29.72
-	GTX Titan(x1)	36.89	26.47
-	GTX Titan(x2)	72.31	42.57
2000 projections (1119.3 GigaUpdates total)			
Present Work	Quadro K2100M	5.16	3.94
-	GTX Titan(x1)	36.22	27.17
-	GTX Titan(x2)	69.95	43.89
VOI is 1025 ² x 1850H			
All systems reading/writing SSD or local RAID array			
Raw GUPS represents FBP calculation only. “SS” or Steady State GUPS is wall-clock rate including filtering, memory transfers, and disk transfers.			

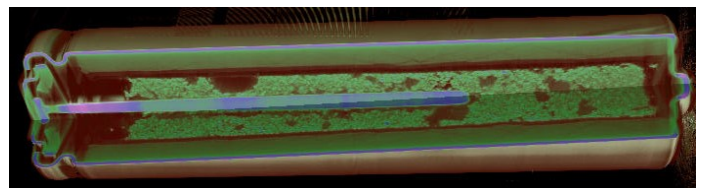


Fig. 3. Visualization of AAA battery imaged by accelerated helical method. (1024x1024x1850 from 1000 projections, 5.1° half-cone angle).

[5] E. Fontaine and H. H. S. Lee, “Optimizing Katsevich image reconstruction algorithm on multicore processors, in *Proc. Int. Conf. Parallel Distrib. Syst.*, Hsinchu, Taiwan: IEEE, 2007, pp. 467–474.

[6] G. Yan, J. Yian, S. Zhu, C. Qin, Y. Dai, F. Yang, et. al., “Fast Katsevich algorithm based on GPU for helical cone-beam computed tomography”, *IEEE Trans. Inf. Technol. Biomed.*, 2010, vol. 14, no. 4, pp. 1053–1061.

[7] S. Steckmann, M. Knaup, and M. Kachelrieß, “Hyperfast general-purpose cone-beam spiral backprojection with voxel-specific weighting,” *IEEE Nuclear Science Symposium Conference Record*, 2008, pp. 5426–5433.

[8] J. Yang, “Cone beam cover method: An approach to performing backprojection in Katsevich’s exact algorithm for spiral cone beam CT”, *Journal of X-Ray Science and Technology*, 2004, vol. 12, no. 4, pp. 199–214.

General Thresholding Representation for the L_p Regularization and Its Application in Computed Tomography

Chuang Miao and Hengyong Yu

Abstract--The l_1 norm minimization has been widely used to recover sparse signals/images inspired by the compressive sensing (CS) theory. In order to obtain sparser solution, the l_p ($0 < p < 1$) regularization method has attracted an increasing interest, which is a generalized version of the well-known l_1 regularization. In this paper, we report an approximate general analytical thresholding representation for the l_p ($0 < p < 1$) regularization. Our formula can be reduced to the well-known soft-threshold filtering for l_1 regularization and the hard-threshold filtering for l_0 regularization. We integrate the *general* threshold representation formulas into an iterative thresholding framework for computed tomography (CT) reconstruction with l_p regularization. Numerical simulations are performed to demonstrate application and evaluate the performance of the algorithms. Our results show that the proposed algorithms outperforms the state-of-the-art reweighted algorithm in terms of the sparsity enhancement, convergence speed, reconstruction accuracy, image quality and parameters sensitivity. The generalized threshold representation for l_p regularization has a great potential for all the CS inspired applications with l_p regularization.

1. Introduction

The well-known l_1 regularization has been widely used to relax the l_0 regularization problem, which can also produce sparse solutions for the sparsity problems. Nevertheless, the l_1 regularization may yield inconsistent results and fails to recover the optimal original signal with the least measurement. Naturally, a promising direction towards l_p ($0 \leq p \leq 1$) norm (l_p regularization) has attracted a great attention, which can generate a sparser solution. The l_p regularization is a nonconvex, nonsmooth, and non-Lipschitz optimization problem. It is nontrivial to perform a thorough theoretical analysis and efficient algorithms for solutions. By conducting a phase diagram study [1], Xu *et al* demonstrated that: (1) the l_p regularizations can generate sparser solutions than l_1 regularization. As the value of p decreases, the l_p

regularization generates sparser solution; (2) the $l_{1/2}$ regularization somehow plays a representative role among all l_p regularizations. When $p \in (1/2, 1)$, the $l_{1/2}$ regularization always yields the best sparse solution and when $p \in (0, 1/2)$, the performance of l_p has no significant difference.

Similar to the l_1 regularization, there are two approaches to solve the large-scale l_p regularization. One is the reweighted norm algorithm, and the other is the thresholding algorithm. The reweighted norm algorithm converts the l_p regularization into a format of l_1 regularization by employing a weighting function. Then the algorithms for solving l_1 regularization can be applied immediately, i.e., l_1 -reweighted [2] and generalized l_1 -greedy algorithms [3]. The thresholding algorithm is a simple iterative process followed by a thresholding operation. Recently, Xu *et al* discovered that the solution of the $l_{1/2}$ regularization can be analytically expressed in a thresholding form, distinguishing it from other l_p ($p \neq 2/3$) regularizations [1]. Besides the iterative thresholding algorithms for l_0 , $l_{1/2}$ and l_1 regularizations, we are also interested in finding an iterative thresholding algorithm for other l_p ($0 < p < 1$) regularizations. Recently, we derived a recursive solution for any l_p ($0 < p < 1$) regularization in a thresholding form [4]. Here, we will optimize the initialization scheme to obtain a quasic-analytic form and demonstrate its application for CT reconstruction in terms of a *general* iterative thresholding algorithm. The *general* iterative threshold filtering algorithms are adequate and efficient for large-scale problems in CS-based applications, and the regularization parameters have specific meanings and are easy to choose.

The rest of this paper is organized as follows: **in Section II**, we will summarize the recursive *general* thresholding expression and derive the quasic-exact analytical formula for any l_p regularization with $0 < p < 1$; **in Section III**, we will apply the proposed *general* thresholding algorithm to CT image reconstruction with numerical simulations and evaluate its the performance. Finally, **in Section IV**, we will make a conclusion.

2. Method

2.1. Problem Description

We consider the following linear system

$$\mathbf{y} = \mathbf{A}\mathbf{x} + \boldsymbol{\varepsilon}, \quad (1)$$

where $\mathbf{A} \in \mathbb{R}^M \times \mathbb{R}^N$ is a given $M \times N$ matrix, $\mathbf{y} = (y_1, \dots, y_M)^T \in \mathbb{R}^M$ is the observation or measurement, and $\boldsymbol{\varepsilon} \in \mathbb{R}^M$ is the measurement noise. When the system is ill-

C. Miao and H.Y. Yu are from the Department of Biomedical Engineering and VT-WFU School of Biomedical Engineering and Sciences, Wake Forest University Health Sciences, Winston-Salem, NC, 27157. This work was partially supported by the NSF CAREER Award CBET-1149679 and an NSF collaborative grant DMS-1210967. This work was also support by China Scholarship. Email: hengyong-yu@ieee.org.

posed, our goal is to recover $\mathbf{x} = (x_1, \dots, x_N)^T \in \mathbb{R}^N$ from the observation \mathbf{y} such that \mathbf{x} has the sparsest structure (\mathbf{x} has the fewest nonzero components). This sparsity problem can be modeled as

$$\min_{\mathbf{x} \in \mathbb{R}^N} \|\mathbf{x}\|_p \quad \text{s.t.} \quad \mathbf{y} = \mathbf{A}\mathbf{x}, \quad (2)$$

where $0 < p < 1$ and $\|\mathbf{x}\|_p$ is called l_p norm in \mathbb{R}^N defined as

$$\|\mathbf{x}\|_p = (\sum_{i=1}^N |x_i|^p)^{1/p}. \quad (3)$$

The sparsity problem can be frequently transformed into the following l_p regularization problem:

$$\min_{\mathbf{x} \in \mathbb{R}^N} \{\|\mathbf{y} - \mathbf{A}\mathbf{x}\|^2 + \lambda \|\mathbf{x}\|_p^p\}, \quad (4)$$

where $\|\cdot\|_p$ denotes the l_p norm defined by Eq. (3), and $\lambda > 0$ is a regularization parameter to balance the least square term and the penalty term.

2.2. Threshold Filtering Algorithm for l_p Regularization

Any solution of l_p regularization problem defined by Eq. (4) is a l_p solution. A l_p problem permits a thresholding representation, that is, there is a thresholding function h such that an iterative threshold filtering algorithm can be defined for any of its l_p solution. A thresholding function h is characterized by its threshold value T and defining function φ ,

$$h(x) = \begin{cases} \varphi(x), & |x| > T \\ 0, & \text{otherwise} \end{cases}. \quad (5)$$

A diagonally nonlinear mapping H can be deduced from h ,

$$H(\mathbf{x}) = (h(x_1), h(x_2), \dots, h(x_N))^T. \quad (6)$$

Hence, any of its l_p solution can be obtained by the iterative thresholding algorithm

$$\mathbf{x}^{k+1} = H(\varnothing(\mathbf{x}^k)) \quad (7)$$

where \varnothing is an affine transform from \mathbb{R}^N to \mathbb{R}^N , and can be defined as

$$\varnothing(\mathbf{x}) = \mathbf{x} + \mu \mathbf{A}^T (\mathbf{y} - \mathbf{A}\mathbf{x}) \quad (8)$$

where μ is a small positive parameter to control the step of each iteration. Once the thresholding function h is well defined, the iterative thresholding algorithm for any l_p regularization can be obtained.

2.3. General Thresholding Representation for l_p ($0 < p < 1$) Regularization

To develop the general thresholding representation for any l_p ($0 < p < 1$) solution, we need to find the thresholding function $h_{\lambda,p}$ which is characterized by its threshold value $T_{\lambda,p}$ and the defining function $\varphi_{\lambda,p}$. Following the same derivation in [1], it is easy to verify that the threshold value $T_{\lambda,p}$ and the defining function $\varphi_{\lambda,p}$ can be obtained by considering the following problem. Given any fixed $\mathbf{x} = (x_1, x_2, \dots, x_N)^T \in \mathbb{R}^N$, let us consider

$$y_i = \arg \min_{y_i \in \mathbb{R}} \{(y_i - x_i)^2 + \lambda |y_i|^p\}, \quad \lambda > 0. \quad (9)$$

Because all the components share the same thresholding function, let us omit the sub-index i for abbreviation. The general format of the problem can be written as

$$y = \operatorname{argmin}_y \{(x - y)^2 + \lambda |y|^p\}, \quad \lambda > 0, 0 < p < 1. \quad (10)$$

It equals to

$$\begin{cases} y = \operatorname{argmin}_{y \geq 0} \{(x - y)^2 + \lambda y^p\}, \lambda > 0, 0 < p < 1 \\ y = \operatorname{argmin}_{y < 0} \{(x - y)^2 + \lambda (-y)^p\}, \lambda > 0, 0 < p < 1 \end{cases} \quad (11)$$

Because the threshold function is symmetric, we only consider the case $y \geq 0$ in the following derivations and the results can be directly extended to the case $y \leq 0$.

2.3.1 Threshold Value $T_{\lambda,p}$

Let F denotes the objective function

$$F = (y - x)^2 + \lambda y^p. \quad (12)$$

The solution of Eq.(9) implies that F should achieve its minimum value. When $x \geq T_{\lambda,p}$, the first order optimality condition of y implies

$$2(y - x) + \lambda p y^{p-1} = 0. \quad (13)$$

From Eq.(12), we have $\lambda y^p = F - (y - x)^2$ and substitute it into Eq. (13), we arrive

$$(2 - p)y^2 - 2x(1 - p)y + p(F - x^2) = 0. \quad (14)$$

Because $F = x^2$ when $y = 0$, F should also be equal to x^2 at the critique point $T_{\lambda,p}$ we are interested. Substitute $F = x^2$ into Eq.(14), we have the non-zero solution

$$y = \frac{2x(1-p)}{2-p}. \quad (15)$$

Substitute Eq. (15) into Eq. (12) and let $F = x^2$, we arrive at

$$x^2 = \left(x - \frac{2x(1-p)}{2-p}\right)^2 + \lambda \left(\frac{2x(1-p)}{2-p}\right)^p, \quad (16)$$

which yield the threshold value $T_{\lambda,p}$ by solving x

$$T_{\lambda,p} = \frac{2-p}{2} (1-p)^{\frac{p-1}{2-p}} \lambda^{\frac{1}{2-p}}. \quad (17)$$

2.3.2 General Recursive Thresholding Representation

By reformatting Eq. (13), we have

$$y = x - \frac{\lambda p}{2} y^{p-1}, \quad (18)$$

which is a typical fixed-point problem. From Eq. (18), let

$\psi(y) = x - \frac{\lambda p}{2} y^{p-1}$ we immediately have the following recursive formula,

$$y^{k+1} = \psi(y^k), \text{ given any } y^0, k > 0 \quad (19)$$

Combining Eqs. (19) and (17), we immediately obtain the final thresholding function in a general formula

$$h_{\lambda,p}(x) = \begin{cases} x - \operatorname{sign}(x) \frac{\lambda p}{2} (y^k(|x|))^{p-1}, & k \rightarrow \infty, |x| > \frac{2-p}{2} (1-p)^{\frac{p-1}{2-p}} \lambda^{\frac{1}{2-p}} \\ 0, & \text{otherwise} \end{cases} \quad (20)$$

Denoting $t = x - y$, Eq. (18) can be simplified to,

$$t = \frac{\lambda p}{2} (x - t)^{p-1}, \quad (21)$$

which implies an recursive solution for t

$$\begin{cases} t^{k+1}(x) = \frac{\lambda p}{2} (x - t^k)^{p-1}, & k > 0. \\ \text{Given any } t^0 \end{cases} \quad (22)$$

Combining Eqs. (22) and (17), we immediately obtain an alternative final thresholding function in a general formula

$$h_{\lambda,p}(x) = \begin{cases} x - \operatorname{sign}(x) t^k(|x|), & k \rightarrow \infty, |x| > \frac{2-p}{2} (1-p)^{\frac{p-1}{2-p}} \lambda^{\frac{1}{2-p}} \\ 0, & \text{otherwise} \end{cases} \quad (23)$$

Because t usually is very small, a small iterative number k can results in very good approximation.

2.3.3. Quasic-exact Analytical Representation

Since we are interested in developing an accurate yet analytical thresholding representation, we realize that the proposed recursive general thresholding solution can be simplified to approximate the solution very well in a few iteration numbers by choosing appropriate initial values, which results in quasic-exact and analytic representation. By investigating the initial value and select the iteration number carefully, we can derive several concise candidates for the

analytical thresholding expression. This will lead to the *general* threshold filtering algorithm directly. Here we show some possible choices of initial values and the iteration number and give the corresponding approximate analytical thresholding expressions. For convenience, we employ the alternative iterative thresholding solution in Eqs. (22) and (23). x_T and y_T are input and output values at the critical points.

i. $t^0(|x|) = 0$ and the iteration number $N = 2$

$$h_{\lambda,p}(x) = \begin{cases} x - \operatorname{sgn}(x) \cdot \frac{\lambda p}{2} \left(|x| - \frac{\lambda p}{2} |x|^{p-1} \right)^{p-1}, & |x| > \frac{2-p}{2} (1-p)^{\frac{p-1}{2-p}} \lambda^{\frac{1}{2-p}} \\ 0, & \text{otherwise} \end{cases} \quad (24)$$

ii. $t^0(|x|) = |x| - y_T$ and $N = 2$

$$h_{\lambda,p}(x) = \begin{cases} x - \operatorname{sgn}(x) \cdot \frac{\lambda p}{2} \left(|x| - \frac{p}{2} (1-p)^{\frac{p-1}{2-p}} \lambda^{\frac{1}{2-p}} \right)^{p-1}, & |x| > \frac{2-p}{2} (1-p)^{\frac{p-1}{2-p}} \lambda^{\frac{1}{2-p}} \\ 0, & \text{otherwise} \end{cases} \quad (25)$$

iii. $t^0(|x|) = x_T - y_T$ and $N = 2$

$$h_{\lambda,p}(x) = \begin{cases} x - \operatorname{sgn}(x) \cdot \frac{\lambda p}{2} \left(|x| - \frac{\lambda p}{2} \left(|x| - \frac{p}{2} (1-p)^{\frac{p-1}{2-p}} \lambda^{\frac{1}{2-p}} \right)^{p-1} \right)^{p-1}, & |x| > \frac{2-p}{2} (1-p)^{\frac{p-1}{2-p}} \lambda^{\frac{1}{2-p}} \\ 0, & \text{otherwise} \end{cases} \quad (26)$$

iv. $t^0(|x|) = \alpha |x|^{p-1}$ and $N = 1$

Because $t^0(|x|)$ pass through $(x_T, x_T - y_T)$, we have $\alpha = \frac{\lambda p}{2^{2-p}} \left(\frac{1-p}{2-p} \right)^{p-1}$ and $t^0(|x|) = \frac{\lambda p}{2^{2-p}} \left(\frac{1-p}{2-p} \right)^{p-1} |x|^{p-1}$. The final approximate analytical thresholding expression is

$$h_{\lambda,p}(x) = \begin{cases} x - \operatorname{sgn}(x) \cdot \frac{\lambda p}{2} \left(|x| - \frac{\lambda p}{2^{2-p}} \left(\frac{1-p}{2-p} \right)^{p-1} |x|^{p-1} \right)^{p-1}, & |x| > \frac{2-p}{2} (1-p)^{\frac{p-1}{2-p}} \lambda^{\frac{1}{2-p}} \\ 0, & \text{otherwise} \end{cases} \quad (27)$$

v. $t^0(|x|) = \alpha (|x| - y_T)^{p-1}$ and $N = 1$

Similarly, $t^0(|x|)$ pass through $(x_T, x_T - y_T)$, we have $\alpha = \lambda \left(\frac{p}{2} \right)^{2-p} (1-p)^{p-1}$ and $t^0(|x|) = \lambda \left(\frac{p}{2} \right)^{2-p} (1-p)^{p-1} (|x| - y_T)^{p-1}$. The final approximate analytical thresholding expression is

$$h_{\lambda,p}(x) = \begin{cases} x - \operatorname{sgn}(x) \cdot \frac{\lambda p}{2} \left(|x| - \lambda \left(\frac{p}{2} \right)^{2-p} (1-p)^{p-1} \left(|x| - (1-p)^{\frac{1}{2-p}} \lambda^{\frac{1}{2-p}} \right)^{p-1} \right)^{p-1}, & |x| > \frac{2-p}{2} (1-p)^{\frac{p-1}{2-p}} \lambda^{\frac{1}{2-p}} \\ 0, & \text{otherwise} \end{cases} \quad (28)$$

3. Results

It has been shown that smaller p has stronger sparsity enhancement than a larger one [3]. In order to verify the sparsity enhancement property of our derived analytic thresholding representation, we implemented and incorporated the developed formulas into the classical SART reconstruction framework. A numerical modified Shepp-Logan phantom was used to perform simulations. We assumed a representative circular scanning locus of radius 538.5 mm and fan-beam geometry. Over a 360° range, 984 projections were uniformly acquired. For each projection, 222 detector cells were equiangularly distributed, which defines a field of view of 249.2 mm in radius and an iso-center spatial resolution of 2.3 mm. Using the simulated sinogram and discrete gradient transform, the SART-type general thresholding algorithm was implemented by employing the same algorithm in [5] except

different thresholding formula was used. All the reconstructed image sizes are 128 × 128 with the pixel size comparable to the detector cell size. We selected the second quasic-exact analytic formula in Eq. (25) as the approximate thresholding formula. In order to compare the performance of different value of p fairly, we developed a parameter selecting scheme. A good regularization parameter λ should balance the weight of the least square term and the penalty term in Eq. (4). By assuming the least square term (residual error) as a constant, we derived a relationship of the regularization parameters between different p for fair comparison as follows,

$$\lambda_1 \|x\|_{p_1}^{p_1} = \lambda_2 \|x\|_{p_2}^{p_2}, \quad (29)$$

where x represents the ground truth, p_1 and p_2 are two different p values. We vary p in (0, 1] and the number of views range from 5 to 15. To overcome the local minimum problem, the initialization is selected as follow: for each view number, we fixed the iteration number as 10000 and the images are reconstructed with $p=1.0$ and λ range from 1×10^{-6} to 1×10^{-2} . The reconstruction with the smallest root-mean-square-error (RMSE) is selected as the initialization for different p . The corresponding optimal λ for $p=1.0$ is used to calculate the optimal λ for other p by Eq. (29). With this initialization strategy, for each p , we run the reconstruction algorithm 5000 iterations where we found that either the reconstruction is accurate (i.e. RMSE < 10^{-3}) or the RMSE curve levels off. As shown in Fig. 1, the accurate reconstruction (i.e. RMSE < 10^{-3}) is occurred at 14 views for $p=1.0$. When p is reduced a little bit (i.e. $p=0.9$), it yields a dramatic drop in the number of views to obtain accurate image reconstruction. While the accurate reconstruction for all $p < 1$ is occurred at 9 views, the smaller p can reach a smaller RMSE.

For a fair comparison, in the same SART framework, we implemented the reweighted algorithm proposed in [3] using the discrete gradient transform with the weighting function selected as $\omega = \frac{1}{\sqrt{|\nabla u|^2 + \eta}}$, where ∇u is the gradient magnitude image and η is a small number to avoid singularity. We selected $\eta = 10^{-4}$ for all the experiments. The view number is selected as 9 where the proposed general threshold filtering algorithm can reconstruct images accurately when $0 < p < 1$. In order to select the best initialization from the reconstruction with $p=1.0$, we vary λ from 10^{-8} to 10^{-3} and fixed the iteration number as 20000 where we observed the RMSE either level off or too slow to convergence (i.e. $\lambda = 10^{-8}$). Because $\lambda = 10^{-7}$ yields the smallest RMSE, the corresponding reconstructed image is selected as the initialization.

With the optimal initializations for the general threshold filtering algorithm and the reweighted algorithm, we reconstructed images with $p=0.1, 0.9$ and 1.0 . For the general threshold filtering algorithm, the regularization parameter λ was selected according to Eq. (29) and the iteration number was fixed as 5000. For the reweighted algorithm, the parameter λ was selected by cross-validation by varying λ in $[10^{-11}, 10^{-3}]$ and the iteration number was fixed as 200000 for $p=0.1$ and 0.9 where the RMSE either level off or too slow to convergence. When $\lambda > 10^{-3}$, the reweighted algorithm crashes. The reconstructed images and the RMSE curves are shown in Figs. 2 & 3, respectively. For both of the algorithms,

$p=1$ cannot accurately reconstruct the image. While the general threshold filtering algorithm can accurately reconstruct images with $p=0.1$ and 0.9 from 9 views, the reweighted algorithm failed to accurately reconstruct the images. For both of the algorithms, $p=0.1$ has smaller RMSEs compare to $p=0.9$.

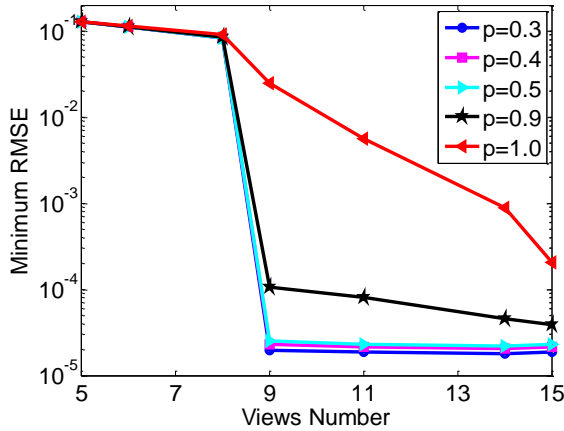


Figure 1. Image recovery plots for the general threshold filtering algorithm.

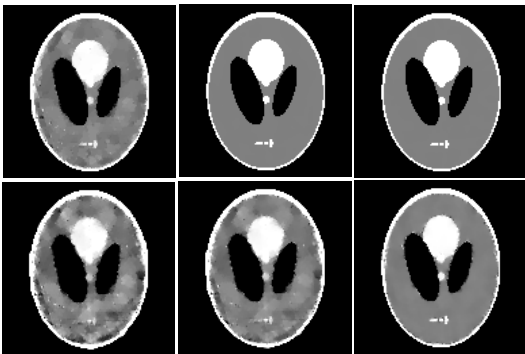
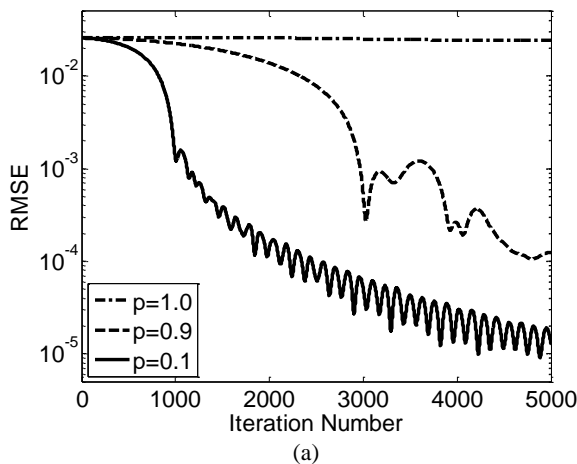
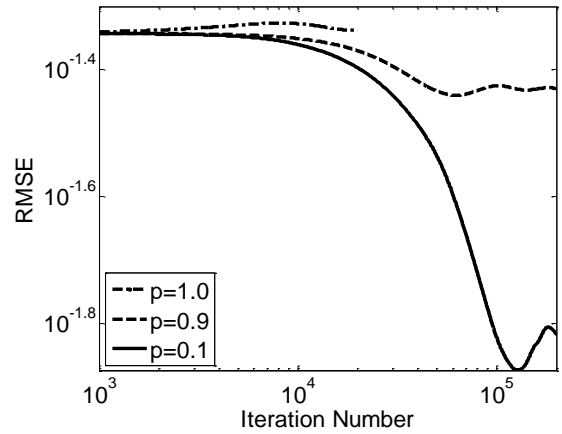


Figure 2. Reconstructed images from 9 views. The top and bottom rows are reconstructed by the general-threshold filtering and reweighted algorithms, respectively. From the left to right column, the images correspond to $p=1.0$, 0.9 and 0.1 , respectively. For the general-threshold filtering algorithm, the iteration numbers are 5×10^3 for $p=0.1$, $p=0.9$ and $p=1$. For the reweighted algorithm, the iteration numbers for $p=1.0$, $p=0.9$ and $p=0.1$ are 2×10^4 , 6×10^4 and 1.3×10^5 , respectively.



(a)



(b)

Figure 3. RMSE curves for (a) the general threshold filtering algorithm and (b) the reweighted algorithm from 9 views with optimal regularization parameters. For the general threshold filtering algorithm, the iteration number for $p=1.0$, 0.9 and 0.1 are 5×10^3 . For the reweighted algorithm, the iteration numbers for $p=1.0$, 0.9 and 0.1 are 2×10^4 , 2×10^5 and 2×10^5 , respectively.

4. Conclusions

In this paper, we derived several quasic-exact and analytic thresholding formulas for general l_p ($0 < p < 1$) nonconvex regularization problem and obtained the corresponding general threshold filtering algorithm. Comparing to the reweighted algorithm, our proposed general threshold filtering algorithm achieves a substantial reduction in the necessary number of views for accurate reconstruction of the Shepp-Logan phantom. In addition, the proposed general threshold filtering algorithm has advantages in terms of image quality, reconstruction accuracy, convergence speed and parameters sensitivity. Due to the limited space, we did not show details of the correctness of the numerical experiments, the convergence properties of the iterative thresholding representation, the error bounds and the accuracy of different approximate analytical thresholding formulas (Formula 2 in Eq. (25) is actually the least accurate one). In the near future, we will perform more experiments with realistic data to compare the performance of each algorithm. We believe this work can provide a better tool for the sparse solution of CS based regularization problems.

5. References

- [1]. Xu, Z.B., et al., *Representative of $L1/2$ Regularization among Lq ($0 < q \leq 1$) Regularizations: an Experimental Study Based on Phase Diagram*. Acta Automatica Sinica, 2012. 38(7).
- [2]. Candès, E., M. Wakin, and S. Boyd, *Enhancing Sparsity by Reweighted $\ell 1$ Minimization*. Journal of Fourier Analysis and Applications, 2008. 14(5-6): p. 877-905
- [3]. Zhu, J. and X. Li, *A generalized greedy algorithm for image reconstruction in CT*. Applied Mathematics and Computation, 2013. 219(10): p. 5487-5494.
- [4]. Yu, H. and C. Miao, *General thresholding representation for the Lp regularization problem*. International Symposium on Biomedical Imaging, 2014, to appear.
- [5]. Yu, H. and G. Wang, *SART-type Half-threshold Filtering Approach for CT Reconstruction*. under review.

GPU-based Implementation for Interior Tomography

Rui Liu and Hengyong Yu

Abstract— Narrowing the x-ray beam to focus on a specific region of interest (ROI) can reduce potential radiation dose and result in the so-called interior problem. It has been proved that the interior problem can be uniquely and stably solved by minimizing the ROI's total variation (TV) if the imaging object is piecewise constant or polynomial, which is called interior tomography. To implement the interior tomography, the soft threshold filtering (STF) method was applied with a pseudo inverse of discrete gradient transform (GDT) for TV minimization. However, the iterative nature of interior reconstruction algorithm is slow in sequential implementation. In this work, we combine the interior reconstruction and GPU based acceleration technique for practical applications with fan-beam and cone-beam geometry.

Keywords—*Computed Tomography (CT); Interior Tomography; Compressed Sensing (CS); GPU; Interior Reconstruction*

1. INTRODUCTION

One of the common methods to reduce the radiation risk is to narrow the x-ray beam to focus on particular lesion region (interior scan). Interior scan is commonly desirable for cardiac CT^[1] and nano-CT^[2], which results in the interior problem. In the compressive sensing (CS) framework, it has been proved that the interior problem can be uniquely and stably solved regularized by prior knowledge of certain sub-region of interest^{[3]-[5]}. Inspired by the CS theory, images subjected to sparsity constraints are able to be accurately reconstructed from a few projections, which can be implemented in the simultaneous algebraic reconstruction technique (SART) framework with soft-threshold filtering (STF) methods^{[6]-[8]}. Because the discrete gradient transform (DGT) is non-invertible, the SFT method cannot be directly applied for total variation (TV) minimization. This problem can be addressed by adopting an alternative invertible sparse transforms or constructing a pseudo inverse of DGT^[6]. To minimize the TV, one can use the steepest descent method or the STF with a pseudo inverse of DGT. In order to speedup the reconstruction speed, parallel computing is usually adopted to accelerate these algorithms. Modern graphic processing unit (GPU) is suitable for single instruction multiple data (SIMD) computing model and compute unified device architecture (CUDA)^[9] is rapidly exploited in many research fields including medical imaging. In this paper, we will apply the ordered subset SART

(OS-SART) reconstruction framework with STF and the parallel computing^[10] to make the CS-based interior tomography practical.

2. ALGORITHM DESIGN

The image (volume) to be reconstructed is labeled as $\mathbf{f} \in \mathbf{R}^N$ and the projection is denoted as $\mathbf{p} \in \mathbf{R}^M$. The projection process in a discrete form can be modeled as $\mathbf{p} = \mathbf{A}\mathbf{f} + \mathbf{e}$, where $\mathbf{A} \in \mathbf{R}^{M \times N}$ is the system matrix and $\mathbf{e} \in \mathbf{R}^M$ represents the measurement noise. Various projection models (such as linear interpolation method, grid method, Siddons' method^[11], area based method^[12], distance driven method^[13] and footprint method^[14]) have been developed to compute the elements of \mathbf{A} . We adopt a modified Siddons' method as projection model and pixel driven as back-projection model.

Inspired by CS theory, a regularization item is introduced into the OS-SART framework for accurate interior reconstruction when the projection is insufficient. Due to the non-sparse property of the most medical images, an appropriate sparse transform is necessary before the regularization. Taking Ψ as the sparse transform, the objective function can be rewritten as

$$\hat{\mathbf{f}} = \arg_f \min \|\Psi\mathbf{f}\|_1 \text{ s.t. } \|\mathbf{p} - \mathbf{A}\mathbf{f}\|_2^2 \leq \varepsilon. \quad (1)$$

The optimization problem (1) can be directly applied for CT image reconstruction. When Ψ represents DGT, $\|\Psi\mathbf{f}\|_1$ can be defined as $\|\mathbf{f}\|_{TV}$ which is the l_1 norm of DGT of \mathbf{f} . To solve (1), we usually minimize $\|\mathbf{f}\|_{TV}$ and $\|\mathbf{p} - \mathbf{A}\mathbf{f}\|_2^2$ alternatively. $\|\mathbf{p} - \mathbf{A}\mathbf{f}\|_2^2$ can be minimized by the OS-SART algorithm. $\|\mathbf{f}\|_{TV}$ minimization can be achieved by the STF. The image \mathbf{f} is first transformed into the DGT domain to \mathbf{g} . Given the prior knowledge of its TV value τ , a binary search is performed to find an optimal threshold ω for SFT. Then the filtered \mathbf{g} is inversely transformed with ω according to the formula in [6].

The OS-SART divides the projection data into several subsets for a faster convergence rate. These subsets participate the reconstruction process in an alternating fashion. Theoretically speaking, the larger the number of subsets is, the faster the convergence rate is. However, the image quality may be decreased with the increase of subset number. To further accelerate the convergence, the fast weighting in the FISTA is also adopted in our implementation.

3. GPU ACCELERATION

The STF requires high computational cost. We choose CUDA based GPU implementation to accelerate the reconstruction algorithms.

R. Liu and H.Y. Yu are from the Department of Biomedical Engineering and VT-WFU School of Biomedical Engineering and Sciences, Wake Forest University Health Sciences, Winston-Salem, NC, 27157. This work was partially supported by the NSF CAREER Award CBET-1149679. Corresponding author email: hengyong-yu@ieee.org.

Considering a circular trajectory, the geometrical symmetry is applied in our implementation. The projection weightings in all angles can be calculated from the first $\pi/4$ scanning range. The cosine and sine values, source positions, the detector elements coordinates in initial position and object elements coordinates are all loaded into constant memory for higher efficiency. Meanwhile, configuring the threads number being multiple of 32 in one block is a good choice. We choose 32×32 as one block size for back projection. The OS-SART is implemented with each subset as one projection in one angle, and the threads block is configured as (256, 1, 1). In cone-beam geometry, the projection thread block is configured as (32, 32) for one angle. The Siddons' algorithm is adopted in our projection model. The pre-allocated array element number should be no less than the largest intersects with the object element edges. We adopt a modified Siddons' algorithm to avoid pre-assigning memory^[15]. This algorithm first calculates the intersections of the compact support of the 2D/3D image and the current x-ray path. Beginning with the incident point, the algorithm applies the same clipping algorithm to individual pixel/voxel bounding box to calculate the image index j and its weight $a_{i,j}$. Considering the direction of the x-ray path, the exit point of the current pixel/voxel is set as the incident point of its neighbor pixel/voxel and this process will be repeated until the current incident point is the exit point of the compact support. Pixel-driven backprojection is adopted in our implementation. Projection matrix can be applied to accelerate the process mapping the point in world coordinate to detector indices. On the other hand, single object point back projection usually needs interpolation on the detector. As suggested by the peers, texture fetching can be applied to accelerate the interpolation process in hardware, and we adopted the method similar to Li et al.^[16]. For every voxel, the bounding convex polygon is calculated, and only the detector elements inside the polygon need to be considered.

The DGT is a key process to calculate the TV of an image. For an individual DGT value $D(f_{i,j,k})$ at the position (i, j, k) , it involves four values $(f_{i+1,j,k}, f_{i,j+1,k}, f_{i,j,k+1}$ and $f_{i,j,k})$ which are not continuously stored in GPU memory. The DGT is not intensive in arithmetic computation but memory bandwidth. To reduce the data latency, we divide the volume into $8 \times 8 \times 8$ sub volumes that overlapped on the boundary and loaded into the shared memory in cone-beam case. In fan-beam case, the image is divided into 32×32 sized overlapped sub-image with the same strategy. Because the value in last index of the sub image is the first index of its adjoining sub image, if the threads in each block is allocated as (t_x, t_y) and the image size is (N_x, N_y) . The block number for DGT calculation is $(\lfloor (N_x + t_x - 2)/(t_x - 1) \rfloor, \lfloor (t_y - 2)/(t_y - 1) \rfloor)$. Similarly, the block number for 3D DGT can be calculated with the same formula.

Finding an optimal threshold after the DGT is indispensable to accelerate the convergence of STF. It is a dichotomy process which is also applicable in GPU. The Thrust library is applied for common algorithms such as sorting and linear transform. The prior knowledge of the intermediate discrete gradient image can be estimated from the roughly reconstructed image by the FBP method in 2D case or FDK method in 3D case. The pseudo inverse transform will be applied to recover the image from the DGT domain. It is implemented in GPU according to equations (3.8) to (3.11) in [6]. The memory bandwidth problem can also be solved by shared memory.

When both of the projection data and image volume are large, it is impossible to load these two data sets into one device memory simultaneously. Although pinned memory technique and zero-copy technique in CUDA can be used to partly solve this problem by exposing the CPU memory address to the GPU device, it is inappropriate for iterative reconstruction which updates the imaging object frequently. This is a high burden for PCI bus and large data latency will

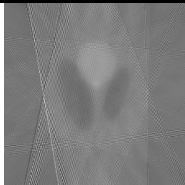
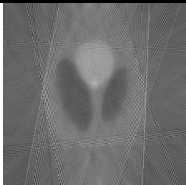
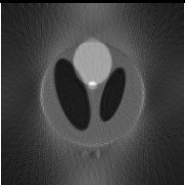
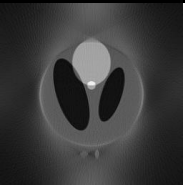
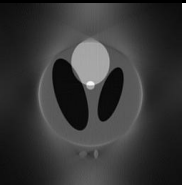



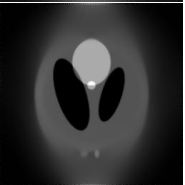
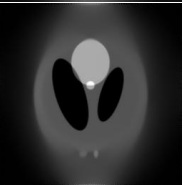

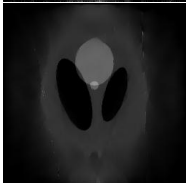



Projection Number	17	21	72	180	360
OS-SART					
OS-SART+ Steepest Descent based TV minimization					
OS-SART + STF based TV minimization					

Figure 1 Comparison of OS-SART and the corresponding TV minimization versions with different projection numbers; it is found that both the steepest descent and STF based TV minimization perform well compared with OS-SART for interior reconstruction.

occur. To solve this problem, two Tesla GPUs are used. Both the image volume and the projection data are divided in two sub-parts without data redundancy. When more than two Tesla GPUs are available, dedicated scheme should be designed to split the image volume and projection data accordingly.

4. NUMERICAL EXPERIMENTS

To minimize TV for interior reconstruction, the steepest descent and STF methods were integrated into the OS-SART. A flat panel detector was assumed. The source to object distances and source to detector distances were 50cm and 100cm, respectively. The detector length was 45cm, the object was compactly supported in a disk with radius 10cm, and the scanning range was from 0 to 2π . The sinogram was truncated with 25% on both sides to simulate an interior scan with GPU. The fan-beam reconstruction was tested with resolution $256^2, 512^2, 1024^2$ and 2048^2 ; correspondingly, the detector resolutions are 300, 600, 1200 and 2400, respectively. This CS-based interior reconstruction was tested with 17, 21, 72, 180 and 360 projections. The iteration number was 50. Some representative results were in Figure 1.

The computational cost of the STF for 2D fan-beam reconstruction in different image resolutions and projection numbers are listed in Table 1. We could see that the computational cost was proportional to the projection number and it also exponentially grew with the image resolution doubling. We also tested the STF method on CPU with image resolutions 1024^2 and 2048^2 under projection number 17 to 360. The reconstruction time and speedup are both listed in Figure 2. We can observe that the speedup was more significant when the image was with larger resolutions, and the speedup would be larger when the projection was less sufficient. Our analysis also showed that most of the computational cost was used for projection and backprojection operations for image sizes 1024^2 and 2048^2 . We also found that the STF method could slightly save computational cost especially when the image resolution was high.

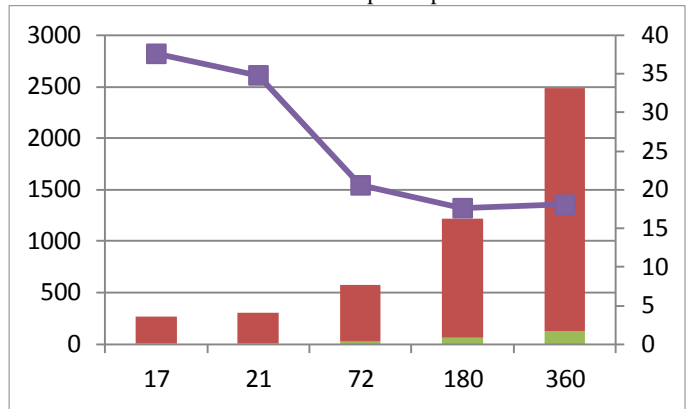
Table 1 GPU based STF reconstruction time (seconds) for 50 iterations with 2D fan-beam geometry, different projection numbers and image resolutions.

	17	21	72	180	360
256	1.1318	1.2775	3.6525	8.7095	17.1106
512	2.5505	3.0415	9.3782	22.7653	45.1335
1024	7.0190	8.4435	26.8415	65.6050	130.6528
2048	23.4480	28.3035	90.2208	220.8985	439.1520

For cone-beam geometry, the system parameters were the same with additional detector height 45cm and the object height 20cm. The single GPU acceleration for the OS-SART plus STF-based TV minimization was tested with the 512^3 sized modified Shepp-Logan phantom. The projection number was 100 with detector resolution 512^2 and the iteration number was 50. Comparing the OS-SART plus STF-based TV minimization and conventional OS-SART algorithm, the computational costs are 505.834 seconds and 475.906 seconds. The time difference mainly comes from the STF operation which occupies 19.328 seconds. The computational cost is

relative small to find the optimal threshold ω_{y_0} . The SD-based TV minimization spent 567.841 seconds. Analyzing by a CUDA profile software, the projection process occupied 56.3% of the time and backprojection occupied 37.6% of the time in one iteration. On average, the backprojection from 100 projection views to 512^3 sized volume in one iteration costs 3.58s, in this case the GUPS is 17.88. It can be seen that the STF-based TV minimization method can reconstruct promising volume in cone-beam and most of the aliasing comes from the divergence of the x-ray. The SD-based method can reconstruct the volume better when the image is piecewise constant with more computational cost compared to the STF-based TV minimization.

1024 × 1024 Image reconstruction time from 50 iterations with CPU vs. GPU and the speed up curve



2048 × 2048 Image reconstruction time from 50 iterations with CPU vs. GPU and the speed up curve

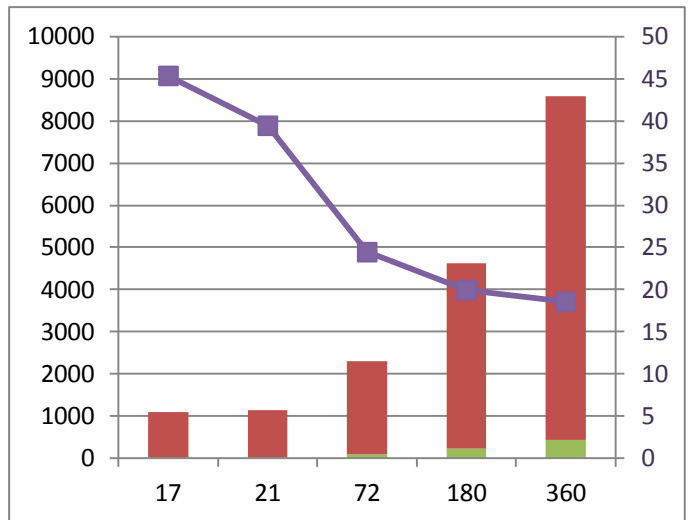


Figure 2: The red bars and green bars represent CPU based and GPU based reconstruction cost (in seconds, marked on left vertical axis) with 50 iterations, respectively. The purple curves are the speed up ratio of GPU implementation to CPU implementation metric on right vertical axis.

The CS-based interior reconstruction was also tested on real clinical dataset from 180 projections. The SD-based TV minimization and STF-based TV minimization were tested with the real patient interior scan. We can see that the

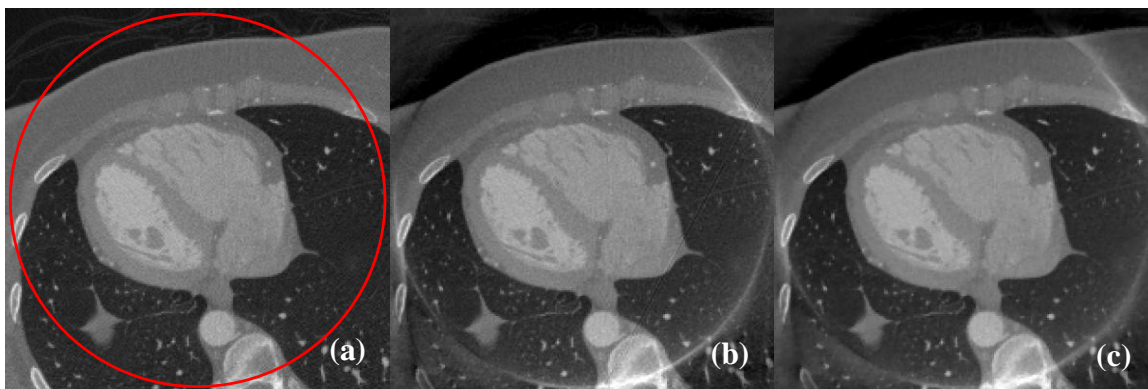


Figure 3: Comparison of SD-based TV minimization reconstruction (b) and STF-based TV minimization reconstruction with respect to the reference image (a).

reconstruction results are comparable (see Figure 3). The RMSE (Root-mean-square deviation) is measured in the region inside the red circle of Figure 3 (a). The RMSE of Figure 3(b) is 36.25HU, while the RMSE of Figure 3(c) is 35.05HU. It indicates that the STF-based TV minimization outperforms than SD-based TV minimization in CS-based interior reconstruction.

The OS-SART is also tested for the multiple GPUs acceleration. We reconstructed a 3D $512 \times 512 \times 512$ image with single floating precision. The detector size was 600×600 , the projection number was 72, and the iterative number was 30. The computational cost was 658.46 seconds in single GPU device, the cost was reduced to 189.85 seconds with two GPU devices, and it can be further reduced to 130.63 seconds with 3 devices.

5. CONCLUSION

The x-ray CT is the broadly applied imaging modality for non-destructive diagnosis and image-guided intervention. The CS theory and interior reconstruction have been investigated to reduce the potential of x-ray exposure hazard. The DGT is usually used as the sparse transform. To overcome the non-invertible problem of the DGT for TV minimization, pseudo-inverse was constructed for the STF-based method for CS-based interior tomography.

The GPU boosts the CS-based interior tomography for practical applications. Our experimental results show that the OS-SART plus STF-based TV minimization method runs slightly faster than the SD-based TV minimization and reconstruct promising results in fan-beam geometry using one GPU for acceleration. In the cone-beam geometry experiments, the STF-based method outperforms a little bit than the SD-based method for few-view projections. Comparing with the CPU-based implementation in fan-beam geometry, the speedup is higher when the projection number is smaller or the image size is larger. Therefore, the GPU parallelization is suitable for CS-based interior tomography especially for large-scale volume reconstruction. By analyzing the timeline in cone-beam reconstruction, it is found that the projection and backprojection operations dominate the reconstruction cost in the STF-based method. In the near future, we will investigate other projection and backprojection models for possible high-

efficient GPU implementation to further reduce the reconstruction time.

REFERENCES

- [1] J. Liu and Q. Hu, "Cardiac CT Image Reconstruction Based on Compressed Sensing," *Procedia Eng.*, vol. 29, pp. 2235–2239, 2012.
- [2] G. Wang, "The meaning of interior tomography," in *Acoustics, Speech and Signal Processing (ICASSP), 2011 IEEE International Conference on*, 2011, pp. 5764–5767.
- [3] J. Yang, H. Yu, W. Cong, M. Jiang, and G. Wang, "Higher-order total variation method for interior tomography," in *SPIE Optical Engineering+ Applications*, 2012, p. 85061B–85061B.
- [4] Y. Ye, H. Yu, and G. Wang, "Exact Interior Reconstruction with Cone-Beam CT," *Int. J. Biomed. Imaging*, vol. 2007, pp. 1–5, 2007.
- [5] Y. Ye, H. Yu, and G. Wang, "Exact interior reconstruction from truncated limited-angle projection data," *J. Biomed. Imaging*, vol. 2008, pp. 5:1–5:6, 2008.
- [6] H. Yu and G. Wang, "A soft-threshold filtering approach for reconstruction from a limited number of projections," *Phys. Med. Biol.*, vol. 55, no. 13, pp. 3905–3916, Jul. 2010.
- [7] H. Yu and G. Wang, "SART-Type Image Reconstruction from a Limited Number of Projections with the Sparsity Constraint," *Int. J. Biomed. Imaging*, vol. 2010, Apr. 2010.
- [8] I. Daubechies, M. Defrise, and C. De Mol, "An iterative thresholding algorithm for linear inverse problems with a sparsity constraint," *Commun. Pure Appl. Math.*, vol. 57, no. 11, pp. 1413–1457, 2004.
- [9] D. Luebke, "CUDA: Scalable parallel programming for high-performance scientific computing," in *Biomedical Imaging: From Nano to Macro, 2008. ISBI 2008. 5th IEEE International Symposium on*, 2008, pp. 836–838.
- [10] J. Deng, "Parallel computing techniques for computed tomography," 2011.
- [11] R. L. Siddon, "Fast calculation of the exact radiological path for a three-dimensional CT array," *Med. Phys.*, vol. 12, no. 2, pp. 252–255, 1985.
- [12] H. Yu and G. Wang, "Finite detector based projection model for high spatial resolution," *J. X-Ray Sci. Technol.*, vol. 20, no. 2, pp. 229–238, 2012.
- [13] B. D. Man and S. Basu, "Distance-driven projection and backprojection in three dimensions," *Phys. Med. Biol.*, vol. 49, no. 11, pp. 2463–2475, Jun. 2004.
- [14] Y. Long, J. A. Fessler, and J. M. Balter, "3D Forward and Back-Projection for X-Ray CT Using Separable Footprints," *IEEE Trans. Med. Imaging*, vol. 29, no. 11, pp. 1839–1850, Nov. 2010.
- [15] F. J. Erik Sundermann, "A Fast Algorithm to Calculate the Exact Radiological Path Through a Pixel Or Voxel Space," 1998.
- [16] N. Li, H.-X. Zhao, S.-H. Cho, J.-G. Choi, and M.-H. Kim, "A fast algorithm for voxel-based deterministic simulation of X-ray imaging," *Comput. Phys. Commun.*, vol. 178, no. 7, pp. 518–523, Apr. 2008.

Solid lung nodule volumetry: effects of dose reduction and reconstruction algorithms

Stefano Young and Michael F. McNitt-Gray

Abstract—Measuring the volume of solid pulmonary nodules on thoracic CT is a key task for staging cancer and measuring therapy response. Dose reductions and different reconstruction algorithms could change reader performance in this task, but their effects are still not well understood. More quantitative studies are needed to demonstrate the effects of dose and reconstruction algorithm on nodule volumetry. We devised an experiment using simulated reduced-dose CT scans, based on the raw sinogram data from clinical patient scans, to compare semi-automated volumetry at clinical dose with volumetry at 25%, 10%, and 3% of our clinical dose protocols. We also compared volumetry on images reconstructed with B45f and I50f strength 3 kernels on a Siemens Definition Flash workstation. For lesions > 1 cm in effective diameter, the readers' repeatability at clinical dose was similar to the inter-dose reproducibility at all dose levels (+/-15%). Reproducibility also seemed to be unaffected by changing reconstruction kernels. However, it remains a challenge to isolate the effects of dose and reconstruction algorithm from other sources of reader variability in the clinical setting.

Index Terms—Lung nodules, volumetry, thoracic CT, dose reduction, reconstruction algorithms, repeatability, inter-dose reproducibility.

I. INTRODUCTION

There is great interest in reducing the dose in thoracic CT protocols, particularly with the potential reimbursement of lung cancer screening in the near future. With more patients potentially receiving CT scans, it becomes more important to ensure that thoracic CT protocols provide high-quality information to the physician with a minimum of radiation dose. However, it is not obvious how far to reduce the dose in chest CT without increasing image noise to the point of sacrificing the high standard of care that we have come to expect from CT.

To reduce thoracic CT dose without sacrificing standard of care, an important prerequisite is to demonstrate that our dose reductions do not degrade the quality of quantitative measurements in the lung. In particular, estimating the volume of solid pulmonary nodules is a critical measurement, both for staging lung cancer and for measuring progression or stability of disease. It is so important that various societies

have published guidelines on how to manage these findings when they appear on thoracic CT exams [1,2]. Although lung nodule volumetry is critical to patient management and various guidelines exist in the literature, there remains a great deal of variability in the execution of this quantitative measurement.

Gavrielides et al. illustrated that scan dose and reconstruction algorithm are factors which could potentially affect the variability in lung nodule volumetry, though there is not yet consensus on the effects of these factors [3]. Only a few published studies have attempted to quantify how dose affects readers' measurement variability when measuring clinical lesions. In one study, investigators performed two consecutive low-dose and two consecutive standard-dose scans for each patient [4]. An observer then clicked each nodule, and volumes were automatically calculated by a commercial algorithm. For the consecutive low-dose scans, they found inter-scan relative volume differences between -38% and 60% (95% confidence limits). For the standard-dose scans, confidence limits were between -27% and 40%. The authors acknowledged, however, that they could not directly compare performance at the two dose levels due to protocol differences; in particular the slice thickness. In another study, investigators scanned each patient twice; once at standard dose and once at ultra-low dose. Two readers measured nodule volumes at both dose levels. Inter-dose relative volume differences ranged from -23.4% to 26.2% for reader 1 and -25.1% to 28.9% for reader 2 [5]. In the same study, they found intra-dose, inter-reader differences ranging from -9.7% to 8.3% at standard dose and -12.6% to 12.4% at ultra-low dose. The difference between inter- and intra-dose results illustrates the importance of inter-scan patient factors like positioning and breath hold. The difference between intra-dose results at standard and ultra-low dose suggests that one or both readers became slightly less precise at ultra-low dose. The authors concluded, however, that dose did not affect reader performance, based on comparing their inter-dose results with other studies' inter-scan results at standard dose.

We devised novel experiments to investigate the effects of scan dose and reconstruction algorithm on lung nodule volumetry. These experiments involved simulated reduced-dose scans based on the raw data from a single clinical CT scan for each patient. This document explains the experimental design and the results of those experiments, as well as discusses some example scenarios for relating the results to dose reduction in the clinical setting.

Stefano Young is with the University of California Los Angeles, Los Angeles, CA 90024 USA (e-mail: stefanoyoung@mednet.ucla.edu).

Michael F. McNitt-Gray is with the University of California Los Angeles, Los Angeles, CA 90024 USA (e-mail: mmcnettgray@mednet.ucla.edu).

II. MATERIALS AND METHODS

Our experiments involved three main steps: simulating reduced-dose scans (Section II.A), validating our simulations on phantom data (Section II.B), and designing a reader study for evaluating reader variability in lung nodule volumetry (Section II.C).

A. Simulating reduced-dose scans

Repeat scanning patients for research purposes can lead to unnecessary radiation dose, so these types of studies have typically been limited to two dose levels per patient. Recently, researchers demonstrated that it is possible to simulate multiple reduced-dose CT scans by exporting the raw sinogram data from a single clinical CT scan and applying an appropriate noise model. A variety of noise models have been summarized by Zabic et al [6]. The simulation approach has various benefits, including being able to explore the dose space efficiently without unnecessary radiation exposure and isolate dose effects from motion effects, which are clinically unavoidable even if the patient stays on the table between scans.

We adapted Zabic's approach and used concepts from Massmouzadeh et al. [7] to simulate reduced-dose sinograms from a series of thoracic CT scans acquired from our Siemens Definition Flash scanner under IRB approval. Through a research agreement with Siemens, we have the tools to extract individual readings from the raw sinogram files. All scans were adult patients acquired with the following technical parameters: 120 kV, 0.5 sec rotation time, 250-285 ref mAs, B45f kernel, 1-mm slice thickness, and CareDose 4D (tube-current modulation). In our simulations, we modeled dose reduction by scaling the tube-current modulation function by a constant factor. The raw CT data were exported from the scanner, and then we simulated reduced-dose sinograms in parallel on a multi-CPU computing cluster for speed. After simulating reduced-dose sinograms, we imported the sinograms back to the scanner workstation and reconstructed using the same kernel and slice thickness as we used clinically. The reconstructed images were then loaded into our group's quantitative imaging workstation software to take advantage of the semi-automated contouring tools available.

B. Validation of reduced-dose simulations

To validate our reduced-dose simulations, we performed a comparison between water phantom scans at various dose levels and phantom simulations at the same dose levels. We compared mean and standard deviations of the Hounsfield-unit values at different locations within one slice, and we found good agreement at all dose levels. While this is not a definitive demonstration of agreement between clinical and simulated scans, it gave us confidence that we could generate reduced-dose image series across the range of dose levels supported by our scanner model.

C. Reader study design

Under IRB approval, we exported the raw sinogram data for 68 patients with at least one suspicious nodule. From these,

we selected a subset of 35 "measurable" lesions based on language in the Quantitative Imaging Biomarkers Alliance (QIBA) profile document on nodule volume change measurement, namely: "tumor margins are sufficiently conspicuous and geometrically simple enough to be recognized on all images". The QIBA profile also specified a minimum effective diameter of 1 cm. Thus, we ruled out the smallest lesions and lesions which were attached to vessels or pleural walls. We selected only one lesion per patient to avoid potential bias due to a large number of lesions coming from the same scan. For each of the patients with a lesion meeting the QIBA criteria, we used the clinical scan to simulate reduced-dose sinograms at 25%, 10%, and 3% of the clinical dose. We started at just 25% of clinical dose because lung nodules are known to be high-contrast. In terms of CTDIvol, our clinical protocol corresponded to 20.9 mGy in the 32-cm CTDI phantom, so the 3% dose level would be less than 1 mGy.

After simulating reduced-dose sinograms for all 35 scans, we imported them back to the scanner workstation and reconstructed with two different kernels: B45f and I50f strength 3. All images were reconstructed at 1-mm slice thickness. We then imported the DICOM images to our group's quantitative imaging workstation software for semi-automated contouring [8]. All image series were anonymized to hide the patient and dose information. We asked three trained lab technologists to contour the lesions using a divide-and-conquer approach. Starting at the lowest dose (3%), each reader received a list of the 35 lesions in random order, where the reconstruction algorithm for each lesion was also assigned randomly (without replacement). Due to the difference in appearance between the reconstruction kernels, we felt this would reduce bias, and the readers would have difficulty distinguishing a change in recon kernel from a change in dose. The readers repeated this process at 10% and 25% dose, but clinical dose followed a slightly different design. At clinical dose, the image series were duplicated and randomly inserted into the reading list to get an estimate of the readers' intra-dose repeatability.

For statistical analysis, there are various options for displaying and analyzing volumetry data. One of the difficulties that arises is isolating the dose dependence and algorithm dependence from other factors. Our research question was really a question of agreement or reproducibility of nodule volumetry across doses and reconstruction algorithms, so we used analyses inspired by Bland and Altman [9]. For the clinical repeatability data, we calculated relative differences between two volume measurements made on the identical image series. For comparing volumetry across dose levels, we calculated relative differences between clinical and reduced-dose volumes (i.e. inter-dose reproducibility) as follows:

$$100 \times \frac{V_{\text{clinical}} - V_{\text{reduced}}}{\frac{1}{2}(V_{\text{clinical}} + V_{\text{reduced}})} \quad (1)$$

An analogous form was used to calculate the inter-dose, inter-algorithm reproducibility.

III. RESULTS

Nodule effective diameters ranged from approximately 7-35 mm, with the majority of the nodules less than 20 mm in effective diameter and a few larger nodules (Figure 1). Because the QIBA criteria were applied visually before contouring, there were a number of sub-cm nodules in the final dataset.

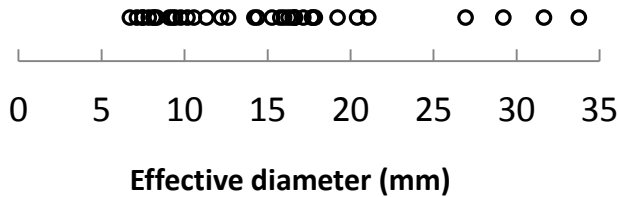
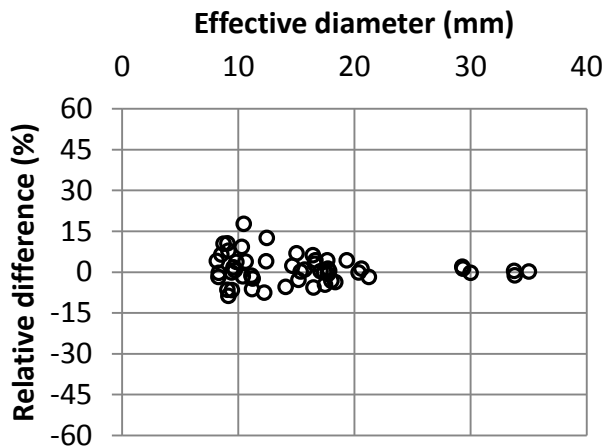


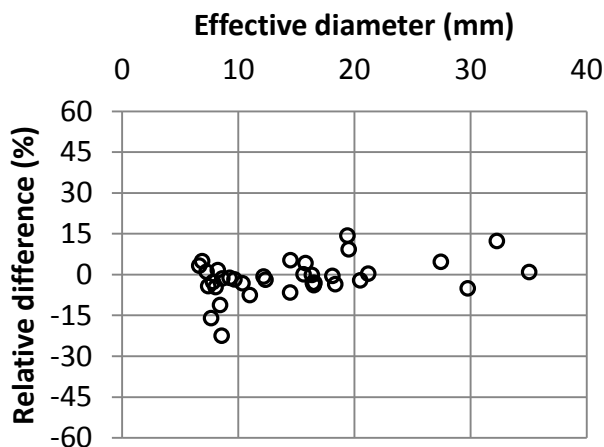
Figure 1 - Nodule sizes ranged from approximately 7-35 mm effective diameter, with the majority of nodules < 20 mm. Results are for reader 1 at clinical dose (B45f kernel).

A. Clinical (intra-dose) repeatability and inter-dose reproducibility with B45f kernel

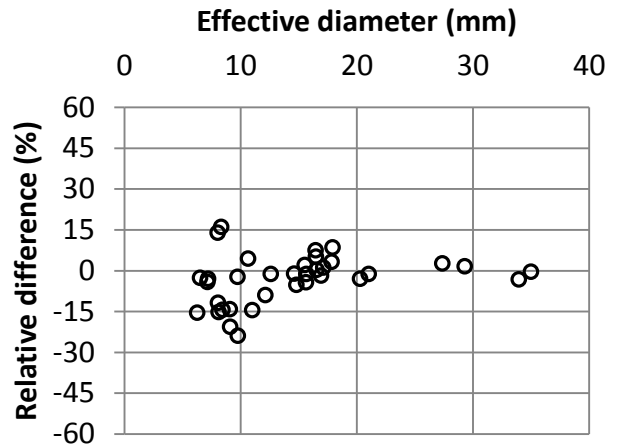
Clinical (~20.9 mGy)



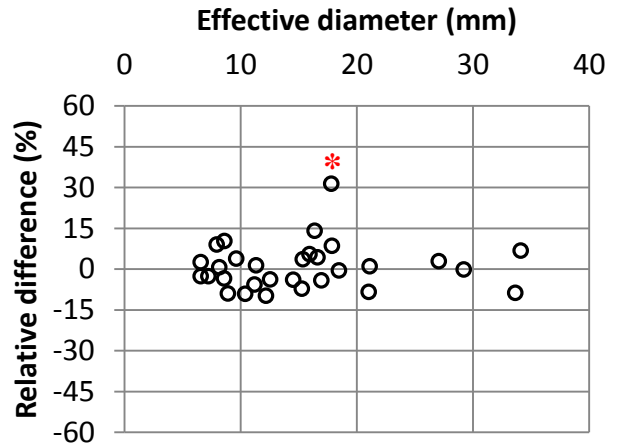
25% (~5.2 mGy)



10% (~2.1 mGy)



3% (~0.6 mGy)

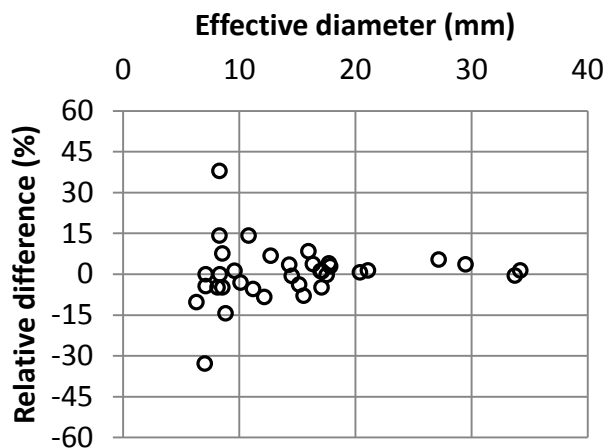


In the following results, we pooled the measurements from all three readers. In the clinical repeatability (intra-dose) experiment, the 95% confidence interval (CI_{95}) was -9.1% to 11.3% relative differences. At 25% dose, CI_{95} was -14.6% to 12.1%. At 10% dose, CI_{95} was -20.3% to 14.4%. At 3% dose, CI_{95} was -15.5% to 17.4%. For effective diameters > 1 cm, most of the relative differences were between +/-15% at all dose levels. One suspicious outlier at 3% dose is marked (*) for discussion.

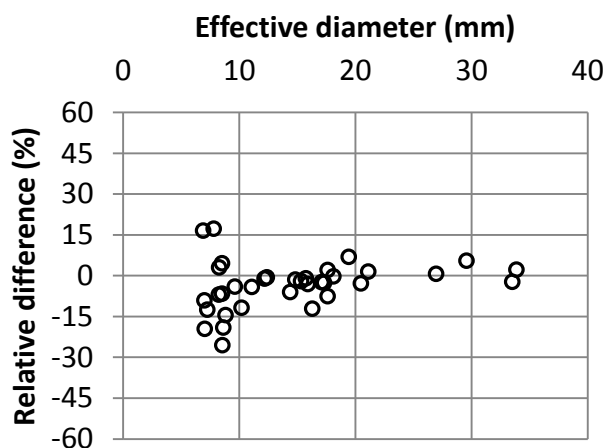
B. Inter-dose reproducibility with I50f kernel strength 3

We repeated the inter-dose reproducibility experiments in Section III.A using images reconstructed with the SAFIRE I50f kernel, strength 3. Relative volume differences were measured with respect to the same B45f clinical reference volumes as in the previous section.

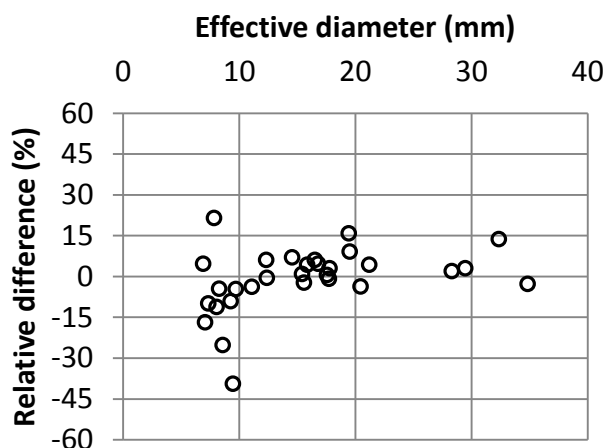
25% (~5.2 mGy)



10% (~2.1 mGy)



3% (~0.6 mGy)



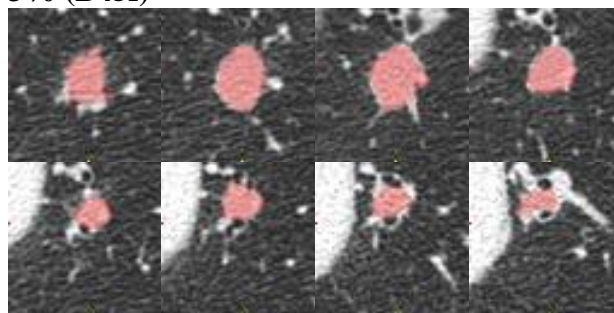
At 25% dose, CI_{95} was -20.0% to 20.8% relative difference. At 10% dose, CI_{95} was -20.5% to 13.8%. At 3% dose, CI_{95} was -23.7% to 21.9%. As in Section III.A, for effective diameters > 1 cm, most of the relative differences were between $\pm 15\%$.

IV. DISCUSSION

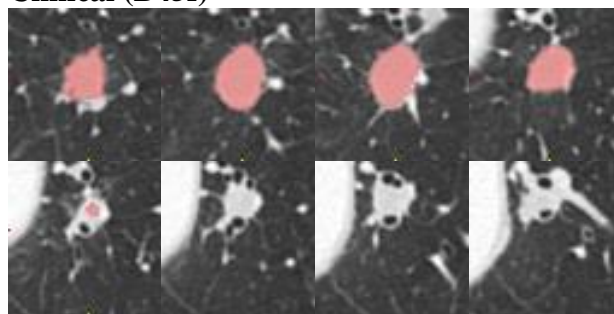
Considering nodule effective diameters > 1 cm, all but one of the volume differences fell within the range of $\pm 15\%$ across all dose-reconstruction combinations in this study. Inter-dose reproducibility seemed to agree with the clinical repeatability for larger nodules. Most of the nodules with $|volume\ differences| > 15\%$ corresponded to smaller nodules, which would not be considered to meet the QIBA criteria.

In the one case in Section III.A where a larger nodule had an inter-dose volume difference $> 30\%$ (below), it was still difficult to isolate the effects of dose from reader variability effects.

3% (B45f)



Clinical (B45f)



Since the readers started with the 3% dose lesions and ended with the clinical lesions, we concluded that the differences above were most likely due to a change in the reader's decision-making process as the reader became comfortable with the task over time, rather than a change due to perceiving additional contrast or reduced noise at the clinical dose level.

V. CONCLUSIONS

For solid nodules satisfying the QIBA criteria for "measurable" lesions, volumetry seemed to be independent of dose and reconstruction algorithm across the range of dose levels and algorithms that we simulated in this study.

REFERENCES

- [1] H. Macmahon, J. H. M. Austin, G. Gamsu, C. J. Herold, J. R. Jett, D. P. Naidich, E. F. Patz, and S. J. Swensen, "Guidelines for Management of Small Pulmonary Nodules Detected on CT Scans : A Statement from the Fleischner Society," *Radiology*, vol. 237, no. 2, pp. 395–400, 2005.
- [2] M. K. Gould, J. Fletcher, M. D. Iannettoni, W. R. Lynch, D. E. Midthun, D. P. Naidich, and D. E. Ost, "Evaluation of patients with pulmonary nodules: when is it lung cancer?: ACCP evidence-based clinical practice guidelines (2nd edition).," *Chest*, vol. 132, no. 3 Suppl, p. 108S–130S, Sep. 2007.
- [3] M. A. Gavrielides, L. M. Kinnard, K. J. Myers, and N. Petrick, "Noncalcified lung nodules: volumetric assessment with thoracic CT.," *Radiology* 251(1), 26-37 (2009).
- [4] C. Rampinelli, E. De Fiori, S. Raimondi, G. Veronesi, and M. Bellomi, "In vivo repeatability of automated volume calculations of small pulmonary nodules with CT.," *AJR. Am. J. Roentgenol.* 192(6), 1657–1661 (2009).
- [5] P. A. Hein, V. C. Romano, P. Rogalla, C. Klessen, A. Lembecke, L. Bornemann, V. Dicken, B. Hamm, and H.-C. Bauknecht, "Variability of semiautomated lung nodule volumetry on ultralow-dose CT: comparison with nodule volumetry on standard-dose CT.," *J. Digit. Imaging* 23(1), 8-17 (2010).
- [6] S. Zabić, Q. Wang, T. Morton, and K. M. Brown, "A low dose simulation tool for CT systems with energy integrating detectors.," *Med. Phys.*, vol. 40, no. 3, p. 031102, Mar. 2013.
- [7] P. Massoumzadeh, S. Don, C. F. Hildebolt, K. T. Bae, and B. R. Whiting, "Validation of CT dose-reduction simulation," *Med. Phys.*, vol. 36, no. 1, p. 174, 2009.
- [8] M. S. Brown, R. Pais, P. Qing, S. Shah, M. F. McNitt-Gray, J. G. Goldin, I. Petkovska, L. Tran, and D. R. Aberle, "An architecture for computer-aided detection and radiologic measurement of lung nodules in clinical trials.," *Cancer Inform.* 4, 25–31 (2007).
- [9] J. Bland and D. Altman, "Measuring agreement in method comparison studies," *Stat. Methods Med. Res.*, vol. 8, no. 135, 1999.

Considerations on an Advanced Adaptive Filter

Harald Schöndube, Rainer Raupach and Karl Stierstorfer

I. INTRODUCTION

The photon statistics of CT projection measurements can be modeled quite accurately as a Poisson or compound Poisson distribution. In many cases, the simplifying assumption of modeling CT projection noise as an attenuation-dependent Gaussian distribution can be made. In other words, the noise associated with a given measured value depends on the attenuation of this particular ray. This means that for non-isotropic objects (i.e., objects that are not “round” with respect to their CT attenuation) the noise in the CT projections depends on the projection direction and as a result pixel noise in the reconstructed image will be anisotropic. This so-called “directionality” of the image pixel noise depends on the extend of the non-isotropy (or “eccentricity”) of the object.

The so-called adaptive filter is an established method to reduce the directionality of image noise in CT images [1], [2]. By applying an attenuation-dependent filtering to the raw fan-beam data it attempts to equalize the quantum statistics of all projections that contribute to a given image. The adaptive filter can be realized by first applying a 2D linear low-pass filter to each projection and then performing a ray-wise attenuation-dependent mixing of the filtered data with the original unfiltered data. The mixing factor therefore determines the adaptive filter strength of each element; it is chosen with the aim to equalize the projection noise of the projection data, i.e., the projection featuring the minimal maximum attenuation value stays entirely unfiltered.

However, every linear filtering operation comes with a corresponding loss of resolution at high-contrast edges in the object. To mitigate this effect combining the adaptive filter with edge-restoring algorithms has been considered [3]. In this case, a second image would be reconstructed from unfiltered data and then mixed with the original image according to the strength of edges as detected in the image by an edge detection algorithm. However, while effectively restoring high-contrast edges this approach removes the effectiveness of the adaptive filter in regions close to the edge.

In this work, the results of an investigation of an edge-preserving, rather than edge-restoring approach are presented. While the performance of edge preservation is not influenced compared to the edge-restoration described above, the effectiveness of the adaptive filters along edges in the object is at least partially retained with our approach.

II. ALGORITHM DESCRIPTION

A. Notation

We denote 2D parallel CT projection data as $g(p, \vartheta)$, where p is the distance of a particular ray from the iso-center and

The authors are with Siemens AG, Healthcare Sector, Siemensstr. 1, 91301 Forchheim, Germany. Contact: harald.schoendube@siemens.com

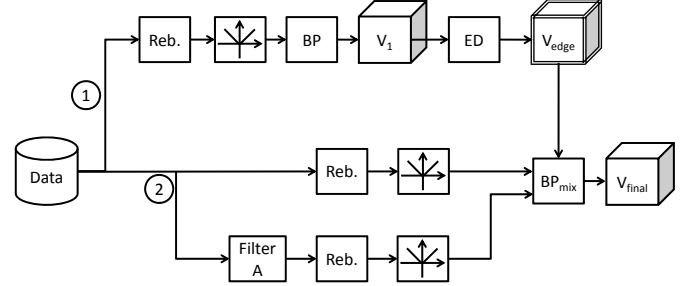


Fig. 1. Flow chart of our proposed algorithm.

ϑ denotes the projection angle; in this notation the Radon transform of an object $f(\underline{x})$ is expressed as

$$g(p, \vartheta) = \int_{-\infty}^{\infty} f(p\underline{\theta} + t\underline{\theta}^{\perp}) dt,$$

for $0 \leq \vartheta \leq \pi$ with $\underline{\theta} = [\cos(\vartheta), \sin(\vartheta)]^T$ and $\underline{\theta}^{\perp} = [-\sin(\vartheta), \cos(\vartheta)]^T$. We furthermore denote ramp-filtered parallel CT data as $\check{g}(p, \vartheta)$, such that the filtered backprojection of $g(p, \vartheta)$ can be written as

$$f(\underline{x}) = \int_0^{\pi} \check{g}(\underline{x} \cdot \underline{\theta}, \vartheta) d\vartheta.$$

B. An advanced adaptive filter

Our proposed algorithm, dubbed “advanced adaptive filter reconstruction” (AAFR), is based on applying the edge-dependent mixing on the filtered raw data during the backprojection step rather than in image domain. A flow-chart of the procedure is shown in figure 1. It comprises of two main steps (marked ① and ② in the flowchart, respectively):

In the first step, an image volume V_1 is reconstructed from the original unfiltered data by means of applying a filtered backprojection (marked as a sequence of rebinning, ramp filter and backprojector BP in the flow chart). V_1 is then fed into an edge detector ED , resulting in an edge volume V_{edge} . Note that for each pixel, V_{edge} should not only contain information about edge strength but also about the direction of a potentially detected edge at the given pixel’s location.

In a second step, the data is first filtered using the “filter A”, which is best chosen as being equivalent to the adaptive filter described above. Both the filtered and the non-filtered data are rebinned, ramp filtered, and then fed into a modified backprojector BP_{mix} . Here, the backprojected data component for target pixel \underline{x} and projection angle ϑ is computed as a linear combination of the filtered and non-filtered data:

$$\check{g}_{BP}(\underline{x} \cdot \underline{\theta}, \vartheta) = \alpha(\underline{x}, \vartheta) \check{g}(\underline{x} \cdot \underline{\theta}, \vartheta) + (1 - \alpha(\underline{x}, \vartheta)) \check{g}_A(\underline{x} \cdot \underline{\theta}, \vartheta),$$

where $\check{g}_A(p, \vartheta)$ denotes (after ramp-filtering and rebinning) the data filtered by filter “A”, while $\check{g}(p, \vartheta)$ stands for the

respective unfiltered data. The mixing factor $\alpha(\underline{x}, \vartheta)$ depends both on \underline{x} and ϑ and is determined from V_{edge} in dependence of the edge significance at \underline{x} along the direction $\underline{\theta}^\perp$:

$$\alpha(\underline{x}, \vartheta) = h\left(\frac{|\cos(\vartheta)S_x(\underline{x}) + \sin(\vartheta)S_y(\underline{x})|}{N(\underline{x})}\right),$$

where $S_x(\underline{x})$, $S_y(\underline{x})$ and $N(\underline{x})$ respectively denote the gradient along x - and y -directions and the noise level at location \underline{x} as determined from V_{edge} . The edge significance function $h(\lambda)$ is a smooth function that maps the edge SNR to a scalar significance value with $h(0) = 0$, $h(\lambda) = 1$ if λ is larger than a threshold value λ_{max} , and $0 \leq h(\lambda) \leq 1$ for all values of λ . In other words, if the edge SNR along $\underline{\theta}$ at \underline{x} is large, the algorithm considers the edge component at \underline{x} parallel to the backprojected ray as not being negligible and $\alpha(\underline{x}, \vartheta)$ is set to a value such that the non-filtered data $\check{g}(\underline{x} \cdot \underline{\theta}, \vartheta)$ is the predominant component in the backprojected value $\check{g}_{\text{BP}}(\underline{x} \cdot \underline{\theta}, \vartheta)$.

C. Linear filter variant

A second variant of our method, which is included here for completeness, would be to apply a linear filter instead of the adaptive filter for the “filter A” step. Additionally to the edge-dependent factor, an adaptive weight according to the eccentricity of the object would then be applied in the mixing step of the backprojector BP_{mix} . However, this approach introduces additional image artifacts and is therefore not a preferred solution.

An example is shown in figure 2, which shows images reconstructed from the same simulated CT data set: On the left side, a “classical” adaptive filter followed by an FBP reconstruction was applied. On the right side, the “linear filter” variant of our proposed method was applied (with the mixing in the BP_{mix} step limited to the adaptive weight without applying an edge-dependent factor). It can clearly be seen from this figure, that additional artifacts are introduced by this approach.

The reason for this lies in the non-commutativity of adaptive weighting and ramp filtering: If we denote the filtered and the non-filtered dataset with $g_1(p, \vartheta)$ and $g_2(p, \vartheta)$, respectively and the (channel-dependent) adaptive weights as $w(p, \vartheta)$ we have the following expression for the “classical” adaptive mixing:

$$g_{\text{adfil}}(p, \vartheta) = w(p, \vartheta)g_1(p, \vartheta) + (1 - w(p, \vartheta))g_2(p, \vartheta).$$

Applying the convolution kernel $K(p)$ we obtain

$$\begin{aligned} \check{g}_{\text{adfil}}(p, \vartheta) &= K(p) * g_{\text{adfil}}(p, \vartheta) \\ &= K(p) * (w(p, \vartheta)g_1(p, \vartheta) + (1 - w(p, \vartheta))g_2(p, \vartheta)). \end{aligned}$$

On the other hand, applying the adaptive mixing in the back-projection step means commuting convolution with $K(p)$ and weighting with $w(p, \vartheta)$, which is not identical to $\check{g}_{\text{adfil}}(p, \vartheta)$, since

$$\begin{aligned} &K(p) * (w(p, \vartheta)g_1(p, \vartheta) + (1 - w(p, \vartheta))g_2(p, \vartheta)) \\ &= K(p) * w(p, \vartheta)g_1(p, \vartheta) + K(p) * (1 - w(p, \vartheta))g_2(p, \vartheta) \\ &\neq w(p, \vartheta)K(p) * g_1(p, \vartheta) + (1 - w(p, \vartheta))K(p) * g_2(p, \vartheta) \end{aligned}$$

holds.

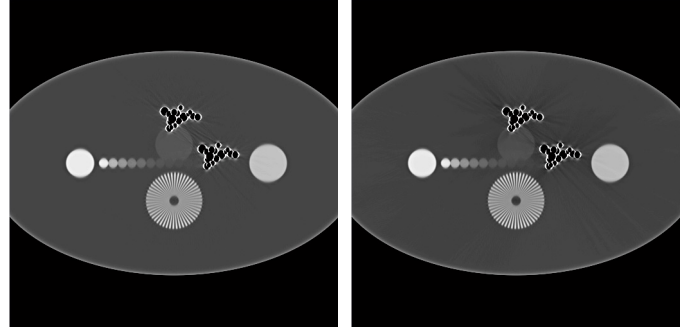


Fig. 2. Images from simulated CT data: (left) reconstructed using the “classical” adaptive filter followed by FBP; (right) applying a linear filter to the data and applying an adaptive mixing between the filtered and non-filtered data during the backprojection step.

Parameter	Data set 1	Data set 2
Acquisition mode	Single-Source Spiral	Single-Source Spiral
Collimation	32 x 1.2 mm	64 x 0.6 mm
Pitch factor	1.2	0.55
Tube voltage	100 kV	140 kV
Q. ref. mAs	180	600
Reconstructed FOV	300 mm	300 mm
Slice width	1.5 mm	0.6 mm
Kernel	B40f	B40s

TABLE I
OVERVIEW OF THE ACQUISITION AND RECONSTRUCTION PARAMETERS OF DATA SET 1 AND DATA SET 2.

III. RESULTS

In the following, some results obtained with a prototype implementation will be shown and discussed. The images shown here were obtained from two different data sets, designated as “data set 1” and “data set 2”, respectively, in the remainder of this report; see table I for details about acquisition and reconstruction parameters.

A. Algorithm performance

Tested with data set 1, the AAFR algorithm delivers good results. Figure 3 shows a comparison with a standard WFBP reconstruction with classical adaptive filter. The reduction of directed noise while maintaining edge sharpness is clearly recognizable. In figure 4 the adaptive filter in the WFBP reconstruction was parameterized for a stronger noise reduction such that it corresponds to the setting of “filter A” for the AAFR reconstruction. In this case, the resulting level of directed noise and streak artifacts is quite comparable to the one obtained with AAFR, albeit at the cost of a loss of edge sharpness which does not incur when applying our proposed AAFR method.

The eccentricity of the scan object of data set 2 is markedly stronger than the one of data set 1. Therefore, the level of directed noise and streak artifacts is much higher and the data set is more challenging for our proposed AAFR method. From figure 5 it can be seen that careful parameter optimization is necessary, as otherwise two types of artifacts are prone to appear:

- “ghost structures” along high-contrast edges, especially manifesting themselves as fine lines along bones;



Fig. 3. Images reconstructed from data set 1: AAFR (left), reference WFBP with classical adaptive filter (right), c/w : 40/300.

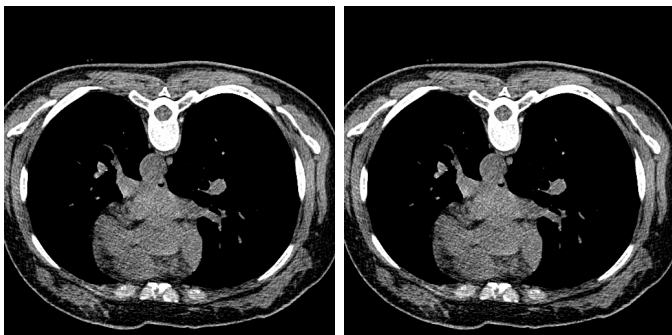


Fig. 4. Images reconstructed from data set 1: AAFR (left), reference WFBP with classical adaptive filter and stronger parameterization (right), c/w : 40/300.

- regions along soft tissue boundaries, in which the noise level is visibly higher than in homogeneous regions in the interior of the organ.

The arrows in figure 5 each point to one example of these two kinds of artifacts.

An analysis shows that the first artifact is caused by an imbalance between the adaptive filter applied to the data and the image-based edge detection: Consider a pixel close to, but not directly adjacent to a high-contrast edge. If the distance from the edge is large enough, it will be not marked as being in the neighborhood of the edge. Consequently, the filtered

data will be used for backprojection. If, however, the distance from the edge is smaller than the maximum extent of the adaptive filter in projection domain, the filtered CT value will still have a different expectation value than the unfiltered one due to the edge blurring caused by the filter. Thus, the ghost structures appear. In other words, the artifact generation process is comparable as if the image had been filtered by a low-pass filter and then mixed with the original unfiltered image according to the result of the edge detector, with the edge detection parameters not matched to the extent of the low-pass filter.

A somewhat higher noise around detected edges is actually inherent to our method due to the edge-dependent mixing between filtered and non-filtered data. The second artifact can therefore not fully be prevented; it can however be mitigated by ensuring a smooth transition between using filtered and non-filtered data.

In consequence, it is necessary to parameterize the edge detector such that its result matches the extent of the adaptive filter in projection domain and such that a smooth transition between the use of filtered and non-filtered data in the back-projector is ensured. In practice, we have realized this behavior by applying a spatial filter to $\alpha(\underline{x}, \vartheta)$. In this way, we enlarge the area of regions with high edge significance (i.e. regions in which edges are assumed to be close by) at the one hand and smoothen the transition between regions with high and low edge significance at the other hand. The result of this technique with using a 7×7 pixel boxcar filter is shown in figure 6. It can be seen that the ghost structures along bone edges are eliminated completely, while the impact of the unequal noise distribution along soft tissue edges on image perception is also visibly reduced. On close inspection one might perceive a somewhat degraded image sharpness compared to the default parameterization of the AAFR and the reference WFBP. We have thus also applied a modified filtering where a maximum filter of size 3×3 pixel was applied, followed by a 5×5 boxcar filter. The result is shown in figure 7; image sharpness is maintained better than with the simple 7×7 boxcar, this comes, however, at the cost of the non-uniform noise at tissue

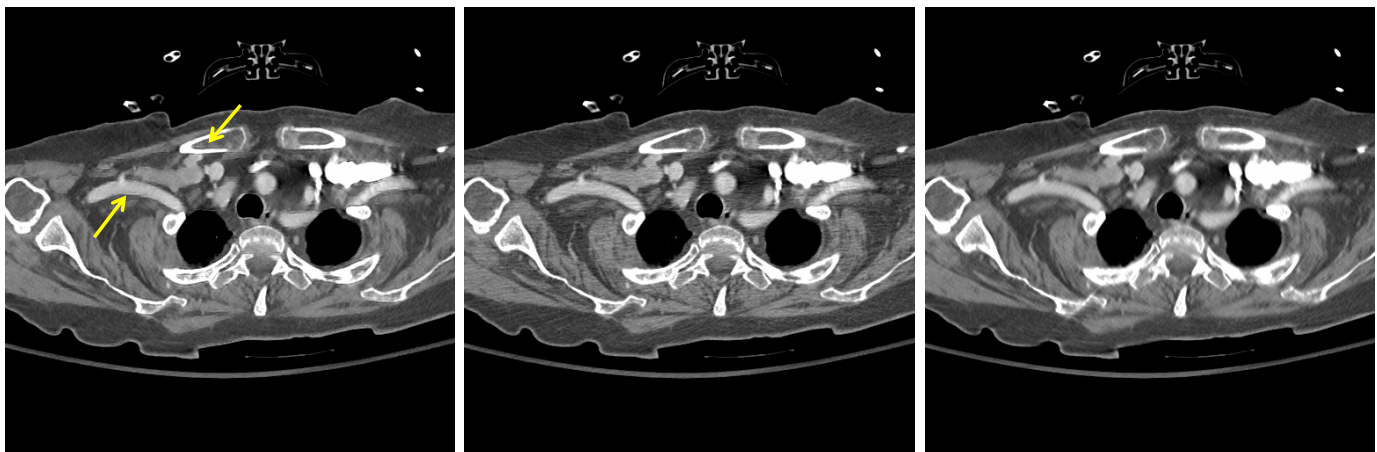


Fig. 5. Images reconstructed from data set 2: AAFR (left), reference WFBP with classical adaptive filter (center), WFBP with classical adaptive filter and stronger parameterization (right), c/w : 50/500.

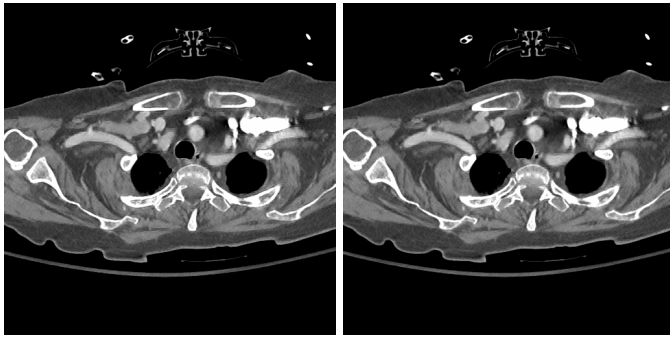


Fig. 6. Images reconstructed from data set 2: AAFR with 7x7 boxcar filter on edge significance matrix (left), AAFR “default” (right), c/w: 50/500.

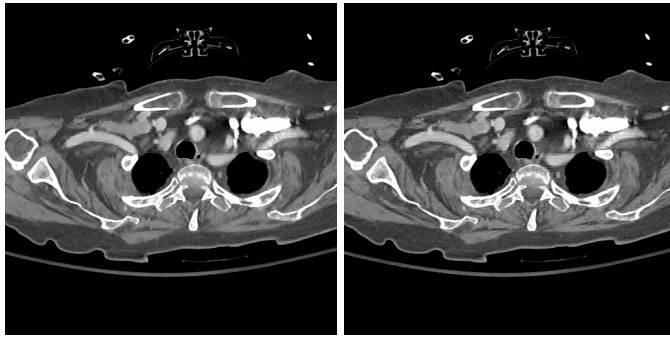


Fig. 7. Images reconstructed from data set 2: AAFR with 3x3 maximum and 5x5 boxcar filter on edge significance matrix (left), AAFR “default” (right), c/w: 50/500.

boundaries being more visible again (cf. figure 6).

B. Comparison to image-domain mixing

As a simpler approach for an edge-preserving reconstruction involving filtered and non-filtered data, backprojecting both data sets separately and then applying an edge-dependent mixing in image space has previously been proposed [3]. Compared with our proposed method, this setup does not allow for a choice between non-filtered and filtered data depending on projection direction and edge orientation, instead the non-filtered data will be used for all projection directions in the neighborhood of a given edge. Hence, data contributions that belong to a projection direction perpendicular to the edge can not be smoothed in this case. However, those contributions are exactly the ones that are “responsible” for streak artifacts perpendicular to the edge. The resulting effect can be recognized in figures 8 and 9: In the first figure, a comparison of our proposed AAFR method vs. the described edge-dependent image mixing approach is shown for data set 1. Since the object shown in this data set features a relatively low eccentricity, the difference between the two methods is more or less negligible. However, for data set 2, which shows a stronger level of eccentricity, the situation is different: Figure 9 displays the comparison for the same AAFR configuration as in figure 6.¹ Here, remaining streak artifacts perpendicular to

¹Note that to ensure a fair comparison, the same processing was applied to the edge detection input for the image-domain mixing approach as used in the corresponding AAFR configuration.

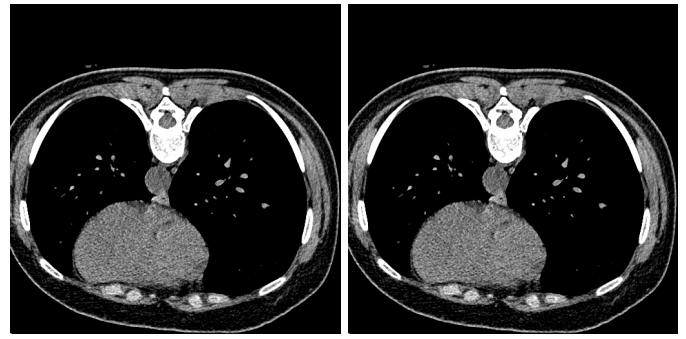


Fig. 8. Comparison AAFR (left) vs. edge-dependent image mixing (right) for data set 1, c/w: 40/300.

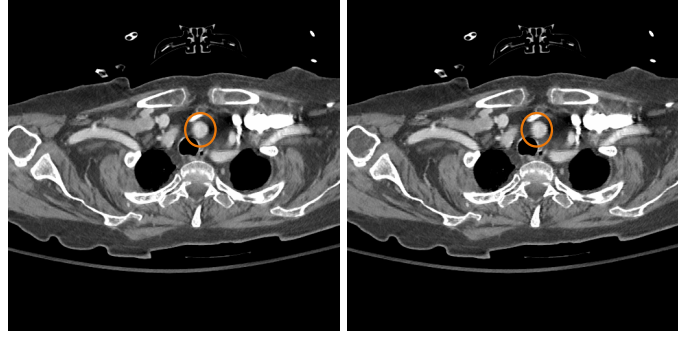


Fig. 9. Comparison AAFR (left) vs. edge-dependent image mixing (right) for data set 2, AAFR configuration as in figure 6, c/w: 50/500.

edges present in the object can clearly be recognized in the image reconstructed with the simpler image-domain mixing, while these artifacts are not present in the image reconstructed with our AAFR method.

IV. CONCLUSION

We have presented a new approach for extending the well-known adaptive filter with an edge-dependent backprojection step to allow for a stronger filter parameterization while maintaining image sharpness. An evaluation shows that obtaining good image quality in terms of edge preservation while effectively reducing directed noise and streak artifacts is possible. Careful parameter optimization is necessary to adapt the result of the edge detection routine to the extent of the filter applied in projection domain. Compared to a simpler image-domain mixing approach the AAFR method yields a superior reduction of streak artifacts, especially perpendicular to edges present in the imaged object.

REFERENCES

- [1] Marc Kachelrieß, Oliver Watzke, and Willi A. Kalender. Generalized multi-dimensional adaptive filtering for conventional and spiral single-slice, multi-slice, and cone-beam CT. *Medical Physics*, 28(4):475–490, April 2001.
- [2] Jiang Hsieh. Adaptive streak artifact reduction in computed tomography resulting from excessive x-ray photon noise. *Medical Physics*, 25(11):2139–2147, November 1998.
- [3] Gengsheng Zeng. View-based noise modeling in the filtered backprojection MAP algorithm. In *Proceedings of the second international Conference in X-ray Computed Tomography (Salt Lake City, USA)*, pages 103–106, June 2012.

Improved Trajectories in C-Arm Computed Tomography for Non-Circular Fields of View

Magdalena Herbst, Frank Schebesch, Martin Berger, Rebecca Fahrig, Joachim Hornegger and Andreas Maier

Abstract—In C-arm computed tomography, the field of view (FOV) is often not sufficient to acquire certain anatomical structures, e.g. a full hip or thorax. Recently proposed methods to extend the FOV use a fixed detector displacement and a 360° scan range to double the radius of the FOV. These trajectories are designed for circular FOVs. However, there are cases in which the required FOV is not circular but rather an ellipsoid. In this work, we show that the use of a dynamically adjusting detector offset can reduce the required scan range when using a non-circular FOV. Furthermore, we present an algorithmic approach which determines the minimal required scan ranges for arbitrary FOVs given a certain detector size. Our results indicate a promising reduction of the necessary scan range especially for ellipsoidal objects. Additionally initial reconstruction results of our method yielded comparable results as when using a fixed detector offset with a full 360° rotation.

I. INTRODUCTION

In computed tomography (CT), the maximum size of the reconstructable field of view (FOV) is a relevant factor. The diameter of a C-arm CT's FOV is typically determined by its detector size and might therefore be limited. Thus, it might be too small to cover certain anatomical areas of interest as for example the hip, the chest or both knees simultaneously.

One solution to increase the FOV is to displace the detector array and adjust the scan range accordingly [1], [2], [3]. The maximal radius of the FOV can be doubled if a displacement of half the detector range is used. Consequently, only half of the extended FOV is acquired with a single projection. Prior to reconstruction these truncated projections are then rebinned to a complete data set which covers the fully extended FOV. One drawback of these methods is, that a full 360° scan range is required to sample the extended FOV completely. Conventional C-arm CT scanners typically do not allow for such high scan ranges and even state-of-the-art robot-mounted systems might not be able to use a 360° scan range in certain angulations. This might be due to an irregular patient position as for example when scanning knees under weight-bearing conditions [4], [5].

Currently these trajectories and their reconstruction methods are designed for circular FOVs, but many anatomical structures may be better described by a non-circular boundary, for example by using ellipses. In this work, we propose a numerical approach that determines the minimally required scan range for arbitrary shaped FOVs, given a certain detector size.

Magdalena Herbst, Frank Schebesch, Martin Berger, Joachim Hornegger, and Andreas Maier are with the Pattern Recognition Lab, Department of Computer Science, Friedrich-Alexander-Universität Erlangen-Nürnberg. Joachim Hornegger and Andreas Maier are with Erlangen Graduate School in Advanced Optical Technologies (SAOT). Rebecca Fahrig is with the Department of Radiology, Stanford University, Stanford, CA, USA.

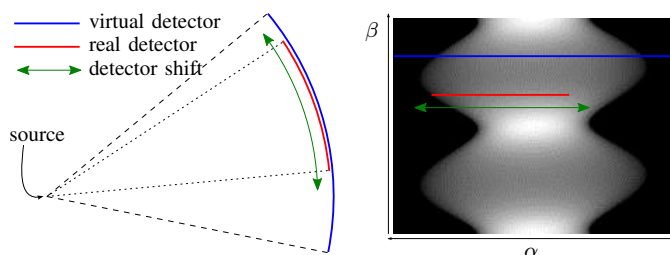


Fig. 1: Rotation of detector around source equals shift of the detector in the sinogram

II. MATERIALS AND METHODS

A. Correspondences in the Sinogram

In a sinogram of a complete rotation, i.e. a scan range of 360° , every ray is detected twice [6]. These rays are also known as complementary rays. The corresponding line integrals resulting of the complementary rays are equal and their position in the sinogram can be described by the relation

$$f(\alpha, \beta) = f(-\alpha, \beta + \pi + 2\alpha) . \quad (1)$$

B. Proposed Algorithm

Subsequently, we consider simple objects that are used to represent various shapes of possible FOVs. For example ellipsoids could be used to represent an outline of a hip slice, or two circles that are positioned off-center could be a suitable FOV for a cross-section of two knees. Now we define a virtual detector that is large enough to cover the whole object such that none of the acquired projections suffer from data truncation. Then a ground truth sinogram is generated using the defined FOV model and an arbitrary but non-zero density distribution within the FOV. For simplicity we assume a constant density over the entire FOV and use the mean density value of water. If the object has non-uniform diameters, e.g. like an ellipse, it is visible in the sinogram that there are line integrals that do not intersect the object, i.e. their sum is zero (cf. Fig. 1, right side). That means that this data is not necessary for reconstruction. Consequently, the idea is to move the detector in such a way that only non-zero line integrals are collected in each projection.

This motion of the detector is illustrated in Fig. 1. The projection of a single angle taken with the virtual detector is depicted by the blue line and represents a single line of the sinogram. The red line represents the real detector and its corresponding data in the sinogram. Moving the red line in the sinogram to the left and right is equivalent to rotating

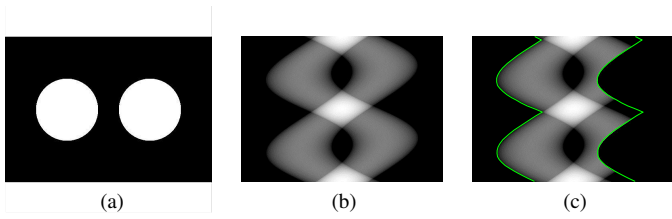


Fig. 2: Shape of the knees, sinogram of the knees and example for data acquired with a smaller detector with dynamic offset

the real detector while performing the rotation of the whole C-arm system. The rotational movement of the detector can be described with the angle between the central ray of the virtual detector and the central ray of the real detector. It will change while rotating the whole C-arm and can be described as a function of β . In this way, only segments of interest are acquired in the sinogram. The most intuitive way of rotating the detector is to follow the contour of the object in the sinogram (cf. Fig. 2). Hence, a minimal amount of background is scanned. If this movement is performed and a full data set should be acquired, the following constraints have to be fulfilled:

- First, the detector has to be large enough to cover the data for a rotation angle where the object outline is narrowest.
- Second, the detector has to be at least as wide as half of the object outline's widest position in the sinogram. Otherwise the object can not be covered with an off-center acquisition.

If the detector size given by the first requirement is equal to the detector size given by the second requirement, we would have a circular FOV and could use a static off-centered detector with a 360° scan range. In case the first requirement leads to a smaller detector size than the second requirement, we can use the proposed dynamic detector offset to reduce the scan range necessary for a full data acquisition.

In Fig. 2, we visualize the proposed detector motion by a simple example. Fig. 2(a) shows an object that represents the cross section of the shape of two knees by using two uniform circles. Fig. 2(b) depicts the full virtual sinogram of the object and Fig. 2(c) shows the data that is acquired if the proposed movement of the detector is realized. The superimposed lines represent the sinogram boundaries of the rotated detector.

C. Determining the Minimally Required Scan Range

In order to check whether the acquired data is sufficient for reconstruction, at first the truncated sinogram is completed by using the approach described in Algorithm 1. First, the actually acquired projection data is written into the sinogram. Positions in the sinogram which have a value of zero are assumed to be missing rays. Next, these are filled by their corresponding rays given by the redundancy condition Eq. (1). After this completion step, the sinogram is compared to the ground truth. If some data is still missing, the acquired data set is not complete. If there are no differences between the completed sinogram and the ground truth, the acquired

Algorithm 1 Sinogram Completion

```

for all  $(\alpha, \beta)$  do
  if  $f(\alpha, \beta)$  was acquired with the trajectory then
     $f(\alpha, \beta) = f(\alpha, \beta)$ 
  else
     $f(\alpha, \beta) = f(-\alpha, \beta + \pi + 2\alpha)$ 
    interpolation is required in this step
  end if
end for

```

data set is complete and therefore sufficient to perform the reconstruction.

We now focus on the derivation of a numerical approach to determine the minimal scan range such that the virtually extended sinogram is still complete. The proposed algorithm to solve this problem is presented in Algorithm 2. To determine the minimally required scan range $\Delta\beta_{min}$ for an arbitrary FOV and a given detector size, we perform a grid search over all possible starting angles $\beta_{Start} \in [0^\circ, 360^\circ]$ and over all possible scan ranges $\Delta\beta \in [180^\circ, 360^\circ]$. First, the minimally required rotation for every starting point is determined by starting with a small $\Delta\beta$. Then we increase it until the data set is complete. Next, the overall minimal $\Delta\beta$ and the corresponding β_{Start} is chosen as a final result. For the step size in angular direction, the angular spacing between the generated projections is used, which also limits the accuracy of the determined minimum scan range.

Subsequently, we present a selection of scanning configurations for the example depicted in Fig. 2. Fig. 3 shows an incomplete configuration with $\beta \in [53^\circ, 299^\circ]$. Fig. 3(a) shows the acquired sinogram, Fig. 3(b) shows the sinogram after the completion step using Algorithm 1 and the white areas in Fig. 3(c) depict the detected missing rays. The two missing areas correspond to each other by Eq. (1), thus, to fill the missing areas it is sufficient to acquire only one of them.

Algorithm 2 Find the minimal complete set for given object and detector size

```

 $\Delta\beta_{min} = \infty$ 
 $\beta_{Start, min} = 0$ 
for all  $\beta_{Start}$  do
   $\Delta\beta = 180^\circ$ 
  while data set is not complete do
    Acquire data with  $\beta_{Start}$  and  $\Delta\beta$ 
    Complete sinogram with Algorithm 1
    if data set is complete then
      if  $\Delta\beta < \Delta\beta_{min}$  then
        Save the values for the new minimal set:
         $\Delta\beta_{min} = \Delta\beta$  and  $\beta_{Start, min} = \beta_{Start}$ 
      end if
    else
      Increase  $\Delta\beta$ 
    end if
  end while
end for

```

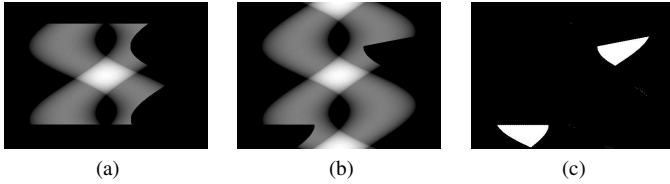


Fig. 3: Acquired data is not sufficient for a complete data set.

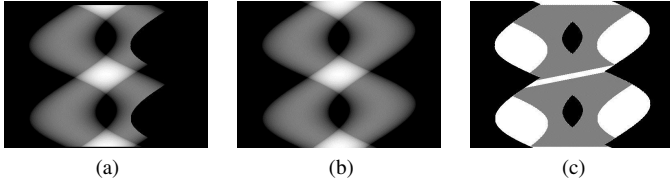


Fig. 4: More data acquired than the minimal complete data set.

In this configuration, the detector follows the left boundary in the sinogram. Because of this the range of β has to be extended towards the bottom of the sinogram until the lower of the two missing areas is covered completely.

Fig. 4 shows a scanning configuration with $\beta \in [10^\circ, 357^\circ]$. Here, more than the minimal complete data set is acquired. Fig. 4(a) shows the acquired sinogram, Fig. 4(b) shows the sinogram after completion and the gray areas in Fig. 4(c) depict the redundantly acquired data. The range of β could be reduced in the upper part of the sinogram.

In Fig. 5 a minimal complete data set with a scan range of $\beta \in [53^\circ, 357^\circ]$ is shown. Fig. 5(a) shows the acquired sinogram, Fig. 5(b) shows the resulting completed sinogram and Fig. 5(c) shows the acquired redundant areas. With this configuration, there are no missing parts and no redundant areas that can be left out without losing data that is required for the complete data set.

All algorithms were implemented using CONRAD, an open source software for simulation and reconstruction of CT data (see [7]).

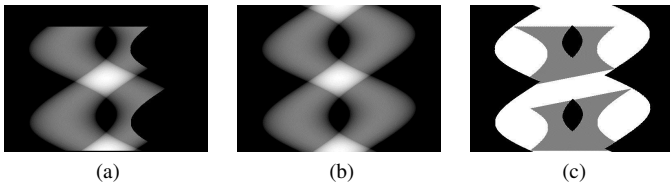


Fig. 5: Exactly the minimal complete data set is acquired.

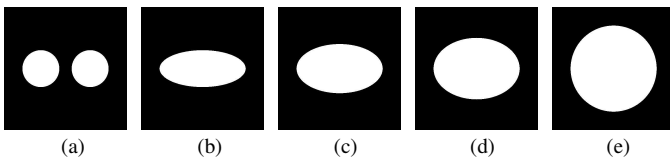


Fig. 6: Different shapes

Object	Diameter in x-direction	Diameter in y-direction
Two circles	358.4 mm	153.6 mm
Ellipse 1	358.4 mm	153.6 mm
Ellipse 2	358.4 mm	204.8 mm
Ellipse 3	358.4 mm	256 mm
Circle	358.4 mm	358.4 mm

TABLE I: Dimensions of the different objects

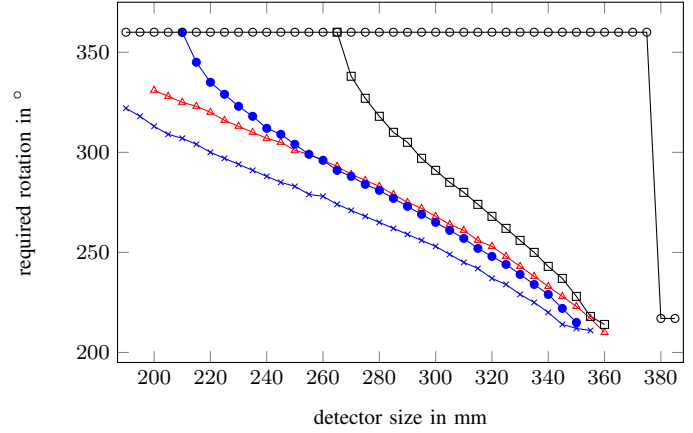


Fig. 7: Required rotation for different objects and detector sizes. Two Circles (\blacktriangle), Ellipse 1 (\times), Ellipse 2 (\bullet), Ellipse 3 (\blacksquare), Circle (\circ)

III. EVALUATION AND RESULTS

A. Evaluation

In Fig. 6 we show the different FOVs that were used for evaluation of the minimally required scan range for different detector sizes. Fig. 6 shows the off-center circles introduced above, Fig. 6(b) to Fig. 6(d) depict ellipses with varying diameter in y-direction and Fig. 6(d) shows a uniform circle. For detailed parameters of the shapes we refer to TABLE I. For our simulations we generated 360 projections for the full scan using an angular increment of 1° . The focal length was set to 574 mm and the virtual detector had 501 elements with a spacing of 1 mm leading to a virtual fan angle of approximately 47° .

B. Results

Fig. 7 shows the required rotation depending on the detector size for the different objects. For non-circular objects the graphs clearly depict the connection between detector size used and the minimally required scan range. Further we can see that a reduction of the FOV in one direction also reduces the minimally required scan range when the detector size is fixed. At the point where the detector size is greater than the large diameter of the FOV, the trajectory degenerates to a normal short scan approach. For the uniform circle only two possibilities exist. In case the detector is big enough to cover the circle, then a normal short scan [8] is sufficient. If the detector is too small for the circle, a full 360° scan range needs to be acquired. For objects that have different dimensions in

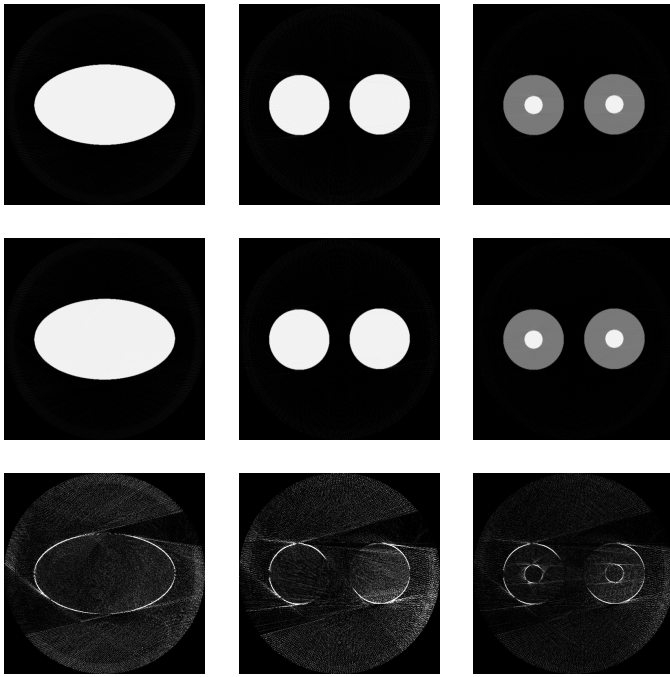


Fig. 8: Reconstruction results, top: reconstruction of the original sinogram, middle: reconstruction of the trajectory result, bottom: difference images. The gray scale window for the reconstruction results is $[0, 1.05]$ and for the difference images $[0, 0.05]$. The maximal difference for the ellipse is 0.232, for the two circles 0.256 and for the modified two circles 0.125.

x- and y-direction, a smaller rotation range is sufficient for a complete data set compared to a circumscribed circular object.

As a proof of concept of our approach, we conducted image reconstructions. First we reconstructed the sinogram using a full 360° scan range, then the rebinned sinogram for the minimally determined scan-range is reconstructed. A visual comparison of both reconstruction results is shown in Fig. 8 for an ellipse and for the object containing two circles. To show that our method is indeed independent of the intensity distributions with the FOVs we also adjusted the two circles with additional high-density objects in their center. The images show the reconstruction result for the full virtual sinogram (top row), for the minimally complete sinogram (middle row) and the difference image between both of them (bottom row). The reconstruction results of the full virtual sinogram as well as the completed sinogram are in good agreement with each other, showing only minor deviations at the object boundaries. For a quantitative evaluation we also computed the relative root-mean-square-error (rRMSE) for the reconstruction results. We determined an rRMSE of 1.11%, 1.15% and 0.66% for the ellipse, the two circle and the modified two circles, respectively.

IV. DISCUSSION

In this work we present a method that is capable to determine the minimally required scan range for extended and arbitrary shaped FOVs given a certain detector size. FOV extensions using a fixed detector displacement produce a circular

FOV with the double radius compared to a centered detector [1], [2]. This comes with the cost that projections need to be acquired over a scan range of 360° . Due to space restrictions or limitations given by the scanner geometry, these large scan ranges are sometimes not feasible in an interventional suite. The presented approach, however, enables FOV shapes that are tailored to the actual object and automatically determines the minimally required scan-range to allow for an automatic trajectory planning. We show in Fig. 7 that this can result in a substantial reduction of the required scan range, especially for FOVs that are similar to ellipsoids with different semi-axis lengths.

We assume that the detector is movable throughout the C-arm's global rotation movement, which is already feasible with state-of-the-art C-arm CT scanners. The reconstruction results show that our minimally acquired sinogram achieves an almost identical reconstruction when compared to the reconstruction from the 360° reference sinogram. The difference images in the bottom row of Fig. 8 reveal that most of the deviations are located at the objects' boundaries. We related this to the data completion step where the incomplete sinogram is filled by simple bi-linear interpolation. Thus, inaccuracies are introduced in the sinograms which subsequently leads to the observable loss of spatial resolution in the reconstruction domain. In a yet to be developed online filtered back-projection algorithm, we expect less resolution loss.

In terms of noise we expect the method to be as robust as any filtered back-projection-type reconstruction method. We expect that common noise reduction methods will be applicable with minor modifications [9]. Furthermore, truncation correction can be applied as in any C-arm scan [10].

For future work, we plan to analytically derive a formula that gives the relation between detector size and minimally required scan range. Furthermore, we will investigate the extension to three dimensional FOV shapes.

V. SUMMARY

In C-arm computed tomography, the detector is often too small for the region of interest. Recent trajectories are designed for circular field of views (FOVs). This configuration allows two minimal sets: the short scan and the large volume scan.

For imaging of certain parts of the human body, the required FOV may be non-circular, e.g. for imaging of the thorax, abdomen, or knees. In this paper, we presented a numerical method to investigate scan length vs. detector size in arbitrary objects for fan-beam geometry. We further showed that there exists a continuum of solutions for some non-circular objects and that reconstruction from such trajectories yields image qualities comparable to a full scan acquisition.

REFERENCES

- [1] D. Schäfer and M. Grass, "Cone-beam filtered back-projection for circular X-ray tomography with off-center detector," in *Proceeding of the 10th International Meeting on Fully Three-Dimensional Image Reconstruction in Radiology and Nuclear Medicine, Beijing, PR China, 2009*, pp. 86–89.
- [2] H. Kunze and F. Dennerlein, "Cone beam reconstruction with displaced flat panel detector," in *Proceeding of the 10th International Meeting on Fully Three-Dimensional Image Reconstruction in Radiology and Nuclear Medicine, Beijing, PR China, 2009*, pp. 138–141.

- [3] G. Wang, "X-ray micro-CT with a displaced detector array," *Medical physics*, vol. 29, no. 7, pp. 1634–1636, 2002.
- [4] A. Maier, J.-H. Choi, A. Keil, C. Niebler, M. Sarmiento, A. Fieselmann, G. Gold, S. Delp, and R. Fahrig, "Analysis of vertical and horizontal circular c-arm trajectories," in *SPIE Medical Imaging*. International Society for Optics and Photonics, 2011, pp. 796 123–796 123.
- [5] J.-H. Choi, R. Fahrig, A. Keil, T. F. Besier, S. Pal, E. J. McWalter, G. S. Beaupré, and A. Maier, "Fiducial marker-based correction for involuntary motion in weight-bearing C-arm CT scanning of knees. Part I. Numerical model-based optimization," *Medical physics*, vol. 40, no. 9, p. 091905, 2013.
- [6] G. L. Zeng, *Medical Image Reconstruction*. Springer, 2010.
- [7] A. Maier, H. Hofmann, M. Berger, P. Fischer, C. Schwemmer, H. Wu, K. Müller, J. Hornegger, J.-H. Choi, C. Riess, A. Keil, and R. Fahrig, "CONRAD - A software framework for cone-beam imaging in radiology," *Medical Physics*, vol. 40, no. 11, 2013.
- [8] D. L. Parker, "Optimal short scan convolution reconstruction for fan beam CT," *Medical physics*, vol. 9, no. 2, pp. 254–257, 1982.
- [9] A. Maier, L. Wigström, H. Hofmann, J. Hornegger, L. Zhu, N. Strobel, and R. Fahrig, "Three-dimensional anisotropic adaptive filtering of projection data for noise reduction in cone beam CT," *Medical Physics*, vol. 38, no. 11, pp. 5896–5909, 2011.
- [10] F. Dennerlein and A. Maier, "Region-Of-Interest Reconstruction on medical C-arms with the ATRACT Algorithm," in *Proc. SPIE 8313*, SPIE, Ed., San Diego, California, USA, 2012, pp. 8313–8347.

Reduction of Dose by Focusing the X-Ray Beam to a Specific Region of Interest: Monte Carlo Assessment

M. Buğrahan Oktay and Frederic Noo

Abstract—We investigate the reduction in dose out of the region of interest by filtering the X-ray beam to focus on the specific region of interest by means of Monte Carlo simulations. We use the Geant4 simulation toolkit that describes the interactions of the particles with matter. We created a simple mathematical phantom that includes kidneys, heart, spine, rib-cage and lungs. All organs and bones are describes by simple mathematical shapes by using Geant4. We performed simulations concentrating on two different region-of-interest (ROI) : kidneys and heart and for two different body sizes. The effect of a bow-tie filter was approximated by a Gaussian attenuation profile. Our results showed that when the X-ray source is filtered to focus on the specific organ, the energy deposited in outside of the ROI was dramatically reduced.

I. INTRODUCTION

The importance of the diagnostic CT is evidenced by the annual increase in the number of CT scans performed which is currently about 85 million annually. It has the tremendous impact on cancer and emergency medicine and remains an invaluable diagnostic technique. CT the largest contributor to medical radiation exposure among the US population can expose patients to cumulative radiation doses that may increase patient’s likelihood of developing cancer and other health problems.

A CT examination with effective dose of 10 mSv may be associated with an increase in the possibility of fatal carcinogenics. In addition a radiation exposure in childhood (5-10% if all CT scans in US are pediatric) may result in very small but increased risks of leukemia and brain tumors [1]. This becomes a large public health problem when large number of the population goes under a CT scans. Therefore, research focusing on methods to reduce the radiation dose from CT could shift benefit/risk balance further to benefit side.

In this paper, we investigate the reduction in the dose (energy deposit) by using a specific region focused X-Ray beam by means of Monte Carlo simulations. In section II, we discuss the simulation parameters, phantom and the software used. We concentrate on scanning two different regions, kidneys and heart for two different body sizes. We investigate the reduction in energy deposits by means of delivering the required dose to the region of interest, while preserving the surrounding areas. To different body sizes were used in simulations. These are

M. B. Oktay and F. Noo and are with the Utah Center for Advanced Imaging Research, Radiology Department, University of Utah, Salt Lake City, UT 84018 USA (e-mail: noo@uclair.med.utah.edu and bok-tay@uclair.med.utah.edu)

referred to as “Slim” and “Fat” and created by only changing the trunk size while the organ and bones sizes are kept fixed. The kidney scans are discussed in section III and the heart scans are discussed in section IV. We present our conclusions and future work in section V.

II. SIMULATION

A. Software

We use Geant4 software. Geant4 is a Monte Carlo simulation Toolkit, describing the interaction of particles with matter. It is widely used from High Energy Physics to medical physics. It provides sophisticated physics packages and an advanced geometry component. Further details can be found in [2].

B. Geometry

We created a simple mathematical phantom by using simple geometrical shapes provided in Geant4. We created objects representing the kidneys, lungs, heart, spine and rib cage. The kidneys, lungs and spine are represented by elliptical tubes which satisfies the equation

$$\left(\frac{x - x_{\text{off}}}{a}\right)^2 + \left(\frac{y - y_{\text{off}}}{b}\right)^2 \leq 1; \quad z_{\text{min}} \leq z \leq z_{\text{max}} \quad (1)$$

The heart is represented by a 5 cm radius sphere centered at $(x, y, z) = (1.5, -2.0, 20.15)$ cm. The rib cage is made of 12 elliptical rings centered at the origin. Each ring is 1.4 cm in height and thickness of 0.5 cm. They are separated by 1.4 cm starting from $z = 0.1$ cm to $z = 35$ cm. The left lung is set to be smaller than the right lung and the heart is shifted to the left. All geometrical objects were defined in G4VUserDetectorConstruction class of Geant4. The dimensions and offsets of the objects are summarized in Table I. The frontal view of the phantom is shown in Figure 1 and a cross sectional view of the phantom is shown in Figure 5.

The kidneys and heart are made of soft tissue. The spine and ribs are made of bone material and the lungs are made of lung tissue. All objects are placed in an elliptical tube (trunk) made of water. All the materials can be defined by using “G4Material” class of Geant4. The materials and densities used are summarized in Table II.

C. Beam

We used a fan beam for all simulations. The X-Ray source is located 57 cm away from the origin and rotated around the

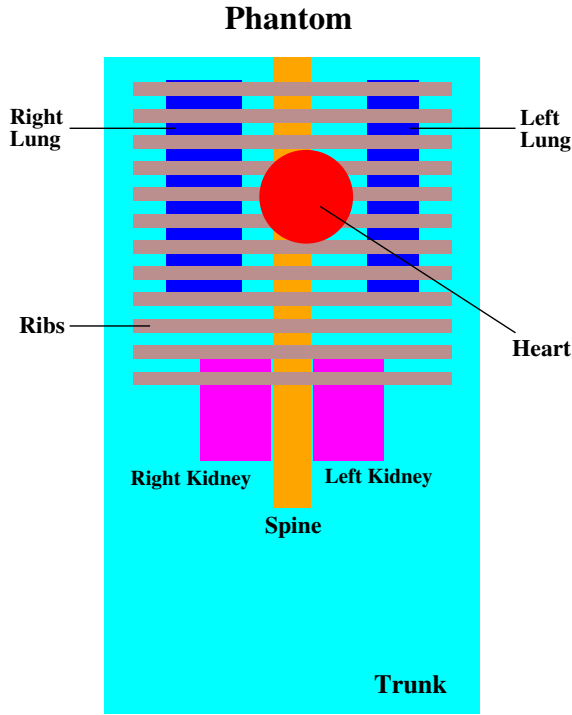


Fig. 1. Frontal view of the phantom created with Geant4.

Object	a	b	x_{off}	y_{off}	z_{off}	z_{min}	z_{max}
Trunk - Slim	20	10	0	0	0	-35	35
Trunk - Fat	25	15	0	0	0	-35	35
Left Kidney	3.75	1.5	6.0	6.0	-2.5	-8.0	2.5
Right Kidney	3.75	1.5	-6.0	6.0	-2.5	-8.0	2.5
Spine	2.0	2.5	0	5.5	11	-13	35
Left Lung	2.75	6.0	10.75	0	0	-20.5	20.5
Right Lung	4.05	6.0	-9.45	0	0	-20.5	20.5
Heart	5.0	5.0	1.5	-2.0	20.15	-	-

TABLE I

PARAMETERS USED IN PHANTOM. ALL UNITS ARE IN CENTIMETERS. TWO DIFFERENT TRUNK SIZES WERE USED WHILE ALL THE ORGAN AND BONE SIZES KEPT FIXED.

isocenter of the phantom. Each scan is done at 360 degrees in 1 degree intervals, $N_\lambda = 360$. At each rotation angle, λ , the beam is uniformly sampled by $N_{\Delta\phi} = 400$ directions between the tangent points of the object (see Figure 2) and $N_{in} = 300$ photons were sent at each direction. We define the total beam energy per scan can as

$$\text{Total Beam Energy} = E_\gamma \times N_{\Delta\phi} \times N_{in} \times N_\lambda \quad (2)$$

where E_γ is the photon energy. Mono-energetic X-ray beam energy was used between 10 and 120keV in 5 keV intervals.

We estimated the bow tie filter attenuation profile. The bow tie filter reduces the X-ray fluence as a function of increasing fan angle θ from the central ray. In our simulations, this effect is approximated by a Gaussian profile factor $p(\theta) = \exp(-\eta\theta^2)$ resulting in $N_{in} \times p(\theta)$ photons in each direction. The factor η is calculated for the maximum fan angle $\theta = 26^\circ$ and set to be 11.18.

Object	Material	Density [g/cm^3]
Kidneys and Heart	Soft Tissue	0.9896
Lungs	Lung Tissue	1.4862
Ribs and Spine	Bone Material	0.2958
Trunk	Water	1.0

TABLE II
MATERIALS USED IN PHANTOM.

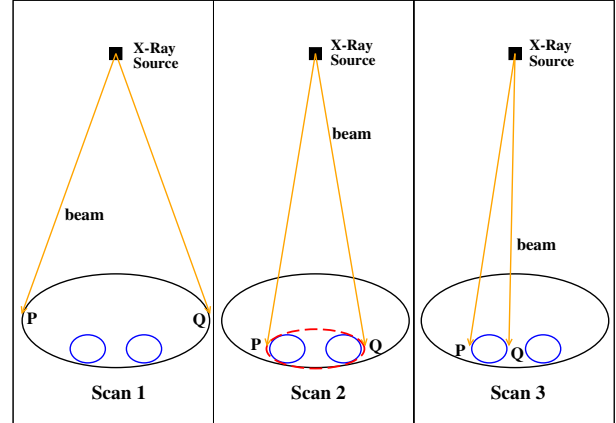


Fig. 2. Three different beams for kidney scans. Only kidneys are shown for illustration. Third scan is repeated for both kidneys and results are combined.

D. Errors

Since performing Monte Carlo simulations is a timely process, we estimated errors for 40, 60, 80 and 100 keV cases. In each case the simulation is repeated 10 times with different initial conditions.

III. KIDNEY SCANS

We performed three different scans concentrated on three different focused area. In the first scan, “Scan 1” in Figure 2, The X-Ray beam was focused on the entire trunk. In the second case, “Scan 2”, the beam is concentrated on a smaller elliptical region that contains both kidneys. The radii for the small elliptical region are $a = 10.0$ cm and $b = 2.5$ cm. The third scan, “Scan 3”, was focused on an individual kidney. In this case, the kidneys were scanned separately and the results from both scans were combined. The points **P** and **Q** in Figure 2 represent the tangent points of the shape being scanned, therefore the fan angle changed with changing rotation angle λ . The beam’s z -coordinate was set to be $z = -2.5$ cm which corresponds to the middle of the kidneys. Each simulation is repeated for two different trunk sizes.

In order to understand the effect of the focused beams, the fractional energy deposited for each object were calculated according to

$$f_j(E) = \frac{\text{Energy Deposited in the Region}}{\text{Total Beam Energy}} \quad (3)$$

where the “Total Beam Energy” is given in Eq. (2) and $j = \{1, 2, 3\}$ corresponds to the first, second and third scans,

respectively.

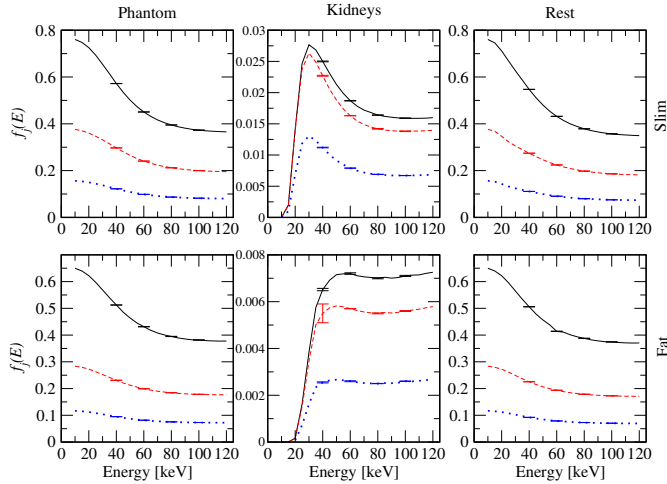


Fig. 3. The fractional energy deposited $f(E)$ for Phantom, Kidneys and the Rest for both slim and fat trunk sizes. Errors are estimated for 40, 60, 80 and 100 keV cases. Solid (black) = $f_1(E)$, dashed (red) = $f_2(E)$ and dotted (blue) = $f_3(E)$. Top row corresponds to Slim, and bottom row corresponds to Fat trunk sizes.

The fractional energy deposited for each scan is shown in Figure 3 for the “Phantom”, “Kidneys” and the “Rest” for both slim and fat trunk sizes. In Figure 3, “Phantom” refers to entire phantom while “Rest” refers to the Phantom where the kidneys are excluded (e.g., entire volume surrounding the kidneys). Since the beam is focused to a smaller region for each scan, the fractional energy deposited is also smaller as one expects.

Further information can be gathered by plotting the ratios of $f(E)$'s relative to the first scan. This is illustrated in Figure 4. When the X-Ray beam is focused on the smaller elliptical area (Scan 2) rather than the entire phantom and in the phantom without the kidneys (Rest) reduce approximately by a factor of 2 both in the Slim and Fat body types. The energy deposited in the kidneys reduces by approximately 10 percent. On the other hand, in Scan 3 where each kidney is scanned separately and the results are combined, the energy deposited in the Phantom and Rest is roughly reduced by a factor of 5 in both sizes while the reduction in the kidneys is roughly 2.5 relative to the Scan 1.

IV. HEART SCANS

The heart was the other region of interest where we investigated the effects of the focused beam. We followed the same strategy used for the kidneys scans. We performed two different scans. In the first scan (Scan 1), the beam was directed between the tangent points of the trunk (exactly the first scan of previous section) while in the second case (Scan 2), the beam was focused on the heart only (see Figure 5). Because the heart is located in between the lungs and surrounded by the rib cage, we varied the z -coordinate of our fan beam. We repeated the simulations for each scan at two different

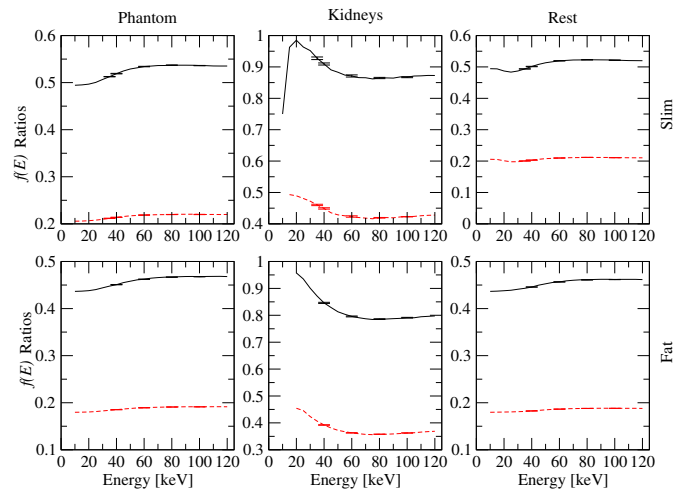


Fig. 4. The ratios of $f(E)$'s relative to the first case. $f_2(E)/f_1(E)$ (black solid lines) is the energy deposit ratio of second case to the first one. $f_3(E)/f_1(E)$ (red dashed lines) is the ratio of the third case to the first one. First row is for the Slim and the second row is for the Fat trunk size.

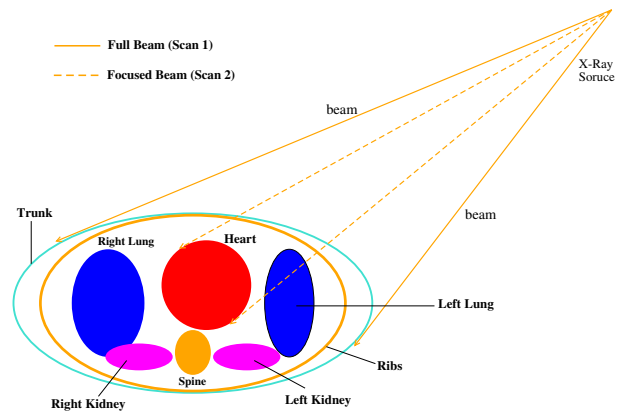


Fig. 5. Cross sectional view of the mathematical phantom. Solid lines represents the full beam while dashed lines represent the focused beam.

z positions ($z = 20.15$ and $z = 19.0$ cm) and averaged our results.

The fractional energy deposited $f(E)$ in the heart, phantom and the area outside of the heart (Rest) for each scan is shown in Figure 6. When the beam is focused on the heart only, the energy deposited in the heart and other areas decreased as expected.

Savings in energy deposited in each area can be seen better by plotting the ratios of the fractional energy deposits as illustrated in Figure 7. In the case of the slim body size, $f_2(E)/f_1(E)$ ratio for the heart is approximately between 0.8 to 0.9 while this ratio goes below 0.8 in the case of fat body size. Similarly, $f_2(E)/f_1(E)$ ratio for the Phantom and the Rest is approximately 0.5 for slim body size and slightly lower than 0.5 for fat body size.

V. CONCLUSIONS AND FUTURE WORK

We have studied the savings in energy deposited both in the ROI and outside of the ROI with a simple mathematical

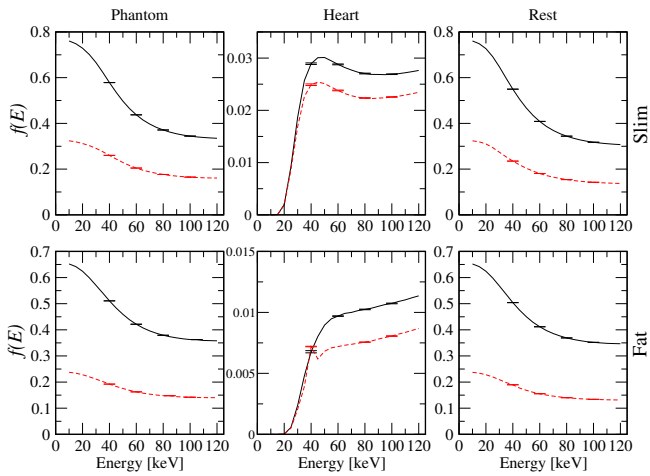


Fig. 6. Fractional Energy Deposits $f(E)$ for the entire phantom, heart and the rest. Solid lines = Scan 1 (black) and dashed lines = Scan 2 (red). Top row is for the slim and bottom row is for the fat body sizes.

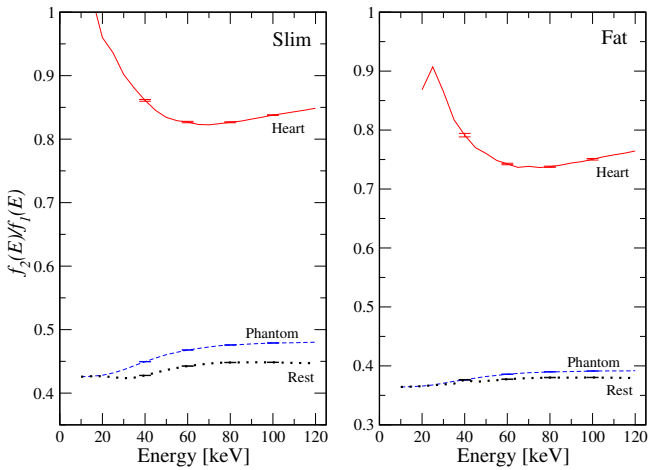


Fig. 7. Ratios of the fractional energy deposits in Phantom, Heart and Rest for both Slim (left) and Fat (right) body sizes. Solid lines = Heart (red), dashed lines = Phantom (blue) and dotted lines = Rest (black).

phantom created by the Geant4 simulation toolkit. We used a fan beam and performed 360 degree scans on the kidneys and heart. Our results clearly show that when the beam was filtered to focus on the specific region (ROI) rather than the entire phantom, the energy deposited in the areas outside of the region of interest dramatically reduced which demonstrates the potential of these studies. We currently perform these studies on anatomically correct voxelized phantoms and investigate the effect on the image quality.

REFERENCES

- [1] Pearce MS, Salotti JA, Little MP, McHugh K, Lee C, Kim KP, Howe NL, Ronckers CM, Rajaraman P, Sir Craft AW, Parker L, Berrington de Gonzalez A. "Radiation exposure from CT scans in childhood and subsequent risk of leukaemia and brain tumours: a retrospective cohort study", *The Lancet* 2012.
- [2] <http://geant4.cern.ch/>

Grating Based Differential Phase Contrast CT Imaging without Mechanical Phase Stepping

Yongshuai Ge, Ke Li, John Garrett, and Guang-Hong Chen

Abstract—Grating-based x-ray differential phase contrast CT (DPC-CT) often uses a phase stepping procedure that involves sequential grating stepping and sequential x-ray exposures to achieve phase measurement. This means that the otherwise continuous CT data acquisition has to be divided into several interleaved time sequences, between which the system waits for the grating to be translated into the next phase stepping position. This also implies that the grating position can not be fixed. Considering that the grating would be potentially mounted in a fast-rotating gantry, this would add a potential source of mechanical instability. To accelerate the data acquisition speed and improve the mechanical stability of of DPC-CT, a new interferometer setup was developed and integrated into an experimental DPC-CT system. In this method, one of the gratings used in DPC-CT was divided into separate rows, each with a specially-designed offset with respect to the neighboring row. This design allows any four neighboring detector rows to achieve an effective phase stepping routine within a single x-ray exposure and at a fixed grating position. Initial phantom experiments have demonstrated that the new interferometer design can generate highly accurate DPC-CT images at the same data acquisition speed of conventional absorption CT.

I. INTRODUCTION

Grating-based x-ray differential phase contrast CT (DPC-CT) has shown promise for use in medical imaging. One potential limitation of the current implementation method is the speed of the data acquisition: a so-called phase stepping technique has been used as the standard approach to help extract x-ray phase information [1], [2]. In this method, the acquisition of each DPC projection at each projection angle is divided into several sub-acquisitions; each sub-acquisition requires one of the gratings to be moved by a fraction of the period of the x-ray diffraction pattern before an x-ray intensity measurement is performed. In the end, a total of 4 to 8 x-ray measurements are needed at each projection angle. The requirement of multiple-exposure and stop-and-move of the grating significantly decrease the data acquisition speed of DPC-CT. Further, considering the gratings must be mounted into a gantry that rotates together with the tube-detector assembly with the image object, the phase stepping routine adds a potential source of mechanical instability because the grating position can not be fixed with respect to the gantry.

To speed up the data acquisition speed of DPC-CT and improve its mechanical stability, a new DPC-CT setup with a novel grating design was developed in this work. The method enables a continuous single-shot DPC-CT data acquisition

without the need to translate the grating position and/or multiple x-ray intensity measurements. A grating interferometer system based on this new design has been fabricated and integrated into an experimental DPC-CT system at our institution, and initial physical phantom experiments have been performed for validation and performance assessment.

II. METHODS

The phase stepping procedure has been used in DPC-CT to help capture the lateral shift of the periodic interference pattern, the dimension of which is on the order of a few microns thus is much smaller than the pixel size of most x-ray detectors used in medical imaging. A partially (usually 50%) transmissive analyzer grating, commonly referred to as the G2 grating, is moved sequentially a fraction ($1/M$) of the period of the interference pattern for M times. The x-ray intensity modulations behind the G2 grating is thus low-pass filtered without loss of phase information. The result can be modeled as the following sinusoidal function with high enough accuracy to describe this intensity modulation:[1], [2]

$$I^{(k)}(x, y) = I_0(x, y) + I_1(x, y) \cos \left[2\pi \frac{k}{M} + \varphi(x, y) \right], \quad (1)$$

where I_0 denotes the DC value of the sinusoidal curve and represents the conventional absorption contrast signal, while φ denotes the DPC signal and can be extracted from $I^{(k)}$ via

$$\varphi(x, y) = \tan^{-1} \left[\frac{\sum_{k=1}^M I^{(k)}(x, y) \sin(2\pi k/M)}{\sum_{k=1}^M I^{(k)}(x, y) \cos(2\pi k/M)} \right]. \quad (2)$$

Since there are three unknowns in Eq. (1), at least three x-ray exposures acquired at three distinct phase step positions are needed to extract the phase signal. Most often, the phase stepping technique requires a relatively long time to acquire a complete dataset to perform the phase retrieval. This long time process has become one major bottleneck for the DPC-CT applications in medical imaging. Moreover, due to the movement during the data acquisition procedures, it also degrades the mechanical stability of the grating interferometer. Such instability is especially problematic for tomographic imaging systems which require the gratings to be mounted onto rotating gantries.

In this work, we report a novel interferometer design that is able to achieve single-shot data acquisition like a standard CT imaging modality. In this new design, the only modification is for the G2 grating. Figure 1 shows the schematic illustration of the new design. The idea behinds such design is to split the M phase stepping data points registered in one given detector

Y. Ge, and J. Garrett are with Department of Medical Physics, University of Wisconsin-Madison, Madison, WI

K. Li and G.-H. Chen are with Department of Medical Physics and Department of Radiology, University of Wisconsin-Madison, Madison, WI

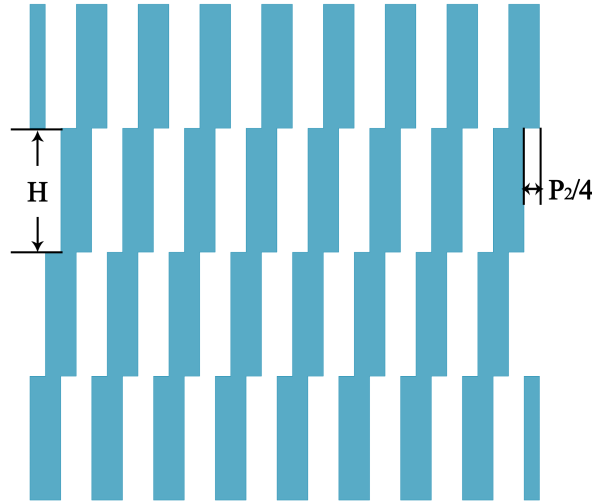


Fig. 1. Schematic illustration of the new G2 grating design. Each row has a height of H , and equal to the detector pixel width, i.e., $48 \mu\text{m}$ in our design. At the same time, each row is laterally shifted by a distance of $P_2/4$ with respect to adjacent rows, where P_2 denotes the period of the x-ray interference pattern.

pixel into M different neighboring detector pixels along the vertical direction. In other words, by using this new G2 design, we will be able to incorporate different detector rows with different phase step k .

As indicated on Figure 1, the conventional parallel-structured G2 grating was modified into a staircase structure. For our new G2 grating, we set the total number of phase steps to four, i.e., $M = 4$. Thus, each row owns a horizontal offset from one another and the lateral shift is equal to a quarter of the period of the x-ray interference fringe pattern. This design allows x-ray intensity at four neighboring detector rows to correspond to four distinct phase stepping positions. What's more, the height of every single row has the same dimension of a detector pixel, i.e., $48 \mu\text{m}$ in our design. Such small enough pixel size, in fact, would not make too much influence on the image quality.

$$\begin{aligned}
 I^{(1)}(u, v) &= I(u, v - 1), \\
 I^{(2)}(u, v) &= I(u, v), \\
 I^{(3)}(u, v) &= I(u, v + 1), \\
 I^{(4)}(u, v) &= I(u, v + 2).
 \end{aligned} \tag{3}$$

By using of this new G2 grating design, now we have to make a combination on any four adjacent detector pixels to generate a complete effective phase stepping dataset. This can be done with the help of equations in Eq. (3). Once obtained this interpolated dataset, the phase signal can be retrieved through Eq. (1). The I_0 and I_1 can all be extracted in the similar way.

A new G2 grating based on this design was fabricated and installed on our experimental DPC-CT benchtop system. The specifications of this grating are presented in Table I. The benchtop incorporates a CMOS flat panel detector with $48 \mu\text{m}$ isotropic pixel size across a 2048×1024 array (Rad-ikon Shad-o-Box 2048, Sunnyvale, CA) and a microfocus x-ray

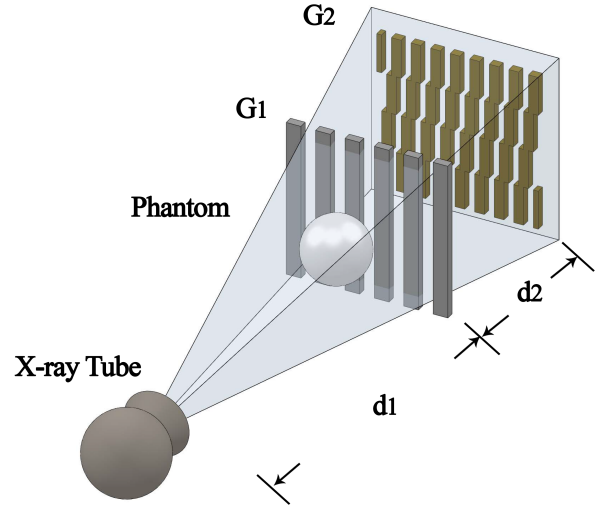


Fig. 2. DPC-CT system setup with the new G2 grating.

TABLE I
GRATING SPECIFICATIONS.

	G ₁	G ₂
Pitch (μm)	8.0	4.8
Duty cycle (%)	50	50
Depth (μm)	40	60
Size (cm^2)	7×7	5×5

tube (Hamamatsu L13021, Japan). The tube was operated at 40 kVp and $175 \mu\text{A}$. The arrangement of the experimental setups is illustrated in Fig. 2.

TABLE II
SETUP ARRANGEMENTS.

	Distance (cm)
Source to G1, d_1	108.4
G1 to G2, d_2	21.7
Source to isocenter	95.4
Source to detector	131.6

The new grating design and DPC data acquisition method was firstly validated by acquiring a DPC projection image of a physical phantom. The phantom is a polytetrafluoroethylene (PTFE) tube with an inner diameter of 9.2 mm and a wall thickness of 1.9 mm.

The second phantom we used in this verification is shown in Fig. 3. The container is made from a acrylic tube, whose outer diameter is 9.55 mm and has a wall of 1.50 mm thick. Balls with various diameters (denoted as D) are arranged into the tube which is filled with ordinary vegetable oil. From the top to the bottom, there are 10 layers:

- One Polyoxymethylene (POM) ball, $D=6.34$ mm
- Seven Polystyrene (PS) balls, $D=1.99$ mm
- one POM ball, $D=6.34$ mm

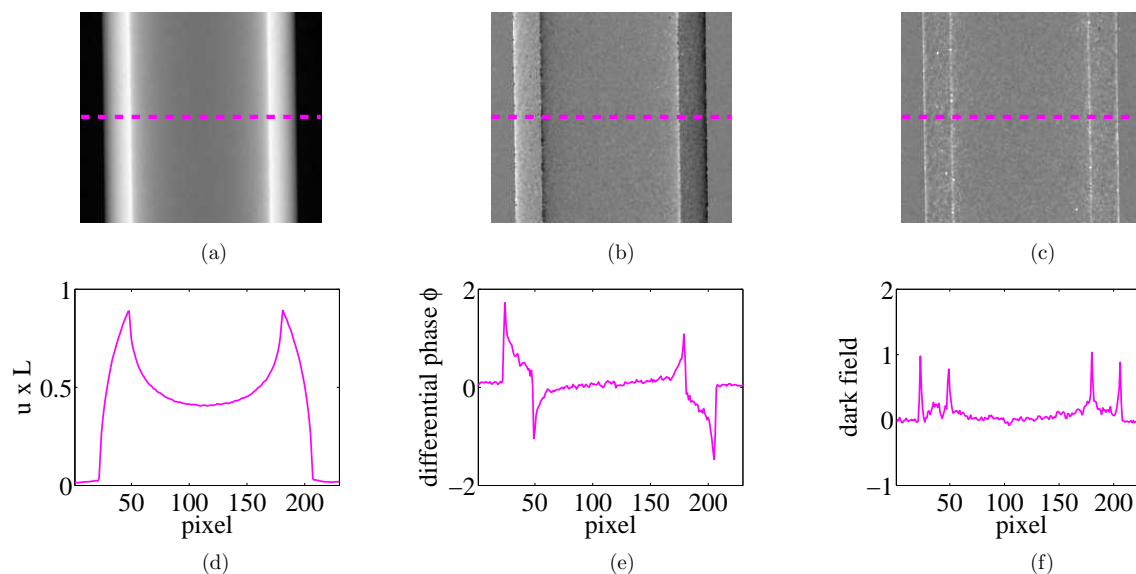


Fig. 4. Results from the PTFE tube phantom. (a) is the conventional x-ray absorption image, (b) is the differential phase contrast image, and (c) is the dark field image; (d)-(f) are measured line profiles corresponding to each image.

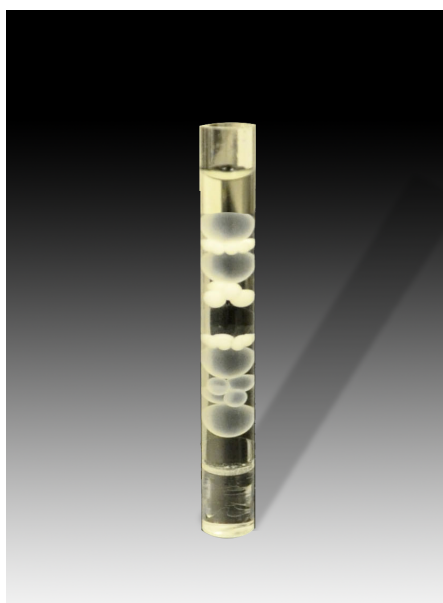


Fig. 3. Photo of the physical phantom scanned during the experiment. There are 28 spheres soaked in oil.

- Four PS balls, $D=3.18$ mm
- One acrylic ball, $D=6.34$ mm
- Seven PS balls, $D=1.99$ mm
- One POM ball, $D=6.34$ mm
- Four POM balls, $D=3.18$ mm
- One POM, $D=6.34$ mm
- One acrylic ball, $D=6.34$ mm

Visually, the POM material is most opaque, the PS material is in the middle, and acrylic is the most transparent medium.

III. RESULTS

Figure 4 shows absorption contrast, DPC, and dark field projection images of the PTFE tube acquired using the new G2 grating. A single x-ray exposure was adequate to generate these images. Figure 5-6 show CT images of the second phantom. These results show that the new grating can successfully generate CT image with three different contrast mechanisms.

IV. SUMMARY AND CONCLUSIONS

In this study, an x-ray differential phase contrast imaging method with a new grating interferometer design was developed to achieve DPC-CT imaging without mechanical phase stepping. This method removes the need for performing multiple exposures at each projection view thus removes the technique hurdle that prevents DPC-CT from achieving the same data acquisition speed of conventional x-ray absorption CT. More importantly, this method allows all of the gratings used in DPC-CT to stay static relative to the tube-detector assembly, therefore it should significantly improve the mechanical stability of the x-ray interferometer. This is particularly meaningful for CT acquisitions that requires the gratings to be mounted into a high-speed rotary gantry. Due to these advantages, this method is expected to greatly facilitate DPC-CT imaging's translation into clinical applications.

REFERENCES

- [1] A. Momose, S. Kawamoto, I. Koyama, Y. Hamaishi, H. Takai, and Y. Suzuki, "Demonstration of x-ray Talbot interferometry," *Jpn. J. Appl. Phys., Part 2* **42**(7B), pp. 866–8, 2003.
- [2] T. Weitkamp, A. Diaz, C. David, F. Pfeiffer, M. Stampanoni, P. Cloetens, and E. Zeigler, "X-ray phase imaging with a grating interferometer," *Opt. Exp.* **12**(16), pp. 6296–304, 2005.

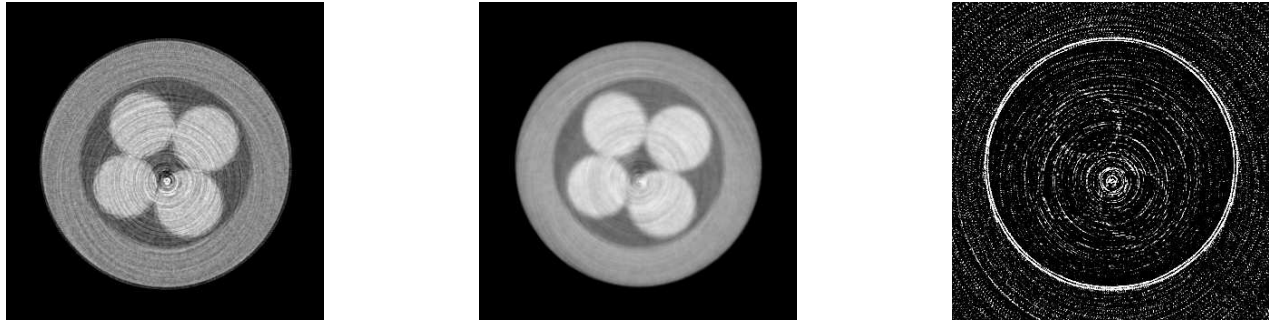


Fig. 5. Axial images of the top fourth PS layer of the second phantom. From the left to right, they are the absorption image with display range of $[0.07, 0.03]$, the phase image with display range of $[3.85, 3.21] \times 10^{-7}$, and the dark field image with display range of $[0.30, 0.20]$.

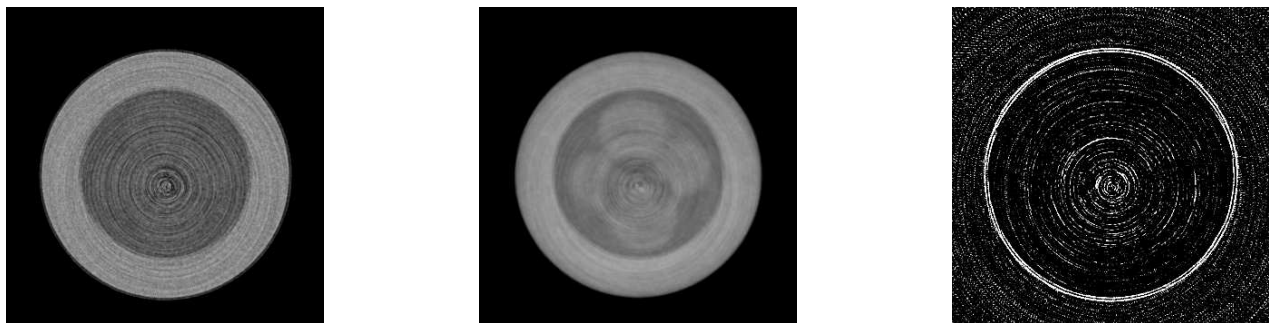


Fig. 6. Axial images of the bottom POM layer of the second phantom. From the left to right, they are the absorption image with display range of $[0.07, 0.03]$, the phase image with display range of $[3.85, 3.21] \times 10^{-7}$, and the dark field image with display range of $[0.30, 0.20]$.

X-ray phase-contrast computed tomography in helical mode without phase stepping

Mathias Marschner, Marian Willner, Julia Herzen, Peter B. Noël and Franz Pfeiffer

Abstract—Grating-based X-ray phase-contrast computed tomography has gained significant attention in recent years due to the fact that it can be used with incoherent, polychromatic sources. However, phase-contrast CT measurements still require longer measurement time compared to conventional CT. This is mainly a result of the need to perform a stepping of the gratings to obtain the phase information. Several methods have been proposed to increase measurement speed and to circumvent the need for a phase stepping procedure, e.g. Moirée fringe scanning. In this method the object is scanned over Moirée fringes in the interferogram to sample a stepping curve. We extend this method to the tomographic case which enables a continuous helical acquisition without stepping the gratings. A helical movement along the tomographic axis is used to simultaneously rotate the sample and scan over the Moirée fringes. We present first experimental results of this helical fringe-scanning phase-contrast CT.

I. INTRODUCTION

X-ray computed tomography is a widely used tool for medical and industrial applications including clinical diagnosis. Phase sensitive X-ray techniques are an interesting alternative method for imaging weakly absorbing materials. There, the linear attenuation coefficient is small compared to the refractive index decrement. The refraction is responsible for changes in the phase of the X-ray waves. Consequently, better image quality and contrast can be achieved when using phase information [1]. Several methods for phase-contrast imaging have been developed and some have been transferred to conventional laboratory-based X-ray tube sources.

Grating interferometry relies on transmission gratings in the X-ray beam and enables high sensitivity phase measurements even with laboratory sources [2]. Several studies explore the possible benefit of using this method for biomedical imaging [3].

In many applications, fast image acquisition is of great importance. So far, acquisition times with phase-contrast CT are long compared to conventional attenuation-based CT. The prevailing measurement procedure relies on translation of one of the gratings. This so called phase stepping procedure is a limiting factor in the reduction of the acquisition time. Further, the need for precise translation of the gratings implies a demanding stability condition. Additionally, a continuous motion of a rotating gantry is impossible if a phase stepping has to be done for each projection.

Mathias Marschner, Marian Willner and Franz Pfeiffer are with the Chair of Biomedical Physics & IMETUM, Technische Universität München, 85748 Garching, Germany.

Julia Herzen is with the Institute of Materials Research, Helmholtz-Zentrum Geesthacht, 21502 Geesthacht, Germany

Peter B. Noël is with the Department of Radiology, Technische Universität München, 81675 München, Germany

In medical CT systems a helical scanning procedure is used to extend the field of view and reduce measurement time [4]. There are first theoretical and simulation studies on helical scanning procedures for PCCT [5], [6], [7]. However, none of these methods eliminate the need for a phase stepping for each single projection. Recently, several procedures were proposed to circumvent this need for a phase stepping at each rotation step. Interlaced phase stepping [8] combines rotation step and phase step. This way, a continuous rotation is possible. However, the gratings still need to be moved which implies the same stability conditions as a normal phase stepping procedure. Also, the translation of the grating is of limited speed and accuracy and therefore limits rotation speed and image quality.

Fringe analysis is one approach that can be used to retrieve the phase without the need of a phase stepping procedure. However, the disadvantage of single-shot approaches of this kind is a decrease in spatial resolution [9].

The reverse projection method [10] also enables phase retrieval without the need of a stepping procedure. This is achieved by a linear approximation of the stepping curve at the steepest point. However, this entails that the retrieved phase is only correct for small values what effectively decreases the dynamic range of the system. Also, to obtain both absorption and phase-contrast information, two interferograms at opposing angles have to be recorded, so a scan over 360 degrees is needed. An interferogram is the raw image recorded by the detector containing the information that arises due to the interference of the X-rays. Furthermore, the dark-field signal cannot be simultaneously obtained by this method. A similar approach [11] reconstructs a combined image containing information both from attenuation and refraction also from only one interferogram. However, it does not allow to obtain separate maps of the absorption and refraction of the measured object.

One could imagine to record a full stepping curve without moving the gratings by use of a scanning setup [12]. Here, the gratings are fixed while the sample is moved. A deliberate misalignment of the gratings G_1 and G_2 (mismatch of inter grating distance $d' = d + \Delta d$) leads to Moirée fringes. These correspond to a spatially dependent intensity profile on the detector. In a phase stepping configuration the image would ideally be uniform and change its intensity dependent on the relative grating positions. Therefore, different positions on the detector correspond to different relative positions of the gratings in a traditional phase stepping approach. When combining these different areas a stepping curve can be obtained as illustrated in fig. 1. Here, the sample is moved over different detector positions instead of a translation of the gratings.

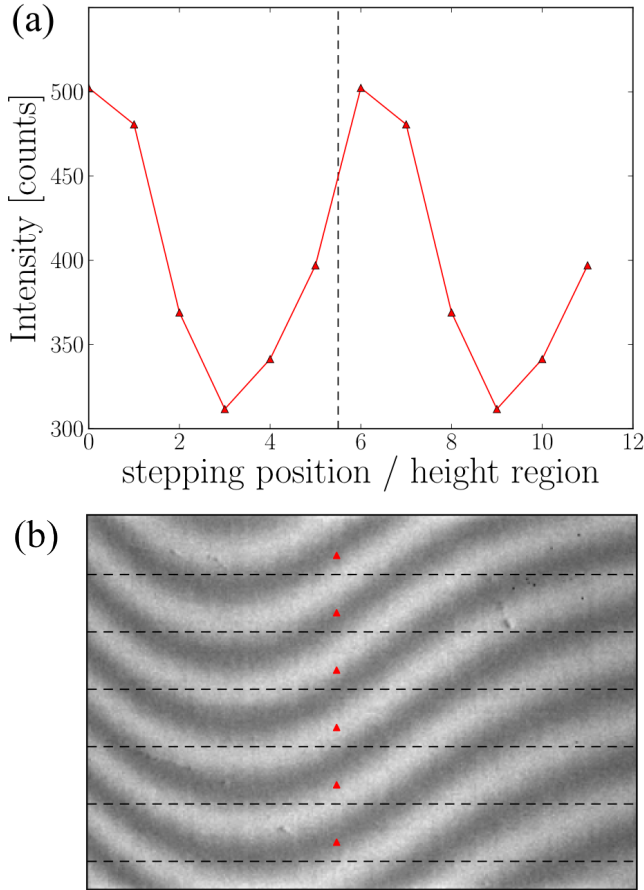


Fig. 1. The interferogram (b) shows Moiré fringes introduced by deliberate mismatch of the relative position of G_1 and G_2 . A stepping curve can be obtained by combining the height regions, marked by dashed lines. (a) shows an exemplary stepping curve that is obtained by using the pixels marked by red triangles.

Thereby, the same region of the sample is recorded at different fringe phases. This way, a stepping is performed without translating the gratings and a differential phase projection can be obtained.

In contrast to the single-shot techniques, the full information that is available with a phase stepping scan is also obtained with the scanning method. The need to translate the gratings with a precision of fractions of the grating pitch is eliminated. Note, a precision to a fraction of $5 \mu\text{m}$ is necessary. The movement of the sample only needs to be precise to pixel sizes which range from $50 \mu\text{m}$ for mammography systems to over $500 \mu\text{m}$ for clinical CT systems. Therefore, the requirement for precision of the essential stepping movement is relaxed. Additionally, the field of view of such a system is not limited by the size of the gratings or the detector. Recently, a commercial mammography system was converted to a grating interferometry system [13] using the described fringe scanning approach. It features multiple commercially available gratings and several line detectors. However, the sample still needs to be recorded at least three times to obtain a stepping curve.

We propose a method to extend the scanning setup to

the tomographic case, where the translation of the sample is achieved by a helical motion of the tomographic axis. With our proposed method a continuous helical rotation of the sample or the gantry can be used, because no stepping of the gratings is needed. As explained earlier, this increases the measurement speed and is also beneficial for the stability of the system. In contrast to single-shot techniques, there is no inherent loss in resolution. Further, due to the scanning approach the field of view is extended in vertical direction which enables the imaging of objects larger than the field of view of the system.

II. HELICAL PHASE SCANNING

A scanning-type system similar to the one in [12] is realized by upward motion of the tomographic axis during rotation. The pitch is defined by the upwards movement per detector height and slice thickness:

$$p = \frac{\Delta h}{H}, \quad (1)$$

with Δh being the upwards movement per rotation and H the detector height. The number of helical rotations corresponds to the number of phase steps M that are recorded for each slice. For each angle, the same slice has to be in the field of view at least three times, each at a different fringe phase. That means that the pitch has to be lower than $p \leq 1/3$. To be able to use a standard processing algorithm, a full period of the stepping curve has to be sampled at equidistant positions. Therefore, the vertical movement per rotation is dependent on the period of the Moiré fringes in the interferogram, or vice versa. After $M + 1$ rotations, the phase of the Moiré fringe has to be the same as before the first rotation. This leads to the fact that the period P of the fringes has to be

$$P = \frac{M + 1}{k} \Delta h, \quad (2)$$

with k being the number of fringes in the interferogram.

III. EXAMPLE AND APPLICATION

A. Grating interferometer setup

A Talbot-Lau interferometer was used to experimentally test the proposed method. It consists of three gratings G_0 , G_1 , and G_2 made out of gold with periods of $5.4 \mu\text{m}$. The absorption gratings G_0 and G_2 have a height of 60 to $70 \mu\text{m}$. The phase grating G_1 was designed to give a phase shift of π at 27 keV and has a height of $5.2 \mu\text{m}$. The setup was operated in a symmetric configuration with inter grating distances of $\overline{G_0 G_1} = \overline{G_1 G_2} = 85.70 \text{ cm}$. The X-rays are generated by a ENRAF Nonius rotating anode X-ray tube with a Molybdenum target which is operated at 40 kVp and 70 mA . A PILATUS II single photon counting detector by *Dectris*, Switzerland was utilized. It features a field of view of 487×195 pixels with a pixel size of $172 \times 172 \mu\text{m}^2$. The measured phantom consists of three plastic rods of PMMA, LDPE and POM respectively, each with a diameter of approximately 6 mm . They were measured in a tube with a diameter of 3 cm , filled with water which was itself put in a water bath to avoid phase wrapping artifacts.

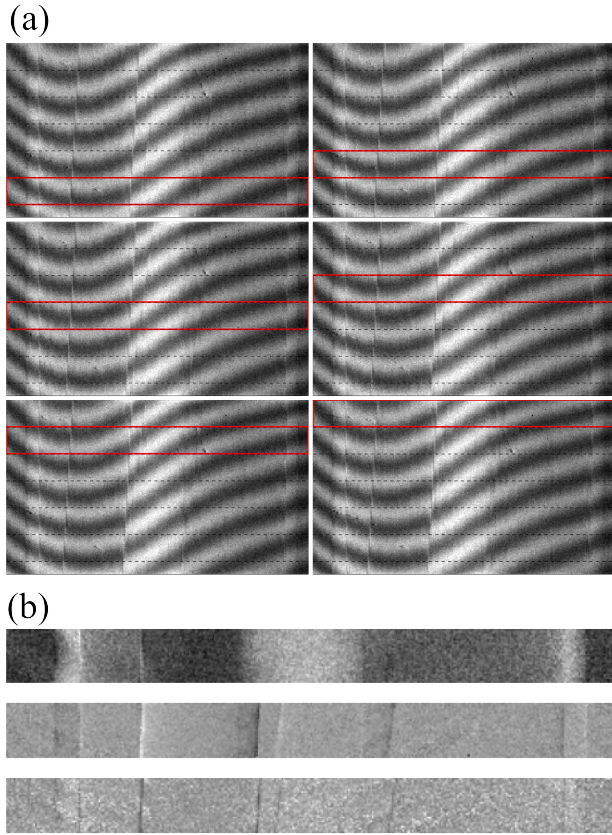


Fig. 2. Six interferograms (a), each recorded at the same angle but at different heights because of the helical movement, are combined to obtain a phase stepping. The areas marked with a red box are used to obtain a transmission, differential phase and dark-field projection (b, from top to bottom). The complementarity between attenuation- and phase-contrast is clearly visible: the LDPE rod in between the POM and PMMA rod has a low refractive index but a high linear attenuation coefficient.

B. Helical phase scanning setup

In our experiment, the period of the Moiré fringes is approximately 35 pixels. The Moiré fringes were tuned by intentionally misaligning the gratings G_1 and G_2 . An upward movement per rotation of $\Delta h = 30$ px was used to sample one period of the stepping curve over the course of $M = 6$ rotations. That means that the sample was moved upwards by 0.05 pixels after each interferogram. Figure 2 shows interferograms recorded for each rotation at the same angle. The sample is moved upwards during the rotation step. Additionally, flat-fields, which are projections without the sample, are recorded after each rotation. These are necessary because of drifts of the phase of the Moiré pattern induced by temperature changes in the gratings. More advanced processing algorithms could remove the need to record flatfields during the measurement, e.g. by tracking the drift of the fringes in areas without sample.

The regions of interest that are combined to one stepping series are indicated by red boxes. Standard processing in form of a least-squares fit is used to extract the attenuation, differential phase and dark-field projections.

The exposure time for each interferogram was 1 s and therefore 6 s for each projection. During the tomographic scan

600 projections were recorded for each rotation. Each region of the sample has to be imaged $M = 6$ times, therefore the number of rotations needed and with that the total exposure time depends on the size of the sample. Also, in the rotations at the beginning and in the end, only part of the sample is in the field of view, if the detector is not moved together with the sample. Consequently, $M - 1$ additional rotations are needed to scan the whole sample. If the sample is larger than the field of view of the detector, more rotations are necessary leading to a longer total exposure time for the sample. However, each region of the sample has a fixed exposure time of $t_{total} = MN_{\theta}t$. In this experiment this total exposure time was 1 hour.

The height of the detector used is $H \times s = 195$ pixels, therefore the pitch is $p \approx 0.15$. After 6 rotations, only $M\Delta h = 6 \times 30$ pixels = 180 pixels of the detector have been used. This is due to the constraint that a complete stepping curve has to be sampled. Thus, an integer multiple of fringes has to be in the region of $M + 1$ rotations. With a fringe period of 35 pixels and $M = 6$ rotations, this leads to an active area of 180 px. To use the whole detector for imaging, the fringe period needs to be tuned to fit the height of the detector:

$$kP = (M + 1)\Delta h. \quad (3)$$

Due to grating imperfections and polychromatic sources this can be a challenging task.

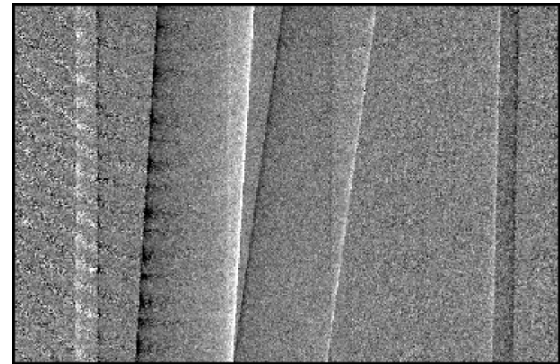


Fig. 3. The projections obtained from the combination of the height regions can then be assembled to form a full projection that is even larger than the field of view of the system. The non-uniform period of the fringes in with standard processing algorithms lead to remaining fringes in the projections. They are also visible in the differential phase projection shown here.

C. Experimental results

Figure 3 shows the differential phase projection of the measured phantom consisting of three plastic rods. As indicated in fig. 2, $M = 6$ phase steps were taken from six projections recorded at the same angle but after increasing number of rotations and therefore different heights. These were then combined to form a phase stepping series. Standard processing was used to extract the attenuation, differential phase and darkfield projections. The size of the retrieved projections is 365×240 pixels. In principle, there is no limit on the vertical size of the sample scanned. Just one additional rotation is

needed when the size of the sample increases by Δh . As a result, the limited vertical field of view of the detector and the gratings is overcome.

Imperfect and inhomogeneous gratings lead to non-uniform fringes over the field of view. This does not disturb the quality of the projections as long as the period of the fringes is constant over the whole interferogram. But in the case of our experiment, the fringe period is smaller in the left part of the interferograms than in the middle and in the right part. Therefore, in this region, the sampled stepping curve is not of exactly one period. Standard processing then leads to an error that is dependent on the fringe phase of the interferogram. This results in remaining fringes in the differential phase projections as visible in the left part of the processed differential phase projection shown in fig. 3. It was not possible to achieve a more homogeneous distribution of the fringes with the available gratings. Future grating from improved fabrication processes may be more homogeneous which will make alignment procedure less challenging. Also, more advanced processing methods are able to retrieve the phase information correctly even from not completely sampled stepping curves.

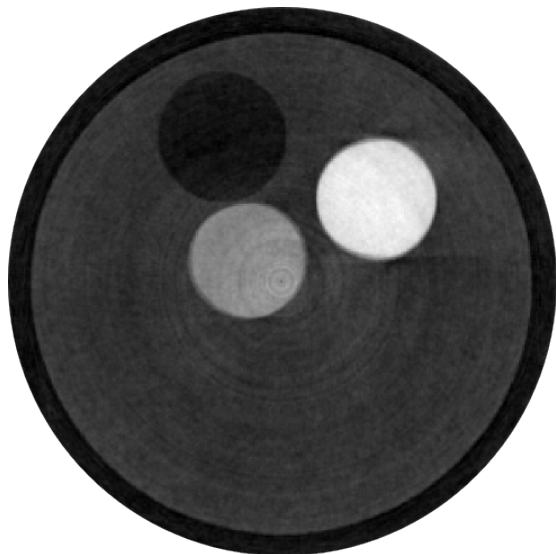


Fig. 4. The acquired differential phase projections can be used to reconstruct the distribution of the refractive index decrement of the measured sample. This figure shows an axial slice of the tomographic reconstruction. The three phantom materials (POM, PMMA and LDPE in descending intensity) are clearly visible.

The combined and processed projections were then used for a tomographic reconstruction. First, the vertical displacement of the projections due to the helical motion was corrected. Then, standard filtered backprojection in combination with a Hilbert filter kernel was used to reconstruct the distribution of the refractive index decrement. Figure 4 shows an axial slice of the tomographic reconstruction of the measured sample. The three plastic rods are clearly visible in the tube filled with water. There are visible ring artefacts that arise due to inhomogeneous gratings and detector response. These are not caused by the helical measurement procedure and also occur

in traditional phase-stepping acquisitions.

IV. CONCLUSION

It was shown that using a helical motion to scan over different areas of the fringe pattern a phase stepping can be performed. This procedure simultaneously yields conventional attenuation, differential phase and dark-field projections. Further, it was illustrated that this technique can be applied to tomographic scans using a grating interferometer without the need for the translation of the gratings. With fixed gratings the stability of the system is less critical. Due to the fact that no stepping procedure is necessary, the acquisition time is only limited by the exposure time. In traditional phase stepping acquisitions, the speed of the stepping motors is a limiting factor. A continuous rotation is enabled for sufficiently short exposure times. Additionally, the scanning nature of this method enables imaging of larger samples without the need for larger area gratings and detectors. In conclusion, this is an important step towards industrial and clinical application of grating-based phase-contrast computed tomography.

REFERENCES

- [1] A. Momose, "Recent Advances in X-ray Phase Imaging," *Japanese Journal of Applied Physics*, vol. 44, pp. 6355–6367, Sept. 2005.
- [2] F. Pfeiffer, T. Weitkamp, O. Bunk, and C. David, "Phase retrieval and differential phase-contrast imaging with low-brilliance X-ray sources," *Nature Physics*, vol. 2, pp. 258–261, Mar. 2006.
- [3] F. Pfeiffer, J. Herzen, M. Willner, M. Chabior, S. Auweter, M. Reiser, and F. Bamberg, "Grating-based X-ray phase contrast for biomedical imaging applications.," *Zeitschrift für medizinische Physik*, vol. 23, pp. 176–85, Sept. 2013.
- [4] W. Kalender, "Technical foundations of spiral CT.," *Seminars in ultrasound, CT, and MR*, vol. 15, no. 2, pp. 81–89, 1994.
- [5] Z. Qi, P. Thériault-Lauzier, N. Bevins, J. Zambelli, K. Li, and G.-H. Chen, "Helical x-ray differential phase contrast computed tomography," *Proc. of SPIE*, vol. 7961, pp. 79611Q–79611Q–6, Mar. 2011.
- [6] J. Li, P. Zhu, and Y. Sun, "An approximate reconstruction method for helical cone-beam differential phase-contrast computed tomography images.," *Physics in medicine and biology*, vol. 57, pp. 2347–56, Apr. 2012.
- [7] J. Fu, M. Willner, L. Chen, R. Tan, K. Achterhold, M. Bech, J. Herzen, D. Kunka, J. Mohr, and F. Pfeiffer, "Helical differential X-ray phase-contrast computed tomography," *Physica Medica*, Feb. 2014.
- [8] I. Zanette, M. Bech, A. Rack, G. Le Duc, P. Tafforeau, C. David, J. Mohr, F. Pfeiffer, and T. Weitkamp, "Trimodal low-dose X-ray tomography.," *Proceedings of the National Academy of Sciences of the United States of America*, vol. 109, pp. 10199–204, June 2012.
- [9] H. Wen, E. E. Bennett, M. M. Hegedus, and S. Rapacchi, "Fourier X-ray scattering radiography yields bone structural information.," *Radiology*, vol. 251, pp. 910–8, June 2009.
- [10] P. Zhu, K. Zhang, Z. Wang, Y. Liu, X. Liu, Z. Wu, S. A. McDonald, F. Marone, and M. Stampanoni, "Low-dose, simple, and fast grating-based X-ray phase-contrast imaging," *Proceedings of the National Academy of Sciences of the United States of America*, vol. 107, no. 31, pp. 13576–13581, 2010.
- [11] P. C. Diemoz, P. Coan, I. Zanette, a. Bravin, S. Lang, C. Glaser, and T. Weitkamp, "A simplified approach for computed tomography with an X-ray grating interferometer.," *Optics express*, vol. 19, pp. 1691–8, Jan. 2011.
- [12] C. Kottler, F. Pfeiffer, O. Bunk, C. Grunzweig, and C. David, "Grating interferometer based scanning setup for hard x-ray phase contrast imaging," *Review of Scientific Instruments*, vol. 78, no. 4, p. 043710, 2007.
- [13] E. Roessl, H. Daerr, T. Koehler, G. Martens, and U. van Stevenaal, "Clinical boundary conditions for grating-based differential phase-contrast mammography," *Philosophical Transactions of the Royal Society A: Mathematical, Physical and Engineering Sciences*, vol. 372, Mar. 2014.

Fast Splitting-Based Ordered-Subsets X-Ray CT Image Reconstruction

Hung Nien and Jeffrey A. Fessler

Abstract—Using non-smooth regularization in X-ray computed tomography (CT) image reconstruction has become more popular these days due to the recent resurgence of the classic augmented Lagrangian (AL) methods in fields such as total-variation (TV) denoising and compressed sensing (CS). For example, undersampling projection views is one way to reduce radiation dose in CT scans; however, this causes strong streak artifacts in FBP images that degrade image quality. To overcome this problem, the split Bregman (SB) method, an alias of the AL method in the context of ℓ_1 -regularized image reconstruction problems, has been investigated using strong non-smooth TV and sparsity regularizations. Unfortunately, existing SB-based methods are slow due to the iterative updates for the challenging inner least-squares problem. This paper proposes to solve X-ray CT image reconstruction problems with TV or sparsity regularization using a splitting-based ordered-subsets (OS) algorithm, split OS-LALM, and evaluates the proposed algorithm using a few-view X-ray CT image reconstruction problem with TV regularization. Experimental results show that the proposed algorithm significantly accelerates the convergence of X-ray CT image reconstruction with non-smooth TV regularization over the standard (linearized) SB method and demonstrates the effectiveness of OS acceleration with splitting-based algorithms.

I. INTRODUCTION

X-ray computed tomography (CT) is a non-invasive medical procedure that images the attenuation properties, such as the density distribution, of the body. It is incredibly useful and important in the medical community, while the growing concern about radiation dose from CT scans comes from the increased use of CT procedures. In the past three decades, the average American's dose from medical exposure (not including radiotherapy) has increased from 0.54 mSv in 1982 to 3.0 mSv in 2006, where CT procedures account for about half of the collective dose from all medical procedures [1]. Compared with the natural background yearly dose of 3.6 mSv, the standard radiation dose used currently can increase the possible risk of cancers, especially for body screening with multiple scans.

Using fewer projection views in a CT scan is one way to reduce radiation dose, but such undersampling causes strong streak artifacts that degrade FBP image quality. To reduce streak artifacts, the split Bregman (SB) method [2], a fast convex optimization method using variable splitting technique, has been investigated using total-variation (TV) and sparsity regularizations. Unfortunately, existing SB-based

methods for few-view CT image reconstruction, especially for 3D CT, can be slow due to the challenging inner least-squares problem with a highly shift-variant Hessian [3–5]. For example, [3] suggested solving the inner least-squares problem of the SB method using up to 100 iterations of the conjugate gradient (CG) method, that is, hundreds of forward/back-projection pairs for a single outer-loop image update! Although the forward/back-projection operations in few-view CT are less time-consuming than in clinical CT, using hundreds of forward/back-projection pair for a single image update remains undesirable.

To solve the problem of the difficult inner least-squares problem in SB methods, Ramani *et al.* [6] introduced an additional auxiliary variable that separates the shift-variant and approximate shift-invariant parts of the statistically weighted quadratic data-fitting term so that one can find an appropriate circulant preconditioner for the better-conditioned inner problem and solve the inner problem efficiently using the preconditioned conjugate gradient (PCG) method. The acceleration is significant in 2D CT [6]; however, in 3D CT, due to the cone-beam geometry, it is much harder to find a good preconditioner for the inner least-squares problem, and the method in [6] has yet to achieve the same acceleration as in 2D CT.

Considering the same variable splitting scheme as in [6], this paper proposes to solve X-ray CT image reconstruction problem with TV or sparsity regularization using a linearized augmented Lagrangian (AL) method [7, 8] that replaces the difficult inner least-squares problem by a simple majorization-minimization procedure (a gradient descent that guarantees monotone decreasing of the cost value) and more importantly, is suitable for ordered-subsets (OS) [9] acceleration. For instance, suppose M ordered subsets are used for acceleration. The proposed splitting-based OS algorithm takes roughly $1/M$ forward/back-projection pair for a single image update! Therefore, compared with existing SB methods, we perform many more image updates in a given reconstruction time, leading to faster convergence.

The remainder of the paper is organized as follows. Section II introduces the problem formulation and derives the proposed splitting-based OS algorithm for solving regularized least-squares problems. Section III considers solving few-view X-ray CT image reconstruction problem with penalized weighted least-squares (PWLS) criterion using the proposed algorithm and reports the experimental results comparing a linearized SB method with our method. Finally, we draw conclusions in Section IV.

H. Nien and J. A. Fessler are with the Department of Electrical Engineering and Computer Science, University of Michigan, Ann Arbor, MI 48105, USA. This work is supported in part by NIH grant R01-HL-098686 and by an equipment donation from Intel Corporation. The authors thank GE Healthcare for providing sinogram data in our experiments.

II. PROPOSED METHOD

A. Split OS-LALM: OS-LALM with an additional split

Consider a regularized least-squares problem:

$$\hat{\mathbf{x}} \in \arg \min_{\mathbf{x} \in \Omega} \left\{ \frac{1}{2} \|\mathbf{y} - \mathbf{A}\mathbf{x}\|_2^2 + \Phi(\Theta\mathbf{x}) \right\}, \quad (1)$$

where \mathbf{A} is the system matrix, \mathbf{y} is the noisy measurement, Θ is an analysis regularization matrix, Φ is some convex (and possibly non-smooth) potential function, and Ω denotes the convex set for a box constraint (usually the non-negativity constraint) on \mathbf{x} . For example, in (anisotropic) TV-regularized image restoration problems, Θ is a finite difference matrix, and Φ is an ℓ_1 norm, probably with some weighting. The minimization problem (1) is non-trivial in general since Θ might not be an identity matrix, and Φ can be non-smooth. One typical way to solve this problem is to use the SB method [2] that introduces an auxiliary variable for the vector $\Theta\mathbf{x}$ and decomposes the convex optimization problem into a series of simpler penalized least-squares problems. However, when $\mathbf{A}'\mathbf{A}$ is highly shift-variant, the SB method can be slow due to the iterative inner updates.

To develop a faster algorithm, instead of solving (1) using the SB method, we consider solving an equivalent constrained minimization problem:

$$\begin{aligned} (\hat{\mathbf{x}}, \hat{\mathbf{u}}, \hat{\mathbf{v}}) \in \arg \min_{\mathbf{x}, \mathbf{u}, \mathbf{v}} \{g(\mathbf{u}) + \Phi(\mathbf{v}) + \iota_\Omega(\mathbf{x})\} \\ \text{s.t. } \mathbf{u} = \mathbf{A}\mathbf{x}, \mathbf{v} = \Theta\mathbf{x} \end{aligned} \quad (2)$$

using the linearized AL method [7, 8]:

$$\begin{cases} \mathbf{x}^{(k+1)} \in \arg \min_{\mathbf{x}} \left\{ \iota_\Omega(\mathbf{x}) + \check{\theta}_k(\mathbf{x}; \mathbf{x}^{(k)}) + \check{\phi}_k(\mathbf{x}; \mathbf{x}^{(k)}) \right\} \\ \mathbf{u}^{(k+1)} \in \arg \min_{\mathbf{u}} \left\{ g(\mathbf{u}) + \frac{\rho}{2} \|\mathbf{A}\mathbf{x}^{(k+1)} - \mathbf{u} - \mathbf{d}^{(k)}\|_2^2 \right\} \\ \mathbf{v}^{(k+1)} \in \arg \min_{\mathbf{v}} \left\{ \Phi(\mathbf{v}) + \frac{\eta}{2} \|\Theta\mathbf{x}^{(k+1)} - \mathbf{v} - \mathbf{e}^{(k)}\|_2^2 \right\} \\ \mathbf{d}^{(k+1)} = \mathbf{d}^{(k)} - \mathbf{A}\mathbf{x}^{(k+1)} + \mathbf{u}^{(k+1)} \\ \mathbf{e}^{(k+1)} = \mathbf{e}^{(k)} - \Theta\mathbf{x}^{(k+1)} + \mathbf{v}^{(k+1)}, \end{cases} \quad (3)$$

where $g(\mathbf{u}) \triangleq \frac{1}{2} \|\mathbf{y} - \mathbf{u}\|_2^2$, ι_Ω is the characteristic function of the convex set Ω that handles the box constraint on \mathbf{x} , \mathbf{d} and \mathbf{e} are the scaled Lagrange multipliers of the split variables \mathbf{u} and \mathbf{v} , respectively, and $\rho > 0$ and $\eta > 0$ are the corresponding AL penalty parameters. The functions $\check{\theta}_k(\mathbf{x}; \mathbf{x}^{(k)})$ and $\check{\phi}_k(\mathbf{x}; \mathbf{x}^{(k)})$ are two separable quadratic surrogate (SQS) functions that majorize the quadratic AL penalty terms

$$\theta_k(\mathbf{x}) \triangleq \frac{\rho}{2} \|\mathbf{A}\mathbf{x} - \mathbf{u}^{(k)} - \mathbf{d}^{(k)}\|_2^2 \quad (4)$$

and

$$\phi_k(\mathbf{x}) \triangleq \frac{\eta}{2} \|\Theta\mathbf{x} - \mathbf{v}^{(k)} - \mathbf{e}^{(k)}\|_2^2 \quad (5)$$

at $\mathbf{x} = \mathbf{x}^{(k)}$, respectively. Let L_1 and L_2 denote the maximum eigenvalues of $\mathbf{A}'\mathbf{A}$ and $\Theta'\Theta$, respectively, it follows that

$$\begin{cases} \check{\theta}_k(\mathbf{x}; \mathbf{x}^{(k)}) \\ \propto \frac{\rho}{2t_1} \|\mathbf{x} - (\mathbf{x}^{(k)} - t_1\mathbf{A}'(\mathbf{A}\mathbf{x}^{(k)} - \mathbf{u}^{(k)} - \mathbf{d}^{(k)}))\|_2^2 \\ \check{\phi}_k(\mathbf{x}; \mathbf{x}^{(k)}) \\ \propto \frac{\eta}{2t_2} \|\mathbf{x} - (\mathbf{x}^{(k)} - t_2\Theta'(\Theta\mathbf{x}^{(k)} - \mathbf{v}^{(k)} - \mathbf{e}^{(k)}))\|_2^2, \end{cases} \quad (6)$$

where $t_1 \triangleq 1/L_1$ and $t_2 \triangleq 1/L_2$. The majorizations remove the entanglement of \mathbf{x} introduced by \mathbf{A} and Θ , leading to simple inner updates in (3) using proximal mappings.

As can be seen in (3), introducing an additional split variable \mathbf{v} only modestly changes the updates from the one-split linearized AL iterates [7, 8]. Letting $h_k \triangleq \iota_\Omega + \check{\phi}_k$, the two-split linearized AL iterates (3) become the one-split linearized AL iterates with an iteration-dependent regularization term h_k , where the effect of h_k is fully determined by the \mathbf{v} - and \mathbf{e} -updates in (3)! Hence, we can easily rewrite the two-split linearized AL iterates (3) to the two-split gradient-based linearized AL iterates:

$$\begin{cases} \mathbf{s}^{(k+1)} = \rho \nabla \ell(\mathbf{x}^{(k)}) + (1 - \rho) \mathbf{g}^{(k)} \\ \mathbf{x}^{(k+1)} \in \text{prox}_{(\rho^{-1}t_1)h_k}(\mathbf{x}^{(k)} - (\rho^{-1}t_1) \mathbf{s}^{(k+1)}) \\ \mathbf{g}^{(k+1)} = \frac{\rho}{\rho+1} \nabla \ell(\mathbf{x}^{(k+1)}) + \frac{1}{\rho+1} \mathbf{g}^{(k)} \\ \mathbf{v}^{(k+1)} \in \text{prox}_{\eta^{-1}\Phi}(\Theta\mathbf{x}^{(k+1)} - \mathbf{e}^{(k)}) \\ \mathbf{e}^{(k+1)} = \mathbf{e}^{(k)} - \Theta\mathbf{x}^{(k+1)} + \mathbf{v}^{(k+1)}, \end{cases} \quad (7)$$

where ℓ denotes the quadratic data-fitting term in (1), and prox_f denotes the proximal mapping of f defined as:

$$\text{prox}_f(\mathbf{z}) \triangleq \arg \min_{\mathbf{x}} \left\{ f(\mathbf{x}) + \frac{1}{2} \|\mathbf{x} - \mathbf{z}\|_2^2 \right\}. \quad (8)$$

Since both ι_Ω and $\check{\phi}_k$ are separable, the \mathbf{x} -update of the two-split gradient-based linearized AL iterates (7) has a closed-form solution:

$$\mathbf{x}^{(k+1)} = \left[\mathbf{x}^{(k)} - \frac{1}{\rho L_1 + \eta L_2} (\mathbf{s}^{(k+1)} + \boldsymbol{\sigma}^{(k+1)}) \right]_\Omega, \quad (9)$$

where $[\cdot]_\Omega$ denotes an operator that projects a vector onto Ω , and

$$\boldsymbol{\sigma}^{(k+1)} \triangleq \eta \Theta' (\Theta\mathbf{x}^{(k)} - \mathbf{v}^{(k)} - \mathbf{e}^{(k)}) \quad (10)$$

is the search direction attributed to the regularization term. Finally, the two-split gradient-based linearized AL method (7) is an extension of the one-split gradient-based linearized AL method, so we can accelerate it by using OS and the deterministic downward continuation approach proposed in [7, 8]. For the OS version, we replace the gradients in (7) with the subset gradients $M\nabla \ell_m$ for $m = 1, \dots, M$, where ℓ_1, \dots, ℓ_M are M smaller quadratic functions that satisfy $\ell = \ell_1 + \dots + \ell_M$ and the ‘‘subset balance condition’’ [9]:

$$\nabla \ell(\mathbf{x}) \approx M\nabla \ell_1(\mathbf{x}) \approx \dots \approx M\nabla \ell_M(\mathbf{x}). \quad (11)$$

When OS is used for acceleration, we call our proposed algorithm split OS-LALM, by an analogy of the SB method.

B. Applications

In this paper, we consider a regularized least-squares problem with a general composite convex regularizer $\Phi(\Theta\mathbf{x})$. As mentioned before, when Θ is a finite difference matrix and Φ is a weighted ℓ_1 norm, (1) becomes a TV-regularized image reconstruction problem. In this case, the \mathbf{v} -update in (7) can be solved efficiently using soft-thresholding, and the constant $L_2 \triangleq \lambda_{\max}(\Theta'\Theta) = 4d$, where d denotes the number of neighbors we considered in the finite difference operator. Furthermore, when Θ is the discrete framelet transform matrix [10] and Φ is an ℓ_1 norm, (1) becomes a frame-based image

reconstruction problem [11]. In this case, the \mathbf{v} -update can also be solved using soft-thresholding, and $L_2 = 1$ because the discrete framelet is a tight frame. In fact, the proposed algorithm is even more general. For example, consider introducing one more split for the box constraint on \mathbf{x} . In this case, we can use non-separable (but probably tighter) quadratic surrogate functions with non-diagonal (e.g., circulant) Hessian matrices to majorize θ_k and ϕ_k in (3) because the additional split variable takes care of the box constraint.

III. EXPERIMENTAL RESULTS

This section evaluates our proposed algorithm (7) using the statistically weighted few-view X-ray CT image reconstruction problem with TV regularization:

$$\hat{\mathbf{x}} \in \arg \min_{\mathbf{x} \in \Omega} \left\{ \frac{1}{2} \|\mathbf{y} - \mathbf{A}\mathbf{x}\|_{\mathbf{W}}^2 + \text{TV}(\mathbf{x}) \right\}, \quad (12)$$

where \mathbf{A} is the system matrix of a CT scan, \mathbf{y} is the noisy sinogram, \mathbf{W} is the statistical weighting matrix, and $\text{TV}(\cdot)$ denotes an anisotropic TV regularization term. To solve (12) using the proposed algorithm, we simply replace \mathbf{A} and \mathbf{y} in (1) by the weighted forward projection operator $\mathbf{W}^{1/2}\mathbf{A}$ and the weighted noisy sinogram $\mathbf{W}^{1/2}\mathbf{y}$, respectively, and let $\Theta \triangleq \mathbf{C}$ denote a finite difference matrix and Φ denote a weighted ℓ_1 norm.

Computing L_1 , the maximum eigenvalue of $\mathbf{A}'\mathbf{W}\mathbf{A}$, is sometimes impractical because the power iteration might take hundreds of forward/back-projections for finding that number, while the number changes with different weighting matrix \mathbf{W} , even for a fixed geometry. In practice, we simply use $\mathbf{L}_1 \triangleq \text{diag}\{\mathbf{A}'\mathbf{W}\mathbf{A}\mathbf{1}\}$ to construct the SQS of the quadratic AL penalty term θ_k [7, 8]. This also provides voxel-dependent step sizes for image updates in (9). One can also generalize L_2 to a diagonal matrix \mathbf{L}_2 by considering a “weighted” quadratic AL penalty term of the second split [12]. However, in this paper, we just use $L_2 = 4d$ for simplicity.

We reconstructed a $512 \times 512 \times 122$ image from an undersampled chest axial CT scan. The size of the original sinogram is $888 \times 64 \times 642$ (half scan), and we uniformly undersampled the number of projection views from 642 to 81 (about 12.6% of projection views are used for reconstruction). Instead of using the standard SB-based method [3], we used a linearized SB method as the baseline reconstruction method because it has no iterative inner updates and is much easier for imposing box constraints on \mathbf{x} . Let **OS-LALM- M - ρ - η** denote the proposed algorithm using M subsets with AL penalty parameters ρ and η , where “ $\rho = c$ ” denotes the deterministic downward continuation [7, 8]. When $\rho = 1$, the proposed algorithm happens to be the linearized SB method [13].

The number of subsets M is varied from 1 to 5 for investigating different amounts of OS acceleration. The AL penalty parameter η was hand-tuned for fastest convergence and remained the same throughout the experiment for fair comparison. Intuitively, η determines the step sizes for image updates in (9), especially when the deterministic downward continuation approach is used. Empirically, choosing ηL_2 that is about 2% to 10% of L_1 (or the median of the diagonal entries of \mathbf{L}_1) usually exhibits fast convergence of the proposed

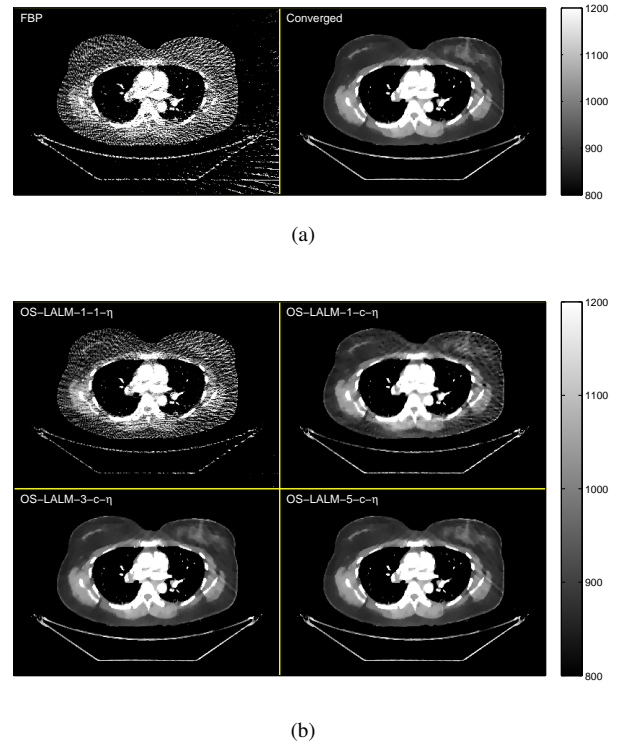


Fig. 1: Chest CT: cropped images [displayed from 800 to 1200 HU] from the central transaxial plane of (a) the initial FBP image $\mathbf{x}^{(0)}$ and the reference reconstruction \mathbf{x}^* , and (b) the reconstructed images $\mathbf{x}^{(100)}$ at the 100th iteration using the proposed algorithm with different AL penalty parameters. When $\rho = 1$, the proposed algorithm reverts to the linearized SB method.

algorithm. Finally, the total number of iterations is set to be 100. In this case, 100 undersampled forward/back-projection pairs, about 13 full forward/back-projection pairs, are used for the reconstruction.

Figure 1 shows the initial FBP image and the almost converged reference reconstruction together with the reconstructed images of the proposed algorithm with different parameters. As can be seen in Figure 1(a), the initial FBP image exhibits strong streak artifacts due to the undersampled projection views, and these streak artifacts are reduced significantly in the reference reconstruction by applying TV regularization. Figure 1(b) demonstrates the effectiveness of our proposed algorithm. With the deterministic downward continuation (i.e., $\rho = c$), the proposed algorithm shows less streak artifacts in the reconstructed images, and the reduction is more effective for larger M . Figure 2 shows the convergence rate curves (RMS differences between the reconstructed image $\mathbf{x}^{(k)}$ and the reference reconstruction \mathbf{x}^* as a function of iteration) of the proposed algorithm with different AL penalty parameters. As can be seen in Figure 2, the proposed algorithm shows substantial acceleration with continuation and ordered subsets. For example, the RMS difference of OS-LALM-5- c - η reaches 10 HU within 50 iterations, while the linearized SB method (OS-LALM-1-1- η) is still far away from the optimum (about

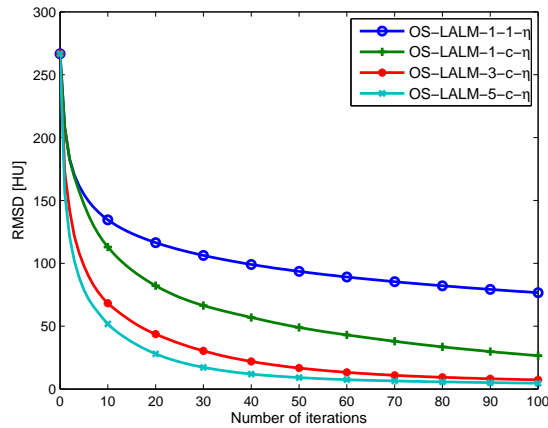


Fig. 2: Chest CT: RMS differences between the reconstructed image $\mathbf{x}^{(k)}$ and the reference reconstruction \mathbf{x}^* as a function of iteration using the proposed algorithm with different AL penalty parameters. When $\rho = 1$, the proposed algorithm reverts to the linearized SB method.

90 HU in RMS difference). Finally, note that algorithms with OS typically are not convergent. The algorithms enter a “limit cycle” in which updates stop approaching the optimum. However, as can be seen in Figure 2, the cyan curve (OS-LALM-5-c- η) is below 5 HU at the 100th iteration and keeps decreasing after that. This demonstrates the gradient error tolerance of our proposed splitting-based OS algorithm.

IV. CONCLUSION

In this paper, we proposed a splitting-based ordered-subsets (OS) algorithm, split OS-LALM, for solving weighted least-squares X-ray computed tomography (CT) image reconstruction problems with a general composite convex regularizer. To demonstrate our proposed algorithm, we investigated solving a few-view X-ray CT image reconstruction problem with total-variation (TV) regularization. Experimental results showed that the proposed algorithm exhibits fast convergence rate and excellent gradient error tolerance when OS is used for acceleration. The same technique can also be applied to 3D clinical CT with complicated (e.g., non-smooth) regularization terms.

REFERENCES

- [1] “Ionizing radiation exposure of the population of the United States,” Tech. Rep. 160, National Council on Radiation Protection and Measurements (NCRP), 2009.
- [2] T. Goldstein and S. Osher, “The split Bregman method for L1-regularized problems,” *SIAM J. Imaging Sci.*, vol. 2, no. 2, pp. 323–43, 2009.
- [3] B. Vandeghinste, B. Goossens, J. D. Beenhouwer, A. Pizurica, W. Philips, S. Vandenberghe, and S. Staelens, “Split-Bregman-based sparse-view CT reconstruction,” in *Proc. Intl. Mtg. on Fully 3D Image Recon. in Rad. and Nuc. Med.*, pp. 431–4, 2011.
- [4] B. Vandeghinste, B. Goossens, R. Van Holen, C. Vanhove, A. Pizurica, S. Vandenberghe, and S. Staelens, “Combined shearlet and TV regularization in sparse-view CT reconstruction,” in *Proc. 2nd Intl. Mtg. on image formation in X-ray CT*, pp. 37–40, 2012.
- [5] Y. Li, P. T. Lauzier, J. Tang, and G.-H. Chen, “Bregman regularized statistical image reconstruction method and application to prior image

- constrained compressed sensing (PICCS),” in *Proc. SPIE 8668 Medical Imaging 2013: Phys. Med. Im.*, p. 86683A, 2013.
- [6] S. Ramani and J. A. Fessler, “A splitting-based iterative algorithm for accelerated statistical X-ray CT reconstruction,” *IEEE Trans. Med. Imag.*, vol. 31, pp. 677–88, Mar. 2012.
- [7] H. Nien and J. A. Fessler, “Accelerating ordered-subsets X-ray CT image reconstruction using the linearized augmented Lagrangian framework,” in *Proc. SPIE 9033 Medical Imaging 2014: Phys. Med. Im.*, p. 903332, 2014.
- [8] H. Nien and J. A. Fessler, “Fast X-ray CT image reconstruction using the linearized augmented Lagrangian method with ordered subsets,” *arXiv: 1402.4381*, 2014. Submitted to *IEEE Trans. Med. Imag.*
- [9] H. Erdoğan and J. A. Fessler, “Ordered subsets algorithms for transmission tomography,” *Phys. Med. Biol.*, vol. 44, pp. 2835–51, Nov. 1999.
- [10] I. Daubechies, B. Han, A. Ron, and Z. Shen, “Framelets: MRA-based constructions of wavelet frames,” *Appl. Comput. Harmon. Anal.*, vol. 14, pp. 1–46, Jan. 2003.
- [11] J. Cai, S. Osher, and Z. Shen, “Split Bregman methods and frame based image restoration,” *SIAM J. Multiscale Model. Simul.*, vol. 8, no. 2, pp. 337–69, 2009.
- [12] H. Nien and J. A. Fessler, “Combining augmented Lagrangian method with ordered subsets for X-ray CT reconstruction,” in *Proc. Intl. Mtg. on Fully 3D Image Recon. in Rad. and Nuc. Med.*, pp. 280–3, 2013.
- [13] H. Nien and J. A. Fessler, “A convergence proof of the split Bregman method for regularized least-squares problems,” *arXiv: 1402.4371*, 2014.

Tomographic image reconstruction from continuous projections

Jeroen Cant, Willem Jan Palenstijn, Gert Behiels, Jan Sijbers

Abstract—An important design aspect in tomographic image reconstruction is the choice between a step-and-shoot protocol versus continuous X-ray tube movement for image acquisition. A step-and-shoot protocol implies a perfectly still tube during X-ray exposure, and hence involves moving the tube to its next position only in between exposures.

In a continuous movement protocol, the tube is in a constant motion. The angular integration of the rays inherently produces blurred projections. Conventional reconstruction from such projections leads to blurred reconstructed images, and therefore the projection angles are kept small. Important advantages of a continuous scanning protocol are shorter acquisition times and less demands on modality construction from a mechanical point of view.

In this work, the continuous protocol is extended with continuous projections, in which the X-ray source is continuously emitting X-rays over larger angles. The focal spot motion can no longer be ignored and is modeled in the reconstruction. The reconstruction quality is compared with the equivalent step-and-shoot counterpart showing improved results for region of interest tomography.

I. INTRODUCTION

X-ray projections for tomographic image reconstruction can be acquired in different ways. In a *step-and-shoot* protocol, the X-ray tube and detector are stationary during the X-ray projection and move to a next location only in between exposures [1]. While this protocol is the easiest from an image reconstruction point of view, it poses severe constraints on the design of the modality and typically leads to a longer acquisition time.

In the *continuous* acquisition mode, the tube is in a constant motion and projections are acquired over small angles. In a spiral CT scanner, the X-ray tube and the table are in a constant motion. This enables a heavily reduced acquisition time compared to the original step-and-shoot modality [2]. For breast tomosynthesis, the tube is in a continuous movement and emits short X-ray bursts at specific intervals, which also enables a shorter acquisition time and thus increases patient comfort [3].

Most reconstruction algorithms applied to projection data that are acquired in a continuous acquisition mode, however, still assume a stationary source and detector during exposure. Any focal spot movement during exposure is considered unwanted because the angular integration of X-rays produces blurring in the projections which leads to decreased image quality. Protocols are designed in such a way that this effect

is limited as much as possible, either by a low tube rotation speed or short exposure time [3] [4].

In this work, the continuous acquisition model is taken one step further. *Continuous exposures* are studied, whereby the X-ray tube *continuously* emits radiation over larger angles while moving through the acquisition path. In this model, focal spot motion can no longer be neglected and needs to be modeled in the reconstruction.

Motion related reconstruction artifacts have already been studied extensively in the literature. Object motion during acquisition of the different projections creates inconsistencies between the projection images, leading to reconstruction artifacts unless the motion is modeled and incorporated in the reconstruction algorithm [5]. A common example of subject motion occurs in imaging of a thorax when a patient cannot hold his breath. Another motion related artifact is caused by unwanted motion of the tube or detector, e.g., due to mechanical drifting [6]. The focal spot motion of the continuous exposures, however, differs from the previous motion examples as it is incorporated into the acquisition protocol by design. Recently, investigations have been made for modeling small focal spot motion to improve reconstruction quality in breast tomosynthesis [7].

In our work, the effect on the image quality of reconstructions modeling continuous exposures is studied and compared with reconstructions from a step-and-shoot model with equal total radiation dose and number of projections. As will be demonstrated, for specific applications such as region of interest tomography, reconstructions from continuous exposures may significantly improve the image quality of the equivalent step-and-shoot protocol, at the cost of decreasing spatial resolution outside the region of interest.

The concept of continuous projections and the integration in the SIRT algorithm is worked out in section II. In section III the Fourier sampling behaviour of the continuous projections is analysed. Section IV contains experiments on various phantoms. The conclusion can be found in section V.

II. METHODS

In this section, the concept of continuous projections is explained for parallel beam geometry. Generalization to other geometries is straightforward.

A. Continuous projections

The attenuation of an X-ray beam in the case of a step-and-shoot protocol, further referred to as a ‘*static*’ projection, can

JC, WJP and JS are with the iMinds-Vision Lab, University of Antwerp, Belgium. JC and GB are with Agfa Healthcare NV, Belgium. Corresponding author: jeroen.cant2@uantwerpen.be

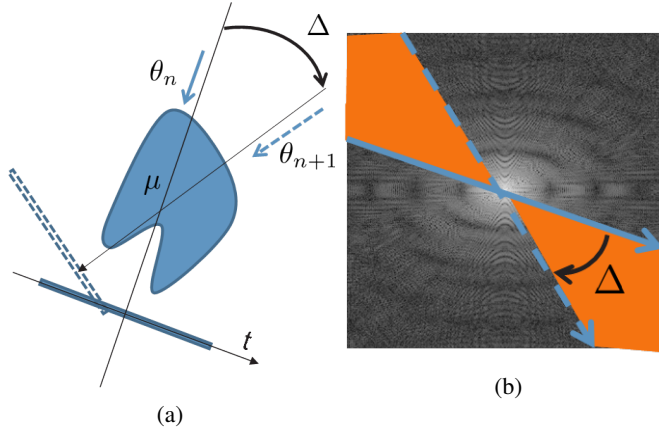


Fig. 1: (a) shows an example image acquisition geometry. Parallel beam projections are acquired at angles $\theta_n = n\Delta$ with $n = 1, \dots, N$. (b) shows the corresponding lines of these projections in the Fourier space. In a *continuous* acquisition, the detector integrates photons between θ_n and θ_{n+1} and hence gathers information about a wedge of angular width Δ in the Fourier space.

be expressed as follows:

$$I_n^s(t) = I_0 \exp \left(- \int_{L_{t,\theta_n}} \mu(x,y) ds \right) \quad (1)$$

with $(x,y) = (r \cos \theta_n - s \sin \theta_n, r \sin \theta_n + s \cos \theta_n)$. Furthermore, I_0 is the intensity measured by the detector without object and I the intensity after attenuation by the object. The attenuation coefficients of the imaged object are represented by $\mu(x,y)$, and the line integral is taken over the X-ray beam L_{t,θ_n} from source to detector as illustrated in Fig. 1a.

After dividing the projection data by I_0 , taking the logarithm and inversion, the discretized version of Eq.(1) can be expressed as a linear combination of the attenuation coefficients in \mathbf{x} along the path of the ray:

$$b_i = \sum_j a_{i,j} x_j \quad (2)$$

where b_i represents projection pixel i . The image vector \mathbf{x} is the discrete representation of μ , and the weight of the attenuation coefficient at image pixel x_j is $a_{i,j}$, which is related to the intersection length of the ray with this pixel.

The combination of Eq. (2) for all projection pixels leads to a system of linear equations

$$\mathbf{b} = \mathbf{A} \mathbf{x} \quad (3)$$

where $\mathbf{A} = \{a_{i,j}\}$ represents the system matrix, \mathbf{x} the vector of unknown attenuation coefficients in the discrete representation of μ and \mathbf{b} the vector of the entire projection data.

In case of *continuous* projections, each projection value $I_n^c(t)$ is the result of the integration of photons during rotation of the source-detector system from θ_n to $\theta_{n+1} = \theta_n + \Delta$. When the same total radiation dose is administered and the X-ray

source and detector move with constant angular velocity, the measured intensity is given by:

$$I_n^c(t) = \frac{I_0}{\Delta} \int_{\alpha=\theta_n}^{\theta_{n+1}} \exp \left(- \int_{L_{t,\alpha}} \mu(x,y) ds \right) d\alpha. \quad (4)$$

with $(x,y) = (r \cos \alpha - s \sin \alpha, r \sin \alpha + s \cos \alpha)$. For simplicity, the tube is assumed to emit a constant intensity. Also, the delay for reading out the detector is neglected. A more refined model for the emitted energy is presented by [7].

To obtain a discrete formulation of Eq. (4), S rays are sampled between θ_n and θ_{n+1} . Eq. (2) is modified to:

$$b_i = - \log \left(\frac{1}{S} \sum_{s=0}^{S-1} \exp \left[- \sum_j a_{i,j,s} x_j \right] \right) \quad (5)$$

where $a_{i,j,s}$ now represents the weight of the attenuation coefficient at position j for the beam arriving at detector pixel i with angle $\theta_n + \frac{s}{S}\Delta$.

The sampling factor S should be chosen high enough to correctly sample the full area between the corresponding lines in the Fourier space as illustrated in Fig. 1b. The coefficients $a_{i,j,s}$ can be obtained by modelling the sampled continuous projections system as a static projections system with $S \times N$ projections.

B. Continuous SIRT

The system of equations (3) can be solved using the well known Simultaneous Iterative Reconstruction Technique (SIRT) algorithm, which can be written in matrix formulation as [8]:

$$\mathbf{x}^{(k+1)} = \mathbf{x}^{(k)} + \mathbf{C} \mathbf{A}^T \mathbf{R} (\mathbf{b} - \mathbf{A} \mathbf{x}^{(k)}),$$

where $\mathbf{x}^{(k)}$ represents the reconstructed image at iteration k and \mathbf{C} and \mathbf{R} the diagonal matrices with the inverse column and row sums of the system matrix \mathbf{A} , respectively. The operation $\mathbf{A} \mathbf{x}^{(k)}$ corresponds to a so called *forward projection*, and the transpose \mathbf{A}^T is referred to as the *backprojection* operator. With static exposures, this forward projection comes down to a weighted sum of image pixel values on a ray from source to detector, using an interpolation scheme between all pixels that are partially intersected by this ray. Similarly, the backprojection is a weighted redistribution of a value across the same image pixels in the neighbourhood of that ray.

For the protocol with continuous projections, the forward and backward projectors are adapted. Instead of backprojecting a value along a single ray, this value is distributed across S rays corresponding to S source-detector positions of each exposure. The forward projector is modeled by S rays matching our sampled continuous exposure.

III. FOURIER ANALYSIS

For a parallel beam geometry, the effect of uniformly moving the source while constantly emitting radiation can intuitively be understood from the Fourier-slice theorem. This theorem states that for parallel beams, the Fourier transform of a static projection $p(x)$ of an image $f(x)$ is equal to a slice $s(k_x)$ in F , the Fourier transform of f . Stated otherwise,

each projection p ‘samples’ the Fourier space F of our image formed by the attenuation coefficients μ .

Where static projections represent lines in the Fourier space, a *continuous* projection will integrate all rays between angles θ_n and θ_{n+1} and thus gather information from the entire area in the Fourier space between the two corresponding lines of the static projections (Fig. 1b).

Conceptually, one can easily understand that when acquiring only a few static projection images, the Fourier space of the image will be severely undersampled and hence the reconstructed image will contain reconstruction artifacts. This can be seen in Fig. 2, where the reconstruction from only 10 projections shows streak artifacts.

Since the continuous projections sample the whole area between the corresponding lines of the start and end angle in the Fourier space of the image, it can be expected that this technique produces reconstructions with less streak artifacts. In the following section the reconstruction algorithm based on these continuous projections is compared with static reconstruction algorithms under various circumstances.

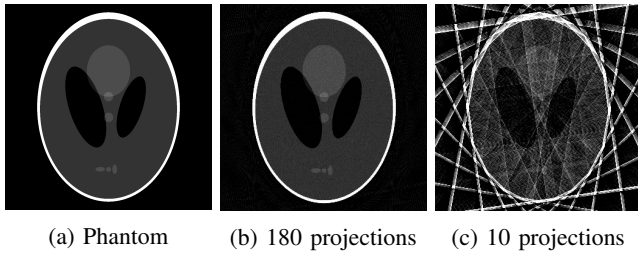


Fig. 2: SIRT reconstructions of a Shepp-Logan phantom (a) with 180 (b) and 10 (c) projections, showing typical streak artifacts.

IV. EXPERIMENTS

A. Reconstruction comparison between static and continuous projections.

To illustrate the effect of continuous vs static projections, the root mean square error (RMSE) for SIRT reconstructions from static and continuous projections on the Shepp-Logan phantom was compared as a function of the number of projections. The static projections were equally distributed along 180 degrees and the continuous projections integrated all rays between two consecutive static projections. 1000 iterations were performed for all reconstructions. The SIRT algorithm used for the continuous projections was modified as described in section II-B by sampling the rays in the angular range of the projections. For a limited number of projections, the continuous exposures resulted in a lower RMSE. With increasing number of projections, the difference between both methods vanished (see Fig. 3).

The continuous projections approach was also applied to the XCAT [9] phantom, with the center of source-detector rotation in the left lung. One can easily notice from Fig. 5 that the resolution improved in the rotation center, but decreased with increasing distance from this rotation center compared to the static reconstruction. This suggests that continuous projections

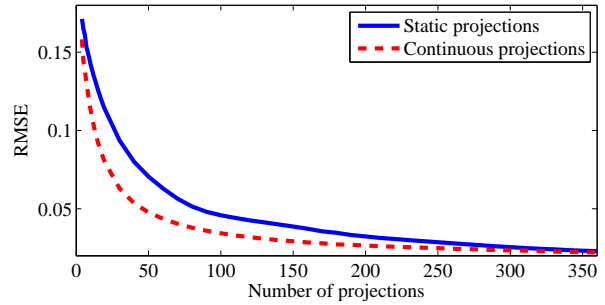


Fig. 3: RMSE for SIRT reconstructions in function of the number of projections. All projections angles were distributed evenly over a total acquisition angle of 180 degrees.

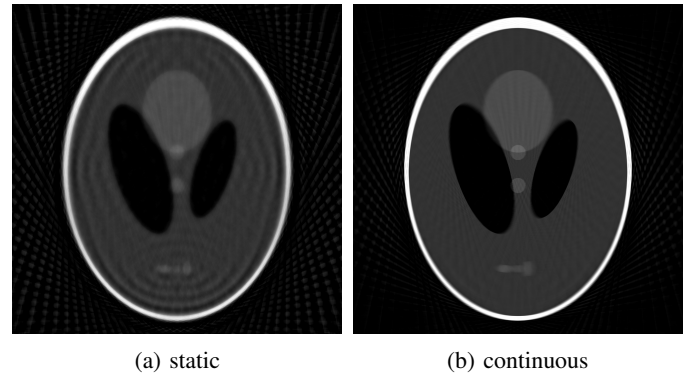


Fig. 4: Reconstruction of the Shepp Logan phantom, using 45 static (a) and continuous (b) projections.

might be of use in region of interest tomography, e.g., during surgery when a physician is only interested in a fast and accurate reconstruction of a local region of the patient.

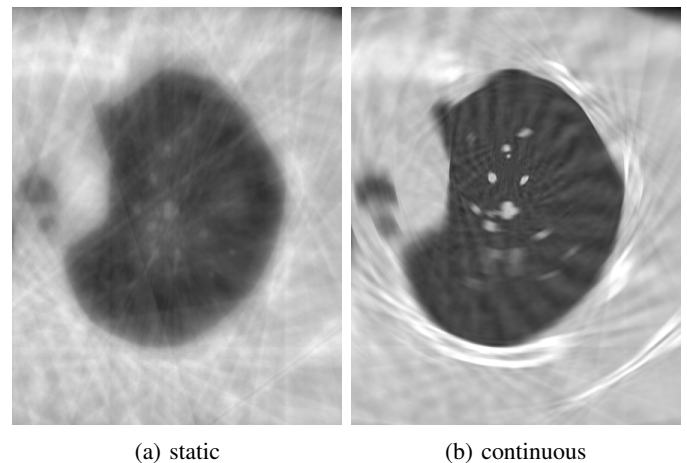


Fig. 5: Reconstruction of the XCAT phantom, using only 20 static (a) and fully continuous (b) projections with rotation center in left lung. Both images are displayed with equal contrast settings.

Besides an improved image quality around the rotation center, artifacts can be observed due to the motion of the tube outside this center. To analyze this further, projections of

two phantoms were reconstructed. The first phantom (Fig. 6a) consists of concentric circles, centered in the tube-detector rotation center. In Fig. 6b & 6c, reconstructions from 20 static projections and 20 continuously acquired exposures are shown, respectively. Whereas the static reconstruction shows many artifacts, the continuous reconstruction is nearly perfect.

The second phantom in Fig. 6d consists of 10 radial lines, distributed evenly over 360°. The reconstruction from 20 continuous projections in Fig. 6f smeared the radial lines along concentric circles, centered in the tube-detector rotation center. The angle of this smearing corresponds to the covered angle of the continuous projections.

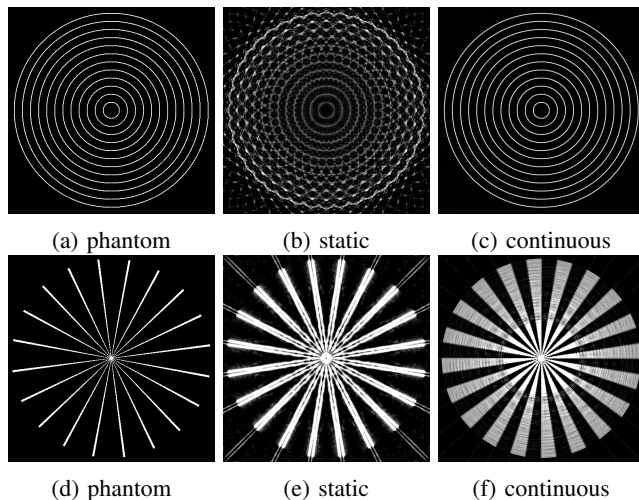


Fig. 6: Circles phantom (a) with static (b) and continuous (c) reconstruction, showing nearly perfect reconstruction for the continuous projections. The radial lines phantom (d) illustrates the concentric nature of the artifacts in continuous reconstruction (f). Contrast was enhanced in all images for easier visibility.

B. Noisy projections

The previous experiments were performed with noiseless projections. As noiseless imaging is not a realistic scenario, the effect of adding Poisson noise in the sinograms on the reconstruction quality of continuous projections was investigated. Reconstructions of static and fully continuous projections were compared, both methods using the same radiation dose per projection and an equal number of projections.

The artifacts along arcs centered around the tube-detector rotation center, as discussed in section IV-A, can also be seen in the continuous reconstruction from noisy projections (see Fig. 7).

V. CONCLUSION

An acquisition protocol was investigated with continuous exposures involving an X-ray source that continuously moves while continuously emitting radiation. The motion of the X-ray source was modeled in the reconstruction algorithm. A comparison with a conventional step-and-shoot acquisition protocol using the same total radiation dose and number of

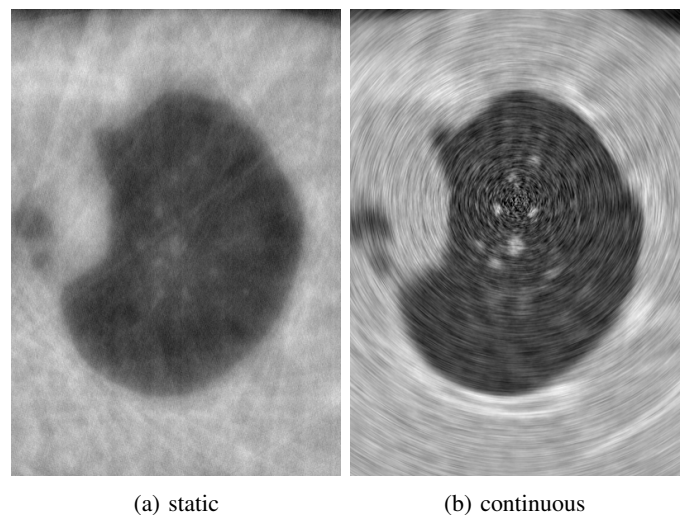


Fig. 7: Reconstruction of the XCAT phantom, using 20 static (a) and fully continuous (b) noisy projections. We have used 300 iterations of SIRT used in both cases. Both images are displayed with equal contrast settings.

projections showed reduced artifacts and improved contrast and resolution around the tube-detector rotation center.

ACKNOWLEDGEMENT

This work was funded by the Agency for Innovation by Science and Technology in Flanders (IWT). Networking support was provided by the EXTREMA COST Action MP1207.

REFERENCES

- [1] J. Hsieh *et al.*, "Step-and-shoot data acquisition and reconstruction for cardiac x-ray computed tomography," *Medical Physics*, vol. 33, no. 11, p. 4236, 2006.
- [2] W. Kalender *et al.*, "Single-breath-hold spiral volumetric ct by continuous patient translation and scanner rotation," *Radiology*, vol. 173, no. 2, p. 414, 1989.
- [3] A. Smith, "Fundamentals of breast tomosynthesis," *White Paper, Hologic Inc., WP-00007*, 2008.
- [4] H. U. Kerl *et al.*, "Evaluation of a continuous-rotation, high-speed scanning protocol for micro-computed tomography," *Journal of computer assisted tomography*, vol. 35, no. 4, pp. 517–23, 2011.
- [5] I. Al-Shakhrah *et al.*, "Common artifacts in computerized tomography: A review," *Applied Radiology*, vol. 32, no. 8, pp. 25–32, 2003.
- [6] W. A. Kalender *et al.*, "Flat-detector computed tomography (FD-CT)," *European radiology*, vol. 17, no. 11, pp. 2767–79, Nov. 2007.
- [7] K. Michielsen *et al.*, "Patchwork reconstruction with resolution modeling for digital breast tomosynthesis," *Medical Physics*, vol. 40, no. 3, pp. 1–10, 2013.
- [8] J. Gregor *et al.*, "Computational analysis and improvement of SIRT," *IEEE transactions on medical imaging*, vol. 27, no. 7, pp. 918–24, Jan. 2008.
- [9] W. P. Segars *et al.*, "Realistic ct simulation using the 4d xcat phantom," *Medical physics*, vol. 35, no. 8, pp. 3800–3808, 2008.

Preliminary Evaluation of Dental Cone-beam CT Image from Reduced Projection Data by Constrained-TV-minimization

Zheng Zhang, Xiao Han, Budi Kusnoto, E. Y. Sidky and Xiaochuan Pan

Abstract—Cone-beam computed tomography (CBCT) has gained increasing acceptance in general dentistry and orthodontics during the past decade. Nevertheless, dental CBCT delivers considerable radiation dose, which raises concern about the potential risk. One of the approaches to lower the radiation dose in CBCT data acquisition is to reduce the total number of projections. However, image quality may be degraded when current analytic-based algorithms are used for reconstructing images from sparse-view CBCT data. Recently, many optimization-based algorithms have been investigated for image reconstruction from data containing reduced projections. In this work, we apply the adaptive-steepest-descent (ASD)-projection-onto-convex-set (POCS) algorithm to reconstructing images from full (300)- and sparse (151 and 76)-view dental CBCT data sets. The result shows that the ASD-POCS algorithm can reconstruct from 300-view and 151-view data images with quality comparable to, or improved over the clinical images. The ASD-POCS reconstruction from 76-view data has visibly degraded quality, but may still yield potential practical utility in certain clinical tasks.

I. INTRODUCTION

Cone-beam computed tomography (CBCT) has gained increasing acceptance in general dentistry and orthodontics during the past decade [1], [2]. Dental CBCT provides three-dimensional images, which eliminate superimposition and distortion effects existing in two-dimensional X-ray imaging. The three-dimensional images enable clinicians to have more accurate anatomic information and more intuitive observation of structures of interest. Meanwhile, two-dimensional X-ray images, such as projection radiographs, can still be generated from the three-dimensional image.

Although dental CBCT possesses many advantages, concerns about potential radiation risk exist because it generally delivers more radiation dose than conventional 2D X-ray imaging [3]. In particular, because children and adolescents are more sensitive to radiation [4], it is of great merit to lower the imaging dose in the CBCT scans for them. One way to lowering the imaging dose is to reduce the total number of projections while maintaining the exposure per projection the same. However, image reconstruction from sparse-view data often poses challenge to clinically used reconstruction algorithms, and results in inferior image quality, which may affect diagnosis or assessment.

Z. Zhang, X. Han, E. Y. Sidky and X. Pan are with The University of Chicago.

B. Kusnoto is with Departments of Orthodontics, the University of Illinois at Chicago.

Recently, a great body of studies has been carried out to develop optimization-based algorithms for exploiting image reconstruction from sparse-view data. One of such algorithms is adaptive-steepest-descent (ASD)-projection-onto-convex-set (POCS) algorithm [5]–[9], which has demonstrated the potential to improve image quality and to reconstruct images with practical utilities in non-conventional conditions. In this work, we perform optimization-based image reconstruction by using the ASD-POCS algorithm from dental CBCT data. In particular, we focus on sparse-view image reconstructions.

II. MATERIALS AND METHODS

A. CBCT Imaging System

In the work, we collect data with an i-CAT CBCT system (Imaging Sciences International, Hatfield, PA). In the i-CAT system, the distances from the source to the rotation axis and to the detector are 49.35 *cm* and 71.03 *cm*, respectively. The detector consists of a 480×384 array with an element size of 0.508×0.508 *mm*². The diameter of the field-of-view (FOV) is about 13 *cm* within the transverse plane.

B. Data Acquisition

A patient data set was collected at 300 views over 2π . The patient was scanned with tube voltage of 120 kV and tube current of 20 mAs. The measured data contain truncation because the scan FOV is insufficient to cover the entire object support. We refer to the 300-view data as the full data, from which we extracted sparse-view data sets at 151 and 76 views uniformly distributed over 2π . We then perform image reconstruction from the full- and sparse-view data sets.

C. Optimization-Based Imaging Model

In an optimization-based reconstruction, the model data \mathbf{g}_0 and image \mathbf{f} are vectors with M pixels and N voxels, respectively, and a discrete-to-discrete (D-D) linear model links the two vectors [5]–[7], which can be written as:

$$\mathbf{g}_0 = \mathcal{H}\mathbf{f}. \quad (1)$$

\mathcal{H} denotes the system matrix of size $M \times N$. We employ a ray-driven projection model to calculate elements of \mathcal{H} . The properties of \mathcal{H} are affected by the data sampling, for example, the number of projection views.

D. Optimization-Based Reconstruction

In this work, we consider the constrained-TV-minimization program

$$\mathbf{f}^* = \operatorname{argmin} \|\mathbf{f}\|_{\text{TV}} \quad \text{s.t.} \quad \mathbf{f} \geq 0 \quad \text{and} \quad D(\mathbf{f}) \leq \epsilon, \quad (2)$$

where $D(\mathbf{f}) = |\mathcal{H}\mathbf{f} - \mathbf{g}|$ denotes the Euclidean-data divergence, \mathbf{g} are measured data, and ϵ is a pre-selected, positive parameter for accommodating inconsistencies between data and the model. We use the ASD-POCS algorithm [5]–[9] that has been developed previously to solve the optimization program in Eq. (2). The algorithm uses alternately the POCS to reduce the data divergence and the TV gradient descent to lower the image TV. In the study, we reconstructed images from the acquired full data and the extracted sparse-view data sets by using the ASD-POCS algorithm. The reconstructed image array size is $536 \times 536 \times 440$, with a voxel size of $0.3 \times 0.3 \times 0.3 \text{ mm}^3$.

E. Image Evaluation

In the work, we focus on evaluating sparse-view ASD-POCS reconstructions that if they can yield clinical utilities; while the full-view ASD-POCS result is shown as the upper bound for sparse-view reconstructions, and we want to investigate if ASD-POCS algorithm can improve the image quality in current dental CBCT imaging protocols. We obtain clinical images from the i-CAT CBCT system, which are reconstructed by use of the FDK algorithm [10]. These clinical images are used as the gold standard for evaluating ASD-POCS reconstructions. We carry out two evaluation studies: a visualization study for assessing the quality of ASD-POCS reconstructions, and an accuracy study [11] to evaluate the accuracy of those images when used as diagnostic cephalometric analysis and measurement (in orthodontics and oral surgery purposes).

In the visualization study, we compare ASD-POCS reconstructions to the clinical images by using the cross-sectional CBCT images. Two-dimensional sets of lateral and posterior-anterior cephalograms are generated from 3D CBCT images by using software Dolphin 3D (Dolphin Imaging & Management Solutions, Chatsworth, CA). The two-dimensional images are evaluated by observers recruited from UIC School of Dentistry, including orthodontic residents, orthodontic faculties, oral surgery faculties, oral surgery residents and oral and maxillofacial radiologists. In the study, observers blindly evaluate the two-dimensional images of the clinical images, the full- and sparse-view ASD-POCS reconstructions, respectively [12]. Observers assess each image if it yields diagnostic acceptance ("yes" is recorded as 1 and "no" as 0), and rank each image on a visual analog scale from 1 to 10 (1 is the poorest quality and 10 is the best quality). Statistical analyses, such as Cochran test, McNemar test, Friedman test, and Wilcoxon test, are conducted based on observers' evaluation.

In the accuracy study to determine the landmark locations, we evaluate two-dimensional images, such as lateral

cephalograms and posterior-anterior cephalograms. We enroll orthodontists to label and trace 65 anatomical landmarks in these two-dimensional images. Inter and intra observer reliabilities are tested and found consistent.

III. RESULTS

A. Cross-Sectional Images

We first compare cross-sectional CBCT images between the clinical image and the ASD-POCS reconstructions from full- and sparse-view data sets. We display in Fig. 1 the clinical image within two transverse slices and one sagittal slice, and use white boxes to enclose structures of root canals in Fig. 1a, sinus in Fig. 1b, and aerated mastoid bone in Fig. 1c, respectively. Those structures are of great interest in many applications in general dentistry as well as orthodontics. For detailed comparison between the clinical image and ASD-POCS reconstructions, we display in Figs. 2-4 zoomed-in images within those ROIs.

Reconstruction from 300-view data (full data) We first compare ROI images in the full-view ASD-POCS reconstruction to those in the clinical image, which are shown in Figs. 2-4. By comparing the root canals in Fig. 2, we observe that the full-view ASD-POCS reconstruction is comparable to the clinical image, with slightly enhanced contrast and improved sharpness. In Fig. 3, closer inspection of the sinus reveals that the full-view ASD-POCS reconstruction has better defined boundaries of the structures. In Fig. 4, rich details can be found within the aerated mastoid bone in the full-view ASD-POCS result, which appear to be somewhat obscured in the clinical image.

Reconstruction from 151-view data We then compare the ROIs in the 151-view ASD-POCS result to those in the clinical image as well as in the full-view ASD-POCS reconstruction in Figs. 2-4. Observation can be made that the 151-view ASD-POCS reconstruction is comparable to the clinical image. We also notice that the 151-view ASD-POCS result shows better sharpness of the sinus structures than the clinical image in Fig. 3. In Fig. 4, there are still more details of the complex structures within the aerated mastoid bone in the 151-view ASD-POCS reconstruction than in the clinical image. Moreover, we notice that the reduction of view numbers from 300 to 151 appears to have a less noticeable impact on ASD-POCS reconstructions.

Reconstruction from 76-view data Finally, we inspect the ROIs in the image reconstructed from 76-view data in Figs. 2-4 by use of the ASD-POCS algorithm. Comparing to the corresponding ROIs in the clinical image and in the full-view ASD-POCS reconstruction, the 76-view ASD-POCS result is visibly degraded due to substantial data reduction. However, in Figs. 2 and 3 we can still delineate the inner contour of the root canals and the sinus. By inspecting the fine structures within the aerated mastoid bone in Fig. 4, we observe that the 76-view ASD-POCS result shows comparable sharpness to the clinical image. Those results indicate that the 76-view ASD-POCS reconstruction may

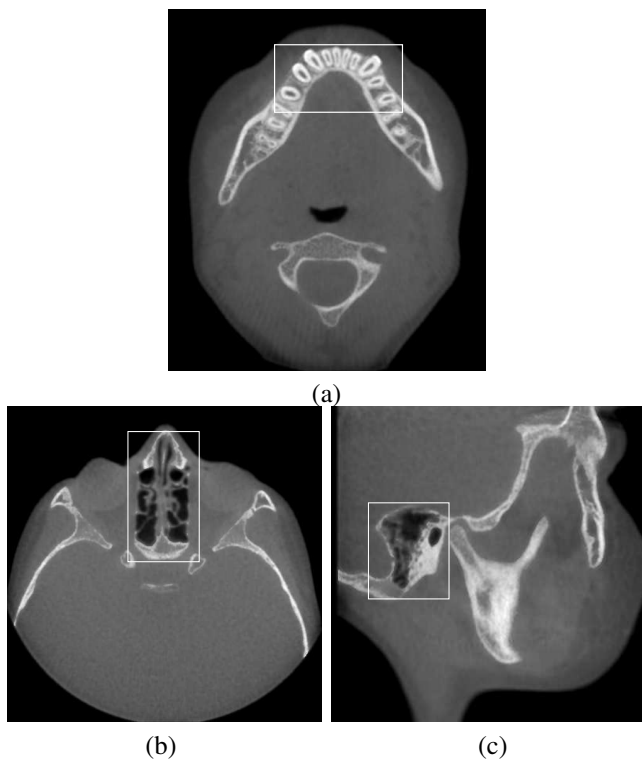


Figure 1. Images of the patient within transverse slices (a, b) and within a sagittal slice (c). ROIs are enclosed by solid boxes, which show root canals (a), sinus (b), and aerated mastoid bone (c). Display window: [-1000, 1800] HU.

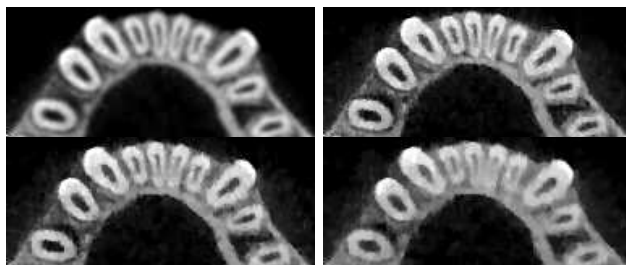


Figure 2. Zoomed-in view of ROI in (a) of Fig. 1. Top left: clinical image; Top right: ASD-POCS image reconstructed from 300-view data; Bottom left: ASD-POCS image reconstructed from 151-view data; Bottom right: ASD-POCS image reconstructed from 76-view data. Display window: [0, 1800] HU.

possess potential utility for certain clinical tasks that do not need very detailed information.

B. Human Observer Study

We carried out human observer study for qualitative assessment. Professionals participate the study to evaluate the lateral cephalograms and the posterior-anterior cephalograms. The results demonstrate that the full-view ASD-POCS result is more favorable relative to the clinic image. The 151-view ASD-POCS reconstruction still produces results comparable to the clinical images, which can be used for the routine diagnosis. When the projection number is pushed down to 76, although observers consider that the 76-view ASD-POCS reconstruction is a little inferior to

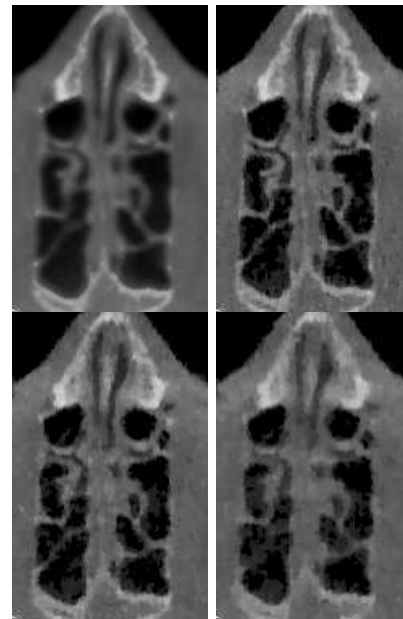


Figure 3. Zoomed-in view of ROI in (b) of Fig. 1. Top left: clinical image; Top right: ASD-POCS image reconstructed from 300-view data; Bottom left: ASD-POCS image reconstructed from 151-view data; Bottom right: ASD-POCS image reconstructed from 76-view data. Display window: [-1000, 1500] HU.

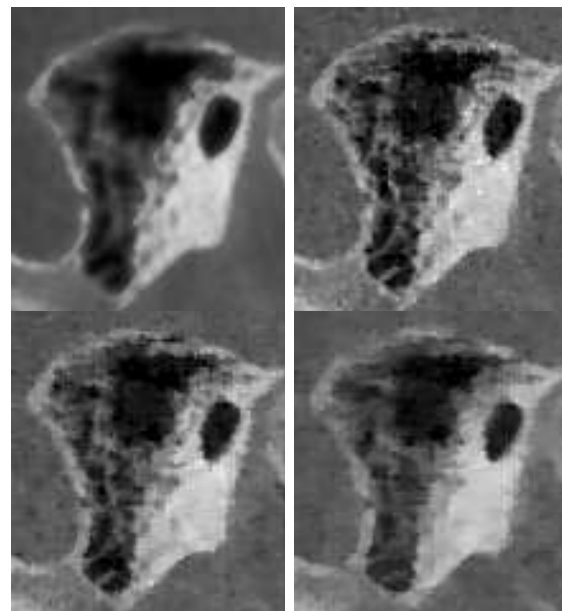


Figure 4. Zoomed-in view of ROI in (c) of Fig. 1. Top left: clinical image; Top right: ASD-POCS image reconstructed from 300-view data; Bottom left: ASD-POCS image reconstructed from 151-view data; Bottom right: ASD-POCS image reconstructed from 76-view data. Display window: [-800, 1300] HU.

the clinical image when evaluating the posterior-anterior cephalograms, there are still few differences between them in the lateral cephalograms. In particular, observers consider the lateral cephalogram generated from the 76-view ASD-POCS reconstruction can be used for orthodontic diagnosis.

C. Accuracy Study

In the accuracy study, orthodontists were recruited to trace 65 cephalometric landmarks. Average error of the location of the 65 cephalometric landmarks was found to be $(1.07 \text{ mm} \pm 0.68 \text{ mm})$ for the 2D images from 151-view ASD-POCS reconstruction, which is comparable to the i-CAT CBCT gold standard $(1.00 \text{ mm} \pm 0.50 \text{ mm})$ when used for cephalometric measurements and analyses. In some instances, even the 2D images from the 76-view ASD-POCS reconstruction still produced clinically acceptable accuracy $(1.44 \text{ mm} \pm 0.86 \text{ mm})$.

IV. DISCUSSIONS

In this work, we have investigated the application of the ASD-POCS algorithm to reconstructing images from full- and sparse-view patient data collected with an i-CAT CBCT system. We evaluated the ASD-POCS reconstructions from full data as well as sparse-view data sets containing 151 and 76 views, and compared them to the clinical image. We first carried out visualization for assessing the image quality by using the CBCT cross-sectional images; we then carried out human observer study for evaluating the diagnostic acceptance of the ASD-POCS reconstructions, based on lateral cephalograms and posterior-anterior cephalograms; finally, we conducted accuracy study to evaluate the accuracy of those images when used as diagnostic cephalometric analysis and measurement (in orthodontics and oral surgery purposes). Results show that ASD-POCS reconstruction from full data is comparable to, or better than the current clinical image. The 151-view ASD-POCS reconstruction is also comparable to the clinical image, and can be used for the routine diagnosis. The 76-view ASD-POCS reconstruction, although visibly degraded in the cross-sectional images, is comparable to the clinical image when using the lateral cephalogram. The work suggests that the ASD-POCS algorithm may be used for dental CBCT image reconstruction from data containing reduced projections, which lowers the imaging dose and yields images of practical utility.

V. ACKNOWLEDGMENTS

We thank Abdelrahman Salem and Pardeep Kaur (The University of Illinois at Chicago) for carrying out the observer study and the accuracy study. This work was supported in part by NIH R01 Grant Nos. CA120540, CA158446, and EB000225. The contents of this article are solely the responsibility of the authors and do not necessarily represent the official views of the National Institutes of Health.

REFERENCES

- [1] J. Ludlow, L. Ludlow, and S. Brooks, "Dosimetry of two extraoral direct digital imaging devices: NewTom cone beam CT and Orthophos Plus DS panoramic unit," *Dentomaxillofacial Radio.*, vol. 32, pp. 229 – 234, 2003.
- [2] J. Ludlow, L. Ludlow, S. Brooks, and W. Howerton, "Dosimetry of 3 CBCT devices for oral and maxillofacial radiology: CB Mercuray, NewTom 3G and i-CAT," *Dentomaxillofacial Radio.*, vol. 35, pp. 219 – 226, 2005.
- [3] J. Roberts, N. Drage, J. Davies, and D. Thomas, "Effective dose from cone beam CT examinations in dentistry," *British Journ. Radio.*, vol. 82, pp. 35 – 40, 2008.
- [4] T. Underhill, I. Chilvarquer, K. Kimura, R. Langlais, W. McDavid, J. Preece, and G. Barnwell, "Radiobiologic risk estimation from dental radiology. Part I. Absorbed doses to critical organs," *Oral surg., Oral med., Oral Path., Oral Radio., & Endoont.*, vol. 66, pp. 111 – 120, 1988.
- [5] E. Y. Sidky, K.-M. Kao, and X. Pan, "Accurate image reconstruction from few-views and limited-angle data in divergent-beam CT," *J. X-Ray Sci. and Technol.*, vol. 14, pp. 119–139, 2006.
- [6] E. Y. Sidky and X. Pan, "Image reconstruction in circular cone-beam computed tomography by constrained, total-variation minimization," *Phys. Med. Biol.*, vol. 53, pp. 4777–4807, 2008.
- [7] X. Pan, E. Y. Sidky, and M. Vannier, "Why do commercial CT scanners still employ traditional, filtered back-projection for image reconstruction?" *Inverse Probl.*, vol. 25, p. 123009, 2009.
- [8] J. Bian, J. H. Siewerdsen, X. Han, E. Y. Sidky, J. L. Prince, C. A. Pelizzari, and X. Pan, "Evaluation of sparse-view reconstruction from flat-panel-detector cone-beam CT," *Phys. Med. Biol.*, vol. 55, pp. 6575–6599, 2010.
- [9] X. Han, J. Bian, D. R. Eaker, T. L. Kline, E. Y. Sidky, E. L. Ritman, and X. Pan, "Algorithm-enabled low-dose micro-CT imaging," *IEEE Trans. Med. Imag.*, vol. 30, pp. 606–620, 2011.
- [10] L. A. Feldkamp, L. C. Davis, and J. W. Kress, "Practical cone-beam algorithm," *J. Opt. Soc. Am. A*, vol. 1, pp. 612–619, 1984.
- [11] A. Salem, "Feasibility study on the reduced-projection-algorithm for 2D cephalograms," *MS thesis, University of Illinois at Chicago*, 2014.
- [12] P. Kaur, "Evaluation radiographic orthodontic records image quality derived from CBCT," *MS thesis, University of Illinois at Chicago*, 2014.

Old Ideas New Again: A System Concept for Fast CT Using Semi-Conventional Approaches

G. M. Besson

Abstract- A system concept is introduced with the potential to achieve much faster data acquisition than currently possible in third-generation CT using extensions of known technologies.¹

I. INTRODUCTION

Viewed under a specific lens, the history of computed tomography (CT) developments can be characterized as a quest for speed and coverage. While the pencil-beam data acquisition geometry of EMI's first system, which took five minutes to acquire the data for a single slice, may perhaps be described as optimal for scanning a phantom or other fixed object, the realities of human imaging have led to a constant drive for faster data acquisition. This drive led first to the CT "generations," and then to the "slice wars," wherein per historical convention the EMI translate/rotate geometry is called first generation, and the "rotate/rotate" arrangement is referred to as third generation (jointly rotating source-and-detector assembly). The second generation was an intermediate step long forgotten; more significant are the departures represented by fourth- and fifth generations to be described shortly.

Speed and Coverage in Third Generation CT

The evolution from first generation to third-generation, the current de-facto standard geometry, initially enabled the acquisition of single slice data acquisition in the order of 1 second. Indeed the General Electric (GE) platform of the 1980s was known as the "High-Speed." The c. 1990 introduction of slip-ring gantries enabled continuous rotation for an arbitrary period of time and supported helical/spiral CT scanning. While in retrospect "obvious" this step went against the conventional wisdom of the times that best image quality was achieved in step-and-shoot acquisition. In fact helical data acquisition opened the door to organ scanning within a breath-hold, and proved extremely valuable in multiple clinical applications. The next step that provided the platform for significant CT application advances was the introduction of true multi-row detector systems in 1998 by the major vendors. A commercial "slice-war" ensued through the introduction of systems with larger and larger z-axis coverage and number of detector rows; this emphasis started subsiding with the availability of 64 or 128 row-detector systems with 150 to 180 rotation-per-minute (RPM) capability. However, at least one vendor put out a stake with the introduction in 2005 a 320-

detector row system capable of organ coverage in a single rotation for specific applications, such as cardiac CT.

Cardiac CT Imaging, Electron-Beam Tomography

Cardiac imaging using early 1980s CT technology was challenging at best: while the concepts of prospective and retrospective gating were known, the temporal resolution limitation was simply overwhelming: this is the period of time when half-scan reconstruction was suggested to reduce the possibility that motion would introduce image artifacts suggestive of aortic dissection. The concept of electron-beam tomography (EBT) imaging was introduced by Haimson [1] and developed into commercial reality by Imatron [2]. EBT, also known as fifth-generation CT, enabled data acquisition of one or two slices in the order of 50 ms, a time frame sufficient for "freezing cardiac motion." EBT however suffered from a lack of instantaneous power, complexity, and high cost; 3rd generation multi-row detector systems in the early 2000s developed cardiac capabilities competitive with EBT.

Historical Variants: Fourth-Generation and the Mayo Clinic's DSR

In fourth generation CT, an x-ray source revolves inside a circle (or arc of a circle) of stationary detectors centered on isocenter (whereas in 3rd-generation geometry, the detector arc is centered at the source); a fan-beam projection is formed overtime with vertex at a given detector cell location.

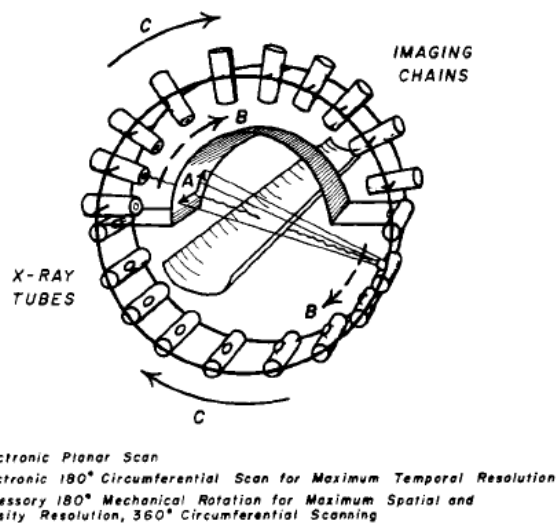


Fig. 1. Schematic for the Mayo clinic's DSR, from [3].

G. Besson is with ForeVision Technologies Corporation. Part of this work was done while the author was with Analogic Corporation.

The Dynamic Spatial Reconstructor (DSR) developed at the Mayo clinic in the early 1980s [3] relied on multiple image

chains (x-ray tube coupled to a two-dimensional image-intensifier detector) mounted on a rotating gantry to achieve fast volumetric imaging, cf. Fig. 1.

II. A NOVEL HYBRID SYSTEM DESIGN CONCEPT

A. Forces on X-Ray Tubes

The mechanical forces exerted on a rotating x-ray CT tube vary as a function of angular velocity ω per the relation: $f = m r \omega^2$. At constant flux per rotation, the power requirement on the tube increases with ω , and in most designs so does the mass of the x-ray source. For illustration, taking (arbitrarily) $m \propto \omega^{0.2}$ leads to the force relationship plotted in Fig. 2. It appears difficult at this time to expect tube technologies to evolve to support, say, a factor 10 increase in rotation speed from today's ≈ 200 RPM capability.

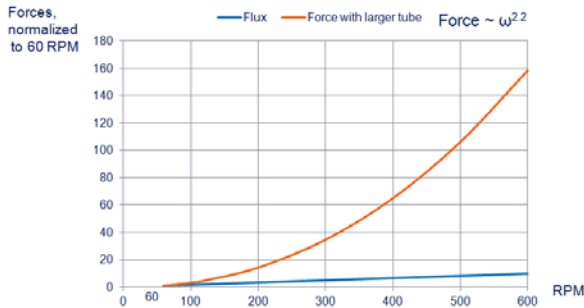


Fig. 2. Flux requirements and applied forces for x-ray tubes on a rotating gantry, angular velocity given in RPMs. The plot assumes the tube mass varies as $m \propto \omega^{0.2}$. 75 RPM was achieved in the late 1990s, while today's fastest systems support 200 RPM or slightly more.

B. Packing a Third Generation Gantry

A patent to Franke [4] describes a rotating gantry packed with three image chains. Simple geometry calculations indicate that this is an upper limit in typical medical imaging geometries. A prototype using two image-intensifier-based image chains (the "Morphometer") was developed in 1988 by CGR [5]. Siemens has recently commercialized a CT scanner with two imaging chains, the most recent version under the name "Somatom Force." In these embodiments, the second imaging chain has a limited angle detector that does not cover the full imaging field-of-view [6].²

C. A Hybrid Approach

While designing x-ray tubes capable of withstanding much higher forces appears daunting, it is not clear that such limitations would carry over to detectors. Modern CT detectors are relatively compact solid state devices with no moving parts and in principle could be designed to accept large accelerations. Taking this hypothesis as a working assumption, consider a system with two concentric rotating gantries, respectively the "source drum" ("external") and "detector drum" ("internal") and an angularly-extended detector arc, as shown schematically in Fig. 3 in "artist

² In the following I often use the term "detector" to mean the detector and associated data-acquisition-system (DAS) electronics.

rendition." The proposed concept relies on: (1) a decoupling of the source rotation support from the detector rotation support; (2) concomitant observation of a source at a range of azimuthal angles; (3) utilization of a multiplicity N_s of x-ray sources; (4) use of a wider-angle detector extent and of a detector arc centered on iso-center; (5) a new anti-scatter grid architecture with lamellas substantially oriented parallel to the main gantry plane; (6) introduction of a sparse view acquisition geometry, termed "view bunching."

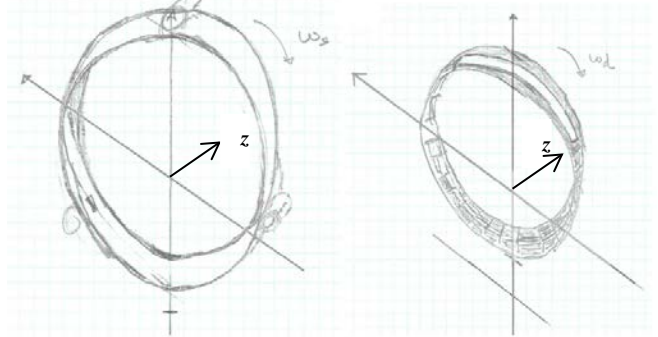


Fig. 3. Left: Three-dimensional rendition of an x-ray source drum (rotation at angular velocity ω_s) comprising three tubes; Right: Rendition of an independently rotating detector drum (ω_d), with an extended angular range, a drum aperture permitting x-ray illumination therethrough, and anti-scatter grids arranged parallel to the main gantry plane.

D. Theory of Operation

In one exemplary embodiment appropriate for medical imaging such as illustrated in Fig. 4, the detector arc covers about $4\pi/3$ radians, and the beam aperture in the detector drum about $2\pi/3$ radians. Accordingly a given x-ray source is in view of the detector (and acquires un-truncated projections) for a period of time T_s given by:

$$T_s(\omega_d - \omega_s) = 2\pi/3. \quad (1)$$

Writing $r_\omega = \omega_d/\omega_s$ and choosing that the angular range covered by a source during the time T_s be at least equal to the angle interval $\Delta\theta_s = 2\pi/N_s$ between two (equi-angularly distributed) sources minus a fraction k , we impose:

$$T_s\omega_s \geq (1 - k)\Delta\theta_s, \quad (2)$$

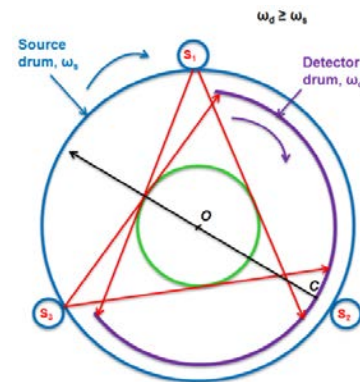


Fig. 4. Conceptual diagram for a CT system with two independently rotating gantries, one supporting N_s x-ray sources ($N_s = 3$ illustrated), the second an angularly-extended detector arc.

from which:

$$r_{\omega} \leq 1 + \frac{N_s}{3(1-k)} \quad (3)$$

E. How Fast?

Data acquisition speed ratios as compared to third generation geometry are given by $(r_{\omega} - 1)$ assuming all x-ray sources in detector view can be counted as active and listed in Table I.

TABLE I
RATIOS OF DATA ACQUISITION VELOCITIES VS. THIRD GENERATION

$k \rightarrow$	0	0.25	0.33	0.50
Ns=3	1	1.33	1.49	2.00
Ns=6	2	2.67	2.99	4.00
Ns=12	4	5.33	5.97	8.00

F. View Bunching

When detector drum rotation is increased beyond the upper bound given by setting $k=0$ in (3), angular source data acquisition develops “gaps” and I term the result as “view bunching,” illustrated in Fig. 5.

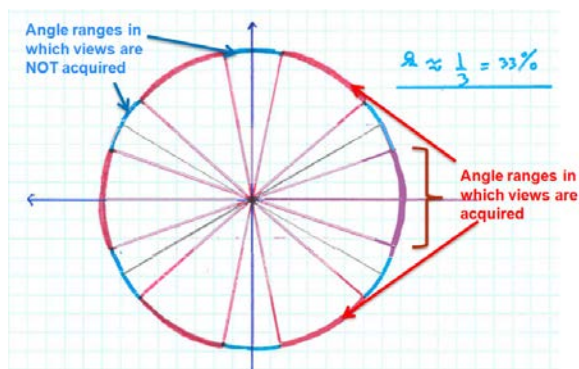


Fig. 5. Sparse view acquisition in a pattern of “view bunching” occurs when the constraint (3) for $k=0$ is not met.

It is noted that some early sampling theorems support un-even sampling; see for instance Papoulis [7].

III. SUPPORTIVE TECHNOLOGIES AND TRENDS

Development of an actual system per the above design concept will depend on the feasibility of adapting and/or further developing current technologies in the following areas.

A. Bearings

Bearing technologies include mechanical bearings (ball or roller-based); magnetic bearings; and air bearings, wherein air is passed at a high pressure through a porous material to support the rotating drum. A concept for two independent coaxial drum rotations can be found, for example, in [8].

B. Detector Electronics

It is desirable to reduce the detector depth along a source-to-detector central line so as to minimize the spacing between the two gantry drums. Current CT detector technology has

been evolving in this direction, with the recent introduction of integrated detectors wherein the analog-to-digital electronics is completely contained within the geometric shadow of one detector cell x-ray absorption element; from which point-on communications are digital. If need be, more voluminous digital electronics could be rearranged further along the z-axis outside the primary x-ray beam projection, although “deeper” gantries are unappealing to the patient.

C. Compact X-Ray Sources and Generators

X-ray tubes tend to be heavy and voluminous sub-systems. However, Rand et al in 1991 described a concept [9] later implemented commercially [10] with the 2004 introduction of “rotating-envelope designs,” whereby significantly less bulky x-ray tube inserts are possible; Fig. 6 shows an exemplary embodiment of such technology in the Straton tube insert. However even for such tubes, the high-voltage (HV) power system remains quite large indeed.

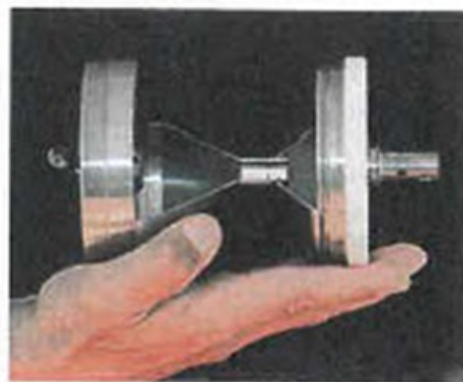


Fig. 6. Photo of a partly disassembled “hand-held” Straton tube from [11]. While the overall bulk and mass of a complete Straton tube and HV power supply cannot be properly inferred from this photo, the illustration is nonetheless indicative of a significant step down in size as compared to competitive tubes.

Power switching from one HV generator to several x-ray tubes is a desirable and known technology.

D. Distributed X-Ray Sources

Various technologies are being investigated that could potentially lead to truly distributed array sources: several configurations are then possible, including in the limit true dual 4th-generation geometry with a complete ring of stationary sources and a rotating detector.³

E. Data Acquisition Multiplexing

In the illustrated geometry, for $N_s \geq 4$ several tubes are in detector view. Grid switching enables rapid on-and-off cycling of x-ray tube emissions, which allows time-multiplexing between the various sources. Alternatively or in combination, spectral multiplexing might be used when an energy-resolving detector is available. Time multiplexing will increase tube-power requirements.

³ This configuration has the advantage of eliminating the cone-angle problem associated with 5th-generation geometry.

A. Cardiac CT

As discussed above, cardiac imaging has historically been a key driver for various aspects of CT technology. Effective data acquisition at 500 to 1,000 RPMs might open the door to improved imaging with better temporal resolution.

B. Scatter Correction

The trend toward detectors with much increased coverage along the rotation axis (z -axis) would be associated with the detection of much increased scattered radiation in the absence of counter-measures. Scatter in CT is a difficult problem as correcting for single events is not sufficient while at the same time the diffusion approximation does not necessarily apply; accordingly a method of choice to reduce the key scatter-to-primary ratio has been the introduction of so-called multi-directional anti-scatter grids (ASG) comprising lamellas crossing at angles. In the proposed approach, uni-directional lamellas would have to be oriented substantially parallel to the gantry main plane (orthogonal to z), since the detector will collect data from a given source at a variety of angles with respect to the central vector CO of Fig. 4. Such a geometry is less favorable to the blocking of “in irradiated-slice” single-scatters but comparable in efficacy to uni-directional lamellas oriented along the z -axis for blocking multiple scatter events.

C. Multi-Spectral Imaging

As discussed in the Multiplexing paragraph above, the proposed architecture might naturally leverage progress in multi-spectral imaging to enable simultaneous data acquisition from more than one x-ray source.

D. Compressed Sensing

Today there is much interest in the area of compressed sensing, that is the possibility of achieving in some sense similar image quality in most cases from a reduced acquired data set. The CT system concept described above naturally leads to a version of sparse sampling, where the views are acquired in bunches separated by gaps. Research is needed to determine whether the promise of compressed sensing applies in this instance.

E. Photon Counting CT

Photon counting technologies promise “noise-less” data acquisition and energy discrimination; the later capability in particular would enable spectral multiplexing of two or more x-ray tubes and thus support the proposed architecture.

F. Reduced Dose CT

Reduced dose CT can be obtained via a combination of hardware and software approaches. On the hardware side, direct conversion detectors do not require a light reflector and thus potentially offer geometric efficiency limited only by the ASG. Software methods that leverage *a-priori* information to limit inversion noise-amplification and to perform image-level noise reduction are applicable to this proposed architecture.

A. CT Architecture Evolution

A natural “slice-wars” milestone is the ability to image an organ in a rotation using wide z -detector coverage. Will there be a role for systems with faster rotation and smaller z -aperture, re-balancing costs between detector and sources and finding an improved operating point between scatter rejection and dose efficiency?

B. A First Most Likely Embodiment?

The above system concept outlines a potential path for much higher effective rotation and data acquisition speeds, at the price of a number of trade-offs, including costs, complexity, and scatter rejection efficiency. Accordingly a first-implementation might be to a photon-counting system with a relatively narrow z -aperture; such as 20-mm. With a moderate 33% amount of view-bunching, such a system with six sources and two HV generators could support (Table I) a data acquisition speed of up to three times that of third generation; or about 600 RPMs using today’s tube technology. Such a system with for illustration 32×0.625 -mm detector rows might enable a detector without ASG, and thus a low-dose platform, while providing coverage similar to a system with a 60-mm z -aperture.

ACKNOWLEDGMENT

I am happy to thank Daniel Abenaim, John O’Connor, John Percival and Eric Zanin for negotiating a work environment conducive to the germination of this concept.

REFERENCES

- In this brief description only a few references are given; many relevant and significant papers are not listed, and I have made no systematic attempt to address questions of priority. The full paper will be available at: <https://sites.google.com/site/guybessonselectedpublications/>
- [1] J. Haimson, “Method and apparatus incorporating no moving parts, for producing and selectively directing x-rays to different points on an object,” *US Patent No. 4,158,142*, 1979.
 - [2] D. P. Boyd and M. J. Lipton, “Cardiac computed tomography,” *Proc. IEEE*, 71(3), pp. 298-307, 1983.
 - [3] R. A. Robb, E. A. Hoffman, L. J. Sinak, L. D. Harris, and E. L. Ritman, “High-speed three-dimensional x-ray computed tomography: the dynamic spatial reconstructor,” *Proc. IEEE*, 71(3), pp. 308-319, 1983.
 - [4] K. Franke, “Tomographic apparatus for producing transverse layer images,” *US Patent No. 4,150,293*, 1979.
 - [5] D. Saint-Felix et al., “*In vivo* evaluation of a new system for 3D computerized angiography,” *Phys. Med. Biol.*, 39, pp. 583-595, 1994.
 - [6] T. G. Flohr et al., “First performance evaluation of a dual-source CT (DSCT) system,” *Eur. Radiol.*, 16, pp. 256-268, 2006.
 - [7] A. Papoulis, *Probability, random variables and stochastic processes*. 3rd Ed., McGraw-Hill, 1991.
 - [8] A. P. Tybinkowski and R. Swain, “Dual gantry bearing for combined tomography scanner,” *US Patent No. 7,020,233*, 2006.
 - [9] R. E. Rand, D. P. Boyd, and K. R. Peschmann, “Rotating x-ray tube with external bearings,” *US Patent No. 4,993,055*, 1991.
 - [10] P. Schardt et al., “New x-ray tube performance in computed tomography by introducing the rotating envelope tube technology,” *Med. Phys.*, 31(9), pp. 2699-2706, 2004.
 - [11] W. A. Kalender, *Computed Tomography*. 3rd Ed., Publicis, 2011.

Mitigating cone-beam artifacts via shift-variant data usage for large cone-angle scans

Jed D. Pack, Kai Zeng, Adam Budde, Zhye Yin, Bruno De Man

Abstract—Clinical CT scanners with a cone-angle that is large enough to cover the entire heart have been introduced by two vendors. Such scanners allow the heart to be scanned at a single phase (temporal window) and can enable dynamic imaging of the heart or brain for advanced analysis such as perfusion and functional assessments. These scanners must use advanced reconstruction methods if they are to produce images that are free of cone-beam artifacts. In previous work [1], an approach that helps mitigate such artifacts for the case of a short-scan data acquisition was described. If a full-scan of data is available, however, reconstruction of a larger volume is possible. Herein, an approach is described for leveraging the main idea of [1] in order to mitigate artifacts in the portion of the image volume that does not always project onto the detector during a full axial scan.

I. INTRODUCTION

In clinical CT (especially cardiac CT), it is often a goal to scan as large a volume as possible within a certain small time window (e.g., in a single rotation or even less). An axial scan tends to be the best way to achieve this goal with today’s clinical scanners since we want to measure data that covers the same section of the patient at all views (to the extent possible) in order to maximize the region that has sufficient data for reconstruction. Even in an axial scan, however, there are voxels that project onto the detector for only a subset of the views. This paper is mostly concerned with voxels that project onto the detector for an angular range of between ~ 180 and 360 degrees for a full axial scan (measured in terms of ray rotation while ignoring the cone angle). It is reasonable to think of reconstructing such voxels from a full-scan since the set of missing frequencies associated with these voxels is only moderate. If the scan were a short-scan, however, many of these same voxels would be measured on a set of views that provides highly incomplete frequency information. We will call the region containing such voxels the “corner” region, since these voxels are located in the corners of an image of the xz - or yz -planes, as seen in figure 1.

One way to reconstruct the corner region is to use a view weighting function that depends not only on the ray, but also on the voxel position along the ray. There are several examples of such functions in the literature [2]–[7]. In some cases, the volume is divided into sectors and a short-scan reconstruction is done for each sector (N-segment [3], Combination-Weighted-FDK [6]). In other cases, a view weighting function that varies smoothly as a function of both voxel and ray is

Jed D. Pack, (Kai Zeng), Zhye Yin, and Bruno De Man are all with (or formerly with) GE Global Research Center, Niskayuna, NY, USA; Adam Budde is with GE Healthcare, Waukesha, WI, USA.

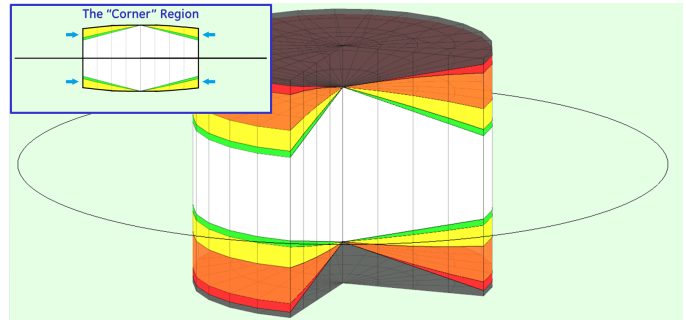


Fig. 1. A cut-away view of the cone-beam imaging volume. The colored regions represent volumes that are seen on the detector for different (wedge geometry) view angle ranges as follows: 360 degrees (white), between 270 and 360 degrees (green), between 180 and 270 degrees (yellow), between 90 and 180 degrees (orange), between 0 and 90 degrees (red), 0 degrees (black). The current paper is primarily concerned with reconstructing voxels in the green and yellow regions.

employed (Hybrid-Tent-FDK [2], Extended-Parallel-BP [4], 3D-Weighted-FDK [5], Extended-FDK [7]).

Each of these view weighting-based approaches works by amplifying the influence of rays that project onto the detector whenever the conjugate ray projects off of the detector (as a means of compensating for the missing conjugate ray data). The functions are made smooth in order to avoid streaky artifacts oriented along rays that are measured at the edge of the detector. Essentially, each voxel is “seen” only for a partial-scan, so the view weighting for that voxel bears a lot of similarity to the view weighting functions commonly used in partial-scan or short-scan reconstruction (e.g., Parker weighting [9]).

However, as has been described previously [1], when the cone angle is non-zero, view weighting can only approximately handle the data redundancy in frequency (Fourier/Radon) space. This approximation becomes quite poor for cone angles of several degrees or more. The “Butterfly” technique [1] has been developed to handle this redundancy much more accurately for partial-scan reconstructions. The goal of the current paper is to leverage this same technique to improve image quality in the “corner” region of a full-scan reconstruction, in much the same way as view weighting methods were extended from partial-scan techniques to full-scan techniques.

II. METHOD

The high-level idea in [1] is to produce two reconstructions (each from a different view weighting function) and then to combine the good frequency information in each using

2D (slice-by-slice) filtering to produce a final image volume with significantly reduced cone-beam artifacts. The filtering is usually shift-invariant and can therefore be done using 2D FFTs.

The frequency data handling in the corner region of a full-scan is quite shift-variant and will therefore involve approximations and/or added computation. There are many ways to handle this. One way is to apply a finite number of shift-invariant filters and then to combine them with spatially-dependent weighting functions. One such implementation of the algorithm flow (in cone-parallel or wedge geometry) is as follows, and has been used to produce the relevant images herein:

- 1) Perform fan-to-parallel rebinning of each row separately (this results in the wedge geometry).
- 2) Apply a ramp filter to each row of data.
- 3) Apply length correction (cosine cone weighting).
- 4) Backproject, while applying a first weighting function to produce reconstruction A.
- 5) Backproject, while applying a second weighting function to produce reconstruction B.
- 6) For each image slice (i) that includes the corner region:
 - Loop azimuthally over several angles (α):
 - Apply a smooth mask M_α (oriented at angle α) to the i th slice of both reconstructions (A and B)
 - Compute the 2D FFT of both slices
 - Blend the two FFT slices using a weighting function W_α to produce a blended FFT image
 - Compute the 2D IFFT to produce the blended image
 - Sum the resulting blended images across all α values to produce the final image for the i th slice.

As the first three steps are common (e.g., [5], [8]), the details of these steps are omitted in favor of details on the remaining steps. The weighting functions for reconstructions A and B must be selected as well as the image masking functions (M_α) and the Fourier blending function (W_α). Details of each of these is respectively given in one of the following subsections.

A. View (Backprojection) Weighting

As in the case of [1], the idea is to do two reconstructions with significantly different view weighting (or backprojection weighting) functions, so as to produce a pair of image volumes in which the cone beam artifacts are oriented along different directions (and therefore frequencies). Fourier domain blending can then be used to select the best frequencies from each volume in order to remove such artifacts to the extent possible.

In general, view weighting functions can depend on voxel location and view angle (four scalar parameters in all). However, in view of the fact that rotating a voxel around the z -axis should only shift the view weighting function by the same angle, the view weighting function can be built in a coordinate frame that rotates with view angle around the z -axis—specifically, (s, t, z) , where the unit vector in the s direction for a given view always points orthogonal to the rays (thus the s coordinate determines which detector column a voxel will project onto). We adopt the convention that s

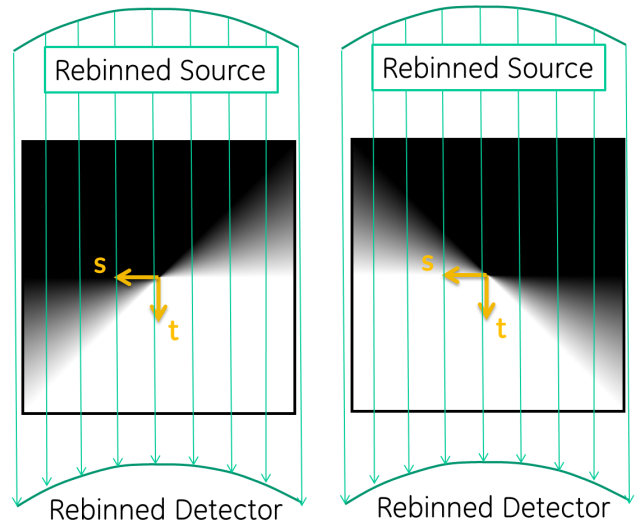


Fig. 2. View weighting functions used herein (displayed in the st -plane). In general these functions can also depend on radius and z . Left: reconstruction A. Right: reconstruction B.

points generally from the left side of the detector toward the right side (as seen from the source) and t points generally away from the source rather than toward it. Using this coordinate frame eliminates the dependence on view angle, so we are left with a weighting function that can be stored as a lookup table that is a function of three scalar parameters rather than four.

There are many (s, t, z) view weighting functions that can accomplish our goal satisfactorily. However, a few guidelines can be given. For example, the function for reconstruction A should be the mirror image of the function for reconstruction B in the s direction. Also, for any given voxel, the view range used in reconstruction B should always be higher in angle than the view range used in reconstruction A.

For completeness, the view weighting function used to produce the images in this paper is now given. This function is a further simplification of the above in that it can be parameterized by a single parameter (azimuthal angle in the st -plane) rather than the three parameters described previously. The function is given here:

$$w(x, y, z, \theta) = w_r(s, t, z) \quad (1)$$

$$w_r(s, t, z) = \begin{cases} w_a(\phi), & \text{if } t > 0, \text{ for reconstruction A} \\ w_a(-\phi), & \text{if } t > 0, \text{ for reconstruction B} \end{cases} \quad (2)$$

$$\phi = \arctan(s/t) \quad (3)$$

The function w_r is only defined for $t > 0$ above. The remainder of w_r is defined so as to ensure that the usual normalization condition is met (weighting of conjugate rays must sum to one). Specifically, when $t < 0$, $w_r(s, t, z) = 1 - w_r(-s, -t, z)$; when $t = 0$, the value is chosen to ensure continuity. In our implementation, w_a is as follows:

$$w_a(\phi) = \begin{cases} \phi/(\pi/4), & \text{if } \phi < \pi/4 \\ 1, & \text{otherwise} \end{cases} \quad (4)$$

Figure 2 displays these functions in the st -plane.

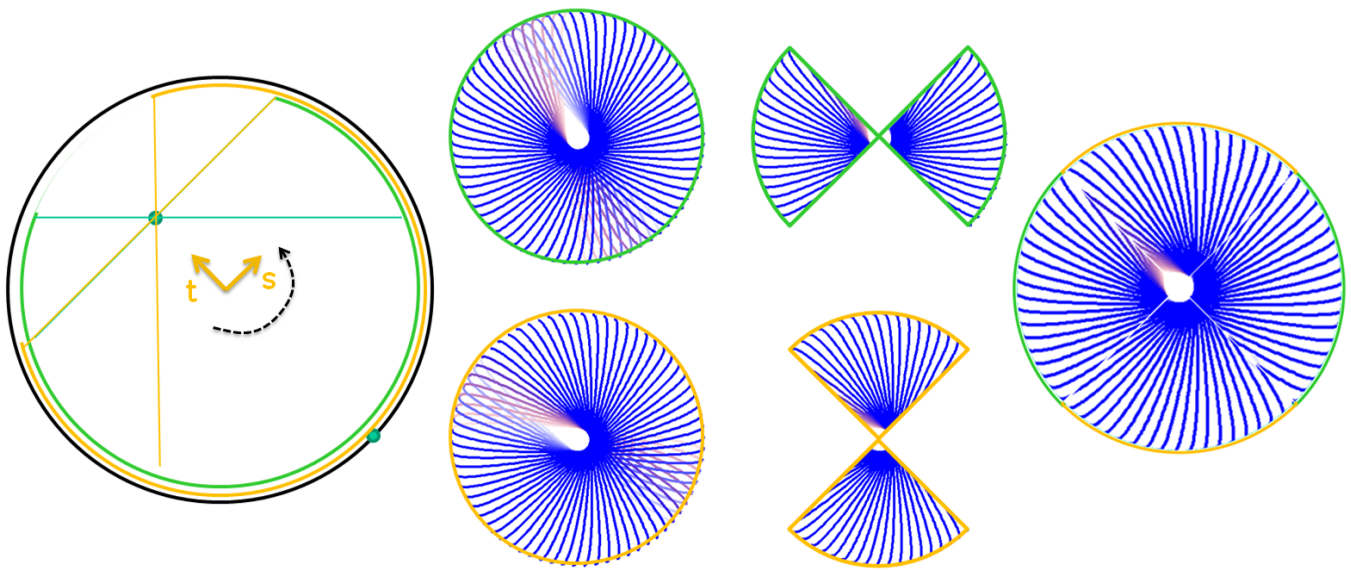


Fig. 3. First (left-most) panel: The views used to reconstruct a voxel in the corner region at the indicated location are highlighted in green (for reconstruction A) and orange (for reconstruction B). Second panel: The resulting contributions to Fourier space are indicated with the color on each interior curve indicating the level of extrapolation if the voxel is only seen for 180 degrees: from blue (none) through purple (minor) to bright red (most significant extrapolation). Fourier data from views with a full view weight are rendered in a darker color than those with $w < 1$. Third panel: After Fourier masking. Last panel: Combined Fourier data represented in the final image. See [1] for further background/explanation on this type of figure.

B. Image Masking

For each voxel in the corner region, there is a critical view at which it is farthest from the source, and therefore projects onto the detector at a minimum cone angle. This critical angle is at the center of the view range for which this voxel is seen on the detector. The set of voxels that have their critical angle within a particular small range all are associated with similar artifact orientations, and therefore require similar Fourier blending. We can, therefore form image masks that select such voxels for a series of small view ranges that together span a full 180 degrees. This would result in a series of binary masks, each of which was set to one only within a pair of opposing sectors, as shown in the top panel of figure 4. The sum of all such masks is one everywhere since each voxel is represented in exactly one such mask. As is often the case in CT reconstruction, however, sudden transitions can result in visible artifacts. As a result, these masks should be smoothed in the azimuthal angle direction on concentric circles. In our implementation this smoothing had an angular width of $\pi/14$, which matched the angular width of the original sectors (we used a total of 14 masks). Several of the masks are shown on the bottom panel of figure 4.

Alternatively, the smoothing can have a wider angular range for circles that are near the boundary of the corner region since voxels that are nearer this boundary are seen on the detector over a wider angular range than those farther from this boundary. Also, the image masking can optionally be done after (instead of before) Fourier blending.

C. Fourier Blending

As shown in figure 3, data mishandling artifacts can be minimized if the Fourier blending selects 90 degrees worth

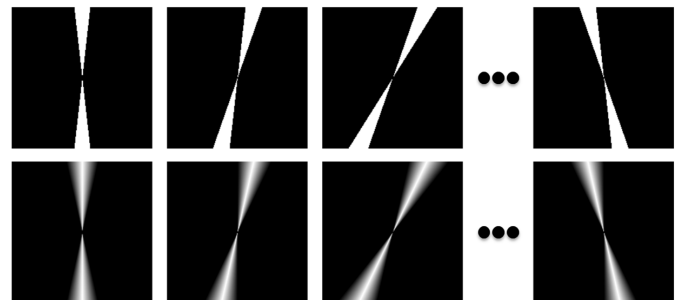


Fig. 4. Image domain masks (M_α) are shown both without (top) and with (bottom) azimuthal blending.

of Fourier data from each reconstruction (reconstruction A and B). Fortunately, this strategy also minimizes the impact of views in which the backprojection of extrapolated data is done. Extrapolated data can be useful for approximating very low frequencies, but such data can also produce streaks in the image around the edges of high contrast structures (e.g., ribs) if it is used to fill in higher spatial frequency regions of Fourier space. A uniform smoothing in the Fourier domain (windowing in the spatial domain) not only shrinks the spatial extent of our filter, but it also allows for extrapolated data to be used at the very low frequencies while removing its influence at the higher frequencies. At the same time, streaks due to object motion are reduced since this introduces an effect that is somewhat analogous to Parker weighting [9]. The results in this paper were produced using a Gaussian smoothing of the filter in frequency space with a standard deviation of 0.3 mm^{-1} . A small amount of azimuthal smoothing can also be included in the Fourier masks (we again used $\pi/14$) to compensate for the finite number of image masks.

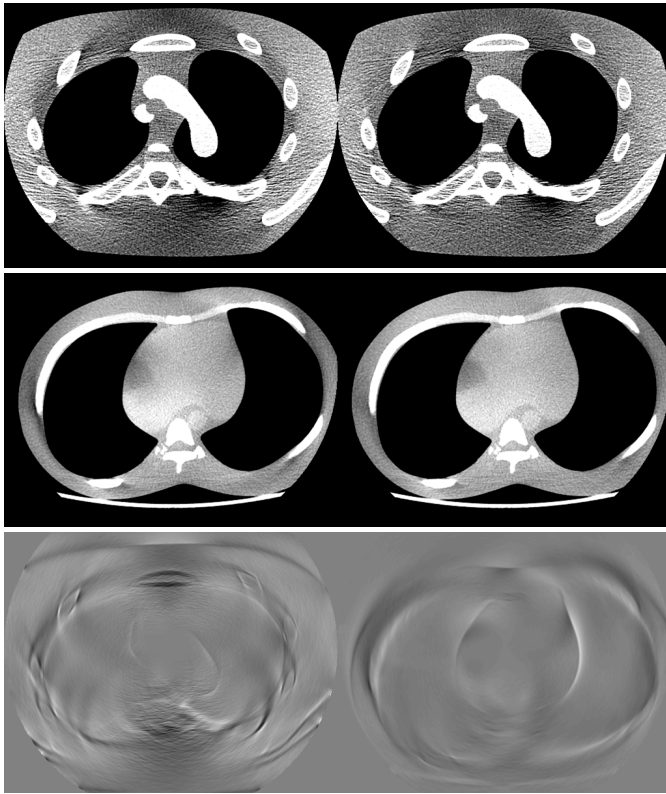


Fig. 5. Top panel: nCAT reconstructions. Center panel: Reconstructions of wide-cone CT data of a physical phantom. In the upper panels, the left image uses the view weighting from [7], while the right image is the result of the proposed method. The bottom panel shows a difference image (between the two methods) for nCAT (left) and real data (right). All images use a display FOV of 300mm and a 350 HU window and represent slices that are 4.4 mm from the edge of the 160 mm coverage volume (so as to include voxels that have close to 180 degrees worth of views). In each case, some improvement is achieved by using the proposed method rather than the baseline method.

D. Comparison Method

As a baseline, we compared our algorithm with an algorithm that performs steps 1-3 identically to the proposed method, but then does a single backprojection step using the weighting given in [7].

III. RECONSTRUCTION RESULTS AND DISCUSSION

In figure 5, we show results that illustrate the artifact reduction provided by the Full-scan Butterfly method. Data for the nCAT phantom [10] (top panel) was simulated with CatSim [11] in the cardiac region. The number of views, columns, and rows simulated was 984, 888, and 256 respectively. The detector had a cone angle of 14.6 degrees. Real data for an *Anthropomorphic Upper Abdomen Phantom* (Kyoto Kagaku, Japan, central panel) was acquired on a prototype Revolution CT system (GE Healthcare, Waukesha, WI). Reconstructions were performed using the baseline method and the method proposed here, and the difference between the two is shown in the bottom panel.

As is the case for [1], we note that this algorithm can alternatively be performed in the native geometry. For example, one could employ filtering (a view dependent derivative followed by a Hilbert transform performed on curves at the intersections

of the detector surface with planes that intersect the source trajectory tangentially), view-weighting in the (s, t, z) space (modified to account for the geometry), and backprojection with an inverse distance weight.

It should also be noted that although the current algorithm has been described in the context of a full-scan reconstruction, wherein voxels in the “non-corner” region are reconstructed with equal contributions from all views, data usage can be varied throughout the entire volume in order to provide the best balance between noise, artifacts, and temporal resolution.

IV. CONCLUSIONS

The proposed method produces high quality images from wide-cone full-scan data. The improvements come at a higher algorithm complexity and computational cost and may not be significant enough to justify use of this approach for some applications, particularly if the cone angle is small. In wide-cone clinical CT, however, such improvements are worth the effort as they provide an even larger high IQ image volume.

ACKNOWLEDGEMENTS

The authors would like to thank Brian E. Nett and Jiang Hsieh for their contributions, including guidance, suggestions, provision of data, etc.

REFERENCES

- [1] Pack J D, Yin Z, Zeng K, Nett B E, “Mitigating cone-beam artifacts in short-scan CT imaging for large cone-angle scans”, *Fully 3D Image Reconstruction Meeting 2013*, p. 300, 2013.
- [2] Grass M, Kohler T, Proska R, “3D cone-beam CT reconstruction for circular trajectories” *Phys. Med. Biol.* **45** 329, 2000.
- [3] Hsieh J, “N-segment cone beam reconstruction algorithm for single circular orbit CT”, *Radiology*, 225(P) 253, 2002.
- [4] Kachelries M, Knaup M, Kalender W A, “Extended parallel backprojection for standard three-dimensional and phase-correlated four-dimensional axial and spiral cone-beam CT with arbitrary pitch, arbitrary cone-angle, and 100% dose usage.” *Med Phys* 31, 1623, 2004.
- [5] Tang X, Hsieh J, Nilsen R A, Hagiwara A, Thibault J, and Drapkin E, “A three-dimensional weighted cone beam filtered backprojection (CB-FBP) algorithm for image reconstruction in volumetric CT under a circular source trajectory”, *Phys. Med. Biol.*, 2005.
- [6] Mori S, et. al., “A combination-weighted Feldkamp-based reconstruction algorithm for cone-beam CT” *Phys. Med. Biol.*, 2006.
- [7] Grimmer R, et al. “Cone-beam CT image reconstruction with extended z range.” *Med. Phys.* 36, 3363, 2009.
- [8] Feldkamp L A, Davis L C, and Kress J W, “Practical cone-beam algorithm”, *J Opt Soc Am*, 1, 612, 1984.
- [9] Parker D L, “Optimal short-scan convolution reconstruction for fan-beam CT,” *Medical Physics*, 9, p. 254, 1982.
- [10] Segars W P, Tsui B M W, Frey E C, Fishman E K, “Extension of the 4D NCAT phantom to dynamic X-ray CT simulation,” *Nuclear Science Symposium Conference Record*, 5, 3195, 2003.
- [11] De Man B, Basu S, Edic P, Iatrou M, Tower B, Chandra N, Dunham B, McOlash S, Sainath P, Shaughnessy C, Williams E, “CatSim: a new computer assisted tomography simulation environment”, *SPIE Medical Imaging*, 2007.

Efficient and Exact C-arm Cone-Beam Imaging for Axially Extended Field-of-View using the Ellipse-Line-Ellipse Trajectory

Zhicong Yu, Günter Lauritsch, Joachim Hornegger, Frédéric Noo

Abstract—C-arm computed tomography for axially long field-of-view is an important extension to the current C-arm 3D imaging capability and can be crucial in some intra-operative cases. Recently, a novel data acquisition geometry, i.e., the Ellipse-Line-Ellipse trajectory, was proposed for this new technique. It has been shown that this trajectory satisfies mechanical motion constraints of a C-arm system and provides excellent geometrical characteristics for cone-beam image reconstruction. This work makes good use of these characteristics and develops an efficient and exact image reconstruction scheme using the general CB-FBP reconstruction theory. We demonstrate this scheme by computer simulations with a modified FORBILD head phantom.

I. INTRODUCTION

C-arm Computed Tomography (CT) is an innovative technique that allows a C-arm system to produce 3D images using a set of cone-beam (CB) projections. Clinical reports (e.g., [1]) have shown that this new technique is becoming more and more useful in the interventional room, such as neurovascular imaging, interventional procedure guidance and post-surgery assessment. These reports have demonstrated that C-arm CT can reduce treatment related complications and improve interventional efficacy and safety.

However, current C-arm CT uses a circular short scan for data acquisition, which limits the imaging ability along the axial direction, i.e., along the centerline of the patient table. This limitation has been reported in hepatic vascular imaging where the entire liver is of interest [1]. In general, the axially-short coverage limitation is an issue whenever imaging an axially-long organ is needed in intra-operative cases, e.g., the entire spine or the whole aorta. Hence, development of C-arm CT for axially extended field-of-view (FOV) is needed in the interventional room. For convenience, we call this new development as extended-volume C-arm CT.

Significant effort has been made to achieve the extended-volume C-arm CT [2]. Three data acquisition geometries were investigated, namely, the reverse helix [3], [4], the arc-extended-line-arc (AELA) [5] and the ellipse-line-ellipse (ELE) [6]. The major challenge of extended-volume

C-arm CT is that the projection data are axially truncated due to limited detector size. To overcome this challenge, efficient and exact R-line based reconstruction algorithms are the best candidates; an R-line is a segment of line that connects two points on a connected source trajectory. However, the reverse helix cannot provide sufficient R-line coverage in the region-of-interest (ROI), hence exact and efficient cone-beam (CB) image reconstruction is difficult for the reverse helical trajectory. The AELA trajectory has sufficient R-line coverage, but it is not continuous and induces x-ray exposure pause. The ELE trajectory is continuous and has sufficient R-line coverage in the ROI. Therefore, it is the best candidate for extended-volume C-arm CT.

Geometrical characteristics of the ELE trajectory have been thoroughly studied in [6], [2], and efficient and exact image reconstruction scheme using the differentiated back-projection (DBP) algorithm has been proposed [7]. To reduce computational cost, the DBP method has to first perform image reconstruction on R-line surfaces and then data rebinning from R-line surfaces to Cartesian coordinate system. The former step increases implementation complexity and the latter step may cause unnecessary resolution loss. To overcome these problems, the filtered-back-projection (FBP)-type R-line based reconstruction algorithms are of interest.

This work aims at developing an efficient and exact image reconstruction scheme for the ELE trajectory based on the general CB-FBP reconstruction theory [8], [9], [10]. Although different reconstruction schemes have been proposed for various circle-plus trajectories [11], [12], none of them are readily applicable to the ELE trajectory. The scheme for a circle-plus-line trajectory [11] cannot solve the problem at hand, because an R-line of the ELE trajectory may involve two elliptical arcs and one line. The scheme for a general circle-plus trajectory [12] cannot be used neither: the ELE trajectory usually uses short scan due to mechanical motion constraints of a C-arm system, but this scheme requires the general circle to be closed. To apply the general CB-FBP theory to the ELE trajectory, a new reconstruction scheme needs to be developed.

This paper is organized as follows. First, in Section II, we describe the geometry of the ELE trajectory and clarify the criteria for ROI design. Next, in Section III, we review the general CB-FBP reconstruction theory and explain the new reconstruction scheme for the ELE trajectory. Then, we demonstrate the proposed reconstruction scheme in Section IV by computer simulations using a modified FORBILD head phantom. We conclude this work in Section V.

Z. Yu and F. Noo are with Department of Radiology, University of Utah, Salt Lake City, USA; G. Lauritsch is with Siemens AG, Healthcare Sector, Forchheim, Germany; J. Hornegger is with Pattern Recognition Lab, University of Erlangen-Nuremberg, Erlangen, Germany. This work was partially supported by a grant of Siemens AG, Healthcare Sector and by the U.S. National Institutes of Health (NIH) under grant R21 EB009168 and R01 EB007236. Its contents are solely the responsibility of the authors and do not necessarily represent the official views of the NIH. The concepts presented in this paper are based on research and are not commercially available.

II. ELE TRAJECTORY

A. Geometry

The ELE trajectory lies on a cylindrical surface that is centered on the long-axis of the patient table as shown on the left of Figure 1. Without loss of generality, we will only consider one basic cycle of this trajectory, i.e., the bottom half of the left of Figure 1. For convenience, we will simply call this basic cycle the ELE trajectory in subsequent sections.

The ELE trajectory is composed of two elliptical arcs that are connected by a segment of line. We call these two elliptical arcs the upper and lower T-arcs, respectively, whereas the segment of line is called the T-line. In the attached (x, y, z) coordinate system, the ELE trajectory is centered on the z -axis and mirror symmetric relative to the (x, y) -plane. The T-arcs are perpendicular to the (x, z) -plane and the T-line is parallel to the z -axis; see the right of Figure 1.

Let λ and γ_m be a polar angle and a fan angle, respectively. We denote $\underline{a}_u(\lambda)$ and $\underline{a}_l(\lambda)$ as vertex points on the upper and lower T-arcs, respectively, and refer to $\underline{b}(z)$ as a vertex point on the T-line. Let R be the radius of the cylindrical surface. We refer to the z coordinate of the center of the upper (resp. lower) T-arc as H (resp. $-H$), and the z coverage of each T-arc as $2\Delta H$. Mathematically, any vertex point on this ELE trajectory can be expressed by one of the following equations

$$\begin{aligned}\underline{a}_u(\lambda) &= (R \cos \lambda, R \sin \lambda, \mathcal{H}(\lambda))^T, \\ \underline{b}(z) &= (R \cos \gamma_m, -R \sin \gamma_m, z)^T, \\ \underline{a}_l(\lambda) &= (R \cos \lambda, R \sin \lambda, -\mathcal{H}(\lambda))^T,\end{aligned}$$

where $\lambda \in [-\gamma_m, \pi + \gamma_m]$ and $z \in [-\mathcal{H}(\gamma_m), \mathcal{H}(\gamma_m)]$ with $\mathcal{H}(\lambda) = H + \Delta H \cos \lambda$. For more details, we refer to [6].

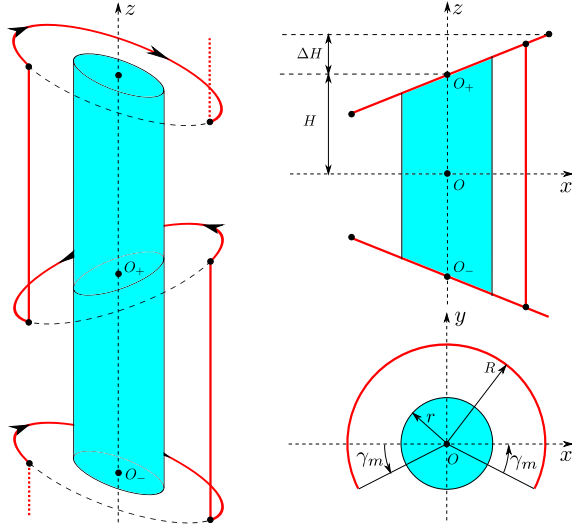


Fig. 1. Left: a complete ELE trajectory. We focus on one basic cycle: the bottom half of the trajectory on the left. Top right: orthogonal projection of the basic cycle of the ELE trajectory onto the (x, z) -plane. Bottom right: orthogonal projection of the basic cycle onto the (x, y) -plane. The light blue cylinder indicates the ROI.

B. ROI Design

There are three types of R-lines for the ELE trajectory: EL R-lines that connect the lower T-arc to the T-line, LE R-lines

that connect the T-line to the upper T-arc, and EE R-lines that connect the two T-arcs. Let the radius of the region-of-interest (ROI) be r . According to [6], full R-line coverage in the ROI can be achieved by the following configurations:

$$\gamma_m = \arcsin(r/R) \quad \text{and} \quad \Delta H/H = r/R.$$

C. R-line Selection

For a given point of interest, there may be more than one R-line through it. In this work, we select the shortest R-line, as the same as that was used in [7]. The R-lines that are used for image reconstruction of the ROI that is inside the convex hull of the ELE trajectory and below the (x, y) -plane are shown in the left of Figure 2. These R-lines are either EL or EE, and they together provide full R-line coverage in the ROI; see the right of Figure 2. The ELE trajectory is mirror symmetric relative to the (x, y) -plane, so is the R-line coverage. Hence, the R-lines for image reconstruction of the ROI that is inside the convex hull and above the (x, y) -plane can be obtained similarly to those in Figure 2.

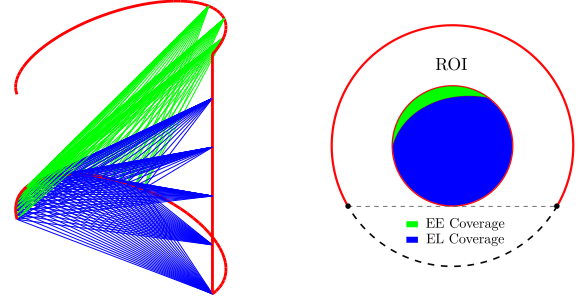


Fig. 2. Left: illustration of R-lines that are used for image reconstruction of the ROI that is inside the convex hull of the ELE trajectory and below the (x, y) -plane. Right: the R-line coverage of the ROI in the (x, y) -plane. Blue: EL R-lines; green: EE R-lines.

III. RECONSTRUCTION METHOD

A. General CB-FBP Reconstruction Theory

In this subsection, we review the general CB-FBP reconstruction theory [8], [9], [10]. We use the same notations as those were used in [10]. Let $\underline{a}(\lambda)$ be a point on a trajectory curve that starts from $\underline{a}(\lambda_s)$ and ends at $\underline{a}(\lambda_e)$. Let $\underline{a}'(\lambda)$ be the derivative of $\underline{a}(\lambda)$ with respect to λ , and let \underline{x} be a point that is located on the line that connects $\underline{a}(\lambda_s)$ and $\underline{a}(\lambda_e)$. For illustration, see Figure 3. Let \underline{e}_0 be the unit vector pointing from $\underline{a}(\lambda)$ to \underline{x} , and let

$$\underline{e}_1 = \frac{\underline{a}'(\lambda) - (\underline{a}'(\lambda) \cdot \underline{e}_0)\underline{e}_0}{\|\underline{a}'(\lambda) - (\underline{a}'(\lambda) \cdot \underline{e}_0)\underline{e}_0\|} \quad \text{and} \quad \underline{e}_2 = \underline{e}_1 \times \underline{e}_0,$$

so that \underline{e}_0 , \underline{e}_1 and \underline{e}_2 form a Cartesian coordinate system. In the plane that is spanned by \underline{e}_1 and \underline{e}_2 , we define

$$\underline{e} = \cos \phi \underline{e}_1 + \sin \phi \underline{e}_2 \quad \text{and} \quad \underline{e}^\perp = \underline{e} \times \underline{e}_0,$$

where ϕ is the polar angle from \underline{e}_1 to \underline{e} in the plane that is spanned by \underline{e}_1 and \underline{e}_2 . Note that, when ϕ is identical to $\pi/2$ or $3\pi/2$, the plane spanned by \underline{e}^\perp and \underline{e}_0 is tangent to the trajectory curve.

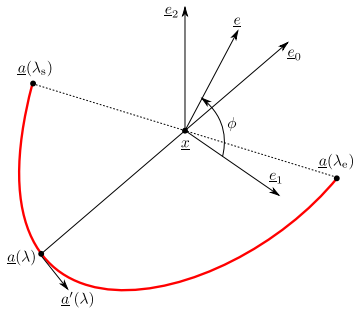


Fig. 3. Illustration for the general CB-FBP reconstruction theory.

Let $g(\lambda, \underline{x})$ be the line integral of the attenuation coefficients along the line that goes through $\underline{a}(\lambda)$ and \underline{x} , and let $g'(\lambda, \underline{x})$ be the derivative of $g(\lambda, \underline{x})$ with respect to λ . Now, consider an arbitrary Radon plane that contains \underline{x} with normal \underline{n} . This plane intersects the trajectory curve (bounded by \underline{a}_s and \underline{a}_e) at positions $\lambda_1, \lambda_2, \dots, \lambda_{N(\underline{n}, \underline{x})}$, with $N(\underline{n}, \underline{x})$ being the number of intersections. To address contributions of the projections corresponding to all these intersections, we introduce a weighting function, denoted as $M(\lambda, \phi; \underline{x})$, such that it satisfies the equation below

$$\sum_{k=1}^{N(\underline{n}, \underline{x})} M(\lambda_k, \phi_k; \underline{x}) = 1, \quad (1)$$

where ϕ has the same geometrical meaning as that in Figure 3. According to the general CB-FBP theory [8], [9], [10], \underline{x} can be reconstructed by the formula below:

$$f(\underline{x}) = -\frac{1}{2\pi} \int_{\lambda_s}^{\lambda_e} \frac{g_F(\lambda, \underline{x})}{\|\underline{x} - \underline{a}(\lambda)\|} d\lambda, \quad (2)$$

where

$$g_F(\lambda, \underline{x}) = \int_0^\pi c(\lambda, \phi; \underline{x}) g_H(\lambda, \phi, \underline{x}) d\phi, \quad (3)$$

with

$$c(\lambda, \phi; \underline{x}) = -\frac{1}{2} \left(\frac{\partial q}{\partial \phi} \right) (\lambda, \phi, \underline{x}), \quad (4)$$

$$q(\lambda, \phi; \underline{x}) = \text{sign}(\cos \phi) M(\lambda, \phi; \underline{x}), \quad (5)$$

and

$$g_H(\lambda, \phi, \underline{x}) = \int_{\pi}^{\pi} \frac{1}{\pi \sin \gamma'} g'(\lambda, \cos \gamma' \underline{e}_0 + \sin \gamma' \underline{e}_1^\perp) d\gamma'. \quad (6)$$

It is important to note that if $M(\lambda, \phi; \underline{x})$ is piecewise constant, $c(\lambda, \phi; \underline{x})$ will be a combination of pulse functions, which means only a finite filtering lines on the detector will be needed for reconstruction of \underline{x} .

B. Filtering Lines

Now, we focus on $M(\lambda, \phi; \underline{x})$, $c(\lambda, \phi; \underline{x})$, and the corresponding filtering lines. We denote the ROI that is inside the convex hull ROI_C , and refer to ROI_U and ROI_L as the portions of ROI_C that are above and below the (x, y) -plane, respectively. For convenience, we only clarify our choice of $M(\lambda, \phi; \underline{x})$ and the corresponding filtering lines for ROI_L .

Similar results can be obtained for ROI_U due to the mirror symmetry of the ELE trajectory.

Let \underline{x} be the point of interest, and let $\mathcal{R}(\underline{x})$ be the shortest R-line that goes through \underline{x} . We denote the trajectory curve that is bounded by $\mathcal{R}(\underline{x})$ as $\mathcal{S}(\underline{x})$. Let Π be a Radon plane that contains \underline{x} . By construction, there will be one or three intersections between $\mathcal{S}(\underline{x})$ and Π . In case that there is only one intersection, the value of $M(\lambda, \phi; \underline{x})$ is 1. In case that there are three intersections, we label them according to the order that the ELE trajectory goes through the plane, namely the first, second and third intersections. We design the $M(\lambda, \phi; \underline{x})$ according to the order of these intersections; see Table I. With the M function defined as in Table I, $c(\lambda, \phi; \underline{x})$ will be zero for most Radon planes, except for those tangent to the trajectory at the current view point or through the endpoints of $\mathcal{S}(\underline{x})$.

TABLE I
M FUNCTION USED FOR ROI_L

intersection order	M value
1st of three intersections	+1
2nd of three intersections	+1
3rd of three intersections	-1
1st of one intersection	+1

We select the filtering lines according to the M function defined in Table I. For this purpose, at each view point, we first project $\mathcal{S}(\underline{x})$ and the critical Radon planes onto the detector, and then study the value of $c(\lambda, \phi; \underline{x})$. Two types of R-lines may be associated to \underline{x} , i.e., EL R-lines and EE R-lines, depending on the location of \underline{x} . For an EL R-line, the projections of $\mathcal{S}(\underline{x})$ onto the detector when viewing from the lower T-arc and the T-line are illustrated in the left and right of Figure 4, respectively. It is observed that $c(\lambda, \phi; \underline{x})$ is non-zero only along \mathcal{C}_1 and \mathcal{L}_1 , which are parallel and tangent to the projections of the lower T-arc, respectively.

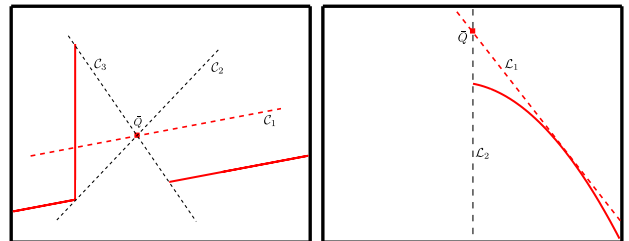


Fig. 4. Projections of an EL R-line segment onto the detector. Left: viewing from the lower T-arc; right: viewing from the T-line. Point \bar{Q} is the projection of \underline{x} , and $c(\lambda, \phi; \underline{x})$ is zero everywhere except for \mathcal{C}_1 and \mathcal{L}_1 .

For an EE R-line, when the view point is located on the lower T-arc, there are two cases regarding the relation between the filtering lines and the projection of $\mathcal{S}(\underline{x})$, as shown in Figure 5. However, in both cases, the filtering lines corresponding to non-zero $c(\lambda, \phi; \underline{x})$ are the same, namely \mathcal{C}_1 , which is parallel to the projection of the lower T-arc. Similarly, when the view point is located on the T-line or on the upper T-arc, $c(\lambda, \phi; \underline{x})$ is zero everywhere except for the filtering lines that are tangent to the projections of the lower T-arc, as shown by \mathcal{L}_1 in Figure 6.

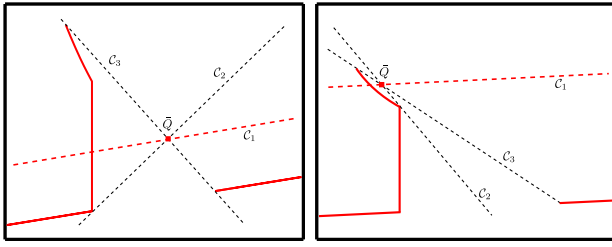


Fig. 5. Projections of an EE R-line segment onto the detector when the view point is located on the lower T-arc. Point \bar{Q} is the projection of \underline{x} , and $c(\lambda, \phi; \underline{x})$ is zero everywhere except for \mathcal{C}_1 .

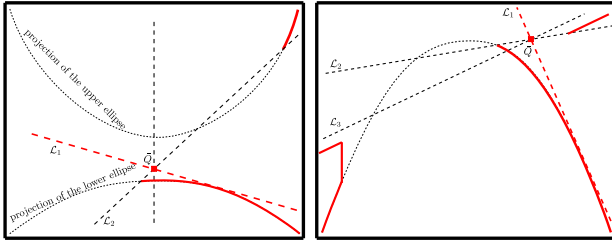


Fig. 6. Projections of an EE R-line segment onto the detector when the view point is located on the T-line (left) or on the upper T-arc (right). Point \bar{Q} is the projection of \underline{x} , and $c(\lambda, \phi; \underline{x})$ is zero everywhere except for \mathcal{L}_1 .

Based on the above analysis, for ROI_L , $g_H(\lambda, \phi, \underline{x})$ in Equation 6 should be calculated along the lines that are parallel to the projection of the lower T-arc when the view point is on the lower T-arc, and along the lines that are tangent to the projection of the lower T-arc when the view point is on the T-line or on the upper T-arc. It is important to note that the filtering lines \mathcal{L}_1 are drawn for illustration purpose. In reality, because the scan radius is much larger than the length of the T-line, the parabola is wide open and \mathcal{L}_1 is usually quite flat.

C. Reconstruction Scheme

The reconstruction scheme for ROI_L consists of three steps using the M function listed in Table I. They are: i) view-dependent differentiation, ii) Hilbert transform along \mathcal{C}_1 or \mathcal{L}_1 , and iii) back-projection along R-line segments.

IV. COMPUTER SIMULATION

We demonstrate our reconstruction scheme using a modified FORBILD head phantom [7]. The largest slice of this phantom is in disk shape at $z = 0$ cm of radius 12 cm. We adopted a flat panel detector with pixel size of $0.06 \text{ cm} \times 0.06 \text{ cm}$, a scan radius of 30 cm and a source-to-detector of 45 cm. For the ELE trajectory, we chose $H = 5$ cm, $\Delta H = 2$ cm and $\gamma_m = 24^\circ$. For each T-arc, 500 CB projections were generated, whereas for the T-line, 61 CB projections were generated. All CB projections were acquired with quarter detector pixel shift, and each pixel value was calculated as the average of the values corresponding to 8 uniformly distributed sub-regions.

We performed image reconstruction according to Section III-C. For the view-dependent differentiation, we adopted the Noo's scheme [13], and selected 0.001 for the resolution control parameter ε . The reconstruction results are shown in Figure 7. For comparison, we also illustrate the reconstruction

results obtained by only using the lower T-arc (Top right) and by using the lower T-arc and T-line together (bottom right). Compared to the result in the white box on the left, these results have significant CB artefacts. These results demonstrates the validity of the proposed reconstruction scheme.

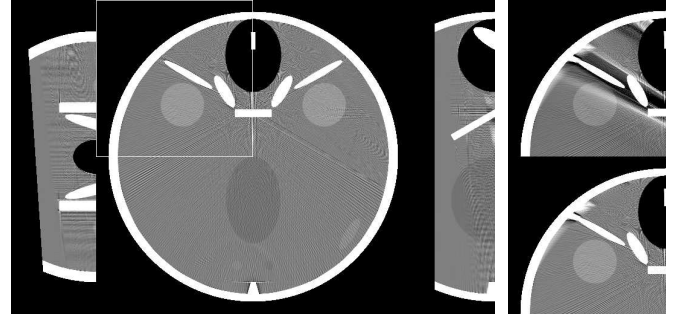


Fig. 7. Reconstruction results of the modified FORBILD head phantom. In the left figure, from left to right: coronal slice at $y = 6$ cm; transverse slice at $z = 0$ cm; sagittal slice at $x = 0$ cm. In the right figure, from top to bottom: results using only the lower T-arc; results using the lower T-arc and the T-line together. Gray scale window: $[0, 100]$ HU.

V. CONCLUSION AND DISCUSSION

We have proposed a reconstruction scheme for the ELE trajectory using the general CB-FBP theory. Computer simulation results show that efficient and exact C-arm long-object CB imaging is achievable using such a scheme.

The proposed reconstruction scheme avoids vertical filtering lines and thus allows data truncation in the axial direction. However, to what extent the truncation is allowed is not clear at this stage. This issue of detector requirement will be addressed in our future research.

REFERENCES

- [1] M. J. Wallace et al., "Three-dimensional C-arm cone-beam CT: applications in the interventional suite," *J. Vasc. Interv. Radiol.*, 2008.
- [2] Z. Yu, "C-arm Computed Tomography with Extended Axial Field-of-View," Ph.D. dissertation, University of Erlangen-Nuremberg, 2013.
- [3] S. Cho et al., "Exact reconstruction of volumetric images in reverse helical cone-beam CT," *Med. Phys.*, 2008.
- [4] Z. Yu et al., "FDK-type reconstruction algorithms for the reverse helical trajectory," in *Proc. of MIC.* IEEE, 2011.
- [5] Z. Yu et al., "Line plus arc source trajectories and their R-line coverage for long-object cone-beam imaging with a C-arm system," *Phys. Med. Biol.*, 2011.
- [6] Z. Yu et al., "Ellipse-Line-Ellipse source trajectory and its R-line coverage for long-object cone-beam imaging with a C-arm system," in *Proc. of SPIE*, 2012.
- [7] Z. Yu et al., "Extended-volume image reconstruction using the Ellipse-Line-Ellipse trajectory for a C-arm system," in *Proc. of Fully 3D*, 2013.
- [8] A. Katsevich, "Theoretically exact FBP-type inversion algorithm for spiral CT," *SIAM J. Appl. Math.*, 2002.
- [9] G.-H. Chen, "An alternative derivation of katsevichs cone-beam reconstruction formula," *Med. Phys.*, 2003.
- [10] F. Noo, *Informatics in Medical Imaging*, ser. Imaging in Medical Diagnosis and Therapy, 2012, ch. 13 Principles of three-dimensional imaging from cone-beam projection data.
- [11] A. Katsevich, "Image reconstruction for the circle and line trajectory," *Phys. Med. Biol.*, 2004.
- [12] A. Katsevich, "Image reconstruction for a general circle-plus trajectory," *Inverse Problems*, 2007.
- [13] F. Noo et al., "A new scheme for view-dependent data differentiation in fan-beam and cone-beam computed tomography," *Phys. Med. Biol.*, 2007.

New Inversion Formula for the X-ray Transform and its Application to CT reconstruction

Steven Oeckl¹

Abstract—We present an inversion formula for the X-ray transform that differs in many ways from well-known results: The formula is valid for arbitrary dimensions and provides therefore an uniform approach for fan- and cone-beam Computerized Tomography. Instead of using the formula of Grangeat for linking the X-ray transform and the Radon transform the presented formula is based on a relation between the X-ray transform and the extended Radon transform. Additionally, we don't have to deal with the derivative of the Crofton symbol which is usually a discontinuous function. Applying the new formula we achieve reconstruction algorithms of filtered backprojection and filtered layergram type. The performance of the proposed algorithms is shown using simulated data.

I. INTRODUCTION

THE (divergent) X-ray transform is the mathematical modell for Computerized Tomography (CT). The two dimensional (2D) and the three dimensional (3D) X-ray transform is related to fan-beam and cone-beam CT, respectively. Analytical reconstruction algorithms are therefore based on the inversion of the X-ray transform especially for dimensions $n \in \{2, 3\}$.

Instead of inverting the 2D X-ray transform usually the 2D Radon transform in combination with an appropriate transformation is used to derive reconstruction algorithms for fan-beam CT, see for example [1]. In case of cone-beam CT several inversion formulas for the 3D X-ray transform are well-known, see [2], [3], [4] [5], [6]. The mentioned formulas have all in common that the inversion formula for the 3D Radon transform serves as a starting point for the proof and Grangeat's formula [7] is used to achieve a relation between the 3D Radon transform and the 3D X-ray transform. Furthermore in every formula one has to deal with the derivative of the Crofton symbol which is usually a discontinuous function and therefore causes numerical challenges.

In this contribution we present a different approach for deriving an inversion formula for the X-ray transform for arbitrary dimensions. The derivation starts with a new formula for inverting the n-dimensional extended Radon transform. Then we make use of a new relation between the extended Radon transform and the X-ray transform. Using this approach we avoid the derivative of the Crofton symbol. Details on all results of this contribution can be found in [8].

In section two we provide the basic definitions and notations for this contribution. An inversion formula for the extended Radon transform is shown in section three. The

relation between the extended Radon transform and the X-ray transform is content of the fourth section. In section five we present an inversion formula for the n-dimensional X-ray transform. An inversion formula for the extended X-ray transform will be presented in section six. The derivation of reconstruction algorithms based on the new inversion formulas is demonstrated in section seven. Section eight is reserved for results and we finish the contribution with a conclusion in section nine.

II. PRELIMINARIES

Throughout this paper let $n \in \mathbb{N}$ be a natural number with $n \geq 2$ and let $r \in \mathbb{R}^+$ be a positive real number. We define $\mathbb{N}_0 := \mathbb{N} \cup \{0\}$, $\mathbb{R}_*^n := \mathbb{R}^n \setminus \{0\}$, and $\Omega_r^n := \{x \in \mathbb{R}^n : \|x\| < r\}$ the open n-dimensional ball with radius r . Let $S^{n-1} := \{x \in \mathbb{R}^n : \|x\| = 1\}$ be the n-dimensional unit sphere and $H^\alpha(\Omega_r^n)$ the Sobolev space of order $\alpha \in \mathbb{R}^+ \cup \{0\}$. The space of test functions is denoted by $D(\Omega_r^n)$ and the Schwartz space by $S(\mathbb{R}^n)$. Let f be an appropriate function. For $x \in \mathbb{R}^n$ we define the translation $\mathcal{T}_x f := f(\cdot - x)$ and for $c \in \mathbb{R}^+$ the dilatation $\mathcal{V}_c f := f(c \cdot)$. We define the convolution $\mathcal{C}_g f := \int_{\mathbb{R}^n} f(x)g(\cdot - x) dx$ and the Fourier transform $\hat{f} := \frac{1}{(2\pi)^{n/2}} \int_{\Omega_r^n} f(x)e^{-i\langle x, \cdot \rangle} dx$. The Riesz potential \mathcal{I}^α is defined for $\alpha \in \mathbb{R}$ with $\alpha < n$ by $(\mathcal{I}^\alpha f)^\wedge := |\cdot|^{-\alpha} \hat{f}$. For $f \in L^2(\Omega_r^n)$ and $(\theta, t) \in S^{n-1} \times \mathbb{R}$ the operator $\mathcal{R}^r f(\theta, t) := \mathcal{R}_\theta^r f(t) := \int_{\Omega_r^n} f(x)\delta(\langle x, \theta \rangle - t) dx$ is called *Radon transform*.

III. INVERSION OF THE EXTENDED RADON TRANSFORM

We introduce analogous to [9] the extended Radon transform as follows: Let $f \in L^2(\Omega_r^n)$ and $(y, t) \in \mathbb{R}_*^n \times \mathbb{R}$. The operator

$$\tilde{\mathcal{R}}^r f(y, t) := \tilde{\mathcal{R}}_y^r f(t) := \int_{\Omega_r^n} f(x)\delta(\langle x, y \rangle - t) dx$$

is called *extended Radon transform*. The extended Radon transform is also well-defined for $f \in S(\mathbb{R}^n)$. In this case we write $\tilde{\mathcal{R}}$ instead of $\tilde{\mathcal{R}}^r$.

In [9] it was also pointed out that $\tilde{\mathcal{R}}^r f$ is homogeneous of degree -1 , i.e. for $\theta \in S^{n-1}$ we have $\tilde{\mathcal{R}}_{\rho\theta}^r f(\rho \cdot) = \rho^{-1} \tilde{\mathcal{R}}_\theta^r f$. For $\alpha, \beta \in \mathbb{R}$ with $\alpha \geq \beta - (n-1)/2 \geq 0$ and $f \in H^\alpha(\Omega_r^n)$ we have further

$$\mathcal{I}^{-\beta} \tilde{\mathcal{R}}_{\rho\theta}^r f(\rho \cdot) = \rho^{-(\beta+1)} \mathcal{I}^{-\beta} \tilde{\mathcal{R}}_\theta^r f. \quad (1)$$

The next result shows an inversion formula for the extended Radon transform.

¹Fraunhofer-Entwicklungszentrum Röntgentechnik EZRT, Fürth, Germany, a division of the Fraunhofer-Institute for Integrated Circuits IIS in cooperation with the Fraunhofer IZFP

Theorem III.1. Let $f \in H^{(n-1)/2}(\Omega_r^n)$, $\omega \in S^{n-1}$, $g \in L^1(\mathbb{R}^n)$ rotationally symmetric with $(\cdot)^{-1}g(\cdot) \in L^1(\mathbb{R})$ and $c_g := \int_0^\infty \rho^{-1}g(\rho\omega) d\rho \neq 0$. Then we have

$$f = \frac{1}{2c_g} (2\pi)^{1-n} \int_{\mathbb{R}^n} \mathcal{I}^{1-n} \tilde{\mathcal{R}}_y^r f(\langle \cdot, y \rangle) g(y) dy.$$

IV. RELATION BETWEEN X-RAY TRANSFORM AND EXTENDED RADON TRANSFORM

For $f \in L^1(\mathbb{R}^n)$, $a \in \mathbb{R}^n$, $\theta \in S^{n-1}$ and $k \in \mathbb{N}_0$ with $k < n$ we define

$$\begin{aligned} \mathcal{D}^k f(a, \theta) &:= \mathcal{D}_a^k f := \int_0^\infty \rho^k f(a + \rho\theta) d\rho, \\ \mathcal{D} f(a, \theta) &:= \mathcal{D}_a f(\theta) := \mathcal{D}_a^0 f(\theta). \end{aligned}$$

The operator \mathcal{D} is called *X-ray transform*. We call \mathcal{D}^k *generalized X-ray transform* and we define the abbreviations

$$\begin{aligned} \mathcal{G}^k f(a, \theta) &:= \mathcal{G}_a^k f(\theta) := \mathcal{D}_a^k f(\theta) + \mathcal{D}_a^k f(-\theta), \\ \mathcal{G} f(a, \theta) &:= \mathcal{G}_a f(\theta) := \mathcal{D}_a f(\theta) + \mathcal{D}_a f(-\theta). \end{aligned}$$

The relation between the X-ray transform and the Radon transform has been investigated in detail, see [10], [11], [12], [7] and [13]. Instead of using a linkage between the X-ray transform and the classical Radon transform, we derive a relation between the X-ray transform and the extended Radon transform.

Theorem IV.1. Let $\alpha \in \mathbb{R}^+$ with $\alpha \geq \max\{0; (n-3)/2\}$, $f \in H^\alpha(\Omega_r^n)$, $\beta \in \mathbb{R}^+$ with $\beta > n-3/2$, $\varphi \in H^\beta(\Omega_r^n)$ and $a \in \mathbb{R}^n$. Then we have

$$\begin{aligned} \int_{S^{n-1}} \mathcal{D}_a f(\theta) \mathcal{I}^{2-n} \mathcal{R}_\theta^r \varphi(0) d\theta \\ = \int_{\Omega_r^n} \mathcal{I}^{2-n} \tilde{\mathcal{R}}_y^r f(\langle a, y \rangle) \varphi(y) dy. \end{aligned}$$

It can be shown that the formulas for linking the Radon transform and the X-ray transform in [7] and in [11] can be derived from Theorem IV.1, not only for the case $n=3$, but for all $n \geq 2$.

V. INVERSION OF THE X-RAY TRANSFORM

Let $\Lambda \subset \mathbb{R}$ be a closed interval. The curve that corresponds to a path $\phi : \Lambda \rightarrow \mathbb{R}^n$ is denoted by $\Gamma_\phi := R(\phi) \subset \mathbb{R}^n$. The set of all paths where the corresponding curve is lying outside of Ω_r^n is defined by $\Phi^{n,r}(\Lambda) := \{\phi : \Lambda \rightarrow \mathbb{R}^n \mid R(\phi) \subset \mathbb{R}^n \setminus \Omega_r^n\}$. Within this paper we make always use of an admissible path ϕ , i.e. $\phi \in \Phi^{n,r}(\Lambda)$ and $\int_\Lambda \|\phi(\lambda) - r\|^{n-1} d\lambda < \infty$. This condition ensures that the X-ray transform depending on an admissible path ϕ which is defined for $\lambda \in \Lambda$ and $\theta \in S^{n-1}$ by

$$\mathcal{D}_\phi f(\phi(\lambda), \theta) := \mathcal{D}_{\phi(\lambda)} f(\theta)$$

turns into a continuous operator $\mathcal{D}_\phi : L^2(\Omega_r^n) \rightarrow L^2(\Gamma_\phi \times S^{n-1})$.

In [2] it was shown that a stable inversion of the X-ray transform can be performed if the path fulfills the so-called *Tuy conditions*, i.e. $\phi \in \Phi^{n,r}(\Lambda)$ is bounded, continuous, differentiable a.e., and for all $(x, \theta) \in \Omega_r^n \times S^{n-1}$ there

exists an element $\lambda \in \Lambda$ such that $\langle x, \theta \rangle = \langle \phi(\lambda), \theta \rangle$ and $\langle \phi'(\lambda), \theta \rangle \neq 0$. Obviously, for the same $\lambda \in \Lambda$ and all $\rho \in \mathbb{R} \setminus \{0\}$ the equations $\langle x, \rho\theta \rangle = \langle \phi(\lambda), \rho\theta \rangle$ and $\langle \phi'(\lambda), \rho\theta \rangle \neq 0$ are also valid.

Based on a Tuy path we define for $\theta \in S^{n-1}$ and $s \in \mathbb{R}$ the *Crofton symbol* by $n_\phi(\theta, s) := \#\{\lambda \in \Lambda : \langle \phi(\lambda), \theta \rangle = s\}$. For $\rho \in \mathbb{R}$ we get immediately $n_\phi(\rho\theta, \rho s) = n_\phi(\theta, s)$.

Using the Crofton symbol we define a function that is important for the inversion of the X-ray transform: Let $\phi \in \Phi^{n,r}(\Lambda)$ be a Tuy path, $\lambda \in \Lambda$ and $y \in \Omega_r^n$. We define

$$t_{\phi, \lambda, r}(y) := |\langle \phi'(\lambda), y \rangle| n_\phi(y, \langle \phi(\lambda), y \rangle)^{-1}. \quad (2)$$

The function $t_{\phi, \lambda, r}$ is even and homogeneous of degree 1, because we have

$$\begin{aligned} t_{\phi, \lambda, r}(-y) &= |\langle \phi'(\lambda), -y \rangle| n_\phi(-y, \langle \phi(\lambda), -y \rangle)^{-1} \\ &= |\langle \phi'(\lambda), y \rangle| n_\phi(y, \langle \phi(\lambda), y \rangle)^{-1} = t_{\phi, \lambda, r}(y) \end{aligned}$$

and for $\rho := \|y\|$ and $\theta := y/\|y\|$ we get

$$\begin{aligned} t_{\phi, \lambda, r}(\rho\theta) &= |\langle \phi'(\lambda), \rho\theta \rangle| n_\phi(\rho\theta, \langle \phi(\lambda), \rho\theta \rangle)^{-1} \\ &= \rho |\langle \phi'(\lambda), \theta \rangle| n_\phi(\theta, \langle \phi(\lambda), \theta \rangle)^{-1} = \rho t_{\phi, \lambda, r}(\theta). \end{aligned}$$

The structure of the presented inversion formula for the X-ray transform is essentially based on the following result.

Lemma V.1. Let $\beta, z \in \mathbb{R}^+$ with $z < r$ and $\beta > \max\{1, n-3/2\}$, $\phi \in \Phi^{n,r}(\Lambda)$ a Tuy path with $t_{\phi, \lambda, r} \in H^\beta(\Omega_r^n)$ for $\lambda \in \Lambda$, $g \in D(\Omega_r^n)$ rotationally symmetric with $g|_{\Omega_\alpha^n} \equiv 0$, $e \in S(\mathbb{R}^n)$, $\omega \in S^{n-1}$, $c_g := \int_0^\infty \rho^{-1}g(\rho\omega) d\rho \neq 0$ and

$$\varphi_{\phi, \lambda, e, g} := \frac{1}{c_g} \mathcal{I}^{-1} \tilde{\mathcal{R}}_{(\cdot)} e(\langle \phi(\lambda), \cdot \rangle) g(\cdot) t_{\phi, \lambda, r}(\cdot). \quad (3)$$

Then we have $\varphi_{\phi, \lambda, e, g} \in H^\beta(\Omega_r^n)$ and

$$\mathcal{I}^{2-n} \mathcal{R}_\theta^r \varphi_{\phi, \lambda, e, g}(0) = 2(2\pi)^{n-2} \mathcal{G}_{\phi(\lambda)}^{n-2} \mathcal{C}_e \hat{t}_{\phi, \lambda, r}(\theta). \quad (4)$$

The next theorem shows an inversion formula for the n-dimensional X-ray transform.

Theorem V.2. Let $\beta \in \mathbb{R}^+$ with $\beta > \max\{1, n-3/2\}$, $f \in L^2(\Omega_r^n)$, $\phi \in \Phi^{n,r}(\Lambda)$ a Tuy path with $t_{\phi, \lambda, r} \in H^\beta(\Omega_r^n)$ for $\lambda \in \Lambda$. Then we have for almost every $x \in \Omega_r^n$

$$f(x) = (2\pi)^{-1} \int_\Lambda \int_{S^{n-1}} \mathcal{D}_{\phi(\lambda)} f(\theta) \mathcal{G}_{\phi(\lambda)}^{n-2} \mathcal{T}_x \hat{t}_{\phi, \lambda, r}(\theta) d\theta d\lambda.$$

Proof. Let $g \in D(\Omega_r^n)$ be rotationally symmetric with $g|_{\Omega_\alpha^n} \equiv 0$ and $c_g := \int_0^\infty \rho^{-1}g(\rho\omega) d\rho \neq 0$ for $\omega \in S^{n-1}$. Since the Riesz potential is self-adjoint we get using Theorem III.1 and $c := (2\pi)^{1-n}/2$ for an arbitrary $e \in S(\mathbb{R}^n)$

$$\begin{aligned} \int_{\mathbb{R}^n} f(t) e(t) dt &= \int_{\mathbb{R}^n} \frac{c}{c_g} \int_{\Omega_r^n} \mathcal{I}^{1-n} \tilde{\mathcal{R}}_y^r f(\langle t, y \rangle) g(y) dy e(t) dt \\ &= \int_{\mathbb{R}^n} \frac{c}{c_g} \int_{\Omega_r^n} \int_{\mathbb{R}} \mathcal{I}^{1-n} \tilde{\mathcal{R}}_y^r f(s) \delta(s - \langle t, y \rangle) ds g(y) dy e(t) dt \\ &= \frac{c}{c_g} \int_{\Omega_r^n} \int_{\mathbb{R}} \mathcal{I}^{1-n} \tilde{\mathcal{R}}_y^r f(s) \int_{\mathbb{R}^n} e(t) \delta(s - \langle t, y \rangle) dt ds g(y) dy \\ &= \frac{c}{c_g} \int_{\Omega_r^n} \int_{\mathbb{R}} \mathcal{I}^{1-n} \tilde{\mathcal{R}}_y^r f(s) \tilde{\mathcal{R}}_y e(s) ds g(y) dy \\ &= \frac{c}{c_g} \int_{\Omega_r^n} \int_{\mathbb{R}} \mathcal{I}^{2-n} \tilde{\mathcal{R}}_y^r f(s) \mathcal{I}^{-1} \tilde{\mathcal{R}}_y e(s) ds g(y) dy. \quad (5) \end{aligned}$$

Using the substitution $s = \langle \phi(\lambda), y \rangle$ and using the definition of $\varphi_{\phi,\lambda,e,g}$ from (3) yields

$$\begin{aligned}
& \frac{c}{c_g} \int_{\Omega_r^n} \int_{\mathbb{R}} \mathcal{I}^{2-n} \tilde{\mathcal{R}}_y^r f(s) \mathcal{I}^{-1} \tilde{\mathcal{R}}_y e(s) ds g(y) dy \\
&= \frac{c}{c_g} \int_{\Omega_r^n} \int_{\Lambda} \mathcal{I}^{2-n} \tilde{\mathcal{R}}_y^r f(\langle \phi(\lambda), y \rangle) \mathcal{I}^{-1} \tilde{\mathcal{R}}_y e(\langle \phi(\lambda), y \rangle) \\
&\quad \times |\langle \phi'(\lambda), y \rangle| n_{\phi}(y, \langle \phi(\lambda), y \rangle)^{-1} d\lambda g(y) dy \\
&= \frac{c}{c_g} \int_{\Omega_r^n} \int_{\Lambda} \mathcal{I}^{2-n} \tilde{\mathcal{R}}_y^r f(\langle \phi(\lambda), y \rangle) \\
&\quad \times \mathcal{I}^{-1} \tilde{\mathcal{R}}_y e(\langle \phi(\lambda), y \rangle) t_{\phi,\lambda,r}(y) d\lambda g(y) dy \\
&= \frac{c}{c_g} \int_{\Lambda} \int_{\Omega_r^n} \mathcal{I}^{2-n} \tilde{\mathcal{R}}_y^r f(\langle \phi(\lambda), y \rangle) \\
&\quad \times \mathcal{I}^{-1} \tilde{\mathcal{R}}_y e(\langle \phi(\lambda), y \rangle) g(y) t_{\phi,\lambda,r}(y) dy d\lambda \\
&= c \int_{\Lambda} \int_{\Omega_r^n} \mathcal{I}^{2-n} \tilde{\mathcal{R}}_y^r f(\langle \phi(\lambda), y \rangle) \varphi_{\phi,\lambda,e,g}(y) dy d\lambda. \quad (6)
\end{aligned}$$

Since $\varphi_{\phi,\lambda,e,g} \in H^{\beta}(\Omega_r^n)$ (Lemma V.1) we can apply Theorem IV.1. Together with Lemma V.1 we get

$$\begin{aligned}
& c \int_{\Lambda} \int_{\Omega_r^n} \mathcal{I}^{2-n} \tilde{\mathcal{R}}_y^r f(\langle \phi(\lambda), y \rangle) \varphi_{\phi,\lambda,e,g}(y) dy d\lambda \\
&\stackrel{IV.1}{=} c \int_{\Lambda} \int_{S^{n-1}} \mathcal{D}_{\phi(\lambda)} f(\theta) \mathcal{I}^{2-n} \mathcal{R}_{\theta}^r \varphi_{\phi,\lambda,e,g}(0) d\theta d\lambda \\
&\stackrel{V.1}{=} (2\pi)^{-1} \int_{\Lambda} \int_{S^{n-1}} \mathcal{D}_{\phi(\lambda)} f(\theta) \mathcal{G}_{\phi(\lambda)}^{n-2} \mathcal{C}_e \hat{t}_{\phi,\lambda,r}(\theta) d\theta d\lambda. \quad (7)
\end{aligned}$$

Concluding (5), (6), and (7) yields

$$\begin{aligned}
& \int_{\mathbb{R}^n} f(t) e(t) dt = \\
& (2\pi)^{-1} \int_{\Lambda} \int_{S^{n-1}} \mathcal{D}_{\phi(\lambda)} f(\theta) \mathcal{G}_{\phi(\lambda)}^{n-2} \mathcal{C}_e \hat{t}_{\phi,\lambda,r}(\theta) d\theta d\lambda. \quad (8)
\end{aligned}$$

Let $e_{\gamma} := e_{\gamma,n}^{\text{Gaub}} := \frac{1}{(2\pi)^{n/2} \gamma^n} e^{-\frac{\|\cdot\|^2}{2\gamma^2}}$ be the n-dimensional Gaussian function and choose the arbitrary function e in (8) as $e_{\gamma}(\cdot - x)$. For $\gamma \rightarrow 0$ we get for almost every $x \in \Omega_r^n$

$$f(x) = (2\pi)^{-1} \int_{\Lambda} \int_{S^{n-1}} \mathcal{D}_{\phi(\lambda)} f(\theta) \mathcal{G}_{\phi(\lambda)}^{n-2} \mathcal{T}_x \hat{t}_{\phi,\lambda,r}(\theta) d\theta d\lambda.$$

□

VI. INVERSION OF THE EXTENDED X-RAY TRANSFORM

For $f \in L^2(\Omega_r^n)$, $a \in \mathbb{R}^n$ and $y \in \mathbb{R}_*^n$ we define

$$\tilde{\mathcal{D}}f(a, y) := \tilde{\mathcal{D}}_a f(y) := \int_0^{\infty} f(a + ty) dt.$$

The operator $\tilde{\mathcal{D}}$ is called *extended X-ray transform*. The extended X-ray transform is homogeneous of degree -1 , i.e. for $a \in \mathbb{R}^n$, $\rho \in \mathbb{R}^+$ and $\theta \in S^{n-1}$ we have $\tilde{\mathcal{D}}_a f(\rho\theta) = \rho^{-1} \tilde{\mathcal{D}}_a f(\theta)$, see [14].

The next result shows an inversion formula for the extended X-ray transform.

Theorem VI.1. *Let $\beta \in \mathbb{R}^+$ with $\beta > \max\{1, n - 3/2\}$, $f \in L^2(\Omega_r^n)$, $\phi \in \Phi^{n,r}(\Lambda)$ a Tuy path with $t_{\phi,\lambda,r} \in H^{\beta}(\Omega_r^n)$*

für $\lambda \in \Lambda$ and $\mathcal{W}_a := \mathcal{T}_a + \mathcal{T}_{-a}$ für $a \in \mathbb{R}^n$. Then we have for almost every $x \in \Omega_r^n$

$$f(x) = (2\pi)^{-1} \int_{\Lambda} \int_{\mathbb{R}^n} \tilde{\mathcal{D}}_{\phi(\lambda)} f(y) \mathcal{W}_{(\phi(\lambda)-x)} \hat{t}_{\phi,\lambda,r}(y) dy d\lambda.$$

VII. RECONSTRUCTION ALGORITHMS

Using Theorem V.2 we derive reconstruction algorithms of filtered backprojection type. Depending on the number of approximations we achieve shift-variant or shift-invariant filtering. The first of maximal two approximations is nearly the same as in the standard filtered backprojection algorithm for fan-beam geometry, see [14], and should therefore cause no artefacts in an usual CT setup.

An algorithm of filtered layergram type based on Theorem VI.1 is also shown. In this case no approximations are necessary.

A. Filtered Backprojection

The inner integral concerning S^{n-1} in the inversion formula in Theorem V.2 depends on the reconstruction point $x \in \Omega_r^n$ and must be calculated for every x . To achieve a backprojection algorithm we need to show that the value of the inner integral is equal for all reconstruction points lying on a single ray starting at a curve position $\phi(\lambda)$. Therefore we define for $u \in \mathbb{R}_*^n$ and $v \in \mathbb{R}^n$ with $v \neq u$ the mapping $U_{u,v} : \mathbb{R}^n \rightarrow \mathbb{R}^n$ such that $U_{u,v} \left(\frac{u-v}{\|u-v\|} \right) = \frac{u}{\|u\|}$. Obviously, $U_{u,v}$ is a rotation and therefore unitary. The corresponding Operator $\mathcal{U}_{u,v} : L^1(\mathbb{R}^n) \rightarrow L^1(\mathbb{R}^n)$ is defined by $f \mapsto \mathcal{U}_{u,v} f := f(U_{u,v}(\cdot))$.

Applying the X-ray transform to a translation can be expressed as a combination of appropriate rotation operators and the X-ray transform, i.e. for $a, x \in \mathbb{R}^n$ and $k \in \mathbb{N}_0$ with $k < n$ we have

$$\mathcal{G}_a^k \mathcal{T}_x = \left(\frac{\|a-x\|}{\|a\|} \right)^{k+1} \mathcal{U}_{a,x} \mathcal{G}_a^k \mathcal{U}_{a,x}^* \mathcal{V}_{\frac{\|a-x\|}{\|a\|}}. \quad (9)$$

Since $t_{\phi,\lambda,r}$ is homogeneous of degree 1, we get for $c \in \mathbb{R}^+$

$$\mathcal{V}_c \hat{t}_{\phi,\lambda,r} = c^{-(n+1)} \hat{t}_{\phi,\lambda,cr}. \quad (10)$$

Combining (9) and (10) yields the following variant of Theorem V.2: Let $\beta \in \mathbb{R}^+$ with $\beta > \max\{1, n - 3/2\}$, $f \in L^2(\Omega_r^n)$, $\phi \in \Phi^{n,r}(\Lambda)$ a Tuy path with $t_{\phi,\lambda,r} \in H^{\beta}(\Omega_r^n)$ for $\lambda \in \Lambda$, $c := (2\pi)^{-1}$ and $c_{\phi(\lambda),x} := \frac{\|\phi(\lambda)-x\|}{\|\phi(\lambda)\|}$. Then we have for almost every $x \in \Omega_r^n$

$$f(x) = c \int_{\Lambda} c_{\phi(\lambda),x}^{-2} \int_{S^{n-1}} \mathcal{D}_{\phi(\lambda)} f(\theta) g_{x,\phi,\lambda,c_{\phi(\lambda),x}r}(\theta) d\theta d\lambda$$

with

$$g_{x,\phi,\lambda,c_{\phi(\lambda),x}r}(\theta) := \mathcal{U}_{\phi(\lambda),x} \mathcal{G}_{\phi(\lambda)}^{n-2} \mathcal{U}_{\phi(\lambda),x}^* \hat{t}_{\phi,\lambda,c_{\phi(\lambda),x}r}(\theta).$$

1) *Backprojection with Shift-Variant Filtering:* If for all $x \in \Omega_r^n$ and $\lambda \in \Lambda$ the estimation $\|x\| \ll \|\phi(\lambda)\|$ holds, then we approximate $\hat{t}_{\phi,\lambda,c_{\phi(\lambda),x}r} \approx \hat{t}_{\phi,\lambda,r}$ and get $f \approx \tilde{f}_1$ with

$$\tilde{f}_1(x) := c \int_{\Lambda} c_{\phi(\lambda),x}^{-2} \int_{S^{n-1}} \mathcal{D}_{\phi(\lambda)} f(\theta) g_{x,\phi,\lambda,r}(\theta) d\theta d\lambda. \quad (11)$$

For an arbitrary reconstruction point $x \in \Omega_r^n$ and an arbitrary curve position $\lambda \in \Lambda$ we define

$$m_{\phi,\lambda,r}(x) := \int_{S^{n-1}} \mathcal{D}_{\phi(\lambda)} f(\theta) g_{x,\phi,\lambda,r}(\theta) d\theta. \quad (12)$$

Let $L_{a,\theta} := \{a + \rho\theta : \rho \in \mathbb{R}^+\} \subset \mathbb{R}^n$ be the ray with starting point $a \in \mathbb{R}^n$ and direction $\theta \in S^{n-1}$. For $x_1, x_2 \in L_{a,\theta}$ we have $\frac{a-x_1}{\|a-x_1\|} = \frac{a-x_2}{\|a-x_2\|}$. This yields $\mathcal{U}_{a,x_1} = \mathcal{U}_{a,x_2}$ and therefore $m_{\phi,\lambda,r}(x_1) = m_{\phi,\lambda,r}(x_2)$. This shows that it is not necessary to calculate (12) for every point $x \in \Omega_r^n$. It is sufficient to calculate the value of (12) for every ray $L_{\phi(\lambda),\theta}$ at an arbitrary point $x \in L_{\phi(\lambda),\theta}$. This value can be backprojected along $L_{\phi(\lambda),\theta}$ because the value holds for every other point on this ray. Therefore we have a backprojection algorithm.

Due to the operator $\mathcal{U}_{\phi(\lambda),x}^*$ in $g_{x,\phi,\lambda,r}$ the value of (12) changes if the ray for which we have to calculate (12) changes. We can therefore interpret (12) as a shift-variant filtering. Calculating the filter consists essentially of determining $\hat{t}_{\phi,\lambda,r}$ and computing the generalized X-ray transform of $\hat{t}_{\phi,\lambda,r}$.

2) *Backprojection with Shift-Invariant Filtering*: If we approximate in (11) additionally $\mathcal{G}_{\phi(\lambda)}^{n-2} \mathcal{U}_{\phi(\lambda),x}^* \hat{t}_{\phi,\lambda,r}(\theta) \approx \mathcal{G}_{\phi(\lambda)}^{n-2} \hat{t}_{\phi,\lambda,r}(\theta)$, then we have $f \approx \tilde{f}_2$ with

$$\tilde{f}_2 := c \int_{\Lambda} c_{\phi(\lambda),x}^{-2} \int_{S^{n-1}} \mathcal{D}_{\phi(\lambda)} f(\theta) \tilde{g}_{x,\phi,\lambda,r}(\theta) d\theta d\lambda \quad (13)$$

and

$$\tilde{g}_{x,\phi,\lambda,r}(\theta) := \mathcal{U}_{\phi(\lambda),x} \mathcal{G}_{\phi(\lambda)}^{n-2} \hat{t}_{\phi,\lambda,r}(\theta).$$

We still have a backprojection in (13) and the inner integral concerning S^{n-1}

$$\int_{S^{n-1}} \mathcal{D}_{\phi(\lambda)} f(\theta) \mathcal{U}_{\phi(\lambda),x} \mathcal{G}_{\phi(\lambda)}^{n-2} \hat{t}_{\phi,\lambda,r}(\theta) d\theta$$

is a convolution of $\mathcal{D}_{\phi(\lambda)} f$ with $\mathcal{G}_{\phi(\lambda)}^{n-2} \hat{t}_{\phi,\lambda,r}$. Therefore formula (13) is a filtered backprojection with shift-invariant filtering.

B. Filtered Layergram

Since the preliminaries for applying the approximations in the previous section are not always fulfilled we show another reconstruction algorithm. This algorithm is based on the inversion formula for the extended X-ray transform and is of filtered layergram type, i.e. a filtering is performed after an unfiltered backprojection. Because no approximation is necessary, the algorithm is theoretically exact.

Using Theorem VI.1 and the homogeneity of $\tilde{\mathcal{D}}$ we get the following result: Let $\beta \in \mathbb{R}^+$ with $\beta > \max\{1, n-3/2\}$, $f \in L^2(\Omega_r^n)$ and $\phi \in \Phi^{n,r}(\Lambda)$ a Tuy path with $t_{\phi,\lambda,r} \in H^\beta(\Omega_r^n)$ for $\lambda \in \Lambda$. Then we have for almost every $x \in \Omega_r^n$

$$f(x) = \frac{1}{2\pi} \int_{\Lambda} h_{f,\phi,\lambda,r}(\phi(\lambda) - x) + h_{f,\phi,\lambda,r}(x - \phi(\lambda)) d\lambda$$

with

$$h_{f,\phi,\lambda,r} := \int_{\mathbb{R}^n} \|y\|^{-1} \mathcal{D}_{\phi(\lambda)} f(y/\|y\|) \hat{t}_{\phi,\lambda,r}(\cdot - y) dy.$$

The function $h_{f,\phi,\lambda,r}$ is a convolution of $\|\cdot\|^{-1} \mathcal{D}_{\phi(\lambda)} f(\cdot/\|\cdot\|)$ with $\hat{t}_{\phi,\lambda,r}$. If the projection data $\mathcal{D}_{\phi(\lambda)} f(\theta)$ is given for all $\theta \in S^{n-1}$, then we can determine $\mathcal{D}_{\phi(\lambda)} f(y/\|y\|)$ for all $y \in \mathbb{R}^n$

by performing a backprojection. A subsequent weighting by $\|\cdot\|^{-1}$ yields $\|y\|^{-1} \mathcal{D}_{\phi(\lambda)} f(y/\|y\|)$ for all $y \in \mathbb{R}^n$. Therefore we have an algorithm of filtered layergram type where the filtering has to be performed after every backprojection step.

VIII. RESULTS

Generating results using the proposed algorithms is in progress and will be finished for the final version of this paper.

IX. CONCLUSION

We've showed in this paper CT reconstruction algorithms based on a new inversion formula for the X-ray transform. Although the formula is only valid for paths fulfilling the Tuy conditions the presented approaches for deriving reconstruction algorithms are also applicable to non Tuy paths if small reconstruction artefacts are allowed. Finishing the implementation of the algorithms and comparing the results to state-of-the-art reconstruction algorithms are the next steps.

REFERENCES

- [1] A. C. Kak and M. Slaney, *Principles of Computerized Tomographic Imaging*. IEEE Press, 1998.
- [2] H. K. Tuy, "An inversion formula for cone-beam reconstruction," *SIAM Journal on Applied Mathematics*, vol. 43, no. 3, pp. 546–552, 1983.
- [3] M. Defrise and R. Clack, "A cone-beam reconstruction algorithm using shift-variant filtering and cone-beam backprojection," *IEEE Transactions on Medical Imaging*, vol. 13, no. 1, pp. 186–195, March 1994.
- [4] H. Kudo and T. Saito, "Derivation and implementation of a cone-beam reconstruction algorithm for nonplanar orbits," *IEEE Transactions on Medical Imaging*, vol. 13, no. 1, pp. 196–211, March 1994.
- [5] A. Louis, "Development of algorithms in computerized tomography," in *The Radon Transform, Inverse Problems, and Tomography*, G. Olafsson and E. T. Quinto, Eds., 2006, pp. 25–42.
- [6] A. Katsevich, "An improved exact filtered backprojection algorithm for spiral computed tomography," *Advances in Applied Mathematics*, vol. 32, no. 4, pp. 681–697, 2004.
- [7] P. Grangeat, "Mathematical framework of cone-beam reconstruction via the first derivative of the radon transform," in *Lecture Notes in Mathematics*, G. T. Herman, A. K. Louis, and F. Natterer, Eds. Springer, 1991, vol. 1497, pp. 66–97.
- [8] S. Oeckl, "Die Faltung als regularisierte Eigenschaft in der Röntgen-Computertomographie," Ph.D. dissertation, Universität des Saarlandes, 2014 (submitted).
- [9] F. Natterer, *The Mathematics of Computerized Tomography*. John Wiley & Sons, 1986.
- [10] C. Hamaker, K. T. Smith, D. C. Solmon, and S. L. Wagner, "The divergent beam x-ray transform," *Rocky Mountain Journal of Mathematics*, vol. 10, no. 1, pp. 253–283, 1980.
- [11] B. D. Smith, "Image reconstruction from cone-beam projections: Necessary and sufficient conditions and reconstruction methods," *IEEE Transactions on Medical Imaging*, vol. 4, no. 1, pp. 14–25, March 1985.
- [12] I. M. Gel'fand and A. B. Goncharov, "Recovery of a compactly supported function starting from its integrals over lines intersecting a given set of points in space," *Soviet Math. Dokl.*, vol. 34, no. 2, pp. 373–376, 1987.
- [13] V. P. Palamodov, "Inversion formulas for the three-dimensional ray transform," in *Lecture Notes in Mathematics*, G. T. Herman, A. K. Louis, and F. Natterer, Eds. Springer, 1991, vol. 1497, pp. 53–62.
- [14] F. Natterer and F. Wübbeling, *Mathematical Methods in Image Reconstruction*. SIAM, 2001.

Data Consistency Conditions for 2D Truncated Parallel Projections

Rolf Clackdoyle and Laurent Desbat

Abstract-- New data consistency conditions (DCC) have been derived for parallel projections in two dimensions, which have the remarkable feature that they can be applied to truncated projections. We show the derivation of these conditions and illustrate a potential application to motion detection and compensation.

I. INTRODUCTION

In the context of image reconstruction, data consistency conditions (DCC), also called range conditions, are mathematical descriptions of the redundancies in projection measurements. These conditions can usefully decouple the tomographic reconstruction problem from other systematic effects in the measurement model. For example, if the target specimen (usually a patient in the medical imaging scenario) undergoes an abrupt rigid motion, the measurement model now consists of both a very large linear tomographic system as well as a handful of nonlinear parameters that describe the motion and the time point when the motion occurred. If DCC are available for the tomographic model, then the small number of nonlinear parameters can be estimated by requiring the adjusted model to satisfy the DCC, which is usually a far easier task than repeated reconstructions using trial nonlinear parameters. This technique has found numerous applications in various areas of medical imaging, including in x-ray CT (e.g. [Bas00, Pat02, Def03, Hsi04, Yu07, Maz10, Tan11]).

The most well-known DCC are those of Helgason-Ludwig (HL) [Lud66, Hel80], which apply to the Radon transform in parallel projection geometries. Others have been established for fanbeam, cone-beam, exponential, and attenuated transforms and for different formats such as for Fourier transformed sinograms. (For example DCC: [Jon38, Nat83, Fin83, Edh86, Agu95, Pat02, Che05, Yu06, Lev10, CID13]). Only a few of these DCC allow subsets of a full tomographic set of data to be examined for consistency. For example, with the HL conditions, the order zero condition is that the projection sums are constant, so any number of projections can be checked for consistency of their DC terms. Similarly, any two parallel projections can will determine the degree-1 polynomial specified in the HL DCC, and other projections can then be checked against this polynomial. Convenient descriptions of DCC

where subsets of projections can be checked exist in a few cases, see [CID13] for an example using cone-beam projections. This flexibility to apply DCC to subsets of measurements increases their usefulness in applications.

With the advent of true ROI reconstruction in the plane (see [Cla10] for an overview), it is important to consider the situation of truncated projections. To our knowledge, no DCC are known to exist that can treat truncated projections, with the exception of the differential form given in [Joh30], which has the both the advantage and disadvantage of applying locally to fully 3D measurements; they cannot directly be used for just two truncated cone-beam projections for example.

We announce here what we believe to be the first DCC that can handle truncated parallel projections in the plane. We provide a simple proof of the consistency which we illustrate with simulations. We then discuss how these new DCC might be applied in practice, using a toy problem (for illustration) that involves motion detection of a known tumour-like object.

II. THEORY

We let $f(x, y)$ represent the unknown density function, and $p(\phi, r)$ be the parallel projection of f defined by

$$p(\phi, r) = \int_{-\infty}^{\infty} f(r\alpha + s\beta) ds \quad (1)$$

where $\phi \in (-\pi/2, \pi/2)$ and $\alpha = (\cos\phi, \sin\phi)$, $\beta = (-\sin\phi, \cos\phi)$. Now, for each non-negative n , we consider a weighted backprojection of $p(\phi, r)$, where the weight depends on n . The projection $p(\phi, \cdot)$ will be weighted by $\tan^n\phi / \cos\phi$ prior to backprojection. The singularity near $\pm\pi/2$ will be dealt with by only considering $|\phi| < \pi/2 - \epsilon$ as will be discussed below, but to simplify the derivation we ignore this detail for now. The weighted backprojection is given by

$$b_n(x, y) = \int_{-\pi/2}^{\pi/2} p(\phi, (x, y) \cdot \alpha) \frac{\tan^n\phi}{\cos\phi} d\phi \quad (2)$$

Since the system is shift-invariant, the behavior of the weighted backprojection can be completely characterized by its point response function (PRF), so we first examine this PRF, and then show how it leads to consistency conditions in the form of polynomials of degree n which can accommodate truncation of the projections.

A direct substitution of equation 1 into equation 2, followed by the substitution $s = (x, y) \cdot \beta - s'$ yields

$$b_n(x, y) = \int_{-\pi/2}^{\pi/2} \int_{-\infty}^{\infty} f(((x, y) \cdot \alpha)\alpha + s\beta) \frac{\tan^n\phi}{\cos\phi} ds d\phi \quad (3a)$$

R. Clackdoyle is with the Laboratoire Hubert Curien, CNRS UMR 5516, Saint Etienne, France (e-mail: rolf.clackdoyle@univ-st-etienne.fr).

L. Desbat is with the TIMC-IMAG laboratory, CNRS UMR 5525, and Joseph Fourier University, Grenoble, France (e-mail laurent.desbat@imag.fr).

This work was partially supported by the Agence Nationale de la Recherche (France), project "DROITE," number ANR-12-BS01-0018.

$$= \int_{-\pi/2}^{\pi/2} \int_{-\infty}^{\infty} f((x, y) - s'\beta) \frac{\tan^n \phi}{|s'| \cos \phi} |s'| ds' d\phi \quad (3b)$$

$$= \int_{-\infty}^{\infty} \int_{-\infty}^{\infty} f((x, y) - (x', y')) \frac{(-x')^n}{(y')^n |y'|} dx' dy' \quad (3c)$$

$$= \int_{-\infty}^{\infty} \int_{-\infty}^{\infty} f(x - x', y - y') h_n(x', y') dx' dy' \quad (3d)$$

where the point response function is

$$h_n(x, y) = \frac{(-1)^n x^n}{y^{n+1}} \text{sgn}(y) \quad (4)$$

Equation 3c was obtained from equation 3b by performing the polar-to-rectangular coordinate change of variables $(x', y') = (-s' \sin \phi, s' \cos \phi)$, with $dx' dy' = |s'| ds' d\phi$.

Note that for $n = 0$, the point response function becomes $h_0(x, y) = 1/|y|$ and the backprojection $b_0(x, y)$ is equal to an unweighted integration in the x -direction of $f(x, y)$.

We continue the derivation to arrive at our main result.

$$b_n(x, y_0) = \int_{-\infty}^{\infty} \int_{-\infty}^{\infty} f(x', y') h_n(x - x', y_0 - y') dx' dy' \quad (5a)$$

$$= \int_{-\infty}^{\infty} \int_{-\infty}^{\infty} f(x', y') \frac{(x' - x)^n}{(y_0 - y')^{n+1}} \text{sgn}(y_0 - y') dx' dy' \quad (5b)$$

$$= c_0 + c_1 x + c_2 x^2 + \dots + c_n x^n \quad (5c)$$

where we consider y_0 to be held constant and c_k is given by

$$c_k = (-1)^k \binom{n}{k} \times \int_{-\infty}^{\infty} \int_{-\infty}^{\infty} f(x', y') \frac{(x')^{n-k}}{(y_0 - y')^{n+1}} \text{sgn}(y_0 - y') dx' dy' \quad (6)$$

The new consistency conditions for 2D parallel projections can now be stated as follows:

Theorem: Suppose that a sinogram $p(\phi, r)$ satisfies equation 1 for some density function f . For y_0 chosen such that the line $y = y_0$ does not intersect the compact support of f , and for any non-negative integer n , the weighted backprojection b_n (equation 2) evaluated along the line segment $[(x_a, y_0), (x_b, y_0)]$ is a polynomial function of x , of degree at most n . That is,

$$b_n(x, y_0) = c_0 + c_1 x + c_2 x^2 + \dots + c_n x^n \quad x \in [x_a, x_b] \quad (7)$$

Note that by choosing y_0 such that the line $y = y_0$ does not intersect the support of f , all potential singularities vanish. The expression for c_k given by equation 6 no longer contains a singular kernel because the support of f restricts the integration range to exclude $y = y_0$. Furthermore, with the compact support of f not touching the line $y = y_0$, we see that there must exist some small ε such that the projection of the support of f at any angles $|\phi| \in [\pi/2 - \varepsilon, \pi/2]$ will miss the line segment $[(x_a, y_0), (x_b, y_0)]$, and therefore, for (x, y) on the line segment, this small ε range of angles will not contribute to $b(x, y)$ given by equation 2, and thus the $\tan^n \phi / \cos \phi$ singularity is avoided.

According to the theorem, testing the DCC for a parallel beam system can be achieved by simply performing a weighted backprojection onto a line segment outside the object, and verifying that the values on the line segment form a polynomial

of the correct degree. The advantage of these DCC over the HL or other published conditions is that some projection truncation is allowed: only those lines which contribute to the backprojection $b_n(x, y_0)$ for $x_0 \in [x_a, x_b]$ are needed. In the simulations section below, we illustrate the large amount of projection truncation that can be sustained while still being able to check the DCC of the measurements.

Since the backprojection is only performed along a line segment rather than a 2D volume, the computational cost is very low. Furthermore, the number of points along taken along the line can be chosen to trade off between computational effort and the accuracy desired to check the polynomial. For our simulations (see below) we examined only orders $n = 0, 1, 2$ yet we chose about 100 points on the line segment.

For each backprojection of order n , a different weight is required. However, many different backprojections can be computed in parallel as only the weight depends on n .

III. AN ILLUSTRATION OF DCC

A. Phantom and acquisition geometry

To illustrate the DCC we used a simple phantom made up of elliptical regions of constant density. Parallel beam projections of this phantom were obtained by computing exact line-lengths passing through the component ellipses. The phantom consists of a large elliptical shell of outer axes lengths 25 units x 40 units with several smaller elliptical features inside. The outer component of the elliptical shell is horizontally centered in the coordinate system but is displaced 10 units in the vertical direction (so its center is at $(0, -10)$). The phantom details are presented in Table 1, and Fig. 1 shows a sketch of it.

A non-truncated sinogram $p(\phi, r)$ was created of this phantom, for 1600 projections ϕ over the range $[-\pi/2, \pi/2]$ with 2560 samples for $r \in [-25, 25]$. Also, a truncated sinogram $p^t(\phi, r)$ was considered which was the same as $p(\phi, r)$ by extracting the 1024 central samples for $r \in [-10, 10]$ in each projection. This truncated sinogram corresponds to the field-of-view (FOV) of diameter 20 indicated in Fig. 1. The two sinograms are displayed in Fig 2. Note the heavy truncation of sinogram $p^t(\phi, r)$: every projection is truncated either on one side, or the other, or on both sides.

Table1: Ellipse Parameters

Ellipse	Center	(Dx, Dy)	Density
1a	(0, -10)	(40, 25)	0.5
1b	(0.5, -10)	(38, 24)	-0.5
2	(-5, -12)	(8.75, 8.75)	0.1
3	(2, -7)	(3.75, 2.5)	0.1
4	(4, 0)	(5, 2.5)	0.1
5	(-7, -1)	(1.25, 2.5)	0.1
6	(-3, 0)	(1.25, 1.25)	0.1
7	(-4, -4)	(2.5, 2.5)	0.2
8	(-2, -3.5)	(1.5, 1.5)	0.2

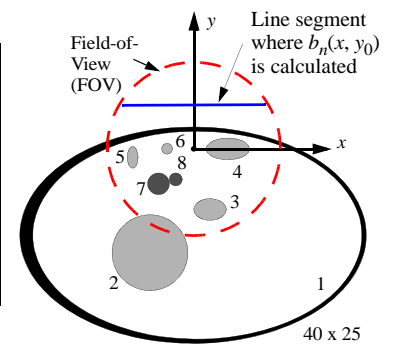


Fig 1. Illustration of the phantom, showing also the FOV corresponding to the truncated sinogram, and also the line-segment along which the backprojections were calculated for verifying data consistency.

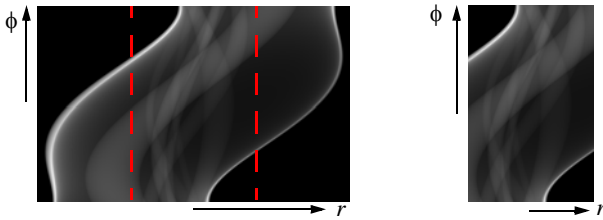


Fig 2. Sinograms. Left: the full 1600 projections (vertical axis) of 2560 elements each for large coverage of 50 units in diameter. The red lines show the boundary of the FOV indicated in Fig. 1. Right: the 1600 x 1024 truncated sinogram extracted from full sinogram, covering the 20 units diameter FOV shown in Fig 1.

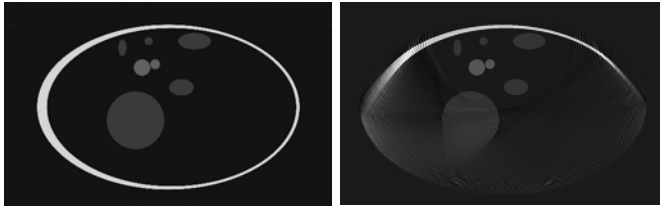


Fig 3. Reconstructions. Left: a FBP reconstruction of the full object from the full sinogram of Fig. 2. The reconstruction size was 1024 x 1024. Right: a conjugate gradient reconstruction from a downsampled 800 x 512 version of the truncated sinogram. The image size is 256 x 256. (Greyscale windows are not the same.)

Reconstructions from the two sinograms of Fig. 2 are shown in Fig. 3. From the full data, a standard filtered back-projection (FBP) reconstruction was performed. Accurate (“exact”) ROI reconstruction from such truncated sinograms was only theoretically established in 2007 [Def07], but no suitable analytic reconstruction technique is known at this time. The image of Fig. 3 (right) was achieved by using a conjugate gradient method to minimize a least-squares criterion with a small amount of regularization. This ROI reconstruction from truncated data is computationally intensive.

B. Verifying data consistency conditions

From the simulated sinogram, the weighted backprojection functions $b_n(x, y_0)$ defined by equation 2 were calculated for the line segment $y = y_0$ with $y_0 = 5$ and $x \in [-8, 8]$ as illustrated in Fig. 1. We now drop the fixed y_0 and just write $b_n(x)$ for short. We only examined cases $n = 0, 1, 2$ and the backprojection was performed for 101 samples along the line segment, spaced every 0.16 units apart. The plots of Fig. 4 show least-squares fits of the backprojections b_n to polynomials of degree n . We note the excellent polynomial fits of the correct degree, as predicted by the theory.

The central observation here is that to perform the back-projections $b_n(x)$, only the truncated sinogram was necessary. All lines (sinogram entries) necessary to calculate the back-projection were available because the line-segment lies inside the FOV of Fig. 1. Thus we have found (and numerically verified) necessary DCC for the truncated sinogram $p^l(\phi, r)$.

IV. AN APPLICATION OF DCC

As an illustration of potential applications of truncated projection DCC, we consider a dynamic version of our phantom and illustrate how the DCC can be applied to search for 3 motion parameters.

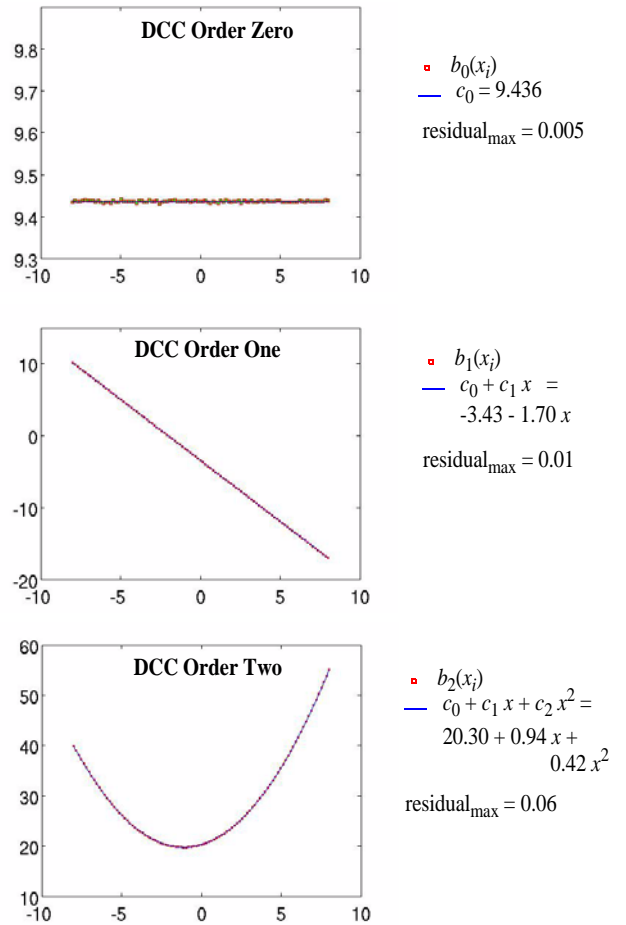


Fig 4. Data Consistency Conditions. The backprojections $b_0(x)$, $b_1(x)$, $b_2(x)$ were fit respectively to polynomials of degree 0, 1, 2. The three graphs show the original 101 values x_i along the line $x \in [-8, 8]$ and, superimposed, the best fit polynomial. The residual values are also listed.

A. Dynamic phantom

We define a dynamic version of the phantom which changes during the course of the scan and therefore the projections will not be consistent. The dynamic nature of the phantom is described by 3 nonlinear parameters, and the objective is to search for these parameters by minimizing inconsistency. For the dynamic phantom, ellipses 7 and 8 undergo a horizontal oscillatory motion (such as a tumour moving due to respiration). It is assumed that the shape and density of the “tumour” are known, but not the three motion parameters (t_0, t_1, A) defined below, and not the rest of the phantom.

We assume that the projections are gathered over T seconds uniformly, so $\phi_t = (\pi/T)t - \pi/2$. The centers of ellipses 7 and 8 are now $\Gamma_t(-4, -4)$ and $\Gamma_t(-2, -3.5)$ where

$$\Gamma_t(x, y) = \begin{cases} \left(x + \frac{A}{2} - \frac{A}{2} \cos\left(2\pi \frac{t-t_0}{t_1-t_0}\right), y \right) & \text{if } t \in [t_0, t_1] \\ (x, y) & \text{otherwise} \end{cases} \quad (8)$$

For our simulation we use $T = 18$ seconds and $(t_0, t_1, A) = (2, 17, 7)$. Fig. 5 illustrates the motion.

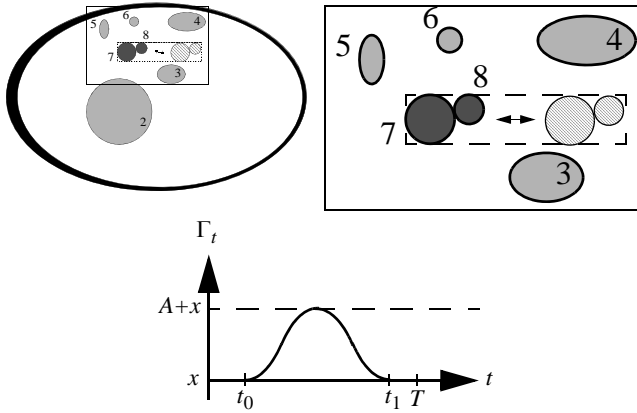


Fig 5. Dynamic Phantom details. Upper row: phantom and magnified insert illustrating horizontal motion of ellipses 7 and 8. Bottom: graph of the function Γ_t . The motion starts at t_0 and ends at initial position at t_1 . The distance travelled in each direction is A .

B. Sinogram and reconstruction of dynamic data

As before, the (truncated) projections were simulated by using line-length calculations, but through the dynamic phantom described above. Fig. 6 shows the resulting sinogram and the reconstruction obtained from this sinogram. It is an interesting curiosity that the movement of disks 7 and 8 does not cause only a lateral blurring, but seems to suggest a triangular motion.

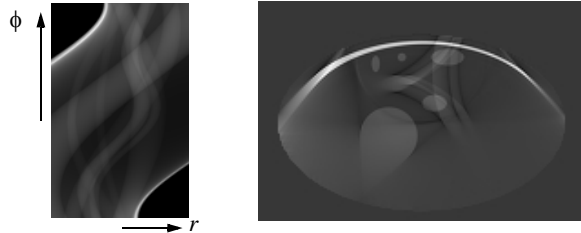


Fig 6. Left: sinogram p^{dyn} of the dynamic phantom, same parameters as in Fig. 2(right). Conjugate gradient reconstruction from the sinogram at left; same parameters as in Fig 3(right). Note that complicated blurring caused by motion.

C. Using DCC to identify the motion

We describe here our procedure for using DCC to estimate the three motion parameters of the tumour from the projections p^{dyn} of the dynamic phantom. We introduce non-negative cost functions $C_n(p)$ which are zero when the (truncated) sinogram is consistent. Recalling that b_n is the backprojection of p along the line segment, we define $C_n(p)$ to be the residual of the best degree- n polynomial fit to b_n . That is,

$$C_n(p) = \min_{q \in Q_n} \|q - b_n\|^2 \quad (9)$$

where Q_n is the set of all polynomials of degree n .

Since we know the tumour properties, from a set of motion parameters (t_0, t_1, A) we can simulate its position at time t and thereby construct a simulated tumour sinogram $p_{t_0, t_1, A}^{\text{sim}}$. If we successfully estimate its motion parameters, they can be subtracted from the measurements p^{dyn} to give consistent data. So, we define a cost function $c(t_0, t_1, A)$ as follows:

$$c(t_0, t_1, A) = \sum_{n=1}^2 C_n(p^{\text{dyn}} - p_{t_0, t_1, A}^{\text{sim}}) \quad (10)$$

We used the Downhill Simplex method (see ‘‘amoeba’’ [Pre03]) to minimize $c(t_0, t_1, A)$ starting from four vertices of an initial simplex of $(t_0, t_1, A) = (1.5, 16, 6), (3, 16, 6), (1.5, 17.5, 6), (1.5, 16, 7.5)$ with respective costs 0.27, 0.88, 0.31, 0.63. We obtained, after 204 evaluations of the cost function, the values $(\tilde{t}_0, \tilde{t}_1, \tilde{A}) = (1.98, 16.99, 7.03)$ with a cost of 0.19 (which was slightly lower than the cost at the ‘‘true’’ motion parameters $(t_0^*, t_1^*, A^*) = (2, 17, 7)$).

In Fig. 7 we show the sinogram $p_{\tilde{t}_0, \tilde{t}_1, \tilde{A}}^{\text{sim}}$ of the estimated movement of the tumour, which we subtract from the measured sinogram p^{dyn} to give a corrected sinogram $p^{\text{dyn}} - p_{\tilde{t}_0, \tilde{t}_1, \tilde{A}}^{\text{sim}}$ which is the most consistent possible according to our procedure. We performed a motion-corrected reconstruction from this consistent sinogram, and in comparing with Fig. 6 we note that the motion artifacts have been virtually eliminated.

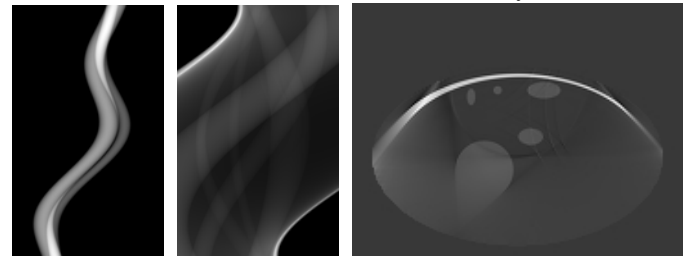


Fig 7. Motion correction by DCC. Left: DCC estimated motion $p_{\tilde{t}_0, \tilde{t}_1, \tilde{A}}^{\text{sim}}$ in measured sinogram p^{dyn} . Center: Sinogram after motion component has been subtracted: $p^{\text{dyn}} - p_{\tilde{t}_0, \tilde{t}_1, \tilde{A}}^{\text{sim}}$. Right: Reconstruction obtained from corrected sinogram, showing dramatically reduced motion artifacts (compare to Fig. 6).

V. DISCUSSION AND CONCLUSIONS

We have derived necessary DCC for truncated parallel projections. We believe these to be the first published DCC for truncated projections. The conditions were applied to a toy problem in motion estimation and compensation to illustrate their potential for practical applications.

DCC for truncated *fanbeam* projections are possible using the same principles as shown here, but the backprojection step would be more elaborate, probably requiring 2D interpolations.

The backprojection weight functions are closely related to expressions appearing in recently-published fanbeam DCC [Cla13]. The link can be seen by considering the virtual fanbeam approach (see [Cla10] for a description) applied to the truncated parallel projections.

VI. REFERENCES

- [Agu95] V. Aguilar and P. Kuchment. ‘‘Range conditions for the multi-dimensional exponential x-ray transform.’’ *Inv. Probs* 11, 977-982, 1995.
- [Bas00] S. Basu and Y. Bresler. ‘‘Uniqueness of tomography with unknown view angles.’’ *IEEE Trans Imag Proc* 9, 1092-1106, 2000.
- [Che05] G.-H. Chen and S. Leng. ‘‘A new data consistency condition for fan-beam projection data.’’ *Med Phys* 32, 961-967, 2005.
- [Cla10] R. Clackdoyle and M. Defrise. ‘‘Tomographic Reconstruction in the 21st Century: Region-of-interest reconstruction from incomplete data.’’ *IEEE Sig Proc Mag.* 27, 60-80, 2010.

- [Cla13] R. Clackdoyle. "Necessary and Sufficient Consistency Conditions for Fanbeam Projections along a Line." *IEEE Trans Nucl Sci*, 60, 1560-1569, 2013.
- [CID13] R. Clackdoyle and L. Desbat. "Full data consistency conditions for cone-beam projections with sources on a plane." *Phys. Med. Biol.* 58, 8437-8456, 2013.
- [Def03] M. Defrise, F. Noo, and H. Kudo. "Improved two-dimensional rebinning of helical cone-beam computerized tomography data using Johns equation." *Inv. Probs* 19, S41-S54, 2003.
- [Def06] M. Defrise, F. Noo, R. Clackdoyle, and H. Kudo. "Truncated Hilbert transform and image reconstruction from limited tomographic data" *Inv. Probs* 22,1037-1053, 2006.
- [Edh86] P.R. Edholm, R.M. Lewitt and B. Lindholm. "Novel properties of the Fourier decomposition of the sinogram." *Proc SPIE* 671, 8-18, 2006.
- [Fin83] D.V. Finch and D.C. Solmon. "Sums of homogeneous function and the range of the divergent beam X-ray transform." *Numer Func Anal and Optimiz* 5, 363-419, 1983.
- [Hel80] S. Helgason. *The Radon Transform*. (Boston: Birkhauser), 1980.
- [Hsi04] J. Hsieh, E. Chao, J. Thibault, B. Grekowitz, A. Horst, S. McOlash and T.J. Myers. "A novel reconstruction algorithm to extend the CT scan field-of-view." *Med. Phys.* 31, 2385-2391, 2004.
- [Joh38] F. John. "The ultrahyperbolic differential equation with four independent variables." *Duke Math. J.* 4, 300-322, 1938.
- [Lev10] M.S. Levine, E.Y. Sidky and X. Pan. "Consistency Conditions for Cone-Beam CT Data Acquired with a Straight-Line Source Trajectory." *Tsinghua Sci Technol* 15, 56-61, 2010.
- [Lud66] D. Ludwig. "The Radon transform on Euclidean space." *Comm. Pure Appl. Math.* 19, 49-81, 1966.
- [Maz10] S.R. Mazin and N.J. Pelc. "Fourier properties of the fanbeam sinogram." *Med. Phys* 37, 1674-1680, 2010.
- [Nat83] F. Natterer. "Computerized tomography with unknown sources." *SIAM J. Appl. Math.* 43, 1201-1212, 1983.
- [Pat02] S.K. Patch. "Consistency conditions upon 3D CT data and the wave equation." *Phys. Med. Biol.* 47, 2637-2650, 2002.
- [Pre03] W.H. Press, S.A. Teukolsky, W.T. Vetterling, B.P. Flannery. *Numerical Recipes in C++* (Cambridge: Masson) 2003.
- [Tan11] S. Tang, X. Mou, Q. Xu, Y. Zhang, J. Bennett and H. Yu. "Data consistency condition-based beam-hardening correction." *Opt. Eng.* 50, 076501(1-13), 2011.
- [Yu06] H. Yu, Y. Wei, J. Hsieh and G. Wang. "Data Consistency Based Translational Motion Artifact Reduction in Fan-Beam CT." *IEEE Trans. Med. Imag.* 25, 792-803, 2006.
- [Yu07] H. Yu and G. Wang. "Data Consistency Based Rigid Motion Artifact Reduction in Fan-Beam CT." *IEEE Trans. Med. Imag.* 26, 249-260, 2007.

Fanbeam Data Consistency Conditions for Applications to Motion Detection

Rolf Clackdoyle, Simon Rit, Jan Hoskovec, Laurent Desbat

Abstract-- New data consistency conditions (DCC) have recently been published for fanbeam projections. We explore the potential of applying fanbeam DCC to detection and tracking of motion of a small known object inside an unknown background without the need for image reconstruction. Two scanning geometries are considered that have different data consistency properties. A downhill simplex search for 3 nonlinear parameters by minimizing inconsistency was successful. Various issues on the use of fanbeam DCC are discussed.

I. INTRODUCTION

In image reconstruction from projections, the simple line-integral model presents a large system of linear equations. Data consistency conditions (DCC) analytically describe the redundancies in this integral equation, and they can play a useful role in image reconstruction. The idea is that by verifying the DCC of the measured data, other systematic and possibly nonlinear effects can be identified and possibly corrected before performing the tomographic reconstruction step. It was probably Natterer who pioneered this approach over 30 years ago, when he explored the use of consistency conditions on the attenuated Radon transform to identify unknown attenuation coefficients from SPECT emission measurements [Nat83]. This general approach has been followed numerous times, with a range of medical imaging applications in PET, SPECT and CT. See for example, [Nat93, Gli94, Men99, Bas00, Erl00, Pat02, Wei03, Lay05, Yu07, Tan11, Def12] among others.

At the heart of such approaches are the consistency conditions themselves. These are mathematical equations that describe the consistency (arising from redundancy) of the measurements. For the simple (non-attenuated) line-integral model which is valid for CT imaging, the well-known Helgason-Ludwig (HL) conditions [Lud66] [Hel80] apply, and are particularly useful because they can be expressed in terms of subsets of parallel projections. In other words, consistency of a sub-collection of measured projections can be checked without

obtaining a full collection of projections. The situation for subsets of fanbeam projections is more complicated although such consistency conditions for linear trajectories have recently been published [Cla13].

In this work, we are only concerned with unknown density functions in the plane, and with fanbeam projections. The purpose is to explore the use of fanbeam consistency conditions and study issues that might arise in applications. We define an artificial 2D problem in motion detection which is both challenging yet within reach of fanbeam consistency methods.

II. FANBEAM PROJECTIONS AND CONSISTENCY CONDITIONS

As usual in classical tomography, we let $f(x, y)$ represent the unknown density function. We define a fanbeam projection $g(v_\lambda, \cdot)$ with x-ray source at position v_λ , by

$$g(v_\lambda, \phi) = \int_0^\infty f(v_\lambda + l\alpha_\phi) dl \quad (1)$$

where $\alpha_\phi = (\cos \phi, \sin \phi)$ with ϕ ranging over some interval of length at most 2π which may depend on the source position v_λ . The source trajectory is parameterized by $\lambda \in \Lambda$ for some bounded interval Λ . Our example trajectories will be a straight line segment, and a conventional circular scan.

Fanbeam consistency conditions can be stated for the case of a straight line trajectory that does not cut through the object. By rotating and translating the coordinate system if necessary, we can assume that the straight line trajectory is the y -axis (so $v_\lambda = (0, \lambda)$), and that the object lies entirely in the $x > 0$ half-plane. In this situation, the range of ϕ is $(-\pi/2, \pi/2)$. Now for any fixed non-negative n strictly less than the number of measured projections N , we convert each projection to a scalar function $J_n(\lambda)$ as follows:

$$J_n(\lambda) = \int_{-\pi/2}^{\pi/2} g(v_\lambda, \phi) \frac{\tan^n \phi}{\cos \phi} d\phi \quad (2)$$

If the projections are consistent, i.e. if g satisfies equation 1 for some f , then $J_n(\lambda)$ is a polynomial in λ of degree at most n . These necessary conditions are easily verified and also turn out to be sufficient [Cla13].

The case $n = 0$ has been known in various guises for some time [Fin83, Noo02, Che05, Lev10] (see the discussions in [Tan12] and [Cla13]), and this case has the following special feature which will be relevant for the studies presented in sections III and IV below. For $n = 0$, the expression $J_0(\lambda) = \int g(v_\lambda, \phi) / \cos \phi d\phi$ is a constant (does not depend on λ) and the constant is given by

R. Clackdoyle is with the Laboratoire Hubert Curien, CNRS UMR 5516, Saint Etienne, France (e-mail: rolf.clackdoyle@univ-st-etienne.fr).

S. Rit is with the CREATIS laboratory, CNRS UMR 5220 and INSERM U1044, Lyon, France (e-mail: simon.rit@creatis.insa-lyon.fr).

J. Hoskovec is with the Université Jean Monnet, Saint Etienne, France (e-mail: jan.hoskovec@univ-st-etienne.fr)

L. Desbat is with the TIMC-IMAG laboratory, CNRS UMR 5525, and Joseph Fourier University, Grenoble, France (e-mail: laurent.desbat@imag.fr).

This work was partially supported by the Agence Nationale de la Recherche (France), project "DROITE," number ANR-12-BS01-0018, and partially supported by a grant from the Région Rhône-Alpes (ARC6).

$$J_0 = \iint \frac{f(x, y)}{x} dx dy \quad (3)$$

We notice therefore that any translation of the object in the direction parallel to the trajectory line (the y direction) will not affect this constant. Furthermore, equation 3 remains constant even when replacing $f(x, y)$ by $f_1(x, y) + f_2(x, y + t)$ for any translation t of the f_2 component of f . So multiple pieces of the object translating independently in the trajectory direction also leave J_0 unchanged.

III. MATERIALS AND METHODS

A. Phantom description

We used a highly simplified 2D phantom consisting of two components. The static component is a bounding elliptical shell containing 5 ellipses, and we refer to this phantom as f_1 . The second component, referred to as f_2 , consists of two disks undergoing motion during the simulated measurement procedure. Tables 1 and 2 give details of the ellipses making up the static and dynamic components of the phantom. Note that D_x and D_y refer to the full axis lengths of the ellipses.

For the dynamic component of the phantom, an oscillatory motion of amplitude A occurs in the horizontal direction during the time period $[t_0, t_1]$ where $0 \leq t_0 < t_1 \leq T$ and where T is the total duration. We take $T = 10$ seconds in this work. The precise description of the motion is given by $\Gamma_t(x, y) = (\bar{x}_t, y)$ if $t \in [t_0, t_1]$ and $\Gamma_t(x, y) = (x, y)$ otherwise, where

$$\bar{x}_t = x + \frac{A}{2} \left(1 - \cos \left(2\pi \frac{t - t_0}{t_1 - t_0} \right) \right) \quad (4)$$

The amplitude of the motion is fixed at some value in the range $A \in [3, 9]$. The standard motion parameters used in the simulations will be $(t_0, t_1, A) = (1, 8, 7)$. The phantom is illustrated in Fig 1.

It is assumed that the static component of the phantom in Table 1 is unknown, but that the dynamic component in Table 2 is known except for the motion parameters (t_0, t_1, A) . The main purpose of these experiments is to determine if the motion parameters can be extracted from projection measurements without (or before) performing image reconstruction. If

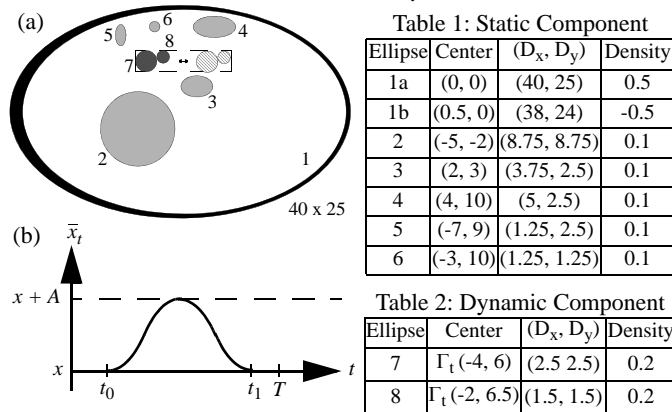


Fig 1. Illustration of the phantom. (a) scale drawing of the positions of the component ellipses, also showing the extent of the motion for $A = 7$. (b) plot of the motion function given by equation 4.

the motion parameters can be determined, then a full dynamic reconstruction is possible because the moving component is then fully specified, and can be subtracted from the projections leaving the static part which can then be fed to any standard reconstruction algorithm.

B. Measurement geometry 1: linogram mode

In the first measurement geometry, the x-ray source trajectory follows a straight line $v_\lambda = (\lambda, 20)$ for $\lambda \in \Lambda = [-25, 25]$. A total of 101 projections are taken along the line, starting at the position $(-25, 20)$ and ending at $(+25, 20)$ in steps of 0.5. The source is assumed to move at constant speed along the line, during the collection time of $T = 10$ seconds, so $\lambda = 50t/T - 25$. Each projection is considered to be instantaneously measured, with a temporal spacing of 0.1 seconds between projections.

For this geometry, a suitable range of ϕ would be $\phi \in [-\pi, 0]$, however we assume a flat immobile detector with “equispaced” sampling (in the terminology of [Kak88]) positioned along the line $y = -15$. Using the equispaced variable x_d instead of ϕ , our projection measurements become

$$\bar{g}(v_\lambda, x_d) = \int_0^\infty f(v_\lambda + l\gamma_{\lambda, x_d}) dl \quad (5)$$

where γ_{λ, x_d} is the unit vector leaving the source at $v_\lambda = (\lambda, 20)$ and pointing at the detector position $(x_d, -15)$. To ensure that there is no truncation of these projections for the larger static phantom, the detector extent runs from $(-140, -15)$ to $(140, -15)$. See Fig 2(a).

When the appropriate changes of variables are applied to equation 2, we find that

$$J_n(\lambda) = \int_{-\infty}^\infty \cos \gamma \bar{g}(v_\lambda, x_d) (x_d)^n dx_d \quad (6)$$

where γ here refers to the angle of incidence of the ray with the detector, so $\cos \gamma = 35 / \sqrt{35^2 + (x_d - \lambda)^2}$.

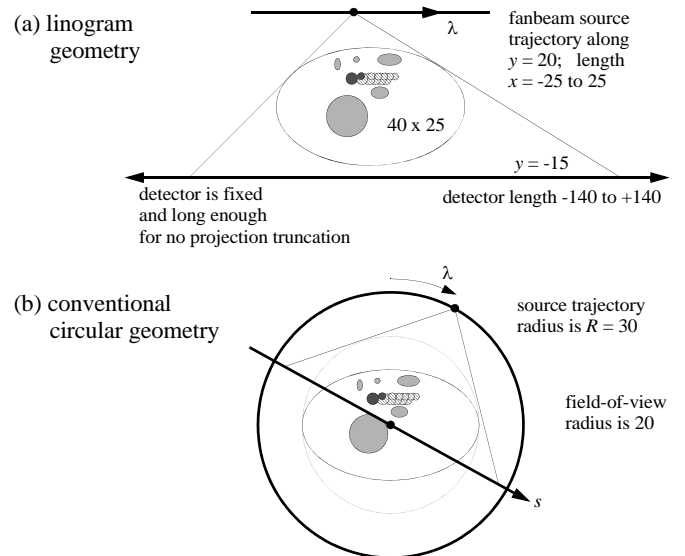


Fig 2. The two scanning geometries. (a) The linogram geometry, drawn to scale except for the extent of the detector which is long enough to avoid truncated projections. (b) The conventional circular scanning geometry.

This geometry, of parallel detector and trajectory, is the well-known linogram geometry [Edh87], and the quantity $\cos\gamma \bar{g}(v_\lambda, x_d)$ is a linogram. The finite length of the trajectory segment however, means that the system is tomographically incomplete so mathematically-correct image reconstruction is not possible.

The 101 linogram projections were simulated using analytic line-length calculations for the elliptical elements in the phantom, with dynamic parameters $(t_0, t_1, A) = (1, 8, 7)$ and $T = 10$ seconds. The simulated linogram is shown in Fig 3(a). Using the known dynamic component of the phantom, the unknown motion parameters (t_0, t_1, A) were sought by applying the DCC (equation 6) of orders $n = 1, 2, 3$ and calculating the residuals of the polynomial fits. If incorrect motion parameters are used to model the linogram projections, then resulting DCC may not be satisfied. Note that order $n = 0$ is not useful because the motion is parallel to the trajectory and order zero consistency is always maintained in that case.

An optimization cost function $F_n(t_0, t_1, A)$ was formed for each feasible triple (t_0, t_1, A) by simulating linograms \bar{g}^s of the dynamic component of the phantom (using pixelized representations to avoid “inverse crime”) and computing DCC functions $J_n^s(\lambda)$ from them according to equation 5. The difference $J_n^{\text{data}}(\lambda) - J_n^s(\lambda)$ was fit to an n -degree polynomial in λ to determine a residual vector $r_n(t_0, t_1, A)$ (recalling from equation 2 that consistency implies that $J_n(\lambda)$ is a polynomial of degree at most n). If $r_n = 0$ then the subtraction of the simulated movement from the measurement represented a consistent linogram and the unknown motion parameters were considered to be found. The cost function was defined as $F_n = \|r_n\| / \|J_n^{\text{data}} - J_n^s\|$.

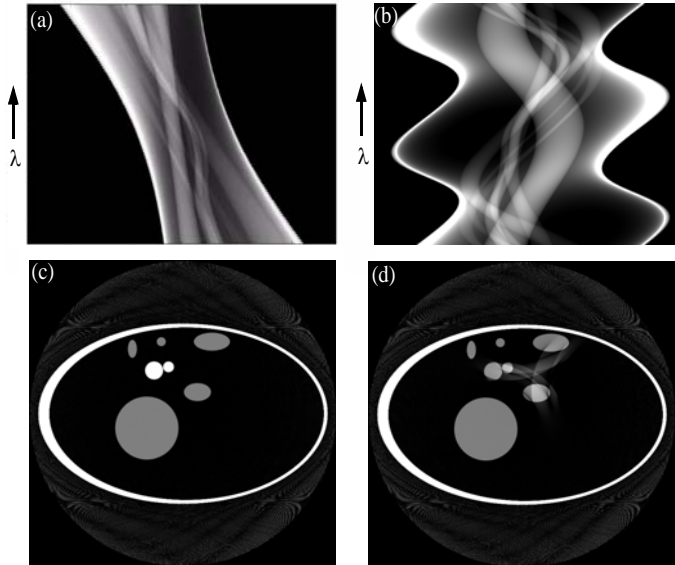


Fig 3. Top row: (a) linogram and (b) fanbeam sinogram simulations of the phantom with moving feature (more evident in linogram than sinogram). Bottom row: FBP reconstruction from (d) dynamic sinogram above and (c) from the sinogram of the frozen $t = 0$ instant of the phantom. The horizontal movement manifested itself as a triangular-shaped blurring in the reconstruction.

C. Measurement geometry 2: circular trajectory

The second fanbeam geometry is standard, consisting of 600 projections taken over a circular source trajectory of radius 30. Thus $v_\lambda = (30 \sin\lambda, 30 \cos\lambda)$ for $\lambda \in [0, 2\pi]$, and we note the clockwise motion of the source, starting at the “12 o’clock” position. The projections are collected at constant speed over $T = 10$ seconds, so $\lambda = 2\pi t/T$. The projections were simulated on a “virtual” flat detector passing through the origin and oriented perpendicularly to the tangent of the source motion; we use s for the detector variable. The projections are now represented by $\widehat{g}(\lambda, s) = \int_0^\infty f(v_\lambda + l\mu_{\lambda,s}) dl$ where $\mu_{\lambda,s}$ is the unit vector pointing from the source to the s -position on the detector which is $(s \cos\lambda, -s \sin\lambda)$. See Fig. 2(b). The fanbeam sinogram for this 360° circular scan is shown in Fig.3(b). Standard FBP reconstructions are shown in Figs.3(d) and 3(c) respectively for the dynamic phantom and for a static version of the phantom, frozen at $t = 0$.

For circular trajectories, fanbeam consistency can be achieved by converting an entire fanbeam dataset to parallel projections and using the standard HL conditions (e.g. [Pat01, Yu07]). Alternatively, fanbeam projections can be handled pairwise by considering the line connecting two sources as a pseudo trajectory, and applying the DCC of equation 2. With only two sources on the trajectory, only the $n = 0$ term is available (it is possible to check for equality of J_0 for two values of λ , but higher order polynomials cannot be handled). Recalling the restriction that the trajectory line not intersect the object, we find that there are a total of 96,000 pairs (pseudo trajectories).

We write $J(\lambda_i, j)$ for the DCC value corresponding to source λ_i with the (pseudo) trajectory line connecting the two sources λ_i and λ_j . Note that the cosine term in equation 2 is with respect to angle ϕ measured perpendicularly to the pseudo trajectory line. Furthermore the projection is equispaced, not equiangular (using the [Kak88] terminology) so a change of variables is needed. We skip the details of this derivation and present the final formula, which is

$$J(\lambda_i, j) = \int_{-\infty}^{\infty} \frac{\widehat{g}(\lambda_i, s)}{|R \cos(\mu/2) - s \sin(\mu/2)|} \frac{R}{\sqrt{R^2 + s^2}} ds \quad (7)$$

where $R = 30$ is the trajectory radius, and $\mu = \lambda_j - \lambda_i$ is the signed angular difference between the two source locations. Zeroth order consistency of a pair of projections simply means that

$$J(\lambda_i, j) = J(\lambda_j, i) \quad (8)$$

Note that if the line connecting sources λ_i and λ_j is horizontal then the pseudo trajectory is parallel to the motion of the dynamic component of the phantom, so even though projections λ_i and λ_j were of different temporal phases of the object, consistency of order zero is still maintained in this situation.

IV. RESULTS AND DISCUSSION

A. The linogram scan

The cost function was calculated on a coarse grid throughout the feasible range and its behavior was studied. For order $n = 0$, it was found to be virtually constant, correctly reflecting the known theory that any horizontal motion would remain consistent for this linogram geometry. For orders $n = 1, 2, 3$ a single deep global minimum was found at the correct motion parameters as shown in the plots of Fig. 4. The few isolated local minima lay in shallow “bowls” in different locations for the different orders, suggesting that a single cost function of $F = F_1 + F_2 + F_3$ would be suitable. The cost function was re-calculated and re-examined after adding 3% Gaussian noise to the linogram data elements. The resulting plots (not shown here) were very similar except the global minimum increased slightly for $n = 1, 2, 3$.

The downhill simplex method was used for the nonlinear optimization of F_n using each of the four value of n . In each case, the routine converged in roughly 200 to 300 iterations, with the following results. For each of $n = 0, 1, 2, 3$ respectively, the estimated parameters were $(t_0, t_1, A) = (0,56, 9,97, -0,04)$, $(0,99, 8,01, 7,05)$, $(0,98, 8,00, 7,03)$, $(1,02, 8,00, 6,83)$ (recalling that the true motion parameters were $(1, 8, 7)$).

Further studies are underway, including using different true motion parameters, different initialization locations, and quantifying the effects of additive noise in the projection data.

B. The circular scan

The order zero DCC condition was calculated for every pair of source points whose connecting line (pseudo trajectory) lay outside the 20 cm field-of-view. For each pair, the percent

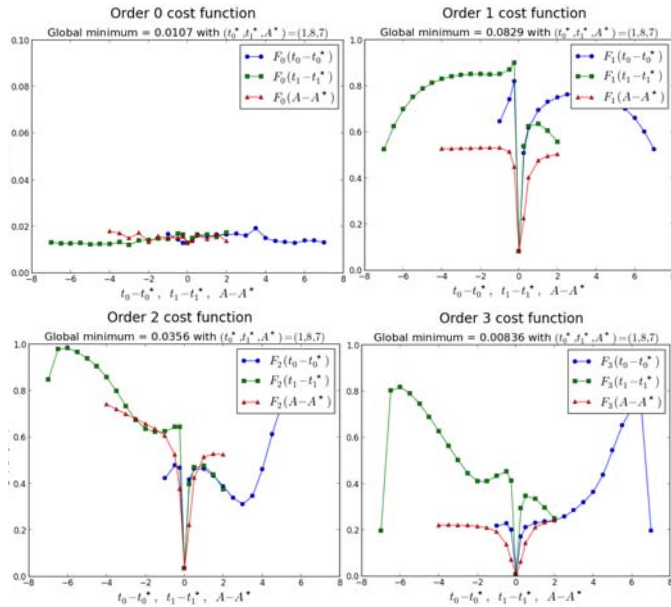


Fig 4. Perpendicular intersection plots through the global minimum of the cost function $F_n(t_0, t_1, A)$ for each of $n = 0$ (top left); $n = 1$ (top right); $n = 2$ (bottom left); $n = 3$ (bottom right). The vertical scale for $n = 0$ is magnified 10 times with respect to the other three scales. The plots illustrate the abrupt fall of the cost function in the immediate neighborhood of the true motion parameters.

relative difference was calculated. The results were grouped into parallel trajectory lines because the horizontal or nearly horizontal lines would not reveal inconsistency, being aligned with the movement of the dynamic component.

At a fixed orientation, there were always 160 parallel trajectory lines, 80 on each side of the field-of-view (FOV). These lines varied from 20 cm to 30 cm from the center of the system. We grouped the lines as shown in Fig 5, and displayed the *average* percent relative difference over all the parallel lines lying on one side of the FOV. We also plotted the average relative difference for just the lines between 20 cm and 25 cm from the center, because they represent source pairs that are more separated temporally: from 1.83 second minimal separation to 2.67 seconds of separation, whereas consecutive sources are only separated by 0.017 seconds. (For the pairs of source positions that cross the starting point, the lines between 20 cm and 25 cm from the center respectively have temporal separation between 8.17 and 7.33 seconds.)

The results of the graph show two effects. One is that, as predicted by the theory, the horizontal (0° or 180°) movement does not cause inconsistency, because horizontal and nearly horizontal trajectory lines showed very low relative differences. The other effects are due to temporal behavior of the phantom. Each condition compares one pair of snapshots and there are many instances when the phantom can be in the same position for the two snapshots. The 1 second immobile period at the start and the 2 seconds at the end maintain consistency during these periods, as do snapshots that are temporally symmetric about the midpoint of the motion, which occurs at $t = 4.5$ seconds. The flat region in Fig 5 near 160 degrees is attributed to this symmetry effect.

We note that the average relative errors appear quite small, all under 0.5%, but it is important to note that the mass of the moving part of the phantom is a small fraction of the total. The total number of lines (conditions $J(\lambda_i, j) = J(\lambda_j, i)$) in this simulation was 96000. These conditions could be exploited in a similar way to those of the linogram to provide estimates of the motion parameters.

The flat areas of the plot of Fig 5 can be used to roughly identify the *direction* of the motion, because a strictly linear motion will enforce two angles, separated by 180 degrees, for which consistency will generally hold.

V. SUMMARY AND CONCLUSIONS

With two different fanbeam geometries, various features of the application of DCC have been explored. The order zero condition can not detect motion parallel to the trajectory, but can potentially be used to detect the direction of linear movement. In our simulations, the higher order conditions could be used to build a suitable cost function for finding three motion parameters for a simple motion of a known component of the phantom. The DCC are linear in the components of the image, so they might become swamped if a large static background object were involved. There are many potential applications of fanbeam DCC, and we have illustrated various approaches and and discussed their features and limitations.

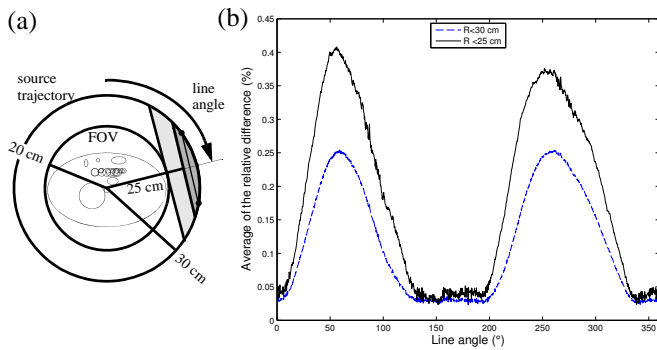


Fig 5. Average relative differences. (a) illustration of a group of parallel trajectory lines showing the $R < 30$ cm group (shaded) and $R < 25$ cm group (light shading). (b) Plot of average relative difference as a function of line angle for all lines (lower curve) and for just those lines closer than 25 cm (upper curve).

VI. REFERENCES

- [Bas00] S. Basu and Y. Bresler. "Uniqueness of tomography with unknown view angles." *IEEE Trans Imag Proc* 9, 1092-1106, 2000.
- [Che05] G.-H. Chen and S. Leng. "A new data consistency condition for fan-beam projection data." *Med Phys* 32, 961-967, 2005.
- [Cla13] R. Clackdoyle. "Necessary and Sufficient Consistency Conditions for Fanbeam Projections along a Line." *IEEE Trans Nucl Sci.* 60, 1560-1569, 2013.
- [Def12] M. Defrise, A. Rezaei and J. Nuyts. "Time-of-flight PET data determine the attenuation sinogram up to a constant." *Phys. Med. Biol.* 57, 885-899, 2012.
- [Edh87] P.R. Edholm and G.T. Herman. "Linograms in image reconstruction from projections." *IEEE Trans. Med. Imag.* MI-6, 301-307, 1987.
- [Erl00] K. Erlandsson, D. Visvikis, W.A. Waddington and P. Jarritt. "Truncation Reduction in Fan-Beam Transmission Scanning Using the Radon Transform Consistency Conditions." *IEEE Trans. Nuc. Sci.* 47, 989-993, 2000.
- [Fin83] D.V. Finch and D.C. Solmon. "Sums of homogeneous function and the range of the divergent beam X-ray transform." *Numer Func Anal and Optimiz* 5, 363-419, 1983.
- [Gli94] S.J. Glick, B.C. Penney, M.A. King and C.L. Byrne "Noniterative Compensation for the Distance-Dependent Detector Response and Photon Attenuation in SPECT Imaging" *IEEE Trans. Med. Imag.* 13, 363-374, 1994.
- [Hel80] S. Helgason. *The Radon Transform*. (Boston: Birkhauser), 1980.
- [Kak88] A.C. Kak and M. Slaney. *Principles of Computerized Tomographic Imaging* (New York: IEEE Press) 1988.
- [Lay05] C.M. Laymon, M. Swadley, J.E. Bowsler, T. Blodgett and S.K. Ziolk. "Evaluation of Sinogram Consistency Conditions for Identifying Artifactual PET Attenuation Images". *Conf Rec of the 2005 Nucl Sci Symp and Med Imag Conf* 3, 1611-1614, 2005.
- [Lev10] M.S. Levine, E.Y. Sidky and X. Pan. "Consistency Conditions for Cone-Beam CT Data Acquired with a Straight-Line Source Trajectory." *Tsinghua Sci Technol* 15,56-61, 2010.
- [Lud66] D. Ludwig. "The Radon transform on Euclidean space." *Comm. Pure Appl. Math.* 19, 49-81, 1966.
- [Men99] C. Mennessier, F. Noo, R. Clackdoyle, G. Bal and L. Desbat. "Attenuation correction in SPECT using consistency conditions for the exponential ray transform." *Phys. Med. Biol.* 44, 2483-2510, 1999.
- [Nat83] F. Natterer. "Computerized tomography with unknown sources." *SIAM J. Appl. Math.* 43, 1201-1212, 1983.
- [Nat93] F. Natterer. "Determination of tissue attenuation in emission tomography of optically dense media." *Inv. Probs* 9, 731-736, 1993.
- [Noo02] F. Noo, M. Defrise, R. Clackdoyle and H. Kudo. "Image reconstruction from fan-beam projections on less than a short scan." *Phys. Med. Biol.* 47, 2525-2546, 2002.
- [Pat01] S.K. Patch. "Moment conditions indirectly improve image quality." *Contemp. Math.* 278, 193-205, 2001.
- [Pat02] S.K. Patch. "Consistency conditions upon 3D CT data and the wave equation." *Phys. Med. Biol.* 47, 2637-2650, 2002.
- [Tan11] S. Tang, X. Mou, Q. Xu, Y. Zhang, J. Bennett and H. Yu. "Data consistency condition-based beam-hardening correction." *Opt. Eng.* 50, 076501(1-13), 2011.
- [Tan12] S. Tang, Q. Xu, X. Mou and X. Tang. "The mathematical equivalence of consistency conditions in the divergent-beam computed tomography." *J. X-ray Sci. Tech.* 20, 45-68, 2012.
- [Wel03] A. Welch, W. Hallett, P. Marsden and A. Bromiley "Accurate Attenuation Correction in PET using Short Transmission Scans and Consistency Information." *IEEE Trans Nucl Sci* 50, 427-432, 2003.
- [Yu07] H. Yu and G. Wang. "Data Consistency Based Rigid Motion Artifact Reduction in Fan-Beam CT." *IEEE Trans. Med. Imag.* 26, 249-260, 2007.

Motion Compensated Fan-Beam CT by Enforcing Fourier Properties of the Sinogram

Martin Berger, Andreas Maier, Yan Xia, Joachim Hornegger and Rebecca Fahrig

Abstract—In computed tomography involuntary patient motion can lead to a severe degradation of image quality. Most of the motion estimation methods rely on additional information, such as fiducial markers or an ECG signal. In contrast, data driven motion estimation exists which aims to estimate the motion directly from the acquired projections. This is typically achieved by the optimization of an error metric that is either defined in the image or in the projection domain. In this work, we present a novel data driven error function for motion compensation in fan-beam CT and its combination with a simple motion compensation scheme. The new method operates entirely in the fourier domain of the sinogram, by enforcing zero energy regions of the spectrum. Qualitative and quantitative results show that the proposed method is able to remove most of the motion artifacts, yielding a relative root mean square error of 7.09% compared to 20.35% for the motion corrupted reconstruction.

Keywords—Computed Tomography, C-arm CT, Motion Compensation, Image Reconstruction

I. INTRODUCTION

In computed tomography (CT) patient or scanner motion can lead to severe motion artifacts, typically observable as streaking. This is due to the fact that the acquired projections are no longer consistent with the trajectory assumed for image reconstruction. Detection and compensation of such motion during the image reconstruction process can substantially increase the image quality. However, often additional information is necessary to detect the motion. For example external markers which are clearly visible in the projection images can be attached to estimate the patient motion [1]. The assumption here is that the detected surface motion correlates to the motion at the volume of interest (VOI), which might not always be true. In the field of cardiovascular imaging, motion artifacts can be reduced by ECG-gating. Here only a subset of the acquired projections from similar heart phases is built by exploiting information of the ECG signal that was acquired during the scan. However, the ECG data might not correspond exactly with the heart motion and reconstruction of such a subset can also cause undersampling artifacts [2].

To allow for a motion compensated reconstruction independent of additional information sources the motion needs to be directly estimated from the acquired data. This type of motion estimation typically requires an iterative minimization of error metrics, where the motion is estimated such that the error metric is minimized. The metrics can be defined directly in the reconstructed image domain, but also in the sinogram

space [3]. For parallel-beam geometry, it has been shown that the two-dimensional Fourier transform of the sinogram contains triangular shaped regions that have an absolute value close to zero [4]. Recently this concept has been extended to the fan-beam case [5]. In this work we utilize the findings of [5] and propose an error metric and motion estimation scheme that is entirely based in the fourier domain of the sinogram.

II. MATERIALS AND METHODS

A. Fourier Properties of the Sinogram

In Fig. 3(f) an example spectrum of a sinogram is shown which clearly depicts the triangular regions. The size and orientation of these regions depend on the maximum distance of the object to the center of rotation r_p , as well as the source-to-patient distance L and the detector-to-patient distance D . According to [5] the spectral zero regions for a flat detector can be described by

$$\left| \frac{\omega}{\omega - \xi(L + D)} \right| > \frac{r_p}{L}, \quad (1)$$

where ω and ξ are the frequency variables corresponding to the projection angles and the detector rows, respectively. The triangular regions are by definition designed for objects centered in the rotation center. However, potential patient or scanner motion violates this requirement. Hence, the overall energy in the triangular spectral regions increases.

B. Error Measure for Motion Compensation

We now introduce the cumulative energy, i.e. the sum of squared absolute values inside the triangular regions, as an objective function for patient motion correction. The error measure can be written as

$$e(\mathbf{P}) = \left\| \mathbf{F}_\xi \mathbf{P} \mathbf{F}_\omega \circ \mathbf{W} \right\|_{\mathbb{F}}^2, \quad (2)$$

where $\mathbf{P} \in \mathbb{R}^{M \times N}$ is the sinogram with N projections of length M on its columns. $\mathbf{F}_\xi \in \mathbb{R}^{M \times M}$ and $\mathbf{F}_\omega \in \mathbb{R}^{N \times N}$ denote discrete fourier transform (DFT) matrices, corresponding to DFTs along the detector and the projection angles, respectively. $\mathbf{W} \in \mathbb{R}^{M \times N}$ is a binary matrix that evaluates to one where (1) is true and to zero otherwise. Further, $\|\cdot\|_{\mathbb{F}}^2$ is the squared Frobenius norm and \circ denotes the element-wise matrix multiplication.

For the correction of the two-dimensional patient motion we assume simple one-dimensional detector translations. Optimization of (2) requires frequent evaluations of the error function including the 2D fourier transform. We utilize the shift-theorem to move the detector translation after the 1D

Rebecca Fahrig is with the Department of Radiology, Stanford University, Stanford, CA, USA. Martin Berger, Andreas Maier, Yan Xia and Joachim Hornegger are with the Pattern Recognition Lab, Department of Computer Science, Friedrich-Alexander-Universität Erlangen-Nürnberg. This work has been supported by the Research Training Group 1774 "Heterogeneous Image Systems", funded by the German Research Foundation (DFG).

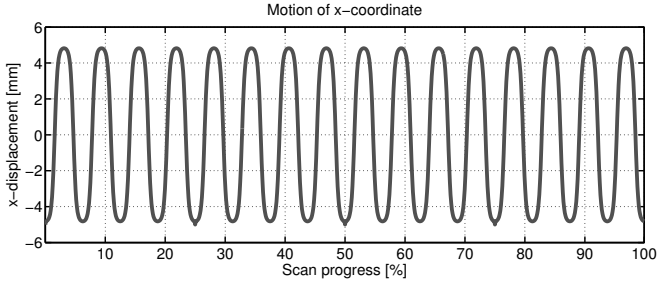


Fig. 1. Simulated periodic translation along the x-axis over the scan progress.

fourier transform along the detector. Let t_n be the translation of the n-th projection, then (2) can be rewritten as

$$[t_1, \dots, t_N] = \arg \min_{[t_1, \dots, t_N]} \left\| ((\mathbf{F}_\xi \mathbf{P}) \mathbf{T}) \mathbf{F}_\omega \circ \mathbf{W} \right\|_{\mathbb{F}}^2, \quad (3)$$

$$\text{with } \mathbf{T} = \begin{pmatrix} e^{-i\frac{2\pi\xi}{M}t_1} & \dots & 0 \\ \vdots & \ddots & \vdots \\ 0 & \dots & e^{-i\frac{2\pi\xi}{M}t_N} \end{pmatrix}.$$

$\mathbf{T} \in \mathbb{R}^{N \times N}$ is a matrix that has the phase factors on its diagonal and is zero elsewhere. Note, that $\mathbf{F}_\xi \mathbf{P}$ is independent of t_n and can thus be precomputed prior to optimization. Thus, additional evaluations of (3) only require a 1D fourier transform along the projection angles.

C. Gradient Computation

For a more robust numerical optimization it is advantageous to have an analytically derived gradient of the cost function [6]. In the following we derive the partial derivatives of (3) with respect to the detector shifts t_n . First, we build the derivative of the Frobenius norm, where $\text{Tr}(\cdot)$ denotes the trace and \mathbf{H} the Hermitian operator. We used the identity $\|\mathbf{X}\|_{\mathbb{F}}^2 = \text{Tr}(\mathbf{X}\mathbf{X}^{\mathbf{H}})$ and define $\mathbf{X} = ((\mathbf{F}_\xi \mathbf{P}) \mathbf{T}) \mathbf{F}_\omega \circ \mathbf{W}$.

$$\frac{\partial}{\partial t_n} \|\mathbf{X}\|_{\mathbb{F}}^2 = \text{Tr} \left(\left(\frac{\partial}{\partial t_n} \mathbf{X} \right) \mathbf{X}^{\mathbf{H}} + \mathbf{X} \left(\frac{\partial}{\partial t_n} \mathbf{X} \right)^{\mathbf{H}} \right) \quad (4)$$

To evaluate (4) we need to derive the partial derivatives of \mathbf{X} .

$$\begin{aligned} \frac{\partial}{\partial t_n} \mathbf{X} &= \frac{\partial}{\partial t_n} \left(((\mathbf{F}_\xi \mathbf{P}) \mathbf{T}) \mathbf{F}_\omega \circ \mathbf{W} \right) \\ &= \left((\mathbf{F}_\xi \mathbf{P}) \frac{\partial}{\partial t_n} \mathbf{T} \right) \mathbf{F}_\omega \circ \mathbf{W} \\ &= \left((\mathbf{F}_\xi \mathbf{P}) \left(-i \frac{2\pi\xi}{M} \exp(-i\frac{2\pi\xi}{M}t_n) \mathbf{J}^{nn} \right) \right) \mathbf{F}_\omega \circ \mathbf{W} \\ &= (\mathbf{E}) \mathbf{F}_\omega \circ \mathbf{W} \end{aligned} \quad (5)$$

Here \mathbf{J}^{nn} is a single-entry matrix, which is one at (n, n) and zero elsewhere. $\mathbf{E} \in \mathbb{R}^{M \times N}$ can be interpreted as follows. First we shift the projections by t_n directly in the fourier domain. Subsequent multiplication by $-i\frac{2\pi\xi}{M}$ is equivalent to the derivative over the shifted projections. With \mathbf{J}^{nn} we then select the n-th projection and set the others to 0. Because \mathbf{E} has only one non-zero column, the fourier transform over the rows, \mathbf{F}_ω , degenerates to a simple vector multiplication

$$(\mathbf{E}) \mathbf{F}_\omega = \mathbf{e}_n \mathbf{f}_n^\omega,$$

Parameter	Symbol/Unit	High-quality	Low-quality
Source-patient-distance	L	600	600
Detector-patient-distance	D	0	0
Approx. object extent [mm]	r_p	122.5	122.5
#Detector cells	M	1240	620
Detector spacing [mm]	du	0.25	0.5
#Projections	N	892	240
Angular spacing [degree]	$d\beta$	0.404	1.5
Reconstruction size	$R_x \times R_y$	2048 × 2048	2048 × 2048
Pixel size	[mm × mm]	0.125 × 0.125	0.125 × 0.125
Absorption model	-	monochromatic	monochromatic
Photon Energy	[keV]	80	50
#Photons	-	-	30000

TABLE I. SIMULATION PARAMETERS USED FOR THE EVALUATION.

where $\mathbf{e}_n \in \mathbb{R}^{M \times 1}$ is the n-th column of \mathbf{E} and $\mathbf{f}_n^\omega \in \mathbb{R}^{1 \times N}$ is the n-th row of \mathbf{F}_ω . Considering the use of a fast fourier transform (FFT) the complexity reduces from $\mathcal{O}(MN \log(N))$ to $\mathcal{O}(MN)$.

Because \mathbf{X} is already computed when evaluating the error function (3), the gradient computation does not require an additional FFT and can be implemented efficiently.

III. EVALUATION AND RESULTS

A. Evaluation

To evaluate our method we used the central slice of the FORBILD head phantom¹. The experiments consisted of a high quality, noise free scan, but also a low quality, noisy simulation to investigate the method's behaviour under more realistic conditions. The geometric, as well as the reconstruction parameters used for the simulations are presented in Table I.

Affine motion of the head phantom has been simulated as an accelerated periodic translation around the x-axis, denoted as $t_x(\beta)$. The motion model can be described by

$$t_x(\beta) = \hat{t}_x \left(\frac{2}{1 + \exp(a \cos(k\beta))} - 1 \right), \quad (6)$$

where \hat{t}_x is the amplitude, k is the number of periods per scan, and a is an acceleration factor. For our simulation we chose $\hat{t}_x = 5$ mm, $k = 16 \text{ deg}^{-1}$ and $a = 4$. Fig. 1 depicts a plot of the x-axis translation over the scan progress.

The evaluation procedure for both, low-quality and high-quality simulations, was as follows. First we analytically computed the sinogram for the motion corrupted but also for the motion free case. As a reference we also rendered the phantom directly in the reconstruction space, where we used the attenuation coefficients as pixel intensities. Note that the attenuation coefficients are energy dependent, hence the low-quality differs from the high-quality ground truth phantom. All simulations have been carried out using the open source software CONRAD [7].

For the minimization of the cost-function (3) we used the L-BFGS algorithm, where we provided the partial derivatives as given by (4). To compute the mask \mathbf{W} the object extent r_p is required. We estimated r_p from the sinogram by measuring

¹www.imp.uni-erlangen.de/phantoms

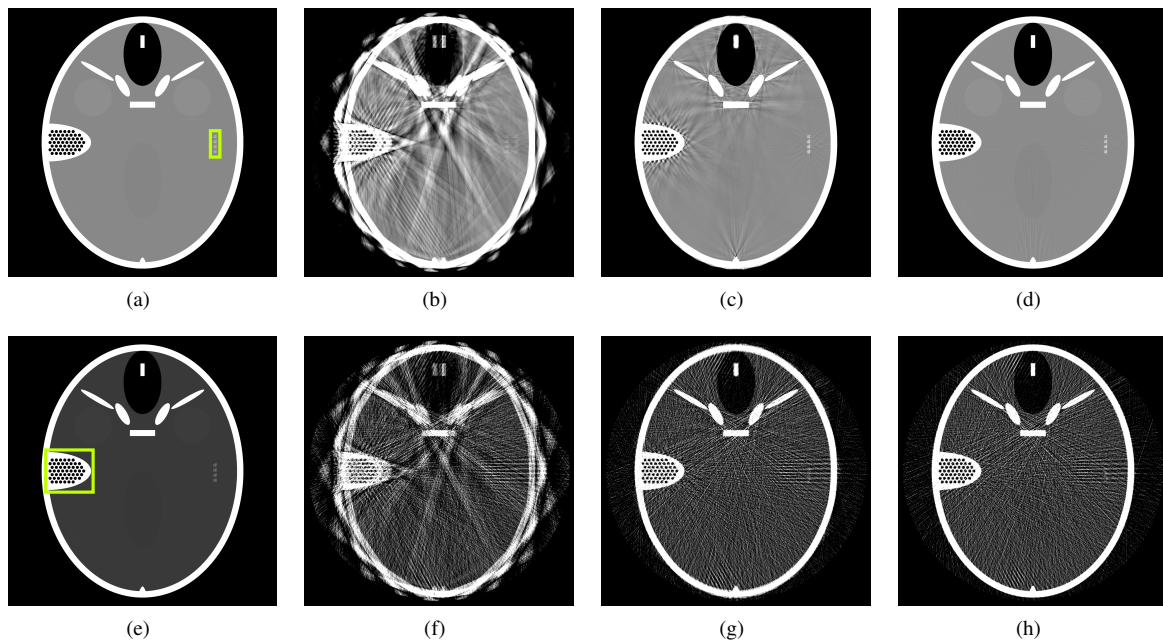


Fig. 2. Qualitative reconstruction results for the high-quality (top row) and the low-quality (bottom row) simulations. From left to right: Ground truth rendering, motion corrupted, motion corrected and the motion free reconstruction. Visualization windows are $[0.07, 0.27]$ for the top and $[0.07, 0.80]$ for the bottom row.

the maximum distance between the projection boundaries (see Table I). The optimization was done repeatedly using a multi-resolution approach. The sinogram scaling factors were 0.25, 0.5 and 1 and a zero vector was used for initialization. The optimized shifts were incorporated into the reconstruction as described in [8].

For a quantitative evaluation we computed the relative root mean square error (rRMSE) of the motion corrupted, the corrected and the motion-free reconstruction with respect to the corresponding ground truth. The rRMSE is defined as

$$rRMSE(\mathbf{R}, \mathbf{G}) = \frac{1}{\hat{I}_g} \|\mathbf{R} - \mathbf{G}\|_F$$

where \mathbf{R} is the reconstructed and \mathbf{G} the ground truth image and \hat{I}_g the intensity range of \mathbf{G} .

B. Results

Figure 2 shows the reconstruction results for the high (top row) and low-quality (bottom row) simulations. In both cases the image quality improved substantially when comparing the corrected to the motion corrupted reconstructions. The proposed method was able to restore edges, especially at the lateral boundaries. However, in the high-quality simulations we still observe some residual streaking artifacts compared to the reference reconstruction where no motion was present. For the low-quality simulations our approach yielded comparable results to the motion free reconstruction.

The sinograms and their spectra are depicted in Fig. 3 for the high-quality simulations. The motion and its correction is clearly visible in the spatial domain. This observation is supported by the corresponding spectra, where we clearly see a reduced energy in the superimposed triangular regions. This is in agreement with the actual error function values provided in Table II.

Measure		With motion	Corrected	Reference
High-quality	rRMSE [%]	20.35	7.09	2.48
	$e(\mathcal{P}) [\times 10^6]$	1648.49	32.35	0.34
Low-quality	rRMSE [%]	25.12	13.97	12.57
	$e(\mathcal{P}) [\times 10^6]$	109.55	6.32	4.12

TABLE II. ERROR FUNCTION AND RMSE VALUES FOR THE MOTION CORRUPTED, THE CORRECTED AND THE REFERENCE SPECTRA.

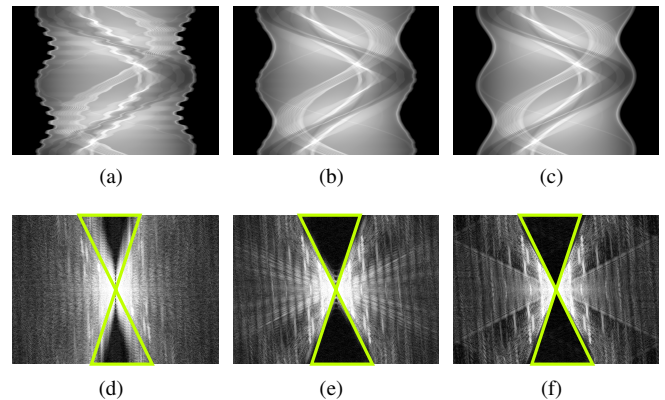


Fig. 3. Sinograms (top row) and their logarithmically scaled spectra (bottom row) for the noise-free projections. From left to right: motion corrupted, motion corrected and the motion free reference. Visualization windows are $[1.0, 5.5]$ for the sinograms and $[1.5, 5.0]$ for the log-spectra.

In Fig. 4 we can see a detailed view of the reconstructed area around the phantom's resolution pattern for the noise-free data. In comparison to the motion corrupted reconstruction, where the pattern is no longer visible, the proposed method could restore the pattern adequately. However, we can see some loss of information compared to the motion free reconstruction. For the noisy data a close-up of the phantom's ear is shown in Fig. 5. Compared to the non-corrected reconstruction, our

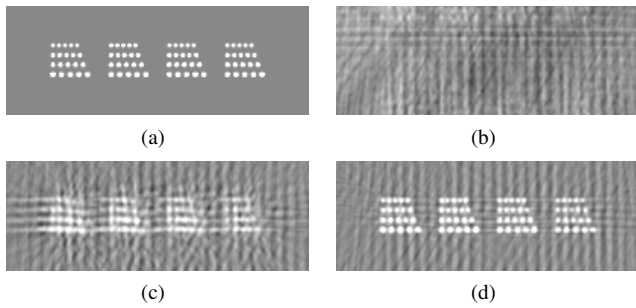


Fig. 4. The reconstructed resolution pattern for the high quality simulations. From (a) to (d): Ground truth, motion corrupted, motion corrected and motion free reconstruction. The region's position is superimposed in Fig. 2(a).

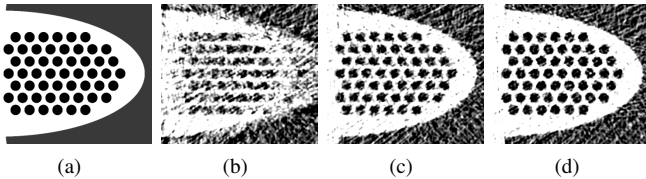


Fig. 5. The reconstructed left ear in case of the noisy data. From left to right: Ground truth, motion corrupted, motion corrected and motion free reconstruction. The region's position is superimposed in Fig. 2(e).

method was able to restore the encapsulated air bubbles, yielding similar results to those seen in the motion free reconstruction.

To get an impression of how accurate the translations were estimated, we forward projected the moving phantom's center position to the detector for each projection. In Fig. 6 the forward projected (gray, solid line) and the estimated translations (orange, dashed line) are plotted for the high-quality simulations. The plot shows that our approach reliably estimated the translational effect of the motion. A very similar result was obtained for the low-quality case.

IV. DISCUSSION

Our evaluation shows promising results for ideal high-quality data without noise. Because the error function is defined in the fourier domain we show that the method also works for low-quality simulations which contain a significant amount of noise. Compared to the reconstructions without motion correction, our approach improved image quality substantially. For the low-quality case the motion compensated reconstruction yielded comparable results to those of the reference reconstruction without motion. This is in line with the achieved quantitative results as shown in Table II.

In case of the high-quality data our method was able to restore most of the structures, yet we still observe some remaining motion-based artifacts. This limitation might be due to our relatively simple motion model which only takes detector shifts into account. Shifting the detector can effectively only compensate for that part of the motion that was parallel to the detector. It does not take potential scaling of the projections into account that occur from motion orthogonal to the detector. The resulting residual artifact is represented by small ripples in the corrected sinogram in Fig. 3(b). In Fig. 6 we show that when we only consider the motion parallel to the detector, the

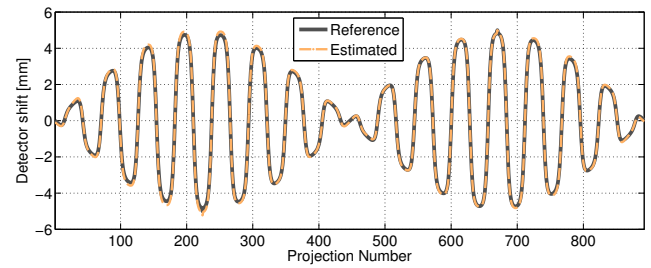


Fig. 6. Forward projection of the phantom's center (solid line) compared to the estimated detector shifts (dashed line), for the high-quality data.

optimization of our error measure is capable of estimating the motion with high accuracy.

A simulated periodic motion along the x-axis was used for this proof of concept. Evaluations with a more realistic patient motion will be part of future work. Further, we plan to extend the underlying fourier properties to a cone-beam formulation where we also want to incorporate short-scans. This would then allow its application on real C-arm CT data.

V. CONCLUSION

In this work we present a novel data driven error function for motion compensation in fan-beam CT. Further we introduce its combination with a simple motion compensation scheme by incorporating projection shifts. We also derive the gradient and show that its computation can be implemented efficiently. Our qualitative and quantitative results show that the proposed method is able to correct most of the motion artifacts.

REFERENCES

- [1] J.-H. Choi, R. Fahrig, A. Keil, T. F. Besier, S. Pal, E. J. McWalter, G. S. Beaupré, and A. Maier, "Fiducial marker-based correction for involuntary motion in weight-bearing C-arm CT scanning of knees. Part I. Numerical model-based optimization," *Medical Physics*, vol. 40, no. 9, p. 091905, 2013.
- [2] C. Schwemmer, C. Rohkohl, G. Lauritsch, K. Müller, and J. Hornegger, "Residual motion compensation in ECG-gated interventional cardiac vasculature reconstruction," *Physics in Medicine and Biology*, vol. 58, no. 11, p. 3717, 2013.
- [3] S. Ens, J. Ulrici, E. Hell, and T. Buzug, "Automatic motion correction in cone-beam computed tomography," in *Nuclear Science Symposium Conference Record (NSS/MIC), 2010 IEEE*, 2010, pp. 3248–3251.
- [4] P. R. Edholm, R. M. Lewitt, and B. Lindholm, "Novel Properties Of The Fourier Decomposition Of The Sinogram," in *Proc. SPIE 0671, Physics and Engineering of Computerized Multidimensional Imaging and Processing*, T. F. Budinger, Z.-H. Cho, and O. Nalcioglu, Eds. International Society for Optics and Photonics, 1986, pp. 8–18.
- [5] S. R. Mazin and N. J. Pelc, "Fourier properties of the fan-beam sinogram," *Medical Physics*, vol. 37, no. 4, pp. 1674–80, 2010.
- [6] J. Nocedal and S. J. Wright, *Numerical Optimization*. Springer New York, 1999, vol. 2.
- [7] A. Maier, H. G. Hofmann, M. Berger, P. Fischer, C. Schwemmer, H. Wu, K. Müller, J. Hornegger, J.-H. Choi, C. Riess *et al.*, "CONRAD A software framework for cone-beam imaging in radiology," *Medical Physics*, vol. 40, no. 11, p. 111914, 2013.
- [8] D. Schaefer, J. Borgert, V. Rasche, and M. Grass, "Motion-Compensated and Gated Cone Beam Filtered Back-Projection for 3-D Rotational X-Ray Angiography," *Medical Imaging, IEEE Transactions on*, vol. 25, no. 7, pp. 898–906, 2006.

Redundancies in X-ray images due to the epipolar geometry for transmission imaging

André Aichert, Nicole Maass, Yu Deuerling-Zheng, Martin Berger, Michael Manhart, Joachim Hornegger, Andreas K. Maier and Arnd Doerfler

Abstract—In Computer Vision, the term epipolar geometry describes the intrinsic geometry between two pinhole cameras. While the same model applies to X-ray source and detector, the imaging process itself is very different from visible light. This paper illustrates the epipolar geometry for transmission imaging and makes the connection to Grangeat’s theorem, establishing constraints on redundant projection data along corresponding epipolar lines. Using these redundancies, a geometric consistency metric is derived. Our metric could be applied to any pair of transmission images and could be used for pose refinement, calibration correction and rigid motion estimation in fluoroscopy and flat detector computed tomography (FD-CT). In addition to the theoretical contribution, this paper investigates the properties and behavior of the metric for the purpose of re-calibration of an FD-CT short scan for narrow angular range.

I. INTRODUCTION

In order to reconstruct a 3D image from a number of 2D X-ray projections, one requires accurate knowledge of the underlying projection geometry. The trajectory for CT reconstruction is either assumed fixed by construction or are calibrated before acquisition. Artifacts in the reconstruction may arise from inaccuracies of the calibration and unpredictable or non-reproducible scanner motion. This is also equivalent to rigid movement of the patient in medical scenarios.

Each image is associated with a projection matrix, which uses the same pinhole camera model as it is common in Computer Vision. The analogy opens up a field of established methods which are ready for application to transmission imaging problems [1], [2]. This paper studies the connection between the epipolar geometry of two projections and Grangeat’s theorem [3] in order to exploit redundancies in the projection data for image-based optimization of the assumed projection geometry after an acquisition. Both the epipolar geometry and Grangeat’s Theorem have previously been used for this purpose [4], [5], but their connection has not been established. In contrast to [6], [5], the work of Debbeler et al. [4] does not require reconstruction and uses a relatively simple and fast metric on 2D projections. We

Joachim Hornegger, Andreas K. Maier, André Aichert, Martin Berger and Michael Manhart are associated with the Pattern Recognition Lab, Friedrich-Alexander-Universität Erlangen-Nürnberg, Germany; Nicole Maass and Yu Deuerling-Zheng with the Siemens AG, Healthcare Sector, Erlangen and Forchheim, Germany; Arnd Doerfler and André Aichert with Department of Neuroradiology, Universitätsklinikum Erlangen, Germany; Andreas K. Maier with the Erlangen Graduate School in Advanced Optical Technologies (SAOT)

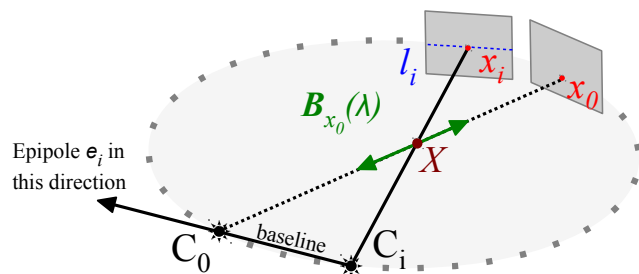


Figure 1. Epipolar geometry of two source positions C_0 and C_i from a circular trajectory. An image point $x_0 \cong P_0 X$ on the detector is back-projected to a ray $B_{x_0}(\lambda)$. The line $l_i \cong F x_i$ is the projection of that ray from C_i to the corresponding detector plane and hence contains the projection $x_i \cong P_i X$ and the projection of the other source $e_i \cong P_i C_0$, called the epipole. It follows that the line can be written as the join of the image point with the epipole $l_i \cong e_i \times x_i$.

derive a new formulation of that metric based on epipolar geometry, which allows us to model the reliability in a certain direction given a specific trajectory. Finally, we will investigate accuracy, precision and robustness of the X-ray source and detector, specifically for subsets of a short scan trajectory of an FD-CT C-arm system.

II. EPIPOLAR REDUNDANCIES IN X-RAY IMAGES

A. Epipolar Geometry

The term epipolar geometry describes the relative geometry between two pinhole cameras defined by their projection matrices P_0 and P_i . We rely on the real projective n-space $\mathbb{P}^n = \mathbb{R}^{n+1} \setminus \{0\}$ and introduce an equality relation

$$\mathbf{a} \cong \mathbf{b} \Leftrightarrow \mathbf{a}, \mathbf{b} \in \mathbb{P}^n, \exists \lambda \in \mathbb{R}, : \lambda \mathbf{a} - \mathbf{b} = \mathbf{0} \quad (1)$$

for the equivalence classes of scalar multiples. We will denote the location of the X-ray source as $\mathbf{C} \cong (-t\mathbf{R}, 1)^T \cong \text{kernel}(\mathbf{P}) \in \mathbb{P}^3$, for the projection matrix $\mathbf{P} \cong \mathbf{K}[\mathbf{R}|\mathbf{t}] \in \mathbb{R}^{4 \times 3}$, according to the notation common in Computer Vision. The projection matrix \mathbf{P} maps a world point in real projective three-space $\mathbf{X} \in \mathbb{P}^3$ to an image point on the detector in the real projective plane $\mathbf{x} \cong (u, v, 1)^T \cong \mathbf{P}\mathbf{X} \in \mathbb{P}^2$. We will work with a large number of views, but consider only two pairs of projection matrices and images (P_0, I_0) and (P_i, I_i) at a time. For convenience, a lower index denotes the view number, for example, $x_i \cong P_i X$ is a point in projective two-space on image I_i . W.l.o.g., we will use the index 0 as a reference view.

Suppose that the same world point is seen by two cameras as $\mathbf{x}_0 \cong \mathbf{P}_0\mathbf{X}$ and $\mathbf{x}_i \cong \mathbf{P}_i\mathbf{X}$. The intensity of a pixel \mathbf{x}_0 on the detector is the line integral along the back-projection ray $\mathbf{B}_{\mathbf{x}_0}(\lambda) \cong \mathbf{P}_0^+\mathbf{x}_0 + \lambda\mathbf{C}_0$, where \cdot^+ denotes the pseudo inverse. There exists a 3×3 matrix of rank 2 called the fundamental matrix \mathbf{F}_0^i defined up to scale which maps a point \mathbf{x}_0 on the reference image I_0 to a line $\mathbf{l}_i \cong \mathbf{F}_0^i\mathbf{x}_0$ on I_i . The epipolar line \mathbf{l}_i is the forward projection of a back-projection ray from a point on I_0 to I_i . Since the projection of $\mathbf{B}_{\mathbf{x}_0}$ is the line \mathbf{l}_i and $\mathbf{B}_{\mathbf{x}_0}$ contains the source position \mathbf{C}_0 , the line \mathbf{l}_i must also contain the projection of \mathbf{C}_0 to the i -th image called the epipole $\mathbf{e}_i \cong \mathbf{P}_i\mathbf{C}_0$. Hence epipolar lines form a bundle around the epipole $\mathbf{l}_i \cong \mathbf{e}_i \times \mathbf{x}_i$. The fundamental matrix can be expressed directly in terms of the projection matrices

$$\mathbf{F}_0^i \cong [\mathbf{e}_i]_{\times} \mathbf{P}_i \mathbf{P}_0^+ \quad (2)$$

where $[\mathbf{e}_i]_{\times}$ denotes the skew symmetric matrix representing the cross-product with the epipole. See also Figure 1 for an intuitive example and [1] for a thorough discussion.

B. 3D Radon Transform on Epipolar Planes

1) *Notation:* The key to finding redundancies imposed by this geometry is that the source positions \mathbf{C}_0 , \mathbf{C}_i and any back-projection ray $\mathbf{B}_{\mathbf{x}_0}$ define a plane, which contains both epipolar lines. There is a pencil of such planes around the line joining the source positions. We will now establish a relationship between the observed intensities along epipolar lines and the plane integral of the object over this epipolar plane. We call the plane $\mathbf{E} \cong \text{join}(\mathbf{B}_{\mathbf{x}_0}, \mathbf{C}_i) \cong (\mathbf{n}^T, -n)^T \in \mathbb{P}^3$ with normal \mathbf{n} and signed distance from the origin n . W.l.o.g. assume that the origin of our coordinate system is in the (finite) X-ray source \mathbf{C}_0 with the z -axis pointing in orthogonal direction to an epipolar plane containing the back-projection ray $\mathbf{B}_{\mathbf{x}_0}$. In this coordinate system the plane equation becomes $\mathbf{E} \cong (0, 0, 1, 0)^T$, hence we need only consider x and y coordinates in the following. For points $\mathbf{x}_0^T \mathbf{l}_0 = \mathbf{b}$ on the epipolar line we introduce the notation $F_{\mathbf{x}_0}(r) := f(r \cdot \cos(\varphi), r \cdot \sin(\varphi), 0)$, where r is the distance to $\mathbf{C}_0 \cong (0, 0, 0, 1)^T$ and φ is the ray direction within the plane \mathbf{E} and $f: \mathbb{R}^3 \rightarrow \mathbb{R}$ denote the absorption coefficients of our object. $F_{\mathbf{x}_0}$ essentially samples f along the ray $\mathbf{B}_{\mathbf{x}_0}$.

2) *2D Radon Transform ρ_{I_0} along epipolar lines:* We start from the X-ray intensity

$$I(u, v) = I_{\text{tube}} \cdot \exp\left(-\int F_{\mathbf{x}_0}(r) dr\right) \quad (3)$$

detected in $\mathbf{x}_0 \cong (u, v, 1)^T$ attenuated by an object f along the ray $\mathbf{B}_{\mathbf{x}_0}$ with initial intensity I_{tube} . The X-ray projection for a single detector point on the 2D plane reads

$$\ln\left(\frac{I_{\text{tube}}}{I(u, v)}\right) = \int F_{\mathbf{x}_0}(r) dr = \int f\left(\begin{array}{c} r \cdot \cos(\varphi) \\ r \cdot \sin(\varphi) \\ 0 \end{array}\right) dr \quad (4)$$

where a single angle φ defines the ray, because by choice of coordinate system the source is in the origin. The distance to the origin r defines a point on that ray. Finally, the integral over an epipolar line $\mathbf{l}_0 \cong \mathbf{e}_0 \times \mathbf{x}_0$ in the polar coordinates of \mathbf{E} is

$$\rho_{I_0}(\mathbf{l}_0) = \iint f\left(\begin{array}{c} r \cdot \cos(\varphi) \\ r \cdot \sin(\varphi) \\ 0 \end{array}\right) dr d\varphi \quad (5)$$

3) *3D Radon Transform ρ_f over the epipolar plane:* The 3D radon transform of the object at \mathbf{E} is the plane integral

$$\rho_f(\mathbf{E}) = \iiint f(x, y, z) \delta((x, y, z, 1) \cdot \mathbf{E}) dx dy dz = \iint f(x, y, 0) dx dy \quad (6)$$

If we write the same plane integral in terms of the polar coordinates, we get the relationship with the integral over the epipolar line \mathbf{l}_0 . The Jacobian determinant of the polar transformation of the x - y -plane is exactly

$$\det(\mathbf{J}_{\Phi}) = r \cdot \cos(\varphi)^2 + r \cdot \sin(\varphi)^2 = r \quad (7)$$

which yields

$$\begin{aligned} \rho_f(\mathbf{E}) &= \iint f(x, y, 0) dx dy = \iint f(\Phi(\varphi, r)) \det(\mathbf{J}_{\Phi}) dr d\varphi \\ &= \iint f\left(\begin{array}{c} r \cdot \cos(\varphi) \\ r \cdot \sin(\varphi) \\ 0 \end{array}\right) r dr d\varphi \neq \rho_{I_0}(\mathbf{l}_0) \end{aligned} \quad (8)$$

We observe for cone-beam projections, that the integrals over epipolar lines generally differ by a weighting with the distance to the X-ray source. In the following, we will derive a formulation of a derivative of the epipolar plane integral which happens to cancel out that weighting factor.

C. Grangeat's theorem

The relationship between line integrals on the projection image and plane integrals of the object has been investigated in a different context by Grangeat [3], [7]. For the moment, we restrict ourselves to a single projection image. If we assume w.l.o.g. that the origin of the u - v -plane is located in the principal point, we can write the epipolar line

$$\mathbf{l} \cong (\cos(\psi + \frac{\pi}{2}), \sin(\psi + \frac{\pi}{2}), -t)^T \quad (9)$$

in terms of an angle ψ and distance t from principal point \mathbf{p} . The point \mathbf{o} is the orthogonal projection to that line. The 2D radon transform for \mathbf{l} is

$$\rho_I(\mathbf{l}) = \iint I(u, v) \delta((u, v, 1) \cdot \mathbf{l}) du dv \quad (10)$$

Figure 2 (a) reveals the geometric relationships between the 2D radon transform $\rho_I(\mathbf{l})$ and the 3D radon transform of the object $\rho_f(\mathbf{E})$. The 3D distance from \mathbf{C} to the line \mathbf{l} is exactly the distance to the image plane within a projection in direction of t . Its orthogonal projection must therefore be again \mathbf{o} . It follows that the lines $\text{join}(\mathbf{p}, \mathbf{o})$ and $\text{join}(\mathbf{C}, \mathbf{o})$ are orthogonal to \mathbf{l} . An arbitrary point \mathbf{x} on \mathbf{l} can be written

in terms of the angles κ (between \mathbf{E} and the principal ray) and φ (between \mathbf{o} and \mathbf{x} measured at \mathbf{C}). The distance from \mathbf{C} to \mathbf{l} is then $\cos(\varphi)r$ and the focal distance $\cos(\kappa)\cos(\varphi)\cdot r$ (via triangle $\mathbf{p}, \mathbf{C}, \mathbf{o}$).

Now, we apply Grangeat's trick and look at the derivative of $\rho(\mathbf{E})$ with respect to the distance to the origin n .

$$\frac{d}{dn}\rho_f(\mathbf{E}) = \frac{d}{dn} \iint F_{\mathbf{x}}(r)r \, dr d\varphi = \iint \frac{d}{dn} F_{\mathbf{x}}(r)r \, dr d\varphi \quad (11)$$

Observe in Figure 2 (b) that there is a relationship $dn = \sin(d\kappa) \cdot \cos(\varphi)r$. Because for small angles $\sin(d\kappa) = d\kappa$ it holds

$$\frac{d\kappa}{dn} = \frac{1}{\cos(\varphi)r} \quad (12)$$

and by chain rule we obtain

$$\frac{d}{dn} F_{\mathbf{x}}(r)r = \frac{d}{d\kappa} \frac{1}{\cos(\varphi)} F_{\mathbf{x}}(r) \quad (13)$$

Since the angle φ is small (bounded by half fan-angle), the cosine is almost one and we ignore it in our computations. We also ignore that \mathbf{n} is tilted slightly out of the detector plane, because κ is small. We can compute the derivative w.r.t t instead of n .

$$\begin{aligned} \frac{d}{dn}\rho_f(\mathbf{E}) &\stackrel{d\kappa \approx 0}{=} \iint \frac{d}{d\kappa} \frac{1}{\cos(\varphi)} F_{\mathbf{x}}(r) \, dr d\varphi \\ &\stackrel{\varphi \text{ small}}{\approx} \frac{d}{d\kappa} \iint F_{\mathbf{x}}(r) \, dr d\varphi \stackrel{\kappa \text{ small}}{\approx} \frac{d}{dt}\rho_I(\mathbf{l}) \end{aligned} \quad (14)$$

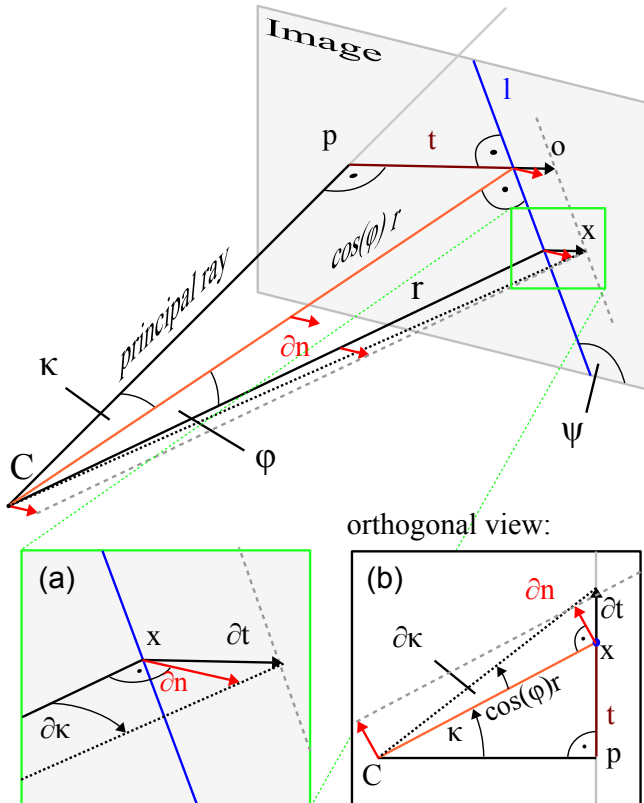


Figure 2. Grangeat's theorem: relationship between angle κ and normal n .

D. Definition of the metric

The main result of this paper and the connection between Equations 2 and 14 is that for a point \mathbf{x}_0 on I_0 we find redundant information in the i -th view (P_i, I_i)

$$M_0^i(\mathbf{x}_0) := \left(\frac{d}{dt}\rho_{I_0}(\mathbf{e}_0 \times \mathbf{x}_0) - \frac{d}{dt}\rho_{I_i}(\mathbf{F}_0^i \mathbf{x}_0) \right)^2 \approx 0 \quad (15)$$

The equation states, that given an image pair I_0 and I_i , a point \mathbf{x}_0 defines two corresponding epipolar lines $\mathbf{e}_0 \times \mathbf{x}_0$ and $\mathbf{F}_0^i \mathbf{x}_0$, whose line integrals derived w.r.t t are approximately the same. This is assuming the projection is accurately known. We expect the line integrals to differ more or less, depending on the geometric accuracy of the epipolar plane, respectively the projection parameters.

As discussed in Section II-B1, there is a pencil of such epipolar planes and each defines a pair of redundant line integrals. Figure 3 shows the epipolar lines of two views along with their respective derivative of the radon transform. We define the epipolar consistency metric as the sum over the squared differences between a selection of corresponding epipolar lines. To exclude planes which do not intersect the projection images and to control the sampling, we select points $\mathcal{X}_0^i \subset \mathbb{P}^2$ on I_0 , such that the resulting epipolar lines are evenly spaced, all intersect the images and that their maximal distance inside image bounds is no more than k pixels. We devise the following algorithm to select \mathcal{X}_0^i for a finite epipole:

- 1) Find the most distant corner of I_0 to the epipole

$$\mathbf{e}_0^i \cong \mathbf{P}_0 \cdot \mathbf{C}_i \quad (16)$$

and call its distance m .

- 2) Compute the angular step $d\alpha$, such that

$$\tan(d\alpha) = \frac{k}{m} \quad (17)$$

- 3) Find minimal and maximal angles $\alpha_{min}, \alpha_{max}$, so that any line

$$\mathbf{l}_\alpha = ((\cos(\alpha), \sin(\alpha), 0)^T + \mathbf{e}_0) \times \mathbf{e}_0 \quad (18)$$

intersects at least one image.

- 4) Compute the set \mathcal{X}_0^i via

$$\mathcal{X}_0^i = \{ \mathbf{x}_0 \in \mathbb{P}^2 : \mathbf{x}_0 \cong (\cos(\alpha), \sin(\alpha), 0)^T + \mathbf{e}_0 \\ \forall j \in \mathbb{N} : \alpha = \alpha_{min} + j \cdot d\alpha < \alpha_{max} \} \quad (19)$$

In this formulation, the points in \mathcal{X}_0^i lie on a circle around \mathbf{e}_0 , no matter the radius. For (almost) infinite epipoles $\mathbf{e}_0 \cong (e_x, e_y, \epsilon)^T$, $\epsilon \approx 0$, one can simply assume it were finite and sufficiently far away. We can now express the metric as

$$M_0^i = \frac{1}{|\mathcal{X}_0^i|} \sum_{\mathbf{x}_0 \in \mathcal{X}_0^i} \left(\frac{d}{dt}\rho_{I_0}(\mathbf{x}_0 \times \mathbf{e}_0) - \frac{d}{dt}\rho_{I_i}(\mathbf{F}_0^i \mathbf{x}_0) \right)^2 \quad (20)$$

divided by the number of line pairs $|\mathcal{X}_0^i|$. The derivatives of the 2D radon transform $\frac{d}{dt}\rho_I$ can be pre-computed.

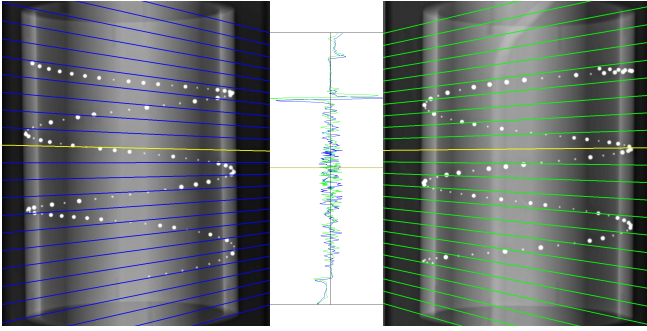


Figure 3. Two views with epipolar lines aligned to a plot of the derivative of the line integrals for the left image (blue) and right image (green). Notice a shift in the signals due to imperfect geometry.

Finally, we sum up all those pairs of views, which change during optimization. If we want to optimize over parameters in \mathbf{P}_0 , for example, we need not compute redundancies between (\mathbf{P}_i, I_i) and (\mathbf{P}_j, I_j) for $i \neq 0 \neq j$, because they remain constant if only \mathbf{P}_0 changes: $M_0 = \sum_i M_0^i$.

III. EXPERIMENTS AND RESULTS

A. Materials and methods

We validate against the digital phantom with random beads in a full 360° rotation presented in [4] (512×512 px projections, 1000 mm source-detector distance, phantom of diameter ~ 100 mm). In addition, we conducted an experiment for this work using a 120° sweep of 190 projections showing a real PDS2 calibration phantom using a sequence of a Siemens C-arm system. Using [8] we computed the C-arm projection matrices from the projections of the metal beads in the calibration phantom and obtained an average re-projection error of about 1.3 pixels (image size 960×1240 px, bead size about 8 – 12 px), which we also verified by visual inspection. These projection matrices are the gold standard. In order to prove the robustness of our method, we use the raw projection data directly from the scanner, without corrections of any kind (i.e. no I_0 correction, no correction for varying tube voltage etc.). We use a non-linear optimizer without gradient (Powell-Brent). In order to investigate accuracy, precision and stability of our method, we conduct a series of random studies over a rigid transformation in world space. As an intuitive and meaningful error metric, we compute the distance between the bead centers projected with the ground truth versus the current projection. This error is more informative, since the method itself is entirely image based, while quantities in millimeters and degrees of world space depend on overall scaling and most of the parameters a highly interdependent.

1) *Sampling of radon space:* In case of a circular trajectory, the epipole moves on a straight line from plus infinity, through the image to minus infinity. The epipolar lines are almost parallel, when the epipole is far away. When we align the detector v -axis with the axis of rotation, epipolar lines in most views will be almost parallel to the u -axis. This is visualized in Figure 4, where all the samples taken

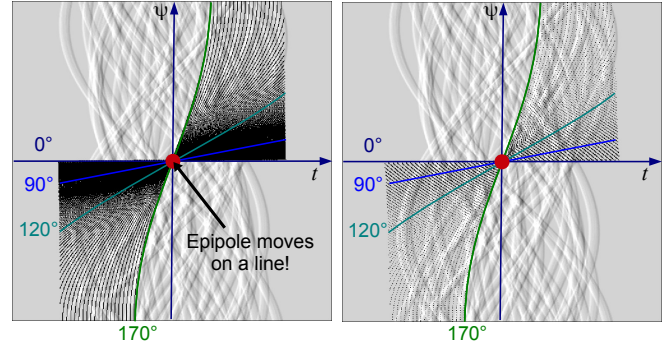


Figure 4. Derivative of the radon transform of the digital phantom. Samples for a 170° rotation about Y-axis with a maximum distance between epipolar lines of one pixel (left) and 5 pixels (right). Sampled locations in black.

from radon space are marked with a black dot. Note that a line bundle corresponds to a sinoid curve in Radon Space. Also note a linear trajectory of the epipole leads to a single intersection point of all sinoids. This is because the epipole itself moves on a line, which is represented in a single point in radon space, and that line is contained in any of the line bundles. Through the definition of \mathcal{X}_0^i , we can easily adjust the number of lines, hence the sampling in radon space.

2) *Dependency on direction of epipolar lines:* We expect the method to be reliable whenever the epipole is close to the image or even inside the image. The epipole is inside the image when the two views are related dominantly by a forward-backward translation, including opposing views. For cases, where the epipolar lines are almost parallel, we get little information in their direction (the direction of the integrals) but only orthogonal to them. Note that a pure translation parallel to the image plane results in parallel epipolar lines, a translation orthogonal to the image plane leaves the epipole in the center of the image. Rotations around the source merely apply a 2D homography to the image. As a general motion is a combination of these effects, we can predict which geometries will give reliable information and in which spatial direction. Observe, for example Figure 4, where sampling is dense close to the $\psi = 0$ axis (horizontal). This is a property of any circular trajectory. The epipole is within the image for views within \pm fan angle from the opposing view. For an opening angle of 40° this is just about 10 of all views. The method is thus much more robust for optimizing parameters orthogonal to the plane of rotation (usually denoted v -direction of the detector). Only for opposing views is it similarly reliable in both u and v directions. This is a problem especially for short scans, as visualized in the shape of the graphs in Figure 5, which show a long and narrow valley in u -direction.

B. Random study

1) *Accuracy:* First, the gold standard geometry is assumed and optimized w.r.t the metric to find the distance of the closest minimum. Any change away from the gold standard is an inaccuracy. We obtained a mean accuracy over all projections of ~ 0.25 px and a maximum of 1.00 px.

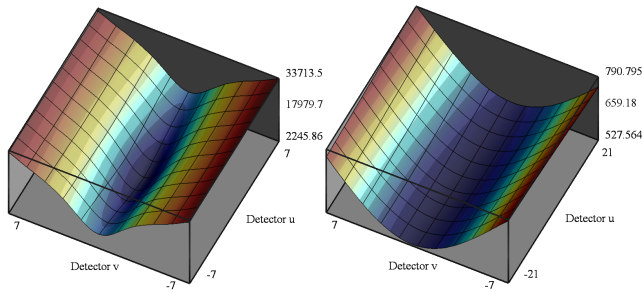


Figure 5. Plots of the epipolar consistency metric for detector shifts u and v for the numerical 360° phantom and the real 120° PDS2 phantom. Note the minimum can be located much more clearly in u -direction for 360° data.

2) *Precision*: The second step is to randomly disturb the optimal pose by a random set of parameters. The disturbances are uniformly distributed in a range of ± 5 mm for the translations and ± 0.05 radians $\approx \pm 2.8^\circ$ for the rotations. We present results for only one representative projection at a sample size of $n = 30$. We were able to reduce the mean pixel error from ~ 2.4 px to ~ 0.2 px (maximum error was 0.7 px).

3) *Stability*: Finally, we conducted another random study with extreme disturbances of ± 25 mm for the translations and ± 0.25 radians $\approx \pm 14^\circ$ for rotations and observe the range of parameters, for which optimization is successful. We found that of $n = 100$ samples drawn, with an average error of ~ 10 px we were able to recover the pose up to an error of < 1 px in 51 cases. The minimum initial error of the unsuccessful cases was 7.0 px and the mean initial error, which could be corrected for was 9.3 px.

4) *Ultra short scan*: Due to the direction of the epipolar lines for narrow angular range (compare Section III-A2), we conduct the random studies for the 120° data only w.r.t to the world Y -position of the source (similar to detector v) of the projection at 60° primary angle. This is currently a major limitation and subject of future work. The result of an initial random study for $n = 100$ and ± 25 mm offsets are a reduction of the mean error down from ~ 9.7 px to ~ 0.01 px with a maximum error of ~ 0.1 px. The same study for detector shift u would fail and even increase the mean error. This example shows, that a correct optimization strategy must be found.

IV. CONCLUSION

We present a new formulation for redundancies in transmission imaging data based on the epipolar geometry between pairs of views. We make the connection from Grangeat's theorem to the epipolar geometry of two X-ray projections, which enables us to express corresponding line integrals in the projection data using the fundamental matrix. We further derived a consistency metric, which exploits redundancies of these line integrals to optimize the projection geometry. We are presenting a fast algorithm to compute that metric and observe some of its properties, including robustness to varying X-ray tube parameters and

its ability to correct 3D parameters, without the need for 3D reconstruction. The understanding of the underlying epipolar geometry gives us control over the sampling in radon space and it helps us identify geometries for which the metric is reliable. An initial random study using projections of a numerical and physical phantoms suggest that the metric can indeed find practical use in a multitude of applications related to the estimation of projection geometry. We believe that its potential applications range from pose estimation in fluoroscopy, tracking of a rigid object in X-ray projections, automatic re-calibration of the imaging system for FD-CT reconstruction up to the detection, estimation and correction of rigid patient movement. Future work should investigate different approaches to optimization, such as finding subsets to avoid dependencies in the optimization, evaluate real data sets and compare computation speed versus precision with other approaches to calibration correction.

Acknowledgments: This work was supported by Spitzencluster Medical Valley, Verbund Bildgebende Diagnostik: Teilprojekt BD 16 FKZ: 13EX1212.

Disclaimer: The concepts and information presented in this paper are based on research and are not commercially available.

REFERENCES

- [1] R. I. Hartley and A. Zisserman, *Multiple View Geometry in Computer Vision*. Cambridge University Press, ISBN: 0521623049, 2000.
- [2] O. Faugeras, *Three-dimensional computer vision: a geometric viewpoint*, ser. Artificial intelligence. MIT Press, 1993.
- [3] P. Grangeat, "Mathematical framework of cone beam 3d reconstruction via the first derivative of the radon transform," in *Mathematical Methods in Tomography*, ser. Lecture Notes in Mathematics, G. Herman, A. Louis, and F. Natterer, Eds. Springer Berlin Heidelberg, 1991, vol. 1497, pp. 66–97.
- [4] C. Debbeler, N. Maass, M. Elter, F. Dennerlein, and T. M. Buzug, "A new ct rawdata redundancy measure applied to automated misalignment correction," in *Proceedings of the Fully Three-Dimensional Image Reconstruction in Radiology and Nuclear Medicine (Fully3D)*, 2013, p. 264.
- [5] W. Wein and A. Ladikos, "Detecting patient motion in projection space for cone-beam computed tomography," in *MICCAI 2011 Proceedings*, ser. Lecture Notes in Computer Science. Springer, Sep. 2011.
- [6] Y. Kyriakou, R. M. Lapp, L. Hillebrand, D. Ertel, and W. A. Kalender, "Simultaneous misalignment correction for approximate circular cone-beam computed tomography," *Phys Med Biol*, vol. 53, no. 22, pp. 6267–6289, Nov 2008.
- [7] T. Buzug, *Computed Tomography: From Photon Statistics to Modern Cone-Beam CT*. Springer, 2008.
- [8] A. Maier, J. H. Choi, A. Keil, C. Niebler, M. Sarmiento, A. Fieselmann, G. Gold, S. Delp, and R. Fahrig, "Analysis of Vertical and Horizontal Circular C-Arm Trajectories," in *Proc. SPIE Vol. 7961*, SPIE, Ed., 2011, pp. 7961 231–7961 238.

Geometrical Jitter Correction in Computed Tomography

Nicole Maass, Frank Dennerlein, André Aichert, and Andreas Maier

Abstract—In computed tomography and tomosynthesis perspective projections of an object are measured from different views. These projections are correlated to each other as they image the same object. Quantification of their consistency constitutes a cost function, which allows to reduce misalignment artifacts. Previously, a promising cost function for perspective projection consistency quantification has been proposed and evaluated for global misalignment artifact reduction [1]. In this work we evaluate the ability of that cost function to quantify and improve misalignment artifacts that originate from unreproducibly wobbling scanner components. The evaluation is done for scans with circular trajectories using mathematical simulations and measurements.

I. INTRODUCTION

In computed tomography, misalignment artifacts degrade reconstructed CT images if the geometrical information of each view are in bad agreement with the real positions and orientations of the CT scanner’s components (source, object, detector). Thus, there are numerous methods published in literature on that issue. Some of these methods place markers in the field of measurement or perform dedicated calibration measurements in order to calibrate a reproducible trajectory [2]–[4]. In this work we are focusing on methods that do not require markers, dedicated calibration measurements, or reproducible system trajectories [5]–[8]. We use the cost function that has been proposed in reference [1] and evaluate its ability to correct not only global misalignment, as it has been shown in reference [1], but also projection-specific misalignment (jitter). Additionally, we give further insights into intermediate results that allow to assess the efficiency of the cost function for the optimization of a particular geometry parameter with a given trajectory.

II. METHOD

A. Flat detector geometry

Without loss of generality, we use the flat detector cone–beam CT geometry from reference [1] throughout this work, as it is sketched in Figure 1. Cone–beam projections

$$p(\lambda, u, v) = \int_{-\infty}^{\infty} dt f(\mathbf{s}(\lambda) + t\mathbf{t}(\lambda, u, v)) \quad (1)$$

of the object $f(x, y, z)$ are measured from N source positions λ_n . The scalar lambda parameterises the piecewise continuous

Dr. N. Maass and Dr. Frank Dennerlein are with the Siemens AG, Healthcare Sector, Erlangen, Germany. André Aichert and Dr. Andreas Maier are with the Pattern Recognition Lab, Department of Computer Science, Friedrich–Alexander–University Erlangen–Nueremberg, Erlangen, Germany. Dr. Andreas Maier is with the Erlangen Graduate School in Advanced Optical Technologies (SAOT). Corresponding author: nicole.maass@siemens.com

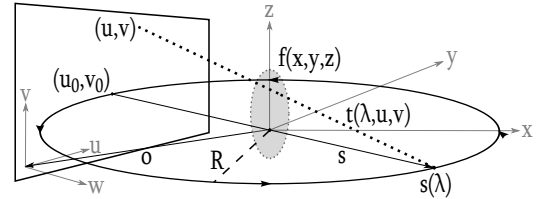


Fig. 1. Illustration of the circular 3D cone–beam acquisition geometry with a flat panel detector.

trajectory $\mathbf{s}(\lambda)$, that contains all source positions $\mathbf{s}(\lambda_n)$. The coordinates u and v parameterise the flat detector pixel’s columns and rows, respectively, such that the triple (n, u, v) uniquely describes one specific ray (line integral) through the object $f(x, y, z)$.

B. Radon planes

Picking two different source positions $\mathbf{s}(\lambda_n)$ and $\mathbf{s}(\lambda_{\hat{n}})$ we have already fixed two points of a Radon plane. We choose an angle ψ , with $-\frac{\pi}{2} \leq \psi < \frac{\pi}{2}$, as a third parameter which identifies one plane from that set of planes. With these three parameters (n, \hat{n}, ψ) we are able to uniquely identify a Radon plane that contains the source positions $\mathbf{s}(\lambda_n)$ and $\mathbf{s}(\lambda_{\hat{n}})$. The actual meaning of ψ is unimportant for the remainder of this work; we can just think of it as the angle between the normal vector of the plane and some (almost) arbitrarily chosen reference vector. Varying ψ from $-\frac{\pi}{2}$ to $\frac{\pi}{2}$ we get all Radon planes that contain the source positions $\mathbf{s}(\lambda_n)$ and $\mathbf{s}(\lambda_{\hat{n}})$ of views n and \hat{n} , respectively.

For practical implementations, ψ needs to be discretized in an appropriate step size $d\psi = \frac{\pi}{N_\psi}$. Throughout this work we use equiangular sampling of ψ with $N_\psi = 768$. Obviously, not every possible Radon plane intersects with the projection images of both views (n and \hat{n}), as the size of each projection image is limited. We define the function $m(n, \hat{n})$ to count the number of Radon planes that intersect with the detectors of both views, i.e. $0 \leq m(n, \hat{n}) < N_\psi$.

C. Radon domain consistency

In reference [9] an intermediate function $S(s, \mu, \lambda)$ over the previously discussed Radon planes is derived. Note that the parameterization of the Radon plane is done by the view λ and a line on that view’s detector plane, which is defined by the distance to the image origin s and an angle μ . Either notation refers to a Radon plane in 3D object domain.

In reference [1] it has been shown that redundancies in that intermediate function can be used to quantify the rawdata consistency and that this consistency criterion can be used for

global misalignment correction. Thereby, the overall rawdata consistency criterion from reference [1] does not distinguish specific projections but calculates a sum over all Radon planes of all combinations of two different views n and \hat{n} :

$$\hat{c}_{\text{RP}} = \sqrt{\sum_{n=0}^{N-1} \sum_{\mu=-\pi/2}^{\pi/2} \sum_{l=-L_{\text{max}}}^{L_{\text{max}}} (g_3(n, \mu, l) - g_3(\hat{n}, \hat{\mu}, \hat{l}))^2}, \quad (2)$$

where $g_3(n, \mu, l)$ of reference [1] corresponds to $S(s = l, \mu, \lambda = \lambda_n)$ in reference [9]. In equation 2 a Radon plane is described by the triple (n, μ, l) , which corresponds to picking one view's source position $\mathbf{s}(\lambda_n)$ and one line on the detector of that view. $g_3(\hat{n}, \hat{\mu}, \hat{l})$ is the corresponding second measurement of the Radon intermediate function, with $\mathbf{s}(\lambda_{\hat{n}})$ being the second intersection of the Radon plane with the source trajectory (the first time is at $\mathbf{s}(\lambda_n)$) and $(\hat{\mu}, \hat{l})$ describes the line on that second view's detector.

D. Projection-specific cost function

Using the parameterization of a Radon plane introduced in section II-B, we reformulate the overall rawdata consistency cost function of equation (2) to

$$c_{\text{RP}} = \sum_{n=0}^{N-1} \sum_{\hat{n}=n+1}^{N-1} c_{\text{PP}}(n, \hat{n}), \quad \text{with} \quad (3)$$

$$c_{\text{PP}}(n, \hat{n}) = \frac{\sqrt{\sum_{\psi=0}^{N_\psi-1} (g_3(n, \mu, l) - g_3(\hat{n}, \hat{\mu}, \hat{l}))^2}}{m(n, \hat{n})} \quad (4)$$

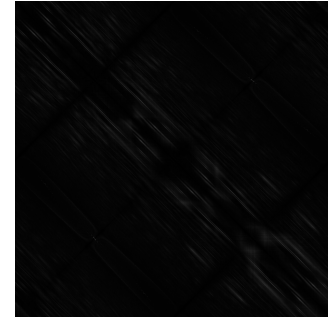
being the normalized contribution of one projection pair (PP) to the cost function. Note that $\mu, l, \hat{\mu}$, and \hat{l} are functions of the Radon plane which is uniquely defined by the triple (n, \hat{n}, ψ) , as discussed earlier. In order to obtain comparable cost function contributions from each pair of projections, we have modified equation (2) by 1) calculating the norm only over all planes of one pair of projections instead of all available Radon planes of all projection pairs and 2) normalizing $c_{\text{PP}}(n, \hat{n})$ with the count function $m(n, \hat{n})$.

In figure 2(a) a 2D plot of the function $c_{\text{PP}}(n, \hat{n})$ is shown using $n \in [0, N-1], \hat{n} \in [0, N-1]$. The plot is created from the simulated projection data of the Forbild head phantom described in section II-F. Thereby the correct geometry was used for calculations, such that all values different from 0 are numerical errors. These numerical errors introduce a constant offset into the cost function c_{RP} . We did not observe that this offset affects the optimization procedure which is performed using this cost function.

E. Jitter correction

With the formulation of a normalized projection pair-wise cost function $c_{\text{PP}}(n, \hat{n})$ in equation (4) we can easily define a cost function that considers the consistency of one particular projection n with all other projections:

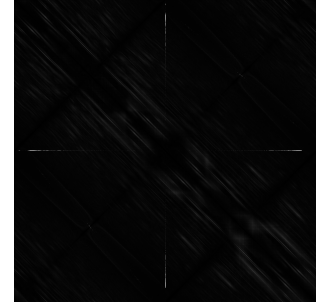
$$c_n = \sum_{\hat{n}=0}^{N-1} c_{\text{PP}}(n, \hat{n}). \quad (5)$$



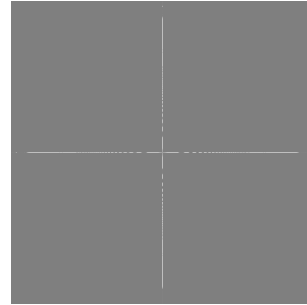
(a) $c_{\text{PP}}(n, \hat{n})$ without dejusts, showing numerical errors only



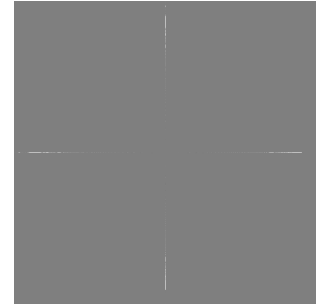
(b) $c_{\text{PP}}(n, \hat{n})$ with axial dejust $i_{n=300, \Delta v_0} = 1$



(c) $c_{\text{PP}}(n, \hat{n})$ with lateral dejust $i_{n=300, \Delta u_0} = 1$



(d) difference: $2(b) - 2(a)$



(e) difference: $2(c) - 2(a)$

Fig. 2. Projection pair cost $c_{\text{PP}}(n, \hat{n})$ using projection data of the Forbild head phantom simulations. The number of projections of this dataset is $N = 600$ and therefore the plots have 600×600 pixels with each pixel showing the (normalized) inconsistency of the Radon domain intermediate function of all Radon planes that were found for that pair of projections. Note that due to the symmetry $c_{\text{PP}}(n, \hat{n}) = c_{\text{PP}}(\hat{n}, n)$ it is unnecessary to label the axis. The grayscale window is $C/W = 0.3/0.6$ for standard images and $C/W = 0/0.6$ for difference images.

The cost functions c_n and $c_{\text{PP}}(n, \hat{n})$ implicitly depend on the geometry of all projections as the intersection line (n, μ, l) of a Radon plane (n, \hat{n}, ψ) with the detector of view number n changes with the geometry of views n or \hat{n} , as visualized in figure 2. Equation (5) means summing up row or column number n in a 2D plot of $c_{\text{PP}}(n, \hat{n})$. Since we are mainly interested in changes of the function c_n while varying the geometry (which refers to subfigures 2(d) and 2(e)), we have dropped the dependency of this function on the overall geometry and explicitly denote its dependency on geometry changes in equation (6).

For every geometry parameter under consideration, we define a base step size, which is the optimization resolution and maps the continuous physical parameters on an integer

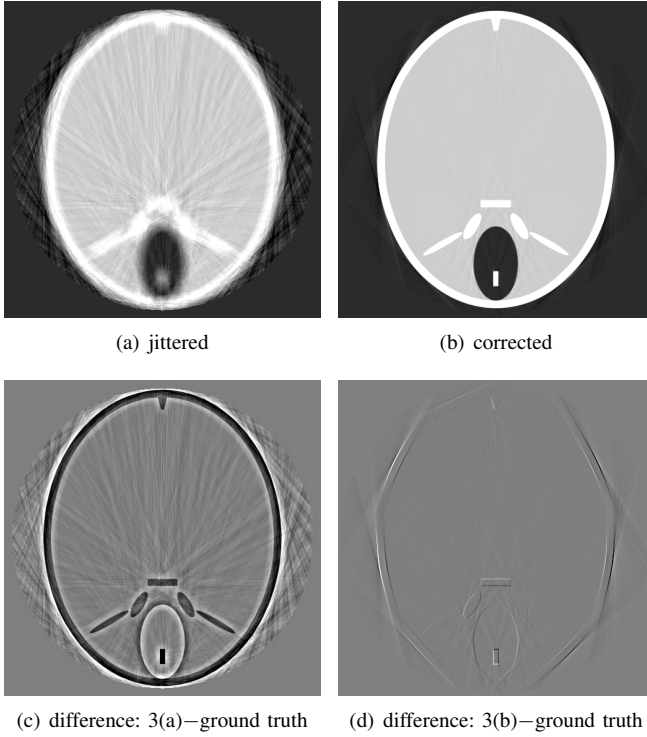


Fig. 3. Head phantom simulations with jitter added on the lateral and axial detector position: $u_{0,n} = u_0 \pm 20 \cdot \Delta u_0$, $v_{0,n} = v_0 \pm 20 \cdot \Delta v_0$. Grayscale window: Standard images $C/W = 0.01/0.03 \text{ mm}^{-1}$; difference images $C/W = 0.0/0.03 \text{ mm}^{-1}$.

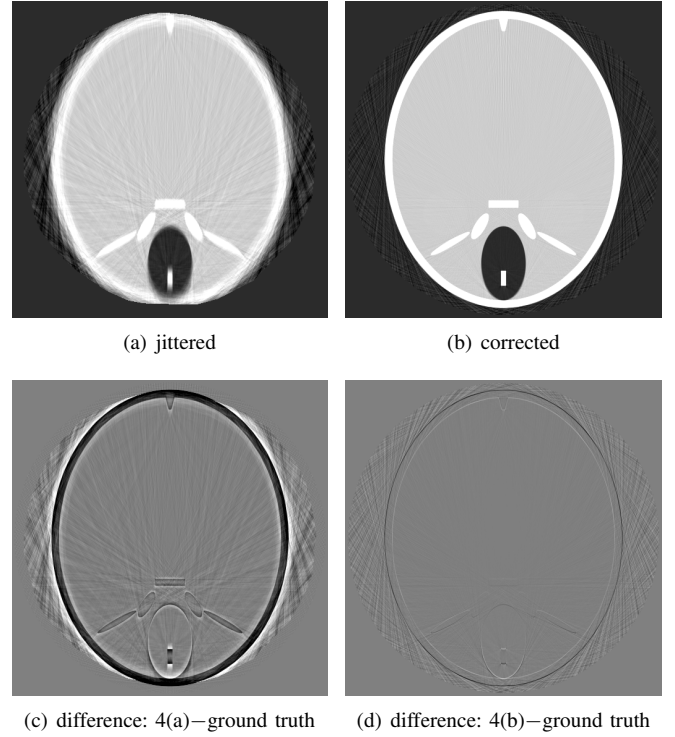


Fig. 4. Head phantom simulations with jitter added on the source-object distance (R) and source-detector distance (D): $R_n = R \pm 20 \cdot \Delta R$, $D_n = D \pm 20 \cdot \Delta D$, with $\Delta R = 7.5 \text{ mm}$ and $\Delta D = 12 \text{ mm}$. Grayscale window: Standard images $C/W = 0.01/0.03 \text{ mm}^{-1}$; difference images $C/W = 0.0/0.03 \text{ mm}^{-1}$.

grid. Considered geometry parameters and their base step sizes are:

- lateral detector offset $\Delta u_0 = 1.0 \text{ px}$
- axial detector offset $\Delta v_0 = 1.0 \text{ px}$
- detector slant $\Delta b = 0.15^\circ$
- source-object distance $\Delta R = 0.01 \cdot R$
- source-detector distance $\Delta D = 0.01 \cdot D$

For optimization, we calculate

$$i_{n,\Delta}^{\min} = \underset{i \in [-20,20]}{\operatorname{argmin}} (c_n(i \cdot \Delta)), \quad (6)$$

with Δ being the geometry parameter under consideration. The search range of ± 20 steps is arbitrarily chosen here and should be adapted to the expected jitter deviations of a given system.

After finding the minimum cost function value of projection n for geometry parameter Δ the trajectory correction is applied before the next view is considered. To avoid the introduction of offsets by systematic errors of the trajectory (e.g. parameter drift), we process the projections in bit-reversal order. After processing all projections with one geometry parameter under consideration, the next geometry parameter Δ is used. After processing all projections with all geometry parameters, one iteration is considered to be completed. The process of jitter correction can be repeated iteratively.

F. Experiments

We use simulations of the Forbild head phantom to prove the concept with known ground truth. The simulations were

performed using an ideal circle trajectory with source trajectory radius of $R = 750 \text{ mm}$, source-detector-distance $D = 1200 \text{ mm}$, $N = 600$ projections equiangularly distributed on a full circle, and 512×512 detector pixels with $0.8 \times 0.8 \text{ mm}$. Reconstructions use a $512 \times 512 \times 512$ voxel grid with 0.5 mm isotropic voxel size, but only the central slice is presented. In a first experiment we simulate a combination of uniformly distributed lateral (u_0) and axial (v_0) detector jitter of up to ten pixel in each direction. In a second experiment we simulate a combination of uniformly distributed source-object distance jitter (R) and source-detector distance jitter (D) of up to 10% each. We present reconstruction results with the jittered geometry configuration and after application of three iterations of the jitter optimization proposed in section II-E.

In addition to the simulation, we show a CT measurement of a car key. The dataset has $N = 1440$ projections equiangularly distributed on a full circle using $R = 100 \text{ mm}$ source-object distance, $D = 450 \text{ mm}$ source-detector distance, and about 1000×750 detector pixels with a size of $0.15 \times 0.15 \text{ mm}$. The projection data of this measurement are severely truncated in about half of the projections in order to measure the object with high spatial resolution (i.e. high magnification). The industrial CT scanner, which has acquired those data, does not suffer from noticeable wobbling of measurement components such that we can use the dataset trajectory as ground truth (after global misalignment correction according to reference [1]). We add uniformly distributed artificial jitter on each of the scanning parameters (one at a time) and run the optimization

algorithm for exactly that scanning parameter. In an additional experiment we add artificial jitter on three scanning parameters at a time (v_0 , u_0 , and b) and run the optimization algorithm for exactly those scanning parameters.

For presentation we choose a 512×512 pixel slice with 0.015 mm isotropic pixel size that contains tiny high contrast objects, which are the cross sections of wires connecting a chip with a circuit board. Figure 5 gives an overview of the complete dataset, its field-of-measurement, and the slices presented in figure 6.

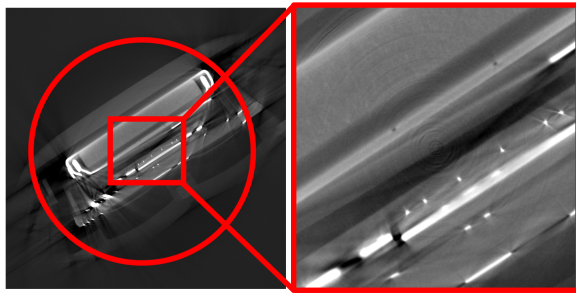


Fig. 5. Overview of the car key dataset delineating the field of measurement (red circle) and the area presented in figures 6 and 7 (red rectangle). The grayscale window is $C/W = 0.1/0.25 \text{ mm}^{-1}$.

III. RESULTS

A. Head phantom simulations

In figures 2(b) and 2(c) there is the visualization of $c_{pp}(n, \hat{n})$ while dejusting projection number n . It is noticeable that the effect of dejusting projection n is restricted to exactly the line (column) which is used in c_n . A dejust of just one detector pixel causes a signal in the plots that is clearly visible. It is further noticeable that there are projection pairs including projection number n where the effect of the dejust cannot be observed clearly. There are even some negative values on line n in figure 2(b). We conclude that for each parameter there are some projection pairs that are less suited for consistency quantification than others. This observation helps predicting which parameters can be optimized for a given trajectory.

However, in figure 2 there is only the effect of one dejusted projection (for visualization). In the experiment we have randomly dejusted every projection (by up to 10 steps) and applied the proposed jitter optimization algorithm (searching up to 20 steps) using c_n as a cost function. The results of the first experiment dejusting u_0 and v_0 simultaneously is presented in figure 3; the result of the second experiment dejusting R and D is presented in figure 4. In both experiments we can notice that the artificial jitter severely degrades the image quality, such that many structures are hardly noticeable. The proposed jitter correction algorithm significantly improves the image quality in both experiments, however, slight dejusts remain.

B. Car key measurement

Figure 6 presents the results of the car key dataset after dejustment of single geometry parameters. Figure 7 presents the results after simultaneous dejustment of three geometry

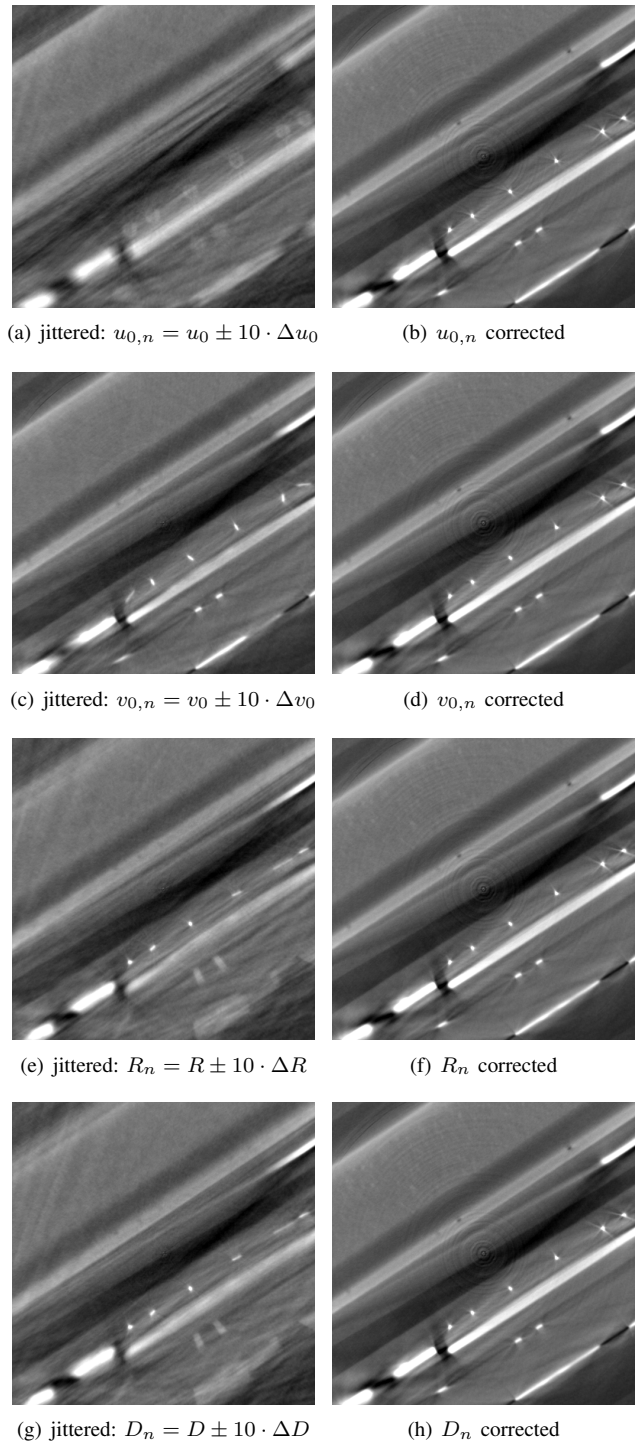


Fig. 6. Car key dataset with artificial jitter added on various circle trajectory parameters (left column) and after two iterations of jitter correction (right column). Grayscale window $C/W = 0.10/0.25 \text{ mm}^{-1}$

parameters (u_0 , v_0 , and b) with difference images provided for comparison with the ground truth reconstruction. The artificially introduced jitter severely degrades the image quality (left column) and the proposed jitter correction algorithm is able to recover the original image quality in all cases (right column). No noticeable artifacts remain in standard images; in difference images slight differences remain, which are not

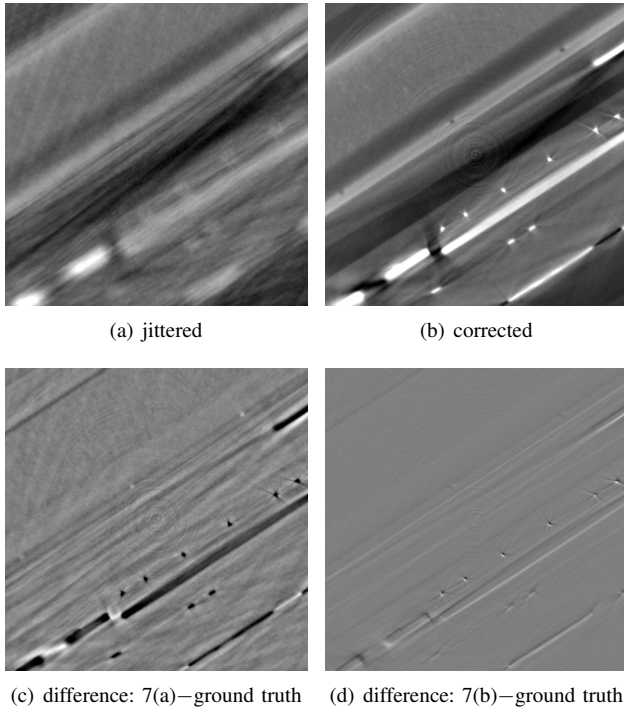


Fig. 7. Car key dataset with artificial jitter added on the axial detector offset (v_0), the lateral detector offset (u_0), and the detector slant (b) and the correction after two iterations. Grayscale window: Standard images $C/W = 0.10/0.25 \text{ mm}^{-1}$; difference images $C/W = 0.0/0.25 \text{ mm}^{-1}$.

necessarily artifacts but could also result from an overall shift of the object.

In order to give more insight into the method, we plot the jitter for the optimization of the v_0 parameter in figure 8. From the plot it can be seen that the remaining jitter is one optimization step or less.

In figure 9 we plot all $N = 1440$ cost functions c_n that are evaluated during the first iteration of optimization in v_0 -direction. Every single cost function is very smooth, has a unique minimum within the search range, and would also allow for gradient decent optimization (which is not done in this work).

Figures 5–9 originate from a measured real world dataset that has about 50% of its projections severely laterally truncated (all projections are axially truncated).

IV. CONCLUSION

We have evaluated the use of a rawdata consistency quantification method based on a Radon intermediate function for the optimization of geometrical jitter in circular computed tomography scans. The results are promising regarding ability, reliability, and stability of the method. For a final conclusion a larger number of real world measurements will be used.

Disclaimer: The concepts and information presented in this paper are based on research and are not commercially available.

REFERENCES

[1] C. Debbeler, N. Maass, M. Elter, F. Dennerlein, and T. M. Buzug, "A new CT rawdata redundancy measure applied to automated misalignment

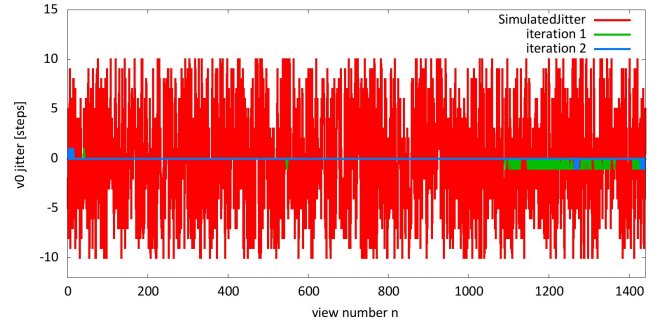


Fig. 8. Simulated jitter (red) $i_{n,\Delta v_0}$ in v_0 direction and remaining deviation from the ground truth $i_{n,\Delta v_0} - i_{n,\Delta v_0}^{\min}$ after a given number of iterations. The red jitter values correspond to figure 6(c) and the blue jitter values correspond to figure 6(d).

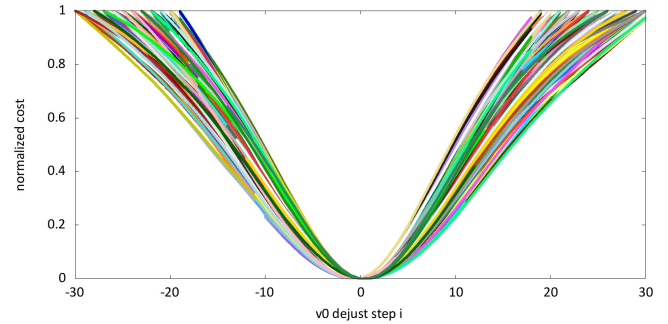


Fig. 9. Plot of the cost functions $c_n \left((i_{n,\Delta v_0} - i_{n,\Delta v_0}^{\min}) \Delta v_0 \right)$ for $n \in [0, N - 1]$ and $i \in [-20, 20]$. Each of the $N = 1440$ plots is separately normalized. These are the cost functions whose minima $i_{n,\Delta v_0}^{\min}$ are searched during the first iteration of Δv_0 jitter correction of the car key dataset. The shift of each plot towards its minimum allows for efficient visualization.

correction," in *Proceedings of the 12th International Meeting on Fully 3D Image Reconstruction*, 2013.

[2] C. Mennessier, R. Clackdoyle, and F. Noo, "Direct determination of geometric alignment parameters for cone-beam scanners," *Physics in Medicine and Biology*, vol. 54, no. 6, p. 1633, 2009. [Online]. Available: <http://stacks.iop.org/0031-9155/54/i=6/a=016>

[3] S. Simbt, F. Dennerlein, and J. Boese, "Markerbasiertes Online Kalibrierverfahren für die CT-Rekonstruktion," in *Bildverarbeitung für die Medizin*, 2010, pp. 157–161.

[4] S. Sawall, M. Knaup, and M. Kachelrieß, "A robust geometry estimation method for spiral, sequential and circular cone-beam micro-CT," *Medical Physics*, vol. 39, no. 9, pp. 5384–5392, 2012. [Online]. Available: <http://link.aip.org/link/?MPH/39/5384/1>

[5] J. Wicklein, H. Kunze, W. A. Kalender, and Y. Kyriakou, "Image features for misalignment correction in medical flat-detector CT," *Medical Physics*, vol. 39, no. 8, pp. 4918–4931, 2012. [Online]. Available: <http://link.aip.org/link/?MPH/39/4918/1>

[6] F. Dennerlein and A. Jerebko, "Geometric jitter compensation in cone-beam CT through registration of directly and indirectly filtered projections," in *Nuclear Science Symposium Conference Record (NSS/MIC)*, 2012, pp. 2892–2895.

[7] D. Panetta, N. Belcari, A. Del Guerra, and S. Moehrs, "An optimization-based method for geometrical calibration in cone-beam CT without dedicated phantoms," *Phys. Med. Biol.*, vol. 53, pp. 3841–3861, 2008.

[8] A. Kingston, A. Sakellariou, T. Varslot, G. Myers, and A. Sheppard, "Reliable automatic alignment of tomographic projection data by passive auto-focus," *Medical Physics*, vol. 38, no. 9, pp. 4934–4945, 2011. [Online]. Available: <http://link.aip.org/link/?MPH/38/4934/1>

[9] M. Defrise and R. Clack, "A cone-beam reconstruction algorithm using shift-variant filtering and cone-beam backprojection," *IEEE TMI*, vol. 13, no. 1, pp. 186–195, March 1994.

An Efficient Technique For Multi-Phase Model Based Iterative Reconstruction

Shiyu Xu, Debashish Pal and Jean-Baptiste Thibault

Abstract—Multi-phase scan is a fundamental CT acquisition technology used in a variety of applications such as cardiac CT and perfusion CT. Model-based iterative reconstruction (MBIR) has already demonstrated significant IQ improvements that can provide significant noise reduction with improved resolution that are essential for such applications. However the challenge is to efficiently reconstruct multi-phase scans. The simplest way is to perform MBIR reconstruction on each individual phase data in a sequential order or in a parallel computing framework. However, these approaches either lead to increase in overall compute time or reduce the patient throughput due to more computing resources being utilized for a single patient. Alternatively due to the views shared among the adjacent phases, it is possible to reuse the geometric coefficient calculations and to reconstruct multiple image volumes simultaneously. The proposed approach involves joint optimization of the MBIR cost-function to estimate images from all phases simultaneously. In this paper, the efficiency and feasibility of multi-phase reconstruction is investigated. First a quantitative metric is derived for estimating the improvement in the efficiency, then the improvement is verified using an implementation of the prototype algorithm. It is demonstrated using a cardiac multi-phase data that the proposed algorithm improves the computational efficiency with no change in the IQ compared to sequential MBIR reconstruction. It is also concluded that the improvement is dependant on the type of the optimization algorithm and the compute architecture.

Index Terms—Cardiac CT, multi-phase scan, MBIR, perfusion CT.

I. INTRODUCTION

Technology for X-ray detection in cone-beam (CB) geometry is rapidly improving and offers potential of performing fast high-resolution volume CT imaging. However, to optimally build such systems, the problem of CB image reconstruction needs to be fully understood. Statistical iterative methods (IR) exhibit particularly promise since it provides the flexibility of accurate physical noise modeling and geometric system description. Recently invented IR technique, model based iterative reconstruction (MBIR) [1], [2], significantly improves image quality (IQ) compared to conventional filtered back-projection (FBP). Iterative reconstruction suffers from an inherent challenge in terms of compute time compared to FBP due to multiple iterations needed for convergence and each iteration involves forward/back-projections using a complex geometric system model.

Shiyu Xu is with the Department of Electrical and Computer Engineering, Southern Illinois University Carbondale, IL, 62901 USA (e-mail: shiyu.xu@gmail.com).

Debashish Pal and Jean-Baptiste Thibault is with Advanced Science and Engineering Group, GE Healthcare 3000 N Grandview Blvd W1180 Waukesha, WI 53188 USA.

Multi-phase reconstruction using MBIR poses an additional challenge of reconstructing multiple images volumes corresponding to different phases. Multi-phase scanning involves acquiring CT data at different time instants and is widely used in a variety of applications such as cardiac and perfusion CT. In cardiac CT [3], [4], multi-phase scans are typically used to identify images at a quiescent phase with least motion artifacts. Reconstructions from multi-phase scan data can also be used to generate the motion signature which can then be applied to correct the motion artifact and in turn to improve temporal resolution [5]. A typical multi-phase scan in cardiac axial CT is demonstrated in Fig. 1(a), where view ranges for the adjacent phases partially overlap. In perfusion CT [6], multi-phase scan enables the potential to view crucial information such as blood flow (arterial and venous) and function in the heart, brain, joints and other parts of the body. In a non-cardiac axial perfusion CT geometry adjacent phases share the same view range and the data for all phases are totally co-located.

One simple way of reconstructing multiple volumes corresponding to different phases using MBIR is to reconstruct each phase sequentially, which is easy to implement but increases the reconstruction time by a factor of k , which is the number of phase. If several parallel computing nodes are available, reconstruction for each phase can be distributed amongst different nodes and all phase reconstructions are performed simultaneously. In this case, a K -time speed up is gained compared to the sequential reconstructions. However, utilizing more compute resources for a single exam reduces the patient throughput which is critical in the CT work flow. A more efficient approach is proposed in this paper in which the image volumes corresponding to different phases are jointly reconstructed on the same compute node as described in section II-A. The efficiency is gained due to the fact that the views among adjacent phases are shared and hence the geometric model calculations can be shared during the forward/back-projections. Additional details about the memory organization of the sinograms are shown in section II-B. The improvement in the efficiency is demonstrated using cardiac multi-phase data in section III.

II. METHODS

A. Multi-phase reconstruction framework

The joint objective function for a multi-phase scan can be constructed as:

$$\Phi(\mu) = \sum_{k=1}^K \sum_{i=1}^M (y_i - \sum_{j=1}^N a_{i,j} \mu_{k,j})^2 w_{k,i}$$

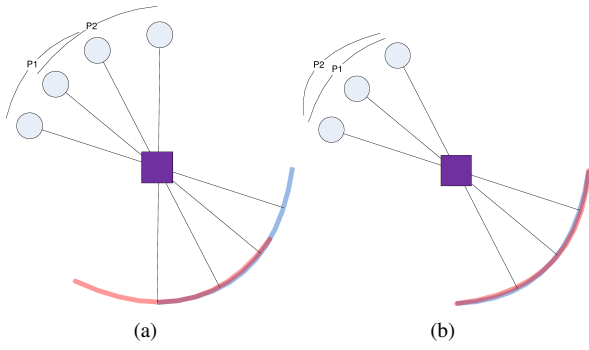


Fig. 1. Schematic geometry of multi-phase scan with partial and full overlap in the views.

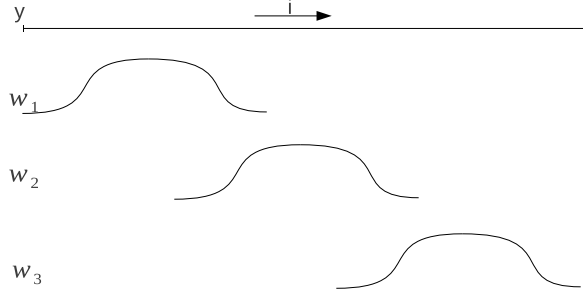


Fig. 2. Schematic demonstration of the projection data and statistical weights used for multi-phase MBIR reconstruction.

$$+\beta \sum_{k=1}^K \sum_{j=1}^N \sum_{m \in N_j} \kappa_{k,m} \kappa_{k,j} \rho(\mu_{k,j} - \mu_{k,m}), \quad (1)$$

where $i \in [1, M]$ indexes the projection data from all phases that needs to be reconstructed; $j \in N$ is the voxel index; $k \in K$ is the phase index; N_j is an index set of j -th voxel's neighbors. The first term in the objective function Φ is the data-fidelity to minimize the data mis-match, where y is the projection data; w_k is a vector of statistical weights and is constructed separately for each phase k ; $a_{i,j}$ is the system coefficient calculated by a distance driven (DD) forward model. The system matrix coefficients are shared by all the phases. μ_k is the image volume estimated for the k -th phase. The second term in the objective function Φ is a prior term where ρ is q-GGMRF potential function [1], [2], $\kappa_{k,j}$ are spatially varying regularization coefficients and β controls the tradeoff between the data-fidelity and prior.

An example of the projection data and statistical weights for a cardiac three-phase reconstruction is shown in fig. 2. The projection data and weights are vectors of dimension M . The index i represents the detector index with the view index being the slowest variable. The windowing function shown in the figure are cardiac gating function for each phase. The gating function is applied on the statistical weights to reduce motion artifacts [7]. As explained in eq. 1, the projection data spans all the phases but the gating function imposes limit on the number of views actually used for reconstructing a particular phase.

Iterative coordinate descent (ICD) [2] is used as the optimization technique to solve eq. 1. ICD is a greedy optimization algorithm in which the voxels are updated using a sequence

of one-dimensional functions. In the case of multi-phase reconstruction, the K -dimensional vector μ_k is estimated by solving the function,

$$\begin{aligned} \mu_{k,j}^{n+1} = \arg \min_{\mu_{k,j} \geq 0} \{ & \theta_{1,kj}(\mu_{k,j} - \mu_{k,j}^n) \\ & + \frac{1}{2} \theta_{2,kj}(\mu_{k,j} - \mu_{k,j}^n)^2 \\ & + \beta \sum_{m \in N_j} \kappa_{k,j} \kappa_{k,m} \rho(\mu_{k,j} - \mu_{k,m}^n) \}, \end{aligned} \quad (2)$$

which leads to the update step,

$$\mu_{k,j}^{n+1} = \mu_{k,j}^n - \frac{\theta_{1,kj} + \sum_{m \in N_j} \kappa_{k,j} \kappa_{k,m} \rho'(\mu_{k,j} - \mu_{k,m}^n)}{\theta_{2,kj} + \sum_{m \in N_j} \kappa_{k,j} \kappa_{k,m} \rho''(\mu_{k,j} - \mu_{k,m}^n)}, \quad (3)$$

where the first and second derivative of ρ is computed using the functional substitution method [2]. $\theta_{1,j}$ is a K -dimensional gradient vector and $\theta_{2,j}$ is a K -dimensional diagonal matrix for voxel index j . The elements of these matrices are computed as,

$$\begin{aligned} \theta_{1,kj} &= \sum_i a_{i,j} (e_{k,i} w_{k,i}), \\ \theta_{2,kj} &= \sum_i a_{i,j}^2 w_{k,i}. \end{aligned} \quad (4)$$

e_k is the error sinogram and is maintained separately for every phase. The error sinogram is first computed as,

$$e_{k,i} = \sum_j a_{i,j} \mu_{k,j}^0 - y_i, \quad (5)$$

and it is updated after every voxel update,

$$\begin{aligned} e_{k,i} &= e_{k,i} + \Delta e_{k,i}, \\ \Delta e_{k,i} &= a_{i,j} (\mu_{k,j}^{n+1} - \mu_{k,j}^n). \end{aligned} \quad (6)$$

The efficiency in the multi-phase reconstruction can be achieved by reusing the system coefficients $a_{i,j}$ to compute the error sinogram for all phases. The error sinogram is then consumed to compute the first and second derivatives of the cost-function as shown in eq. 4. However, this approach requires more memory than a sequential processing or parallel processing. The proposed method requires K M -dimensional error sinogram, and statistical weight and K N -dimensional image volume. The efficiency improvement in a multi-phase framework depends on the number of coefficients shared amongst the phases. For example, in a clinical scan with an average heart rate of 65 bpm and gantry rotation speed of 0.35 s over 984 views, a three phase scan with 5% phase difference will have total 1080 views. A very crude calculation of the efficiency ratio using the proposed approach is $\eta = \frac{642 \times 3}{1080} = 1.78$. In the subsequent sections, a more accurate metric is used to compute the efficiency achieved with the proposed approach.

B. Memory organization and voxel processing

The update equation in eq. 3 consists of multiple steps of data operation and memory access in a general computer model shown in Fig. 3 where the local buffer could be on-chip SRAM or cache, Mem represents main memory

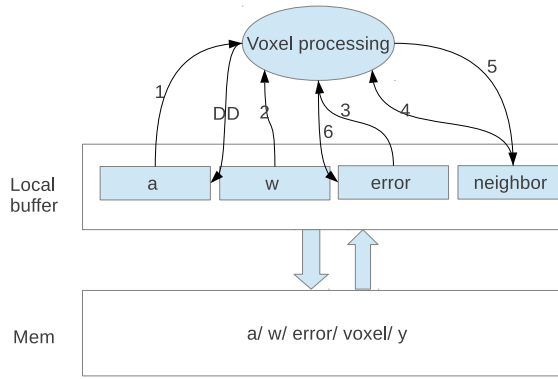


Fig. 3. k -dimensional vector update in a general computer.

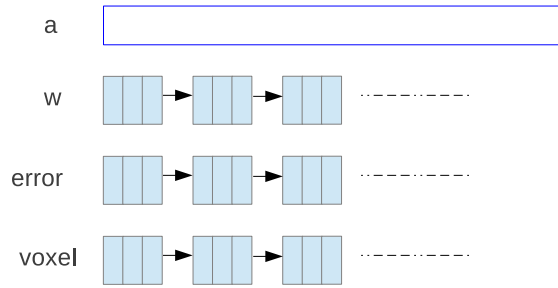


Fig. 4. Memory organization for a three-phase reconstruction in physical memory line.

system (off-chip). These steps are summarized as below:

Voxel processing:

- 1: The system coefficients a_{ij} are generated using DD model and written back to Mem through a -buffer.
- 2: After fetching operation 1/2/3, θ_1 and θ_2 are computed by Eq. 4 for k -dimensional vector, μ_k .
- 3: k -dimensional vector, μ_k and its neighbors are fetched by operator 4 to compute ρ' and ρ'' .
- 4: The k -dimensional vector, μ_k is updated simultaneously by Eq. 3 and is written back to Mem by operator 5.
- 5: Consequently, the error sinogram is updated using Eq. 6 by operator 6.

In the above operations, memory access operations 1/2/3/4/5 can take as high as 80% of total computing cost. Therefore, it is crucial to organize the data in a more efficient way. A potential memory arrangement is to interlace the phase data as a package and to store it in a continuous physical memory line. By using the burst mode, reading weight $w_{x,i}$ at any phase can also fetch other phase $w_{y,i}$ to fill in one cache line, which can hide the memory latency to read other phase data. Fig. 4 demonstrates the memory organization for accessing data in a three-phase reconstruction. This allows reading one element which brings in all other elements automatically by a burst mode to update the 3-dimensional voxel vector using the shared system matrix coefficients.

Interleaved non-homogeneous (NH) and homogeneous voxel selection is used to speed up convergence by focusing the computation where it is most needed [2]. During each

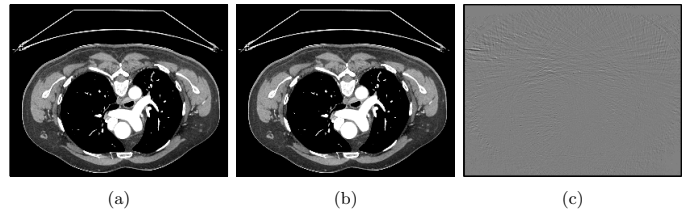


Fig. 5. IQ comparison of the center slices reconstructed using multi-phase MBIR and individual MBIR at target phase (75% of the RR cycle). (a) shows the slice reconstructed by multi-phase MBIR; (b) shows the slice reconstructed by individual MBIR; (c) shows the reconstruction difference between the multi-phase MBIR and individual MBIR

non-homogenous update, a set of voxel indices are selected based on their update magnitudes. In the multi-phase MBIR framework, the same set of voxel indices is used to update images from all phases. This set of voxel indices is selected based on the sum of update magnitudes from all phases as given below:

$$m(j) = \sum_1^K |\mu_{k,j}^{n+1} - \mu_{k,j}^n|. \quad (7)$$

III. EXPERIMENTS AND RESULTS

A. Image quality validation

A cardiac CT clinical data is used to demonstrate the feasibility of multi-phase MBIR image reconstruction. The data is acquired in GE Discovery 750HD using a pitch of 0.2 with a gantry rotation speed of 0.35 s. Images are reconstructed at 66%, 75% and 83% of the RR cycle. Individual MBIR reconstructions of the phases are also performed to generate reference results. This comparison is performed to perform a sanity check on the implementation. It is clear from Eq. 1 that the cost function of a single MBIR reconstruction should converge to the same image as the multi-phase reconstruction for a given phase. All the images are reconstructed in a 70 cm field-of-view with a 418×418 matrix inside a zROI of dimension 13. A total of 99 slices are reconstructed as MBIR requires extra slices to be reconstructed outside the zROI. 4 iterations of ICD are used to reconstruct all the images. The dimension of the projection data used for multi-phase and single MBIR reconstruction is , $1080 \times 888 \times 64$ and $642 \times 888 \times 64$, respectively. As explained in section II-A, the size of the error sinogram and statistical weight sinogram for multi-phase reconstruction is $3 \times 1080 \times 888 \times 64$. In contrast, the size of these sinograms are the same as the projection data for a single phase MBIR reconstruction.

Fig. 5 and Fig. 6 show the IQ comparison of the central slice of the zROI using the proposed multi-phase MBIR and separate MBIR reconstructions at the two phase locations. Hence a sanity check on the implementation is performed demonstrating that within the same number of iterations multi-phase MBIR reconstruction produces IQ comparable to separate MBIR reconstructions performed at the given phases.

In Section II, a rough estimation on the acceleration ratio is presented. A more thorough metric to evaluate the efficiency gained by doing multi-phase reconstruction over separate MBIR reconstructions is described here. In the best case

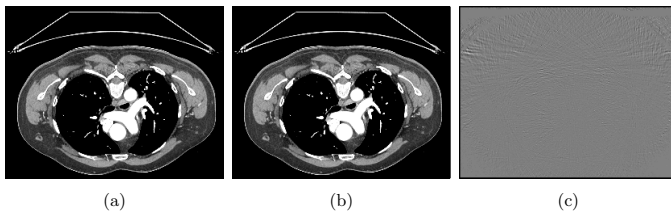


Fig. 6. IQ comparison of the center slices reconstructed using multi-phase MBIR and individual MBIR at right phase (83% of the RR cycle). (a) shows the slice reconstructed by multi-phase MBIR; (b) shows the slice reconstructed by individual MBIR; (c) shows the reconstruction difference between the multi-phase MBIR and individual MBIR

scenario when all the phases share exactly the same number of views (*i.e.* axial perfusion CT), fetching one system matrix coefficient can be reused K (number of phases) times and this would hold for every fetch operation. However typically this would depend on the amount of overlap between the phases. The metric can be specific to every detector element and will indicate the efficiency of the fetch operation for every detector element. For the sake of simplicity, this metric is averaged across all detector elements and is shown in Eq. 8 below.

$$\eta = \frac{\sum_{k=1}^K \sum_j (\sum_i I_{i \in k} I_{(a_i, j \neq 0)})}{\sum_j \sum_i I_{(a_i, j \neq 0)}}, \quad (8)$$

where I is an indicator function; $I_{(a_i, j \neq 0)}$ counts the number of non-zero geometric coefficients corresponding to the j -th voxel and i -th detector index. $I_{i \in k}$ counts the number of phases that share detector index i . The ratio η is the efficiency gained due to shared system coefficients. A ratio of 3 demonstrates the best-case scenario for a 3-phase reconstruction and with 100% overlap in the views, while in the case of the scan used in section III-A the efficiency metric is evaluated as 2.3. This implies that the performance of a 3-phase reconstruction on the scan used in the previous section will be $3/2.3 \approx 1.3$ times a single phase MBIR reconstruction.

B. Practical efficiency measurement

The multi-phase MBIR algorithm is implemented and is run on a multi-thread environment to evaluate the actual improvement in the efficiency. The performance of a 3-phase MBIR reconstruction is measured to be $3/1.4 = 2.1$ times a single phase MBIR reconstruction. The reason of slower performance than the predicted one is due to time spent in memory access. It is to be noted that all the efficiency metrics computed in the previous sections ignore the memory access time. Since the multi-phase MBIR reconstructions need bigger sinograms than a single phase MBIR reconstruction, the memory access time may have a significant impact in negating the efficiency gained due to sharing the system matrix coefficients. In contrast, the best-case performance is measured to be $3/2.1 = 1.5$ times a single phase MBIR reconstruction. The best-case situation is shown in Fig. 1(b).

IV. CONCLUSION

In this paper, a multi-phase MBIR algorithm is presented for reconstructing data from a multi-phase scan. The multi-phase

scans have overlapping view ranges and as a result the geometric model calculations are shared in the proposed algorithm reducing the compute time. It is shown that the multi-phase MBIR algorithm is a better alternative than performing individual MBIR reconstructions sequentially without impacting the final image quality. It is shown that the images obtained with individual MBIR reconstructions are almost identical to the images obtained with the multi-phase MBIR reconstruction algorithm. The minor difference in convergence rate can be caused due to the fact the update mask used in the non-homogenous update is different in the two implementations. The efficiency improvement is measured with a 3 phase reconstruction at 66%, 75%, and 83% using a clinical dataset on a particular implementation of the algorithm available in-house. The efficiency is gated by the memory access as the multi-phase algorithm requires larger arrays for the sinograms. To optimize the memory access, the data from all the phases is interlaced into a continuous physical memory line which can then be accessed in a burst mode to update all the image volumes simultaneously. Finally the measurements are based on ICD algorithm which is a sequential algorithm and may have a different memory access pattern than a simultaneous update algorithms such as PCG, OS-SPS. In addition the efficiency achieved is highly dependant on the compute platform itself. In the future, more study is required to evaluate the efficiency for techniques that are based on simultaneous updates. The image model used in this study is still an indicator function and can be expanded to include more kinetic models as proposed in [8] for cardiac multi-phase scans.

ACKNOWLEDGMENT

This work is supported by GE healthcare.

REFERENCES

- [1] J.-B. Thibault, K. D. Sauer, C. A. Bouman, and J. Hsien, "A three-dimensional statistical approach to improved image quality for multislice helical CT," *Med. Phys.*, vol. 34(11), pp. 4526–4544, 2007.
- [2] Z. Yu, J.-B. Thibault, C. A. Bouman, K. D. Sauer, and J. Hsien, "Fast model-based x-ray CT reconstruction using spatially non-homogeneous icd optimization," *IEEE Transactions on image processing*, vol. 20(1), pp. 161–75, 2011.
- [3] H. W. Goo, "State-of-the-art ct imaging techniques for congenital heart disease," *Korean J Radiol.*, vol. 11(1), pp. 4–18, 2010.
- [4] T. C. Gerber, B. Kantor, and E. E. Williamson, "Computed tomography of the cardiovascular system," in *Computed Tomography of the Cardiovascular System*. Dordrecht: CRC Press, 2007, p. 556.
- [5] A. Isola, C. Metz, M. Schaap, S. Klein, M. Grass, and W. Niessenc, "Cardiac motion-corrected iterative cone-beam CT reconstruction using a semi-automatic minimum cost path-based coronary centerline extraction," *Computerized Medical Imaging and Graphics*, vol. 36, pp. 215–226, 2012.
- [6] A. Konstas, G. G. T.-Y. Lee, and M. Lev, "Theoretic basis and technical implementations of ct perfusion in acute ischemic stroke, part 1: Theoretic basis," *AJNR.*, vol. 30, pp. 662–668, 2009.
- [7] P. DL, "Optimal short scan convolution reconstruction for fanbeam CT," *Med. Phys.*, vol. 9(2), pp. 254–257, 1982.
- [8] Z. Yu, J.-B. Thibault, J. Wang, C. A. Bouman, and K. D. Sauer, "Kinetic model for motion compensation in Computed Tomography," *11th International Meeting on Fully Three-Dimensional Image Reconstruction in Radiology and Nuclear Medicine*, pp. 466–469, 2011.

Multiscale Interior Tomography using 1D Generalized Total Variation

Minji Lee, John P. Ward, Michael Unser and Jong Chul Ye*

Abstract—We propose a method for accurate and fast reconstruction of the interior of a 2D or 3D tomographic image from its incomplete local Radon transform. Unlike the existing interior tomography work with 2D total variation, the proposed algorithm guarantees exact recovery using a 1D generalized total variation semi-norm for regularization. The restrictions placed on an image by our 1D regularizer are much more relaxed than those imposed by the 2D regularizer in previous works. Furthermore, to further accelerate the algorithm up to a level of clinical use, we propose a multi-resolution reconstruction method by exploiting the Bedrosian theorem for the Hilbert transform. More specifically, as the high frequency part of the image can be quickly recovered using Hilbert transform thanks to the Bedrosian equality, we show that computationally expensive iterative reconstruction can be applied only for the low resolution images in downsampled domain, which significantly reduces the computational burden. We demonstrate the efficacy of the algorithm using circular fan-beam and helical cone-beam data.

I. INTRODUCTION

In x-ray computed tomography (CT), reconstruction of region of interest (ROI) from local projection data has been called for to reduce radiation exposure in imaging specific organs such as heart, or to reduce size of x-ray detector for cost saving. Using the backprojection filtration (BPF) method [1], it was shown that the ROI that cannot cover the whole object can be determined uniquely when the intensity of subregions inside the field of view (FOV) are known *a priori* [2], [3]. However, in general, it is difficult to know the intensity inside the object. Consequently, using the 2D total variation, the authors in [4] showed that unique reconstruction is possible if the images are piecewise constant. In those papers, while the images were assumed to be piecewise polynomial, the regularization term was 2D and fairly complex, which led the authors to focus on piecewise linear images [5]. Furthermore, the iterative procedure to reconstruct the interior images under the regularization is quite complicated, which prohibits its use in clinical environment.

As in those papers, we seek to reconstruct images that are piecewise smooth; i.e., the domain where the image is defined can be decomposed into a finite number of subdomains such that the image is a smooth function on each piece. However, our approach generalizes the ideas developed in [5] with a simplified 1D formulation, and as a result, we are able to perfectly reconstruct new classes of functions. In particular, we can reconstruct any image that is a generalized L-spline along a collection of lines passing through the region of interest.

M. Lee and J. C. Ye are with Bio Imaging & Signal Processing Lab, Department of Bio & Brain Engineering, KAIST, Korea. J. P. Ward and M. Unser are with Bioimaging Group, EPFL, Switzerland.

Here L is a differential operator that can be more general than an n -th order derivative. For example, we can reconstruct images whose 1D restrictions are non-polynomial exponential B-splines, and which are not covered by the previous works.

To further accelerate the algorithm up to a level of clinical use, we propose a multi-scale reconstruction method that separately reconstructs low frequency part and high frequency part of the 1D signal at different resolution. More specifically, thank to the Bedrosian equality for the Hilbert transform, even for the truncated Hilbert transform, we can show that high frequency part of the signal can be recovered accurately using one step Hilbert transform. Therefore, the computationally expensive iterative reconstruction can be performed only to reconstruct the low frequency part of the signal after down-sampling, which allows its fast implementation. We verify the efficacy of the algorithm using 2D fan-beam and 3D cone-beam reconstruction with realistic acquisition parameters.

II. MATHEMATICAL BACKGROUNDS

A. Differentiated Backprojection and Hilbert Transform

In helical cone-beam CT, the scanning trajectory is expressed as

$$\vec{r}_0(\lambda) = \left(R \cos(\lambda), R \sin(\lambda), \frac{h}{2\pi} \lambda \right)^T, \quad (1)$$

where λ is the rotation angle of x-ray source, R the distance from the source to rotation axis, and h the pitch of helical trajectory. If $h = 0$, the acquisition geometry is reduced to a 2D fan-beam geometry. From helical cone-beam scanning, we can get the cone-beam projection data of a 3D object function $f(\vec{r})$, and it can be expressed as

$$P(\vec{r}_0, \hat{\beta}) = \int_0^\infty ds f(\vec{r}_0 + s\hat{\beta}), \quad \hat{\beta} \in S^2 \quad (2)$$

with the unit vector $\hat{\beta}$ of projection direction from a x-ray source location at \vec{r}_0 . From this projection data, the differentiated backprojection (DBP) at the 3D point \vec{r} can be computed by [1]

$$g(\vec{r}) = \frac{-1}{2\pi} \int_{\lambda_1}^{\lambda_2} \frac{d\lambda}{|\vec{r} - \vec{r}_0(\lambda)|} \frac{\partial}{\partial q} P(\vec{r}_0(q), \hat{\beta}(\lambda, \vec{r})) \Big|_{q=\lambda}. \quad (3)$$

In this equation, $\frac{\partial}{\partial q} P(\vec{r}_0(q), \hat{\beta}(\lambda, \vec{r})) \Big|_{q=\lambda}$ means differentiation of projection with respect to the source trajectory, and $\int_{\lambda_1}^{\lambda_2} \frac{d\lambda}{|\vec{r} - \vec{r}_0(\lambda)|}$ refers the backprojection with cone-beam weighing. Here, λ_1 and λ_2 are determined by a PI line through \vec{r} . This PI line is unique for any point inside the helix, so

there must be unique λ_1 and λ_2 for \vec{r} . Now, with a slight abuse of notation, if we define DBP data and attenuation image restricted on the PI line as

$$g(x) := g(\vec{r}_0(\lambda_1) + x(\vec{r}_0(\lambda_2) - \vec{r}_0(\lambda_1))) \quad (4)$$

$$f(x) := f(\vec{r}_0(\lambda_1) + x(\vec{r}_0(\lambda_2) - \vec{r}_0(\lambda_1))) \quad (5)$$

Then, we have the following 1D Hilbert transform relationship

$$g(x) = \frac{1}{\pi} \text{P.V.} \int_{-\infty}^{\infty} \frac{dx'}{x-x'} f(x') = \mathcal{H}f(x) \quad (6)$$

where P.V. denotes the Cauchy principal value. For the case of 2D fan-beam geometry, the PI line is not unique and we can choose infinitely many PI lines that pass through \vec{r} . Among these, we use a set of PI lines that are parallel to each other to simplify the implementation.

B. Interior Tomography Formulation

If the DBP data $g(x)$ is available for all x , the reconstruction of $f(x)$ can be simply done by performing inverse Hilbert transform \mathcal{H}^{-1} , which is equal to $-\mathcal{H}$. However, in the case of interior tomography problem, the detector is truncated; so, the DBP data is only available within $x_1(e_1, e_2)$. The main problem of such truncated Hilbert transform is the existence of the null space. More specifically, there exists non-zero $\nu(x)$ such that

$$\mathcal{H}\nu(x) = 0, \quad x \in (e_1, e_2). \quad (7)$$

Indeed, $\nu(x)$ can be expressed using an appropriate DBP data $h(x)$ outside of the ROI:

$$\nu(x) = -\frac{1}{\pi} \int_{\mathbb{R} \setminus (e_1, e_2)} \frac{dx'}{x-x'} h(x'). \quad (8)$$

Then, a required interior tomography formulation is to find an appropriate regularization term that suppresses the signal belonging to the null space of the truncated Hilbert transform. Note that $\nu(x)$ in (8) is differentiable in any order due to the removal of the origin in the integrand.

III. MAIN CONTRIBUTIONS

A. Exact Recovery under Generalized TV Penalty

To generalize the TV to meet the goal, we consider a regularization with respect to a Fourier multiplier operator L that is defined on $L_2(\mathbb{R})$ and satisfies two conditions. First, for any interval $E = (e_1, e_2) \subset \mathbb{R}$, we require L to map $C_c^\infty(E)$ to $C_c(E)$. Second, the null space of L , denoted as \mathcal{N}_L , should consist of entire functions. An example of such an operator is a constant coefficient differential operator

$$L := a_K D^K + a_{K-1} D^{K-1} + \dots + a_1 D + a_0 \quad (9)$$

where $K \geq 1$, D denotes the distributional derivative on \mathbb{R} , and each a_k is a real number. In this example, the finite-dimensional null space consists of linear combinations of exponential functions multiplied by polynomials. For an operator L and an interval $E \subset \mathbb{R}$, we formally define the *generalized total variation semi-norm*

$$\|f\|_{TV(L;E)} := \|Lf\|_{L_1(E)} \quad (10)$$

which is valid when $Lf \in L_1(E)$. In order to ensure that this semi-norm is valid for a larger class of functions, we use the dual formulation

$$\|f\|_{TV(L;E)} := \sup_{h \in C_h} \int_E f(x) L^* h(x) dx \quad (11)$$

where $C_h = \{h \in C_c^\infty(E), \|h\|_{L_\infty} \leq 1\}$. As in [4], our results are based on the fact that $\nu(x)$ in (8) is infinitely smooth in E . Suppose, furthermore, the signal $f(x)$ to be reconstructed is a generalized L-spline, where L is a finite-order operator. It is this disparity between the infinitely smooth $\nu(x)$ and the finitely smooth $f(x)$ that allows us to have perfect reconstruction.

Theorem 1. *Let $f_0(x)$ be a generalized L-spline such that*

$$Lf_0(x) = \sum_{n=1}^N a_n \delta(x - x_n) \quad (12)$$

on E . Then, the following minimization problem

$$\arg \min_f \|f\|_{TV(L;E)} \quad \text{subject to } \mathcal{H}f_0(x) = \mathcal{H}f(x), \quad x \in E$$

has the unique solution equal to $f_0(x)$.

B. Multi-Resolution Decomposition Using Bedrosian Equality

Unlike the previous works [5], our regularization is based on 1D TV semi-norm. Therefore, the optimization problem is much less complex. In addition, we now propose a multi-scale decomposition method that further reduces the computational complexity.

1) *Low frequency reconstruction:* To reconstruct $f(x)$ from its truncated Hilbert transform, we split it into low-pass and high-pass components. This is accomplished by convolving with a function ϕ whose Fourier transform Φ satisfies:

- For some $\omega_0 > 0$, $\Phi(\omega) = 1$ when $|\omega| < \omega_0$ and $\Phi(\omega)$ has fast decay for $|\omega| > \omega_0$;
- Φ is even, smooth, and decreasing for $|\omega| > \omega_0$

In this paper, we use a spline for ϕ . Then, the low-pass component $f_L(x)$ is given by convolving $a_f^{-1} \phi(a_f)$ with $f(x)$, for some dilation factor $a_f > 0$. This can be easily implemented using spline wavelet transform and taking the lowest band signal. Furthermore, the low-pass component $f_L(x)$ can be recovered from the corresponding low-pass component of the DBP data $g(x)$ since the Hilbert transform preserves the bandwidth as observed in

$$G(\omega) = \mathcal{F}\{\mathcal{H}f\}(\omega) = -i \text{sgn}(\omega) F(\omega). \quad (13)$$

Thanks to (13), we can reconstruct the $f_L(x)$ from the down sampled DBP data $g_L(x)$. For the recovery of the resulting low-pass band $f_L(x)$, we make the following assumption.

Assumption 1. *f_L is well modeled as an L-spline for some Fourier multiplier operator L .*

Under this assumption, f_L is reconstructed using the iterative algorithm with TV semi-norm regularization. The implementation of the iterative step will be explained in detail later.

2) *High frequency reconstruction*: After reconstructing $f_L(x)$, the high-pass component $f_H(x)$ is the complement. Note in particular that the Fourier transform of f_H is identically zero in a neighborhood of the origin. This allows us to compute f_H using Bedrosian's theorem for the Hilbert transform.

Theorem 2 (Bedrosian). *Let $f, g \in L_2(\mathbb{R})$. Suppose that the Fourier transform of f , denoted by $F(\omega)$, vanishes for $|\omega| > \omega_0$, with $\omega_0 > 0$, and the Fourier transform of g , denoted by $G(\omega)$, vanishes for $|\omega| < \omega_0$; then*

$$\mathcal{H}\{f(x)g(x)\} = f(x)\mathcal{H}g(x). \quad (14)$$

Since we only have exact data for $\mathcal{H}f(x)$ on a restricted interval $E = (e_1, e_2)$, we apply a band-limited finite length window $w(x)$ before computing the inverse Hilbert transform. Bedrosian's theorem implies that

$$w(x)g_H(x) = w(x)\mathcal{H}f_H(x) = \mathcal{H}\{w(x)f_H(x)\} \quad (15)$$

as long as the support of $W(w)$ is contained in a neighborhood of the origin that is disjoint from the support of $F_H(w)$. Here, we use the characteristic function of the interval $E = (e_1, e_2)$. Solving for f_H in (15), we get

$$f_H(x) = \frac{-\mathcal{H}\{w(x)g_H(x)\}}{w(x)}, \quad x \in E. \quad (16)$$

IV. IMPLEMENTATION

A. Low Frequency Signal Reconstruction

To recover the low frequency signal, we first take downsampling of the original DBP by wavelet decomposition and taking the lowest frequency band (see Fig. 1). From the downsampled DBP signal, the low frequency part of signal is reconstructed using projection onto convex sets (POCS) algorithm, and the reconstructed signal is then upsampled to the original resolution signals. This procedure takes much less time than iterative reconstruction of the original full-resolution DBP signal. For POCS implementation, the following five convex constraint sets are used:

$$\begin{aligned} C_1 &= \{f(x) \in L^2(\mathbb{R}) : f(x) = 0, x \notin (b_1, b_2)\} \\ C_2 &= \{f(x) \in L^2(\mathbb{R}) : \mathcal{H}f(x) = g(x), x \in (e_1, e_2)\} \\ C_3 &= \{f(x) \in L^2(\mathbb{R}) : \|f\|_{TV(L;E)} \leq \tau\} \\ C_4 &= \{f(x) \in L^2(\mathbb{R}) : \int_{b_1}^{b_2} dx f(x) = P(\vec{r}_0(\lambda_1), \hat{\beta}(\lambda_1, \vec{r}))\} \\ C_5 &= \{f(x) \in L^2(\mathbb{R}) : f(x) \geq 0, \forall x\}, \end{aligned}$$

Here, (b_1, b_2) denotes the approximate object boundary. The projection to each constraint is quite straightforward except for the projection on C_3 , the generalized TV norm constraint. It turns out that the projection on C_3 from a point f_0 can be implemented as the following denoising step.

$$\hat{f} = \arg \min_f \{\|f - f_0\|_2^2 + 2\lambda\|f\|_{TV(L;E)}\} \quad (17)$$

for an appropriate Lagrangian parameter. Using the definition of the generalized TV semi-norm, the optimization problem is given by

$$\sup_{h \in C_h} \min_f \{\|f - f_0\|_2^2 + 2\lambda\langle f, L^*h \rangle\}, \quad (18)$$

whose optimal solution of the inner minimization is given by $\hat{f} = f_0 - \lambda L^*h$. So, (18) can be reformulated with respect to the dual variable:

$$\min_{h \in C_h} \left\{ \lambda^2 \|L^*h\|_{L_2(E)}^2 - 2\lambda \langle f_0, L^*h \rangle \right\}. \quad (19)$$

Then, the optimal solution \hat{h} can be obtained by gradient projection method

$$h_k = P_{C_h} (h_{k-1} - 2t_k \lambda L (\lambda L^* h_{k-1} - f_0)) \quad (20)$$

when t_k denotes the k -th step size, P_{C_h} denotes the projection on the convex set C_h , and $2\lambda L (\lambda L^* h_{k-1} - f_0)$ is the gradient of the cost function in (19). For super-linear convergence rate, we implement the algorithm based on Nesterov method.

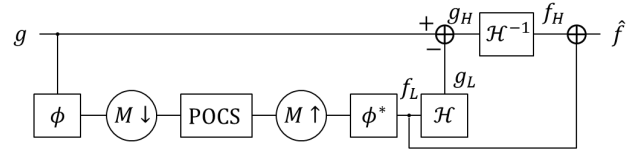


Fig. 1. Multi-resolution reconstruction flowchart.

B. High Frequency Signal Reconstruction

After low frequency reconstruction, the reconstructed low frequency signal is upsampled using wavelet reconstruction. The upsampled low resolution image is then transformed using Hilbert transform to extract the high frequency residual DBP signals. Then, the resulting high frequency residual signal is applied to an inverse Hilbert transform to obtain high frequency signal. Finally by adding the reconstructions of low and high frequency, we can get the interior tomography with the original resolution (see Fig. 1).

V. NUMERICAL RESULTS

A. Circular Fan-Beam CT

The first reconstruction result was obtained with circular fan-beam projection. The 2D phantom is 512×512 size with 1×1 mm² size pixel. The number of detector array is 400 with 1 mm pitch, and the number of views is 1200. The distance from source to rotation axis is 800 mm, and the distance from source to detector is 1400 mm. The radius of FOV is about 113 mm, so for each PI line, the truncation rate (length of support divided by length of FOV) is from 0 to 0.95. In Fig. 2, the first image in (a) is the original ground truth. Fig. 2(b)(c) show the low and high frequency reconstruction images respectively, and the final reconstruction is shown in Fig. 2(d), which is nearly identical to the original signal.

B. Helical Cone-Beam CT

The second simulation is 3D cone-beam CT with helical trajectory. The resolution of the phantom is $512 \times 512 \times 512$ voxels with voxel size $1 \times 1 \times 1$ mm³. The distances from source to rotation axis and from source to detector are same with the circular fan-beam simulation. The detector resolution is 450×109 pixels with pitch of 1×1 mm², so the radius of

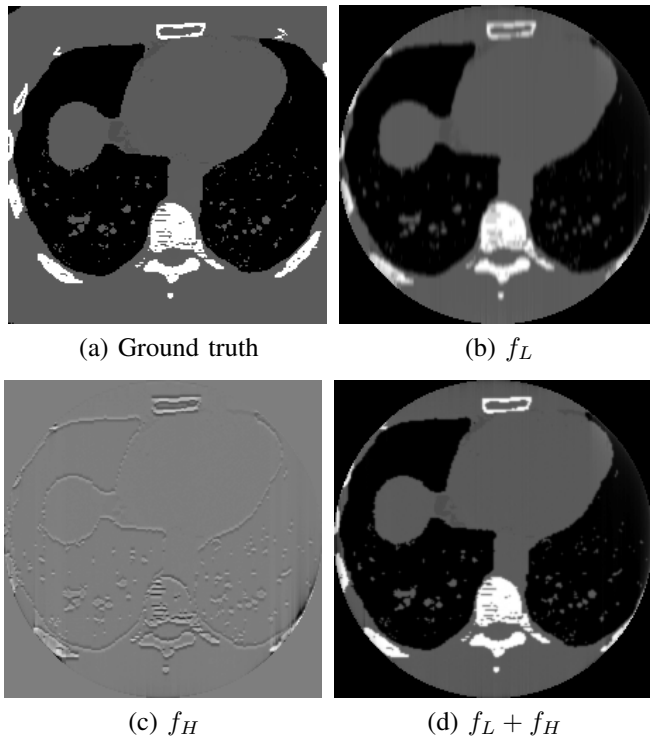


Fig. 2. 2D fan-beam reconstruction: (a) ground truth, (b) low frequency signal reconstruction, (c) high frequency signal reconstruction, and (d) the final reconstruction result.

FOV is about 127 mm. For helical scanning trajectory, the number of rotations is 3, the helical pitch h is 100 mm, and the number of views is 1200 per rotation. First, the object was reconstructed in PI line space, and then by regridding process, the final reconstruction of about 250 slices was obtained.

Fig. 3 is the reconstruction result in FOV for the helical cone-beam CT. Even for helical cone-beam CT, the original 3D problem can be converted into many 1D problems on the PI line, so what we need to do is repeat the 1D reconstruction processes for all PI lines. In the first column, transection, coronal, and sagittal planes are shown, and for each row, the line profile whose location is indicated by white line in the plane image was plotted. The total computational time was less than 14 minutes, which corresponds to about 3 seconds for each slice.

VI. CONCLUSIONS

Using the differentiated back projection, an interior tomography problem in 2D or 3D can be converted to a 1D truncated Hilbert transform problem. Due to the existence of the null space in the truncated Hilbert transform, appropriate regularization is necessary. To overcome the complexity and restriction of the existing 2D-TV regularization approach, this paper proved that 1D generalized TV semi-norm penalty is more relaxed but still sufficient to guarantee the perfect recovery. Moreover, by exploring the Bedrosian theorem, we demonstrated that the computational expensive iterative reconstruction can be performed at very coarse resolution, which significantly reduces the computational complexity. The simulation result shows the proposed algorithm can produce

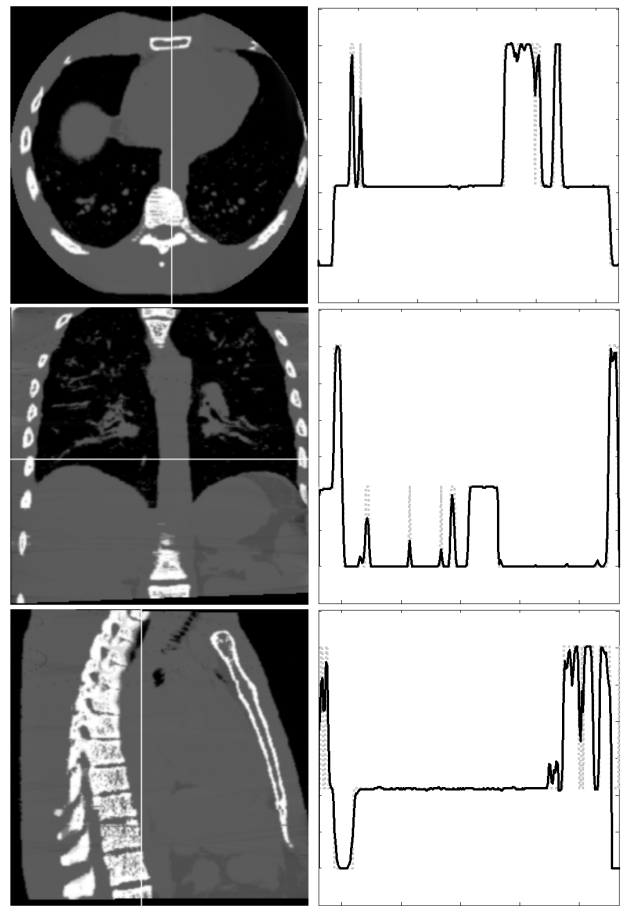


Fig. 3. Reconstruction images and line profiles with 3D inner organ phantom and helical cone-beam scanning

high quality reconstruction for both 2D and 3D geometries, and its computational time can be significantly reduced down to practical level even for helical cone-beam CT.

ACKNOWLEDGMENT

MJL and JCY were supported by the National Research Foundation of Korea (NRF) grant No.2009-6081089, and Samsung Electronics. The research leading to these results by JPW and MU has received funding from the European Research Council under the European Union's Seventh Framework Programme (FP7/2007-2013) / ERC grant agreement n 267439.

REFERENCES

- [1] Yu Zou and Xiaochuan Pan, "Image reconstruction on pi-lines by use of filtered backprojection in helical cone-beam ct," *Physics in medicine and biology*, vol. 49, no. 12, pp. 2717, 2004.
- [2] M. Defrise, F. Noo, R. Clackdoyle, and H. Kudo, "Truncated Hilbert transform and image reconstruction from limited tomographic data," *Inverse Problems*, vol. 22, no. 3, pp. 1037, 2006.
- [3] M. Courdurier, F. Noo, M. Defrise, and H. Kudo, "Solving the interior problem of computed tomography using *a priori* knowledge," *Inverse problems*, vol. 24, no. 6, pp. 065001, 2008.
- [4] H. Yu and G. Wang, "Compressed sensing based interior tomography," *Physics in medicine and biology*, vol. 54, no. 9, pp. 2791, 2009.
- [5] Jiansheng Yang, Hengyong Yu, Ming Jiang, and Ge Wang, "High-order total variation minimization for interior tomography," *Inverse problems*, vol. 26, no. 3, pp. 035013, 2010.

Application of incremental algorithms to CT image reconstruction for sparse-view, noisy data

Sean Rose¹, Martin S. Andersen², Emil Y. Sidky¹, and Xiaochuan Pan¹

Abstract—This conference contribution adapts an incremental framework for solving optimization problems of interest for sparse-view CT. From the incremental framework two algorithms are derived: one that combines a damped form of the algebraic reconstruction technique (ART) with a total-variation (TV) projection, and one that employs a modified damped ART, accounting for a weighted-quadratic data fidelity term, combined with TV projection. The algorithms are demonstrated on simulated, noisy, sparse-view CT data.

I. INTRODUCTION

In iterative image reconstruction (IIR) there can be a large disconnect between practical iterative algorithms and the optimization problems that motivate their design. Particularly for image reconstruction from sparse-view CT data with its associated ill-conditioned linear system model, the number of required iterations for accurate solvers of relevant optimization problems can be much greater than 1,000. When iteration numbers are this large, the trajectory of the image estimates can be quite important because practical application of IIR dictates iteration numbers on the order of ten – well short of convergence.

The usual strategy for obtaining useful images rapidly is to employ algorithms that process the data sequentially [1,2]. In particular, for sparse-view CT we have been developing the adaptive-steepest-descent - projection-onto-convex-sets (ASD-POCS) algorithm [3], which is sequential in that it employs ART for the data agreement step. The algorithm has been shown to yield useful images at low iteration numbers [4]. While we have also used ASD-POCS for accurate solution of constrained TV-minimization, the algorithm is not guaranteed to converge and parameter selection is not straight-forward when accurate solution is desired.

Recently, an incremental framework [5,6] has been developed from which sequential iterative algorithms can be derived that both yield useful images at low iteration numbers and converge to the solution of a designed optimization problem. The reason why such a framework

can be helpful for IIR algorithm development is that many design principles such as maximum entropy, maximum likelihood (ML), and sparsity exploitation are a form of optimization. It is not clear that truncating the iteration of the optimization problem solver will yield images that reflect the intentions of the designed optimization problem. With the incremental framework, where initial convergence is rapid, there may be a stronger link between early image estimates and the solution to the designed optimization.

In this work, we motivate and investigate the use of TV-constrained data-discrepancy minimization for sparse-view image reconstruction from noisy CT data. Two different data agreement terms are compared: a Euclidean distance between estimated data and input data, and a weighted quadratic where the weighting reflects the model used for generating the simulated noise. Accurate solution of the designed optimization, solved using the Chambolle-Pock (CP) algorithm, is compared to image estimates obtained at low iteration numbers for algorithms derived from the incremental framework.

II. METHODS

Using a generic linear model for X-ray projection

$$\mathbf{g} = X\mathbf{f}, \quad (1)$$

ideal gradient magnitude image (GMI) sparsity exploiting image reconstruction is formulated as

$$\mathbf{f}^* = \arg \min_{\mathbf{f}} \|\nabla \mathbf{f}\|_1 \text{ such that } X\mathbf{f} = \mathbf{g}, \quad (2)$$

where X is the system matrix representing X-ray projection; \mathbf{f} is the image, \mathbf{g} is the sinogram; ∇ is a finite differencing implementation of the spatial gradient of the image; and the objective function $\|\nabla \mathbf{f}\|_1$ is the TV of the image \mathbf{f} . The specified optimization problem seeks, among all images that agree with the data perfectly, the one with minimum TV. When noise or other inconsistency is present in the data, the strict equality of Eq. (2) cannot be satisfied and this constraint must be relaxed

$$\mathbf{f}^* = \arg \min_{\mathbf{f}} \|\nabla \mathbf{f}\|_1 \text{ such that } \|X\mathbf{f} - \mathbf{g}\|_2 \leq \epsilon, \quad (3)$$

where ϵ is a parameter of the optimization that puts a tolerance on the allowable data discrepancy. While this

¹The University of Chicago, Department of Radiology MC-2026, 5841 S. Maryland Avenue, Chicago IL, 60637.

²Technical University of Denmark, Department of Applied Mathematics and Computer Science, Lyngby, Denmark

optimization problem can be used for GMI sparsity-exploiting image reconstruction, it is somewhat inconvenient in that the parameter ϵ must be searched.

For this work, we formulate the GMI sparsity exploiting optimization with a constraint on the TV instead of the data discrepancy

$$\mathbf{f}^* = \arg \min_{\mathbf{f}} \frac{1}{2} \|\mathbf{X}\mathbf{f} - \mathbf{g}\|_2^2 \text{ such that } \|\nabla\mathbf{f}\|_1 \leq \gamma, \quad (4)$$

where now the parameter γ constrains the image TV. This form is particularly convenient for phantom studies to test the effectiveness of GMI sparsity-exploiting image reconstruction, because γ can be set to the value derived from the test phantom. In this way, both ideal and noisy data studies can be conducted using Eq. (4). In the ideal case the data fidelity term can be driven to zero, while in the noisy case the objective minimum will likely be nonzero and positive. Moreover, employing a TV constraint allows easy comparison of GMI sparsity-exploiting image reconstruction with different data fidelity terms. As an example of such an alternative, which we investigate below, we employ the maximum-likelihood data fidelity for uncorrelated Gaussian noise

$$\mathbf{f}^* = \arg \min_{\mathbf{f}} \frac{1}{2} (\mathbf{X}\mathbf{f} - \mathbf{g})^T \text{diag}(\mathbf{v})^{-1} (\mathbf{X}\mathbf{f} - \mathbf{g})$$

such that $\|\nabla\mathbf{f}\|_1 \leq \gamma, \quad (5)$

where \mathbf{v} represents the variance of the data noise model.

All of the optimizations stated above can be solved by a first-order algorithm such as that of Chambolle and Pock [7,8], but the required iteration number for a useful image can be large. One can also employ the incremental framework to derive sequential algorithms that solve both Eqs. (4) and (5). Following Ref. [6], we write down in Algorithm 1 an instance of an incremental algorithm for the optimization problem in Eq. (5).

III. RESULTS

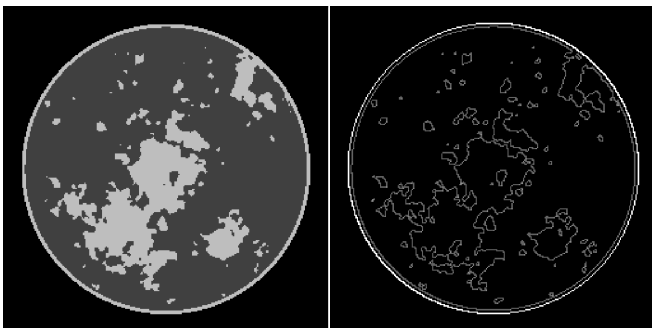


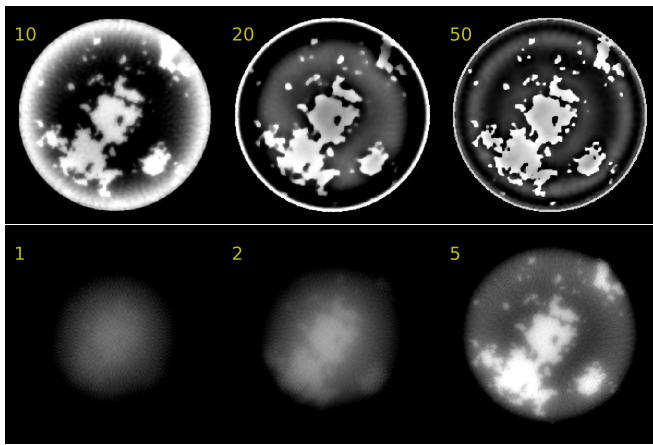
Fig. 1. Breast phantom for CT and its corresponding gradient-magnitude image (GMI). Left is the linear attenuation map of the phantom in the gray scale window $[0.174, 0.253] \text{ cm}^{-1}$. Right is the GMI $[0.0, 0.1] \text{ cm}^{-1}$ that serves to illustrate that the test phantom is sparse in the GMI.

Algorithm 1 Pseudocode for N steps of an incremental algorithm instance for solving the TV-constrained optimization problem in Eq. (5). Note that this algorithm also applies to Eq. (4) by setting $\mathbf{v} = 1$. The integer M is the total number of measurements in the sinogram. The parameters t_0, ρ and α all affect rate of convergence, but for the simulations here where iteration numbers are low, ρ and α are fixed to one and zero, respectively. The parameter t_0 is determined by the value that yields the smallest data discrepancy within a fixed number of iterations. The parameter γ belongs to the optimization problem, and for the simulations presented here it is always set to the TV of the test phantom. The projection in line 14, which finds the image closest to \mathbf{h}_M with TV less than or equal to γ , is carried out by the CP algorithm [7,8].

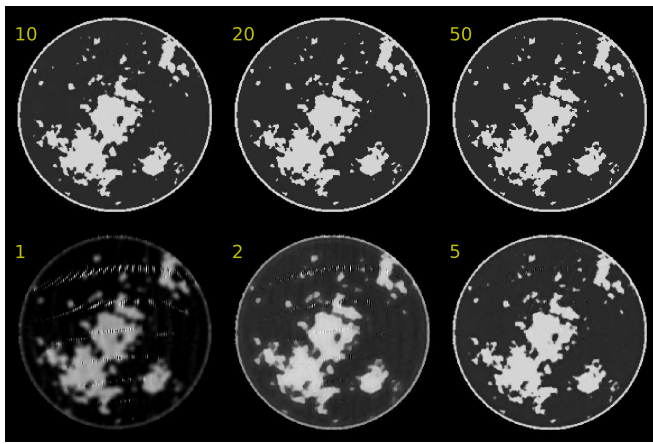
- 1: select algorithm parameters:
 - 2: $t_0 \in (0, \infty)$; $\rho \in (0, 2)$; $\alpha \in [0, 1]$
 - 3: select TV constraint parameter γ
 - 4: initialize \mathbf{f}_0
 - 5: $n \leftarrow 0$
 - 6: **repeat**
 - 7: $\mathbf{h}_0 \leftarrow \mathbf{f}_n$
 - 8: $t_n \leftarrow t_0 / (n + 1)^\alpha$
 - 9: $i \leftarrow 0$
 - 10: **repeat**
 - 11: $\mathbf{h}_{i+1} \leftarrow \mathbf{h}_i - \rho \mathbf{x}_i \frac{(\mathbf{x}_i^T \mathbf{h}_i - g_i)}{\|\mathbf{x}_i\|_2^2 + v_i/t_n}$
 - 12: $i \leftarrow i + 1$
 - 13: **until** $i \geq M$
 - 14: $\mathbf{f}_{n+1} \leftarrow \rho \text{proj}_{\{\mathbf{f} \mid \|\nabla\mathbf{f}\|_1 \leq \gamma\}}(\mathbf{h}_M) + (1 - \rho)\mathbf{h}_M$
 - 15: $n \leftarrow n + 1$
 - 16: **until** $n \geq N$
-

To demonstrate the utility of the Algorithm 1, we conduct image reconstruction studies with ideal and noise sparse-view projection data. The digital phantom shown in Fig. 1 emulates breast CT and it consists of 256×256 pixel array. For the ideal data study, the projection data are obtained by use of Eq. (1) so that the system matrix employed in data generation and image reconstruction are identical. The projection data consist of 100 projections onto a 512-bin linear detector array. The source-detector and source-isocenter distances are modeled to be 72cm and 36cm, respectively. The sampling of this configuration is clearly not sufficient for direct or implicit inversion of Eq. (1) because the number of image pixels exceeds the number of measurements.

a) Noiseless study: Exploiting GMI sparsity with TV-constrained optimization, we solve Eq. (4) setting $\gamma = \gamma_0$, the true value obtained from the test phantom. We state without showing results that the true phantom can be recovered exactly in the numerical sense under these



Chambolle-Pock



incremental

Fig. 2. Progression of image estimates for both CP and incremental algorithms for the case of noiseless projection data. The iteration number is indicated in each panel.

conditions. The more important point for our purpose is how quickly can a useful image be obtained. We solve Eq. (4) by use of both CP and the incremental instance shown in Algorithm 1, setting $\nu = 1$. Intermediate iterates are shown up to 50 iterations in Fig. 2. One can immediately see the advantage of Algorithm 1 as a visually accurate reconstruction appears already at 10 iterations while the CP results are not close to the phantom for any of the shown images. This difference is not specific to these two algorithms. Rather it stems from a well-known feature of algorithms that process the data sequentially versus those that do not. The point of interest here is that we have the rapid initial convergence with Algorithm 1, and as the iterations continue the image estimate is guaranteed to converge to a solution of Eq. (4).

b) Noisy study: For the remainder of the results, image reconstruction is performed on simulated data including noise. The same discrete-to-discrete model generates the mean sinogram, but noise realizations are drawn from a Gaussian distribution, where the covariance is taken to be diagonal and the variance at each sample is the one over the transmitted number of photons. The integrated incident

number of photons per view per detector bin is modeled to be 2×10^5 , corresponding to a fairly low intensity that might be used in an actual breast CT scan. In this simulation the only source of inconsistency is due to the noise model, and we know exactly what probability distribution function governs the noise realization selection. All other sources of inconsistency: continuous object model, beam hardening, scatter, partial volume averaging, etc., which would be present in actual CT data are suppressed. In this way, we can isolate and address two questions: (1) within the parameters of the simulation what is the impact of using the ML motivated weighted quadratic in Eq. (5) as opposed to the isotropic quadratic of Eq. (4) in terms of the solution to the respective optimization problems, and (2) if there is difference between solutions of these problems, will this difference be reflected in the images generated by Algorithm 1 when the iteration is severely truncated, i.e. 10 to 20 iterations.

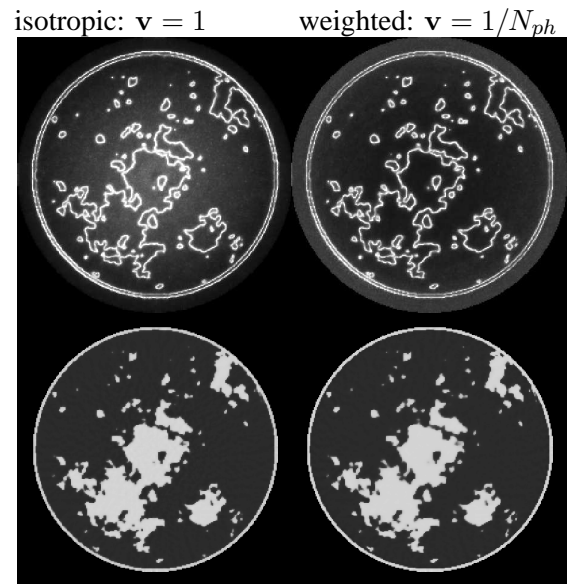


Fig. 3. Image standard deviation (top row, $[0,0,0.005] \text{ cm}^{-1}$) and mean (bottom row, $[0.174,0.253] \text{ cm}^{-1}$) estimated from accurate solution of Eq. (5) for 1000 realizations of noisy data. The left and right columns correspond respectively to an isotropic data fidelity and a one-over-transmission-intensity ($1/N_{ph}$) weighted quadratic motivated by the ML principle. The mean image RMSE from the truth is $2.19 \times 10^{-3} \text{ cm}^{-1}$, left, and $2.10 \times 10^{-3} \text{ cm}^{-1}$, right.

Employing the CP algorithm, the mean and standard deviation of the solution to Eq. (5) using $\gamma = \gamma_0$, the true TV of the phantom, are estimated from 1000 noise realizations and are shown in Fig. 3. The bias for both isotropic and ML weighting is low as both image means are visually close to the phantom. The estimated standard deviation images are more interesting, showing structure that reflects the object. In both cases the image standard deviation is reduced dramatically by the use of the TV constraint except for at pixels near to those corresponding to nonzero values of the phantom's GMI.

This phenomenon was also observed in the fully sampled case in Ref. [9]. We do observe a difference in the background of these images and it does appear that the ML weighting yields a lower standard deviation in the middle of the image. Going toward the image periphery, the isotropic weighting appears to result in a slightly lower standard deviation. Overall, the ML weighting lowers the image standard deviation with respect to isotropic weighting without increasing bias.

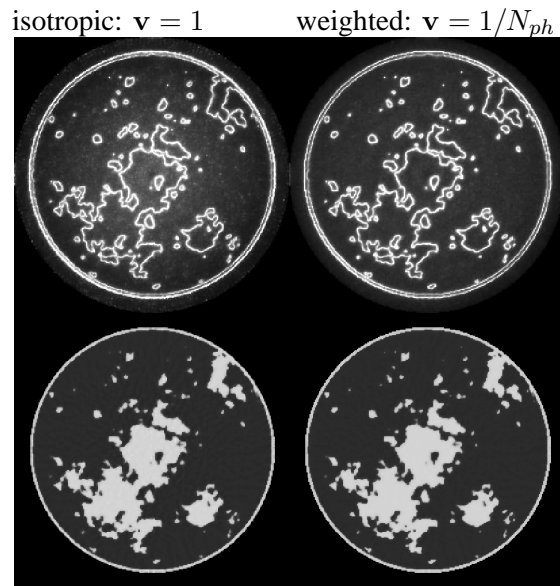


Fig. 4. Same as Fig. 3 except that results are obtained after 20 iterations of Algorithm 1. For both isotropic and ML weighting, the algorithm t_0 is selected to yield the lowest value of the data fidelity at the last iteration. The mean image RMSE from the truth is $3.14 \times 10^{-3} \text{ cm}^{-1}$, left, and $2.21 \times 10^{-3} \text{ cm}^{-1}$, right.

Turning to the use of Algorithm 1, we have verified (results not shown) using a single noise realization that we obtain an accurate solution to Eq. (5) in 1000 iterations. The interest here, however, is in use of Algorithm 1 at low iteration number. A parallel set of results are shown in Fig. 4 obtained by use of Algorithm 1 and stopping at 20 iterations. Again the TV constraint is set to the phantom TV, but because the iteration is truncated an additional parameter t_0 has a large effect on the reconstructed image. For this preliminary work we have selected this parameter as described in the figure caption, but there is a bias-variance trade-off associated with t_0 , which would need to be fully explored for a more complete understanding. Nevertheless we do observe an effect of the different weightings even though the iteration is severely truncated. The ML weighting for the given t_0 settings yields a visually lower standard deviation background and a lower RMSE between mean and phantom.

IV. SUMMARY

We have applied the incremental framework of Refs. [5,6] to generate an algorithm instance of TV constrained,

data discrepancy minimization for CT image reconstruction. The algorithm yields an accurate solution to the designed optimization problem at large iteration numbers and can provide a useful image at low iteration numbers. To demonstrate the utility of this framework, we apply the algorithm to two different TV constrained optimization problems with different data discrepancy terms. We observe with preliminary results from a controlled simulation that at low iteration numbers we may be able to (1) accurately recover the image from under-sampled data by use of the TV constraint and (2) obtain a more favorable variance-bias trade-off by use of the weighted quadratic term.

V. ACKNOWLEDGMENT

MSK was supported by Grant No. ERC-2011-ADG 20110209 from the European Research Council. This work was also supported in part by NIH R01 Grant Nos. CA158446, CA120540, and EB000225. The contents of this article are solely the responsibility of the authors and do not necessarily represent the official views of the National Institutes of Health.

REFERENCES

- [1] R. Gordon, R. Bender, and G. T. Herman, "Algebraic reconstruction techniques (ART) for three-dimensional electron microscopy and X-ray photography," *J. Theor. Biol.*, vol. 29, pp. 471–481, 1970.
- [2] J. Qi and R. M. Leahy, "Iterative reconstruction techniques in emission computed tomography," *Phys. Med. Biol.*, vol. 51, no. 15, pp. R541–R578, 2006.
- [3] E. Y. Sidky and X. Pan, "Image reconstruction in circular cone-beam computed tomography by constrained, total-variation minimization," *Phys. Med. Biol.*, vol. 53, pp. 4777–4807, 2008.
- [4] E. Y. Sidky, X. Pan, I. Reiser, R. M. Nishikawa, R. H. Moore, and D. B. Kopans, "Enhanced imaging of microcalcifications in digital breast tomosynthesis through improved image-reconstruction algorithms," *Med. Phys.*, vol. 36, pp. 4920–4932, 2009.
- [5] D. P. Bertsekas, "Incremental proximal methods for large scale convex optimization," *Math. Program.*, vol. 129, pp. 163–195, 2011.
- [6] M. S. Andersen and P. C. Hansen, "Generalized row-action methods for tomographic imaging," *Numer. Alg.*, pp. 1–24, 2013, <http://dx.doi.org/10.1007/s11075-013-9778-8>.
- [7] A. Chambolle and T. Pock, "A first-order primal-dual algorithm for convex problems with applications to imaging," *J. Math. Imag. Vis.*, vol. 40, pp. 120–145, 2011.
- [8] E. Y. Sidky, J. H. Jørgensen, and X. Pan, "Convex optimization problem prototyping for image reconstruction in computed tomography with the Chambolle-Pock algorithm," *Phys. Med. Biol.*, vol. 57, pp. 3065–3091, 2012.
- [9] T. Köhler and R. Proksa, "Noise properties of maximum likelihood reconstruction with edge-preserving regularization in transmission tomography," in *Proceedings of the 10th International Meeting on Three-Dimensional Image Reconstruction in Radiology and Nuclear Medicine*, 2011, pp. 263–266.

GPU Accelerated Structure-Exploiting Matched Forward and Back Projection for Algebraic Iterative Cone Beam CT Reconstruction

William M. Thompson and William R. B. Lionheart

Abstract—Algebraic iterative reconstruction algorithms have been the subject of much research into problems of limited data CT reconstruction. However, their use for practical problems, particularly for high resolution systems and corresponding large volume sizes, has often been considered unfeasible due to their high computational demands. For cone beam geometry, we present a highly parallel adaptation of Siddon’s algorithm for discrete forward and back projection, based on exploitation of structure in the pattern of the cone beam rays. The proposed algorithm has been implemented for nVidia GPUs using CUDA, resulting in speedup of an order of magnitude when tested against a non-structure exploiting parallel CPU implementation of Jacobs’ algorithm. The work is presented in the context of circular scan, flat panel detector micro CT, but could easily be adapted to other scanning trajectories and detector configurations.

I. INTRODUCTION

Cone beam x-ray micro CT is now a widely-used imaging technique in materials science [1], and also in other applications such as non-destructive testing, oil exploration and semiconductor manufacture for example. In such applications, there is currently a drive towards faster acquisition times, motivated by a variety of reasons including higher throughput scanning, dose reduction and higher temporal resolution four dimensional imaging. To this end, the use of algebraic iterative reconstruction algorithms involving total variation (TV) minimisation (e.g. [2], [3]) is the subject of much current research. Such algorithms have particularly high utility in these applications, as objects of interest often consist of homogeneous materials with a piecewise constant structure. A typical problem may involve calculating distribution of pore sizes based on analysis of a segmented volume, for example.

At the core of any algebraic iterative reconstruction algorithm are the projection matrix A , and its transpose, representing back projection; these are formed from a discrete model of the projection process, for which many choices exist. A common choice is to represent the rays as straight lines, and to consider the lengths of intersection with a regular grid of voxels. Then the discrete forward projection of the n^{th} ray is given by

$$p_n = \sum_{i,j,k} l_n(i,j,k)x(i,j,k), \quad (1)$$

where $l_n(i,j,k)$ represents the length of intersection, and $x(i,j,k)$ is the value of the CT attenuation coefficient function

Henry Moseley X-ray Imaging Facility and School of Mathematics, University of Manchester. Corresponding author: William R. B. Lionheart, E-mail: bill.lionheart@manchester.ac.uk.

in the voxel with x , y and z indices (i,j,k) . All such $l_n(i,j,k)$ together form the projection matrix A ; however, due to the size of the system, these values are usually not stored but are computed on the fly during forward or back projection.

Siddon’s algorithm [4] gives an efficient way to calculate the values of $l_n(i,j,k)$ by following rays through the volume. Subsequent work ([5], [6], [7], [8]) has refined Siddon’s algorithm somewhat, and more recently, a new approach has been proposed [9]. However, all of these methods are presented in the general case of a single ray, and do not exploit any structure in the pattern of multiple rays.

A typical cone-beam micro CT scanner consists of a micro-focus x-ray source located opposite a square flat panel detector; the object under inspection is rotated in the path of the beam to change the projection angle. Typical detector resolutions can be 2048×2048 pixels or higher, with resulting reconstructed volume size of 2048^3 voxels; therefore, in order to enable algebraic iterative reconstruction of realistically sized experimental data sets within reasonable time scales, it is essential to make the discrete forward and back projection operations as fast as possible. For this reason, in practical applications it is often the case that a different discrete model is used for back projection than that used for forward projection. In such cases, the matrix representing back projection is not the exact transpose of the projection matrix, which may have a negative impact on algorithm convergence. Our work has focused on implementations where the same model is used for both, creating a matched forward and back projector pair.

The work presented here discusses acceleration of Siddon’s algorithm in the cone beam case, by exploiting structure in the rays. Although the work is presented in the specific case of a flat panel detector, the method is also equally applicable to curved detectors. The work is presented in the context of forward projection, but it should be noted that the implementation of the corresponding matched back projector uses the same method for the calculation of the ray-voxel intersection lengths, but with obvious differences in how these are used.

II. SIDDON’S ALGORITHM

Siddon noted that since most of the $l_n(i,j,k)$ are zero, rather than summing (1) over all voxels, it is much more efficient to follow the path of each ray through the volume, summing over only the non-zero values.

Considering only the two-dimensional case initially, and adopting the notation of [5], let a ray have end points

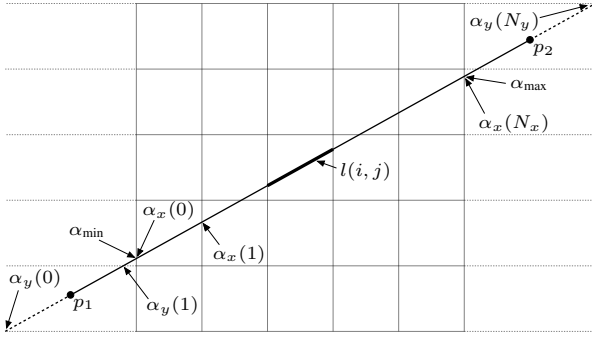


Fig. 1: Parametric representation of rays in Siddon's algorithm

$p_1 = (p_{1x}, p_{1y})$ and $p_2 = (p_{2x}, p_{2y})$, and assume $p_{1x} \neq p_{2x}$ and $p_{1y} \neq p_{2y}$; the degenerate cases can be handled trivially. Let $p = (p_x, p_y)$ be any point along the ray; then we have the parametric representation

$$p_x(\alpha) = p_{1x} + \alpha(p_{2x} - p_{1x}), \quad (2)$$

$$p_y(\alpha) = p_{1y} + \alpha(p_{2y} - p_{1y}), \quad (3)$$

where $\alpha \in \mathbb{R}$ and $\alpha \in [0, 1]$ for points on the ray between p_1 and p_2 .

Without loss of generality, assume that the reconstruction grid consists of isotropic cubic voxels of unit size, with the grid origin at the lower left corner. In reality, the source and detector geometry can be simply scaled and translated to fit. Define the grid by its edges, the surfaces $x = i$ and $y = j$, where $i \in \{0, \dots, N_x\}$ and $j \in \{0, \dots, N_y\}$, and denote these respectively as the x and y planes.

Let $\alpha_x(i)$ and $\alpha_y(j)$ represent the α values at the intersection points of the ray with the i^{th} x plane and j^{th} y plane, as shown in figure 1; then

$$\alpha_x(i) = \frac{i - p_{1x}}{p_{2x} - p_{1x}}, \quad \alpha_y(j) = \frac{j - p_{1y}}{p_{2y} - p_{1y}}. \quad (4)$$

Note that these points are not restricted to intersections lying within the grid.

Denote the values of α at the ray's grid entry and exit points by α_{\min} and α_{\max} . These may be calculated easily from the α_x and α_y values at the grid extremities. Denote the indices of the first intersected x and y planes *after the ray enters the grid* by respectively i_{\min} and j_{\min} . Similarly, denote the indices of the last intersected x and y planes, up to and including the grid edge, by respectively i_{\max} and j_{\max} . Again, these may be calculated from the α_x and α_y values at the grid extremities.

Using these calculated indices, we now form arrays $\alpha_x[\cdot]$ and $\alpha_y[\cdot]$ containing the α values of every intersection point of the ray with the x and y planes:

$$\alpha_x[i_{\min}, \dots, i_{\max}] = [\alpha_x(i_{\min}), \dots, \alpha_x(i_{\max})], \quad (5)$$

$$\alpha_y[j_{\min}, \dots, j_{\max}] = [\alpha_y(j_{\min}), \dots, \alpha_y(j_{\max})]. \quad (6)$$

We then sort the elements of $\{\alpha_{\min}, \alpha_x[\cdot], \alpha_y[\cdot]\}$ in ascending order, forming the single array $\alpha_{xy}[\cdot]$, containing the α values of every intersection point of the ray with the grid edges, in monotonically increasing order. Note that in the construction

of the $\alpha_{xy}[\cdot]$ array, duplicate values of α_x and α_y are not included. These values correspond to intersections of the ray with the corner (or in 3D, also an edge) of a voxel.

Now we loop through all points in the $\alpha_{xy}[\cdot]$ array and calculate the x and y voxel indices and intersection lengths. For each $m \in \{1, \dots, N_v\}$, where N_v is the total number of intersections, the x and y indices i_m and j_m are given by

$$i_m = \left\lfloor p_x \left(\frac{\alpha_{xy}[m] + \alpha_{xy}[m-1]}{2} \right) \right\rfloor, \quad (7)$$

$$j_m = \left\lfloor p_y \left(\frac{\alpha_{xy}[m] + \alpha_{xy}[m-1]}{2} \right) \right\rfloor. \quad (8)$$

Then the intersection length for each voxel is given by

$$l(i_m, j_m) = (\alpha_{xy}[m] - \alpha_{xy}[m-1]) \cdot d_{\text{conv}}, \quad (9)$$

where d_{conv} is the Euclidean length of the ray.

The algorithm can be generalised to 3D by following essentially the same procedure to create an $\alpha_z[\cdot]$ array, and then forming the total sorted array $\alpha_{xyz}[\cdot]$.

In CPU implementations of Siddon's algorithm, or any of its derivatives, we can parallelise by simply distributing the rays among available threads. However, this approach treats all rays independently, and as such does not exploit any structure. It is also not ideal for GPU implementations, since these algorithms necessitate a high level of conditional branching. This causes the GPU threads to take different execution paths, a phenomenon known as warp divergence, which can have serious consequences for performance. Memory access patterns are also unlikely to be well-structured, with similar impact on performance.

III. STRUCTURE-EXPLOITING CONE BEAM ALGORITHM

Defining the cone beam geometry as in figure 2, the key to our approach for accelerating Siddon's algorithm in the cone beam case is the observation that for any projection angle and u coordinate on the detector, the projection of this ray in the z direction onto the x - y plane is completely independent of the detector v coordinate. Hence, for any such ray, the values of α_x and α_y , and the x and y voxel indices, are also independent of the detector v coordinate. Therefore, we seek to decompose the ray tracing algorithm into a component in x - y and a component in z .

As a first step, we order the volume so that z is the fastest increasing dimension, and order the projections with detector v coordinate fastest increasing. Then the loop over detector v coordinate can be brought into the core of the ray tracing algorithm, resulting in far more localised memory access patterns. This approach leads to significant performance increase, but the calculation of the ray tracing parameters in the z direction is still dependent on components in x and y , and the algorithm still needs a high level of conditional branching.

In order to make the z component completely independent, we first make the additional assumption that the cone angle is less than or equal to 45° . By cone angle here, we mean the angle that the rays corresponding to the minimum and maximum detector v coordinates make with the x - y plane, assuming the detector is symmetric. Note that, at least in the

case of most laboratory based micro CT scanners, this is a realistic assumption. The effect of this is that, if we consider the reconstruction volume as being composed of columns of voxels in the z direction for constant x and y , then any ray will intersect either one or two voxels in each column it passes through.

Consider any ray with $p_{1z} < p_{2z}$, and let the projection of this ray in the z direction onto the x - y plane have associated $\alpha_{xy}[\cdot]$ array as in the 2D version of Siddon's algorithm. Now consider the m^{th} entry in this array; then the parametric value of the next intersection with a z plane, α_z , and the z index of the first intersected voxel in the currently intersected column, k , are given by

$$\alpha_z = \frac{k+1-p_{1z}}{p_{2z}-p_{1z}}, \quad k = \lfloor p_z(\alpha_{xy}[m]) \rfloor, \quad (10)$$

where

$$p_z(\alpha) = p_{1z} + \alpha(p_{2z} - p_{1z}). \quad (11)$$

Figure 3 shows the locations of the points $\alpha_{xy}[m]$, $\alpha_{xy}[m+1]$ and α_z along the ray in each of the two possible cases. Now let $\alpha_{\min} = \min(\alpha_{xy}[m+1], \alpha_z)$; then in both cases, the intersection lengths with the intersected voxel or voxels are given by

$$l(i_m, j_m, k) = (\alpha_{\min} - \alpha_{xy}[m]) \cdot d_{\text{conv}}, \quad (12)$$

$$l(i_m, j_m, k+1) = (\alpha_{xy}[m+1] - \alpha_{\min}) \cdot d_{\text{conv}}, \quad (13)$$

where i_m and j_m are the x and y indices of the currently intersected column of voxels. Note that in the single voxel case, the length assigned to the second voxel is simply zero.

For rays with $p_{1z} > p_{2z}$, we have the similar formulae

$$\alpha_z = \frac{k-p_{1z}}{p_{2z}-p_{1z}}, \quad k = \lfloor p_z(\alpha_{xy}[m]) \rfloor, \quad (14)$$

$$l(i_m, j_m, k) = (\alpha_{\min} - \alpha_{xy}[m]) \cdot d_{\text{conv}}, \quad (15)$$

$$l(i_m, j_m, k-1) = (\alpha_{xy}[m+1] - \alpha_{\min}) \cdot d_{\text{conv}}. \quad (16)$$

Rays with $p_{1z} = p_{2z}$ are a trivial two-dimensional sub-case and can be handled separately in situations when they arise. However, for the CT systems this work has been developed

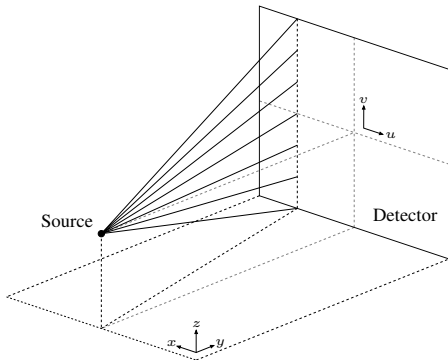


Fig. 2: The flat panel cone beam geometry, showing the exploited structure in the rays

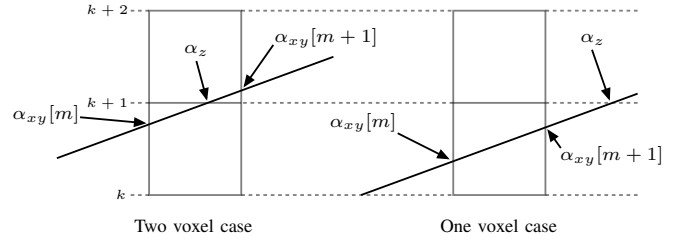


Fig. 3: Ray tracing parameters in the z direction for the one voxel and two voxel cases

for, the detector usually has an even number of pixels and this case need not be considered.

These equations form the basis of CUDA kernels for discrete forward and back projection. For each projection angle, the kernel is launched with thread blocks allocated for each detector u coordinate; each thread within a block is then assigned a detector v coordinate. The 2D $\alpha_{xy}[\cdot]$ arrays and associated x and y voxel indices for each u coordinate are calculated as a CPU process, and copied to the GPU memory asynchronously. In practice, these arrays can often simply be pre-computed and stored for all projection angle and u coordinate pairs.

Threads in each block loop through the pre-calculated $\alpha_{xy}[\cdot]$ array, effectively tracing the rays corresponding to all detector v coordinates simultaneously in lock-step. This process is essentially the same for forward and back projection, but the exact implementation differs in each case. At each point in the loop, the threads only access volume memory locations corresponding to the same column of voxels, keeping the memory access patterns localised. For back projection, values for the whole column of voxels are accumulated in shared memory before writing to global device memory. Multiplication by d_{conv} is performed only once; at the end for forward projection, and at the beginning for back projection. In practice, division by $p_{2z} - p_{1z}$ is replaced by multiplication by its reciprocal; since these values depend only on detector v coordinate, the values may easily be pre-computed and stored. This gives a significant performance increase, since division in CUDA maps to 16 instructions, versus a single instruction for a multiplication.

Note that since both the single voxel and two voxel intersection cases are covered by the same update equations, this results in a CUDA kernel with very few conditional branches; we need only make a decision before the main loop whether p_{2z} is greater than or less than p_{1z} to decide which set of equations to use. The vertical dimension of the detector is padded to a multiple of the CUDA warp size; hence all threads follow the same branch and warp divergence is eliminated.

Due to the limited amount of memory available on the GPU, the controlling host CPU process performs an outer loop over projection angles. For forward projection, data for the whole volume are copied to the device before starting the loop, while for back projection, it is necessary to accumulate the volume and copy this back at the end. All other host-device and device-host memory transfers are asynchronous, keeping GPU idle

	FP time (s)	BP time (s)
Jacobs, CPU, 32 threads	100	200
Inner v loop Jacobs, CPU, single thread	292	367
Inner v loop Jacobs, CPU, 32 threads	18	65
New, GPU	5.9	7.1

TABLE I: Comparison of timings for the GPU implementation

time low.

IV. RESULTS

Our algorithm has been implemented in CUDA, and has been profiled and tuned for nVidia devices of compute capability 2.0. Table I shows timings for forward and back projection for a synthetic data test problem consisting of 720 cone beam projections of size 512×512 , into a volume of size 512^3 . We compared the CUDA implementation of the new algorithm against a parallel CPU implementation of Jacobs' algorithm, and serial and parallel CPU implementations of Jacobs' algorithm with inner loop over the detector v coordinate. Timings for the GPU code include the time taken for host-device and device-host memory transfers. The test hardware was a dual CPU Intel Xeon 3.1GHz machine with 64GB RAM and nVidia Quadro 6000 GPU, featuring 448 CUDA cores and 6GB onboard RAM. The operating system was Windows 7 Professional, using CUDA version 5.5. Hyperthreading was enabled.

Comparing the GPU version of our new algorithm to the parallel implementation of the Jacobs algorithm, our results show speedups of approximately 19 and 28 times respectively for forward and back projection. Comparing the new algorithm against the optimised CPU implementation of Jacobs' algorithm with inner loop over v , respective speedups of 3 and 9 times are observed. We attribute the comparatively greater speedup for back projection to the elimination of the OpenMP atomic operations which are necessary for volume updates in the parallel CPU implementations. However, back projection is still significantly slower than forward projection, since although the volume is updated in columns, the method is still essentially ray driven.

Raw performance of the algorithm in terms of the GUPS metric was measured at 40.1 GUPS for forward projection, and 28.9 GUPS for back projection. This was calculated by counting the exact number of updates made in each case to the volume or projection data, and dividing by the kernel run time as measured by the nVidia nSight profiler. While this performance for back projection falls substantially short of that given by the latest implementations submitted for the RabbitCT benchmark, it should be noted that back projection as part of a matched forward and back projector pair is a fundamentally different problem to that of a highly optimised, standalone voxel driven back projector.

The new algorithm has also been tested in algebraic iterative reconstruction methods for real experimental data sets, with varying numbers of projections of size 1024×1024 into a 1024^3 volume. Figure 4 compares a slice from an FDK reconstruction of a 400 projection scan of an Aluminium rod, at a resolution of 0.7 microns, with a reconstruction using a combined steepest descent and TV minimisation algorithm.

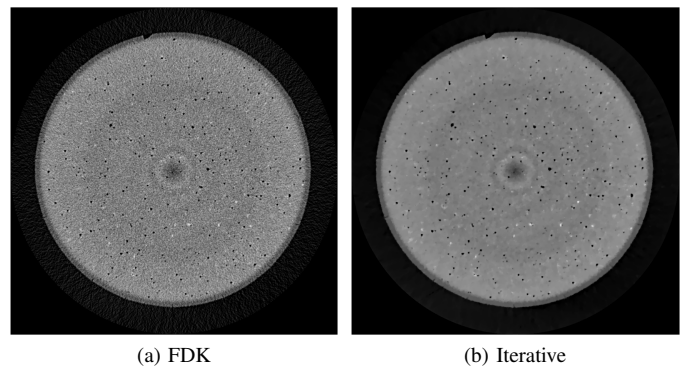


Fig. 4: Example slice from reconstruction of 400 projection experimental data set

The iterative reconstruction shows clearly lower noise level while maintaining the main features of interest, resulting in a volume which is much easier to segment. Using the new algorithm, iterative reconstruction times for this type of data set are in the order of minutes, rather than hours for our original parallel Jacobs implementation.

V. CONCLUSIONS

Due to the computation time, our previous work in application of algebraic iterative reconstruction techniques to micro CT problems has been limited to studying the effects on a central two-dimensional slice through the volume. The new algorithm presented here now allows us to apply such methods to realistic problem sizes with experimental data in full 3D, within reasonable time scales.

Our plans for future development of this work include implementations designed to cope with larger size reconstruction volumes, where the entire volume does not fit into the GPU memory, and testing and optimising the code for the latest generation of GPU devices.

REFERENCES

- [1] E. Maire and P. J. Withers, "Quantitative x-ray tomography," *International Materials Reviews*, vol. 59, no. 1, pp. 1–43, 2014.
- [2] E. Y. Sidky and X. Pan, "Image reconstruction in circular cone-beam computed tomography by constrained, total-variation minimization," *Physics in Medicine and Biology*, vol. 53, no. 17, p. 4777, 2008.
- [3] X. Pan, E. Y. Sidky, and M. Vannier, "Why do commercial CT scanners still employ traditional, filtered back-projection for image reconstruction?" *Inverse Problems*, vol. 25, no. 12, p. 123009, 2009.
- [4] R. L. Siddon, "Fast calculation of the exact radiological path for a 3-dimensional CT array," *Medical Physics*, vol. 12, no. 2, pp. 252–255, 1985.
- [5] F. Jacobs, E. Sundermann, B. D. Sutter, and I. Lemahieu, "A fast algorithm to calculate the exact radiological path through a pixel or voxel space," *J. Comput. Inform. Technol.*, vol. 6, pp. 89–94, 1998.
- [6] M. Christiaens, B. D. Sutter, K. D. Bosschere, J. V. Campenhout, and I. Lemahieu, "A fast, cache-aware algorithm for the calculation of radiological paths exploiting subword parallelism," in *Journal of Systems Architecture, Special Issue on Parallel Image Processing*, 1998.
- [7] G. Han, Z. Liang, and J. You, "A fast ray-tracing technique for TCT and ECT studies," in *Nuclear Science Symposium, 1999. Conference Record. 1999 IEEE*, vol. 3, 1999, pp. 1515–1518 vol.3.
- [8] H. Zhao and A. J. Reader, "Fast ray-tracing technique to calculate line integral paths in voxel arrays," in *Nuclear Science Symposium Conference Record, 2003 IEEE*, vol. 4, Oct 2003, pp. 2808–2812 Vol.4.
- [9] H. Gao, "Fast parallel algorithms for the x-ray transform and its adjoint," *Medical Physics*, vol. 39, no. 11, pp. 7110–7120, 2012.

Duality-based projection-domain tomography solver for splitting-based X-ray CT reconstruction

Madison G. McGaffin Jeffrey A. Fessler

Abstract—Model-based image reconstruction (MBIR) for X-ray CT produces high quality images from relatively low-dose scans, but the high computational cost of MBIR algorithms prevent them from being used ubiquitously in the clinic. Variable splitting with the alternating directions methods of multipliers (ADMM) provides rapidly converging algorithms by decomposing the challenging MBIR optimization problem into an iterated sequence of simpler subproblems. Variable splitting algorithms have achieved state-of-the-art performance in 2D, but replicating those successes in 3D has proved difficult. In this paper, we consider a simple splitting algorithm that decomposes the reconstruction problem into a nonnegative denoising problem and a quadratic tomography problem. Unlike prior work, we solve the tomography problem with a novel duality-based approach that yields convergent algorithms similar to ordered subsets methods and iterated filtered backprojection. We show some promising preliminary results.

I. INTRODUCTION

Consider the following statistical X-ray CT reconstruction problem [15]

$$\hat{\mathbf{x}} = \underset{\mathbf{x} \geq \mathbf{0}}{\operatorname{argmin}} \left\{ J(\mathbf{x}) = \frac{1}{2} \|\mathbf{A}\mathbf{x} - \mathbf{y}\|_{\mathbf{W}}^2 + R(\mathbf{x}) \right\}, \quad (1)$$

with noisy sinogram data $\mathbf{y} \in \mathbb{R}^M$, system matrix $\mathbf{A} \in \mathbb{R}^{M \times N}$, statistical weights $\mathbf{W} = \operatorname{diag}_i\{w_i\}$, and convex edge-preserving regularizer R . The optimization problem (1) is impractical or impossible to solve in closed form due to the large dimension of \mathbf{x} , the nonnegativity constraint and the nonquadratic regularizer. Consequently, solving (1) requires an iterative optimization routine, but unfortunately this is a challenging problem to solve efficiently. Gradient-based simultaneous algorithms that update all pixels of \mathbf{x} simultaneously appear to be better-equipped to take advantage of modern highly-parallel hardware. However (1) presents several challenges for gradient-based methods:

- 1) the CT projection (\mathbf{A}) and backprojection (\mathbf{A}') operations, which are both required to compute an update direction for simultaneous gradient-based methods, are computationally expensive; and
- 2) the reconstruction cost function J is difficult to precondition, especially for 3D reconstruction [3], [4], [9], [18].

In this paper, we consider a variable splitting algorithm that decomposes (1) into an image-space denoising problem and a quadratic “tomography” minimization problem involving the

M. G. McGaffin and J. A. Fessler are with the Dept. of Electrical Engineering and Computer Science, University of Michigan, Ann Arbor, MI 48109 USA. (email: mcgaffin@umich.edu, fessler@umich.edu)

Supported in part by NIH grant R01-HL-098686 and equipment donations from Intel Corporation.

CT system matrix. The primary contribution of this paper is a novel duality-based approach to this tomography problem.

II. VARIABLE SPLITTING

Variable splitting with ADMM is a technique to solve a challenging optimization problem, *e.g.*, (1), with an iterated set of simpler subproblems [9], [11]–[13]. Let $\mathbf{v} \in \mathbb{R}^N$. Instead of directly solving (1), we solve the constrained problem

$$\hat{\mathbf{x}} = \underset{\mathbf{x}}{\operatorname{argmin}} \min_{\mathbf{v} \geq \mathbf{0}} \frac{1}{2} \|\mathbf{A}\mathbf{x} - \mathbf{y}\|_{\mathbf{W}}^2 + R(\mathbf{v}) \quad \text{s.t. } \mathbf{x} = \mathbf{v}. \quad (2)$$

The augmented Lagrangian for this constrained problem is

$$\mathcal{L}(\mathbf{x}, \mathbf{u}; \boldsymbol{\eta}) = \frac{1}{2} \|\mathbf{A}\mathbf{x} - \mathbf{y}\|_{\mathbf{W}}^2 + R(\mathbf{v}) + \frac{1}{2} \|\mathbf{x} - \mathbf{v} + \boldsymbol{\eta}\|_{\boldsymbol{\Gamma}}^2, \quad (3)$$

where $\boldsymbol{\Gamma} \succ \mathbf{0}$. The alternating directions method of multipliers (ADMM) iterations leads to two subproblems:

$$\begin{cases} \mathbf{x}^{(n+1)} = \underset{\mathbf{x}}{\operatorname{argmin}} \frac{1}{2} \|\mathbf{A}\mathbf{x} - \mathbf{y}\|_{\mathbf{W}}^2 + \frac{1}{2} \|\mathbf{x} - \mathbf{v}^{(n)} + \boldsymbol{\eta}^{(n)}\|_{\boldsymbol{\Gamma}}^2, \\ \mathbf{v}^{(n+1)} = \underset{\mathbf{v} \geq \mathbf{0}}{\operatorname{argmin}} \frac{1}{2} \|\mathbf{v} - \mathbf{x}^{(n+1)} - \boldsymbol{\eta}^{(n)}\|_{\boldsymbol{\Gamma}}^2 + R(\mathbf{v}), \\ \boldsymbol{\eta}^{(n+1)} = \boldsymbol{\eta}^{(n)} + \mathbf{x}^{(n+1)} - \mathbf{v}^{(n+1)}. \end{cases} \quad (4)$$

The \mathbf{x} and \mathbf{v} updates do not need to be performed exactly to ensure convergence [2]; empirically, more accurate solutions accelerate convergence.

We choose $\boldsymbol{\Gamma}$ to be diagonal. The \mathbf{v} update is then a penalized weighted least squares denoising problem. There are many algorithms to solve this class of problem, and it can be solved quickly even for large problems and non-smooth regularizers [7], [8]. Hereafter we focus on the more challenging tomography \mathbf{x} update. Note that many splitting-based algorithms have inner steps similar to the \mathbf{x} update we study here [9], [13]. The techniques in the following section can be applied to those algorithms as well.

III. THE TOMOGRAPHY SUBPROBLEM

Though the \mathbf{x} update in (4) is a theoretically simple unconstrained quadratic minimization problem, solving for $\mathbf{x}^{(n+1)}$ is challenging in practice [9], [10]. The popular family of gradient-based methods share the form:

$$\begin{cases} \mathbf{r}^{(m)} = \mathbf{A}\mathbf{x}^{(m)} - \mathbf{y}, \\ \mathbf{g}^{(m)} = \mathbf{A}'\mathbf{W}\mathbf{r}^{(m)} + \boldsymbol{\Gamma}(\mathbf{x}^{(m)} - \mathbf{v}^{(n)} + \boldsymbol{\eta}^{(n)}), \\ \mathbf{d}^{(m)} = \mathbf{f}^{(m)}(\mathbf{g}^{(m)}), \\ \mathbf{x}^{(m+1)} = \mathbf{x}^{(m)} + \mathbf{d}^{(m)}. \end{cases} \quad (5)$$

The function $\mathbf{f}^{(m)} : \mathbb{R}^N \rightarrow \mathbb{R}^N$ is an iteration-dependent preconditioning and step-size computing step. Preconditioning modifies the search direction such that $\mathbf{d}^{(m)}$ “points” more toward the global minimizer \mathbf{x}^* . The ideal, and unrealizable, preconditioner would rapidly implement the inverse of the cost function Hessian

$$\mathbf{f}_{\text{ideal}}(\mathbf{g}) = \mathbf{P}_{\text{ideal}}\mathbf{g} = [\mathbf{A}'\mathbf{W}\mathbf{A} + \mathbf{\Gamma}]^{-1}\mathbf{g}. \quad (6)$$

Many practical approximations to $\mathbf{P}_{\text{ideal}}$ have been proposed involving diagonal matrices, circulant operators and the FFT [3], [4], [9], [13], [18]. Unfortunately the shift-varying nature of the Hessian, induced by the statistical weights \mathbf{W} and geometrical properties of \mathbf{A} , make designing a highly effective preconditioner challenging.

A. Duality approach

Instead of solving the tomography problem directly with a gradient-based method, we introduce an auxiliary variable $\mathbf{u} \in \mathbb{R}^M$ and consider the following equivalent saddle-point problem:

$$\mathbf{x}^{(n+1)} = \underset{\mathbf{x}}{\text{argmin}} \max_{\mathbf{u}} \left\{ \mathcal{S}(\mathbf{x}, \mathbf{u}) = (\mathbf{A}\mathbf{x} - \mathbf{y})'\mathbf{W}\mathbf{u} + \frac{1}{2} \left\| \mathbf{x} - \mathbf{v}^{(n)} + \boldsymbol{\eta}^{(n)} \right\|_{\mathbf{\Gamma}}^2 - \frac{1}{2} \|\mathbf{u}\|_{\mathbf{W}}^2 \right\}. \quad (7)$$

Performing the inner maximization yields the original quadratic function in (4):

$$\nabla_{\mathbf{u}}\mathcal{S} = \mathbf{W}(\mathbf{A}\mathbf{x} - \mathbf{y}) - \mathbf{W}\mathbf{u} = \mathbf{0}, \quad (8)$$

$$\mathbf{u}(\mathbf{x}) = \mathbf{A}\mathbf{x} - \mathbf{y}, \quad (9)$$

$$\mathcal{S}(\mathbf{x}, \mathbf{u}(\mathbf{x})) = \frac{1}{2} \|\mathbf{A}\mathbf{x} - \mathbf{y}\|_{\mathbf{W}}^2 + \frac{1}{2} \|\mathbf{x} - \mathbf{v} + \boldsymbol{\eta}\|_{\mathbf{\Gamma}}^2, \quad (10)$$

so solving (7) (*i.e.*, finding the saddle point), solves the quadratic \mathbf{x} update problem.

We observe that $\mathcal{S}(\mathbf{x}, \mathbf{u}_0)$ is convex and continuous in \mathbf{x} for all \mathbf{u}_0 , and $\mathcal{S}(\mathbf{x}_0, \mathbf{u})$ is concave and continuous in \mathbf{u} for all \mathbf{x}_0 . By Sion’s minimax theorem [14], we can reverse the order of the minimization and maximization steps in (7),

$$\min_{\mathbf{x}} \max_{\mathbf{u}} \mathcal{S}(\mathbf{x}, \mathbf{u}) = \max_{\mathbf{u}} \min_{\mathbf{x}} \mathcal{S}(\mathbf{x}, \mathbf{u}), \quad (11)$$

to find the saddle point. In other words, instead of solving the image-space primal problem, we can solve the projection-domain dual problem.

We compute the minimizing value of \mathbf{x} in terms of \mathbf{u} ,

$$\mathbf{x}(\mathbf{u}) = \mathbf{v}^{(n)} - \boldsymbol{\eta}^{(n)} - \mathbf{\Gamma}^{-1}\mathbf{A}'\mathbf{W}\mathbf{u}, \quad (12)$$

and plug (12) into (7) to yield the quadratic dual problem:

$$\mathbf{u}^* = \underset{\mathbf{u}}{\text{argmax}} \left\{ D(\mathbf{u}) = -\frac{1}{2} \mathbf{u}'(\mathbf{W} + \mathbf{W}\mathbf{A}\mathbf{\Gamma}^{-1}\mathbf{A}'\mathbf{W})\mathbf{u} + \mathbf{u}'\mathbf{W}(\mathbf{A}(\mathbf{v}^{(n)} - \boldsymbol{\eta}^{(n)}) - \mathbf{y}) \right\}. \quad (13)$$

There are many options for solving (13), and as in the primal problem, a natural family of algorithms are the gradient-based

methods. The general form of a gradient-based algorithm in the dual domain is:

$$\begin{cases} \mathbf{p}^{(m)} = \mathbf{W}(\mathbf{y} + \mathbf{u}^{(m)} + \mathbf{A}(\mathbf{\Gamma}^{-1}\boldsymbol{\gamma}^{(m)} - \mathbf{v}^{(n)} + \boldsymbol{\eta}^{(n)})), \\ \mathbf{q}^{(m)} = f^{(m)}(\mathbf{p}^{(m)}), \\ \mathbf{u}^{(m+1)} = \mathbf{u}^{(m)} + \mathbf{q}^{(m)}, \\ \boldsymbol{\gamma}^{(m+1)} = \boldsymbol{\gamma}^{(m)} + \mathbf{A}'\mathbf{W}\mathbf{q}^{(m)}, \end{cases} \quad (14)$$

with $\mathbf{u}^{(0)} = \mathbf{0}$, $\boldsymbol{\gamma}^{(0)} = \mathbf{0}$, and $f^{(m)}$ a preconditioning and step-size computing operation in the projection domain. After a number of iterations, we update \mathbf{x} with (12) and return to the outer iterations of the ADMM algorithm (4),

$$\mathbf{x}^{(n+1)} = \mathbf{x}(\mathbf{u}^{(m)}) = \mathbf{v}^{(n)} - \boldsymbol{\eta}^{(n)} - \mathbf{\Gamma}^{-1}\boldsymbol{\gamma}^{(m)}. \quad (15)$$

As a practical matter, we can warm-start this dual problem by saving the final values of $\mathbf{u}^{(m)}$ and $\boldsymbol{\gamma}^{(m)}$ between \mathbf{x} updates and use those instead of $\mathbf{u}^{(0)} = \mathbf{0}$ and $\boldsymbol{\gamma}^{(0)} = \mathbf{0}$.

B. Projection-domain group coordinate ascent algorithm

Ordered subsets (OS) algorithms [1], [5] partition the system matrix, weights and data into disjoint subsets by view, $\{S_k\}_{k=1}^K$, such that

$$\mathbf{A}'\mathbf{W}(\mathbf{A}\mathbf{x}^{(m)} - \mathbf{y}) \approx \frac{N_{\beta}}{|S_k|} \sum_{\beta \in S_k} \mathbf{A}_{\beta}'\mathbf{W}_{\beta}(\mathbf{A}_{\beta}\mathbf{x}^{(m)} - \mathbf{y}_{\beta}). \quad (16)$$

The right hand side of (16) is used in OS methods as an approximate gradient that requires the forward- and back-projection of only $|S_k|$ views instead of N_{β} . This gradient approximation is accurate when $\mathbf{x}^{(m)}$ is far from the solution and when the subsets contain enough views, but for $\mathbf{x}^{(m)}$ near the solution and smaller subsets, OS algorithms without relaxation approach limit cycles around the solution.

In the projection (dual) domain, an analogy to ordered subsets is group coordinate ascent (GCA). A GCA algorithm divides \mathbf{u} into K groups, $\mathbf{u} = [\mathbf{u}_0, \dots, \mathbf{u}_{K-1}]$ and iteratively maximizes over each group while holding the others constant. Even if the maximization is performed approximately with a minorize-maximize step, the algorithm is convergent [16].

The following algorithm for solving (13) uses $f^{(m)}$ to apply the linear preconditioner \mathbf{P}_k and computes the optimal step length for each group. For all groups $k = 0, \dots, K-1$ perform

the following:

$$\begin{cases} \mathbf{p}_k^{(m)} &= \mathbf{W}_k \left(\mathbf{y} + \mathbf{u}_k^{(m)} \right. \\ &\quad \left. + \mathbf{A}_k \left(\Gamma^{-1} \gamma^{(m+\frac{k}{K})} - \mathbf{v}^{(n)} + \boldsymbol{\eta}^{(n)} \right) \right), \\ \mathbf{q}_k^{(m)} &= \mathbf{P}_k \mathbf{p}_k^{(m)}, \\ \mathbf{d}_k^{(m)} &= \mathbf{A}_k' \mathbf{W}_k \mathbf{q}_k^{(m)}, \\ \alpha_k^{(m)} &= - \frac{\left(\mathbf{q}_k^{(m)} \right)' \mathbf{p}_k^{(m)}}{\left(\mathbf{q}_k^{(m)} \right)' \mathbf{W}_k \mathbf{q}_k^{(m)} + \left(\mathbf{d}_k^{(m)} \right)' \Gamma^{-1} \mathbf{d}_k^{(m)}}, \\ \mathbf{u}_k^{(m+1)} &= \mathbf{u}_k^{(m)} + \alpha_k^{(m)} \mathbf{q}_k^{(m)}, \\ \gamma^{(m+\frac{k+1}{K})} &= \gamma^{(m+\frac{k}{K})} + \alpha_k^{(m)} \mathbf{d}_k^{(m)}. \end{cases} \quad (17)$$

These updates are iterated for $m = 1, \dots, N_{\text{iter-dual}}$. In the context of an ADMM algorithm with warm-starting, $N_{\text{iter-dual}} = 1$ or 2 appears to be sufficient.

C. Comparison to image-space algorithms

While (17) is written in a convenient form for implementation, the behavior of the algorithm is unclear. To compare (17) and traditional ordered subsets algorithms, we rewrite some of the steps in terms of \mathbf{x} using (15):

$$\begin{cases} \mathbf{r}_k^{(m)} &= \mathbf{A}_k \mathbf{x}^{(m+\frac{k}{K})} - \mathbf{y}_k, \\ \mathbf{u}_k^{(m+1)} &= \mathbf{u}_k + \alpha_k^{(m)} \mathbf{P}_k \mathbf{W}_k \left(\mathbf{u}_k^{(m)} - \mathbf{r}_k^{(m)} \right), \\ \mathbf{x}^{(m+\frac{k+1}{K})} &= \mathbf{x}^{(m+\frac{k}{K})} \\ &\quad - \alpha_k^{(m)} \Gamma^{-1} \mathbf{A}_k' \mathbf{W}_k \mathbf{P}_k \mathbf{W}_k \left(\mathbf{r}_k - \mathbf{u}_k \right), \end{cases} \quad (18)$$

with $\mathbf{x}^{(0)} = \mathbf{v}^{(n)} - \boldsymbol{\eta}^{(n)}$.

Recall that the group assignments are arbitrary and each loop through all the groups requires only one total forward and back-projection. The algorithm given in (18) will converge to the solution to the \mathbf{x} -update equation, $\mathbf{x}^{(n+1)}$, though possibly not monotonically in the primal cost function. This flexibility in subset selection is very different from traditional OS algorithms that require judicious design of the subsets to satisfy the subset approximation (16).

The step size computation guarantees monotone convergence in the dual function, so we have some flexibility in designing the projection-domain preconditioners \mathbf{P}_k . One interesting choice is

$$\mathbf{P}_k^{\text{IFBP}} = \mathbf{W}_k^{-1} \mathbf{F}_k \mathbf{W}_k^{-1}, \quad (19)$$

where the \mathbf{F}_k are positive-definite ramp filters. If Γ^{-1} is chosen to correct for the nonuniform spatial sampling of the CT system, (18) resembles an iterated filtered backprojection algorithm for solving the \mathbf{x} update subproblem (7):

$$\mathbf{x}^{(m+\frac{k+1}{K})} = \mathbf{x}^{(m+\frac{k}{K})} - \alpha_k^{(m)} \Gamma^{-1} \mathbf{A}_k' \mathbf{F}_k (\mathbf{A}_k \mathbf{x} - \mathbf{y}_k - \mathbf{u}_k). \quad (20)$$

D. Simplified step size computation

As the number of groups increases, the forward- and back-projections are no longer the only considerable computational costs of the dual group coordinate ascent algorithm (17). In particular the step size computation, which includes an inner product on two image-sized vectors, becomes relatively computationally expensive. To mitigate this we replace the step size computation with a minorize-maximize step. Let $\mathbf{M}_k \succeq \mathbf{A}_k \Gamma^{-1} \mathbf{A}_k'$ be diagonal. All the entries of \mathbf{A}_k and Γ are nonnegative, so we use the easily-computed majorizer [1]:

$$\mathbf{M}_k = \text{diag}_i \{ [\mathbf{A}_k \Gamma^{-1} \mathbf{A}_k' \mathbf{1}]_i \}. \quad (21)$$

The following modified dual ascent algorithm performs no inner products and only a few diagonal matrix multiplications:

$$\begin{cases} \mathbf{p}_k^{(m)} &= \mathbf{W}_k \left(\mathbf{y} + \mathbf{u}_k^{(m)} \right. \\ &\quad \left. + \mathbf{A}_k \left(\Gamma^{-1} \gamma^{(m+\frac{k}{K})} - \mathbf{v}^{(n)} + \boldsymbol{\eta}^{(n)} \right) \right), \\ \mathbf{q}_k^{(m)} &= -(\mathbf{W}_k + \mathbf{W}_k \mathbf{M}_k \mathbf{W}_k)^{-1} \mathbf{p}_k^{(m)}, \\ \mathbf{u}_k^{(m+1)} &= \mathbf{u}_k^{(m)} + \mathbf{q}_k^{(m)}, \\ \gamma^{(m+\frac{k+1}{K})} &= \gamma^{(m+\frac{k}{K})} + \mathbf{A}_k' \mathbf{W}_k \mathbf{q}_k^{(m)}. \end{cases} \quad (22)$$

This algorithm is more practical than (17) when the number of groups is very large (e.g., one group for each view). We do not expect that using a majorizer will considerably slow convergence, because $\mathbf{A}_k \Gamma^{-1} \mathbf{A}_k'$ shrinks as the number of views in the k th group decreases.

IV. PRELIMINARY EXPERIMENTS

As a preliminary experiment, we instantiated a $1024 \times 1024 \times 192$ -pixel XCAT phantom and generated simulated data for an axial scan with a GE Lightspeed scanner [17] with 888 channels, 64 rows, and 984 views. We simulated Poisson noise and reconstructed onto a $512 \times 512 \times 96$ -pixel grid without the nonnegativity constraint and using a 26-neighbor edge-preserving regularizer with the smooth Fair potential. All calculations were performed on an NVIDIA Tesla C2050.

The proposed variable splitting algorithm used $\Gamma = \text{diag}_j \{ [\mathbf{A}' \mathbf{W} \mathbf{A}]_{jj} \}$. We solved the denoising subproblem with group coordinate descent [8] and performed the \mathbf{x} update with the tomography solver using one view per group and the simplified step size calculation (22). We looped through all the views in the tomography algorithm once per outer iteration and visited the views in random order.

To provide a preliminary comparison, we plotted cost function against iteration for the proposed algorithm, ordered subsets with separable quadratic surrogates Nesterov's 1983 first-order acceleration [6] with 8, 10, 12 and 16 subsets. All algorithms perform one forward- and back-projection per outer iteration; each algorithm took approximately one minute per (outer) iteration. See Figure 1. The proposed algorithm converges faster than all the accelerated OS algorithms. Figure 3 illustrates the cost function of each algorithm as a function of iteration, and Figure 2 shows the center slice of $\mathbf{x}^{(5)}$ after five iterations of the proposed algorithm.

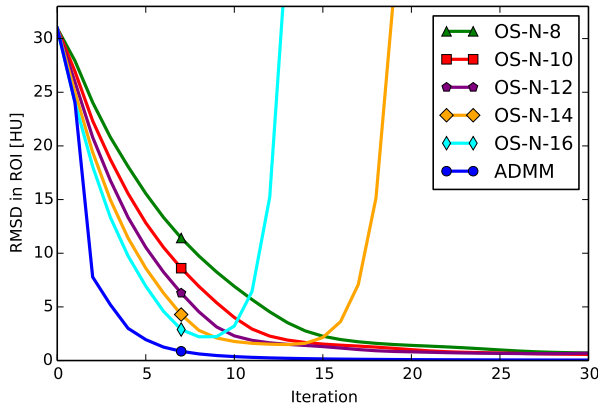


Fig. 1: Root mean squared difference of the proposed algorithm and OS-SQS-Nesterov by iteration to a converged reference image. The proposed algorithm converges considerably more quickly than OS-SQS-Nesterov with any tested number of subsets.

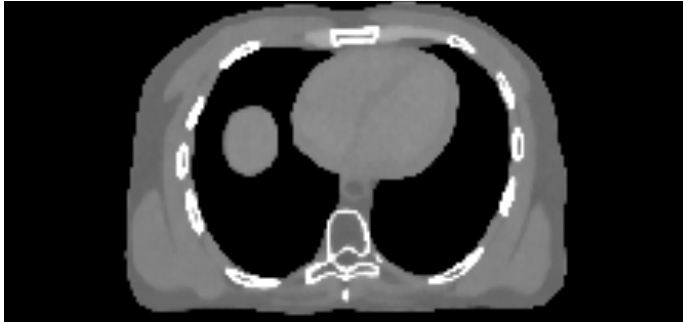


Fig. 2: Image after 5 iterations of proposed algorithm; center slice shown in a [800,1200] HU window.

V. CONCLUSIONS AND FUTURE WORK

We proposed a novel duality-based method to solve an inner quadratic tomography subproblem for a variable splitting algorithm. The reconstruction algorithm appears to converge rapidly in preliminary experiments, and we intend to perform a more thorough investigation of its performance.

The duality-based approach to the tomography problem presented here is applicable beyond the simple splitting-based algorithm in this paper, and it offers an efficient solution to the challenging 3D “tomography problem” that appears in many splitting-based reconstruction algorithms. Future work will explore more efficient methods to solve the projection-domain dual problem.

REFERENCES

- [1] H. Erdoğan and J. A. Fessler. Ordered subsets algorithms for transmission tomography. *Phys. Med. Biol.*, 44(11):2835–51, November 1999.
- [2] J. Eckstein and D. P. Bertsekas. On the Douglas-Rachford splitting method and the proximal point algorithm for maximal monotone operators. *Mathematical Programming*, 55(1-3):293–318, April 1992.
- [3] J. A. Fessler and S. D. Booth. Conjugate-gradient preconditioning methods for shift-variant PET image reconstruction. *IEEE Trans. Im. Proc.*, 8(5):688–99, May 1999.

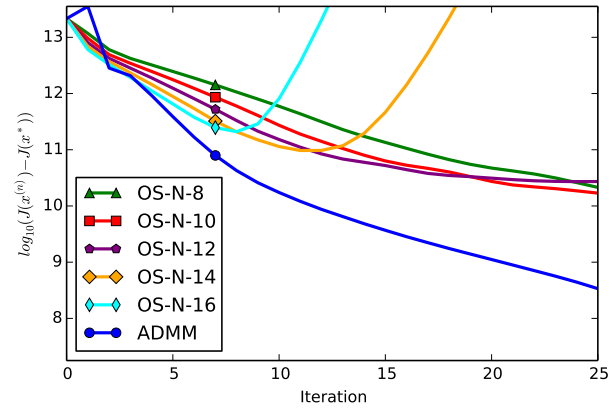


Fig. 3: Cost function values of the proposed algorithm and OS-SQS-Nesterov by iteration relative to the converged reference.

- [4] L. Fu, Z. Yu, J-B. Thibault, B. D. Man, M. G. McGaffin, and J. A. Fessler. Space-variant channelized preconditioner design for 3D iterative CT reconstruction. In *Proc. Intl. Mtg. on Fully 3D Image Recon. in Rad. and Nuc. Med.*, pages 205–8, 2013.
- [5] H. M. Hudson and R. S. Larkin. Accelerated image reconstruction using ordered subsets of projection data. *IEEE Trans. Med. Imag.*, 13(4):601–9, December 1994.
- [6] D. Kim, S. Ramani, and J. A. Fessler. Accelerating X-ray CT ordered subsets image reconstruction with Nesterov’s first-order methods. In *Proc. Intl. Mtg. on Fully 3D Image Recon. in Rad. and Nuc. Med.*, pages 22–5, 2013.
- [7] M. McGaffin and J. A. Fessler. Sparse shift-varying FIR preconditioners for fast volume denoising. In *Proc. Intl. Mtg. on Fully 3D Image Recon. in Rad. and Nuc. Med.*, pages 284–7, 2013.
- [8] M. G. McGaffin and J. A. Fessler. Fast edge-preserving image denoising via group coordinate descent on the GPU. In *Proc. SPIE 9020 Computational Imaging XII*, page 90200P, 2014.
- [9] M. G. McGaffin, S. Ramani, and J. A. Fessler. Reduced memory augmented Lagrangian algorithm for 3D iterative X-ray CT image reconstruction. In *Proc. SPIE 8313 Medical Imaging 2012: Phys. Med. Im.*, page 831327, 2012.
- [10] H. Nien and J. A. Fessler. Combining augmented Lagrangian method with ordered subsets for X-ray CT image reconstruction. In *Proc. Intl. Mtg. on Fully 3D Image Recon. in Rad. and Nuc. Med.*, pages 280–3, 2013.
- [11] H. Nien and J. A. Fessler. Splitting-based statistical X-ray CT image reconstruction with blind gain correction. In *Proc. SPIE 8668 Medical Imaging 2013: Phys. Med. Im.*, page 86681J, 2013.
- [12] L. Pfister and Y. Bresler. Model-based iterative tomographic reconstruction with adaptive sparsifying transforms. In *Proc. SPIE 9020 Computational Imaging XII*, 2014.
- [13] S. Ramani and J. A. Fessler. A splitting-based iterative algorithm for accelerated statistical X-ray CT reconstruction. *IEEE Trans. Med. Imag.*, 31(3):677–88, March 2012.
- [14] M. Sion. On general minimax theorems. *Pacific J. Math.*, 8(1):171–6, 1958.
- [15] J-B. Thibault, K. Sauer, C. Bouman, and J. Hsieh. A three-dimensional statistical approach to improved image quality for multi-slice helical CT. *Med. Phys.*, 34(11):4526–44, November 2007.
- [16] P. Tseng and S. Yun. A coordinate gradient descent method for nonsmooth separable minimization. *Mathematical Programming*, 117(1-2):387–423, 2009.
- [17] J. Wang, T. Li, H. Lu, and Z. Liang. Penalized weighted least-squares approach to sinogram noise reduction and image reconstruction for low-dose X-ray computed tomography. *IEEE Trans. Med. Imag.*, 25(10):1272–83, October 2006.
- [18] Z. Yu, L. Fu, D. Pal, J-B. Thibault, C. A. Bouman, and K. D. Sauer. Nested loop algorithm for parallel model based iterative reconstruction. In *Proc. Intl. Mtg. on Fully 3D Image Recon. in Rad. and Nuc. Med.*, pages 197–200, 2013.

Iterative CT Reconstruction using Models of Source and Detector Blur and Correlated Noise

Steven Tilley II, Jeffrey H. Siewerdsen, and J. Webster Stayman

Abstract—Statistical model-based reconstruction methods derive much of their advantage over traditional methods through more accurate forward models of the imaging system. Typical forward models fail to integrate two important aspects of real imaging systems: system blur and noise correlations in the measurements. This work develops an approach that models both aspects using a two-stage approach that includes a regularization deblurring operation followed by generalized penalized weighted least-squares reconstruction. Different reconstruction noise models including standard uncorrelated and correlated presumptions were explored. Moreover, different imaging systems were investigated in which blur was dominated by source effects, dominated by detector effects, or by a combination of source and detector blur. The proposed reconstruction approach that models the correlated noise demonstrated the best performance across all scenarios with the greatest benefits for increased source blur and for reconstructions with finer spatial resolution. This suggests potential application of the method for high resolution systems like dedicated flat-panel cone-beam CT (e.g., head, extremity, dental, mammography scanners) where system resolution is limited by both source and detector blur effects and noise correlations in measurement data are traditionally ignored.

Index Terms—High spatial resolution CT, Model-based Reconstruction, Generalized Least-Squares Estimation.

I. INTRODUCTION

Model-based tomographic reconstruction techniques have demonstrated better dose utilization and noise versus image quality tradeoff than traditional methods [1]. Such advantages are, in part, due to the integration of improved forward models that more accurately represent the physics and noise processes of acquisition and detection. Forward models of varying complexity can be designed to incorporate different imaging system characteristics, such as source and detector blur [2][3]. While recent studies [4] suggest that blur modeling may not yield substantial improvements for current diagnostic CT scanners and scan protocols, the advantages of blur modeling are dependent on target spatial resolutions and system geometries. For example, degradations in spatial resolution are potentially much more important in systems like dedicated flat-panel cone-beam CT that has been developed for high spatial resolution applications (e.g., temporal bone, extremity, dental imaging). The intrinsic spatial resolution in these systems is limited by both detector and source blurring effects. Detector blur tends to be dominated by light spread in the scintillator as opposed to detector aperture effects, since the pixel size tends to be small compared to the scintillator blur. Source blur is also often more pronounced in such systems due to the compact geometries (short source-to-detector distances) and the use of fixed anode

sources with focal spots that are larger than their rotating anode counterparts.

Thus, higher fidelity forward models like those in [2][3] that incorporate system blur offer an opportunity to recover lost spatial resolution. However, those approaches and nearly all traditional model-based reconstruction methods make an important assumption about the underlying noise model that is potentially quite inaccurate for flat-panel systems that use indirect detection. Specifically, the conversion of primary quanta to secondary quanta in the scintillator of an indirect detector imparts spatial correlations in the measurement noise. These correlations are visibly evident in gain scan acquisitions, yet the standard assumption for statistical model-based reconstruction is to presume that the measurements are independent. Despite this noise model mismatch, model-based approaches have demonstrated an advantage in cone-beam CT [1]. However, we hypothesize that additional advantages can be attained when more accurate noise modeling is integrated in the reconstruction, particularly in high spatial resolution applications in which system blur is also modeled.

Previous work [5] has shown that integrating a correlated noise model into the reconstruction process allows for improved tradeoffs between noise and resolution. In [5], a linearization of the data that included a deblurring operation followed by penalized generalized weighted least-squares reconstruction was introduced and applied to an imaging system with equal amounts of source and detector blur. The work presented here further generalizes the methodology of [5] to consider regularized deblurring of projection data and extends the investigations to systems with varying degrees of source and detector blur. Specifically, we consider scenarios where source blur is dominated by source effects, or dominated by detector effects, or is a mixture of source and detector effects to find where blur and correlated noise modeling yields the greatest advantage. Understanding this relationship has important implications for hardware design in cone-beam CT systems, including choices in the system geometry, focal spot size, scintillator thickness, etc.

In the following sections, the generalized reconstruction approach with system blur and a correlated noise model is introduced and investigated. Three different noise models - white noise, uncorrelated noise with unequal variances, and generalized correlated noise - are compared in simulated CT studies, and the improved performance using the correlated noise model is demonstrated

II. METHODS

A. Forward Model and Correlated Noise Model

The system model for a general CT system with indirect detection is illustrated in Figure 1. The mean measurement model that we adopt for development of the reconstruction algorithm has the following form:

$$\bar{y} = \mathbf{B}_d \mathbf{B}_s \mathbf{G} \exp(-\mathbf{A}\mu) \quad \mathbf{G} = \mathbf{D}\{g\} \quad (1)$$

which uses a monoenergetic formulation of Beer's law where the image volume is denoted by μ , the projection operation

Steven Tilley II, Jeffrey H. Siewerdsen, and J. Webster Stayman are with the Department of Biomedical Engineering, Johns Hopkins University, Baltimore, MD 21212 USA (phone: 410-955-1314; fax: 410-955-1115; e-mail: web.stayman@jhu.edu).

This work supported in part by NIH grants R21EB014964 and T32EB010021

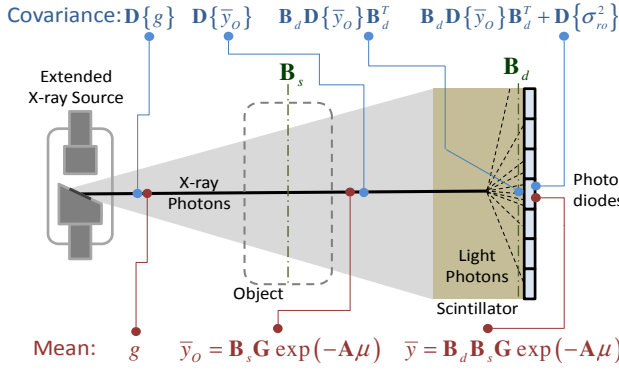


Fig. 1. System model for a generalized indirect detector cone-beam CT system. Following the generation and transit of photons (left to right), the mean number of quanta and the covariance associated with those quanta are modeled. Specifically, the mean distribution of x-ray photons at generation (g) is both attenuated by the object and undergoes spatial blurring due to the extended source. In the detector, additional blur due to light spread in the scintillator is modeled yielding the form for the mean measurement model. Noise undergoes a similar propagation through the system starting with independent photon noise with variance equal to the mean. Changes in the mean due to attenuation in the object modify these variances, which then exhibit spatial spreading (correlation) in the scintillator. Finally, these correlated measurements may be modified with the addition of (independent) readout noise.

is represented by the system matrix \mathbf{A} , and the diagonal matrix \mathbf{G} denotes a gain associated with each detector ray (i.e. x-ray fluence). (The notation $\mathbf{D}\{\cdot\}$ denotes the operator that puts the vector operand onto the diagonal elements of a diagonal matrix.) Two linear blur operators are included that model the effects of source blur, \mathbf{B}_s , and detector blur \mathbf{B}_d separately. This model is an approximation, particularly for source blur, since source effects are depth-dependent. However, for objects that are relatively thin (without a substantial change in magnification across the volume) this is a convenient and reasonable approximation.

The propagation of noise through the imaging system is also illustrated in Figure 1. Photons generated at the x-ray source are presumed to be independent with a variance equal to their mean (e.g., a Gaussian approximation to a Poisson distribution) yielding a diagonal covariance matrix. Some x-ray photons are attenuated in the object modifying these variances by their survival probabilities as well as spatial spreading due to source blur; however, the noise remains uncorrelated at this point. In the detector, individual x-ray photons are converted to many light photons, which spread spatially (detector blur) and correlate the noise. Lastly, photodiodes convert light photons to a digital signal with possible readout noise (presumed independent and Gaussian with standard deviation equal to σ_{ro}). This results in the following model for the distribution of noise in the measurements:

$$y \sim \text{Gaussian}(\bar{y}, \mathbf{K}_y) \quad \mathbf{K}_y = \mathbf{B}_d \mathbf{K}_q \mathbf{B}_d^T + \mathbf{K}_r$$

$$\mathbf{K}_q = \mathbf{D}\{\sigma_{q\text{quantum}}^2\} = \mathbf{D}\{\bar{y}_o\} \quad \mathbf{K}_r = \mathbf{D}\{\sigma_{ro}^2\} \quad (2)$$

with the following covariance matrices: \mathbf{K}_q represents pre-detection uncorrelated quantum noise, \mathbf{K}_r denotes uncorrelated readout noise, and \mathbf{K}_y is the covariance associated with the measurement vector y .

As in [5], rather than trying to solve the generalized nonlinear least-squares reconstruction problem, we choose to

transform the measurements to obtain a linear least-squares objective function. Specifically, we may compute estimated line integrals using the follow equation

$$\hat{l}(y) = -\log(\mathbf{G}^{-1} \mathbf{B}^{-1} y). \quad (3)$$

This transformation includes the familiar normalization (\mathbf{G}^{-1}) and logarithm operations, but also includes a deblurring of projection data represented by \mathbf{B}^{-1} .

Ideally, this deblurring would remove spatial resolution losses associated with both the source and detector blur suggesting that

$$\mathbf{B}^{-1} \approx [\mathbf{B}_d \mathbf{B}_s]^{-1} \quad (4)$$

Unfortunately, such an inverse may not exist, or the inverse is highly ill-conditioned, yielding computational difficulties and potential noise amplification. Instead, we adopt the following regularized pseudo-inverse

$$\mathbf{B}^{-1} = [\mathbf{B}_s^T \mathbf{B}_d^T \mathbf{B}_d \mathbf{B}_s + \lambda \mathbf{I}]^{-1} \mathbf{B}_s^T \mathbf{B}_d^T. \quad (5)$$

This transformation allows for regularized inversion of the source and detector blurs and includes a parameter λ to control the strength of the regularization. (Here, we have adopted a magnitude regularization scheme, but other options, including pairwise roughness penalties, could also be applied.)

Applying the linearization in (3) suggests the following generalized penalized weighted (linear) least-squares reconstruction objective function:

$$\hat{\mu} = \text{argmin} \|\hat{l}(y) - \mathbf{A}\mu\|_{\mathbf{K}_l}^2 + \beta R(\mu)$$

$$= [\mathbf{A}^T \mathbf{K}_l^{-1} \mathbf{A} + \beta \mathbf{R}_\mu]^{-1} \mathbf{A}^T \mathbf{K}_l^{-1} \hat{l}(y). \quad (6)$$

which encourages a fit between the line integral estimates and the projected image volume estimate. In this case, we have adopted a quadratic regularization term which leads to a closed form solution with penalty strength governed by the scalar parameter β . Central to the data fitting is a weighting by the inverse of the covariance associated with the estimated line integrals. Thus, an expression \mathbf{K}_l is required. As in [5], propagating the measurement covariance \mathbf{K}_y through the transformation in (3), one can show that the covariance of the line integral estimates may be approximated as

$$\mathbf{K}_l \approx \mathbf{D}\left\{\frac{1}{\mathbf{B}^{-1} \bar{y}}\right\} \mathbf{B}^{-1} \mathbf{K}_y [\mathbf{B}^{-1}]^T \mathbf{D}\left\{\frac{1}{\mathbf{B}^{-1} \bar{y}}\right\} \quad (7)$$

While the estimator in (6) is fully specified with the definitions in (5) and (7), there are a number of practical concerns in performing this optimization.

B. Practical Implementation

For typical CT systems, it is impractical to store and invert most of the matrices defined above. Thus, the action of the matrices is implemented functionally. This includes projection and backprojection functions, shift-invariant blur functions implemented using Fourier methods, and computation of \mathbf{K}_l through serial application of each of its components. The measured data were used as an approximation for \bar{y} in (7), and \mathbf{K}_q in (2) was approximated from measurements by $\mathbf{D}\{\mathbf{B}^{-1} y\}$.

The matrix inverses require special treatment as well. For shift-invariant blur functions, (5) may be computed directly using Fourier domain division. The action of the remaining three matrix inverses in (6) are computed using conjugate gradient (CG) based approximation.

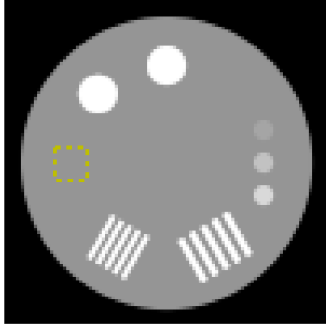


Fig. 2. Two-dimensional digital phantom used for performance investigations. The phantom comprises low and high-contrast targets and two sets of line pairs. A square region of interest in a uniform region of the phantom is indicated with a dashed line showing where variance in the reconstructed image is computed.

Noting that (6) can be rewritten as

$$S\hat{\mu} = b \quad (8)$$

$$b = A^T K_l^{-1} \hat{l}(y) \quad (9)$$

$$S = A^T K_l^{-1} A + \beta R_\mu \quad (10)$$

we see that the inverse in (9) can be approximated with one CG loop, whereas approximating (8) requires a nested loop with an inner CG loop to estimate the inverse in (10) and an outer CG loop to solve (8).

In this work, the inner loop K_l inversions in (10) were performed using a maximum of 100 CG iterations, and the outer loop inversion in (8) used a maximum of 250 CG iterations. The inversion in (9) used a maximum 1000 CG updates. All optimization code was written in Python with calls to external GPU libraries for fast projection and backprojection operations.

C. Simulation Experiments

To investigate the performance of the proposed reconstruction approach, simulation experiments were conducted using the phantom in Figure 2. The system geometry used a 100x100 axial image reconstruction with 0.1 mm voxels and a 1D detector array of 150 pixels with

0.14 mm pitch. The source-to-detector distance was 400 mm and source-to-axis distance was 200 mm. Projection data were obtained for 360 angles over 360°. Predetection quantum noise was simulated using a Gaussian distribution with a constant 10^5 photons in the unattenuated beam (with variance equal to mean). For these initial studies, readout noise variance was set to 0.

We compared reconstructions using the generalized penalized weighted least-squares approach of (6) using three different noise models: 1) The correlated noise model described in (7); 2) a white Gaussian noise model; and 3) an uncorrelated Gaussian model that presumed each measurement had a variance equal to its mean (approximating a Poisson random variable). Additionally, we consider three different blur scenarios with Gaussian source and detector blurs. Specifically, three imaging systems were modeled with: 1) detector dominated blur (2.121 pixels FWHM detector, 0.001 pixels FWHM source blur); 2) equally distributed blur, (1.5 pixels FWHM source and detector blur); and 3) source dominated blur (0.001 pixels FWHM detector, 2.121 pixels FWHM source blur). We performed a dual parameter sweep (β and λ) for each noise model and blur scenario combination.

To compare images, bias and variance were calculated for each reconstruction. Bias was calculated using a reconstruction of noiseless data according to the following:

$$bias = \|\hat{\mu}_{noiseless} - \mu_{true}\|^2 \quad (11)$$

The variance was calculated as the spatial variance over a flat part of a reconstruction (indicated with dashed line in Fig. 2).

III. RESULTS

Fig. 3. shows plots of bias versus variance for each of the reconstruction noise models and each of the three different

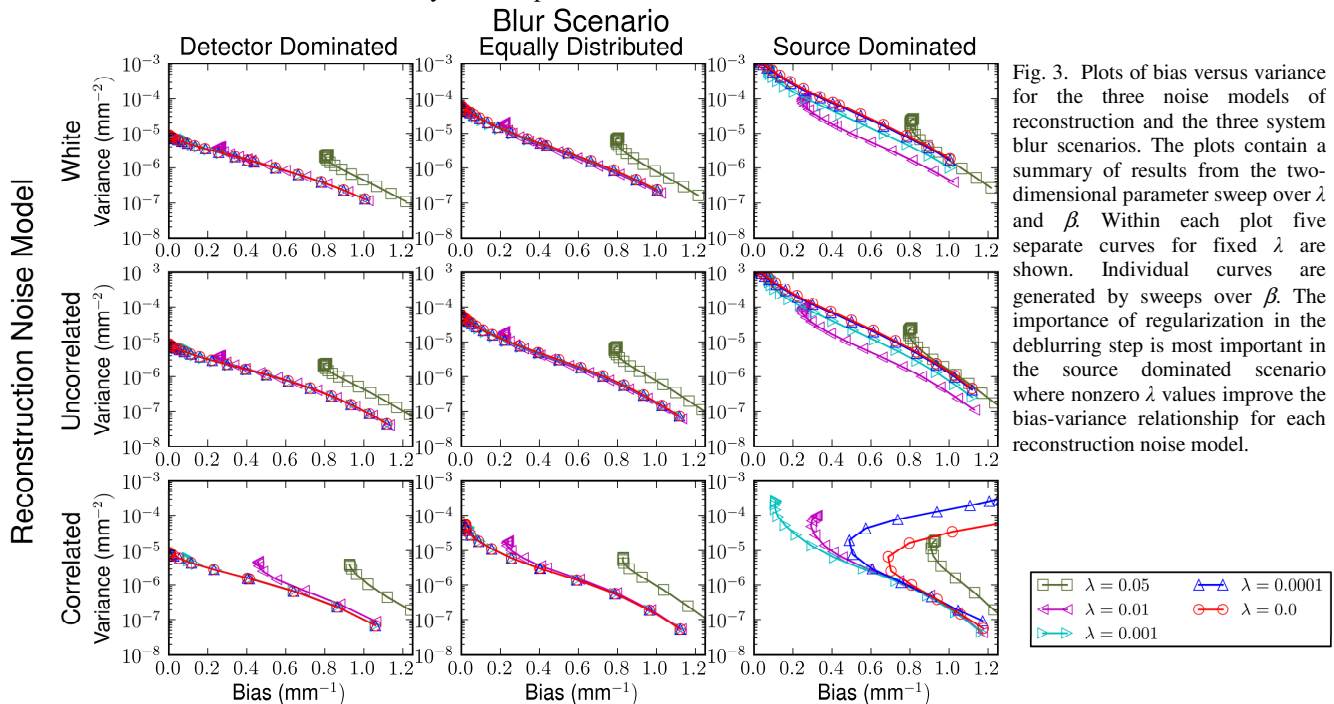


Fig. 3. Plots of bias versus variance for the three noise models of reconstruction and the three system blur scenarios. The plots contain a summary of results from the two-dimensional parameter sweep over λ and β . Within each plot five separate curves for fixed λ are shown. Individual curves are generated by sweeps over β . The importance of regularization in the deblurring step is most important in the source dominated scenario where nonzero λ values improve the bias-variance relationship for each reconstruction noise model.

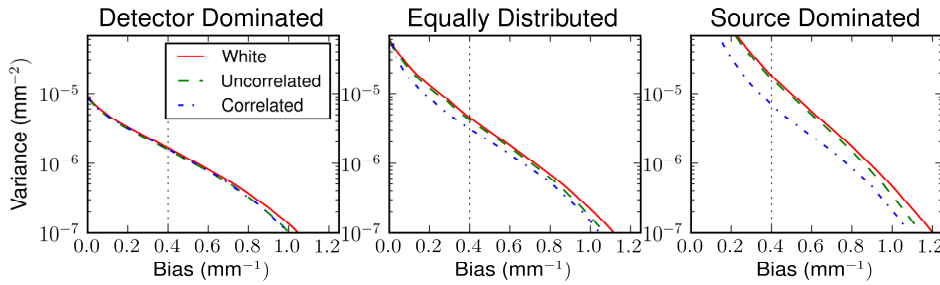


Fig. 4. Bias-variance plots for each blur scenario with optimal selection of (λ, β) . These plots illustrate the relative performance of each reconstruction noise model. In the detector blur dominated scenario, the three models perform comparably. In both the equal blur and source dominated blur scenarios, the correlated noise model shows the best performance and the white noise model shows the worst performance. The relative gain of the correlated noise model is greatest in the source blur dominated scenario.

blur scenarios. In particular this investigation shows the relative performance of different methods across a wide range of regularization strengths for the deblurring operation (λ) and for reconstruction (β). Within each plot of Fig. 3 there are five curves representing the bias versus variance performance for a fixed value of λ and varying β . In the case of detector dominated blur, there was little or no benefit from using a regularized de-blur. It appears that the added bias due to increased λ did not improve the noise tradeoff, and the added bias becomes a detriment at higher values of λ .

Similar trends are evident in the case of equal source and detector blurs. That is, the regularization in the deblurring step does not appear to improve the bias-variance tradeoff and at higher λ , this added regularization is detrimental.

The situation is different for the case of source dominated blur. In this case, increased regularization in the deblurring step improves the bias-variance tradeoff. However, the relationship is more complex and depends on

the noise model in the reconstruction. For the white noise and uncorrelated noise models, $\lambda=0.01$ is optimal over much of the bias range; however, the optimal λ decreases at lower bias levels (as induced by small β values). For the correlated noise model, there appears to be a single optimal λ value over the range with $\lambda=0.001$. The correlated noise plots also show unusual behavior for very low β values when λ is also low. Specifically, lower β appear to increase bias. This is likely due to ringing in the reconstruction for (nearly) unregularized solutions.

To compare the three noise models with each other, we consolidated the above sweeps into a single curve for each noise model by selecting the (λ, β) pair that achieves the best performance for each bias level. These results are summarized in Fig. 4.

When the blur is dominated by the detector, the overall image quality is better than the other blur scenarios, and the three noise models perform similarly. Equivalence between the white and correlated models is not unexpected since correlations are due to detector blur and the deblurring preprocessing operation decorrelates the noise, making the noise model white. However, it is somewhat surprising that the incorrect uncorrelated noise model with nonuniform variances performs similarly, suggesting relatively low variations in mean measurements for this small object.

When blur is predominately due to the x-ray source, the overall image quality is worse, but the advantage in using the correlated noise model is highest. In this scenario, none of the noise is initially correlated, and the deblurring step introduces correlations in the data. The uncorrelated noise model appears to be an improvement over the white noise model, with the advantage of the correlated noise model diminishing for higher bias levels. In this high bias regime there is less advantage to blur and correlation modeling when the reconstructed images have coarser spatial resolution. In effect, if a coarse resolution image is desired, it doesn't matter if the blur comes from intrinsic system blur or from regularization. The equal blur scenario falls in-between the other two scenarios for performance and interpretation. The rank ordering of methods is the same as the source blur dominated case, with a smaller difference between the three noise models.

Fig. 5 shows bias matched reconstructions generated using each noise model in each blur scenario. Bias was matched at approximately 0.4 mm^{-1} (indicated by the dotted lines in Fig 3) and an optimal (λ, β) pair was applied for each noise model. These reconstruction results illustrate the trends in Fig 3. When blur is predominately attributed to the source,

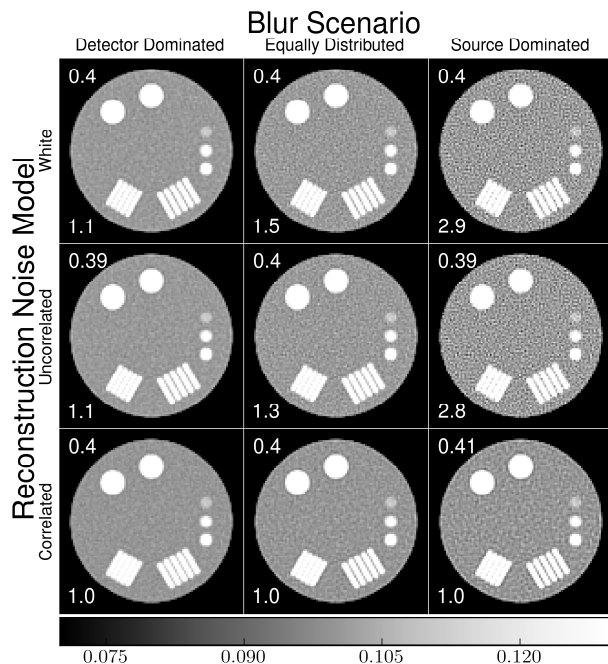


Fig. 5. Bias matched reconstructions for each blur scenario and reconstruction noise model. The bias of each reconstruction is shown in the top left (approximately 0.4 mm^{-1}), and the relative variance (the ratio of the noise variance in the reconstruction relative to the correlated noise variance) is shown in the bottom left of each image. Improved image quality (i.e., reduced noise) for the correlated noise model is evident in the equal blur and source blur dominated cases.

using the correlated noise model results in a substantial reduction in noise. The noise reduction is less when the blur is equally distributed between source and detector, and is marginal when the blur is caused predominately by the detector.

IV. DISCUSSION

In this work a generalized approach for reconstructing CT data with system blur and measurement correlations was introduced. The two step process involved a regularized deblurring step followed by a generalized penalized weighted least-squares reconstruction. Different noise models for the reconstruction were investigated including an approach that explicitly models the propagation of noise through the system and preprocessing. This explicit correlated model outperforms standard (uncorrelated) noise model choices. The benefits are greatest with more source blur, but are evident in a more typical scenario of balanced source and detector blur.

The proposed approach has potential application in tomographic systems that demand high spatial resolution and minimum noise/dose. Possible applications include flat-panel cone-beam CT systems, including dedicated dental, head, extremities, and mammography systems.

V. REFERENCES

- [1] A. S. Wang, J. W. Stayman, Y. Otake, G. Kleinszig, S. Vogt, G. L. Gallia, a J. Khanna, and J. H. Siewerdsen, "Soft-tissue imaging with C-arm cone-beam CT using statistical reconstruction," *Phys. Med. Biol.*, vol. 59, no. 4, pp. 1005–1026, Feb. 2014.
- [2] D. F. Yu, J. a Fessler, and E. P. Ficaro, "Maximum-likelihood transmission image reconstruction for overlapping transmission beams.," *IEEE Trans. Med. Imaging*, vol. 19, no. 11, pp. 1094–105, Nov. 2000.
- [3] B. Feng, J. a Fessler, and M. a King, "Incorporation of system resolution compensation (RC) in the ordered-subset transmission (OSTR) algorithm for transmission imaging in SPECT.," *IEEE Trans. Med. Imaging*, vol. 25, no. 7, pp. 941–9, Jul. 2006.
- [4] C. Hofmann, M. Knaup, and M. Kachelriess, "Do We Need to Model the Ray Profile in Iterative Clinical CT Image Reconstruction?," 2013, p. 403.
- [5] J. W. Stayman, W. Zbijewski, S. Tilley II, and J. Siewerdsen, "Generalized Least-Squares CT Reconstruction with Detector Blur and Correlated Noise Models," pp. 1–4.

CT Reconstruction of Surfaces from Binary Objects

Stefan Sawall, Jan Kuntz, Joscha Maier, Barbara Flach, Sören Schüller, and Marc Kachelrieß

Abstract—The extraction of polygonal objects from computed tomography (CT) reconstructions is a common task in several applications, e.g. for finite element analysis of bone biomechanics. Usually, a voxel volume is reconstructed from the acquired rawdata using an appropriate reconstruction algorithm. In a subsequent step global or local thresholds are applied to obtain a set of points on the object surface which undergo a polygonization. The result is a polygonal surface representation of the object. This process is governed by a variety of parameters, each of them is influencing the final result and thus requires careful calibration. To overcome this issue we propose a reconstruction algorithm that directly reconstructs the vertices of a polygonal surfaces. As typical meshes contain up to several million triangles we employ a spatial subdivision structure to speed up the ray-polygon-intersection tests and which in turn also allows for a performant application of regularizations on the obtained meshes. The preliminary results in the herein presented feasibility study indicate that the proposed method allows for a highly accurate reconstruction of polygonal surfaces from measured rawdata within reasonable time. This boosts several applications, e.g. the easy and fast construction of antropomorphic phantoms for simulations or for 3D printing models from CT scans.

I. INTRODUCTION

POLYGONAL representations of objects obtained from computed tomography (CT) reconstructions are used in a variety of applications. Examples include finite element simulations (FEM) of biomechanical properties of bones [1], [2], the construction of antropomorphic phantoms used in the simulation of imaging modalities [3] or for 3D printing. In most cases the acquired rawdata are reconstructed onto a discrete voxel grid, i.e. a volume, by an appropriate image reconstruction algorithm. In a subsequent step features of interest are segmented manually or by applying global and/or local thresholds, which are dependent on a variety of parameters based on the chosen methodology [4]. The therefrom obtained binary voxel objects are converted to polygonal objects using appropriate algorithms, e.g. the marching cubes method or more sophisticated methods like the ball pivoting algorithm [5], [6], which again might be dependent on several tweakable parameters. Errors introduced due to a miscalibration in any of the required parameters might accumulate along this pre-processing pipeline and degrade the quality of the obtained polygonal object representation in terms of accuracy and degree of refinement. This process is illustrated in figure 1. To avoid these disadvantages we propose to directly reconstruct polygonal objects, i.e. meshes, and to perform an iterative

refinement of the mesh vertex positions such that the difference of a forward projection through this object and the acquired rawdata is minimized, similar to the idea proposed in [7]. As a typical object, however, might contain up to several million polygons, we employ a spatial subdivision structure to allow for a rapid computation of intersection lengths through the considered meshes. In the following we will restrict ourselves to meshes which are solely constructed from triangles, as these are the most commonly used primitives. We also assume that all provided meshes are watertight in the ray direction, i.e. any arbitrary ray intersecting this object results in an equal number of inbound and outbound intersections.

II. MATERIALS AND METHODS

A. Ray-Triangle Intersection

Let us define a triangle (in three dimensional space) as

$$T(\mathbf{o}, \mathbf{a}, \mathbf{b}) = \{\mathbf{o} + \lambda_1 \mathbf{a} + \lambda_2 \mathbf{b} \mid 0 \leq \lambda_i, \lambda_1 + \lambda_2 \leq 1\}. \quad (1)$$

where \mathbf{o} is one of the triangle's edges, and \mathbf{a} and \mathbf{b} are vectors pointing from this edge to the other two edges (see fig. 2). The definition is such that the normal vector $\mathbf{n} = \mathbf{a} \times \mathbf{b}$ is pointing away from the object. We now need to find out, whether our ray $\mathbf{s} + \lambda \Theta$, originating at the source position \mathbf{s} and heading in direction Θ , intersects the triangle, i.e. whether there exist $\lambda_1, \lambda_2 \geq 0$ with $\lambda_1 + \lambda_2 \leq 1$ such that

$$\mathbf{s} + \lambda \Theta = \mathbf{o} + \lambda_1 \mathbf{a} + \lambda_2 \mathbf{b}. \quad (2)$$

To do so, let us first compute $D = \mathbf{n} \cdot \Theta = (\mathbf{a} \times \mathbf{b}) \cdot \Theta$. If D is zero our ray is either parallel or lies within the plane defined by the triangle. Now, let $\mathbf{c} = \mathbf{o} - \mathbf{s}$ and $\mathbf{m} = \Theta \times \mathbf{c}$, multiply (2) by $\Theta \times \mathbf{a}$ to obtain

$$\lambda_2 = -\frac{(\Theta \times \mathbf{a}) \cdot \mathbf{c}}{(\Theta \times \mathbf{a}) \cdot \mathbf{b}} = +\frac{\mathbf{m} \cdot \mathbf{a}}{D}$$

and check if $0 \leq \lambda_2 \leq 1$. If this is not the case, the ray is not intersecting the triangle. If this is the case, we are done. Otherwise we continue by multiplying (2) with $\Theta \times \mathbf{b}$ and find

$$\lambda_1 = -\frac{(\Theta \times \mathbf{b}) \cdot \mathbf{c}}{(\Theta \times \mathbf{b}) \cdot \mathbf{a}} = -\frac{\mathbf{m} \cdot \mathbf{b}}{D}.$$

If $0 \leq \lambda_1$ and if $\lambda_1 + \lambda_2 \leq 1$ we know that the ray is intersecting the triangle. The intersection is found by multiplying (2) with \mathbf{n} as

$$\lambda = \frac{\mathbf{n} \cdot \mathbf{c}}{D}.$$

If $\mathbf{n} \cdot \Theta > 0$ the intersection point is the point where the ray exits the object. If $\mathbf{n} \cdot \Theta < 0$ the ray enters the object. To speed up the calculation one may rather regard the quantities $\hat{\lambda}_1 =$

Dr. Stefan Sawall, Dr. Jan Kuntz, Joscha Maier, Barbara Flach, Sören Schüller, and Prof. Dr. Marc Kachelrieß: Medical Physics in Radiology, German Cancer Research Center (DKFZ), Im Neuenheimer Feld 280, Heidelberg, Germany.

Corresponding author: stefan.sawall@dkfz.de

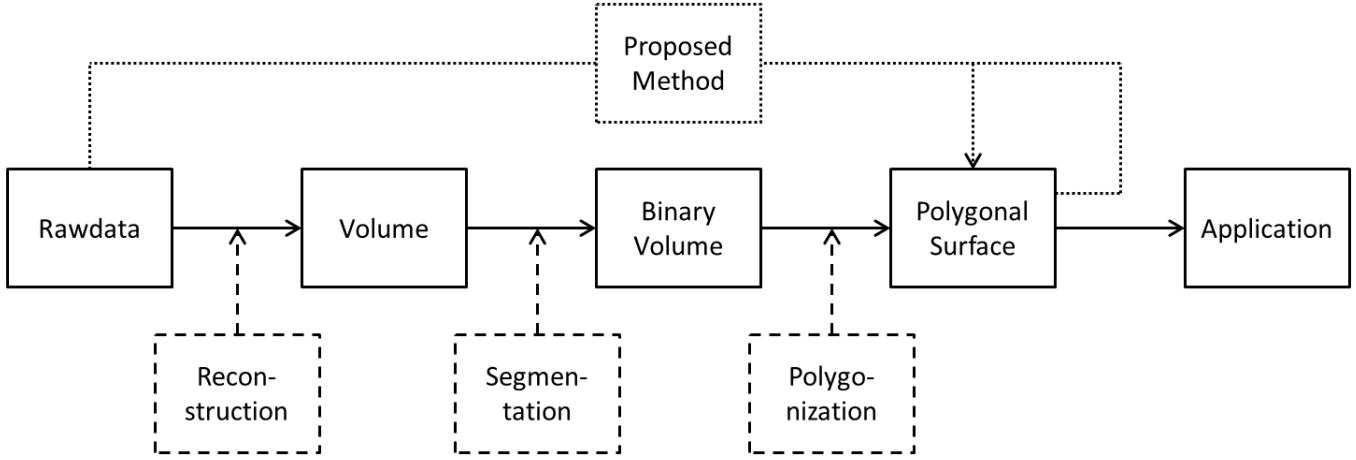


Fig. 1. Overview of the process resulting in a polygon mesh based on measured rawdata. The usual operations are framed by dashed lines while the proposed method is illustrated using dotted lines.

$\lambda_1 \mathbf{n} \cdot \Theta$ and $\hat{\lambda}_2 = \lambda_2 \mathbf{n} \cdot \Theta$ and then perform the computations without the divisions. In case $\mathbf{n} \cdot \Theta > 0$ we have an intersection if $0 \leq \hat{\lambda}_1, \hat{\lambda}_2$ and if $\hat{\lambda}_1 + \hat{\lambda}_2 \leq \mathbf{n} \cdot \Theta$. If $\mathbf{n} \cdot \Theta < 0$ we may simply replace Θ by $-\Theta$, then carry out the intersection calculations, and at the very end replace λ by $-\lambda$.

B. Spatial Subdivision

As typical objects contain up to several million triangles, simple bruteforce intersection tests are computationally not feasible. E.g. the computation of intersection lengths for 1000 projection images through an object containing 10^6 triangles with a detector size of 1000×1000 pixels would require the computation of 10^{15} ray-triangle-intersection tests. To overcome this issue we use a spatial subdivision structure proposed recently [8]. In particular, an octree is used in the following. An octree in three-dimensional space is a tree structure with each node in general containing eight child nodes. If we consider the root node to be the bounding box of our triangulated objects these child nodes correspond to equally sized spatial subdivisions, i.e. rectangular boxes, of this bounding box. These nodes will be referred to as internal nodes in the following. This subdivision process continues by subdividing each child node in eight boxes again. If the space enclosed by such a subbox does not contain any triangles, it will no further be used to spawn new child nodes. I.e. its parent node rejects this child node and thus the number of childs is reduced by one. As soon as certain termination criteria are met the process stops. The subdivision in our case stops as soon as no new subboxes can be generated that contain at least 16 triangles. The triangles contained in a subbox are stored in a so-called external child node. If the intersections of a ray with an object shall be computed the octree is traversed. I.e., it is ensured that the ray intersects with the bounding box of the root node. If this is not the case the procedure is terminated. If the ray intersects the root node all internal child nodes are recursively checked for an intersection. If any of these nodes contains an external child node the intersection points with the triangles enclosed therein are computed. Using

this spatial subdivision scheme ensures that the number of triangles that have to be considered per ray is highly reduced and thus performance is increased by several orders of magnitude.

C. Mesh Optimization

Given the measured rawdata \mathbf{p} we wish to adapt our triangle mesh to these data by finding new vertex positions such that the difference between the measured data and simulated intersection lengths $\mathbf{L}(\mathbf{r})$, as a function of the N vertices $\mathbf{r} = (\mathbf{r}_{x_1}, \mathbf{r}_{y_1}, \mathbf{r}_{z_1}, \dots, \mathbf{r}_{x_N}, \mathbf{r}_{y_N}, \mathbf{r}_{z_N})$, is minimized. We assume that a valid initial mesh is provided, e.g. by a reconstruction of \mathbf{p} , segmentation and triangulation of the obtained volume followed by a successful registration in either image space (3D-3D) or rawdata space (2D-3D). Note that sophisticated algorithms already exist to achieve this task [9], [10]. The alignment of the vertices to the rawdata can be performed by optimizing the following cost function:

$$C(\mathbf{r}) = \|\mathbf{p} - \mu \mathbf{L}(\mathbf{r})\|_2^2 + \eta R(\mathbf{r}). \quad (3)$$

The term $\eta R(\mathbf{r})$ therein denotes a penalty term with the weight η that allows for a regularization of the obtained mesh, e.g. by Geometric Laplacian (GL) to constrain the smoothness of a given vertex \mathbf{r}_k as proposed in reference [11]:

$$GL(\mathbf{r}_k) = \mathbf{r}_k - \frac{\sum_{m \in n(\mathbf{r}_k)} l_m^{-1} \mathbf{r}_m}{\sum_{m \in n(\mathbf{r}_k)} l_m^{-1}} \quad (4)$$

Therein, $n(\mathbf{r})$ denotes the set of vertices adjacent to \mathbf{r}_k , and l_k is the Euclidian distance from vertex \mathbf{r}_m to vertex \mathbf{r}_k . The cost function in eq. 3 can easily be extended to include other effects, e.g. a finite focal spot size or a finite detector aperture. Note that the used spatial subdivision structure allows for a highly performant application of local and global mesh regularization schemes. However, we restrict ourselves to $\eta = 0$ in the feasibility study presented herein and only consider binary objects, i.e. by choosing the linear attenuation coefficient as $\mu = 1$. Hence the linear attenuation coefficient will be dropped

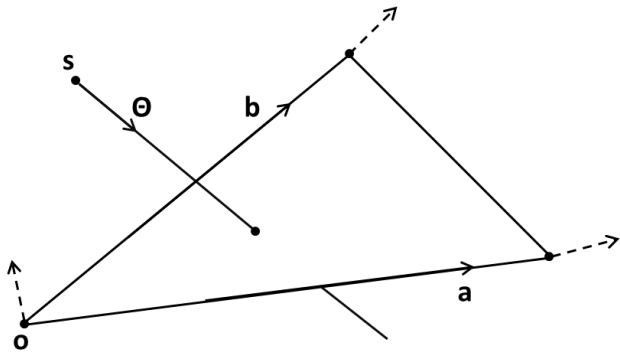


Fig. 2. Overview of the triangle formed by o, a, b , a ray originating at the source s heading in direction d and intersecting at point Q^* . The dashed lines indicate a translation of the vertices due the proposed refinement scheme.

in the following considerations. As the intersection lengths through a mesh are the distances between consecutive entrance and exit points, the cost function might also be given as

$$C(\mathbf{r}) = \|\mathbf{p} - \sum_{i \in I} (\mathbf{O}_i - \mathbf{I}_i)\|_2^2 \quad (5)$$

with $\mathbf{O} = \mathbf{O}(\mathbf{r})$ and $\mathbf{I} = \mathbf{I}(\mathbf{r})$ being all $I \in \mathbb{N}$ respective entrance and exit points. An optimization of this cost function, and hence of the desired mesh, can be performed using ,e.g., the gradient descent method. The required derivatives of (5), omitting constants, for all rays $J \in \mathbb{N}$ with respect to the vertex coordinates are

$$\nabla_{\mathbf{r}} C(\mathbf{r}) = - \sum_{j \in J} \left[(p_j - L_j) \left(\sum_{i \in I} \frac{\partial \mathbf{O}_i}{\partial \mathbf{r}} - \sum_{i \in I} \frac{\partial \mathbf{I}_i}{\partial \mathbf{r}} \right) \right]. \quad (6)$$

The derivatives of the entrance and exit points, $\partial \mathbf{I} / \partial \mathbf{r}$ and $\partial \mathbf{O} / \partial \mathbf{r}$, can easily be obtained from the equations governing the ray–triangle–intersection computations. Optimized vertex positions can be obtained as

$$\mathbf{r}^{k+1} = \mathbf{r}^k + t \nabla_{\mathbf{r}} C(\mathbf{r}^k) \quad (7)$$

with t being the step size and $k \in \mathbb{N}$ being the iteration number. To speed up convergence our implementation uses a non–linear conjugate gradient descent employing a Polak–Ribière conjugation with a backtracking line search [12]. We further employ an ordered subset update scheme as it is known from the ordered subset simultaneous algebraic reconstruction (OSSART) [13], i.e. the updates are successively performed from orthogonal directions.

D. Simulations

To illustrate the feasibility of the proposed method the triangulated mesh of a lumbar vertebra with a size of about $60 \text{ mm} \times 60 \text{ mm} \times 40 \text{ mm}$ containing about 70000 triangles obtained from BodyParts3D is used in the presented simulation study (see fig. 3) [14]. As the choice of the segmentation threshold is a common source of errors in the extraction of triangulated surfaces from CT scans this will be used as

an example in the following. In particular, a miscalibrated threshold results in an erroneous scaling of the obtained mesh. This issue is emulated by simulating 360 projection images in a circular trajectory of the vertebra with 1000×1000 detector pixels per projection and a pixel size of $400 \mu\text{m}$. The source–detector–distance is 930 mm and the distance between source and isocenter is 570 mm. To simulate an erroneous segmentation the proposed algorithm was initialized with a scaled version of the original vertebra. The scaling by a factor of 0.9 was performed around its center of mass. This corresponds to a maximum deviation of about 6 mm which is by far larger than typical voxel sizes in CT. The algorithm was stopped as soon as the summed changes of the vertex positions in consecutive iterations were smaller than 10^{-4} mm.

III. RESULTS

Using a scaled version of the vertebra as initialization for the proposed method, the algorithm converged after 450 iterations. Figure 3 shows the wireframe of the vertebra, a projection obtained using the reference mesh, difference images between this initial projection and the ones obtained in a given iteration, and a series of color–coded deviation maps. The latter were obtained using CloudCompare (EDF R&D, Telecom ParisTech, Paris, France) and represent the signed distance of the reference mesh, i.e. the unscaled vertebra, compared to the mesh obtained in a given iteration. As can be seen a comparison between the unscaled vertebra and the mesh used to initialize the algorithm, i.e. the vertebra scaled by 0.9, shows severe deviations in the order of up to 6 mm. Note that distances are not computed between corresponding triangles in both models but between the surfaces closest to each other and thus the color-coded deviation maps are not entirely blue but also reddish colors appear. After about 150 iterations larger planar areas are already well reconstructed and only show small errors while edges still exhibit deviations in the order of 6 mm. At iteration 300 almost all vertices are reconstructed illustrated by the greenish colors. However, still deviations in the order of 3 mm remain at the edges of the object. The deviation-map obtained after 450 iterations illustrates that the vertebra could be completely reconstructed from the given rawdata with errors remaining in the order of a few micrometers. A similar conclusion can be drawn from the difference images between projections obtained in a given iteration and the one obtained from the reference mesh. The shown differences, due to the choice of $\mu = 1$ directly showing differences in intersection lengths, are almost zero after 450 iterations, illustrating that the vertebra was fully recovered.

IV. CONCLUSION AND DISCUSSION

This feasibility study illustrates that the proposed method is capable of reconstructing triangle meshes from a given set of rawdata. As this task can be achieved in reasonable time in the scale of minutes it is a promising perspective to obtain highly detailed meshes from CT scans without the flaws of the usual methodology including several parameter dependent segmentation and triangulation steps. Future research might include an estimation of the number of required projection images,

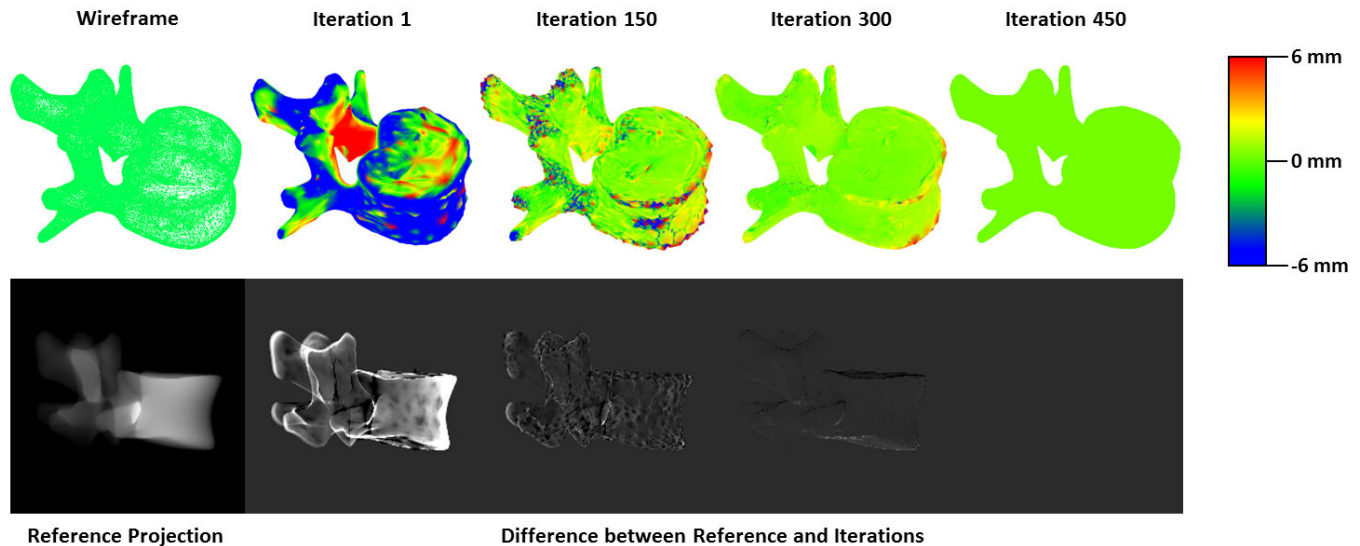


Fig. 3. The top row shows the color-coded deviation maps for iterations 1, 150, 300, 450. The bottom row shows the initial projection image of the reference vertebra and the differences of the same projection to the results obtained in each iteration. The projection image is windowed $C = 30$ mm, $W = 60$ mm and difference images are windowed $C = 2$ mm, $W = 6$ mm.

the processing of multi-material objects and the integration of the proposed method into complex scan protocols, i.e. with a reasonable anatomical background.

ACKNOWLEDGEMENTS

The high-speed projection simulator RayConStruct-PS, including the fast ray-triangle intersector, and the high-speed image reconstruction software RayConStruct-IR were provided by RayConStruct® GmbH, Nürnberg, Germany.

REFERENCES

- [1] A. Torcasio, X. Zhang, H. Van Oosterwyck, J. Duyck, and G. Lenthe, "Use of micro-CT-based finite element analysis to accurately quantify peri-implant bone strains: a validation in rat tibiae," *Biomechanics and Modeling in Mechanobiology*, vol. 11, no. 5, pp. 743–750, 2012.
- [2] D. Lacroix, A. Chateau, M.-P. Ginebra, and J. A. Planell, "Micro-finite element models of bone tissue-engineering scaffolds," *Biomaterials*, vol. 27, no. 30, pp. 5326 – 5334, 2006.
- [3] W. Segars, D. Lalush, and B. M. W. Tsui, "A realistic spline-based dynamic heart phantom," *Nuclear Science, IEEE Transactions on*, vol. 46, no. 3, pp. 503–506, 1999.
- [4] W. Elmasry, H. Mofteh, N. El-Bendary, and A. Hassanien, "Performance evaluation of computed tomography liver image segmentation approaches," in *Hybrid Intelligent Systems (HIS), 2012 12th International Conference on*, 2012, pp. 109–114.
- [5] W. E. Lorensen and H. E. Cline, "Marching Cubes: A high resolution 3D surface construction algorithm," *SIGGRAPH Comput. Graph.*, vol. 21, no. 4, pp. 163–169, 1987.
- [6] F. Bernardini, J. Mittleman, H. Rushmeier, C. Silva, and G. Taubin, "The ball-pivoting algorithm for surface reconstruction," *Visualization and Computer Graphics, IEEE Transactions on*, vol. 5, no. 4, pp. 349–359, 1999.
- [7] C. Soussen and A. Mohammad-Djafari, "Polygonal and polyhedral contour reconstruction in computed tomography," *Image Processing, IEEE Transactions on*, vol. 13, no. 11, pp. 1507–1523, 2004.
- [8] S. Sawall, M. Baer, M. Brehm, M. Knaup, and M. Kachelrieß, "Fast computation of projections from triangulated surfaces," in *Fully 3D Image Reconstruction, 12th International Meeting on*, 2013, pp. 304–308.
- [9] C. Sinthanayothin and W. Tharanon, "3D-3D registration: Surface rendering plus skull and soft tissue registration," in *Industrial Electronics and Applications, IST IEEE Conference on*, 2006, pp. 1–5.
- [10] P. Steininger, M. Neuner, H. Weichenberger, G. C. Sharp, B. Winey, G. Kametriser, F. Sedlmayer, and H. Deutschmann, "Auto-masked 2D/3D image registration and its validation with clinical cone-beam computed tomography," *Physics in Medicine and Biology*, vol. 57, no. 13, p. 4277, 2012.
- [11] G. Lavoué, "A roughness measure for 3d mesh visual masking," in *Proceedings of the 4th Symposium on Applied Perception in Graphics and Visualization*, New York, NY, USA, 2007, pp. 57–60.
- [12] J. R. Shewchuk, "An introduction to the conjugate gradient method without the agonizing pain," Pittsburgh, PA, USA, Tech. Rep., 1994.
- [13] H. Hudson and R. Larkin, "Accelerated image reconstruction using ordered subsets of projection data," *Medical Imaging, IEEE Transactions on*, vol. 13, no. 4, pp. 601–609, 1994.
- [14] BodyParts3D. [Online]. Available: <http://lifesciencedb.jp/bp3d/>

Statistical Framework For Synthetic Object Addition to CT Projections

Stanislav Žabić¹, Kevin M. Brown¹, Brendan Eck²

Abstract—In this paper we present a statistical framework for adding synthetic objects of arbitrary size to raw X-ray CT data on a system with energy integrating detectors. In CT projections, added objects change both the mean signal as well as the noise distribution. To add synthetic objects to CT data, we attenuate individual projections accordingly and account for those changes, based on the conditional variance theorem. This method allows for the addition of both hypodense and hyperdense lesions of arbitrary size, independent of reconstruction technique. Simulations with analytic phantoms over 1000 noise realizations showed that the proposed statistical framework agrees with the ground truth.

I. INTRODUCTION

Synthetic objects are often added to clinical computed tomography (CT) data in order to evaluate computer aided diagnosis (CAD) algorithms, to evaluate image perception, and to compare image quality of various reconstruction algorithms. A review of the literature on studies which add synthetic objects to CT data shows a wide variety of applications and approaches, as we will discuss in detail in Section II. The size of added objects varies from relatively small, low contrast liver lesions, larger lung nodules to high contrast implants. Objects added to liver and lungs can range anywhere from 1mm to 10mm in diameter and can have contrast of 5HU (Hounsfield units) for lesions to one-hundred or more in the case of the lung nodules. Lesions are typically hypodense (negative contrast) and nodules are invariably hyperdense (positive contrast). If we also consider the possibility of adding implants, added objects can be even several hundred HU or more.

All approaches that we have reviewed in the literature assume that the data with the added object approximately inherits statistical properties of the background data. This certainly seems reasonable for relatively small objects or objects with low attenuation. However, noise properties of CT data are dominated by the statistics of x-ray generation and attenuation, and we expect that whenever we add or take something out of the CT data, we necessarily change not only the mean values, but also the statistical properties of the data. No work that we have reviewed took this into careful consideration, nor argued at what point the size and attenuation of the added object relative to the background interfere with the statistical properties enough to be concerned.

In this paper we assume that the x-ray portion of the CT data is well approximated by the Poisson distribution and that the distribution of detector noise is known. With those assumptions we present a very simple statistical framework for synthetic object addition to CT projections which claims to agree with the assumed model on the first two statistical moments (mean and variance).

II. STATE OF THE ART

Ambrosini [1] argues that a good simulation of lung nodules must have anatomical shape similar to real lung nodules

for objective testing of CAD applications for abnormality detection. Their technique of modeling the size, shape and attenuation of the synthetic objects is valuable and in this paper we assume that size, shape and attenuation of the synthetic object is known.

Li et. al. [7] study techniques for simulation of lung nodules. They consider three types of synthetic nodule simulation: 1) synthetic nodules are added to a physical or mathematical phantom, 2) nodules are either segmented out from the real clinical images or 3) computer generated. For types 2) and 3), the nodules are added to the reconstructed clinical images. The advantage of adding nodules to the clinical images is that it creates a volume with realistic anatomy. Earlier work on this subject is by Hoe et. al. [5] with liver lesions. Studies of Li [7] and Hoe [5] motivate us to take a step further in developing a realistic framework that uses existing clinical data without lesions or nodules, and adds synthetic ones which can then be used for observer studies.

Madsen [8], [9], [10] et. al. are interested in lung nodule addition based on a library of nodules extracted from clinical image volumes. Abnormalities are added in the image space and images are used in image perception studies. Shin [13] et. al. and Kazantzakis [6] et. al. developed a similar tool, which also adds virtual pulmonary nodules to CT data, and this is the only paper that we identified which also has some statistical considerations. The objects are added and synthetic noise is simulated with heuristically determined patterns and levels in the image space using a blending technique based on an early work in digital imaging by Porter and Duff [11], interestingly of the *Star Wars* cinema franchise. Our motivation is to create a framework based on a more accurate noise model of CT data.

Falck et. al. [3] use realistic liver lesions which are segmented from real clinical cases and added to phantom data using an image domain blending technique described in [4]. Images to which synthetic nodules are introduced, come from a statistical reconstruction algorithm, SAFIRE, and they are subsequently used for image quality (IQ) performance testing of that algorithm. The authors do not offer much details on the accuracy of the blending technique, simply stating that the simulations inherit noise magnitude and characteristics of the target data-set to a large extent, but that extent has not been quantified. The image reconstruction algorithm used in this study belongs to a class of statistical reconstruction algorithms, which use the knowledge of the statistical properties of the data in the process of image formation. A successful object blending technique must be tailored to this specific algorithm. This means that if we wish to compare performance between two different reconstruction algorithms, we also need to modify the blending technique. This motivates us to create an object insertion strategy which adds an object to the data accurately regardless of its size and attenuation *before* the images are reconstructed to allow for an independent IQ comparison for any reconstruction algorithm.

¹ Philips Healthcare, ², Case Western Reserve University, Cleveland, OH

As an additional argument for a more careful consideration of the object size, we also quote Wang's [14] talk at the RSNA meeting in 2013, where he indicated the need for a statistically accurate addition of larger synthetic implants to interventional cone-beam CT data. Clearly, large implants will at one point change the noise characteristics of the target data set.

The final motivation for our work comes from Wunderlich and Noo [16], who derived the analytical formula of image covariance in direct fan-beam CT reconstruction and used a channelized hoteling observer (CHO) for modeling the performance in a simulated lesion detection task. The phantom used in their study is fully analytical and certain images contain the lesion while others do not. The task of the observer is to recognize whether the lesion is present or not. Their study can now be extended to clinical data to which *signal present* data could be obtained by adding synthetic lesions using our statistical framework.

III. ASSUMPTIONS AND THE PROBLEM STATEMENT

Suppose that an X-ray is generated with the flux of N_a photons, where a indicates a tube current and that we have a CT system with energy integrating detectors with a fixed integration period during the scan. Before the X-ray reaches the detector, it attenuates through an object with an attenuation μ_1 and according to the monochromatic Beer's law, the mean number of detected photons is:

$$y_{a,l_1} = N_a e^{-l_1},$$

where $l_1 = \int_r \mu_1 dl$ is the line integral of the object μ_1 along ray r .

In practice, this mean number is not available because the recorded value is corrupted by noise. In fact, on a system with energy integrating detectors, we record the signal which can be modeled as

$$\hat{s}_{a,l_1} = AP(N_a e^{-l_1}) + \mathcal{D},$$

where A is the electronic gain, $\mathcal{P}(m)$ indicates Poisson realization with mean m and \mathcal{D} indicates zero-mean detector electronic noise realization with variance $\sigma_{\mathcal{D}}^2$. We described this model in details in [17] which heavily relies on earlier work by Whiting et. al [15].

Assuming that the noise from X-ray photons and the detector are independent random variables, according to the model in [15], we have the following result for the first two statistical moments of the signal \hat{s}_{a,l_1} :

$$\begin{aligned} \text{Mean}(\hat{s}_{a,l_1}) &= Ay_{a,l_1} & \text{and} \\ \text{Var}(\hat{s}_{a,l_1}) &= A^2 y_{a,l_1} + \sigma_{\mathcal{D}}^2. \end{aligned} \quad (1)$$

Our goal is to add an object with a different attenuation function μ_2 to the original object. If we do that, then the combined line integral along ray r is $l = l_1 + l_2$, where $l_2 = \int_r \mu_2 dl$. Since the added object can consist of parts which have a negative contrast, we require that the tube current b in the combined object scan satisfies

$$b \leq \min\{ae^{l_2}, a\}. \quad (2)$$

If $l_2 > 0$, then we can keep $b = a$, but otherwise, $b < a$, which happens if the added object has a negative attenuation in certain views. The mean number of detected photons in a combined object scan will be

$$y_{b,l} = N_b e^{-l}.$$

There are some important practical considerations that stem from condition (2). Namely, if we are adding a hyperdense object to the data, then we need to introduce more noise only to the parts of the CT data that penetrate through the added object. But, if a synthetic object has some negative line integrals, then, roughly speaking, we resort to adding noise to the projections of the background data, since noise removal is a much more difficult task and is really the job of a CT reconstruction algorithm. *Adding noise to the background* is a good description of the meaning when we write $b < a$. In that case, background data must be acquired at a higher dose if we wish to achieve the noise levels of the target volume with the synthetic lesion which contains hypodense regions.

Let us assume that condition (2) holds. We claim that the following formula gives us a signal where a synthetic object is inserted into the existing object, while satisfying the first two statistical moments (1) for tube current b

$$\hat{s}_{a \rightarrow b, l_1 + l_2} = \frac{A a - b e^{-l_2}}{a - b e^{-l_2}} \mathcal{P}\left(\frac{b e^{-l_2}}{a - b e^{-l_2}} \frac{\hat{s}_{a, l_1}}{A}\right) + \mathcal{D} \sqrt{1 - \frac{b^2 e^{-2l_2}}{a^2}}, \quad (3)$$

whenever $a > b e^{-l_2}$, otherwise $\hat{s}_{a \rightarrow b, l_1 + l_2} = \hat{s}_{a, l_1 + l_2}$.

One can see that for $\hat{s}_{a \rightarrow b, l_1 + l_2}$ we have

$$\text{Mean}(\hat{s}_{a \rightarrow b, l_1 + l_2}) = Ay_{b, l}, \quad \text{and}$$

$$\text{Var}(\hat{s}_{a \rightarrow b, l_1 + l_2}) = A^2 y_{b, l} + \sigma_{\mathcal{D}}^2,$$

by following the steps of the proof in the Appendix of [17]. Just take $\alpha = a$ and $\beta = b e^{-l_2}$, where α and β are symbols used in [17]. The key part that allows us to prove our claim is *conditional variance theorem* [2] which we discussed in details in [17].

IV. SIMULATION STUDY

In this section, we verify theoretical results from the previous section using a mathematical phantom. To simplify our simulation and underline the importance of the conditional variance principle for the Poisson part of the noise model, we will assume that the detector noise \mathcal{D} is not present. Detector noise is not a dominant source of noise for the dose levels selected for the experiment, which is another reason why we excluded it from our experiments in this paper. We use the analytical simulations to demonstrate the effectiveness of our model, but the method itself is not restricted just to the simulations. Results with real data and electronic noise will be presented in our poster at the conference.

We start with three analytical phantoms p , p_1 and p_2 where phantom p is simply a sum of p_1 and p_2 . Line integrals corresponding to the phantom p will be denoted as l and they are calculated along rays that form a realistic CT cone-beam geometry. Similarly, line integrals of the phantom p_1 will be denoted as l_1 and line integrals of the phantom p_2 will be denoted as l_2 . We will simulate noisy CT projections for the phantoms p and p_1 and then we will add phantom p_2 to p_1 using the formula (3). The role of the phantom p_2 is that of an arbitrary synthetic lesion, nodule or an implant added to the background data p_1 . We will demonstrate that the mean and noise variance of 1000 noisy image reconstructions with FBP for the direct noise simulations on phantom p and reconstructions from data calculated with formula (3) are the same. We are adding a large object to exaggerate the effects of the noise, but the method is not limited to the object size.

We will perform the experiment twice, first with object p_2^+ which contains entirely positive line integrals (Fig. 1. d)

and second with object p_2^- which has negative line integrals (Fig. 1. e). When adding an object with positive values, the attenuation in combined data will be higher in areas that correspond to the added object, so we expect the noise to go up in those areas. However if an added object has negative values, the attenuation will be lower in those areas than in the background. As argued in the previous section, we cannot decrease the noise in projections, so we resort to adding noise to the background. The mathematical expression that reflects this is in condition (2). In our experiment with object p_2^+ , we can keep $a = b = 100mA$, but in our experiment with object p_2^- , condition (2) forces us to choose tube current for the background to be $a = 100mA$ and for the targeted simulation, we chose $b = 69mA$ since the minimum line integral through the added object in that case is -0.37 . Throughout this experiment, the integration period was simulated at the fixed length of $417\mu s$.

Let indices (i, j) denote detector channels (i) and views (j) in this simulation. We make 1000 three noisy sets with mean values $y_{b,l}(i, j) = N_b(i)e^{-l(i,j)}$, $y_{a,l_1}(i, j) = N_a(i)e^{-l_1(i,j)}$ and $y_{b,l_1}(i, j) = N_b(i)e^{-l_1(i,j)}$, using the Poisson noise generator, such as the one described in [12]. Details on how to obtain N_a and N_b for a system are in [17]. The noisy data sets are denoted as

$$\begin{aligned}\hat{y}_{b,l}(i, j) &= \mathcal{P}(y_{b,l}(i, j)), \\ \hat{y}_{a,l_1}(i, j) &= \mathcal{P}(y_{a,l_1}(i, j)) \quad \text{and}, \\ \hat{y}_{b,l_1}(i, j) &= \mathcal{P}(y_{b,l_1}(i, j)).\end{aligned}$$

Note that in our experiment with the positive object p_2^+ , because of $a = b$, we do not need the third simulation \hat{y}_{b,l_1} .

We will then create three new data sets by *adding* the object p_2 to the background p_1 using three different methods. The first method is derived from our formula (3)

$$\hat{y}_{a \rightarrow b, l_1 + l_2}(i, j) = \frac{a - be^{-l_2(i,j)}}{a} \mathcal{P}\left(\frac{be^{-l_2(i,j)}}{a - be^{-l_2(i,j)}} \hat{y}_{a,l_1}(i, j)\right),$$

and the two other methods obtain the new data by simply adding the line integrals $l_2(i, j)$ to $l_1(i, j)$

$$\begin{aligned}\hat{z}_{b, l_1 + l_2}(i, j) &= \hat{y}_{b, l_1}(i, j)e^{-l_2(i,j)}, \\ \hat{z}_{a, l_1 + l_2}(i, j) &= \hat{y}_{a, l_1}(i, j)e^{-l_2(i,j)}.\end{aligned}$$

Again, the last simulation $\hat{z}_{a, l_1 + l_2}$ is skipped for object p_2^+ , which contains only positive line integrals because $a = b$.

We reconstruct all the obtained data-sets into images using a classical fan beam, filter-back-projected reconstruction algorithm and calculate mean value and variance for all 1000 noise realizations. Results are summarized in Figures 2-5. One can see that the images from data obtained with formula (3) mean and variance agrees very well with the direct simulations and that naive approaches fail to do so.

V. CONCLUSION AND DISCUSSION

We have demonstrated a feasible and accurate statistical framework for adding synthetic objects to CT data using simulations. Simulations performed on the mathematical phantom validates the theoretical considerations when detector noise is not present. We will also present results with the real data at the conference. One of the drawbacks of our work is that we do not incorporate the object material and its spectral properties into our simulation tool, which will be a topic of our future research. Another limitation is that

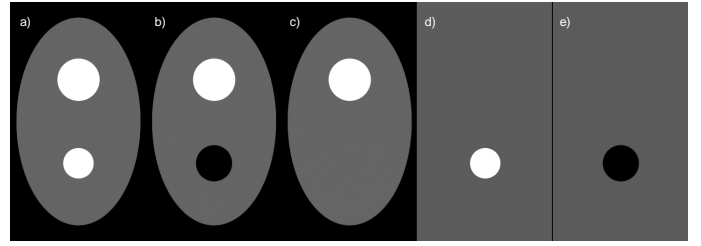


Fig. 1. Image a) represents the full phantom $p_1 + p_2^+$ and image b) represents the full phantom $p_1 + p_2^-$. Image c) represents the background p_1 . Image d) is the hyperdense object p_2^+ and e) is the hypodense object p_2^- which we add to the background. Background p_1 contains an outer ellipse with the long axis of 350mm and short axis of 210mm and HU of 0. The circle at the top has diameter of 70mm and 750HU. Hyperdense object p_2^+ is one circle at the bottom with diameter of 50mm and HU of 1000 when added to the background. Hypodense object p_2^- is one circle at the bottom with diameter of 50mm and HU of -310 when added to the background. Window for all images is 50 HU, images a) - c) are centered at 0 HU and d) and e) are centered at -1000HU.

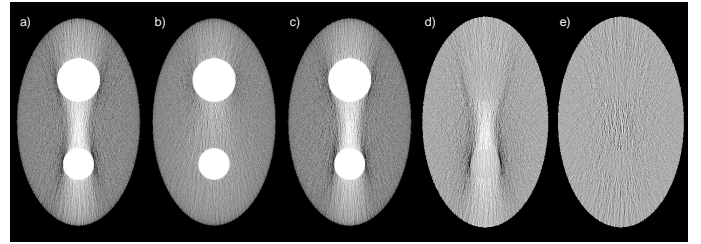


Fig. 2. Simulation results: Images a) b) and c) represent mean of reconstructions from 1000 noise realizations for the hyperdense experiment described in Section IV. Image d) is the ratio image a) divided by b) and image e) is the ratio image a) divided by c). Image a) is for the full object and data $\hat{y}_{a,l}$, image b) is for the data \hat{z}_{a,l_1} and image c) is for the data \hat{y}_{a,l_1+l_2} . Naive approach in image b) underestimated the realistic mean from image a) and our method in c) completely agrees with image a), which is also seen in the ratio images. For images a) - c) is window 50 HU and center 0HU. For images d) - e), window is 0.02 and center is 1

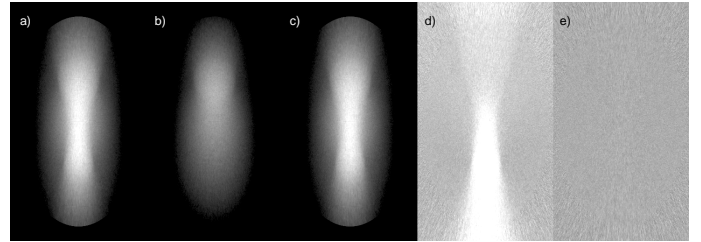


Fig. 3. Simulation results: Images a) b) and c) represent variance of reconstructions from 1000 noise realizations for the hyperdense experiment described in Section IV. Image d) is the ratio image a) divided by b) and image e) is the ratio image a) divided by c). Image a) is for the full object and data $\hat{y}_{a,l}$, image b) is for the data \hat{z}_{a,l_1} , image c) is for the data \hat{y}_{a,l_1+l_2} . Naive approach in images b) underestimated the realistic variance from image a) and our method in d) completely agrees with image a), which is also seen in the ratio images. For images a) - c) is window 6000 and center 4000HU. For images d) - e), window is 1.5 and center is 1.

the objects are inserted into the background using only the additive rule. Another interesting topic would be to develop a similar framework in case the precedence rule, which would be convenient when a user wishes to superimpose objects into the existing background. Nevertheless, with a relatively simple framework, we addressed some of the most important limitations of previously published works on this topic: in our work, objects are added statistically accurately, independently of their size and attenuation and our method does not depend on the

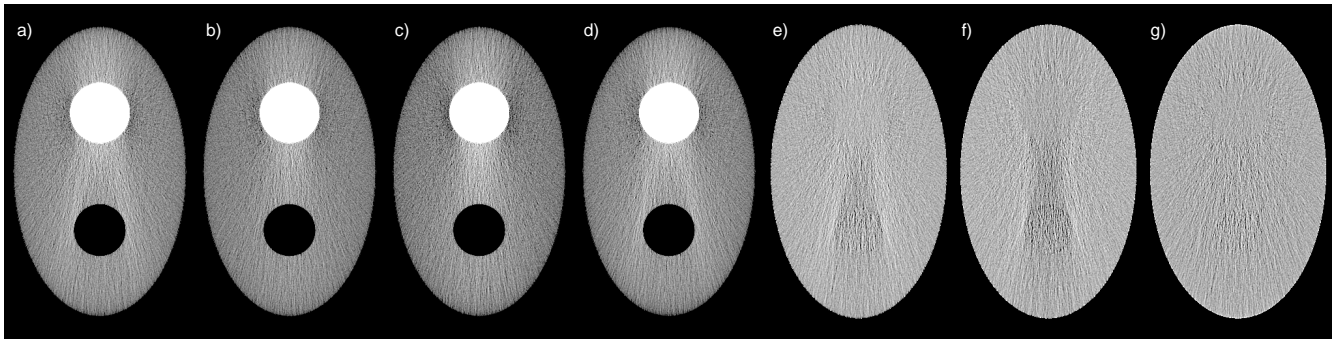


Fig. 4. Simulation results: Images a) b) c) and d) represent mean of reconstructions from 1000 noise realizations for the hypodense experiment described in Section IV. Image e) is the ratio image a) divided by b) and image f) is the ratio image a) divided by c) and image g) is the ratio image a) divided by d). Image a) is for the full object and data $\hat{y}_{b,l}$, image b) is for the data \hat{z}_{a,l_1} , image c) is for the data \hat{z}_{b,l_1} and image d) is for the data $\hat{y}_{a \rightarrow b, l_1 + l_2}$. Naive approach in images b) and c) do not agree the realistic means from image a) and our method in image d) completely agrees with image a), which is also seen in the ratio images. For images a) - d) is window 50 HU and center 0HU. For images e) - g), window is 0.02 and center is 1.

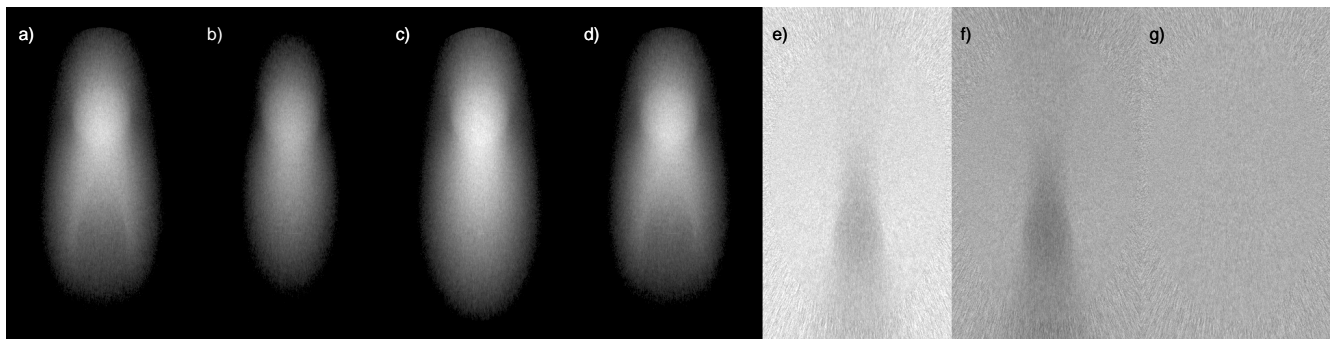


Fig. 5. Simulation results: Images a) b) c) and d) represent variance of reconstructions from 1000 noise realizations for the hypodense experiment described in Section IV. Image e) is the ratio image a) divided by b) and image f) is the ratio image a) divided by c) and image g) is the ratio image a) divided by d). Image a) is for the full object and data $\hat{y}_{b,l}$, image b) is for the data \hat{z}_{a,l_1} , image c) is for the data \hat{z}_{b,l_1} and image d) is for the data $\hat{y}_{a \rightarrow b, l_1 + l_2}$. Naive approach in images b) and c) do not agree the realistic variance from image a) and our method in image d) completely agrees with image a), which is also seen in the ratio images. For images a) - d) is window 6000 and center 4000HU. For images e) - g), window is 1.5 and center is 1.

reconstruction method, being a projection-based simulation.

REFERENCES

- [1] R. D. Ambrosini and W. G. O'Dell *Realistic simulated lung nodule dataset for testing CAD detection and sizing*, Medical Imaging 2010: Computer Aided Diagnosis, Proc. of SPIE, Vol. 7624
- [2] G. Casella and R. Berger, *Statistical Inference*, Duxbury Resource Center, Pacific Grove, CA, 2001.
- [3] C. von Falck, V. Bratanova, T. Rodt, B. Meyer, S. Waldeck, F. Wacker, H. Shin, *Influence of Sinogram Affirmed Iterative Reconstruction of CT Data on Image Noise Characteristics and Low-Contrast Detectability: An Objective Approach*, PLoS ONE 8(2): e56875.
- [4] C. von Falck, T. Rodt, S. Waldeck, D. Hartung, B. Meyer, F. Wacker, H. Shin, *A systematic approach towards the objective evaluation of low-contrast performance in MDCT: combination of a full-reference image fidelity metric and a software phantom*, European Journal of Radiology 81 (2012) 3166 3171
- [5] C. Hoe, E. Samei, D. P. Frush, D. M. Delong, *Simulation of Liver Lesions for Pediatric CT*, Radiology, vol. 238, no. 2, February 2006, 699-705
- [6] K. Karantzevelos, H. Shin, S. Jördens, B. King, K. Ringe, D. Hartung, F. Wacker, C. von Falck, *Development and Evaluation of a Software Tool for the Generation of Virtual Liver Lesions in Multidetector-Row CT Datasets*, Acad Radiol 2013; 20:614-620
- [7] X. Li, E. Samei, D. M. Delong, R. P. Jones, A. M. Gaca, C. L. Hollingsworth, C.M. Maxfield, C. W. Carrico, D. P. Frush, *Three-dimensional simulation of lung nodules for pediatric multidetector array CT*, The British Journal of Radiology, 82 (2009) 401-411.
- [8] M. T. Madsen, K. S. Berbaum, A. N. Ellingson, B. H. Thompson, B.F. Mullan, R. T. Caldwell, *A New Software Tool for Removing, Storing, and Adding abnormalities to Medical Images for Perception Research Studies*, Acad. Radiol. 2006; 13:305-312
- [9] M. T. Madsen, K. S. Berbaum, A. Ellingson, B. H. Thompson, B. F. Mullan, *Lesion removal and lesion addition algorithms in lung volumetric data sets for perception studies*, Proc. of SPIE Vol. 6146 61460T-1
- [10] M. T. Madsen, K. S. Berbaum, K. M. Schartz, R. T. Caldwell, *Improved implementation of the abnormality manipulation software tools*, Proc. of SPIE Vol. 7966 796612-1
- [11] T. Porter and T. Duff, *Compositing Digital Images*, Computer Graphics, Vol 18, No3, July 1984.
- [12] G. W. Press, B. P. Flannery, S. A. Teukolsky, W. T. Vetterling, *Numerical recipes in C (2nd ed.): the art of scientific computing*, Cambridge University Press, New York, NY, USA (1992).
- [13] H. Shin, M. Blietz, B. Frericks, S. Baus, D. Savellano, M. Galanski, *Insertion of Virtual pulmonary nodules in CT data of the chest: developments of a software tool*, Eur. Radiol. (2006), 16:2567-2574,
- [14] A. S. Wang, J. W. Stayman, Y. Otake, J. H. Siewerdsen, *Synthetic Cone-beam CT for Determining Patient- and Task-specific Minimum-dose Techniques in Repeat Scans* RSNA 2013, SST14-04
- [15] B. R. Whiting, P. Massoumzadeh, O. A. Earl, J. A. O'Sullivan, D. L. Snyder, J. F. Williamson, *Properties of preprocessed sinogram data in x-ray computed tomography*, Med Phys. 33, 3290-3303 (2006).
- [16] A. Wunderlich and F. Noo, *Image covariance and lesion detectability in direct fan-beam x-ray computed tomography*, Phys. Med. Biol. 53, 2471 2493 (2008).
- [17] S. Žabić, Q. Wang, T. Morton, K. M. Brown, *A low dose simulation tool for CT systems with energy integrating detectors*, Med Phys. 2013 Mar; 40(3):031102.

Development of a Cardiac CT Simulation Platform: an Integration of 4D Anthropomorphic Phantom with Stent Models and an Accurate CT Projector

George S.K. Fung, Karl Stierstorfer, Katsuyuki Taguchi, W. Paul Segars,
Herbert Bruder, Matthew Fuld, Thomas G. Flohr, Benjamin M.W. Tsui

Abstract – The aim of this research is to develop a cardiac CT simulation platform by integrating a realistic 4D anthropomorphic phantom, with a beating heart and coronary stent models, and an accurate CT projection data simulator. This enhanced simulation platform has the advantages of utilizing realistic models of human anatomy and coronary stent without voxelization, the realistic cardiac beating and coronary artery motion, and accurate modeling of the characteristics of clinical CT systems. First, we modeled different heart motion curves and heart rates for the 4D NURBS-based XCAT phantom to represent different cardiac beating patterns. Second, we modeled primitive-based coronary stent models using multiple stent parameters and these stent models moved according to the corresponding coronary tree motion of the XCAT phantom at different cardiac phases. Third, the DRASIM CT projection data simulator was enhanced to trigger the generation of the dynamic phantoms at the required cardiac phases before running the projection data simulation for all projection views according to the specific rotation speed and cardiac beating patterns. We employed our new simulation platform to perform a series of cardiac CT angiography simulation to study the effect of stent diameters on artificial lumen attenuation, and the effect of heart rates on the motion artifacts for stents deployed at different coronary branches. In our results, our new simulation platform shows its capability in the generation of clinically realistic cardiac CT images with realistic motion artifact. Significant increase in the error of intra-lumen attenuation is observed as the stent diameter decreases from 4mm to 2.5mm which might be caused by the system spatial resolution. Moreover, minor to moderate motion artifacts are observed for stents located in LAD and LCX at the heart rate 50 and 70 bpm whereas RCA stent suffers much more significant motion artifacts even at low heart rate. In conclusion, we have developed a unique 4D XCAT/DRASIM CT simulation platform, which provides a powerful tool for the design and optimization of CT scanners, scanning protocols, and image reconstruction methods for cardiac CTA studies.

I. INTRODUCTION

Non-invasive cardiac CT is one of the most demanding and challenging diagnostic CT applications. Due to the rapid beating heart and small and complex anatomic structure of coronary arteries, both high temporal and high spatial resolution conditions are required to virtually freeze the cardiac motion and to accurately image the fine coronary structure. Over the last few decades, various advancements in the methods and technologies of CT have been developed and progressively improving the CT image quality and lower the radiation dose for cardiac and other clinical applications [1]. At the same time, CT scanners have become exceedingly complex and any protocol or design optimization studies become a big challenge. It is impractical to optimize the large number of parameters of imaging protocols and design settings in modern CT systems based on human subject studies due to the prohibitive high cost and unnecessary radiation dose concerns. On the other hand, it is equally impractical to perform optimization studies on physical phantoms as those cannot realistically mimic the true clinical scenario in general, such as fabricating an anatomically realistic physical beating heart phantom. Therefore, the most promising practical approach to these optimization studies is through realistic computer simulation [2] using realistic human-model phantom and accurate CT simulator. It is crucially important to understand that without a highly realistic anthropomorphic phantom and a physics- and geometric-accurate CT projection data simulator, the studies might lead to clinical irrelevant, or even misleading, conclusions. Another major merit of using computer generated phantoms in simulation studies is that the exact anatomy and motion of the phantom are known, thus providing the ground truth for quantitative evaluation.

Previously, we have developed a complete CT/human-model simulation package [3] by integrating the eXtended CArdiac-Torso (XCAT) phantom [4], a computer generated Non-Uniform Rational B-Spline (NURBS) surface based phantom that provides a realistic model of human anatomy, and the Deterministic RAdiological SIMulation (DRASIM) (developed by Siemens Healthcare) CT projection data simulation program [5]. In this paper, we have further enhanced our simulation platform by modeling realistic cardiac beating motion using heart cycle curve, modeling realistic integrated models of human anatomy and coronary stent without voxelization, and adding the support of dynamic phantom by the CT projection simulator. We employed our new simulation platform to perform a series of cardiac CT angiography simulation to study the effect of stent diameters on in-stent false enhancement, and the effect

Manuscript received February 12, 2014. This work was partly supported by Siemens-JHU research grant.

G. S. K. Fung, K. Taguchi, and B. M. W. Tsui are with the Department of Radiology, Johns Hopkins University, Baltimore, MD 21287 USA (e-mail: gfung2@jhmi.edu).

K. Stierstorfer, H. Bruder, M. Fuld, and T. Flohr are with the Siemens Healthcare, Forchheim, Germany.

W. P. Segars is with the Department of Radiology, Duke University, Durham, NC 27710, USA.

of heart rates on the motion artifacts for different coronary branches and scanner settings.

II. METHODS

Essentially, the simulation platform consists of multiple components: 4D XCAT and stent phantom, DRASIM simulator, and projection data generation. The schema and data flow diagram of the integration is depicted in Figure 1.

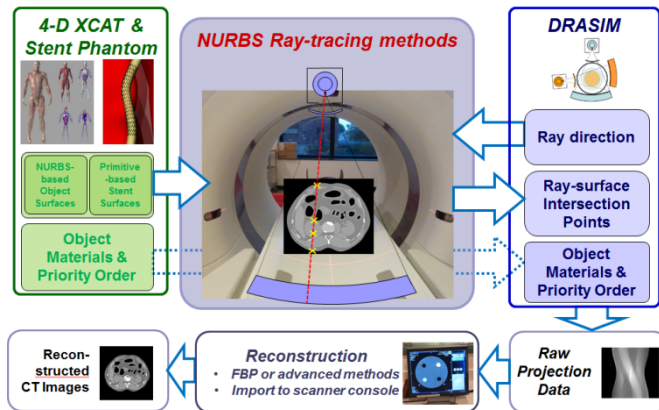


Figure 1. The schema and dataflow diagram of the 4D XCAT/DRASIM integration

A. Realistic 4D digital phantom of human and stent models

The XCAT phantom [4] is a whole-body computer model of the human anatomy based on NURBS surfaces. Unlike other phantoms based on simple mathematical primitives or voxelized phantoms, the XCAT provides an accurate representation of the complex human anatomy using over 2,000 NURBS surfaces and has the advantage that its organ shapes can be changed according to the anatomical parameters to realistically model anatomical variations of the patients. For the XCAT cardiac motion, it was originally determined from tagged MRI data of a normal human. The motion is depicted as a large collection of 3-D motion vectors with each defined for each control point in each myocardial surface: 5 surfaces for left ventricle including endocardial border, epicardial border, and 3 mid-myocardial surfaces between endo-epicardial borders; endo- and epicardial borders for right ventricle. Heart motion curve (as shown in Figure 2) could be used to define the contraction point at specific cardiac phase in which the heart deforms from end-diastole to end-systole then back to end-diastole. With the heart motion curve, the users have the capability to adjust the motion of the myocardium at any time points, the quiet phase of a cardiac cycle, and change the ratio of the duration of systole and diastole phases.

Coronary stent is a small metal framework that deployed in the coronary arteries to maintain the arteries open and the myocardial blood supply in the treatment of coronary heart disease. Basically, most stents are built by interconnecting a series of basic units which called “rings” or “cells” with “link strut”. A typical structural pattern of a ring can be approximately represented as sinusoidal curve.

In our stent model, we employed 6 parameters: location of the stent in the arteries; length and radius of the stent; the cell height; the cell gap, and the strut thickness. The rings were parallel to the tangent of the centerline of the arteries. The neighbor rings were joined together by link struts. For simplicity, we represented the stents as interconnected cylindrical struts as shown in Figure 3. The material was defined as stainless steel and the strut thickness was fixed to 0.1mm. Since the stent was deployed inside the artery, the NURBS surface of the artery was deformed to match the size and extend of the stent. Moreover, we made an assumption the motion of the arteries did not change due to deployment of stents. Therefore, the stents moved with the corresponding centerline of the moving coronary arteries.

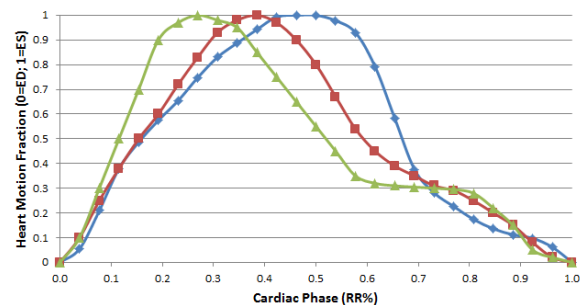


Figure 2. A number sample heart motion curves to define different heart beat motion patterns

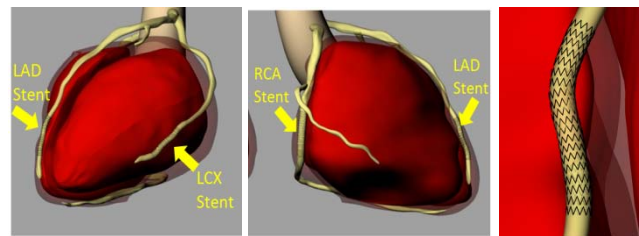


Figure 3. Rendered images of the XCAT heart phantom and stent models deployed at LAD, LCX and RCA branches

B. Accurate CT projection simulator

The DRASIM software package [5], developed by Siemens Healthcare, is a CT projection data simulation program which allows simulation of x-ray transmission data based on a narrow beam assumption. Since DRASIM is developed by the research department of the manufacturer, it has all the necessary parameters that need to accurately reproduce the projection data generated by actual Siemens clinical CT scanners. DRASIM can accurately model a detailed list of CT scanner specific parameters, such as focus size and the detector aperture with oversampling, the motion of the focal spot on the anode plate, and the polychromatic x-ray beam. However, original DRASIM only works with simple geometric phantoms composed of multiple simple geometric primitive objects, such as spheres, ellipsoids, and cylinders.

C. Projection data generation with 4D phantom

We employed the dynamic-link library (DLL) approach to integrate the 4D XCAT phantom and the DRASIM software programs. The new NURBS-based DLL was loaded into the DRASIM program when it was called at runtime only. One of the main component of the DLL was the efficient ray-tracing algorithm for NURBS surfaces, which included Bezier clipping method, bounding volume hierarchy representation, and fast ray-box intersection calculation, as part of the development of the CT projector for the XCAT phantom [6]. Due to the extremely high spatial resolution of the projection rays, additional work has been performed in fine-tuning the stopping tolerance for the recursive subdivision process in Bezier clipping method in order to achieve highly accurate ray-sum calculation. Additional logic has been designed to keep track the incident and exit sequence of the casting ray through a surface using the surface normal at intersection point in order to achieve highly robust ray-sum calculation.

As the heart and stents were at different phases at every single projection view for the simulation studies of beating heart, the XCAT and stent phantoms were needed to be generated at the specific corresponding phase at the starting of every projection view generation. The users were allowed to save all the generated phantoms at required phases to save the time for phantom generation. However, the disk space required for thousands instances of the phantoms could be extremely large.

D. Cardiac CTA simulation and evaluation

The data acquisition parameter settings of DRASIM were based on the Definition Flash dual-source CT scanner (Siemens Healthcare). The geometry settings, including source to center distance, center to detector distance, number of detector channels, number of views per rotation, fan angle of the detector, filters, and many other were specified accordingly. To isolate the beam hardening effect, a monoenergetic x-ray source of 75 keV and tube current setting of 320mAs per rotation were employed for all simulations. Oversampling of 3x3 on focus and detector elements was employed. The CT image reconstruction was performed by short-scan Parker-weighting filtered back projection. 2304 view/rot, 0.6mm collimator

The simulation platform was employed on a series of coronary CTA studies. In the first study, we studied the effect of stent diameters on artificial lumen attenuation coronary arteries and stents. The coronary arteries and the left ventricular blood pool were enhanced to 300HU. The diameters of the stents tested were ranging from 2.5mm to 4mm. Stents were deployed at all 3 arteries. To isolate the motion artifacts from spatial resolution, static phantom at mid-diastolic phase was used. The figure-of-merit was

$$\text{Artificial Lumen Attenuation (ALA)}(\%) = \left(\frac{\text{mean measured HU inside stent}}{\text{true HU inside stent}} - 1 \right) * 100\%$$

In the second study, we studied the effect of heart rates on the motion artifacts for different coronary branches. The rotation speed of the scanner was 0.28s/rotation. The beating heart model was tested at 4 different heart rates (HRs), i.e., 50, 70, 90, and 110bpm. The figure of merit used was

$$RMSE = \sqrt{\frac{1}{n_x n_y} \sum_0^{n_x-1} \sum_0^{n_y-1} [r(x,y) - t(x,y)]^2}$$

III. RESULTS AND DISCUSSIONS

As shown in Figure 4, ALA increases from 3.4% to 25.6% as the RCA stent diameter decreases from 4mm to 2.5mm due to system spatial resolution. At this slice, stents at both LAD and RCA suffer similar degradations in terms of ALA and are higher LCX for each of stent size. It could be explained as the orientations of stents at LAD and RCA are closed to vertical whereas the LCX one is oblique with the transaxial plane which leads to larger lumen area thus less effect from the system spatial resolution.

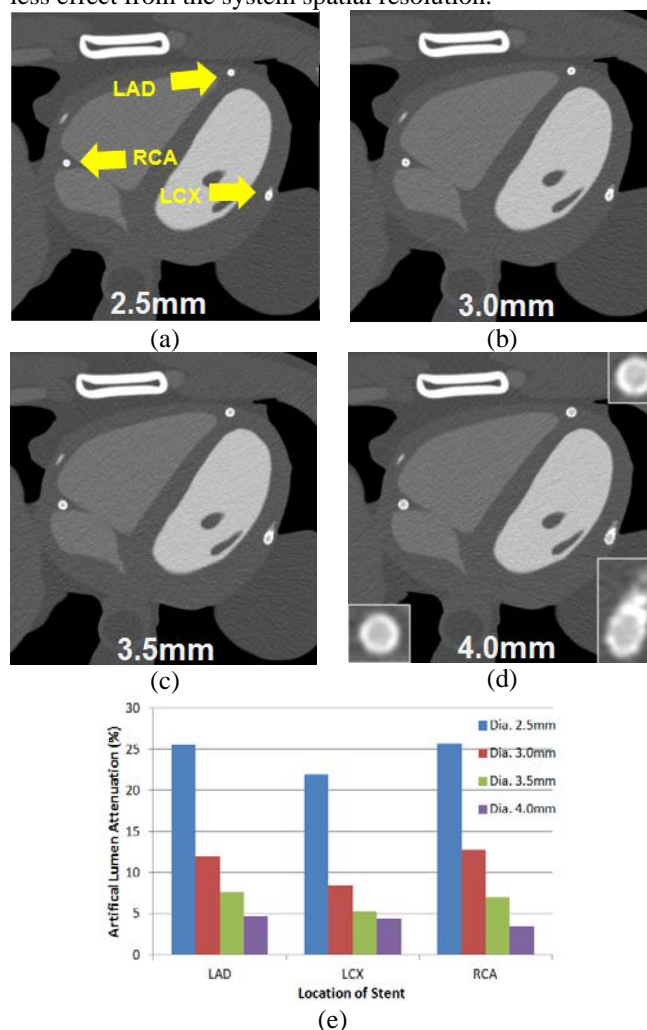


Figure 4. Coronary CTA simulation using static heart at mid-diastolic phase and the stents with the diameter of (a) 2.5mm, (b) 3.0mm, (c) 3.5mm, and (d) 4.0mm. (e) The ALA for stents with different dia. at LAD, LCX, and RCA.

As shown in Figure 5, RMSE was used to measure the degree of motion artifacts with reference to the images from static CTA simulation. It is apparent that the simulated CTA images the blood pool border of left ventricle suffers significant motion artifacts at high heart rates (70, 90 and 110 bpm). For all heart rates, LAD stents always suffer the least motion artifacts, LCX stents suffer intermediate artifacts, and RCA stents suffer the most serious motion artifacts. It is fully explainable as, it is known that, in most patients, LAD has least motion whereas RCA has the biggest motion. Also, qualitatively, we also observe that LAD and LCX suffer minor to moderate motion artifacts at the heart rate 50 and 70 bpm. However, RCA suffers very significant motion artifacts even at heart rate as low as 50bpm.

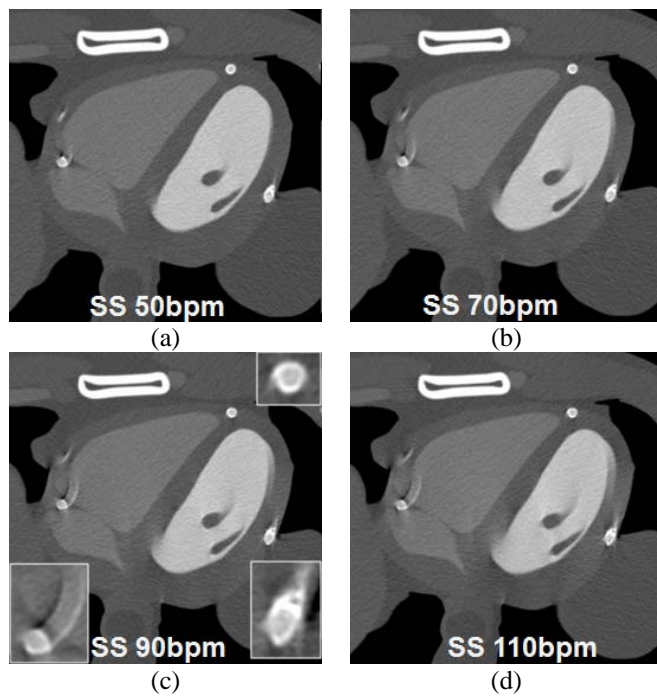


Figure 4. Coronary CTA simulation with single-source CT with coronary stents and heart beating at (a) 50bpm, (b) 70bpm, (c) 90 bpm, and (d) 110bpm. (e) The ALA for stents with different heart rates at LAD, LCX, and RCA.

We have further investigated the effect of different scanning protocols, which are single source and dual source scan modes, on motion artifacts at different heart rates and stent locations. We have found DSCT achieves lower RMSE than SSCT for all HRs and all stent locations. For *LAD* & *LCX*, DSCT provides moderate motion artifacts improvement depending on HRs (~19% on avg.). For *RCA*, DSCT achieves dramatic improvement in RMSE than using SSCT (~36%), but still suffers from significant motion artifacts, especially at high HRs

IV. CONCLUSION

In conclusion, we have developed a unique 4D XCAT/DRASIM CT simulation platform, which enables highly realistic cardiac CTA simulation with clinical CT systems. The platform provides a powerful tool for the design and optimization of CT scanners, scanning protocols, and image reconstruction methods for cardiac CTA studies. We have utilized the new platform for the evaluation of our newly developed motion compensation methods for the reduction of motion artifacts [7].

ACKNOWLEDGEMENT

We thank Drs. E. Fishman and S. Kawamoto for their helpful discussions and suggestions.

REFERENCES

- [1] Ohnesorge, B.M., Flohr, T.G., Becker, C.R., Knez, A., and Reiser, Multi-slice and dual-source CT in cardiac imaging, 2nd ed., Springer-Verlag (2007).
- [2] Segars, W. P. and Tsui, B. M. W., "MCAT to XCAT: The evolution of 4-D computerized phantoms for imaging research," Proceedings of the IEEE, 97(12), 1954-1968 (2009).
- [3] Fung G.S.K., Stierstorfer K., et al., "A realistic CT/Human-Model Simulation Package," Proc. 2nd Int. Conf. on Image Formation in X-ray CT, 66-69 (2012).
- [4] Segars, W. P., Sturgeon, G., Mendonca, S., Grimes, J., and Tsui, B. M. W., "4D XCAT phantom for multimodality imaging research," Medical Physics, 37(9), 4902-4915 (2010).
- [5] Stierstorfer, K., "DRASIM: A CT-simulation tool," Internal Report, Siemens Healthcare.
- [6] Segars, W. P., Mahesh, M., Beck, T.J., Frey, E. C., and Tsui, B. M. W., "Realistic CT simulation using the 4D XCAT phantom," Medical Physics, 35(8), 3800-3808 (2008).
- [7] Bruder, H., Fung G.S.K., Rohkohl C., Allmendinger T., and Stierstorfer, K., "Validation of Motion Artifact Metric Optimization Reconstruction (MAM)," submitted to 3rd CT Meeting (2014).

Axial Cone Beam BPF/DBPF Reconstruction with 3D Weighting and Butterfly Filtering

Shaojie Tang, Wenqing Wang and Xiangyang Tang*

Abstract— The backprojection-filtration and differentiated backprojection with Hilbert filtering (BPF/DBPF) algorithms are originally derived for exact helical and axial image reconstruction from cone beam (CB) and fan beam projection data, respectively. To extend their applications in axial CB scan for reconstruction of three-dimensional (3D) images, we have proposed its integration with a 3D weighting scheme (namely 3D weighted CB-BPF/DBPF algorithm), in which we've found that, the artifacts due to cone angle can be significantly reduced by the 3D weighting, but the post-backprojection (post-BP) Hilbert filtering induces severe streak artifacts in images located away from the central plane determined by the circular source trajectory. To eliminate the streak artifacts caused by the post-BP Hilbert filtering, we propose to integrate the 3D weighted axial CB-BPF/DBPF algorithm with paired Butterfly filtering in this paper. Using the Forbield head phantom that is rigorous in reconstruction accuracy inspection, we evaluate the proposed algorithm and verify that, by incorporating the paired Butterfly filtering, the 3D weighted axial CB-BPF/DBPF algorithm at least performs as well as the 3D weighted axial CB-FBP algorithm in reconstruction accuracy.

Index Terms— Reconstruction, Filtered backprojection, Backprojection-filtration, Differentiated backprojection

I. INTRODUCTION

Approximate cone beam (CB) reconstruction algorithms for a circular trajectory (namely axial CB scan) have been extensively employed in CT imaging for medical and industrial applications [1, 2]. However, since the circular trajectory does not satisfy the data sufficiency condition (DSC) [3], CB artifact appears and worsens with increasing cone angle. Though the reconstruction algorithms associated with helical/spiral [4-9] or 'circle plus' [10-11] trajectories have been proposed to meet the DSC, the axial CB scan is still the most desirable in practice for physiological and interventional imaging in the clinic, which drives the CT image reconstruction community to explore solutions for reducing, if not eliminating, CB artifacts existing in the images reconstructed from axial CB scan data, especially when the cone angle becomes relatively large [12].

Weighting schemes have been proposed for CB filtered backprojection (CB-FBP) algorithms to reduce the artifacts

caused by cone angle to a clinically acceptable level. Among all the solutions in this category, the three-dimensional (3D) weighted CB-FBP algorithm is of merit and has found its applications in clinical multi-detector row CT scanners [9, 12]. By giving a favorable weight to the ray out of a conjugate ray pair with the smaller cone angle, the artifacts due to conjugate ray inconsistency and longitudinal detector truncation, both are consequences of the cone angle, can be effectively reduced.

The algorithms of backprojection-filtration and differentiated backprojection with Hilbert filtering algorithm (BPF/DBPF henceforth) are originally derived for exact helical and axial image reconstruction from cone beam and fan beam projection data, respectively [7, 13]. Its major advantage is the capability of reconstructing a region of interest (ROI), leading to the success of dealing with data truncation in practical situations wherein data truncation is inevitable. To extend the BPF/DBPF algorithm's application in axial CB scan, we have proposed to integrate the BPF/DBPF algorithm with 3D weighting (namely 3D weighted axial CB-BPF/DBPF algorithm) [14]. Preliminary results show that the 3D weighted CB-BPF/DBPF algorithm can work as well as the 3D weighted CB-FBP algorithm in terms of CB artifact reduction. However, the post-BP Hilbert filtering is in fact not accurate (see section V), resulting in severe streak artifacts along the Hilbert filtering's orientation in reconstructed images at the spots where the object varies abruptly [14-16].

Recently, the so-called Butterfly filtering has been proposed by Pack *et al* to reduce the artifacts caused by the data null and redundancy in a partial (270°) CB scan [17]. With resort to a pair of orthogonal Butterfly filters in spatial-frequency domain, the artifacts caused by the data null and redundancy can be mitigated to an unnoticeable level. Recognizing the fact that the artifact generated by the post-BP Hilbert filtering in the 3D weighted CB-BPF/DBPF algorithm is orientation-specific and the Butterfly filtering is good at suppressing orientation-specific artifacts, we propose in this paper to incorporate the Butterfly filtering into the 3D weighted axial CB-BPF/DBPF algorithm (namely 3D weighted axial CB-BPP/DBPF with Butterfly filtering) and conduct an evaluation to verify its performance.

II. THEORETICAL BACKGROUND

The derivation of BPF and DBPF algorithms starts at different points, but ends up with a common algorithmic structure. We present the proposed algorithm under the DBPF framework.

A. CB Geometries for Axial Scan and Reconstruction

The native CB geometry is shown in Fig. 1 (a), where O - xyz represents the coordinate system. S is the focal spot of x-ray

Manuscript received on Jan. 31, 2014. This work was partially supported by NIH (grant P50-AG025688).

Shaojie Tang and Wenqing Wang are with the School of Automation, Xi'an University of Posts and Telecommunications, Xi'an, Shaanxi 710121, China. Shaojie Tang was also with the Department of Radiology and Imaging Sciences, Emory University, Atlanta, USA. (e-mail: tangshaojie@xupt.edu.cn)

Xiangyang Tang is with the Department of Radiology and Imaging Sciences, Emory University School of Medicine, Atlanta, GA 30322, USA, (*corresponding author e-mail: xiangyang.tang@emory.edu).

source, and $P(x, y, z)$ denotes a point within the object to be imaged. The ray emanating from S and passing $P(x, y, z)$ is determined by its view angle η , fan angle γ , and cone angle α . In the native CB geometry, the circular trajectory is expressed as

$$ST(\eta) = (R \sin \eta, R \cos \eta, 0), \eta \subseteq (\eta_{\min}, \eta_{\max}), \quad (1)$$

where η_{\min} and η_{\max} denote start and end of the source trajectory.

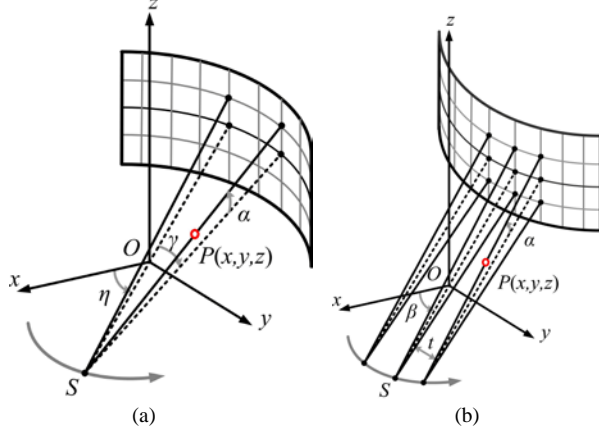


Fig. 1. The schematic of native cone beam (a) and cone-parallel (b) geometries.

Through a row-wise fan-to-parallel rebinning, the native CB geometry is converted into the cone-parallel geometry shown in Fig. 1 (b). The ray emanating from focal spot S and passing through $P(x, y, z)$ is uniquely determined by its view angle β , distance t from the axis of rotation (AOR), and cone angle α . In the cone-parallel geometry, significantly improved noise uniformity and image generation speed can be attained.

B. Conjugate Ray Inconsistency in Cone-parallel Geometry

The conjugate ray inconsistency means that, due to cone angle, the conjugate rays that are 180° apart in β are not identical. In the cone-parallel geometry, the ray corresponding to $(\alpha_c, \beta_c, t_c) = (\alpha_c, \pi + \beta, -t)$ is conjugate to the ray associated with (α, β, t) .

C. Axial CB-FBP Algorithm in Cone-parallel Geometry

The 3D weighted axial CB-FBP algorithm in the cone-parallel geometry can be expressed as [9, 12]

$$f(x, y, z) \approx \frac{\pi}{\beta_{\max} - \beta_{\min}} \int_{\beta_{\min}}^{\beta_{\max}} \cos \alpha w_{3d}(\alpha, \beta, t, l) \tilde{s}(\alpha, \beta, t) d\beta, \quad (2)$$

$$\tilde{s}(\alpha, \beta, t) = s(\alpha, \beta, t) \otimes h(t), \quad (3)$$

where $h(t)$ is the ramp filtering kernel in parallel beam, and $s(\alpha, \beta, t)$ denotes the rebinned projection data. Let l denote the distance between the image and central planes, the weighting function $w_{3d}(\alpha, \beta, t, l)$ meets the normalization condition

$$w_{3d}(\alpha, \beta, t, l) + w_{3d}(\alpha_c, \beta_c, t_c, l) = 1. \quad (4)$$

In a full scan ($\beta_{\max} - \beta_{\min} = 2\pi$), $w_{3d}(\alpha, \beta, t, l)$ is designed as [13]

$$w_{3d}(\alpha, \beta, t, l) = w_{3d}(\alpha, l) = \frac{\tan^{k(|l|)}(|\alpha_c|)}{\tan^{k(|l|)}(|\alpha_c|) + \tan^{k(|l|)}(|\alpha|)}. \quad (5)$$

D. Axial BFP/DBPF Algorithm in Cone-parallel Geometry

If we modify the definition of $\tilde{s}(\alpha, \beta, t)$ in Eq. (3) as

$$\tilde{s}(\alpha, \beta, t) = \frac{\partial}{\partial t} s(\alpha, \beta, t). \quad (6)$$

Eq. (2) can be converted into

$$-2\pi H_\theta f(x, y, z) \approx b_\theta(x, y, z) = \frac{\pi}{\beta_{\max} - \beta_{\min}} \int_{\beta_{\min}}^{\beta_{\max}} \cos \alpha w_{3d}(\alpha, \beta, t, l) \operatorname{sgn}(\sin(\beta - \theta)) \tilde{s}(\alpha, \beta, t) d\beta, \quad (7)$$

where H_θ denotes the Hilbert transform along the direction $(-\sin\theta, \cos\theta, 0)$ [7, 13]. Using a finite Hilbert inverse transform, one can approximately determine the object function $f(x, y, z)$ from the differentiated backprojection (DBP) image $b_\theta(x, y, z)$.

E. Butterfly Filtering

Pack *et al* proposed the approach of Butterfly filtering to deal with the data null and redundancy in spatial-frequency domain corresponding to a partial $[0^\circ, 270^\circ)$ CB scan [17]. Illustrated in Fig. 2 is an example of the Butterfly filter pair.

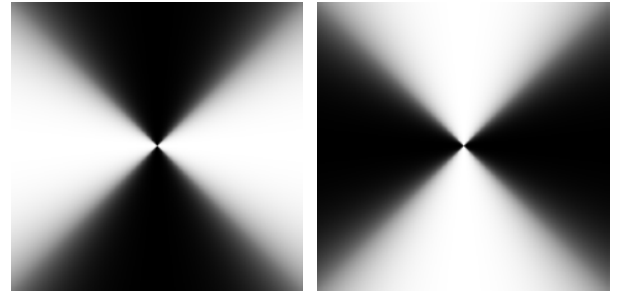


Fig. 2. A pair of Butterfly filters that are orthogonal in the frequency domain.

III. NUMERICAL EVALUATION

A. Parameters of CT System, Scan and 3D Weighting

The proposed algorithm is evaluated using the Forbild head phantom [18] simulated in an axial scan under the native CB geometry and rebinned into the cone-parallel geometry. In computer simulation, the distance from x-ray source to the AOR of CT gantry is assumed 541.0mm and the detector is with 64×0.625 mm z-dimension at the AOR. 1160 projection views are acquired along the angular range $[0^\circ, 360^\circ)$. The weighting parameter $k(|l|)$ in $w_{3d}(\alpha, \beta, t, l)$ is empirically determined in Ref. [12] and reused here. The matrix of reconstructed transaxial images is 512×512 , with a field of view (FOV) 256×256 mm², leading to a voxel size $0.5 \times 0.5 \times 0.625$ mm³.

B. Scan Range and post-BP Hilbert Filtering Orientation

The full axial scan data are used to evaluate the proposed algorithm. According to Ref. [7, 13], as a full scan corresponds to angular range $[0^\circ, 360^\circ)$, there should be no limitation on the orientation along which the post-BP Hilbert filtering is carried out. We carry out the post-BP Hilbert filtering and the Butterfly filtering along the 0° (horizontal in reconstructed image) and 90° (vertical) directions, respectively. As an extension, we also investigate the case wherein only partial scan data in angular range $[0^\circ, 270^\circ)$ is available. By decomposing $[0^\circ, 270^\circ)$ into two sub-angular ranges $[0, 180^\circ)$ and $[90^\circ, 270^\circ)$, the post-BP

Hilbert filtering and Butterfly filtering can only be implemented along the 0° and 90° directions, respectively, according to Ref. [7, 13]. Note that no 3D weighting is implemented in the partial scan case since not every ray is associated with a conjugate ray.

IV. PRELIMINARY RESULTS

In the performance evaluation and verification, the outermost slice is selected as the reconstruction plane. Presented in Fig. 3 (a) and (b) are images reconstructed by the CB-FBP algorithm without and with the 3D weighting, respectively, and that in Fig. 3 (c) is their difference. Fig. 3 clearly shows that CB artifact is significantly reduced, if not eliminated, by the 3D weighting in the CB-FBP algorithm.

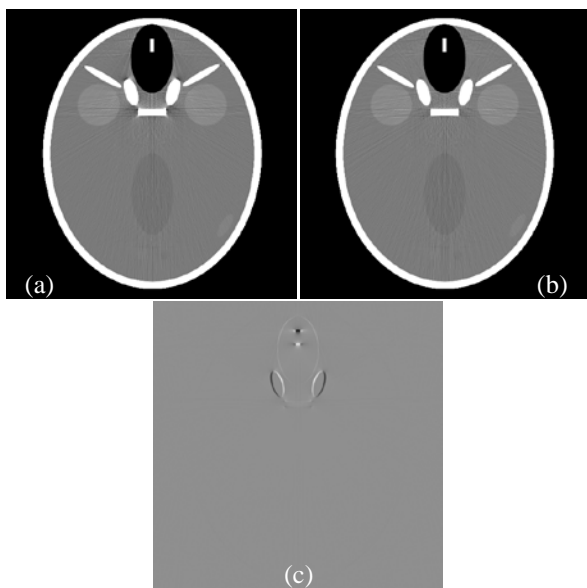


Fig. 3. Images reconstructed from full (360°) axial scan data by the CB-FBP algorithm without (a) and with (b) 3D weighting, and their difference (c).

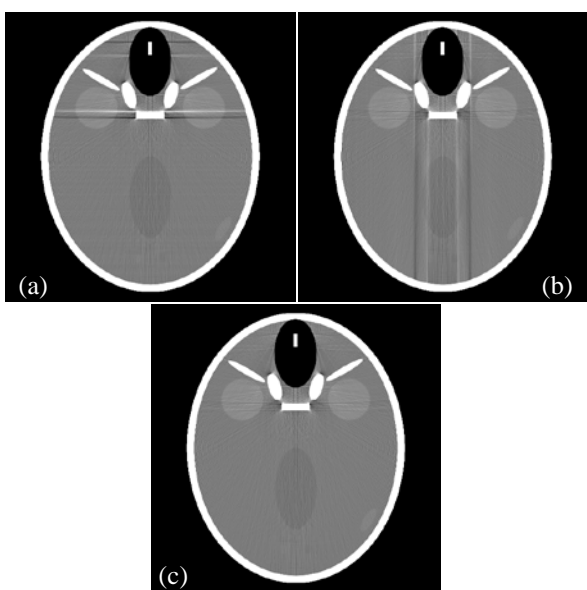


Fig. 4. Images reconstructed from CB full-scan data by the axial CB-BPF/DBPF algorithm without 3D weighting and with the Hilbert filtering carried out at orientation of (a) 0° and (b) 90° , and (c) the synthesized image.

Presented in Fig. 4 (a) and (b) are the images reconstructed by the CB-BPF/DBPF algorithm from full scan data with the Hilbert filtering carried out along 0° and 90° , respectively, in which no 3D weighting is employed. By applying the Butterfly filter pair on the images in Fig. 4 (a) and (b), we get the synthesized image in Fig. 4 (c), showing that the artifacts caused by the post-BP Hilbert filtering along both horizontal and vertical directions can be reduced, if not removed, to a unnoticeable level. The layout of Fig. 5 is the same as that in Fig. 4, except for that the images are reconstructed by the CB-BPF/DBPF algorithm with the 3D weighting. Presented in Fig. 5 (d) is the difference between the images in Fig. 4 (c) and Fig. 5 (c), showing that the 3-D weighting indeed reduces the CB artifacts significantly, while the artifact caused by the Hilbert filtering are eliminated by the paired Butterfly filtering.

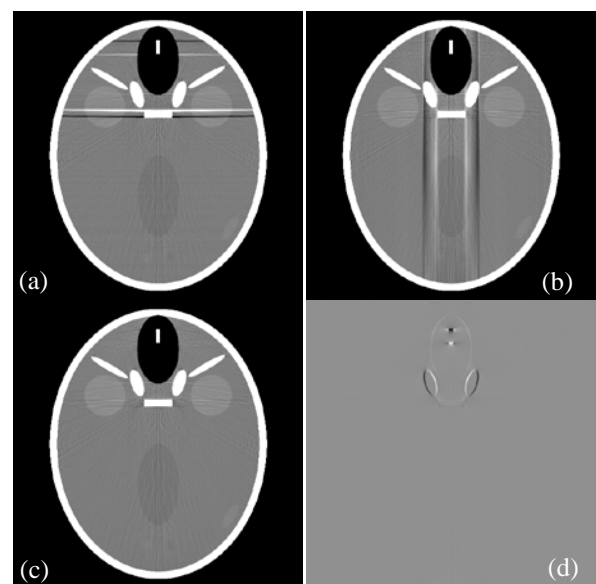


Fig. 5. Images reconstructed from CB full-scan data by the axial CB-DBPF algorithm with 3D weighting with the Hilbert filtering carried out at orientation of (a) 0° and (b) 90° , and (c) the synthesized image, as well as (d) the difference between Fig. 4 (c) and Fig. 5 (c).

Displayed in Fig. 6 (a) and (b) are the images reconstructed by the CB-BPF/DBPF algorithm from data in the angular ranges $[0^\circ, 180^\circ)$ and $[90^\circ, 270^\circ)$, respectively. Note that no 3D weighting can be applied in the reconstruction to get these two images, since only half-scan data in the cone-parallel geometry is available in each case. Hence, CB artifact exists in the image shown in Fig. 6 (c), while the streak artifacts are removed by the paired Butterfly filtering. It should be noted that, to obtain the projection data within the range $[0^\circ, 270^\circ)$ in the cone-parallel geometry, the corresponding angular range in the native CB geometry is larger than $[0^\circ, 270^\circ)$ but smaller than $[0^\circ, 360^\circ)$.

V. DISCUSSIONS AND CONCLUSIONS

A 3D weighted axial CB-BPF/DBPF algorithm integrated with paired Butterfly filtering is proposed here for CB image reconstruction from axial CB scan data. The 3D weighting has been previously proposed by us for the CB-DBPF to suppress CB artifacts, while the paired Butterfly filtering proposed here

is to suppress the severe streak artifacts caused by the post-BP Hilbert filtering. Since the BPF/DBPF algorithm for image reconstruction in CB axial scan is theoretically approximate, the performance of the proposed algorithm needs to be investigated thoroughly. In this work, we conduct a performance evaluation via simulation study, and the preliminary results show that the integration of 3-D weighting with paired Butterfly filtering in the CB-BPF/DBPF algorithm works well as anticipated, enabling the proposed algorithm for CB axial scan wherein the cone angle is relatively large.

We used to speculate that the occurrence of severe streak artifacts after the post-BP Hilbert filtering in the 3D weighted CB-BPF/DBPF algorithm [14] may be due to a corruption by the residual CB artifact that cannot be removed by the 3D weighting. It is our current understanding that the BPF/DBPF algorithm is originally derived for exact helical reconstruction on PI-lines/chords and exact axial reconstruction from fan beam projection data, respectively [7, 13]. In axial CB scan, once the image plane is away from the central plane determined by the x-ray source trajectory, the BPF/DBPF algorithm is no longer accurate. Fortunately, the reconstruction inaccuracy mainly manifests itself as streak artifacts aligned with the orientation along which the Hilbert filtering is carried out. Thus, the paired Butterfly filtering that is orientation-specific can be utilized to remove the streak artifacts effectively and efficiently [17]. However, it should be noted that the paired Butterfly filtering may compromise the proposed algorithm's capability of dealing with data truncation, because, two orthogonal directions, other than just one direction in the original BPF/DBPF algorithm, have to be taken care in the reconstruction.

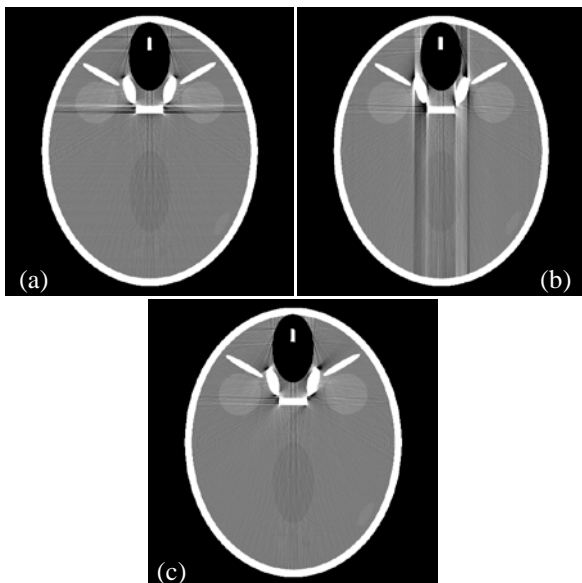


Fig. 6. Images obtained by the axial CB-DBPF algorithm without 3D weighting from data in angular range $[0^\circ, 180^\circ)$ (a) and $[90^\circ, 270^\circ)$ (b), corresponding to Hilbert filtering carried out at 0° and 90° , respectively. The image in (c) is synthesized from (a) and (b) via paired Butterfly filtering.

We believe that the proposed 3D weighted axial CB-BPF/DBPF algorithm is novel from the standpoint of reconstruction algorithm development, though its extension

from the original BPF/DBPF algorithm [7, 13] to the algorithm proposed in this work is quite heuristic. In addition, we'd like to indicate that, under the BPF algorithmic framework, an axial CB-BPF reconstruction algorithm has been proposed in the literature [15]. It is believed that the 3D weighting scheme and Butterfly filtering presented in this paper are also applicable to the CB-BPF algorithm published in Ref. [15]. Further work to investigate the proposed algorithm's robustness over noise and larger cone angle is under the way and the results will be promptly reported in our near future publication.

REFERENCES

- [1] L. A. Feldkamp, L. C. Davis and J. W. Kress, "Practical cone-beam algorithm," *J. Opt. Soc. Am. A*, vol.1, pp.612, 1984.
- [2] G. Wang, T. H. Lin, P. C. Cheng and D. M. Shinozaki, "A general cone-beam reconstruction algorithm," *IEEE Trans. Med. Imaging*, vol.12 pp.486, 1993.
- [3] H. Tuy, "An inversion formula for cone-beam reconstruction," *SIAM J. Appl. Math.*, vol.43, pp.546, 1983.
- [4] H. Kudo, F. Noo and M. Defrise, "Cone-beam filtered-backprojection algorithm for truncated helical data," *Phys. Med. Biol.*, vol.43, pp.2885, 1998.
- [5] M. Defrise, F. Noo and H. Kudo, "A solution to the long-object problem in helical cone-beam tomography," *Phys. Med. Biol.*, vol.45, pp.623, 2000.
- [6] A. Katsevich, "Analysis of an exact inversion algorithm for spiral cone-beam CT," *Phys. Med. Biol.*, vol.47, pp.2583, 2002.
- [7] Y. Zou and X. Pan, "Exact image reconstruction on PI-lines from minimum data in helical cone-beam CT," *Phys. Med. Biol.*, vol.49, pp.941, 2004.
- [8] X. Tang and J. Hsieh, "A filtered backprojection algorithm for cone beam reconstruction using rotational filtering under helical source trajectory," *Med. Phys.*, vol.31, pp.2949, 2004.
- [9] X. Tang, J. Hsieh, R. A. Nilsen, S. Dutta, D. Samsonov and A. Hagiwara, "A three-dimensional-weighted cone beam filtered backprojection (CB-FBP) algorithm for image reconstruction in volumetric CT-helical scanning," *Phys. Med. Biol.*, vol.51, pp.1, 2006.
- [10] F. Noo, R. Clack, T. A. White and T. J. Roney, "The dual-ellipse cross vertex path for exact reconstruction of long objects in cone-beam tomography," *Phys. Med. Biol.*, vol.43, pp.797, 1998.
- [11] X. Tang and R. Ning, "A cone beam filtered back-projection (CB-FBP) reconstruction algorithm for a circle-plus-two-arc orbit," *Med. Phys.*, vol.28, pp.1042, 2001.
- [12] X. Tang, J. Hsieh, A. Hagiwara, R. A. Nilsen, J-B Thibault and E. Drapkin, "A three-dimensional weighted cone beam filtered backprojection (CB-FBP) algorithm for image reconstruction in volumetric CT under a circular source trajectory," *Phys. Med. Biol.*, vol.50, pp.3889, 2005.
- [13] F. Noo, R. Clackdoyle and J. D. Pack, "A two-step Hilbert transform method for 2D image reconstruction," *Phys. Med. Biol.*, vol.49, pp.3903, 2004.
- [14] X. Tang, S. Tang and Y. Yang, "Improving axial image reconstruction by off-centering ROI with data truncation and 3D weighted cone beam DBPF algorithm," *The 11th International Meeting on Fully Three-Dimensional Image Reconstruction in Radiology and Nuclear Medicine*, pp.371, Potsdam, Germany, 2011.
- [15] L. Yu, Y. Zou, E. Y. Sidky, C. A. Pelizzari, P. Munro and X. Pan, "Region of interest reconstruction from truncated data in circular cone-beam CT," *IEEE Trans. Med. Imaging*, vol.25, pp.869, 2006.
- [16] D. Schäfer, M. Grass and P. van de Haar, "FBP and BPF reconstruction methods for circular X-ray tomography with off-center detector," *Med. Phys.*, vol.38, pp.S85, 2011.
- [17] J. D. Pack, Z. Yin, K. Zeng and B. E. Nett, "Mitigating cone-beam artifacts in short-scan CT imaging for large cone-angle scans," *The 12th International Meeting on Fully Three-Dimensional Image Reconstruction in Radiology and Nuclear Medicine*, pp.300, Potsdam, Germany, 2013.
- [18] G. Lauritsch and H. Bruder, "head phantom," <http://www.imp.uni-erlangen.de/phantoms/head/head.html>, 1998.

Reduction of Cone Artifacts in CT with Incomplete Source Trajectories

Johan Sunnegårdh, Harald Schöndube, Thomas Flohr

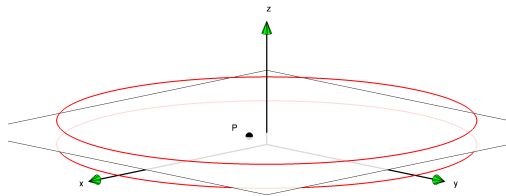


Fig. 1. Incompleteness of circular x-ray source trajectory.

Abstract—In medical CT, incomplete x-ray source trajectories such as the circular and high-pitch dual source helical trajectories are frequently used, mainly due to their superior temporal properties. The increasingly large detectors of modern CT systems in combination with data incompleteness may lead to image artifacts. We present a modified Regularized Iterative Filtered Backprojection (RIFBP) algorithm which allows for improved reduction of these artifacts by incorporating certain prior knowledge. Unlike iterative methods employing non-quadratic regularization, e.g. ℓ^1 -norm minimization, the prior knowledge is only used for reducing artifacts and does not affect resolution or noise texture notably. Experiments on high-pitch dual source scans of an anthropomorphic thorax phantom demonstrate the improved artifact reduction of the proposed method.

I. INTRODUCTION

In cone-beam computed tomography, to allow for exact and stable image reconstruction, the x-ray source trajectory has to satisfy the Tuy-Smith condition [1], [2]: for each point P in the object to be reconstructed, all planes containing P are required to intersect the x-ray source trajectory at least once. Data are assumed to be untruncated. Therefore, only x-ray source points that contribute with measurements of P are to be considered.

In medical applications X-ray source trajectories that do not satisfy the Tuy-Smith condition are frequently used. Examples of such trajectories are the single/multiple circle trajectory and the High-Pitch Dual Source (HPDS) trajectory [3]. Although these trajectories do not allow for exact reconstruction, they have advantages in situations where high temporal resolution is required.

Fig. 1 illustrates data acquisition with two circular x-ray source trajectories. Obviously, if the point P is outside the planes defined by the source trajectories, no near-axial planes passing through P intersect any of the source trajectories.

Fig. 2 illustrates the situation for HPDS data acquisition with pitch factor 3.2. Here, each source-detector system illuminates the point P slightly more than 90° . Between the

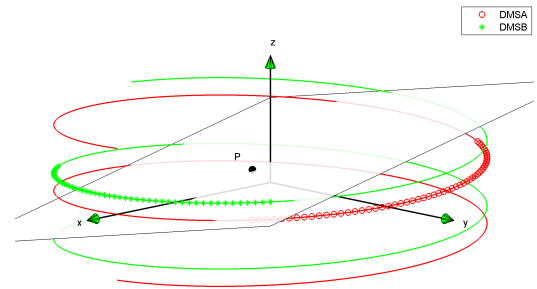


Fig. 2. Incompleteness of the HPDS x-ray source trajectory with a pitch factor of 3.2. The red o-markings and green *-markings indicate segments of x-ray source trajectories contributing with measurements of P .

two contributing source trajectory segments, planes that do not intersect any of the contributing trajectories can be placed.

Cone artifacts, *i.e.*, artifacts that are directly related to the cone beam geometry of the data acquisition, are caused by (i) non-exactness of the reconstruction algorithm and (ii) by incomplete data. Artifacts caused by the non-exactness of the reconstruction algorithm can be suppressed by linear (Regularized) Iterative Filtered Backprojection (RIFBP) methods [4], while incomplete data artifacts require incorporation of some kind of additional information.

In the following section, RIFBP and related notation are introduced. This is followed by a presentation of Edge-RIFBP, which improves reconstruction by incorporating prior information about the sharpness of high-contrast edges. Edge-RIFBP was previously proposed in [5] as a method for wind-mill artifact reduction. In the results section, reconstructions without iteration (Weighted Filtered Backprojection (WFBP) [6]), reconstruction with linear RIFBP, and results with Edge-RIFBP are compared. Finally, conclusions and open points are summarized.

II. MATERIALS AND METHODS

A. Regularized Iterative Filtered Backprojection (RIFBP)

In the past, Iterative Filtered Backprojection (IFBP) methods have been successfully applied for artifact reduction in a wide variety of tomographic reconstruction problems. A review of early works on IFBP is found in [7].

We use a vector/matrix notation for representing images and data, and linear operations. The vector $\mathbf{p}_{\text{in}} \in \mathbb{R}^M$ denotes input projection data and the vector $\mathbf{f} \in \mathbb{R}^N$ denotes an image. The matrix $\mathbf{Q} \in \mathbb{R}^{N \times M}$ denotes a reconstruction operator, and the matrix $\mathbf{P} \in \mathbb{R}^{M \times N}$ denotes a forward projector. In our case, \mathbf{Q} is the Weighted Filtered Backprojection (WFBP) [6], and \mathbf{P} is the forward projection by Joseph [8].

The authors are with Siemens Healthcare, Forchheim, Germany

Typically, RIFBP is initialized with a WFBP reconstruction $\mathbf{f}_0 = \mathbf{Q}\mathbf{p}_{\text{in}}$. This is followed by iterative application of the RIFBP update equation

$$\mathbf{f}_{k+1} = \mathbf{f}_k - \alpha(\mathbf{Q}(\mathbf{P}\mathbf{f}_k - \mathbf{p}_{\text{in}}) + \beta\mathbf{R}\mathbf{f}_k) \quad (1)$$

The regularization operator $\mathbf{R} \in \mathbb{R}^{N \times N}$ is a high-pass filter which, in combination with the parameter β , controls the smoothness of the final result.

For a better understanding of the role of $\beta\mathbf{R}$, we note that $\mathbf{Q}\mathbf{P} \in \mathbb{R}^{N \times N}$, *i.e.* forward projection followed by reconstruction, can be approximated as a low-pass filtering $\mathbf{L} \in \mathbb{R}^{N \times N}$ plus artifact generation $\mathbf{A} \in \mathbb{R}^{N \times N}$:

$$\mathbf{Q}\mathbf{P} = \text{Smoothing}(\mathbf{L}) + \text{Artifact generation}(\mathbf{A}). \quad (2)$$

By substituting $\mathbf{R} = (\mathbf{I} - \mathbf{L})/\beta$ in (1), where \mathbf{L} is an approximation of the smoothing due to interpolations in $\mathbf{Q}\mathbf{P}$ and the apodization of the rampfilter in \mathbf{Q} , we get

$$\begin{aligned} \mathbf{f}_{k+1} &= (1 - \alpha)\mathbf{f}_k + \alpha(\mathbf{L}\mathbf{f}_k + \mathbf{Q}(\mathbf{p}_{\text{in}} - \mathbf{P}\mathbf{f}_k)) \quad (3) \\ &= (1 - \alpha)\mathbf{f}_k + \alpha(\mathbf{Q}\mathbf{p}_{\text{in}} - \underbrace{(\mathbf{Q}\mathbf{P} - \mathbf{L})}_{\text{artifact operator } \mathbf{A}} \mathbf{f}_k) \quad (4) \end{aligned}$$

Thus, for $\alpha = 1$, the update step may be seen as subtracting of artifacts $(\mathbf{Q}\mathbf{P} - \mathbf{L})\mathbf{f}_k$ from an image $\mathbf{Q}\mathbf{p}_{\text{in}}$ which has artifacts. Note that if \mathbf{L} is smoother than $\mathbf{Q}\mathbf{P}$ (β high), the result becomes smoother than $\mathbf{Q}\mathbf{p}_{\text{in}}$, and conversely, if \mathbf{L} is sharper than $\mathbf{Q}\mathbf{P}$ (β low), the result becomes sharper than $\mathbf{Q}\mathbf{p}_{\text{in}}$.

If the spectral radius of

$$\Delta \triangleq \mathbf{I} - \alpha(\mathbf{Q}\mathbf{P} + \beta\mathbf{R}) = \mathbf{I} - \alpha(\mathbf{I} + \mathbf{Q}\mathbf{P} - \mathbf{L}) \quad (5)$$

is strictly less than one, the RIFBP method converges to the fixed point

$$\begin{aligned} \mathbf{f}_\infty &= (\mathbf{I} - \Delta)^{-1}\mathbf{Q}\mathbf{p}_{\text{in}} = (\mathbf{Q}\mathbf{P} + \beta\mathbf{R})^{-1}\mathbf{Q}\mathbf{p}_{\text{in}} = \\ &= (\mathbf{I} + \mathbf{Q}\mathbf{P} - \mathbf{L})^{-1}\mathbf{Q}\mathbf{p}_{\text{in}} = (\mathbf{I} + \mathbf{A})^{-1}\mathbf{Q}\mathbf{p}_{\text{in}}. \quad (6) \end{aligned}$$

To avoid undesired modification of certain structures, *e.g.* high frequencies, or image regions, an operator $\mathbf{G} \in \mathbb{R}^{N \times N}$ which suppresses these structures or regions from the correction image may be applied in each update step:

$$\mathbf{f}_{k+1} = (1 - \alpha)\mathbf{f}_k + \alpha(\mathbf{Q}\mathbf{p}_{\text{in}} - \mathbf{G}(\mathbf{Q}\mathbf{P} - \mathbf{L})\mathbf{f}_k). \quad (7)$$

The fixed point of this update step is

$$\mathbf{f}_\infty = (\mathbf{I} + \mathbf{G}(\mathbf{Q}\mathbf{P} - \mathbf{L}))^{-1}\mathbf{Q}\mathbf{p}_{\text{in}}. \quad (8)$$

In the following, for simplicity we will restrict the discussion to the case $\alpha = 1$, *i.e.*,

$$\mathbf{f}_{k+1} = \mathbf{Q}\mathbf{p}_{\text{in}} - \mathbf{G}(\mathbf{Q}\mathbf{P} - \mathbf{L})\mathbf{f}_k. \quad (9)$$

Details on the operator \mathbf{G} are given in Section II-D.

B. Improved artifact reduction

The RIFBP method is able to perfectly suppress cone artifacts caused by non-exactness of the reconstruction \mathbf{Q} . However, in the case of incomplete source trajectories, there is no unique solution to be found by the data fidelity term $\mathbf{Q}(\mathbf{P}\mathbf{f}_k - \mathbf{p}_{\text{in}})$. Therefore, RIFBP is not necessarily convergent, and if it converges, artifacts will remain in the final result.

To further reduce artifacts, incorporation of additional information is necessary. Typically, this is accomplished by replacing the linear regularization \mathbf{R} with a non-linear regularization, *e.g.* the Geman-McClure prior [9], which enforces piecewise smoothness onto the final image. Although this approach efficiently reduces artifacts, it also leads to modified contrast and resolution properties, which may be undesired.

Here, we employ a different approach based on the following observations:

- 1) The input volume to $(\mathbf{Q}\mathbf{P} - \mathbf{L})$ in equation (9) is solely used for generating artifacts to be subtracted from $\mathbf{Q}\mathbf{p}_{\text{in}}$. Therefore this volume has to contain the structures that cause cone artifacts, but does not necessarily need to faithfully represent the object to be reconstructed.
- 2) The intensity of cone artifacts is an order of magnitude smaller than that of structures causing cone artifacts. Therefore, only high-contrast edges need to be considered for artifact reduction.
- 3) In medical CT, high-contrast edges (bone/soft tissue, soft tissue/air) may be considered step functions. During data acquisition and reconstruction, the highest frequencies of these edges are lost, leading to failure to accurately reproduce the artifacts with $(\mathbf{Q}\mathbf{P} - \mathbf{L})$.

These observations motivate the introduction of an “edge recovery operator” $F : \mathbb{R}^N \rightarrow \mathbb{R}^N$ which reduces contrast in low-contrast regions, and more importantly restores high-contrast edges prior to artifact generation:

$$\mathbf{f}_{k+1} = \mathbf{Q}\mathbf{p}_{\text{in}} - \mathbf{G}(\mathbf{Q}\mathbf{P} - \mathbf{L})F(\mathbf{f}_k). \quad (10)$$

This type of method was first proposed by Hsieh [10] for reduction of cone artifacts in the single circle source trajectory. In the following, (10) in combination with the edge recovery operator described in the next section (first presented in [5]) will be referred to as Edge-RIFBP.

C. The edge recovery operator F

The purpose of the edge recovery operator is to restore high-contrast edges, and to further reduce contrast in low contrast regions.

For each output voxel f_i^{out} , a set Ω_i consisting of the corresponding f_i^{in} and neighboring input voxels is considered. Furthermore, given the input parameter $m \in [0, 1]$, the following entities are calculated:

$$\Omega_{i,\text{min}} = \min(\Omega_i), \quad (11)$$

$$\Omega_{i,\text{max}} = \max(\Omega_i), \quad (12)$$

$$\Omega_{i,\text{median}} = \text{median}(\Omega_i), \quad (13)$$

$$\Omega_{i,\text{contrast}} = \Omega_{i,\text{max}} - \Omega_{i,\text{min}}, \quad (14)$$

$$\Omega_{i,L} = \Omega_{i,\text{min}} + m \cdot \Omega_{i,\text{contrast}}, \text{ and} \quad (15)$$

$$\Omega_{i,H} = \Omega_{i,\text{max}} - m \cdot \Omega_{i,\text{contrast}}. \quad (16)$$

TABLE I
RECONSTRUCTION PARAMETERS

Voxel volume in-plane sampling distance	Δ_{xy}	0.68mm
Voxel volume cross-plane sampling distance	Δ_z	0.3mm
Median filter dimensions	k_x, k_y, k_z	1,1,15
Contrast threshold	T	300HU
Relative contrast margin	m	0.05
Transition function shape	γ	0.25
WFBP redundancy weight	Q	0.8

Now, given a contrast threshold T , the condition

$$\Omega_{i,\text{contrast}} < T \vee f_i^{\text{in}} < \Omega_{i,L} \vee f_i^{\text{in}} > \Omega_{i,H} \quad (17)$$

is evaluated. If this condition is true, the neighborhood is classified as a low-contrast region, and f_i^{out} is set to $\Omega_{i,\text{median}}$. Otherwise, the neighborhood is assumed to contain a high-contrast edge, and f_i^{out} is set to $g(f_i^{\text{in}}|\Omega_{i,L}, \Omega_{i,H}, \gamma)$.

The function $g(\cdot|L, H, \gamma)$ describes a transition between L and H , and is defined by

$$g(x|L, H, \gamma) = \frac{\text{sign}(x') |x'|^\gamma (H - L)}{2} + \frac{L + H}{2}$$

$$x' = 2 \frac{(x - \frac{L+H}{2})}{H - L}. \quad (18)$$

For $\gamma = 1$, the transition is linear, and for γ close to zero, the transition resembles a step function.

D. Experiments

Although the method should work also for reducing artifacts between the circles in the multiple circle source trajectory, experiments have only been done for the HPDS spiral source trajectory with pitch factor 3.2 so far. To examine the effectiveness of the proposed method, the Turbell clock phantom [11] and an anthropomorphic thorax phantom were used. Reconstruction parameters are listed in Table I. The scanning geometry is illustrated in Fig. 2.

Since cone artifacts are caused by high-contrast edges orthogonal to the z -axis, the dimensions of the neighborhood Ω_i of the edge recovery operator were chosen to be $\pm 2.5\text{mm}$ along the z -axis and 0mm in the xy -plane.

The linear operator L in (10) was selected to be a separable spatially invariant linear filter approximating the frequency characteristics of QP in the iso-center. Although such a filter cannot perfectly model the spatially dependent behavior of QP , the effects of the mismatch between QP and L were observed to be small, as long as the image matrix was large enough to harbor the frequency content produced by the reconstruction Q .

To further reduce possible unwanted effects of the algorithm, the operator G in (10) was selected to be a cylindrically symmetric spatially invariant linear filter with frequency characteristics

$$G(u, v, w) = \begin{cases} 1, & \rho < \rho_L \\ \cos^2\left(\frac{\pi}{2} \frac{\rho - \rho_L}{\rho_H - \rho_L}\right), & \rho_L \leq \rho < \rho_H \\ 0, & \rho_H \leq \rho \end{cases}, \quad (19)$$

where $\rho = \sqrt{u^2 + v^2}$. The cut-off frequencies were set to $\rho_L = 2.5\text{lp/cm}$ and $\rho_H = 5.0\text{lp/cm}$. The use of a filter G

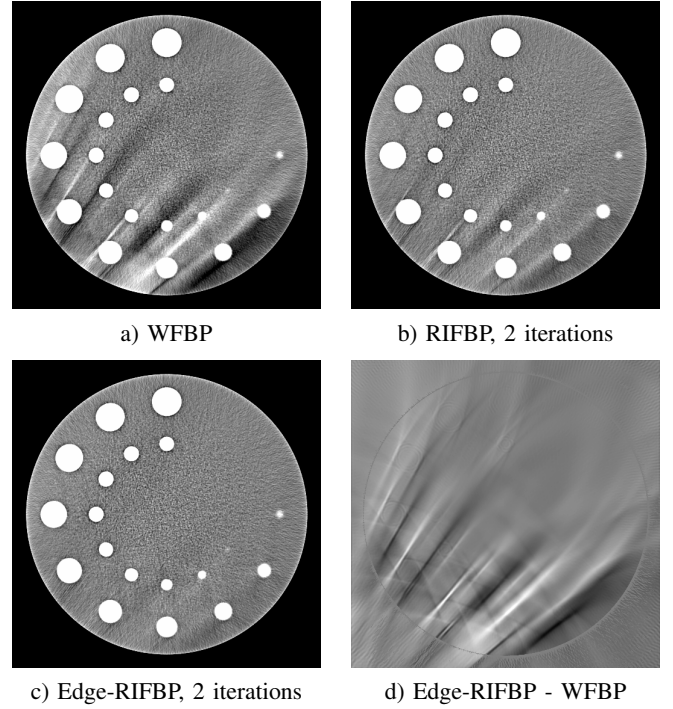


Fig. 3. Reconstructions of the Turbell sphere clock phantom [11]. Greyscale window: (C : 0HU, W : 200HU).

to reduce in-plane frequency content is motivated by the observation that cone artifacts consist mainly of low frequencies in-plane, and have higher frequencies along the z -axis.

III. RESULTS

Fig. 3 shows reconstructions of the Turbell sphere clock phantom at $z = -3\text{mm}$ with a greyscale window width of 200HU. The phantom consists of a water cylinder filled with spheres with an attenuation of 1000HU. Due to the high contrast between the spheres and the water background, strong artifacts occur in the WFBP reconstruction in Fig. 3a. For acquisitions with pitch factor less than 1.5, cone artifacts are normally perfectly suppressed with the RIFBP algorithm [4]. However, due to the incompleteness of the HPDS trajectory, artifacts remain in the RIFBP reconstruction as shown in Fig. 3b. It is worth noting that the RIFBP reconstruction does not improve much if the number of iterations is increased (not shown). Fig. 3c shows the reconstruction result with Edge-RIFBP. Although some artifacts remain, the result is much better than for RIFBP. As shown in Fig. 3d, the difference between Edge-RIFBP and WFBP consists mainly of artifacts.

To examine the behavior of Edge-RIFBP in a more realistic scenario, experiments were made with a physical anthropomorphic thorax phantom. The results are shown in Fig. 4. Again, strong cone artifacts appear in the WFBP result in Fig. 4a. These artifacts are alleviated but not perfectly suppressed by the RIFBP in Fig. 4b. With Edge-RIFBP, the result is much better: as shown in Fig. 4c, remaining artifacts are rather due to beam-hardening than related to the cone-beam geometry. Fig. 4d shows the difference between Edge-RIFBP and WFBP. Although some ringing artifacts around high-contrast structures can be seen, the amplitudes of these artifacts



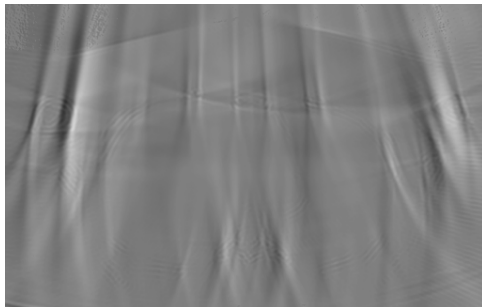
a) WFBP



b) RIFBP, 2 iterations



c) Edge-RIFBP, 2 iterations



d) Edge-RIFBP - WFBP

Fig. 4. Reconstructions of an anthropomorphic thorax phantom. Greyscale window ($C : 0\text{HU}, W : 300\text{HU}$)

are less than 1% of the local contrast.

IV. CONCLUSION

It has been demonstrated that Edge-RIFBP efficiently reduces cone artifacts for HPDS data acquisitions with pitch factors up to 3.2, without affecting image noise texture or resolution. By carefully selecting the linear operators L and G , undesired modification of high-contrast edges is avoided.

The optimal selection of the operator G remains to be determined: on the one hand, to enable correction for all frequencies, it is desirable to have G resembling the identity

matrix as much as possible, on the other hand any unwanted modification of high-contrast edges has to be avoided.

One possible side effect of the algorithm is the introduction of new artifacts due to erroneous recovery of high-contrast edges. However, this effect has not been observed in the experiments.

In comparison with the similar algorithm [10], the Edge-RIFBP algorithm relies on local contrast information rather than segmenting to known attenuation values (water, bone, ...). For the HPDS and multiple circle trajectories, using the local contrast information might be more beneficial because (i) the attenuation of bone varies due to density variations and beam-hardening, and (ii) the local contrast information in Qp along the z -axis in the interior of the scan range is relatively reliable. However, for the single circle trajectory, and for the borders of the HPDS and multiple circle trajectories, stronger assumptions about the attenuation values may be necessary.

REFERENCES

- [1] H. K. Tuy, "An Inversion Formula for Cone-Beam Reconstruction," *SIAM Journal on Applied Mathematics*, vol. 43, no. 3, pp. 546–552, 1983.
- [2] B. D. Smith, "Image reconstruction from cone-beam projections: necessary and sufficient conditions and reconstruction methods," *IEEE Trans Med Imaging*, vol. 4, no. 1, pp. 14–25, 1985. [Online]. Available: <http://dx.doi.org/10.1109/TMI.1985.4307689>
- [3] H. Bruder, M. Petersilka, H. Mehldau, W. Heidinger, T. Allmendinger, B. Schmidt, R. Raupach, C. Thierfelder, K. Stierstorfer, and T. Flohr, "Flash imaging in dual source CT (DSCT)," in *Proceedings of the SPIE, Medical Imaging 2009*, S. E. and J. Hsieh, Eds., vol. 7258, 2009, p. 72580D.
- [4] J. Sunnegårdh and P.-E. Danielsson, "Regularized iterative weighted filtered backprojection for helical cone-beam CT," *Medical Physics*, vol. 35, no. 9, pp. 4173–4185, 2008. [Online]. Available: <http://link.aip.org/link/?MPH/35/4173/1>
- [5] J. Sunnegårdh and K. Stierstorfer, "A new method for windmill artifact reduction," in *12th International Meeting on Fully Three-Dimensional Image Reconstruction in Radiology and Nuclear Medicine. Lake Tahoe, CA, USA*, 2013.
- [6] K. Stierstorfer, A. Rauscher, J. Boese, H. Bruder, S. Schaller, and T. Flohr, "Weighted FBP—a simple approximate 3D FBP algorithm for multislice spiral CT with good dose usage for arbitrary pitch," *Physics in Medicine and Biology*, vol. 49, no. 11, pp. 2209–2218, 2004.
- [7] X.-L. Xu, J.-S. Liow, and S. C. Strother, "Iterative algebraic reconstruction algorithms for emission computed tomography: A unified framework and its application to positron emission tomography," *Medical Physics*, vol. 20, no. 6, pp. 1675–1684, 1993.
- [8] P. M. Joseph, "An improved algorithm for reprojecting rays through pixel images," *IEEE Transactions on Medical Imaging*, vol. 1, no. 3, pp. 192–196, 1982.
- [9] S. Geman and D. E. McClure, "Statistical methods for tomographic image reconstruction," *Bulletin of the International Statistical Institute*, vol. 52, pp. 5–21, 1987.
- [10] J. Hsieh, "A practical cone beam artifact correction algorithm," in *IEEE Nuclear Science Symposium Conference Record*, vol. 2, 2000, pp. 15/71–15/74.
- [11] H. Turbell, "Cone-Beam reconstruction using filtered backprojection," PhD thesis 672, Department of Electrical Engineering, Linköping University, Linköping, Sweden, February 2001.

Bilateral filtering for x-ray phase-contrast imaging

Sebastian Allner, Thomas Koehler, Andreas Fehringer, Marian Willner, Franz Pfeiffer, and Peter B. Noël

Abstract—Phase contrast computed tomography (PCCT) suffers from severe noise when aiming towards dose-comparable preclinical scans. To reduce the noise level bilateral filters can be used which can exploit the three different registered signals this imaging modality provides. Here, we propose a different derivation for the value dependent filter part built on a covariance-based weighting scheme. Furthermore, we will introduce a covariance analysis method to investigate noise correlation and reveal the advantages of 3D versus 2D filtering. We will also show the improvement from taking complementary image information into account. Finally we compare the filter derived in the proposed way with the standard range filter and present bilateral filter result for grating-based phase contrast reconstructions of a human artery sample at different noise levels.

I. INTRODUCTION

In the last decade phase contrast imaging which provides absorption, phase, and scattering information about the sample has undergone a remarkable development [1]. The enhanced soft tissue contrast [2], [3], this method provides is especially useful in computed tomography and yields complementary data to standard absorption imaging. However, the image acquisition entails major challenges like the phase stepping procedure or an absorbing analyzer grating after the sample which reduce the image statistics significantly. In a preclinical context the applicable dose to utilize grating-based phase contrast imaging is limited. Therefore, the resulting reconstructions exhibit lowered photon statistics. This lowered statistics leads to increased noise and decreased image quality. This is even more apparent in coronal slices of the phase reconstruction due to low frequency noise. One way to improve image quality is to use iterative reconstruction techniques [4], [5], [6]. Another possibility to treat noise is image post processing. The bilateral filters in this work reduce the noise while preserving edges in the sample. Whereas the standard range filter is represented by a normal Gaussian distribution we apply a more physically motivated approach. In [7], an extension of the bilateral filter was introduced that exploits the edge information from the absorption and phase image. However, this algorithm does not take into account that the noise power spectra in the two images are very different. Specifically, the absorption image has predominantly high-frequency noise, whereas the phase image suffers from low-frequency noise. The goal of this

work is to include this additional piece of information into the bilateral filter.

II. MATERIALS AND METHODS

A. Bilateral filtering

The concept of bilateral filtering [8] is based on a weighting scheme for neighboring pixels. The general form of a bilateral filter contains a distance dependent domain filter part $d(x, x')$ and a gray value dependent range filter part $r(f(x), f(x'))$:

$$\tilde{f}(x) = \frac{1}{N(x)} \int_{-\infty}^{\infty} f(x') d(x, x') r(f(x), f(x')) dx', \quad (1)$$

with x being the position of the central pixel, x' the positions of neighboring pixels and $N(x)$ a normalization factor. While the domain filter accounts for local weighting of neighboring pixels the range filter part enforces the value dependent component to prevent filtering across edges. For domain and range filter parts normally a Gaussian distribution is applied either with the squared pixel distance for the domain or the squared value difference for the range filter part:

$$d(x, x') \propto \exp\left(-\frac{(x - x')^2}{2\sigma_d^2}\right), \quad (2)$$

$$r(f(x), f(x')) \propto \exp\left(-\frac{(f(x) - f(x'))^2}{2\sigma_f^2}\right), \quad (3)$$

with σ_d being the standard deviation of the filter kernel size and σ_f the noise standard deviation of the considered reconstruction values (e.g. absorption noise σ_a). However, in those formulations no influence of the noise behavior or the correlation between different image bands is present. In this work we are including those into our model. The different registered signals of grating-based phase contrast imaging are from this point forward referred as bands.

We start the derivation of the new bilateral filter by the following Gaussian model for the noise distribution in two voxels in two bands:

$$g(n_1, n_2, n_3, n_4) \propto \exp\left(\frac{1}{2} (n_1, n_2, n_3, n_4) S (n_1, n_2, n_3, n_4)^T\right), \quad (4)$$

where n_1 and n_2 are the noise values of the two considered voxels in one band, n_3 and n_4 in the other complementary band. The matrix S is the inverse of the covariance matrix of the two two-band voxels. Since each voxel has in our case two bands (absorption and phase) the covariance

S. Allner, A. Fehringer, M. Willner and F. Pfeiffer are with the Chair of Biomedical Physics, Technische Universität München, Munich, Germany.

T. Koehler is with Philips Technologie GmbH, Innovative Technologies, Hamburg, Germany and Institute for Advanced Study, Technische Universität München, Munich, Germany.

P.B. Noël is with the Department of Radiology, Technische Universität München, Munich, Germany.

matrix between two pixel is a 4×4 matrix. Symmetry arguments and a locally constant noise level lead to:

$$C = \begin{pmatrix} c_{11} & c_{12} & c_{13} & c_{14} \\ c_{21} & c_{11} & c_{14} & c_{13} \\ c_{13} & c_{14} & c_{33} & c_{34} \\ c_{14} & c_{13} & c_{34} & c_{33} \end{pmatrix}, \quad (5)$$

$$S = C^{-1}, \quad (6)$$

with $s_{kl} = (S)_{kl}$ being the elements of the inverted covariance matrix. The variables are in the order (a_i, a_j, p_i, p_j) with i being the treated central voxel and j the other voxels of the weighting array. This makes the upper left 2×2 matrix the noise correlation of the absorption signal, the bottom right 2×2 matrix the noise correlation of phase and the other matrix entries the linkage between absorption and phase noise.

The idea for new range filter is to set it proportional to the marginal likelihood that a certain difference is observed in the two bands, given the assumption that the true values of the two voxels are the same in both bands. In order to calculate this marginal likelihood, we introduce the difference of the band values Δa and Δp and with $n_2 = \Delta a - n_1, n_4 = \Delta p - n_3$ into equation (4). The marginal likelihood can then be calculated by integrating over all possible noise realizations which result in the same observed differences Δa and Δp :

$$r \propto \int_{-\infty}^{\infty} \int_{-\infty}^{\infty} \exp\left(\frac{1}{2}(n_1, \Delta a - n_1, n_3, \Delta p - n_3) \cdot S(n_1, \Delta a - n_1, n_3, \Delta p - n_3)^T\right) dn_1 dn_3.$$

Exploiting also the symmetry of S this leads to:

$$r \propto \exp\left(\frac{\Delta a^2}{4}(s_{12} - s_{11}) + \frac{\Delta a \Delta p}{2}(s_{14} - s_{13}) + \frac{\Delta p^2}{4}(s_{34} - s_{33})\right). \quad (7)$$

Note that for the case of completely uncorrelated noise where all off-diagonal elements of S vanish, the range filter boils down to the one proposed in [7] except for the detail that the noise variance of the difference is used instead of the noise level in the image.

B. Investigated filters

We applied the filters to absorption and phase reconstructions recovered from filtered back-projection (FBP). All following filter formulas are mentioned for just one band but can be transferred to the other by replacing a by p . The investigated filter based on equation (7) is referred as **covariance-based filter**, which takes additional information from the other band and noise correlations of the datasets into account:

$$\tilde{a}_i = \frac{1}{N_i} \sum_{j \in \mathcal{N}_i} a_j d(x_i, x_j) \exp\left(\frac{\Delta a_{ij}^2}{4}(s_{12} - s_{11}) + \frac{\Delta a_{ij} \Delta p_{ij}}{2}(s_{14} - s_{13}) + \frac{\Delta p_{ij}^2}{4}(s_{34} - s_{33})\right), \quad (8)$$

where x_j is the considered voxel in the neighborhood \mathcal{N}_i of the central voxel x_i . We compared this filter to the standard Gaussian bilateral filter, where the image bands are treated separately, the **single-band filter**:

$$\tilde{a}_i = \frac{1}{N_i^a} \sum_{j \in \mathcal{N}_i} a_j d(x_i, x_j) \exp\left(-\frac{\Delta a_{ij}^2}{2\sigma_a^2}\right), \quad (9)$$

and the **multi-band filter** [7] which exploits the complementarity of the additional band and can be written as:

$$\tilde{a}_i = \frac{1}{N_i} \sum_{j \in \mathcal{N}_i} a_j d(x_i, x_j) \exp\left(-\frac{\Delta a_{ij}^2}{2\sigma_a^2} - \frac{\Delta p_{ij}^2}{2\sigma_p^2}\right). \quad (10)$$

It uses the edge information from both bands to recover more reliable weights but does not consider noise correlation.

C. Correlation Analysis

We used a covariance analysis in the image domain for determining the noise correlation. Subvolumes of the size of the filter array are selected in a background area in order to acquire independent noise measurements. To guarantee the independence of the different measurements a minimum distance between the subsets is considered. Because one can assume the noise correlation to be equal over the field of view and symmetric due to the FBP algorithm the covariance matrices between the central and the neighboring voxels have to be calculated only once.

D. Scanning parameters

The filters were applied to image data of a human artery which was measured at a symmetric grating-based Talbot-Lau interferometer lab setup with a rotating anode source and a photo counting detector. All gratings have a period of $5.4 \mu\text{m}$ and an inter grating distance of 80 cm. The formalin-fixed sample was put into a 3 cm tube and imaged in a water bath. The x-ray tube was operated at 40 kVp resulting in an effective energy of $\approx 27 \text{keV}$. The sample was measured with 11 phase steps and different exposure times per step (long exposure: 3.6 s, medium exposure: 0.4 s and short exposure: 0.144 s).

III. RESULTS

A. Influence of 2D or 3D filtering

The filter kernel size plays an important role in post processing with filters. However, in computed tomography there is also the possibility to filter across slices and thus

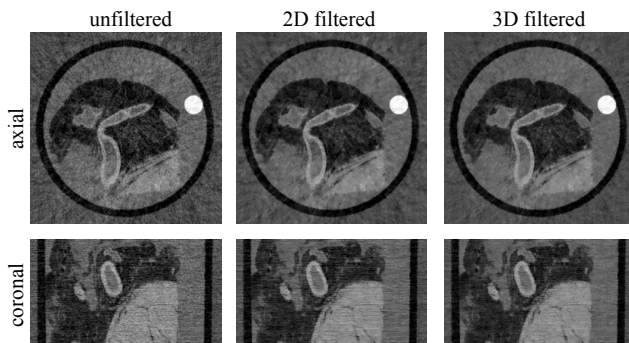


Figure 1. The unfiltered, 2D and 3D single-band results of an axial and a coronal slice from phase FBP.

to work on volume data. Because of the random orientation of structures three-dimensional (3D) filtering provides more statistics and therefore yield improved results. The kernel size has to be adapted reasonably because small kernels may not cover enough values and too large kernels require long computation time. In this study we used a Gaussian domain filter with the size of $\sigma_d = 4$ px and the filter was truncated at a distance of 8 px. Figure 1 exhibits an axial slice in the top row and a coronal slice in the bottom row of a phase signal reconstruction of the human artery sample. These single-band filtered images have a reduced noise amplitude compared to the unfiltered FBP whereas the 3D-filtered slice provides the best results due to improved statistics. Additionally the differential phase projections cause low frequency noise in axial images and introduce strong noise streaks in the coronal slices due to slice-independent FBP reconstruction. These streaks are contained in 2D filtering but reduced in 3D post processing. From this point 3D filtering is used because of its improved results.

B. Integrating complementary information

Pure domain filters like a simple Gaussian or mean filter smooth over edges and features of the approximate size of their kernel. Bilateral filtering prevents this by taking the photometric distance and the noise standard deviation into account. However, when an edge or feature is in the range of noise it is washed out. This unwanted behavior is partially overcome by the multi-band or covariance-based filter because they include the registered complementary band information of grating-based phase contrast imaging.

Figure 2 shows a detail image view of the absorption signal of an artery wall which is obstructed by noise in the unfiltered absorption image. It can not be distinguished from the formalin because absorption signal has much lower soft tissue contrast than the phase image. The single- and multi-band filter reduce the noise level by approximately the same amount, and the covariance-based filter decreases noise even further. However, on the inner edges of the artery wall the multi-band and covariance-based versions recover a more prominent edge than the single-band bilateral filter because the range filter part is influenced by the higher phase signal contrast. The best result is achieved by the covariance-based

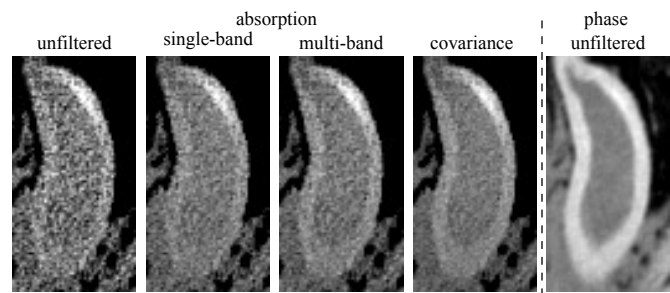


Figure 2. A detail image of the different filter results of the absorption signal of an artery wall. The image to the right shows the same detail in the phase image.

filter combining the small noise amplitude and the additional edge information of the complementary phase band.

C. Filtering different image qualities

Figure 3 shows the three investigated filter results for the absorption and the phase signal for different exposure times. All filters reduce the noise range in the images but the best result is achieved with the covariance-based filter. The filters which use more bands achieve a better result via an improved weighting. This is most apparent at the artery walls of the absorption images where the complementary phase band saves the filter from smoothing over faint edges. Additionally the edges appear less jagged in the multi-band and even a little less in the covariance-based filter image. This effect can be observed in the medium exposure absorption or the short exposure phase image at the top border of the specimen. In this example the absorption signal benefits more from the phase image because the setup has a high phase sensitivity.

IV. CONCLUSION

We showed that the bilateral filter derived with the correlation approach reduces the noise range significantly in comparison to the standard Gaussian formulation. It improves the image quality by optimizing the filter weights. Incorporating more bands in the weighting process and thus using complementary data decreases the possibility to smooth over faint features, especially when dealing with shorter exposure times. The covariance-based filter accounts for the noise correlation in the signals and weights correlated voxels less. However, this influence is not visible in the images and the main benefit stems from the use of the variance of the difference instead of the variance of the noise in the image itself. Particularly when using the 3D filtering the effect of including off-diagonal elements of the inverse covariance matrix is small. There only a few voxels in the same slice differ considerably in weighting compared to the large amount of uncorrelated weights as the noise is not correlated in different axial slices. However, bilateral filtering offers the possibility to perform phase contrast computed tomography with shorter exposure times leading toward dose-comparable preclinical scans.

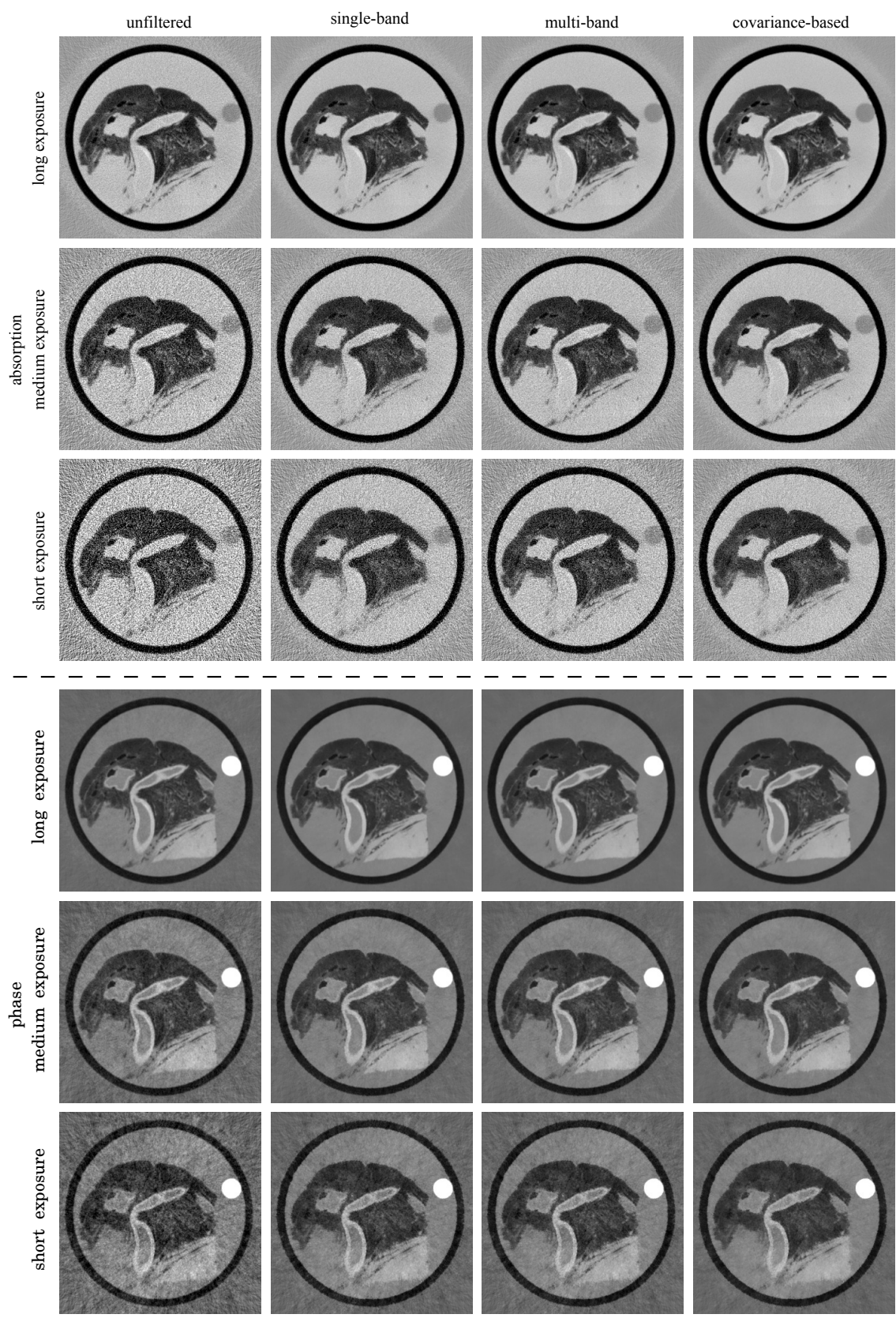


Figure 3. The absorption and phase reconstructions of good, medium and poor image quality with their bilateral filter results.

REFERENCES

- [1] F. Pfeiffer, C. Kottler, O. Bunk, and C. David, "Hard X-Ray Phase Tomography with Low-Brilliance Sources," *Physical Review Letters*, vol. 98, no. 10, p. 108105, Mar. 2007. [Online]. Available: <http://link.aps.org/doi/10.1103/PhysRevLett.98.108105>
- [2] F. Pfeiffer, O. Bunk, C. David, M. Bech, G. L. Duc, A. Bravin, and P. Cloetens, "High-resolution brain tumor visualization using three-dimensional x-ray phase contrast tomography," *Physics in Medicine and Biology*, vol. 52, no. 23, p. 6923, 2007. [Online]. Available: <http://stacks.iop.org/0031-9155/52/i=23/a=010>
- [3] A. Bravin, P. Coan, and P. Suortti, "X-ray phase-contrast imaging: from pre-clinical applications towards clinics," *Physics in Medicine and Biology*, vol. 58, no. 1, p. R1, 2013. [Online]. Available: <http://stacks.iop.org/0031-9155/58/i=1/a=R1>
- [4] T. Koehler, B. Brendel, and E. Roessl, "Iterative reconstruction for differential phase contrast imaging using spherically symmetric basis functions," *Medical Physics*, vol. 38, no. 8, 2011.
- [5] T. Gaass, G. Potdevin, P. B. Noël, A. Tapfer, M. Willner, J. Herzen, M. Bech, F. Pfeiffer, and A. Haase, "Compressed sensing for phase contrast ct," *AIP Conference Proceedings*, vol. 1466, no. 1, 2012.
- [6] D. Hahn, P. Thibault, A. Fehring, M. Bech, P. B. Noël, and F. Pfeiffer, "Bone artifact reduction in differential phase-contrast ct," *Fully3D*, 2013.
- [7] T. Koehler and E. Roessl, *Simultaneous de-noising in phase contrast tomography*. American Institute of Physics, 2012, pp. 78–83. [Online]. Available: <http://dx.doi.org/10.1063/1.4742272>
- [8] C. Tomasi and R. Manduchi, *Bilateral filtering for gray and color images*. Institute of Electrical and Electronics Engineers, 1998, pp. 839–846. [Online]. Available: <http://dx.doi.org/10.1109/ICCV.1998.710815>

Metal artifact reduction using l_1 and non-local penalties with iterative sinogram correction

Kyungsang Kim^{a,b}, Jong Chul Ye^b, Georges El Fakhri^a and Quanzheng Li^{a,*}

Abstract—Metal artifact reduction is a challenging issue in CT reconstruction. Due to insufficient measurements after passing through the metal object, the break down of the inconsistency in attenuation sinogram results in severe streak artifacts in the reconstructed image. In this project, we propose a metal artifact reduction method using l_1 norm and non-local penalties with iterative sinogram correction, where the 3D in-painting algorithm is iteratively used to estimate the sinogram in the iteratively updated metal regions. Metal and non-metal images using l_1 norm and non-local penalties are reconstructed separately. The split Bregmann algorithm and the generalized non-local formula were applied to solve the optimization problems associated with l_1 norm and non-local penalties. Both body phantom simulations and real dental CT experiments verify that the proposed method can significantly reduce the metal artifacts and provide more clear details of the image structure.

I. INTRODUCTION

Metal artifact reduction (MAR) is a crucial and challenging issue in the computed tomography (CT) reconstruction. High attenuation coefficients in metal objects significantly decrease the total number of photons, the severe beam-hardening effect, referred as the metal artifact, leads to artifacts such as dark stripes between metal objects and shining stripes in metal and surrounding tissues. Specifically, if the number of detected photon is close to zero after passing through metal objects, the consistency of measurements breaks down, meaning the linear relationship of measurements in projection space does not exist any more [1]. For example, metal objects such as implant and gold crown are popularly used, which results in severe metal artifacts in reconstructed dental CT images.

To deal with the MAR problem in CT imaging, sinogram correction methods using interpolation [2], [3], segmentation [4], [5] and in-painting [6], [7], [8], [9] have been widely used. Sinogram correction methods remove metal regions in the projection domain, and then fill the estimated values for metal parts in the sinogram using interpolation, segmentation and in-painting based methods. In addition, iterative reconstruction methods [10], [11], [12] have been proposed for MAR, which can provide more accurate results at the expense of higher computational cost, compared with conventional filtered back-projection (FBP) algorithm. More interestingly, metal region reconstruction using a compressed sensing based sparsity constraint has been also proposed in [13] where the method solves a l_1 minimization using the FOCal Underdetermined System Solver (FOCUSS) algorithm with only few views.

In this paper, we propose a novel MAR method that consists of both a new iterative sinogram correction algorithm and advanced iterative reconstruction schemes for metal and non-metal images. We first propose a novel iterative sinogram correction method using an iterative metal region filling method with a 3D in-painting method proposed by Garcia [14], where metal regions in sinogram are estimated by the discrete cosine transform (DCT) based in-painting method. After estimation of metal and non-metal sinograms, we propose iterative reconstruction methods using l_1 and non-local penalties for metal and non-metal images, respectively. For the metal image reconstruction using l_1 penalty, we exploit the alternating split Bregman algorithm [15], which is the alternating-direction method of multipliers (ADMM) algorithm for solving the l_1 penalty. Furthermore, we used the generalized non-local penalty [16], [17] for the non-metal image reconstruction, which provides the general formula for the non-local penalty. We validate our method using both a simulated digital body phantom data and real dental data. The results demonstrate the proposed method provides the significant improvement on metal artifacts reduction compared to the conventional FBP. In addition, we accelerate the proposed method by implementing forward and backward projectors using GPU [18], so the proposed method is considerably practical and can be easily applied in real clinics.

II. METHOD

A. Iterative sinogram correction

The first step in the proposed method is the sinogram correction. In this step the accurate metal region detection is critical to fully utilize the original sinogram which is pre-converted by the negative logarithm from original measurements. Thus, we propose an iterative sinogram correction that updates metal regions iteratively. In Fig. 1, we describe the flowchart of the iterative sinogram correction. First, we reconstruct an initial image using the conventional FBP, and then threshold the background values and extract the initial metal image. The size of the initial metal regions in sinogram are over-estimated by forward projection of the initial metal image. Therefore, we calculate difference between the estimated sinogram in the metal regions and original sinogram. If the difference is less than a specific value ϵ , we consider that small difference regions are not metal regions. In our method, $\epsilon = 0.1$ was used. We then remove those regions from the metal regions and update a new estimated metal region. For several iterations, metal regions can be more accurately defined. Finally, the metal sinogram is calculated by subtracting non-metal

^aCenter for Advanced Medical Imaging Sciences, Massachusetts General Hospital and Harvard Medical School; ^bBio Imaging Signal Processing Lab., Dept. of Bio&Brain Engineering, Korea Advanced Institute of Science and Technology

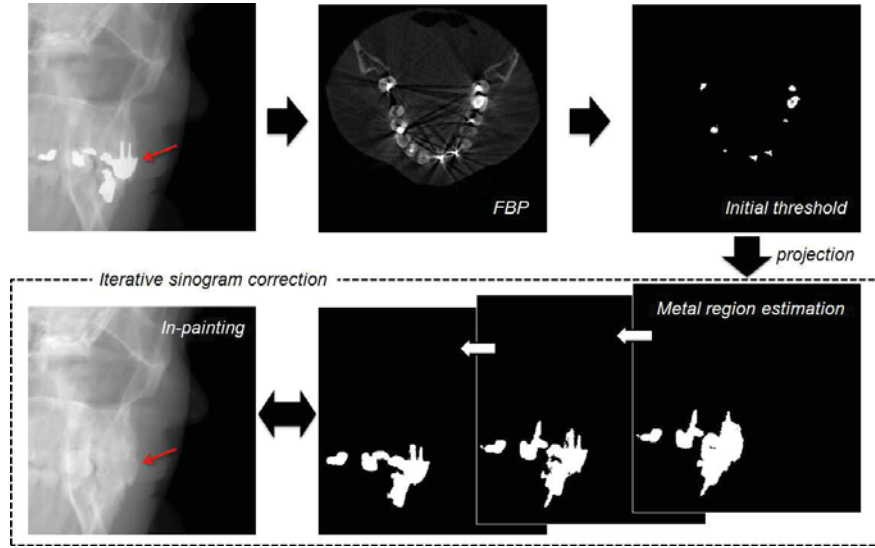


Fig. 1. Flowchart of the iterative sinogram correction.

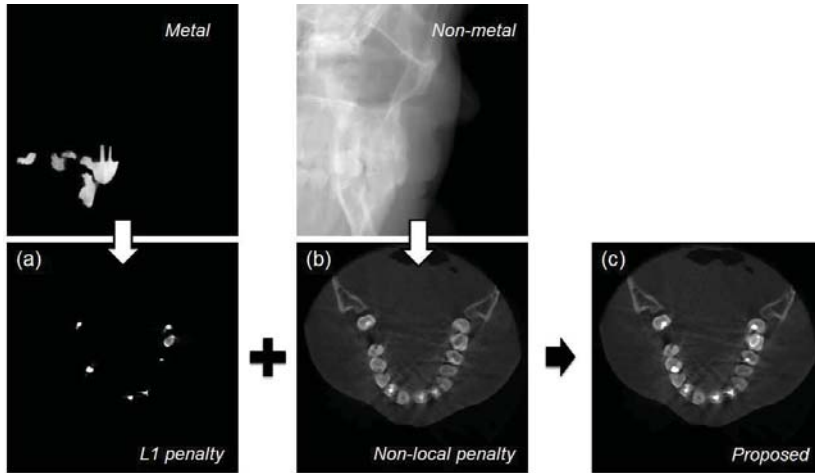


Fig. 2. Iterative reconstruction using (a) l_1 and (b) non-local penalties for metal and non-metal images, and (c) final image is the sum of both images.

sinogram from original sinogram. During all the iterations, the sinogram in the metal region is estimated using a DCT based 3D in-painting method [14]. The in-painting algorithms, which have been used as state-of-the-art sinogram correction method in MAR for several years [6], [7], [8], [9], fill smoothly varying values in the metal region because the intensity varies smoothly along spatial and angular directions in sinogram if metal objects do not exist.

B. Iterative reconstruction

The second step in the proposed method is to reconstruct metal and non-metal images separately and iteratively as shown in Fig. 2. In this step we optimize two cost functions for metal and non-metal images, respectively. Specifically, we define the original sinogram y , metal sinogram y_m and

non-metal (background) sinogram y_b . Corresponding to each sinogram, metal image x_m , non-metal image x_b and the final image x are defined. The first cost function using the l_1 penalty for the metal image is as follows:

$$\min_{x_m} \frac{1}{2} \|y_m - \mathbf{A}x_m\|_2^2 + \lambda \|x_m\|_1, \quad (1)$$

where \mathbf{A} denotes the system matrix of projection in cone-beam geometry, and λ is a control parameter to keep the balance between the data fitting term and the penalty term.

Then, the second cost function using the non-local penalty for the non-metal image is as follows [19]:

$$\min_{x_b} \frac{1}{2} \|y_b - \mathbf{A}x_b\|_2^2 + \beta R(x_b), \quad (2)$$

where the generalized non-local formula is that

$$R(x_b) = \sum_j \frac{1}{p} \left(\sum_{k \in \Omega} w_{jk}(x_b) (|x_{b,j} - x_{b,k}|)^2 \right)^{p/2}, \quad (3)$$

$$w_{jk}(x) = \exp \left(- \frac{\|\mathbf{f}_j(x) - \mathbf{f}_k(x)\|_{\mathbf{h}}}{\sigma^2} \right), \quad (4)$$

and

$$\|\mathbf{f}_j(x) - \mathbf{f}_k(x)\|_{\mathbf{h}} = \sqrt{\sum_{l=1}^{N_p} h_l (x_{j_l} - x_{k_l})^2}, \quad (5)$$

where β is also control parameter to keep the balance between the data fitting term and the penalty term, σ is a filtering parameter and Ω is the neighbors. N_p is the number of pixels in a patch, h_l is the normalized inverse distance between pixel j_l and k_l in which $\sum_l h_l = 1$. In this paper, $\Omega = 5 \times 5 \times 5$, $N_p = 3 \times 3 \times 3$, $\beta = 0.1$, $\sigma = 0.001$ and $p = 2$ were used.

III. OPTIMIZATION

A. Metal image reconstruction using l_1 penalty

In the alternating split Bregman method, Eq. (1) can be expressed as follows [15]:

$$(x_m^{n+1}, u^{n+1}) = \min_{x_m, u} \frac{1}{2} \|y_m - \mathbf{A}x_m^n\|_2^2 + \lambda_1 \|u^n\|_1 + \frac{\lambda_2}{2} \|x_m^n - u^n - b^n\|_2^2, \quad (6)$$

$$b^{n+1} = b^n + \alpha(u^{n+1} - x_m^{n+1}). \quad (7)$$

where the initial $b^0 = 0$, α is a constant for the update b , and we then solve two minimizations for x_m and u alternatively. Solution for each subproblem is as follow:

$$x_m^{n+1} = x_m^n - \frac{\sum_{i=1}^{n_i} a_{ij} (\bar{y}_{m,i}^n - y_{m,i}) + \lambda_2 (x_j^n - u_j^n - b_j^n)}{\sum_{i=1}^{n_i} a_{ij} \gamma_i + \lambda_2}, \quad (8)$$

$$u^{n+1} = \text{shrink}\{x_m^{n+1}, \lambda^*\} = \max(x_m^{n+1} - \lambda^*, 0), \quad (9)$$

$$b^{n+1} = b^n + \alpha(u^{n+1} - x_m^{n+1}), \quad (10)$$

where $\lambda^* = \lambda_1/\lambda_2$, $\gamma_i = \sum_j^{n_j} a_{ij}$, $\bar{y}_{m,i}^n = \sum_{j=1}^{n_j} a_{ij} x_{m,j}^n$ and n_i and n_j denote the number of pixels of sinogram and image, respectively. Here, $\sum_{i=1}^{n_i} a_{ij} \gamma_i$ can be pre-calculated. In this paper, $\alpha = 1$ and $\lambda^* = \lambda_1 = 0.001$ were used.

B. Non-metal image reconstruction using non-local penalty

Eq. (2) is differentiable, thus the solution is calculated using the first and second derivatives:

$$x_{b,j}^{n+1} = x_{b,j}^n - \frac{\sum_{i=1}^{n_i} a_{ij} (\bar{y}_{b,i}^n - y_{b,i}) + \beta \dot{R}(x_{b,j}^n)}{\sum_{i=1}^{n_i} a_{ij} \gamma_i + \beta \ddot{R}(x_{b,j}^n)}, \quad (11)$$

where

$$\bar{y}_{b,i}^n = \sum_{j=1}^{n_j} a_{ij} x_{b,j}^n, \quad (12)$$

$$\dot{R}(x_{b,j}^n) = \sum_{k \in \Omega} w_{j,k}(x_b^n) (x_{b,j}^n - x_{b,k}^n), \quad (13)$$

$$\ddot{R}(x_{b,j}^n) = \sum_{k \in \Omega} w_{j,k}(x_b^n). \quad (14)$$

Finally, the reconstructed image of the proposed method is the sum of x_m and x_b .

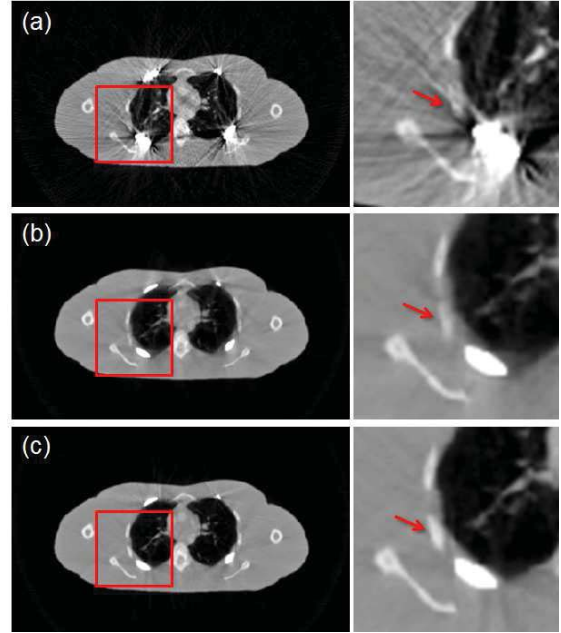


Fig. 3. Reconstruction images of (a) FBP and the proposed method using (b) initial sinogram correction and (c) iterative sinogram correction.

IV. EXPERIMENTAL RESULTS

We evaluate the performance of the proposed method using both digital body phantom data and real dental CT data. In the body phantom simulation, several ribs are setup as metal subjects to generate metal artifacts. We then simulated CT measurements using polychromatic spectrums. In Fig. 3, we validated the effect of iterative sinogram correction as well as the image quality improvement, and compared the proposed method with the conventional FBP. Metal artifacts in Fig. 3(a) were significantly reduced as shown in Figs. 3(b) and 3(c). In addition, details of Fig. 3(c) were more clear than that of Fig. 3(b), which means that the accurate metal region estimation is important for the recovery of edge structures near metal objects. The results demonstrated that the iterative sinogram correction improves the details of image, and the proposed method reduces the metal artifact significantly.

We also performed an *in vivo* experiment using real dental CT data. The reconstructed image of FBP and the proposed method were compared In Fig. 4. Since there are several implants and gold crown in the data, severe metal artifacts were observed in the FBP reconstruction. However, the proposed method significantly reduced metal artifacts. In addition, the edge of both metal and non-metal images was more clear.

Particularly, the non-local penalty with a novel optimization framework was exploited for the reconstruction of the non-metal image, . In Fig. 5, we compared non-metal images of FBP and the proposed method. It clearly demonstrated that the iterative reconstruction using non-local penalty can reduce noise variance while preserving edge directions and could be an excellent choice of low dose image reconstruction for MAR.

Furthermore, we implemented forward and backward pro-

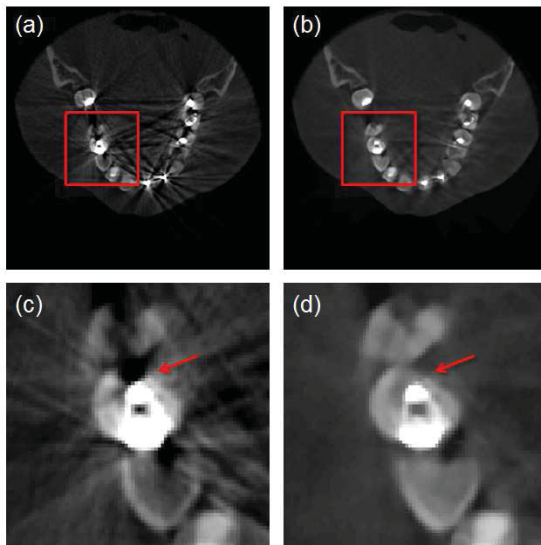


Fig. 4. Reconstruction images of (a) FBP and (b) the proposed method, and (c) and (d) are region of interests of FBP and the proposed method, respectively.

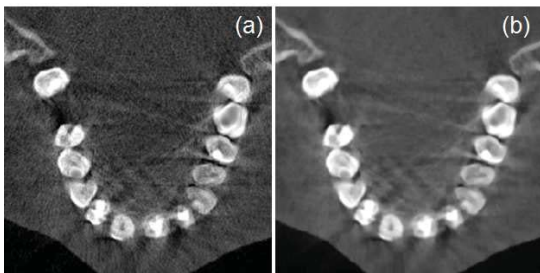


Fig. 5. Reconstructed non-metal images of (a) FBP and (b) the proposed method.

jectors using GPU, where the Nvidia Tesla C2070 with compute unified device architecture (CUDA) was exploited. In our geometry, the $512 \times 512 \times 320$ image with $608 \times 616 \times 455$ sinograms takes 17s for one iteration. Comparing to the Intel i7-2670 CPU, the reconstruction time of the proposed method using GPU was 270 times faster than using CPU, so the proposed method can be easily applied in real clinics.

V. CONCLUSIONS

In conclusion, we proposed a metal artifact reduction method using l_1 and non-local penalties with iterative sinogram correction. The proposed method consists of two steps, one is a novel iterative sinogram correction, and another one is the iterative reconstructions of metal and non-metal images using l_1 and non-local penalties, respectively. To exploit l_1 and non-local penalties, we proposed a novel optimization framework using the split Bregman algorithm and the generalized non-local formula. The results of both body phantom simulation and real dental experiments showed our proposed algorithm can significantly reduce metal artifacts and provide more clear details. In addition, GPU implementation of the

proposed method demonstrated the feasibility to apply this method in real clinics.

REFERENCES

- [1] J. Hsieh, "Computed tomography: principles, design, artifacts, and recent advances." SPIE, 2009.
- [2] W. A. Kalender, R. Hebel, and J. Ebersberger, "Reduction of CT artifacts caused by metallic implants," *Radiology*, vol. 164, no. 2, pp. 576–577, 1987.
- [3] A. H. Mahnken, R. Raupach, J. E. Wildberger, B. Jung, N. Heussen, T. G. Flohr, R. W. Günther, and S. Schaller, "A new algorithm for metal artifact reduction in computed tomography: in vitro and in vivo evaluation after total hip replacement," *Investigative radiology*, vol. 38, no. 12, pp. 769–775, 2003.
- [4] H. Yu, K. Zeng, D. K. Bharkhada, G. Wang, M. T. Madsen, O. Saba, B. Policeni, M. A. Howard, and W. R. Smoker, "A segmentation-based method for metal artifact reduction," *Academic radiology*, vol. 14, no. 4, pp. 495–504, 2007.
- [5] Y. Zhang, L. Zhang, X. R. Zhu, A. K. Lee, M. Chambers, and L. Dong, "Reducing metal artifacts in cone-beam CT images by preprocessing projection data," *International Journal of Radiation Oncology Biology Physics*, vol. 67, no. 3, pp. 924–932, 2007.
- [6] M. Bal and L. Spies, "Metal artifact reduction in CT using tissue-class modeling and adaptive prefiltering," *Medical physics*, vol. 33, pp. 2852–2859, 2006.
- [7] Y. Kim, S. Yoon, and J. Yi, "Effective sinogram inpainting for metal artifacts reduction in X-ray CT images," in *International Conference on Image Processing*. IEEE, 2010, pp. 597–600.
- [8] Y. Zhang, Y.-F. Pu, J.-R. Hu, Y. Liu, and J.-L. Zhou, "A new CT metal artifacts reduction algorithm based on fractional-order sinogram inpainting," *Journal of X-ray science and technology*, vol. 19, no. 3, pp. 373–384, 2011.
- [9] H. S. Park, J. K. Choi, K.-R. Park, K. S. Kim, S.-H. Lee, J. C. Ye, and J. K. Seo, "Metal artifact reduction in CT by identifying missing data hidden in metals," *Journal of X-ray science and technology*, vol. 21, no. 3, pp. 357–372, 2013.
- [10] G. Wang, D. L. Snyder, J. O'Sullivan, and M. Vannier, "Iterative deblurring for CT metal artifact reduction," *IEEE Transactions on Medical Imaging*, vol. 15, no. 5, pp. 657–664, 1996.
- [11] B. De Man, J. Nuyts, P. Dupont, G. Marchal, and P. Suetens, "An iterative maximum-likelihood polychromatic algorithm for CT," *IEEE Transactions on Medical Imaging*, vol. 20, no. 10, pp. 999–1008, 2001.
- [12] C. Lemmens, D. Faul, and J. Nuyts, "Suppression of metal artifacts in ct using a reconstruction procedure that combines map and projection completion," *IEEE Transactions on Medical Imaging*, vol. 28, no. 2, pp. 250–260, 2009.
- [13] J. Choi, K. S. Kim, M. W. Kim, W. Seong, and J. C. Ye, "Sparsity driven metal part reconstruction for artifact removal in dental CT," *Journal of X-ray Science and Technology*, vol. 19, no. 4, pp. 457–475, 2011.
- [14] D. Garcia, "Robust smoothing of gridded data in one and higher dimensions with missing values," *Computational Statistics & Data Analysis*, vol. 54, no. 4, pp. 1167–1178, 2010.
- [15] T. Goldstein and S. Osher, "The split Bregman method for L1-regularized problems," *SIAM Journal on Imaging Sciences*, vol. 2, no. 2, pp. 323–343, 2009.
- [16] G. Gilboa and S. Osher, "Nonlocal linear image regularization and supervised segmentation," *Multiscale Modeling & Simulation*, vol. 6, no. 2, pp. 595–630, 2007.
- [17] A. Elmoataz, O. Lezoray, and S. Bougleux, "Nonlocal discrete regularization on weighted graphs: a framework for image and manifold processing," *Image Processing, IEEE Transactions on*, vol. 17, no. 7, pp. 1047–1060, 2008.
- [18] G. Sharp, N. Kandasamy, H. Singh, and M. Folkert, "GPU-based streaming architectures for fast cone-beam CT image reconstruction and demons deformable registration," *Physics in medicine and biology*, vol. 52, no. 19, pp. 5771–5783, 2007.
- [19] S. Kindermann, S. Osher, and P. W. Jones, "Deblurring and denoising of images by nonlocal functionals," *Multiscale Modeling & Simulation*, vol. 4, no. 4, pp. 1091–1115, 2005.

Scatter deconvolution in X-ray cone-beam CT using data consistency

Changhwan Kim, Miran Park, Younghun Sung, Jae Hak Lee, Jiyoung Choi, and Seungryong Cho

Abstract

This study was conducted to demonstrate the feasibility of using data consistency as a criterion of optimizing scatter convolution kernel for scatter correction in cone-beam CT. By utilizing data consistency, one can iteratively optimize the parameters of a scatter kernel in the deconvolution method. In the optimization, we used a Particle Swarm Optimization (PSO) algorithm for its computational efficiency and its excellence in convergence. For validating our proposed method, we performed a simulation study using the XCAT phantom, and also performed an experimental study using the ACS head phantom. The results showed that the proposed method substantially improves the accuracy of the deconvolution method. The beauty of the proposed method is that an accurate and robust scatter correction can be achieved from a single cone-beam scan without using any auxiliary hardware.

1. Introduction

Scatter constitutes a dominant source of image artifacts in cone-beam CT, and numerous methods for scatter correction have been developed [1, 2]. The deconvolution method is one of the correction methods that deconvolves projection data using appropriate scatter kernels. This method has the advantages of convenience in scanning and of computational efficiency. However, it has been reported that the deconvolution method may be less accurate than other scatter correction methods such as Monte Carlo method [2].

Accuracy of the deconvolution method largely depends upon the scatter kernel and its parameters. The kernel and its parameters are in general determined empirically, and therefore may not apply well to diverse situations in clinical scans. Empirical determination process itself can be cumbersome and inaccurate to certain degree. To improve the accuracy of deconvolution method, we made use of the data consistency condition in this work. Data consistency, one

of the fundamental properties of Radon transform [3], provides a useful criterion that is independent of the view-angles of parallel-beam and therefore can be utilized for scatter kernel optimization. Data consistency is challenged by physical factors such as scatter, suboptimal calibration, and data truncation. Under the condition that other factors are managed within a tolerable level or can be neglected, data consistency will depend largely on the scatter component. In other words, data consistency can be used to provide an index of the amount of scatter contamination in the data.

In this work, we used the data consistency which tells that sum of the line integrals in the mid-plane of cone-beam data after fan-parallel rebinning should be a constant throughout the entire scanning angles. Mid-plane cone-beam data basically constitute fan-beam data, and a rebinning process that converts the fan-beam to parallel-beam is required to meet the data consistency. We then used the data consistency to secure that the optimal scatter kernel can be obtained for scatter correction. For optimizing the parameters of a scatter kernel iteratively, we used the so-called Particle Swarm Optimization (PSO) algorithm. We performed a simulation study using the XCAT phantom which is a numerical human body phantom, and also performed an experiment study using the ACS head phantom. We demonstrated that the data consistency can help improve the scatter correction substantially.

2. Method

2.1. Deconvolution method

The deconvolution method originates from an assumption that the scatter component can be estimated by a spatial convolution of the primary signal with a scatter kernel. The scatter kernel determines the magnitude and distribution of the scatter component [4, 5]. Accuracy of the deconvolution method largely depends on the shape of a scatter kernel. Various scatter kernel models have been proposed for improving the accuracy of scatter correction [6, 7]. In this work, we used an asymmetric scatter kernel proposed by Josh Star-Lack et al. [7], which is believed to outperform other kernels. In their model, the scatter signal can be estimated as follows :

This work was supported in part by the NRF grant NRF-2013M2A2A9043476, KIRAMS grant, and by the MEST grant R0001270 and R0001376 in Korea.

C. Kim, M. Park, and S. Cho* are with Korea Advanced Institute of Science and Technology, Daejeon, Korea (e-mail: scho@kaist.ac.kr). Y. Sung, J. Lee, and J. Choi are with Samsung Advanced Institute of Technology, Suwon, Korea.

$$I_s = (1 - \gamma\tau(x,y))((I_p A_f)^{*} h_s) + ((\gamma\tau(x,y) I_p A_f)^{*} h_s) \quad (1)$$

$$A_f = A (I_p/I_0)^\alpha \ln(I_0/I_p)^\beta \quad (2)$$

$$h_s = \exp(-r^2/2\sigma_1^2) + B \cdot \exp(-r^2/2\sigma_2^2) \quad (3)$$

where A_f is amplitude factor, h_s is form function, I_p is the primary estimate, τ is thickness estimate, γ is a proportional constant, I_p is attenuated primary signal, and I_0 is unattenuated primary signal. The parameters $\alpha, \beta, A, B, \sigma_1$, and σ_2 are the fitting parameters that will determine the shape of a scatter kernel. The key contribution of our work is to determine these parameters iteratively using the data consistency condition without any further empirical processes.

2.2. Data consistency

Data consistency in 2D, one of the fundamental properties of Radon transform, tells that the total attenuation in a parallel-beam geometry should remain constant from view to view. In other words, if we sum up the measured parallel projection data for each view, the sum should be a constant independent of the view-angle.

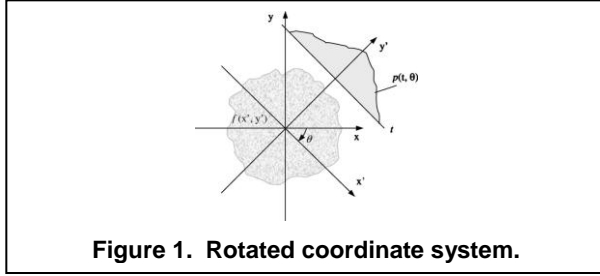


Figure 1. Rotated coordinate system.

$$\begin{aligned} \int_{-\infty}^{\infty} p(t, \theta) dt &= \int_{-\infty}^{\infty} dt \int_{-\infty}^{\infty} f(x', y') dy' \\ &= \iint_{-\infty}^{\infty} f(x', y') dx' dy' \\ &= \iint_{-\infty}^{\infty} f(x, y) dx dy \\ &= \int_{-\infty}^{\infty} p(t, 0) dt \end{aligned} \quad (4)$$

To apply this condition, we used only mid-plane of projection data. Also, we converted fan-beam projection data to parallel-beam projection data by a process called fan-parallel rebinning [8] because data consistency condition is valid only in parallel-beam geometry.

2.3. Fan-parallel rebinning

Both fan and parallel-beam geometries are shown in Fig. 2. β is the fan-beam source angle, γ is the fan-angle, θ is the parallel angle, and t is the radial parallel coordinate. s is the virtual fan-beam detector coordinate and D is the distance of the source point from the origin.

The relationship between (θ, t) and (β, γ) is given by Eq. (5) and (6). Using this relationship, we converted the fan-beam projection data to parallel-beam projection data.

$$\begin{cases} \theta = \beta + \gamma \\ t = s \cos \gamma \end{cases} \quad (5)$$

$$\begin{cases} \theta = \beta + \arctan\left(\frac{s}{D}\right) \\ t = \frac{sD}{\sqrt{(s^2 + D^2)}} \end{cases} \quad (6)$$

2.4. PSO algorithm

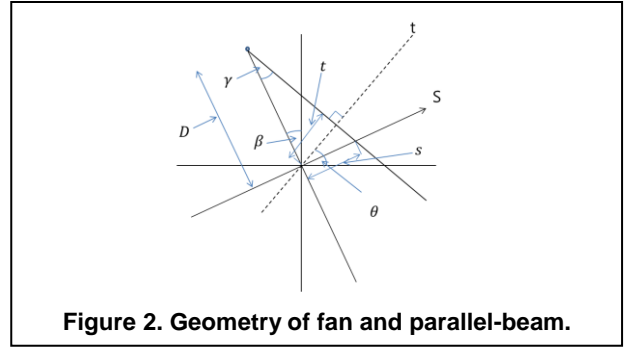


Figure 2. Geometry of fan and parallel-beam.

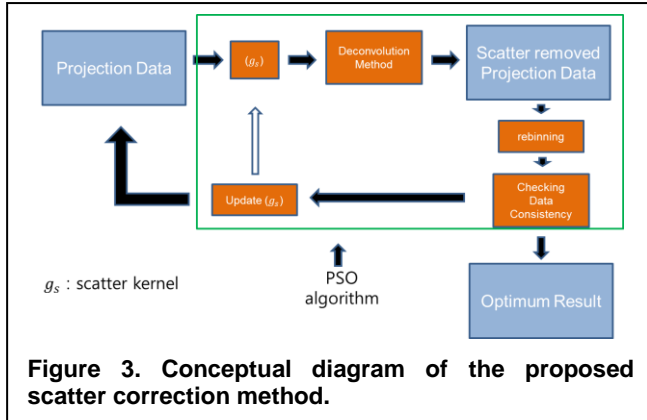
The key step of this work is to find the optimum parameters of a scatter kernel. While changing the parameters iteratively, the optimum is sought for which satisfies the data consistency best. However, this strategy can be challenging for its computational burden; all possible parameters in a certain range should be checked collectively.

For an efficient implementation of the optimization, we incorporated the PSO algorithm [9]. PSO algorithm is one of the optimization algorithms that find a best element out of available alternatives, and it simulates the foraging process of a bunch of creatures. PSO algorithm has advantages of simplicity in its implementation and its relatively fast convergence to the global optimum compared to other algorithms. There are two conditions that need to be met in the PSO algorithm. Agents or particles, which stand for individuals in swarm, should share information each other during iterations. And, they should move based on the shared information. When better positions of the agents are found, then the movement of the swarm will be updated and guided by these. The process is repeated and by doing so it is hoped

that a satisfactory solution will eventually be reached within a reasonable number of iterations.

2.5. Proposed scatter correction method

A conceptual diagram of the proposed scatter correction method is shown in Fig. 3. The procedures are explained below:



1. Initially set up the parameters of the scatter kernel model.
2. Apply the deconvolution method with a selected kernel and remove the scatter component.
3. Rebin the scatter-removed projection data from fan-beam to parallel-beam geometry.
4. Check whether the data satisfies data consistency condition or not.
5. Iterate 1-4 steps with PSO algorithm until data consistency is met to a satisfactory level.
6. Acquire the optimum parameters of the scatter kernel model and the optimum scatter correction result.

3. Results

3.1. Simulation study

Using the XCAT phantom, we acquired cone-beam projection data and added the scatter noise on the projection data by use of a specific kernel which is assumed to be unknown. With scatter-contaminated projection data, we applied the proposed scatter correction method.

In the scatter-free projection data, data consistency is

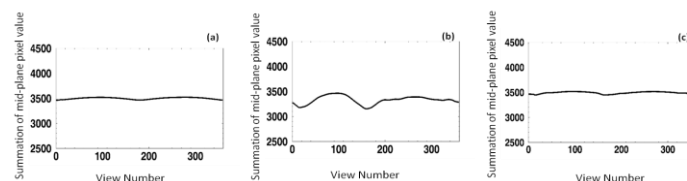


Figure 4. Data consistency graph of scatter-free projection data (a), scatter-contaminated projection data (b), and scatter-corrected projection data (c)

well preserved as shown in Fig. 4 (a). But, in the scatter-contaminated case, there is a pronounced variation of sum of line integrals as can be seen in Fig. 4 (b). Fig. 4 (c) shows data consistency profile of the scatter-corrected data by use of the proposed method, and it demonstrates that the scatter components are successfully corrected. We introduced an inconsistency level to assess scatter correction quantitatively as defined in Eq. (7). The inconsistency level was used as a criterion in the iterative procedure of optimizing the parameters.

$$Inconsistency\ level = \frac{std(value)}{average(value)} \times 100(\%) \quad (7)$$

Table 1. Inconsistency levels of each data consistency graph.

(a)	(b)	(c)
0.529	2.473	0.593

In Table 1, we summarize the inconsistency level values of the corresponding data. The inconsistency level has been much reduced after scatter correction.

The reconstructed images from scatter-free, scatter-added, and scatter-corrected projection data are shown in Fig. 5. Image artifacts caused by the scatter component are clearly seen in (b), and the artifacts are substantially removed by use of the proposed method. For a quantitative assessment, we used Structural Similarity Index (SSIM). Table 2 shows that the image accuracy has been much improved after scatter correction.

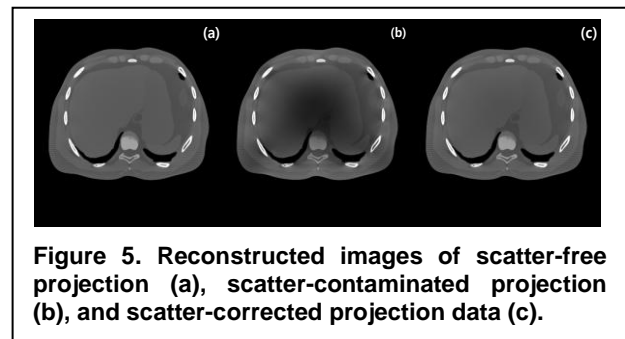


Table 2. SSIM of reconstructed images of scatter-contaminated (a) and scatter-corrected (b) projection data

(a) scatter-contaminated	(b) scatter-corrected
0.8804	0.9752

3.2. Experimental study

We also applied the proposed method to the experimentally acquired data using the ACS head phantom and our bench-top CT system.

Table 3. Inconsistency levels of data consistency of scatter-contaminated and corrected projection data.

(a) scatter-contaminated	(b) scatter-corrected
1.769	0.537

The inconsistency level measures are also summarized in Table 3. In Fig. 6, the reconstructed images from the original data and scatter-corrected projection data are shown, respectively. Image artifacts are clearly seen in (a), and the artifacts are successfully removed by use of the proposed method. The line profiles of reconstructed images in Fig. 7 also shows that the cupping artifact from scatter component is successfully removed by use of the proposed method.

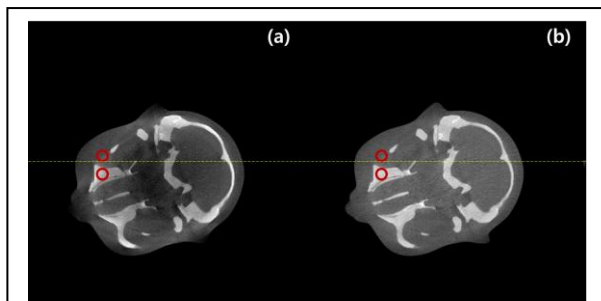


Figure 6. Reconstructed images of scatter-contaminated projection data (a), and scatter-corrected projection data (b).

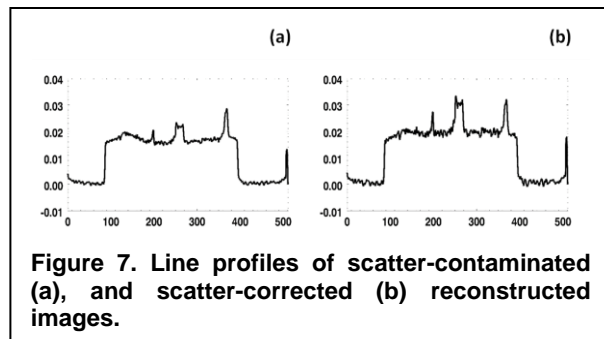


Figure 7. Line profiles of scatter-contaminated (a), and scatter-corrected (b) reconstructed images.

Table 4. CNR of scatter-contaminated and corrected projection data.

(a) scatter-contaminated	(b) scatter-corrected
0.85	1.26

We calculated CNR values of the ROI marked as red circles in Fig. 6. CNR value increased from 0.85 to 1.26 as the scatter was corrected.

4. Conclusion

In this work, we proposed an improved deconvolution method for scatter correction by use of data consistency. The results from both numerical and experimental studies confirmed that the proposed method can efficiently correct for the scatter without additional scans or hardware equipments.

5. References

- [1] Ernst-Peter Rührnschopf and Klaus Klingenberg, "A general framework and review of scatter correction methods in x-ray cone-beam computerized tomography. Part 1: Scatter compensation approaches", *Med.Phys.*, 2011, pp. 4296-4311.
- [2] Ernst-Peter Rührnschopf and Klaus Klingenberg, "A general framework and review of scatter correction methods in cone beam CT. Part 2: Scatter estimation approaches", *Med.Phys.*, 2011, pp. 5186-5199.
- [3] F. Natterer, *The Mathematics of Computerized Tomography*, Philadelphia: SIAM, 2001.
- [4] L. A. Love and R. A. Kruger, "Scatter estimation for a digital radiographic system using convolution filtering", *Med.Phys.*, 1987, pp. 178-185.
- [5] J. A. Seibert and J. M. Boone, "X-ray scatter removal by deconvolution", *Med.Phys.*, 1988, pp. 567-575.
- [6] B. Ohnesorge et al, "Efficient object scatter correction algorithm for third and fourth generation CT scanners", *Eur.Radiol.*, 1999, pp. 563-569.
- [7] Josh Star-Lack et al, "Efficient scatter correction using asymmetric kernels", in *Proceedings SPIE.*, 2009, p 72581Z
- [8] Avinash C. Kak and Malcolm Slaney, *Principles of Computerized Tomographic Imaging*, NY: IEEE Press, 1988
- [9] J. Kennedy and R. C. Eberhart, "Particle swarm optimization", in *Proceedings IEEE Neural Networks*, 1995, pp. 1942-1948.

A Sparse Monte Carlo Method for High-Speed, High-Accuracy Scatter Correction for Soft-Tissue Imaging in Cone-Beam CT

Wojciech Zbijewski, Alejandro Sisniega, J. Webster Stayman, John Yorkston, Nafi Aygun, Vassili Koliatsos, and Jeffrey H. Siewerdsen

Abstract—Cone-beam CT (CBCT) offers the capability for novel, point-of-care imaging platforms dedicated and optimized to specific diagnostic tasks, many with stringent demands on quantitative accuracy, image uniformity, and detectability of low-contrast soft-tissue structures that exceed conventional image quality limits. For example, a CBCT system is now under development for imaging of traumatic brain injury at the point-of-care, employing a compact scanning geometry and requiring a new level of image quality / radiation dose performance beyond that of previous CBCT applications. Among the major challenges to image quality, uniformity, and dose is x-ray scatter, motivating the development of a high-speed, high-fidelity scatter estimation and correction methodology to yield artifact free images with contrast resolution sufficient for the task of detecting small, fresh bleeds (~1 mm diameter, 50 Hounsfield Unit contrast). We report a fast and accurate approach for Monte Carlo (MC) based scatter correction that advances computational speed to practical levels and accuracy in scatter fluence estimation well beyond that of simple parametric approaches. A novel methodology combining GPU acceleration, variance reduction techniques, simulations with low number of photons and with a reduced number of projection angles (sparse MC) augmented by kernel denoising yields a computation time of ~2 min. Uniformity in reconstructions of a realistic head phantom is improved by ~60% compared to an uncorrected image and by ~20% compared to an "oracle" correction based on constant scatter fraction. The sparse MC framework is also suitable to integration with novel reconstruction methods (e.g., model-based penalized weighted least squares) under development to advance CBCT image quality beyond conventional limits to a level required by challenging application in brain imaging.

Index Terms—X-ray Scatter, Monte Carlo Simulation, Artifact Correction, CT Reconstruction, Head CT.

I. INTRODUCTION

Increased awareness of the healthcare burden of traumatic brain injury (TBI), estimated to result in >\$76B in direct and indirect costs, has generated a growing interest in imaging technologies for assessment of brain injury directly at the point-of-care or even within the environment where TBI frequently occurs (e.g., athletic or war theater). Such

This work was supported in part by academic-industry partnership with Carestream Health (Rochester NY).

W. Zbijewski, A. Sisniega, J. W. Stayman, and J. H. Siewerdsen are with the Department of Biomedical Engineering, Johns Hopkins University, Baltimore, MD 21212 USA (phone: 410-955-1305; fax: 410-955-1115; e-mail: wzbijewski@jhu.edu).

J. Yorkston is with Carestream Health, Rochester, NY.

N. Aygun is with Dept. of Radiology and V. Koliatsos is with Dept. of Neurology, Johns Hopkins University, Baltimore, MD.

technology could also find application in other settings where visualization of acute brain injury is essential for proper diagnosis and treatment, e.g. in assessment of concussion or intracranial hemorrhage in the Emergency Department or Intensive Care Unit. Flat-panel detector (FPD)-based CBCT systems provide an excellent platform for development of point-of-care imaging. Research underway at our institution is developing such technology for high quality imaging of the brain in platforms well suited to such challenging application areas and imaging tasks [Fig. 1 (A)]. One of the significant challenges in such application is the required level of contrast and image uniformity. For the task of detecting fresh intraparenchymal blood associated with acute injury, the contrast is ~50 Hounsfield Units (HU), and the size of a bleed can be as small as ~1 mm in diagnosis of mild TBI. As shown in Fig. 1(B), current generation CBCT systems can detect such contrast levels for >2 mm detail size, but lack image uniformity compared to conventional CT [Fig. 1(C)]. This loss of uniformity is largely caused by shading artifacts due to increased scatter inherent to CBCT. The proposed imaging system involves a compact geometry to facilitate portability, further increasing scatter magnitude. Moreover, the need to minimize radiation dose likely prohibits the use of an antiscatter grids. Consequently, a scatter correction algorithm capable of high-accuracy scatter fluence

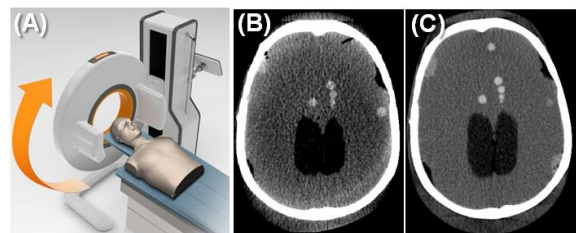


Fig. 1. High-quality CBCT head imaging. (A) Mock illustration of a dedicated CBCT scanner for application in the ICU and other point-of-care settings for high-quality imaging of the head and neck, intracranial hemorrhage, and traumatic brain injury. (B) Reconstruction of a head phantom with simulated bleeds obtained on a current generation CBCT employing scatter grid and basic scatter and beam hardening corrections. (C) Reconstruction of the same phantom on clinical CT.

estimation is essential to achieving the desired level of image quality in head CBCT.

Monte Carlo (MC) simulations provide accurate scatter estimates, but have been considered too computationally expensive for application in scatter correction. Recently, MC simulation engines have been successfully ported onto GPUs [1, 2], providing a convenient parallel platform for fast MC on desktop computers.

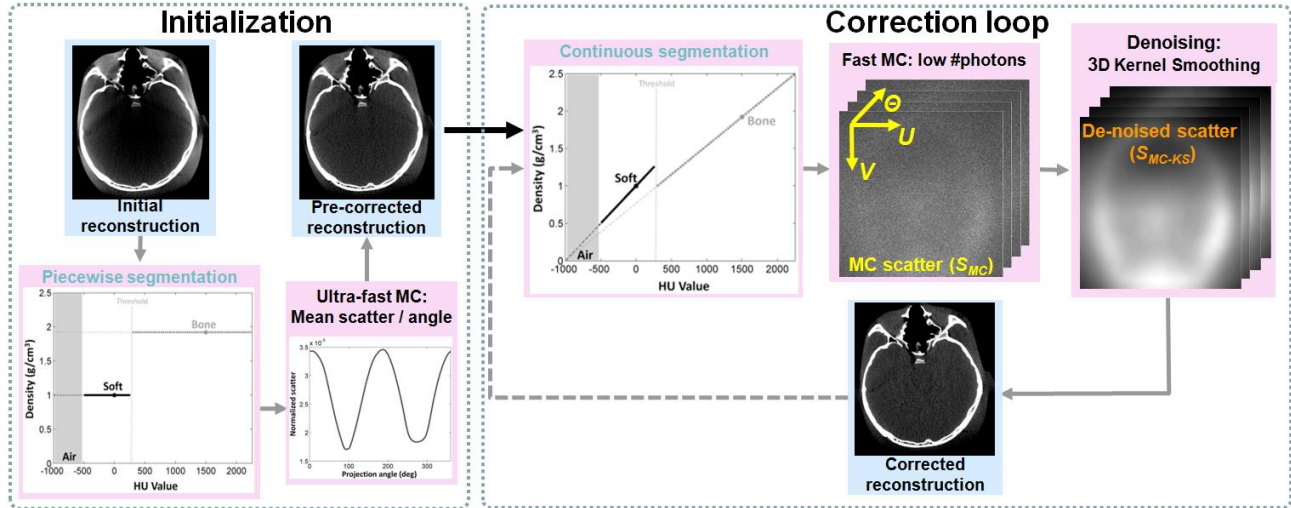


Fig. 2. Workflow of the proposed rapid MC-based scatter correction algorithm, consisting of an initial baseline correction facilitating accurate segmentation in the subsequent correction employing rapid MC-GPU with low number of photon tracks and de-noising of the scatter estimates.

We have combined GPU-based MC simulations of x-ray scatter with GPU-optimized variance reduction (VR) techniques, introduced in the general theory of MC to provide acceleration by improving signal-to-noise ratio (SNR) in the scatter estimates obtained within a given simulation time. Further acceleration of MC is possible by decreasing the number of tracked photons. The resulting speed-up is offset by decreased SNR in the estimates, but successful de-noising of the scatter distributions with 3-dimensional iterative Richardson-Lucy fitting has been demonstrated [3]. This approach exploits the smoothness of scatter in the detector plane and in projection angle. Here we employ a non-iterative (and thus potentially faster) de-noising algorithm (kernel smoothing, KS). We combine this approach with GPU-enabled MC simulation with VR and investigate additional speed-up through a reduction in the number of simulated projections (sparse angular sampling). The proposed approach is tested on experimental data pertinent to head CBCT, demonstrating accurate correction within 2 min simulation time.

II. METHODS

A. GPU-Accelerated Monte Carlo Simulator

The GPU implementation of the MC x-ray transport model is based on MC-GPU v1.1 (code.google.com/p/mcgpu/). In-house additions to the simulator [2] include a probabilistic model of tungsten anode x-ray spectra with arbitrary filtration, and an analytical model of energy-dependent detection in CsI:Tl scintillator.

The GPU-accelerated MC package employs variance reduction through Interaction Splitting, whereby every interacting photon is split into several virtual photons, followed by Forced Detection, whereby virtual photons are deterministically ray-traced toward a randomly selected detector pixel. The implementation of VR was optimized for parallel execution on a GPU [2]. For a head CBCT geometry, VR achieved ~6x improvement in SNR over MC-GPU with no VR at equal runtime [2].

B. A Fast MC Scatter Correction Pipeline

The proposed scatter correction pipeline is illustrated in Fig. 2. In the initialization phase, the initial CBCT reconstruction is segmented by simple thresholding, and a fixed nominal density ("piecwise" segmentation) is assigned to each tissue (bone, soft-tissue, and air). GPU-accelerated MC simulation of the segmented reconstruction is performed using an extremely low number of photons (simulation times of <1 min). The resulting scatter estimates are too noisy to yield accurate correction even with de-noising, but are sufficient to estimate the mean scatter per projection, allowing for a baseline correction.

The corrected reconstruction is then segmented using a second-pass "continuous" tissue model, where the density of each tissue is now allowed to vary in a linear manner based on the HU value. The initial, baseline correction facilitates this approach by reducing gross HU inaccuracies. The use of the continuous model is essential to e.g. avoid under-correction due to over-estimate of scatter absorption in the skull (occurring when the skull is simulated as uniform layer of cortical bone).

GPU-based MC is then applied to the segmented volume. The number of photons is again sparse – low enough to yield practical correction times – but greater than in the initialization phase, so that the resulting scatter distribution S_{MC} can be de-noised to yield an accurate scatter estimate for the correction (S_{MC-KS}):

$$S_{MC-KS}(u, v, \theta) = \frac{\sum_{u_i, v_i, \theta_i} K_{KS}(u, v, \theta, u_i, v_i, \theta_i) S_{MC}(u_i, v_i, \theta_i)}{\sum_{u_i, v_i, \theta_i} K_{KS}(u, v, \theta, u_i, v_i, \theta_i)} \quad (1),$$

where u, v are the detector coordinates, θ is projection angle, and index i runs through the scatter sinogram. K_{KS} is a 3-dimensional Gaussian kernel applied to the distance between two points in the (u, v, θ) space; the FWHM of the kernel is denoted as σ_{KS} . In the studies presented here, the numerical values of σ_{KS} in the spatial and angular dimensions are equal when expressed in pixels for (u, v) and degrees for θ . Note that Eq. (1) allows estimation of the

signal at locations (u, v, θ) located outside of the lattice (u_i, v_i, θ_i) where the noisy input data (S_{MC}) are provided. This allows for estimation of the complete scatter sinogram from simulations done only at a sparse subset of projection angles with no need for interpolation.

C. Experimental Setup

An FPD-based imaging bench is configured in a geometry envisioned for head CBCT as shown in Fig. 1 (A). The SDD is ~ 700 mm, and the SAD is ~ 500 mm. The system employs a PaxScan 4343 FPD (Varian Imaging Products, Palo Alto, CA) with a 250 mg/cm^2 CsI:Tl screen and $0.139 \times 0.139 \text{ mm}^2$ native pixel size; the data is binned to 0.556 mm^2 pixel size. The studies involved a head phantom consisting of a natural skull embedded in uniform water-equivalent (Rando) body material (The Phantom Laboratory, Salem, NY) with spherical contrast-detail patterns in the cranium ($\sim 1\text{-}15$ mm diameter range, ~ -100 - $+200$ HU contrast range). The phantom is imaged at 100 kVp (+2 mm Al, +0.2 mm Cu) and 0.25 mAs/projection; 360 projections are collected at 1° increments.

Reconstructions employed the Feldkamp algorithm using 0.5 mm^3 voxels, Hann apodization and a cutoff at 0.5 of the Nyquist frequency. In each case, bone-induced beam hardening was corrected (after scatter correction) using a variation of the two-pass Joseph-Spital approach [4]. GPU-based MC scatter estimation was executed on an Nvidia GTX 780 Ti GPU with 2880 CUDA cores and 3 GB on-board memory (Nvidia, Santa Clara, CA).

The accuracy of the correction was assessed by evaluating the uniformity of the reconstructions. A region-of-interest (ROI) consisting of the complete intra-cranial volume was chosen inside a 10 mm thick slab in the superior orbital region of the head, where the cranium is filled only with the brain-equivalent Rando material. The ROI was thus expected to be uniform; deviations from uniformity were measured by computing the standard deviation of voxel values in the ROI (denoted as nonuniformity, NU). While this metric includes both the effects of noise and artifact, it

is assumed that for the same projection dataset, changes in NU primarily reflect changes in the artifact level, with lower values of NU indicating more uniform images.

III. RESULTS

Fig. 4 (A) shows a gold standard MC result computed from the head phantom reconstruction with 10^{11} photons/projection (no VR was applied). A noisy distribution obtained with 10^8 photons/projection (and x1000 shorter runtime) [Fig. 4 (B)] is successfully restored with KS to a similar level of noise and detail as the gold standard, as shown in Fig. 4 (C). Fig. 5 demonstrates the relationship between the uniformity in the scatter corrected reconstructions, the number of simulated photon histories, and the size of the smoothing kernel (again without VR). The size of σ_{KS} yielding minimal NU increased with increasing number of photons, reflecting increased noise in the MC scatter estimates. Very small kernels ($\sigma_{KS} = 10$

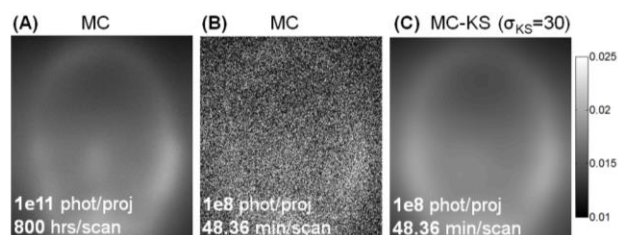


Fig. 4. (A) A gold-standard MC scatter simulation of the head phantom using 10^{11} photons/projection is compared with MC simulations with 10^8 phot/proj (B), along with the corresponding result of 3D KS (C).

pixels/degrees, likely smaller than typical scatter PSF) are insufficient even for 10^8 phot/proj, whereas simulation with a very low number of photons yielded artifacts in the corrected images even for σ_{KS} close to the optimum [Fig. 5 (B)]. For large kernels, the performance was similar across the entire range of numbers of photon histories; in this case, MC-KS converged to a correction with uniform scatter estimation per projection and exhibited overcorrection.

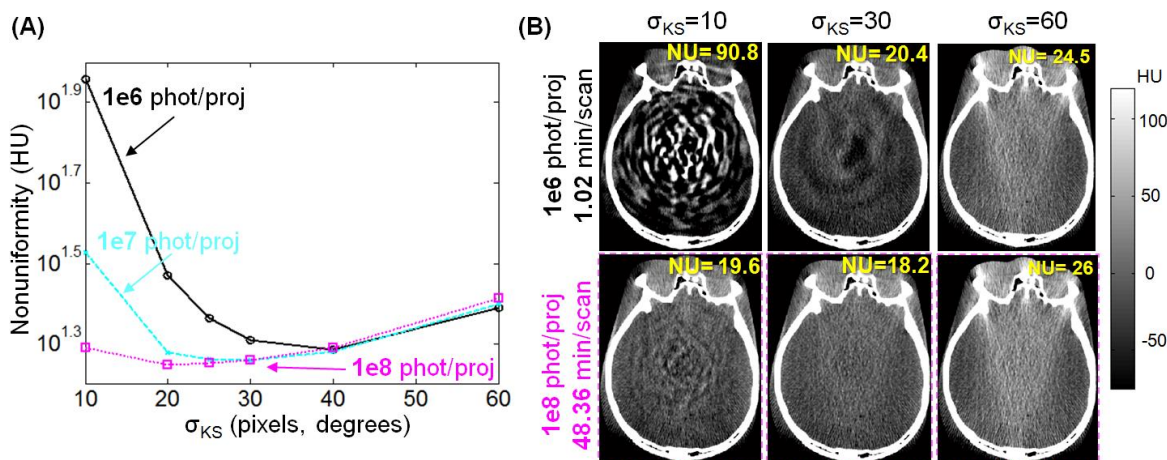


Fig. 5. (A) The nonuniformity NU in reconstructions obtained using MC-KS scatter correction as a function of the number of simulated photons and the size of the 3D smoothing kernel σ_{KS} . (B) MC-KS scatter corrected reconstructions obtained using MC with 10^6 photons/projection (top row) and 10^8 photons/projection (bottom row) and various sizes of the smoothing kernel.

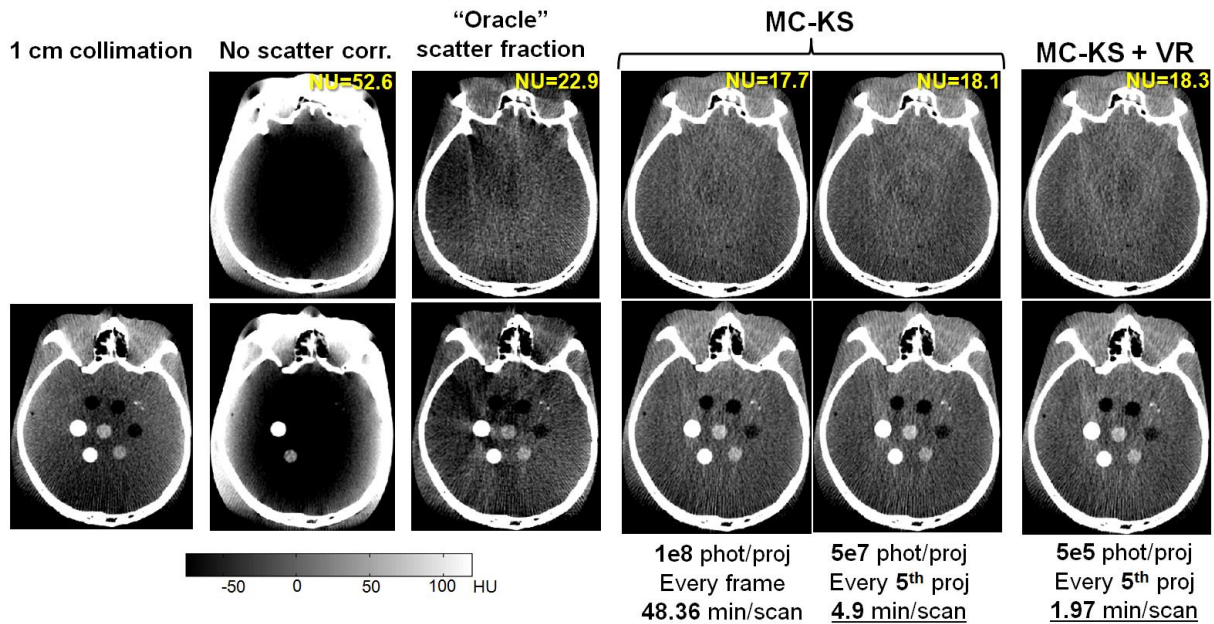


Fig. 6. Comparison of CBCT head phantom reconstructions without scatter correction, with a basic scatter correction and with MC-KS scatter correction. Highly uniform reconstructions with significantly reduced artifacts are achievable within ~ 2 min/scan using accelerated MC simulations.

Scatter-corrected reconstruction obtained with MC-KS with 10^8 phot/proj in Fig. 5 achieved a high level of uniformity, but the simulation time (~ 50 min) is prohibitive for many clinical applications. While the potential for further reduction in the number of simulated photons without sacrificing uniformity certainly exists [as demonstrated e.g. by the 10^7 phot/proj MC-KS curve in Fig. 5 (A)], an alternative approach was investigated that combines MC with a low number of photons with sparse sampling of the projection angles. Example results are shown for the head phantom in Fig. 6. Reconstruction of a thinly collimated scan with reduced scatter is compared with a reconstruction with no scatter correction (initial volume in the scatter correction pipeline of Fig. 2), reconstruction with an "oracle" constant scatter fraction correction (scatter in each projection estimated as a constant fraction of the signal in the center of the shadow of the object, where the fraction is estimated from an MC simulation), and three examples of MC-KS. For MC-KS, the kernel sizes were chosen to minimize NU . MC-KS with no VR, 10^8 phot/proj and no projection subsampling shows considerable improvement over uncorrected image ($\sim 60\%$ reduction in NU), noticeable improvement over the "oracle" correction ($\sim 20\%$ reduction in NU and reduction in artifacts) and similar (or slightly better) uniformity as the collimated scan (no NU estimate is available due to the limited field of view). A very similar level of uniformity was exhibited by MC-KS correction with $5 \cdot 10^7$ phot/proj (no VR) and simulation of every 5th projection, requiring less than 5 min simulation time per scan. Even shorter simulation time of only 2 min/scan achieved a comparable level of uniformity and artifact when MC-KS was combined with variance reduction, using fewer photons in the VR simulation, but giving a noise level similar to that of plain

MC with $\sim 30x$ more photon histories.

IV. DISCUSSION

Monte Carlo-based scatter correction in head CBCT imaging was achieved within ~ 2 min simulation time by employing a combination of sparse sampling in the number of photons and projection angles with variance reduction, GPU acceleration, and denoising via kernel smoothing. The ability to achieve accurate scatter estimation with sparse sampling of projections can be advantageous for MC acceleration because of the potentially better load balancing associated with tracking of a large number of photons concentrated within fewer frames (compared to simulating fewer photons for all projection angles). Such tradeoffs are a subject of ongoing work. The proposed approach relies on an accurate segmentation of the reconstructed volume; current results show a $\sim 20\%$ degradation in uniformity when the continuous object model is replaced with the simpler piecewise model. Segmentation algorithms, tissue models and associated calibration methods are under investigation. Integration with model-based image reconstruction for further enhancement of soft tissue detectability will be pursued, initially as a pre-correction step in a Penalized Weighted Least Squares approach operating on line integral data. The algorithm will be validated in a series of benchtop studies and deployed on the dedicated CBCT scanner currently under development at for high-quality imaging of the head and neck.

REFERENCES

- [1] A. Badal et al. "Accelerating Monte Carlo simulations of photon transport in a voxelized geometry using a massively parallel GPU," *Med. Phys.*, 2009.
- [2] A. Sisniega et al., "Monte Carlo study of the effects of system geometry and antiscatter grids on cone-beam CT scatter distributions," *Med. Phys.*, 2013.
- [3] W. Zbijewski et al. "Efficient Monte Carlo based scatter artifact reduction in cone-beam micro-CT," *IEEE TMI*, 2006.
- [4] P. M. Joseph et al. "A method for correcting bone induced artifacts in computed tomography scanners," *J. Comput. Assist. Tomogr.* 1978.

Deformable 3D–2D Registration for CT and its Application to Low Dose Tomographic Fluoroscopy

Barbara Flach, Jan Kuntz, Marcus Brehm, Rolf Kueres, Sönke Bartling, and Marc Kachelrieß

Abstract—4D intervention guidance by low dose tomographic fluoroscopy opens up the possibility to make interventions faster and saver. To do so, a prior volume of the patient is acquired at the beginning of the intervention and is then continuously updated using a very low number of low dose cone-beam projections during the intervention. To update the prior, which is also known as the running prior, a deformable registration that robustly works with sparse target data is required. Volume-to-volume registration, however, suffers from streak artifacts contained in the target volumes that are reconstructed from a very low number of projections. To overcome this drawback, we here introduce a new deformable volume-to-rawdata registration algorithm.

The proposed 3D–2D registration computes a displacement vector field that maximizes the agreement of a CT volume and the acquired rawdata. The registration is constrained by a regularization term in accordance with a fluid-based diffusion. Optimizing the rawdata term and the regularization term is done in an alternating manner. The agreement with the rawdata is optimized by a conjugate gradient method for non-linear functions, while the regularization is realized by convolution of the vector fields with Gaussian kernels.

Based on measured data from an in-vivo pig we show that the results of our 3D–2D deformable registration do not depend as strong on the number of projections used for defining the target position as the results of the demons algorithm do. This opens the opportunity to increase the temporal resolution of the running prior technique, and in consequence to increase the robustness of low dose tomographic fluoroscopy.

Index Terms—computed tomography (CT), flat detector CT, interventional radiology, minimally-invasive interventions, under-sampled reconstructions, deformable registration

I. INTRODUCTION

MINIMALLY-INVASIVE interventions become more and more important due to a quicker recovery of the patient and a reduced risk of infections [1]. These interventions are often guided by projective fluoroscopy providing temporally resolved projection (2D+time) data. But those projection images show only a superposition of the patient's anatomy and therefore the navigation through more complex structures is difficult because the images are ambiguous. Continuously displaying 3D volumes would obviously help but for clinical

Barbara Flach, Dr. Jan Kuntz, Marcus Brehm, Rolf Kueres, and Prof. Dr. Marc Kachelrieß: Medical Physics in Radiology, German Cancer Research Center (DKFZ), 69120 Heidelberg, Germany.

Barbara Flach, Dr. Jan Kuntz, and Prof. Dr. Marc Kachelrieß: Institute of Medical Physics, University of Erlangen–Nürnberg, 91052 Erlangen, Germany.

Dr. Sönke Bartling: Personalized Interventional Oncotherapy, German Cancer Research Center (DKFZ), 69120 Heidelberg, Germany and Institute for Clinical Radiology and Nuclear Medicine, University Medical Center Mannheim, 68167 Mannheim, Germany.

Corresponding author: barbara.flach@dkfz.de

acceptance the dose level needs to be as low as in projective fluoroscopy.

Recently we published the PrIDICT algorithm for low dose tomographic fluoroscopy which provides temporally resolved volume (3D+time) data at the same dose level as projective fluoroscopy [2], [3]. This becomes possible using a high quality prior volume acquired before the intervention showing the patient's anatomy and extracting only the position of the interventional material out of very few projections acquired during the intervention. Figure 1 shows some time frames of such a reconstruction. To make the PrIDICT algorithm more robust regarding movements of the patient we extended it by the running prior technique [4]. A deformable volume-to-volume (3D–3D) registration based on the demons algorithm [5] is used to correct for motion between the prior scan and the current position of the patient represented by a reconstruction of the latest intervention projection data. In addition, each projection is incorporated into the resulting running prior volume to account for low-contrast objects appearing during the intervention like bleedings.

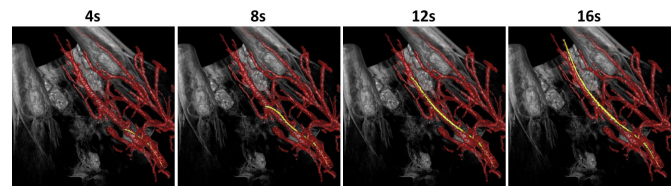


Fig. 1. Volume renderings of an intervention guided by low dose tomographic fluoroscopy. The anatomy is shown in gray, the vasculature in red and the guidewire in yellow.

The quality of the registration highly depends on the quality of the target volumes. If those are reconstructed from too few projections, e.g. to ensure a high temporal resolution of the running prior, the image quality is deteriorated and therefore the results of the registration are not acceptable [6]. To avoid the influence of reconstruction artifacts we here introduce a deformable volume-to-rawdata (3D–2D) registration calculating a displacement vector field (DVF) $u(\mathbf{r})$ that gives a displacement for each voxel.

The existing 3D–2D registration literature is typically restricted to rigid transformations [7]–[10]. A deformable 3D–2D registration based on motion vector fields is suggested by Wang et al. [11] who minimize the cost function for matching an volume to projection data by a conjugate gradient (CG) method. Prümmer et al. [12] propose a deformable 3D–2D registration with curvature regularization and solve it by discrete cosine transforms.

Here we introduce a new 3D–2D registration with a fluid–based diffusion regularization to get a fair comparison to the demons algorithm which works with this regularization.

II. MATERIALS AND METHODS

The potential workflow of an intervention guided by our low dose tomographic fluoroscopy will start with the acquisition of a high quality prior volume f_P reconstructed from about $N_P = 600$ projections. Afterwards, maybe with a short break inbetween, the intervention starts. To reach a dose level as low as in projective fluoroscopy only very few interventional projections $10 \leq N_I \leq 20$ per half rotation were acquired. They serve for the reconstruction of the interventional material and for the adaptation of the prior.

A. Low Dose Tomographic Fluoroscopy

The volumes shown during the intervention, which we refer to as the time frames $f_{TF,i}$, must not show undersampling artifacts. For this reason we apply the PrIDICT algorithm [2], [3]. It uses the information about the anatomy of the high quality prior volume f_P and combines it with the temporally resolved interventional material. Ideally the rawdata difference between the latest acquired projections p_i consisting of e.g. $N_I = 15$ projections and the forward projection of the prior volume f_P in the same geometry shows only the interventional material and some noise. A reconstruction of this difference is deteriorated by streak artifacts because of the high undersampling. We use the fact that the interventional material is very small and of high contrast. Hence, the reconstructed difference volume is sparse and we reduce its L_0 –norm by setting all insignificant voxels to zero. The result of this step is a volume showing only the interventional material which is added to the prior volume for display. Summarizing,

$$f_{TF,i} = f_P + \phi \left(X^{-1}(p_i - X(f_P)) \right),$$

with X being the x–ray transform and ϕ being the sparsifying transformation setting insignificant voxels to zero.

This algorithm is extended by replacing the static prior volume f_P by the running prior $f_{RP,i}$, with $f_{RP,0} = f_P$. This running prior $f_{RP,i}$ evolves from the last running prior $f_{RP,i-1}$ by a non–rigid deformation with the DVF \mathbf{u}_i resulting from a registration explained more detailed in section II–B for a fixed i . Additionally to this deformation step we use the latest acquired rawdata p_i to replace the information of older projections in the deformed running prior of the last time step $\hat{f}_{RP,i}(\mathbf{r}) = f_{RP,i-1}(\mathbf{r} + \mathbf{u}_i(\mathbf{r}))$. This is done by forward projecting $\hat{f}_{RP,i}$ in the same geometry as the projections p_i are acquired, by subtracting these forward projections from the p_i , and by adding the reconstruction of the difference to the deformed running prior of the last step $\hat{f}_{RP,i}(\mathbf{r})$:

$$f_{RP,i} = \hat{f}_{RP,i} + X^{-1}(p_i - X\hat{f}_{RP,i}).$$

B. 3D–2D Registration

In reference [4] the DVF $\mathbf{u}(\mathbf{r})$ is determined by a registration of the last running prior $f_{RP,i-1}(\mathbf{r})$ to the current position of the patient defined by a reconstruction of the latest

$N_T = 60$ projections, a volume–to–volume registration. This leads to a lower temporal resolution than that of the displayed interventional material which is reconstructed from $N_I = 15$ projections. One would prefer to have the same temporal resolution for both which means $N_T = N_I$. But using such a low number of projections for the target volume leads to non–acceptable results of a volume–to–volume registration because of the streak artifacts in the target image. To avoid this we decided to compare the deformed volume and the projection data in the rawdata domain leading to a volume–to–rawdata registration.

Such a 3D–2D registration aims at finding the DVF $\mathbf{u}(\mathbf{r})$ maximizing the correlation of a volume and the rawdata. This corresponds to minimizing the functional

$$S[\mathbf{u}] = \|\mathbf{X}m(\mathbf{r} + \mathbf{u}(\mathbf{r})) - p\|_2^2, \quad (1)$$

with $m(\mathbf{r})$ being the model volume which is to be deformed, in our case the last running prior $f_{RP,i-1}(\mathbf{r})$, and p the rawdata defining the target position of the model consisting of N_T projections. This problem is ill–conditioned and therefore we have to constrain the problem by additional requirements on $\mathbf{u}(\mathbf{r})$. Typically, (1) is minimized iteratively and therefore we can introduce a temporal variable t where the development of the DVF over the iterations corresponds to the temporal evolution of the DVF $\mathbf{u}(\mathbf{r}, t)$. That means the DVF $\mathbf{u}(\mathbf{r}, k\Delta t)$ belongs to the result of iteration k and we introduce $\mathbf{u}^{(k)}(\mathbf{r}) := \mathbf{u}(\mathbf{r}, k\Delta t)$. Back to the constraints, we use a fluid–based diffusion registration [13], [14] and ask for a smooth DVF $\mathbf{u}(\mathbf{r}, t)$ as well as a smooth velocity vector field $\mathbf{v}(\mathbf{r}, t) = \partial_t \mathbf{u}(\mathbf{r}, t)$. To achieve smoothness of a vector field $\mathbf{w}(\mathbf{r}, t) = (w_1(\mathbf{r}, t), w_2(\mathbf{r}, t), w_3(\mathbf{r}, t))^T$ the following term has to be minimized:

$$R[\mathbf{w}] = \sum_{d=1}^3 \sum_{\mathbf{r} \in \Omega} \langle \nabla_{\mathbf{r}} w_d(\mathbf{r}, t), \nabla_{\mathbf{r}} w_d(\mathbf{r}, t) \rangle,$$

with $\langle \cdot, \cdot \rangle : V \times V \rightarrow \mathbb{R}$ the inner product on a vector space V and $\nabla_{\mathbf{r}} = (\partial_{x_1}, \partial_{x_2}, \partial_{x_3})^T$ the spatial derivative in \mathbf{r} . To summarize the registration should minimize the following cost function

$$C[\mathbf{u}] = S[\mathbf{u}] + \beta R[\mathbf{u}] + \gamma R[\partial_t \mathbf{u}]$$

with β and γ being regularization parameters that have to be chosen according to the problem.

For efficient calculation we separate the minimization terms and thus introduce a linking term

$$C[\bar{\mathbf{u}}, \underline{\mathbf{u}}] = S[\bar{\mathbf{u}}] + \sigma \|\bar{\mathbf{u}} - \underline{\mathbf{u}}\|_2^2 + \beta R[\underline{\mathbf{u}}] + \gamma R[\partial_t \underline{\mathbf{u}}].$$

The solution can be approximated by minimizing in an alternating manner

$$C[\bar{\mathbf{u}}] = S[\bar{\mathbf{u}}] + \sigma \|\bar{\mathbf{u}} - \underline{\mathbf{u}}\|_2^2, \quad (2)$$

with fixed $\underline{\mathbf{u}}$ and

$$C[\underline{\mathbf{u}}] = \sigma \|\bar{\mathbf{u}} - \underline{\mathbf{u}}\|_2^2 + \beta R[\underline{\mathbf{u}}] + \gamma R[\partial_t \underline{\mathbf{u}}], \quad (3)$$

with fixed $\bar{\mathbf{u}}$.

The first problem (2) is solved by a conjugate gradient (CG) method for non–linear functions [15]. The linking term

$\sigma\|\bar{\mathbf{u}} - \mathbf{u}\|_2^2$ is accounted for by initializing the CG step by the result \mathbf{u} originating from the last minimization of problem (3). The second problem (3) can be solved by convolution of the DVF $\mathbf{u}(\mathbf{r}, t)$ and the velocity vector field $\mathbf{v}(\mathbf{r}, t) = \partial_t \mathbf{u}(\mathbf{r}, t)$ with Gaussian kernels [16], [17]. Since the iterations can be regarded as temporal development of the deformation the velocity field belongs to the update part for which the displacement field $\mathbf{u}^{(k)}$ is adjusted to get $\mathbf{u}^{(k+1)}$.

We end up with the registration algorithm shown in algorithm 1.

Algorithm 1 Deformable 3D–2D registration algorithm with alternating minimization of dissimilarity by CG algorithm for non-linear functional $S[\mathbf{u}]$ and minimization of regularization by convolution with Gaussian kernels.

Initialize:

$$\begin{aligned} \mathbf{u}^{(0)}(\mathbf{r}) &= 0 && \text{or a given DVF} \\ \mathbf{g}^{(0)}(\mathbf{r}) &= \nabla_{\mathbf{u}} S[\mathbf{u}^{(0)}(\mathbf{r})] && \text{gradient} \\ \mathbf{d}^{(0)}(\mathbf{r}) &= -\mathbf{g}^{(0)}(\mathbf{r}) && \text{conjugate search direction} \end{aligned}$$

Iterate:

Smooth velocity field to model fluid motion

$$\mathbf{d}^{(k)}(\mathbf{r}) = K_{\text{fluid}} * \mathbf{d}^{(k)}(\mathbf{r})$$

Determine step length λ by backtracking line search [18] to minimize

$$\|\mathcal{X}m(\mathbf{r} + \lambda \mathbf{d}^{(k)}(\mathbf{r}) + \mathbf{u}^{(k)}(\mathbf{r} + \lambda \mathbf{d}^{(k)}(\mathbf{r}))) - p\|_2^2$$

Update DVF

$$\mathbf{u}^{(k+1)}(\mathbf{r}) = \lambda \mathbf{d}^{(k)}(\mathbf{r}) + \mathbf{u}^{(k)}(\mathbf{r} + \lambda \mathbf{d}^{(k)}(\mathbf{r}))$$

Smooth DVF to model diffusive motion

$$\mathbf{u}^{(k+1)}(\mathbf{r}) = K_{\text{diffusive}} * \mathbf{u}^{(k+1)}(\mathbf{r})$$

Calculate forces for next iteration

$$\begin{aligned} \mathbf{g}^{(k+1)}(\mathbf{r}) &= \nabla_{\mathbf{u}} S[\mathbf{u}^{(k+1)}(\mathbf{r})] \\ \rho &= \max \left\{ 0, \frac{\mathbf{g}^{(k+1)\top}(\mathbf{g}^{(k+1)} - \mathbf{g}^{(k)})}{\mathbf{g}^{(k)\top} \mathbf{g}^{(k)}} \right\} \\ \mathbf{d}^{(k+1)}(\mathbf{r}) &= -\mathbf{g}^{(k+1)}(\mathbf{r}) + \rho \mathbf{d}^{(k)}(\mathbf{r}) \end{aligned}$$

Note that this algorithm, apart from the calculation of the forces, is similar to the demons algorithm as described in reference [13] and as implemented for the results here and in reference [4].

C. Datasets

We applied the proposed algorithm to a dataset where the carotid of a pig was probed with a guidewire. The data for the prior volume consist of $N_p = 600$ projections distributed over a full rotation and were acquired within 20 s at 80 kV tube voltage and 50 mA tube current. During the intervention we acquired 120 projections per full rotation at a sampling rate of 30 frames per second. From these data we use only every fourth projection for our investigations resulting in $N_1 = 15$

projections per half rotation used for reconstruction of each time frame. Between the prior and the intervention scan the pig was moved manually while there was almost no motion except for the interventional material during the intervention scan itself. Based on the dataset we compare the registration results using the demons algorithm as described in reference [13] and the proposed 3D–2D registration with $N_T = \{60, 30, 15, 8\}$ projections. Both registrations are initialized by the same DVF $\mathbf{u}^{(0)}$ resulting from an affine registration.

III. RESULTS

The comparison of the errors with different N_T in figure 2 shows exemplarily on one slice that the registration results from the demons algorithm strongly depend on the number of projections while the registration results from the proposed 3D–2D registration are stable and do not show this effect. As ground truth $f_{\text{GT}}(\mathbf{r})$ we take the reconstruction from all available projections. The residual error in image domain is defined as the difference $f_P(\mathbf{r} + \mathbf{u}(\mathbf{r})) - f_{\text{GT}}(\mathbf{r})$ respectively the initial error as $f_P(\mathbf{r}) - f_{\text{GT}}(\mathbf{r})$ and in rawdata domain $\mathcal{X}f_P(\mathbf{r} + \mathbf{u}(\mathbf{r})) - p$ respectively $\mathcal{X}f_P(\mathbf{r}) - p$.

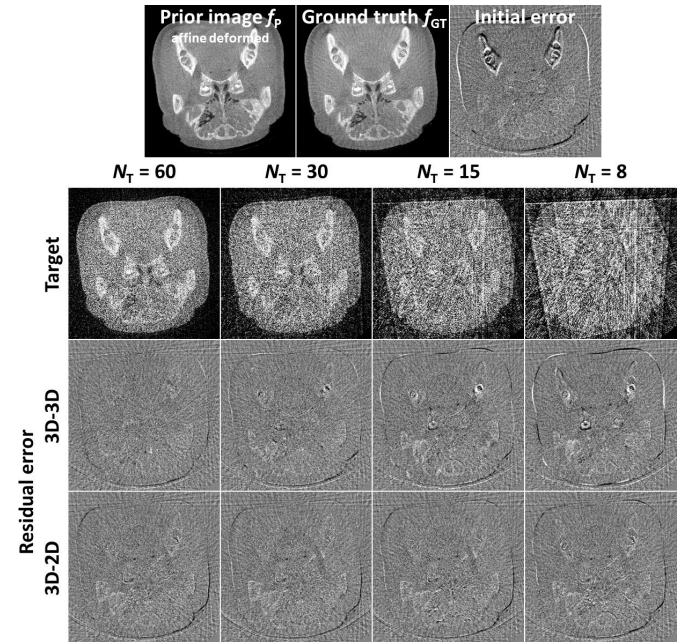


Fig. 2. Comparison of registration results from a 3D–3D registration and a 3D–2D registration with different numbers of projections. The images are shown at a gray scale window of $C = 0$ HU, $W = 1500$ HU. The error images are shown at a gray scale window of $C = 0$ HU, $W = 1000$ HU.

Since our aim is to use only $N_T = N_1 = 15$ projections for the registration we compared both registrations especially for this case. Figure 3 shows the residual errors for $N_T = 15$ in image domain by further slices of the dataset and in rawdata domain.

It demonstrates that both algorithms improve the matching as can be seen comparing with the initial error. In most parts of the image 3D–2D registration is superior to the 3D–3D registration, e.g. in areas pointed to by arrows. A similar result can be observed in rawdata domain. This is not surprising

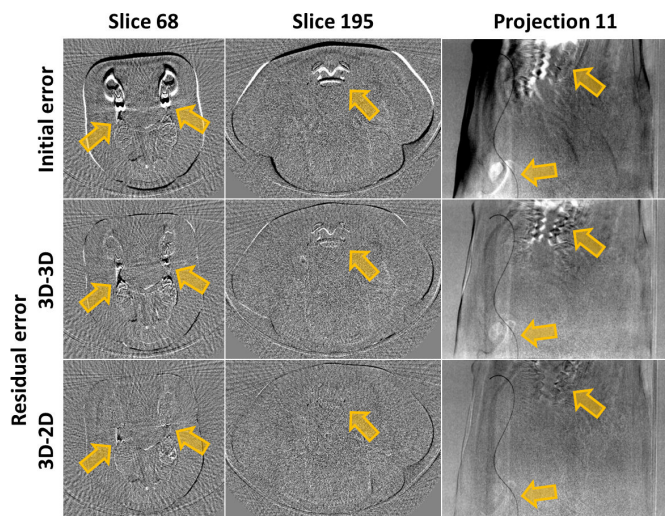


Fig. 3. Comparison of residual errors in image and in rawdata domain for $N_T = 15$ projections. The images are shown at a gray scale window of $C = 0$ HU, $W = 1000$ HU and the rawdata images at a window of $C = 0, 0$, $W = 1.0$.

since with 3D–2D registration this expression is explicitly minimized. Both observations are confirmed by the objective results shown in table I where we analyzed the error in the image domain defined by $E_{\text{img}} = \|f_P(\mathbf{r} + \mathbf{u}(\mathbf{r})) - f_{\text{GT}}(\mathbf{r})\|_2^2 / \|f_{\text{GT}}(\mathbf{r})\|_2^2$ and in the rawdata domain defined by $E_{\text{raw}} = \|\mathbf{X}f_P(\mathbf{r} + \mathbf{u}(\mathbf{r})) - p\|_2^2 / \|p\|_2^2$. We calculated the norms only in parts not affected by truncation.

TABLE I
ERRORS OF DIFFERENT REGISTRATION APPROACHES IN IMAGE AND RAWDATA DOMAIN.

	Initial	3D–3D	3D–2D
E_{raw}	$28.06 \cdot 10^{-4}$ = 100 %	$10.66 \cdot 10^{-4}$ = 38 %	$6.85 \cdot 10^{-4}$ = 24 %
E_{img}	0.061 = 100 %	0.042 = 68 %	0.037 = 60 %

IV. CONCLUSION AND DISCUSSION

Our investigations on improving the temporal resolution of the running prior are promising. The registration results show that the matching in rawdata domain offers the potential to reduce the number of projections used for the registration to $N_T = N_I = 15$. Although the registration is here introduced for CT with the X–ray transform it can easily be applied also to other imaging techniques by replacing the X–ray transform, for example by the Fourier transform in MRI.

ACKNOWLEDGEMENT

This study was supported by the Deutsche Forschungsgemeinschaft (DFG) under grant KA 1678/6-1. The high performance compute hardware was provided by the Universitätsbund Erlangen–Nürnberg e.V., Erlangen, Germany. Parts of the reconstruction software were provided by RayConStruct® GmbH, Nürnberg, Germany.

REFERENCES

- [1] A. Brill, J. Fleshman Jr., B. Ramshaw, S. Wexner, and O. Kaidar-Person, “Minimally invasive procedures: what family physicians need to know,” *The Journal of family practice*, vol. Suppl, pp. S1–22, Nov. 2005.
- [2] J. Kuntz, R. Gupta, S. Schönberg, W. Semmler, M. Kachelrieß, and S. Bartling, “Real-time X–ray–based 4D image guidance of minimally invasive interventions,” *European Radiology*, Jan. 2013.
- [3] J. Kuntz, B. Flach, R. Kueres, W. Semmler, M. Kachelrieß, and S. Bartling, “Constrained reconstructions for 4D intervention guidance,” *Phys. Med. Biol.*, vol. 58, no. 10, pp. 3283–3300, May 2013.
- [4] B. Flach, J. Kuntz, M. Brehm, R. Kueres, S. Bartling, and M. Kachelrieß, “Low dose tomographic fluoroscopy: 4D intervention guidance with running prior,” *MedPhys*, vol. 40, no. 10, p. 101909, Oct. 2013.
- [5] J. Thirion, “Image matching as a diffusion process: an analogy with Maxwell’s demons,” *Medical Image Analysis*, vol. 2, no. 3, pp. 243–260, Sep. 1998.
- [6] B. Flach, J. Kuntz, M. Brehm, R. Kueres, S. Bartling, and M. Kachelrieß, “Up-to-date prior knowledge via motion correction for low dose tomographic fluoroscopy,” *Proceedings of the 12th International Meeting on Fully Three-Dimensional Image Reconstruction in Radiology and Nuclear Medicine*, pp. 193–196, Jun. 2013.
- [7] X. Chen, R. Gilkeson, and B. Fei, “Automatic 3D-to-2D registration for CT and dual-energy digital radiography for calcification detection,” *Med. Phys.*, vol. 34, no. 12, pp. 4934–4943, Dec. 2007.
- [8] D. Fu and G. Kuduvali, “A fast, accurate, and automatic 2D–3D image registration for image-guided cranial radiosurgery,” *Med. Phys.*, vol. 35, no. 5, pp. 2180–2194, May 2008.
- [9] J. Kim, F. Yin, Y. Zhao, and J. Kim, “Effects of x–ray and CT image enhancements on the robustness and accuracy of a rigid 3D/2D image registration,” *Med. Phys.*, vol. 32, no. 4, pp. 866–873, Apr. 2005.
- [10] R. Munbodh, D. Jaffray, D. Moseley, Z. Chen, P. Knisely, P. Cathier, and J. Duncan, “Automated 2D–3D registration of a radiograph and a cone beam CT using line-segment enhancement,” *MedPhys*, vol. 33, no. 5, pp. 1398–1411, May 2006.
- [11] J. Wang and X. Gu, “High-quality four-dimensional cone-beam CT by deforming prior images,” *PMB*, vol. 58, no. 2, pp. 231–246, Jan. 2013.
- [12] M. Prümmer, J. Hornegger, M. Pfister, and A. Dörfler, “Multi-modal 2D–3D non-rigid registration,” *Proceedings of SPIE on Medical Imaging*, vol. 6144, pp. 297–308, Mar. 2006.
- [13] T. Vercauteren, X. Pennec, Y. Perchant, and N. Ayache, “Diffeomorphic demons: Efficient non-parametric image registration,” *NeuroImage*, vol. 45, no. 1 Suppl, pp. S61–S72, Mar. 2009.
- [14] J. Modersitzki, *Numerical Methods for Image Registration*. Oxford University Press, 2004.
- [15] J. Shewchuk, *An introduction to the conjugate gradient method without the agonizing pain*. Pittsburgh, PA, USA: Carnegie Mellon University, 1994.
- [16] P. Cachier and N. Ayache, “Regularization methods in non-rigid registration: II. isotropic energies, filters and splines,” INRIA, Tech. Rep. 4243, Aug. 2001.
- [17] P. Cachier, E. Bardinnet, D. Dormont, X. Pennec, and N. Ayache, “Iconic feature based nonrigid registration: the PASHA algorithm,” *Computer Vision and Image Understanding*, vol. 89, no. 23, pp. 272–298, 2003.
- [18] J. Nocedal and S. Wright, *Numerical optimization*. Springer Verlag, 1999.

Nesterov’s Method for Accelerated Penalized-Likelihood Statistical Reconstruction for C-arm Cone-Beam CT

Adam S. Wang, J. Webster Stayman, Yoshito Otake, Gerhard Kleinszig, Sebastian Vogt,
and Jeffrey H. Siewerdsen

Abstract—C-arm cone-beam CT offers great potential in image-guided interventions, but conventional analytic reconstruction methods are associated with limited image quality, particularly for soft-tissue imaging. While model-based iterative reconstruction (IR) methods improve image quality and/or reduce radiation dose, long reconstruction time limits utility in clinical workflow. Additionally, in contrast to diagnostic CT, C-arm cone-beam CT (CBCT) involves complexities of lateral truncation, an incomplete orbit, and relatively few projections. Lateral truncation in particular slows reconstruction convergence and introduces large errors in the reconstruction. Faster IR algorithms are therefore essential for broader adoption in CBCT-guided procedures. This work examines the acceleration achieved by modifying the ordered-subset, separable quadratic surrogates algorithm for solving the penalized-likelihood (PL) objective to include Nesterov’s method, which utilizes “momentum” from image updates of previous iterations to better inform the current iteration and provide significantly faster convergence. Reconstruction performance was assessed in C-arm CBCT of an anthropomorphic head phantom and cadaveric torso, demonstrating that Nesterov’s method provides equivalent image quality while reducing the reconstruction time by an order of magnitude. Despite the slower convergence of IR with truncated C-arm CBCT, implementation of Nesterov-accelerated PL reconstruction on relatively inexpensive GPUs reduced reconstruction time from ~100 min for the ordered subset, separable quadratic surrogates method to as little as ~2 min.

Index Terms—Iterative Reconstruction, Cone-Beam CT, Radiation Dose, Image-Guided Surgery, Truncation

I. INTRODUCTION

Advances in model-based iterative reconstruction (IR) methods for x-ray CT and cone-beam CT (CBCT) imaging have led to numerous studies demonstrating the benefits of improved image quality and/or reduced radiation dose [1]–[3]. However, the increased reconstruction time (up to several hours, even on commercial systems) is a major drawback that limits the use of IR in many applications, especially those that require timely images as part of the clinical workflow. For example, potential applications of IR for CBCT include the use of C-arms in image-guided surgery for verifying device placement (orthopedic surgery) and providing high-quality, low-dose intraoperative checks against normal tissue complication (e.g., intracranial

This work is supported by NIH fellowship F32-EB017571, an AAPM Research Seed Funding grant, and academic-industry partnership with Siemens Healthcare, XP Division.

A. S. Wang, J. W. Stayman, Y. Otake, and J. H. Siewerdsen are with the Department of Biomedical Engineering, Johns Hopkins University, Baltimore, MD 21205 USA (e-mail: {adamwang, web.stayman, otake, jeff.siewerdsen}@jhu.edu).

G. Kleinszig and S. Vogt are with Siemens Healthcare, Erlangen, Germany (e-mail: {gerhard.kleinszig, sebastian.vogt}@siemens.com).

hemorrhage in neurosurgery) [4][5]. Such applications demand image reconstructions on the order of minutes rather than hours.

Accelerating iterative reconstruction is an active area of research and can be addressed using a number of possible solutions, including hardware and/or algorithmic improvements. For example, the separable quadratic surrogates (SQS) method iteratively solves the penalized-likelihood (PL) reconstruction problem using a highly parallelizable approach that can leverage advances in parallel computing such as GPUs, but convergence can still be slow. Further compounding the challenge, lateral truncation of projections is typical in C-arm CBCT due to the relatively small field of view (FOV). Expanding the reconstruction FOV beyond the C-arm “complete data” FOV is important in IR methods to enforce consistency of the line integral of the reconstruction with the measurements, but the problem is generally ill-conditioned. Image regularization can improve conditioning of the problem, but truncated data and/or sparse sampling leads to even slower convergence.

A common acceleration technique divides the projections into ordered subsets (OS) to accelerate the reconstruction by a factor approximately equal to the number of subsets. Even so, convergence typically requires hundreds of iterations and can take hours. While conventional SQS updates the image without any “memory” of previous updates, the algorithm can be modified to carry “momentum” from previous updates to better inform the current update. Kim *et al* recently demonstrated such a method [6], combining OS-SQS with Nesterov’s method [7] to achieve faster convergence in penalized weighted least squares (PWLS) for CT reconstructions. The work below extends Nesterov’s method to acceleration of PL reconstruction in C-arm CBCT in the context of image-guided surgery, with a particular emphasis on how acceleration can help overcome convergence issues associated with truncated data. Performance is assessed relative to SQS in an anthropomorphic head phantom for truncated and untruncated data, and demonstrated in a cadaveric torso emulating a scenario of CBCT-guided abdominal surgery.

II. METHODS

A. Statistical Reconstruction Algorithms

The PL framework enables statistical image reconstruction by first applying a basic Poisson statistics model to the data:

$$y_i \sim \text{Poisson}(I_{0,i}e^{-l_i}), \quad (1)$$

where y are the raw projections, I_0 is the number of incident photons, and $l = \mathbf{A}\mu$ are the line integrals computed for system matrix \mathbf{A} (forward-projection) and image volume μ .

PL then formulates the reconstruction as the solution to an optimization problem, where the objective $\Phi(\mu; y)$ comprises the log-likelihood function $L(\mu; y)$ of the data and image regularization by a roughness penalty $R(\mu)$ with strength β :

$$\hat{\mu} = \underset{\mu}{\operatorname{argmax}}\{\Phi(\mu; y) \triangleq L(\mu; y) - \beta R(\mu)\}, \quad (2)$$

Ignoring constant terms, the log-likelihood function is:

$$L(\mu; y) \cong -\sum_i I_{0,i} e^{-l_i} + y_i l_i, \quad (3)$$

and the image roughness is calculated as:

$$R(\mu) = \sum_j \sum_{k \in \mathcal{N}_j} w_{jk} \psi(\mu_j - \mu_k), \quad (4)$$

where j indexes all voxels, k indexes the voxels in a neighborhood \mathcal{N}_j about voxel j (first-order neighborhood in this work), w_{jk} are the weights within a neighborhood (unity in this work), and ψ is the penalty function.

The OS-SQS method [8] is often employed to solve Eq. (2) and utilizes highly parallelizable forward and backprojection operators and voxel-wise operations of volumes. The starting image $\mu^{(0)}$ can be initialized by the filtered backprojection (FBP) reconstruction (although a common alternative is a zero image). When M subsets are used (providing acceleration by approximately a factor of M), the algorithm is run for N iterations as follows (Algorithm 1, denoted SQS- M):

Algorithm 1: SQS with M Ordered Subsets (SQS- M)

Initialize $\mu = \mu^{(0)}$	
Pre-compute $\gamma_m = \mathbf{A}_m \mathbf{1}$, for $m = 1, 2, \dots, M$	
For $n = 1, 2, 3, \dots, N$	
For $m = 1, 2, 3, \dots, M$	
$l = \mathbf{A}_m \mu$	(5)
$\dot{h}_i = y_i - I_{0,i} e^{-l_i}, \forall i \in S_m$	(6)
$\dot{L} = M[\mathbf{A}_m^T \dot{h}]$	(7)
$c_i(l_i) = \begin{cases} 2I_{0,i}(1 - e^{-l_i} - l_i e^{-l_i})/l_i^2, & l_i > 0 \\ I_{0,i}, & l_i = 0 \end{cases}$	(8)
$d = M[\mathbf{A}_m^T (\gamma \cdot c(l))]$	(9)
$\Delta_j = -\frac{\dot{L}_j + \beta \sum_{k \in \mathcal{N}_j} w_{jk} \dot{\psi}(\mu_j - \mu_k)}{d_j + \beta \sum_{k \in \mathcal{N}_j} 2w_{jk} \omega_{\psi}(\mu_j - \mu_k)}$	(10)
$\mu = [\mu + \Delta]_+$	(11)

where \mathbf{A}_m and \mathbf{A}_m^T are the forward and backprojection operators, respectively, for subset m ; γ_m are the projections of a volume of all ones; S_m are the projections in subset m ; i and j index detector pixels and volume voxels, respectively; \dot{L} and d are the gradient and curvature of the likelihood surrogates, respectively; \cdot denotes an element-wise product of two vectors; $\dot{\psi}$ and ω_{ψ} are the derivative and curvature of the penalty function surrogates, respectively; Δ is the image update; and $[\cdot]_+$ is a nonnegativity constraint. In this work, the edge-preserving Huber penalty was used, with

$$\psi_H(x) = \begin{cases} x^2/(2\delta), & |x| \leq \delta \\ |x| - \delta/2, & |x| > \delta \end{cases}, \quad (12)$$

$$\omega_{\psi_H}(x) = 1/\max(|x|, \delta), \quad (13)$$

where δ is used to control the degree of edge preservation by controlling the width of the quadratic penalty region about 0.

Despite the OS acceleration, SQS- M convergence can be very slow. Significant acceleration can be achieved by adapting Nesterov's method [7] with improved momentum weights [9] to accumulate momentum from image updates Δ (denoted $-D^{-1}M\nabla\Psi_m(\mu)$ in [6]). The algorithm is run for N iterations and M subsets as follows (Alg. 2, denoted Nes- M):

Algorithm 2: Nesterov Acceleration of SQS- M (Nes- M)

Initialize $z = v = \mu = \mu^{(0)}, t = 1$	
For $n = 1, 2, \dots, N$	
For $m = 1, 2, \dots, M$	
Compute Δ	
$z = [\mu + \Delta]_+$	(14)
$v = v + t\Delta$	(15)
$t = (1 + \sqrt{1 + 4t^2})/2$	(16)
$\mu = (1 - \frac{1}{t})z + \frac{1}{t}[\mu^{(0)} + v]_+$	(17)

where z is the current image estimate; v is the cumulative momentum from all image updates; t is a scalar that increases approximately linearly with each subiteration; and μ is now a state variable that linearly combines the current image estimate with the cumulative momentum added to the initial image. The image update Δ is computed as usual [Eqs. (5)–(10)]. The additional computational expense of Nesterov's method is minimal: it requires just one additional volume v in memory storage (the implementation can eliminate the intermediate variable z), and the additional computation of v and μ are multiply-and-add, voxel-wise operations of volumes that can be performed in parallel.

B. Experimental Setup

The performance of the SQS- M and Nes- M algorithms were compared on CBCT data acquired using an x-ray test bench and a prototype mobile C-arm capable of CBCT (modified PowerMobil, Siemens Healthcare). Studies employed an anthropomorphic head phantom containing a natural skeleton and simulated soft-tissue inserts as well as a cadaveric torso emulating an abdominal surgery scenario. The test bench incorporated a 43×43 cm² flat-panel detector (PaxScan 4343CB, Varian Medical Systems, 0.278² mm² pixel size) providing little or no lateral truncation (of the head phantom). The C-arm employed a 30×30 cm² detector (PaxScan 3030+, Varian Medical Systems, 0.388² mm² pixel size) with realistic lateral truncation (Fig. 1). The acquisition technique and geometry of the test bench replicated that of the C-arm – 100 kVp tube voltage, 80 mAs total exposure, 198 projections over ~178° orbit, 60 cm SAD, and 120 cm SDD.

The SQS and Nes algorithms were fully implemented using custom CUDA libraries to leverage the parallel computing capabilities of GPUs. Unless otherwise noted, the separable footprints (SF-TT) projector was used due to its greater accuracy [10]. The effect of M was quantified for integer divisors of the number of projections – thus, $M \in \{66, 33, \dots, 1\}$. Lastly, reconstruction parameters were set at $I_0 = 8000$, $\beta = 200$ (for the bench data, and $\beta = 80$ for the C-arm data to compensate for the smaller detector array), $\delta = 10^{-4}$, and 0.6³ mm³ voxel size.

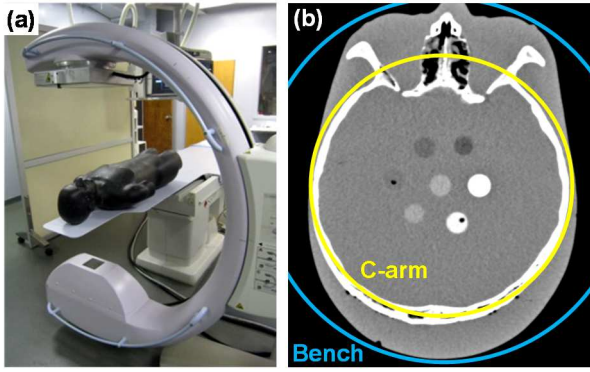


Fig. 1. (a) C-arm with anthropomorphic head phantom. (b) The bench and C-arm FOV are depicted with respect to a CT image of the phantom, display window $[-400\ 400]$ HU.

Different reconstruction algorithms (e.g., Nes-11 vs SQS-1) were compared by assessing how many iterations n_A were required for algorithm A to achieve the same objective value as n_B iterations of algorithm B:

$$\min n_A \text{ s.t. } \Phi(\mu_A^{(n_A)}; y) \geq \Phi(\mu_B^{(n_B)}; y). \quad (18)$$

In this way, the acceleration factor (AF) of algorithm A could be determined in relation to algorithm B:

$$\text{AF}(n_B) = n_B/n_A, \quad (19)$$

which for SQS- M , produces the familiar $\text{AF} \approx M$. Additionally, the root mean square difference (RMSD) between $\mu^{(n)}$ and a ‘‘converged’’ reconstruction μ^* was used to quantify image accuracy as a function of iteration.

III. RESULTS

A. Untruncated Reconstructions of the Head

Test bench images of the head phantom were reconstructed using the SQS- M algorithm run for 1000 iterations for each M , and the acceleration factors relative to SQS-1 demonstrated the speedups associated with SQS- M (Fig. 2). As expected, SQS- M achieved AF up to M (although the AF tends to fall off due to suboptimal limit cycles, as seen with SQS-66). The Nes- M algorithm was similarly run for 100 iterations each and demonstrated much greater AF than SQS- M . For example, Nes-11 exhibited AF = 357 at 10^4 equivalent SQS-1 iterations, and the AF continued to monotonically increase with more iterations,

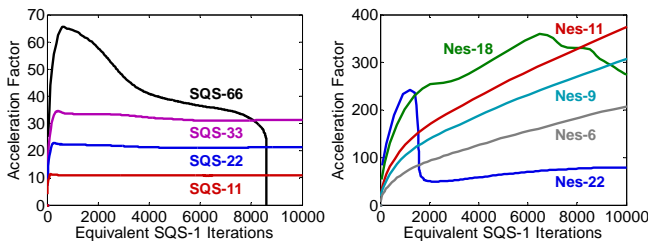


Fig. 2. Acceleration factor for SQS and Nes relative to SQS-1 (note the different y-axis scaling). (a) SQS-66 reaches a suboptimal limit cycle and cannot further improve the objective, while SQS- $\{33, 22, 11\}$ achieve the same objective as 10^4 iterations of SQS-1 in $\{321, 469, 922\}$ iterations, respectively, and provide AF approximately equal to M . (b) On the other hand, Nes- $\{22, 18\}$ exhibit unstable, non-monotonic acceleration, while Nes- $\{11, 9, 6\}$ achieve the same objective as 10^4 iterations of SQS-1 in only $\{28, 34, 50\}$ iterations, giving AF of $\{357, 294, 200\}$, respectively.

suggesting a faster rate of convergence than SQS and increasingly more benefit from additional iterations. The AF also appeared to be proportional to M (for $M \leq 11$). For $M > 11$, the reconstruction may not converge due to limit-cycle issues or instability, since momentum from each subset only contains information from a few projections, which may lead the reconstruction to false local optima.

The converged reference volume μ^* was achieved with 3000 iterations of Nes-1 followed by 3000 iterations of SQS-1 and was confirmed to have greater objective value than any of the other reconstructions. The convergence of SQS- M and Nes- M was assessed by the RMSD with μ^* in a region encompassing soft-tissue simulating inserts (Fig. 3). For SQS reconstructions, SQS-66 most rapidly reduced RMSD in early iterations but quickly leveled out after achieving 2.0 HU † accuracy in 140 iterations, while SQS-33 was capable of RMSD = 1.0 HU after 260 iterations. On the other hand, Nes-18 only required 15 iterations to achieve RMSD = 2.0 HU, and Nes-11 achieved RMSD = 1.0 HU in 21 iterations.

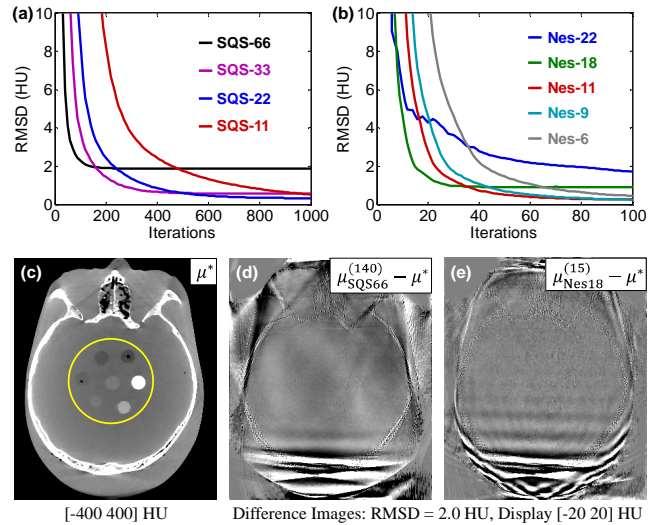


Fig. 3. Accuracy of image reconstructions. (a) For RMSD = 2.0 HU, the fewest iterations required for SQS was $M=66, N=140$ and (b) for Nes was $M=18, N=15$. (Note the different x-axis scaling.) If better convergence (e.g., RMSD < 1 HU) is required, Nes exhibits an even greater reduction in iterations relative to SQS. (c) Reference volume μ^* and circular region used for RMSD evaluation annotated in yellow. The SQS and Nes difference images [(d) and (e), respectively] show residual high frequency structure at edges and residual streaks at the posterior of the skull arising from the incomplete orbit (178°).

B. Truncated Reconstructions of the Head

For the truncated C-arm projections, the AF followed a similar trend as the untruncated bench data, with Nes-11 providing a stable, monotonic increase in AF up to $345\times$ for 10^4 equivalent SQS-1 iterations. However, analysis of RMSD illustrated the challenge of truncated projections, particularly due to missing data outside the C-arm FOV and the slow convergence in those regions (Fig. 4). Both SQS and Nes were unable to achieve RMSD as low as their counterparts in the untruncated data, in large part due to

† The conversion in attenuation units from mm^{-1} to HU was made using the approximation: $0.02 \text{ mm}^{-1} = 1000 \text{ HU}$.

influence from the large errors outside the C-arm FOV (RMSD >180 HU outside the C-arm FOV). The algorithms therefore require more iterations even for a higher RMSD than in untruncated data, with SQS-33 achieving 4.0 HU RMSD in 197 iterations and Nes-11 in 21 iterations. Even so, Nes-11 provided a 9.4× reduction in the number of iterations required with SQS-33. Additionally, large M (e.g., SQS-66, Nes-22) resulted in unstable reconstructions and was susceptible to divergence from the optimal solution with too many iterations. Even moderate values of M for Nes exhibited some degree of divergent behavior, and improving stability is the subject of ongoing work.

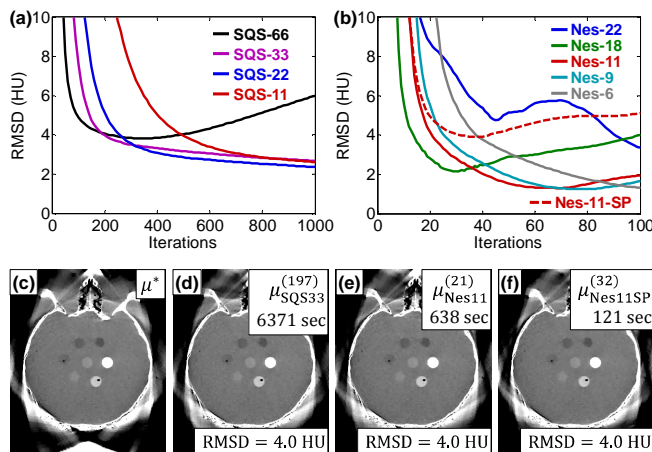


Fig. 4. Convergence and accuracy in truncated data. (a) SQS and (b) Nes reconstructions of truncated projections provided reconstructions with $\text{RMSD} < 4$ HU but were subject to divergence at a large number of iterations. (c) The converged solution μ^* shows a reasonably accurate reconstruction inside the C-arm FOV. An RMSD of 4.0 HU was achieved by (d) 197 iterations of SQS-33 in 6371 sec, (e) 21 iterations of Nes-11 in 638 sec, and (f) 32 iterations of Nes-11 with the simpler Siddon/Peters (SP) projectors in 121 sec. Display window [-400 400] HU.

While the above results all used the SF-TT projector, preliminary investigation with faster, less accurate projectors (e.g., ray-driven Siddon forward projector [11] and voxel-driven Peters backprojector [12], denoted SP) was also able to yield RMSD of 4.0 HU but required a greater number of iterations (32 iterations for Nes-11-SP) since the overall RMSD was increased due to the unmatched projectors. Nevertheless, the SP projectors may be useful if the benefit of increased speed outweighs the cost of additional iterations – e.g., in near-real-time CBCT for image-guided surgery.

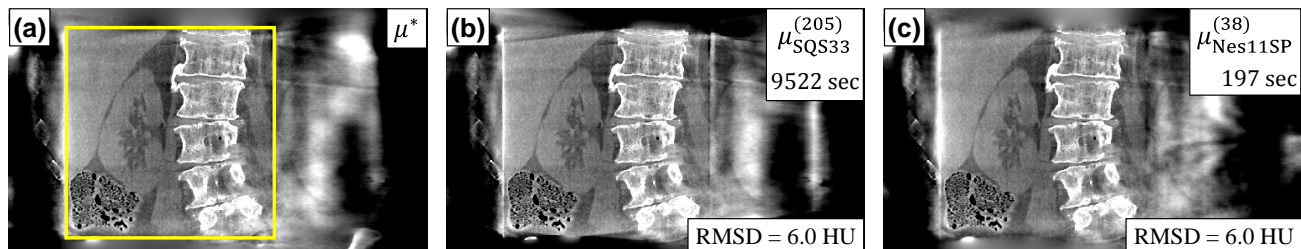


Fig. 5. Accelerated reconstruction of a cadaveric torso in CBCT-guided surgery. (a) Coronal slice of the reference reconstruction μ^* of a cadaveric torso. The reconstruction FOV encompassed the axial extent of the abdomen, while the C-arm FOV (outlined in yellow) covers the right kidney, liver, spine, and small pockets of gas in the bowels. (b) SQS-33 provided $\text{RMSD} = 6.0$ HU (measured in an ROI around the kidney) in 205 iterations (9522 sec), while (c) Nes-11-SP provided the same RMSD in 38 iterations (197 sec). Display window [-500 500] HU.

C. Reconstruction Time with GPU Implementation

Reconstruction times for C-arm CBCT were measured for the full head volume ($300 \times 360 \times 300$ voxels) on a PC workstation with a single GPU (EVGA GeForce GTX Titan Black Superclocked Signature). Relative to the SQS-11 time per iteration, SQS-33 added an additional 7.94% computational time cost (primarily due to regularizing and updating the volume for each subset), while Nes-11 only added 1.34% cost (Table I). Conversely, the faster SP projectors dramatically reduced the time per iteration by almost a factor of 8 since it is particularly well-suited for efficient parallel implementation. An RMSD of 4 HU could be accomplished in ~11 min for Nes-11 SF-TT, while the faster SP projectors allowed reconstruction in just over 2 min (121 sec). Therefore, Nesterov’s method (Nes-11) alone reduced reconstruction time by 10.0× over SQS (SQS-33), and faster projectors enabled an additional speedup of 5.3× over SF-TT with the same RMSD.

TABLE I. RECONSTRUCTION TIME FOR A FULL HEAD VOLUME ($300 \times 360 \times 300$ VOXELS) AT FIXED $\text{RMSD} = 4$ HU.

	SQS-11 SF-TT	SQS-33 SF-TT	Nes-11 SF-TT	Nes-11 SP
Time/Iter (sec)	29.96	32.34	30.36	3.79
Cost/Iter	—	+7.94%	+1.34%	-87.3%
Iterations	494	197	21	32
Total Time (sec)	14800	6371	638	121

D. Truncated Reconstructions of the Abdomen

The same analysis of SQS and Nes algorithms was performed in reconstructions of fully truncated C-arm projections of a cadaveric torso (Fig. 5). Because of the larger object size, the reconstructed volume was increased to $500 \times 350 \times 300$ voxels and a balance between reconstruction time and RMSD was found with SQS-33 providing 6.0 HU RMSD in 205 iterations (9522 sec), while Nes-11-SP was able to do so in only 38 iterations (197 sec = 3.3 min). Compared to the head reconstruction, the abdomen reconstruction required more iterations even for a higher RMSD due to the greater degree of truncation and missing data. However, the acceleration of Nes- M -SP relative to SQS- M was just as pronounced, with a 48.3× reduction in reconstruction time, demonstrating the applicability of the algorithm to objects with even more severe truncation.

IV. DISCUSSION AND CONCLUSION

Nesterov's method offers dramatic reduction in reconstruction time by accelerating convergence of the conventional ordered subset SQS algorithm. With faster Siddon-Peters type projectors, a GPU implementation of Nesterov-accelerated SQS was capable of providing a volumetric reconstruction of the head in ~2 minutes, despite the challenge of fully truncated C-arm CBCT projections, which leads to an ill-conditioned problem and slower convergence due to the large amount of missing data. Conventional FBP reconstruction is still faster than iterative reconstruction since by definition it requires only a single backprojection (cf., multiple forward/backprojections for IR). For example, FBP reconstruction of the head volume only required 19.3 sec [18.0 sec for filtering (implemented on GPU, but not yet fully optimized for run time) and 1.3 sec for backprojection]. Nonetheless, such reconstruction speed further facilitates incorporation of IR methods in image-guided interventions, with corresponding benefits to image quality and reduced radiation dose.

Ongoing work includes integration of other methods for addressing lateral truncation, e.g., a fit of projection data to an elliptical model of the volume. Using coarser voxels outside the C-arm FOV (i.e., a multi-resolution volume) could provide further acceleration, since accuracy outside the FOV is not as critical. Simultaneous use of multiple GPUs has been investigated to reduce forward and backprojection time for the SF-TT projector by distributing the projections within each subset among the GPUs, whereas the already fast SP projectors were unable to take advantage of multiple GPUs due to the overhead cost of transferring data between GPUs. For example, a GPU workstation with 3× GTX Titan's reduced the time per iteration of the head volume to 15.52 sec (2.1× reduction, cf. Table I) for Nes-11, but increased the time to 6.84 sec (1.8× increase) for Nes-11-SP. Future work includes derivation of a method for selecting M a priori to maximize acceleration and minimize instability for a given level of RMSD as well as incorporation of a convergence criterion for terminating the reconstruction at an appropriate number of iterations.

REFERENCES

- [1] D. Marin, R. C. Nelson, S. T. Schindera, S. Richard, R. S. Youngblood, T. T. Yoshizumi, and E. Samei, "Low-tube-voltage, high-tube-current multidetector abdominal CT: improved image quality and decreased radiation dose with adaptive statistical iterative reconstruction algorithm--initial clinical experience," *Radiology*, vol. 254, no. 1, pp. 145–153, 2010.
- [2] P. J. Pickhardt, M. G. Lubner, D. H. Kim, J. Tang, J. A. Ruma, A. M. del Rio, and G.-H. Chen, "Abdominal CT with model-based iterative reconstruction (MBIR): initial results of a prospective trial comparing ultralow-dose with standard-dose imaging," *Am. J. Roentgenol.*, vol. 199, no. 6, pp. 1266–1274, 2012.
- [3] A. S. Wang, J. W. Stayman, Y. Otake, G. Kleinszig, S. Vogt, G. L. Gallia, A. J. Khanna, and J. H. Siewerdsen, "Soft-tissue imaging with C-arm cone-beam CT using statistical

- reconstruction," *Phys. Med. Biol.*, vol. 59, no. 4, pp. 1005–1029, 2014.
- [4] A. I. Qureshi, A. D. Mendelow, and D. F. Hanley, "Intracerebral haemorrhage," *Lancet*, vol. 373, no. 9675, pp. 1632–1644, 2009.
- [5] L. Zrinzo, T. Foltynie, P. Limousin, and M. I. Hariz, "Reducing hemorrhagic complications in functional neurosurgery: a large case series and systematic literature review: Clinical article," *J. Neurosurg.*, vol. 116, no. 1, pp. 84–94, 2012.
- [6] D. Kim, S. Ramani, and J. A. Fessler, "Accelerating X-ray CT ordered subsets image reconstruction with Nesterov's first-order methods," in *Proc. Intl. Mtg. on Fully 3D Image Recon. in Rad. and Nuc. Med.*, 2013, pp. 22–25.
- [7] Y. Nesterov, "Smooth minimization of non-smooth functions," *Mathematical Programming*, vol. 103, pp. 127–152, 2005.
- [8] H. Erdogan, J. A. Fessler, and H. Erdoğan, "Ordered subsets algorithms for transmission tomography," *Phys. Med. Biol.*, vol. 2835, no. 11, pp. 2835–2851, 1999.
- [9] P. Tseng, "Approximation accuracy, gradient methods, and error bound for structured convex optimization," *Mathematical Programming*, vol. 125, pp. 263–295, 2010.
- [10] Y. Long, J. A. Fessler, and J. M. Balter, "3D forward and back-projection for X-ray CT using separable footprints," *Med. Imaging, IEEE Trans.*, vol. 29, no. 11, pp. 1839–1850, 2010.
- [11] R. L. Siddon, "Prism representation: a 3D ray-tracing algorithm for radiotherapy applications," *Phys. Med. Biol.*, vol. 30, no. 8, p. 817, 1985.
- [12] T. M. Peters, "Algorithms for fast back-and re-projection in computed tomography," *Nucl. Sci. IEEE Trans.*, vol. 28, no. 4, pp. 3641–3647, 1981.

Patient-bounded Extrapolation for 3D Region of Interest Reconstruction in C-arm CT

Yan Xia, Sebastian Bauer, Andreas Maier, Martin Berger, and Joachim Hornegger

Abstract—Three-dimensional (3D) region of interest (ROI) imaging with C-arm systems provides anatomical information in a predefined 3D target region at a considerably low X-ray dose. A necessary initial step prior to a 3D acquisition is to isocenter the patient with respect to the target to be scanned. To this end, two low-dose fluoroscopic X-ray acquisitions are usually applied from anterior-posterior (AP) and medio-lateral (ML) views. In this paper, we present a patient-bounded extrapolation method that makes use of these non-collimated fluoroscopic images to improve image quality in 3D ROI reconstruction. The algorithm first extracts the 2D patient contours from the AP and ML images. These 2D contours are then combined to estimate a volumetric model of the patient. Forward-projecting the shape of the model at the eventually acquired C-arm rotation views gives the patient boundary information in the projection domain. In this manner, we are in the position to substantially improve image quality by enforcing the extrapolated line profiles to end at the known patient boundaries, derived from the 3D shape model estimate. The proposed method is evaluated on five clinical datasets with different degrees of truncation. The proposed algorithm achieved a relative root mean square error (rRMSE) of 0.7% with respect to non-truncated data, even in the presence of severe truncation, compared to 8.7% from a state-of-the-art heuristic extrapolation.

I. INTRODUCTION

Three-dimensional (3D) C-arm based region of interest (ROI) tomography that provides anatomical information in a predefined target region at considerably low X-ray dose is a valuable tool in interventional radiology for therapy planning and guidance, particularly for neurointerventions. However, ROI imaging leads to laterally truncated projections from which conventional reconstruction algorithms generally yield images with severe truncation artifacts.

A major category of truncation correction methods is based on estimating the missing data using a heuristic extrapolation procedure, such as symmetric mirroring of projection images (Ohnesorge *et al.* [1]), water cylinder extrapolation (Hsieh *et al.* [2]), square root extrapolation (Soubelle *et al.* [3]) and hybrid extrapolation (Zellerhoff *et al.* [4]). Although these methods can be carried out without *a priori* information, they rely on heuristics. The degree of accuracy of these extrapolation estimates highly depends on the level of truncation.

Later, Maltz *et al.* [5] observed that the thickness of the patient could be estimated by calculating water-equivalent thicknesses, so that the unknown patient boundary can be

Y. Xia, M. Berger, A. Maier and J. Hornegger are with the Pattern Recognition Lab, Friedrich-Alexander-University Erlangen-Nuremberg, Germany. Y. Xia and J. Hornegger are also with the Erlangen Graduate School in Advanced Optical Technologies (SAOT), Germany. S. Bauer is with Siemens AG, Healthcare Sector, Germany.

Disclaimer: The concepts and information presented in this paper are based on research and are not commercially available.

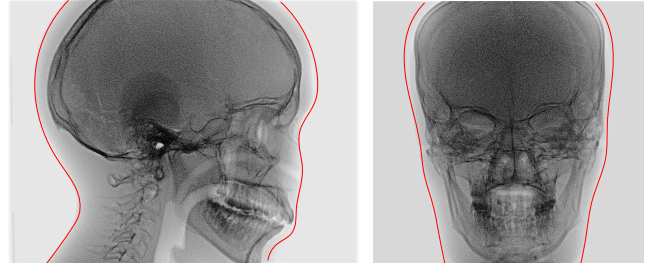


Fig. 1: Illustration of two short fluoroscopic X-ray pulses from ML view (left) and AP view (right), respectively. The red outlines indicate the extracted boundary information.

approximated. However, in practice, the presence of any non-water tissue may result in a substantial over- or underestimation of the actual object thickness.

In contrast, Wiegert *et al.* [6] and Kolditz *et al.* [7] suggested that patient size and shape information can be obtained from an *a priori* low-dose CT scan if available. By forward-projection of this *a priori* CT volume, the collimated regions in the ROI acquisition can be extended in an accurate manner.

In this paper, we present a patient-bounded extrapolation method that leads to major improvements in the quantitative accuracy of 3D ROI imaging, even in the presence of severely truncated data. The method does not require any additional hardware and can be readily integrated into the existing interventional workflow. It is based on the fact that prior to a 3D scan, low-dose fluoroscopic X-ray acquisitions are generally performed from anterior-posterior (AP) and medio-lateral (ML) views, to isocenter the patient with respect to the target to be scanned; see Fig. 1. The fundamental idea of the proposed method is to estimate a 3D shape model of the patient from these low-dose non-truncated fluoroscopic images and then exploit this patient-specific *a priori* shape knowledge for the extrapolation of truncated projections.

II. METHOD

First, we estimate the rough 3D patient shape based on two low-dose fluoroscopic projections, using per-slice ellipse fitting. The details are elaborated in the following sections; also see Fig. 2 for notations.

Contour-bounded Slice-wise Ellipse Fitting

To extract the boundaries, we first compute the gradient image of fluoroscopic projections and detect the edges using an empirically pre-set threshold. Suppose $\mathbf{u}_{lb}^{AP} = (u_{lb}^{AP}, v_i, 1)$, \mathbf{u}_{rb}^{AP} , \mathbf{u}_{lb}^{ML} , and \mathbf{u}_{rb}^{ML} are the homogeneous coordinates of the segmented left and right boundary points at detector row v_i of the 2D fluoroscopic images from AP and ML view. Let $\mathbf{P} \in$

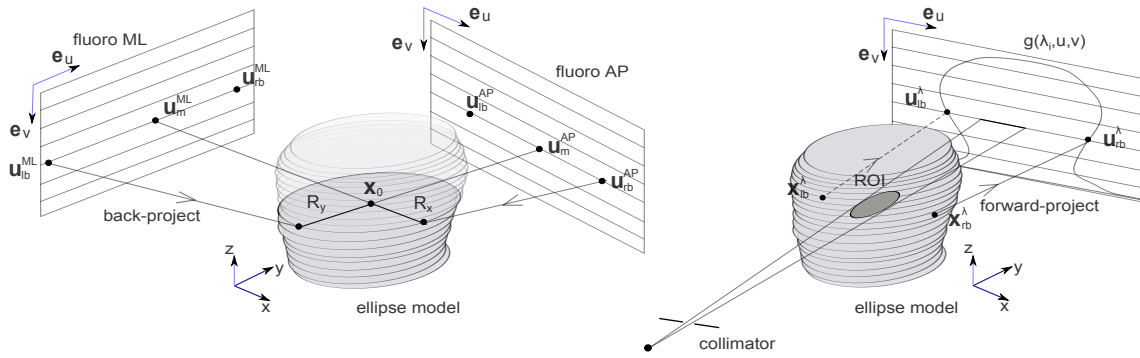


Fig. 2: Illustration of the patient-bounded extrapolation scheme. (Left) Contour-bounded slice-wise ellipse fitting. (Right) Forward-projection of the boundaries of the previously estimated patient shape model at a given C-arm rotation view provides the patient boundary in the projection domain.

$\mathbb{R}^{3 \times 4}$ be the projection matrix that maps position $\mathbf{x} = [x, y, z]$ in the C-arm coordinate frame to a position $\mathbf{u} = [\omega u, \omega v, \omega]$ in the 2D projection plane:

$$\mathbf{u} = \mathbf{P} \begin{bmatrix} \mathbf{x} \\ 1 \end{bmatrix}. \quad (1)$$

The matrix \mathbf{P} can be decomposed as follows:

$$\mathbf{P} = [\mathbf{P}_{13} \mid \mathbf{p}_4] = [\mathbf{AR} \mid \mathbf{At}] \quad (2)$$

where $\mathbf{R} \in \mathbb{R}^{3 \times 3}$ denotes the rotation matrix, $\mathbf{t} \in \mathbb{R}^3$ denotes the translation vector, and $\mathbf{A} \in \mathbb{R}^{3 \times 3}$ the intrinsic parameter matrix.

Then, we can compute the direction unit vector \mathbf{e}_m^{AP} , \mathbf{e}_m^{ML} of the ray that connects the source to the middle point of the two boundaries, i.e., $\mathbf{u}_m^{AP} = (\mathbf{u}_{lb}^{AP} + \mathbf{u}_{rb}^{AP})/2$ and $\mathbf{u}_m^{ML} = (\mathbf{u}_{lb}^{ML} + \mathbf{u}_{rb}^{ML})/2$, as:

$$\mathbf{e}_m^{AP} = \frac{(\mathbf{P}_{13}^{AP})^{-1} \mathbf{u}_m^{AP}}{\|(\mathbf{P}_{13}^{AP})^{-1} \mathbf{u}_m^{AP}\|_2}, \quad \mathbf{e}_m^{ML} = \frac{(\mathbf{P}_{13}^{ML})^{-1} \mathbf{u}_m^{ML}}{\|(\mathbf{P}_{13}^{ML})^{-1} \mathbf{u}_m^{ML}\|_2}, \quad (3)$$

where \mathbf{P}^{-1} denotes the pseudo-inverse of the matrix \mathbf{P} .

Now the ray equations can be expressed as ($t, l \in \mathbb{R}$)

$$\mathbf{l}_m^{AP}(t) = \mathbf{s}^{AP} + t\mathbf{e}_m^{AP}, \quad \text{and} \quad \mathbf{l}_m^{ML}(l) = \mathbf{s}^{ML} + l\mathbf{e}_m^{ML}, \quad (4)$$

where \mathbf{s}^{AP} and \mathbf{s}^{ML} are source positions at AP and ML views, which can be computed using $\mathbf{s} = -\mathbf{P}_{13}^{-1} \mathbf{p}_4$.

Then, the center of the fitted ellipse \mathbf{x}_0 is estimated by computing the intersection of the two rays \mathbf{l}_m^{AP} and \mathbf{l}_m^{ML} . Here, we confine to breaking the problem down to a 2D line intersecting based on the approximation that $\mathbf{s}^{AP} \mathbf{I}_z = \mathbf{s}^{ML} \mathbf{I}_z$ and $\mathbf{e}_m^{AP} \mathbf{I}_z = \mathbf{e}_m^{ML} \mathbf{I}_z = 0$, where $\mathbf{I}_z = [0 \ 0 \ 1]^T$. The third component of \mathbf{x}_0 is given by the corresponding slice position. To obtain the intersection point \mathbf{x}_0 , we establish $\mathbf{s}^{AP} + t\mathbf{e}_m^{AP} = \mathbf{s}^{ML} + l\mathbf{e}_m^{ML}$ and solve for t . Then, substituting t in the first equation of (4) yields:

$$\mathbf{x}_0 = \mathbf{s}^{AP} + \frac{\|(\mathbf{s}^{ML} - \mathbf{s}^{AP}) \times \mathbf{e}_m^{ML}\|_2}{\|\mathbf{e}_m^{AP} \times \mathbf{e}_m^{ML}\|_2} \mathbf{e}_m^{AP}. \quad (5)$$

Now we need to determine the radii R_x , R_y of the ellipse. The line equation of the rays from AP view that connects the patient boundary and source can also be expressed as (e.g. right boundary) $\mathbf{l}_r^{AP}(h) = \mathbf{s}^{AP} + h\mathbf{e}_r^{AP}$, where \mathbf{e}_r^{AP} is computed using \mathbf{u}_{rb}^{AP} accordingly. Suppose \mathbf{x}_r is the point

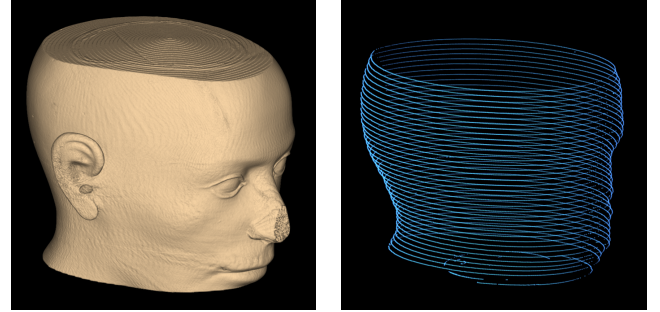


Fig. 3: Visualization of the actual patient shape extracted from a non-collimated 3D reconstruction (left) and the 3D volumetric model estimated from two orthogonal projections with different ellipses in each slice (right).

located on the line \mathbf{l}_r^{AP} that satisfies $\mathbf{x}_r \mathbf{I}_y = \mathbf{x}_0 \mathbf{I}_y$, i.e., with the same y -axis coordinate as \mathbf{x}_0 . Then, the radius along the x -axis R_x can be approximated as follows:

$$R_x = (\mathbf{x}_r - \mathbf{x}_0) \mathbf{I}_x \quad (6)$$

where $\mathbf{I}_x = [1 \ 0 \ 0]^T$ and $\mathbf{I}_y = [0 \ 1 \ 0]^T$.

In analogy, we can use the boundary from ML view to determine the radius of the ellipse along the y -axis R_y .

Patient Boundary Estimation for Arbitrary Angulations

With the estimated ellipse in the volumetric image domain, we can compute the left and right patient boundaries of that ellipse for any given C-arm rotation angle λ as follows:

$$\mathbf{x}_{lb}^\lambda = \mathbf{x}_0 - r\mathbf{e}_u, \quad (7)$$

$$\mathbf{x}_{rb}^\lambda = \mathbf{x}_0 + r\mathbf{e}_u, \quad (8)$$

where $r = \sqrt{(R_y \cos \lambda)^2 + (R_x \sin \lambda)^2}$ and \mathbf{e}_u denotes the unit vector in detector row direction.

Then, we forward-project these voxel positions to 2D projection plane using Eq. (1), also cf. Fig. 2:

$$\mathbf{u}_{lb}^\lambda = \mathbf{P}^\lambda \begin{bmatrix} \mathbf{x}_{lb}^\lambda \\ 1 \end{bmatrix}, \quad \text{and} \quad \mathbf{u}_{rb}^\lambda = \mathbf{P}^\lambda \begin{bmatrix} \mathbf{x}_{rb}^\lambda \\ 1 \end{bmatrix}. \quad (9)$$

The estimated patient left and right boundaries at the detector row v_i and rotation angle λ , i.e., (u_{lb}^λ, v_i) and (u_{rb}^λ, v_i) , can be easily obtained with $u_{lb}^\lambda = \mathbf{u}_{lb}^\lambda \mathbf{I}_x / \mathbf{u}_{lb}^\lambda \mathbf{I}_z$ and $u_{rb}^\lambda = \mathbf{u}_{rb}^\lambda \mathbf{I}_x / \mathbf{u}_{rb}^\lambda \mathbf{I}_z$.

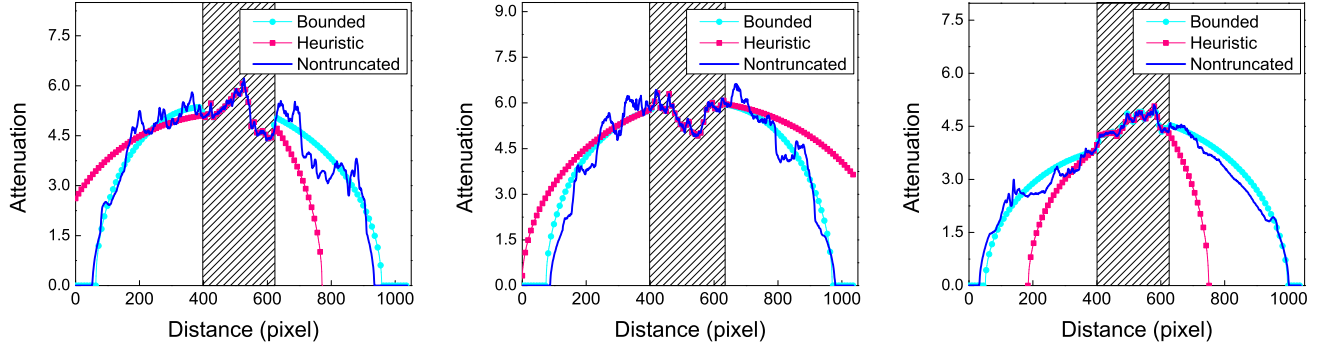


Fig. 4: Comparison of the non-bounded traditional extrapolation and patient-bounded extrapolation in a severe truncation case. Line profiles at projection views of $\lambda = -40^\circ$ (left), $\lambda = 20^\circ$ (middle) and $\lambda = 80^\circ$ (right). Note that the bounded ellipse parameters are estimated using two single projections from $\lambda = -90^\circ$ (ML) and $\lambda = 0^\circ$ (AP). Shaded regions indicate the measured part of projections in ROI scan.

Bounded ROI Projection Profile Extrapolation

Based on the estimated patient boundaries in the ROI scan projection data, we are in the position to apply any extrapolation technique and adapting it according to the restriction that the extrapolated profile must end at the known patient boundaries. In this paper, we adapt the water cylinder approach of Hsieh *et al.* [2] by extending or compressing the initial extrapolated lines to fulfill this restriction. Let $g(\lambda, u, v)$ be the projection data at the detector coordinates (u, v) acquired at angle λ . Then, the extrapolation function is given by

$$\tilde{g}_{\text{wat}}(\lambda, u, v) = 2\mu\sqrt{R^2 - \xi^2(u - u_w)^2} \quad (10)$$

where μ is the water attenuation coefficient, u_w is the location of the fitted cylinder with respect to the detector row and R is the radius. The parameters u_w and R are determined as described in [2].

In contrast to the formulation by Hsieh *et al.*, in Eq. (10) we introduce ξ that serves as a scaling factor to stretch or shrink the extrapolated profiles, which is computed as

$$\xi^2 = \frac{R}{u_b - u_w}, \quad (11)$$

where u_b indicates the left or right boundary (u_{lb} or u_{rb}) we obtained in the previous section.

Bounded Square Root Function Extrapolation

As an alternative, we also investigate the square root function extrapolation that was proposed by Sourbelle *et al.* [3]. The extrapolation function is given as

$$\tilde{g}_{\text{sqr}}(\lambda, u, v) = \sqrt{a \cdot u^2 + b \cdot u + c}. \quad (12)$$

To determine the parameters a , b , and c , the following continuity equations are used:

$$g(\lambda, u_t, v) = \sqrt{a \cdot u_t^2 + b \cdot u_t + c}, \quad (13)$$

$$g'(\lambda, u_t, v) = \frac{b + 2a \cdot u_t}{2g(\lambda, u_t, v)}, \quad (14)$$

where u_t denotes the truncated projection edge and $g'(\lambda, u_t, v)$ is the mean slope value over a small region.

We integrate the patient boundary information into (12) such that the extrapolated profile ends at u_b :

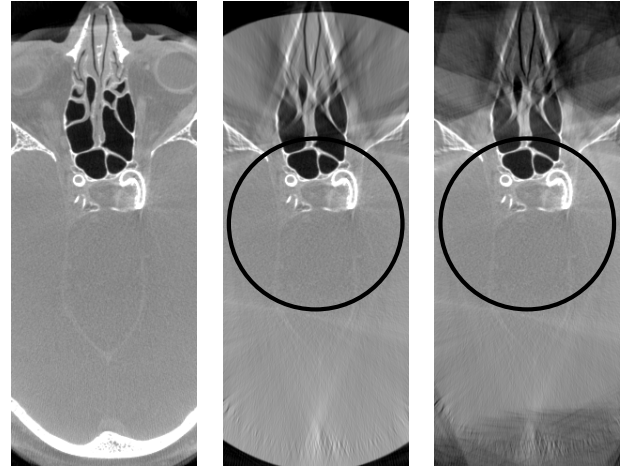


Fig. 5: Transversal slices of the clinical data 1 (medium truncation) reconstructed by FDK from non-truncated data (left), patient-bounded extrapolation (middle), and water cylinder extrapolation (right), in the grayscale window [-1000 HU, 1000 HU]. The black circles indicate the ROI.

$$g(\lambda, u_b, v) = \sqrt{a \cdot u_b^2 + b \cdot u_b + c} = 0. \quad (15)$$

Thus, the three parameters a , b , and c can be determined using these three equations. Note that for both patient bounded extrapolation schemes, we apply a cosine-based smooth weighting on the transition region.

III. EVALUATION

A. Experiment Setup

Five clinical datasets of the patients' head (data courtesy of St. Luke's Episcopal Hospital, Houston, TX, USA) were used to evaluate the proposed method. The datasets were acquired on a C-arm system with 496 projection images (1240×960 px) at the resolution of 0.308 mm/px. Even though a practical implementation would involve the extraction of the patient boundaries from low-dose fluoroscopic data, for proof of concept we here confined to extract the boundaries from two projections ($\lambda = -90^\circ$ and $\lambda = 0^\circ$) of a non-collimated 3D scan. All datasets were virtually cropped to a medium field of view (FOV) and a small FOV and were reconstructed onto a volume of 512^3 with an isotropic voxel size of 0.4 mm³. The

Table I: Quantitative evaluation of truncation corrections for different FOVs. Note that the given RMSE, rRMSE and CC are the average over all five datasets.

	Medium FOV			Small FOV		
	Water cylin. [2]	Bounded water cf. [2]	Bounded sqr. cf. [3]	Water cylin. [2]	Bounded water cf. [2]	Bounded sqr. cf. [3]
RMSE	96.4 HU	30.6 HU	56.1 HU	391.8 HU	43.8 HU	50.6 HU
rRMSE	2.21 %	0.71 %	1.21 %	8.77 %	0.96 %	1.12 %
CC	0.925	0.995	0.992	0.892	0.992	0.991

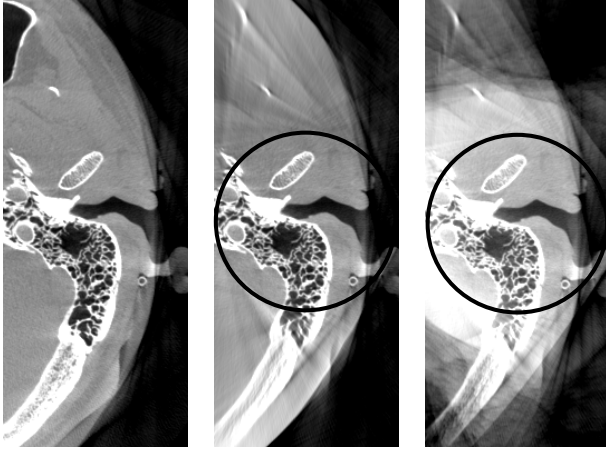


Fig. 6: Transversal slices of the clinical data 2 (off-centered ROI) reconstructed by FDK from non-truncated data (left), patient-bounded extrapolation (middle), and water cylinder extrapolation (right) [-1000 HU, 1000 HU].

original, non-bounded water cylinder extrapolation (Hsieh *et al.* [2]) was investigated as a baseline and compared to our proposed algorithm for the two schemes. To quantify image quality, three quantitative metrics were used: the root mean square error (RMSE), the relative root mean square error (rRMSE) (i.e., the RMSE divided by the total intensity range) and the correlation coefficient (CC).

B. Results

An example of the estimated ellipse model compared to the actual patient shape extracted from reconstruction is shown in Fig. 3. Figure 4 shows the comparison of the heuristic and proposed extrapolation in a severe truncation case. Reconstruction results from the dataset 1, 2, and 3 are presented in Fig. 5-7, respectively. The quantitative evaluation is summarized in Table I. We can see that the proposed method improves the image quality substantially, particularly for severely truncated data. This is due to the fact that non-bounded heuristic extrapolation can not accurately fit the data outside an ROI, while the proposed method yields a much better approximation; see Fig. 4. The reconstructions also show that the proposed method is robust to both severe truncation and off-centered ROIs. Quantitative accuracy is improved considerably: the average RMSE reached 43.8 HU in severe truncation, compared to 391.8 HU from the heuristic method. A relative error of less than 1% was achieved, yielding an error reduction by a factor of 8 compared the heuristic method.

IV. DISCUSSION

The method we proposed in this paper leads to a major improvement in image quality for 3D C-arm based ROI

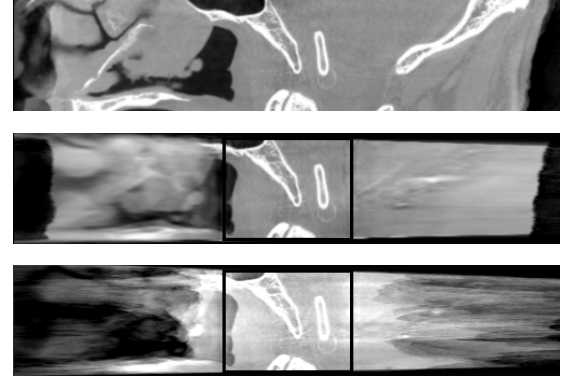


Fig. 7: Sagittal slices of the clinical data 3 (severe truncation) reconstructed by FDK from non-truncated data (top), patient bounded extrapolation (middle), and water cylinder extrapolation (bottom) [-1000 HU, 1000 HU].

imaging. It involves no additional radiation when using the fluoroscopic images, as they are acquired anyway during the patient isocentering process. The model estimation can be readily integrated into the existing interventional workflow without additional hardware. Furthermore, it is well-suited for neurointerventions since: 1) The ellipse is a good model for the head; 2) the low-dose fluoroscopic images are usually non-collimated and cover the entire object of interest. Regarding computation times, both slice-wise ellipse fitting and patient boundary estimation are computationally inexpensive since only the boundary points are involved with small vector/matrix multiplications. Due to their very low radiation dose, a sparse set of fluoroscopic images can be further acquired from different views. In this manner, the detailed patient shape could be estimated using some parametric models such as B-splines.

REFERENCES

- [1] B. Ohnesorge, T. Flohr, K. Schwarz, J. P. Heiken, and J. P. Bae, "Efficient correction for CT image artifacts caused by objects extending outside the scan field of view," *Medical Physics*, vol. 27, no. 1, pp. 39–46, 2000.
- [2] J. Hsieh, E. Chao, J. Thibault, B. Grekowitz, A. Horst, S. McOlash, and T. J. Myers, "A novel reconstruction algorithm to extend the CT scan field-of-view," *Medical Physics*, vol. 31, no. 9, pp. 2385–2391, 2004.
- [3] K. Sourbelle, M. Kachelriess, and W. A. Kalender, "Reconstruction from truncated projections in CT using adaptive detruncation," *European Radiology*, vol. 15, no. 5, pp. 1008–1014, 2005.
- [4] B. Zellerhoff, B. Scholz, E. P. Ruehrschopf, and T. Brunner, "Low contrast 3D-reconstruction from C-arm data," in *Proceedings of SPIE*, 2005, pp. 646–655.
- [5] J. D. Maltz, S. Bose, H. P. Shukla, and A. R. Bani-Hashemi, "CT truncation artifact removal using water-equivalent thicknesses derived from truncated projection data," in *IEEE Engineering in Medicine and Biology Society*, 2007, pp. 2905–2911.
- [6] J. Wiegert, M. Bertram, T. Netsch, J. Wulff, J. Weese, and G. Rose, "Projection extension for region of interest imaging in cone-beam CT," *Acad. Radiol.*, vol. 12, pp. 1010–23, 2005.
- [7] D. Kolditz, Y. Kyriakou, and W. A. Kalender, "Volume-of-interest (VOI) imaging in C-arm flat-detector CT for high image quality at reduced dose," *Medical Physics*, vol. 37, no. 6, pp. 2719–2730, 2010.

Catheter Artifact Reduction (CAR) in Dynamic Cardiac Chamber Imaging with Interventional C-arm CT

Kerstin Müller, Günter Lauritsch, Chris Schwemmer, Andreas K. Maier, Oliver Taubmann,
Bernd Abt, Henning Köhler, Alois Nöttling, Joachim Hornegger and Rebecca Fahrig

Abstract—A C-arm CT system offers the possibility to acquire 2-D high-resolution X-ray images of the patient from different views. These projections can be used for 3-D imaging. Anatomical three-dimensional imaging holds great potential to improve cardiac interventions. However, the image acquisition using a C-arm CT system takes several seconds. A standard FDK reconstruction using all acquired projection images results in a motion blurred image. In order to improve the temporal resolution, an electrocardiogram (ECG) is acquired synchronously with the acquisition and reconstruction is performed only with subsets of projection images, each belonging to a certain heart phase. This retrospective ECG-gating of data from a single C-arm rotation provides only a few projections per heart phase for image reconstruction. This view sparsity leads to prominent streak artifacts and a poor signal-to-noise ratio. Therefore, motion estimation and correction are required for the reconstruction of the cardiac chambers. We recently presented a deformable image registration approach which allows for motion estimation on the initial ECG-gated volumes using a specifically designed imaging protocol. In this paper, an additional step to improve the initial image quality is presented which removes dense objects, i.e. pacing electrodes or catheters, before the deformable 3-D/3-D registration step. The algorithm is evaluated quantitatively and qualitatively on a simulated phantom dataset. The relative root mean square error (rRMSE) was reduced by 27 % and the universal image quality index (UQI) improved by 13 % compared to the algorithm without removing the dense objects from the reconstructions. Finally, the presented algorithmic framework was applied to a first clinical patient dataset and the preliminary results are presented in this paper.

I. INTRODUCTION

In recent years, three-dimensional imaging has become more and more important in the field of cardiac imaging. However, most systems can only be used pre- or post-interventionally. Therefore, need for 3-D imaging directly in the catheter lab has become of major interest in the last years. Interventional 3-D imaging can be performed with an angiographic C-arm CT system already available in most catheter labs in order to perform 2-D fluoroscopic imaging. The 3-D C-arm CT image provides valuable information to the cardiologist directly inside the catheter lab, e.g. for minimally

K. Müller, C. Schwemmer, A. K. Maier, O. Taubmann, and J. Hornegger are with the Pattern Recognition Lab, Department of Computer Science and the Erlangen Graduate School in Advanced Optical Technologies (SAOT), Friedrich-Alexander-Universität Erlangen-Nürnberg, Erlangen, Germany. Email:kerstin.mueller@cs.fau.de. G. Lauritsch, C. Schwemmer and A. Nöttling are with the Siemens AG, Healthcare Sector, Forchheim, Germany. B. Abt and H. Köhler are with the Herz- und Kreislaufzentrum, Rotenburg an der Fulda, Germany. R. Fahrig is with the Department of Radiology, Stanford University, Stanford, CA, USA.

invasive valve procedures or device implantations [1]. For example, in [2], the 3-D reconstruction of the aortic root is used for guidance of a transcatheter aortic valve implantation (TAVI) by overlaying the 3-D reconstruction onto the fluoroscopic images during the deployment of the prosthesis, and for measuring critical anatomical parameters in 3-D image space.

Up to now, pre-operative three-dimensional echocardiographic volumes are used for wall motion analysis for cardiac resynchronization therapy (CRT) procedures in order to find the optimal lead position [3]. Three-dimensional C-arm reconstructions of the cardiac chambers in various heart states directly in the catheter lab would provide valuable information for the cardiologist during the CRT procedure.

For the reconstruction of a temporal sequence of 3-D cardiac images using a C-arm system, a specifically designed contrast and acquisition protocol for dynamic cardiac imaging is required [4]. Due to the design of the imaging protocol, multiple retrospectively ECG-gated reconstructions can be performed. The resulting volumes suffer from noise and streaking artifacts due to sparse view sampling. One possible solution to improve image quality is the use of all acquired projection data in combination with compensation for the cardiac motion in the reconstruction step. The cardiac motion can be estimated by registration of initial 3-D volumes of each heart phase to one reference heart phase. However, the quality of the initial images influences the accuracy of the estimated cardiac motion.

We already investigated different techniques to generate initial images for cardiac motion-estimation via deformable 3-D/3-D image registration [5]. In this paper, an additional catheter artifact removal (CAR) approach is presented to further improve the initial image quality before estimation of the cardiac motion. In our case, a contrast filled catheter and a pacing electrode are always present in the scanning field of view. The presented algorithm is applied to a simulated phantom dataset and to a first clinical patient dataset.

II. DYNAMIC CARDIAC IMAGING

In this section, the new initial image reconstruction method is described as well as the 3-D/3-D registration for cardiac motion estimation. With the estimated motion, a motion-compensated reconstruction is performed using all acquired projection images.

A. 3-D Initial Image Generation

The cardiac motion is estimated on initial 3-D volumes. The initial images are reconstructed by retrospective ECG-gating. A weighting function based on the relative heart phase is introduced into the standard FDK approach, which assigns to each image an impact weight on the reconstruction result. Here, a rectangular window is used. A total of K heart phase volumes can be reconstructed. The resulting reconstructions are denoted as FDK.

Catheter Artifact Removal (CAR): Strong undersampling artifacts are caused by high-density objects like the pigtail catheter or a pacing electrode. Therefore, these objects need to be removed from the 2-D projection images before the reconstruction. The high density objects are identified in the ECG-gated volumes to generate binary 3-D mask volumes for each heart phase. The segmentation process is restricted to a user-defined region of interest (ROI). A thresholding operation is applied with a threshold determined as the mean value inside the defined ROI. The segmented pixels are dilated by a circular object with a radius of 1 voxel. The resulting mask volumes are forward projected into the 2-D projection images which belong to the corresponding heart phase. The 2-D mask images combined with the log-transformed projection images are used for catheter removal. In this paper, a low-frequency-based object masking called Subtract-and-Shift (SaS) is used for the removal of the catheter in the 2-D projection images [6]. The algorithm makes use of the fact that many dense objects do not absorb all incident radiation. Therefore, some remaining anatomical structure is still available within the region overlaid by the object and should be used by an interpolation algorithm.

The resulting projection images are used for ECG-gated filtered backprojection reconstruction to provide volumes without catheters and electrodes. These reconstructions using the catheter removed projections are denoted as cathFDK.

B. Cardiac Motion Estimation

In order to estimate the cardiac motion, one heart phase needs to be chosen as reference phase. The corresponding volume is the reference volume and all other volumes are registered separately to the reference volume. The 3-D motion vector field is derived by optimizing an objective function $\mathcal{L}_{NCC}(\tilde{\mathbf{s}}_{\text{mm}})$, with the vector $\tilde{\mathbf{s}}_{\text{mm}} \in \mathbb{R}^{\tilde{K}_{\text{mm}}}$ denoting the motion model parameters between two heart phases, such that the negative normalized cross correlation (NCC) between the (catheter removed) ECG-gated volumes is minimized. The optimization is performed with an adaptive stochastic gradient descent optimizer. The motion is parameterized by cubic third-order B-splines with uniformly spaced control points $C_s \times C_s \times C_s$. Every control point has its own parameter vector, defining the number of motion model parameters as $\tilde{K}_{\text{mm}} = 3(C_s + 3)^3$. In order to estimate the cardiac motion over the whole scan, the optimization needs to be performed between all $K - 1$ heart phases, resulting in an overall motion vector dimension $K_{\text{mm}} = (K - 1) \tilde{K}_{\text{mm}}$. In this paper, a toolbox for nonrigid registration of medical images called `elastix` is used for the 3-D/3-D motion estimation [7]. A multi-resolution scheme of 4 levels is used with a sampling factor of 2 on each

pyramid level. At the highest image resolution a number of $C_s = 16$ control points are used in each spatial dimension.

C. Motion-compensated Reconstruction

The estimated motion vector field is incorporated into a voxel-driven filtered backprojection reconstruction algorithm which compensates for the motion [8]. The motion correction is applied during the backprojection step by shifting the voxel to be reconstructed according to the motion vector field.

Using no catheter removal for the initial volume reconstruction, the resulting motion-compensated reconstructed volumes are denoted as FDK-MC. When the CAR approach is used for the initial image reconstruction and motion estimation, but the motion-compensated reconstruction is performed with the original measured projection images, the reconstruction is denoted as cathFDK-MC. If the motion-compensated reconstruction utilizes the projection images without catheters and electrodes, the volumes are denoted as cathFDK-MC_i.

III. EXPERIMENTS

A. Phantom Model

A ventricle dataset [9], [10] of a similar design to the XCAT phantom [11] was created. The phantom dataset was simulated with a polychromatic X-ray spectrum. We used a source spectrum $E(b)$ with 36 energy bins from 10 keV to 90 keV, and a time-current product of 2.5 mAs per X-ray pulse. A catheter was simulated coming from the aorta into the left ventricle. The same deformation as for the heart was applied to the catheter. The material of the catheter is similar to copper in order to induce severe streak artifacts in the reconstructions. The material properties of the catheter, bones and the bone marrow have the were chosen according to the mass attenuation coefficients of the NIST X-Ray Table¹. All other structures are assumed to have the same absorption behavior as water with different densities similar to the FORBILD phantom². The density of the contrasted left ventricle bloodpool was set to 2.5 g/cm³, the density of the myocardial wall to 1.5 g/cm³ and the contrasted blood in the aorta to 2.0 g/cm³. Poisson distributed noise was added to the simulated projection stacks such that the noise characteristics of the reconstructed images fit those of the clinical data. As gold standard, static projection images of the phantom with a catheter were generated without noise. The phantom projection data and geometry are publicly available and can be downloaded from <https://conrad.stanford.edu/data/heart>.

The phantom dataset was simulated with similar parameters as used for clinical acquisitions of porcine models [5], [4]. The acquisition simulation was performed over 14.5 s capturing 381 projection images at an angular increment of 0.52° during one C-arm sweep. The isotropic pixel resolution was 0.31 mm/pixel (0.19 mm in isocenter) and the detector size 1240 × 960 pixels. The heart rate was set to 131 bpm. For the phantom dataset, a strict gating was performed, i.e. only one projection per heart cycle is used for reconstruction. A total of 32 heart cycles were acquired resulting in 12 reconstructed

¹<http://physics.nist.gov/PhysRefData/Xcom/html/xcom1.html>

²<http://www.imp.uni-erlangen.de/phantoms/thorax/thorax.htm>

Table I: The rRMSE and UQI of the dynamic phantom model with a catheter for all $K = 12$ heart phases as mean and standard deviation.

Method	rRMSE	UQI
FDK-MC	0.85 ± 0.34	0.84 ± 0.01
cathFDK-MC	0.62 ± 0.43	0.94 ± 0.01
cathFDK-MC _i	0.58 ± 0.52	0.97 ± 0.01

heart phases. Image reconstruction was performed on an image volume of $(25.6 \text{ cm})^3$ distributed on a 256^3 voxel grid.

B. Clinical Data

A clinical patient dataset acquisition was performed using an Artis zeego system (Siemens AG, Healthcare Sector, Forchheim, Germany). The acquisition time was 14 s capturing 381 projection images with 26 f/s at an angular increment of 0.52° during one C-arm rotation. The isotropic pixel resolution was 0.31 mm/pixel (0.19 mm in isocenter) and the detector size 1240×960 pixels. The heart rate was stimulated through external heart pacing to 115 bpm, which is lower than the frequency used for the phantom model (131 bpm). The width of the gating window was set to 10% of the heart cycle, resulting in ≈ 34 projections for the reconstruction of an initial image at a specific heart phase. For this dataset, 10 heart phase volumes were reconstructed at a phase increment of 10%. A volume of 91 ml undiluted contrast agent fluid was administered in the pulmonary artery at a speed of 7 ml/s beginning 13 s before the X-ray rotation was started. The X-ray delay was determined by a test bolus injection. Image reconstruction was performed on an image volume of $(25.6 \text{ cm})^3$ distributed on a 256^3 voxel grid.

IV. RESULTS AND DISCUSSION

A. Phantom Model

For the dynamic phantom data, the 3-D error and a quantitative 3-D image metric can be evaluated. The gold standard image of the non-gated FDK reconstruction using all projections of the static heart phantom of the same heart phase is shown in Fig. 1a. The error as well as the image quality metric were evaluated inside a volume of interest around the ventricle. The region of the catheter was also excluded from the evaluation, since the catheter motion was not in the focus of the cardiac chamber imaging. The relative root mean square error (rRMSE) was used to quantify the 3-D reconstruction error. The results were averaged over all heart phases, resulting in an overall rRMSE. As a 3-D image quality metric the universal image quality index (UQI) was computed [12]. The UQI ranges from -1 to 1 , with 1 as the best overlap between both reconstructions. All results were averaged over the heart phases, resulting in the overall UQI. Looking at the quantitative results in Table I, the cathFDK-MC_i and the cathFDK-MC outperform the FDK-MC reconstructions. For the cathFDK-MC_i, the rRMSE is reduced by 27% and the universal image quality index (UQI) improved by 13% compared to FDK-MC.

The reconstruction results for the phantom data are shown in Fig. 1 for a heart phase of 30%. The non-gated FDK

reconstruction suffers from motion blurring artifacts as can be seen in Fig. 1b. The catheter causes severe streak artifacts in the ECG-gated reconstructions (Fig. 1c). Motion compensation does not eliminate these streak artifacts since the motion estimation is disturbed by them (Fig. 1d). The cathFDK (Fig. 1e) shows less streak artifacts and consequently the corresponding motion compensated image shows a much better image quality (Fig. 1f). In Fig. 1g, the cathFDK-MC_i result is presented, only minor streaking artifacts are visible in the reconstruction. As a post-processing step, the segmented catheter can be added to the cathFDK-MC_i reconstruction (Fig. 1h).

B. Clinical Data

The reconstruction results for the clinical patient dataset are presented in Fig. 2 for a systolic and a diastolic heart phase. It can be seen that artifacts overlay small left ventricular structures in the systolic and diastolic ECG-gated FDK reconstructions (cf. Fig. 2a and 2b, indicated by the arrows). The image quality of the motion-compensated reconstructions using cathFDK-MC_i is improved considerably compared to the initial images (cf. Fig. 2c and 2d).

V. SUMMARY AND CONCLUSION

For cardiac image acquisition with a C-arm CT, it is necessary to include the cardiac motion in the reconstruction. In this paper, we have presented cardiac motion estimation from initial 3-D volume data sets with a deformable B-spline registration. If a dense object is present inside the scan field of view, the undersampled ECG-gated initial images suffer from streak artifacts which disturb the motion estimation. The shadow of the dense object has to be removed from the 2-D projection images as a preprocessing step before the reconstruction of the initial images. Using these volumes, motion is estimated with an improved accuracy. No further image enhancement and processing is needed. For motion-compensated reconstruction of sparse structures like the catheter, different algorithms can be used [13]. The phantom simulation study shows quantitatively the benefit of the proposed method. Clinical preliminary motion-compensated reconstructions of a patient dataset are promising.

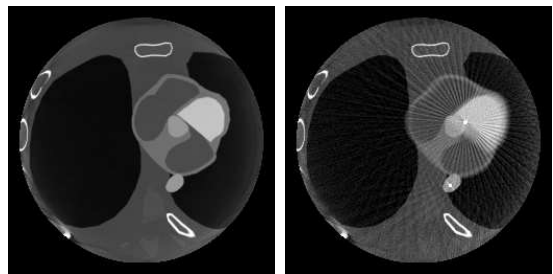
Disclaimer: The concepts and information presented in this paper are based on research and are not commercially available.

ACKNOWLEDGMENT

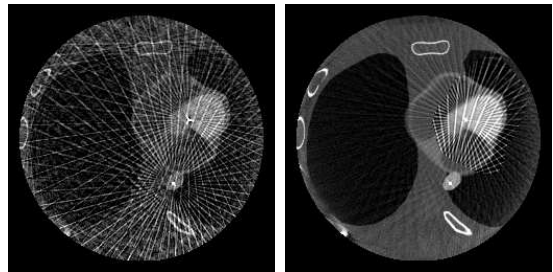
The authors gratefully acknowledge funding support from the NIH grant R01 HL087917 and of the Erlangen Graduate School in Advanced Optical Technologies (SAOT) by the German Research Foundation (DFG) in the framework of the German excellence initiative.

REFERENCES

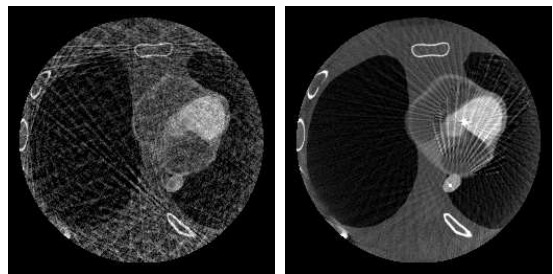
- [1] H. Hetterich, T. Redel, G. Lauritsch, C. Rohkohl, and J. Rieber, "New x-ray imaging modalities and their integration with intravascular imaging and interventions," *Int J Cardiovasc Imaging*, vol. 26, no. 7, pp. 797–808, October 2010.
- [2] M. John, R. Liao, Y. Zheng, A. Nötting, J. Boese, U. Kirschstein, J. Kempfert, and T. Walther, "System to guide transcatheter aortic valve implantations based on interventional C-arm CT imaging," in *MICCAI 2010*, vol. 6361, September 2010, pp. 375–382.



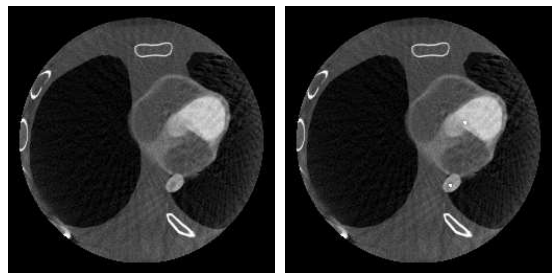
(a) Non-gated FDK of static phantom (b) Non-gated FDK of dynamic phantom



(c) FDK (32 views) (d) FDK-MC



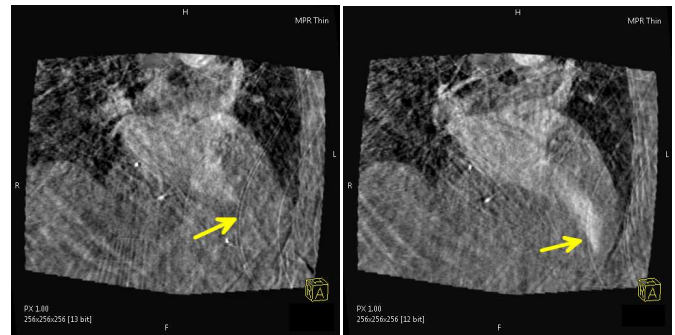
(e) cathFDK (32 views) (f) cathFDK-MC



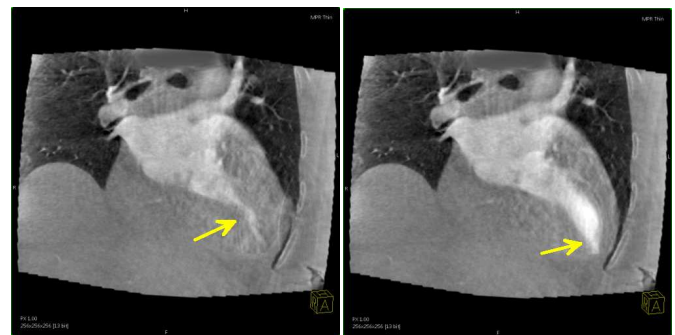
(g) cathFDK-MC_i (h) cathFDK-MC_i with added catheter

Figure 1: Central slice of initial volumes and motion-compensated reconstructions of the phantom model with a catheter and a relative heart phase of $\approx 30\%$ (W 3100 HU, C 780 HU, slice thickness 1 mm).

- [3] M. Döring, F. Braunschweig, C. Eitel, T. Gaspar, U. Wetzels, B. Nitsche, G. Hindricks, and C. Piorkowski, "Individually tailored left ventricular lead placement: lessons from multimodality integration between three-dimensional echocardiography and coronary sinus angiogram," *Europace*, vol. 15, no. 5, pp. 718–727, May 2013.
- [4] S. De Buck, D. Dauwe, J.-Y. Wielandts, P. Claus, C. Koehler, Y. Kyriakou, S. Janssens, H. Heidebuechel, and D. Nuyens, "A new approach for prospectively gated cardiac rotational angiography," in *Proceedings of SPIE Medical Imaging 2013*, vol. 8668, February 2013.



(a) FDK reconstruction of a systolic heart phase (34 views). (b) FDK reconstruction of a diastolic heart phase (34 views).



(c) cathFDK-MC_i of a systolic heart phase. (d) cathFDK-MC_i of a diastolic heart phase.

Figure 2: First results of a clinical patient dataset with the cathFDK-MC_i reconstruction of a systolic and diastolic heart phase (W 2080 HU, C 113 HU, slice thickness 1 mm).

- [5] K. Müller, C. Schwemmer, G. Lauritsch, C. Rohkohl, A. Maier, H. Heidebuechel, S. De Buck, D. Nuyens, Y. Kyriakou, C. Köhler, R. Fahrig, and J. Hornegger, "Image artifact influence on motion compensated tomographic reconstruction in cardiac C-arm CT," in *Proceedings of the Fully3D*, June 2013, pp. 98–101.
- [6] C. Schwemmer, M. Prümmer, V. Daum, and J. Hornegger, "High-density object removal from projection images using low-frequency-based object masking," in *Bildverarbeitung für die Medizin 2010 - Algorithmen - Systeme - Anwendungen*, March 2010, pp. 365–369.
- [7] S. Klein, M. Staring, K. Murphy, M. Viergever, and J. Pluim, "elastix: a toolbox for intensity based medical image registration," *IEEE Trans Med Imaging*, vol. 29, no. 1, pp. 196–205, 2010.
- [8] D. Schäfer, U.fer, J. Borgert, V. Rasche, and M. Grass, "Motion-Compensated and Gated Cone Beam Filtered Back-Projection for 3-D Rotational X-Ray Angiography," *IEEE Trans Med Imaging*, vol. 25, no. 7, pp. 898–906, July 2006.
- [9] A. Maier, H. Hofmann, M. Berger, P. Fischer, C. Schwemmer, H. Wu, K. Müller, J. Hornegger, J.-H. Choi, C. Riess, A. Keil, and R. Fahrig, "Conrad - a software framework for cone-beam imaging in radiology," *Med Phys*, vol. 40, no. 11, pp. 111914–1–8, November 2013.
- [10] K. Müller, A. Maier, P. Fischer, B. Bier, G. Lauritsch, C. Schwemmer, R. Fahrig, and J. Hornegger, "Left ventricular heart phantom for wall motion analysis," in *Proceedings of the IEEE NSS/MIC 2013*, October 2013.
- [11] W. Segars, M. Mahesh, T. Beck, E. Frey, and B. Tsui, "Realistic CT simulation using the 4D XCAT phantom," *Med Phys*, vol. 35, no. 8, pp. 3800–3808, August 2008.
- [12] Z. Wang and A. Bovik, "A universal image quality index," *IEEE Signal Proc Lett*, vol. 9, no. 3, pp. 81–84, March 2002.
- [13] C. Schwemmer, C. Rohkohl, G. Lauritsch, K. Müller, and J. Hornegger, "Residual Motion Compensation in ECG-Gated Interventional Cardiac Vasculature Reconstruction," *Phys Med Biol*, vol. 58, no. 11, pp. 3717–3737, June 2013.

Author Index

A

Abt, B	418
Aichert, A	333, 338
Alessio, A M	29, 99, 173
Allmendinger, T	68
Allner, S	388
Amaya, K	5
Andersen, M S	351
Aygun, N	401
Ayoub, M	117

B

Bartling, S	405
Bauer, S	178, 414
Behiels, G	295
Berger, M	178, 203, 274, 329, 333, 414
Bergner, F	95
Besson, G M	303
Bippus, R	95, 169
Brehm, M	117, 405
Bremer, T	149
Brendel, B	95, 169, 198
Bresler, Y	107
Brown, K M	372
Bruder, H	68, 376
Budde, A	307
Buzug, T M	233

C

Calzado, A.	153
Cammin, J	44, 161
Cant, J	295
Cantwell, B	117
Cao, G	216
Champley, K	149
Chen, B	186, 228
Chen, G-H	21, 283
Chen, L	212
Cho, S	397
Choi, J	397

Clackdoyle, R	249, 319, 324
Coban, S B	194
Cohen, A	220
Constantin, D	13
Cordes, A	233

D

Das, M	236
Davis, A	186
De Man, B	17, 52, 83, 99, 173, 307
Dennerlein, F	178, 338
Desbat, L	319, 324
Deuerling-Zheng, Y	333
Dittman, J	141
Do, S	125, 165
Doerfler, A	91, 333

E

Eck, B	372
Edic, P M	17, 52
Elshahaby, F	25
El Fakhri, G	393

F

Faby, S	117
Fahrig, R	13, 87, 91, 203, 274, 329, 418
Fehringer, A	198, 388
Fessler, J A	103, 291, 359
Firsching, M	141
FitzGerald, P	17, 173
Flach, B	368, 405
Flohr, T G	376, 384
Fuld, M K	25, 376
Fung, G S K	5, 25, 68, 376

G

Gac, N	212
Gagliardi, F	245
Gao, H	83, 220
Garrett, J	283
Ge, Y	283
Geleijns, J	153
Gifford, H C	236
Gilat-Schmidt, T	1, 71, 145, 208
Grass, M	169
Gregor, J	121

H

Hahn, D	198
Han, X	64, 186, 228, 299
Hell, E	75
Herbst, M	274
Hernandez-Giron, I	153
Herzen, J	287
Ho, H	182
Hornegger, J	56, 60, 87, 91, 178, 203, 274, 311, 329, 333, 414, 418
Hoskovec, J	324
Huelsbusch, M	75
Hunter, J F	253
Hsieh, J	216

I

Imai, Y	220
Ishwar, P	133
Ilovea, M	117

J

Jacques, L	191
Jin, Y	17, 83, 173
Joemai, R M S	153

K

Kabus, S	169
Kachelriess, M	75, 117, 368, 405
Kalra, M	165
Karl, W C	125, 133

Khawaja, R	165
Kim, C	397
Kim, D	103
Kim, K	393
Kim, S M	29, 99
Kinahan, P E	29, 99, 173
Kleinfeld, A	60
Kleinszig, G	409
Knaup, M	117
Koehler, H	418
Koehler, T	95, 198, 388
Kojima, S	241
Koliatsos, V	401
Kowarschik, M	33
Kueres, R	405
Kuntz, J	368, 405
Kusnoto, B	299

L

La Riviere, P J	9, 129
Lattimore, B M	253
Lauderbach, L	245
Lauritsch, G	60, 311, 418
Lee, J H	397
Lee, M	347
Levakhina, Y M	233
Li, K	21, 283
Li, Q	393
Li, X	157
Liang, Z	236
Lionheart, W R B	194, 355
Liu, R	261
Liu, X	186

M

Maass, N	87, 333, 338
Maier, A K	87, 91, 178, 203, 274, 329, 333, 338, 414, 418
Maier, J	368
Manhart, M	91, 333
Marschner, M	287
Martin, L	133
McGaffin, M G	359
McNitt-Gray, M F	265
Miao, C	257

Miller, E L	137	Reims, N	141
Mistretta, C A	48	Rigie, D S	9
Montillo, A	52	Rit, S	249, 324
Mory, C	191	Rodet, T	212
Mou, X	79	Rohkohl, C	33, 60, 68
Mueller, K	60, 418	Rose, S	351
Muenzel, D	95	Royalty, K	33
		Rui, X	173

N

Nakada, K	5
Nett, B E	182
Nien, H	291
Noel, P B	95, 198, 287, 388
Noettling, A	418
Noo, F	56, 279, 311

O

Oktay, M B	279
Oeckl, S	315
Otake, Y	409
Overturf, G	245

P

Pack, J D	83, 182, 307
Padole, A	165
Pal, D	343
Palenstijn, W J	295
Pan, X	1, 64, 186, 224, 228, 299, 351
Park, M	397
Parker, L	116
Pearson, E	64, 228
Pelizzari, C A	64
Perlmutter, D S	29, 99
Pfeiffer, F	198, 287, 388
Pfister, L	107
Pohlmann, M	203
Powell, K	117
Pourjabbar, S	165

R

Radley, I	117
Raupach, R	270

S

Samei, E	17
Sanchez, A A	224
Sawall, S	75, 368
Schebesch, F	274
Schmitt, K	56
Schoen, T	141
Schoendube, H	56, 270, 384
Schueller, S	75, 368
Schwemmer, C	60, 418
Segars, W P	376
Sidky, E Y	1, 64, 186, 224, 228, 299, 351
Siewerdsen, J H	111, 363, 401, 409
Sijbers, J	295
Singh, S	165
Sisniega, A	401
Stannigel, K	75
Star-Lack, J	13
Stayman, J W	111, 363, 401, 409
Stierstorfer, K	56, 68, 270, 376
Sukowski, F	141
Sung, Y	397
Sunnegardh, J	384
Szczykutowicz, T P	33, 48

T

Taubmann, O	418
Taguchi, K	5, 44, 161, 376
Tang, J	21
Tang, Q	161
Tang, S	380
Tang, X	380
Thibault, J-B	99, 343
Thompson, W M	355
Tian, X	17
Tilley II, S	111, 363

Tracey, B H 137
Tsui, B M W 25, 376

U

Ulrici, J 75
Unser, M 347

V

Van Buuren, T 245
Vargas, P 129
Veldkamp, W J H 153
Vogt, S 409

W

Wang, A S 409
Wang, G 79
Wang, W 380
Wang, X 157
Ward, J P 253, 347
Ward, W C 253
Wiedmann, U 83
Willey, T M 245
Willner, M 287, 388
Wu, Me 13, 87
Wu, Mi 17

X

Xia, Y 178, 329, 414
Xu, J 25
Xu, S 343

Y

Yamakawa, K 241
Yang, Q 87
Yao, Y 52
Ye, J C 347, 393
Yin, Z 17, 52, 307
Young, S 265
Yorkston, J 401
Yu, H 79, 257, 261
Yu, Z 311

Z

Zabic, S 372
Zbijewski, W 401
Zeng, G L 37
Zeng, K 307
Zhang, Y 79
Zhang, Z 186, 228, 299
Zimmerman, K C 71, 208
Zou, Y 157

